C55.612:977/v.1

Collected Reprints 1977

Atlantic Oceanographic and Meteorological Laboratories

Volume I



June 1978

U.S. DEPARTMENT OF COMMERCE
National Oceanic and Atmospheric Administration

Collected Reprints 1977

Atlantic Oceanographic and Meteorological Laboratories
Miami, Florida 33149

Volume I

June 1978

Boulder, Colorado

U.S. DEPARTMENT OF COMMERCE
Juanita M. Kreps, Secretary

National Oceanic and Atmospheric Administration
Richard A. Frank, Administrator

Environmental Research Laboratories
Wilmot Hess, Director

U. S. Depository Copy

FORWARD

This is the eleventh consecutive year in which the Collected Reprints of NOAA's Atlantic Oceanographic and Meteorological Laboratories have been published for distribution to the libraries of scientific institutions here and abroad. The series provides a single reference source for articles by AOML personnel that have appeared in a broad spectrum of scientific and technical publications.

The Atlantic Oceanographic and Meteorological Laboratories conduct research programs in the areas of physical, chemical, and geological oceanography, sea-air interaction, and marine acoustics. The 1977 edition presents the papers published in that year plus a few that were published in 1976 but were not available for inclusion in that year's volume. The papers are arranged in alphabetical order by first author within each of five groups:

Office of the Director
Physical Oceanography Laboratory
Marine Geology and Geophysics Laboratory
Sea-Air Interaction Laboratory
Ocean Chemistry Laboratory

It is hoped that those recipients with whom we do not already have an exchange arrangement would add the AOML Library to the distribution list for any relevant publications from their institution.

Harris B. Stewart, Jr.
Director
Atlantic Oceanographic
and Meteorological
Laboratories
15 Rickenbacker Causeway
Virginia Key, Florida 33149

CONTENTS

VOLUME I

OFFICE OF THE DIRECTOR

Page

1. Stewart, H. B.

   And Now, IOCARIBE: Carribbean Cooperation: It Works. NOAA Magazine 7, No. 1, 36-38. 1

PHYSICAL OCEANOGRAPHY LABORATORY

2. Beardsley, R.C., H. Mofjeld, M. Wimbush, C.N. Flagg, and J.A. Vermersch, Jr.

   Ocean Tides and Weather-Induced Bottom Pressure Fluctuations in the Middle-Atlantic Bight. Journal of Geophysical Research 82, No. 21, 3175-3182. 4

3. Behringer, D.W., R.L. Molinari, and J.F. Festa.

   The Variability of Anticyclonic Current Patterns in the Gulf of Mexico. Journal of Geophysical Research 82, No. 34, 5469-5476. 12

4. Bush, P.A.

   Bathymetry of the MODE-I Region. Deep Sea Research 23, 1105-1113. (Charts omitted.) 20

5. Chew, F.

   The Advection Effect of Planetary Vorticity on Sea Level Slope in a Western Boundary Current. Marine Geodesy 1, No. 1, 103-116. 35

6. Culverhouse, B.

   Self-Contained Digital Tide Measurement System. NOAA Technical Memorandum ERL AOML-24, 47 pages. 49

7. Festa, J.F.

   Book Review: Physical Oceanography of Estuaries (and Associated Coastal Waters). Bulletin of the American Meteorological Society 58, No. 2, 179-180. 96

Page

8. Hansen, D.V.

A Lagrangian Buoy Experiment in the Sargasso Sea. American Institute of Aeronautics and Astronautics, Technical Committee on Marine Systems and Technologies, Drift Buoy Symposium, Hampton, Virginia, May 22-23, 1976. NASA CP-2003, Session C, Simulation, Sensors, and Data (Dr. Donald Hansen, Chairman) 173-192. 97

9. Hazelworth, J.B.

Oceanographic Variations Across the Gulf Stream Off Charleston, South Carolina, During 1965 and 1966. NOAA Technical Report ERL 383-AOML 25, 73 pages. 116

10. Hazelworth, J.B., S.R. Cummings, S.M. Minton, and G.A. Berberian.

MESA New York Bight Project, Expanded Water Column Characterization Cruise (XWCC 11) NOAA Ship RESEARCHER, September 1976. NOAA Data Report ERL MESA-29, 192 pages.* 192

11. Hazelworth, J.B., S.R. Cummings, R.B. Starr, and G.A. Berberian.

MESA New York Bight Project, Expanded Water Column Characterization Cruise (XWCC 8) NOAA Ship GEORGE B. KELEZ, April 1976. NOAA Data Report ERL MESA-27, 111 pages.* 211

12. Herman, A., and C. Cardwell.

Computer Programs for Simple Lagrangian Processing (SLAP), Users' Guide. NOAA Technical Memorandum ERL AOML-28, 110 pages. 225

13. Herman, A. and D.V. Hansen.

Objective Analysis of Lagrangian Trajectory Data. Proceedings of the American Congress on Surveying and Mapping, 37th Annual Meeting. Washington, D.C., February 27-March 5, 1977, 177-185. 335

* Text only; complete data available from the authors or National Technical Information Service (NTIS).

Page

14. Lee, T.N. and D.A. Mayer.

Low-Frequency Current Variability and Spin-Off Eddies Along the Shelf Off Southeast Florida. Journal of Marine Research 35, No. 1, 193-220. 344

15. Leetmaa, A.

Book Review: Physical Oceanography of Estuaries (and Associated Waters). Limnology and Oceanography 22, No. 5, 975. 372

16. Leetmaa, A.

Effects of the Winter of 1976-1977 on the Northwestern Sargasso Sea. Science 198, No. 4313, 188-189. 373

17. Leetmaa, A.

Observations of Large-Scale Depth Perturbations of the Main Thermocline. Journal of Physical Oceanography 7, No. 5, 746-748. 375

18. Leetmaa, A.

A Study of MODE Dynamics. Deep-Sea Research 24, 733-742. 378

19. Leetmaa, A., P. Niiler, and H. Stommel.

Does the Sverdrup Relation Account for the Mid-Atlantic Circulation? Journal of Marine Research 35, No. 1, 1-10. 388

20. Maul, G.A.

The Annual Cycle of the Gulf Loop Current-Part I: Observations During a One-Year Time Series. Journal of Marine Research 35, No. 1, 29-47. 398

21. Maul, G.A.

Recent Progress in the Remote Sensing of Ocean Surface Currents. Marine Technology Society Journal 11, No. 1, 5-13. 417

22. Maul, G.A.

Variability in the Gulf Stream System. Gulfstream 11, No. 10, 2-7. 426

Page

23. Maul, G.A. and M. McCaslin.

An Assessment of the Potential Contributions to Oceanography From Skylab Visual Observations and Handheld-Camera Photographs. SKYLAB Explores the Earth, NASA SP 380, 339-352. 432

24. Mofjeld, H.O. and M. Wimbush.

Bottom Pressure Observations in the Gulf of Mexico and Caribbean Sea. Deep-Sea Research 24, 987-1004. 446

25. Molinari, R.L.

Synoptic and Mean Monthly 20°C Topographies in the Eastern Gulf of Mexico. NOAA Technical Memorandum ERL AOML-27, 33 pages. 464

26. Molinari, R.L. and A.D. Kirwan, Jr.

Calculations of Differential Kinematic Properties From Lagrangian Observations. American Institute of Aeronautics and Astronautics, Technical Committee on Marine Systems and Technologies, Drift Buoy Symposium, Hampton, Virginia, May 22-23, 1976. NASA CO-2003, 193-209. 499

27. Molinari, R.L. and R.E. Yager.

Upper Layer Hydrographic Conditions at the Yucatan Strait During May, 1972. Journal of Marine Research 35, No. 1, 11-20. 516

28. Molinari, R.L., S. Baig, D.W. Behringer, G.A. Maul, and R. Legeckis.

Winter Intrusions of the Loop Current. Science 198, 505-507. 526

29. Starr, R.B., J.B. Hazelworth, S.R. Cummings, G.A. Berberian.

MESA New York Bight Project Expanded Water Column Characterization Cruise (XWCC 10) NOAA Ship GEORGE B. KELEZ, 28 June-1 July 1976. NOAA Data Report ERL MESA-28, 93 pages.* 529

* Text only; complete data available from the authors or National Technical Information Service (NTIS).

Page

OCEAN CHEMISTRY LABORATORY

30. Atwood, D.K.

Regional Oceanography as it Relates to Present and Future Pollution Problems and Living Resources - Caribbean. Proceedings of IOC/FAO/UNEP International Workshop on Marine Pollution in the Caribbean and Adjacent Regions, Port-of-Spain, Trinidad, 13-18 December 1976. Workshop Report No. 11, 47-79. 539

31. Cantillo, A.Y. and D.A. Segar.

Metal Species Identification in the Environment a Major Challenge for The Analyst. Symposium Volume of the International Conference on Heavy Metals in the Environment, Toronto, Canada, 1977, 183-204. 572

32. Hatcher, P.G. and L.E. Keister.

Carbohydrates and Organic Carbon in New York Bight Sediments as Possible Indicators of Sewage Contamination. Middle Atlantic Continental Shelf and the New York Bight, Special Symposia 2, 1976, M.G. Gross, ed. (the American Society of Limnology and Oceanography, Inc.) 240-248. 594

33. Hatcher, P.G. and D.A. Segar.

Chemistry and Continental Margin Sedimentation. Marine Sediment Transport and Environmental Management, D.J. Stanley and D.J.P. Swift, eds. (John Wiley & Son, Inc.). Chapter 19, 461-477. 603

34. Hatcher, P.G., L.E. Keister, and P.A. McGillivary.

Steroids as Sewage Specific Indicators in New York Bight Sediments. Bulletin of Environmental Contamination and Toxicology 17, No. 4, 491-498. 620

35. Segar, D.A. and G.A. Berberian.

Oxygen Depletion in the New York Bight Apex: Causes and Consequences. Middle Atlantic Continental Shelf and the New York Bight, Special Symposia 2, 1976, M.G. Gross, ed. (the American Society of Limnology and Oceanography, Inc.) 220-239. 628

Page

36. Segar, D.A. and A.Y. Cantillo.

Trace Metals in the New York Bight. Middle Atlantic Continental Shelf and the New York Bight, Special Symposia 2, 1976, M.G. Gross, ed. (the American Society of Limnology and Oceanography, Inc.) 171-198. 648

VOLUME II

MARINE GEOLOGY AND GEOPHYSICS LABORATORY

37. Bennett, R.H.

Pore-Water Pressure Measurements: Mississippi Delta Submarine Sediments. Marine Geotechnology 2, 177-189. 677

38. Bennett, R.H. and J.R. Faris.

AOML Pore Pressure Measurements. Ocean Engineering Technical Bulletin (NDBO) 3, No. 4, p. 3. 690

39. Bennett, R.H., W.R. Bryant, and G.H. Keller.

Clay Fabric and Geotechnical Properties of Selected Submarine Sediment Cores From the Mississippi Delta. NOAA Professional Paper 9, 94 pages. (Pocket insert omitted.) 691

40. Bennett, R.H., D.N. Lambert, and M.H. Hulbert.

Geotechnical Properties of a Submarine Slide Area on the U.S. Continental Slope Northeast of Wilmington Canyon. Marine Geotechnology 2, 245-261. 785

41. Clark, T.L.

FET Pair and Op Amp Linearize Voltage-Controlled Resistor. Electronics 50, No. 9, 111-112. 803

42. Dietz, R.S.

Plate Tectonics: A Revolution in Geology and Geophysics. Tectonophysics 38, 1-6. 805

Page

43. Freeland, G.L. and G.F. Merrill.

The 1973 Bathymetric Survey in the New York Bight Apex: Maps and Geological Implications. NOAA Technical Memorandum ERL MESA-19, 22 pages. 811

44. Freeland, G.L., D.J.P. Swift, W.L. Stubblefield, and A.E. Cok.

Surficial Sediments of the NOAA-MESA Study Areas in the New York Bight. Middle Atlantic Continental Shelf and the New York Bight, Special Symposia 2, 1976, M.G. Gross, ed. (the American Society of Limnology and Oceanography, Inc.) 90-101. 833

45. Goldsmith, V., G.L. Shideler, J.F. McHone, and D.J.P. Swift.

Beach Response in the Vicinity of a Shoreface Ridge System: False Cape, Virginia. Virginia Institute of Marine Science, SRAMSOE, No. 143, June 10-11, 1977, 23-1 - 23-17. 845

46. Hunt, R.E., D.J.P. Swift, and H. Palmer.

Constructional Shelf Topography, Diamond Shoals, North Carolina. Geological Society of American Bulletin 88, 299-311. 862

47. McGregor, B.A.

Geophysical Assessment of Submarine Slide Northeast of Wilmington Canyon. Marine Geotechnology 2, 229-244. 875

48. McGregor, B.A. and R.H. Bennett.

Continental Slope Sediment Instability Northeast of Wilmington Canyon. American Association of Petroleum Geologists Bulletin 61, No. 6, 918-928. 891

49. McGregor, B.A., C.G.A. Harrison, J.W. Lavelle, and P.A. Rona.

Magnetic Anomaly Patterns on Mid-Atlantic Ridge Crest at 26°N. Journal of Geophysical Research 82, No. 2, 231-238. 902

50. Nelsen, T.A., D.A. Mayer, P.G. Hatcher, and W.N. Hess.

New England Offshore Mining Environmental Study: The Character of Particle Dispersion and Water Movement in Massachusetts Bay and Adjacent Waters. Estuarine and Coastal Marine Science 5, 455-465. 910

Page

51. Neumann, A.C., J.W. Kofoed, and G.H. Keller.

Lithoherms in the Straits of Florida, Geology 5, No. 1, 4-10. 921

52. Rona, P.A.

Paleobathymetry of the Crest of Spreading Ridges Related to the Age of Ocean Basins - Comment. Earth and Planetary Science Letters, 35, No. 3, 454-456. 928

53. Rona, P.A.

Plate Tectonics, Energy and Mineral Resources: Basic Research Leading to Payoff. EOS 58, No. 8, 629-639. 931

54. Rona, P.A.

Reply to A.A. Archer's "Comments on 'Plate Tectonics and Mineral Exploration' by P.A. Rona." Natural Resources Forum 1, 196-197. 942

55. Stubblefield, W.L., R.W. Permenter, and D.J.P. Swift.

Time and Space Variation in the Surficial Sediments of the New York Bight Apex. Estuarine and Coastal Marine Science 5, 597-607. 944

56. Swift, D.J.P.

Shelf-Sediment Dynamics. Geotimes 2, No. 6, 19-20. 963

57. Swift, D.J.P., G.L. Freeland, P.E. Gadd, G. Han, J.W. Lavelle, and W.L. Stubblefield.

Morphologic Evolution and Coastal Sand Transport, New York - New Jersey Shelf. Middle Atlantic Continental Shelf and the New York Bight, Special Symposia 2, 1976, M.G. Gross, ed. (the American Society of Limnology and Oceanography, Inc.) 69-89. 965

58. Swift, D.J.P., T. Nelsen, J. McHone, B. Holliday, H. Palmer, and G. Shideler.

Holocene Evolution of the Inner Shelf of Southern Virginia. Journal of Sedimentary Petrology 47, No. 4, 1454-1474. 986

Page

59. Turekian, K.K. and P.A. Rona.

Eastern Atlantic Fracture Zones as Potential Disposal Sites for Radioactive Waste. Environmental Geology 2, 59-62. 1007

60. Young, R.A.

Seaflume: A Device for In-Situ Studies of Threshold Erosion Velocity and Erosional Behavior of Undisturbed Marine Muds. Marine Geology 23, M-11 - M-18. 1011

SEA-AIR INTERACTION LABORATORY

61. Cardone, V.J., D.B. Ross, and M.R. Ahrens.

An Experiment in Forecasting Hurricane Generated Sea States. Proceedings 11th Technical Conference on Hurricanes and Tropical Meteorology of the American Meteorological Society, Miami Beach, Florida, December 13-16, 1977, 688-695. 1019

62. Cardone, V.J., D. Ross, M. Ahrens, J.A. Greenwood, C. Greenwood, and R. Salfi.

Forecasting Hurricane Winds and Waves: A Pilot Study. Final Report to: NOAA Sea-Air Interaction Laboratory and Shell Development Company, December 1976, 45 pages (Abstract only). 1027

63. Hasselmann, K., D.B. Ross, P. Muller, and W. Sell.

Reply to "Comments on 'A Parametric Wave Prediction Model'", by Willard J. Pierson. Journal of Physical Oceanography 7, No. 1, 134-137. 1028

64. Johnson, R.W., I.W. Duedall, R.M. Glasgow, J.R. Proni, and T.A. Nelson.

Quantitative Mapping of Suspended Solids in Wastewater Sludge Plumes in the New York Bight Apex. Journal Water Pollution Control Federation, 2063-2073. 1032

Page

65. Newman, F.C., J.R. Proni, and D.J. Walter.

Acoustic Imaging of the New England Shelf-Slope Water Mass Interfaces. Nature 269, No. 5631, 790-791. 1043

66. Ostapoff, F., S. Worthem, W. Everard.

Surface Meteorological Observations on R/V COLUMBUS ISELIN During Phase III of GATE. NOAA Technical Memorandum ERL AOML-25, 129 pages. 1045

67. Thacker, W.C.

A Spliced Numerical Grid Having Applications to Storm Surge. NOAA Technical Memorandum ERL AOML-26, 22 pages. 1174

68. Thacker, W.C.

A Transformation Relating Temporal and Spatial Spectra of Turbulent Kinetic Energy. NOAA Technical Report ERL 385-AOML 26, 10 pages. 1196

69. Thacker, W.C.

Irregular Grid Finite-Difference Techniques: Simulations of Oscillations in Shallow Circular Basins. Journal of Physical Oceanography 7, No. 2, 284-292. 1206

70. Thacker, W.C.

Reply to "Comments on 'Irregular Grid Finite-Difference Techniques: Simulations of Oscillations in Shallow Circular Basins'" by J.D. Wang. Journal of Physical Oceanography 7, No. 6, 933-934. 1216

71. Thacker, W.C.

"Shear Dispersion" in Time-Varying Flows. NOAA Technical Report ERL 386-AOML 27, 9 pages. 1218

72. Thacker, W.C. and J.W. Lavelle.

Two-Phase Flow Analysis of Hindered Settling. The Physics of Fluids 20, No. 9, 1577-1579. 1227

NOAA Magazine 7, No. 1, 36-38.

And now, IOCARIBE:

Caribbean Cooperation: It Works

BY HARRIS B. STEWART*

IN 1965, on a small French island off Brittany, the Hydrographer of the Royal Netherlands Navy and the Director of the Netherlands Institute for Sea Research generated an idea that blossomed beyond their wildest imaginings.

Two years later, it was adopted as an official program for international cooperation by UNESCO's Intergovernmental Oceanographic Commission.

They called it CICAR—for the Cooperative Investigation of the Caribbean and Adjacent Regions.

Last July, after seven years of work at sea in which 40 research vessels from ten nations participated, CICAR came to an end with a multi-national symposium at Caracas, Venezuela, with more than 100 technical papers presented. These were but the tip of the iceberg; several hundred other papers and reports have been issued, and more will emerge as the last of the field data are analyzed.

How well did CICAR work? Does it deserve to live on in some permutation? For that matter, what was it intended to accomplish? The objectives of the program were spelled out at a Mexico City meeting of the International Coordination Group for CICAR:

—to contribute to the development of marine research in the CICAR region;

—to insure the maximum participation of coastal countries in the region;

—to achieve a better scientific understanding of the region;

—to carry out, rapidly and effectively, certain particular projects of research with well-defined scientific and economic objectives; and

—to establish the basis for further international coordination in the CICAR area.



CICAR provided the occasion for the first official U.S. delegation to be sent to Cuba in recent years, when in 1972 the Havana CICAR meeting included this group, posing at the José Martí airport, (l. to r.), John Bruchs, NMFS; Harris Stewart, AOML; Robert Molinari, AOML; Bernard Zetler, AOML; and John Antoine, Texas A&M University.

All but the second were accomplished successfully, and even that might have been a success had the objective been instead: "maximum *possible* participation of coastal countries". Of the countries in the region, only Colombia, Cuba, Mexico, Venezuela, and the United States were able to field ships, although the Netherlands, France, United Kingdom, Federal Republic of Germany, and the USSR all sent one or more ships from outside the area. Guatemala, Jamaica, Brazil, Panama, and Trinidad and Tobago participated to varying degrees, from having their scientists work on ships of other countries to just showing up at meetings. Except for Cuba, Jamaica, and Trinidad, none of the Caribbean island nations was able to participate, and none of the Central American countries between Mexico and Colombia contributed to the program. In essence, CICAR was the United States, the Soviet Union, Mexico, the Netherlands, the United Kingdom, Colombia and Venezuela, in decreasing order of their degree of participation.

CICAR contributed significantly to the development of marine research in the region, and this is particularly true of Mexico, Colombia, Venezuela, and Trinidad and Tobago. Each of these countries was able to use its participation in CICAR to obtain stronger governmental support for marine research.

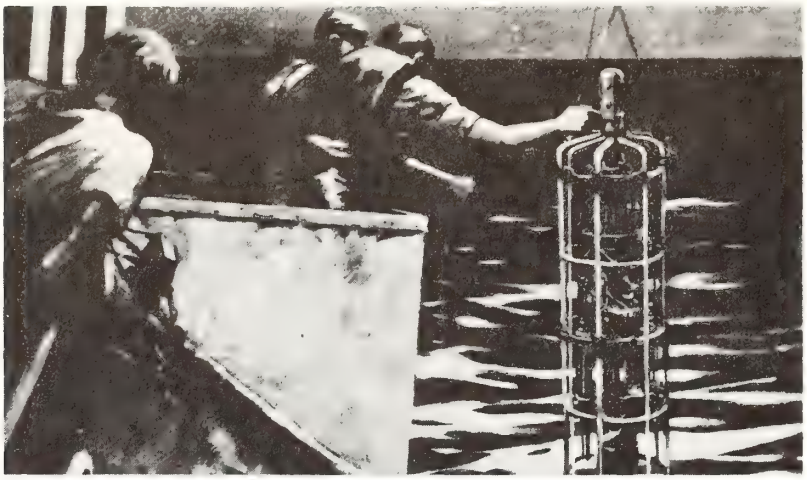
The U.S. was a major contributor to CICAR, with the following sea-going groups involved: NOAA (AOML and the Southeast Fisheries Center of NMFS), Geological Survey, Navy, Coast Guard, Woods Hole Oceanographic Institution, University of Rhode Island, Lamont-Doherty Geological Observatory of Columbia University, Duke University, Florida State University System, University of Miami, Texas A&M University, and the University of Puerto Rico. In

**Dr. Stewart, Director of NOAA's Atlantic Oceanographic and Meteorological Laboratories in Miami, has been for seven years the U.S. National Coordinator for CICAR and has just been appointed as the U.S. Associate for IOCARIBE. He was Chief Scientist on the NOAA-CARIB Expedition in 1972, and has been Chairman of the U.S. Delegations to CICAR meetings in Mexico City, Havana, Port of Spain, Cartagena, and Caracas. He was also the Chairman of the Steering Committee for the July 1976 CICAR-II Symposium and is Editor-in-Chief of the Proceedings of these meetings.*

addition, scientists from numerous other U.S. and Caribbean institutions rode U.S. research vessels during the program. Education and training of Caribbean scientists was an essential element of CICAR and NOAA assisted by having people at NODC for training in the operation of data centers and by running the two-month NOAA-Carib Expedition.

CICAR did indeed achieve a better scientific understanding of the region. Although most of the participating groups from the U.S. and elsewhere were "doing their own thing" rather than working cooperatively on a comprehensive scientific program that somehow never materialized, a tremendous amount of new knowledge was developed. The United States, for example, has published a "Preliminary Bibliography of Published Results of Marine Research by U.S. Scientists in the CICAR Area, 1968–1974" which contains over 400 references. The Soviet Union has a series of publications on the work of its vessels in the CICAR program, and other countries have published CICAR bibliographies (notably the Netherlands, Trinidad and Tobago, and the United Kingdom).

Scientific results presented at the CICAR-II Symposium in Caracas covered a broad spectrum, but representative results in physical oceanography included studies of the circulation in the Cayman Sea, the Gulf of Mexico Loop Current, the physical oceanography of the Cariaco Trench, circulation through the passages between the Atlantic and the Caribbean Sea, effects of upwelling,



Action paintings by Jack Coggins, done aboard NOAA ship Discoverer during 1968 CICAR work off Barbados.



tides in the Caribbean and Gulf of Mexico, and the coastal circulation off Surinam.

A broad range of chemical results dealt with gypsum-organic interactions, the relationship of nutrients to the Amazon River outflow, sources and movements of suspended materials, contamination in coastal lagoons, dissolved carbohydrates off Venezuela, dissolved silica, radionuclides and trace elements in plankton, and salinity structure in the Venezuelan Basin.

Marine geological and geophysical results included the development of a tectonic map of the Caribbean Sea and new knowledge of the complex fault systems of the region, of the nepheloid layer, of sedimentation, of the complex geophysics of the island arc system, of the origin of the Old Bahama Channel, of marine terraces, and calcium carbonate deposition in the Gulf of Mexico.

In the area of sea-air interaction, CICAR resulted in the development of a thermodynamic model for mean monthly sea surface temperature predictions, a better understanding of the role of the atmospheric boundary layer in sea-air interaction processes in the tropics, the development of a climatic heat budget for the Gulf of Mexico, and a much better understanding of the air-sea interactions during squalls and deep convection and of the response of the tropical ocean to meteorological forcing functions.

In marine biology, results ran the gamut from the zonation of fan corals and the biology of Caribbean turtle grass to the dynamics of phytoplankton in an upwelling area, the ecology and toxicity of sponges, and the systematics and distribution of diatoms and dinoflagellates to studies of Caribbean zooplankton, the search for cancer-specific marine antibiotics, studies of the macro-fauna of the area, and new knowledge of coral reefs, the ecology of coastal lagoons, and the regional distributions of the benthic organisms.

In fisheries, CICAR developed new knowledge of shrimp migrations, porgy distribution and migration in the Gulf of Mexico, spawning conditions of fishes in the northeastern Caribbean, potential fish production from coralline shelves, the ecology of juvenile grunts, the distribution of larval lobster recruitment and dispersal as revealed by a surface drift model, the fish fauna of Cuban artificial reefs, the relationship of scarlet prawns to a bottom oil deposit, aquaculture of the sea mussel and the queen conch, the Jamaican spiney lobster, snapper and grouper resources in the region, scallops and mussels, and even an interesting method for inducing spawning and reproduction in molluscs artificially.

The abstracts of the more than 100 papers covering these subjects were published and made available to participants at the Caracas meetings, and the full papers are now in the final stages of preparation for publication by the Inter-governmental Oceanographic Commission of UNESCO and by the Food and Agriculture Organization, both of the United Nations.

The carrying out of specific research projects with well-defined objectives was designed to cover two of CICAR's major

aspects: the CICAR standard sections and the CICAR survey months. These were a series of lines of oceanographic observing stations criss-crossing the Caribbean, the Gulf of Mexico, and certain of the inter-island passes. Every ship working in the area was encouraged to make its observations at these standard stations on these pre-set profiles. Fortunately, many of them did. In addition, several periods were set when every ship that could be made available made observations at the same time—or as nearly at the same time as possible. These were the CICAR Survey Months; probably the best scientific results from CICAR came from these two projects. One of the basic tenets of international cooperation is that it should be limited to those activities that cannot be carried out without such cooperation; these are really the only two CICAR activities that met this criterion. The results, developed primarily by Dr. Robert Molinari of AOML, comprise one of the major scientific results of the CICAR program. His compilation of the work of all the ships that had occupied standard sections during survey months gained immediacy when the Bureau of Land Management needed information to help predict where currents might carry potential oil spills in the Gulf of Mexico. The major relevant work at that time was his, and BLM funded its continuance to a predictive conclusion.

Other than the field work, the major U.S. contribution to CICAR has been by the National Oceanographic Data Center of NOAA's Environmental Data Service. Acting as the CICAR Regional Data Center, NODC has produced bibliographies, data distribution charts, data summaries, on-request data summaries, a Guide to CICAR Data, and has been the willing acceptor of data in all sorts of format from the CICAR participants in spite of their attempt to standardize data submission by developing specific forms, the so-called CICARDI form, for submitting CICAR data. NODC is still trying to get CICAR participants in this country and in others to submit their data to NODC. (An international cooperative effort is no more effective than its ability to exchange data among the participants).

CICAR's field work officially terminated in December of 1975. Both the Intergovernmental Oceanographic Commission, the sponsor of CICAR, and the various countries involved felt that the international cooperative relationships developed during CICAR ought to be continued. The marine scientists in the various Caribbean countries were all talking with each other, the CICAR umbrella facilitated research in the waters of other countries (and restrictions in this area are becoming increasingly bothersome to marine researchers), good science was actually being accomplished by international cooperation that could not have been otherwise done and the CICAR Standard Sections and CICAR Survey Months are the classic examples. Thus it was decided that some mechanism should be established as the basis for future international cooperation and coordination in the Caribbean and its adjacent regions.



Scientific party from several nations poses with officers and Barbados flag aboard the Discoverer during CICAR operations.



Colombian, Venezuelan, and U.S. scientists aboard the Discoverer during the La Guaira to Curtegena leg of NOAA-CARIB, a CICAR training and education cruise in 1972.

The result is that the Intergovernmental Oceanographic Commission has established a CICAR follow-on called the IOC Association for the Caribbean and Adjacent Regions with the acronym IOCARIBE. The first meeting of IOCARIBE was held last July in Caracas, and it was decided that instead of the rather relaxed format of CICAR, IOCARIBE would concentrate on specific projects which would utilize marine science for the benefit of the countries of the Caribbean. The first consideration is that IOCARIBE is to be supported only for six years on a trial basis to see if it can in fact accomplish something worthwhile.

Because the major economic importance of the Caribbean to the nations bordering it is fish, IOCARIBE is concentrating its initial effort on those aspects of marine research that have a significant bearing on fisheries. To this end, a workshop will be convened in 1977 in which physical oceanographers, marine chemists, sedimentologists, marine biologists, and fisheries people will get together to decide what specific projects should be undertaken under IOCARIBE with a view to providing the scientific framework that the Food and Agriculture Organization and others concerned with Caribbean fisheries development need to increase the ability of fishermen within the area to make a livelihood and the people of the area to have a more substantial diet from the sea. This is in sharp contrast to the old CICAR concept of each country "doing its own thing," and the end results should be considerably more applicable to the problems of the area.

The Caribbean is exciting scientifically, as the CICAR participation by United States scientists has indicated. The Caribbean is sensitive politically. IOCARIBE provides a good mechanism for doing good science that will benefit the United States as well as the countries of the region.

That meeting on the Brittany island some eleven years ago spawned a program that has paid off for the IOC, for the Caribbean, for marine science, and for the United States. It is a great game, and NOAA has played a leading role. □

Journal of Geophysical Research 82, No. 21, 3175-3182.

Ocean Tides and Weather-Induced Bottom Pressure Fluctuations in the Middle-Atlantic Bight

R. C. Beardsley,[1] H. Mofjeld,[2] M. Wimbush,[3]
C. N. Flagg,[4] and J. A. Vermersch, Jr.[1]

Five bottom pressure gages were deployed in the Middle-Atlantic Bight during the late winter of 1974. Analysis of the resulting pressure series and neighboring coastal tide gage series shows that tides are the dominant pressure signal in this section of the continental shelf. Most of the remaining pressure fluctuations appear to be forced by meteorological transients. During March 21, 1974, a developing cyclone moving up the coast excited a coherent group of sea level oscillations with characteristic periods of 5–7 hours, which are interpreted here as coastal-trapped edge waves. Spectra of the nontidal pressure series are red, however; most of the nontidal variability is caused by lower-frequency (subtidal) components. The subsurface pressure (SSP) fluctuations do appear coherent over the spatial extent of the array in the most energetic subtidal frequency bands, and estimates made of the relative horizontal SSP gradients indicate that cross-shelf gradient variations are significantly larger than alongshore gradient variations. Some consequences of these large weather-induced gradient fluctuations on the shelf circulation are discussed.

Introduction

During the late winter of 1974, five bottom pressure gages were deployed in the Middle-Atlantic Bight. Analysis of the resulting pressure series and neighboring coastal tide gage series shows that tides are the dominant pressure signal in this section of the continental shelf. Most of the remaining pressure fluctuations appear to be meteorologically forced. Our objective here is to characterize the bottom pressure variability and to examine the spatial and temporal structure of the weather-induced fluctuations.

Three pressure gages were deployed at Marine Ecosystems Analysis (Mesa) program stations 9, 10, and 11 by the Atlantic Oceanographic and Meteorological Laboratories of NOAA as part of the Mesa New York Bight Project (see Figure 1 for station locations). Placed parallel to the Hudson Channel and spaced from the inner shelf out to the shelf break, the Mesa array was designed to measure variations in tides across the shelf. Two other pressure gages were deployed at stations 2 and 3 near 71°W, south of Block Island, by the Massachusetts Institute of Technology (MIT) and the Woods Hole Oceanographic Institution (WHOI). These two gages formed part of a three-element moored array set across the shelf to examine the current and bottom pressure response to meteorological transients.

Four of the five bottom pressure gages produced simultaneous data for the period from March 11 to April 2, 1974. While these overlapping bottom pressure series were obtained in separate programs, they have allowed us to examine the pressure response of a rather broad continental shelf region to winter storms. Intense winter cyclones appear to force a simple low-frequency bottom pressure field which is essentially coherent over the spatial extent of the combined pressure measurement array.

Instrumentation

The bottom pressure records were obtained by using three types of pressure gages. Two Draper Laboratory pressure/temperature recorders [*Wunsch and Dahlen*, 1974] were deployed at stations 2 and 3. These instruments used bonded strain gage transducers and sampled every 7½ min; the gages have an estimated resolution of ±0.3 and ±0.2 cm and an estimated accuracy of ±2.8 and ±3.7 cm, respectively. Only the low-frequency (subtidal) component of the station 2 record was usable because of instrumentally caused high-frequency noise in the record. At Mesa stations 10 and 11, Vibratron pressure gages were deployed which sampled every 7½ min and have an estimated accuracy of ±0.5 cm. A Filloux deep-sea tide gage which used a Bourdon tube–optical lever transducer was deployed at Mesa station 9. Owing to instrumental shifts in the apparent mean pressure, only the last month of this latter series was used. The gage sampled every 30 min and has an estimated accuracy of ±0.5 cm. All pressure instruments were rigidly mounted to bottom anchors.

Coastal sea level records were obtained for the experimental period from the National Ocean Survey for Cape May, Sandy Hook, Woods Hole, and Nantucket Island. To compare bottom pressure series with coastal sea level series, the local atmospheric pressure (in millibars) has been added to the sea surface displacement (in centimeters) to produce synthetic subsurface pressure, or 'SSP,' series.

Tides

The four pressure records were first analyzed by using the response method to determine the harmonic constants for the major tidal constituents M_2, N_2, S_2, O_1, and K_1. The results are listed in Table 1 together with results from a similar analysis for Sandy Hook, New Jersey, as a reference shore station. The three semidiurnal components all increase in amplitude as the depth decreases across the shelf, while the amplitudes of the two diurnal components show little systematic change over the midshelf region. The ratio of the major diurnal to semidiurnal constituents is $R = (K_1 + O_1)/(M_2 + S_2) \doteq 0.24$ for the four shelf records, indicating that the tide is primarily semidiurnal over the Middle-Atlantic Bight. The ratio of M_2/S_2 lies be-

[1] Woods Hole Oceanographic Institution, Woods Hole, Massachusetts 02543.
[2] Atlantic Oceanographic and Meteorological Laboratory, NOAA, Miami, Florida 33149. Present address: PMEL/NOAA, Seattle, Washington 98105.
[3] Nova University, Dania, Florida 33004. Present address: University of Rhode Island, Kingston, Rhode Island 02881.
[4] Massachusetts Institute of Technology/Woods Hole Oceanographic Institution Joint Program in Oceanography, Massachusetts Institute of Technology, Cambridge, Massachusetts 02139.

Copyright © 1977 by the American Geophysical Union.

Paper number 7C0245.

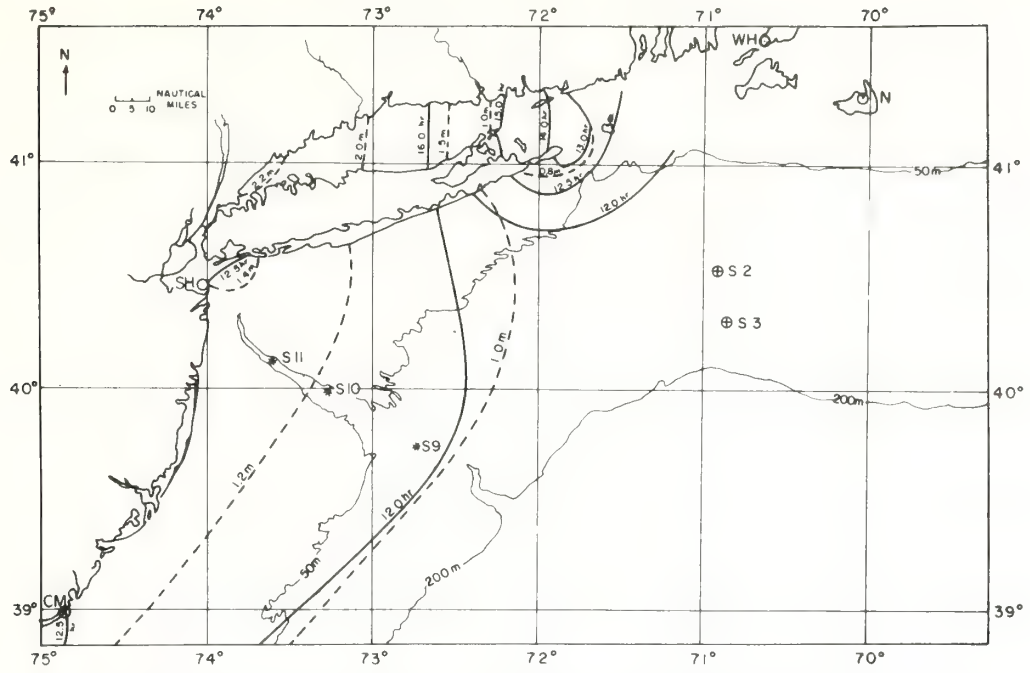


Fig. 1. Bathymetric map of central section of Middle-Atlantic Bight. Isobaths are shown in fathoms (1 fathom = 1.82 m). Positions of shelf and coastal pressure stations are indicated by symbols. Shelf stations Mesa 9, 10, and 11 and MIT/WHOI stations 2 and 3 are denoted by S9, S10, and S11 and S2 and S3, respectively. The positions of the shelf stations were S9, 39°45.6'N, 72°41.8'W; S10, 40°00.0'N, 73°14.3'W; S11, 40°08.1'N, 73°34.4'W; S2, 40°32.6'N, 70°55.6'W; and S3, 40°18.2'N, 70°54.4'W. The coastal stations are Cape May (CM), Sandy Hook (SH), Woods Hole (WH), and Nantucket (N). For completeness we also show the mean corange (dashed lines) and high-water interval (solid lines) charts drawn by *Swanson* [1976].

tween 4.2 and 4.7, which is characteristic of the semidiurnal tide west of Cape Cod.

These results plus other data have been used by *Swanson* [1976] to make mean corange and high- and low-water interval charts for the New York Bight. The mean corange and high-water interval contours found by Swanson are shown in Figure 1 for convenience. This region extends from Cape May, New Jersey, in the south to east of Long Island, New York. Swanson discusses the earlier work by *Redfield* [1958], who used coastal information to estimate the M_2 tide on the shelf. The observed tides at the offshore stations show that Redfield's model is essentially correct for the M_2 constituent to the west of Montauk Point, New York. The discrepancy to the east is attributed by *Swanson* [1976] to the influence of Long Island Sound.

The semidiurnal and diurnal surface tides cause much of the bottom pressure (or SSP) variability observed over the continental shelf. The total pressure variance and percentage contribution caused by the tides for the first 29 days of each data record are listed in Table 1 for the shelf stations and Sandy Hook. A minimum of 80% of the total SSP variance is due to the astronomical tides, and the total variance, like the dominant semidiurnal constituents, decreases significantly in amplitude offshore. Most of the remaining variability is caused by lower-frequency mesoscale and synoptic meteorological fluctuations, which have characteristic periods greater than 2 days. The fraction of the total bottom pressure variance contributed by subtidal components with periods of >31.6 hours is also listed in Table 1 for each shelf station. The subtidal variability (as measured by the variances) decreases by a factor of 15 between Sandy Hook and shelf station 3 near the shelf break. Since the tidal constituents exhibit less amplitude change across the shelf, the percentage contribution to the total pressure variance by subtidal fluctuations decreases offshore toward the shelf break. The subtidal pressure variability should exhibit a seasonal change, so the analysis in Table 1 should be viewed as being representative of late winter or early spring conditions.

Subtidal Pressure Fluctuations

The subtidal bottom pressure fluctuations observed at the four shelf stations are shown as a function of time in Figure 2. Also plotted are synthetic bottom pressure or SSP records from surrounding coastal stations between Cape May and Nantucket. All records have been filtered by using a phase-preserving low-pass filter with a half-amplitude cutoff at a 0.03-cph, or 33.3-hour, period (see *Flagg et al.* [1976] for a complete description of the filter).

The resulting subtidal pressure fluctuations shown in Figure 2 appear to be coherent in both space and time from Cape May to Cape Cod. The pressure fluctuations are approximately in phase and decrease in amplitude toward the shelf

TABLE 1. Amplitude and Phase for the Five Major Tidal Constituents Observed During March–April 1974 at the Four Shelf Stations and at Sandy Hook

	Sandy Hook		Mesa 11		Mesa 10		Mesa 9		MIT/WHOI 3	
	Amplitude, cm	Phase, deg	Amplitude, cm	Phase, deg	Amplitude, cm	Phase, deg	Amplitude, cm	Phase, deg	Amplitude, cm	Phase, deg
Tidal constituent										
M_2	66.0	7	58.9 (62.8)	350 (350)	55.5 (55.9)	351 (347)	49.8 (45.7)	351 (344)	42.2	347 (342)
N_2	16.7	347	13.8	330	12.8	332	11.3	330	10.5	327
S_2	14.8	33	13.1	15	12.5	16	10.6	17	10.1	13
O_1	6.2	168	6.3	169	6.5	170	6.6	181	6.8	178
K_1	10.3	171	10.0	167	9.8	172	9.5	174	8.3	173

	Sandy Hook	Mesa 11	Mesa 10	Mesa 9	MIT/WHOI 3
Standard deviation					
Semidiurnal band					
Amplitude, %	±5.3	±5.1	±4.0	±1.3	±1.2
Phase, deg	±3.0	±2.9	±2.3	±0.8	±0.7
Diurnal band					
Amplitude, %	±29.2	±23.2	±18.1	±3.7	±9.2
Phase, deg	±16.7	±13.4	±10.4	±2.1	±5.3
Total variance, cm²	2685	2132	1805	1387	1056
Variance due to subtidal variability, cm²	265	282	165	21	12
Variance due to tides, %	88.8	84.6	89.0	97.9	96.4
Variance due to subtidal variability, %	9.9	13.2	9.1	1.5	1.2

Values for local water depth, in meters, are as follows: Mesa 11, 37; Mesa 10, 46; Mesa 9, 57; and MIT/WHOI 3, 112. Values for M_2 shown in parentheses are from *Redfield*'s [1958] model. Variances are based on spectral analysis of the first 29 days of each data record; the subtidal band includes all components with periods of ≥31.6 hours.

break; the range at station 3 is 16 cm in comparison to a range of 140 cm at Sandy Hook. Three major storms occurred during the period shown in Figure 2 which produced both large cross-shelf and along-shelf pressure gradients. The first two storms, associated with developing low-pressure systems moving up the Saint Lawrence Valley, generated strong westerly and southwesterly winds over the continental shelf during March 5–6 and March 17–19. The resulting offshore mass flux caused a sea level setdown along the coast, resulting in a strong offshore pressure gradient. On March 30–31 a third low-pressure system moved off the coast near Cape Hatteras and generated northeasterly winds, which caused a strong onshore pressure gradient. Smaller SSP events were generated by less intense storms via the same transient Ekman mechanism.

Autospectra for several pressure records are shown in Figure 3*a* to illustrate the frequency content of the subtidal fluctuations shown in Figure 2. The spectra were computed by using a Danielle window for a 33.75-day period starting either at 2300 UT on February 27 for all stations except 10 and 11 or at 2000 UT on March 9 for stations 10 and 11; only the first nine estimates are plotted. Also shown are the atmospheric pressure spectrum for Sandy Hook and the smoothed spectrum for wind stress observed off Little Egg Inlet, New Jersey, during late winter conditions by *EG&G* [1975]. These spectra show that both the wind stress and the atmospheric pressure variability decrease sharply with increasing frequency; most of the spectral density or power lies in the first three estimates, with characteristic periods greater than 64.8 hours, or 2.7 days. The SSP spectra from both coast and shelf stations exhibit a similar power decrease toward higher frequencies until a sharp power increase occurs in the diurnal tidal band at estimates 6 and 7. This low-frequency spectral gap is more pronounced for the shelf stations, where the diurnal tidal band is relatively more energetic. The coastal and nearshore SSP spectra tend to have a slight spectral density maximum near $f = 0.008$ cph, or 5.2 days; this is due primarily to the presence of the three major storm SSP transients, which have characteristic time scales between 2 and 3 days. Since the SSP spectral densities observed at the coastal stations are typically greater than the atmospheric pressure power at lower frequencies, the nearshore subtidal SSP variability is primarily directly wind driven rather than pressure driven. Using Bermuda atmospheric and sea level records, *Wunsch* [1972] has shown that the SSP variation in the open deep ocean is less than ±1 cm over a frequency range of 0.0025–0.025 cph, a result further demonstrated by *Brown et al.* [1975]. We see here that the 'inverted barometer effect' does significantly reduce the subtidal bottom pressure variability observed near the shelf break.

The coherence and phase of low-frequency SSP fluctuations between different coastal stations are plotted in Figure 3*b*, where the 95% confidence limits for 0.0 and 0.5 true coherence are 0.72 and 0.85, respectively. In general, the estimated coherence of the subtidal SSP fluctuations decreases with increasing frequency and distance. The Sandy Hook–Cape May (SH-CM) and the Woods Hole–Nantucket (WH-N) pairs are sufficiently close to be coherent over the first eight frequency bands shown in Figure 3*b*. All four coastal stations are clearly coherent around estimate 1, with characteristic periods between 4.5 and 13.5 days. This is to be expected, since estimate 1 encompasses the most energetic band shown in Figure 3*a* and the horizontal length scales of midlatitude atmospheric systems exceed the separation scale of these SSP observations. All four stations are also coherent in the diurnal tidal band around estimates 6 and 7.

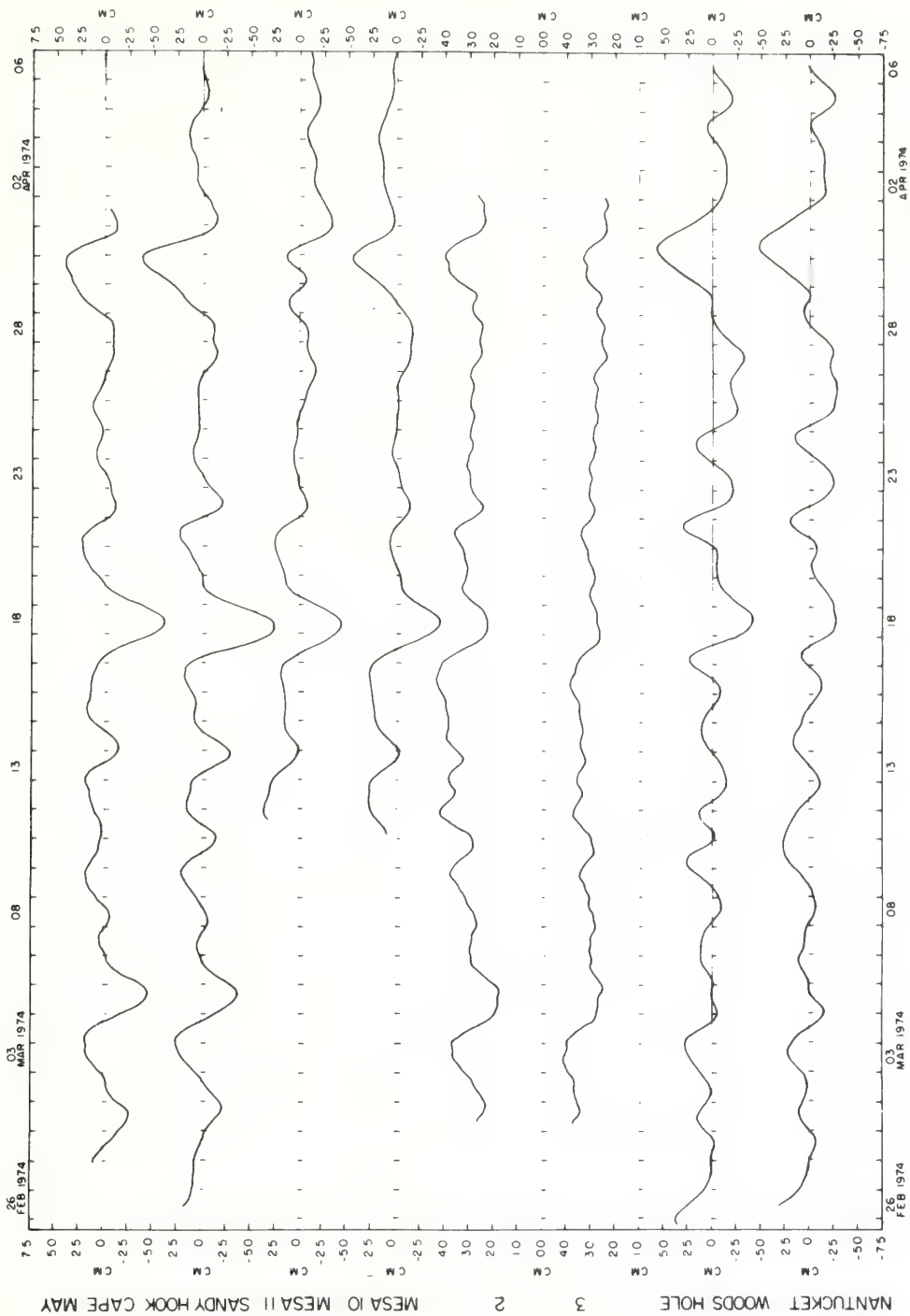


Fig. 2. Subtidal bottom pressure and SSP fluctuations (in centimeters) from four shelf station (Mesa 10 and 11 and MIT/WHOI 2 and 3) and four coastal stations from February 26 to April 6, 1974. All records have been detided by using a phase-preserving convolution low-pass filter with a half-amplitude cutoff at 0.03 cph. All records are aligned in time in vertical direction. Note that because of the relatively small amplitude of the subtidal fluctuations observed at shelf stations 2 and 3 we have enlarged these two records in this figure by a factor of 2.5.

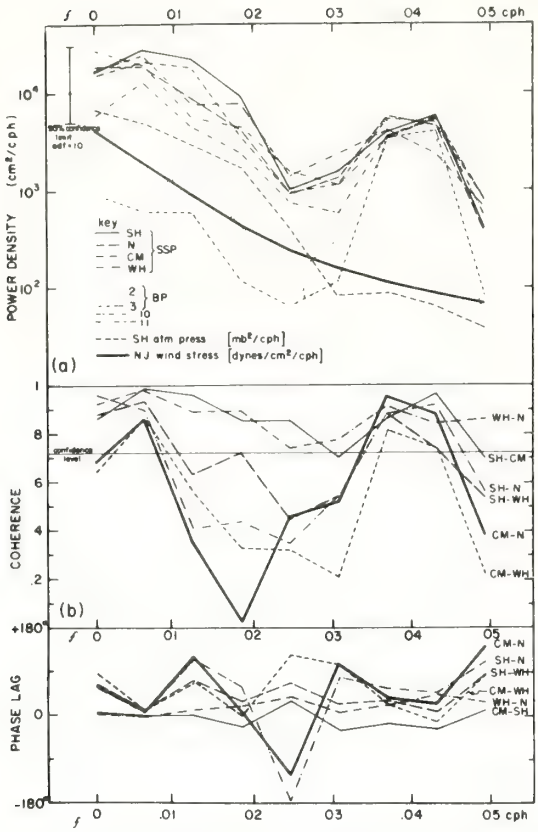


Fig. 3. (*a*) Bottom pressure and SSP from the autospectra from four shelf stations (Mesa 10 and 11 and MIT/WHOI 2 and 3) and four coastal stations. Most of these spectra were completed by using a Danielle window for the 33.75-day period starting at 2300 UT on February 27, and only the first nine averaged estimates are plotted by using a linear frequency scale. The spectra for shelf stations 10 and 11 were computed in a similar manner for the 33.75-day period starting at 2000 UT on March 9. Also shown are the autospectrum of atmospheric pressure for the 33.75-day period starting at 2300 UT on February 27 and the smoothed autospectrum for wind stress observed off Little Egg Inlet, New Jersey, during March and April 1974 and May 1973 by *EG&G* [1975]. (*b*) Coherence spectra for low-frequency SSP fluctuations between different coastal stations. These spectra were computed for the 33.75-day period starting at 2300 UT on February 27. With 5 estimated d.f. the 95% confidence limits for 0.0 and 0.5 true coherence are 0.72 and 0.85, respectively.

The coherence and phase of SSP between different coastal and shelf stations are shown in Figure 4 for the lowest four frequency bands. Pairs with computed coherence exceeding 0.72 (the 95% confidence limit for zero true coherence) are connected by heavy lines. An arrow points to the station in the direction of positive phase lag or, equivalently, positive phase propagation. As is indicated in Figure 3*b*, the coastal records are most coherent in frequency band 1, and fewer record pairs are coherent in bands 2 and 3. While the uncertainty in the phase estimates is quite large, most of the estimated phase lags are consistent with the known eastward propagation of mid-latitude weather patterns. The phase lags shown in Figure 4 for band 1 for all station pairs with a computed coherence exceeding 0.72 (the 95% confidence limit) are consistent with a one-dimensional pressure wave propagating toward 96°T at a speed of 47 km/h, or 26 knots. The estimated wavelength is about 7700 km, corresponding approximately to a mode 4 synoptic wave.

Shelf stations 2 and 3 are close enough to be highly coherent over essentially the entire frequency range examined between 0.003 and 0.5 cph. The same is true for shelf stations 10 and 11, where the phase difference is less than 1 hour over the entire frequency range. SSP at stations 10 and 11 are coherent with Sandy Hook SSP for frequencies between 0.003 and about 0.16 cpd. SSP at both stations 10 and 11 lag Sandy Hook SSP by approximately 4 hours for frequencies less than 0.08 cpd. The two more eastern shelf stations, 2 and 3, are more coherent at lower frequencies with Sandy Hook than with the nearer coastal stations at Woods Hole and Nantucket. These last two stations are located on Vineyard Sound and are presumably more contaminated by local and Gulf of Maine phenomena.

Subtidal Pressure Gradients

Scott and Csanady [1976] have recently developed a local dynamical model to estimate the mean alongshore pressure gradient off a straight coast with simple topography. They have applied this method to coastal current and wind observations made off central southern Long Island during September 1975 and find that the mean sea surface rises toward the northeast with a local alongshore slope of 1.4×10^{-7}. *EG&G* [1976] has made a similar analysis of current and wind data collected off Little Egg Inlet, New Jersey, during February–March 1975 and also finds a mean northward sea surface rise with a local alongshore slope of 2.8×10^{-7}.

The SSP records for the Cape May and Sandy Hook stations are sufficiently coherent with small enough phase lags

TABLE 2. Root-Mean-Square Equivalent Sea Surface Slope Estimated by Using the Variance of the Difference Between SSP Records at Adjacent Stations

Station Pair	rms Equivalent Sea Surface Slope	
	$0.0025 \le f \le 0.034$ cph	$0.0031 \le f \le 0.034$ cph
	Alongshore	
Cape May–Sandy Hook	4.8×10^{-7}	3.8×10^{-7}
	Cross-Shelf	
Sandy Hook–Mesa 11	42.0×10^{-7}	22.7×10^{-7}
Mesa 11–Mesa 10	27.9×10^{-7}	11.5×10^{-7}
MIT/WHOI 2–MIT/WHOI 3	21.4×10^{-7}	10.7×10^{-7}
	Continental Rise	
Site D	5.6×10^{-7}	3.8×10^{-7}

The estimates for station pairs Cape May–Sandy Hook and MIT/WHOI 2–MIT/WHOI 3 and for station pairs Sandy Hook–Mesa 11 and Mesa 11–Mesa 10 were computed for the 33.75-day periods starting at 2300 UT on February 27 and at 2000 UT on March 9, respectively. The site D values are geostrophic estimates of the rms slope variation over the continental rise area inferred from *Thompson*'s [1971] composite kinetic energy spectra at 100 m at site D. Much of the inferred slope variance at side D occurs for periods greater than 16.875 days; the estimated rms sea surface slope for all frequencies below 0.034 cph is 12.5×10^{-7}.

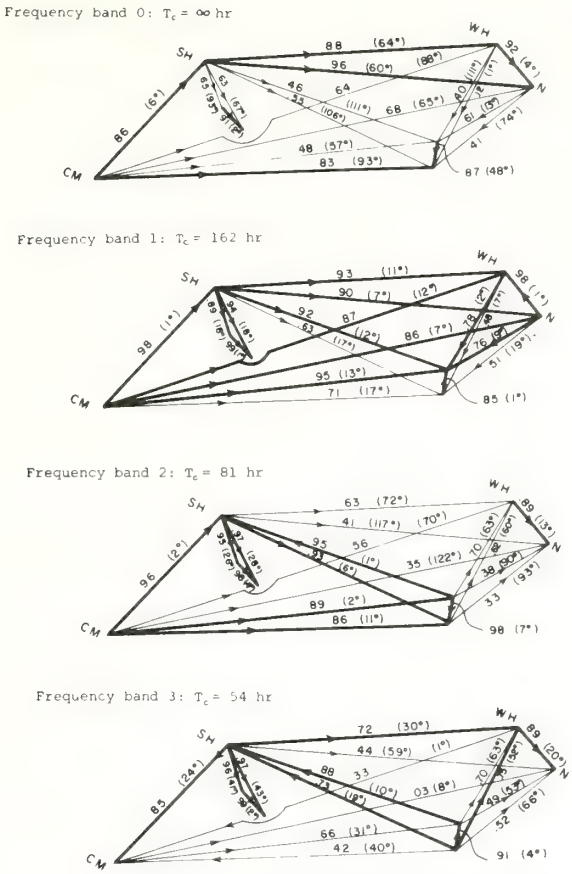


Fig. 4. SSP coherence and phase graphs for selected shelf and coastal stations. Each graph corresponds to a separate frequency band, and only results for the four lowest frequency bands are shown. Pairs with computed coherence exceeding 0.72 (the 95% confidence limit for zero true coherence) are connected by heavy lines. Arrows point in the direction of positive phase propagation.

that we can use the difference between these two records to estimate the low-frequency fluctuations in the alongshore pressure gradient off New Jersey. The offshore pressure gradient fluctuations can also be estimated by using the differences in SSP observed at Sandy Hook and Mesa stations 10 and 11 and MIT/WHOI stations 2 and 3. We have computed the variances of the SSP differences between these pairs of stations, and we list the derived rms or standard deviations of the equivalent sea surface slope in Table 2. The results are presented for two frequency bands, the first encompassing all low-frequency fluctuations with periods between 1.23 and 16.67 days. The second frequency band covers fluctuations with periods between 1.23 and 13.4 days and includes the most energetic band in the wind stress spectra. This second band contains approximately two thirds and one fourth of the total low-frequency variance in the alongshore and cross-shelf SSP gradients, respectively. The results for both bands suggest that the cross-shelf SSP gradient fluctuations both increase toward shore and are significantly larger than the alongshore SSP gradient fluctuations inferred for the New Jersey coast.

Also included in Table 2 are estimates of the rms slope fluctuations anticipated at site D (39°20'N, 70°W), located on the continental rise south of New England. These values are computed by assuming a geostrophic balance between the equivalent sea surface slope and the composite kinetic energy spectrum constructed at 100 m by *Thompson* [1971]. At site D about four fifths of the total variance of the inferred slope variation is caused by motion at frequencies below that resolved in our shelf measurements. The site D values given for the two resolved frequency bands in Table 2 are comparable to the alongshore estimates, suggesting that the alongshelf slope variance is roughly constant across the continental shelf and slope. This suggestion, coupled with the observed significant increase in cross-shelf slope variance, is consistent with the notion that the characteristic horizontal length scale of the dominant atmospheric transients is larger than the characteristic width of the continental shelf.

Using the lower estimate from the second band, we find that during March 1974 the standard deviation of the alongshore surface slope about its mean due to subtidal fluctuations is about 40% larger than the mean slope estimated *EG&G* [1976] for February or March 1975. The maximum subtidal surface slope deviation which occurred during the March 30–31 storm is 1.27×10^{-6}, little over 4 times the estimated mean slope and $3\frac{1}{2}$ times the standard deviation. A histogram of the SSP differences between Sandy Hook and Cape May shows that the number of extreme gradients with low pressure toward the northeast was about double the extreme southwest gradients, a result caused by the asymmetry of the three major storms. The maximum cross-shelf surface slope deviation observed was 83×10^{-7}, which occurred between Sandy Hook and station 11 during the March 30–31 storm.

We should also point out that if the subtidal alongshore current is geostrophic, then the standard deviation of the alongshore current σ_v between adjacent stations is given by $\sigma_v = g/f\sigma_{SS} \doteq 10^7\sigma_{SS}$, where σ_{SS} is the standard deviation of rms sea surface slope as listed in Table 2. Thus the geostrophic rms alongshore current fluctuation between stations 10 and 11 is 11.5 cm/s (for band 2). A rough estimate of the low-frequency rms variation in the alongshore volume flux is 7×10^6 m^3/s, a value about $3\frac{1}{2}$ times the mean alongshore transport estimated by *Beardsley et al.* [1976] from current meter data. While the governing dynamics are certainly more complex, this crude geostrophic estimate of the alongshore transport variation again points out the strong influence of low-frequency meteorological transients in the Middle-Atlantic Bight region.

Pressure Fluctuations at Supratidal Frequencies

An interesting example of above tidal pressure fluctuations was discovered when a tidal signal (predicted by using the observed tidal constituents) was subtracted from the original pressure series at each station. The resultant detided records exhibited mostly subtidal fluctuations and some higher-frequency noise throughout most of the experiment except during March 21, when a group of coherent sea level oscillations was observed (see Figure 5*a*). Between 0600 and 1300 UT on March 21 a large pressure drop occurred which clearly propagated northeastward along the shelf from Cape May to Woods Hole. This initial drop was followed by several oscillations (with average periods between 5.1 and 6.7 hours) which decayed over the next 18 hours. The pressure fluctuations appear to decrease monotonically in amplitude across the shelf, maximum amplitudes being found at the shore stations.

We believe that these coherent pressure fluctuations do represent coastal-trapped edge waves generated by a developing atmospheric low-pressure system which moved up the New England coast and passed over Sandy Hook near 0600 UT on

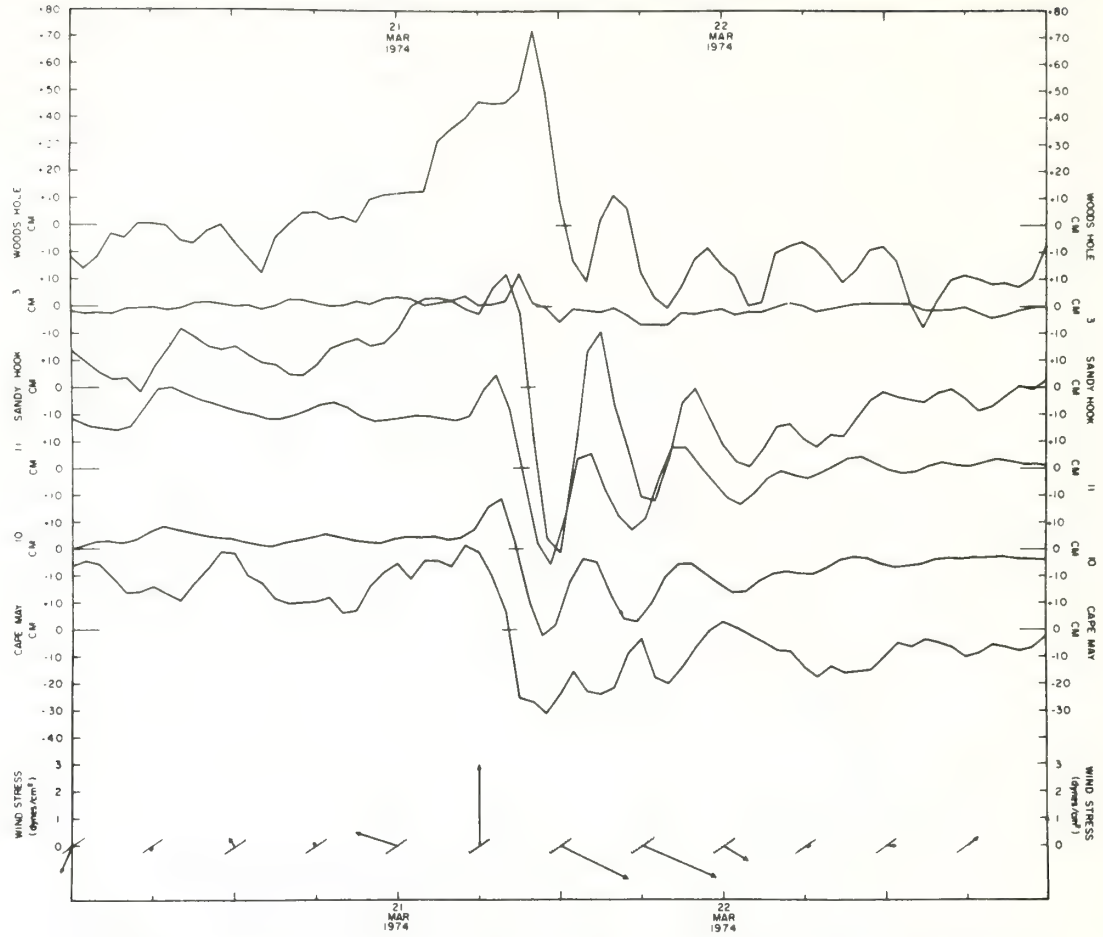


Fig. 5*a*. Detided shelf and coastal SSP records for March 20–33, 1974. The bottom row shows the relative orientation of the wind stress vector and the mean shoreline. Stress was computed from winds observed over the New York Bight apex by using a quadratic drag law $\tau = \rho C_D |\mathbf{W}| \mathbf{W}$, where $C_D = 1.5 \times 10^{-3}$.

March 21. The corresponding surface weather map and storm track are shown in Figure 5*b*. Surface weather maps and the wind stress near Sandy Hook plotted in Figure 3*a* suggest a short initial strong onshore stress quickly followed by a strong (2–4 dyn/cm²) offshore stress component which decayed slowly. The initial pressure drop appears to be the leading member of a short packet of first-mode edge waves which propagate northward along the continental shelf. Edge waves are dispersive, group speed being less than phase speed; thus wave energy was left behind the initial leading pressure drop, which moved in phase with the surface wind stress pattern.

Munk et al. [1956] were the first to suggest that large sea level oscillations observed at Atlantic City and Sandy Hook following hurricanes may be edge waves forced by the moving atmospheric pressure pattern. We have attempted here a quantitative comparison between the observed fluctuations and the two-dimensional free edge wave theories of *Reid* [1958] and *Mysak* [1968] and a numerical model with realistic cross-shelf topography (see Table 3). While the models correctly predict a larger wave period and phase speed to the northeast of the Hudson River Canyon due to an increase in the shelf slope between Sandy Hook and Cape Cod, they generally under-

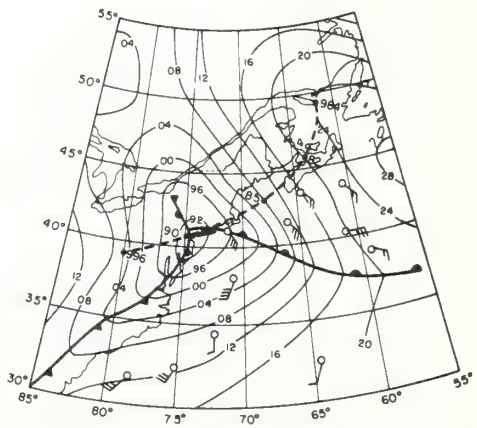


Fig. 5*b*. Weather map showing surface pressure distribution and wind vectors at 0600 UT on March 21. The dashed line shows the track of of the storm center, and dots with numbers indicate the position of the center and center pressure in millibars at 6-hour intervals.

TABLE 3. Comparison Between Wave Periods and Phase Speeds Observed During March 21 and Wave Periods Computed by Using Theoretical Models and a Numerical Model With a Realistic Cross-Shelf Topography

	Observed T, hours	Observed C_p, km/h	Inferred λ ($=TC_p$), km	Theoretical T, hours: *Reid* [1958]	*Mysak* [1968]	Numerical Model
Cape May–Sandy Hook	5.1 ± 0.8	68	344	4.8	4.3	3.9
Sandy Hook–Woods Hole	6.7 ± 0.8	234	1573	6.9	5.0	5.5

All models assume an infinite straight coastline (aligned with the x axis) and a one-dimensional depth profile $h(y)$ which depends only on y, the offshore position. The Reid model considers an infinite 'wedge' shelf, $h = \alpha y$, while Mysak considers a finite wedge shelf joined at a distance L with an ocean of constant depth D. Actual depth profiles across the shelf, slope, and rise region have been used in the numerical model. The periods are computed for the fundamental mode (i.e., the surface elevation decreasing monotonically as $y \to \infty$) by using the observed wavelength λ and topography parameters estimated along transects off Atlantic City and Block Island as input.

estimate the wave periods by ≤25%. We attribute this discrepancy to the sharp bend in the coastline at Sandy Hook, which effectively decreases the slope and broadens the shelf. Both effects tend to increase the period of edge waves.

These and other observations do demonstrate that intense meteorological events (from fast fronts to hurricanes) can excite relatively large-scale high-frequency edge waves which propagate along the mid-Atlantic shelf. such edge wave packets are not commonly observed, and to our knowledge there is no evidence that any large-scale standing oscillations or 'normal' gravity wave modes are effectively excited by atmospheric transients. The decay time scale for the edge waves shown in Figure 5 is roughly 1–2 wave periods. This rapid decay severely limits energy propagation within the Middle-Atlantic Bight between Cape Hatteras and Cape Cod, so we speculate that the effective Q for any possible large-scale normal modes in this region may be small enough to prohibit observation of the mode itself.

Acknowledgments. We want to express our gratitude to C. Wunsch of MIT and J. Dahlen of the Draper Laboratory for making two pressure/temperature recorders available for this experiment and to the crews of the NOAA ship *Researcher*, the USCGC *Hornbeam*, and the tug *Whitefoot* for their considerable help in the field program. W. Brown of UNH has made several helpful suggestions on data presentation and interpretation. This research has been jointly sponsored by the Mesa New York Bight Project through grant 01-5-022-471 to the NOAA Atlantic Oceanographic and Meteorological Laboratory (H.M. and M.W.) and by the National Science Foundation through grants GA-41075, DES 74-03001, and OCE 76-01813 (R.B., C.F., and J.V.). Woods Hole Oceanographic Institution contribution 3888.

REFERENCES

Beardsley, R. C., W. C. Boicourt, and D. V. Hansen, Physical oceanography of the Middle Atlantic Bight, *J. Limnol. Oceanogr., Spec. Symp., 2*, 20–34, 1976.

Beardsley, R. C., and B. Butman, Circulation on the New England continental shelf: Response to strong winter storms, *Geophys. Res. Lett., 1*, 181–184, 1974.

Brown, W., W. Munk, F. Snodgrass, H. Mofjeld, and B. Zetler, Mode bottom experiment, *J. Phys. Oceanogr., 5*(1), 75–85, 1975.

EG&G, Environmental Consultants, Summary of oceanographic observations in New Jersey coastal waters near 38°28'N latitude and 74°15'W longitude during the period May 1973 through April 1974, A report to Public Service Electric and Gas Company, Newark, N. J., 1975.

EG&G, Environmental Consultants, Summary of oceanographic observations in New Jersey coastal waters near 39°28'N latitude and 74°15'W longitude during the period May 1974 through May 1975, A report to Public Service Electric and Gas Company, Newark, N. J., 1976.

Flagg, C. N., J. A. Vermersch, and R. C. Beardsley, 1974 M.I.T. New England shelf dynamics experiment (March 1974) data report, II, The moored array, *Rep. 76-1*, Dept. of Meteorol., Mass. Inst. of Technol., Cambridge, 1976.

Munk, W., F. Snodgrass, and G. Carrier, Edge waves on the continental shelf, *Science, 123*(3187), 127–132, 1956.

Mysak, L. A., Edgewaves on a gently sloping continental shelf of finite width, *J. Mar. Res., 26*(1), 24–33, 1968.

Redfield, A. C., The influence of the continental shelf on the tides of the Atlantic coast of the United States, *J. Mar. Res., 17*, 432–448, 1958.

Reid, R. O., Effect of Coriolis force on edge waves, I, Investigation of the normal modes, *J. Mar. Res., 16*(2), 109–144, 1958.

Scott, J. T., and G. T. Csanady, Nearshore currents off Long Island, *J. Geophys. Res., 81*(30), 5401–5409, 1976.

Swanson, R. L., *Tides, Mesa New York Bight Atlas Monogr.*, vol. 4, 34 pp., New York Sea Grant Institute, Albany, 1976.

Thompson, R., Topographic Rossby waves at a site north of the Gulf Stream, *Deep Sea Res., 18*(1), 1–21, 1971.

Wunsch, C., Bermuda sea level in relation to tides, weather, and baroclinic fluctuations, *Rev. Geophys. Space Phys., 10*(1), 1–49, 1972.

Wunsch, C., and J. Dahlen, A moored temperature and pressure recorder, *Deep Sea Res., 21*(2), 145–154, 1974.

(Received December 1, 1976;
revised March 11, 1977;
accepted March 14, 1977.)

Journal of Geophysical Research 82, No. 34, 5469-5476.

The Variability of Anticyclonic Current Patterns in the Gulf of Mexico

DAVID W. BEHRINGER, ROBERT L. MOLINARI, AND JOHN F. FESTA

Atlantic Oceanographic and Meteorological Laboratories, National Oceanic and Atmospheric Administration, Miami, Florida 33149

A recent twofold increase in the number of temperature observations available in the Gulf of Mexico has prompted a reappraisal of several ideas regarding the temporal variability of the Loop Current in the eastern gulf and the anticyclonic gyre in the western gulf. The analysis includes both synoptic data drawn from 47 cruises in the eastern gulf and monthly maps of temperature at 200 m prepared from observations over the entire gulf. It is found that on average the penetration of the Loop Current into the gulf increases during the winter and spring, reaching a maximum in the early summer, at which time a large anticyclonic eddy probably separates from the loop. It is also found that there are substantial deviations from this average sequence of events; during the past dozen years the period between eddy separations has been as short as 8 months and as long as 17 months. The data coverage of the western gulf is sparse, but there is evidence for the year-round persistence of the anticyclonic gyre and some indications that the gyre may be strongest in summer and winter.

INTRODUCTION

The large-scale circulation in the Gulf of Mexico is dominated by two current systems: the Loop Current in the east and an anticyclonic gyre in the west. The Loop Current enters the eastern gulf through the Yucatan Straits and leaves through the Straits of Florida. Its path between the straits varies with time, frequently forming an anticyclonic loop which extends well north of the Straits of Florida [*Leipper*, 1970; *Maul*, 1975]. The geostrophic transport of the loop relative to deep levels is at least 30×10^6 m^3/s [*Nowlin*, 1972; *Nowlin and Hubertz*, 1972]. This represents a large fraction of the transport of the Gulf Stream, which it ultimately joins downstream. The western gyre is centered at about 24°N in the far western gulf. Its geostrophic transport has been estimated to be about 10×10^6 m^3/s [*Sturges and Blaha*, 1976], and wintertime geoelectrokinetograph measurements across the northern limb of the gyre show maximum surface speeds of 70 cm/s [*Nowlin*, 1972]. There is some evidence that this gyre persists the year round [*Sturges and Blaha*, 1976].

Cochrane [1963] was indirectly the first to propose an annual cycle in the path of the Loop Current. His suggestion was that the path would vary in response to an annual cycle which he found in the strength and cross-stream structure of the surface currents in the Yucatan Straits. Since then, most of what has been learned about the circulation patterns in the eastern gulf has been derived from temperature observations and the geostrophic assumption. It has been shown that the horizontal distribution of temperature in the main thermocline is well correlated with the dynamic topography of the sea surface [*Ichiye*, 1962; *Nowlin and Hubertz*, 1972].

Leipper [1970], on the basis of his analysis of extensive temperature data from 1965 and 1966 and more limited data from a few additional years, cautiously concluded that some changes in the path of the Loop Current may be associated with the seasons. He coined the phrase 'spring intrusion' to describe the growth of the loop into the gulf and the phrase 'fall spreading' to describe the subsequent westward movement of the loop or of a detached eddy.

Leipper's [1970] observations clearly show that an eddy had separated from the loop not long before late August 1965. His data for 1966 can be interpreted as showing that the loop reached a maximum penetration in August and, very likely, shed an eddy at that time [*Molinari*, 1977]. A different timing of these events was observed during a series of cruises in 1969 when the maximum penetration occurred no later than May and a detached eddy was observed to drift westward during the summer [*Cochrane*, 1972]. In 1973, *Maul* [1975] found a cycle in the growth of the loop which was again very similar to that seen by *Leipper* [1970].

Each of the authors cited above has suggested that the pattern of development of the loop may vary from year to year. Some variability is apparent in the differences between the series of observations from 1969 and those from 1966 and 1973. Additional evidence for this variability has been found in observations made during the same month in sequential years [*Nowlin and Hubertz*, 1972]. Nevertheless, the idea of an average annual cycle of spring intrusion and fall spreading has persisted [*Maul*, 1975].

Monthly averages of the distribution of temperature are sources of information on an average annual cycle of the Loop Current. *Whitaker* [1971] has computed monthly averages of the topography of the 22°C temperature surface, and *Robinson* [1973] has computed the monthly averages of temperature at several depths. If the position of the loop is inferred from the 150-m isobath of the 22°C surface, then the annual cycle of the loop which appears in Whitaker's charts shows a maximum intrusion in June and a minimum intrusion in December. A similar analysis of the 22°C isotherm at 150 m from Robinson's charts is ambiguous. Although there are an absolute maximum and an absolute minimum in the intrusion of the loop in May–June and December, respectively, there are also relative maxima in February and October and relative minima in April and August. However, Robinson may have biased the cycle which appears in her charts toward these multiple extremes by the application of a filter which passes the first three annual harmonics. In addition, both Whitaker and Robinson have subjectively smoothed the data to obtain continuity in space and time, thus potentially altering details of the loop cycle.

Less is known about the circulation in the western gulf. Early studies of the western gulf showed a complex system of highs and lows in the dynamic height field of the surface relative to deep levels [*Austin*, 1955; *Duxbury*, 1962]. However, *Nowlin* [1972] analyzed data collected during several winter cruises between 1958 and 1964 and concluded that the central western gulf is dominated in the wintertime by an anticyclonic gyre. *Cochrane* [1972] and *Nowlin and Hubertz* [1972] have

Copyright © 1977 by the American Geophysical Union.

Paper number 7C0714.

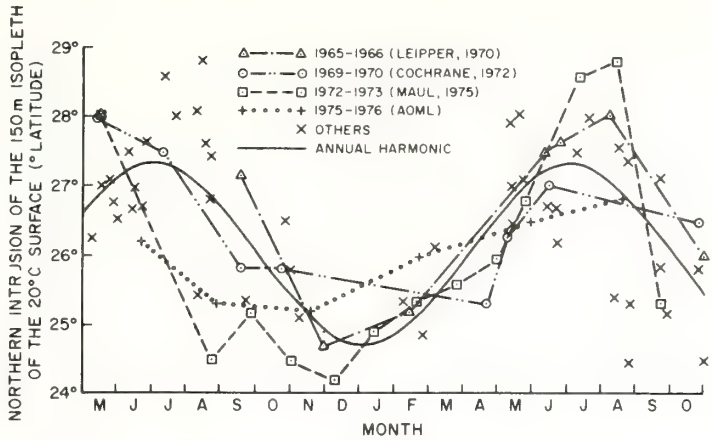


Fig. 1. The penetration of the Loop Current into the Gulf of Mexico versus time of year. The graph is derived from synoptic temperature data, and the penetration is measured by the northern limit of the 150-m isobath of the 20°C isothermal surface. The category 'others' also includes the Leipper, Cochrane, Maul, and AOML cycles where they repeat themselves.

suggested that the gyre is the remnant of an eddy which has separated from the Loop Current and drifted to the west. *Sturges and Blaha* [1976] argue instead that the gyre is driven by the curl of the wind stress and thus is analogous to the major gyres of the world ocean. They argue further that there should be transport maxima in the gyre during the summer and winter which correspond to maxima in the curl of the wind stress at these times.

The object of this study is to reexamine the ideas which have been put forth regarding the time variability of the large-scale circulation in the Gulf of Mexico. In summary, these ideas are (1) that the growth of the Loop Current follows an annual average cycle which includes periods of spring intrusion and fall spreading, (2) that there is significant year-to-year variability in the cycle of the loop, (3) that there is a quasi-permanent anticyclonic gyre in the western gulf, (4) that the strength of the western gyre is maintained by loop eddies which have drifted to the west, or alternatively, (5) that the western gyre is driven by the curl of the wind stress.

A recent increase in the quantity of data available in the gulf has made a reexamination of these ideas worthwhile. In the sections that follow, we first consider the majority of the synoptic data available in the eastern gulf. In this context the phrase 'synoptic data' applies only to data collected during the cruises which had a sufficient areal coverage to define the extent of the Loop Current. The synoptic data include a new series of cruises conducted by the Atlantic Oceanographic and Meteorological Laboratories (AOML) [*Molinari*, 1976]. Finally, because there are more temperature data than those which fit our limited definition of synoptic data, we next use all of the available data to prepare new monthly averaged distributions.

Synoptic Observations

We have used the synoptic data from 47 cruises conducted in the eastern Gulf of Mexico between 1952 and 1976 to construct charts of the topography of the 20°C isothermal surface. The charts which were made from the data collected prior to 1974 have been published by *Molinari* [1977]. He has shown that the position of the 150-m isobath of the 20°C isothermal surface correlates well with the axis of the Loop Current. Thus we have used the northern limit of this 150-m isobath to represent the penetration of the loop at the time of each cruise (Figure 1). In preparing Figure 1 we considered detached eddies to be continuous with the loop if they were located eastward of 90°W longitude. The points which have been derived from data which were reported on by *Leipper* [1970], *Cochrane* [1972], and *Maul* [1975] and from data which were recently collected by AOML are connected by broken lines.

As can be seen in Figure 1, in any month there may be considerable variability in the degree of penetration of the loop into the Gulf. Nevertheless, an annual cycle in the penetration of the loop does emerge from the data. From November through February there is only one observation of an intrusion north of 26°N, and from May through August there are only two intrusions south of 26°N. The period of growth for the loop extends on average through the winter and spring.

We have represented the average cycle by the solid line, which is the mean penetration plus the annual harmonic, $A \cos$

TABLE 1. Season or Month of Eddy Observation and Separation

Year	Month Observed	Month Detached	Season Detached	Source
1952	May			*Molinari* [1977]
1962	Feb.			*Nowlin and McLellan* [1967]
1965	Aug.		summer	*Leipper* [1970]
1966	Aug.		mid-summer	*Molinari* [1977]
1967	June			*Nowlin and Hubertz* [1972]
1968	Aug.	June or July		
1969	May	May		*Molinari* [1977]
1970	Nov.	Nov.		*Cochrane* [1972]
1971	Aug.	Aug.		*Maul* [1975]
1972	May	April		*Maul* [1975]
1973	July	July		*Morrison* [1974]
1974	April	April		*Maul* [1975]
1975	March	Feb.		*Maul* [1975]
1976	Aug.		mid-summer	*Legeckis* [1976] *Molinari et al.* [1977]

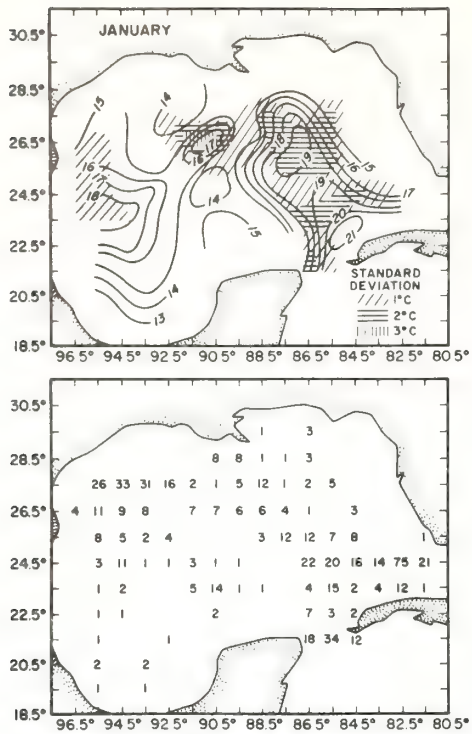


Fig. 2. (Top) Contours of average temperature at 200 m for January. The contour interval is 1°C. The standard deviation is indicated by cross-hatching. (Bottom) The number of temperature observations at 200 m for January.

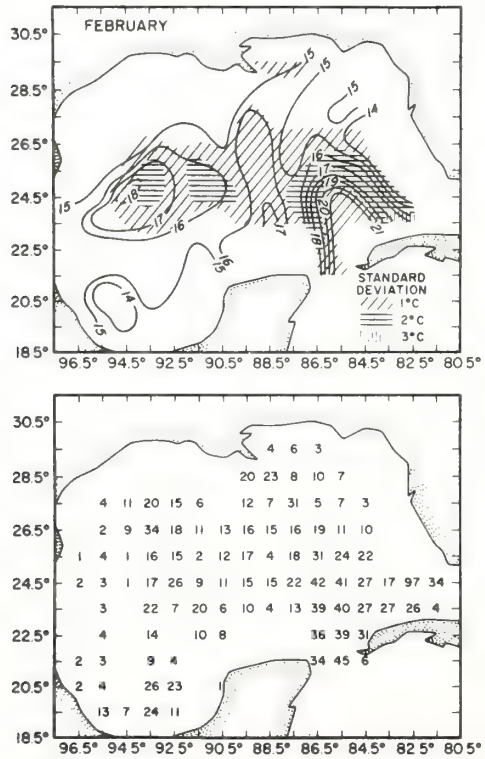


Fig. 3. Same as Figure 2 except for February.

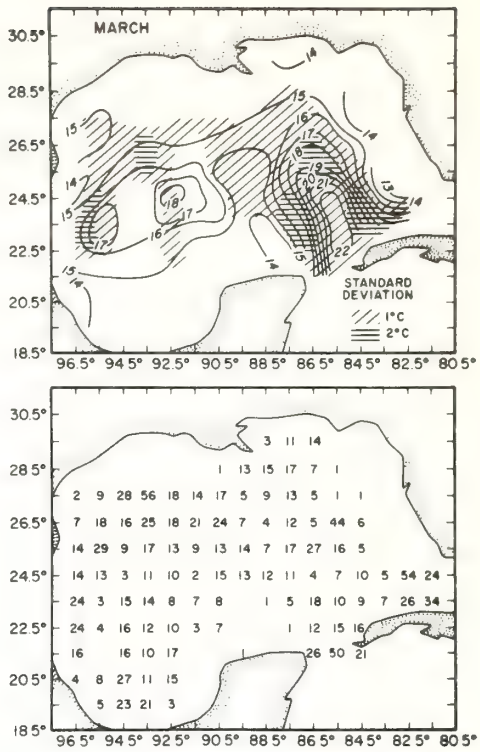


Fig. 4. Same as Figure 2 except for March.

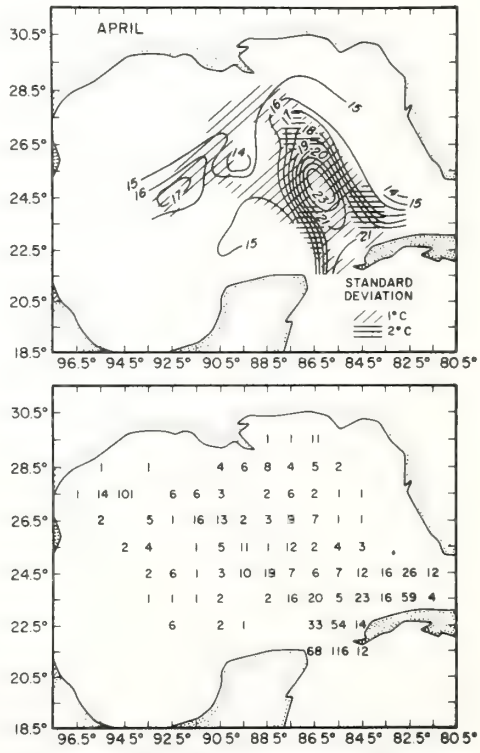


Fig. 5. Same as Figure 2 except for April.

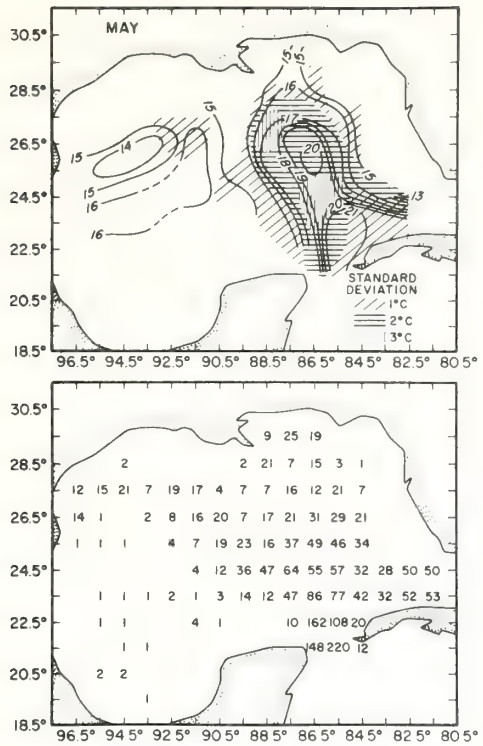


Fig. 6. Same as Figure 2 except for May.

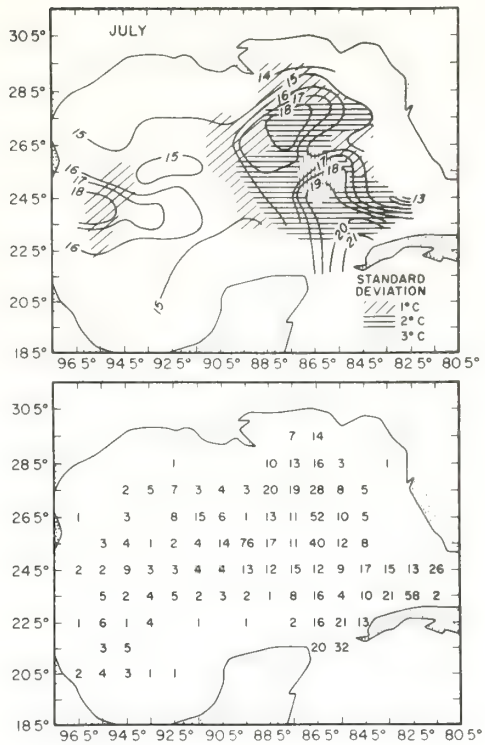


Fig 8 Same as Figure 2 except for July.

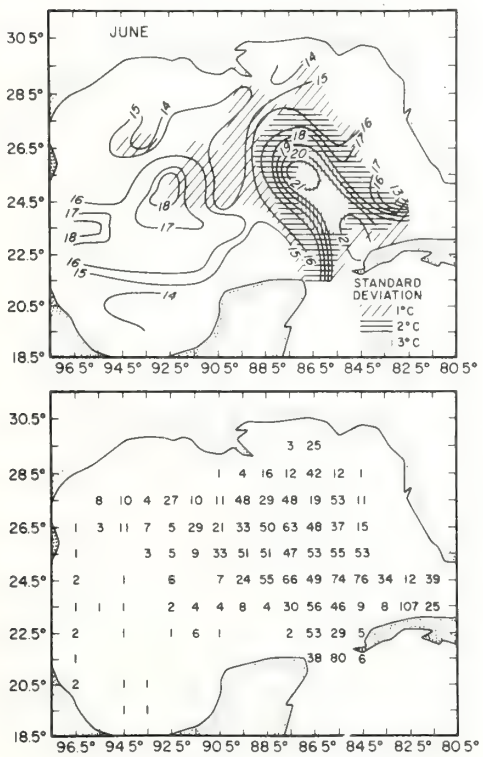


Fig. 7. Same as Figure 2 except for June.

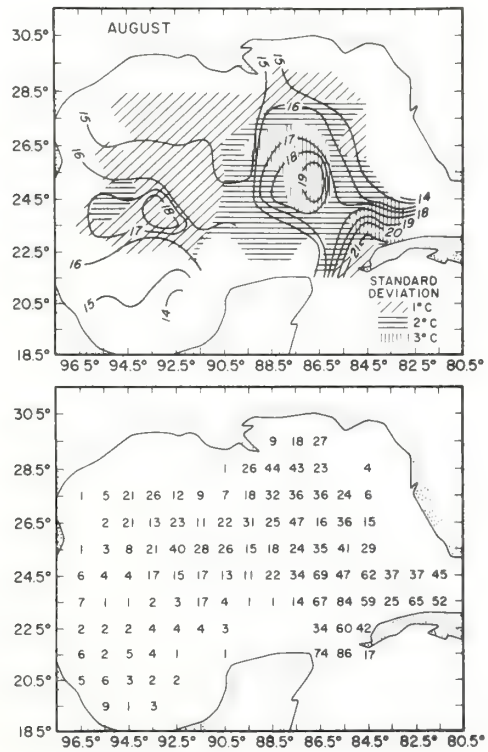


Fig. 9. Same as Figure 2 except for August.

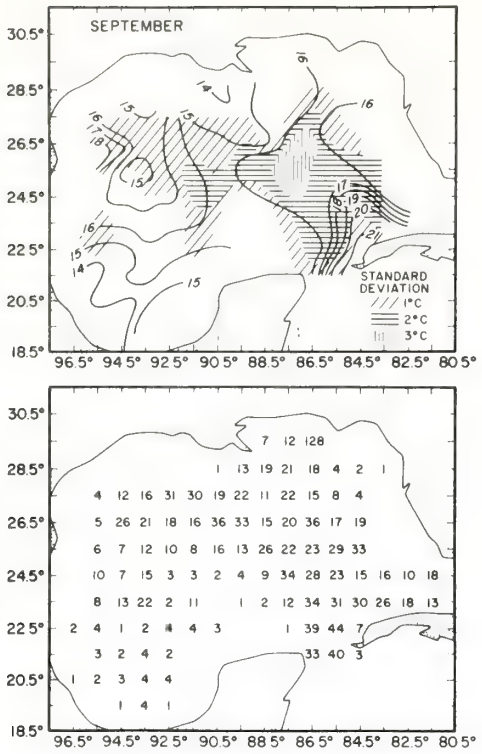


Fig. 10. Same as Figure 2 except for September.

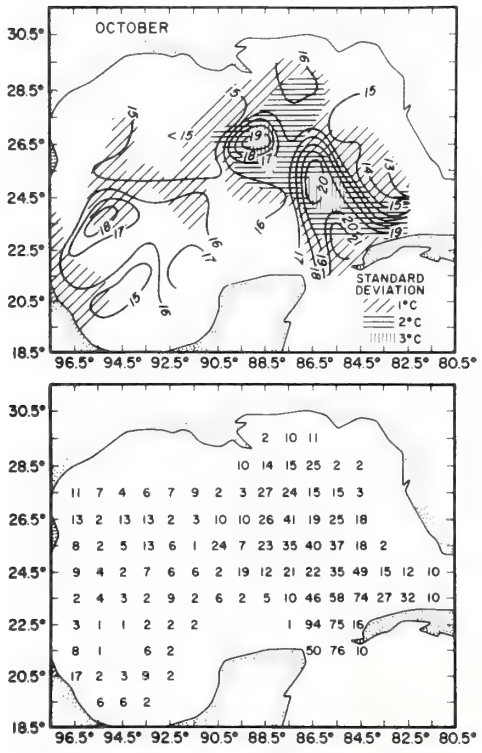


Fig. 11. Same as Figure 2 except for October.

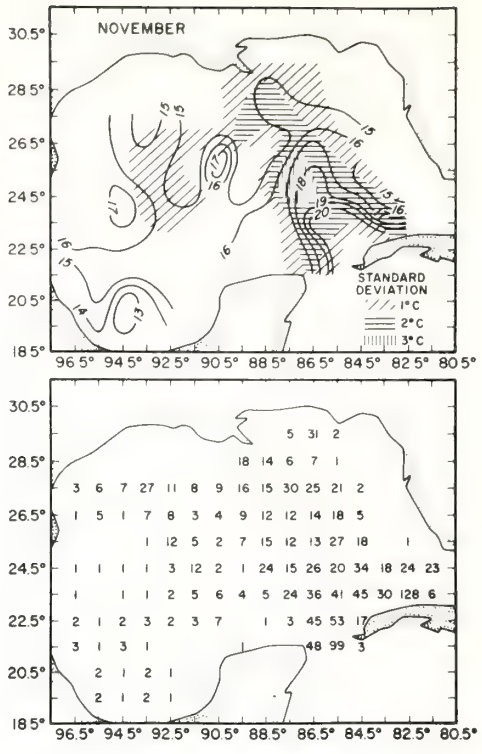


Fig. 12. Same as Figure 2 except for November.

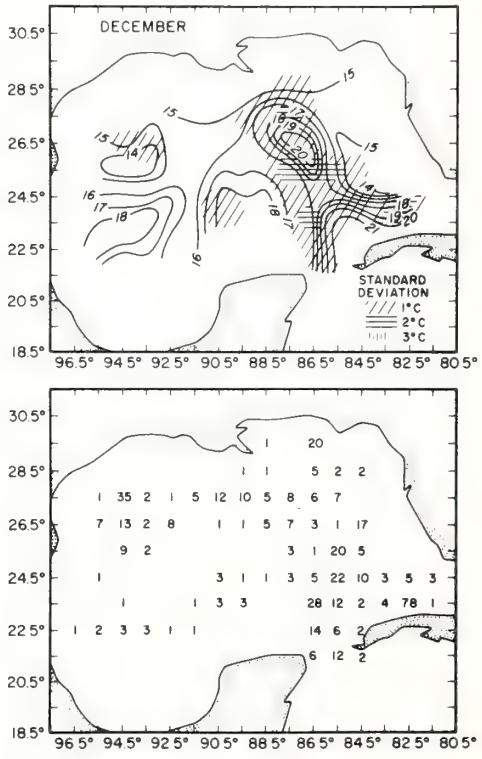


Fig. 13. Same as Figure 2 except for December.

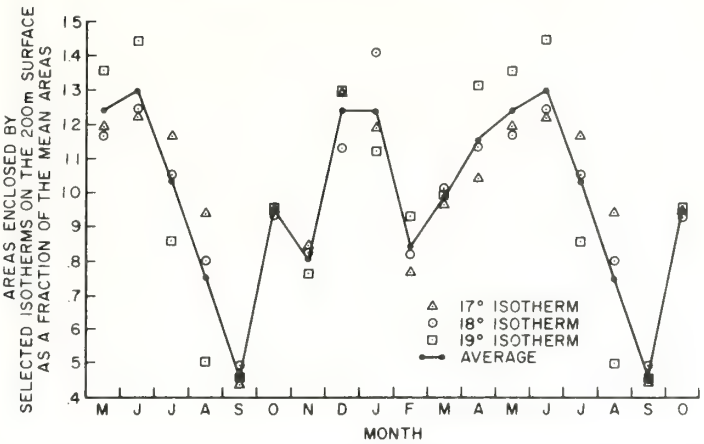


Fig. 14. The penetration of the Loop Current into the Gulf of Mexico versus time of year. The graph is derived from the monthly averaged temperature data, and the penetration is measured by the area enclosed by selected isotherms.

($\omega t - d$), fitted in a least squares sense to the monthly averages of the plotted points. The parameters of the fitted formula are the amplitude, $A = 1.3°$, the phase, $d = 185$ days, and the frequency, $\omega = 1$ cycle/yr, and the mean penetration is 26°N latitude. The average time of occurrence of the maximum intrusion of the loop is the first week in July, but the observations show much variability at that time of year.

Some of the scatter in Figure 1 can be accounted for by fluctuations in the period of the loop cycle. Of the four connected series in Figure 1, only the one derived from *Leipper*'s [1970] data has a period of about 12 months; the remaining three series have periods of at least 15 months, perhaps longer. There is potentially additional information about the period of the loop cycle in the length of time between eddy separations. The evidence clearly shows that eddy separations occurred close to the time of the deepest loop penetrations for the years 1965 [*Leipper*, 1970], 1969 [*Cochrane*, 1972], and 1973 [*Maul*, 1975], and *Leipper*'s [1970] data may be interpreted as showing the same close occurrence of these events in 1966. Since there are no clear-cut counterexamples, it is possible to speculate that the maximum loop penetration and the separation of an eddy are associated events. Table 1 shows the times when by observation or by inference eddies are believed to have separated from the loop. There is great variability in the length of time between separations; it can be as short as 8 months, August 1971 to April 1972, and as long as about 17 months, February 1975 to midsummer 1976. By implication the fluctuations in the period of the loop cycle should be similar.

Monthly Temperature Distributions at 200 m

Average temperatures at 200 m were computed by the National Oceanographic Data Center. The averages were computed for each month and over each 1° square. They include all the data which were collected prior to 1973. Nearly 17,000 observations were available at 200 m, about 13,000 in the eastern gulf and 4000 in the west. This number of observations is about double that used by either *Whitaker* [1971] or *Robinson* [1973].

The distributions of the mean temperature at 200 m, the standard deviations around this mean, and the number of observations used in computing the mean are shown for each month in Figures 2–13. The fields of average temperature have been contoured subjectively, but they have not been smoothed in any other way. Specifically, we have made no attempt to force continuity in time (as both *Whitaker* [1971] and *Robinson* [1973] have done). To do so would have been contrary to our purpose, which was to use all of the temperature data available for a given month to infer a circulation pattern for that month.

The Intrusion of the Loop Current

In the eastern gulf there is an intrusion of warm water which pushes northward between February and July (Figures 3–8). Because the sharpest horizontal gradients in the temperature fields are correlated with the axis of the Loop Current, the temperature distributions in these months imply a continuously increasing northward penetration of the loop into the gulf. In July and August, eddies appear which are clearly separated from the Loop Current. By August the leading edge of the loop has stopped moving northward and has apparently begun to recede (Figure 9). This period of growth and initial recession agrees with the average period that was deduced from the synoptic data summarized in Figure 1. The agreement is not surprising because for these months both analyses use nearly the same raw data.

The eddies which were apparent in July and August have disappeared from the temperature chart for September (Figure 10). However, a patch of high variability does remain around 26°N, 87°W, implying the presence of an eddy at least part of the time. In October the eddy has reappeared in a position further west (Figure 11). Thus the maps suggest that on average an eddy separates from the main Loop Current in July and drifts to the west during the summer and fall. A small eddy appears still farther west in November, but it is defined by only a few observations.

A second intrusion occurs in the temperature maps from October through January. Detached eddies are also apparent in December and January. Although the data coverage is sparse during these months, the temperature distributions are consistent from one month to the next. The secondary intrusion was not anticipated by any previous analysis, including our analysis of the synoptic data.

In order to ease comparisons between the analyses of the synoptic and average data, Figure 14 has been drawn to show the areas enclosed by selected isotherms on the average tem-

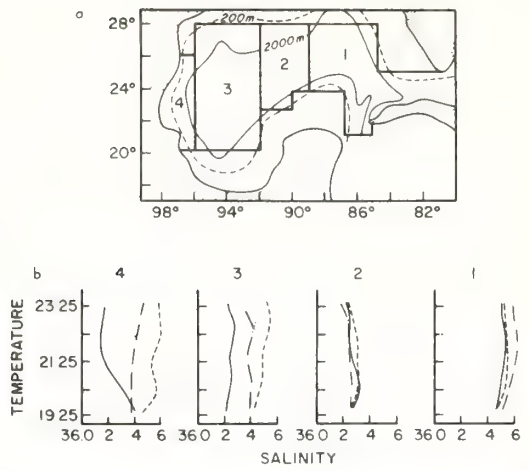


Fig. 15. (*a*) The subregions of the Gulf of Mexico for which seasonal TS relationships were computed (*b*) The seasonal TS curves for the four subregions. The dotted lines are for winter, December–February; solid lines, spring, March–May; dashed lines, summer, June–August; and dash-dot lines, fall, September–November

perature maps; the areas are expressed as fractions of the annual mean. Because it is difficult to correlate a particular average isotherm with the core of the Loop Current (as could be done in the synoptic analysis), we show the fractional areas for the 17°, 18°, and 19° isotherms as well as for the average of the three. The main intrusion in Figure 14 reaches a maximum in June, at approximately the same time as the average maximum intrusion appearing in the synoptic data (Figure 1). However, the secondary intrusion, which in Figure 14 is almost as large as the main intrusion, has no counterpart in Figure 1. This major difference between the two analyses is possible because the average temperature maps for the winter months involve more data than those which fit our definition of synoptic data. For example, the synoptic data for January come from a single cruise reported on by *Maul* [1975]. This cruise provides no data north of 25°N, and yet the deep intrusion which appears in the average temperature map for January is defined in part by observations taken well north of this latitude (Figure 2).

The Gyre in the Western Gulf

The amount of temperature data available in the western gulf at a depth of 200 m is about one third of that available in the east. In some months there are no observations at all over parts of this area. In those months when the data are sufficient, there is a large patch of relatively warm water located at about 24°N (Figures 2–13). Such a feature is consistent with an anticyclonic circulation. The persistence of this feature from month to month is evidence for a permanent anticyclonic gyre.

The feature is well defined and has maximum temperatures of over 18°C during the winter months of December, January, and February. During the summer the feature is most prominent in July. In the spring and fall, when the data coverage is adequate, the warm area appears to be fragmented, and the maximum temperature occasionally falls below 18°C. These variations may be a reflection of variations in the circulation of an associated gyre. *Sturges and Blaha* [1976] have suggested that there should be transport maxima in this gyre during the winter and summer as the result of maxima in the curl of the wind stress.

An alternative to the *Sturges and Blaha* [1976] theory is that the western gyre is periodically renewed by eddies which have separated from the Loop Current and drifted to the west [*Cochrane*, 1972]. As we have already shown above, there is evidence in the average temperature fields of loop eddies which drift westward to at least 89°W by October. Some additional evidence for such eddy movement can be found in the seasonal and regional variability of the warm water salinity maximum, which extends throughout the gulf at an average depth of about 150 m. *Nowlin* [1972] has identified this water with the maximum salinity layer traced by *Wüst* [1964] through the Caribbean basin and designated by him the Subtropical Underwater (SUW). The ultimate source of SUW in the Caribbean and the gulf is the central North Atlantic at 20°–25°N and 30°–50°W [*Wüst*, 1964; *Nowlin*, 1972].

Temperature versus salinity curves were computed for the regions indicated in Figure 15*a*. The parts of those TS curves associated with the salinity maximum are shown in Figure 15*b*. The highest salinities in region 1 occur during the fall when the Loop Current, which transports SUW into the gulf, covers on average the largest part of this region. The maximum value, in excess of 36.6‰, is consistent with the results of *Wüst* [1964]. The salinity maximum in region 2 remains at about 36.3‰ or less throughout the year except during the winter, when it is approximately 36.5‰. This observation is consistent with the renewal of SUW in region 2 by loop eddies drifting westward. Finally, the highest salinities in the western regions 3 and 4 are found during the summer, while the lowest occur during the preceding season, spring. The analysis would then suggest that on average the loop eddies move into the western region during the summer carrying with them the high salinity SUW and, by implication, any eddy momentum which has not dissipated along the way. Thus if the analysis is correct, that component of the circulation of the western gyre which has as its source the loop eddies will show a single summertime maximum. A problem with the analysis is that it cannot account for the location of loop eddies during the spring, when salinities are relatively low in every region west of region 1. This apparent difficulty may disappear when more salinity observations become available, permitting a better spatial resolution of the gulf.

Discussion

Synoptic observations of the Loop Current show much variability from year to year. Yet it is possible to derive from them an average description of the time-dependent behavior of the loop. The essential parts of the description are, first, the growth of the loop into the gulf up to a maximum penetration which coincides with the separation of an eddy and, second, the westward drift of the eddy which leaves behind a Loop Current greatly reduced in its penetration into the gulf. We have found no instance of a recession of the loop which was not preceded by the detachment of an eddy. During the last dozen years there has been one sequence of loop growth and eddy separation per year. On average, the growth of the loop has extended through the winter and spring, and westward drift of the detached eddy has occurred during the summer and fall. This sequence corresponds to that which *Leipper* [1970] found in his pioneering observations of the loop but which he somewhat misleadingly labeled spring intrusion and fall spreading.

As important as the average description of the Loop Cur-

rent cycle is the substantial evidence for large year-to-year fluctuations about the average. The fluctuations are evident in the variability both in the time between maximum penetrations of the loop and in the time between sequential separations of eddies. As we have argued above, these events appear to be related, and thus the period between eddy separations may be used as a measure of the period of the loop cycle. If it is used, then we find that during the past 12 yr there have been periods as short as 8 months and as long as 17 months. The ratio between the number of short periods (less than 1 yr) and the number of long periods (greater than 1 yr) has been about 2:1. The longest of these periods is also one of the best documented. Satellite observations of the sea surface temperature established an eddy separation in February 1975 (*Legeckis* [1976]; see also *Maul* [1975] for an evaluation of satellite observations of the Loop Current), and the series of cruises begun in June 1975 by AOML [*Molinari*, 1976] provided observations of the subsequent behavior of the loop. The observations show that the loop grew steadily from the fall of 1975 through the summer of 1976; the observations suggest a possible separation of an eddy during the summer of 1976 and a repenetration of the northern edge of the loop beyond 26°N by October [*Molinari et al.*, 1977].

Deep penetrations of the Loop Current have occurred in the late fall and early winter of 1974 [*Legeckis*, 1976] and the late fall of 1976 [*Molinari et al.*, 1977]. These deep intrusions are about 6 months out of phase with the average maximum intrusion which occurs in the early summer. It is possible that limited observations of the intrusions associated with long-period cycles can account for the secondary fall-winter intrusion of the loop which appears in the monthly maps of temperature at 200 m.

There is good evidence for the year-round persistence of an anticyclonic gyre in the western Gulf of Mexico. The patch of warm water associated with such a feature appears in each monthly temperature map for which there are sufficient observations. Although there is some evidence for two maxima in the strength of the gyre during the summer and during the winter, the evidence is tenuous.

REFERENCES

Austin, G. B., Jr., Some recent oceanographic surveys of the Gulf of Mexico, *Eos Trans. AGU*, *36*(5), 855, 1955.

Cochrane, J. D., Yucatan Current, *Rep. 63-18A*, p. 6, Dep. of Oceanogr. and Meteorol., A&M Coll. of Tex., College Station, 1963.

Cochrane, J. D., Separation of an anticyclone and subsequent developments in the Loop Current (1969), in *Contributions on the Physical Oceanography of the Gulf of Mexico, Tex. A&M Univ. Oceanogr. Stud.*, vol. 2, Gulf Publishing, Houston, Tex., 1972.

Duxbury, A. C., Averaged dynamic topographies of the Gulf of Mexico, *Limnol. Oceanogr.*, *7*(3), 428, 1962.

Ichiye, T., Circulation and water mass distribution in the Gulf of Mexico, *Geofis. Int.*, *2*(3), 47, 1962.

Legeckis, R., Present and planned satellite observations of the Gulf of Mexico and the Caribbean Sea (abstract), in *Progress in Marine Research in the Caribbean and Adjacent Regions, CICAR-II Symposium, Caracas, Venezuela*, edited by H. B. Stewart, Jr., Intergovernmental Oceanographic Commission, FAO, Unesco, and WMO, Miami, Fla., 1976.

Leipper, D. F., A sequence of current patterns in the Gulf of Mexico, *J. Geophys. Res.*, *75*(3), 637, 1970.

Maul, G. A., An evaluation of the use of the Earth Resources Technology Satellite for observing ocean current boundaries in the Gulf Stream system, *Tech. Rep. ERL 335-AOML*, p. 18, Nat. Oceanic and Atmos. Admin., Boulder, Colo., 1975.

Molinari, R. L., An overview of the Cayman Sea–Gulf of Mexico circulation based on CICAR Survey Month and other data (abstract), in *Progress in Marine Research in the Caribbean and Adjacent Regions, CICAR-II Symposium, Caracas, Venezuela*, edited by H. B. Stewart, Jr., Miami, Fla., 1976.

Molinari, R. L., Synoptic and mean monthly 20°C topographies in the eastern Gulf of Mexico, *Tech. Memo. ERL-AOML 27*, Nat. Oceanic and Atmos. Admin., Boulder, Colo., in press, 1977.

Molinari, R. L., S. Baig, D. W. Behringer, G. A. Maul, and R. Legeckis, Winter intrusions of the Loop Current, *Science*, in press, 1977.

Morrison, J. M., Nutrient and dissolved oxygen distributions in the Gulf of Mexico and adjacent regions, Master's thesis, Tex. A&M Univ., College Station, 1974.

Nowlin, W. D., Jr., Winter circulation patterns and property distributions, in *Contributions on the Physical Oceanography of the Gulf of Mexico, Tex. A&M Univ. Oceanogr. Stud.*, vol. 2, Gulf Publishing, Houston, Tex., 1972.

Nowlin, W. D., Jr., and J. M. Hubertz, Contrasting circulation patterns for the eastern gulf, in *Contributions on the Physical Oceanography of the Gulf of Mexico, Tex. A&M Univ. Oceanogr. Stud.*, vol. 2, Gulf Publishing, Houston, Tex., 1972.

Nowlin, W. D., Jr., and H. McLellan, A characterization of the Gulf of Mexico waters in winter, *J. Mar. Res.*, *25*(1), 29, 1967.

Robinson, M. K., Atlas of monthly mean sea surface and subsurface temperature and depth of the top of the thermocline: Gulf of Mexico and Caribbean Sea, *Tech. Rep. 73-8*, Scripps Inst. of Oceanogr., Univ. of Calif., San Diego, 1973.

Sturges, W., and J. P. Blaha, A western boundary current in the Gulf of Mexico, *Science*, *192*(4237), 367, 1976.

Whitaker, R. E., Seasonal variations of the steric and recorded sea level of the Gulf of Mexico, Master's thesis, Tex. A&M Univ., College Station, 1971.

Wüst, G., *Stratification and Circulation in the Antillean-Caribbean Basins*, part 1, Columbia University Press, New York, 1964.

(Received December 20, 1976;
revised July 20, 1977;
accepted July 26, 1977.)

Deep Sea Research 23, 1105-1113.

Bathymetry of the MODE-I region*

PATRICIA A. BUSH†

(*Received* 10 *November* 1975; *in revised form* 12 *July* 1976; *accepted* 14 *July* 1976)

Abstract—Depth soundings before and during the Mid-Ocean Dynamics Experiment (MODE-I) are integrated to produce bathymetric charts of the MODE-I region at scales of 1:500,000 and 1:250,000. Seven undersea features are named. The southwestern portion of the Bermuda Rise is characterized by rugged bottom topography generally striking north-northeast to south-southwest. Southeast of the Blake Bahama Outer Ridge, a zone of morphology paralleling the regional contours of the lower continental rise and associated deeps along many of the steep slopes on the Bermuda Rise suggest that the submarine terrain may be influenced by erosion by bottom currents.

INTRODUCTION

DURING the spring and summer of 1973 the field work for MODE-I was carried out by scientists from a number of different universities and institutions. The program, designed to investigate the properties of oceanic eddies (mesoscale motions) and their role in the general ocean circulation, is described by HAMMOND (1972). The experimental site (Fig. 1) is an abyssopelagic area extending east from the continental rise of the southeastern extremity of the Blake Bahama Outer Ridge across the Hatteras Plain onto the southwestern portion of the Bermuda Rise (Fig. 2). This region was chosen because it is remote from the Gulf Stream, logistically accessible, and encompasses an area containing both smooth and rough bottom topography.

To evaluate possible effects of the bottom configuration on mesoscale motions, bathymetric data are required. Only a small fraction of the enormous amount of bathymetric information obtained in the last 20 years is available in published form (PASCOE, 1972). LAUGHTON, ROBERTS and GRAVES (1973) catalogued deep ocean bathymetric charts and physiographic diagrams published before 1973. Although some of these charts cover the MODE-I region, as do others by PRATT (1968) and UCHUPI (1971), they are all generalized and reproduced at small scales.

To satisfy the bottom topography requirements for MODE-I, medium-scale bathymetric charts (Chart 1 and Chart 2) have been compiled from depth information collected before and during the experiment (BUSH, 1974). Additional high quality, random trackline sounding data are incorporated when practicable. The presentation of submarine terrain on the charts differs from the standard symbology generally employed by cartographers, i.e. using a single hue, blue, for marine areas and producing differentiation by changes in tone only (SHERMAN, 1972). To depict steep gradients more vividly, the conventional brown land tints are used for bottom features reaching above the 5000-m depth.

---

* MODE Contribution No. 57.

† Physical Oceanography Laboratory, Atlantic Oceanographic and Meteorological Laboratories, Environmental Research Laboratories, National Oceanic and Atmospheric Administration (NOAA), Miami, Florida 33149, U.S.A.

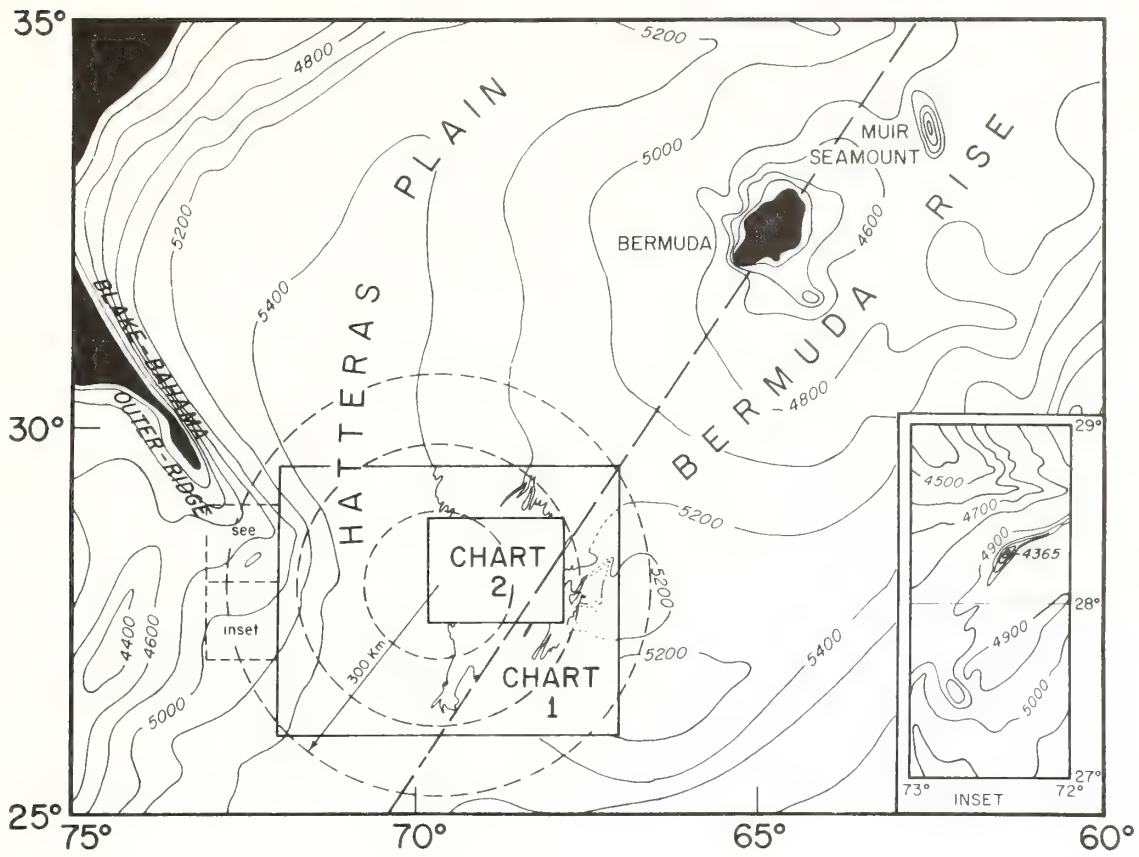


Fig. 1. Geographic limits of Charts 1 and 2. The dashed circles radiating from the center (28°N, 69°40′W) of the MODE-I field experiment area denote accurate mapping (100 km), pattern recognition (200 km), and extended pattern recognition (300 km) areas. Depth curves at 200-m intervals represent only gross features of shape and structure; long dashes show the extended axis of the 100-km wide zone containing the most striking undersea features on the Bermuda Rise in the MODE-I region. The axis parallels the grain of the bottom topography.

INSTRUMENTATION

Various sounding systems were used on the ships collecting the MODE-I bathymetric data. The NOAA ship *Researcher* is equipped with a 12-kHz Harris electronically stabilized narrow beam echo sounder (NBES) with an approximately 3°-wide single vertical effective beam (MAUL, 1970) and a Raytheon PFR calibrated at 800 fathoms s^{-1} (1463 m s^{-1}). The NASA ship *Vanguard* used an AN/UQN1E, which had a flush mounted transducer with a 40°-beam width, while the R.R.S. *Discovery* towed a fish containing a transducer with a beam angle of approximately $\pm 15°$ to half power points.

Other ships were equipped with various echo-sounding systems and transducer beam widths and some used graphical depth recorders calibrated at 1500 m s^{-1}. Vessel speeds ranged from 3 knots (1.54 m s^{-1}) during periods of towing to 14 knots (7.20 m s^{-1}) when steaming between oceanographic stations.

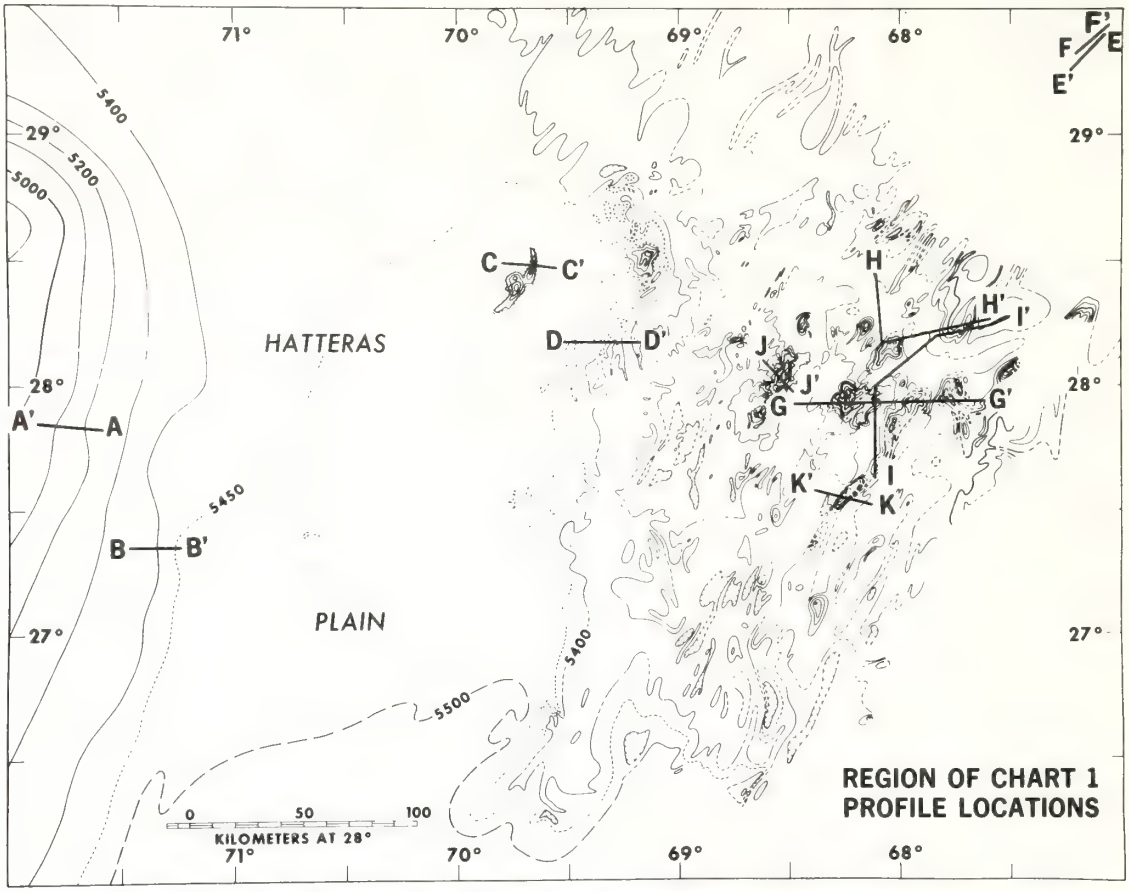


Fig. 2. Region of MODE-I bathymetry detailed on Chart 1. Heavy solid lines show profile placements according to ship trackline directions.

BATHYMETRIC DATA COLLECTION AND COLLATION

Because of diversified interests among participating scientists, depths were sounded intermittently and bathymetric data were collected opportunistically. Standard practices adopted to insure sounding survey accuracy (ADAMS, 1942; JEFFERS, 1960; MCALINDEN and ORLIN, 1969) were not consistent with the primary purpose of the experiment.

The NOAA ship *Researcher* made five cruises over the MODE-I region, generated trackline plots incorporating both satellite and Loran-C fixes, and using a narrow beam echo sounder system, obtained internally consistent bathymetric trackline crossings throughout the experiment. Using *Researcher* echograms and navigational data, bathymetric trackline plots containing maximum and minimum depths were constructed. These plots were used for fitting depth data along other ship tracklines.

The degree of acceptable trackline adjustment required to fit bathymetric data obtained from other ships was weighted according to estimates of the particular vessel's navigational capability, depth measuring system accuracy, data quality control, and knowledge of the sounding sampling rate.

NAVIGATION AND COLLATION OF SHIP TRACKLINES

MODE-I ships used satellite navigation systems or Loran C, or both. The NOAA ship *Researcher* used the SRN-9 satellite system (GUIER, 1966) and the Collins 53L-1/LR-102 Loran-C receiver. The region of study falls within the limits of the approximate groundwave range for Loran-C pairs SS7-W and SS7-Y, and the region is geometrically optimal. Corrections between Loran-C and satellite fixes were negligible during *Researcher* operations.

Few discrepancies in bathymetric fit occur on trackline crossings of the National Aeronautics and Space Administration (NASA) ship *Vanguard* and NOAA ship *Researcher*. Positioning of depth source information collected on the R.R.S. *Discovery* is based on Loran-C fixes because, in general, these were found to be more accurate than the satellite fixes (J. C. Swallow, personal communication). Malfunctioning navigation systems on the R.V. *Trident* and R.V. *Eastward* were reported and subsequent trackline positioning is dubious. Sounding data from the *Trident* are not included with the information shown on Chart 1 and Chart 2. Trackline locations of the *Eastward* are the least well established. On a small part of the *Eastward* trackline plot, errors exceeding 9 km are indicated by sounding discrepancies at other ship track crossings. Generally, errors in *Eastward* trackline positioning relative to those of the *Researcher* and *Vanguard* appear to be less than 4 km, as are those of the NOAA ships *Whiting* and *Mt. Mitchell* using Loran-A control. U.S.N.S. *Keathley* tracklines required a 4.5-km maximum adjustment in the western part of the MODE-I region where bathymetric data from the majority of participating ships determined the configuration of the lower continental rise. R.V. *Chain* and R.V. *Hunt* trackline positions are in good agreement with the *Researcher* and *Vanguard*, with some 3.5-km discrepancies in bathymetric fit. On rare occasions where no satisfactory adjustment was accomplished, short segments of cruise legs have been omitted.

Problems preventing accurate bottom depiction, especially over complex topography, are detailed by many writers, e.g. ADAMS (1942), HOFFMAN (1957), KRAUSE (1962) and COHEN (1970), and will not be reiterated. As MCALINDEN and ORLIN (1969), COHEN (1970), and OUDET (1973) have clearly shown, no foolproof analytical technique exists. Interpretation depends upon the experience and art of the individual analyst.

Trackline locations are superimposed on the depth curves shown on Chart 1 and Chart 2. Not indicated are areas where dense sounding information was collected, primarily aboard the *Discovery* during operation Minimode.

BATHYMETRIC DATA REDUCTION

Automatic cartography is not applicable when navigational control systems and data collection methods are ambiguous (MCALINDEN, 1970; MACKAY, 1972; LAUGHTON, ROBERTS and GRAVES, 1973). Conventional cartographic techniques were applied in the reduction and compilation of bathymetric data collected during MODE-I. Depth source information was read directly from the echo sounder trace. Echograms from the *Researcher*, *Vanguard*, *Eastward*, and *Hunt* (leg III 1/2) were examined for peaks and troughs, and representative sounding values were selected. Except in areas where regional bathymetry was developed, depth data collected on other vessels were recorded at fixed 5- or 10-min time intervals by personnel aboard the different ships or in the laboratories of the various institutions.

Although graphic recordings from the wide beam sources contain a multiplicity of side

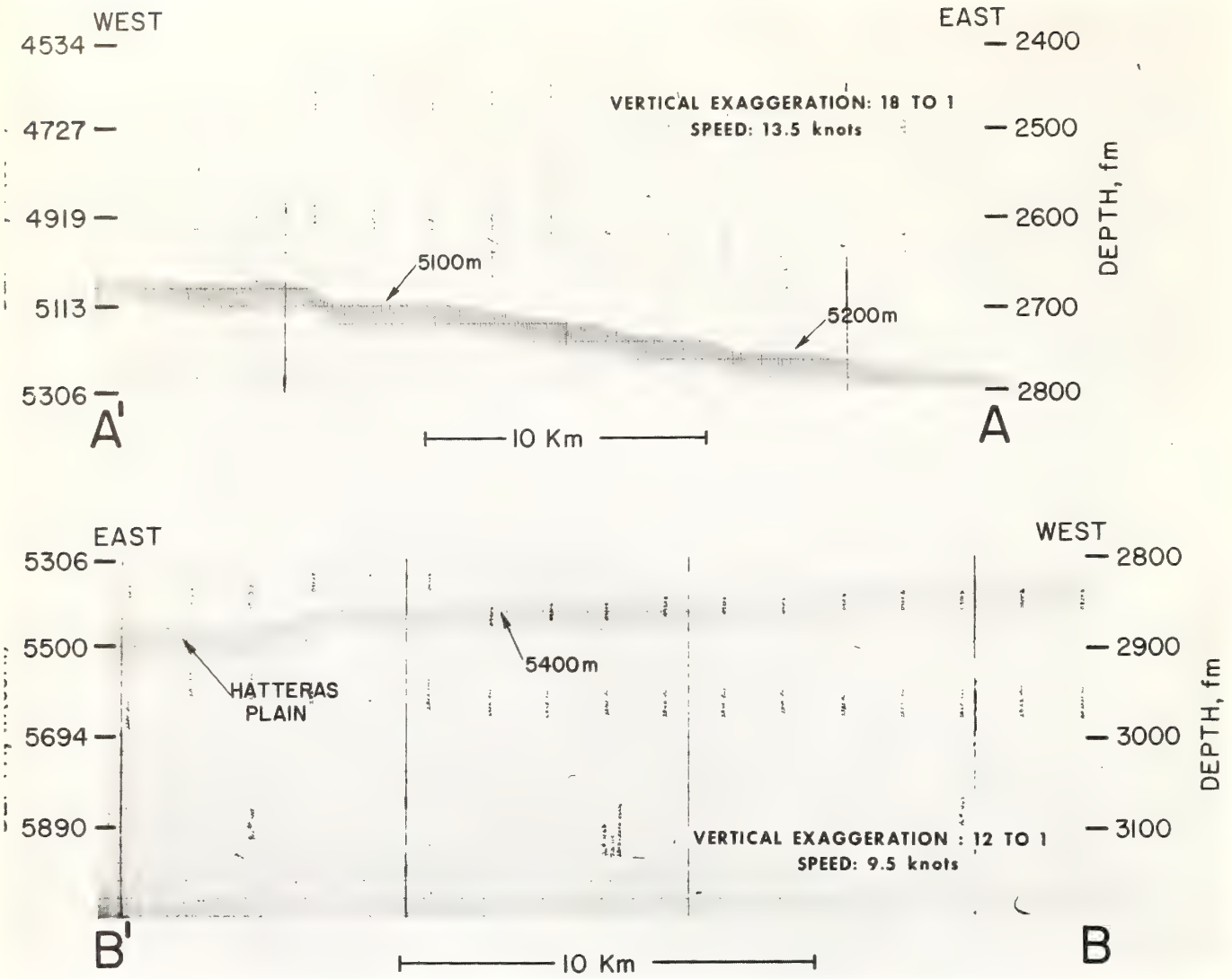


Fig. 3. Precision fathometer records from the *Researcher* showing 'steps' on the lower continental rise.

[facing p. 1108]

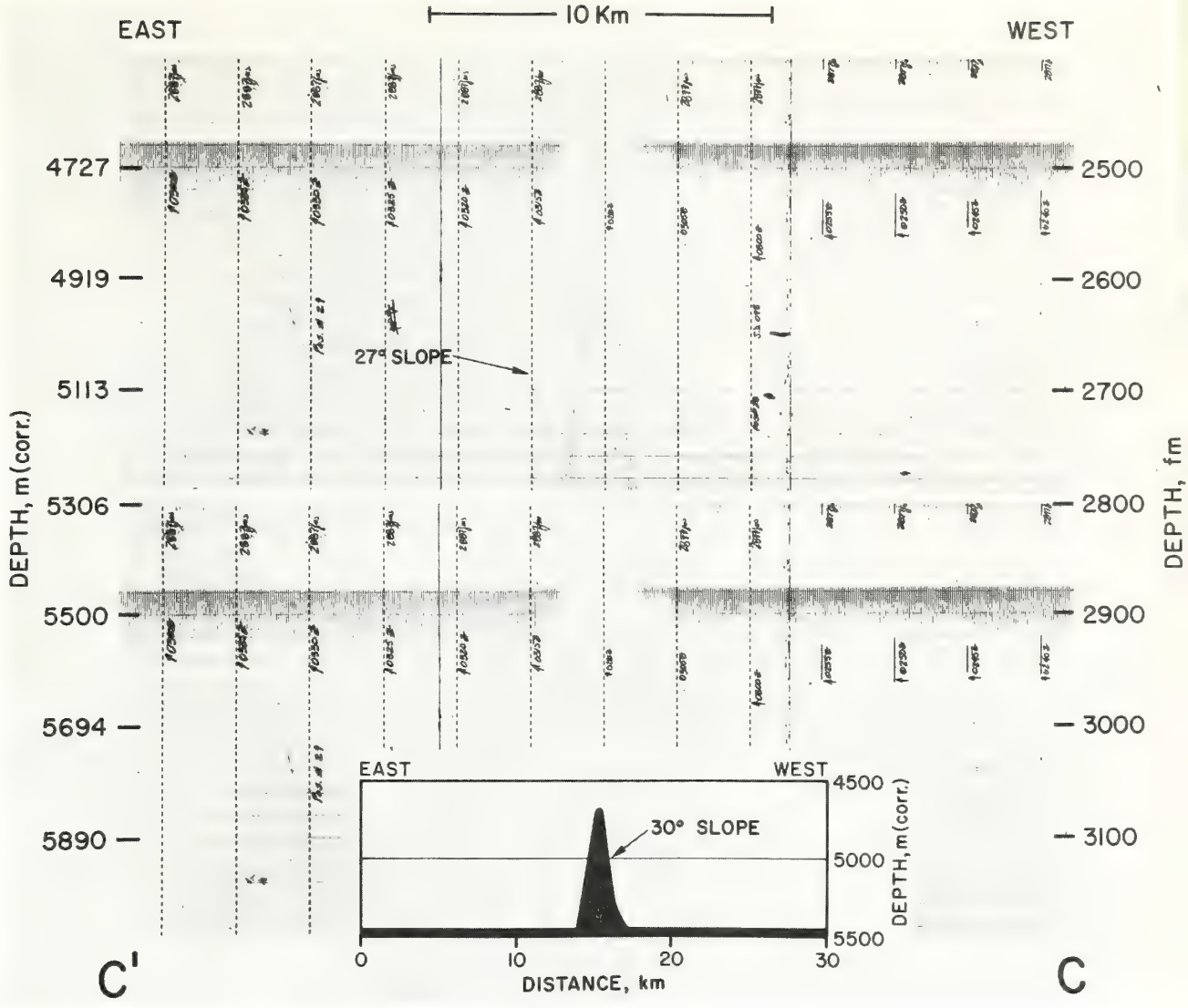


Fig. 4. Precision fathometer record from the *Researcher* crossing over the northeastern peak of Independence Knolls. The echo trace is faint; the inset is a graphic reproduction of a computer profile. Vertical exaggeration of echogram: 18 to 1; profile: 10 to 1.

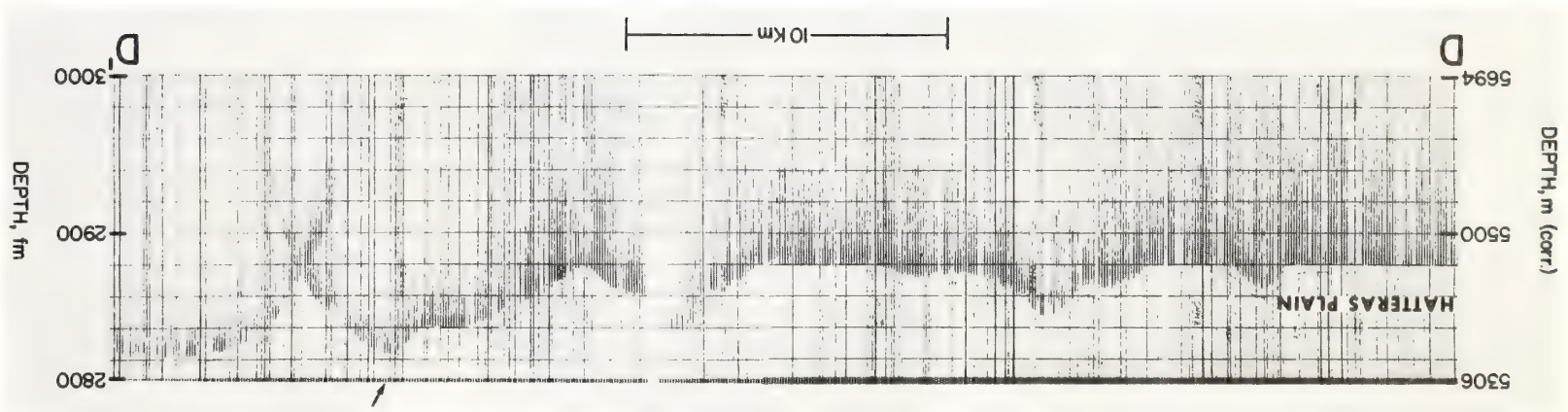


Fig. 5. Precision fathometer record from a *Vanguard* crossing over the Hatteras Plain–Bermuda Rise juncture. Arrow shows a low-amplitude ridge that appears to be about 50 km long (Chart 2) and terminates south of Eastward Knoll. The line above the echo trace was made by shipboard personnel.

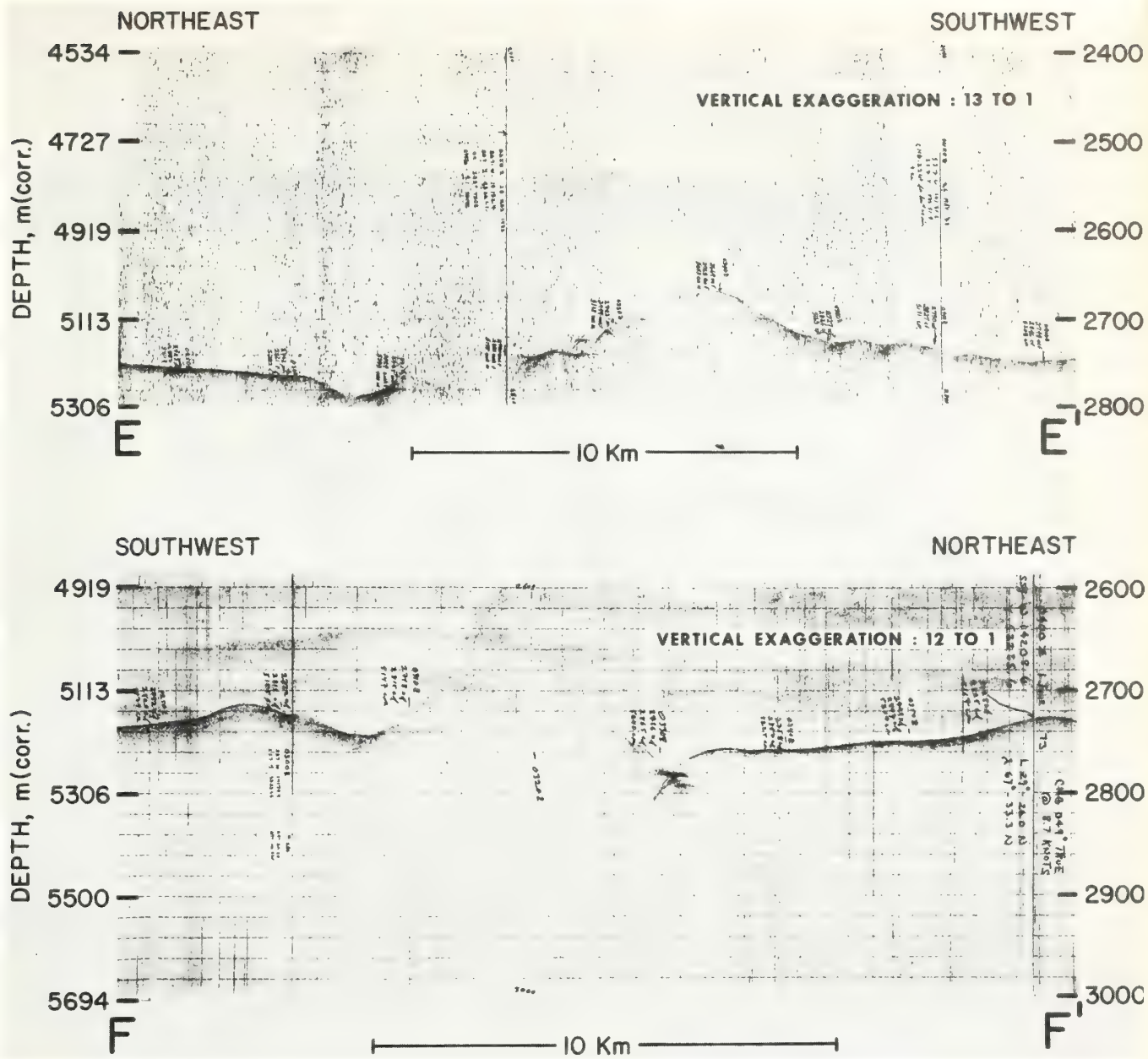


Fig. 6. R.V. *Hunt* echograms collected on different days over the same feature. Ship tracklines were run approximately parallel to one another and about 3 km apart. The vertical range was adjusted after profile E–E′ was recorded to center the echo trace on the paper. The channel to the northeast is normal to the bottom grain and the depression extends northeastward for a distance exceeding 5 km.

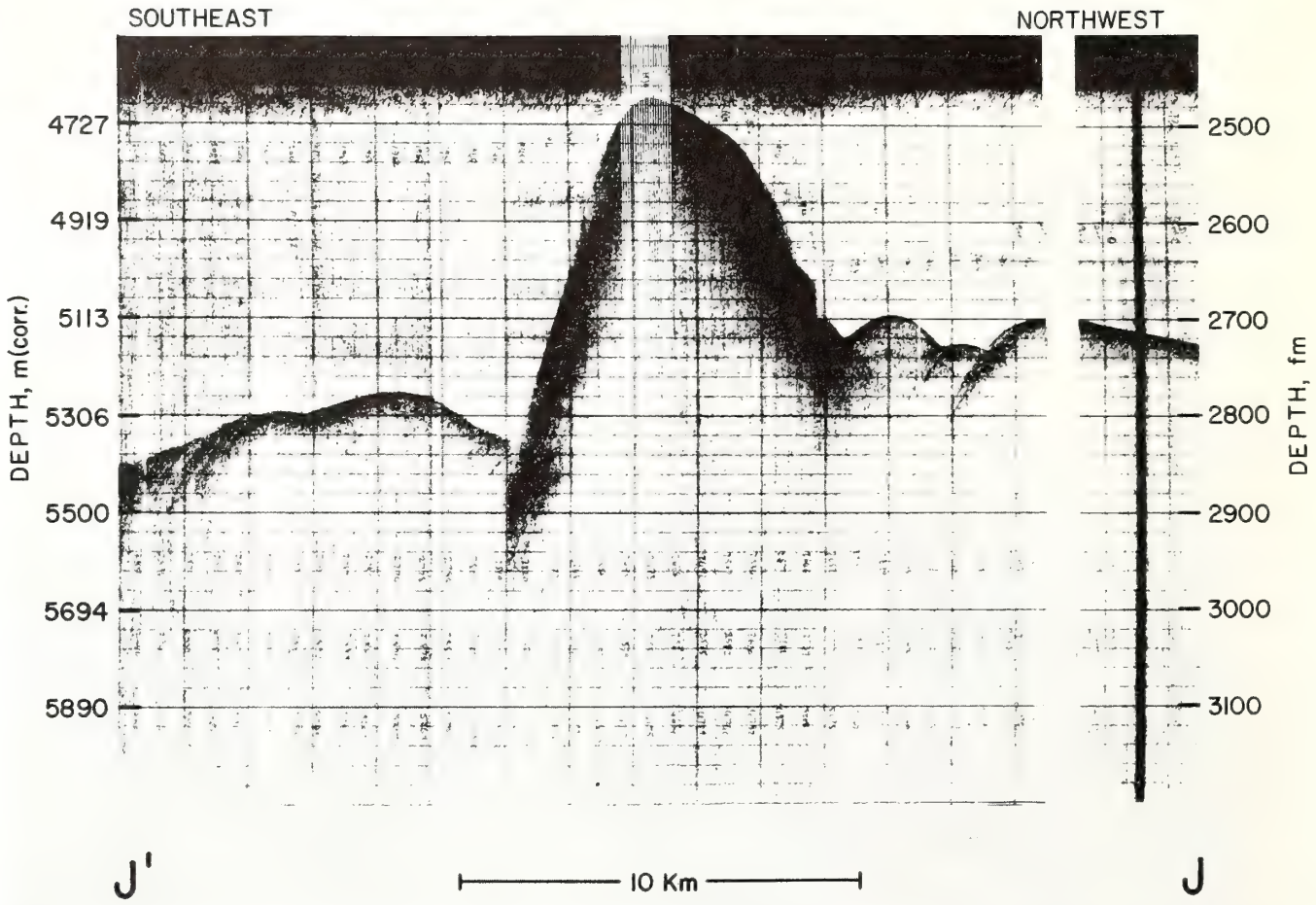


Fig. 8. Echogram collected aboard the *Discovery* over Swallow Knoll; photograph kindly furnished by Dr. J. C. Swallow. The middle peak of the NNE–SSW trending ridge-like feature is about 2.5 km north of this crossing. Note the typical depression at the base of the structure's southeastern slope. Vertical exaggeration: 13 to 1.

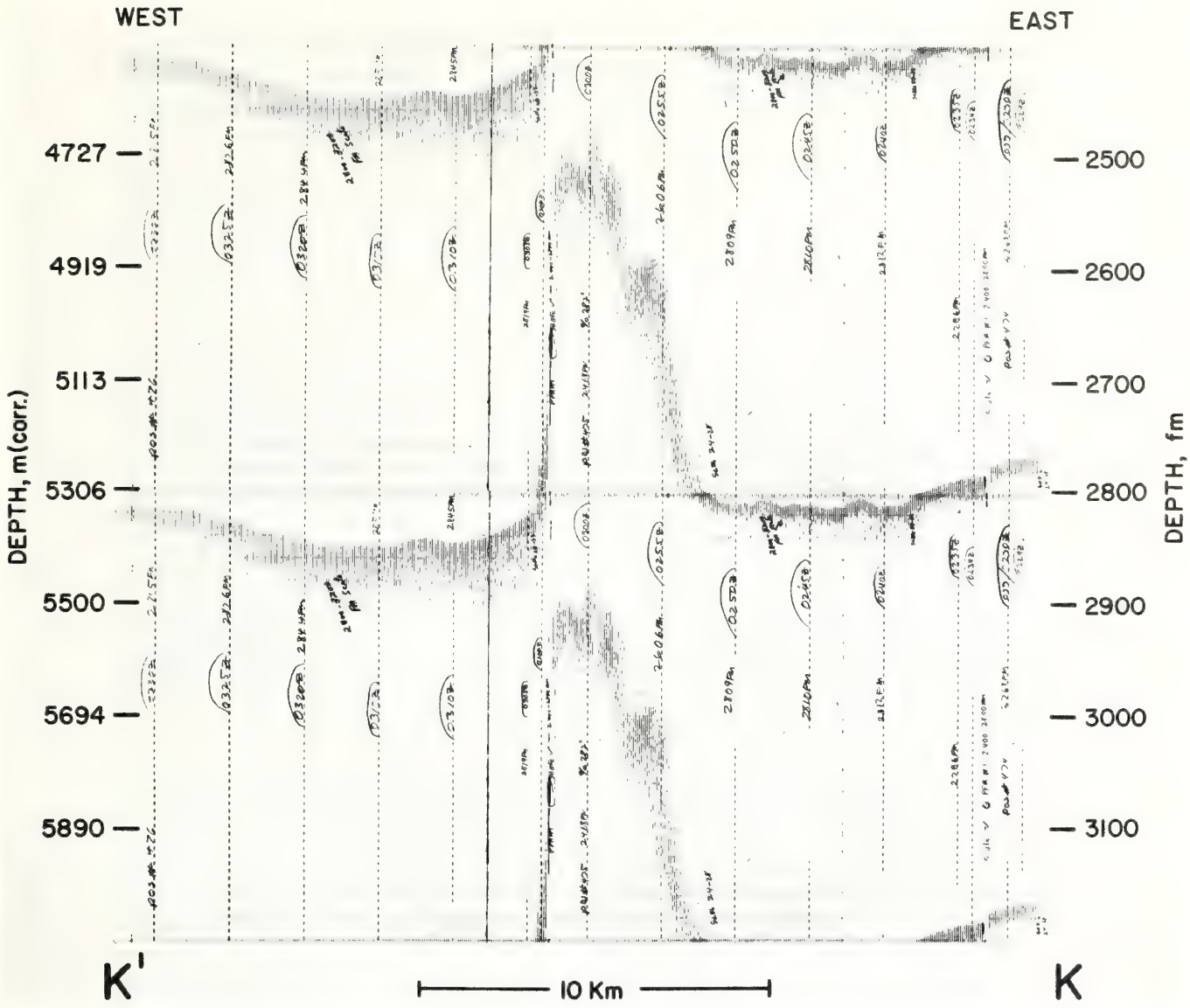


Fig. 9. Precision fathometer record from a *Researcher* crossing over Discovery Ridge. A side echo on the eastern slope of the structure obscures the feature delineation over the crest. The western slope has a 25° gradient before it breaks into a depression at the base of the ridge. Vertical exaggeration: 18 to 1.

echoes or hyperbolae, no correction for slope effect was attempted. In areas of complex and irregular bottom topography as encountered in the eastern portion of the MODE-I region, SHALOWITZ (1930), COHEN (1959), and others have determined that it is virtually impossible to represent the true bottom by slope correction procedures.

Depth information is corrected for sound velocity from area 14 in the tables computed by MATTHEWS (1939). The accuracy sacrificed from the implementation of Matthew's equation for sound speed in deep water (MAUL and BISHOP, 1970) is negligible relative to other errors introduced during opportunistic bathymetric data acquisition and considering the purpose for which the charts are constructed.

CONTINENTAL RISE

West of the study area the generally smooth surface of the lower continental rise is irregular. *Researcher* echograms recorded bottom profiles characterized by hills and valleys west of 72°W. LUSKIN, HEEZEN, EWING and LANDISMAN (1954) reported a similar bottom profile normal to the base of the continental rise and postulated that submarine canyons probably indent the lower part of the rise. Unpublished General Bathymetric Charts of the Ocean (GEBCO) show that two NE–SW trending ridges parallel the 4900-m isobath in this region (Fig. 1, inset). These ridges are 65 and 85 km long; one rises to a least depth of 4365 m and is cut on either side by channels about 40 m deep.

There are steplike successions of flat stretches on the downslope of the continental rise (Fig. 3, profiles A–A′ and B–B′). TOLSTOY and EWING (1949) noted similar steps as the sea floor drops down to the Sohm Plain northeast of Bermuda. The base of the continental rise that extends into the MODE-I region has a typically smooth gradient with a maximum slope of about 1/2°, but apparent 'steps' can be seen occasionally at approximately 100-m intervals.

HATTERAS PLAIN

The 5450-m isobath crossing the northern portion of the Hatteras Plain (Chart 1) is approximated because recorded depths from the echo sounding systems used by the different vessels varied by about 5 m. Depths in the plain reach 5500 m at the southern limits of the MODE-I region, but the depth curve could not be delineated accurately. A form line indicating the approximate location of the 5500-m isobath is shown on Fig. 2. The north–south slope of the portion of the Hatteras Plain sounded during MODE-I is about 1:5000 or 1/5 m km^{-1}.

TOLSTOY and EWING (1949) mention small 'pimples' interrupting the otherwise horizontal ocean floor. Similar protuberances occur at about 27°24′N between 70°37′ and 70°41′W. Only two or three small hills had been found on the Hatteras Plain (HEEZEN and LAUGHTON, 1963, p. 317) before preliminary operations for MODE-I. VOLKMAN (1972) first noted a seamount rising from the flat bottom in this region. Echograms recorded during MODE-I operations show the two peaks of Independence Knolls rising from the plain depth of 5460 m on what appears to be a single NNE–SSW trending base. The southwestern summit of the feature rises over 900 m (BUSH, 1975). Figure 4, profile C–C′, shows the northeastern peak cresting at 4684 m. Between its pinnacle and the 5300-m depth on the west, the knoll gradient exceeds 30°. The eastern side has a gradient of 27° and drops downslope with a steep regularity. A detailed survey over Independence Knolls might provide evidence that this feature is in actuality a double peaked seamount.

At the eastern edge of the plain another abrupt rise, Eastward Knoll, reaches an approximate depth of 4771 m. A least depth of 4730 m (uncorrected) is extrapolated from an

east–west trackline echogram because the echo sounder trace disappears before the vessel passes over the crest. The true position and feature delineation of Eastward Knoll are somewhat obscured by malfunctioning navigational instrumentation. Summits of both Eastward and southwestern Independence knolls are bifurcate.

BERMUDA RISE

As the plains abut the Bermuda Rise undulations on the ocean floor are recorded (Fig. 5, profile D–D′). Echograms collected on the upslope show many small hills and valleys interrupting the surface of the bottom. Although some of the features appear to be continuous, numerous microstructures have dimensions smaller than the sounding line spacing or an amplitude of relief that cannot be resolved on the scales of Charts 1 and 2. The submarine terrain of the plain and rise abutment is pinnate relative to the bottom configuration on the Bermuda Rise.

Bottom topography on the Bermuda Rise trends NNE–SSW. Striking undersea features on the rise in the MODE-I region are contained largely within a zone approximately 100 km wide. The axis of this zone trends N35°E (Fig. 1), paralleling a scarp zone to the east (HEEZEN, THARP and EWING, 1959, p. 76). Echograms between St. George's and the experimental site show the rugged bottom terrain continuing upslope (Fig. 6, profiles E–E′, F–F′). The topographic grain on the Bermuda Rise is parallel to that of the mid-Atlantic Ridge and normal to the axis of the New England Seamount Chain.

The part of the Bermuda Rise sounded during MODE-I demonstrates the topographic complexity of the area. A seamount, an elongated NNE–SSE trending ridge, and several knolls break the undulating bottom (Charts 1–2). Researcher Seamount (Fig. 7, profiles G–G′ and I–I′), sounded extensively from the *Discovery*, has an involuted topography too

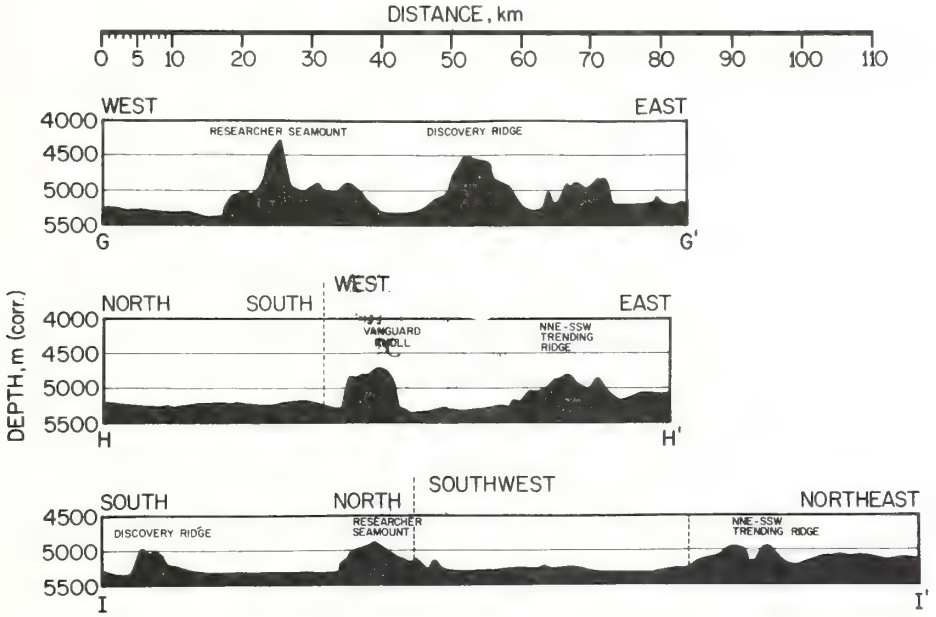


Fig. 7. Graphic reproductions of computer profiles from fathograms collected aboard the *Researcher*. Dashed lines indicate course changes. Vertical exaggeration: 10 to 1.

complicated to portray accurately on medium-scale charts. The seamount pinnacle rises about 1100 m from the surrounding bottom terrain. Five peaks appearing along the quadruply branching apex of the undersea feature are separated from a southeastern summit by a channel trending NNE–SSW. A basin abutting the western edge of the seamount also trends NNE–SSW. The entire structure is a complexity of ridges and channels, hills and valleys. Swallow Knoll (Fig. 8, profile J–J′) has a NNE–SSW trending contiguous axis with a tridentated summit that slopes steeply to the southeast into a depression at the base of the knoll. Vanguard Knoll (Fig. 7, profile H–H′) has two peaks, and Chain Knoll appears to have only one; typical depressions occur at the bases of both mounts. The 100-km extent of Discovery Ridge is assumed because of paucity of depth data. Figure 9, profile K–K′, shows a profile normal to the ridge.

Characteristically many of the structures are partially surrounded at their base by shallow moats, as are those of the New England Seamount Chain (UCHUPI, PHILLIPS and PRADA, 1970) and others in the Pacific Ocean (SCRIMGER and HALLIDAY, 1971). Although DIETZ and MENARD (1953) and others have attributed moats or encircling depressions around seamounts and island bases to crustal depression, PRATT (1968) attributes the depressions southeast of Bermuda to the failure of terrigenous sediment to reach them. The partial burial of seamounts by abyssal plain sediments suggests that these depressions more likely result from erosion or nondeposition rather than loading. Most of the mesomorphology and much of the micromorphology on the Bermuda Rise have associated parallel deeps trending NNE–SSW with many smaller channels cutting normal to the undersea topographic grain.

CONCLUSION

Few geological or geophysical investigations have been undertaken within the MODE-I region, so the genesis of the geomorphology of the area is little known.

SCHNEIDER, FOX, HOLLISTER, NEEDHAM and HEEZEN (1967), using compass oriented seafloor photographs, echograms, and sediment cores show that strong currents occur between the lower continental rise off eastern North America and the adjoining plain. Evidence of parallel ridges and troughs along the regional contours west of the MODE-I region suggests that bottom currents may have some influence in forming the morphology of the lower continental rise.

The *Aries* current measurements (CREASE, 1962) indicate energetic mesoscale motions in the interior of the western North Atlantic. The *Aries* observations show that, on the western edge of the Bermuda Rise, current speeds increase and current directions tend to be more meridional with increasing depth (SWALLOW, 1971).

Many of the steeply sloped undersea structures have associated deeps, and many of the microstructures rising from the bottom have parallel or partially encircling depressions or troughs alongside. Echograms show little sediment accumulation in the channels and troughs. Current erosion is indicated, but MODE-I oceanic eddy studies have not as yet provided supporting evidence because few experiments were conducted at depth. Conversely, it appears that the bottom topography may influence the mesoscale motions (GOULD, SCHMITZ and WUNSCH, 1974; OWENS and BRETHERTON, 1975; FREELAND, RHINES and ROSSBY, 1975).

No far-reaching conclusions can be generated from bathymetric data alone. The nature of the sea bottom in the MODE-I region proves to be more complicated than previously assumed. A 5- to 10-km grid pattern bathymetric survey over the area would provide the

means to depict a submarine terrain of even greater complexity far more accurately than is presently possible.

Acknowledgements—This work was supported in part by the office of the International Decade of Ocean Exploration of the National Science Foundation under funding agreement AG-385.

The bathymetric data reported in this paper result from the efforts of many people. The author is indebted to the officers, technicians, crews, and scientific personnel aboard all the ships employed in echogram collection. Special thanks are given to the MODE-I Chief Scientists for furnishing shiptrack and sounding information. Grateful appreciation is expressed particularly to M. CHAFFEE, Woods Hole Oceanographic Institution, for logistical liaison, to J. MCALINDEN for his helpful cartographic advice, to D. RAHN and R. MULLER, National Oceanic and Atmospheric Administration, National Ocean Survey, Reproduction Division, for their assistance in reproducing the charts, and to D. V. HANSEN for his continued encouragement and support.

REFERENCES

ADAMS K. T. (1942) *Hydrographic manual. Special Publications. United States Coast and Geodetic Survey*, No. 143, revised edition, 940 pp.

BUSH P. A. (1974) MODE region bathymetry. Abstract. *Transactions. American Geophysical Union*, **55**, 679.

BUSH P. A. (1975) Bathymetry of the MODE-I region. *MODE Hot Line News*, No. **70**, 1–2. Woods Hole Oceanographic Institution, Woods Hole, Mass. (Unpublished document.)

COHEN P. M. (1959) Directional echo sounding on hydrographic surveys. *International Hydrographic Review*, **36**, 29–42.

COHEN P. M. (1970) *Bathymetric navigation and charting*, United States Naval Institute, Annapolis, Maryland, 138 pp.

CREASE J. (1962) Velocity measurements in the deep water of the western North Atlantic. *Journal of Geophysical Research*, **67**, 3173–76.

DIETZ R. S. and H. W. MENARD (1953) Hawaiian Swell, deep arch, and subsidence of the Hawaiian Islands. *Journal of Geology*, **61**, 99–113.

FREELAND H. J., P. B. RHINES and H. T. ROSSBY (1975) Statistical observations of the trajectories of neutrally buoyant floats in the North Atlantic. *Journal of Marine Research*, **33**, 383–404.

GOULD W. J., W. J. SCHMITZ, JR. and C. WUNSCH (1974) Preliminary field results for a Mid-Ocean Dynamics Experiment (MODE-I). *Deep-Sea Research*, **21**, 911–931.

GUIER W. H. (1966) Satellite navigation using integral Doppler data—the AN/SRN-9 equipment. *Journal of Geophysical Research*, **71**, 5903–5910.

HAMMOND A. L. (1972) Physical oceanography: planning for a major experiment. *Science*, **176**, 268–269.

HEEZEN B. C. and A. S. LAUGHTON (1963) Abyssal plains. In: *The sea*, M. W. HILL, editor, Interscience, Vol. 3, pp. 312–364.

HEEZEN B. C., M. THARP and M. EWING (1959) The floors of the oceans; I, the North Atlantic. *Special Papers of the Geological Society of America*, **65**, 122 pp.

HOFFMAN J. (1957) Hyperbolic curves applied to echo sounding. *International Hydrographic Review*, **34**, 45–55.

JEFFERS K. B. (1960) *Hydrographic manual. Publications of the United States Coast and Geodetic Survey*, 20–2, 283 pp.

KRAUSE D. C. (1962) Interpretation of echo sounding profiles. *International Hydrographic Review*, **39**, 65–123.

LAUGHTON A. S., D. G. ROBERTS and R. GRAVES (1973) Deep ocean floor mapping for scientific purposes and the application of automatic cartography. *International Hydrographic Review*, **50**, 125–148.

LUSKIN B., B. C. HEEZEN, M. EWING and M. LANDISMAN (1954) Precision measurement of ocean depth. *Deep-Sea Research*, **1**, 131–140.

MACKAY J. M. (1972) Automation of hydrographic surveying. *International Hydrographic Review*, **49**, 149–166.

MATTHEWS D. J. (1939) *Tables of the velocity of sound in pure water and sea water for use in echo-sounding and sound ranging*, H. D. 382, Hydrographic Department, Admiralty, 52 pp.

MAUL G. A. (1970) Precise echo sounding in deep water. *International Hydrographic Review*, **47**, 93–106.

MAUL G. A. and J. C. BISHOP, JR. (1970) Mean sounding velocity. A brief review. *International Hydrographic Review*, **47**, 85–92.

MCALINDEN J. (1970) Oceanographic mapping—the key to Davy Jones's locker. Paper presented at the ASP/ACSM fall Tech. Conference, Denver, Colorado. Published by U.S. Department of Commerce, Rockville, Maryland, 10 pp.

MCALINDEN J. and H. ORLIN (1969) Mapping our new sea frontier. *Surveying and Mapping*, **29**, 71–86.

OUDET L. (1973) The value of a nautical chart. *International Hydrographic Review*, **50**, 149–161.

OWENS B. and F. BRETHERTON (1975) A numerical simulation of the MODE-I statistics. *MODE Hot Line News*, No. **76**, 1–4, Woods Hole Oceanographic Institution, Woods Hole, Mass. (Unpublished document.)

PASCOE L. N. (1972) World bathymetric charts. *International Hydrographic Review*, **49**, 153–160.

PRATT R. M. (1968) Continental shelf and slope of the United States: physiography and sediments of the deep-sea basin. *Professional Papers, United States Geological Survey*, **529-B**, 44 pp.

SCHNEIDER E. D., P. J. FOX, C. D. HOLLISTER, H. D. NEEDHAM and B. C. HEEZEN (1967) Further evidence of contour currents in the western North Atlantic. *Earth and Planetary Science Letters*, **2**, 351–359.

SCRIMGER J. A. and W. HALLIDAY (1971) Bathymetry of Pacific seamounts Bowie and Union. *Deep-Sea Research*, **18**, 123–126.

SHALOWITZ A. L. (1930) Slope corrections for echo sounding. *Special Publications. United States Coast and Geodetic Survey*, No. 165, 23 pp.

SHERMAN J. C. (1972) Topography and submarine mountains: a special problem of terrain representation. *Surveying and Mapping*, **32**, 341–347.

SWALLOW J. C. (1971) The *Aries* current measurements in the western North Atlantic, *Philosophical Transactions of the Royal Society*, (A), **270**, 451–460.

TOLSTOY I. and M. EWING (1949) Atlantic hydrography and the Mid-Atlantic Ridge. *Bulletin of the Geological Society of America*, **60**, 1527–1540.

UCHUPI E. (1971) Bathymetric atlas of the Atlantic, Caribbean and Gulf of Mexico. Woods Hole Oceanographic Institution, Chart No. 3, Ref. No. 71–72. (Unpublished manuscript.)

UCHUPI E., J. D. PHILLIPS and K. E. PRADA (1970) Origin and structure of the New England Seamount Chain. *Deep-Sea Research*, **17**, 483–494.

VOLKMAN G. (1972) A MODE seamount. *MODE Hot Line News*, No. 21, p. 3, Woods Hole Oceanographic Institution, Woods Hole, Mass. (Unpublished document.)

Marine Geodesy 1, No. 1, 103-116.

The Advection Effect of Planetary Vorticity on Sea Level Slope in a Western Boundary Current

Frank Chew

National Oceanic and Atmospheric Administration
Atlantic Oceanographic and Meteorological Laboratories
Miami, Florida

Western boundary currents, such as the Gulf Stream, are often modeled as flows in near cross-stream geostrophic balance with paths that are straight or nearly straight. The effect of planetary vorticity advection on the downstream sea-level slope in these rectilinear flows is re-examined and found negligible. Instead, the re-examination reveals a much greater effect of the ageostrophic component of the horizontal divergence in determining the downstream slope. Overlooked in previous studies is the geostrophic component of the horizontal divergence because of a hidden assumption of parallel flow. To avoid this pitfall, we employ a natural coordinate system to follow precisely the downstream direction. Further, we differentiate between weak geostrophic flows with small accelerations and flows in cross-stream geostrophic balance where downstream acceleration might be appreciable. Two Rossby numbers are employed: a small cross-stream number (≤ 0.01) to describe the near cross-stream balance, and a large downstream number (≤ 0.1) to describe the large downstream accelerations that are found in western boundary flows. Finally, by means of a scale analysis we show that over the whole range of possible Rossby numbers, the advection effect of planetary vorticity on down-

stream sea level slope is negligible compared to the effect of the ageostrophic component of the horizontal divergence. Some new data on the nearshore gradient of the Reynolds stress are also included.

The slope of the sea level along continental boundaries is a controversial issue (Mourad, 1975). In addressing this issue, I will confine attention to the Atlantic coast where the Gulf Stream flows offshore.

Sturges' (1974) discussion of the effect of the Gulf Stream on the sea-level slope along the Atlantic coast contains three elements. The first element concerns deep water steric leveling, and was examined by Fischer (1976). The second element concerns the effect of an offshore Reynolds stress gradient; some recent data provided by Brooks (personal communication, 1976) will serve to assess this element. Sturges' third element concerns a presumed effect of the variation of the Coriolis parameter with latitude, or equivalently, the advection effect of planetary vorticity. He explains it as follows:

> It is generally accepted that the flow in a western boundary current is in geostrophic balance in the cross-stream direction. That is, the momentum balance is given to a very good approximation by
>
> $$fv = i_x g \tag{1}$$
>
> where f is the Coriolis parameter, v is the downstream velocity (here to the north, taken to be in the y direction), i_x is the slope of the sea surface in the x direction, and g is gravity. The total change in level across the flow Δh is given by the cross-stream integral of (1) after rearranging
>
> $$\Delta h = f\langle v\rangle X/g. \tag{2}$$
>
> To see the effect of a current flowing to a different latitude, we differentiate (2) with respect to y:
>
> $$(\partial/\partial y)\Delta h = (f/g)\,(\partial/\partial y)\langle v\rangle X + (\langle v\rangle X/g)\,(\partial f/\partial y). \tag{3}$$
>
> The left-hand side is the meridional slope of sea level along the coast, if the offshore edge of the current is assumed to remain level. . . . The use of (2) for determining sea level slopes is usually called geostrophic leveling.
>
> The first term on the right in (3) is the meridional change in the surface transport per unit depth. The second term is the result of variation of Coriolis parameter with latitude. If these terms can be evaluated they will provide an independent test of the meridional slope . . ."

It will be shown that (3) is misleading because it contains a hidden assumption of parallel flow whose effect, among others, is to discard the geostrophic component of the horizontal divergence. When the assumption is removed, the advection effect of planetary vorticity on downstream sea-level slope is found proportional not to the speed of the horizontal velocity, but to the speed difference between the horizontal velocity and its geostrophic component. This speed difference is small, even where downstream acceleration is appreciable. In consequence, the effect of the advection of planetary vorticity on downstream sea-level slope is negligible compared to the effect of the ageostrophic component of the horizontal divergence.

The Reynolds Stress Gradient

Of the two right-hand terms in (3), Sturges finds the latter one to be dominant. To reconcile the resulting meridional slope i_y with the downstream momentum balance, he uses an equation that is eventually simplified to

$$(\partial/\partial x)\langle u'v'\rangle = -gi_y. \tag{4}$$

According to Sturges, this equation is valid in the "region many kilometers in width extending along the inshore edge of the stream where the speed falls below 30 cm/s . . ." Using the $\langle u'v'\rangle$ data reported by Schmitz and Niiler (1969), Sturges evaluates the left-hand side of (4). Further, he notes, off Miami the stress distribution also shows not only a gradient of the same sign, but one of even larger magnitude. Nevertheless, inspection of the pertinent data reveals that the data are mostly in a region outside where (4) is assumed to hold. Hence Sturges' use of the data represents a shoreward extrapolation.

This extrapolation has no support. Figure 1 is a cross-stream plot of the stress quantity that I. H. Brooks (personal communication, 1976) computed from new data off Miami. The westernmost station at 2 km east of the shoreline shows a small positive $\langle u'v'\rangle$. But the next station 2 km farther east shows a negative $\langle u'v'\rangle$ of over 0.02 m^2/s^2. In the framework of (4), Brooks' data means a sea level sloping up toward the north, the opposite of the slope argued by Sturges.

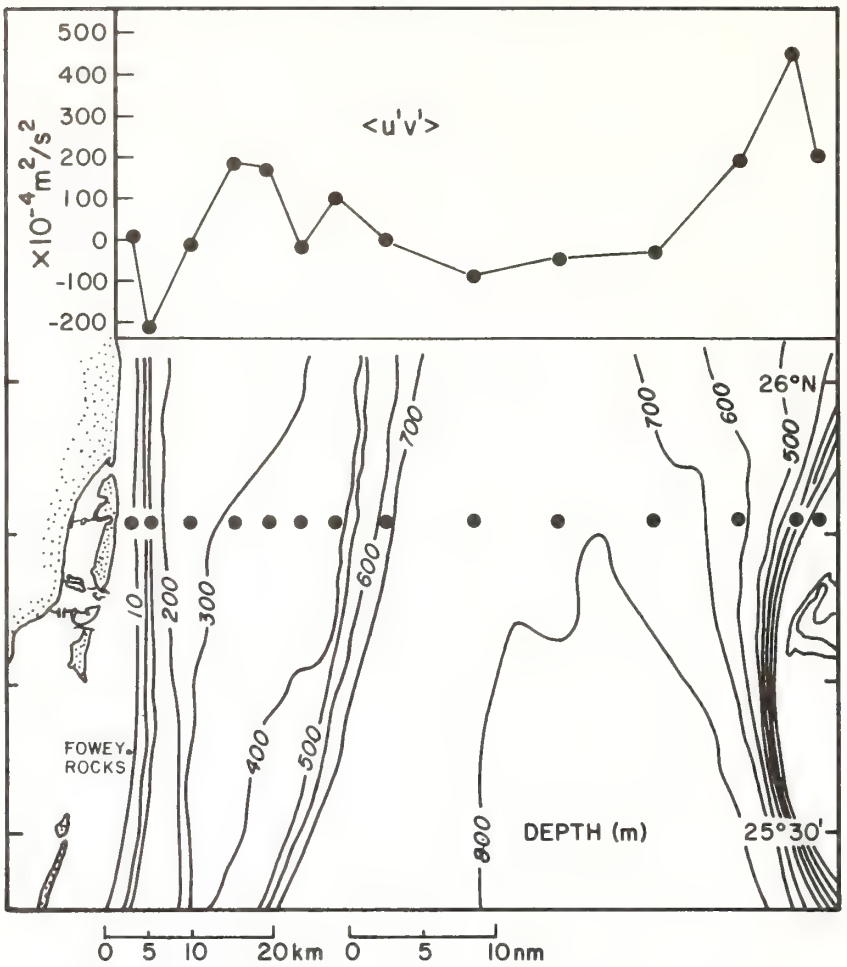


Figure 1. The east–west distribution of <u'v'> off Miami, as computed by Brooks (1976) from data he collected in the period May 16 through August 13, 1974. At each of the 14 stations spanning the channel there were 43–45 measurements of the surface velocity.

The Effect of Planetary Vorticity Advection

The Natural Coordinate System

In order to follow the downstream direction exactly a natural coordinate system is used. Let **V** be the horizontal velocity vector, and **k** the

unit vertical vector positive upward. The unit vector **s** is defined by $\mathbf{V} = V\mathbf{s}$, and so points exactly downstream. The unit vector n is defined by $\mathbf{n} = \mathbf{s} \times \mathbf{k}$ and points to the right of V. The coordinate system is thus a mutually perpendicular frame of curvilinear coordinates that is defined, at any point, by the set of three orthogonal unit vectors (**s**, **n**, **k**).

The Equations of Motion and Rossby Numbers

Let h denote the height of the sea surface above a level surface. Then, in the absence of dissipative or driving (winds or thermohaline) forces, the equation governing the steady state motion of the sea surface is

$$\mathbf{V}\cdot\nabla\mathbf{V} = -\mathbf{k}xf\mathbf{V} - g\nabla h \tag{5}$$

where ∇ is the horizontal del operator. The left-hand term has the components:

$$\mathbf{V}\cdot\nabla\mathbf{V} = V(\partial V/\partial s)\mathbf{s} - KV^2\mathbf{n}, \tag{6}$$

where K is the horizontal flow curvature and KV^2 is the centripetal acceleration. Hence the component of (5) along the flow is the Bernoulli equation

$$(\partial/\partial s)\,(gh + V^2/2) = 0, \tag{7}$$

while the component in the cross-stream direction is

$$KV^2 + fV = g\partial h/\partial n. \tag{8}$$

In oceanographic parlance there is cross-stream geostrophic balance when the ratio of the centripetal to the Coriolis accelerations, a cross-stream Rossby number, is of the order

$$KV^2/fV = KV/f \sim 0.01, \tag{9}$$

where the sign $\sim$ denotes order of magnitude equality. In the Gulf Stream where $V \sim 1 m/s$, the balance holds wherever the radius of curvature is 1,000 km or more; i.e., where the flow is straight or nearly straight. In this case, by neglecting the centripetal acceleration, (8) becomes

$$fV = g\partial h/\partial n. \tag{10}$$

An important feature here is that (10) still allows the flow to accelerate downstream by crossing lines of constant h in accordance with (7), as illustrated in the work of Charney (1955), who modeled the Gulf Stream as an inertial boundary layer. This feature can be made explicit by introducing the coordinate N in the direction of ∇h, and the flow direction Θ relative to lines of constant h, positive toward higher and negative toward lower h. In these coordinates (7) and (10) can be written

$$V\partial V/\partial s = -g\partial h/\partial s = -g(\partial h/\partial N)\sin\Theta, \tag{11}$$

and

$$fV = g\partial h/\partial n = g(\partial h/\partial N)\cos\Theta. \tag{12}$$

In contrast the geostrophic current V_g, obtained by setting the left-hand side of (5) to zero, or equivalently by setting Θ to zero in both (11) and (12), is

$$fV_g = g(\partial h/\partial N). \tag{13}$$

From (11) and (13) we get

$$\sin\Theta = (g\partial h/\partial s)/(g\partial h/\partial N) = -(V\partial V/\partial s)/fV_g, \tag{14}$$

a downstream Rossby number. In a more or less straight flow that accelerates rapidly downstream $\sin\Theta$ is much larger than KV/f.

Confluent and Parallel Flows

The downstream differentiation of (10) gives

$$f(\partial V/\partial s) + V(\partial f/\partial s) = g(\partial/\partial s)(\partial h/\partial n). \tag{15}$$

The right-hand term relating to the downstream change of the cross-stream sea-level slope also contains information on the confluence of the flow. For the rectilinear flow pattern shown in Figure 2A, the orientations of the unit vectors **(s,n)** vary in space. While constant along a straight streamline, **n** changes direction along a normal to the stream-

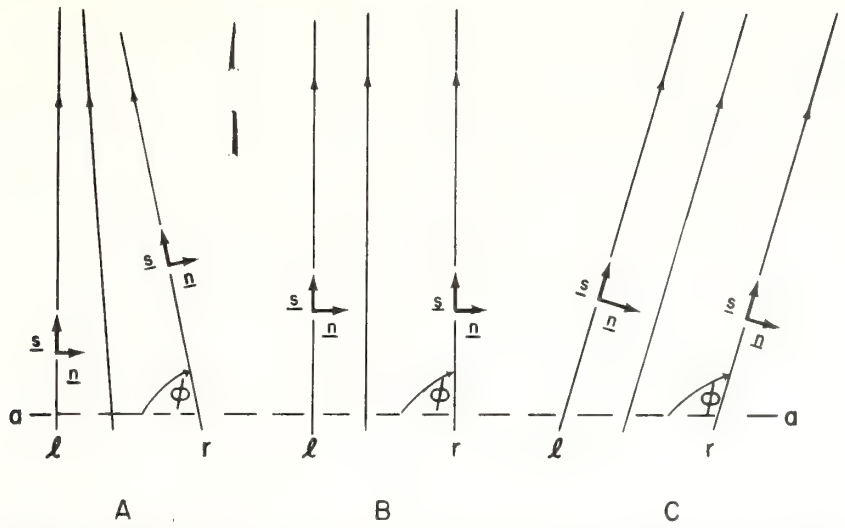


Figure 2. Three schematic patterns of straight flow. The angle ϕ measures the orientation of a streamline with respect to the arbitrary line a-a. 2A represents a confluent flow, 2B and 2C parallel flows. The unit vectors **s** and **n** are also shown.

lines according to

$$(\partial \mathbf{n}/\partial n) = -\mathbf{s}(\partial \phi/\partial n), \tag{16}$$

where ϕ is the angle of a streamline measured positive clockwise from a fixed common reference.

The angle change $(\partial\ \phi/\partial n)$ may be positive, negative, or zero, depending, respectively, on whether the streamlines are difluent, confluent, or parallel. The last case corresponds to streamline patterns illustrated in Figures 2B and 2C. Hence, as detailed in Haltiner and Martin (1957, p. 343) and in Chew (1974), for a straight confluent or difluent flow

$$(\partial/\partial s)(\partial h/\partial n) = (\partial/\partial n)(\partial h/\partial s) - (\partial h/\partial n)(\partial \phi/\partial n). \tag{17}$$

The combination of (10), (15), and (17) gives

$$g(\partial/\partial n)(\partial h/\partial s) = f(\partial V/\partial s) + fV(\partial \phi/\partial n) + V(\partial f/\partial s). \tag{18}$$

And, in turn, its integration across a flow from the streamline ℓ at the

left edge to the streamline r at the right edge, gives

$$g(\partial/\partial s)\,(h_r - h_\ell) = f(\partial/\partial s)\int_\ell^r V\,dn + \int_\ell^r fV(\partial\phi/\partial n)\,dn + \int_\ell^r V(\partial f/\partial s)\,dn. \tag{19}$$

On the right-hand side, the first term represents the effect of downstream change in surface transport; the second term the confluence effect; and, because the total horizontal speed V enters, the third term represents the effect of the total advection of planetary vorticity. These effects, all evaluated between streamlines ℓ and r, jointly determine the difference in downstream sea-level slopes along the same streamlines, as represented on the left-hand side of (19).

The Overlooked Assumption

The straight, parallel flows in Figures 2B and 2C may be obtained from Figure 2A by rotating the streamlines about the line a-a until the angle ϕ is the same for all streamlines. With $(\partial\,\phi/\partial n) = 0$, (19) reduces to

$$g(\partial/\partial s)\,(h_r - h_\ell) = f(\partial/\partial s)\int_\ell^r V\,dn + \int_\ell^r V(\partial f/\partial s)\,dn, \tag{20}$$

which is identical to (3) except for notation. It follows that in (19) the only assumption made is the cross-stream geostrophic balance, while in (3) there is the *additional* assumption of parallel flow.

A Hypothesis and a Scale Analysis

In a stream with characteristic width L, consider the hypothesis that the term $V\partial f/\partial s \equiv V\beta$ dominates the right-hand side of (18). Then order of magnitude consideration gives

$$g(\partial/\partial n)\partial h/\partial s \sim (1/L)g\partial h/\partial s \sim V\beta; \tag{21a}$$

or on substitution from (7) and division by f

$$(V_o/L)\{(V\partial V/\partial s)/fV_o\} \sim (V/f)\beta; \tag{21b}$$

or,

$$(V_o/L)\sin\Theta \sim (V/f)\beta, \tag{21c}$$

on the use of (14). Thus, the hypothesis requires that the order of magnitude of $(V/f)\beta$ be given by the product of (V_g/L) with sin Θ for all possible Θ. Being a characteristic of a given motion system (V_g/L) is a constant for each system. In the Gulf Stream $(V_g/L) \sim 10^{-5}s^{-1}$ for $L \sim 100$ km, and $V_g \sim 1$ m/s. On the other hand, for the segment of the Gulf Stream of interest, $(V/f)\beta \sim 3 \times 10^{-7}/s$, which is another constant. So the hypothesis (21) holds in the one case where sin $\Theta \sim 0.03$. But if the effect of planetary vorticity advection is at all pertinent, the effect should extend over the whole range of possible Θ. Moreover, it is necessary that the effect vanishes with Θ when the flow is along lines of constant h. This suggests that it is the ageostrophic component of $V\beta$ that is pertinent in (18).

Horizontal Divergence and the Advection of Planetary Vorticity

In natural coordinates the horizontal divergence is

$$\nabla\cdot\mathbf{V} = (\partial V/\partial s) + V(\partial\phi/\partial n), \tag{22}$$

the sum of the longitudinal $(\partial V/\partial s)$ and transversal $V(\partial\phi/\partial n)$ divergences (Haltiner and Martin, 1957, p. 314). Hence (18) takes the form

$$g(\partial/\partial n)\partial h/\partial s = f(\nabla\cdot\mathbf{V}) + V\beta, \tag{23}$$

which is the version of the turning equation of Chew (1974, 1975) for steady, rectilinear flows.

As with other large scale flows (e.g., Holmboe *et al.*, 1945, p. 234), the horizontal velocity $\mathbf{V}$ of the Gulf Stream is expressable as the vector sum of a geostrophic and an ageostrophic component:

$$\mathbf{V} = \mathbf{V}_g + \mathbf{V}_a. \tag{24}$$

Therefore,

$$\nabla\cdot\mathbf{V} = \nabla\cdot\mathbf{V}_g + \nabla\cdot\mathbf{V}_a = D_g + D_a, \tag{25}$$

which partitions the horizontal divergence into its geostrophic, D_g, and ageostrophic, D_a, component. A similar partition was used by Stommel (1958, p. 155). From the curl of (5), after discarding its left-hand side,

$$D_g = -(V_g/f)\beta. \tag{26}$$

Hence,

$$f(\nabla \cdot \mathbf{V}) = fD_a + fD_g = fD_a - V_g\beta, \tag{27}$$

and (23) becomes

$$\underset{\text{Banking}}{g(\partial/\partial n)\partial h/\partial s} = \underset{\substack{\text{Ageostrophic} \\ \text{Divergence}}}{fD_a} + \underset{\substack{\text{Ageostrophic} \\ \text{Beta}}}{(V - V_g)\beta}. \tag{28}$$

The left-hand term is the banking term of Chew (1974, 1975); other terms are as labelled. The ageostrophic speed $(V - V_g)$ is generally a function of the acceleration in both the cross- and downstream directions, i.e., of both the flow curvature K and the angle Θ between the flow direction and lines of constant h. To see this, the second equality in (12) is used to rewrite (8) in the form

$$KV^2 + fV = g(\partial h/\partial N)\cos\Theta. \tag{29}$$

Then substituting from (13) and rearranging

$$\begin{aligned} KV^2 &= f(V_g \cos\Theta - V) \\ &= -f\{(V - V_g) + V_g(1 - \cos\Theta)\}. \end{aligned} \tag{30}$$

Or, on solving for $(V\text{-}V_g)$

$$(V - V_g) = -KV^2/f - V_g(1 - \cos\Theta), \tag{31}$$

which reduces to

$$(V - V_g) = -V_g(1 - \cos\Theta) \tag{32}$$

in a straight flow, and further vanishes with Θ. But $(1\text{-}\cos\Theta) \sim \Theta^2/2 \sim 0.01$ even where $\sin\Theta \sim 0.1$. This suggests that the balance of terms in (28) is between the banking and the ageostrophic divergence terms.

Ageostrophic Divergence and Sea Level Slope

In a study of two upstream segments of the Gulf Stream system, Chew (1974) found an approximate equality in the magnitudes of the bank-

ing and the ageostrophic divergence terms. Following (21), in order of magnitude this means

$$Da \sim (V_g/L)\sin\Theta \sim (10^{-5}/s)\sin\Theta. \tag{33}$$

The quantity (V_g/L) is the characteristic magnitude of the lateral shear. As $\sin\Theta \leq 0.1$ generally (Chew, 1974; Molinari, 1976), (33) is consistent with the well-known meteorological fact that where (5) holds the horizontal divergence is an order of magnitude smaller than the lateral shear (Burger, 1958; Phillips, 1963).

For chosen values of KV/f and $\sin\Theta$, the order of magnitudes of both $(V - V_g)$ and D_a are known through (31) and (33). Therefore we can establish the relative magnitudes of the two right-hand terms in (28) for different Rossby numbers. This is done in Table 1 for a Gulf Stream with a radius of curvature of 1,000 km or more. Case 1 in the table represents a large acceleration that is directed almost all downstream. This asymmetry supports a $D_a \sim 10^{-6}s^{-1}$ and a ratio of $(fD_a)/(V - V_g)\beta$ of over 300. The ratio is 100 in the less asymmetric Case 2, where the situation could be mistaken to mean (21), especially if $D_a = -D_g$ so that $\nabla\cdot\mathbf{V} = 0$. The ratio is 60 in the nearly symmetric Case 3, where $\sin\Theta \sim L/R$ and $D_a \sim (V_g/R)$; this is the planetary scale because R is the radius of the earth (Burger, 1958). As the magnitude of the acceleration becomes smaller in the isotropic Case 4 and Case 5, D_a also becomes smaller, but the ratio remains over 10. Finally, in the geostrophic regime of Case 6, where sea level is constant along the flow, both the ageostrophic divergence and the ageostrophic beta terms are zero. Clearly, (28) can be written

$$g(\partial/\partial n)\partial h/\partial s = fD_a. \tag{34}$$

Summary and Conclusion

Two of the three elements in Sturges' discussion of the effect of the Gulf Stream on the sea-level slope along the Atlantic coast are re-examined. In one, we found Sturges' extrapolation of an offshore Reynolds stress gradient unsupported by the observation of I. H. Brooks (personal communication, 1976).

In the other, where a flow in cross-stream geostrophic balance is assumed, we re-examined the effect of planetary vorticity advection on

Table 1

The Relative Magnitude of the Two Right-Hand Terms in (28) for Various Rossby Numbers. All Entries are Computed for Latitude 30°N, where f = $7.3 \times 10^{-5}/s$ and $\beta \equiv \partial f/\partial s \leq 2 \times 10^{-11}\ m^{-1}\ s^{-1}$

Case	*1*	*2*	*3*	*4*	*5*	*6*
Rossby number						
sin Θ	0.1	0.03	0.016	0.01	0.001	0
KV/f	0.01	0.01	0.01	0.01	0.001	0
D_a $(10^{-7}s^{-1})$	10.0	3.0	1.6	1.0	0.1	0
$(V-V_g)$ (m/s)	0.01	0.01	0.01	0.01	0.001	0
fD_a $(10^{-11}s^{-2})$	7.3	2.2	1.2	0.7	0.07	0
$(V-V_g)\,\beta$ $(10^{-13}s^{-2})$	2.0	2.0	2.0	2.0	0.2	0
$fD_a/(V-V_g)\,\beta$	360.0	110.0	60.0	35.0	35.0	

downstream sea-level slope. An overlooked restriction of parallel flow led Sturges to discard the confluence part of the horizontal divergence, i.e., the transversal divergence. When the transversal divergence is restored, and with it the restoration of the geostrophic and other components of the horizontal divergence, the advection of planetary vorticity is found to have only a negligible effect on sea-level slope. This is so because the effect is proportional to the ageostrophic component of the advection, so that over the usual range of Rossby numbers, the effect is one or more orders of magnitude smaller than the effect of the ageostrophic component of the horizontal divergence. In a steady, inviscid Gulf Stream taken as a nearly straight but non-parallel flow, it is the ageostrophic divergence in the stream that determines the change in its downstream sea level slope. Since the sign of the divergence may be positive or negative, it follows that the sea level from Key West to Cape Hatteras may slope either up or down, or up in one segment and down in another.

Acknowledgments

I am grateful to Irving H. Brooks of Nova University, Fort Lauderdale, Florida, for the data in Figure 1, and to Kenneth S. Chew for helping with the presentation.

Part of this paper was presented under the title of "Geostrophic Leveling, One More Assumption" at the Topical Conference on Geodetic Measurement in the Ocean, University of Illinois, Urbana, Ill., June 28–30, 1976.

References

Burger, A. P., 1958, Scale consideration of planetary motions of the atmosphere. *Tellus,* Vol. 10, pp. 195–205.

Charney, J. G., 1955, The Gulf Stream as an inertial boundary layer. Proceedings of the National Academy of Sciences, Vol. 41, pp. 731–740.

Chew, F., 1974, The turning process in meandering currents: a case study. Journal of Physical Oceanography, Vol. 4, pp. 27–57.

Chew, F., 1975, The interactions between curvature and lateral shear vorticities in a mean and an instantaneous Florida Current, a comparison. Tellus, Vol. 27, pp. 606–618.

Fischer, I., 1976, Comments and questions in relation to marine geodesy. Presented at the Topical Conference on Geodetic Measurements in the Ocean, University of Illinois, Urbana, June 28–30.

Haltiner, G. J., and Martin, F. L., 1957, *Dynamical and Physical Meteorology*. New York: McGraw-Hill Book Co., 470 pp.

Holmboe, J., Forsythe, G. E., and Gustin, W., 1945, *Dynamic Meteorology*. New York: John Wiley & Sons, 378 pp.

Molinari, R. L., 1976, The formation of the Yucatan Current based on observations of summer 1971. Journal of Physical Oceanography, Vol. 6, pp. 596–602.

Mourad, A. G., 1975, Marine geodesy. Reviews of Geophysics and Space Physics, Vol. 13, pp. 253–254.

Phillips, W. A., 1963, Geostrophic motion. Review of Geophysics, Vol. 1, pp. 123–176.

Schmitz, W. J., and Niiler, P. P., 1969, A note on the kinetic energy exchange between fluctuations and mean flow in the surface layer of the Florida Current. Tellus, Vol. 6, pp. 814–819.

Stommel, H., 1958, *The Gulf Stream*. Berkeley, California: University of California Press, 202 pp.

Sturges, W., 1974, Sea level slope along continental boundaries. Journal of Geophysical Research, Vol. 79, pp. 825–830.

NOAA Technical Memorandum ERL AOML-24, 47 pages.

NOAA Technical Memorandum ERL AOML-24

SELF-CONTAINED DIGITAL TIDE MEASUREMENT SYSTEM

Benjamin Culverhouse

Physical Oceanography Laboratory

Atlantic Oceanographic and Meteorological Laboratories
Miami, Florida
January 1977

UNITED STATES
DEPARTMENT OF COMMERCE
Elliot L. Richardson, Secretary

NATIONAL OCEANIC AND
ATMOSPHERIC ADMINISTRATION
Robert M. White, Administrator

Environmental Research
Laboratories
Wilmot N. Hess, Director

NOTICE

The Environmental Research Laboratories do not approve, recommend, or endorse any proprietary product or proprietary material mentioned in this publication. No reference shall be made to the Environmental Research Laboratories or to this publication furnished by the Environmental Research Laboratories in any advertising or sales promotion which would indicate or imply that the Environmental Research Laboratories approve, recommend, or endorse any proprietary product or proprietary material mentioned herein, or which has as its purpose an intent to cause directly or indirectly the advertised product to be used or purchased because of this Environmental Research Laboratories publication.

CONTENTS

	PAGE
ABSTRACT	1
1. INTRODUCTION	1
2. DESIGN REQUIREMENTS	2
2.1 Tide Gage	2
2.2 Instrument Support Package	3
3. CONSTRUCTION	4
3.1 Tide Gage	4
3.1.1 Sensors	4
3.1.2 Electronics	10
3.1.3 Power Source	24
3.1.4 Main Frame	26
3.1.5 Pressure Housing	26
3.2 Instrument Support Package	26
3.2.1 Instrument Base	26
3.2.2 Acoustic System	29
4. CALIBRATION AND TESTING	29
4.1 Sensors	29
4.1.1 Pressure	29
4.1.2 Temperature	33
4.2 Electronics	34
4.2.1 Clock Corrections	34
5. RESULTS AND RECOMMENDATIONS	38
5.1 Results	38
5.2 Recommendations	40

CONTENTS

		PAGE
6.	ACKNOWLEDGMENTS	40
7.	REFERENCES	41

FIGURES

Figure 1.	AOML digital tide gage system.	5
Figure 2.	Paroscientific model 2400A digiquartz transducer, and Yellow Springs model 44032 thermistor bead.	6
Figure 3.	Transducer oil interface.	8
Figure 4.	Digiquartz shockmount.	9
Figure 5.	Oil filling the digiquartz.	9
Figure 6.	Tide gage electronics.	11
Figure 7.	Model 64E tape transport.	12
Figure 8.	CR-30, Cassette control card.	13
Figure 9.	CR-21, Head driver card.	14
Figure 10.	CR-12, Motor driver card.	15
Figure 11.	Model 610 timing diagram.	16
Figure 12.	MC-19, Master clock card.	18
Figure 13.	DC-37, Digital thermometer card.	19
Figure 14.	XP-35. Low-level AC counter card.	21
Figure 15.	Power source for the tide measurement system.	25
Figure 16.	Tide gage main frame.	27
Figure 17.	Lower, end plate assembly.	28
Figure 18.	Instrument support package.	28
Figure 19.	Digiquartz frequency vs Pressure.	30
Figure 20A.	Coefficients vs. temperature.	32
Figure 20B.	Digiquartz deviation curve.	32
Figure 21.	Clock deviations as functions of temperature.	35
Figure 22.	Temperature deviations @ 9.35°C.	35
Figure 23.	Temperature deviations @ 14.30°C.	35

Figure 24. Universal curve, cubic fit. 35

Figure 25. Clock deviations vs. cubic fit. 35

Figure 26. Temperature and tide record from MESA deployment of tide gages. 39

SELF-CONTAINED DIGITAL TIDE MEASUREMENT SYSTEM

Benjamin Culverhouse
National Oceanic and Atmospheric Administration
Atlantic Oceanographic and Meteorological Administration
Miami, Florida

ABSTRACT. A digital recording, self-contained tide measurement system for Continental Shelf oceanography is described. Design parameters, construction techniques, sensor calibrations, and system tests are discussed. Pressure and temperature are measured through the use of a high precision quartz crystal and a precision epoxy-coated thermistor. Data are recorded on digital cassettes with a capacity of 11 million bits. Power consumption is extremely low with in-situ recordings of 400 days possible while using an alkaline power source. Time base is supplied by a precision quartz crystal binary clock. Temperature corrections for pressure and time are given. Calibration values are given with coefficients for each pressure transducer stated. Results of MESA deployments are shown, with tide and temperature records.

1. INTRODUCTION

A definite need exists for a high resolution, self-recording, digital tide gage for shallow water applications. It was this need that prompted the Physical Oceanography Laboratory, AOML, Miami, to develop a system that would meet present day needs as well as those in the near future. During the past year five of these systems have been developed through funding from NOAA Marine Ecosystems Analysis (MESA) Program. They are presently deployed in the New York Bight area for a period of six months.

Interest in this tide gage system shown by other laboratories throughout the scientific community is addressed in this technical report. A pressure gage using a vibroton transducer has been developed by Dr. Mark Wimbush (1976) of Nova University and is described in a forthcoming publication. With the information contained here, a scientist could construct a system for his own use.

2. DESIGN REQUIREMENTS

2.1 Tide Gage

The primary consideration in the design of a tide gage system is the accuracy and resolution to which pressure is to be measured. A search was made throughout the industry for a pressure transducer that could meet the most demanding precision reliability, and environmental requirements. Temperature effects related to pressure were also an important factor. Since records of long duration were required, low power consumption by the sensors and electronics was a prerequisite. A compact, durable and reliable instrument support package was needed to assure successful deployments from surface ships. Recovery of the instrument package had to be fail-safe as well as feasible with regard to ship's equipment and capabilities. The design of the tide gage can best be understood if we consider each of the five major component groups separately, that is, sensors, electronics, power source, main frame, and pressure housing.

Selection of the pressure transducer was based on the following requirements;

Pressure range	0-365 psia (250 m)
Accuracy	0.0073 psia (0.5 millibars), when corrected for temperature, hysteresis and drift.
Resolution	0.0004% (0.0016 psia)
Repeatability	0.005% Full Scale (0.02 psia)
Temperature Null Shift	0.0007%/^{o}C
Size	1.0 x 1.5 x 1.5 inches
Power Requirements	+6. VDC., 0.001 ampere

Because of the relatively shallow operating depths of these instruments, pressure fluctuations due to long period waves and wind waves can be of a large magnitude. To remove these unwanted changes by filtering would mean sampling at an extremely fast rate. Since this is not feasible, a technique should be used, whereby the sampling interval is made longer than the wave period, with the pressure value averaged over this longer period. The transducer remains on to obtain maximum resolution and eliminate start-up transients in frequency.

Selection of the temperature sensor was based on the following requirements;

The basic requirement, was that the sensor allow pressure corrections to within 0.2 millibars.

Temperature Range	0 to 32°C
Accuracy	better than 0.1°C
Sensitivity	0.05°C over range
Stability	0.01°C
Repeatability	0.01°C
Time Constant	1 second max. (63% of temp.)

The temperature range (0 to 32°C) allowed for use in tropical waters. The sensors had to be capable of operating at 100% duty cycle for a period of one year.

The design requirements for the electronics portion of the tide gage were varied and many. Of primary importance was the requirement for a clock with timing accuracy to better than 1 ppm (2.5 sec/month) and with a magnetic tape record of tide and temperature for a one-year period, based on an approximate 8-minute sampling interval. To obtain a record of this length required the use of circuitry with very low voltage and current requirements. The accuracy and reliability of this circuitry had to be of the highest quality. Size was also important since the instrument (pressure) housing was to be small in size and weight for ease of handling and deployment.

The power source for the instrument had to supply voltage and current in the amounts capable of sustaining operation for periods longer than one year. This meant the use of power cells that had proven long life and were compact in size. They also had to be dry cells, since gasing could not be tolerated within the instrument housing. The power source had to be small in size and of reliable construction.

For the main frame a one-piece aluminum frame was required for strength without excessive weight. Accessibility to sensors and electronic cards was important, as was ease of wiring the backplane.

The instrument housing requirements were quite simple, since size and weight were the only important factors to be considered. Pressure range for the housing was not an important factor, since an operating depth of only 250 m (365 psi) was required. It was hoped that we could use a design already available.

2.2 Instrument Support Package

The primary requirement for the instrument support package was that it be capable of deploying tide gages in a free-fall mode from a surface ship in water depths up to 275 m and recovering them by means of an acoustic release configuration with flotation. This meant that the system had to be designed

so that a portion of the platform or anchor base would be jettisoned upon receiving an acoustic command signal from the surface, allowing the tide gage, acoustic releases, and instrument base to return to the surface for recovery. Reliability, size, and weight of the package had to be considered very carefully, since one miscalculation could result in loss of equipment as well as the data.

3. CONSTRUCTION

3.1 Tide Gage

The tide gage used is basically an instrument that can record temperature and pressure information on magnetic tape with reference to a preset clock (record count), or a GMT clock. This information can be scanned and logged at a variety of sampling intervals. Pressure range on this particular model is 400 psia, with temperature being 0-32°C. It has a 512-second integration time for data acquisition, since that best meets our needs. Data are logged on 0.150" magnetic cassettes, 300 ft. in length. The data tapes must then be converted to either a 7-/or 9-track IBM compatible tape for processing in our laboratory. The data format in the tide gage is variable to meet user's needs, but is to a large extent dependent upon the resolution of the sensors and electronics being used. The electronics are totally cos/mos design and quite reliable. Total operating power consumption for the gage is less than 2 milliamps, which accounts for the instrument's ability to record in-situ for over one year. The digital tide gage is shown in an exploded view (Figure 1) to illustrate the physical location of the various components and their relationship to each other.

3.1.1 Sensors

The tide gage incorporates two sensors, a quartz crystal pressure transducer (Figure 2) Model 2400A manufactured by Paroscientific Inc., Redmond, Washington, and a thermistor bead, Model 44032, made by the Yellow Springs Inst., Co., Yellow Springs, Ohio. The Model 2400A "digiquartz" is the most suitable pressure transducer now available for this application. It meets or exceeds all the criteria set forth in the design study. The following description of the Model 2400A digiquartz is only a brief outline, since most of the users have prior knowledge. For those not familiar with the Paroscientific transducer, the article by J. Paros (1976) will be most helpful. The digiquartz transducer is a quartz crystal resonator with a frequency of oscillation that varies with pressure. The nominal frequency range for the digiquartz is 40 kHz (0 psia) to 36 kHz (400 psia), and the output signal is a nominal square wave of 4 volts for a 6-volt DC input. Power requirements for the five transducers that AOML has vary from

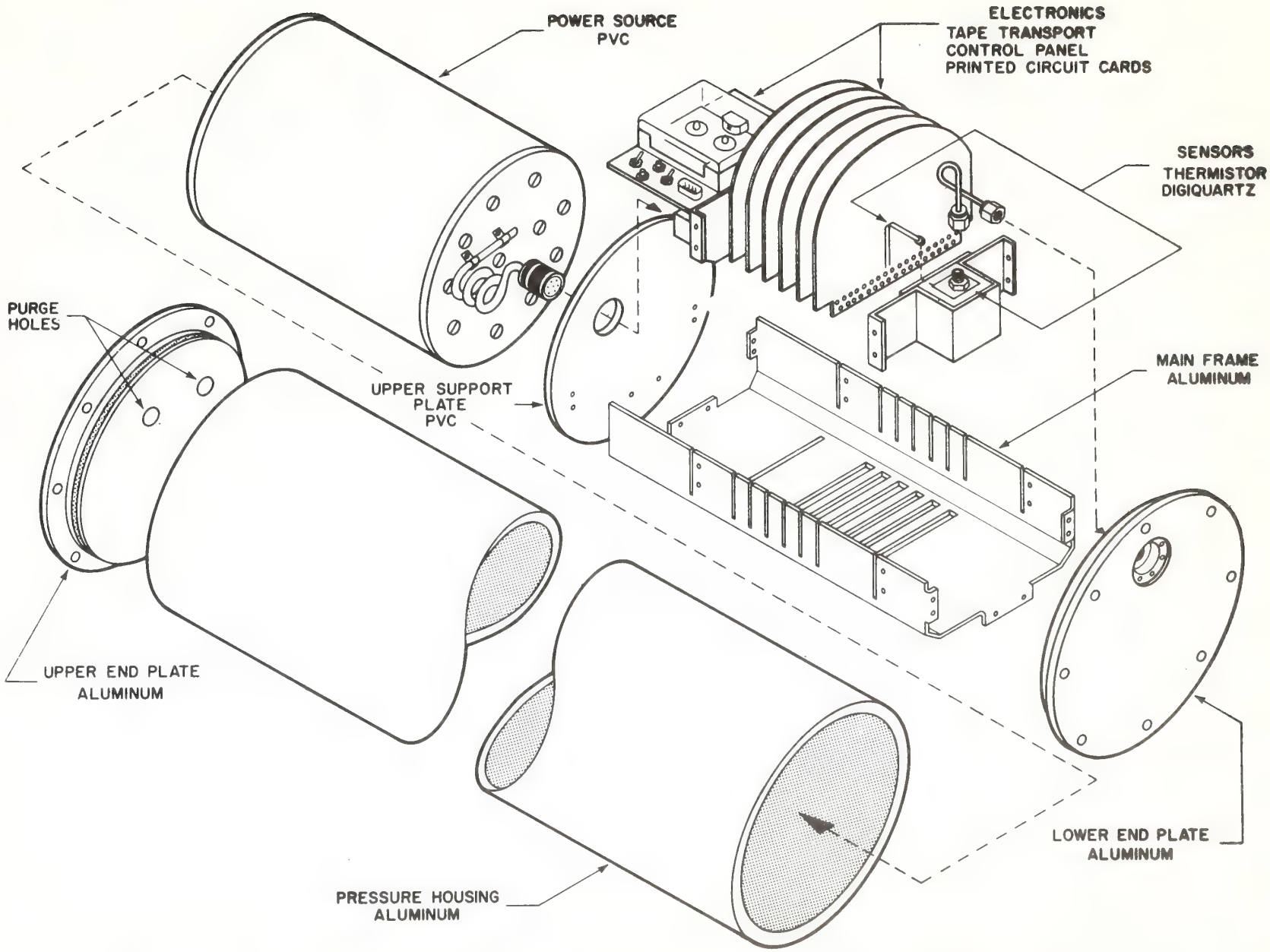


Figure 1. AOML digital tide gage system.

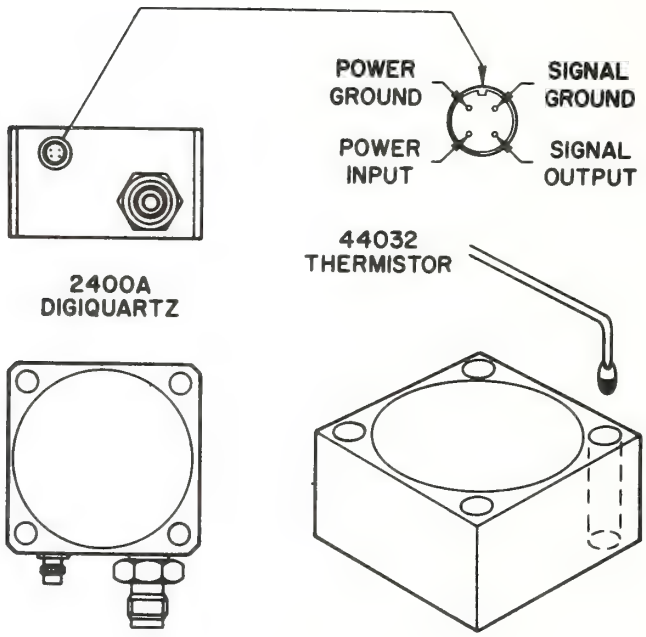


Figure 2. Paroscientific model 2400A digiquartz transducer, and Yellow Springs model 44032 thermistor bead.

about 750 to 900 microamps, which accounts for the extended operational period of the tide gage, since the digiquartz remains "on" constantly once it is deployed. The pressure port for the digiquartz has a Swagelok fitting, #200-1-2. This is connected to a flexible nylon tube which is connected to the tide gage end plate (Figure 3). The plate contains a silicone oil reservoir that is coupled to sea pressure by means of a neoprene rubber diaphragm ~1 mm thick. It is recommended that the digiquartz be shockmounted in the tide gage for maximum protection against shock and vibration. Paroscientific has a shock mount, Model 300A. However, we constructed our own version that serves the purpose nicely. It is made of 1/16" aluminum and rubber sponge material (Figure 4).

Once the digiquartz is mounted in the instrument shock-mount, the bellows must be oil filled. We use silicone oil Dow Corning type 200, 200 cs viscosity. To do this safely, a vacuum pump must be used. A schematic (Figure 5) shows this in detail as it is a very important part of the tide gage preparation. With the transducer connected as shown, evacuate the bellows chamber to 0.1 microns if possible, depending on the pump. Then, with the vacuum level reached, the "T" valve is opened to the oil supply, and the cahmber is filled eliminating any air bubbles which could cause problems. Electrical connections are then made to the electronics portion of the gage by means of a four-conductor shielded cable and transducer plus DP-4S-1, supplied with each transducer.

Temperature measurements for the tide gage are taken inside the transducer housing since the primary purpose for these measurements is to apply corrections to pressure values taken by the digiquartz. Because of its internal placement, the temperature sensor has a time constant of about 31 minutes. The Yellow Springs Model 44032 precision epoxy coated thermistor meets the design requirements set forth in section 2 and is accurate to better than 0.1^{o}C. The thermistor resistance is an exponential function of temperature. The temperature measurement is accomplished by embedding the thermistor bead into one of the digiquartz mounting holes (Figure 2). The mounting hole is then filled with silicone heat transfer compound. The thermistor leads are secured to the digiquartz main body with nylon tie-wraps to prevent movement. Electrical connections are then made to the electronics board. It will be necessary to cover the thermistor leads with shrink tubing or some form of insulation prior to mounting. A more detailed description of the thermistor is given in the electronics section, DC-37 thermometer.

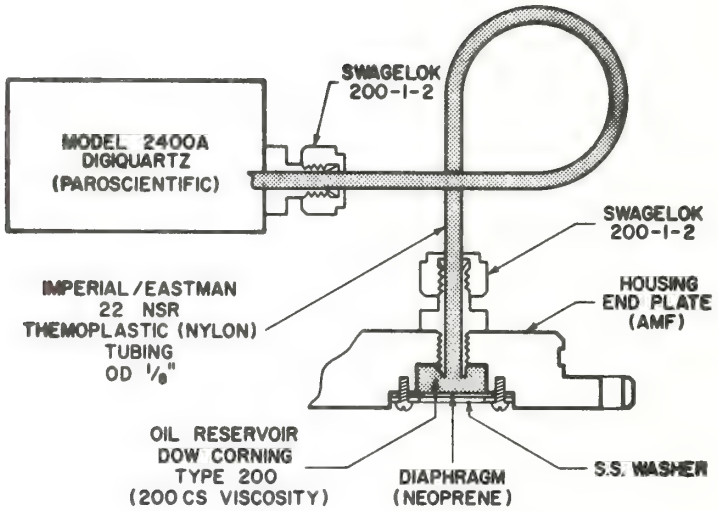


Figure 3. Transducer oil interface.

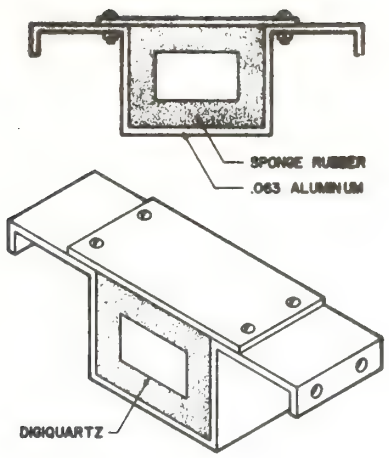


Figure 4. Digiquartz shockmount.

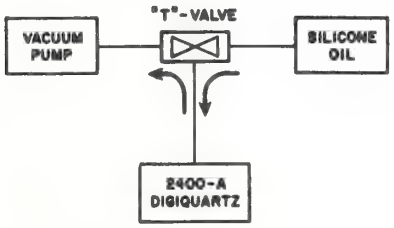


Figure 5. Oil filling the digiquartz.

3.1.2 Electronics

The tide gage electronics (Figure 6) comprises six printed circuit cards and a four-track digital recorder. These components were designed by Winfield Hill and are available from the Sea Data Corporation, Newton, Massachusetts. The series 610 recorder consists of a model 64E tape transport, CR-12 motor driver card, CR-21, head driver card, and CR-30 cassette control card. The XP-35 pressure card, DC-37 temperature card, and MC-19 master clock card make-up the remainder of the data acquisition electronics.

The 64E tape transport (Figure 7) has a gearless direct-drive stepping capstan with take-up clutch. It is approximately 4.4" x 3.9" x 3.7" in size, and will operate in any position. The 64E weighs 2.4 lbs. with stepping accuracy better than 5%. Magnetic tape is a standard 0.150 inch cassette, 0.7 mil thickness, with 800 bits-per-inch (BPI) phase encoding. The 64E is supplied with a 15-pin Jones-type connector (DA-15) and mating plug. Ther are mounting holes on the main frame to facilitate easy packaging. The 610 recorder is a serial recorder that writes four tracks of data, each at a density of 800 bpi, for a total density of 3200 bpi. Each four-bit group is called a character. Tape capacity is approximately 11.5×10^6 bits for a 300' cassette. The recording rate is 100 steps/sec. (400 bits/sec.). Power consumption for the motor and head coils is extremely low when an 18 to 11 volt source is used. Normally current consumption is 300 milliamps or less, during the "write mode".

The CR-12, CR-21, and CR-30 cards are low voltage cos/mos logic type and tested for low leakage. The data format (Table 1) is generated automatically for each record by the CR-30 cassette control card (Figure 8) upon receiving a "record request" from the master clock. The control card has three rising-edge sensitive inputs. The first input steps out an adjustable "record gap", from 4 to 19 blank steps followed by a two-step preamble. The second shifts and records an adjustable amount of data (1 to 99 characters). The third input records a parity character (LCC), completing the data record. Normally all three inputs are triggered together by the master clock, and the operations are completed sequentially. The CR-21 head driver card (Figure 9) contains a 1000-Hz clock that operates the recorder. This card shifts the data, computes parity, generates the phase-encoded head drive, and sends step pulses to the CR-12 motor driver card (Figure 10), which supplies four voltage controlled current sources to drive the four motor coils. This entire timing operation (Figure 11) is dependent upon the pre-selected wiring of the data and gap length counters on the CR-30 card. There are various other application notes that are supplied by

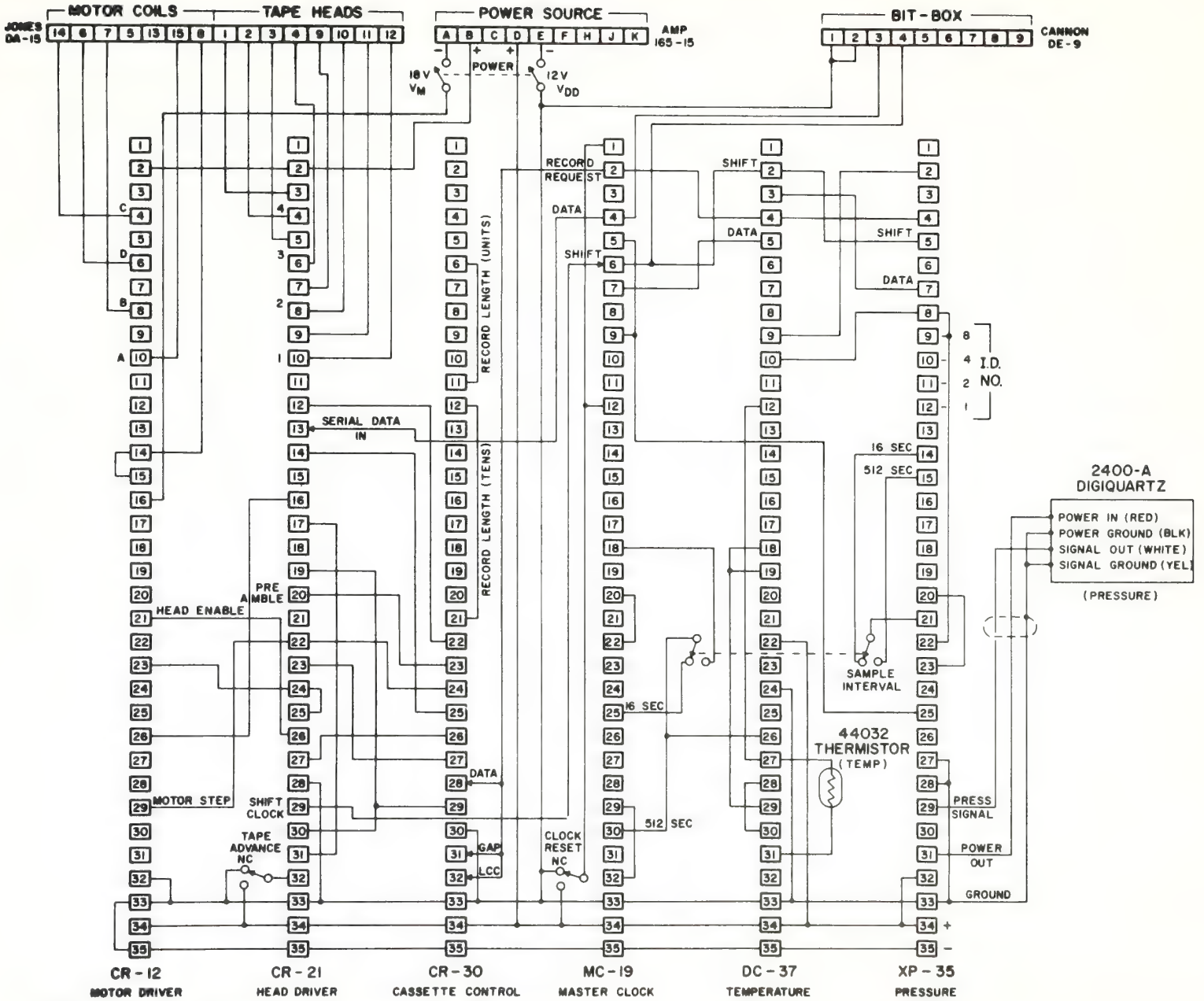


Figure 6. Tide gage electronics.

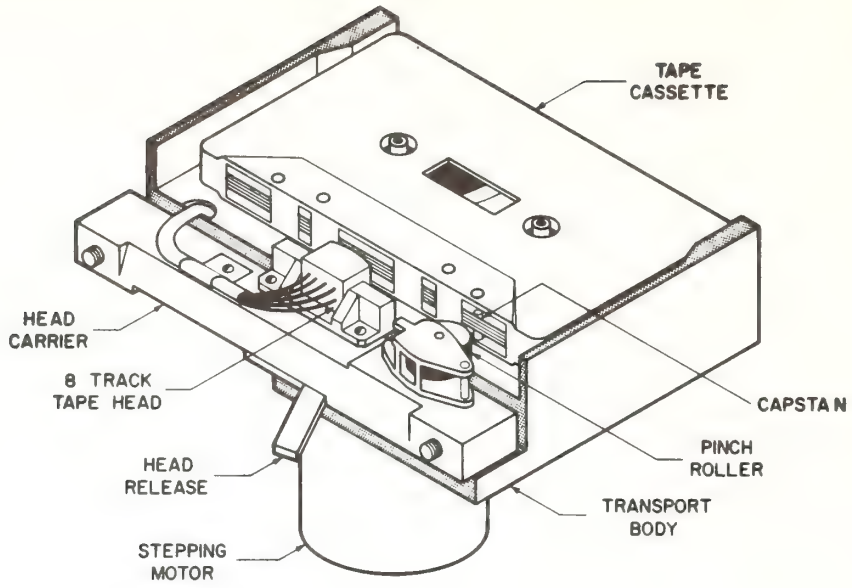


Figure 7. Model 64E tape transport.

DATA RECORD
(30 CHARACTERS)
(120 BITS)

TAPE DIRECTION

CHARACTER	1	2	3	4	5	6	7	8	9	10	11	12	13	14	15	16	17	18	19	20	21	22	23	24	25	26	27	28	29	30
TRACK 1													1	0	MSB					MSB				8	MSB					1
TRACK 2													1	0										4						1
TRACK 3													1	0										2						1
TRACK 4													1	0					LSB				LSB	1					LSB	1

RECORD GAP — PRE-AMBLE — RECORD WORD (5 CHAR. (20 BITS)) — TEMP. WORD (4 CHAR. (16 BITS)) — P. — PRESSURE WORD (5 CHAR. (20 BITS)) — PAR

DATA PARAGRAPH (15 CHAR. (60 BITS)) — BEGINS — ENDS

MSB = MOST SIG. BIT
LSB = LEAST SIG. BIT

Table 1. Data format.

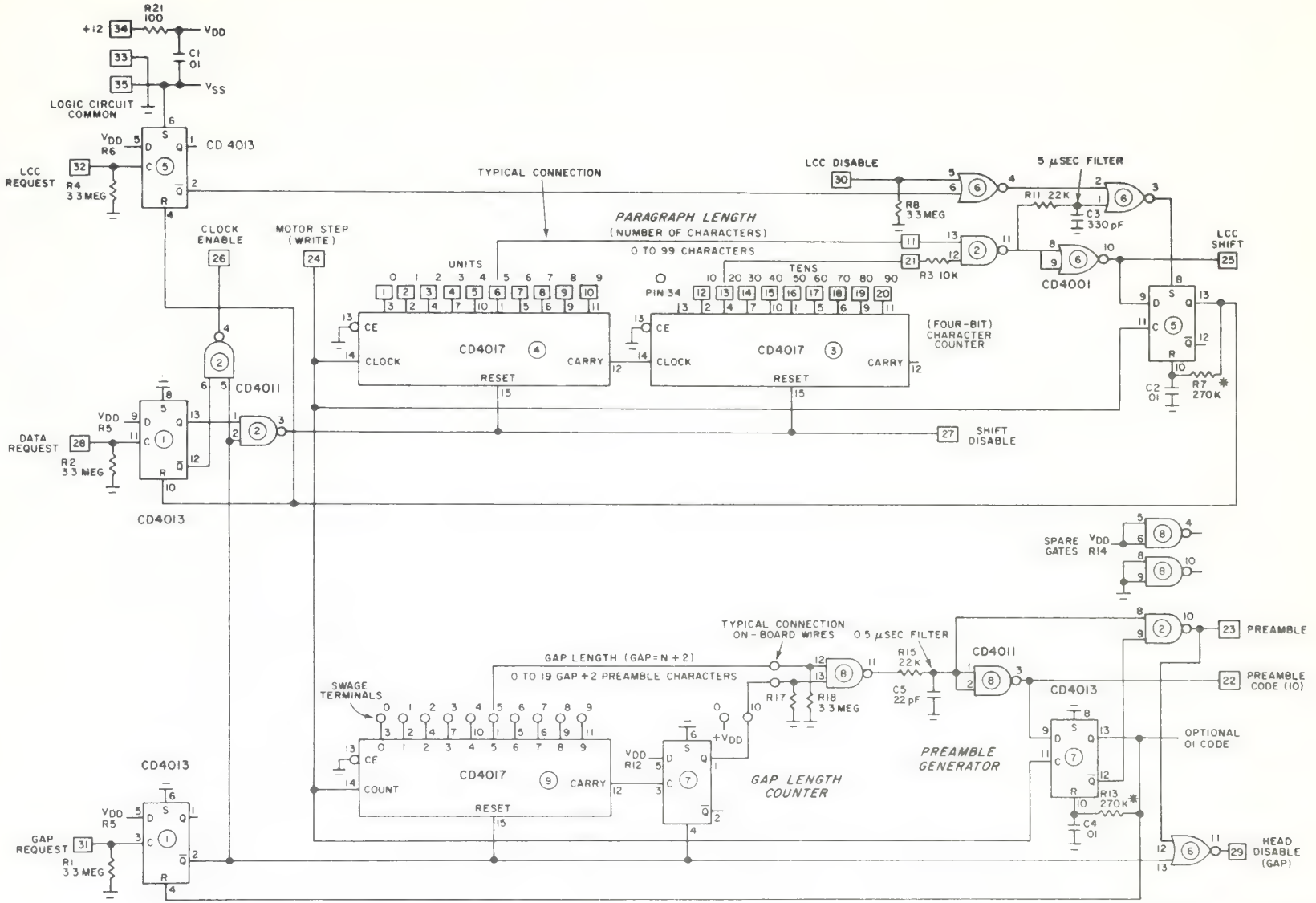


Figure 8. CR-30, Cassette control card.

CR-30
CASSETTE CONTROL
SEA DATA CORPORATION
NEWTON, MASSACHUSETTS

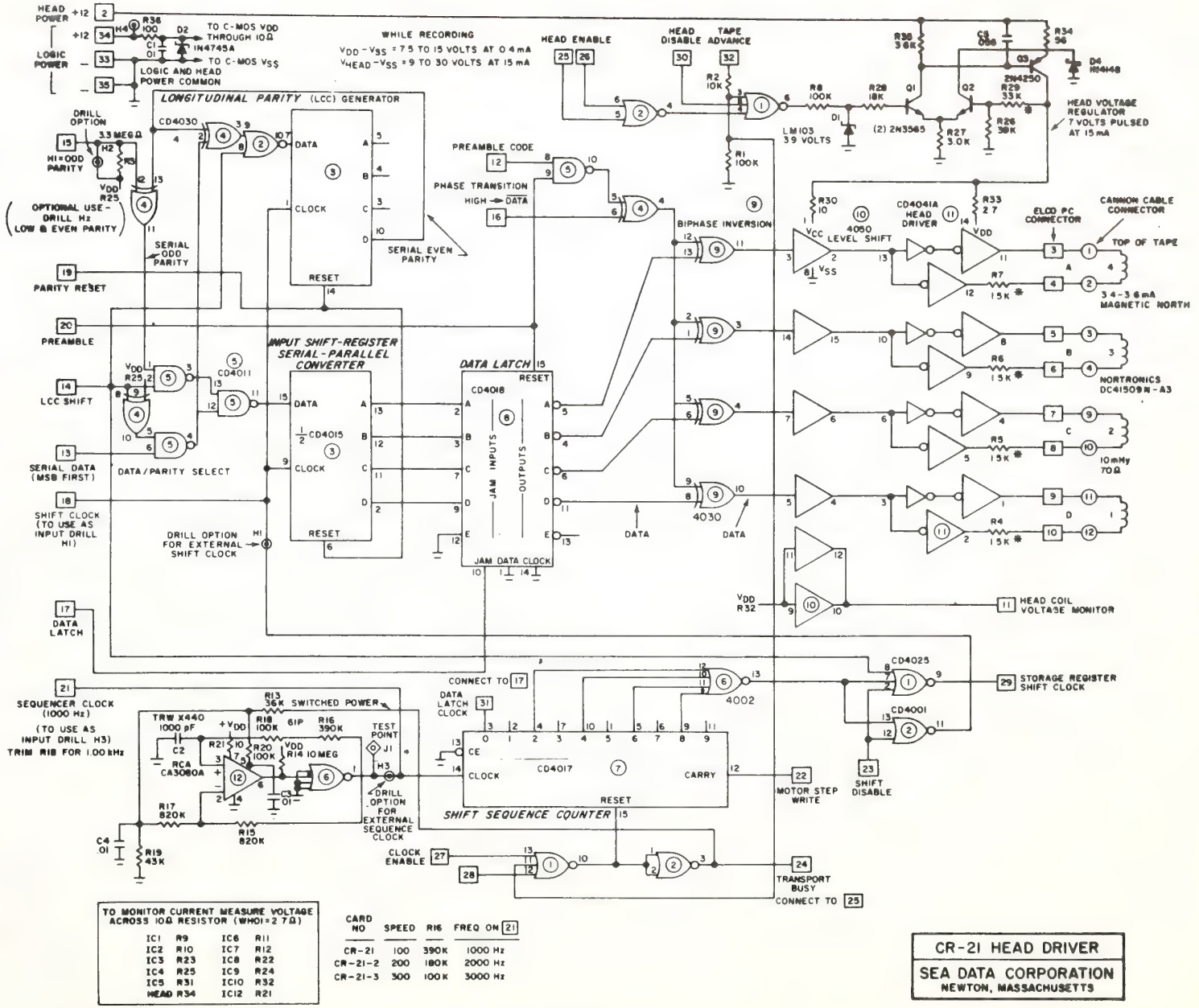


Figure 9. CR-21, Head driver card.

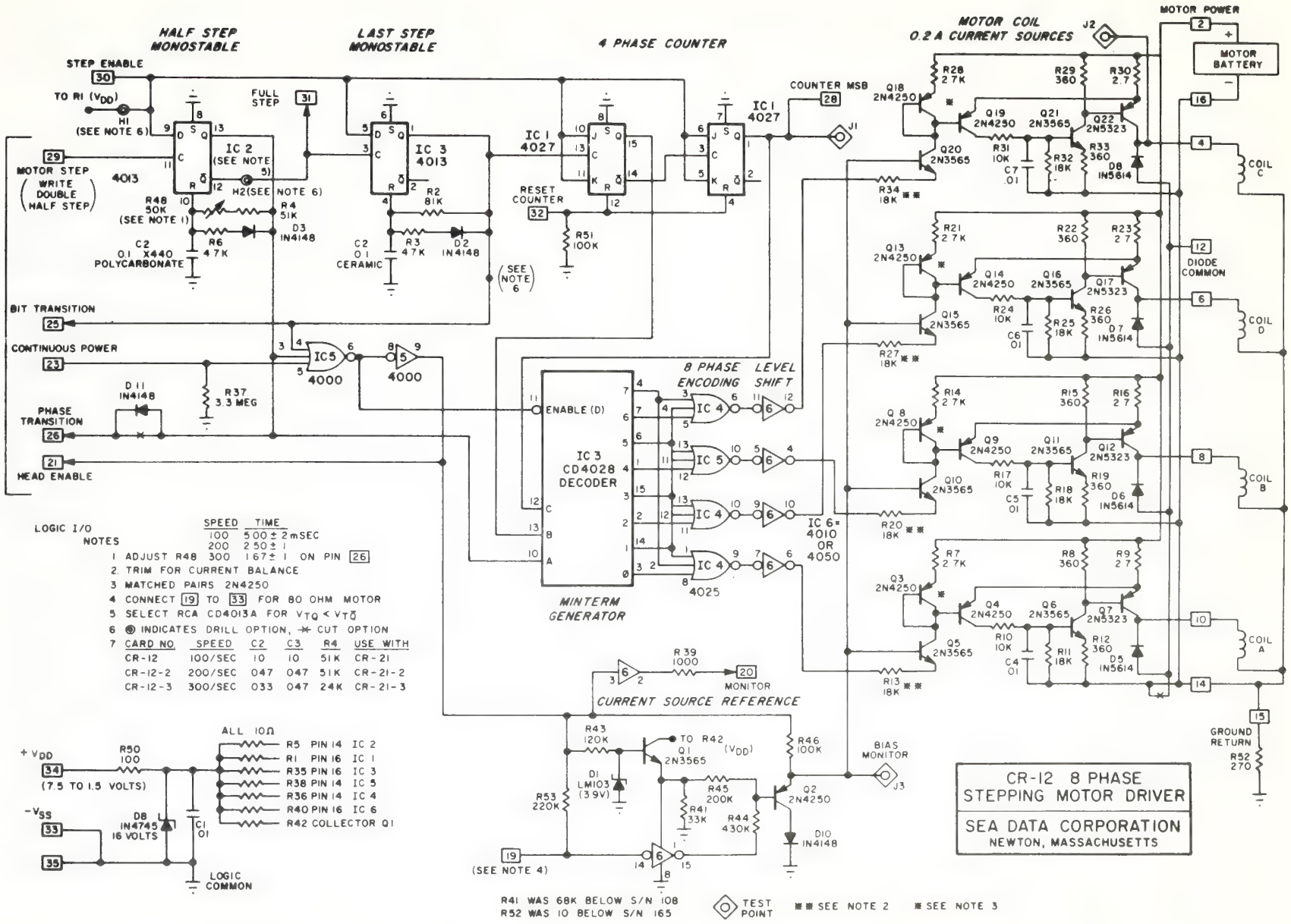


Figure 10. CR-12, Motor driver card.

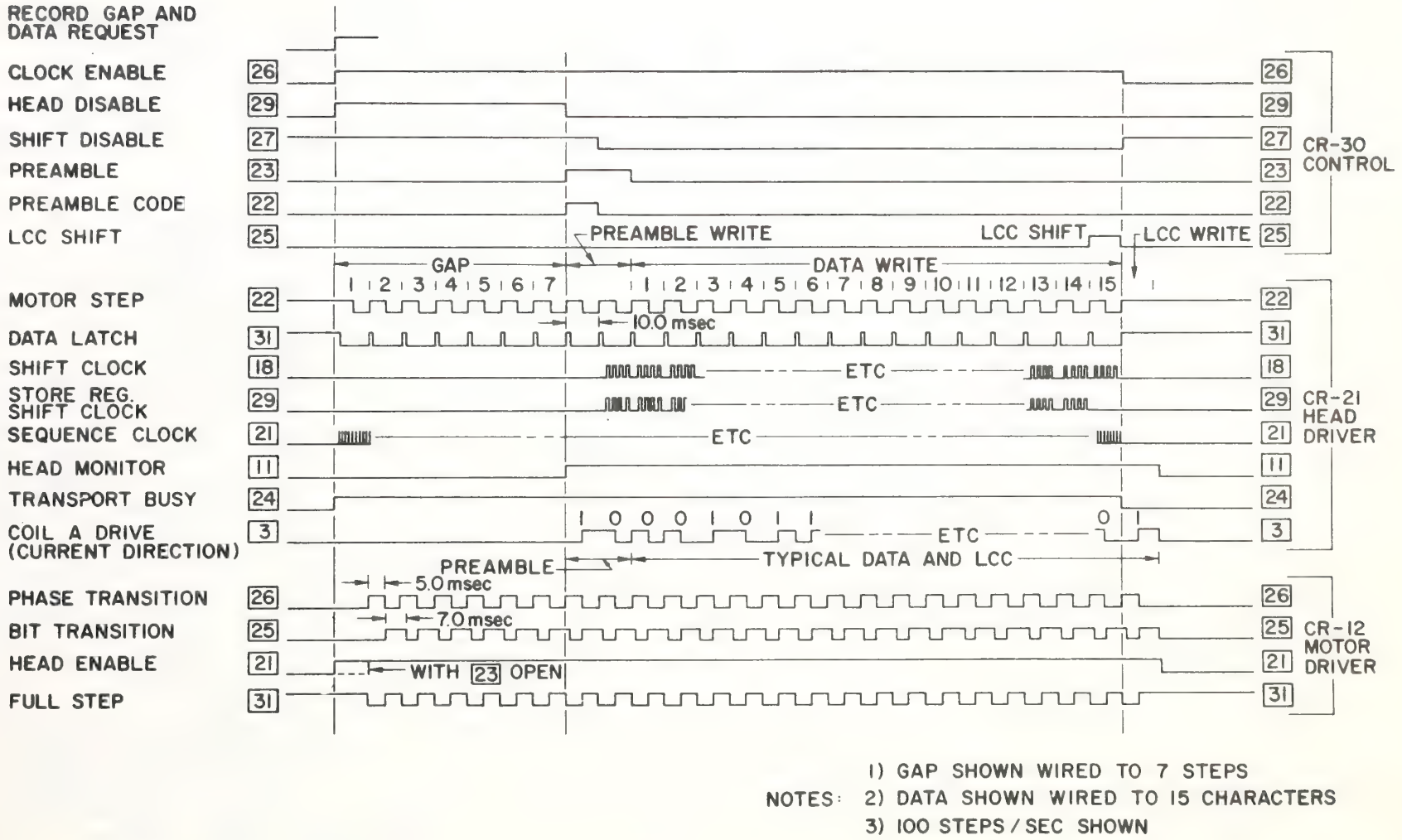


Figure 11. Model 610 timing diagram.

Sea Data when the cards are purchased. An inspection sheet with engineering test data is also supplied with each card. The 610 digital recorder requires only three logic lines to interface it to the remainder of the data acquisition electronics.

The MC-19 master clock (Figure 12) is an unusually versatile quartz clock card. It contains a parallel-resonant oscillator with a quartz crystal that is extremely stable when used with a supply voltage of 8 to 15 volts. The cos/mos oscillator employs a crystal with an NT cut and uses only 50 μ amps of current, with the turning point of the crystal being @ 25°C. The basic frequency of 16,384 Hz (2^{14}) is adjustable at C_5, and it is factory set at 61.03516 μ sec $\pm$ 0.00005. The crystal is laser trimmed and stable to 1 ppm per year. The oscillator circuit also has an amplifier, shaper, level shifter, and buffer. The entire card uses less than 200μ amps of current which makes it highly desirable. There are four separate binary dividers which provide 14 sample rates. There is also a divider for seconds to hours. Pin 12 is a common reset for all dividers. The card also contains a 20-bit binary counter and shift register.

In addition to the time-keeping functions, the MC-19 clock also shifts data that are being received from the DC-37 thermometer and XP-35 counter cards to the CR-21 head drive card for recording. In the gage the clock is being used as a record counter (512 sec.) rather than a real time clock.

On the tide gage main frame there is a small control panel adjacent to the recorder. On this panel there are; the power switch, sample interval switch, tape advance and clock reset buttons, and serial data output connector. With the power switch on, initial activation of the gage is accomplished by depressing the clock reset button. This starts the sampling interval period. This interval is selected by placing the S.I. switch on either 512 or 16 seconds depending on whether field sampling or laboratory checkout is being done. Many other sample rates are available. One important note on the clock reset feature should be mentioned. Once the clock is reset, the first sample interval will be a half-interval only That is, if a 512 interval is selected, the first data shift command will occur in 256 seconds and the second command 512 seconds after the first. This is due to the nature of the electronics and should be noted when processing data tapes. As far as the record count is concerned, a record #1 will appear after the first full interval.

The DC-37 integrating digital thermometer (Figure 13) consists of a YSI thermistor, part #44032 and a Sea Data WHOI style: electronic data collection card, DC-37-5-1-8. The thermometer is accurate to better than 0.1°C without

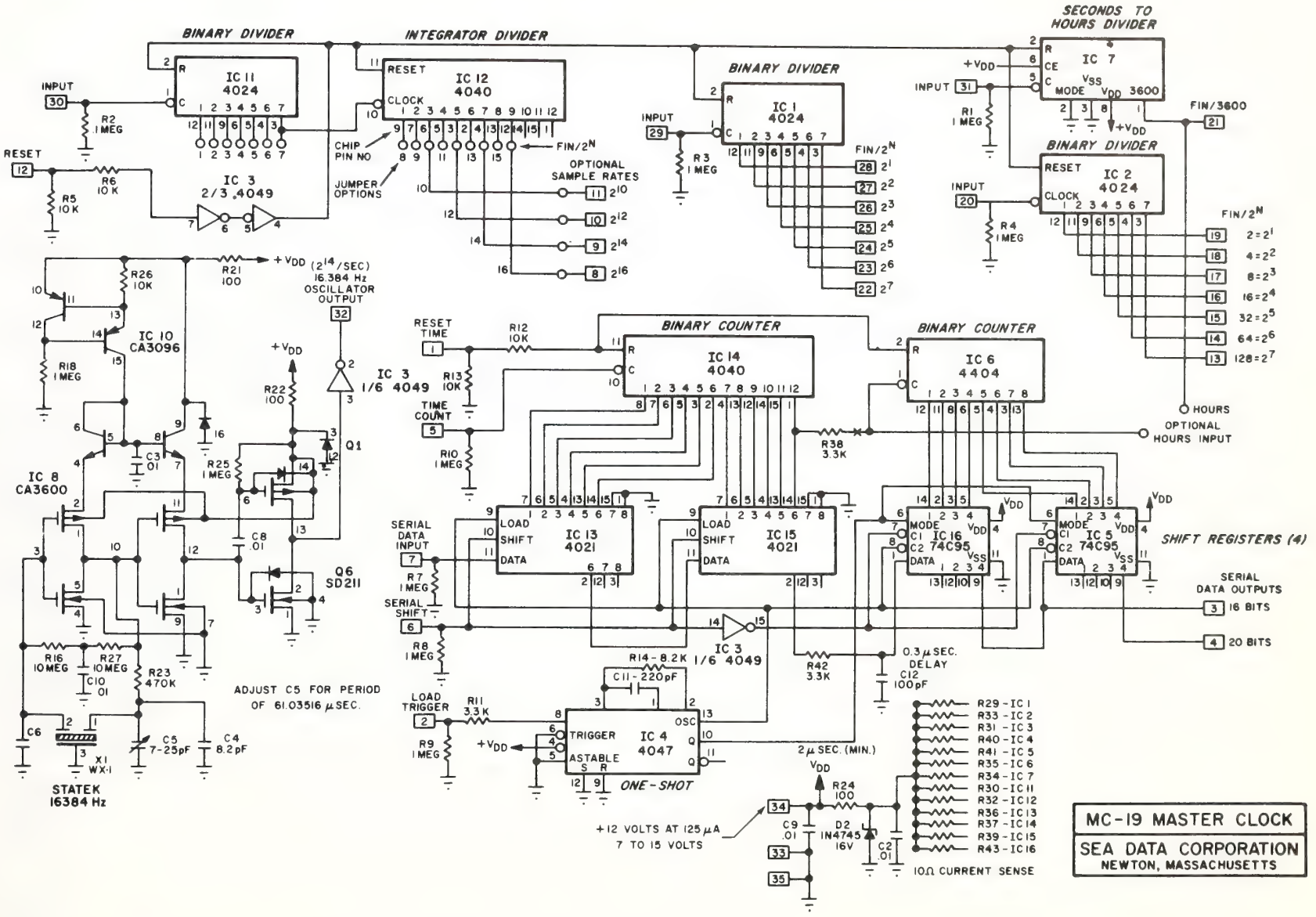


Figure 12. MC-19, Master clock card.

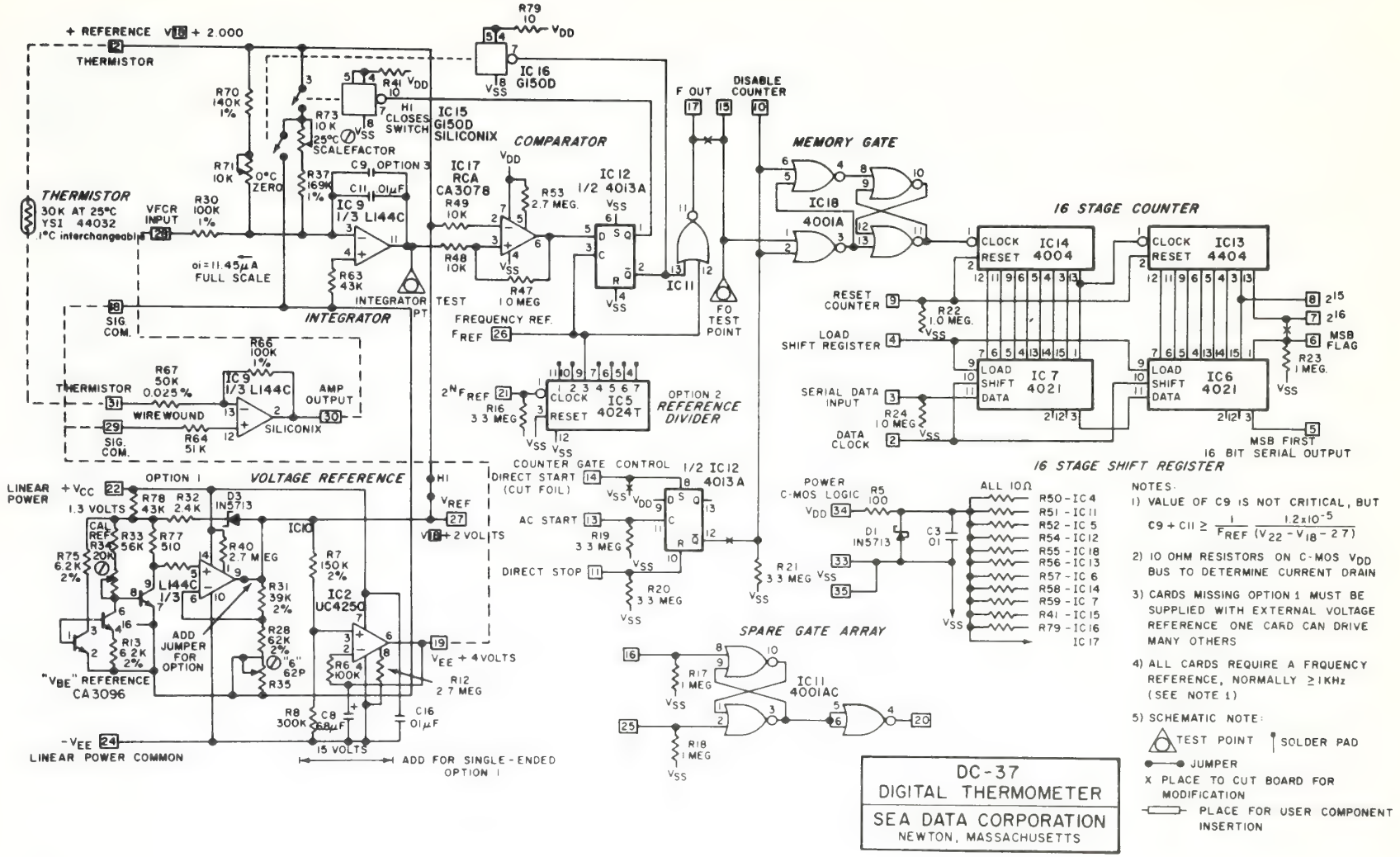


Figure 13. DC-37, Digital thermometer card.

calibration. The 44032 is a precision thermistor which is trimmed before epoxy coating and is accurate and interchangeable to better than .5% or 0.1°C. Sensitivity of the thermistor varies from 4.3%/°C to 5.0%/°C. These thermistors are stable and repeatable to better than 0.01°C per year and are available with 0.01°C calibration and computer curve fitting. The thermistor resistance bears an exponential relationship to temperature as shown in the comparisons between YSI data sheet resistances and measurements made by Jerry Dean (1972) at Woods Hole Oceanographic Institution (Table 2). A most useful formula for thermistors has been developed by Steinhart and Hart (1968) for degrees Kelvin. A modified version of this formula is used for conversion to degrees centigrade;

$$T = \left\{a+b \quad Ln(R_T) + c \quad [Ln(R_T)] \quad ^3\right\}^{-1} - 273.18.$$

This formula can describe thermistors and maximum errors of about 0.001°C over a 30°C range.

The DC-37-5-1-8 is a special version of the Sea Data DC-37 integrating voltage card. This card contains a low power voltage reference, an input operational amplifier, a voltage to frequency converter (VFC), a memory gate, a 16-bit counter, and a 16-bit shift register. The DC-37 option-5 refers to use with the YSI 44032 thermistor, 0.1°C. Option-1 refers to the on-card voltage reference, and option-8 to the temperature measurement range, 0. to 32°C. The normal DC-37-5-1 is used for a 0 to 25°C temperature range. With the input amplifier, the VFC converts a current into frequency for counting and recording. The current-measuring property of the VFC is used to linearize the exponential nature of the thermistor over a 20° span. The DC-37, when combined with the system clock (MC-19), becomes a complete A/D converter. The voltage-to-frequency converter is a precision delta-sigma converter that operates on a charge-balancing principle, where precision quantities of charge are subtracted from the signal current in an integrator. Converters using this method are very accurate and stable, since all parameters depend on ratios of input voltage to reference voltage, output frequency to input frequency, and ratios of resistors. In particular, the output frequency is inversely related to the reference voltage and directly related to a reference frequency. Conversion formulas for temperature counts to °C for the DC-37 thermometer will be discussed in section 4.1.

The XP-35 AC counter (Figure 14) is designed to pperate as a low-level counter for AC (FM) signals in the 1-4 volt region, such as the 2400 A digiquartz signal. The XP-35 contains a shaper, series power regulator, prescale divider, memory gate, sample pulse generator, a 24-bit counter, and a 24-bit shift register.

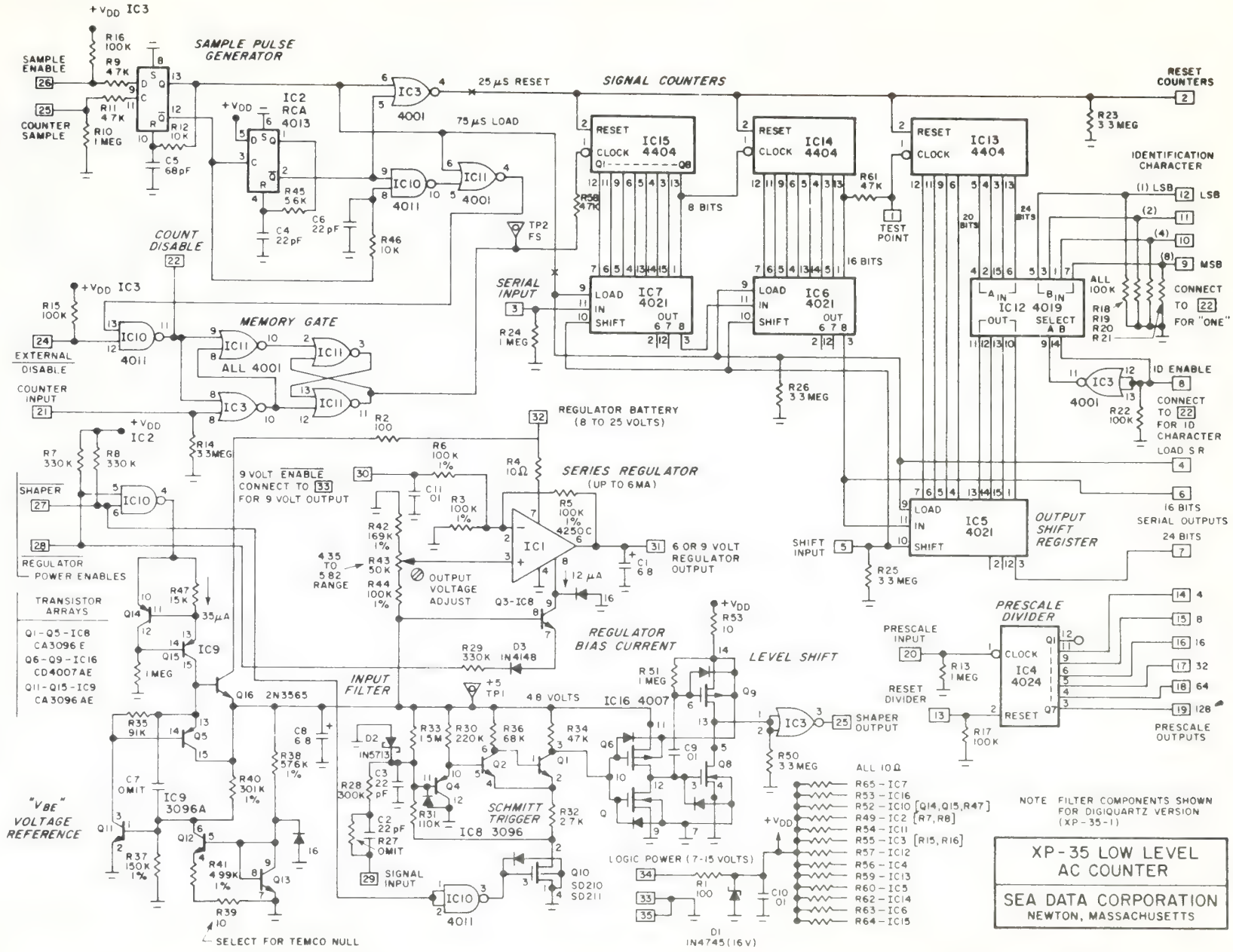


Figure 14. XP-35, Low-level AC counter card.

Table (2)

Temperature vs. Resistance (YSI-44032)

Temperature	YSI Resistance	WHOI Resistance
0°C	94.98 K	95.04 K
5	74.44	74.43
10	58.75	58.69
15	46.67	46.60
20	37.30	37.24
25	30.00	29.94
30	24.27	-----
32	22.33	-----

The shaper section has the following basic circuits: a 4.8-volt voltage reference, an AC input filter, a Schmitt trigger, and a level shift. The voltage reference is provided so that the current drain of the Schmitt trigger is minimized for variations in supply voltage. The input filter, pin 29, controls the sensitivity of the input signal to the trigger circuit and is available in several options. Option one is designed to operate in the 10-70 kHz range which is within the limits of the digiquartz (40-35 kHz). The Schmitt trigger is conventional with the exception that it has been modified to operate at high frequencies with low threshold levels such as 0.25 volts DC, up to 850 kHz. The level shift circuit converts the 4.8 volt level from the trigger circuit into a 12 volt cos/mos logic level,pin-23.

The series regulator provides power for the sensor, in this case the pressure transducer. It has an output voltage of either 6 or 9 volts depending upon the connections made to the card. If pin 30 is connected to pin 33, logic ground, then the output voltage will be 9 volts, otherwise it will be 6 volts. Absolute accuracy of the 6-volt output is 0.5%. The regulator can be turned on with a logic level on pin 28.

The prescale divider is a seven-stage divider that can be used to scale down the FM signal frequency before it goes to the 24-bit counter. For example: a 512-second sampling interval with a transducer frequency spread of 35 to 45 kHz, for all of the quartz transducers, would yield a total count of between 17.92 to 23.04 million counts, an unusually large total count. However, with the prescale divider set on the 1÷8 ratio, a full scale count would be 2.24 to 2.88 x 10^6 count spread. With a register capacity of 1.048 million counts, the result would be two overflows or 2.097152 million counts with an observed count spread of only ∿143 to 783 thousand

counts. The result of this scaling ratio produces a count resolution of ∿0.0004% of full scale (0.1 cm H_2O). Input to the divider is pin 20, with a selection of prescale divider outputs, pins 14 through 19. These outputs can be wired on the instrument backplane, and offer divider ratios of 4, 8, 16, 32, 64, and 128. The selected output is connected to the input of the memory gate, in 21.

The 24-bit counter and 24-bit shift register buffer convert data from a frequency form to a count form and present it in serial bit form for recording on the 610 recorder.

The sample pulse generator, pin 25, generates pulses that load the count contained in the 24-bit signal counter into the serial shift register in preparation for recording. After the data are loaded into the shift registers, the counters are reset. During the time this operation takes place, the memory gate prevents any counts from going to the counter, but at the same time holds in a separate memory the results of any counts that may have occurred during the "on time" of the sample pulse generator. This circuit allows the user to count signals and load them into the shift registers and record them without any count loss from one counting interval to the next. The total number of counts recorded is equal to the exact number of signal pulses that have occurred. This means there is no ± 1 count uncertainty for each individual sample interval when a number of sample intervals are summed.

The 24-bit counter can be considered as an integrator. For example, if the FM signal is counted for a 15-minute period, then there are 900 seconds times the frequency (900 x f) for a total count. The total count is the integrated value of the FM signal during the 15-minute period. To find the actual frequency of this signal, the total count is divided by the counting period of 900, that is, TC/900 = fa. Four bits of the 24-bit counter are set aside, pins 9, 10, 11, and 12, with an optional logic level called I.D. enable, pin 8. When I.D. enable is "high", then the four most significant bits of the shift register become an identification character, that is 1-2-4-8 or any combination thereof up to fifteen, enabling users to identify up to fifteen instrument tapes. This means that the 24-bit counter now becomes a 20-bit counter for pressure frequency. Conversion formulas and correction factors for the XP-35 counter and 2400A digiquartz will be discussed in section 4.1.

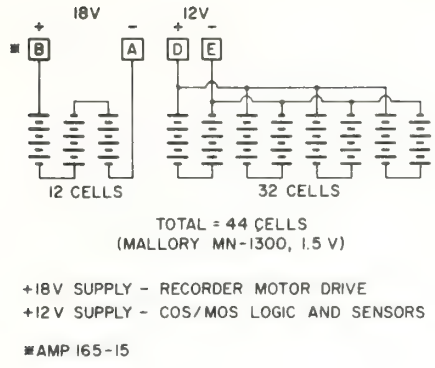
3.1.3 Power Source

Power for the tide measurement system is supplied by a battery pack consisting of forty-four alkaline "D" cells. These cells (Mallory MN-1300) are arranged so that two voltages are available. 18 volts (V_M) is available to drive the stepping motor of the Sea Data, 64E tape transport, while the other, a 12-volt source (V_{DD}), powers the six cos/mos logic cards. The 18-volt source is a series configuration with 12 cells made up in three stacks of four cells each (Figure 15A). The 12-volt source is a series-parallel configuration with 32 cells made up in eight stacks of four cells each.

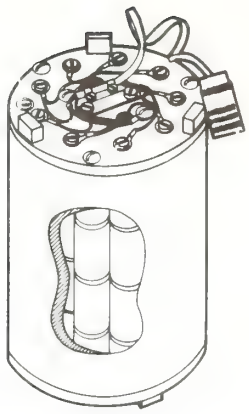
The MN-1300 alkaline battery has a rated capacity of 10 ampere hours under normal conditions. However, at zero degrees centigrade with 1-year shelf derating, a figure of 5-ampere hours per cell is considered a safe rating. Therefore the 5-ampere-hour rating for the 18 volt series stack is twice the 2.5 ampere hours needed for a full tape cassette (300 ft.), since the 64E tape transport can operate from 18 volts down to 12 volts without degrading operation. The 5-ampere-hour rating for each of the four 12-volt parallel stacks in the cos/mos supply provides a 20-ampere-hour rating. The worst-case current drain is less than 2.0 milliamps for the entire cos/mos circuitry including pressure and temperature sensors. On the basis of these values, this section of the power source can operate efficiently for up to 10,000 hours or 416 days.

The alkaline batteries are contained in a polyvinyl chloride (PVC) housing (Figure 15B) approximately six inches in diameter by 10.5 inches in length. There are eleven 1 5/32-inch holes drilled through the PVC housing which position the cells in eleven stacks of four cells each. Figure 15C shows the location of the cells and also the wiring configuration. Stainless buss bars are used to join the various battery stacks. A PVC end plate 3/8" thick is installed on the top and bottom of the power source to hold the batteries in place. The top plate contains spring loaded contacts (Figure 15D) that apply pressure to each battery stack. The bottom plate does not have spring contacts but stainless screws extending approximately 1/16" through the inside of the plate. These screws are not turned as the spring loaded screws on the top plate. Wiring from the power pack to the main frame is accomplished by placing the four power wires in shrink tubing and wiring them to an amphenol series-165, 9-pin connector. The mating connector is located on the main frame.

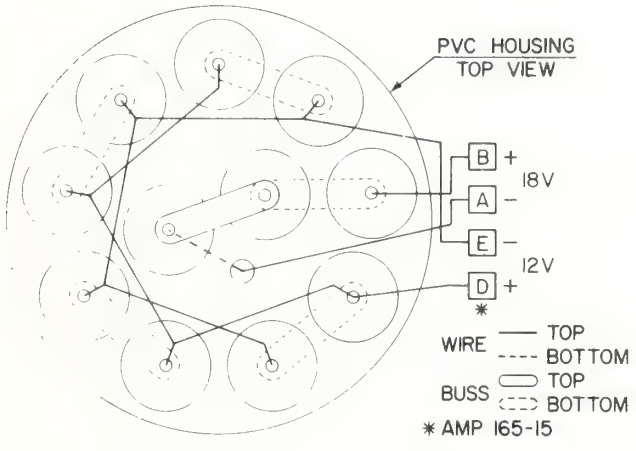
The MN-1300 Mallory alkaline manganese cell was chosen for this application for several reasons. Most importantly, the



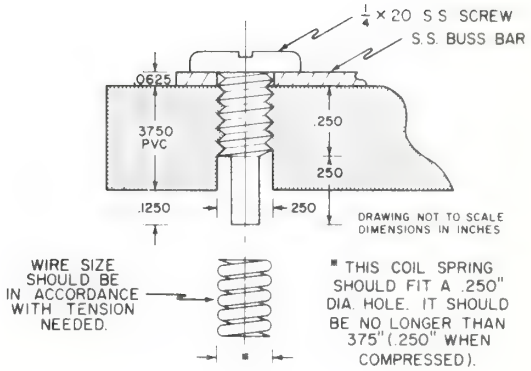
(A)



(B)



(C)



(D)

Figure 15. Power source for the tide measurement system.

MN-1300 has good environmental stability qualities and operates well over a wide range of temperatures (-20°C to +70°C). Because of its rugged construction, it can withstand severe shock and high pressures. Shelf life ratings are excellent, with 90% capacity retained after one year stored @ 21°C. Also the cost of the alkaline cells is low when compared with mercury cells or lithium cells, and they are much more readily available.

3.1.4 Main Frame

The tide gage main frame (Figure 16) is constructed of an aluminum sheet material 0.080" thick and is formed in a "U" shape configuration for maximum support. Slots are milled out of the back plane for mounting the Elco 7008-35 printed circuit card connectors. Slots on each side of the frame guide the PC cards when they are being installed and also give support to the edge of the cards. Three tabs on the top and bottom of the frame are used to mount the frame to the pressure end plate and the upper support PVC plate. Two additional sets of slots are cut in the frame. The upper set is for the tape transport and mounting bracket, and the lower set holds the pressure transducer in its shock mount. All wiring is wire-wrapped; wire gage is #26 with Kynar coating. The wirewrap technique was chosen over soldering for several reasons, the most important being positive contact with no cold solder joints and higher reliability.

3.1.5 Pressure Housing

The tide gage pressure housing is a standard AMF Sea-link Model 284 acoustic release housing with a rating of 1,332 PSI. Construction is of 6061-T6 aluminum with the surface hard anodized. The housing has two end plates with "o-ring" seals that are bolted in place. The upper end plate has purging holes for Freon filling. The lower end plate (Figure 17) is ordered from AMF with the machining completed for the oil reservoir, diaphragm, and transducer mounting hardware. The pressure housing is ∿6.5" outside diameter by 38.0" length All tide gages are purged for ten minutes with Freon #12 and sealed with a minimum of two pounds of Freon pressure before being deployed.

3.2 Instrument Support Package

3.2.1 Instrument Base

The instrument support package (Figure 18) comprises the instrument base (anchor base and instrument platform),

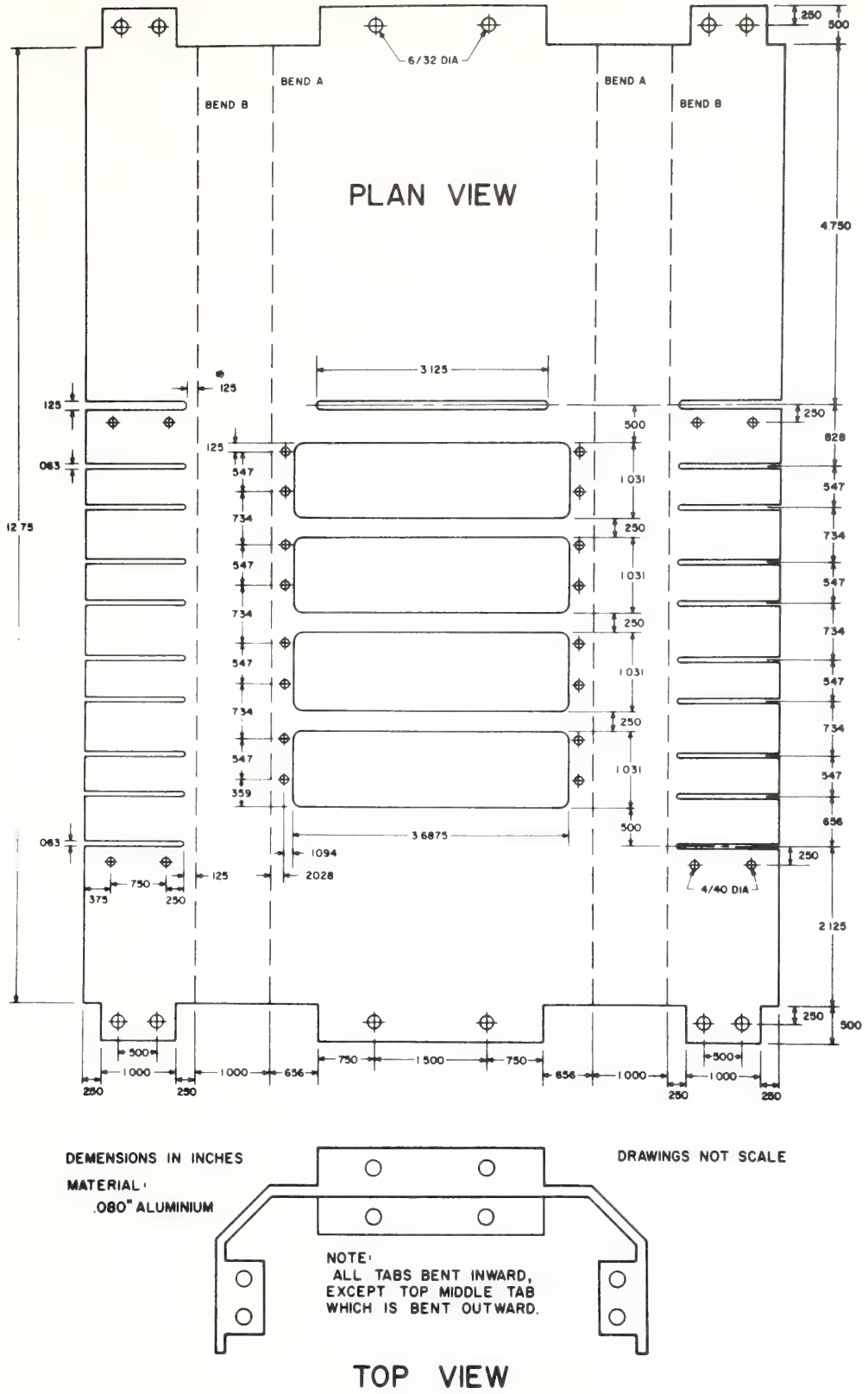


Figure 16. Tide gage main frame.

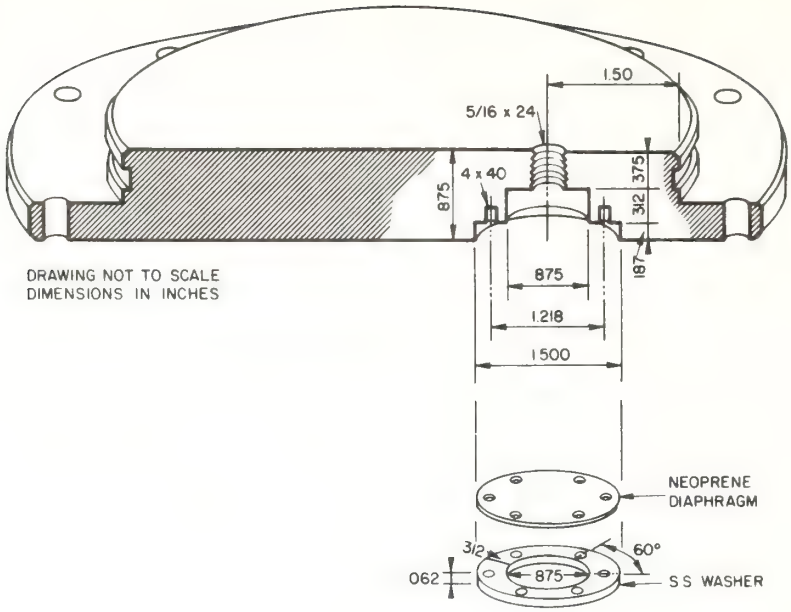


Figure 17. Lower, end plate assembly.

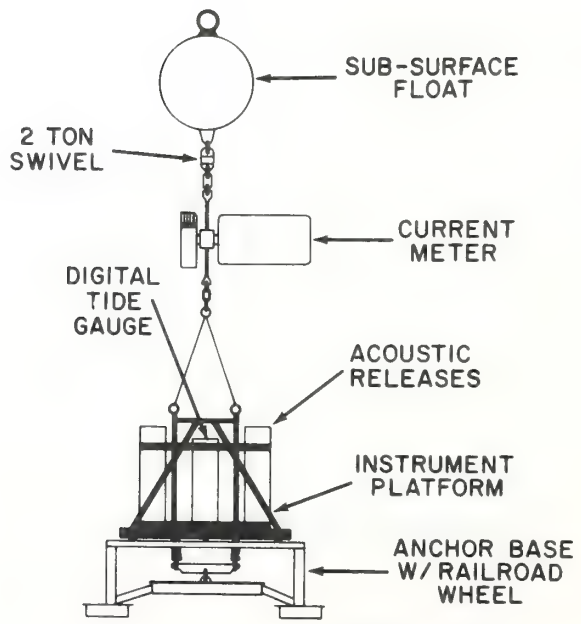


Figure 18. Instrument support package.

the rigging hardware, and a sub-surface float. The upper portion of the instrument base is referred to as the instrument platform, on which is mounted the tide gage and two acoustic releases mounted in tandem. The lower portion is the anchor base, which contains a railroad wheel to insure positive placement on the sea-floor. The sub-surface float is configured for safe margin of positive buoyancy once the anchor base is released. The entire assembly is designed to be deployed in a "free fall" mode.

The tide gage is mounted vertically upon the instrument platform with the pressure interface diaphragm at the lower end. AMF "Sea Link" Model 322 acoustic releases are mounted vertically on each side of the gage with an interconnecting link suspended between the release jaws, which couples the instrument platform to the anchor base at the center point. Activation of either acoustic release allows the instrument platform with tide gage and releases to lift free of the anchor base. The complete support package weights 1925 lb in air and 575 lb in water. Upon release, the instrument platform, current meter, and sub-surface float become ∿330 lb positively buoyant.

3.2.2 Acoustic System

The acoustic system employed with the tide gage is an AMF Sea-Link Shipboard Acoustic Relocator System. It consists of a model 301 receiver/coder and a power amplifier matched to a Model 301 transducer. This system provides a display of bearing angle and slant range to the Model 322 underwater acoustic release units on the instrument platform. Each of the two 322 releases has a different receiver code to prevent interference with other release units and also to afford additional release capability. With this configuration, only one release need be fired to obtain recovery of the system.

4. CALIBRATION AND TESTING

4.1 Sensors

4.1.1 Pressure

To process pressure data obtained from digiquartz pressure transducers, the pressure counts must be converted into pressure in scientific units. At each pressure, a transducer produces an output signal with a particular period. After correction for changes in the sampling interval caused by temperature effects in the clock, the recorded pressure counts can be converted to the transducer period. Figure 19 shows

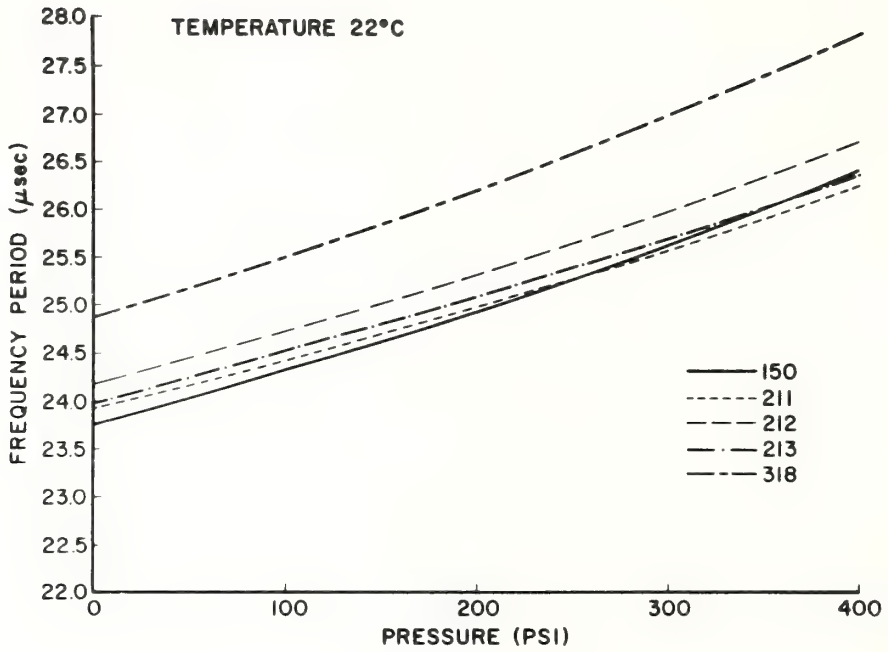


Figure 19. Digiquartz frequency vs pressure.

the periods for the five transducers as functions of applied pressure.

The Engineering Development Laboratory of the National Ocean Survey sponsored a study conducted by the National Bureau of Standards on the characteristics of digiquartz pressure transducers. This study produced an algorithm for the conversion of transducer period to pressure in scientific units:

$P = AS - BS^2$, where P is the pressure; A and B are coefficients; and $S = (1-T_o/T)$, T_o and T being the zero-pressure and measured periods respectively.

In Table 3 typical values for A, B, and T_o are given as functions of temperature. These values were computed by Donald W. Busse of Paroscientific Inc., from calibration data obtained by the Pratt and Whitney Aircraft Company's Florida Research and Development Center in November 1975.

Table 3

Conversion Parameters for Digiquartz, Model 2400-A S/N 318, Period to Pressure in PSI

Temperature	0^o	10^o	21^o
A (psi)	4004.503	4000.835	3997.169
B (psi)	2512.179	2500.858	2495.717
T_o (μs)	24.87405	24.87265	24.87175

As a first approximation, A and B may be considered linear functions of temperature. T_o is a quadratic function of temperature with a minimum period or turnaround point at about 35^oC, according to the manufacturer. Plots of A, B, and T_o versus temperature are shown in Figure 20A.

The values of A, B, and T_o were obtained from period values at 0,200, and 400 psi. The deviation curve (Figure 20B) shows the difference between computed and observed pressures at 21^oC. Except for the isolated deviation at 350 psi, probably due to an error in calibration, the computed pressure is systematically lower than the observed pressure between 0 and 200 psi, and above the observed pressure between 200 and 400 psi. According to Paroscientific Inc., this behavior may be corrected by including a third term CS^3 in the pressure formula. The lower deviation curve in Figure 20B corresponds to increasing pressure from 0 to 400 psi while the upper curve is for

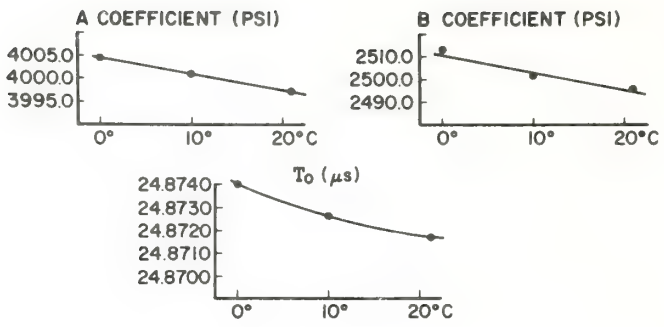


Figure 20A. Coefficients vs. temperature.

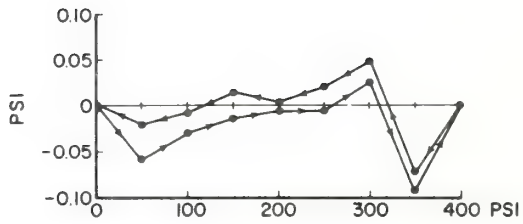


Figure 20B. Digiquartz deviation curve.

decreasing pressure from 400 to 0 psi. The difference between the two curves is the transducer hysteresis for full scale extensions of pressure. In the field under actual conditions, a transducer is subject to about 2 psi fluctuations about a background pressure. The hysteresis associated with fluctuations of this magnitude is negligible.

For further information regarding the digiquartz transducer, contact the manufacturer (Paroscientific Inc.).

4.1.2 Temperature

To process temperature data obtained from the DC-37 integrating thermometer, the observed temperature counts must be converted to degrees centigrade. Using M = observed counts/16384 (reference frequency) and thermistor resistance, $R_T(K\Omega)$, the model thermometer calibration can be described by the following formula:

$$M = \frac{Rx}{R_T + R_{67}} - \frac{Rx}{R_{TO} + R_{67}}$$

$$\frac{M}{R_x} + \frac{1}{R_{TO} + R_{67}} = \frac{1}{R_T + R_{67}}$$

$$\frac{M(R_{TO} + R_{67}) + R_x}{Rx\ (R_{TO} + R_{67})} = \frac{1}{R_T + R_{67}}$$

$$R_T = \frac{R_x\ (R_{TO} + R_{67})}{M(R_{TO} + R_{67}) + R_x} - R_{67}$$

$$R_T = \frac{R_x}{\left(\frac{R_x}{R_{TO} + R_{67}}\right) + M} - R_{67}$$

where:

$R_x = 136.28\ K\Omega$

$R_{TO} = 95.040\ K\Omega$

$R_{67} = 50.00\ K;$

$$R_T = \frac{136.28\ (10)^3}{0.93960 + M} - 50.00\ (10)^3\ (\Omega);$$

$$T = \left\{a + b\ \mathrm{Ln}(R_T) + c\ \left[\mathrm{Ln}\ (R_T)\right]^3\right\}^{-1} - 273.18(^{o}C);$$

* From W. HILL, SEA DATA CORP.

$a = 0.907(10)^{-3}$;

$b = 0.2253(10)^{-3}$;

$c = 0.1136(10)^{-6}$.

These constants derived from Woods Hole Oceanographic Institution data differed by no more than $0.3^{o}C$ from the YSI data but seemed more reliable. Uncalibrated thermistors may vary up to $0.1^{o}C$ from the average data. Temperature measurements accurate to $0.03^{o}C$ can be obtained from calibrated thermistors. Accuracies to $0.005^{o}C$ can be obtained by applying a linear correction for the temperature sensitivity of the DC-37 thermometer card.

4.2 Electronics

4.2.1 Clock Corrections

To obtain accurate harmonic constants, the times at which the pressure samples are taken must be accurately known. The pressure gage clocks are in general temperature-sensitive and have a frequency offset at room temperature. The data processing program is designed to correct the sampling intervals for clock errors; as input parameters, the program requires coefficients in formulas to compute the clock deviation from the ideal frequency . These clock correction formulas and calculations are contributed by Dr. Harold Mofjeld.

Laboratory measurements of the clock deviations were made on 8 Feb. 1975, over a range of temperature for the five S/N clocks to be installed in the new shallow water pressure gages. The clock deviations, with the accuracy of measurement limited by the resolution of the Hewlett-Packard Model 5245L Electronic Counter, are given in Table 4 and plotted in Figure 21 as functions of temperature.

To determine the effects of temperature on the clock deviation, the deviations for each clock relative to the values at $9.35^{o}C$ (Figure 22) and $14.30^{o}C$ (Figure 23) were plotted versus temperature. The deviations relative to the $14.30^{o}C$ values from a narrow envelope with a width comparable to the

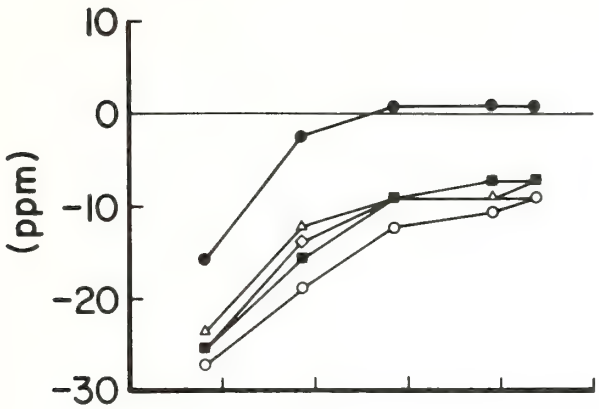


Figure 21. Clock deviations as functions of temperature.

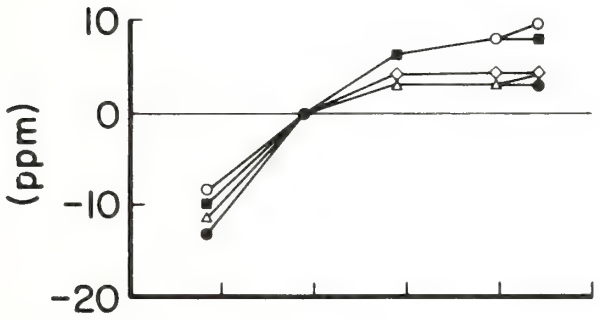


Figure 22. Temperature deviations @ 9.35°C.

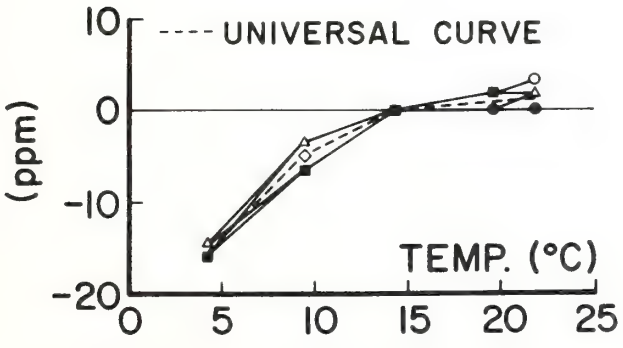


Figure 23. Temperature deviations @ 14.30°C.

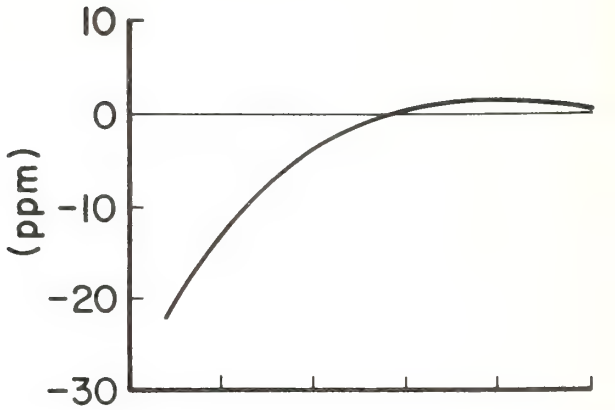


Figure 24. Universal curve, cubic f

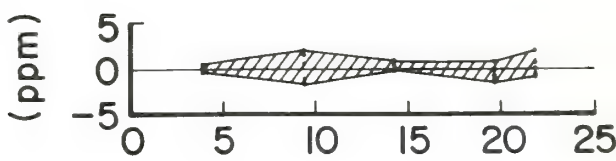


Figure 25. Clock deviations vs. cubic fit.

- • S/N-1
- ◇ S/N-2
- ○ S/N-3
- △ S/N-4
- ▪ S/N-5

TABLE (4)

Measured Clock Deviations

Temperature (°C)	Deviations (parts per million)				
	S/N-1	S/N-2	S/N-3	S/N-4	S/N-5
4.06	-15.56	-25.40	-27.03	-23.76	-25.40
9.35	-2.46	-13.93	-18.84	-12.29	-15.56
14.30	0.82	-9.01	-12.29	-9.01	-9.01
19.74	0.82	-9.01	-10.65	-9.01	-7.37
22.01	0.82	-9.01	-9.01	-7.37	-7.37

Note: All values ± 0.82 ppm

TABLE (5)

Average Clock Deviations Relative to the 14.30°C Value

Temperature (°C)	Deviations (ppm)
4.06	-15.73
9.35	-4.92
14.30	0.00
22.10	1.32

Note: 19.74°C data are not used because of their proximity to the 22.10°C data.

T = Temperature in °C

$u = (T - 14.30^{\circ})/5.00$

f = Actual Frequency

f_o = Ideal Frequency

D = Clock Deviation in parts per million

D* = Clock Deviation relative to the 14.30°C value

$D^* = 10^6 (f - f_o)/f_o - D(14.30^{\circ})$

$D^* = 2.9625\ u - 1.76885\ u^2 + 0.25279\ u^3$

measurement error. Since it is not possible to resolve individual differences in temperature characteristics, a universal curve was fitted to the data in Figure 23 by using a cubic polynomial fitted exactly to the mean of the relative deviations at each temperature. These mean values and the polynomial are given in Table 5 and are plotted in Figure 24.

The total deviation for each clock was found by averaging the differences between the measured deviations for each clock and the cubic polynomial in Table 5. Shown in Table 6 are these averages which, when added to the univeral temperature curve, give the total deviation for each clock as a function of temperature.

Table 6

Average Differences Between the Clock Deviations and the Universal Temperature Curve

	S/N-1	S/N-2	S/N-3	S/N-4	S/N-5
Average =	0.45	-9.71	-12.00	-8.72	-9.38

a_o = Average Clock Deviation

D = Total Clock Deviation for a given Clock

D* = Deviation from the Temperature Curve

$D = D^* + a_o$

The differences between the measured clock deviations and the formula in Table 6 are plotted in Figure 25. The total standard deviation of the differences is 1.08 ppm, which is reasonably close to the resolution of the counter, 0.82 ppm.

5. RESULTS AND RECOMMENDATIONS

5.1 Results

During the past year, five tide gage systems were successfully deployed and recovered in the New York Bight area as part of the MESA program. Tide and temperature records were obtained from three of the instruments; only temperature records were recovered from the remaining two. This was not due to failures in the pressure transducers, but rather to

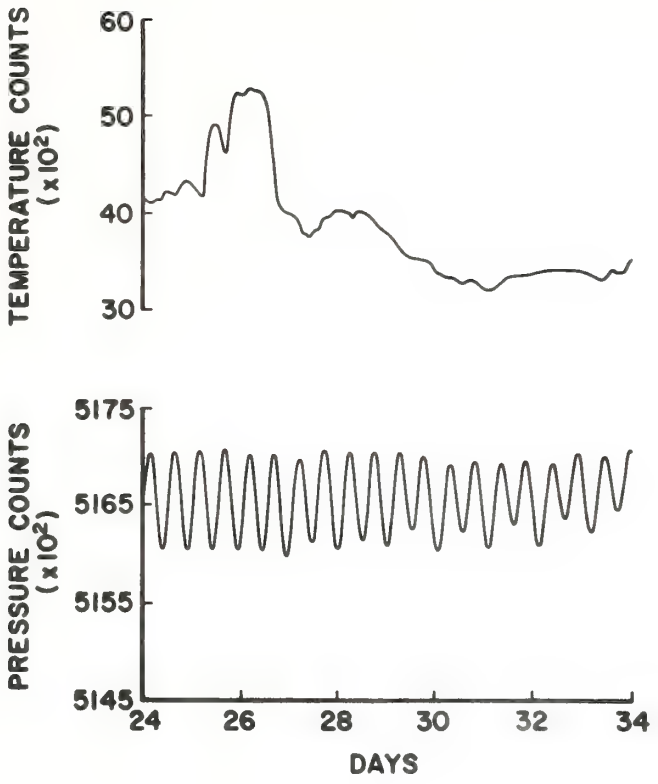


Figure 26. Temperature and tide record from MESA deployment of tide gages.

internal problems with the signal processing electronics. These data are being collected as part of an on-going project to map empirically the tides in the N.Y. Bight and will be used to study storm surges.

A ten-day segment of a temperature and tide record is shown in Figure 26. This record was chosen to illustrate some rather dramatic changes in the temperature and tidal distributions occurring at about the twenty-seventh day and continuing on through the record, but actual numerical analysis reveals much more detail.

5.2 Recommendations

Since the initial design and construction of the tide gages, several items that have come to my attention are important enough to be mentioned here.

It is recommended that the diaphragm be replaced with an oil-seawater interface which is available from Paroscientific in the form of a flexible, oil-filled line attached to the transducer pressure port. This interface can eliminate possible hysteresis and non-repeatability characteristics.

It is further recommended that the shockmount be replaced with a Paroscientific, Model 300-A shockmount. The present shockmount is quite adequate when the transducer is in the gage. However with the transducer removed from the gage, the 300-A offers a greater margin of protection.

The oil for the digiquartz should be outgassed before it enters the transducer bellows and the coiled nylon tubing. This assures that the silicone oil is free from any air particles.

6. ACKNOWLEDGMENTS

The author wishes to thank Dr. Harold O. Mofjeld for his contributions and advice throughout the preparation of this report, especially with regard to the calibration and testing section.

The permission of the Sea Data Corporation to reproduce schematics of the electronic cards is acknowledged.

7. REFERENCES

1. Dean, J. (1972). Nominal thermistor values, Woods Hole Oceanographic Institution. (unpublished manuscript.)

2. Paros, J. (1976). Digital Pressure Transducers. Measurements and Data, Mar/Apr. issue 56, 10, 2, 74-79.

3. Steinhart, J. and Hart, S., (1968). Deep Sea Research, 15, 497-503.

4. Wimbush, M. (1976). An Inexpensive Sea-floor Precision Pressure Recorder. Deep Sea Research, (in press).

USCOMM - ERL

7

Bulletin of the American Meteorological Society 58, No. 2, 179-180.

Physical Oceanography of Estuaries (and Associated Coastal Waters) is a carefully prepared and well-written book that deals with the dynamical processes in estuaries. The subject matter while being far afield from meteorology should, nevertheless, be of interest to those readers concerned with physical oceanography and fluid dynamics. In a brief introduction, the author presents the reader with the jargon used in estuarine studies and distinguishes different types of estuaries, without getting too involved with the details of estuary classifications. The book has been divided into two parts. First, the author introduces the theory governing estuarine dynamics, and then he presents applications of the theory to estuaries throughout the world.

Part 1, Theory, includes chapters on Hydrodynamics, Tidal Phenomena, Circulation, Mixing, and Pollutant Dispersion. In each chapter the author carefully guides the reader through the development of the theory. Estuarine dynamics is a complex subject for which many simplifying assumptions must be made in order to understand the processes involved. In reviewing this book, it is a pleasure to note that the author, for the most part, clearly indicates the assumptions and discusses their limitations. Whenever possible, more than one way of obtaining the same result is presented, and the author carefully indicates the steps taken in the formulations. His mathematical rigor is often complemented by insight based on simple physical arguments.

Part 2, Applications, contains applications of the theory and field observations in over 60 estuaries throughout the world. Chapters are devoted to the estuaries of Great Britian, Europe, Americas (East and West Coast), Asia, Australia, and Japan. Besides enlightening the reader concerning the different types of conditions that have been observed in the estuarine environment, the author has compiled perhaps the most comprehensive synopsis of field observations in estuaries to date. This section alone will make a fine reference for estuarine investigators.

There are two criticisms worth mentioning. In the past few years, a number of mathematical models of estuarine circulation have been developed; however, the theory section includes only analytical methods. The author acknowledges exclusion of these models and cautions the reader about interpreting results from any model. Although I agree with his caution, the same caution must be observed when applying analytical techniques, which are often of limited use. Perhaps, a chapter discussing a few basic types of models and their limitations would have been better than no discussion at all. Although the section on applications gives an excellent summary of observations in numerous estuaries, I would have found equally desirable a more detailed discussion of the circulation features of a few estuaries.

In summary, Dr. Officer's book on estuarine processes is a fine text, one that should make an ideal reference for a graduate course in estuarine dynamics.—*J. F. Festa*

NASA CP-2003, Session C, Simulation, Sensors, and Data (Dr. Donald Hansen, Chairman) 173-192.

SESSION C

Simulation, Sensors, and Data

Chairman: Dr. Donald Hansen,

National Oceanic and Atmospheric Administration,
Atlantic Oceanographic and Meteorological Laboratories

A LAGRANGIAN BUOY EXPERIMENT IN THE SARGASSO SEA

by

Dr. Donald V. Hansen
Atlantic Oceanographic and Meteorological Laboratories
Environmental Research Laboratories
National Oceanic and Atmospheric Administration
Miami, Florida

As indicated, we'll hear from a group of distinguished drifters this morning. In order to be sure we don't run out of time for me, I'll say my piece first. I can make mine a little bit shorter than I'd planned because a number of comments that have already been given set the stage for it. The genesis of my story begins back about 1970 when a number of people in the physical oceanographic community in this country and abroad began thinking and talking about a project to be called the Mid-Ocean Dynamics Experiment (MODE). It was referred to yesterday by Doug Webb and others as the MODE-1 Project. About that time, I began talking to Sam Stevens about the possibility of hitching a free ride, or at least an inexpensive ride, on the French EOLE satellite system, and through the very good offices of Sam and his crack team, we were indeed able to do that. The engineering for the project was done by the Miami Branch of the Engineering Development

The Author: Dr. Hansen received his Ph.D. in Oceanography from the University of Washington in 1964. He worked as a Research Assistant Professor at the University for 1 year before becoming a Research Oceanographer with the Department of Commerce in 1965. He is presently Director, Physical Oceanography Laboratory, Atlantic Oceanographic and Meteorological Laboratories, NOAA, Miami, Florida.

Laboratory of NOAA's National Ocean Survey in Miami. Charlie Kearse described yesterday some of the shipboard procedures and arrangements that were developed by them for us to get these buoys in the water, but what he did not mention was that they also were entirely in charge of the engineering and fitting out of these buoys, and in getting them into the water on what turned out to be extremely short notice. As the project developed, it really didn't go quite as we had planned to have it go, because, due to changes in the scheduling of the MODE Project and of the EOLE Satellite Project, it appeared at a critical time that the two after all were not going to be coincident in time. The EOLE Project was to terminate before the MODE Project went to sea. However, it seemed an interesting and important enough experiment to do in its own right, so we pressed on and did it anyway, almost totally independent of MODE. There was about a 1 month overlap between the termination of this project and the initiation of MODE and, in fact, the buoy that we initially had deployed farthest from the MODE area passed within 30 miles of the central mooring of MODE during the second month of that project.

I want to show you a few slides first to indicate some of the motivation for having done the experiment in the way we did it, and to set the stage to address the question of interpretation which Dean Bumpus raised yesterday with some vigor. If I can see the first slide now, please.

This is an example of a publication that is put out by the Navy. They're called Pilot Charts and show currents and wind to be expected in this region of the Sargasso Sea, what mariners and, in fact, what the rest of us know about surface currents in the Sargasso Sea. I might mention in passing, that all of the data that you can find anywhere on such atlases or charts are, in fact, derived by Lagrangian means. These currents summarized in atlases are about 99 44/100% pure ship drift calculation. They're currents inferred from the deviation of ships from their navigational calculations. The major feature I want to point out here is the fact that all of these current vectors show a very smooth steady flow to the west at

speeds ranging from about a knot to speeds on the order of 1/2 a knot. The MODE Project which you saw illustrated in one of Doug Webb's slides, I believe, was conducted in a circle of about 200 kilometer radius. Figure 2 is a copy of a slide taken from some Soviet work in this region. The Soviets have an active interest in the oceanography of the low latitude Atlantic because they conduct vigorous fisheries activities out there and they have conducted intensive research cruises in this region in 1969 and again in 1971. Figure 2 shows their interpretation of those observations. They're a rather intensive set of observations. Soviet literature is a bit hard to interpret as many of you know, in that they don't document their conclusions by Western standards, but as best one can determine, the observations themselves are good. The interpretation is that the solid dark vectors represent the conventional wisdom about the Antilles Current - the northward and westward flow. Imbedded within them are open vectors which are directed to the southeast, which they interpret as a major countercurrent within the Antilles Current and flowing from someplace just off Florida, all the way down, as a continuous feature, joining the complicated equatorial current system and then flowing off to the east. The light lines you see are where they have intensive sets of observations. The observations consist of moored current meter measurements and shipboard measurements of temperature and salinity, from which are computed the velocity field by classical methods. This is the interpretation of what looks like a rather good set of conventional measurements in the region. When I first saw it, I was a little skeptical to say the least - if it's true, it certainly is rather exciting news to the oceanographic community in general and, in fact, rather embarrassing news to the American oceanographic community: that the Soviets should discover right on our doorstep a very major oceanographic feature about which we have no knowledge. This is a very major current. It is a surface current which, however, extends to about a kilometer deep in the ocean and it has a volume transport approximately equivalent to that of the Gulf Stream or Florida Current as it issues from the Florida Strait and heads up the east coast, which all of you are aware, I am sure, is the major oceanographic feature off the U.S. east coast.

So to try to serve two purposes here--one, we recognized before we went to sea that we would not be able to conduct an experiment in close coordination with the rest of the MODE operations; nontheless, it seemed worthwhile to try to obtain a direct measure of the near surface current structure and its variability in the MODE region. Hence we deployed our buoys along 67°W, immediately to the east of the MODE area, presuming that with the northward and westward drift they would sweep through the MODE area and probably be gone, along the lines of the rather imaginative sketch that Vukovich showed us yesterday, before MODE-I operations began. That was my preliminary guess as to what we might expect in the way of a trajectory development of these buoys when they were deployed, but as you will see, it didn't go quite that way. The idea then was to deploy the buoys so that they would sweep through the surface water in the MODE area before MODE ships came out for that project, except for the southernmost buoy. We learned of the Russian work fairly late in the game and modified the plan to some extent. The buoys were deployed 1° of latitude, 60 miles apart, between 28 north and 25 north. We placed the last one an additional 30 miles south, to place it in the middle of the region where the Soviets claimed to have discovered the countercurrent, to test that particular hypothesis.

Figure 3 shows one of our buoys in the water, using the EOLE satellite tracking system which is exhibited in the side room.

The next slide is of some interest because I think there probably will be additional discussion of this EOLE system today. Figure 4 shows the distribution of position fixes in time for the No. 5 buoy. It shows the hour of the day from midnight to midnight versus day of drift, so the points show the hour and day from time 0 that positions were obtained through the satellite system. They have a quasi-random pattern providing generally 2 - 5 fixes per day which round the clock slowly. The satellite "day" turns out to be something on the order of 23 1/2 hours. This is not a particularly good data distribution for most kinds of analysis we anticipated doing. Once we saw how the data were evolving, we did polynomial fitting

to the X and Y coordinates of the position to provide some smoothing, then we interpolated positions on these polynomial fits at 1-day intervals so we could deal in terms of a fixed time interval. I have a film animation, which we will see, that is the same sort of thing that Doug Webb showed yesterday. It runs rather rapidly so I want to take just a moment to tell you what it contains.

EDITOR'S NOTE: At this point, an animated film sequence showing the drift history of all five buoys was shown.

Figure 5 shows the complete trajectory for the buoy, No. 4, that survived longest. It was retrieved and returned to the laboratory in April 1973.

To speak very breifly about interpretations now, I think that even from this fairly simple experiment, one must begin to make some interpretations and begin to think seriously about how to interpret such data. Some things come fairly immediately to mind--in particular the region where we were exploring the possibility of a major countercurrent. Three of the buoys moved into the region of the supposed countercurrent and pretty much negate the possibility of there being any such countercurrent, and in fact, identified the source of confusion about a countercurrent. It's a sampling problem. The Soviet observations I think are good observations. Their current observations are usually good ones and their shipboard observations are good also. However, they have sampled at fairly widely spaced sections, as one must by traditional methods, and in each of these sections they have found some sort of eddy motion. The error is not in the observation, but in interpretation, in assuming continuity between these various sections. A Lagrangian technique appears to offer much potential for exploring spatial structure in the flow, and offers a fairly economic means for exploring or answering questions about spatial distributions or the existence of particular phenomena.

Another thing that we are working on now--I just have a bare beginning of some things to say about it, another kind of application that has been of interest in oceanography for many decades now is an interest in trying to

predict in a semiquantitative sense the transport or the distribution or dispersion of things dissolved or fine objects scattered in the sea, etc. As an example, the interest is in being able to predict the concentration or the probability of a particular object being in a particular place by an equation in the form:

$$\frac{\partial P}{\partial t} = K_{ij} \frac{\partial 2}{\partial x_i \partial x_j} P$$

In this formulation, K_{ij} is a dispersion coefficient relating the concentration change to the spatial gradient in two dimensions, essentially saying the time change is a diffusion type process related to the gradient, but with a tensor diffusion coefficient. In some classic work by G. I. Taylor dating back to 1921, it's shown that the kind of information that is needed to approach this kind of a problem is, in fact, the Lagrangian information--not Eulerian information, and is laboratory and wind tunnel dynamics, a lot of work over several decades has gone into the problem of trying to establish a relation between Lagrangian and Eulerian statistics. The Eulerian statistics are easier to measure, but for certain problems the Lagrangian statistics are the ones that you really want.

Given a particular particle or particular buoy that has a particular path, one can consider the mean path and the deviations from it, and compute the time lagged autocorrelation. That's what we have done but only for the diagonal components to date.

What we did was to take position data, differentiate it to obtain velocity data, and then compute a statistical function.

The autocorrelation, call it R, is the ensemble average $\overline{V_i(t)V_j(t+\tau)}$.

$V_i(t)$ denotes east or north component of velocity at some time t, and τ a time lag interval.

This is averaged over the ensemble or averaged over all time for the buoy motion. It's a measure of how rapidly the motion loses similarity with itself. At no lag at all the velocity looks exactly like itself so the autocorrelation is equal to the variance. The correlation decays with some structure as time runs on. Figure 6 shows the nature of the autocorrelation function for buoy 4.

The major features of the curve show that the correlation drops to zero on a time scale of about a week or 10 days. That is the Lagrangian time scale for motion in the Sargasso Sea. It also has an oscillatory structure that damps out with increasing lag. It really has validity only out to about 120 days. After that there are too few data points, to draw even tentative conclusions. There are roughly 200 observations going to make up each data point in the beginning of the curve. I don't believe anything out in the tail end of the curve, so basically what is revealed at least during this set of observations is a periodic variability in current having a time scale of about a month--peak to peak here is a lag time of about a month.

The next step to apply this to the dispersion problem is to relate the K_{ij} to the autocorrelation function using logic of G. I. Taylor and others. The result is that the K_{ij} is obtained from the integral of the autocorrelation over time. From a quick calculator integration of the function for buoy 4, I obtained a value 10^7 cm^2/s, which turns out to be a number popular among oceanographers. If one had to guess without knowing anything else it probably would be slightly higher than this, perhaps by a factor of 5 or so.

The other thing you can do--this is a thing that I think Lagrangian techniques are in fact more appropriate for, relative to other kinds of observation and fixed moorings, etc., is to explore not the time correlation behavior but the thing that's really hard to get from moored current meters, the space correlation behavior, because it's really an expensive undertaking to put down a lot of moorings with fixed current meters to explore how currents vary on a time scale of 1 mile - 10 miles - a hundred miles, etc.

By deploying an array of drifters such as we've been discussing here, one can set the initial scale, but as the pattern evolves, it covers quite efficiently a considerable band of space scale. We tried doing that with the buoy data we have here using the buoys in pairs, and in order to get the bulk of data up to some usable level it turns out we don't really have very much data at all yet. In order to try to get the statistics as well behaved as possible, we borrowed a ploy from the field of homogeneous turbulence and worked with buoys in pairs which are separated by a vector having some direction and some length L and decomposed them, presuming that the flow field is isotropic. I really don't have any very good argument to defend that except that the r.m.s. speed in the east directions are approximately the same at about 15 cm/sec, so with a little bit of hand waving we must pass over that question. Then we decomposed the velocity components at buoy pairs into components parallel to and orthogonal to the separation vector between them and computed spatial correlations at fixed times for the parallel and perpendicular components so defined. It turns out, however, that for the space scales covered by this data set, 100-400 km, the correlations are evidently so low that they cannot be distinguished from zero in the quantity of data available. Indications are that probably the spatial correlation is lowest someplace here in the first 100 kilometers or so which is essentially the same sort of thing that was found before and during the MODE experiment for the deep water circulation--deep currents in this same area. I think I've taken about as much time as I ought to. Thank you for your attention. If anyone has any comments, I'll try to respond.

JIM RUSSELL -- U. S. Naval Avionics Facility:
When you assume your isotrophy in your turbulence, what kind of scales are you really looking at in your measurements? Are they fairly large?

Answer -- DR. HANSEN:
Right, the scales we're looking at here are roughly in the 100-500 kilometer range for enough data to be of any significance at all.

JIM RUSSELL -- U. S. Naval Avionics Facility:
And it's also in the surface water rather in the deeper water that we're talking about?

Answer -- DR. HANSEN:
This is strictly the surface water. This was using the buoy that Charlie Kearse showed some slides of yesterday. We had a parachute drogue on them which was at 30 meters depth, so it's really very much in the upper layers of the ocean. The thermocline there is 800 meters deep or so.

JIM RUSSELL -- U. S. Naval Avionics Facility:
Something does bother me about assuming isotrophy there. Did the results you got indicate that assumption may have been o.k.?

Answer -- DR. HANSEN:
I really don't think I can address that. I haven't looked at it carefully. The only think I can say in justification is that the variance in the north-south and in the east-west direction is approximately equal, about 13 and 15 centimeters per second for the r.m.s. speed. There is some indication that in deeper water there probably is some anistrophy, higher energy levels in the north-south direction as compared to the east-west, but it does not show up in this surface data set.

BOB HEINMILLER -- Woods Hole:

There is a little event on your film that caught my eye. There were two buoys--looked like they were very close together--just estimating from the scale 5 and 10 miles--the tail of one about 10 times the tail of the other, both going in the same direction which implies that the speeds for one were considerably, an order of magnitude, higher than the other. I didn't notice that that occured any other time during the film. Have you seen any sort of that? That seems like an awfully high differential.

Answer -- DR. HANSEN:

It does happen other times. You have to see the film several times to detect more of these events, but when we first deployed the buoys I thought we had discovered the center of the ocean circulation because for a period of about 10 days the No. 4 didn't move within the resolution of the satellite, which is about a kilometer there, while buoys north and south of it, particularly one of them north of it, turned and moved toward it and came by at a good rate of speed within about 30 miles, yet the one that was initially deployed there hardly moved for about 10 days. After 10 days it suddenly took off and moved to the south as rapidly as any of them. I interpret that as being indicative of large lateral shears in the flow. In the movies that Doug showed yesterday, you see very much the same sort of thing in the SOFAR float measurements. It looks there as if there are jets imbedded in the flow. They seem to be north-south oriented there but didn't show up quite so much here perhaps because a lot of the statistics may be biased by the fact that the buoys spent a fraction of their time fairly near the Bahama Banks where presumably north-south motion is strongly inhibited and east-west motion parallel to the banks is favored.

CHRIS WELSH -- Virginia Institute of Marine Science(VIMS):

It occurs to me that if you were to put a current meter section out where the Russians did for a long length of time and average over the time to get a climatological circulation, you would still see the countercurrent structure

that they apparently saw simply because when the currents going south, the western boundary, if you want to call it that, structure is apparently more intense from the little worms you have than when they go off to the north.

Answer -- DR HANSEN:

I think that's probably true - if you'd observe just those sections, you likely would see what you interpret as a countercurrent migrating onshore and offshore and north and south or something. I suspect different eddies or different waves or whatever they are occur there at various times. You're probably right. You'd really have to have a very dense set of current meter moorings to be able to resolve the spatial structure in the flow to disabuse yourself of that idea.

PETER HACKER -- JOHN HOPKINS:

I'm worried a little bit about the slippage of the drogues in regions where you do have high lateral shear from the currents you observed and from the winds that are typical in that area. Do you have any kind of a percentage estimate of slippage of the drogue with respect to a water mass?

Answer -- DR. HANSEN:

I haven't put a number on it. We're investigating. We just got all the tropical weather information. We will correlate the local winds with the buoy movements; however, I haven't put a number on it. Maybe Charlie has, I don't know. I think the wind drift for this particular buoy is probably negligable in terms of the currents and the things we see for two reasons: one, the dominant periodicities in the major flow features have a time scale of about a month and you just don't see things like that down there in the weather pattern. You don't expect major wind events in a time scale of a month. Strictly from the engineering point of view, this buoy was about 40-41' long with the major portion of the cross section submerged and, in addition, it has a parachute drogue on it. All indications are that the parachute droges did indeed survive for a time scale of 6 months or better. Bob Heinmiller was one of the last people, I think, to see buoy No. 5 and the reports I have from the appearance of the buoy in the water, the way accessory

floats were arrayed and so on, indicate that the parachute drogue hardware apparently was still on at that time. We recovered one in December after 3 months at sea, and the whole subsurface hardware was essentially in perfect condition then. The one we recovered after 8 months outside the Bahamas had lost its parachute. I don't think it's a serious problem. Did you ever put a number on the windage Charlie?

CHARLIE KEARSE:

I guess I'm just worried. You know, even if it's just 5 or 10 percent--if a flow drifts 100 kilometers downstream or something, at the same time it can be going cross stream 5 of 10 kilometers in a region where you do have intense sheer, it may in fact drift from a countercurrent into the other part of the countercurrent if you do have closely spaced currents.

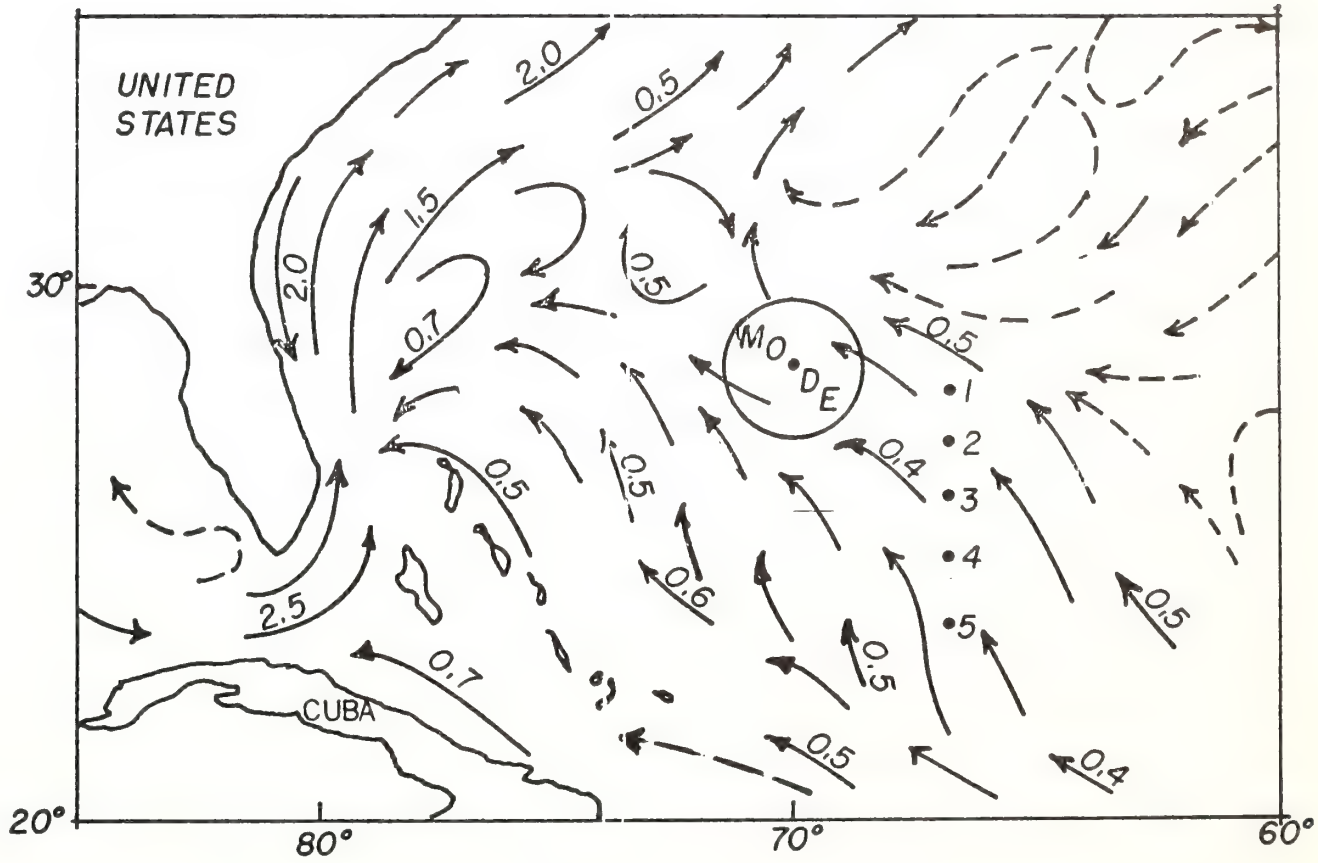


Figure 1. SURFACE CURRENTS IN THE SARGASSO SEA AS TYPICALLY SHOWN IN ATLASES (The MODE-1 region and deployment positions of 5 drifting buoys using the EOLE position locating system are also indicated.

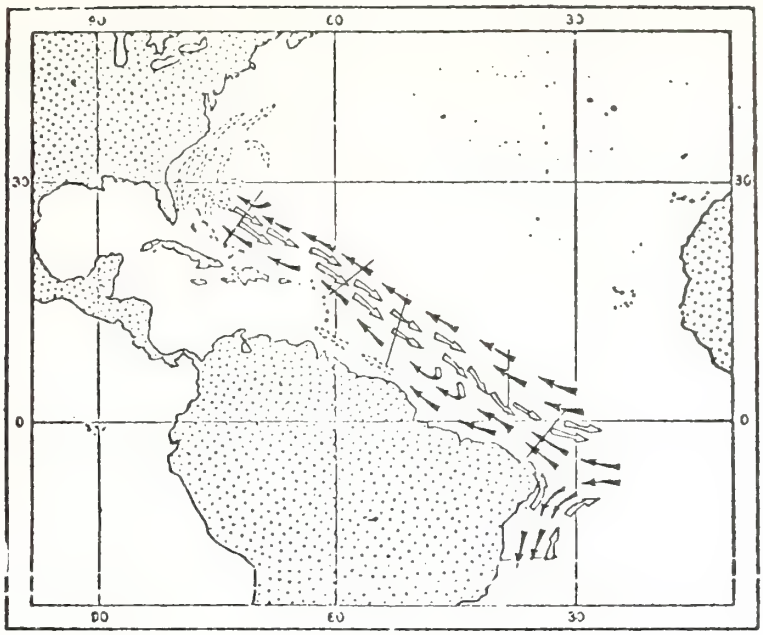


Figure 2 THE ANTILLES COUNTERCURRENT AS HYPOTHESIZED BY V.G. KORT

188

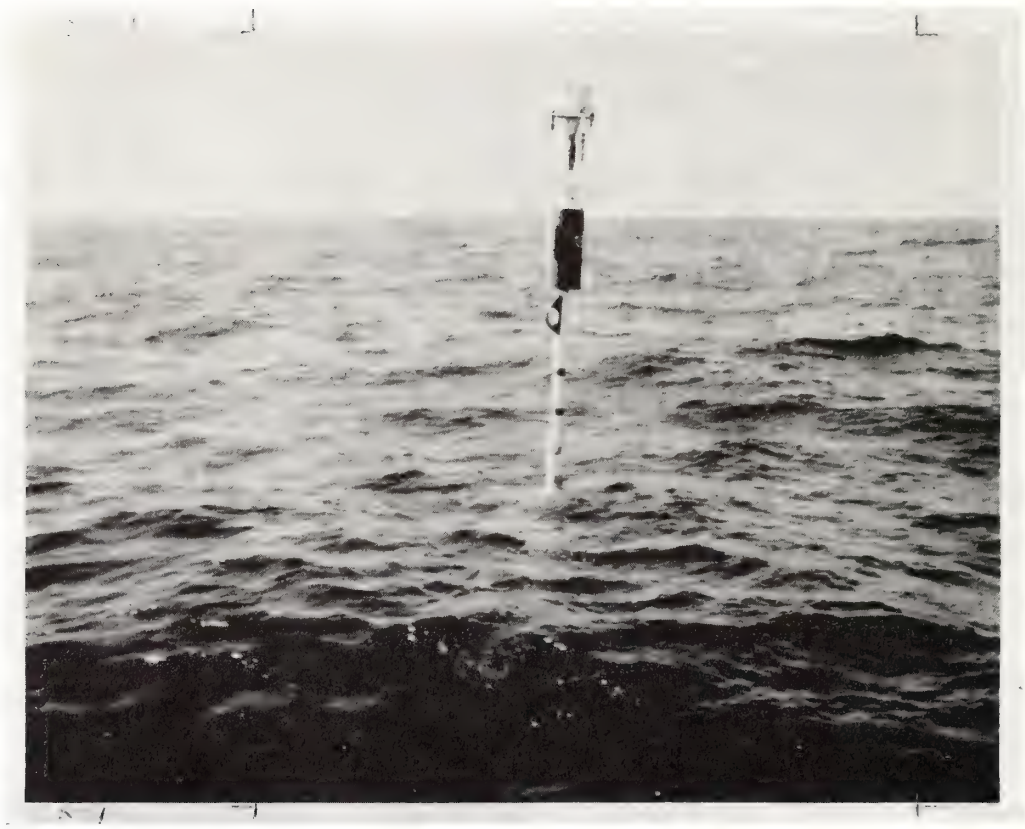


Figure 3 DRIFTING BUOY USING FOLE TRANSPONDER DEPLOYED AT SEA

189

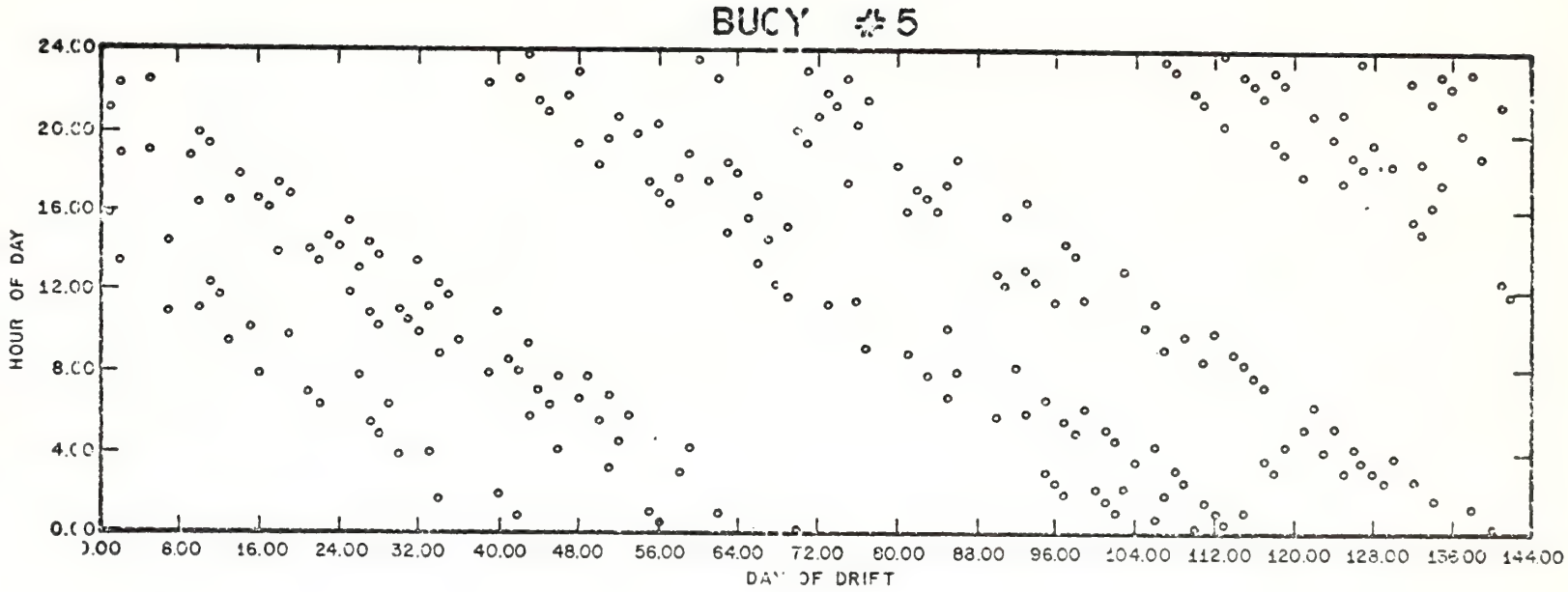


Figure 4 DISTRIBUTION OF EOLE POSITION FIXES IN TIME FOR A DRIFTING BUOY

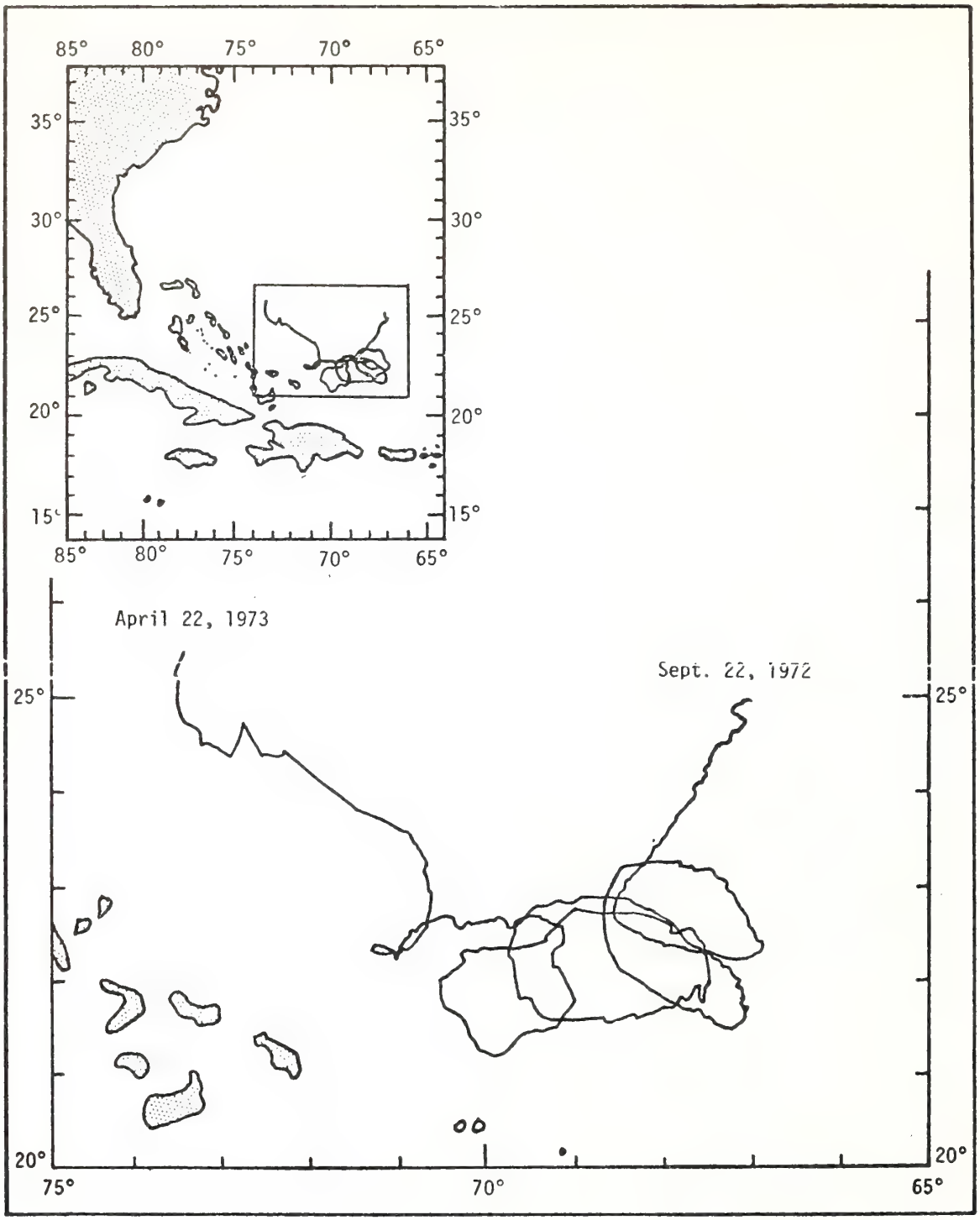


Figure 5 DRIFT TRAJECTORY FOR BUOY No. 4

191

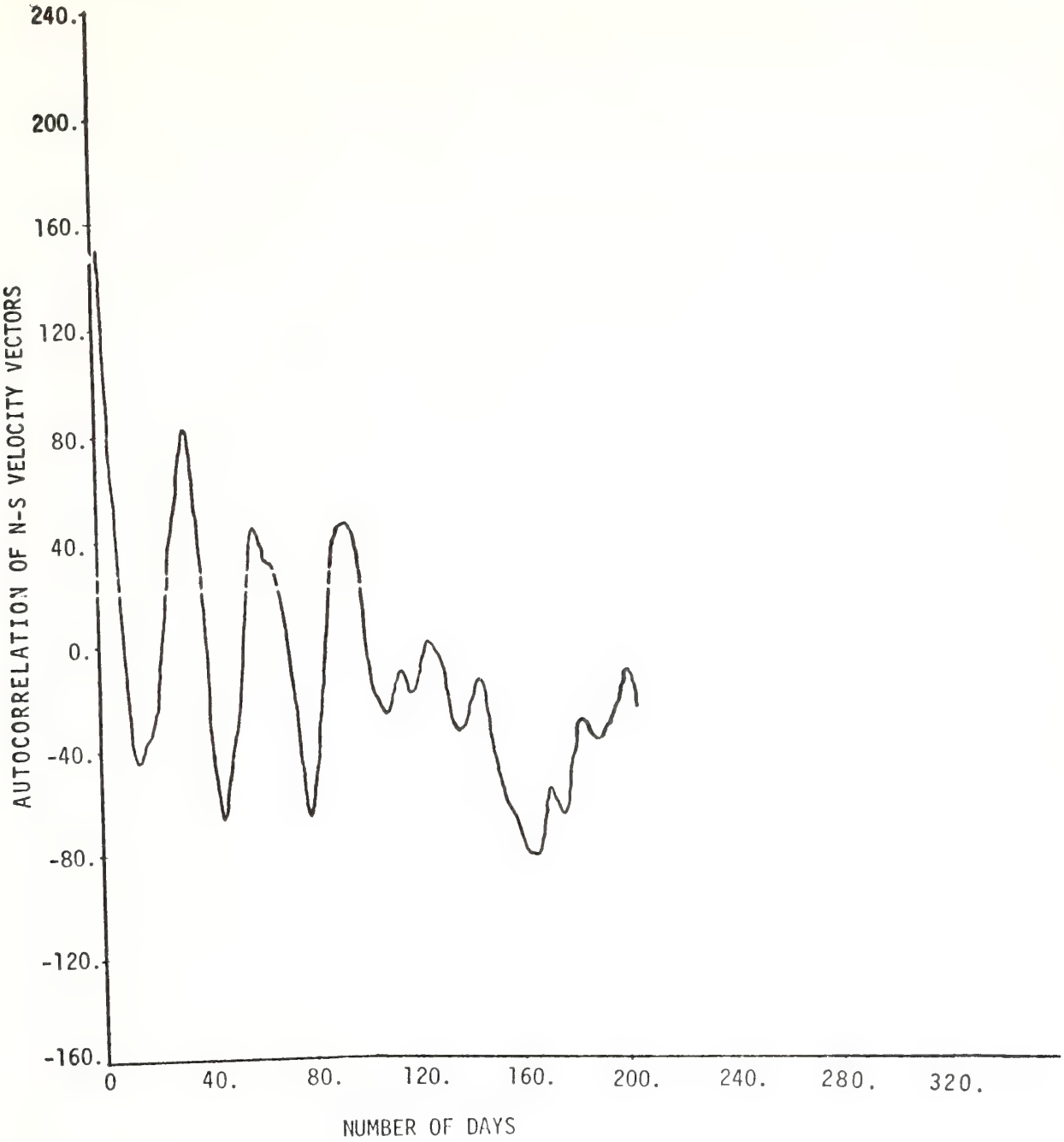


Figure 6 LAGRANGIAN TIME CORRELATION FUNCTION FOR BUOY No. 4

192

NOAA Technical Report ERL 383-AOML 25, 73 pages.

Oceanographic Variations Across the Gulf Stream Off Charleston, South Carolina, During 1965 and 1966

John B. Hazelworth

Atlantic Oceanographic and Meteorological Laboratories
Miami, Florida

September 1976

U.S. DEPARTMENT OF COMMERCE
Elliot Richardson, Secretary
National Oceanic and Atmospheric Administration
Robert M. White, Administrator
Environmental Research Laboratories
Wilmot Hess, Director

Boulder, Colorado

Notice

Mention of a commercial company or product does not constitute an endorsement by NOAA Environmental Research Laboratories. Use for publicity or advertising purposes of information from this publication concerning proprietary products or the tests of such products is not authorized.

CONTENTS

		Page
Abstract		1
1.	INTRODUCTION	1
2.	FIELD OPERATIONS	2
3.	STATION DATA PROCESSING	5
4.	COMPUTER COMPUTATION AND PLOTTING	6
5.	VARIATIONS OF PHYSICAL PROPERTIES	7
	5.1 Temperature	7
	5.2 Salinity	18
	5.3 Dissolved Oxygen	27
	5.4 Sigma-t	36
6.	GEOSTROPHIC CURRENTS AND VOLUME TRANSPORT	46
7.	WATER MASS ANALYSIS	53
8.	OXYGEN-DENSITY RELATIONSHIP	62
9.	ACKNOWLEDGMENTS	71
10.	REFERENCES	71

OCEANOGRAPHIC VARIATIONS ACROSS THE GULF STREAM OFF CHARLESTON, SOUTH CAROLINA, DURING 1965 AND 1966

John B. Hazelworth

The ship Peirce of the United States Coast and Geodetic Survey (U.S.C.&G.S.), now the National Ocean Survey (NOS) of the National Oceanic and Atmospheric Administration (NOAA), conducted a physical oceanographic program across the Gulf Stream off Charleston, South Carolina. The project consisted of a series of cruises, one every two weeks, from August 1965 to July 1966. The primary objectives of the program were to investigate the variability of the physical properties and to record the dynamic variability of the Gulf Stream over a period of one year. This report describes the measurements taken and the methods applied to correct and analyze the hydrographic station data. Cross-sections of each physical property for each cruise are presented. Geostrophic currents and volume transport calculations are presented. Results of water mass analysis by use of the T/S curve and also by use of the oxygen-density relationship are given.

1. INTRODUCTION

The Gulf Stream (specifically the Florida Current) was first described by Ponce de Leon in 1513. Since then numerous men have made observations describing it, and others have advanced theories explaining it. Stommel (1965) has an excellent historical summary in which he states that "even now, after many years of effort, our concept of the Gulf Stream is incomplete." He further states "even today we do not have nearly as much accurate synoptic information about the Gulf Stream as we desire".

With this need in mind, oceanographers from several oceanographic laboratories designated 1965 and 1966 as a period of intense study of the Gulf Stream. The U.S.C.&G.S. planned three projects and designated the ships Explorer and Peirce to carry them out.

The Explorer carried out a series of cruises tracking and monitoring the position of the Gulf Stream meanders northeast of Cape Hatteras. The results of this work have been reported by Hansen (1970)

During the same period, the Peirce was assigned the responsibility of obtaining, as nearly as possible, synoptic data across the Gulf Stream by a series of hydrographic casts. To obtain as accurate and detailed information as possible, the Nansen bottles were spaced relatively close together and the distance between stations was relatively short.

A third project, reported by Wunsch et al. (1969), investigated fluctuations of the Florida Current inferred from sea level tide records.

2. FIELD OPERATIONS

The field operations for the Peirce Gulf Stream project lasted one year. Twenty-seven cruises were planned, one every two weeks. Each cruise lasted three to four days. Cruises 13 and 17 were canceled because of bad weather. Cruises 3, 11, and 19 were shortened for the same reason. Table 1 lists the dates of the cruises and the National Oceanographic Data Center (NODC) cruise numbers.

Table 1. Cruise Dates and NODC Cruise Numbers

Cruise No.	Date	Season	NODC Cruise No.
1	3-8 August 1965	summer	718
2	19-23 August 1965	summer	953
3	1-2 September 1965	summer	515
4	15-18 September 1965	summer	705
5	30 September-3 Oct 1965	fall	718
6	12-15 October 1965	fall	721
7	27-31 October 1965	fall	953
8	11-14 November 1965	fall	980
9	1-4 December 1965	fall	721
10	15-18 December 1965	fall	725
11	5-6 January 1966	winter	953
12	11-14 January 1966	winter	961
14	2-5 February 1966	winter	989
15	16-19 February 1966	winter	766
16	3-6 March 1966	winter	766
18	22-25 March 1966	spring	782
19	5-6 April 1966	spring	723
20	18-21 April 1966	spring	782
21	4-7 May 1966	spring	693
22	18-20 May 1966	spring	737
23	1-3 June 1966	spring	694
24	15-17 June 1966	spring	737
25	28-30 June 1966	summer	737
26	12-15 July 1966	summer	769
27	26-28 July 1966	summer	813

According to the original cruise plan, the ship was to go to about 32°22'N and 79°14'W. At that point the direction of the Gulf Stream was to be determined by means of a parachute current drogue. The cruise track was then laid out at right angles to the current direction. During each cruise, 16 oceanographic stations were taken at 10-mile intervals along a 150-mile track line. After taking station 16, the ship would return to station 13 and reoccupy it as station 17. The ship would then proceed towards shore reoccupying each station, for a total of 29 stations. Approximate station locations are given in Table 2. Starting with cruise 20, the track line was revised as shown in Figure 1. The track line described by the odd numbered stations was the approximate track line for the first 19 cruises. The number within the station identification circle indicates the station number for cruise 1 through 19. Also starting with cruise 20, a near-surface parachute current drogue was set out at each even numbered station from 2 to 20. Each drogue was followed for about 30 minutes to one hour and the average current was computed.

Table 2. Approximate Locations of Gulf Stream Stations

Station No.	Latitude	Longitude
1	32°21'N	79°13'W
2	32°12'N	79°10'W
3	32°05'N	79°03'W
4	31°57'N	78°56'W
5	31°48'N	78°50'W
6	31°38'N	78°44'W
7	31°30'N	78°38'W
8	31°20'N	78°32'W
9	31°11'N	78°26'W
10	31°02'N	78°20'W
11	30°53'N	78°14'W
12	30°44'N	78°08'W
13	30°35'N	78°01'W
14	30°26'N	77°55'W
15	30°17'N	77°50'W
16	30°08'N	77°42'W

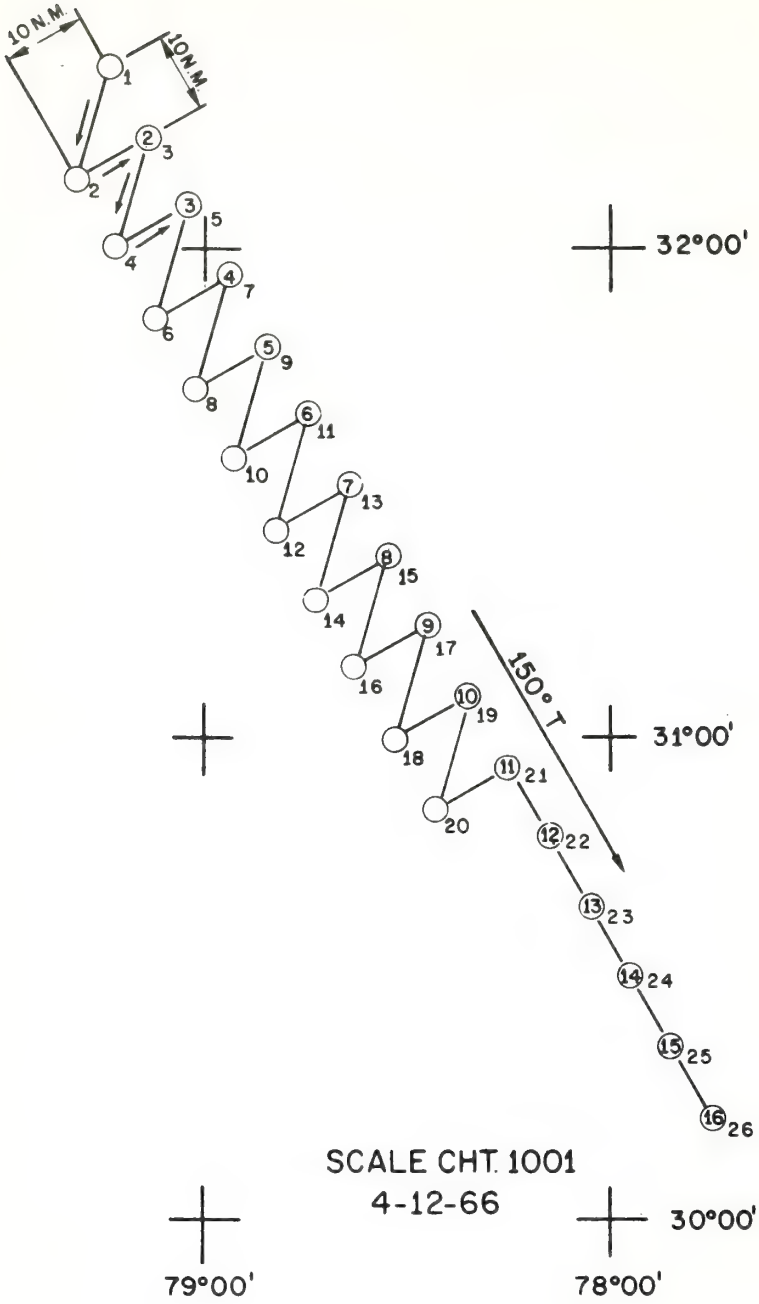


Figure 1. Amended station array, Project OPR-458 Gulf Stream investigation, ship Peirce, 1965-66.

A Nansen cast was taken at each station. Bottles were spaced at 10-m intervals from 0 to 60 m, at 20-m intervals from 60 to 300 m, at 50-m intervals from 300 to 500 m, and at 100-m intervals from 500 m to the bottom. If the station was in water deeper than about 180 m, it was necessary to make two casts.

Primary position locations were determined by LORAN A. Nearshore determinations also were made by HIFIX. Relative positions of the parachute drogues also were made by HIFIX.

Each Nansen bottle held two protected reversing thermometers. In addition an unprotected reversing thermometer was placed on each bottle below 100 m.

3. STATION DATA PROCESSING

Standard thermometer corrections, thermometric depths, and sigma-t values were calculated aboard the ship on a PDP-8 computer. Salinities were determined by using a HYTECH inductive salinometer. Oxygen values were determined by the Winkler method.

At the conclusion of each cruise, the data were processed using standard techniques as outlined by the U.S. Navy Hydrographic Office (1951, 1955). For cruises 1 through 20, the temperature vs. depth, salinity vs. depth, sigma-t vs. depth, oxygen vs. depth and the temperature vs. salinity graphs were hand drawn. Starting with cruise 21, the graphs were drawn by a Cal Comp plotter.

For each cruise, a composite temperature-salinity (T-S) graph was drawn, and individual station observations were compared with it.

When the processing of the serial station data was completed and checked for a cruise, data were sent to the NODC. The NODC calculated sigma-t, specific volume anomaly, dynamic depth, and sound velocity at each observed and standard depth. Temperature, salinity, and oxygen interpolated values also were computed at standard depths.

Before a final computer serial data list was printed, a preliminary listing was reviewed. Sigma-t values were plotted as a check, and hand interpolations of temperature, salinity, and oxygen values at standard depths were made where the computer-calculated values were unacceptable. Final listings were then produced by the NODC.

Unless questioned, the depths of the individual observations are considered to be accurate within 5 m, the temperatures to $\pm$ 0.02°C, and the salinities to $\pm$ 0.01°/oo. When two protected thermometers were used on a Nansen bottle, the average of the two readings was accepted, unless the readings differed by more than 0.05°C. In that case, the more reasonable value was accepted.

One of the following analyses involves seasonal summations of the various oceanographic parameters by station. In these cases, a constant position for each station is assumed. Originally it was intended that station 1 was to be at the same position for all cruises. Successive stations would be located at ten-mile intervals along a straight line at right angles to the current direction. Thus, owing to variation in current direction, the position of a station varied slightly from cruise to cruise. A plot of all stations showed that station 1 varied for all cruises less than one mile. However, the position of each succeeding station ranged over a slightly larger area. Finally station 16 ranged up and down stream from the position given in Figure 1 by as much as 10 miles. It is the opinion of the author that this position variation does not seriously affect the particular analysis, as the position variation for any given station is generally up and down stream and not cross-stream. Also, the greatest position variations occurred at the eastern end of the track line where the parameter variations were the least.

4. COMPUTER COMPUTATION AND PLOTTING

Data sorting and computation of seasonal mean values for each parameter were made by computer. For these mean values, observed data at varying depths could not be used. Rather the interpolated values at standard depths were used. The data were sorted by station and by season, and means were then computed at each standard depth for each oceanographic parameter.

The contour cross-sections were drawn by a Stromberg-Carlson 4020 plotter for each oceanographic parameter for each cruise as well as for seasonal cross-sections. The contour computer program required data at all points of a square matrix. Ideally the points should be equal distances apart. As the data fell far short of these requirements, they had to be manipulated by interpolation procedures. The first interpolation was the computation of standard depths by the NODC. Both observed and standard depth values were used in the matrix computation for the individual cruise cross-sections unless the two were within five meters of each other. Then only the observed values was used. The second interpolation was vertical and linear filling in all points of a 16 x 50 matrix. A third interpolation by weighted means was performed to put the data into a 20 x 20 square matrix. This still was not a true square matrix, as the horizontal distance was 150 miles and the vertical distance was 1000 m.

In spite of the several interpolations, the finished contoured cross-sections agreed quite well with hand drawn ones as long as a sufficient amount of observed data was available. In some cases, holidays occurred. Then interpolation processes took over and the results may be unreliable.

For this reason, on the individual cruise cross-sections each observed data point is indicated by a symbol. The contours also were quite unreliable in the vicinity of a very steep bottom gradient, notably between stations 2 and 3. Station 2 had observed data down to about 50 m and then extrapolated values to 200 m. These values were contoured with the observed values to 200 m at station 3. The results, particularly notable on the water temperature cross-sections, were unacceptable.

The 4020 plots were checked against the original data. Where found to be unreliable the plots were redrawn by hand to fit the original data and then the final contour cross-section plots were drafted.

5. VARIATIONS OF PHYSICAL PROPERTIES

5.1 Temperature

The yearly mean temperature cross-section (Fig. 2) shows that the warmest water appears at the surface in the vicinity of the core of the Gulf Stream. Farther seaward the surface temperature averages about 1°C cooler, while the nearshore end of the time, being somewhat under the environmental influence of the nearby land mass, averaged 3 to 3 1/2°C colder. Water temperature decreased with increased depth. Minimum temperature for the entire cross-section of less than 8°C was observed at stations 3 and 4 in 300 to 350 m. In fact, the water temperature was colder at those stations than at stations 12 through 16 in over 800 m.

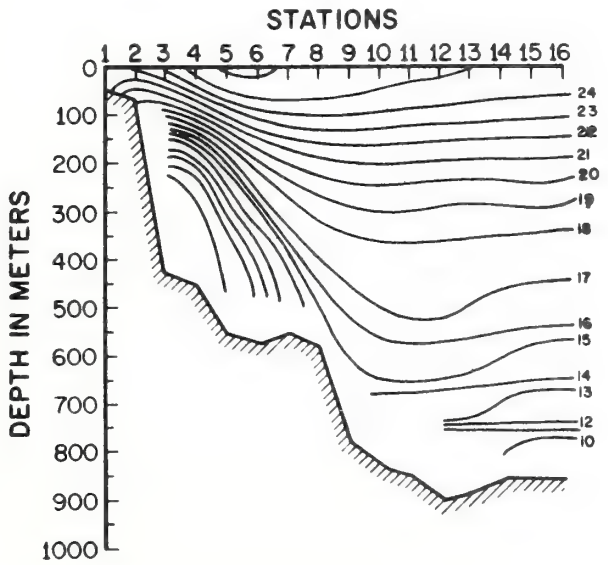


Figure 2. Mean of all cruises water temperature (°C) cross-section.

Throughout the near surface regions (Figs. 3, 4, 5, and 6) seasonal temperature variations were noted. Individual cruise cross-sections are given as Figures 7 through 29. Temperatures were warmest during summer and coldest during winter. The largest seasonal temperature variations were recorded at the nearshore stations. For example, the largest temperature range during the entire year was 9.65°C with a standard deviation of 2.93°C. This was recorded at the surface at station 3. The surface temperature range at station 4 was almost as large, yet the smallest range was found at the next station in the core of the Gulf Stream.

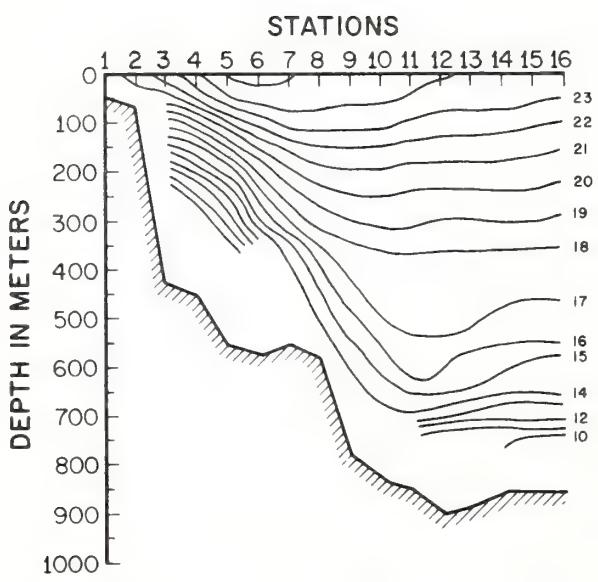


Figure 3. Mean of spring cruises water temperature (°C) cross-section.

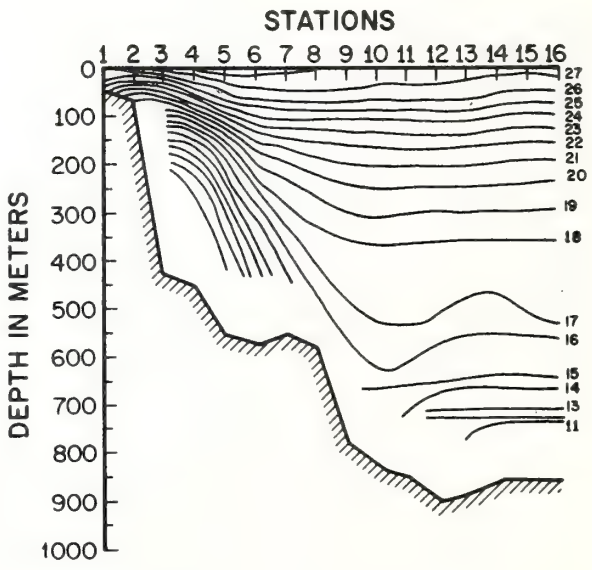


Figure 4. Mean of summer cruises water temperature (°C) cross-section.

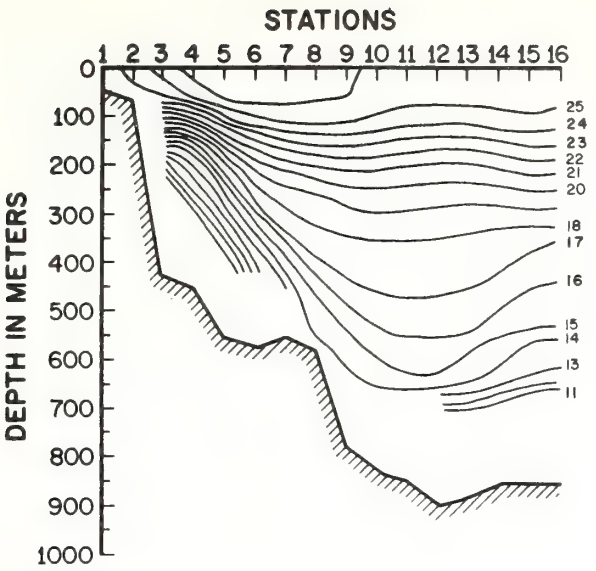


Figure 5. Mean of fall cruises water temperature (°C) cross-section.

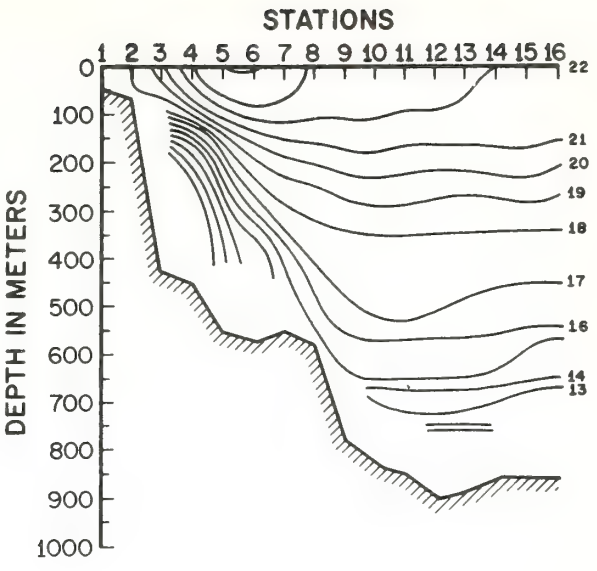


Figure 6. Mean of winter cruises water temperature (°C) cross-section.

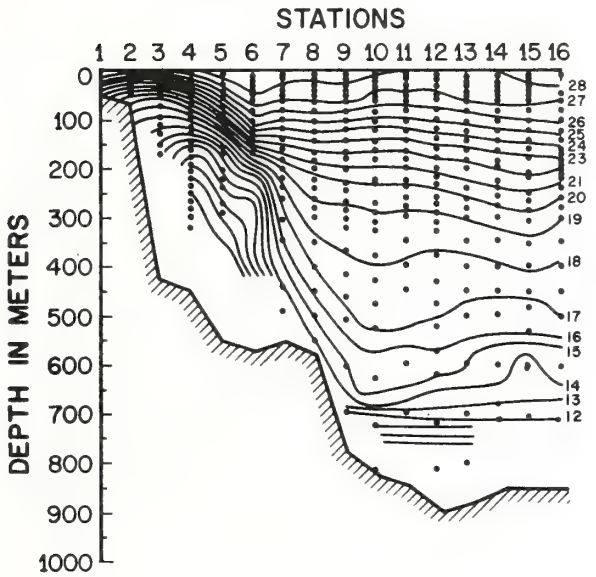


Figure 7. Cruise-1 water temperature (°C) cross-section.

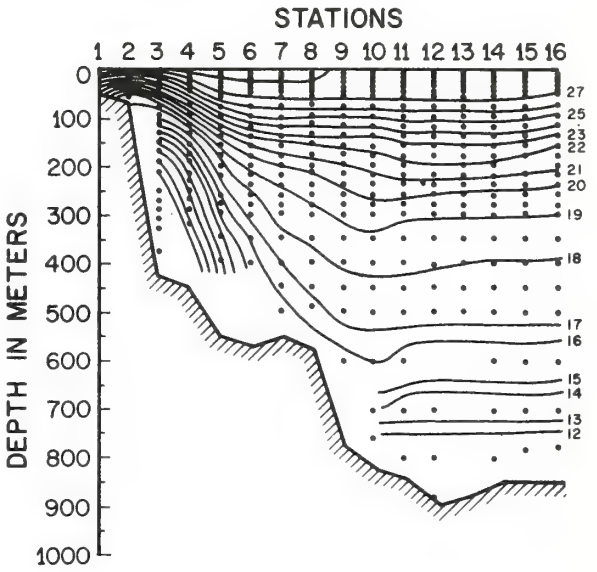


Figure 8. Cruise-2 water temperature (°C) cross-section.

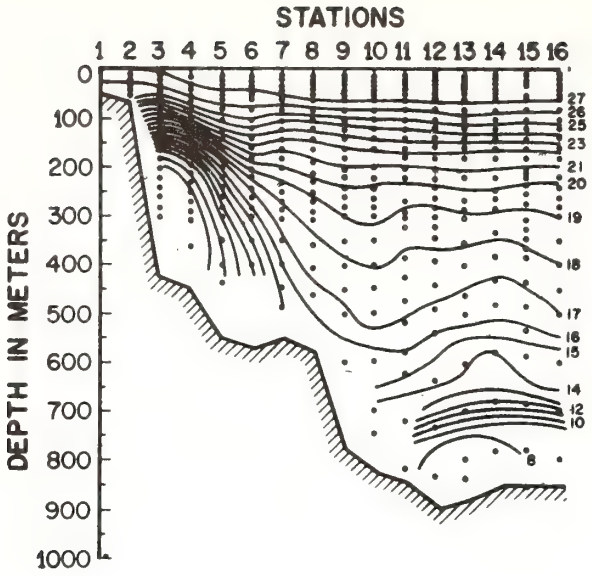


Figure 9. Cruise-4 water temperature (°C) cross-section.

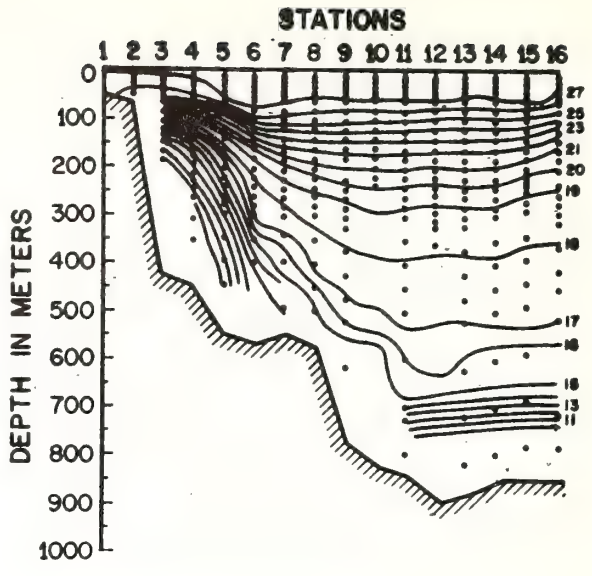


Figure 10. Cruise-5 water temperature (°C) cross-section.

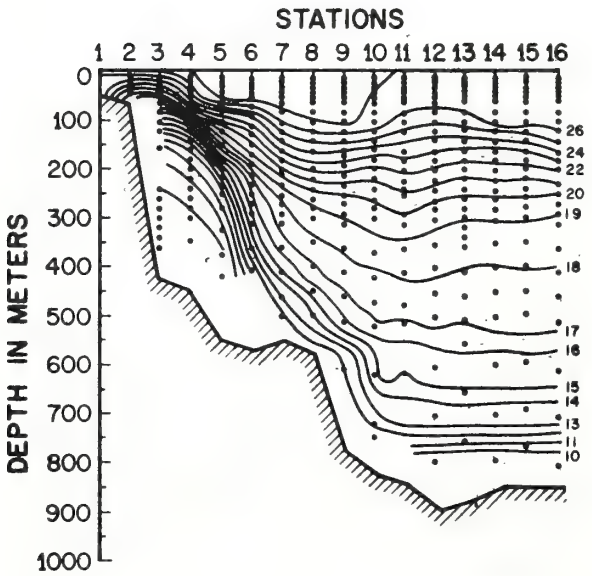


Figure 11. Cruise-6 water temperature (°C) cross-section.

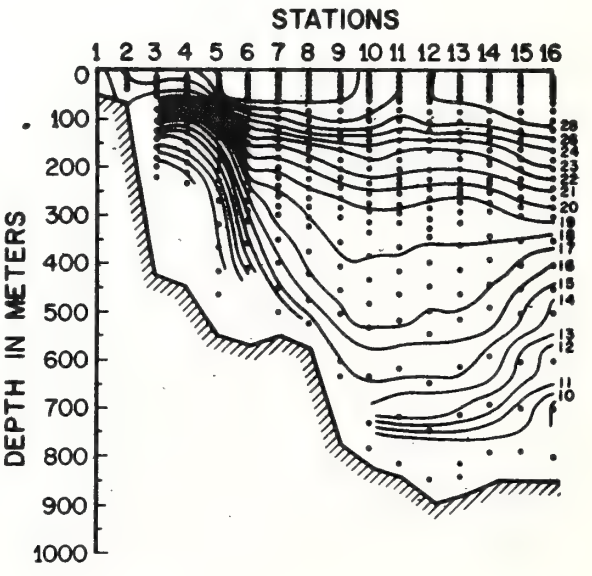


Figure 12. Cruise-7 water temperature (°C) cross-section.

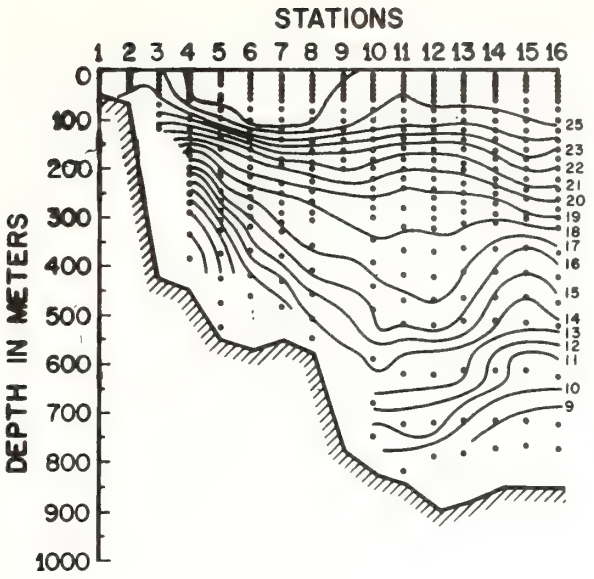


Figure 13. Cruise-8 water temperature (°C) cross-section.

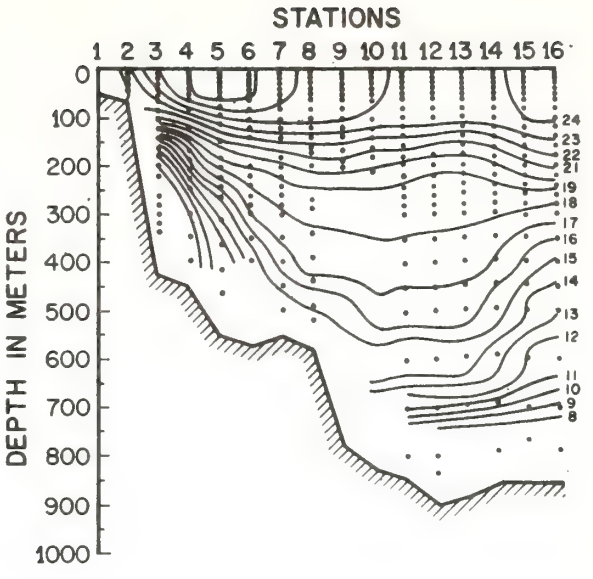


Figure 14. Cruise-9 water temperature (°C) cross-section.

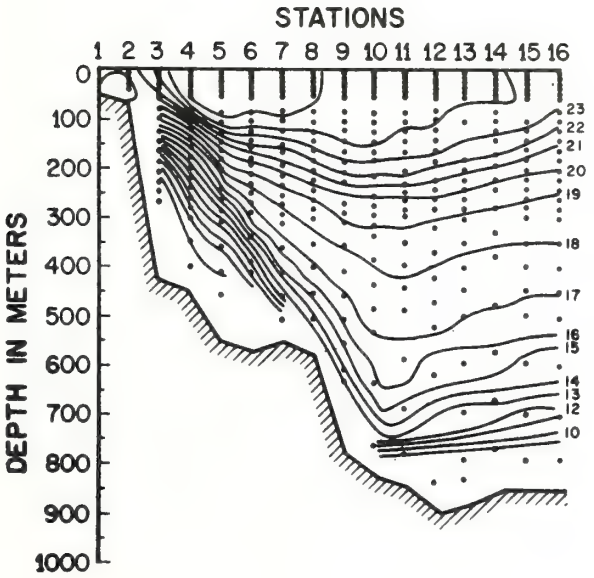


Figure 15. Cruise-10 water temperature (°C) cross-section.

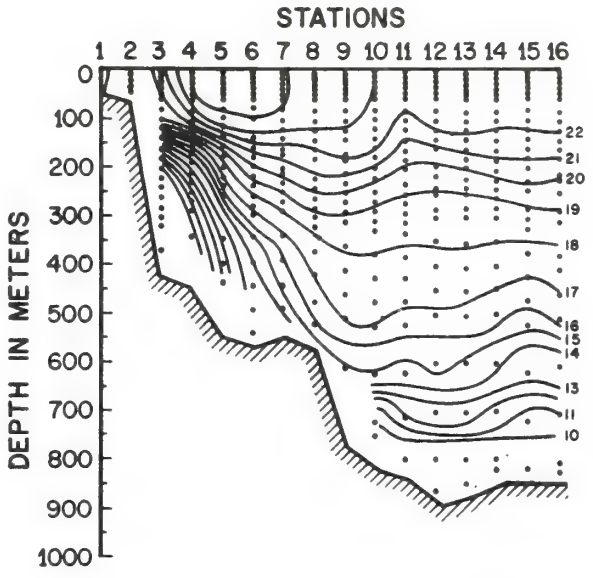


Figure 16. Cruise-12 water temperature (°C) cross-section.

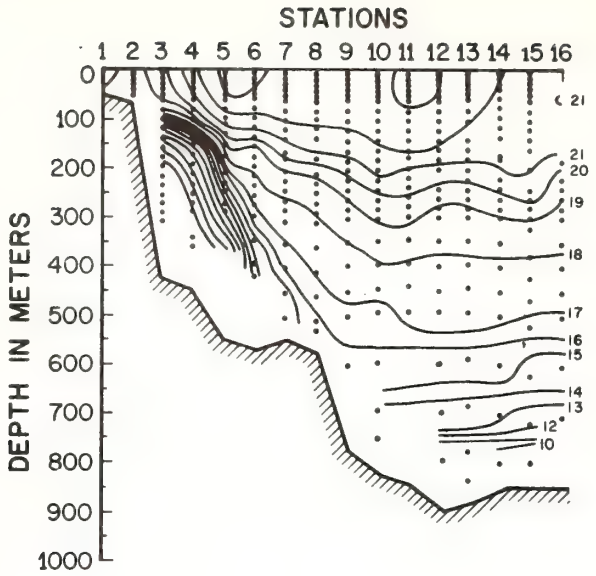


Figure 17. Cruise-14 water temperature (°C) cross-section.

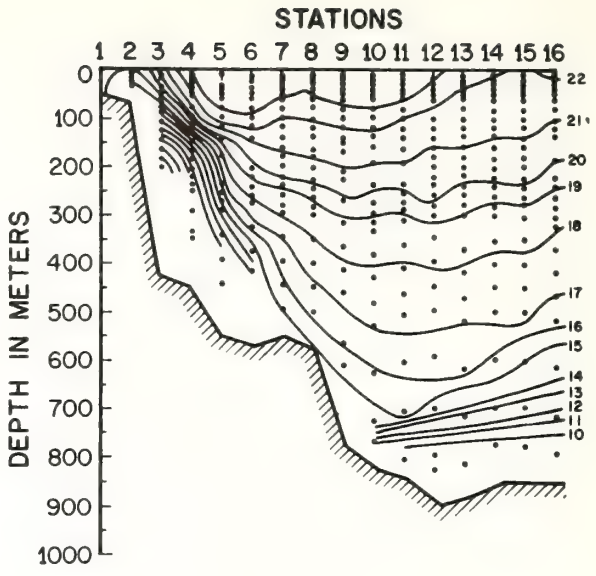


Figure 18. Cruise-15 water temperature (°C) cross-section.

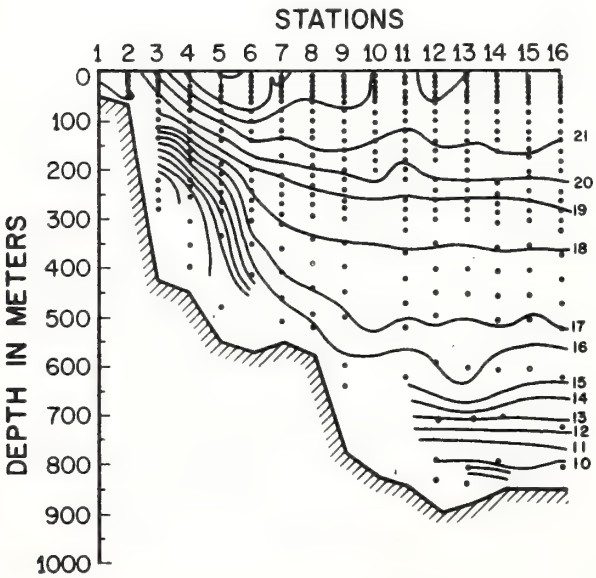


Figure 19. Cruise-16 water temperature (°C) cross-section.

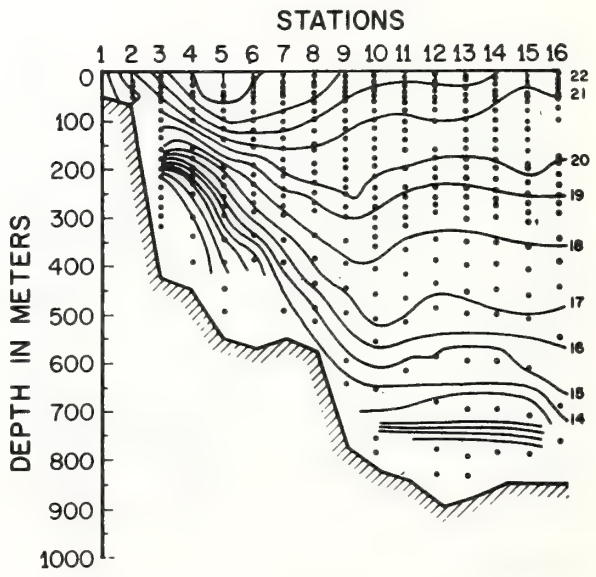


Figure 20. Cruise-18 water temperature (°C) cross-section.

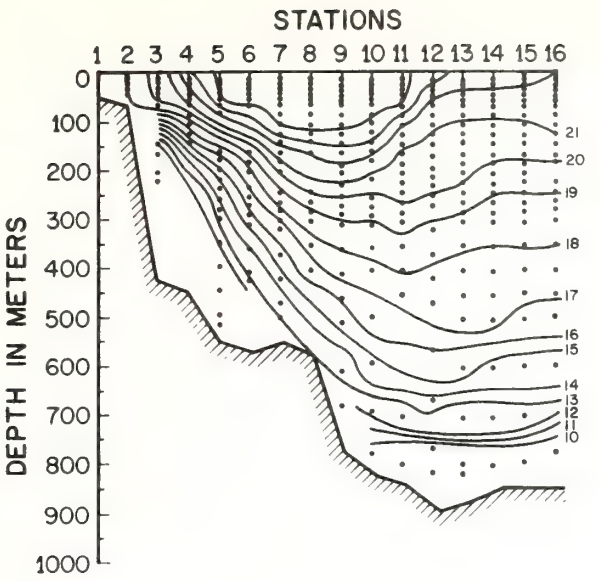


Figure 21. Cruise-19 water temperature (°C) cross-section.

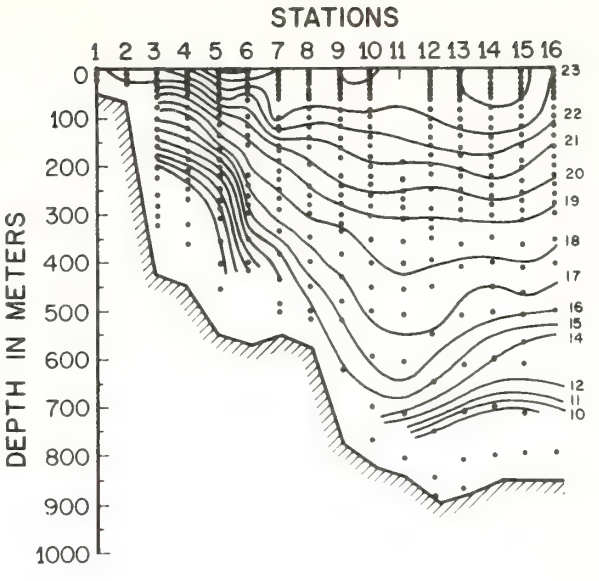


Figure 22. Cruise-20 water temperature (°C) cross-section.

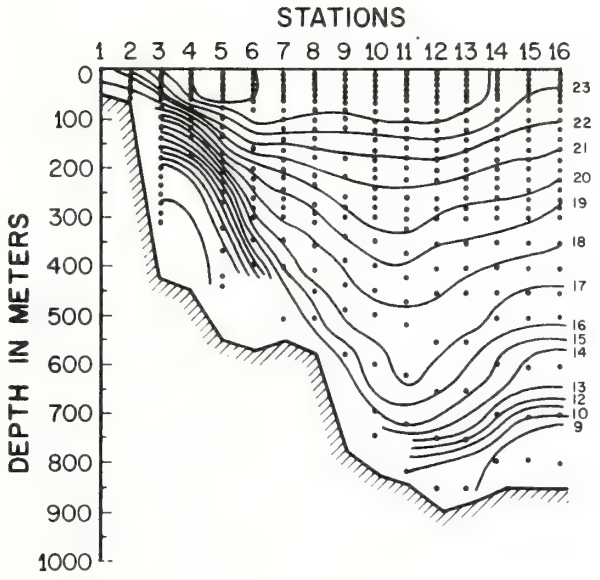


Figure 23. Cruise-21 water temperature (°C) cross-section.

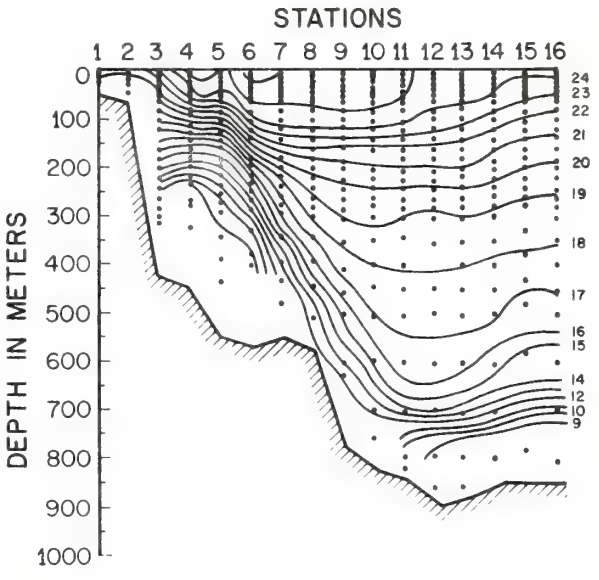


Figure 24. Cruise-22 water temperature (°C) cross-section.

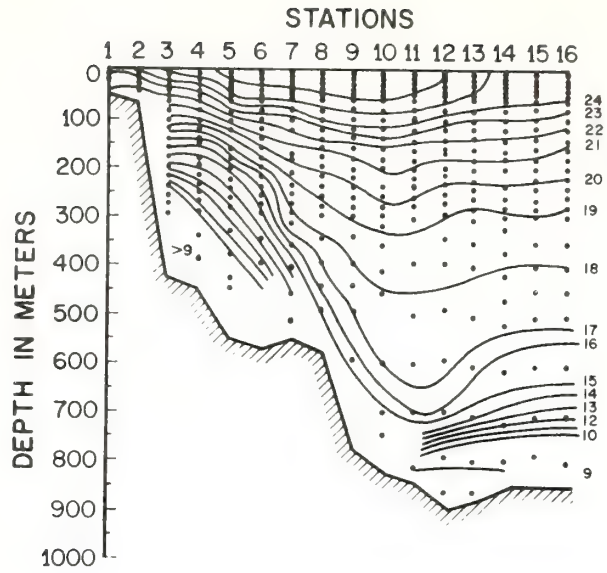


Figure 25. Cruise-23 water temperature (°C) cross-section.

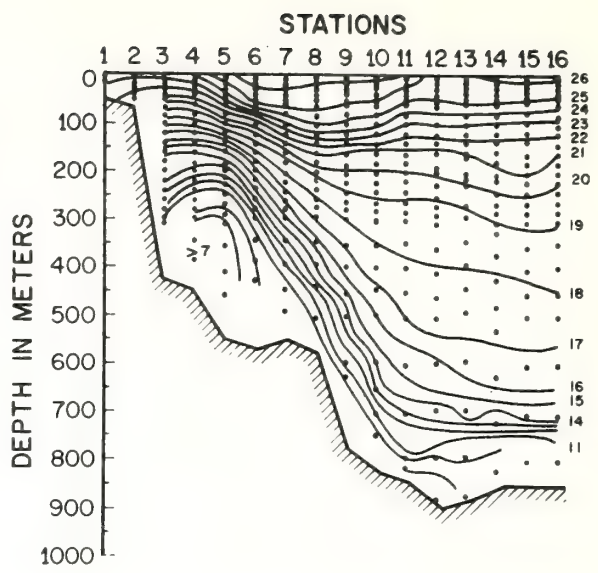


Figure 26. Cruise-24 water temperature (°C) cross-section.

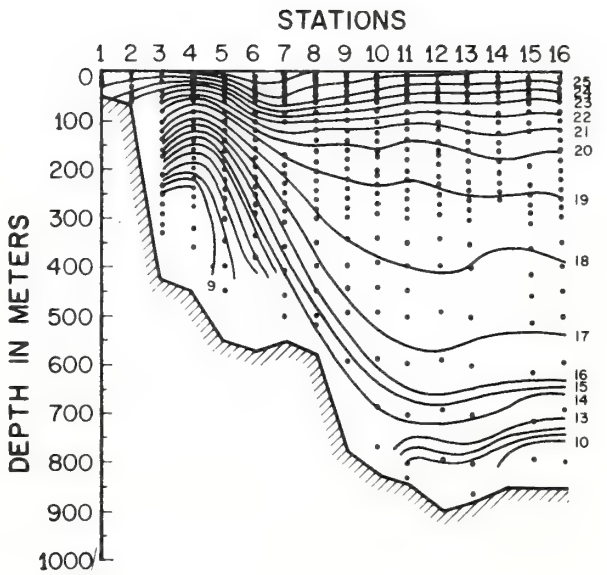


Figure 27. Cruise-25 water temperature (°C) cross-section.

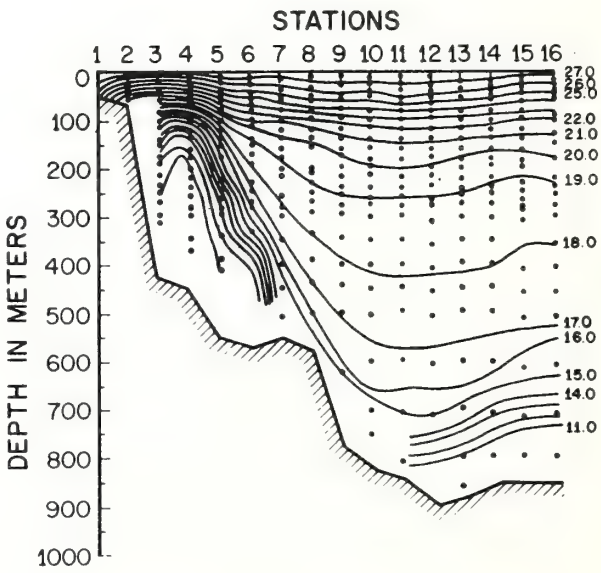


Figure 28. Cruise-26 water temperature (°C) cross-section.

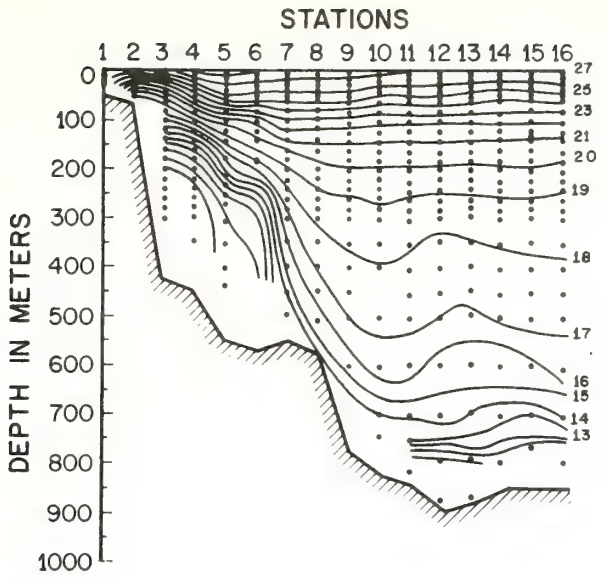


Figure 29. Cruise-27 water temperature (°C) cross-section.

The various physical phenomena that contribute to temperature variation vary in relative importance with depth. From the surface down to about 180-200 m, atmospheric and solar variations are of major importance. Near the bottom, temperature fluctuations are related to water mass movement. Thus the largest fluctuations, having a range of 5° to 10°C, occur at or near the surface over a six-month period. At the bottom, the yearly fluctuations are smaller but significant, varying between 3° and 7°C. Conversely the short term fluctuations at depth are considerably larger than those at the surface. Fluctuations at the bottom as large as 5.5°C occur within two-week periods, and 3° to 4°C variations occur quite frequently. At the surface, cruise-to-cruise temperature variations are usually less than 1°C and seldom exceed 2°C. The large short period bottom fluctuations are definitely geographically oriented. The 3° to 5.5°C variations occur only in the vicinity of stations 3 to 6. At stations 12 to 16 the bottom fluctuations are seldom greater than 2.5°C. Also it is significant that from stations 6 to 16 a large volume of water is found in the vicinity of the 18° isotherm (Worthington, 1959).

Temperature variations related to water mass movement generally are considered to decrease with increasing depth. To some extent this did occur. Seasonal and total means and standard deviations were computed at each standard depth for each station. The standard deviations of all temperature data are graphically presented as Figure 30. This figure indicated that, except for nearshore stations, temperature

variations decrease with increasing depth until a minimum is reached at about mid-depth of 250 to 400 m. Below that depth, temperature variations increased down to 700 m where a secondary maximum is reached. The most unusual temperature variation occurred at station 6 where the maximum standard deviation was recorded at the bottom.

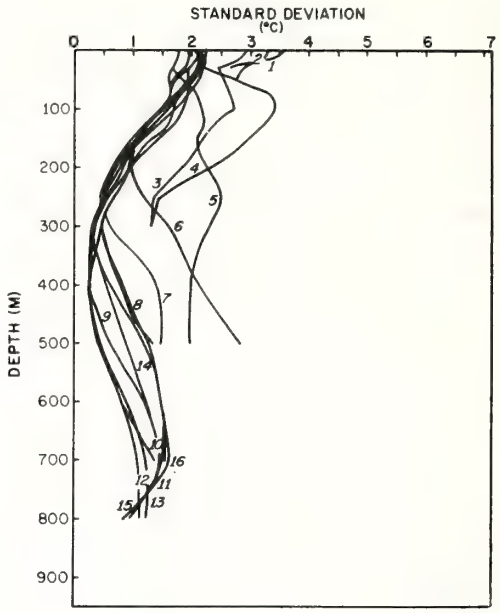


Figure 30. Standard deviations by station obtained by using all temperature data.

The standard deviations for the seasons are graphically presented as Figures 31, 32, 33, and 34. Down to a depth of about 180 to 200 m the standard deviations appear to reflect climatological variations. During summer and winter, surface water variations are low. The surface standard deviations are somewhat larger during spring and fall, indicative of transition periods.

During summer, variations increase with depth to a maximum at about 75 to 100 m, indicative of a shallow mixed layer varying in depth with a strong thermocline below. During winter relatively low standard deviations are recorded from the surface down to about 250 m. These curves indicate a deep mixed layer having relatively little variation with time.

The region of largest standard deviations is found at stations 3, 4, 5, and 6 varying in depth between 50 and 150 m. These large temperature fluctuations reflect variations related to the thermocline, but more importantly, to varying positions or meanderings of the Gulf Stream. Apparently, the velocity core is usually found in the vicinity of stations 5 or 6, but occasionally touches stations 4 or 7.

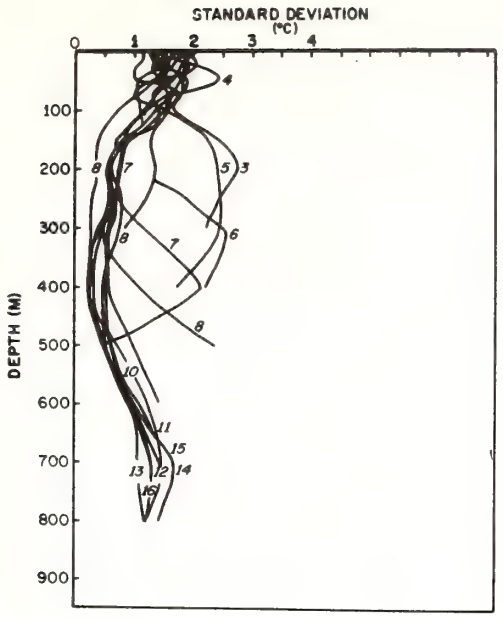


Figure 31. Standard deviations by station, obtained by using spring temperature data.

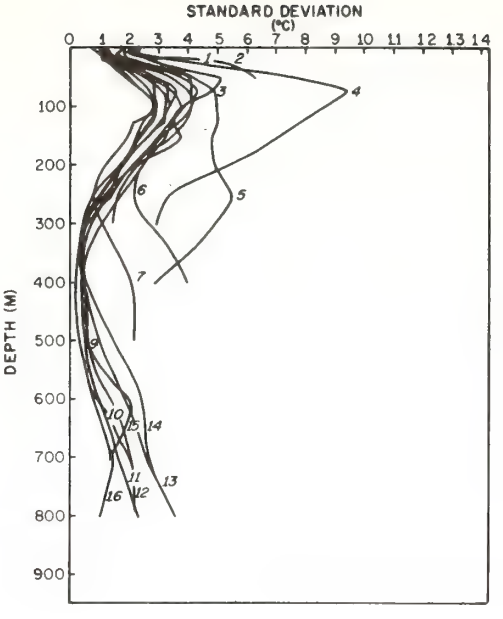


Figure 32. Standard deviations by station, obtained by using summer temperature data.

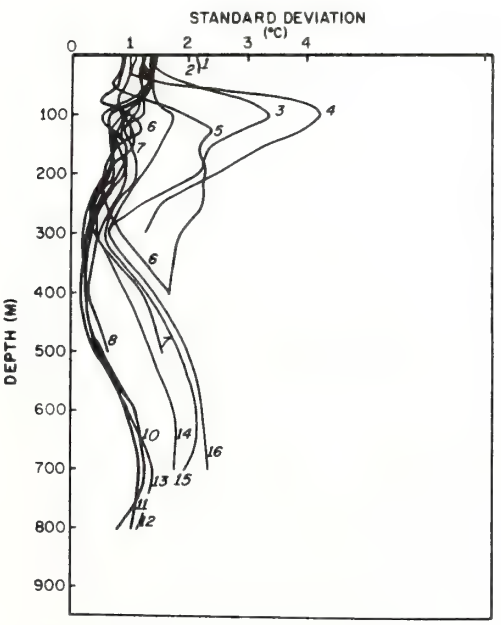


Figure 33. Standard deviations by station, obtained by using fall temperature data.

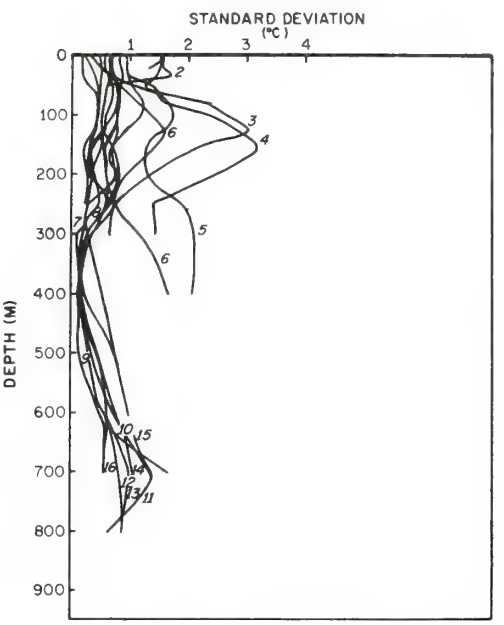


Figure 34. Standard deviations by station, obtained by using winter temperature data.

During the fall, unusually large fluctuations occurred below 300 m at stations 14, 15, and 16. Undoubtedly, they are related to water mass movement, possibly to a counter current at depth (Duing, 1973).

5.2 Salinity

As expected, the mean surface salinity increased with increasing distance from shore. Figure 35 is a cross-section of the mean of all salinity data. A mean value of 36.02°/$_{oo}$ was recorded at station 1, and a mean value of 36.40°/$_{oo}$ was recorded at station 16.

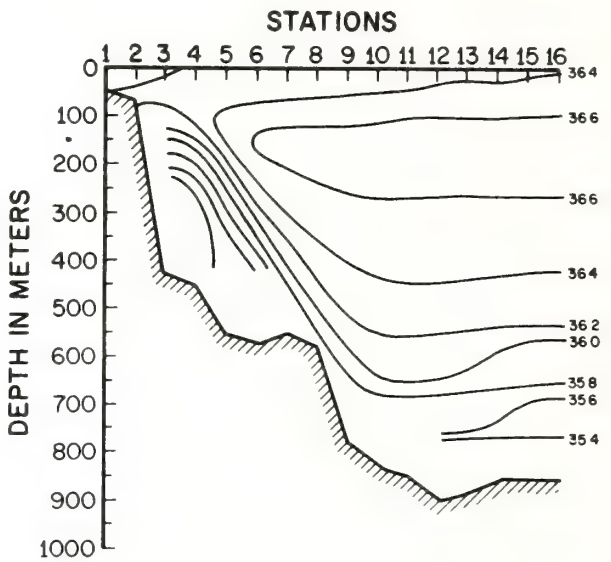


Figure 35. Mean of all cruises salinity cross-section.

Nearshore the maximum salinity of about 36.23°/$_{oo}$ to 36.27°/$_{oo}$ occurs at about 20 to 50 m depth. Below the maximum, the salinity decreases to about 35.12°/$_{oo}$ at the bottom at stations 3, and 4, the lowest value for the entire cross-section.

In the core of the Gulf Stream, the maximum salinity of 36.54°/$_{oo}$ is found at 100 to 125 m. Farther seaward the salinity maximum of about 36.67°/$_{oo}$ to 36.71°/$_{oo}$ is found in a horizontal layer between 100 and 200 m depth. Below the maximum, the salinity gradually decreases to about 35.20°/$_{oo}$ at the bottom.

The surface salinity pattern exhibits considerable seasonal variation. Figures 36, 37, 38, and 39 are the seasonal salinity cross-sections, and figures 40 through 62 are the individual cruise cross-sections. In general, during all seasons the minimum surface values are found at the shoreward end, where a seasonal low of 35.41°/$_{oo}$ occurs during the summer, and the high of 36.34°/$_{oo}$ occurs during the winter.

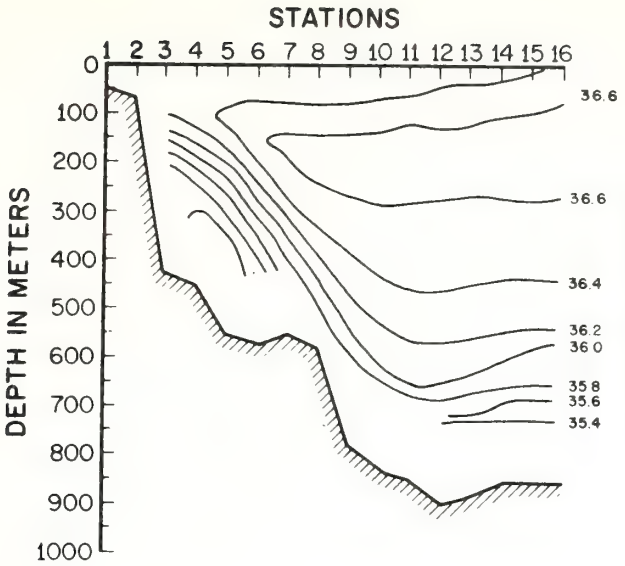


Figure 36. Mean of spring cruises salinity cross-section.

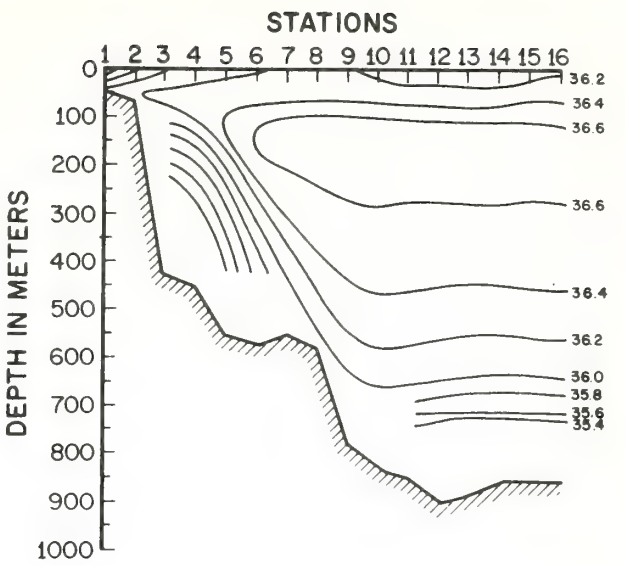


Figure 37. Mean of summer cruises salinity cross-section.

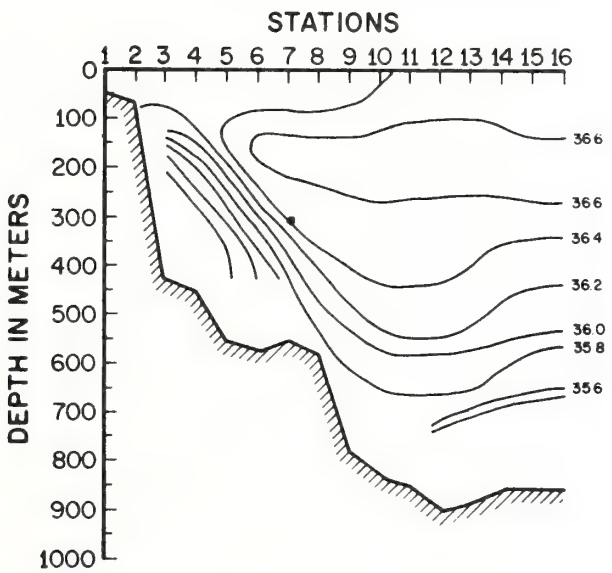


Figure 38. Mean of fall cruises salinity cross-section.

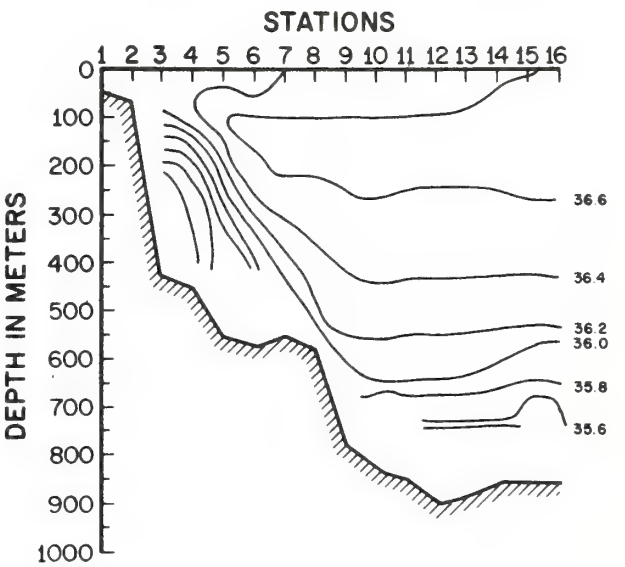


Figure 39. Mean of winter cruises salinity cross-section.

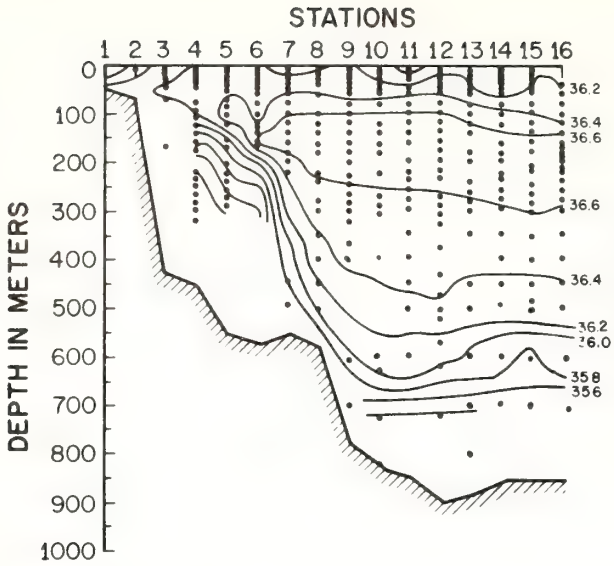


Figure 40. Cruise-1 salinity cross-section.

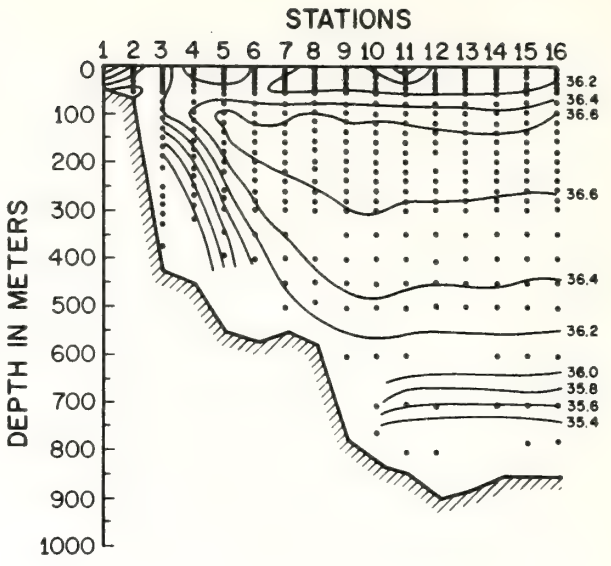


Figure 41. Cruise-2 salinity cross-section.

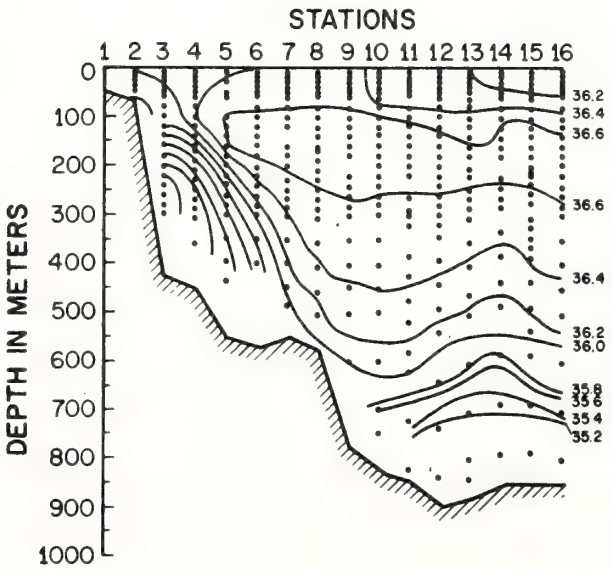


Figure 42. Cruise-4 salinity cross-section.

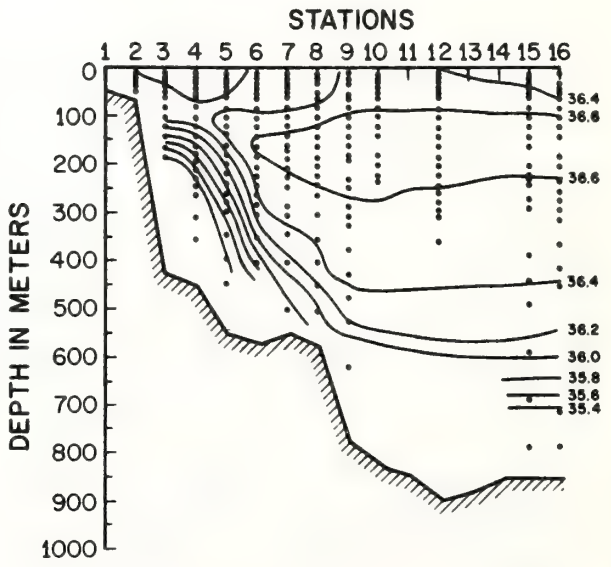


Figure 43. Cruise-5 salinity cross-section.

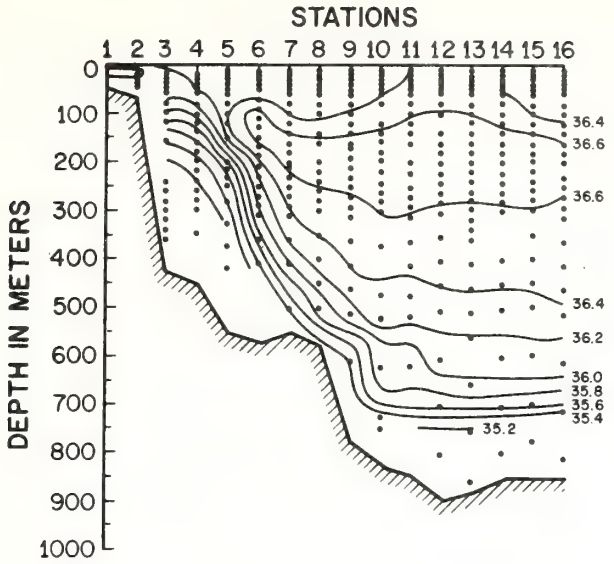


Figure 44. Cruise-6 salinity cross-section.

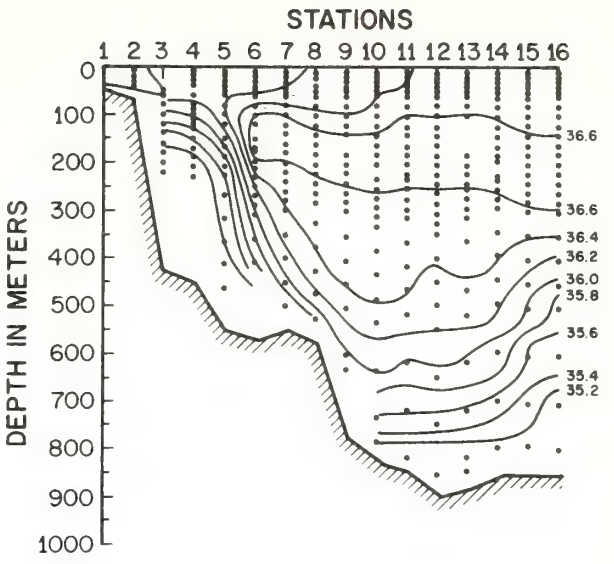


Figure 45. Cruise-7 salinity cross-section.

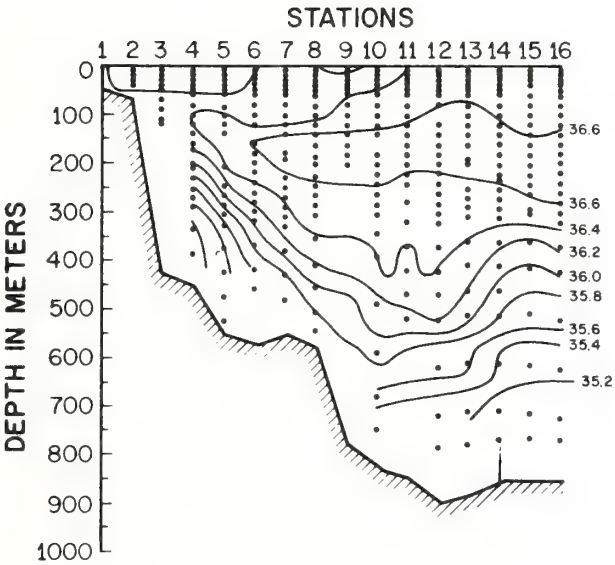


Figure 46. Cruise-8 salinity cross-section.

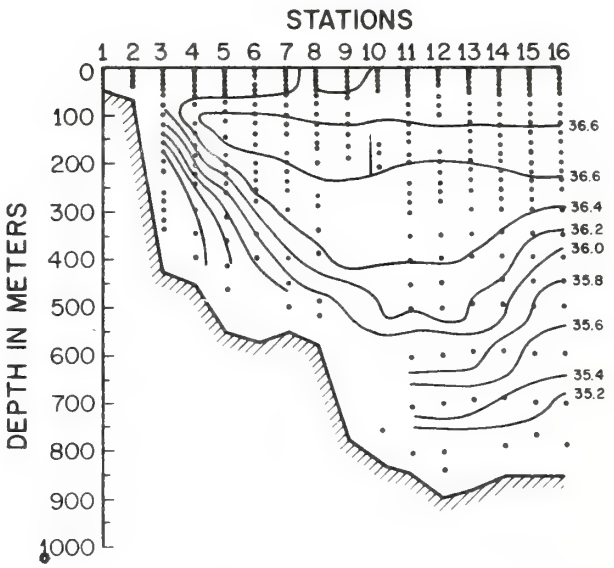


Figure 47. Cruise-9 salinity cross-section.

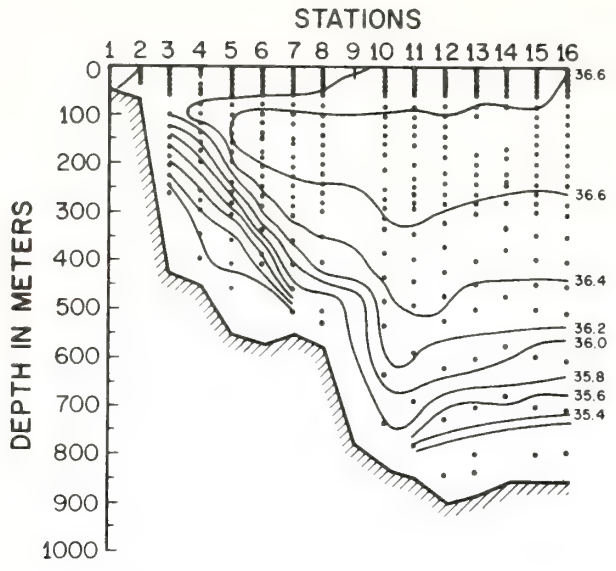


Figure 48. Cruise-10 salinity cross-section.

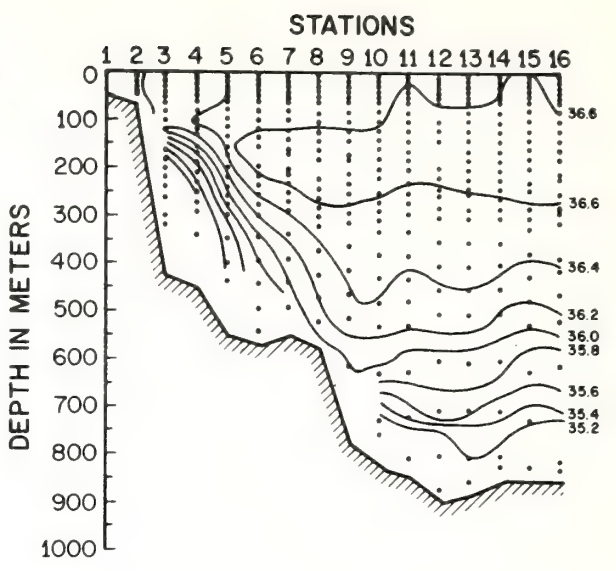


Figure 49. Cruise-12 salinity cross-section.

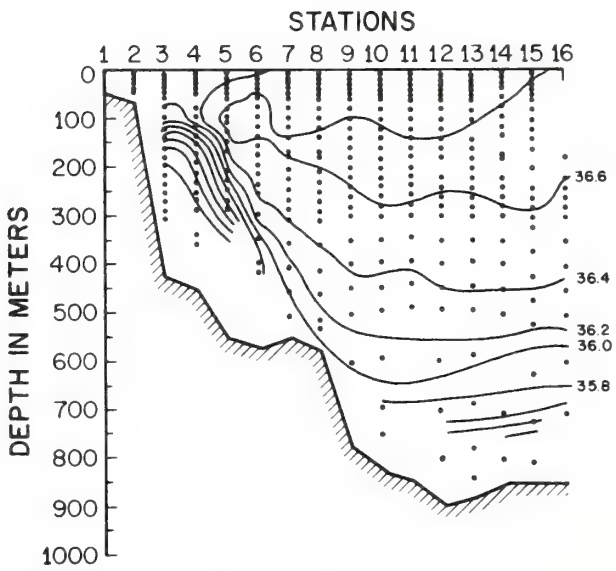


Figure 50. Cruise-14 salinity cross-section.

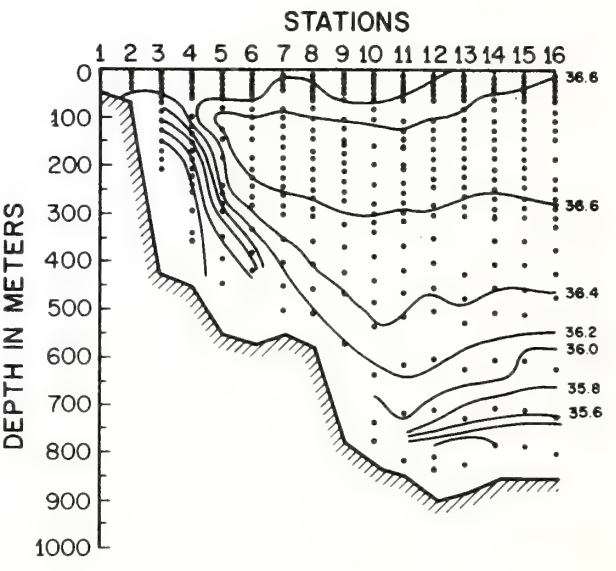


Figure 51. Cruise-15 salinity cross-section.

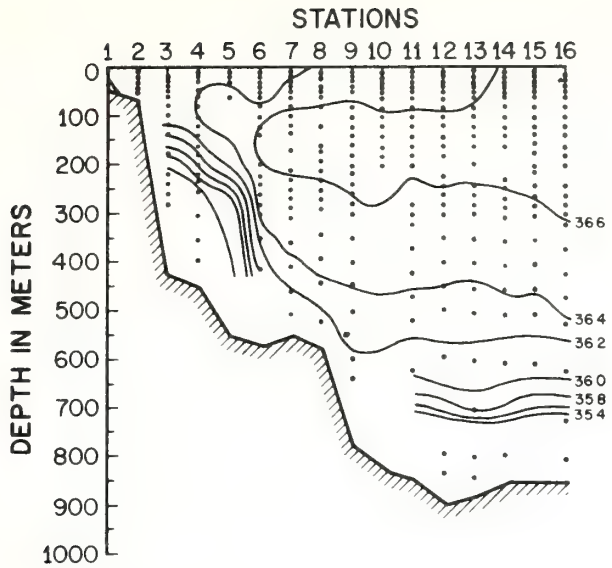


Figure 52. Cruise-16 salinity cross-section.

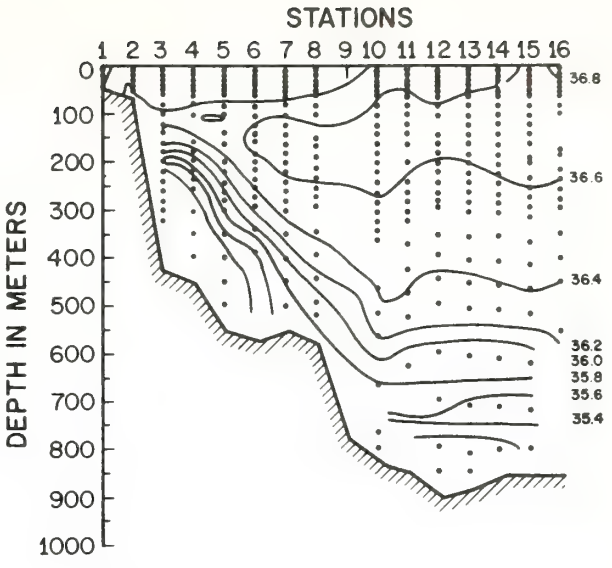


Figure 53. Cruise-18 salinity cross-section.

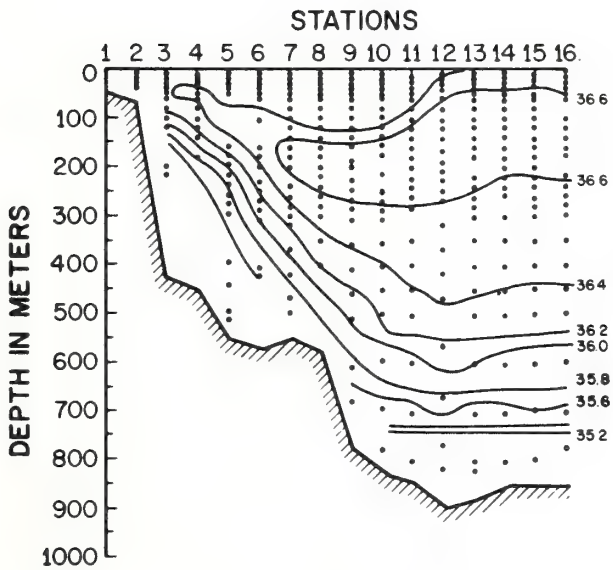


Figure 54. Cruise-19 salinity cross-section.

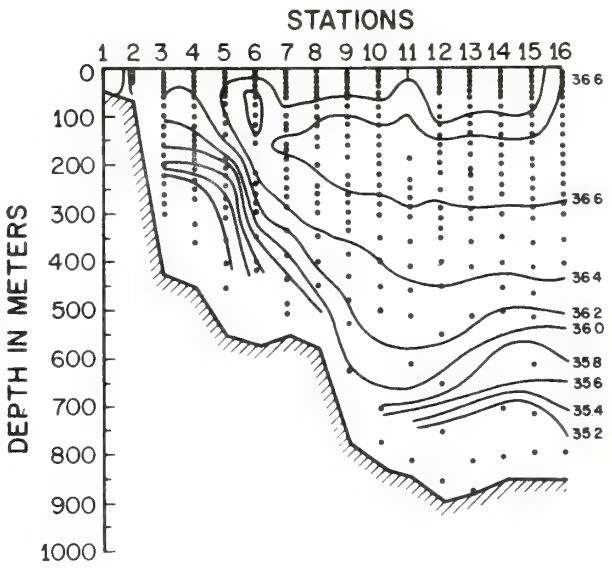


Figure 55. Cruise-20 salinity cross-section.

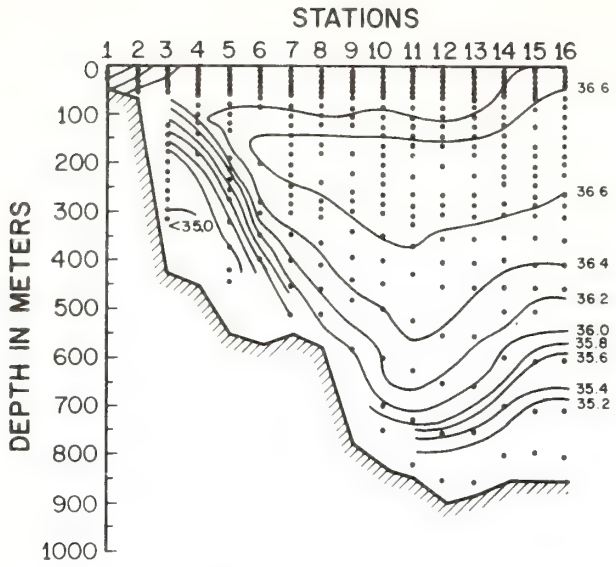


Figure 56. Cruise-21 salinity cross-section.

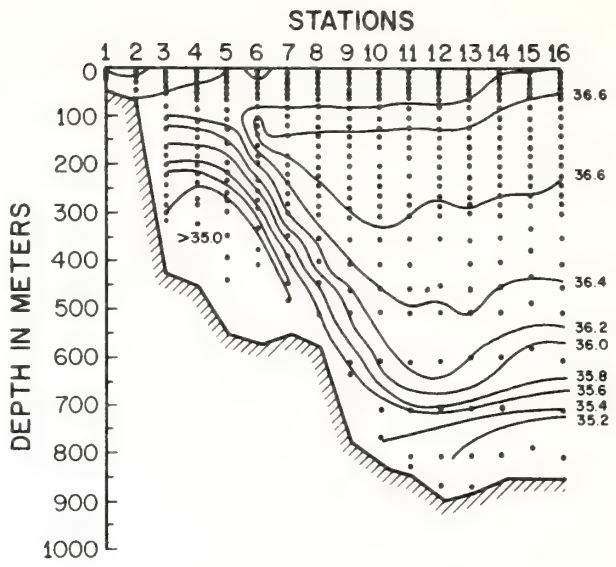


Figure 57. Cruise-22 salinity cross-section.

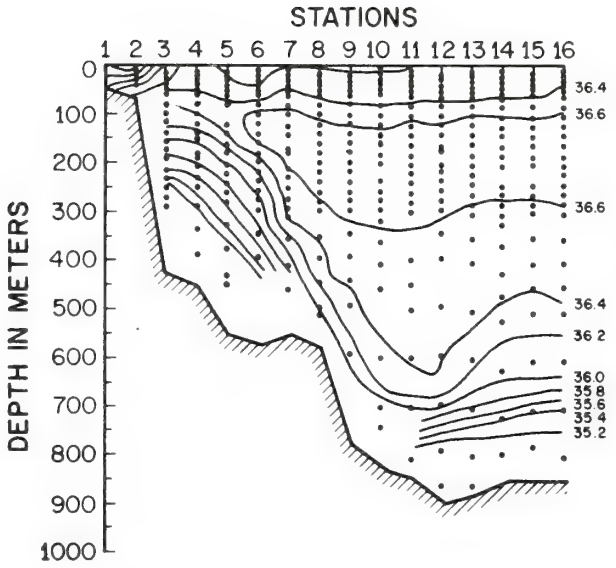


Figure 58. Cruise-23 salinity cross-section.

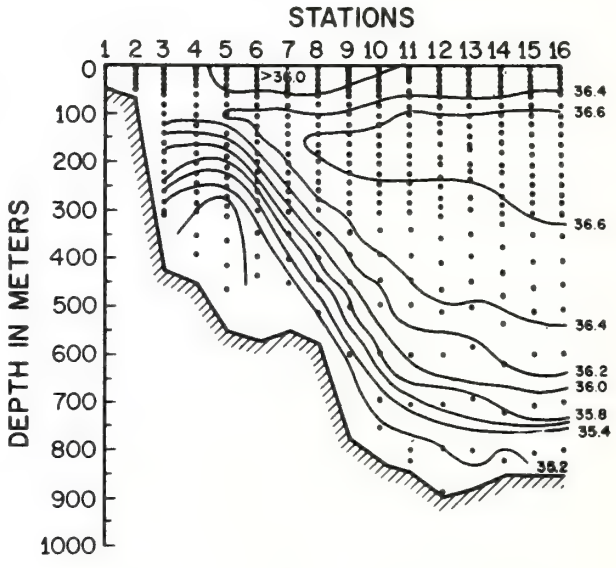


Figure 59. Cruise-24 salinity cross-section.

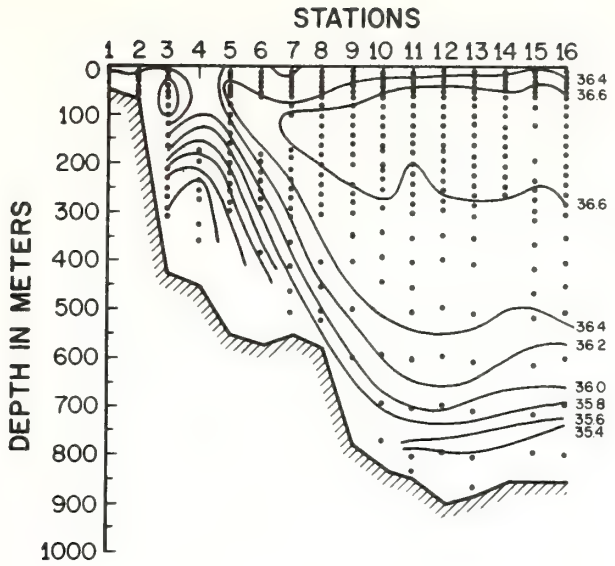


Figure 60. Cruise-25 salinity cross-section.

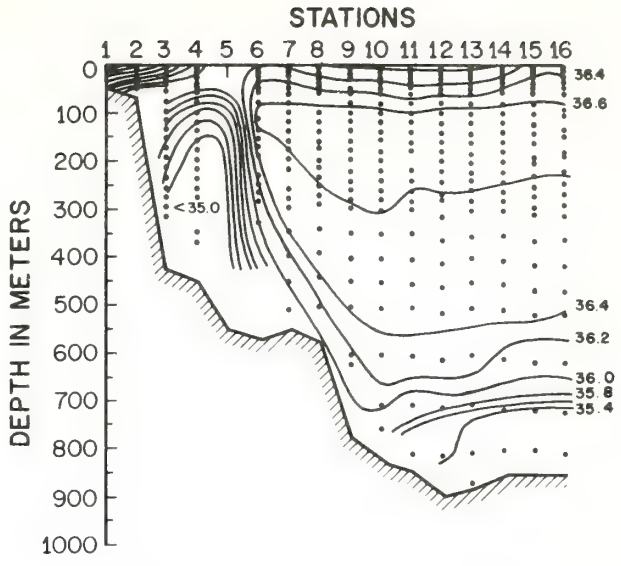


Figure 61. Cruise-26 salinity cross-section.

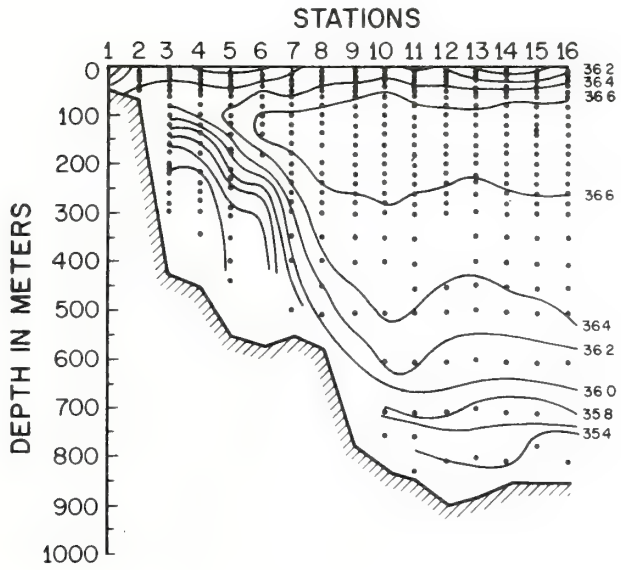


Figure 62. Cruise-27 salinity cross-section.

Coastal water is a mixture of oceanic water and fresh water that has drained from the land. Its salinity depends on the fraction of fresh water and the salinity of the oceanic water. The salinity of offshore surface ocean water is generally greater than 36.00°/₀₀. Surface salinity values less than 36.00°/₀₀ were recorded only during the summer at stations 1, 2, and 3. This indicates that fresh water runoff is most significant during the summer, the period of highest rainfall (Bryson and Hare, 1974). Even at these nearshore stations, the relative high values (all greater than 35.00°/₀₀) indicate that the oceanic water predominates. At all stations the minimum surface salinities occurred during the summer and the maximum during the winter.

The seasonal salinity maximums of 36.71 ± .02°/₀₀ occur in a horizontal lens between 100 and 200 m extending from stations 6 to 16. Minimum salinity for the entire cross-section is found at the bottom in the vicinity of stations 3 and 4. During summer, fall, and winter, the minimum is consistent having a value of 35.02 ± .01°/₀₀. During spring, the minimum rises to 35.17°/₀₀.

Considerable variation was recorded between individual station values at the bottom for stations 8 thru 16 (0.14 to 0.37°/₀₀).

Other than in the near-surface water, the salinity variations are related to dynamic forces. These variations seem to be considerable in some parts of the cross-section and almost non-existent in others. The variations are graphically displayed in Figure 63. For this figure, standard deviations were computed for all cruise data at each station for each standard depth. The resulting curves can be classified into one of three groups, related to water masses and the dynamic forces.

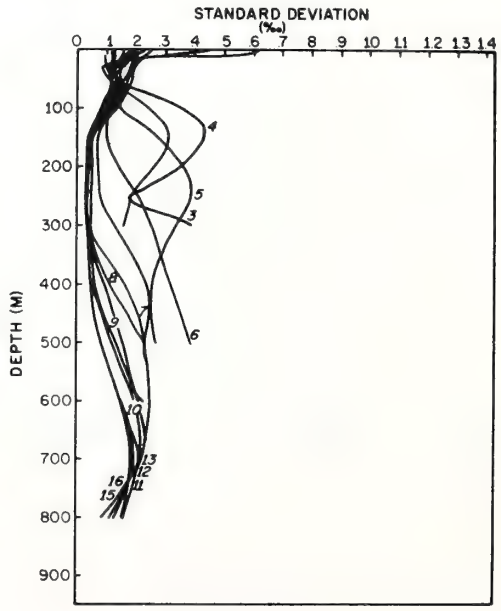


Figure 63. Standard deviations by station obtained by using all salinity data.

The coastal water, stations 1 and 2, exhibit a high salinity variation at the surface that rapidly decreases with depth. Stations 3, 4, and 5 exhibit low surface and near-surface salinity variations that increase with depth until a maximum is reached at about 125 to 250 m. At greater depths, the variation decreases, but it remains greater at the bottom than in the near-surface water.

Stations 8 through 16 exhibit similar salinity variation patterns. The standard deviations from the surface to 100 m are between 0.1 and 0.2. Below 100 m the standard deviations decrease to a minimum of about 0.03 to 0.04 between 150 and 400 m. At greater depths the standard deviations increase to a maximum of about 0.2 at 700 m.

Stations 6 and 7 exhibit a variation pattern that is transitional between 4 and 5 on the one hand and 8 thru 16 on the other.

Of considerable interest are the absolute salinity values at 300 m at stations 3 and 4. At station 3, 38% of the salinity observations are less than 35.00°/$_{oo}$, yet the highest recorded value was 35.66°/$_{oo}$. The standard deviation was an unusually large 0.39°/$_{oo}$. At station 4, 25% of the salinity observations were below 35.00°/$_{oo}$, and the highest recorded was 35.57°/$_{oo}$. This will be discussed further under water masses.

5.3 Dissolved Oxygen

The cross-section mean of all the dissolved oxygen data exhibits a relatively simple pattern (Fig. 64). The maximum surface value is found at station 1. Surface values decrease seaward to station 4. Seaward of station 4, the surface values vary between 4.65 ml/l and 4.76 ml/l. The maximum value for the entire cross-section of 4.96 ml/l is found at the surface at station 1. The maximum values for each station are found in water varying in depth between 10 and 100 m. The values range between 4.96 and 4.69 ml/l.

Below the maximum, oxygen values decrease with increasing depth. The sharpest gradient is found at station 3 where a minimum of 3.24 ml/l is found at 300 m. Similar low values of 3.23 and 3.28 ml/l are found in 800 m at stations 11 and 15. Seaward of station 6, the oxygen gradient between the surface and 600 m is only about 0.05 ml/l per 100 m.

The oxygen patterns for each season (Figs. 65-68) are quite similar to the mean pattern of all the data. That is to say that maximum values are always found in the nearshore water, and the minimum values are found at the bottom. However, definite seasonal patterns exist at all depths.

At any given point on the cross-section, lowest seasonal values are most likely to occur during summer. The maximum summer value of 4.72 ml/l was found at station 11 at 50 m.

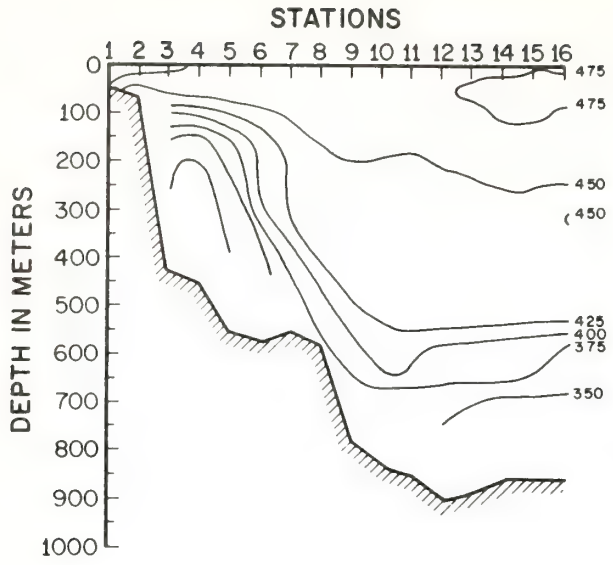


Figure 64. Mean of all cruises oxygen cross-section.

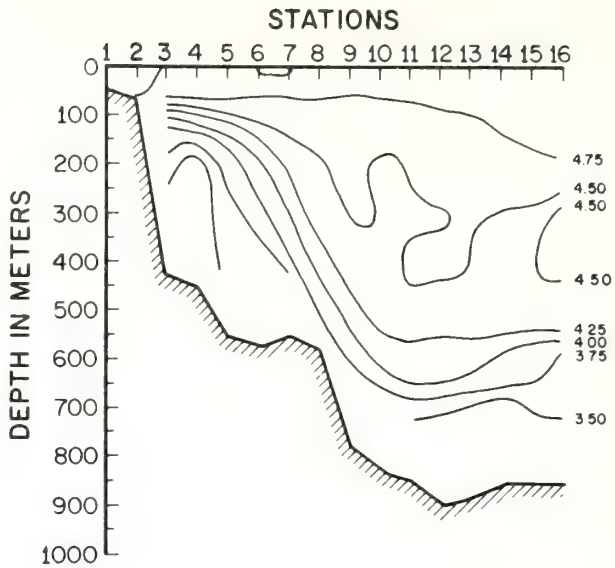


Figure 65. Mean of spring cruises oxygen cross-section.

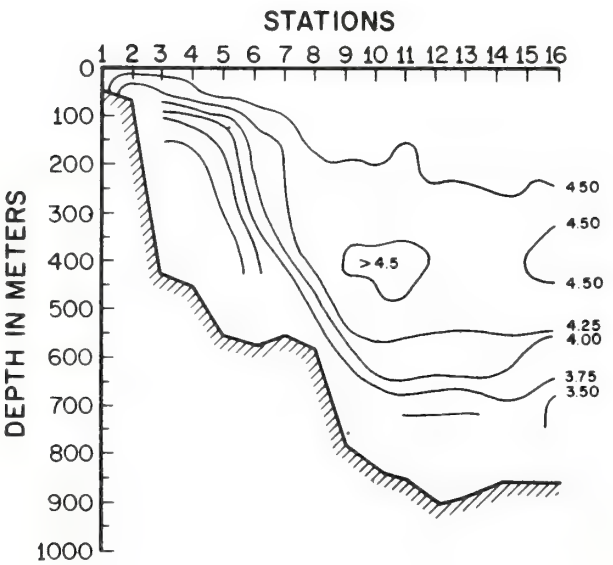


Figure 66. Mean of summer cruises oxygen cross-section.

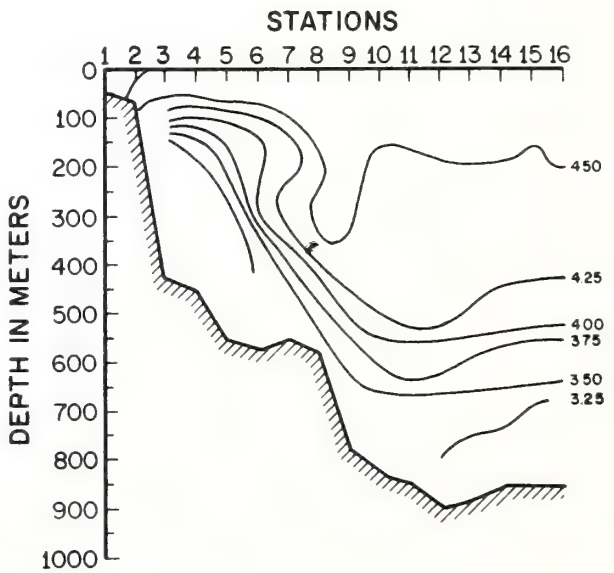


Figure 67. Mean of fall cruises oxygen cross-section.

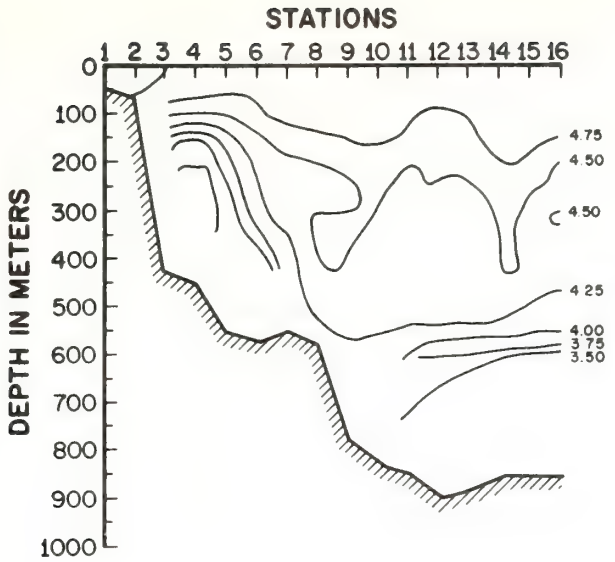


Figure 68. Mean of winter cruises oxygen cross-section.

Values below 3.20 occurred below 150 m at stations 3, 4, and 5 and also below 700 m at station 13. Generally, oxygen values were considerably higher during the winter. The maximum value of 5.38 ml/l was found at station 1 in 20 m of water. Winter minimum values of 3.29 ml/l were recorded at station 4 in 200 m and 3.04 ml/l at station 12 in 800 m of water.

In general, the individual cruise cross-sections are similar to the seasonal ones (Figs. 69-91). One striking feature is masked by the seasonal ones. Generally, the oxygen minimum for a station occurs at the lowest bottle at the station. However, occasionally the minimum observation is reached above the bottom and a slight or sharp increase is recorded at the bottom bottle.

Where the increase in the oxygen value at the bottom is slight, the indication is that the actual oxygen minimum has been reached. This occurs at a sigma-t of 27.12. A sharp increase in the oxygen value at the bottom may indicate a different water mass.

Standard deviations at standard depths for each station using the entire year of data do not form a neat pattern as they do for temperature and salinity (Fig. 92). However, they usually exhibit minimum variation in water less than 100 m. The largest standard deviations are usually recorded at or near the bottom at the seaward end of the line.

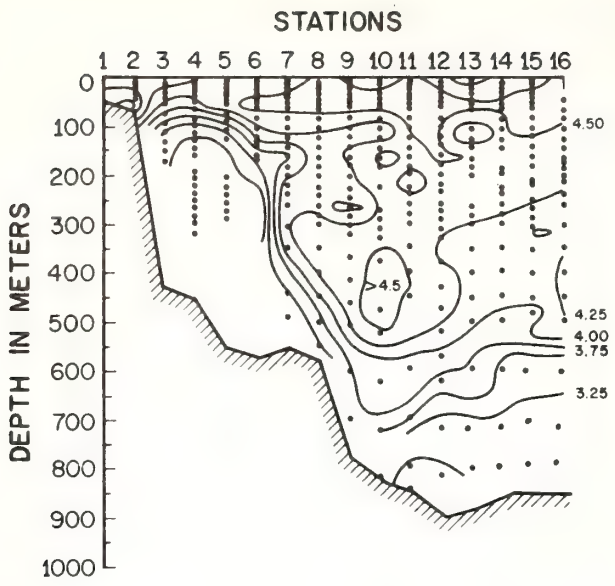


Figure 69. Cruise-1 oxygen cross-section.

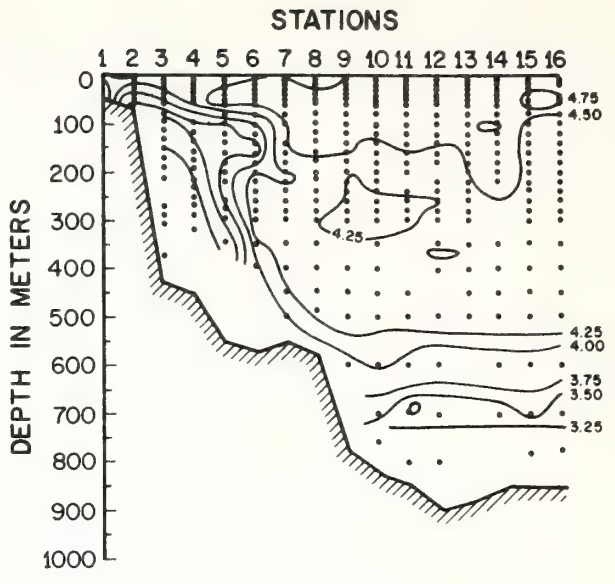


Figure 70. Cruise-2 oxygen cross-section.

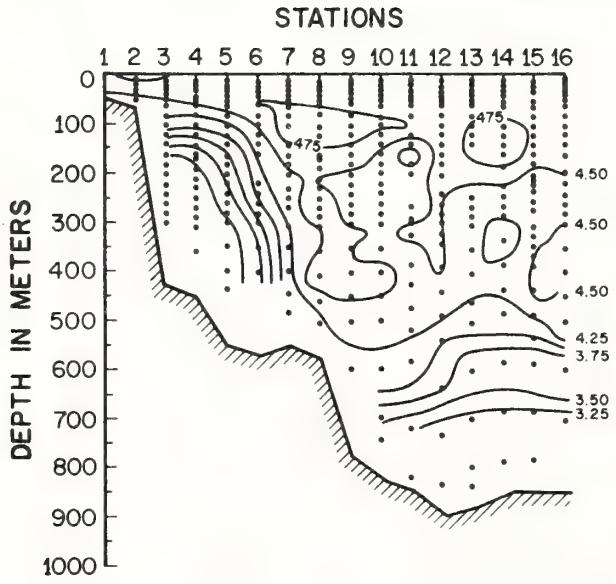


Figure 71. Cruise-4 oxygen cross-section.

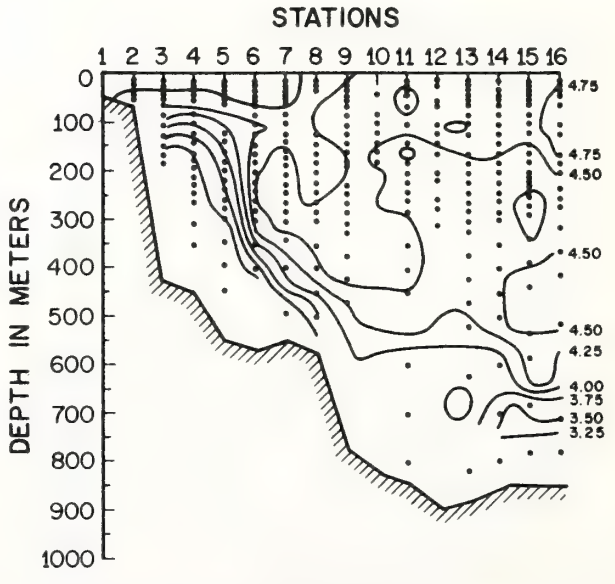


Figure 72. Cruise-5 oxygen cross-section.

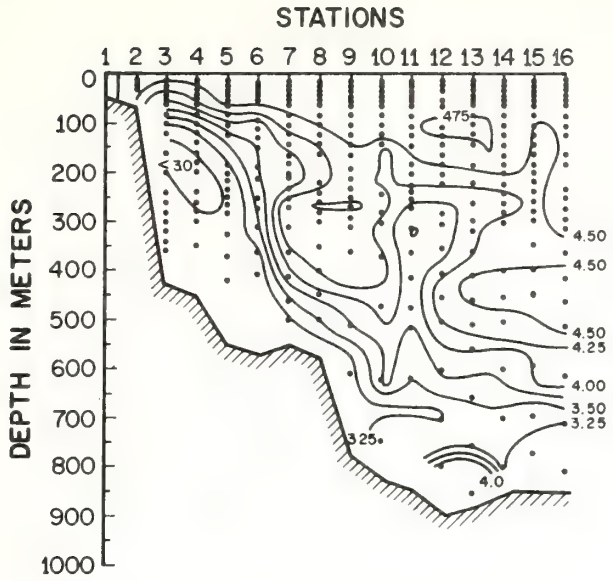


Figure 73. Cruise-6 oxygen cross-section.

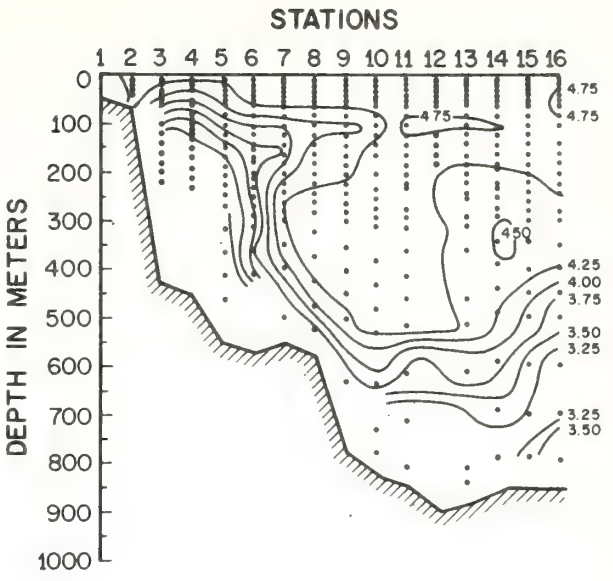


Figure 74. Cruise-7 oxygen cross-section.

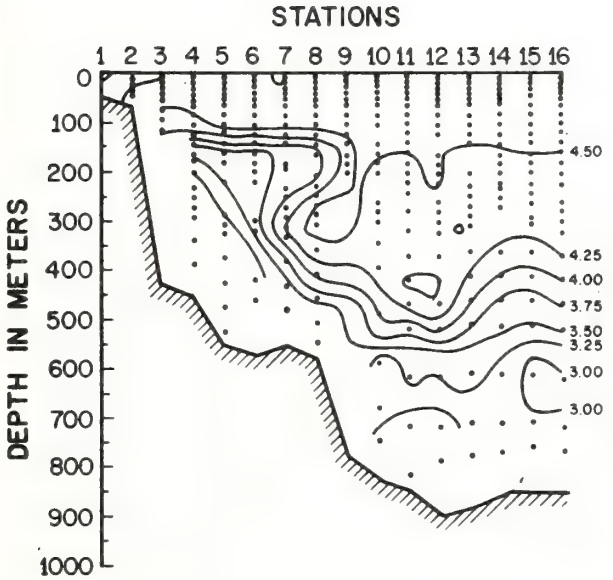


Figure 75. Cruise 8 oxygen cross-section.

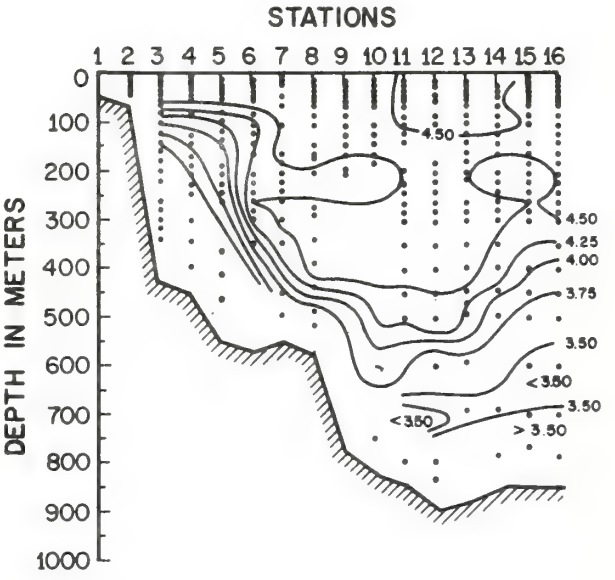


Figure 76. Cruise 9 oxygen cross-section.

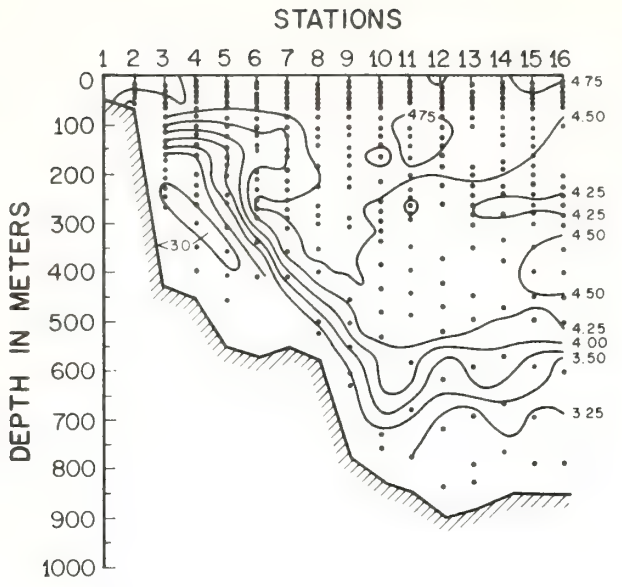


Figure 77. Cruise-10 oxygen cross-section.

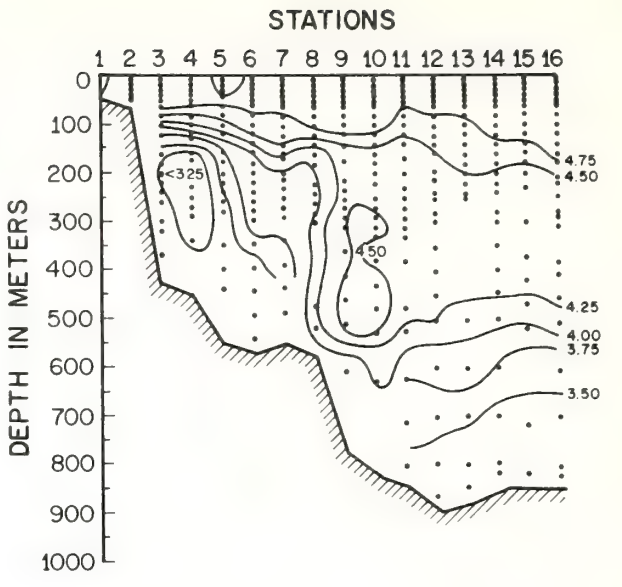


Figure 78. Cruise-12 oxygen cross-section.

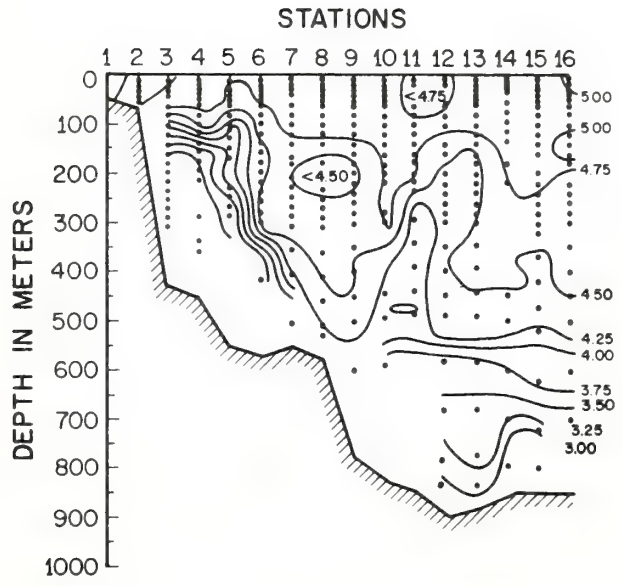


Figure 79. Cruise-14 oxygen cross-section.

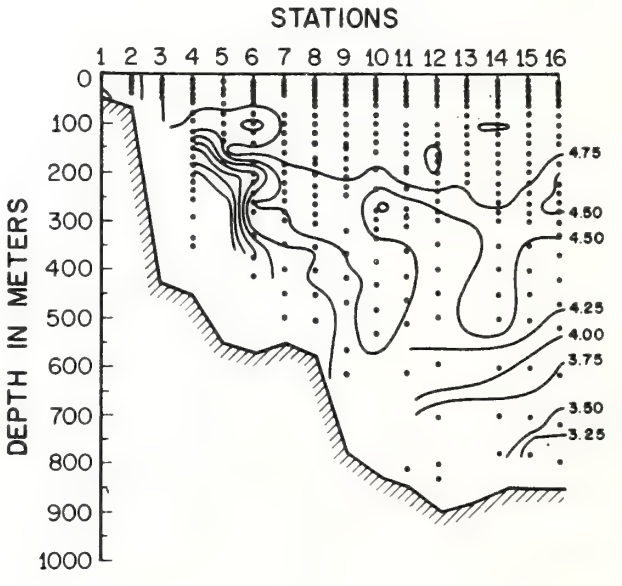


Figure 80. Cruise-15 oxygen cross-section.

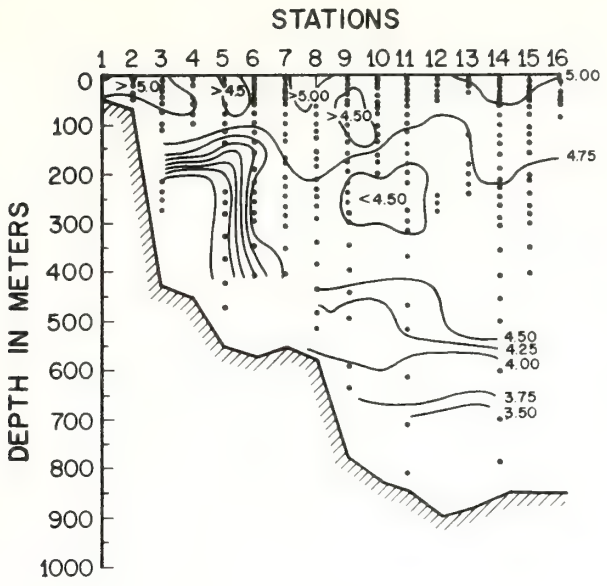


Figure 81. Cruise-16 oxygen cross-section.

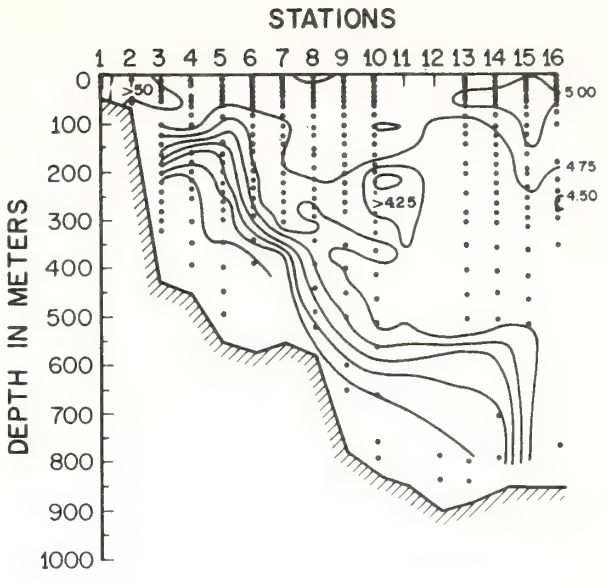


Figure 82. Cruise-18 oxygen cross-section.

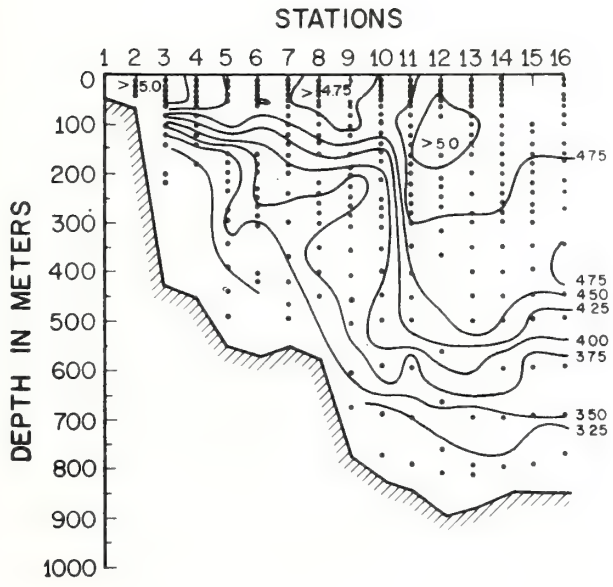


Figure 83. Cruise-19 oxygen cross-section.

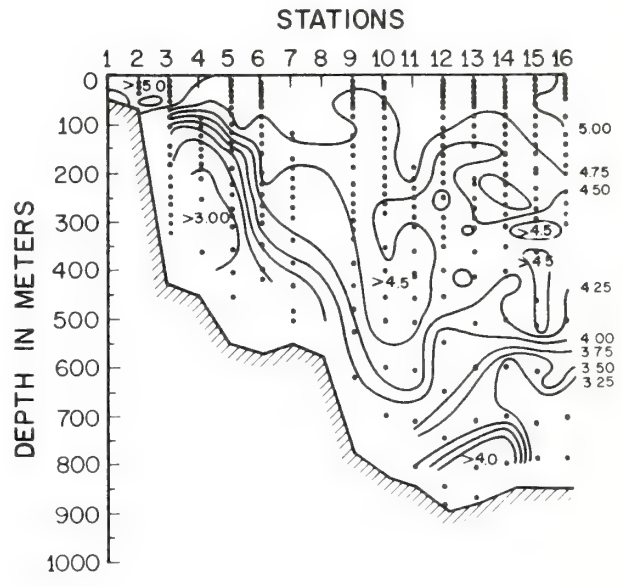


Figure 84. Cruise-20 oxygen cross-section.

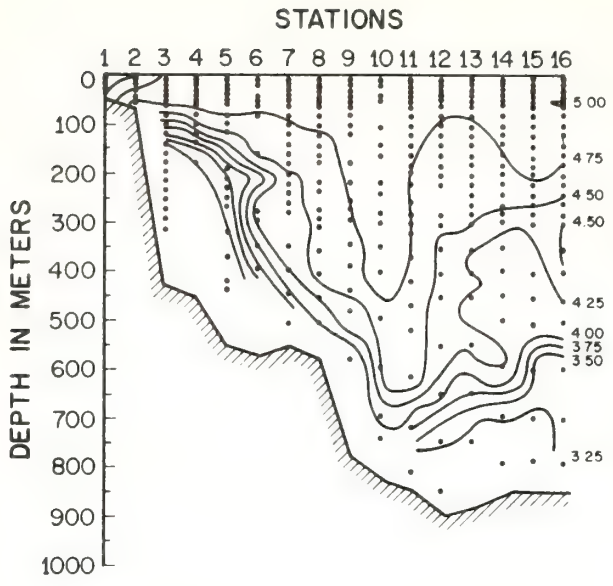


Figure 85. Cruise-21 oxygen cross-section.

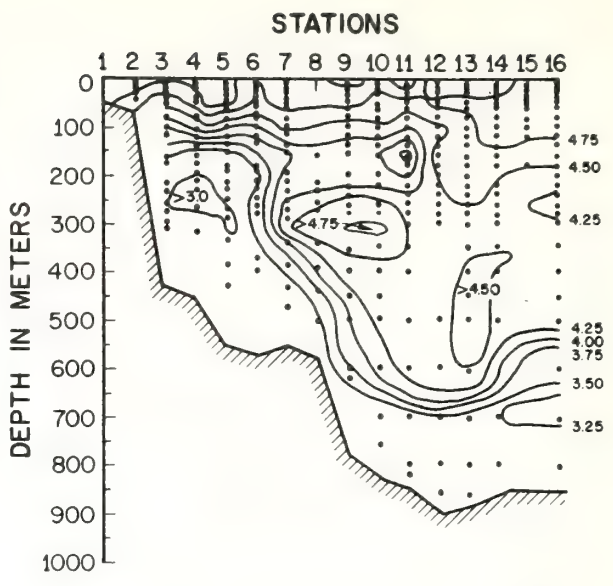


Figure 86. Cruise-22 oxygen cross-section.

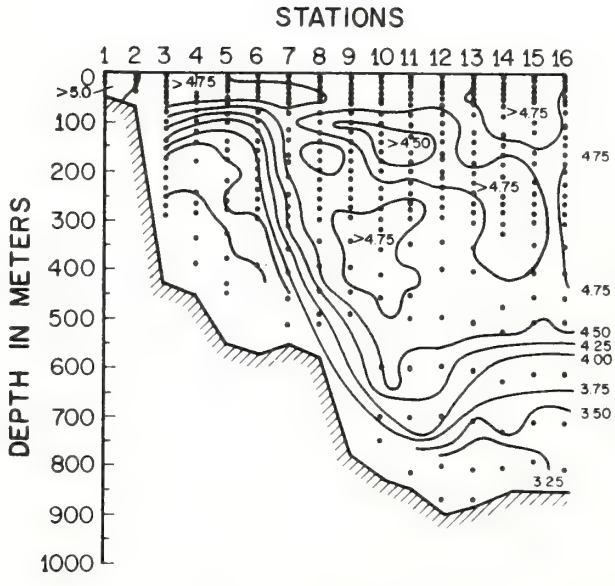


Figure 87. Cruise-23 oxygen cross-section.

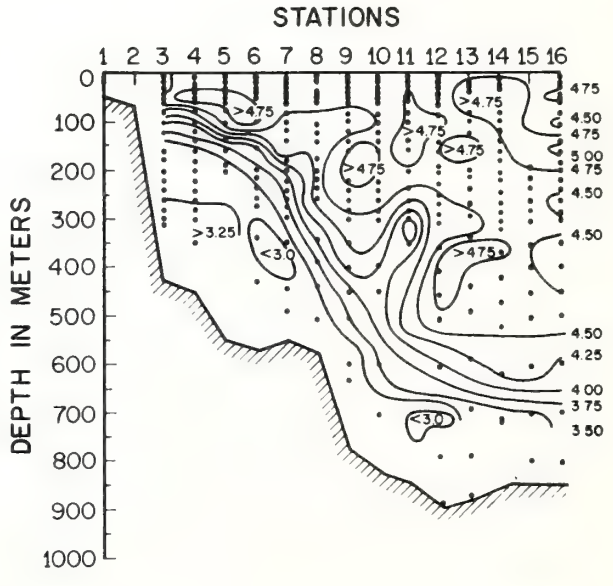


Figure 88. Cruise-24 oxygen cross-section.

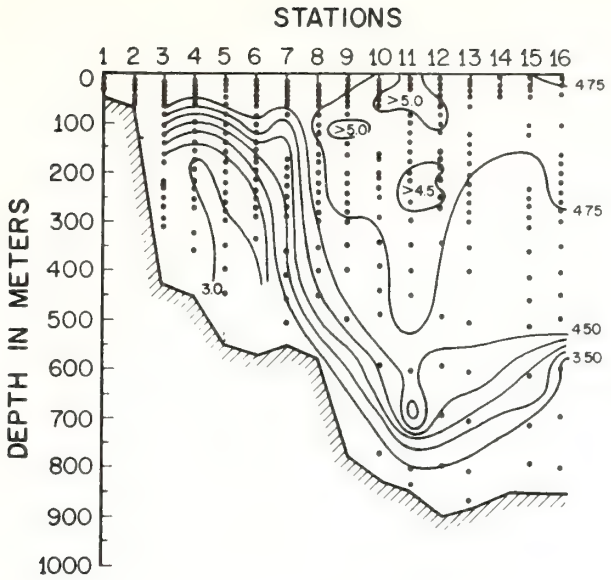


Figure 89. Cruise-25 oxygen cross-section.

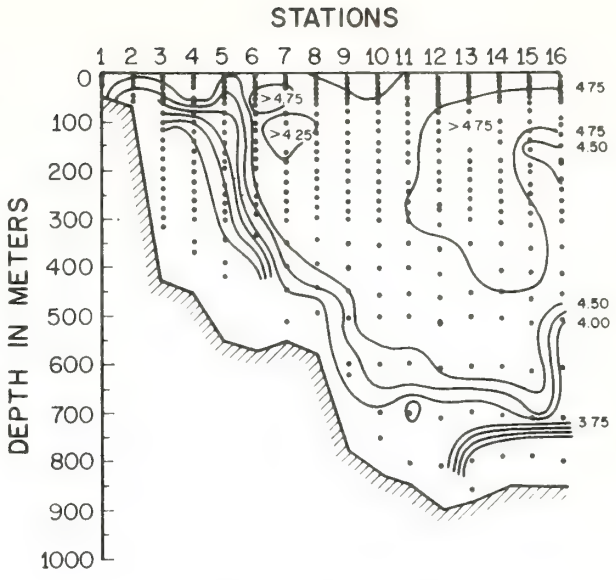


Figure 90. Cruise-26 oxygen cross-section.

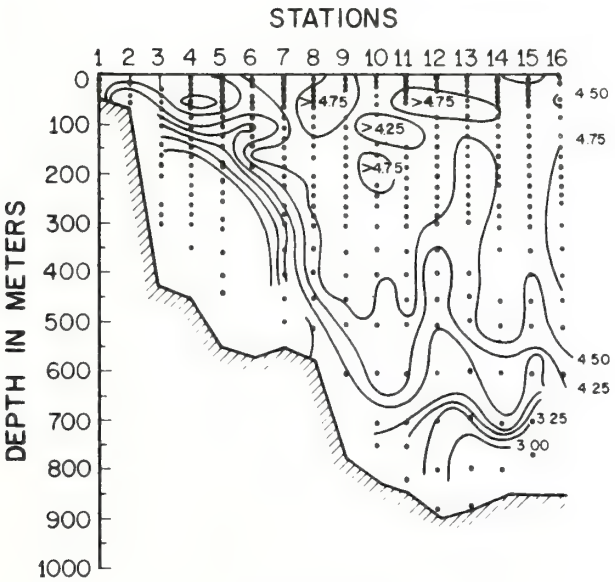


Figure 91. Cruise-27 oxygen cross-section.

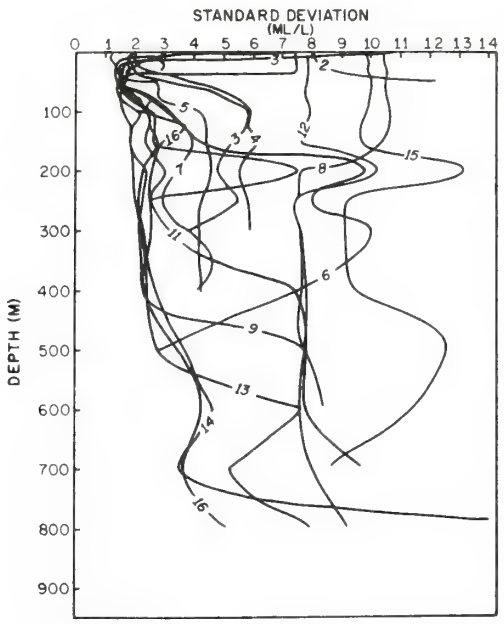


Figure 92. Standard deviation by station, obtained by using all oxygen data.

"Percentage saturation" of oxygen is frequently computed using the formula

$$O_2/O_2' \times 100 = O_2\%$$

where O_2 is the observed oxygen content, O_2' is"100% saturation", 100% saturation is computed from tables derived by Weiss (1970).

The percentage saturation for the near-surface water for all the cruises was close to 100% when computed by seasons. All stations exhibited a percentage saturation between 100% and 104% from the surface to 50 m. Winter was an exception. During winter, nearshore stations did not exhibit 100% saturation, and the rest of the stations exhibited 100% saturation only down to an average depth of 24 m.

The depth of 90% saturation was also computed for each station for each season. All curves were similar. Nearshore 90% of saturation was in 30 to 40 m. Depths increased with increasing distance from shore. The lowest depths were recorded during winter and the highest during the fall. The curves are given as Figures 93-96.

5.4 Sigma-t

The mean cross-section of the entire year of data relates a simple pattern (Fig. 97). The 24.00 isopycnic is found only at stations 5 and 6. This isopycnic line outlines the core of the Gulf Stream in the near-surface water. The 24.20 to 25.20 isopycnic lines slope gently downward from station 1 to station 7 then are generally horizontal out to station 16.

The maximum sigma-t of 27.33, a reflection of the minimum water temperature, is found at station 3 in 300 m. All isopycnic lines from 25.40 to 27.20 slope downward from station 3 to about 8 or 9. Further seaward the isopycnic lines are approximately horizontal.

The seasonal cross sections (figs. 98-101) exhibit patterns similar to the mean cross section of the entire year's data. The maximum sigma-t is always found at the bottom at station 3. No seasonal sigma-t variation is noted at this point, as the values vary only from 27.30 to 27.35. No seasonal variation occurs at the bottom seaward of station 3.

The minimum seasonal isopycnic line is always found including stations 5, 6, and 7. This line varies with the seasonal temperature change from a low of 23.20 during summer to a high 24.80 during winter. As there is almost no variation at the bottom at station 3, the gradient of the isopycnic lines between these areas varies considerably with the season. During summer,

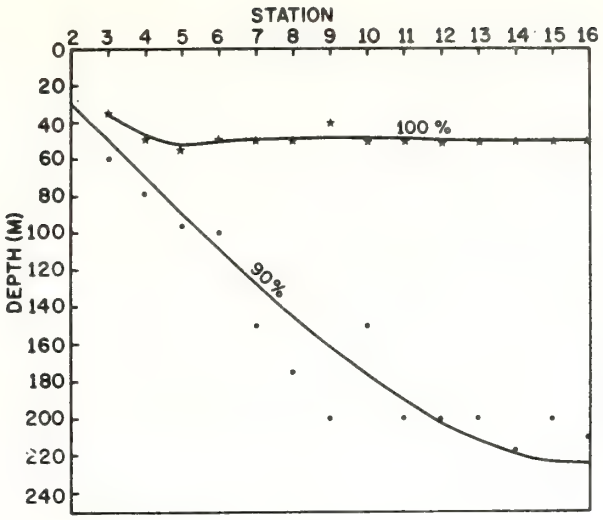


Figure 93. Depth of 100% and 90% oxygen saturation (spring).

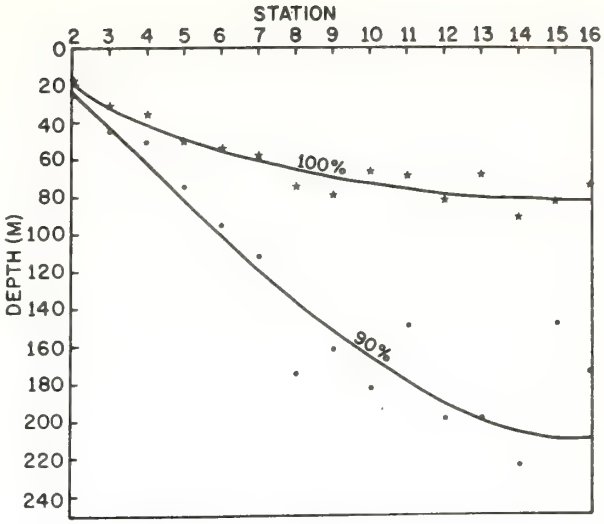


Figure 94. Depth of 100% and 90% oxygen saturation (summer).

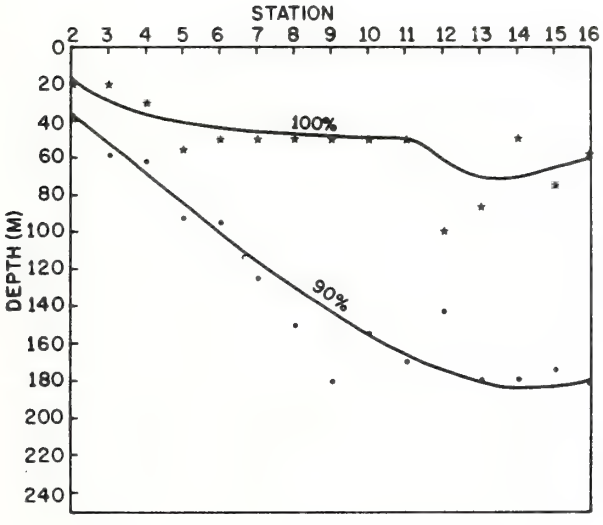


Figure 95. Depth of 100% and 90% oxygen saturation (fall).

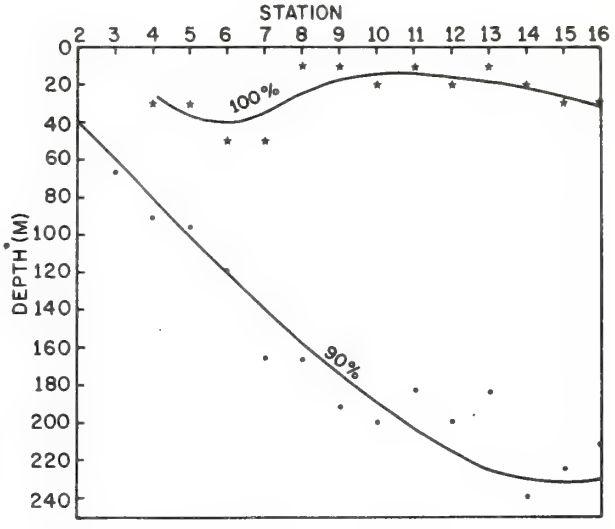


Figure 96. Depth of 100% and 90% oxygen saturation (winter).

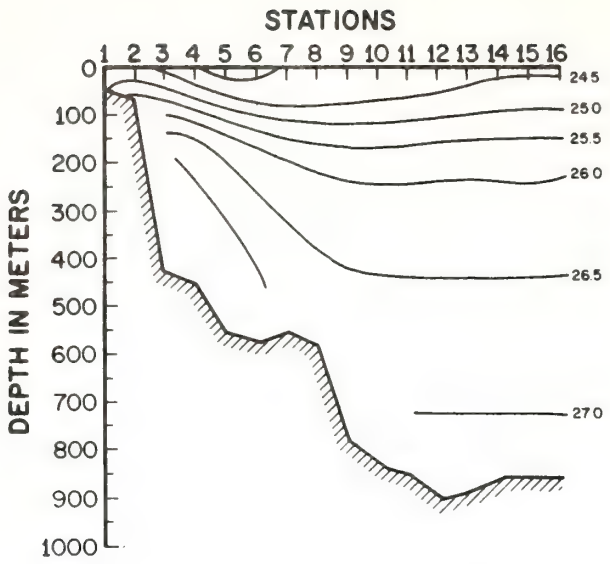


Figure 97. Mean of all cruises sigma-t cross-section.

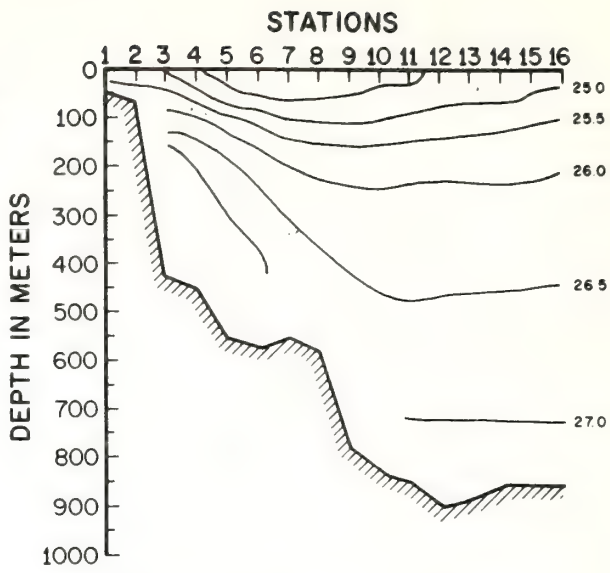


Figure 98. Mean of spring cruises sigma-t cross-section.

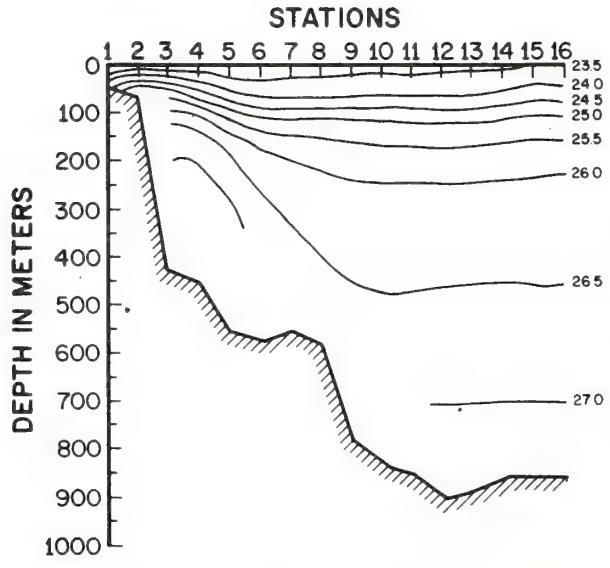


Figure 99. Mean of summer cruises sigma-t cross-section.

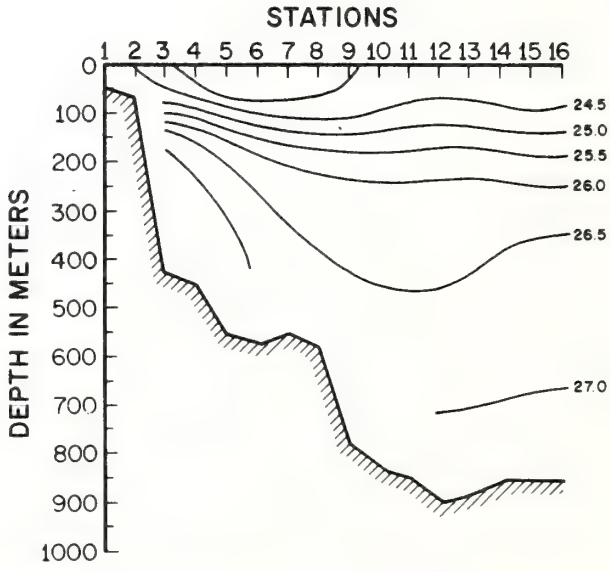


Figure 100. Mean of fall cruises sigma-t cross-section.

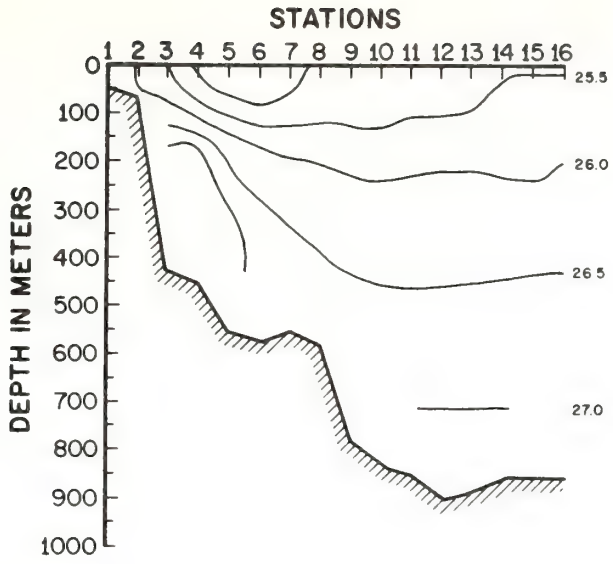


Figure 101. Mean of winter cruises sigma-t cross-section.

a strong seasonal thermocline is very apparent in the upper 200 m, where a gradient of 1.25 per 100 m occurs. In the winter, almost no gradient exists.

In general, the individual cruise sigma-t cross-sections were similar to the seasonal means in their main features (Figs. 102-124). However, seasonal means did mask shorter-term variations that occurred. Figure 125 shows the standard deviations at standard depths for each station, computed using the entire year's data. The largest variation occurred at the surface at station 1. In fact, the largest variations occurred at the nearshore stations reflecting the coastal influence upon these stations.

Away from the nearshore stations, the largest variations occurred at the surface. Exceptions were stations 4 and 5, where in the core of the Gulf Stream the maximum station standard deviations were recorded at about 75 m in depth. Below 200 m standard deviations were quite small, usually less than 0.2.

Variations that were noted occurred in three areas. Usually the lowest density water for a cross-section was found at the surface at stations 5 and 6. However, the lowest density water (20.77) for the entire year's data was found during the summer at station 1. This low density was a reflection of warm land air warming the nearshore water. The nearshore water also had low salinity reflecting the summer rainy season and land runoff.

As previously mentioned, lowest density water was usually found at stations 5 and 6. However, this low density near-

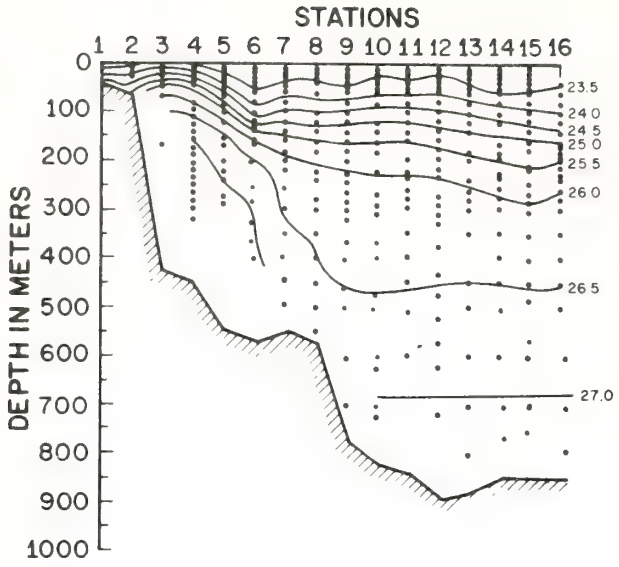


Figure 102. Cruise-1 sigma-t cross-section.

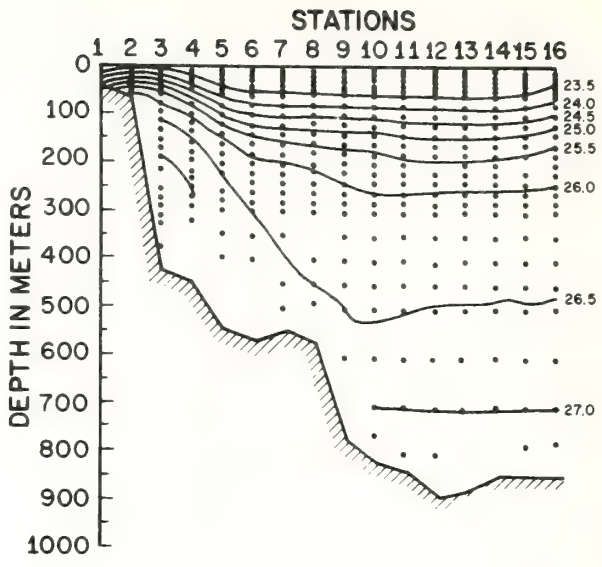


Figure 103. Cruise-2 sigma-t cross-section.

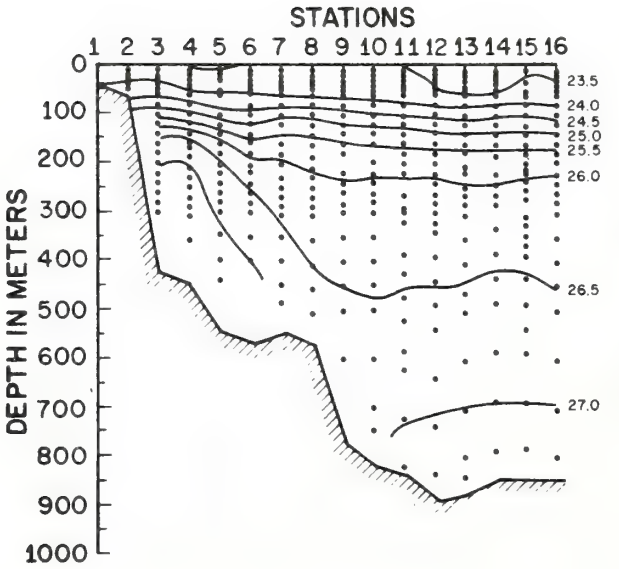


Figure 104. Cruise-4 sigma-t cross-section

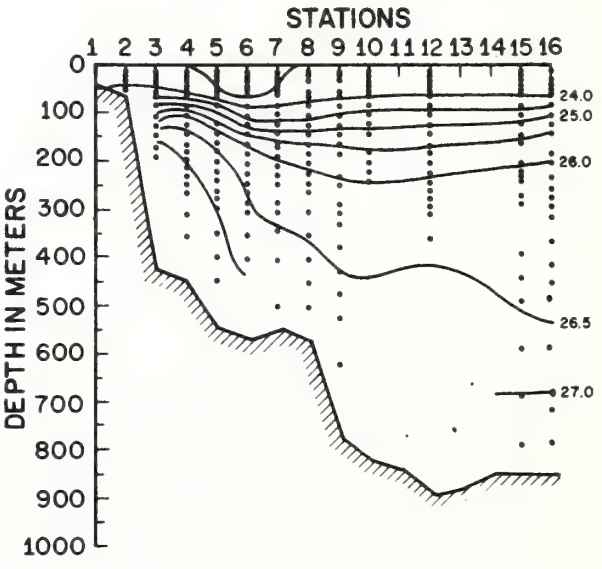


Figure 105. Cruise-5 sigma-t cross-section.

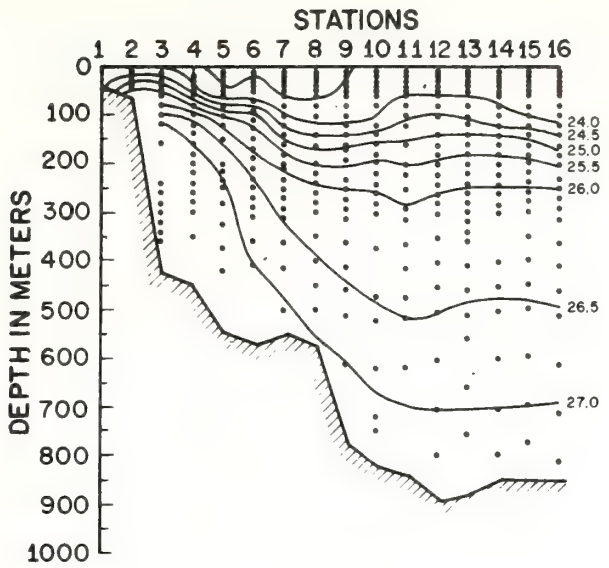


Figure 106. Cruise-6 sigma-t cross-section.

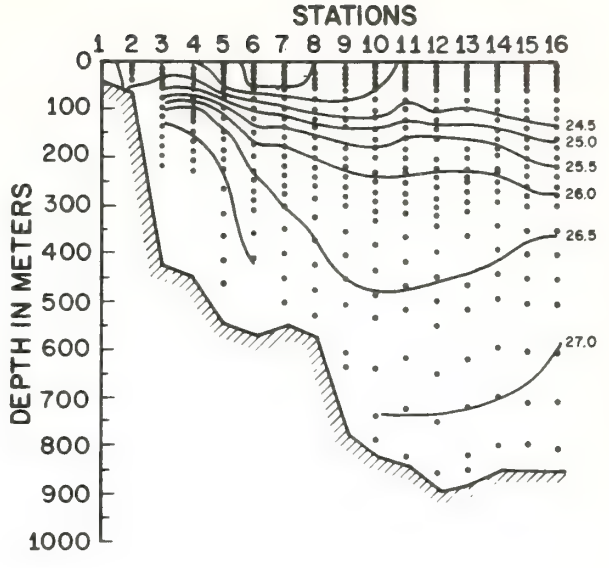


Figure 107. Cruise-7 sigma-t cross-section.

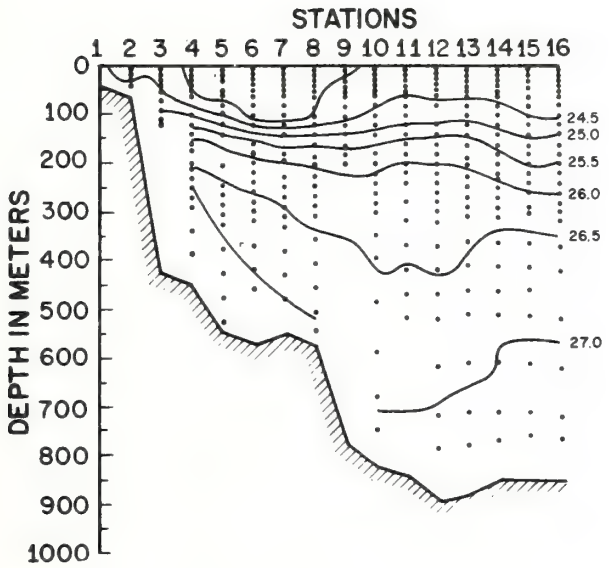


Figure 108. Cruise-8 sigma-t cross-section.

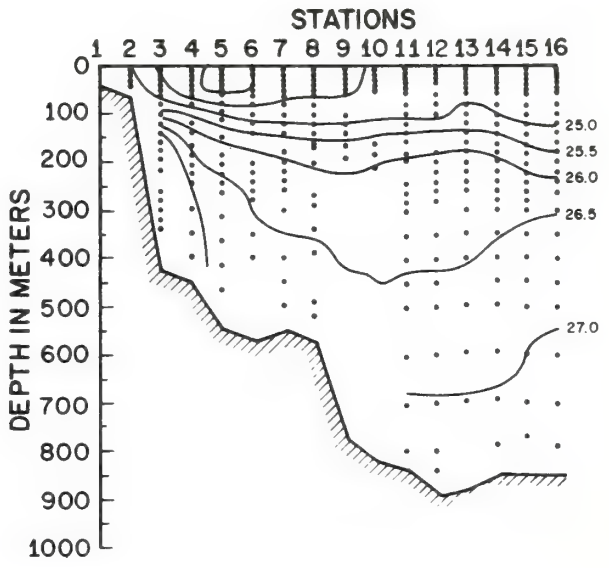


Figure 109. Cruise-9 sigma-t cross-section.

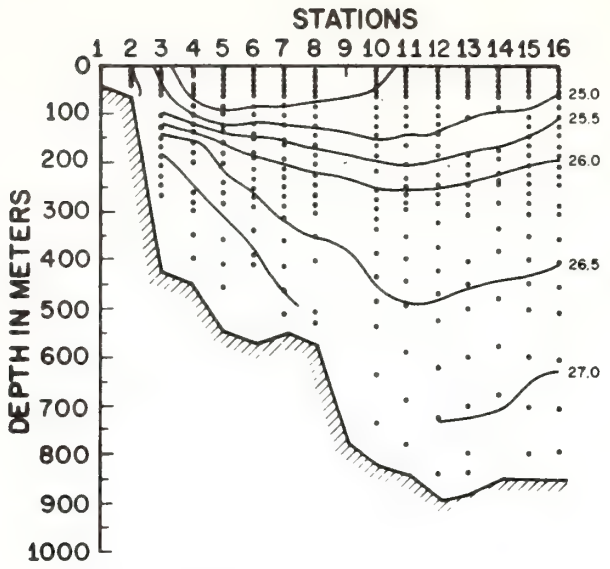


Figure 110. Cruise-10 sigma-t cross-section.

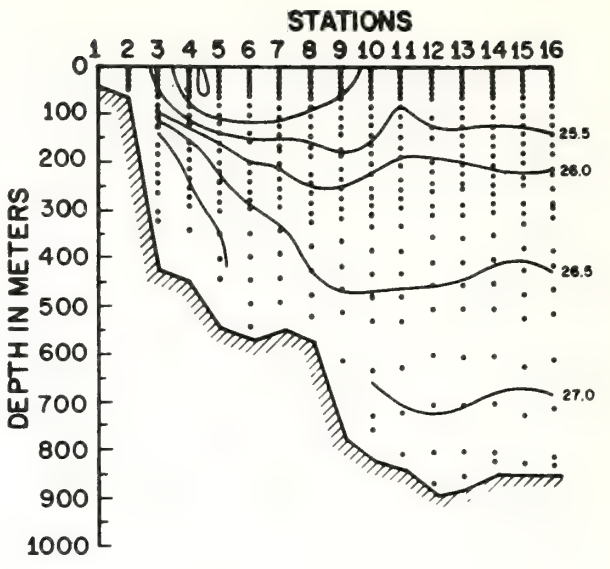


Figure 111. Cruise-12 sigma-t cross-section.

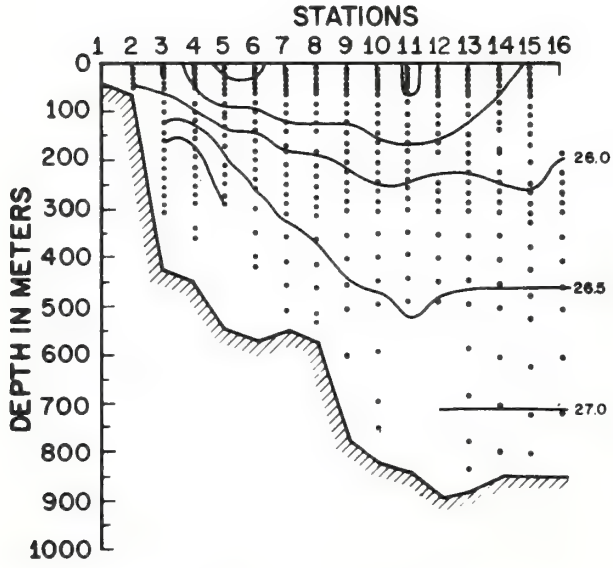


Figure 112. Cruise-14 sigma-t cross-section.

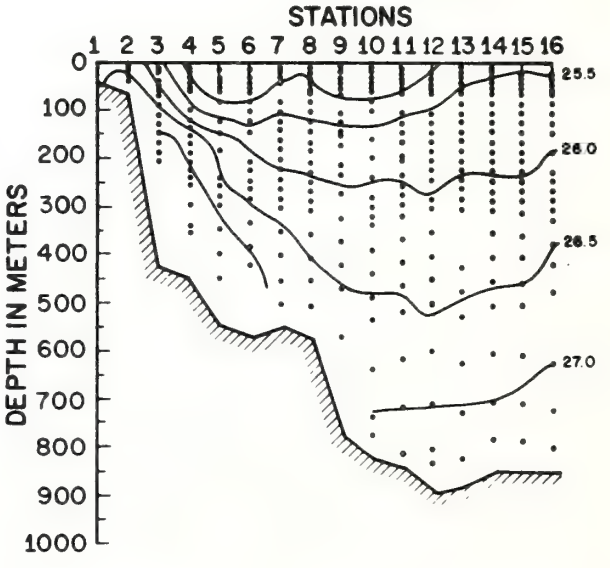


Figure 113. Cruise-15 sigma-t cross-section.

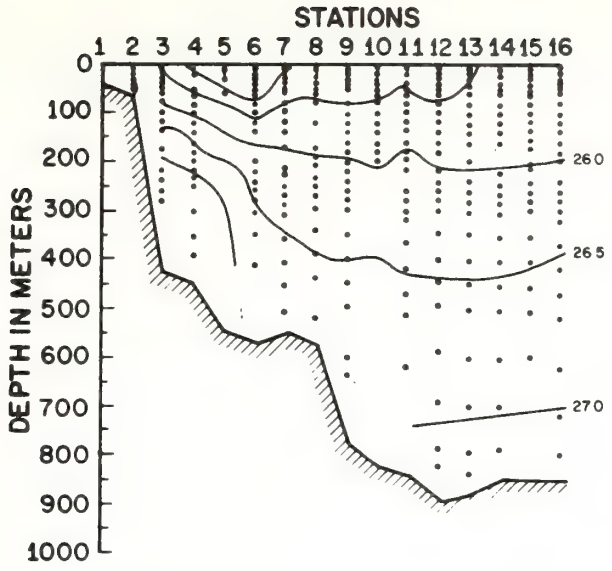


Figure 114. Cruise-16 sigma-t cross-section.

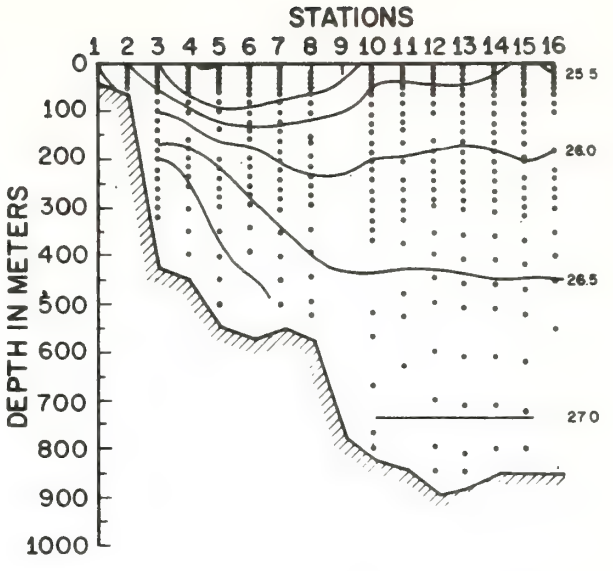


Figure 115. Cruise-18 sigma-t cross-section.

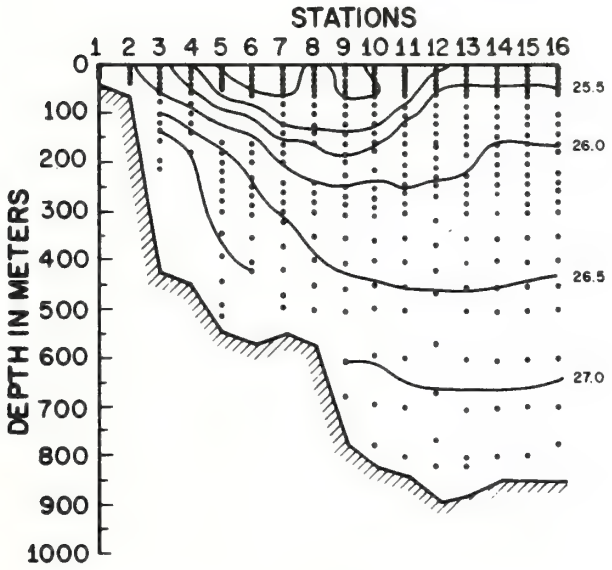


Figure 116. Cruise-19 sigma-t cross-section.

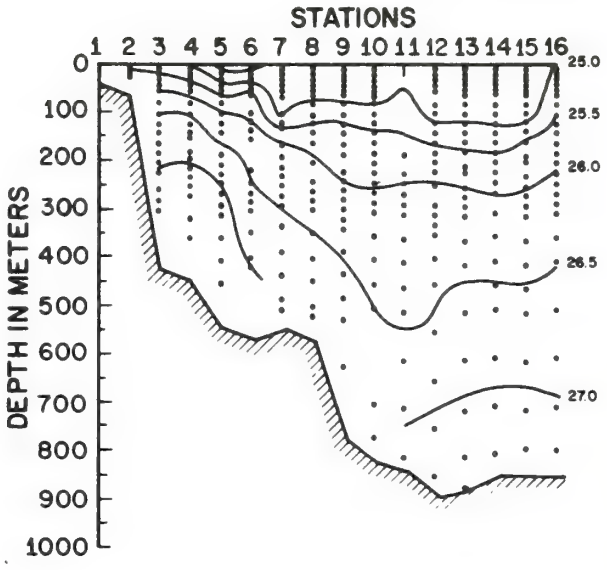


Figure 117. Cruise-20 sigma-t cross-section.

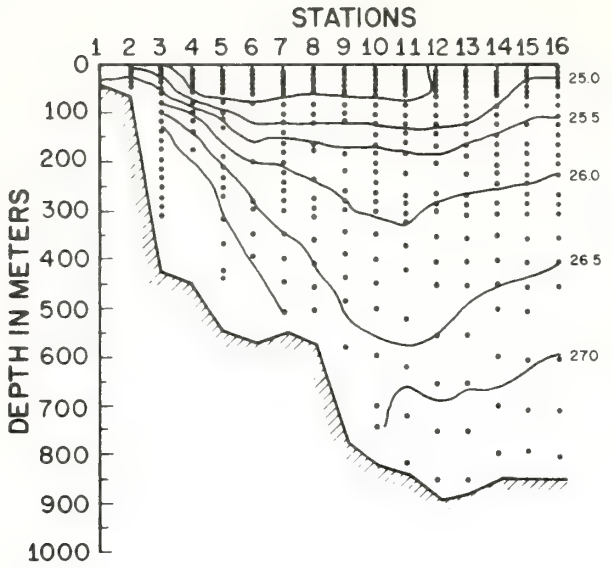


Figure 118. Cruise-21 sigma-t cross-section.

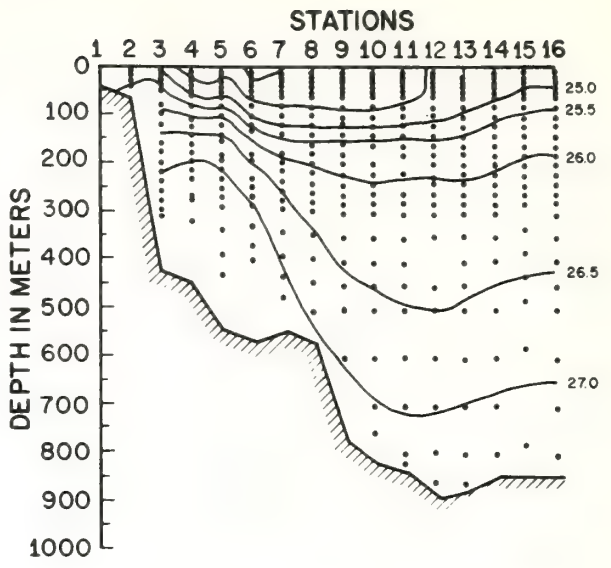


Figure 119. Cruise-22 sigma-t cross-section.

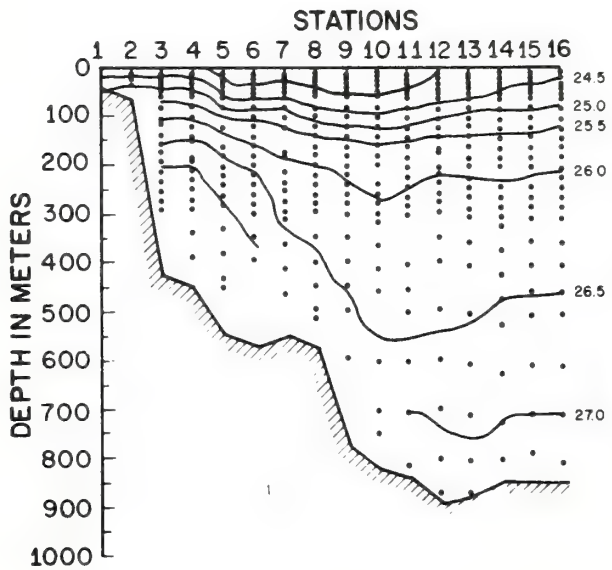


Figure 120. Cruise-23 sigma-t cross-section.

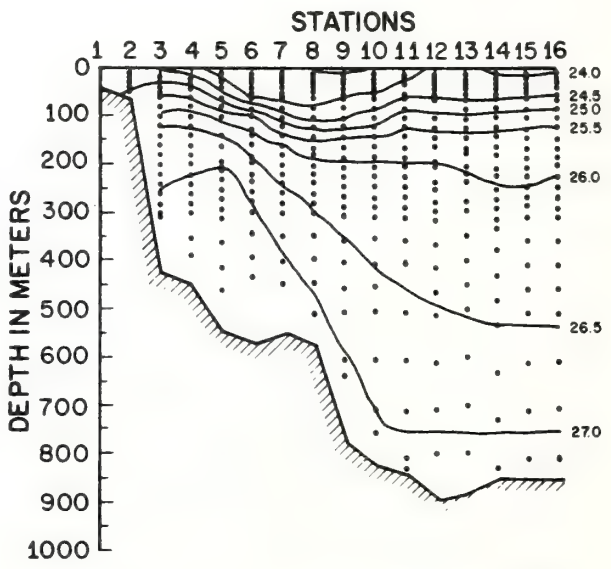


Figure 121. Cruise-24 sigma-t cross-section.

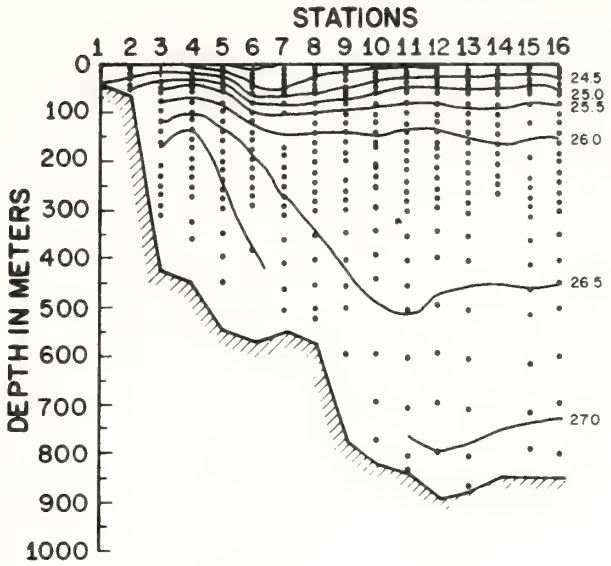


Figure 122. Cruise-25 sigma-t cross-section.

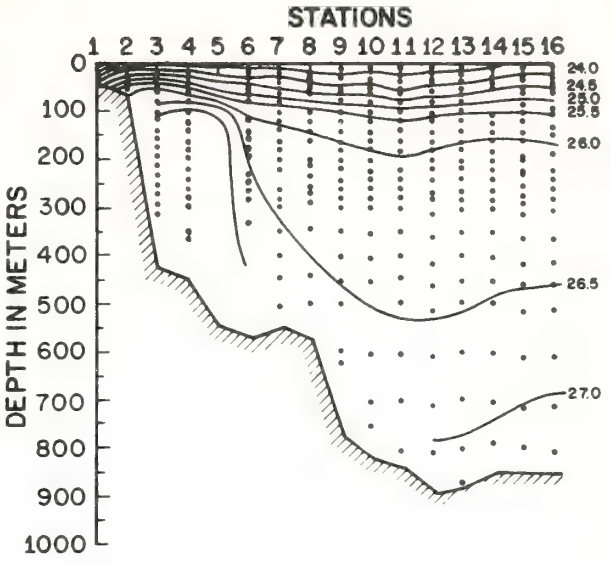


Figure 123. Cruise-26 sigma-t cross-section.

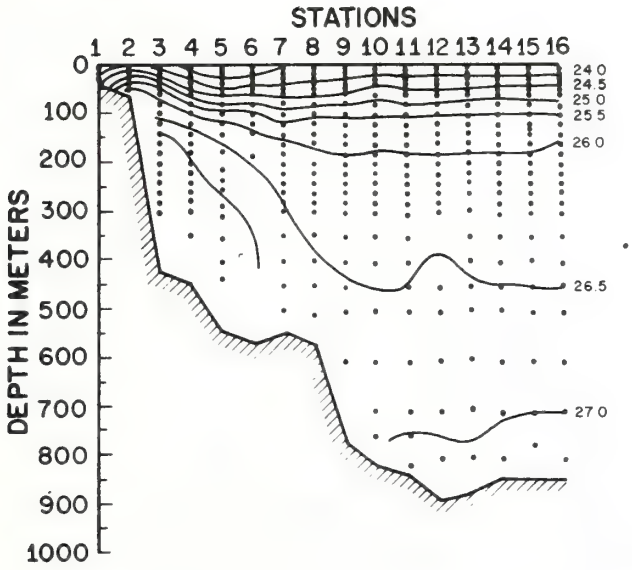


Figure 124. Cruise-27 sigma-t cross-section.

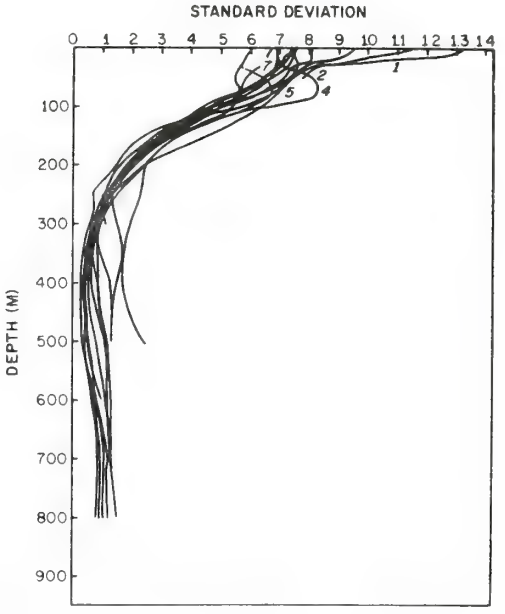


Figure 125. Standard deviations by stations, obtained by using all sigma-t data.

surface water spread from stations 5 through 9 during cruises 19 and 23. Cruise 19 was unique in that the low density water not only spread out horizontally but also extended vertically down to 50 to 100 m.

Cruise 22 also was somewhat unusual. Stations 6 and 10 (Fig. 1) and also their corresponding downstream stations recorded the low surface density water usually associated with this area. Yet a relatively higher density was recorded at station 8, and its corresponding downstream station. This unique water extended to a depth of about 100 m. The higher density resulted from the water temperature at station 8 being about 1.5°C colder than at station 6 and about 2.0°C colder than at station 10.

The third area of unusual variations was located at the bottom at stations 12 and 13. This was the deepest area along the entire cross-section. Usually a sigma-t of about 27.20 to 27.26 was recorded. However, during several cruises, notably 2, 6, 16, and 20, sigma-t's of 27.50 to 27.65 were recorded. Associated with these high densities were unusually low temperatures and high oxygens. Obviously, another water mass had entered the area.

6. GEOSTROPHIC CURRENTS AND VOLUME TRANSPORT

It is standard oceanographic practice to compute space variations in the dynamic height of the sea surface from the observed sub-surface density distribution assuming that a certain deep-level motion may be assumed to be negligible and an isobaric surface essentially level. The dynamic slope of an upper isobaric surface can be found from the variation of specific volume (reciprocal of density) along the isobaric layer. Thus the current at the upper surface relative to any possible current at the lower surface is determined. It is customary in deep water to assume an isobaric surface of 2000 decibars (approximately 2000 m deep) as a so-called layer of no motion.

The Peirce cross-sections were taken crossing the continental shelf and slope. The water depth varied between 30 m and about 900 m.

In similar circumstances, Dietrich (1937) computed the elevations of the sea surface along sections assuming there was a level of no motion in the oxygen minimum layer between 250 and 950 m. Again the Peirce Gulf Stream data were in too shallow water. The oxygen minimum layer was seldom reached. Dietrich, also confronted with this problem, assumed a vanishing horizontal pressure gradient at the bottom. According to Montgomery (1938), this method is very unreliable. Thus, because it appears that no reliable method exists to accurately determine dynamic currents from the early Peirce cruise data, no determinations were made.

Starting with cruise 20, surface drogues were planted in the water at each even (upstream) numbered station and then tracked for 30 minutes to one hour. For purposes of calculating geostrophic currents, the measured currents were assumed to have occurred at both the upstream station and the station directly downstream. The component of the measured current normal to the cross-section was calculated. Geostrophic currents then were computed from the dynamic heights downward from the surface from stations 2 through 10. The method used is described by von Arx (1962).

The surface drogue measurements exhibit a pattern of variability that had already become apparent by the analysis of the temperature-salinity data. The surface drogue measurements indicate that the axis of the Gulf Stream is usually in the vicinity of stations 5 or 6, but on occasion touches stations 4 and 7. The maximum recorded current also varied from cruise to cruise from a low of 141.5 cm/sec during cruise 23 to a high of 218.8 cm/sec during cruise 22. The mean at the core was 178.5 cm/sec. A large variation was recorded at other stations. For example, station 9 varied between a high of 96.6 cm/sec during cruise 20 to a low of 0 during cruise 25.

The current between stations 2 and 3 flowed as part of the Gulf Stream during cruises 21, 22, 26, and 27. During cruises 23, 24, and 25, the current flowed in the reverse direction. Although the water depth in this area varied between 60 and 300 m, the geostrophic current data extended down only to 30 m. The reverse current varied in velocity between 10 and 40 cm/sec. This confirms Bumpus'(1955) report that south of Cape Hatteras a southerly-flowing coastal current was a transient affair.

Generally, the current of the Gulf Stream decreases outward from the core and downward from the surface. However, an increase in velocity with depth does occur locally. For example, during cruise 20, stations 5 to 6 recorded a maximum velocity of 206.8 cm/sec at 75 m. Several other examples were recorded where the maximum station velocity was between 75 and 250 m. Figures 126 to 133 give the current variation across the section at the surface and 100 m. Several examples were noted where the current at 100 m was greater than at the surface.

In this area, the Gulf Stream sometimes extends beyond the entire cross-section, a distance of 90 nautical miles. Station 10, the farthest seaward station that current measurements were made, recorded a mean velocity of 48.0 cm/sec. The velocity cross-section for cruises 20 through 27 are given as Figures 134 through 141. It is to be noted that the axis of the stream is not vertical, but rather exhibits a seaward tilt on nearly every cross-section.

If the geostrophic velocity is computed for each successive layer, the volume transport normal to the lines joining each pair of stations can be computed by summing the products of cross-sectional area and mean velocity for each depth interval. This was done for each Peirce cross-section from cruises 20 to 27. The computational methods for applying the geostrophic

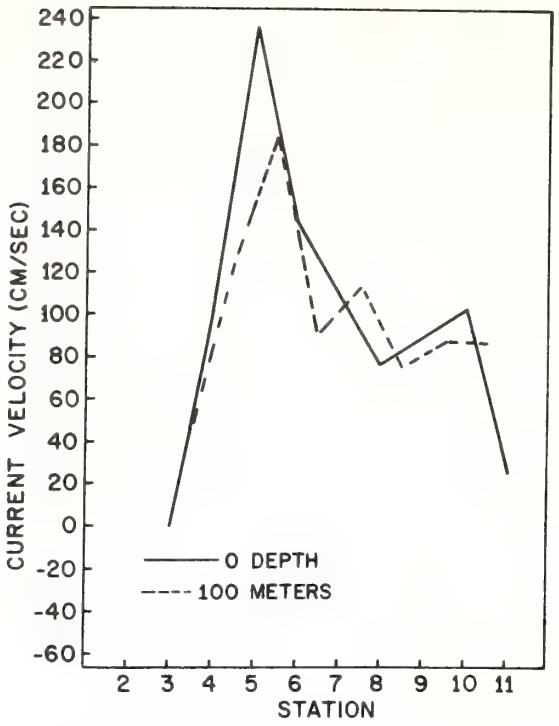


Figure 126. Current velocity at 0 and 100 m for cruise 20.

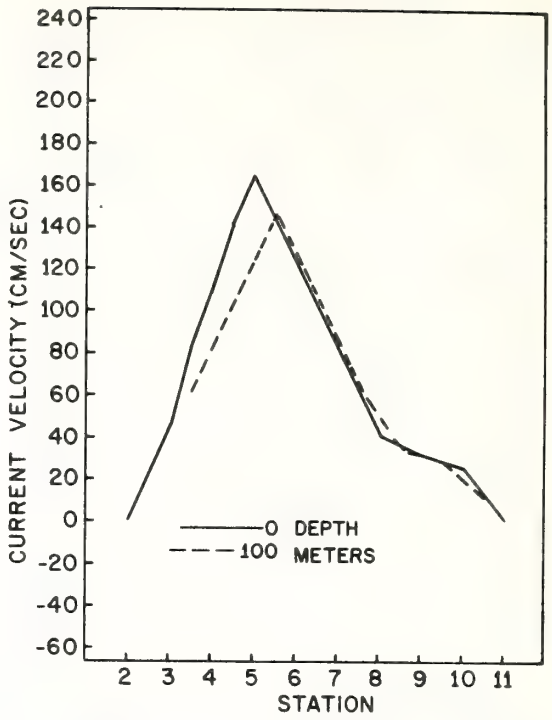


Figure 127. Current velocity at 0 and 100 m for cruise 21.

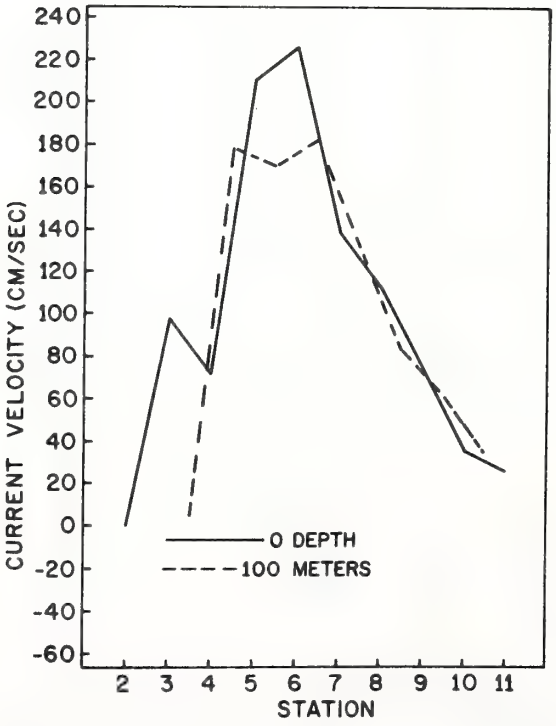


Figure 128. Current velocity at 0 and 100 m for cruise 22.

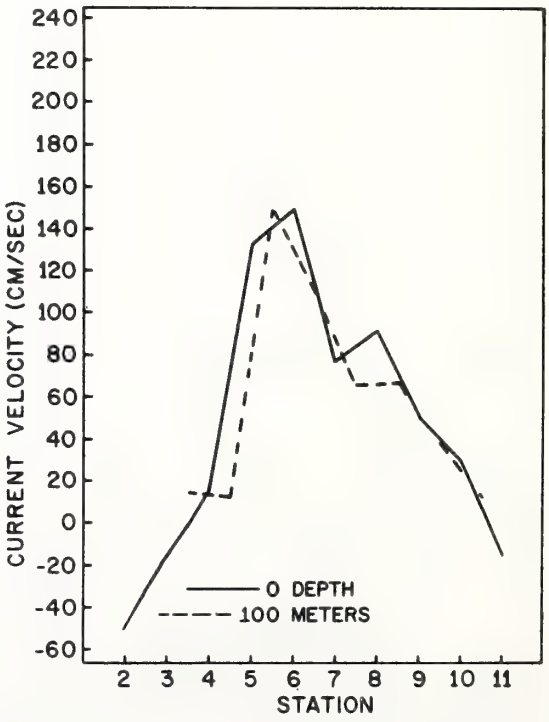


Figure 129. Current velocity at 0 and 100 m for cruise 23.

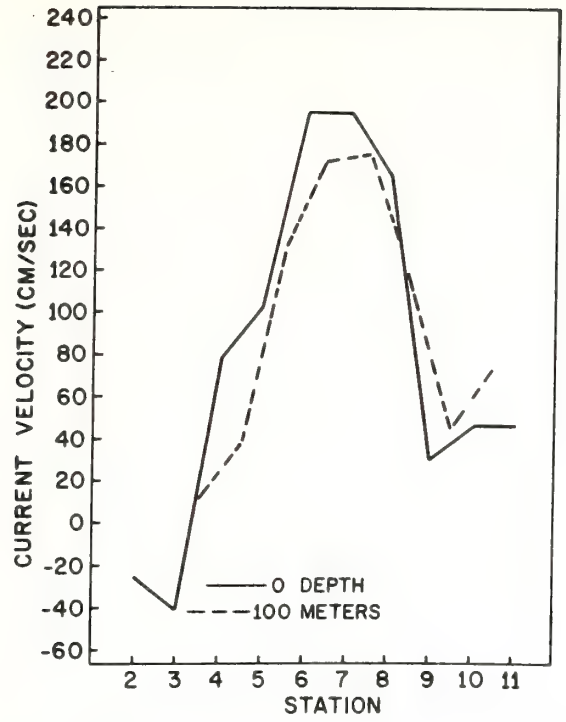


Figure 130. Current velocity at 0 and 100 m for cruise 24.

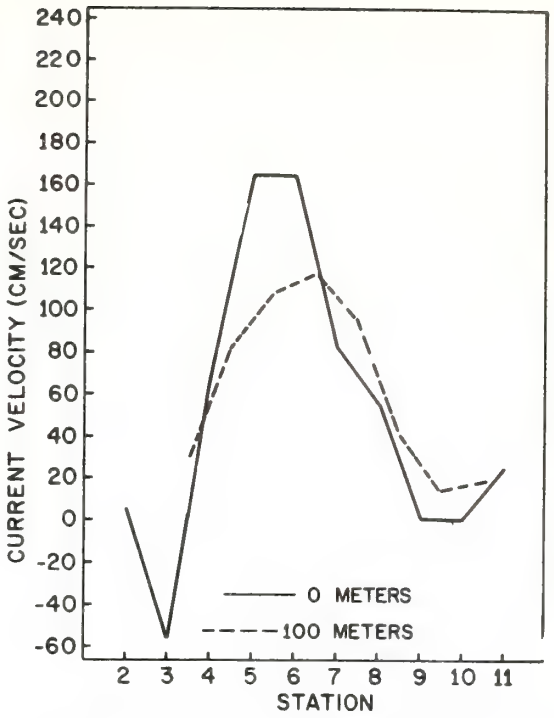


Figure 131. Current velocity at 0 and 100 m for cruise 25.

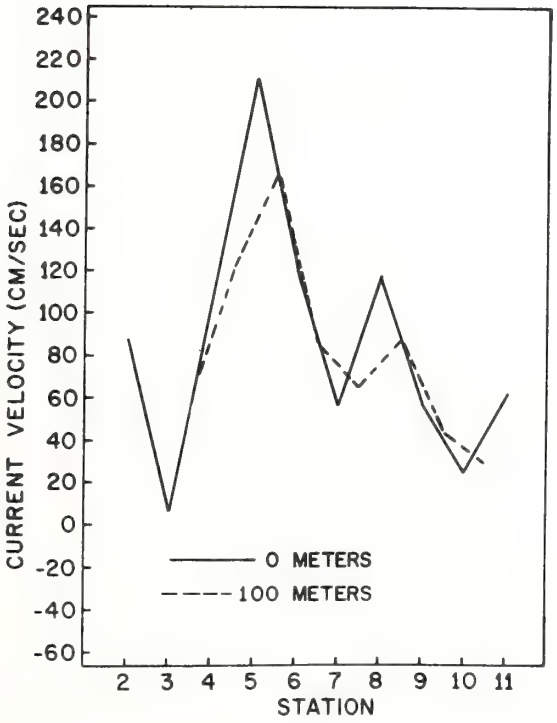


Figure 132. Current velocity at 0 and 100 m for cruise 26.

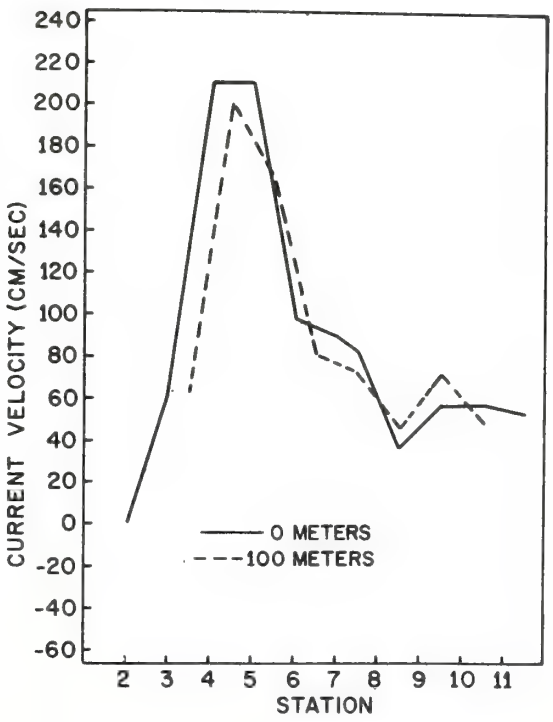


Figure 133. Current velocity at 0 and 100 m for cruise 27.

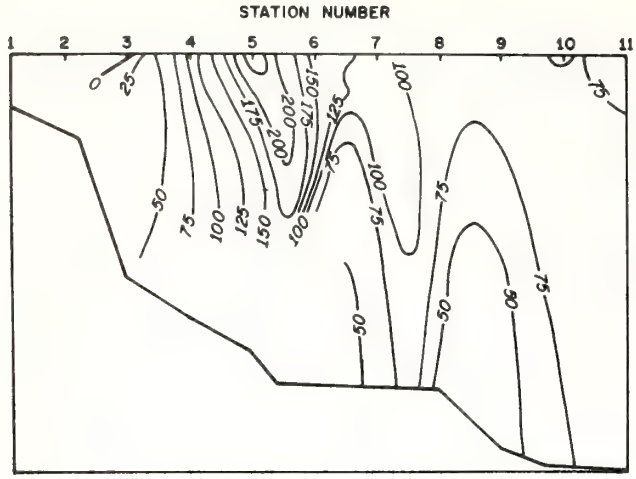


Figure 134. Cruise-20 northern line geostrophic currents (cm/sec).

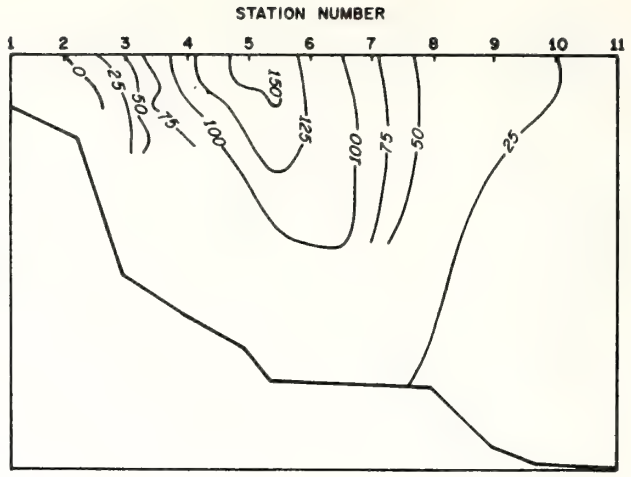


Figure 135. Cruise-21 northern line geostrophic currents (cm/sec).

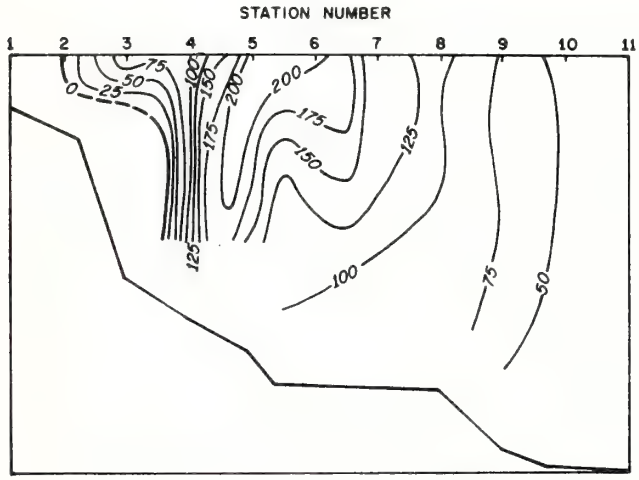


Figure 136. Cruise-22 northern line geostrophic currents (cm/sec).

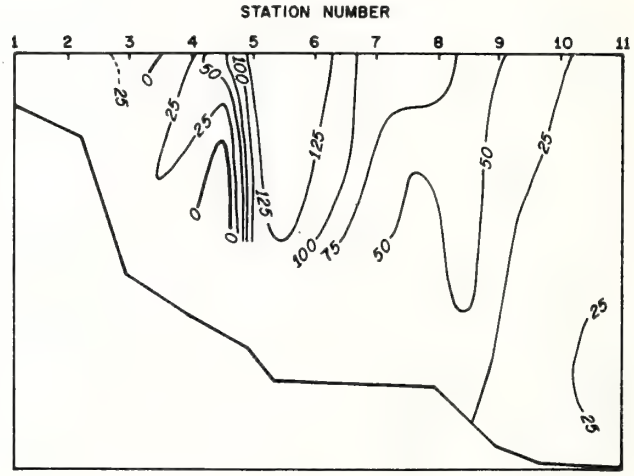


Figure 137. Cruise-23 northern line geostrophic currents (cm/sec).

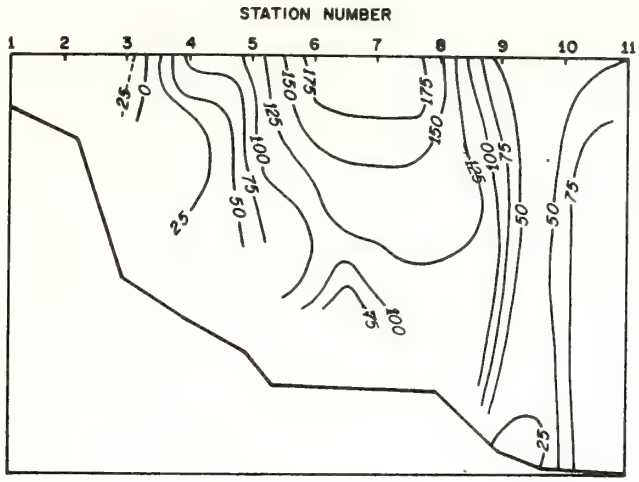


Figure 138. Cruise-24 northern line geostrophic currents (cm/sec).

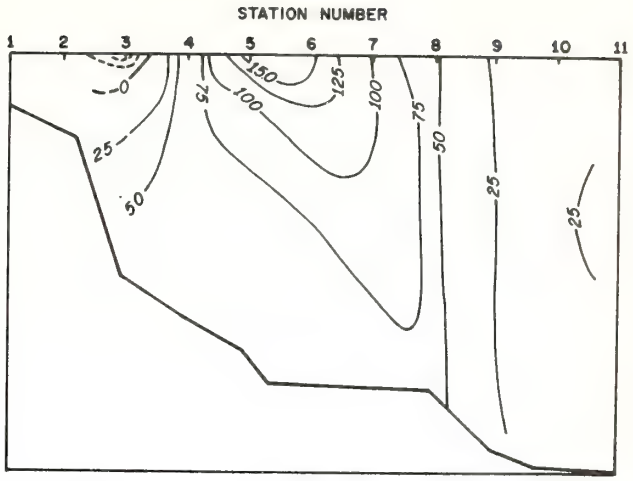


Figure 139. Cruise-25 northern line geostrophic currents (cm/sec).

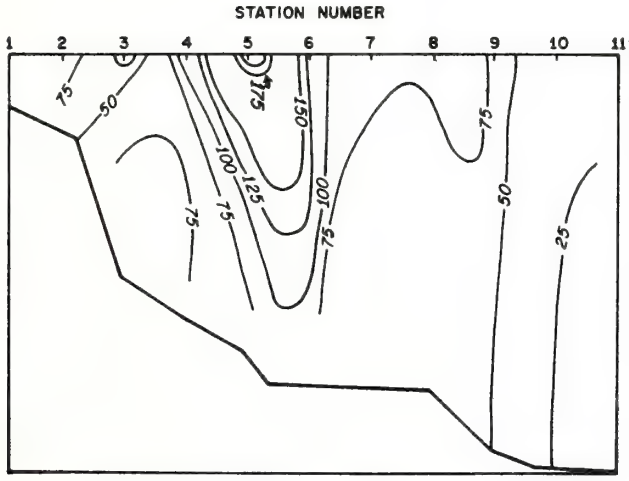


Figure 140. Cruise-26 northern line geostrophic currents (cm/sec).

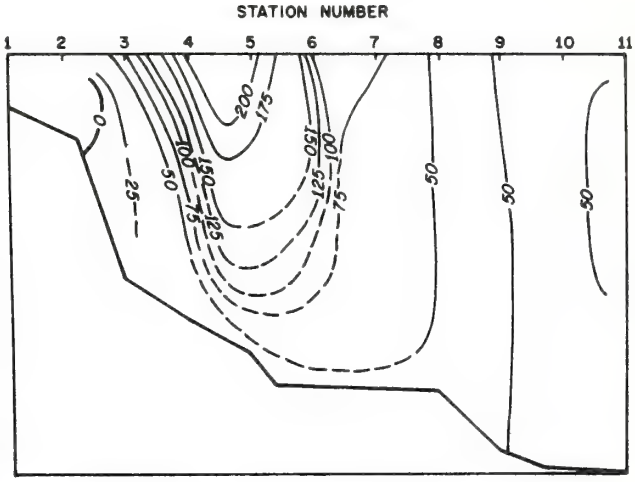


Figure 141. Cruise-27 northern line geostrophic currents (cm/sec).

method are given in H. O. pub 614 (U.S. Navy Hydrographic Office, 1951). Also von Arx (1962) gives a good summary.

These calculations will not accurately reflect the total Gulf Stream volume transport, as several sources of error exist. The surface drogue measurements did not extend completely across the Gulf Stream. As no drogue measurements were made at the seaward end of the line, no volume transport calculations could be made. Additional volume was missed, as the data did not always extend to the bottom.

The accuracy of the volume transport calculations is closely correlated with the accuracy of the surface drogue current measurements. The ship's navigation for the drogue current measurements was by HIFIX. However, the ship's navigation procedure allows its accuracy to be questioned.

Also occupation of oceanographic stations in a current demand a high degree of skill. The ship must maneuver to hold position and also keep a small wire angle to allow the messenger to slide freely and trip the Nansen bottles. But the maneuvering plus drifting in the wind and current may move the ship as much as a mile between the deep and shallow casts in what is nominally the same oceanographic station. During processing of the station data, adjustments were made to give a mean position. Also smoothing of the temperature and salinity data were carried out in the area of overlap between the deep and shallow casts.

Iselin (1940) also was concerned about the various sources of errors inherent in transport calculations. He used tide gage records to prove that his transport values were surprisingly accurate. He concluded that a calculated transport value could be in error by more than 10%, but that the average error of the values was much less.

The individual cruise transport values fluctuate from a low of 25.6×10^6 m^3/sec on cruises 21 and 23 to a high of 65.5×10^6 m^3/sec (Fig. 142). The mean values for the eight cruises are 46.2×10^6 m^3/sec for the north line and 45.3×10^6 m^3/sec for the south line. The mean values appear to be quite reasonable. Schmitz and Richardson (1968) reported the volume transport between Miami and Bimini to be $32 \pm 3 \times 10^6$ m^3/sec, and Iselin (1940) reported various values between 76.4 and 93.5×10^6 m^3/sec for the transport across the Gulf Stream between Montauk Pt., New Jersey, and Bermuda. Iselin noted that his data indicated seasonal periodicity, but thought it did not indicate short period variations. However, he conceded that his computational methods tended to minimuze short-period changes.

Conversely, Von Arx (1962) mentions several reports of diurnal fluctuations in the flow of the Florida Current and Gulf Stream by direct measurements. Von Arx reports "in addition to the tidal variations in the Florida Current, there is an irregular variation of transport based on 24-hour averages taken so as to eliminate the tidal influences. These irregularities show a wide range of variation (by a factor of two) in

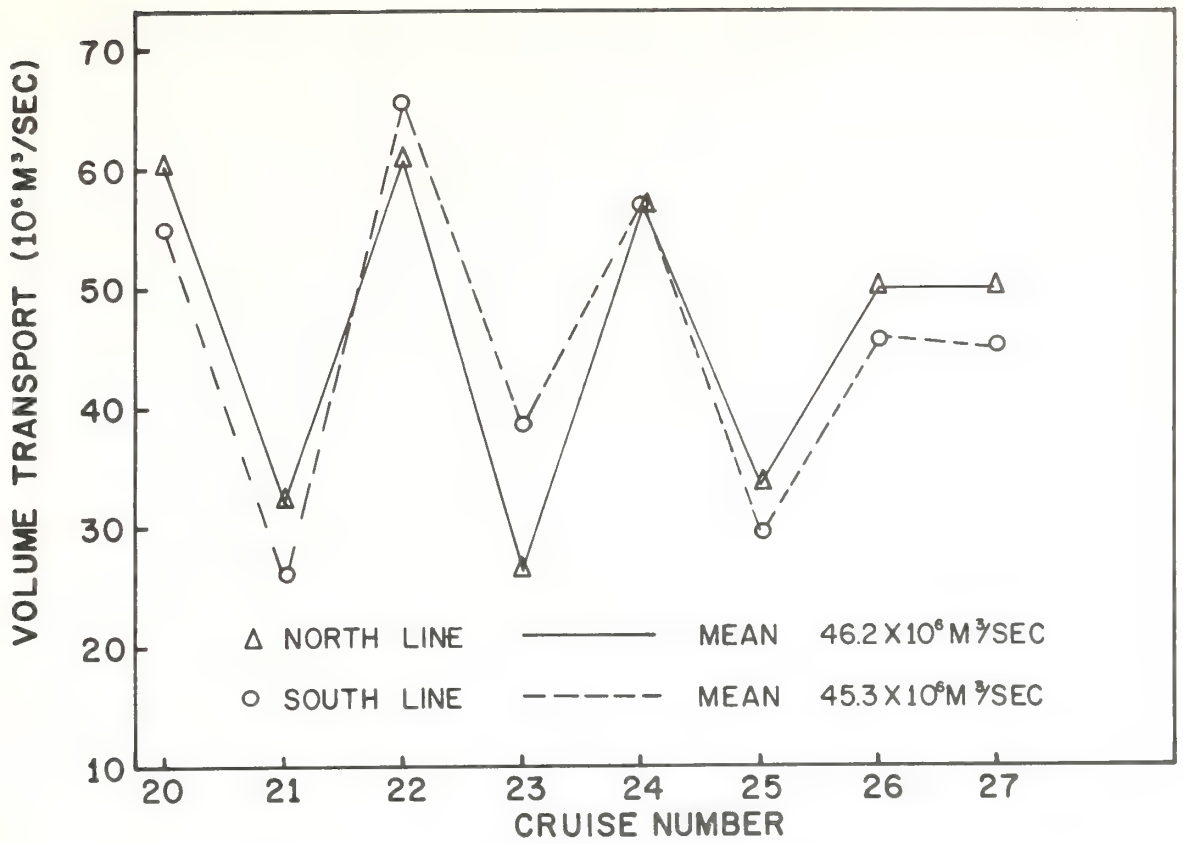


Figure 142. Volume transport across the Gulf Stream for cruises 20-27.

the course of a month and other oscillations having a similar slope but less amplitude." Thus it appears that these transport values are acceptable, having a maximum error of 10 percent.

7. WATER MASS ANALYSIS

It is well established that, as the Gulf Stream flows northward off the east coast of the U.S., its volume of water increases. However, the source of this water has not been well established. It is possible that water mass analysis might indicate the sources of this additional water.

The most widely used method of defining the characteristics of various water masses and of studying their origins and relationships is by the temperature-salinity correlation method first introduced by Helland-Hansen (1918). Since then, the nomenclature of the water masses in the North-Atlantic Ocean has become quite confused, although apparently the water masses themselves have remained essentially the same.

Wright and Worthington (1970) have made a comprehensive report on the nomenclature as used by various authors. Thus a nomenclature discussion here will be limited to that necessary to understand the water masses that occur in the area of interest.

According to Nowlin (1971), the water beneath the surface mixed layer but above the 17°C water is the only distinct water mass formed in the Gulf of Mexico. This water mass, referred to as Continental Edge Water by Wennekins (1959), is characterized by an increase in salinity from about 36.00°/oo to 36.45°/oo between about 25°C and 18°C. Thus the salinity is considerably less for a given temperature than is the water referred to as Yucatan Straits Water by Wennekins.

The water that passes through the Yucatan Straits either passes around the western end of Cuba and directly into the Florida Straits as the Florida Current or flows as the Loop Current in a clockwise direction in the eastern Gulf of Mexico before joining the Florida Current. According to Wust (1964) as well as Nowlin (1971), the water flowing through the Yucatan Straits is made up of the Subtropical Underwater, characterized by an intermediate salinity maximum (36.60 - 36.80°/oo) in depths between 50 and 200 m. Below this is water characterized by an intermediate oxygen minimum in about 400 to 600 m depth, and beneath these is found a remnant of Sub Antarctic Intermediate Water identified by an intermediate salinity minimum in various depths between 700 and 850 m in the Caribbean Sea. Nowlin indicates the depth of this layer varies between 900 and 1100 m in the Gulf of Mexico.

These water masses can be considered the source waters of the Florida Current. Starr (1970) found evidence that some water was added through the Santaren Channel in the central Florida Straits. Farther north, Richardson and Finlen (1967) found indications of water addition to the Florida Current through the Northwest Providence Channel.

Jacobsen (1929) explained all the water in the North Atlantic as combinations of six basic water types; among them was the Antilles Current Water. Iselin (1936) describes the Antilles Current as flowing northwestward along the line of the Bahama Islands and joining the Florida Current north of Little Bahama Bank. Wust (1924) calculated that it supplied the Gulf Stream with about half as much water as does the outflow from the Straits of Florida. The Atlantis took hydrographic stations in this area in February 1932 and April 1933. Iselin (1940) concluded that there was no evidence of a powerful Antilles Current. However, he suggested that, because it is primarily a wind-driven current, as the trades move north-ward in summer the resulting flow might be broader and swifter. He further stated "that on the basis of the present data, the term Antilles Current had best be reserved for the shallow and weak stream of

equatorial water near the islands."

The water found in the Sargasso Sea probably has had more names than any other water mass found in the North Atlantic. Iselin (1936) called it Central Atlantic Water. Its descriptive T-S curve varies from a high of 18°C with a salinity of 36.5°/$_{oo}$ to a low of 4°C with a salinity of 35.00°/$_{oo}$. This water is roughly equivalent to the North Atlantic Central Water described by Sverdrup, et al.(1946). Wright and Worthington (1970) call this water the Western North Atlantic Water. According to Worthington (1959), a considerable part of this water, referred to as 18° water, is formed in the northern part of the Sargasso Sea during the winter. It has a characteristic inflection point close to 300-m depth where the temperature is 17.9 ± 0.3°C and the salinity is 36.50 ± 0.10 °/$_{oo}$. It is hypothesized that these water masses must be the source water for the Gulf Stream in the vicinity of the Peirce cruises.

To define the T-S relationships of the various water masses found in the vicinity of the Peirce cruises, station data from the various source areas were plotted and compared. Figure 143 shows the T-S curve of Continental Edge Water as reported by Wennekens (1959). Also shown are the T-S curves reported by Wennekens (1959) and Iselin (1936) of water in the vicinity of the Yucatan Straits.

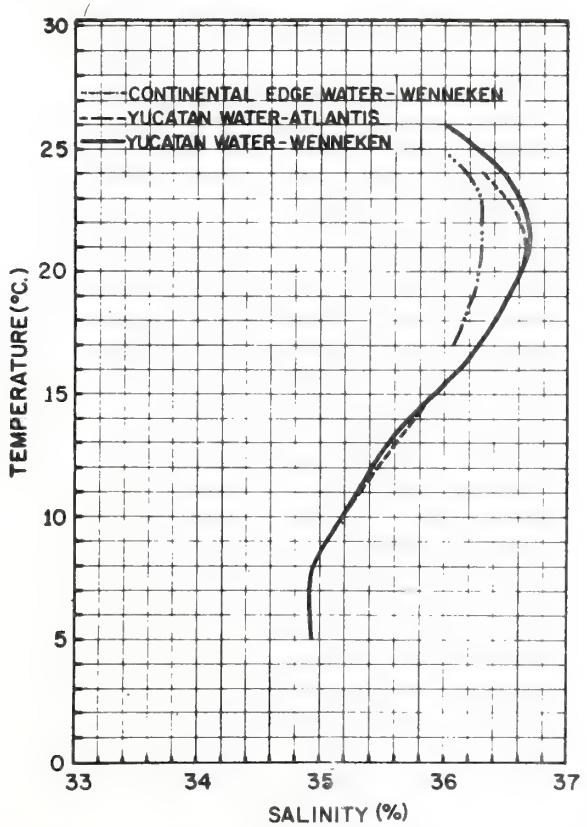


Figure 143. Comparison T/S curves-Continental Edge Water and Yucatan Strait Water.

Comparison curves also were drawn for the water in the vicinity of the Antilles Current. Data were used from the Atlantis cruises of April 1932, and February 1933, the cruise of the Requisite of March 1962, and cruises of the Explorer of April and May 1962 and May 1964. The Explorer and Requisite data are in good agreement below 19°C. As a matter of fact, between 19°C and 11°C and below 6°C, the three curves agree very well. However, between 11°C and 6°C the Requisite and Explorer data exhibit lower salinity values indicating that the Antarctic Intermediate salinity minimum is more prominent than in the Atlantis data. Figure 144 shows these curves.

The Requisite and Explorer also recorded salinity values in the upper 200 m between 36.70°/oo and 37.00°/oo. These values are considerably higher than those recorded by the Atlantis. This great variation in salinity between cruise data is not surprising. Deductions from observations from cruises widely spaced in time may be untrustworthy. This would be especially true in this area, as the Antilles current, according to Iselin (1936), is primarily wind-driven and related to the trades. Defant (1936) indicates that the water in the vicinity of the salinity maximum is a mixture of waters from the southeast and northeast.

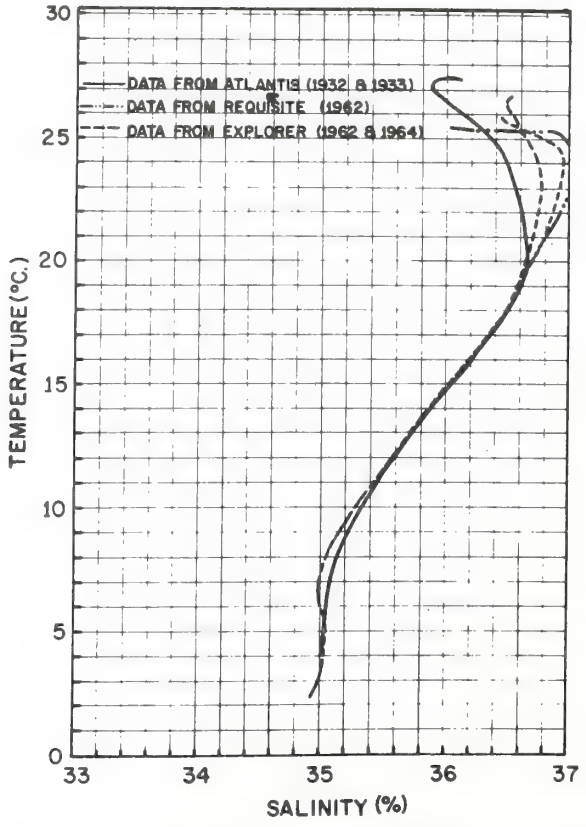


Figure 144. Comparison T/S curves Antilles Current Water.

T-S comparison curves for the water in the Sargasso Sea were drawn using Atlantis data between Chesapeake Bay and Bermuda and Explorer data taken north of the Antilles Current. Between 18°C and 4°C, the limits of the Atlantis data, the two curves are in excellent agreement (Fig. 145). It is not possible to differentiate between water passing through the Yucatan Straits, the Antilles Current, and the water from the Sargasso Sea between 18°C and 22°C. Also Antilles Current Water cannot be differentiated from Sargasso Sea Water between 18°C and 11°C.

Station mean T-S curves for the entire year of data were computed and drawn and are presented as Figure 146. As stations 6 through 16 are very similar, only stations 6, 11, and 16 are shown as examples.

Both surface and maximum salinity values increase with distance from shore, indicating several water masses are crossed. Stations 1 and 2 exhibit a nearshore or coastal water type of local origin. At station 2 Continental Edge Water appears at 30 to 50 m depth. Stations 4 and 5 contain a mixture of Continental Edge Water and water that has passed through the Yucatan Straits (Florida Current Water), the later water type predominating.

Seaward of station 6, water from the Sargasso Sea or Antilles Current predominates.

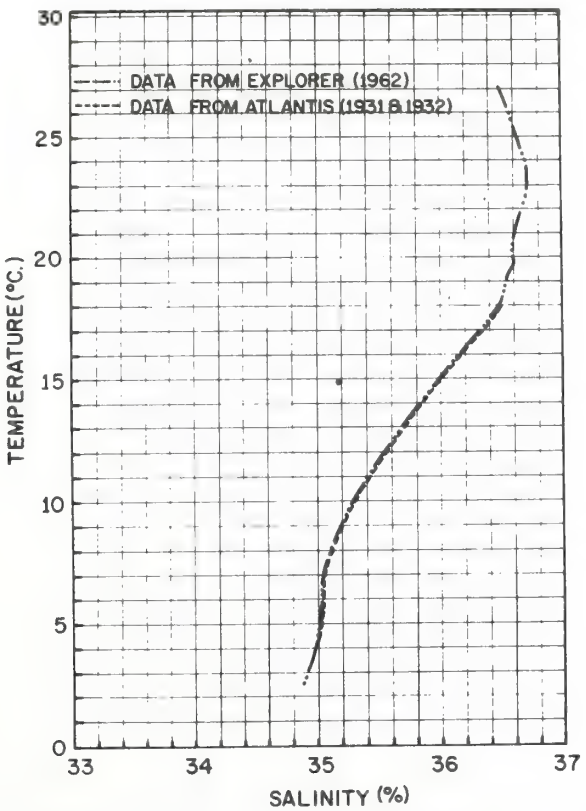


Figure 145. Comparison T/S curves for Sargasso Sea Water.

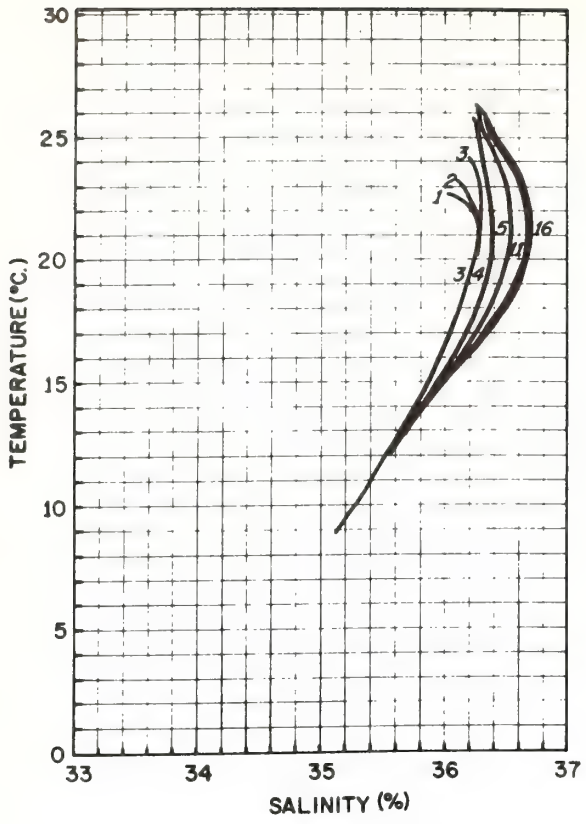


Figure 146. Mean station T/S curves obtained by using all data.

Seasonal mean station T-S curves were computed and given as Figures 147-150. These seasonal T-S curves exhibit patterns similar to the total of all data T-S curves. The same seasonal transition from coastal water to Continental Edge Water to Yucatan Straits Water to Antilles Current Water or Sargasso Sea Water exists. Considerable variation in maximum salinity from season to season was recorded at stations 1 through 6. This indicates considerable variation in the percentage of each water mass in the core of the Gulf Stream. The dominant forces that control the cross-stream mixing must vary with time in a way that is not clear from the mean T-S curves. The T-S curves for stations 7 through 16 coincide during each season.

Seasonal composite station T-S curves were drawn. Figures 151-155 are examples of these curves. Figure 151 shows the composite curves for the spring at station 4. The velocity core of the stream is usually seaward of this station. Identifiable are Continental Edge Water, Yucatan Straits Water, and water that is a mixture of the two. By station 5 (Fig. 152) Yucatan Straits Water predominates; a small amount of water from the Antilles Current can be identified at about 21-23°C during four of the six summer cruises. Station 6 (Fig. 153) still has Yucatan Straits Water predominating. Continental Edge Water no longer is evident. The envelop of T-S curves is relatively wide indicating that during some cruises Antilles Current Water or possibly Sargasso Sea Water has come into the area.

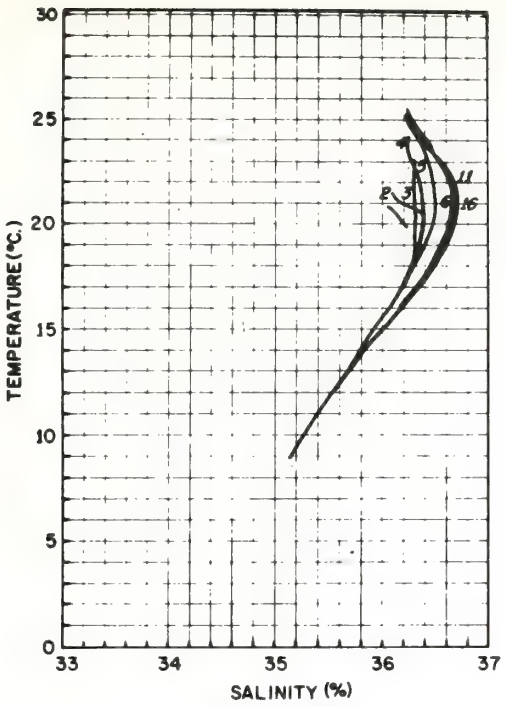


Figure 147. Mean station T/S curves, obtained by using spring data.

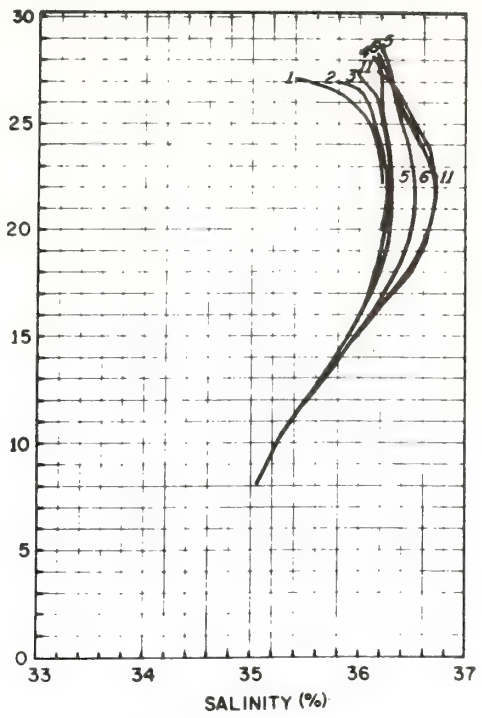


Figure 148. Mean station T/S curves, obtained by using summer data.

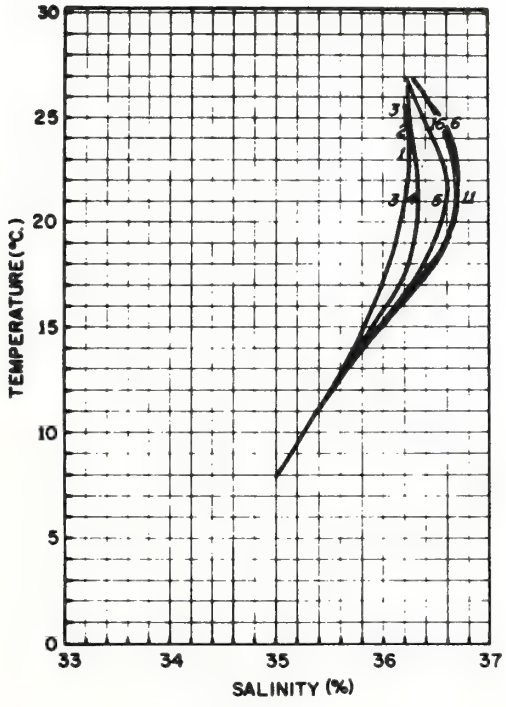


Figure 149. Mean station T/S curves, obtained by using fall data.

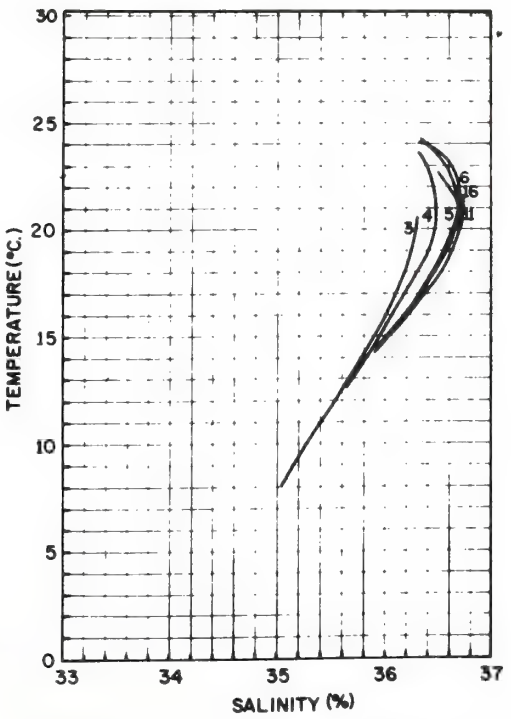


Figure 150. Mean station T/S curves, obtained by using winter data.

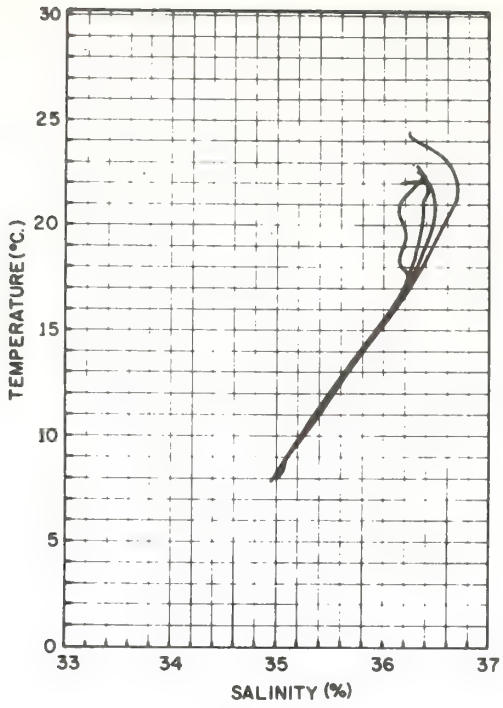


Figure 151. T/S curves for station 4 showing variation by cruise, during spring.

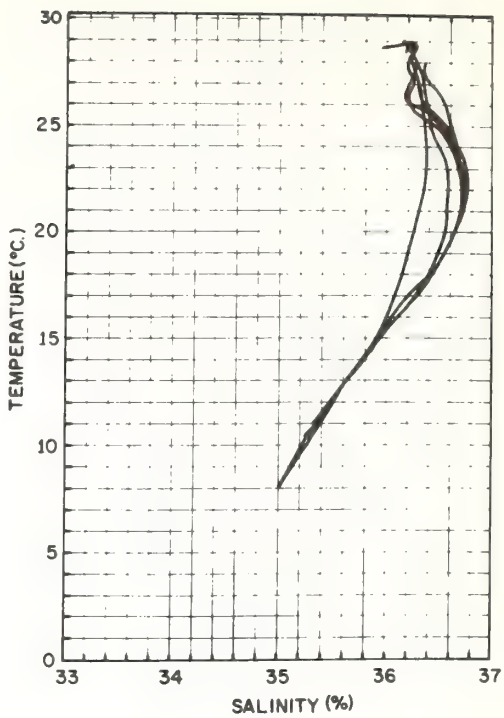


Figure 152. T/S curves for station 5 showing variation by cruise, during summer.

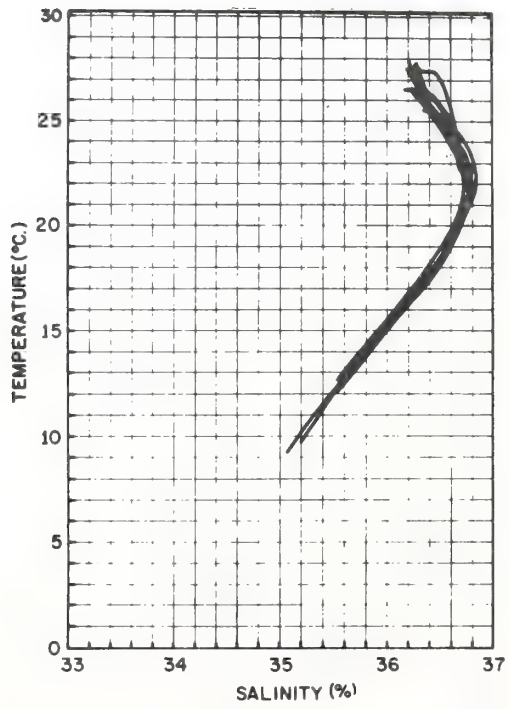


Figure 153. T/S curves for station 6 showing variation by cruise, during fall.

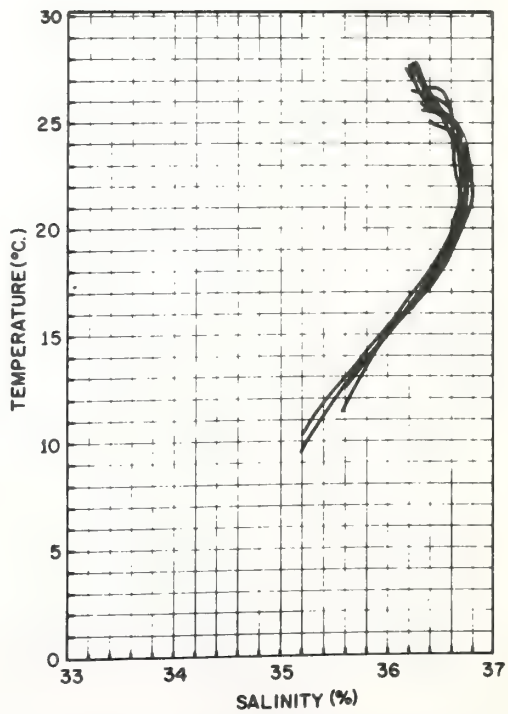


Figure 154. T/S curves for station 7 showing variation by cruise, during winter.

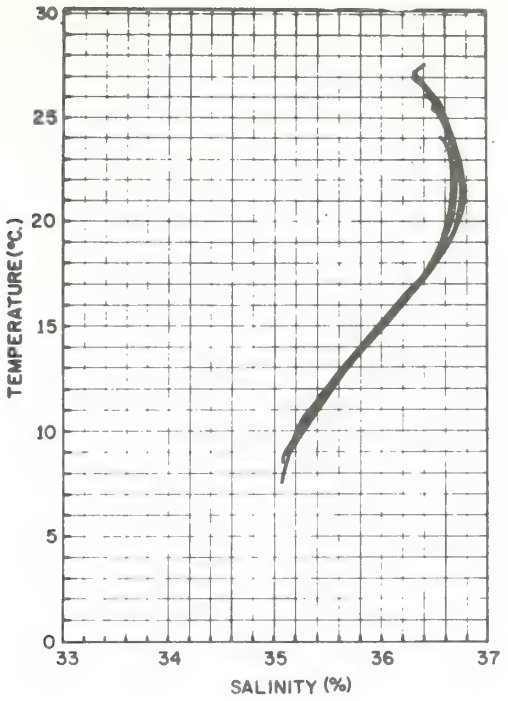


Figure 155. T/S curves for station 16 showing variation by cruise, during fall.

The transition continues at station 7 (Fig. 154). In the upper layers, Antilles Current Water predominates. Below about 20°C Yucatan Straits Water predominates, but Antilles Current Water or Sargasso Sea Water occurs above 15°C during two cruises.

By station 16, Antilles Current Water and Sargasso Sea Water completely predominate (Fig. 155). However, between 9°C and 12°C Yucatan Straits Water occurs during two cruises.

Unusually high sigma-t values occurred during cruises 2, 6, 16, and 20. Sigma-t values between 27.50 and 27.65 were associated with unusually low temperature values and unusually high salinity and oxygen values. This water can be definitely identified as Sargasso Sea Water, while the water above is definitely from the Antilles Current.

As previously mentioned, during cruise 22 the water density was unique. A relatively higher than usual density was recorded at station 5. The water at stations 4 and 6 is identified as Yucatan Straits Water, while at station 5, the surface water is a mixture of Yucatan Straits Water and Continental Edge Water. Below the surface down to at least 100 m, the water is Continental Edge Water. Apparently at some earlier time the Loop Current, west of Florida, entrained this water and carried it along without mixing.

8. OXYGEN-DENSITY RELATIONSHIP

Because use of the temperature salinity relationship was only partially successful in differentiating between the various water masses found in this area, the oxygen-density relationship was used.

Rossby (1936) found that the oxygen-salinity correlation in the Sargasso Sea is different from that in the Yucatan Channel-Florida Straits area. Lowest oxygen concentrations are found in the Straits of Florida. The oxygen-salinity values from the Antilles Current were somewhat between the other two.

To distinguish the water masses in question, Richards and Redfield (1955) defined the correlation between the oxygen concentration and each 0.1 sigma-t unit span of Sargasso Sea Water and examined the anomalies from this correlation of water samples taken across the Yucatan Channel, across the Florida Straits, and along sections across the Gulf Stream. They chose sigma-t rather than salinity because sigma-t increases with depth, so ambiguity is avoided in identifying the depth of the sample. Also surfaces of equal sigma-t are of approximately constant potential density and thus identify the paths of isentropic mixing.

As an extension of the method of Richards and Redfield (1955) oxygen sigma-t correlation curves were constructed for Sargasso Sea Water, Antilles Current Water, Continental Edge Water, and Florida Current Water.

The correlation curve for the Sargasso Sea Water was constructed from 372 observations taken at 16 stations, located 25°-30°N and 65°-72°W during the period February-July 1962.

The correlation curve for the Antilles Current Water was constructed from 679 observations taken at 32 stations during the periods February-June 1962 and May 1964. The stations were north of Hispaniola, Puerto Rico, and the American Virgin Islands and south of 24°N. Both series of observations were taken by the U.S.C.&G.S. ship Explorer.

The correlation curve for the Florida Current Water was constructed from 1443 observations at 108 stations taken during the periods July-December 1961, July-December 1962, and January-June 1963. Only stations located in the center of the Florida Straits between Miami, Florida, and Bimini, Bahama Islands, and between Palm Beach, Florida, and Settlement Point, Bahama Islands, were used. The stations were taken aboard research vessels of the Institute of Marine Science of the University of Miami.

No similar sets of control data were available to identify Continental Edge Water. According to Stefansson et al. (1971) Continental Edge Water has a more variable oxygen-density relationship than Yucatan Straits Water. Generally, it also has a higher oxygen concentration for a given sigma-t in the range 24.0-26.0. High oxygen values that did not fit any of the other oxygen-density curves regularly occurred at station 3. According to the T-S curves, this was Continental Edge Water. These values were used to construct the correlation curve.

The oxygen-sigma-t correlation curves are shown as Figure 156. In all cases, the points on the curves were computed arithmetic means of all oxygen values within a 0.25 sigma-t range.

The water layer is quite thin within certain density ranges, and the number of observations in water having these densities is small, ranging from 4 to 50 samples in each 0.25 sigma-t span. In other cases, the water thickness is considerable within the density range, and the number of observations ranges from 100 to 153.

Also shown in Figure 156 is the oxygen sigma-t correlation curve for the Sargasso Sea Water as computed by Richards and Redfield (1955). The two curves for the Sargasso Sea Water agree quite well except near a sigma-t of 26.00 ± 0.25 where they vary by 0.2 ml/l.

Figure 156 indicates that for sigma-t values greater than 24.75, Florida Current Water has a lower oxygen content than Sargasso Sea Water or Antilles Current Water. For a sigma-t between 25.00 and 27.35, Antilles Current Water has a lower oxygen content than does Sargasso Sea Water. Below a sigma-t of 27.35, oxygen values for Antilles Current Water and Sargasso Sea Water are nearly identical. Within the sigma-t range 24.00 to 24.75, the oxygen content of the three water types is very similar. But at sigma-t values less than 24.00, the oxygen values are higher for water that has passed through the Florida straits. At all sigma-t levels, Continental Edge Water exhibited highest oxygen values.

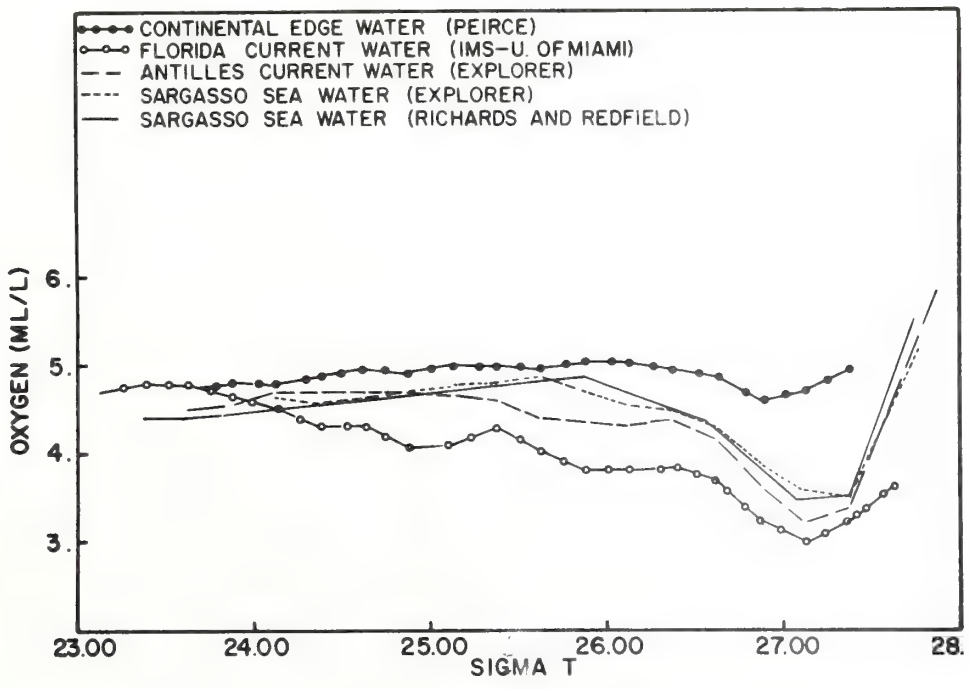


Figure 156. Oxygen-sigma-t correlation curves.

Figure 156 was designed to identify the water type at each data point. From a qualitative view, these oxygen sigma-t correlation curves do not appear to be very reliable between 23.75 and 25.00, but seem fairly reliable at greater depth.

Standard deviations and confidence limits at the 0.95% level of significance were computed for each 0.25 sigma-t group of oxygen values. The results are given in Table 3. Using the means and standard deviations and assuming Gaussian distribution, individual probability of correct identification curves were drawn. The individual values were summed and a mean computed for each water type. The probability of identifying Antilles Current Water correctly for the entire range of sigma-t values is 40%, for Sargasso Sea Water 50%, and for Florida Current Water 70%. Because of its uniqueness, Continental Edge Water was not included in these calculations.

For several reasons, these probability values are lower than the results obtained by actually using the curves to identify the water types. The distribution of the oxygen data does not fit a Gaussian distribution, but rather clusters within about two standard deviations of the mean. Also the lowest probability of correct identification occurs between 24.00 and 25.00, a region of relatively few observations. The probability of correct identification can be raised by assuming that the water type through this region is the same as the water below, which can be identified with a higher degree of reliability. Because of its position of touching only water of much lower oxygen values, Continental Edge Water could be identified with a probability of nearly 100%.

By using Figure 156, all station data were identified as to water source area. The percentage of each water type at each station was then determined. Seasonal means and total means for the entire year's observations of the percentage of each water mass at each station were calculated (Figs. 157-161).

Some identification difficulty was encountered at stations 1 to 5 mainly because information regarding nearshore water was not available. Some degree of uncertainity in identifying water masses does exist. However, the confidence limits presented in Table 3 indicate only a few cases of overlap of confidence limits. Therefore, even though there is some uncertainty in identifying individual observations, the uncertainty is greatly reduced for a mean of values.

Figures 157-161 appear to give a reliable indication of the mean of the percentage of each water mass for the year. A nearshore or coastal water mass exists at stations 1 and 2. Continental Edge Water is found at stations 2, 3, 4, and 5. In general, it extends down to about 100 m in winter and to about 60 m in summer. It is almost non-existent in fall. Florida Current Water predominates at stations 3, 4, 5, and 6 including the core of the Gulf Stream. A small amount of Antilles Current Water and Sargasso Sea Water is found at these stations. Seaward from station 5, the percentage of Florida Current Water decreases. From stations 8 to 16 the percentage varies within a narrow range of 13% to 21%. Strikingly, as elsewhere some Florida Current Water is found over 100 miles to the right of the center of the core. At the

same time, Antilles Current Water and Sargasso Sea Water move towards the core of the Gulf Stream. From station 7 to 16, the amount of Sargasso Sea Water varies from 42% to 58% of the water column. The amount of Antilles Current Water varies between 24% and 39% of the water column.

The seasonal graphs are similar to the yearly mean graph, yet considerable seasonal variation occurs. Continental Edge Water is never recorded seaward of station 5. Yet at station 3 it is 53% of the water column during winter, but only 12% during fall. This is in agreement with Wennekens (1959).

Although Florida Current Water predominates at station 4 and 5 during all seasons of the year, it varies considerably with the season. During summer and fall, it is 90% to 97% of the water column; yet during winter and spring, it is only 48% to 70% of the water column. Sargasso Sea Water is not found in any significant amount at these two stations. Antilles Current Water is found in significant amounts varying between 0 and 21% of the water column. Stations 6 and 7 occupy a transition zone. The amount of Florida Current Water is still significant but decreasing, and the amounts of Sargasso Sea Water and Antilles Current Water are increasing.

Beyond station 7, Sargasso Sea Water predominates. Florida Current Water is usually less than 30% of the water column, and Antilles Current Water was found in highly variable quantities. At times it was the least common of the three water types, yet at other times it was the most common.

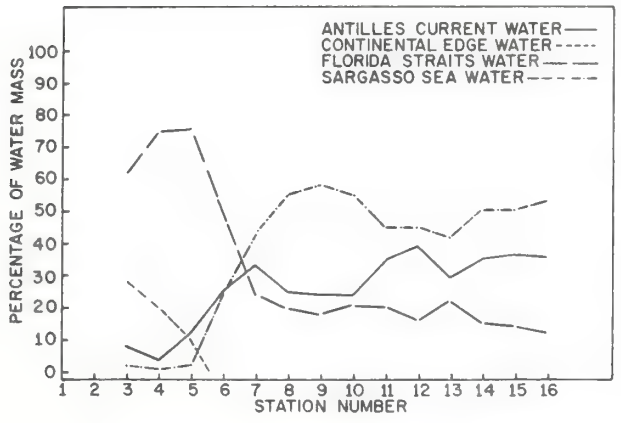


Figure 157. Percentage of each water mass type at each station - total all data.

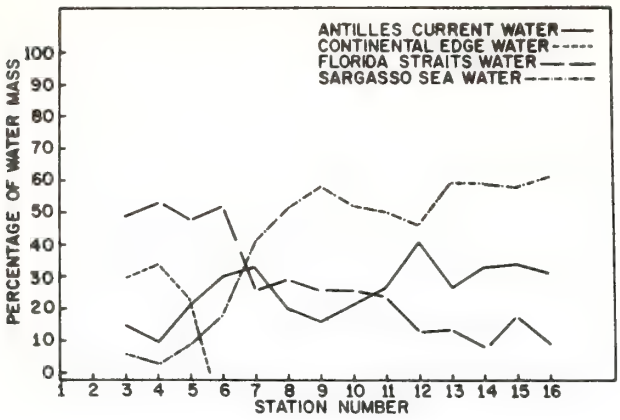


Figure 158. Percentage of each water mass type at each station - spring data.

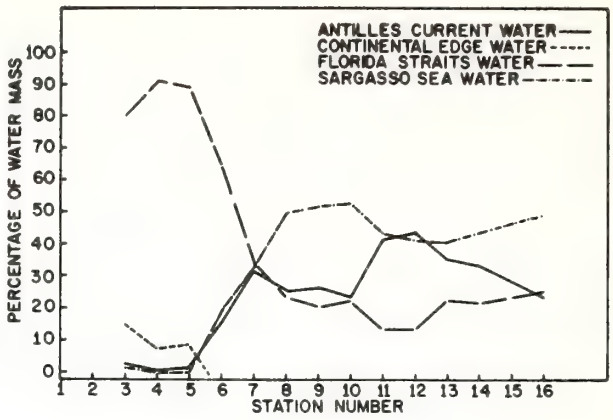


Figure 159. Percentage of each water mass type at each station - summer data.

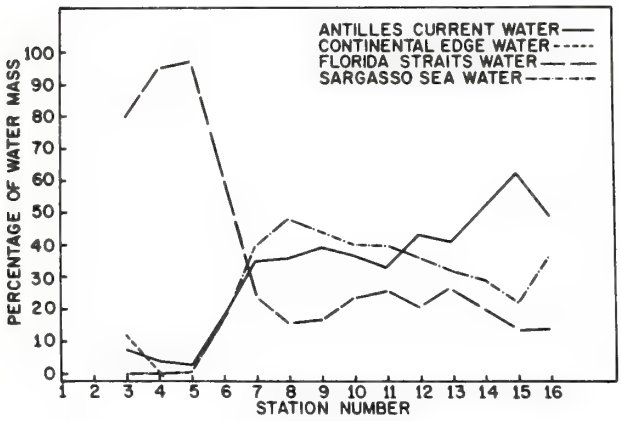


Figure 160. Percentage of each water mass type at each station - fall data.

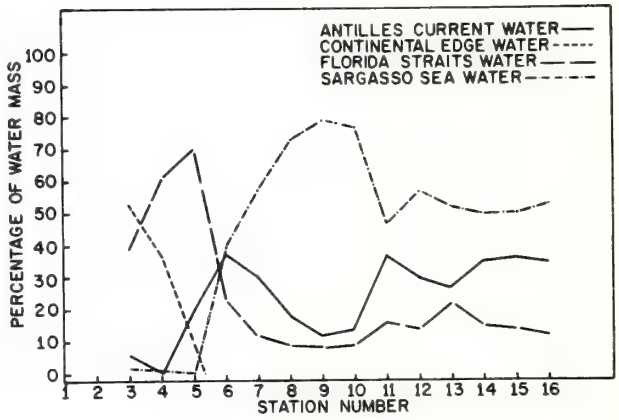


Figure 161. Percentage of each water mass type at each station - winter data.

Table 3. Means, Standard Deviations, and Confidence Limits (95%) For Sigma-t Groups of Oxygen Vaules

Sigma-t Interval	No. of Obs.	Mean Oxygen	Stand. Dev.	Conf. Limits	
		Antilles Current			
23.00-23.25					
23.25-23.50					
23.50-23.75	16	4.51	.11	4.45	4.57
23.75-24.00	43	4.54	.14	4.50	4.58
24.00-24.25	24	4.72	.11	4.67	4.77
24.25-24.50	34	4.70	.18	4.64	4.76
24.50-24.75	54	4.69	.19	4.64	4.74
24.75-25.00	36	4.69	.17	4.63	4.75
25.00-25.25	27	4.65	.16	4.59	4.71
25.25-25.50	28	4.62	.25	4.53	4.71
25.50-25.75	32	4.39	.23	4.31	4.47
25.75-26.00	29	4.34	.23	4.26	4.42
26.00-26.25	41	4.26	.22	4.19	4.33
26.25-26.50	64	4.38	.17	4.34	4.42
26.50-26.75	64	4.13	.22	4.08	4.18
26.75-27.00	69	3.57	.24	3.51	3.63
27.00-27.25	54	3.23	.16	3.19	3.27
27.25-27.50	86	3.34	.25	3.29	3.39
27.50-27.75	124	4.63	.54	4.53	4.73
27.75-28.00	141	5.84	.26	5.80	5.88
		Sargasso Sea			
23.75-24.00	5	4.48	.11	4.39	4.57
24.00-24.25	5	4.65	.11	4.56	4.74
24.25-24.50	4	4.58	. 0	4.58	4.58
24.50-24.75	5	4.64	.11	4.55	4.73
24.75-25.00	11	4.71	.10	4.65	4.77
25.00-25.25	6	4.77	. 0	4.77	4.77
25.25-25.50	46	4.81	.17	4.76	4.86
25.50-25.75	26	4.88	.14	4.83	4.93
25.75-26.00	28	4.72	.27	4.62	4.82
26.00-26.25	22	4.55	.23	4.46	4.64
26.25-26.50	50	4.48	.17	4.43	4.53
26.50-26.75	33	4.30	.20	4.23	4.37
26.75-27.00	23	3.87	.17	3.80	3.94
27.00-27.25	30	3.58	.17	3.52	3.64
27.25-27.50	29	3.49	.22	3.41	3.57
27.50-27.75	40	4.55	.40	4.43	4.67
27.75-28.00	80	5.76	.37	5.65	5.87
		Florida Current			
23.00-23.25	82	4.61	.10	4.59	4.63
23.25-23.50	36	4.73	.17	4.67	4.79
23.50-23.75	47	4.70	.10	4.67	4.73
23.75-24.00	127	4.68	.14	4.66	4.70
24.00-24.25	76	4.66	.20	4.61	4.71
24.25-24.50	105	4.67	.27	4.62	4.72
24.50-24.75	49	4.66	.31	4.57	4.75
24.75-25.00	49	4.47	.39	4.36	4.58
25.00-25.25	48	4.44	.44	4.32	4.56
25.25-25.50	47	4.43	.46	4.28	4.58
25.50-25.75	46	3.91	.48	3.77	4.05
25.75-26.00	47	4.08	.50	3.94	4.22
26.00-26.25	52	3.81	.39	3.67	3.95
26.25-26.50	82	3.84	.38	3.76	3.92
26.50-26.75	81	3.66	.38	3.58	3.74
26.75-27.00	100	3.21	.24	3.16	3.26
27.00-27.25	120	2.99	.18	2.96	3.02
27.25-27.50	153	3.18	.20	3.15	3.21
27.50-27.75	20	3.57	.13	3.51	3.63

It is significant that Antilles Current Water predominates only during the fall. Iselin (1936) noted that during February it was only a very moderate current. However, he concluded that it could be broader and swifter during the summer. Maloney (1967) observed that the Antilles Current exists as a well defined current close to the Bahama bank only during winter. During summer, a broad relatively strong flow exists. Because of travel time delay, the maximum amount of Antilles Current Water would reach this area during the fall.

The highly variable mixing characteristics of the water types are dramatically shown in Figures 162 through 168. These are oxygen sigma-t correlation cross-sections for cruises 1, 12, 14, 19, 21, 22, and 25. Oxygen anomalies were computed by subtracting the oxygen content of Antilles Current Water of the same sigma-t value as given by the correlation curve in Figure 156 from the observed data point.

High positive anomalies are recorded out as far as station 5 down to a depth of 100 m during winter and spring, yet were recorded only at station 1 or not at all during summer and fall. These large positive anomalies fit the definition given by Stefansson et al. (1971) for Continental Edge Water. But these anomalies could also indicate a nearshore water of local origin, because the solubility of oxygen in sea water increases with decreased temperature and salinity.

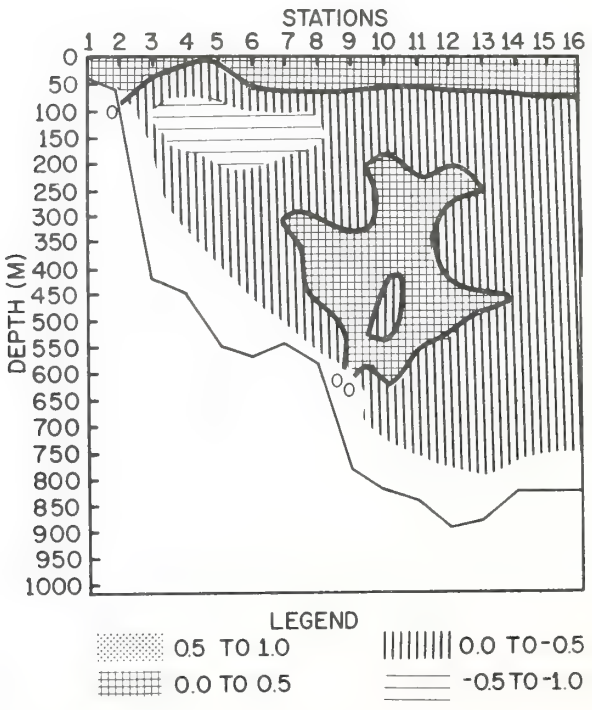


Figure 162. Cruise-1 oxygen anomaly (ml/l) cross-section.

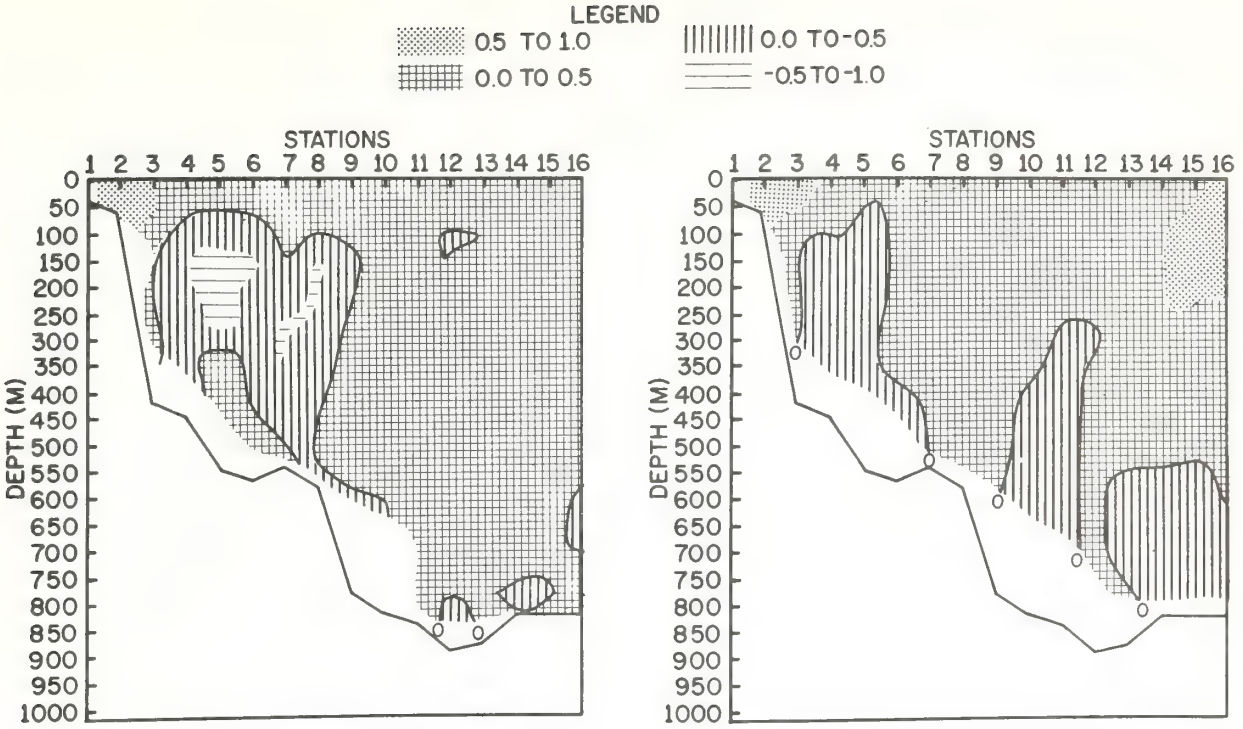


Figure 163. Cruise-12 oxygen anomaly (ml/l) cross-section.

Figure 164. Cruise-14 oxygen anomaly (ml/l) cross-section.

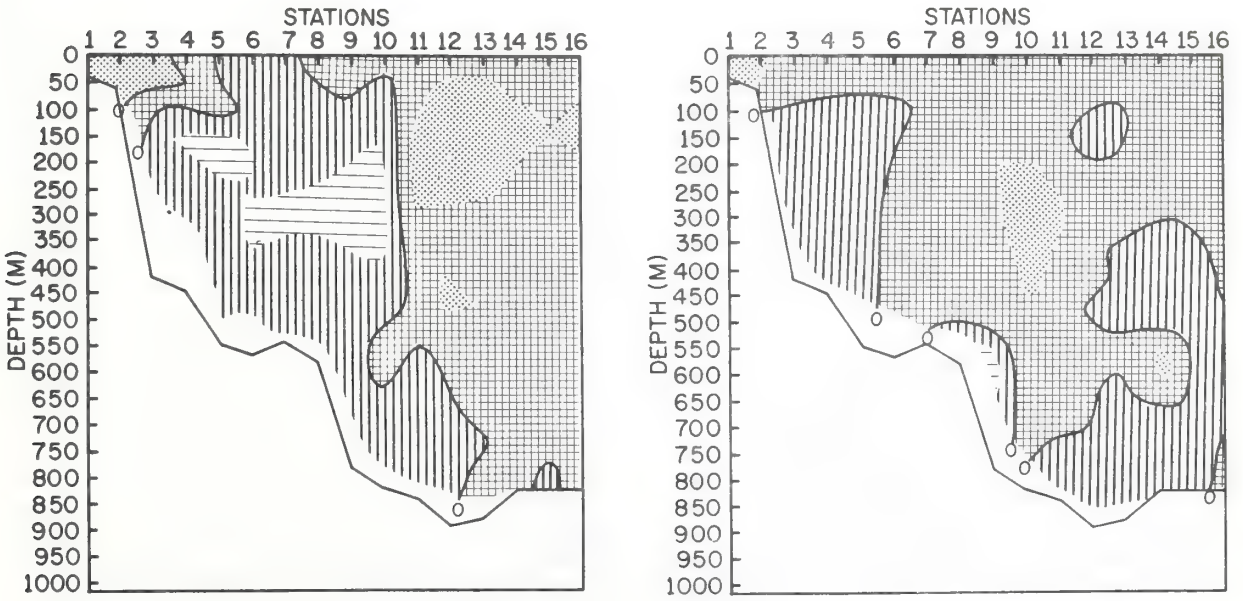


Figure 165. Cruise-19 oxygen anomaly (ml/l) cross-section.

Figure 166. Cruise-21 oxygen anomaly (ml/l) cross-section.

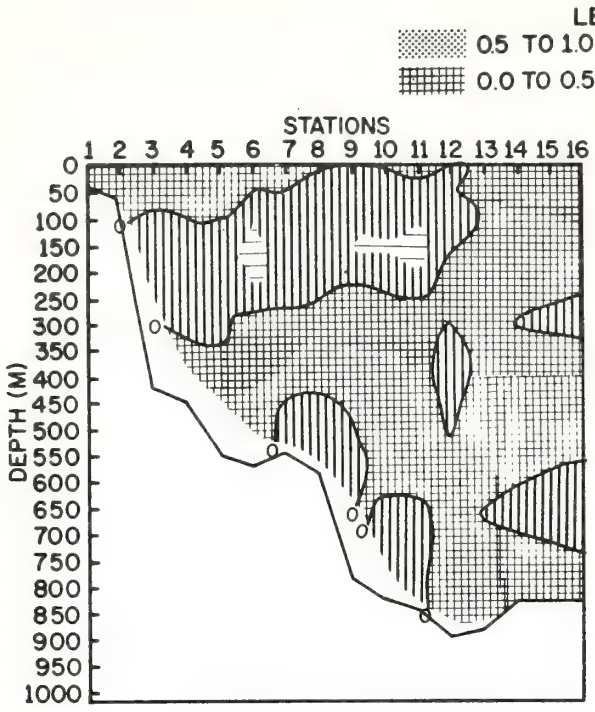


Figure 167. Cruise-22 oxygen anomaly (ml/l) cross-section.

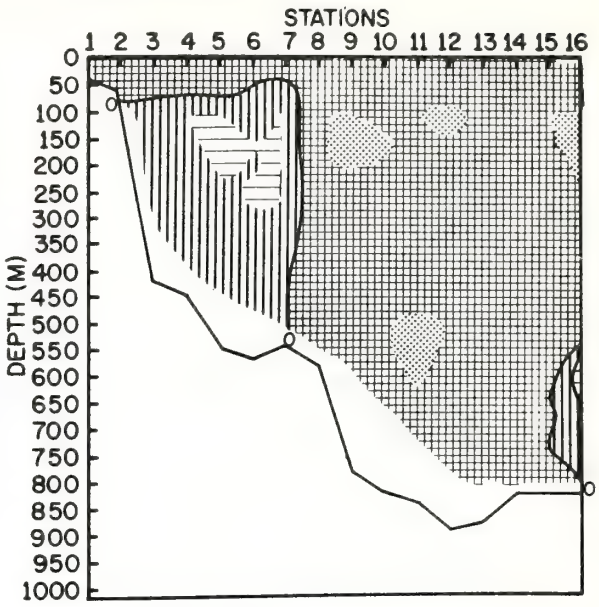


Figure 168. Cruise-25 oxygen anomaly (ml/l) cross-section.

The dramatic variations in water mass movement of the Gulf Stream are very apparent in cruises 14, 19, and 22. Large areas of negative anomalies, indicative of Florida Current Water, spread out from stations 3 to 12 during cruise 22 overriding positive anomaly water. During cruise 19, negative anomalies occur from the surface to the bottom out to station 10. On the other hand, during cruise 14, only a small area of negative anomalies occurs at station 5, the core of the Gulf Stream.

Generally, no clear cut wall of water types exist between the Florida Current Water on the left side and Antilles Current Water and Sargasso Sea Water on the right. Cross current mixing to a varying degree appeared to be the usual situation. However, during cruises 19 and 25, Florida Current Water appeared to be intact on the right side as if a vertical wall existed. Apparently Florida Current Water existed against Sargasso Sea Water and almost no mixing occurred. Only a small amount of Antilles Current Water existed near the surface and below 500 m.

9. ACKNOWLEDGMENTS

Only with the assistance of many people could this paper have been possible. I particularly wish to acknowledge the contributions of Robert B. Starr of NOAA/AOML who provided considerable guidance. David Tyler of the U.S.C&G.S., as Chief Scientist aboard the U.S.C&G.S. ship Peirce, assured consistent high quality field data. Finally, I wish to thank the officers and crew of the U.S.C&G.S. ship Peirce for the long and diligent hours they devoted to collecting the data.

10. REFERENCES

Bryson, R. A. and F. K. Hare, (1974), *Climates of North America, Vol. II of World Survey of Climatology*, Elsevier, New York, 420 p.

Bumpus, Dean F. (1955), The circulation over the continental shelf south of Cape Hatteras. *Transactions, AGU 26*, 601-611.

Defant, A. (1936), Die Troposphare des Atlantischen Ozeans. Idern, 6, I. Teil Schichtung und Zirkulation des Atlantischen Ozeans, 289-411.

Dietrich, Gunter (1937), Die Lage des Meeresoberflache im Druckfeld von Ozean und Atmosphare mit besonderer Beruck-sichtigung des westlichen Nordatlantischen Ozeans und des Golfs von Mexico. Veroffentlichungen des Instituts fur Meereskunde an der Universitat Berlin, Neue Folge, A, *Geogr.-Naturwiss, Heft 33*, 52 p.

Duing, Walter (1973), Some evidence for long period barotropic waves in the Florida Current. *J. of Physical Oceanography, 3*, 343-346.

Hansen, Donald V. (1970), Gulf Stream meanders between Cape Hatteras and the Grand Banks. *Deep Sea Res. 17*, 495-511.

Helland-Hansen, B. (1918), Nogen hydrografiske metoder, Forhand-linger ved de skandinaviske naturforskerer 16 de mote i. Kristiania 10-15 Juli 1916, Oslo.

Iselin, C. O'D. (1936), A study of the circulation of the western North Atlantic. Papers in Physical Oceanography and Meteorology, MIT and WHOI, 4(4), 101 p.

Iselin, C. O'D. (1940), Preliminary Report on Long-Period Variations in the Transport of the Gulf Stream System. Papers in Physical Oceanography and Meteorology, MIT and WHOI, 8(1), 39 p.

Jacobsen, J. P. (1929), Contribution to the Hydrography of the North Atlantic. Dana Exp. 1921-1922, Oceanographical reports 1(3) Copenhagen, 98 p.

Maloney, William E. (1967), A study of the Antilles Current using Moored Current Meter Arrays, TR-199, U.S. Naval Oceanographic Office, Washington, D. C., 142 p.

Montgomery, R. B. (1938), Fluctuations in Monthly Sea Level On Eastern U.S. Coast as Related to Dynamics of Western North Atlantic Ocean. *J. of Marine Research, 1,* 165-185.

Nowlin, W. D. Jr. (1971), Water Masses and General Circulation of the Gulf of Mexico, *Oceanology,* 28-33.

Parr, A. E. (1935), Report on hydrographic observations in the Gulf of Mexico and the adjacent straits made during the Yale Oceanographic Expedition on the "Mable Taylor" in 1932. *Bull. Bingham Oceanographic Coll., V*(I), 93 p.

Richards, F. A. and A. C. Redfield (1955), Oxygen-density relationships in the western North Atlantic. *Deep-Sea Res., 2,* 182-189.

Richardson, W. A. and J. R. Finlen, 1967, The transport of Northwest Providence Channel. *Deep Sea Res., 14,* 361-367.

Rossby, Carl-Gustaf (1936), Dynamics of steady ocean currents in the light of experimental fluid mechanics. *Papers in Physical Oceanogr. & Meteor., 5*(1), 43 p.

Schmitz, William J. and William S. Richardson (1968), On the transport of the Florida Current. *Deep Sea Res., 15,* 679-693.

Starr, Robert B. (1970), An Oceanographic Investigation Adjacent to Cay Sal Bank, Bahama Islands, ESSA Technical Report ERL 167-AOML 2, Washington, D. C. 52 p.

Stefansson, U., L. P. Atkinson, and D. F. Bumpus, (1971), Hydrographic properties and circulation of the North Carolina Shelf and Slope Waters. *Deep Sea Res., 18,* 383-420.

Stommel, Henry (1965), *The Gulf Stream, A Physical and Dynamical Description.* 2nd Ed., U. of Calif. Press, 248 p.

Sverdrup, H. U., M. W. Johnson, and R. H. Fleming (1946), *The Oceans, Their Physics, Chemistry, and General Biology*. Prentice Hall, Englewood Cliffs, N. J. 1087 p.

U. S. Navy Hydrographic Office (1951), Processing Oceanographic Data. By E. C. Lafond, H. O. Pub. No. 614, Washington, D.C. 114 p.

U. S. Navy Hydrographic Office (1955), Instruction Manual for Oceanographic Observations, Second Edition, H. O. Pub. No. 607, Washington, D. C., 210 p.

Von Arx, William S. (1962), *Introduction to Physical Oceanography*. Addison-Wesley, Reading, Mass. 422 p.

Weiss, R. F., (1970), The solubility of Nitrogen, Oxygen, and Argon in Water and Seawater. *Deep Sea Res., 17,* 721-735 p.

Wennekens, M. P., (1959), Water mass properties of the Straits of Florida and related waters. *Bulletin of Marine Science of the Gulf and Caribbean, 9,* 52 p.

Worthington, L. V. (1959), The 18° water in the Sargasso Sea. *Deep Sea Resc., 5,* 297-305.

Wright, W. R., and L. V. Worthington (1970), *The Water Masses of the North Atlantic Ocean, A volumetric census of temperature and salinity,* Serial Atlas of the Marine Environment, Folio 19. American Geographical Society, 5 p.

Wunsch, C., D. V. Hansen, and B. D. Zetler (1969), Fluctuations of the Florida Current inferred from sea-level records. *Deep Sea Resc, 16,* Suppl., 447-470.

Wust, Georg, (1964), *Stratification and Circulation in the Antillean-Caribbean Basins, Part One, Spreading and Mixing of the Water Types, with an Oceanographic Atlas,* Columbia University Press, New York, N. Y. 201 p.

Wust, Georg (1924), Florida und Antillenstrom, eine hydrodynamische Untersuchung. Veroff. Inst. f. Meereskunde. Berlin, N.F.A.: *Geogr.-Naturwiss, Heft 12,* 48 p.

NOAA Data Report ERL MESA-29, 192 pages. (Text only.)

NOAA Data Report ERL MESA-29

MESA NEW YORK BIGHT PROJECT
EXPANDED WATER COLUMN CHARACTERIZATION CRUISE (XWCC 11)
NOAA SHIP RESEARCHER, SEPTEMBER 1976

John B. Hazelworth
Shailer R. Cummings
S. Michael Minton
George A. Berberian

Atlantic Oceanographic and Meteorological Laboratories
Miami, Florida

Marine Ecosystems Analysis Program
Boulder, Colorado
December 1977

UNITED STATES
DEPARTMENT OF COMMERCE
Juanita M. Kreps, Secretary

NATIONAL OCEANIC AND
ATMOSPHERIC ADMINISTRATION
Richard A. Frank, Administrator

Environmental Research
Laboratories
Wilmot N. Hess, Director

NOTICE

The Environmental Research Laboratories do not approve, recommend, or endorse any proprietary product or proprietary material mentioned in this publication. No reference shall be made to the Environmental Research Laboratories or to this publication furnished by the Environmental Research Laboratories in any advertising or sales promotion which would indicate or imply that the Environmental Research Laboratories approve, recommend, or endorse any proprietary product or proprietary material mentioned herein, or which has as its purpose an intent to cause directly or indirectly the advertised product to be used or purchased because of this Environmental Research Laboratories publication.

CONTENTS

	Page
Abstract	1
1. INTRODUCTION	1
2. DATA PRESENTATION	7
3. ACKNOWLEDGMENTS	8
4. REFERENCES	8
5. AREAL AND CROSS-SECTION DISTRIBUTIONS OF TEMPERATURE, SALINITY, AND SIGMA-T	10
6. STATION DATA	17

MESA NEW YORK BIGHT PROJECT
EXPANDED WATER COLUMN CHARACTERIZATION CRUISE (XWCC 11)
NOAA SHIP RESEARCHER
SEPTEMBER 1976

John B. Hazelworth
Shailer R. Cummings
S. Michael Minton
George A. Berberian

During the period 8-27 September 1976, an oceanographic cruise, denoted XWCC-11, was made by the NOAA Ship Researcher in the New York Bight. Bottom mounted pressure gauges were recovered. Physical, chemical, and biological oceanographic data were collected. The objective of the cruise was to supply data to provide a base for analysis of the water movement in the highly impacted ecosystem. This report presents the corrected physical and chemical (nutrient) data, and a preliminary descriptive analysis of the physical data.

Key Words: MESA, New York Bight, Physical Oceanographic Data, Nutrient Data, Neuston Net Tow.

1. INTRODUCTION

This report is a continuation in the Marine Ecosystem Analysis (MESA) Program's series of publications presenting oceanographic data from the New York Bight. In September 1976, an oceanographic cruise was conducted by the Atlantic Oceanographic and Meteorological Laboratories (AOML), Miami, Florida, aboard the NOAA Ship Researcher. The area of investigation was the expanded water column characterization grid covering the central shelf of the New York Bight region.

The cruise was divided into two phases. During the first phase physical, chemical (nutrient and trace metals), and biological (chlorophyll) observations were made at 62 stations, (Fig. 1 and Tab. 1). In addition, Neuston net tows were taken at all stations within 30 miles of shore. The Neuston net tow operation was described in Starr et al., (1977a).

Phase two consisted of a program of biological experiments. Water samples were collected for the determination of several radioactive isotopes. In addition, 26 STD casts were made in support of the biological experiments. Table 2 and Figure 2

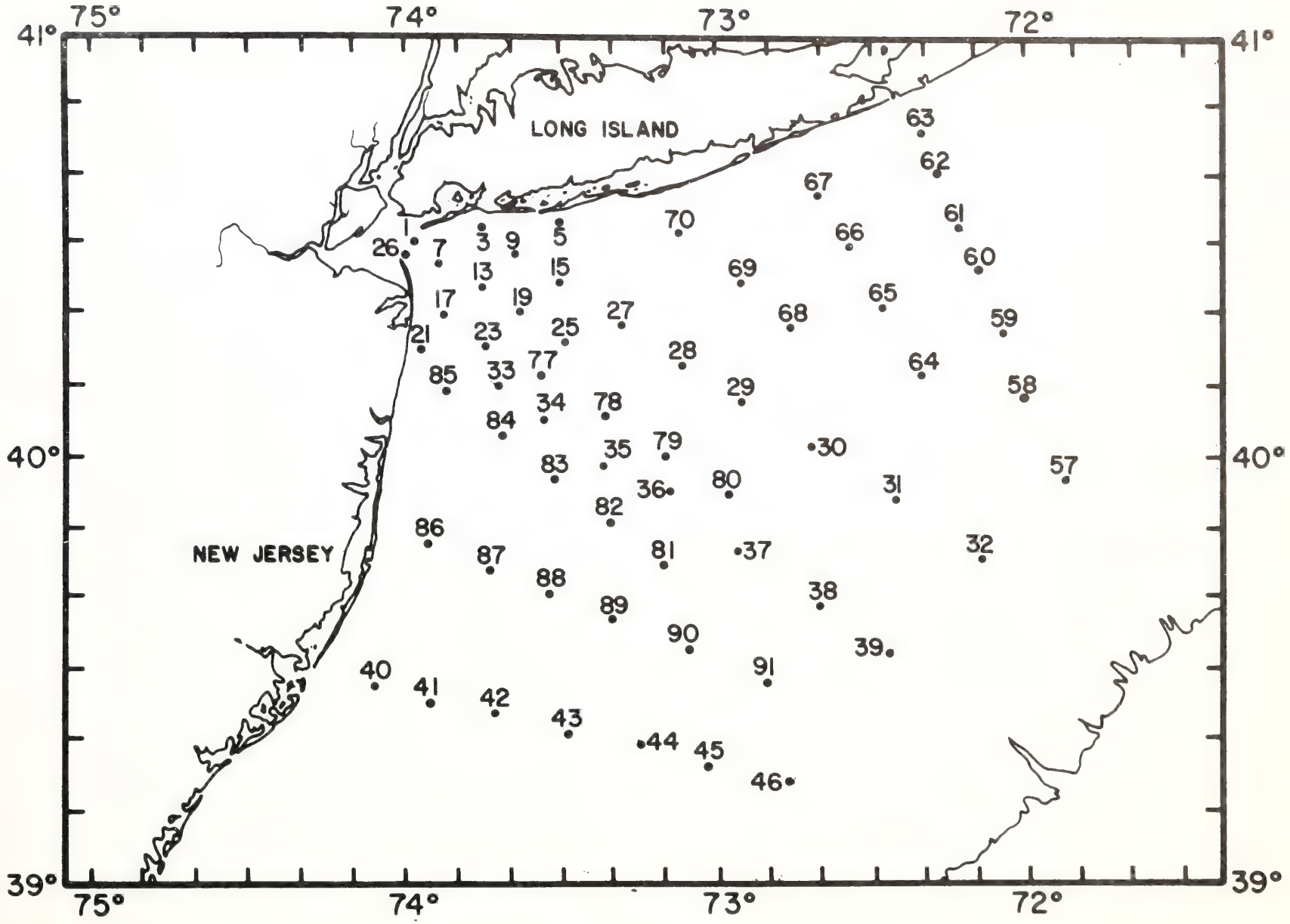


Figure 1. Locations of stations occupied during XWCC-11, first phase.

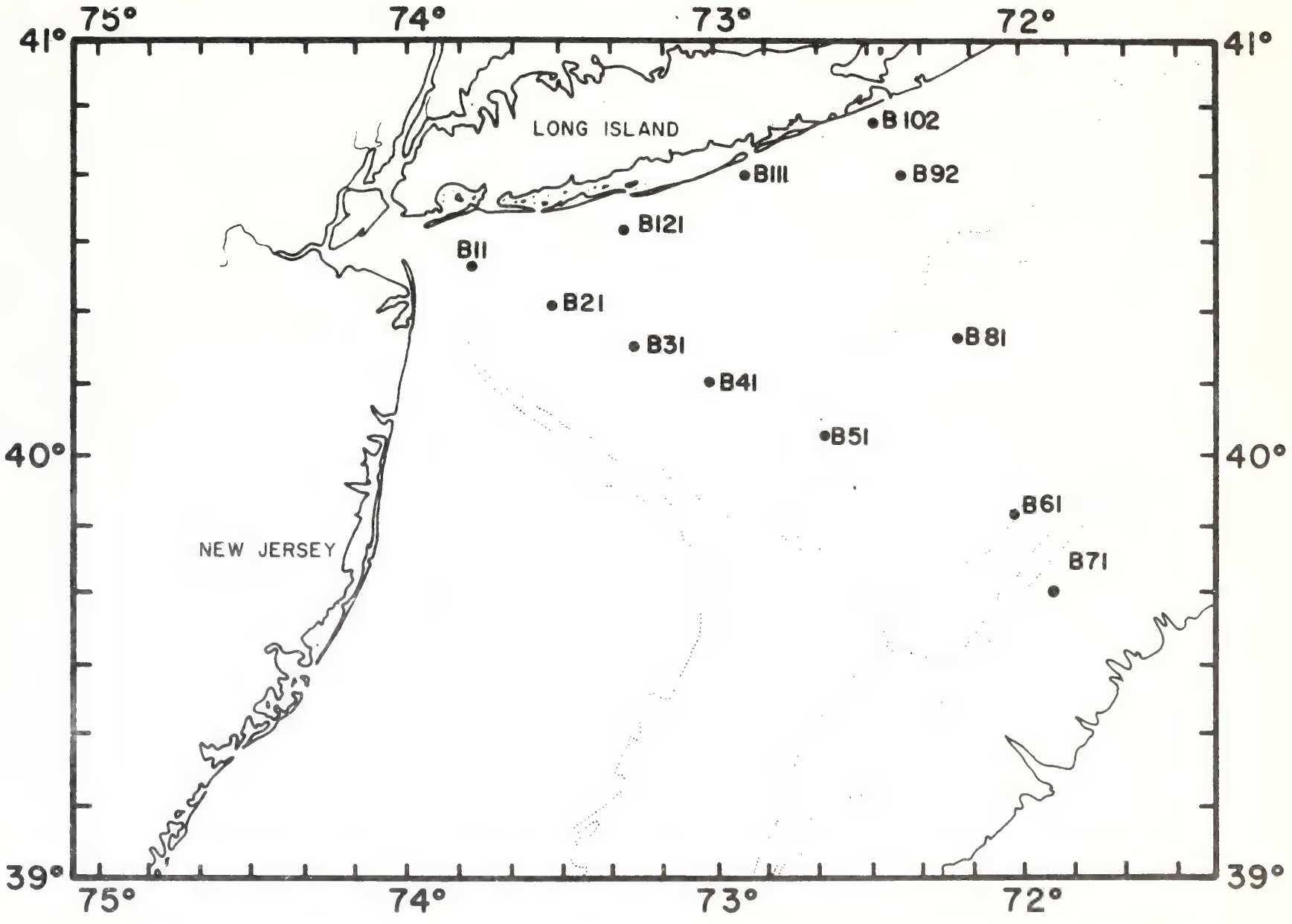


Figure 2. Locations of stations occupied during XWCC-11, second phase.

give the location of these stations. Participating AOML staff members are listed in Table 3.

Table 1. New York Bight Station Positions

Station	Latitude	Longitude	Station	Latitude	Longitude
1	40° 30.2'	73° 57.3'	45	39° 17.0'	73° 1.0'
3	40° 31.5'	73° 48.4'	46	39° 14.0'	72° 45.0'
5	40° 33.3'	73° 32.5'	57	39° 57.0'	71° 52.0'
7	40° 26.9'	73° 53.0'	58	40° 8.0'	71° 58.0'
9	40° 28.3'	73° 39.6'	59	40° 18.0'	72° 4.0'
13	40° 23.3'	73° 47.0'	60	40° 27.0'	72° 9.0'
15	40° 25.2'	73° 30.4'	61	40° 33.0'	72° 13.0'
17	40° 18.5'	73° 51.8'	62	40° 40.0'	72° 16.0'
19	40° 20.2'	73° 37.9'	63	40° 47.0'	72° 20.0'
21	40° 13.5'	73° 56.1'	64	40° 12.0'	72° 20.0'
23	40° 14.8'	73° 45.6'	65	40° 21.0'	72° 28.0'
25	40° 16.9'	73° 28.3'	66	40° 30.0'	72° 34.0'
26	40° 29.0'	73° 59.5'	67	40° 38.0'	72° 40.0'
27	40° 18.0'	73° 17.5'	68	40° 19.0'	72° 46.0'
28	40° 13.5'	73° 7.0'	69	40° 25.0'	72° 55.0'
29	40° 7.0'	72° 54.5'	70	40° 32.0'	73° 7.0'
30	40° 2.0'	72° 41.5'	77	40° 10.5'	73° 34.0'
31	39° 54.0'	72° 25.0'	78	40° 5.0'	73° 21.5'
32	39° 46.0'	72° 7.0'	79	40° .0'	73° 9.5'
33	40° 10.0'	73° 41.5'	80	39° 54.5'	72° 57.0'
34	40° 5.5'	73° 31.5'	81	39° 44.5'	73° 10.0'
35	39° 59.0'	73° 21.5'	82	39° 50.5'	73° 20.5'
36	39° 55.0'	73° 6.5'	83	39° 56.5'	73° 30.5'
37	39° 46.0'	72° 57.0'	84	40° 2.0'	73° 41.0'
38	39° 39.0'	72° 39.5'	85	40° 8.0'	73° 51.5'
39	39° 32.0'	72° 26.0'	86	39° 47.5'	73° 57.0'
40	39° 28.0'	74° 6.0'	87	39° 44.0'	73° 43.5'
41	39° 26.0'	73° 55.5'	88	39° 40.0'	73° 30.0'
42	39° 24.0'	73° 43.0'	89	39° 36.0'	73° 16.5'
43	39° 22.0'	73° 30.0'	90	39° 32.5'	73° 3.0'
44	39° 19.0'	73° 14.0'	91	39° 28.0'	72° 50.0'

Instrumentation used aboard the Researcher, for the collection of physical data, was the same as that described by Charnell, et al., (1976), namely, a Plessey Environmental Systems Model 9040 STD profiler equipped to monitor depth, temperature, and salinity. A General Oceanic Mark V Rosette Sampler equipped with

twelve 1.7 liter Niskin bottles was attached to the STD. Eight 2.5 liter Go-Flo sampling bottles were used on the Rosette sampler to obtain water for trace metals determination. The physical and nutrient data obtained from the water column measurements are presented herein; the operational characteristics of the nutrient-analyses system are found in Starr, et al., (1977b).

Table 2. Station Positions for Phase Two.

Station	Latitude	Longitude	Station	Latitude	Longitude
B11	40° 26.3'	73° 48.2'	B91	40° 39.8'	72° 29.0'
B12	40° 25.6'	73° 48.0'	B92	40° 39.8'	72° 25.0'
B13	40° 25.5'	73° 48.3'	B93	40° 40.0'	72° 25.6'
B14	40° 25.4'	73° 48.2'	B94	40° 40.0'	72° 25.6'
B15	40° 25.6'	73° 48.1'	B95	40° 40.2'	72° 25.6'
B16	40° 25.4'	73° 47.7'	B96	40° 40.2'	72° 25.6'
B21	40° 20.4'	73° 32.5'	B101	40° 46.5'	72° 31.0'
B31	40° 15.0'	73° 16.3'	B102	40° 46.2'	72° 30.1'
B41	40° 10.1'	73° 1.2'	B103	40° 46.2'	72° 30.1'
B51	40° 3.0'	72° 39.1'	B104	40° 46.2'	72° 30.1'
B61	39° 51.0'	72° 01.0'	B111	40° 39.1'	72° 54.9'
B71	39° 39.6'	71° 54.2'	B121	40° 31.8'	73° 18.1'
B81	40° 15.2'	72° 13.7'	B122	40° 31.8'	73° 17.1'

Table 3. Expanded Water Column Characterization Cruise by the NOAA Ship Researcher

Cruise	Date	AOML Personnel
XWCC 11	September 8-27, 1976	John B. Hazelworth, Chief Scientist Adriana Cantillo Shailer Cummings Fred Shields Mike Minton George Berberian

This report is the ninth of a series of reports describing the physical oceanographic measurements in the expanded area.

Earlier cruises were reported by Charnell et al., (1976), Starr et al., (1976, 1977 a, b), Hazelworth and Darnell (1976), Kolitz et al., (1976, 1977), and Hazelworth et al., (1977).

Prior reports, cited above, give detailed information on instrumentation specifications, data collection methods, and data processing techniques. The correction factors required to bring the sensor values into agreement with the water samples as well as the data accuracy, are given in Table 4. The statistical parameters in Table 4 were computed using the following formulas:

$$\text{calibration offset} = \frac{\sum_{i=1}^{N} (\bar{E}_i - W_i)}{N}$$

calibration recheck

$$\bar{X} = \text{mean difference} = \frac{\sum_{i=1}^{N} (I_i - W_i)}{N}$$

$$S_X = \text{standard deviation} = \sqrt{\sum_{i=1}^{N} (I_i - \bar{X})^2} \Big/ (N-1)$$

where N = total number of water samples for entire cruise;
W = water sample value;
$\bar{E}$ = mean electronic sensor value at the depth corresponding to water sample at same depth;
I = corrected interpolated one meter electronic sensor value at the depth corresponding to the water sample value.

Table 4. Correction Factors and Data Accuracy

	Temperature °C	Salinity °/oo	Depth (Meters)
Calibration Offset	+.12	0.0	0.0
Calibration Recheck			
$\bar{X}$	+.02	-0.004	
S_X	.03	.03	
Precision (Repeatability)			±2.5

2. DATA PRESENTATION

Tables of the interpolated data and the corresponding depth profiles of temperature, salinity, and sigma-t are given in Section 6, Station Data. The codes used in the headings are from the National Oceanographic Data Center Manual Series (1964). The tabulated data are given at 1-m intervals from the surface to 50 m and at 10-m intervals thereafter; in addition, pH, oxygen, and nutrient data (from first phase only) are presented at the depths at which water samples were obtained. Profiles were produced from the corrected raw data. The symbols, explained to the left of each horizontal axis and located on the curves at 5-m intervals, identify the parameters. No data are reported for station 26, because of sensor malfunction.

The distributions of temperature, salinity, and sigma-t are presented in Section 5: 1) horizontally at the 1-m depth (Figures 2-4) and 2) vertically along the axis of the Hudson Shelf Valley (Figures 5-7).

3. ACKNOWLEDGMENTS

The authors express their thanks to the officers and crew of the NOAA Ship Researcher, under the command of Capt. Robert Franklin, for the long and diligent hours they devoted to collecting these data. The effort was sponsored by NOAA and funded jointly by the NOAA Environmental Research Laboratories and the MESA Program's New York Bight Project.

4. REFERENCES

Charnell, R. L., M. E. Darnell, G. A. Berberian, B. L. Kolitz, and J. B. Hazelworth (1976): NEW York Bight Project, Water Column Characterization Cruises 1 and 2 of the NOAA Ship Researcher 4-15 March, 5-14 May, 1974 NOAA ERL MESA-18, U. S. Govt. Print. Off., Washington, D. C. 220 pp.

Hazelworth, J. B., B. L. Kolitz, R. B. Starr, R. L. Charnell, and G. A. Berberian (1974): MESA New York Bight Project, Water Column Sampling Cruises #1-5 of the NOAA Ship Ferrel, August-November 1973, MESA Report No. 74-2, U. S. Govt. Print. Off., Washington, D. C. 191 pp.

Hazelworth, J. B., B. L. Kolitz, R. B. Starr, R. L. Charnell, G. A. Berberian, and M. A. Wiselberg (1975): MESA New York Bight Project, Water Column Sampling Cruises #6-8 of the NOAA Ship Ferrel, April - June 1974, NOAA Data Report MESA-1, U. S. Govt. Print. Off., Washington, D. C., 177 pp.

Hazelworth, J. B., B. L. Kolitz, R. B. Starr, R. L. Charnell, G. A. Berberian, and M. A. Weiselberg (1975): MESA New York Bight Project, Water Column Sampling Cruises #9-12 of the NOAA Ship Ferrel, July - November 1974, NOAA Data Report MESA-3 U. S. Govt. Print. Off., Washington, D. C., 233 pp. (Microfiche).

Hazelworth, J. B. and M. E. Darnell (1977): MESA New York Bight Project, Expanded Water Column Characterization Cruises (XWCC-2 and 3) NOAA Ship Researcher, 22 February-5 March, 9-12 April, 1975, NOAA MESA Data Report 23, U. S. Gov't Print. Off., Washington, D. C. (Microfiche).

Hazelworth, J. B., S. R. Cummings, R. B. Starr, G. A. Berberian (1977): MESA New York Bight Project Expanded Water Column Characterization Cruise (XWCC 8) NOAA Ship George B. Kelez, April 1976, NOAA MESA Data Report, U. S. Gov't Print. Off., Washington, D. C., In press.

Kolitz, B. L., J. B. Hazelworth, R. B. Starr, and S. R. Cummings (1976): MESA New York Bight Project. Expanded Water Column Characterization Cruise (XWCC 4-5) NOAA Ship George B. Kelez, May - June 1975, NOAA MESA Data Report-24 U. S. Govt. Print. Off., Washington, D. C. (Microfiche).

Kolitz, B. L., J. B. Hazelworth, R. B. Starr, G. A. Berberian, and S. R. Cummings (1977): MESA New York Bight Project. Expanded Water Column Characterization (XWCC 7) NOAA Ship George B. Kelez, December 1975, NOAA MESA Data Report 26, U. S. Gov't Print. Off., Washington, D. C. (Microfiche). In press.

National Oceanographic Data Center Manual Series (1964): Processing Physical and Chemical Data from Oceanographic Stations, Part 1. Coding and Keypunching, Publication M-2 revised, U. S. Naval Oceanographic Office, Washington, D. C., 117 pp.

Starr, R. B., G. A. Berberian, and M. A. Weiselberg (1976): MESA New York Bight Project, Expanded Water Column Characterization Cruise (XWCC 1) R/V Advance II, January 1975, NOAA Data Report MESA-22, U. S. Gov't Print. Off., Washington, D. C. 43 pp. (Microfiche).

Starr, R. B., J. B. Hazelworth, S. R. Cummings, and G. A. Berberian (1977): MESA New York Bight Project, Expanded Water Column Characterization Cruise (XWCC 10) NOAA Ship George B. Kelez, 28 June - 1 July, 1976, NOAA MESA Data Report, In Press.

Starr, R. B., J. B. Hazelworth, and G. A. Berberian (1977): MESA New York Bight Project, Expanded Water Column Characterization (XWCC 6) NOAA Ship George B. Kelez, September-October 1975, NOAA MESA Data Report 25, U. S. Gov't Print. Off., Washington, D. C. (Microfiche). In press.

5. AREAL AND CROSS-SECTION DISTRIBUTIONS OF TEMPERATURE, SALINITY, AND SIGMA-T

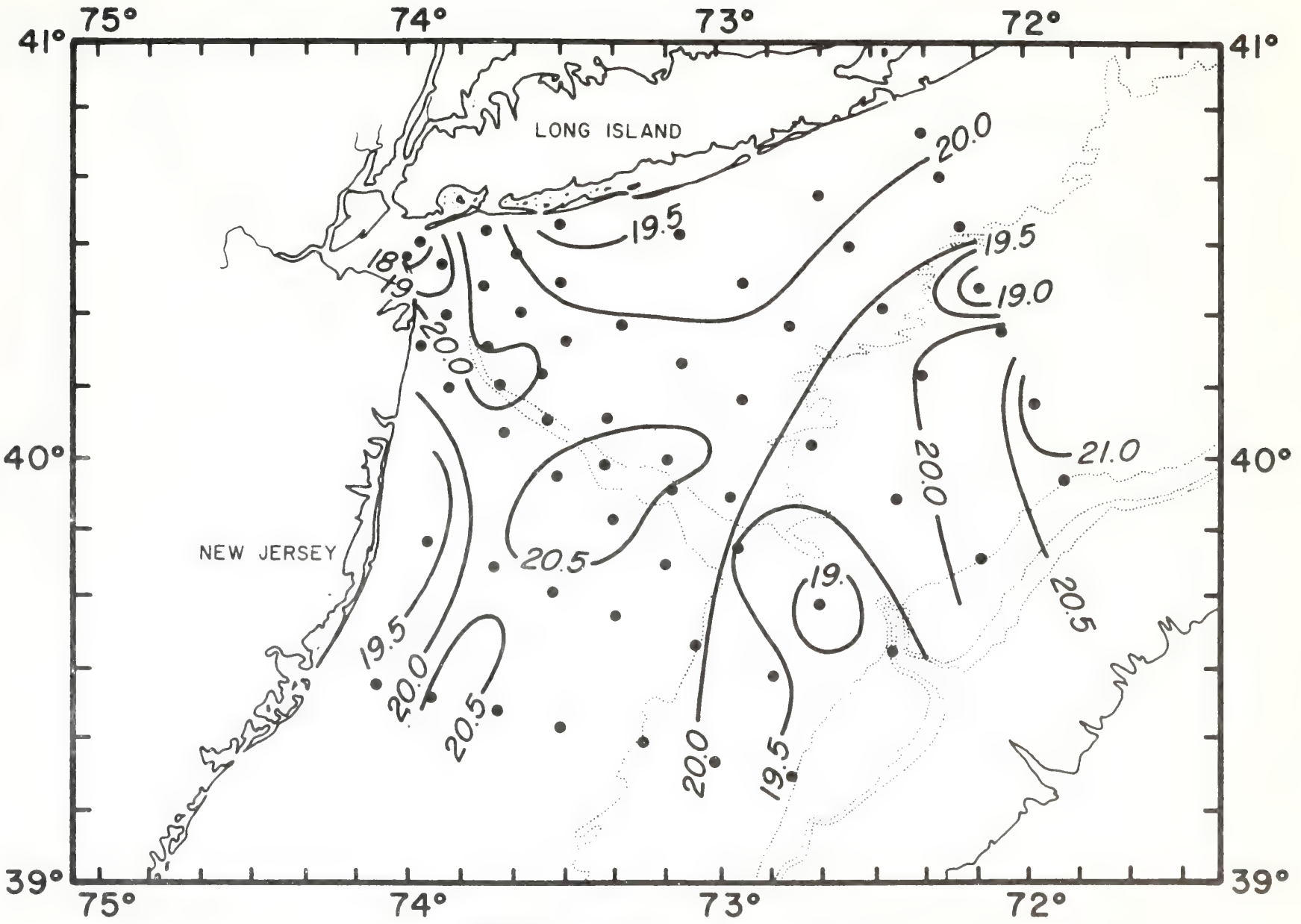


Figure 3. Surface water temperature 9/12/76 - 9/17/76.

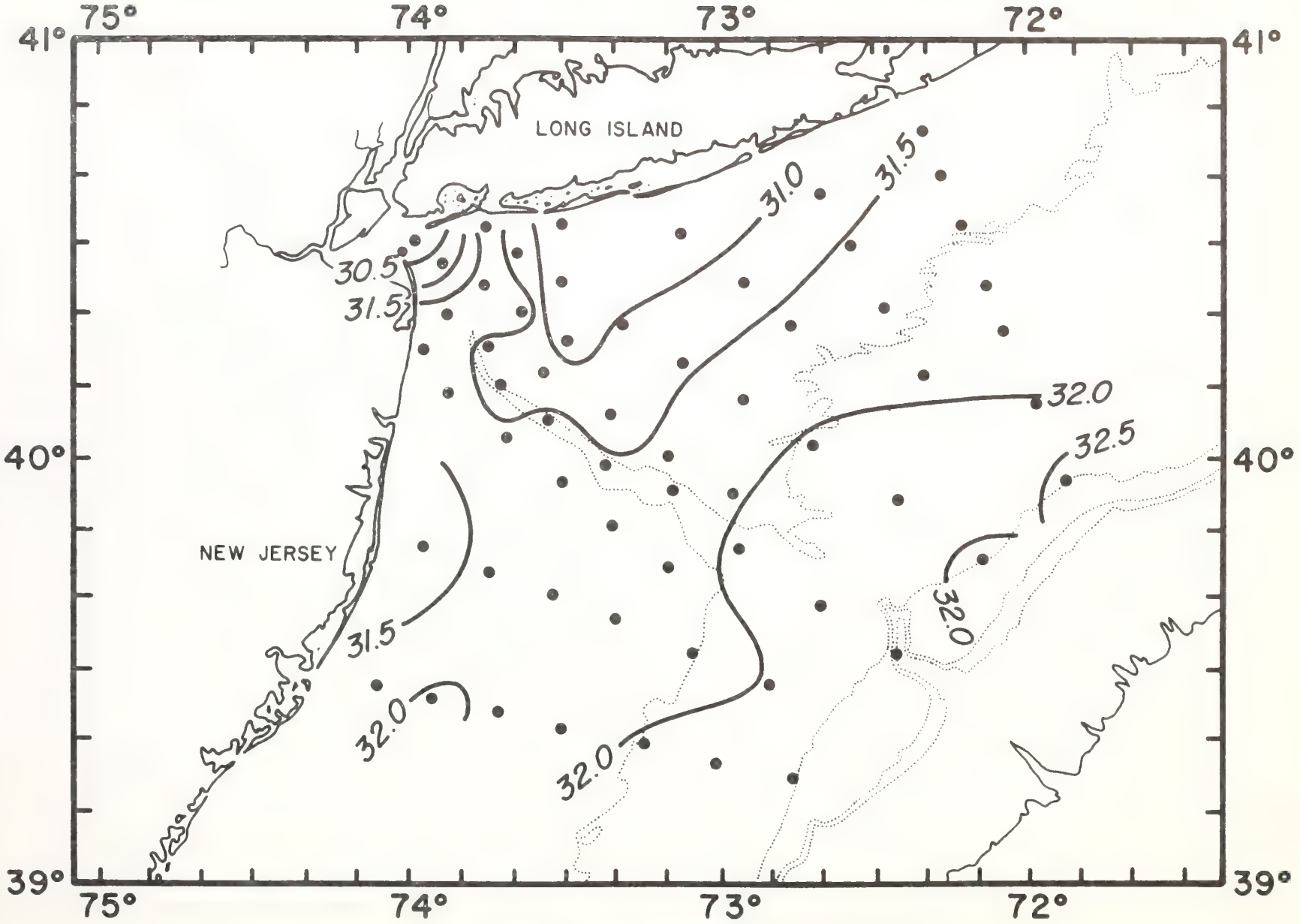


Figure 4. Surface salinities 9/12/76 - 9/17/76.

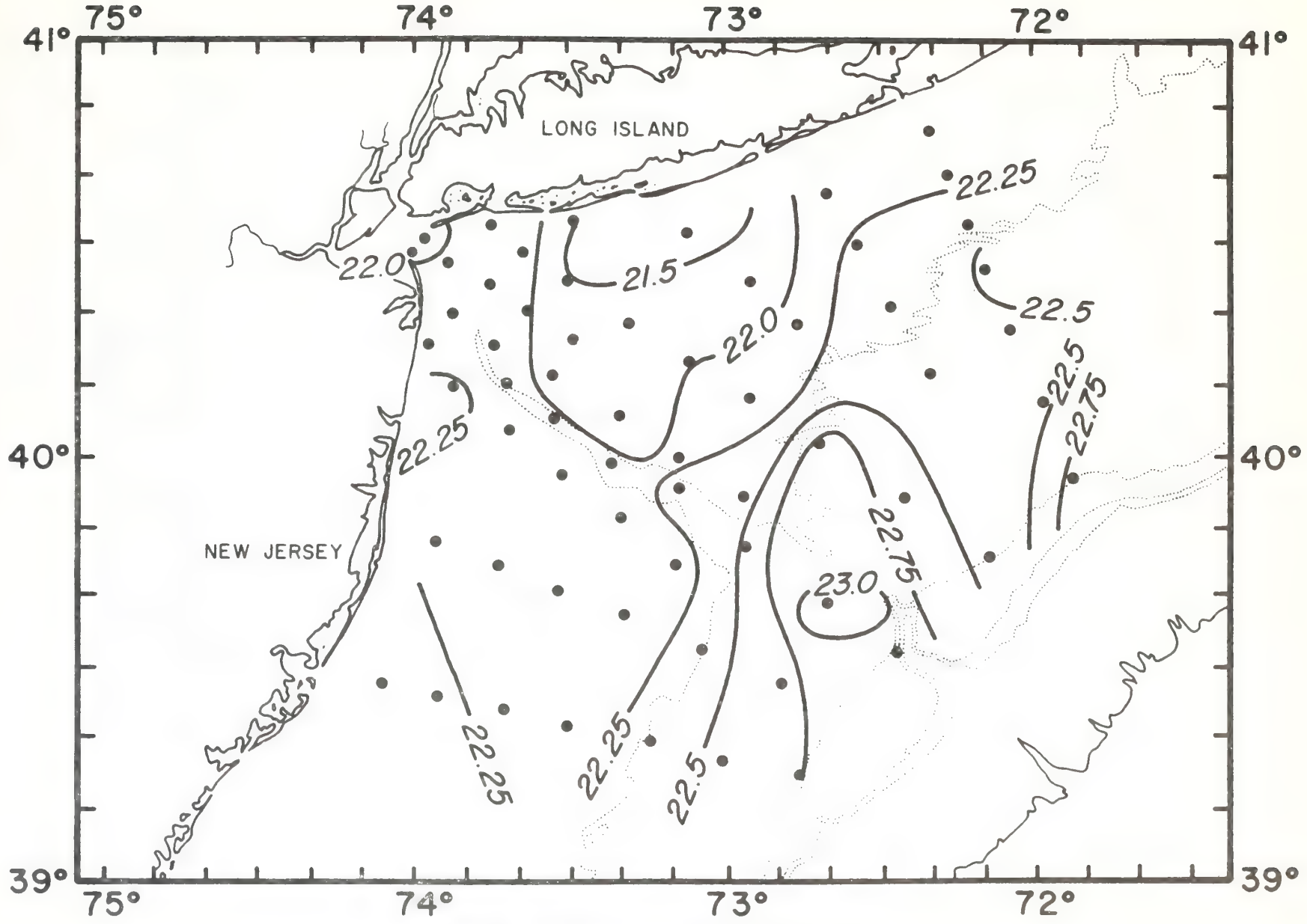


Figure 5. Surface sigma-t 9/12/76 - 9/17/76.

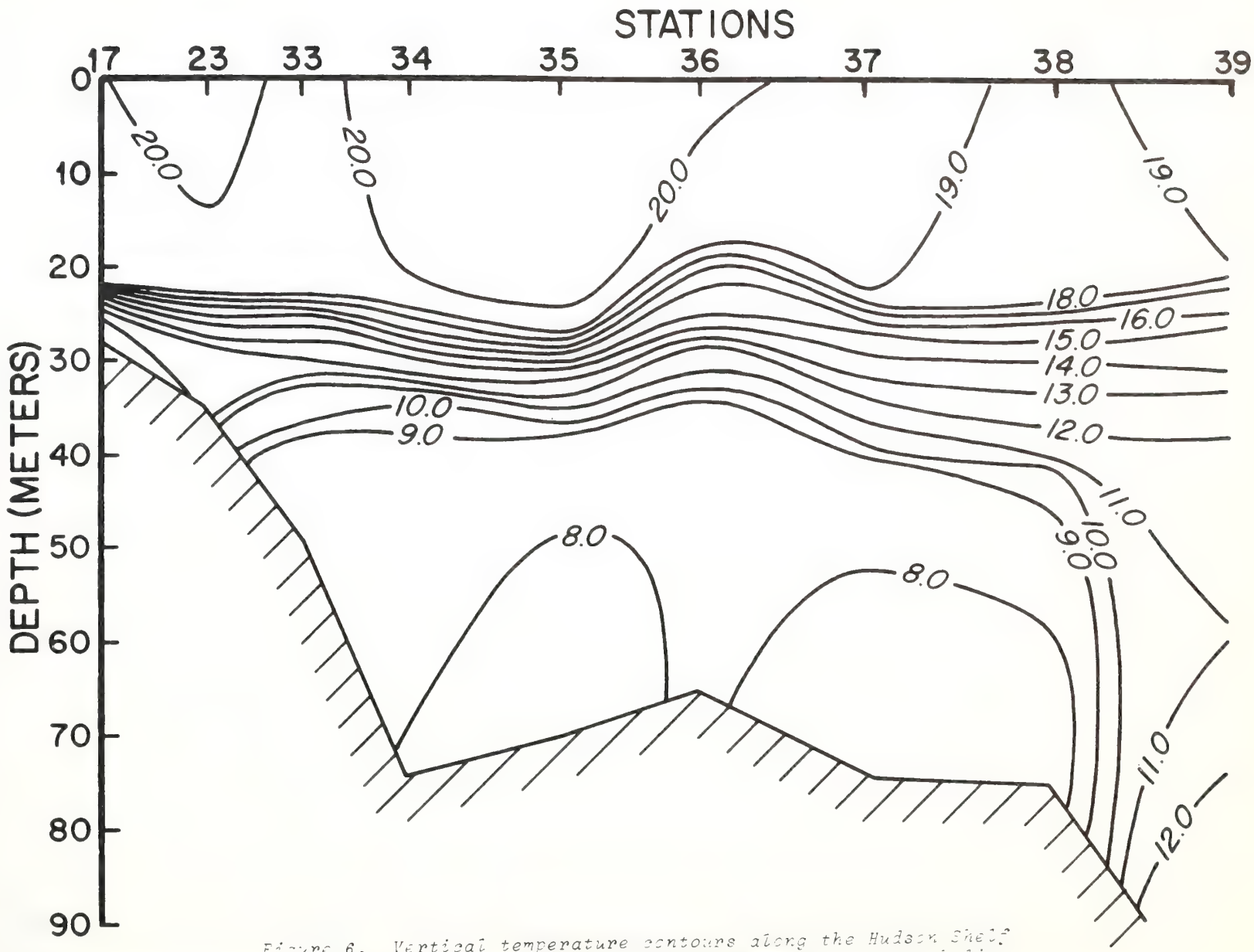


Figure 6. Vertical temperature contours along the Hudson Shelf Valley, 9/12/76 - 9/17/76. Reference Figure 1 for track line.

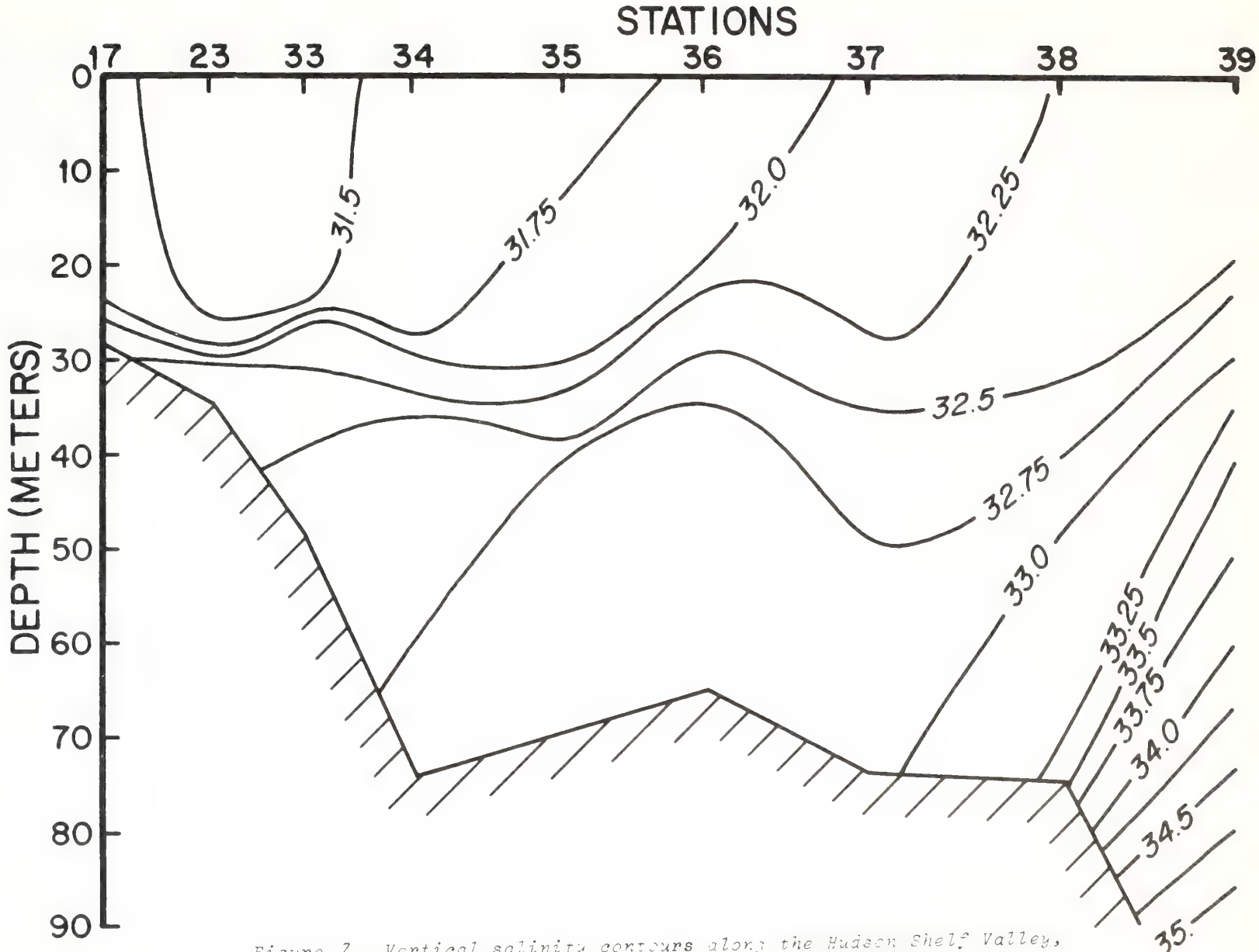


Figure 7. Vertical salinity contours along the Hudson Shelf Valley, 3/12/76 - 3/17/76. Reference Figure 1 for track line.

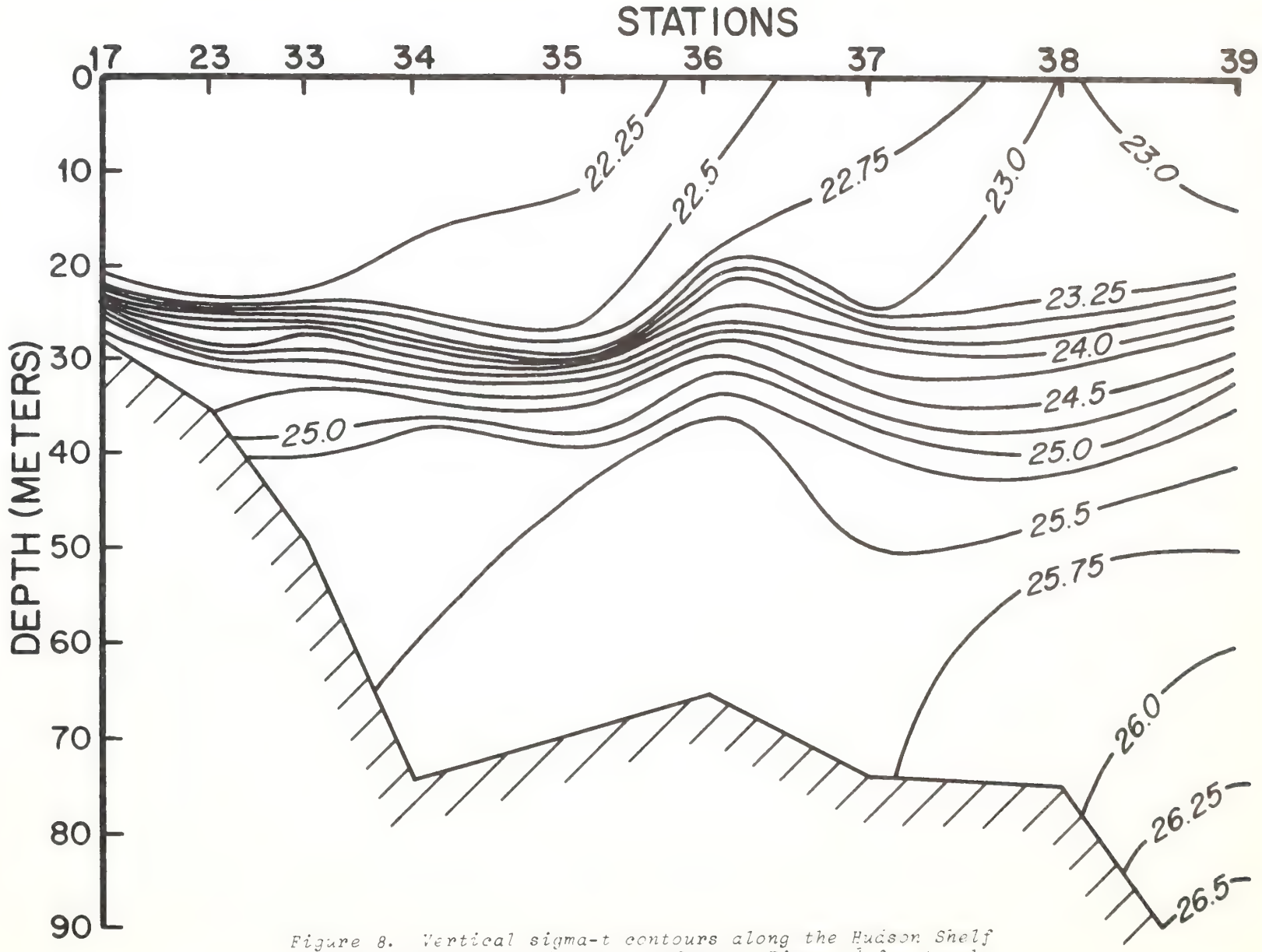


Figure 8. Vertical sigma-t contours along the Hudson Shelf Valley, 9/12/76 - 9/17/76. Reference Figure 1 for track line.

NOAA Data Report ERL MESA-27, 111 pages. (Text only.)

NOAA Data Report ERL MESA-27

MESA NEW YORK BIGHT PROJECT,
EXPANDED WATER COLUMN CHARACTERIZATION CRUISE (XWCC 8)
NOAA SHIP GEORGE B. KELEZ, APRIL 1976

John B. Hazelworth
Shailer R. Cummings
Robert B. Starr
George A. Berberian

Atlantic Oceanographic and Meteorological Laboratories
Miami, Florida

Marine Ecosystems Analysis Program Office
Boulder, Colorado
November 1977

UNITED STATES DEPARTMENT OF COMMERCE
Juanita M. Kreps, Secretary

NATIONAL OCEANIC AND ATMOSPHERIC ADMINISTRATION
Richard A. Frank, Administrator

Environmental Research Laboratories
Wilmot N. Hess, Director

"Mention of a commercial company or product does not constitute an endorsement by NOAA/ERL. Use for publicity or advertising purposes of information from this publication concerning proprietary products or the tests of such products is not authorized."

Page

Abstract 1

1. INTRODUCTION 1

2. DATA PRESENTATION 4

3. ACKNOWLEDGMENTS 4

4. REFERENCES 4

5. AREAL AND CROSS-SECTION DISTRIBUTIONS OF TEMPERATURE, SALINITY, AND SIGMA-T 12

6. STATION DATA

MESA NEW YORK BIGHT PROJECT
EXPANDED WATER COLUMN CHARACTERIZATION CRUISE XWCC 8
(NOAA Ship George B. Kelez)

April 1976

John B. Hazelworth
Shailer R. Cummings
Robert B. Starr
George A. Berberian

During the period 12-16 April 1976, an oceanographic cruise was made by the NOAA Ship Kelez in the New York Bight. The objective of the cruise was to supply data to provide a base for analysis of the water movements in the highly impacted ecosystem. This report presents the corrected physical and chemical (nutrient) data from this cruise.

Key Words: MESA, New York Bight, Physical Oceanographic Data, Nutrient Data

1. INTRODUCTION

This report is a continuation in the Marine Ecosystem Analysis (MESA) Program's series of publications presenting oceanographic data from the New York Bight. In April of 1976, a cruise of 48 stations was conducted by the Atlantic Oceanographic and Meteorological Laboratories (AOML), Miami, Florida, aboard the NOAA Ship Kelez. The instrumentation employed was the same as that described in previous reports (Hazelworth et al., 1974, 1975 a, b, Kolitz et al., 1976) namely, an Inter Ocean Model 513-10 CSTD with associated sensors and equipment. The area of investigation was the expanded New York Bight region (Fig. 1 and Tab. 1). Cruise dates and participating AOML staff members are listed in Table 2. The physical and nutrient data obtained from the water column measurements are presented herein; the operational characteristics of the nutrient-analyses system are found in Starr et al., (1977).

This report is the seventh of a series of reports describing the physical oceanographic measurements in the expanded area. Earlier cruises were reported by Charnell et al., (1976), Starr et al., (1976, 1977), Hazelworth and Darnell (1976), and Kolitz et al. (1976, 1977).

Prior reports, cited above, give detailed information on instrumentation specifications, data collection methods, and data processing techniques. The correction factors and data accuracy are given in Table 3.

Table 1. New York Bight Station Positions

Station	Latitude	Longitude	Station	Latitude	Longitude
1	40°30.2'	73°57.3'	38	39°39.0'	72°39.5'
3	40°31.5'	73°48.4'	39	39°32.0'	72°26.0'
5	40°33.3'	73°32.5'	64	40°12.0'	72°20.0'
7	40°26.9'	73°53.0'	65	40°21.0'	72°28.0'
9	40°28.3'	73°39.6'	66	40°30.0'	72°34.0'
13	40°23.3'	73°47.0'	67	40°38.0'	72°40.0'
15	40°25.2'	73°30.4'	68	40°19.0'	72°46.0'
17	40°18.5'	73°51.8'	69	40°25.0'	72°55.0'
19	40°20.2'	73°37.9'	70	40°32.0'	73° 7.0'
21	40°13.5'	73°56.1'	77	40°10.5'	73°34.0'
23	40°14.8'	73°45.6'	78	40° 5.0'	73°21.5'
25	40°16.9'	73°28.3'	79	40° .0'	73° 9.5'
26	40°29.0'	73°59.5'	80	39°54.5'	72°57.0'
27	40°18.0'	73°17.5'	81	39°44.5'	73°10.0'
28	40°13.5'	73° 7.0'	82	39°50.5'	73°20.5'
29	40° 7.0'	72°54.5'	83	39°56.5'	73°30.5'
30	40° 2.0'	72°41.5'	84	40° 2.0'	73°41.0'
31	39°54.0'	72°25.0'	85	40° 8.0'	73°51.5'
33	40°10.0'	73°41.5'	86	39°47.5'	73°57.0'
34	40° 5.5'	73°31.5'	87	39°44.0'	73°43.5'
35	39°59.0'	73°21.5'	88	39°40.0'	73°30.0'
36	39°55.0'	73° 6.5'	89	39°36.0'	73°16.5'
37	39°46.0'	72°57.0'	90	39°32.5'	73° 3.0'
			91	39°28.0'	72°50.0'

Table 2. Expanded Water Column Characterization Cruise by the NOAA Ship Kelez

Cruise	Date	AOML Personnel
XWCC-8	April 12-16, 1976	Robert B. Starr Chief Scientist George A. Berberian Shailer R. Cummings

Table 3. Correction Factors and Data Accuracy for Cruise XWCC-8

	Temp. °C	Salinity o/oo	Transmissivity	Ph
Correction Factor	+.02	-0.09	N.A.	+.07
Mean Data Accuracy	+.01	- .005		+.01
Standard Deviation	.02	.03		.05

2

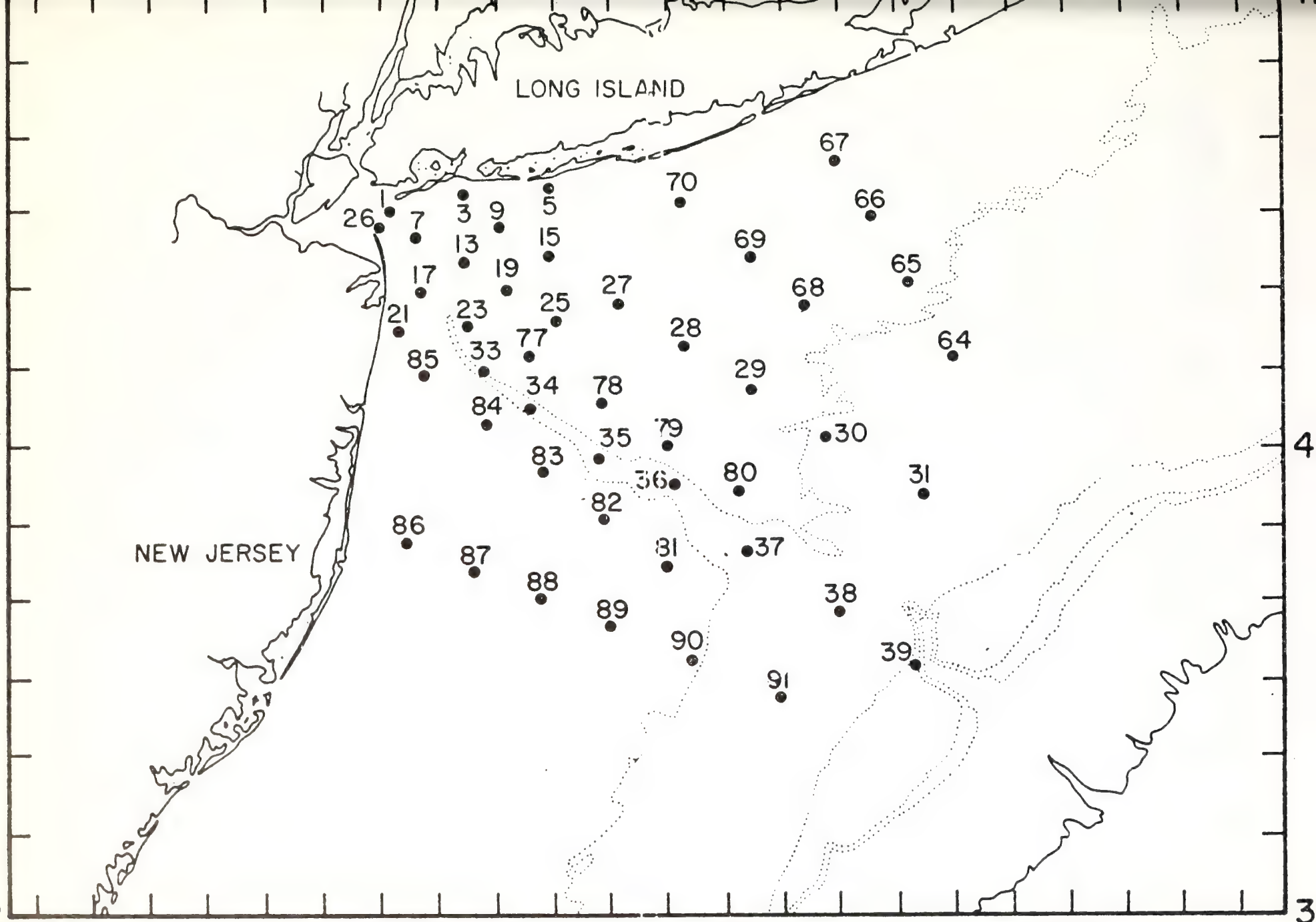


Figure 1. Locations of stations occupied during XWCC-8.

2. DATA PRESENTATION

Tables of the interpolated data and the corresponding depth profiles of temperature, salinity, sigma-t, and transmissivity are given in Section 6, Station Data. The codes used in the headings are from the National Oceanographic Data Center Manual Series (1964). The tabulated data are given at 1-m intervals from the surface to 50 m and at 10 m intervals thereafter; in addition, data are presented at the depths at which water samples were obtained and at the bottom of the cast. Profiles were produced from the corrected raw data. The symbols, explained to the left of each horizontal axis and located on the curves at 5-m intervals, identify the parameters.

The distributions of temperature, salinity, and sigma-t are presented: 1) horizontally at the 1-m depth (Figs. 2-4), and 2) vertically along the axis of the Hudson Shelf Valley (Figs. 5-7).

3. ACKNOWLEDGMENTS

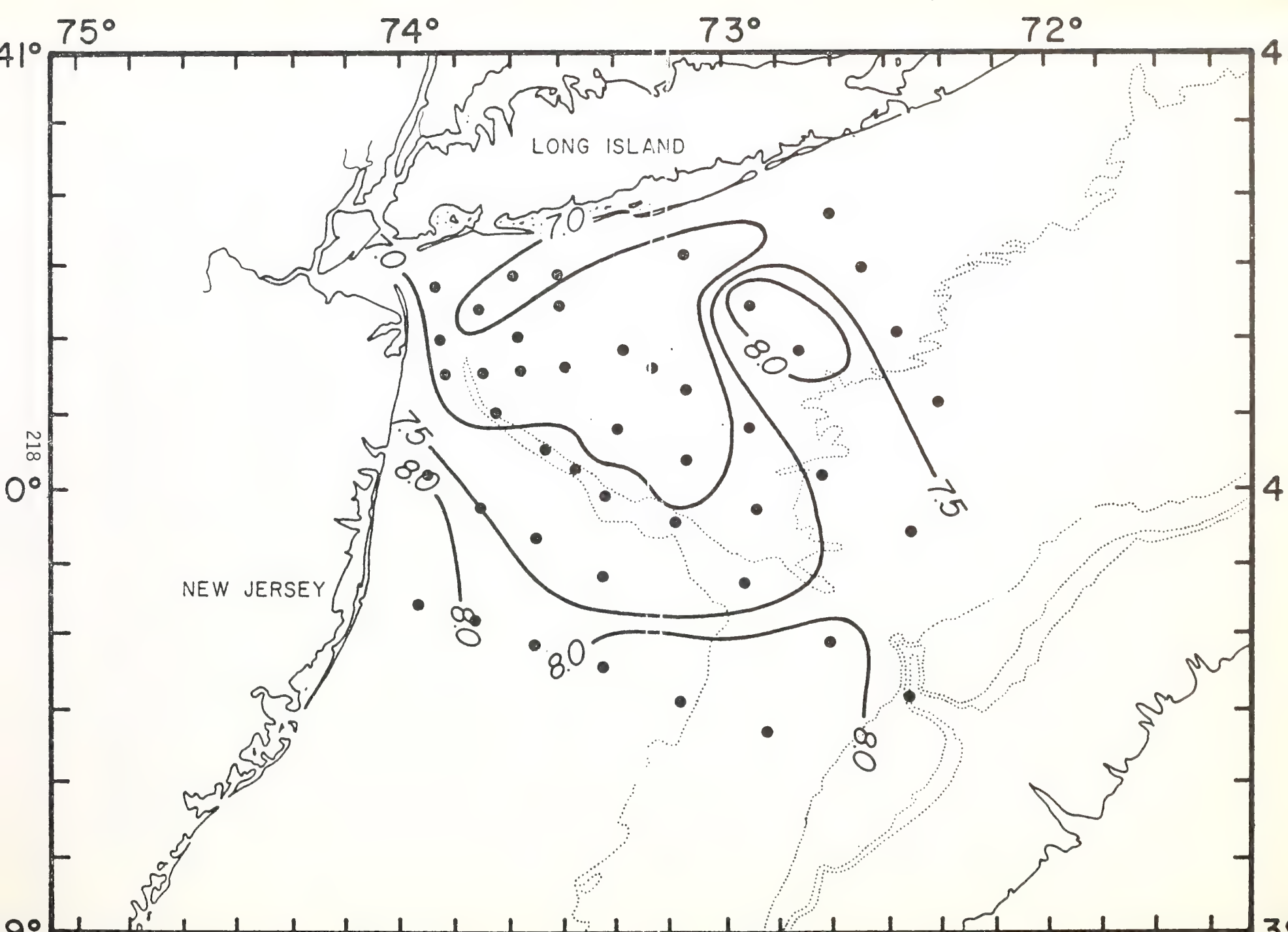
The authors express their thanks to the officers and crew of the NOAA Ship Kelez, under the command of LCDR John Stachelhaus, for the long and diligent hours they devoted to collecting these data. The effort was sponsored by NOAA and funded in part by the NOAA Environmental Research Laboratories and the MESA Program.

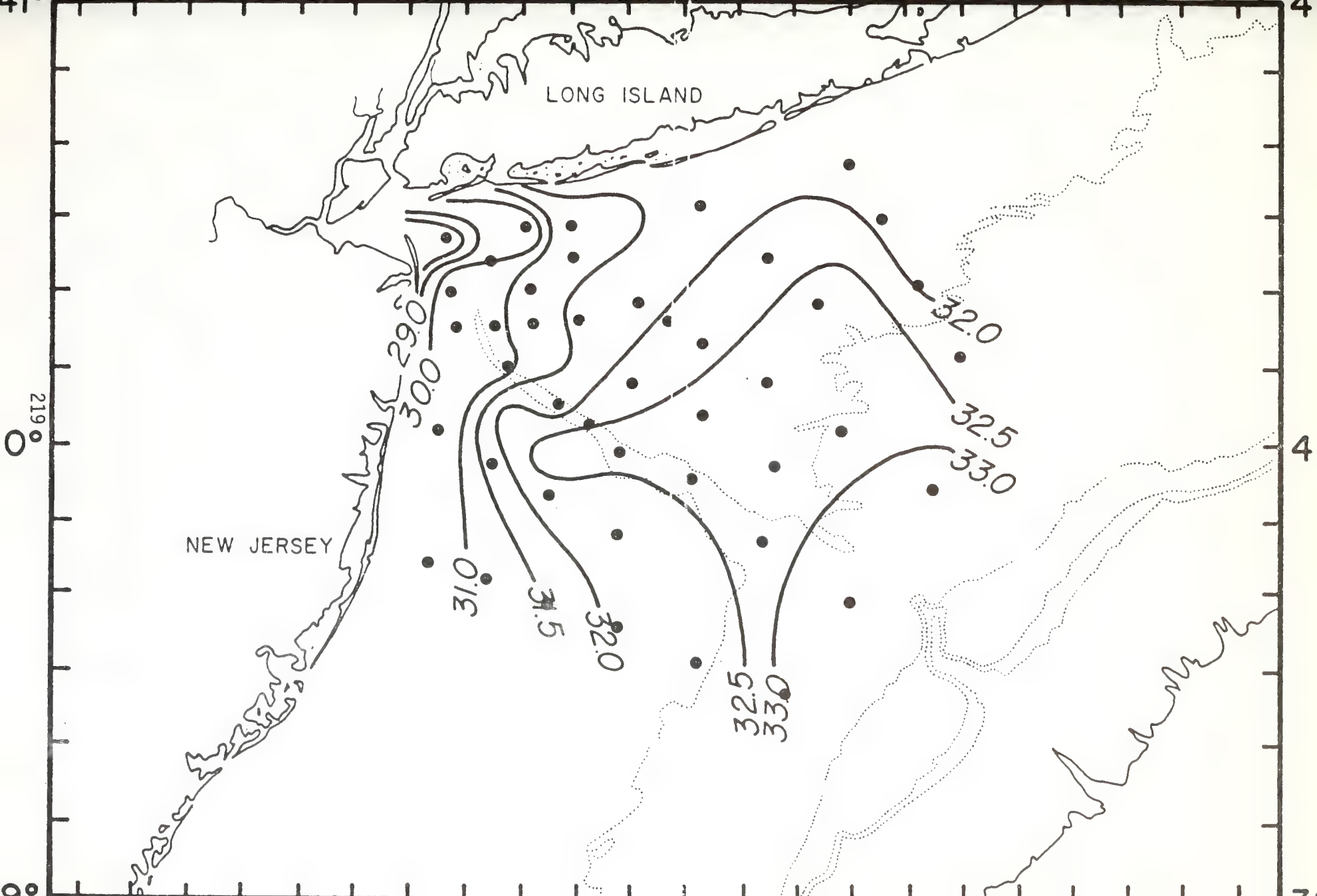
4. REFERENCES

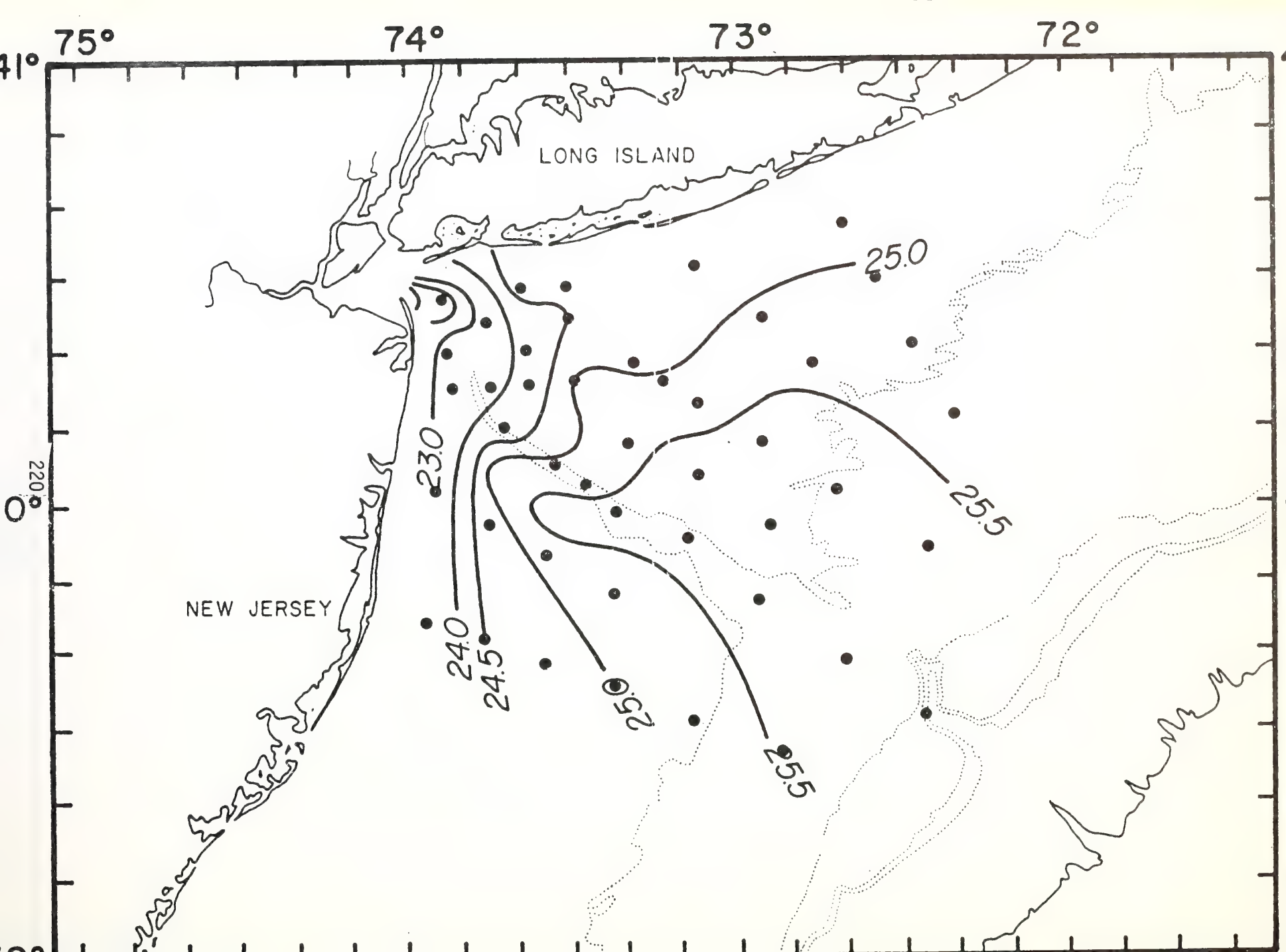
Hazelworth, J. B., B. L. Kolitz, R. B. Starr, R. L. Charnell, and G. A. Berberian (1974): MESA New York Bight Project, Water Column Sampling Cruises #1-5 of the NOAA Ship Ferrel, August-November 1973, MESA Report No. 74-2, U. S. Govt. Print. Off., Washington, D. C. 191 p.

Hazelworth, J. B., B. L. Kolitz, R. B. Starr, R. L. Charnell, G. A. Berberian, and M. A. Weiselberg (1975): MESA New York Bight Project, Water Column Sampling Cruises #6-8 of the NOAA Ship Ferrel, April-June 1974, NOAA Data Report MESA-1, U. S. Govt. Print. Off., Washington, D. C., 177 pp.

Hazelworth, J. B. and M. E. Darnell (1976): MESA New York Bight Project, Expanded Water Column Characterization Cruises XWCC-2 and 3 (NOAA Ship Researcher) 22 February - 5 March, 9 - 12 April, 1975 NOAA MESA Data Report-23, U. S. Gov't Print. Off., Washington, D. C., (Microfiche).


75°
74°
73°
72°
41°
LONG ISLAND
NEW JERSEY
7.0
7.5
8.0
8.0
8.0
8.0
7.5
8.0
218


LONG ISLAND
NEW JERSEY
29.0
30.0
31.0
31.5
32.0
32.5
33.0
32.0
32.5
33.0
219°


75°
74°
73°
72°
41°
220°
LONG ISLAND
NEW JERSEY
25.0
23.0
24.0
24.5
25.0
25.5
25.5

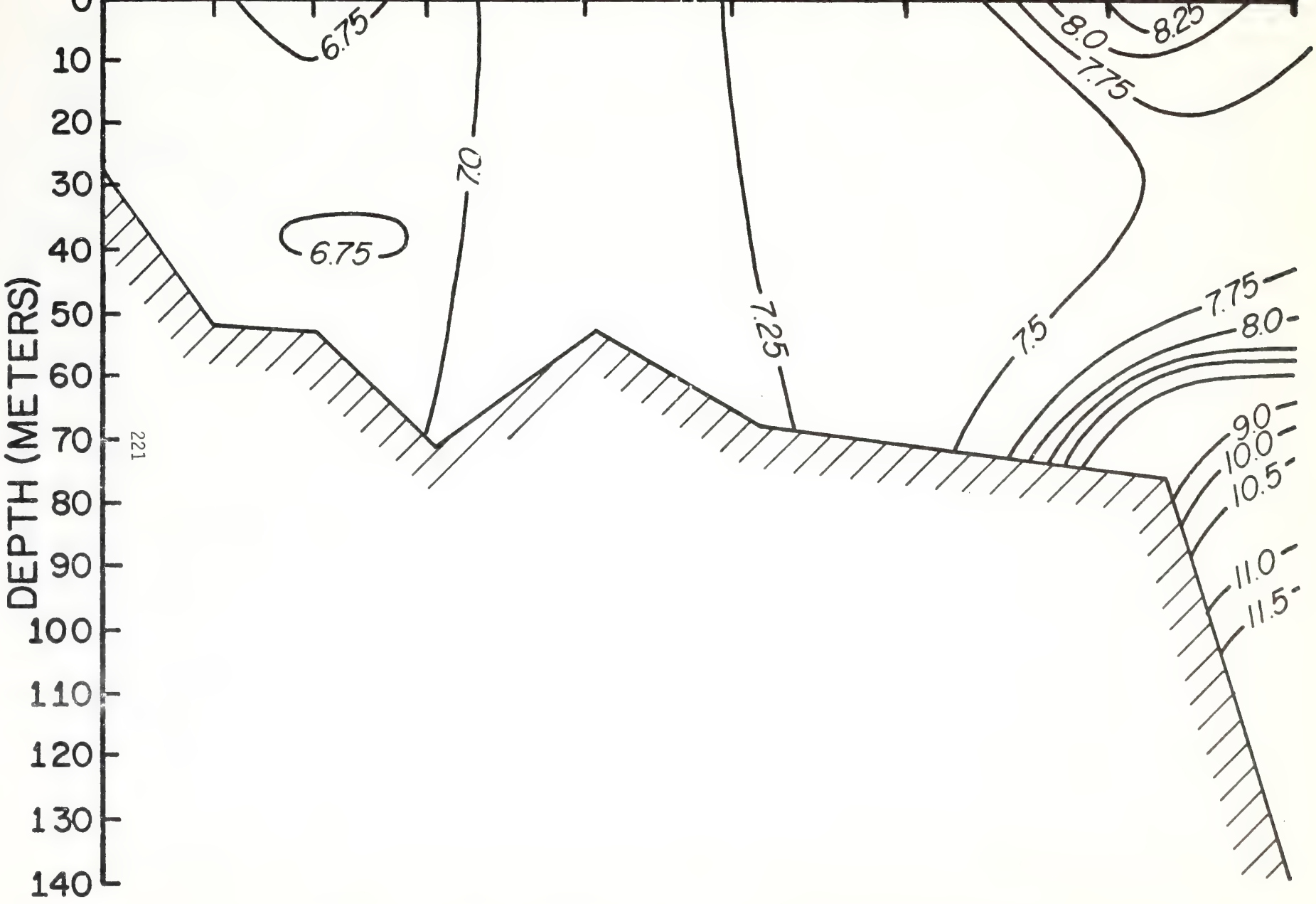


Figure 5. Vertical temperature contours along the Hudson Shelf Valley, 4/12/76 - 4/16/76. Reference Figure 1 for track line.

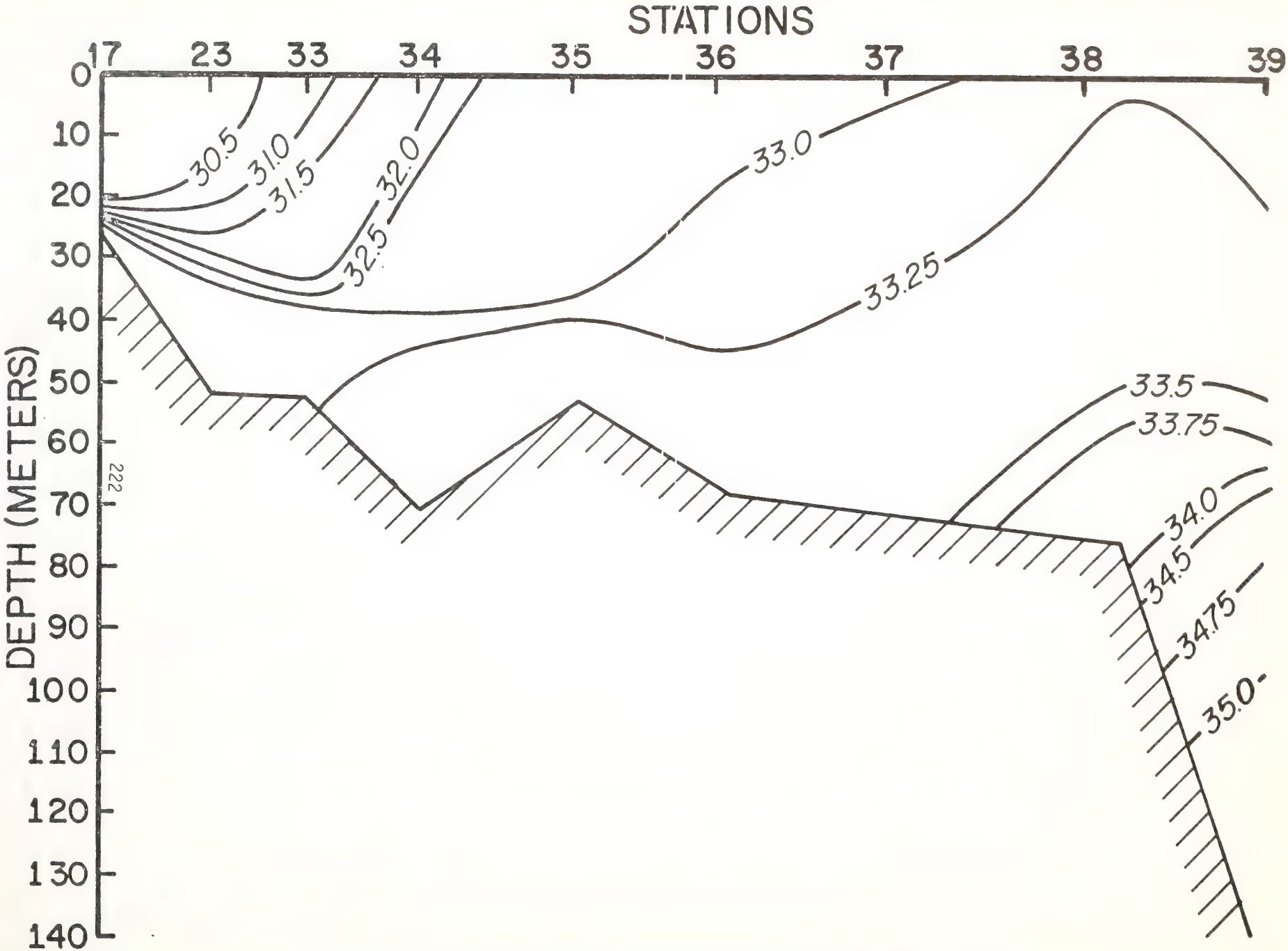


Figure 6. Vertical salinity contours along the Hudson Shelf Valley, 4/12/76 - 4/16/76. Reference Figure 1 for track line.

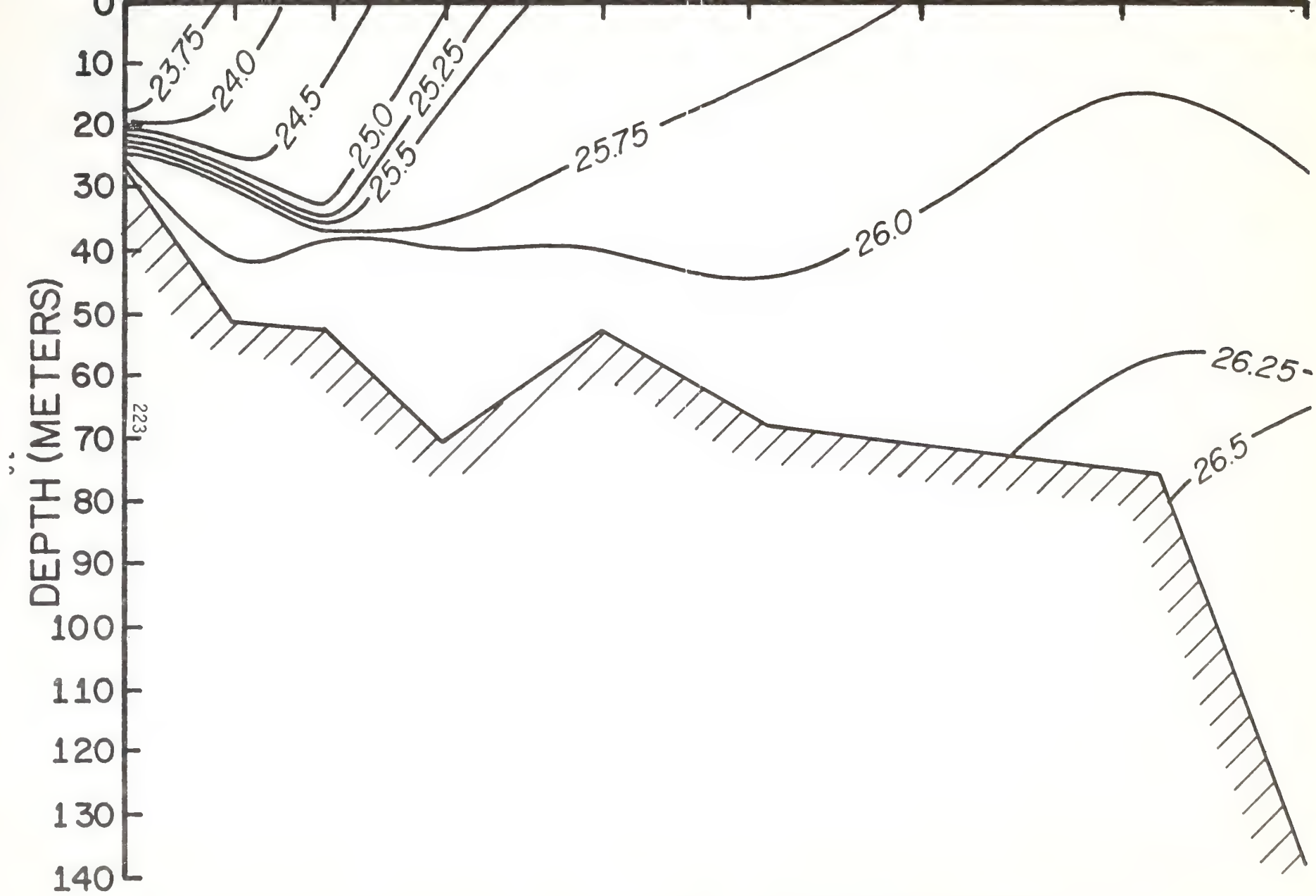


Figure 7. Vertical sigma-t contours along the Hudson Shelf Valley, 4/12/76 - 4/16/76. Reference Figure 1 for track line.

Hazelworth, J. B., B. L. Kolitz, R. B. Starr, R. L. Charnell, G. A. Berberian, and M. A. Weiselberg (1975): MESA New York Bight Project, Water Column Sampling Cruises #9-12 of the NOAA Ship Ferrel, July - November 1974, NOAA Data Report MESA-3 U. S. Govt. Print. Off., Washington, D. C., 233 pp. (Microfiche).

Kolitz, B. L., J. B. Hazelworth, R. B. Starr, G. A. Berberian, and S. R. Cummings (1976): MESA New York Bight Project. Expanded Water Column Characterization Cruise 7 (NOAA Ship Kelez) December 1975, NOAA MESA Data Report-26, U. S. Gov't Print. Off., Washington, D. C. (Microfiche).

Kolitz, B. L., J. B. Hazelworth, R. B. Starr, and S. R. Cummings (1976): MESA New York Bight Project. Expanded Water Column Characterization Cruises XWCC 4 - 5 NOAA Ship Kelez, May - June 1975, NOAA MESA Data Report-24, U. S. Govt. Print. Off., Washington, D. C., (Microfiche).

National Oceanographic Data Center Manual Series (1964): Processing Physical and Chemical Data from Oceanographic Stations, Part 1. Coding and Keypunching, Publication M-2, revised, U. S. Naval Oceanographic Office, Washington, D. C., 117 pp.

Starr, R. B., G. A. Berberian, and M. A. Weiselberg (1976): MESA New York Bight Project, Expanded Water Column Characterization Cruise of the R/V Advance II, January 1975, NOAA Data Report MESA-22, U. S. Gov't Print. Off., Washington, D. C., (Microfiche).

Starr, R. B., J. B. Hazelworth, and G. A. Berberian (1977): MESA New York Bight Project, Expanded Water Column Characterization Cruise 6 of the NOAA Ship Kelez, September - October 1975, NOAA MESA Data Report-25, U. S. Gov't Print. Off., Washington, D. C., (Microfiche).

NOAA Technical Memorandum ERL AOML-28, 110 pages.

COMPUTER PROGRAMS FOR SIMPLE LAGRANGIAN PROCESSING (SLAP), USERS' GUIDE

A. Herman
C. Cardwell

Physical Oceanography Laboratory

Atlantic Oceanographic and Meteorological Laboratories
Miami, Florida
August 1977

UNITED STATES DEPARTMENT OF COMMERCE
Juanita M. Kreps, Secretary

NATIONAL OCEANIC AND ATMOSPHERIC ADMINISTRATION
Richard A. Frank, Administrator

Environmental Research Laboratories
Wilmot N. Hess, Director

CONTENTS

	Page
Abstract	1
1. INTRODUCTION	1
2. DESIGN	1
3. SUBROUTINES	3
3.1 User-called Routines	3
3.2 SLAP-called Routines	5
4. PROGRAM DESCRIPTIONS	7
5. ACKNOWLEDGMENTS	15
6. REFERENCES	16
Appendix A. EXAMPLE OF A SLAP APPLICATION	17
Appendix B. DETERMINATION OF ENGINEERING UNITS	18
Appendix C. PROGRAM LISTINGS	20

COMPUTER PROGRAMS FOR SIMPLE LAGRANGIAN PROCESSING (SLAP), USERS' GUIDE

A. Herman
C. Cardwell

A set of computer programs for automatic processing of Lagrangian buoy drift data is presented. All subroutines are identified in terms of their functions and are further described with methods and restrictions of use. Appendices provide a sample application, determination of engineering units employed in the programs, and printouts of the programs.

1. INTRODUCTION

The computer programs described here completely automate the processing of Lagrangian buoy drift data from a growing data base. The processing includes sorting, plotting of data on a Polyconic or Mercator projection, editing, smoothing data without subjective procedures, and performing simple statistical computations based on computed buoy velocities and accelerations. All required geodetic computations of position, distance, and azimuth are performed on the Fischer Spheroid.

These programs are compatible with the AOML statistical package, FESTSA (Herman and Jacobson, 1975).

The programs at present are run on the NOAA Miami UNIVAC 1108 but can be easily modified to run on any computer with a minimum of 48K words of 32 bits or more, three magnetic tape drives, 50K words of secondary storage (disk or drum), and a plotter capable of accepting Calcomp-like commands. All programs are written in ANSI standard Fortran with the exception of I/O routines, which are written partly in assembly and partly in UNIVAC Fortran V. SLAP is a growing system and addenda to the user's guide will be issued.

2. DESIGN

All routines utilize a labeled common storage area called WORK that is 13900 words long. Secondary storage is limited to the first 50000 words of drum; these are referenced by all routines as unit 33 for words 1-25000 and unit 34 for words 25001 to 50000.

Logical records are 139 words long. Drum physical records are one logical record long, and data base tape physical records are 100 logical records long. The logical records contain the following information.

Word 1	= Buoy identification number
2	= NASA data set number
3	= Latitude in degrees
4	= Longitude in degrees
5	= NASA accuracy estimate in percent (100 = best)
6	= Satellite determined N velocity vector in m/sec
7	= Satellite determined E velocity vector in m/sec
8	= Number (NUM) of 5-word data sets to follow
9-138	= 5-word data sets repeated NUM times with zero fill. The five words are load cell, wind velocity, temperature, atmospheric pressure, and time in days referenced to 1 January 1975 at midnight. The first four words are integer frequency counts.
139	= Year.

The data base is required for all SLAP runs. The first routine to be called after establishing the common block (e.g. Common/Work/Ser (13900)) is SORT. This routine places data on drum unit 33 in the manner specified (see routine description) and tells how many data points you have. All processing routines utilize data from drum unit 33 and rewrite data on unit 33, as described in routine descriptions.

When FESTSA routines are used in conjunction with SLAP, only drum units 2 and 4 can be used.

3. SUBROUTINES

3.1 User-Called Routines

COPI	Produces a copy of any tape in the same format as the original.
CVA	Produces plots of component velocities and accelerations.
DSTAT	Computes means and standard deviations for x-y coordinates and their first differences, and plots a frequency distribution.
DTOTPE	Copies a drum file to a tape.
MAP	Makes a Mercator plot of positions from drum file at a scale of 1:4,000,000.
MAP1	Produces a Polyconic projection plot at a scale of 1:1,000,000 from a drum file.
NASAB	Translates data from NASA format to data base format and writes to data base tape from cards.
NASATP	Creates an AOML data base tape from a NASA archive tape.
NASTAT	Computes and plots statistics of component velocities and accelerations.
PVD	Produces plots of cumulative frequency distribution as a function of distance.
RAW	Produces a smooth plot on a Universal Transverse Mercator projection at 1:250,000 scale.
REPORT	Produces a data report on a 7-track BCD tape in NODC specified format.
SMOOTH	Produces a drum file of daily positions from a drum file of data unequally spaced in time.
SORT	Sorts data base tape file by any combination of buoy ID, time limits, and location limits; creates a drum file of data in chronological order.
SORT2	Sorts two data base tape files in the same manner as SORT.
SPDACC	Produces plots of velocity and accelerations.

User-Called Routines (cont'd.)

TMPLT	Plots time of day as day number for a particular buoy.
TOTP	Creates a SLAP drum file on Unit 33 by combining two DTOTPE files.
TPETOD	Copies a tape file created by DTOTPE on a drum.
TPS	Produces plots and listings of surface temperature, pressure on drogue, and wind speed vs. time.
VCHECK	Deletes all positions from a drum file that would create speeds greater than an input limit, i.e., 2 knots.
VLOOK	Produces plots of cumulative frequency distribution as a function of velocities.
VOLT	Produces a plot of buoy battery voltage vs. time.

3.2 SLAP-Called Routines

AV	Calculates the arithmetic mean of a set of numbers.
BEST	Selects the best sensor value in an orbit.
CDC	Converts CDC 3000 series integer and floating point words to UNIVAC 1108 words.
CLEAR	Zeros work buffer .
CORLAT	Computes auto and cross correlations (available in FESTSA Manual).
CRONO	Sorts a drum file chronologically.
DEG	Converts decimal degrees into degrees-minutes-seconds.
EOF	Writes an end-of-file.
GTSIZ	Determines the length of a tape record.
INPUT	Reads one record from data base tape.
INPT2	Reads data base tapes.
INV	Computes distance and azimuth between geographic positions on the Fischer Spheroid.
HEADER	Creates a data report header in NODC format.
MERC	Computes Cartesian coordinates on a Mercator projection from geographics.
NODC	Creates a data base file in NODC format.
OCW	Converts octal to decimal to binary.
OUT	Writes records to drum.
PCONIC	Computes Cartesian coordinates on a polyconic projection from geographic positions.
PLOT1	Printer plot routine. (available in FESTSA Manual)
POLLY	Computes coefficients for a 3rd-order Orthogonal Polynomial using least squares.
PROCES	Extracts binary non-word-oriented data from NASA archive records.

SPEED	Given two geographics and times - computes midpoint, velocity, velocity components, and azimuths between points.
STATS	Computes means and standard deviations for a data series and its first differences (available in FESTSA Manual).
TPOUT	Reads SLAP file record; copies it to a tape.
UTM	Computes Universal Transverse Mercator positions from geographics on the Fischer Spheroid.
XMAX	Finds the maximum value in an array of numbers.
XMIN	Finds the minimum value in an array of numbers.
ZERO	Initializes data base record to zero.

SUBROUTINE CVA (NUM)

This routine reads NUM logical records from drum unit 33, component velocities and accelerations, and then produces Gould plots of them vs time. Time and the east and north components of velocity and acceleration are printed out.

Method:

1) Distance and azimuths are computed between successive positions which are used for computation of mid-points between positions to which average velocities and accelerations are assigned based on V= D/T and A = V/T.

Geodetic computations are accomplished using the Sodano (1963) equations.

Restrictions: NUM must be $\leq$ 998.

SUBROUTINE DSTAT (NUM)

This routine reads NUM logical records from drum unit 33 and computes Universal Transverse Mercator grid (1958) coordinates from which means and standard deviations are computed for the data and their first differences. Frequency distributions are printer plotted. Fischer Spheroid is used for UTM computations.

This routine has been used to evaluate accuracies of fixes based on data from stationary buoys.

Restrictions: NUM must be $\leq$ 1000

SUBROUTINE DTOTPE (NUM)

Copies NUM logical records in Fortran floating point records from drum unit 33 to tape unit 11 without any tape rewinds. No end-of-file marks are written. The first record written contains only NUM.

Restrictions: NUM must be $\geq$ 1 or a long erroneous loop will result.

SUBROUTINE MAP (NUM)

This routine reads NUM records from drum unit 33 and computes Mercator projection coordinates at the equator relative either to the SW corner of the BC chart it falls on or 80°S at Greenwich. Scaling is set so that all points are plotted within an 8" by 8" area. All values are printed including chart number, and overlays are plotted.

Method:

A table of meridional parts is stored in the computer, and distance computations in Cartesian coordinates are performed as described in Bowditch (1962) page 71. The equations for the Mercator projection can be found in Bomford (1971).

Restrictions: NUM $\leq$ 1000.

SUBROUTINE MAP1 (NUM)

This routine reads NUM logical records from unit 33, computes polyconic coordinates, and plots buoy positions on the Gould Plotter at a scale of 1:1,000,000.

This routine requires a 1 data card in 2F10.3 format with the central meridian of the chart you wish to overlay and the southernmost limit of latitude that your data may approach.

Method:

1) Distances along the central meridian N of 52^{o} vary as follows:

meters = (number of degrees N of 52^{o}) *18.06 + 111279.11

2) Distance of a point in meters x & y from a latitude intersection with the CM is as follows:

$x = Pn \cos \phi$

$y = 1/4\ Pn^2 \sin^2 \phi$

where $P = a/1\text{-}e^2 \sin^2 \phi)^{1/2}$

a = semi-major axis of earth

e = eccentricity of spheroid

ϕ = latitude

n = delta longitude from core in radians.

The above algorithm was derived by simplification of equations in SP5 (1946) yielding positional errors of under 100 meters.

Restrictions: 1) NUM ≤ 998

2) min. latitude $\geq 52^{o}N$

SUBROUTINE NASAB

This routine reads NASA TWERLY CARDS or CARD FORMAT TAPES and transforms the data to the SLAP data base tape format. The output unit is always tape unit 7, and the input is either 5 or 8.

This routine is not ANSI standard and must be modified if a machine other than the UNIVAC 1108 is used.

All input files to this routine must end with an end of file.

SUBROUTINE NASATP

This routine reads NASA Archive tapes and produces a SLAP data base tape. The routine is not ANSI standard in that it utilizes non-standard input/output routines and assembler shift and mask routines.

One data card is required with the number of tapes to be processed in I10 format. The tape input unit is always 'B', and output unit is always 'A'. The input tape is 7-track 800 BPI; both tapes are odd parity.

SUBROUTINE NASTAT (NUM)

Reads NUM logical records from drum unit 33, computes component velocities and accelerations as described in CVA, then performs the same statistics as described in DSTAT. Standard deviations of both computed velocities, accelerations, and their front differences are printed out. Frequency distributions are printer plotted.

This routine is normally used for studying stationary buoys.

Restrictions: NUM $\leq$ 998.

SUBROUTINE PVD (NUM)

This subroutine is used to compute and plot the cumulative frequency distribution function of distances between 0 and 4,000 meters from the mean location. It evaluates system accuracy using stationary buoy data.

Instructions for use:

1) Assign a 9-track tape to Unit A for the Gould Output.

2) CALL PVD (NUM) where NUM is the number of fixes on the drum file.

SUBROUTINE RAW (NUM)

This routine reads NUM records from drum file on unit 33 and produces a Universal Transverse Mercator plot of the buoy trajectory at a scale of 1:250,000.

Geographics, UTM Northings, UTM Eastings, and time are printed. The time is in days relative to the first midnight after the start of the data.

SUBROUTINE REPORT (NUM, TMPMIN)

This routine reads NUM logical records from drum unit 33 and produces a 7-track BCD tape of the buoy data in the specified NODC format on tape unit 7. The approximate minimum surface water temperature encountered by the buoy must be determined in ^{o}C and entered in TMPMIN. Erroneous results will occur if this value is too high or low. Refer to Appendix B for the method used in determining the engineering units.

SUBROUTINE SMOOTH (NUM, DAT1, DAT2)

This routine reads NUM logical records off drum unit 33 and then fits a day's data to a quadratic curve starting with day one and using an orthogonal least squares solution. More days are used if necessary to define the quadratic. The distances to all the points from the curve are computed, and each location is assigned a weight based on the distance. DAT1 is the minimum number of days desired to fit a quadratic curve over for weight determination, and DAT2 is the minimum node interval for splines, also measured in days. Function WATE, the input of which is distance in meters and the output of which is a weight between 0 and 1, accomplishes this. This function is based on an error analysis of the buoy positioning system. N and R are shaping functions for the expression

$$e^{-\left(\frac{\delta}{R}\right)^{2N}}$$

where δ is the input distance in meters computed by SMOOTH. The parameters are N=1, R=8,000 meters, which best fit the error analysis performed for the system. Because N=1 the weighting-equation is Gaussian. This procedure is repeated advancing one day at a time. The weighted positions are now used to least-squares-spline-fit the data. During this procedure, the first and last two days of the data are lost. Data positions at one-day intervals are computed and stored on drum unit 33. NUM now is the number of daily positions on unit 33.

Restrictions: Buoy tracks are limited to 1,000 positions.

For a detailed description of the method used see Herman and Hansen (1977).

SUBROUTINE SORT (NUM)

This routine reads the entire data base from tape unit 8, extracting required data and storing them on drum unit 33. SORT requires a buoy identification number for input and any combination of geographic or time limits. The sorted data will be output in chronological order. It will return in NUM the number of data points found in the sort.

Instructions for use:

1. One data card with up to seven fields in (I10, 6 F10.3) format is required.

Field 1 = Buoy ID

2 = Minimum latitude in degrees

3 = Maximum latitude in degrees

4 = Minimum East longitude

5 = Maximum East longitude

6 = Minimum day count

7 = Maximum day count

Restrictions: If either a minimum or maximum restriction is given, the other must be given also. Maximum latitude cannot equal zero.

SUBROUTINE SORT2 (NUM)

This routine functions exactly as SORT except that it assumes the data base to be on two tapes assigned to tape units 8 & 9.

SUBROUTINE SPDACC (NUM)

This routine reads NUM logical records from drum unit 33, computes speeds and accelerations (not in components), and plots them vs. time on the Gould Plotter. Distances are computed as described in CVA.

SUBROUTINE TMPLT (NUM)

This routine reads NUM logical records from drum unit 33 and plots the time of the fix vs. the day the fix was made. Output is on the Gould Plotter.

Restrictions: NUM $\leq$ 998.

SUBROUTINE TOTP (NUM, IUN1, IUN2)

This utility routine combines two DTOTPE files on separate tapes, IUN1, IUN2, and creates a SLAP drum file on Unit 33.

Instructions for use:

1. Have both DTOTPE files positioned to the proper file on IUN1 and IUN2; then simply CALL TOTP. NUM will be returned and is the total number of records in the newly created SLAP drum file.

SUBROUTINE TPETOD (NUM)

This routine copies a tape of pre-sorted data from tape unit 10 and stores it on drum unit 33.

Restrictions: NUM $\geq$ 1

SUBROUTINE TPS (NUM, TMPMIN)

This routine reads NUM records from a drum file on unit 33, translates frequency counts to surface temperature, pressure, and wind speed; lists and plots all three types of data vs. time in days. Day 1 is taken to January 1, 1975.

The routine expects a nine-track Gould plot output tape to be assigned to tape unit 7.

The approximate minimum surface water temperature encountered by the buoy in ^{o}C must be entered in TMPMIN. Refer to Appendix B for the method used in determining the engineering units.

SUBROUTINE VCHECK (NUM, SPD)

This routine reads NUM logical records from drum unit 33; determines which fixes produce a velocity of greater than SPD, which is the maximum velocity parameter to be entered in knots ; deletes them from the drum file; and corrects NUM accordingly.

This routine computes distances for velocity computations as described in CVA.

A data card containing the deployment time, latitude, and longitude in 3F10.6 format is required for each buoy to be velocity checked.

SUBROUTINE VLOOK (NUM)

This routine computes and plots the cumulative frequency distribution function of velocities between 0 and 400 centimeters per second for a SLAP drum file containing NUM records. The plot is percent vs. velocity.

Instructions for use :

1. Assign a nine-track tape to unit A for the Gould output.

2. CALL VLOOK (NUM) where NUM is the number of fixes on the drum file.

SUBROUTINE VOLT (NUM)

This routine reads NUM records from a drum file on unit 33 and produces a plot of buoy sensor package voltage vs. time in days. Day 1 is taken to be January 1, 1975.

The routine expects a nine-track Gould plot output tape to be assigned for unit A.

5. ACKNOWLEDGMENTS

Card punching and program testing were done by Nancy Holsing. Ideas for many programs came from meetings with Drs. D.V. Hansen, A. Leetmaa and R. Molinari. All work was accomplished at the Atlantic Oceanographic and Meteorological Laboratories, Miami, utilizing a UNIVAC 1108 and PDP 11/40 computer. Mr. D. Pashinski has written two programs which, to

date, have not been incorporated in the package for converting sensor frequency counts to engineering units and outputting them to tape and cards. These routines accept data from the SLAP drum file described in the design section of this report.

6. REFERENCES

Bomford, G., (1971): Geodesy, Oxford, Clarendon Press.

Bowditch, N., (1962): American Practical Navigator, U. S. Govt. Printing Office.

Herman, A., and D. V. Hansen (1977): Objective Analysis of Lagrangian Trajectory Data. In Proceedings of the ACSM 37th Annual Meeting Washington, D. C. Feb. 27-March 5, pp. 177-185.

Herman, A., and Jacobson, R.S., (1975): FESTSA - A System for Time Series Analysis, NOAA, NOS, EDL, Rockville, MD.

Sodano, Emanuel M., (1963): General Non-iterative Solution of the Inverse and Direct Geodetic Problems. Presented at XIII IUGG General Assembly at Berkeley, California.

Tables for a Polyconic Projection of Maps (1946): Special Publication No. 5 (SP5), U. S. Department of Commerce Coast and Geodetic Survey.

Universal Transverse Mercator Grid (1958): Department of Army Technical Manual TM5-241-8, Headquarters, Department of the Army, July.

Appendix A

SLAP Example

Problem: 1) Extract all data for buoy 1174 from data base

2) Edit on basis of a 2-knot velocity

3) Smooth using weighted spline fit

4) Plot on Polyconic at $1:10^6$

Program including control cards:

```
@ N ASG A = PLOTTP.  This assigns a plot type.

@ ASG X   = SLAP, B = DATBSE.  This assigns the program
  and data based type.

@ XQT CUR.  This activates Exec II complex utility routine.

IN X  This loads SLAP

@ I for EXMPLE, EXMPLE.  Fortran compile card.

C Establish common work area

Common/Work/SER (13900)

C Call for a SORT.

Call  SORT (NUM)

C Perform a velocity edit

Call VCHECK (NUM, 2.)

C Complete objective analysis

Call  SMOOTH (NUM, DAT1, DAT2)

C Create plot tape with Polyconic overlay

Call MAP1  (NUM)

Stop

End

XQT EXMPLE

Data Cards
```

Appendix B

Determination of Sensor Values for Buoy Data collected by the Nimbus F Satellite

I. List of sensors

a. Sea surface temperature
b. Wind speed
c. Drogue tension
d. Buoy battery pack voltage

II. Raw Data

a. All data except for voltage are given as instantaneous readings from a modulus 256 counter. Sensor values are a linear function of the rate of change of the counter.

b. Voltages are linearly proportional to the sensor output.

c. Engineering Unit to digital sensor relationships

1. $T = 0.1083 * R-23.833$
   where: T = Temperature in degrees centigrade
   R = Sensor counter rate in counts per day.

2. $W = 0.37931 * RW$
   where: W = Wind speed in miles per hour
   RW = Sensor counter rate in counts per day.

3. $P = 1.3333 * RP-554.6666$
   where: P = Strain gauge pressure between drogue and buoy in pounds per square inch.

4. $V = vv * 0.085$
   where: V = Voltage
   vv = Sensor digital

III. Determination of sensor rate

a. The buoy transmits for one second out of each minute, so within a single orbit there will be many transmissions while the satellite is in range.

1. The first and last transmissions are apt to be incomplete or erroneous and are ignored in processing.

2. The amount of time between good transmissions of sensor information in a single orbit is too short to determine a rate of change, so a single count value is assigned to an orbit.

b. Selection of sensor count value is based on the following considerations:

1. It must be from within a series of slowly increasing counts.

2. The count cannot be such that the rate is determined by change since the previous values create improbable values.

3. The earliest sensor count in an orbit which satisfies the above criteria is selected as representative of the orbit.

Appendix C

Program Listings

```
.I ASV AOMLIO,AOMLIO                                                                    07 JUN 77
ASSEMBLED BY UNIVAC 1108 EXEC II ASSEMBLER   2404 0008A
THIS ASSEMBLY WAS DONE ON 07 JUN 77 AT 18:28:36
000001                                          . *  PROGRAM (CALLABLE BY FORTRAN) WHICH READS A TAPE IN
000002                                          . *  THE BUFFERED MODE AND RETURNS TO THE CALLER THE STATUS
000003                                          . *  (ERROR, ABNORMAL, OR NORMAL) OF THE READ IN ORDER THAT
000004                                          . *  THE CALLER MAY DETERMINE HIS OWN END ACTION.
000005                                          . ***************************************************
000006                                               REGNAM
000007                  000000000311            L201 EQU     0311
000008                  000000000016            U    EQU     016
000009                                          $(1) .
000010                                          AOMLIO* .
000011    01    000000  06 00 13 00 0 000000         S       X11,STATAD
000012          000001  27 00 14 13 1 000000         L       A0,*0),X11      . LOGICAL UNIT
000013          000002  73 02 00 00 0 000036         SSL     A0,30
000014          000003  06 01 14 00 0 000011         S,H2    A0,RD1
000015          000004  27 00 14 13 0 000001         L       A0,1,X11        . BLOCK ADDRESS
000016          000005  06 01 14 00 0 000012         S,H2    A0,RD1+1
000017          000006  27 00 14 13 1 000002         L       A0,*2,X11       . NO. WORDS
000018          000007  06 02 14 00 0 000012         S,H1    A0,RD1+1
000019          000010  74 13 13 00 0 001047         LMJ     X11,TRFS        . READ TAPE
000020          000011  000021 000000          RD1    +       ENDA,0          . END ACTION, UNIT
000021          000012  000000 000000                 +       0,0             . WORD COUNT ,ADDRESS
000022          000013  27 00 13 00 0 000000         L       X11,STATAD
000023          000014  71 13 00 13 0 000003         DL      A0,3,X11        . STATUS WD. ADDRESS
000024          000015  71 12 00 00 0 000000         DS      A0,STATAD       . SAVE
000025          000016  11 16 00 00 0 000001         LN,M    A0,1
000026          000017  06 00 14 13 1 000003         S       A0,*3,X11       . SET BUSY
000027          000020  74 04 00 13 0 000006         J       6,X11           . RETURN
000028                                          ENDA .
000029          000021  42 00 01 00 0 000002         AND     A1,(0777777)    .
000030          000022  25 01 16 00 0 000012         AN,H2   A2,RD1+1        . STARTING ADDR.
000031          000023  06 02 16 00 1 000001         S,H1    A2,*STATAD+1    . NO. WDS. READ
000032          000024  06 00 16 00 1 000000         S       A2,*STATAD      . NTRAN STATUS
000033          000025  27 01 15 00 0 000311         L,H2    A1,L201         . READ STATUS WORD
000034          000026  06 01 15 00 1 000001         S,H2    A1,*STATAD+1    . IN RIGHT HALF
000035          000027  50 00 00 00 0 000014         TZ      A0              .
000036          000030  74 04 00 00 0 000042         J       NOTN            .
000037          000031  53 16 01 00 0 000020         TNE,U   A1,020          . NORMAL READ
000038          000032  74 04 00 13 0 000000         J       0,X11           . YES
000039          000033  73 02 01 00 0 000016         SSL     A1,14           . EOT
000040          000034  74 11 01 00 0 000041         JB   A1,EOF             . YES
000041          000035  73 02 01 00 0 000001         SSL     A1,1            . EOF
000042          000036  74 11 01 00 0 000041         JB   A1,EOF             . YES
000043          000037  27 16 14 00 0 000003         L,U     A0,3            . ERROR
000044          000040  74 04 00 00 0 000042         J       NOTN            .
000045          000041  27 16 14 00 0 000002   EOF   L,U     A0,2            . EOF/EOT
000046          000042  02 00 00 00 1 000000   NOTN  SN      A0,*STATAD      . NTRAN STATUS
000047          000043  74 04 00 13 0 000000         J       0,X11           ..RETURN
000048                                          $(0) .
000049    00    000000                          STATAD       RES    2
000050                                               END  .
              000002  000000777777
```

```
@ ELT AV,1,761122, 49109

000001                  FUNCTION AV(X,N)
000002                  DIMENSION X(1)
000003                  Y=0.
000004                  DO 10 I=1,N
000005               10 Y= Y+X(I)
000006                  AV= Y/N
000007                  RETURN
000008                  END
```

```
. ELT BEST,1,76120), 424 5

000001                  SUBROUTINE BEST(A,B,Y,X,I)
000002                  DIMENSION A(1),B(1)
000003                  IC=2
000004                  DC=256.
000005                  DO 10 J=2,I
000006                  IF((A(J)-A(J-1)).GE.DC) GO TO 10
000007                  IC=J
000008                  DC=A(J)-A(J-1)
000009               10 CONTINUE
000010                  X=B(J)
000011                  Y=A(J)
000012                  RETURN
000013                  END
```

```
@ ELT CDC,1,761209, 42390

000001                COMPILER (FLD=L)
000002                FUNCTION CDC(K,J)
000003                  DOUBLE PRECISION RMAN
000004                INTEGER COMP,BIAS
000005                DATA COMP/0000077777777/,BIAS/0000000002000/
000006                IS=0
000007                FLD(35,1,IS)=FLD(12,1,K)
000008                IF(IS.EQ.0) GO TO 10
000009                K=COMP-K
000010                J=COMP-J
000011              10 FLD(25,11,IEXP)=FLD(13,11,K)
000012                IF(IEXP.LT.BIAS) GO TO 11
000013                IEXP=IEXP-BIAS
000014                FLD(1,12,MAN)=FLD(24,12,K)
000015                FLD(13,23,MAN)=FLD(12,23,J)
000016                RMAN=MAN
000017                RMAN=RMAN/2**35
000018                X=RMAN*2.**IEXP
000019                IF(IS.EQ.1) X=X*-1.
000020                GO TO 12
000021              11 IEXP=BIAS-IEXP+1
000022                FLD(1,12,MAN)=FLD(24,12,K)
000023                FLD(13,23,MAN)=FLD(12,23,J)
000024                RMAN=MAN
000025                RMAN=RMAN/2**35
000026                X=RMAN/(2**IEXP)
000027              12 CDC=X
000028                RETURN
000029                END
```

```
@ ELT CLEAR,1,751023, 60477

000001                  SUBROUTINE CLEAR(DAT)
000002                  DIMENSION DAT(109,100)
000003                  DO 10 I=1,109
000004                  DO 10 J=1,100
000005               10 DAT(I,J)=0.0
000006                  RETURN
000007                  END
```

```
» ELF COPI,1,770607, 656 8

000001                  COMPILER(FLD=EL)
000002                  DIMENSION A(5000)
000003              100 CALL AGBLIO('A',A,5000,L,*)
000004                1 IF(L.EQ.(-1)) GO TO 1
000005                  IF(L.EQ.(-2)) CALL EOF
000006                  IF(L.EQ.(-2)) GO TO 100
000007                  CALL GTSIZ(K,L)
000008                  CALL NTRAN(8,22)
000009                  CALL NTRAN(8,1,L,A,N)
000010                2 IF(N.EQ.(-1)) GO TO 2
000011                  GO TO 100
000012                  END
```

```
⍵ ELT CRONO,1,761122, 49115

000001                SUBROUTINE CRONO(ICT)
000002                DIMENSION ISRT(1000),DAT(139),DAYS(1000)
000003                COMMON/ HY/IV
000004                LOGICAL MOVE
000005                IVD=ICT
000006                DO 1 I=1,1000
000007              1 ISRT(I)=0
000008                REWIND 33
000009                DO 2 I=1,ICT
000010                READ(33)DAT
000011              2 DAYS(I)=DAT(13)
000012                DAYMIN=0.
000013                DAYMAX=999999.
000014                DO 10 I=1,ICT
000015                DO 11 J=1,ICT
000016                IF(DAYS(J).GT.DAYMIN.AND.DAYS(J).LT.DAYMAX)ISRT(I)=J
000017                IF(DAYS(J).GT.DAYMIN.AND.DAYS(J).LT.DAYMAX)DAYMAX=DAYS(J)
000018             11 CONTINUE
000019                DAYMIN=DAYMAX
000020             10 DAYMAX=999999.
000021                DO 12 I=1,ICT
000022                J=I
000023                IF(ISRT(I).EQ.0)GO TO 13
000024             12 CONTINUE
000025             13 ICT=J-1
000026                PRINT 51,(I,DAYS(I),I=1,IVD)
000027                PRINT 50,(I,ISRT(I),I=1,ICT)
000028             51 FORMAT(3(1X,I4,F7.2)     )
000029             50 FORMAT(10(1X,I4,I6))
000030                REWIND 33
000031                L=1
000032                DO 14 I=1,IVD
000033                READ(33)DAT
000034                MOVE=.FALSE.
000035             70 DO 20 J=1,ICT
000036                IF(ISRT(J).EQ.L)  K= J
000037                IF(ISRT(J).EQ.L)   MOVE=.TRUE.
000038                IF(ISRT(J).EQ.L) GO TO 21
000039             20 CONTINUE
000040                L=L+1
000041                IF(L.GT.IVD) GO TO 900
000042                IF(.NOT.MOVE)  GO TO 14
000043                MOVE=.FALSE.
000044             21 LOC=(K-1)*139+500000
000045                CALL NTRAN(1,22)
000046                CALL DMRITE(LOC,139,DAT)
000047                CALL NTRAN(1,22)
000048                L=L+1
000049                IF(L.GT.IVD) GO TO 900
000050             14 CONTINUE
000051            900 CONTINUE
000052                REWIND 33
000053                L=L-1
000054                LOC=500000
```

```
000055                  KILL=0
000056                  DO 16 I=1,17
000057                  CALL READ(LOC,139,DAT)
000058                  CALL BTRAN(1,2,2)
000059                  LOC=LOC+139
000060                  IF(IBIT( DAT(1)),L,IC) WRITE(33) DAT
000061                  IF(IBIT(DAT(1)),L,IC) KILL=KILL+1
000062               16 CONTINUE
000063                  ICT=KILL
000064                  PRINT 800,KILL
000065              800 FORMAT(1X,'KILL=',I10)
000066                  REWIND 33
000067                  RETURN
000068                  END
```

```
$ ELT CVA,1,7706,7, 6649 /

001                SUBROUTINE CVA( 63)
002          C
003          C     GIVES PLOTS OF COMPOLENT VELOCITIES AND ACCELERATIONS IN UNITS OF
004          C      CM/SEC AND CM/SEC/SEC VS TIME IN DAYS
005          C
006                COMMON/WORK/SER(3761),DAT(130),XLAT(1000),XLON(1000),VE(1000),
007               *VN(1000),AE(1000),AN(1000),T(1000),TT(1000),TIME(1000)
008                IF(NUM.GT.998) STOP 2
009                REWIND 63
010                DO 10 I=1,NUM
011                READ (63) DAT
012                IF(DAT(4).LT.180.) DAT(4)=DAT(4)*(-1.)
013                IF(DAT(4).GE.180.) DAT(4)=360.0-DAT(4)
014                XLAT(I)=DAT(3)*0.01745329
015                XLON(I)=DAT(4)*0.01745329
016             10 TIME(I)=DAT(13)*1440.
017                N=NUM-1
018                DO 11 I=1,N
019                T(I)=(TIME(I+1)+TIME(I))/2.
020                CALL SPEED(XLAT(I),XLON(I),XLAT(I+1),XLON(I+1),TIME(I),TIME(I+1),
021               *D4,D5,D6,VE(I),VN(I),D3)
022             11 CONTINUE
023             30 FORMAT(1X,12F10.3)
024                T0=T(1)
025                DO 25 J=1,N
026             25 T(J)=T(J)-T0
027                DO 1 I=1,N
028                T(I)=T(I)/1440.
029                VE(I)=VE(I)*1.666667
030              1 VN(I)=VN(I)*1.666667
031                PRINT 30,(T(K),VE(K),VN(K),K=1,N)
032                NN=N-1
033                DO 20 I=1,NN
034                TT(I)=((T(I+1)+T(I))/2.)-(T(2)/2.)
035                AE(I)=(VE(I+1)-VE(I))/(T(I+1)-T(I))
036             20 AN(I)=(VN(I+1)-VN(I))/(T(I+1)-T(I))
037                PRINT 30,(TT(K),AE(K),AN(K),K=1,NN )
038                CALL SETOVR
039                CALL PLOTS(-45.,-10.,1)
040                CALL SCALE  (T,8.,N,1)
041                CALL SCALE  (TT,8.,NN,1)
042                CALL SCALE  (VE,8.,N,1)
043                CALL SCALE  (VN,8.,N,1)
044                CALL SCALE  (AN,8.,NN,1)
045                CALL SCALE  (AE,8.,NN,1)
046                CALL PLOT(1.,1.,-3)
047                CALL AXIS(0.,0.,12HTIME IN DAYS,-12,15.,0.,T(N+1),T(N+2))
048                CALL AXIS(0.,0.,14HEVEL IN CM/SEC,14,8.,90.,VE(N+1),VE(N+2))
049                CALL LINE(T,VE,N,1,1,3)
050                CALL PLOT(0.,0.,3)
051                CALL PLOT(16.5,0.,-3)
052                CALL AXIS(0.,0.,12HTIME IN DAYS,-12,15.,0.,T(N+1),T(N+2))
053                CALL AXIS(0.,0.,14HNVEL IN CM/SEC,14,8.,90.,VN(N+1),VN(N+2))
054                CALL LINE(T,VN,N,1,1,3)
```

```
0055                CALL PLOT (0.,3.,3)
0056                CALL PLOT (11.,0.,-3)
0057                CALL AXIS(0.,0.,'TIME IN DAYS',-12,8.,0.,TT(NN+1),TT(NN+2))
0058                CALL AXIS(0.,0.,'ACCELERATION IN CM/SEC/SEC',26,8.,90.,AE(NN+1),AE
0059               *(NN+2))
0060                CALL LINE (TT,AE,NN,1,1,3)
0061                CALL PLOT (0.,0.,-3)
0062                CALL PLOT (11.,0.,-3)
0063                CALL AXIS(0.,0.,'TIME IN DAYS',-12,8.,0.,TT(NN+1),TT(NN+2))
0064                CALL AXIS(0.,0.,'ACCELERATION IN CM/SEC/SEC',26,8.,90.,AN(NN+1),AN
0065               *(NN+2))
0066                CALL LINE (TT,AN,NN,1,1,3)
0067                CALL PLOT(0.,0.,999)
0068                CALL BITSET
0069                REWIND 33
0070                RETURN
0071                END
```

```
N ELT DEG,1,760126, 5152.

000001                SUBROUTINE DEG(A,IDG,IMIN,SEC)
000002          C     A IS IN DECIMAL DEGREES
000003                IDG=A
000004                ZMIN=(A-IDG)*60.
000005                IMIN=ZMIN
000006                SEC=(ZMIN-IMIN)*60.
000007                RETURN
000008                END
```

```
@ ELT DSTAT,1,770113, 32795

001                SUBROUTINE DSTAT (NUM)
002          C
003          C      GIVES STATISTICS ON POSITIONS USING THE UTM ROUTINE TO CALCULATE
004          C      THE POSITIONS IN METERS AND DOES STATS USING FESTSA PACKAGE
005          C
006                COMMON/WORK/E(1000),Y(1000),IZ(1000),DAT(139),SER(10361)
007                DATA A/6378206.4 /  ,B/6356583.8/
008                DO 10 I=1,NUM
009                READ(33) DAT
010                IZ(I)=DAT(4)/6.+30.
011                IF(DAT(4).GE.180.) IZ(I)=(DAT(4)-180.)/6.+1
012                IF(DAT(4).LT.180.) DAT(4)=DAT(4)*(-1.)
013                IF(DAT(4).GE.180.) DAT(4)=360.-DAT(4)
014                 XLAT=DAT(3)*0.01745329
015                 XLON=DAT(4)*0.01745329
016                Z=IZ(I)
017                CALL UTM(A,B,XLAT,XLON,Z,Y(I),E(I))
018             10 CONTINUE
019                FY=XMIN(Y,NUM)
020                DO 11 I=1,NUM
021             11 Y(I)=Y(I)-FY
022                CALL NISHUL
023                CALL STRSR1(1,1,1,NUM,0.,1.)
024                CALL STRSR1(2,1,1001,NUM,0.,1.)
025                CALL SMEAN(1,1,3,1)
026                CALL SMEAN(2,1,4,1)
027                CALL STATS(3,1,50,1000.,R,S,T,U)
028                CALL STATS(4,1,50,1000.,R,S,T,U)
029                N=NUM-2
030                CALL CORLAT(1,1,-1,0,2,2,N,0)
031                CALL PLOT1(2,2,1,0,1,2,0,0)
032                CALL CORLAT(2,1,-1,0,1,2,N,0)
033                CALL PLOT1(1,2,1,0,1,2,0,0)
034                RETURN
035                END
```

```
@ ELT,O DTOTPE,1,7,1,6,15, 21570

000001                  SUBROUTINE DTOTPE(NUM)
000002            C     THIS PUTS ANY TYPE OF SORT DATA OUT ONTO A 7 TRACK TAPE
000003                  COMMON/ WORK/DAT(139)
000004                  WRITE(11)NUM
000005                  REWIND 33
000006                  DO 10 I=1,NUM
000007                  READ (33) DAT
000008                  WRITE(11)DAT
000009               10 CONTINUE
000010                  REWIND 33
000011                  RETURN
000012                  END
```

```
@I ASM DIO,DIO,DIO/FEB23                                                    . DIO  1                    07 JUN 77          18:28:38.115
ASSEMBLED BY UNIVAC 1108 EXEC II ASSEMBLER   2404 0008A
THIS ASSEMBLY WAS DONE ON 07 JUN 77 AT 18:28:38
000001                                  . DIO, 1108 DRUM INPUT AND OUTPUT SUBROUTINES                                   . DIO  2
000002                                  . CODED IN FEB 1973 BY D J JOHNSON GFDL PRINCETON                               . DIO  3
000003                                  . SUBROUTINES DREAD AND DWRITE TRANSFER BLOCKS BETWEEN CENTRAL MEMORY            . DIO  4
000004                                  . AND DRUMS TREATED AS A SINGLE VERY LONG ARRAY.  THE TRANSFER MAY BE           . DIO  5
000005                                  . NON-OVERLAPPED OR COMPUTATION OVERLAPPED, IN WHICH CASE SUBROUTINE             . DIO  6
000006                                  . DCHECK VERIFIES PROPER TRANSMISSION.                                          . DIO  7
000007                                          REGNAM                                                                  . DIO  8
000008                                  $(1)%                                                                           . DIO  9
000009                                  DWRITE*. (DRUM ADDRESS,NUM,ARRAY [,STATUS])                                     . DIO 10
000010    01    000000  23 00 01 00 0 000075          LR      R1,(*)DWRITE*)                                            . DIO 11
000011          000001  10 16 02 00 0 000000          LA,14   A2,ONE                  . ONE FOR WRITE                   . DIO 12
000012          000002  74 04 00 00 0 000005          J       IO                                                        . DIO 13
000013                                  DREAD* . (DRUM ADDRESS,NUM,ARRAY [,STATUS])                                     . DIO 14
000014          000003  23 00 01 00 0 000076          LR      R1,(* DREAD*)                                             . DIO 15
000015          000004  10 16 02 00 0 000001          LA,14   A2,TWO                  . TWO FOR READ                    . DIO 16
000016          000005  06 00 16 00 0 000054  IO      S       A2,CALL+5               . OPERATION 1 OR 2                . DIO 17
000017          000006  04 00 01 00 0 000146          SR      R1,LINK                 . STORE NAME FOR ERROR MSG        . DIO 18
000018          000007  06 01 13 00 0 000147          SX,1    B11,LINK+1              . SAVE RETURN REGISTER            . DIO 19
000019          000010  71 13 00 13 0 000001          DL      A0,1,B11                . NUM OF WORDS AND ARRAY          . DIO 20
000020          000011  71 12 00 00 0 000055          DS      A0,CALL+6                                                 . DIO 21
000021          000012  54 02 01 00 0 000766          TLE,2   A1,0766         . CHECK FOR BAD ARRAY ADDRESS             . DIO 22
000022          000013  74 04 00 00 0 000136          J       LOWERR                                                    . DIO 23
000023          000014  25 16 15 00 0 000001          AN,14   A1,1             . SUBTRACT ONE                            . DIO 24
000024          000015  24 00 15 13 1 000001          A       A1,*1,B11       . ADD NUM WORDS                           . DIO 25
000025          000016  55 01 01 00 0 000766          TG,1    A1,0766         . 0766 CONTAINS UPPER LIMIT OF USERS CORE  . DIO 26
000026          000017  74 04 00 00 0 000123          J       MEMERR          . JUMP TO MEM SIZE ERROR                  . DIO 27
000027 U        000020  27 00 17 00 0 000001  OK      L       A3,NTAB$+1              . LOAD ADDRESS OF DRUM1 TABLE     . DIO 28
000028          000021  10 00 04 17 0 000001          L       A4,1,A3                 . LOAD LENGTH OF DRUM 1           . DIO 29
000029          000022  01 00 04 17 0 000003          S       A4,3,A3                 . FAKE ADDRESS OF LAST WRITE      . DIO 30
000030          000023  27 00 15 13 1 000000          L       A1,*0,B11               . GET DRUM ADDRESS                . DIO 31
000031          000024  70 00 15 00 0 000032          JGD     A1,NEXT         . SUBTRACT 1 AND TEST FOR POSITIVE        . DIO 32
000032          000025  27 00 14 00 0 000146  ADDERR  L       A0,LINK                                                   . DIO 33
000033          000026  06 00 14 00 0 000007          S       A0,MSG1                                                   . DIO 34
000034          000027  74 13 13 00 0 001026          PSRINT MSG1,7,1                                                   . DIO 35
                000030  0001 07 000007
000035          000031  74 04 00 00 0 000143          J       BOOBOO                                                    . DIO 36
000036          000032  06 00 15 00 0 000006  NEXT    S       A1,ADDR         . STORE NUMBER OF WORDS TO SKIP ON DRUM    . DIO 37
000037          000033  15 00 04 17 0 000000          AN      A4,0,A3         .SUBTRACT START ADDRESS OF DRUM           . DIO 38
000038          000034  15 00 04 00 0 000015          AN      A4,21           . SUBTRACT NUM OF WORDS TO SKIP           . DIO 39
000039          000035  15 00 04 14 0 000000          AN      A4,0,A0         . SUBTRACT LENGTH OF RECORD               . DIO 40
000040          000036  74 03 04 00 0 000025          JN      A4,ADDERR       . UPPER LIMIT DRUM ADDRESS ERROR          . DIO 41
000041          000037  27 00 16 13 0 000004          L       A2,4,B11                . LOAD CALLING PROGRAMS LINKAGE   . DIO 42
000042          000040  06 00 16 00 0 000060          S       A2,LNKAGE       .                                         . DIO 43
000043          000041  27 00 15 13 0 000003          L       A1,3,B11        . LOAD STATUS WORD OR LINKAGE             . DIO 44
000044          000042  51 07 00 13 0 000003          TNZ,7   3,B11           . TEST FOR LINKAGE                        . DIO 45
000045          000043  74 04 00 00 0 000046          J       STAT            . NOT LINKAGE WORD MUST BE STATUS WORD    . DIO 46
000046          000044  06 00 15 00 0 000060          S       A1,LNKAGE       . STORE LINKAGE WORD                      . DIO 47
000047          000045  27 16 15 00 0 000005          L,14    A1,STATUS       . USE INTERNAL STATUS WORD                . DIO 48
000048          000046  06 00 15 00 0 000057  STAT    S       A1,CALL+8       . FILL IN ADDRESS OF STATUS WORD          . DIO 49
000049 U        000047  74 13 13 00 0 000000  CALL    LMJ     B11,NTRAN                                                 . DIO 50
000050          000050  000000000000                  +       ONE                     . UNIT                            . DIO 51
000051          000051  000000000003                  +       TEN                     . REWIND                          . DIO 52
000052          000052  000000000002                  +       SIX                     . SKIP                            . DIO 53
000053          000053  000000000006                  +       ADDR                                                      . DIO 54
000054          000054  000000000000                  +       $-$                     . READ 2 OR WRITE 1               . DIO 55
```

```
000055          000055  000000000000                    +       $-1                     . NUM OF WORDS                  . DIO 56
000056          000056  000000000000                    +       $-1                     . ARRAY                         . DIO 57
000057          000057  000000000000                    +       $-1                     . STATUS WORD                   . DIO 58
000058          000060  000000000000            LNKAGE  +       $-1                     . LINK                          . DIO 59
000059          000061  27 00 13 00 0 000147             LX      B11,LINK+1      . RESTORE B11                   . DIO 60
000060          000062  51 07 00 13 0 000003             TNZ,7   3,B11           . TEST FOR LINKAGE              . DIO 61
000061          000063  74 04 00 13 0 000005             J       5,B11                                           . DIO 62
000062          000064  27 00 15 00 0 000057             L       A1,CALL+8       . LOAD ADDRESS OF STATUS WORD   . DIO 63
000063          000065  27 00 16 13 0 000001             L       A2,1,B11        . LOAD ADDRESS OF NUM WORDS     . DIO 64
000064          000066  72 01 00 00 0 000076             SLJ     CHECK                                           . DIO 65
000065          000067  74 04 00 13 0 000004             J       4,B11                                           . DIO 66
000066                                          DCHECK*, (STATUS,NUM WORDS)                                     . DIO 67
000067          000070  23 00 01 00 0 000077             LR      R1,(*DCHECK*)                                   . DIO 68
000068          000071  04 00 01 00 0 000146             SR      R1,LINK                                         . DIO 69
000069          000072  06 01 13 00 0 000147             SX,1    B11,LINK+1                                      . DIO 70
000070          000073  71 13 01 13 0 000000             DL      A1,0,B11        . LOAD ADDRESSES OF STATUS AND NUM WORDS . DIO 71
000071          000074  72 01 00 00 0 000076             SLJ     CHECK                                           . DIO 72
000072          000075  74 04 00 13 0 000003             J       3,B11                                           . DIO 73
000073          000076  74 04 00 00 0 000000     CHECK   J       $-$             . A1 AND A2 MUST BE LOADED BEFORE SLJ CHECK. DIO 74
000074          000077  23 00 03 00 0 000100             LR      R3,(33333333)           . LOOP FOR MAX 100 SECONDS . DIO 75
000075          000100  27 00 14 15 0 000000             L       A0,0,A1                                         . DIO 76
000076          000101  53 17 00 00 3 177776             TNE,15  A0,*-1,*0               . -1 TEST               . DIO 77
000077          000102  70 04 03 00 0 000100             JGD     R3,$-2                  . LOOP TIL NOT -1       . DIO 78
000078          000103  53 00 00 16 0 000000             TNE     A0,0,A2                 . IS IT EQUAL TO NUM WORDS . DIO 79
000079          000104  74 04 00 00 1 000076             J       *CHECK          . YES RETURN                    . DIO 80
000080          000105  06 00 14 00 0 000150             S       A0,LINK+2       . NO SAVE STATUS                . DIO 81
000081          000106  23 00 01 00 0 000146             L       R1,LINK         . PICK UP ROUTINE NAME          . DIO 82
000082          000107  04 00 01 00 0 000016             S       R1,MSG2         . AND STORE IT IN MSG2          . DIO 83
000083          000110  74 13 13 00 0 001026             P$RINT  MSG2,7,1                                        . DIO 84
                000111  0001 07 000016
000084 U        000112  27 00 17 00 0 000001             L       A3,NTAB$+1      . PICKUP DRUM1 TABLE ADDRESS    . DIO 85
000085          000113  27 00 14 17 0 000002             L       A0,2,A3         . PICKOUT CURRENT POSITION      . DIO 86
000086          000114  74 13 13 00 0 001063             E$BO    25,MSG3,12      . STORE IN OCTAL FOR MSG3       . DIO 87
                000115  14 0000 000031
000087          000116  74 13 13 00 0 001026             P$RINT  MSG3,5,1                                        . DIO 88
                000117  0001 05 000025
000088          000120  74 13 13 00 0 001032             K$TYPE  MSG3,25                                         . DIO 89
                000121  00 0031 000025
000089          000122  74 04 00 00 0 000143             J       BOOBOO                                          . DIO 90
000090          000123  06 00 15 00 0 000150     MEMERR  S       A1,LINK+2       . SAVE FOR PANIC CALL           . DIO 91
000091          000124  52 01 01 00 0 000766             TE,1    A1,0766         . TEST FOR EXEC 2 LAST WORD ERROR . DIO 92
000092          000125  74 04 00 00 0 000133             J       EXCESS          . NOT BUG , REAL ERROR          . DIO 93
000093          000126  52 16 02 00 0 000001             TE,14   A2,TWO          . IS IT A READ                  . DIO 94
000094          000127  74 04 00 00 0 000020             J       OK              . NO , FINISH WRITE OPERATION   . DIO 95
000095          000130  74 13 13 00 0 001026             P$RINT  MSG4,12,1                                       . DIO 96
                000131  0001 14 000032
000096          000132  74 04 00 00 0 000143             J       BOOBOO                                          . DIO 97
000097          000133  74 13 13 00 0 001026     EXCESS  P$RINT  MSG5,12,1                                       . DIO 98
                000134  0001 14 000046
000098          000135  74 04 00 00 0 000143             J       BOOBOO                                          . DIO 99
000099          000136  06 00 15 00 0 000150     LOWERR  S       A1,LINK+2                                       . DIO100
000100          000137  23 00 01 00 0 000146             L       R1,LINK                                         . DIO101
000101          000140  04 00 01 00 0 000062             S       R1,MSG6                                         . DIO102
000102          000141  74 13 13 00 0 001026             P$RINT  MSG6,10,1                                       . DIO103
                000142  0001 12 000062
000103          000143  27 00 13 00 0 000147     BOOBOO  L       B11,LINK+1                                      . DIO104
000104          000144  27 00 14 00 0 000150             L       A0,LINK+2                                       . DIO105
000105 U        000145  74 04 00 00 0 000000             J       PANIC                                           . DIO106
```

```
000106          000146  112732221624        LINK    'DRUMIO'                                        . DIO107
000107          000147  000157 000000               +       111,$-$                                 . DIO108
000108          000150  000000000000               +       $-1                                     . DIO109
000109          000151  000000000000               +       $-$                                     . DIO110
000110                                      $(0)%                                                   . DIO111
000111      00  000000  000000000001      ONE     + 1                                             . DIO112
000112          000001  000000000002      TWO     + 2                                             . DIO113
000113          000002  000000000006      SIX     + 6                                             . DIO114
000114          000003  000000000012      TEN     + 10                                            . DIO115
000115          000004  000000000026      TWETWO  + 22                                            . DIO116
000116          000005                    STATUS  RES   1                                         . DIO117
000117          000006  000000000000      ADDR    $-$                                             . DIO118
000118          000007  050505050505      MSG1    '       ERROR, DRUM ADDRESS OUT OF RANGE'       . DIO119
                000010  051227272427
                000011  560511273222
                000012  050511112712
                000013  300005243231
                000014  052413052706
                000015  231412050505
000119          000016  050505050505      MSG2    '       ERROR, NTRAN STATUS IN REGISTER A0 '    . DIO120
                000017  051227272427
                000020  560523312706
                000021  230530310631
                000022  323005162305
                000023  271214163031
                000024  122705066005
000120          000025  051127322205      MSG3    ' DRUM FAULT?                                   . DIO121
                000026  130652213154
                000027  050505050505
                000030  050505050505
                000031  050505050505
000121          000032  050605073214      MSG4 ' A BUG IN EXEC 2 WONT ALLOW READING INTO THE LAST WORD OF USER CORE'   122
                000033  051625051235
                000034  121005620534
                000035  242331050621
                000036  212434052712
                000037  061116231405
                000040  162331240531
                000041  151205210630
                000042  310534242711
                000043  052413053230
                000044  122705102427
                000045  120505050505
000122          000046  311512050611      MSG5 'THE ADDRESS OF YOUR ARRAY PLUS NUM WORDS EXCEEDS USER CORE , SEE A0'   123
                000047  112712303005
                000050  241305362432
                000051  270506272706
                000052  360525213230
                000053  052332220534
                000054  242711300512
                000055  351012121130
                000056  053236122705
                000057  162427120556
                000060  053012120506
                000061  600505050505
000123          000062  050505050505      MSG6 '       ERROR, YOUR ARRAY ADDRESS IS LESS THAN USER CORE LIMIT'    . DIO124
                000063  051227272427
                000064  560536243227
```

```
000065  050627270636
000066  050511112712
000067  302305163005
000070  211236300531
000071  150623053230
000072  122705102427
000073  120521162216
000074  310505050505

000075  113427163112
000076  051127120611
000077  111015121020
000100  000177120125
```

END.

SLEUTH CARD

```
PANIC
.TRAN
NTAB$
```

NO END CARD

ERRS IN ELEMENT PRODUCED

```
w ELI EOF,1,77B1,S, 36/54

000001                  SUBROUTINE EOF
000002                  CALL INTRAN(8,22)
000003                  CALL INTRAN(8,9)
000004                  CALL INTRAN(8,22)
000005                  RETURN
000006                  END
```

```
$ ELT FWDGP,1,760412, 48048

000001                SUBROUTINE FWDGP (     ZLAR,ZLOR,AZR,DIST,BR,ZL2,BACAZ)
000002                A=6378206.4
000003                B=6356583.8
000004                   ZDE=1.0E-48
000005                IF (ZA-A+ZB-B) 2600,2700,2600
000006           2600 E2=1.0-((B*B)/(A*A))
000007                F=1.0-B/A
000008                ZA=A
000009                ZB=B
000010           2700 TNB1= (B *SIN (ZLAR))/(A * COS (ZLAR))
000011                B1 = ATAN (TNB1)
000012                COAZ = COS (AZR)
000013                SIB1=SIN (B1) +ZDE
000014                COB1=COS (B1)
000015                TNO1 =   COB1   *   COAZ    / SIB1
000016                COBO =   COB1    *SIN   (AZR)
000017                THETA  = ATAN (TNO1)
000018                DENOM  = COS  (THETA)  *  COBO
000019                IF (DENOM )  3200, 3100,  3200
000020           3100 DENOM = 0.1E-48
000021           3200 TLAM1  =  SIN  (THETA) / DENOM
000022                ZLM1   = ATAN  (TLAM1)
000023                ZLAMA=ABS(ZLM1)
000024                IF(TLAM1) 3400,3600,4100
000025           3400 IF (DENOM) 3500,3600,3700
000026           3500 ZLAM1=3.1415926536-ZLAMA
000027                GO TO 4300
000028           3600 STOP
000029           3700 ZLAM1=6.2831853071-ZLAMA
000030                GO TO 4300
000031           3800 IF(DENOM) 3900,3600,4000
000032           3900 ZLAM1=3.1415926536
000033                GO TO 4300
000034           4000 ZLAM1=0.
000035                GO TO 4300
000036           4100 IF(DENOM) 4200,3600,4250
000037           4200 ZLAM1=3.1415926536+ZLAMA
000038                GO TO 4300
000039           4250 ZLAM1=ZLAMA
000040           4300 COSGB=COBO*COBO
000041                SISGB=1.0-COSGB
000042                ROOT= SQRT(SISGB)
000043                SI2B=SISGB/(1.0-(E2*COSGB))
000044                ZK2=E2*SI2B
000045                ROOT1=SQRT(1.0-ZK2)
000046                ZK1=(1.0-ROOT1)/(1.0+ROOT1)
000047                TODEL=(2.0*THETA)+(ZK1*SIN(2.0*THETA))
000048               1-(((ZK1**2)*SIN(4.0*THETA))/8.0)
000049                DEL1=(DIST*(1.0-ZK1))/(B*(1.0+(.25*ZK1**2)))
000050                TOT=TODEL+DELT
000051                F1=ZK1-((9.0/16.0)*ZK1**3)
000052                F2=(5.0*(ZK1**2))/8.0
000053                F3=(29.0/48.0)*ZK1**3
000054                DTHET=DELT-(F1*COS(TOT)*SIN(DELT))
```

```
000055                1+(F2*COS(2.0*TOT)*SIN(2.0*DELT))
000056                1 - (F3*COS(3.0*TOT) * SIN(3.0*DELT))
000057                 THET2=THETA+DTHET
000058                 IF(ZLAR) 4350,4375,4375
000059           4350 ROOT=-1.0*ROOT
000060           4375 SIB2=ROOT*COS(THET2)
000061                 BCOS=B*SQRT(1.0-(SIB2*SIB2))+ZDE
000062                 TNB2=(A*SIB2)/BCOS
000063                 B2= ATAN(TNB2)
000064                 DEN=-1.0*ROOT*SIN(THET2)+ZDE
000065                 TAZ21=(-1.0*COBO)/DEN
000066                 AZ21=ATAN(TAZ21)
000067                 AZ21=ABS(AZ21)
000068                 IF(TAZ21) 4201,4600,5000
000069           4201 IF(DEN) 4301,4400,4500
000070           4301 BACAZ=3.141592653G-AZ21
000071                 GO TO 5400
000072           4400 STOP
000073           4500 BACAZ=6.2831853071-AZ21
000074                 GO TO 5400
000075           4600 IF(DEN) 4700,4400,4900
000076           4700 BACAZ=3.141592653G
000077                 GO TO 5400
000078           4900 BACAZ=0.
000079                 GO TO 5400
000080           5000 IF(DEN) 5100,4400,5300
000081           5100 BACAZ=3.141592653G+AZ21
000082                 GO TO 5400
000083           5300 BACAZ=AZ21
000084           5400 DLAM2=COBO*COS(THET2)+ZDE
000085                 TLAM2=SIN(THET2)/DLAM2
000086                 ZLAM2=ATAN(TLAM2)
000087                 ZLAM2=ABS(ZLAM2)
000088                 IF(TLAM2) 5700,6100,6500
000089           5700 IF(DLAM2) 5800,5900,6000
000090           5800 TOLAM=3.1415926536-ZLAM2
000091                 GO TO 6900
000092           5900 STOP
000093           6000 TOLAM=6.2831853071-ZLAM2
000094                 GO TO 6900
000095           6100 IF(DLAM2) 6200,5900,6400
000096           6200 TOLAM=3.1415926536
000097                 GO TO 6900
000098           6400 TOLAM=0.
000099                 GO TO 6900
000100           6500 IF(DLAM2) 6600,5900,6800
000101           6600 TOLAM=3.141592653G+ZLAM2
000102                 GO TO 6900
000103           6800 TOLAM=ZLAM2
000104           6900 TWOOT=THETA+THET2
000105                 DLON=TOLAM-ZLAM1
000106                 T1=1.0-F/2.0
000107                 T2=1.0-(.5*T1*ZK1)
000108                 T3=T2-ZK1**2/4.0
000109                 T4=F*T3*DTHET
000110                 T5=E2*ZK1*COS(TWOOT)*SIN(DTHET)/4.0
000111                 T6=E2*ZK1**2* COS(2.0*TWOOT)* SIN(2.0*DTHET)/16.0
000112                 DL=DLON-(COBO*(T4-T5+T6))
```

```
000113                ZL2=ZLO+DL
000114                ABZL2= ABS(ZL2)
000115                IF(ABZL2-3.141592653590) 17000,17000,17000
000116          17000 IF(ZL2) 17100,17200,17200
000117          17100 ZL2=ZL2+6.2831853071
000118                GO TO 2900
000119          17200 ZL2=ZL2-6.2831853071
000120           2900 RETURN
000121                END
```

```
: ELT GTSIZ,1,70,209, 42 ,33

000001                  SUBROUTINE GTSIZ(K,L)
000002                  L=0
000003                  FLD(18,18,L)=FLD(0,18*K)
000004                  RETURN
000005                  END
```

```
» ELT HEADER,1,770301, 4,700

000001                SUBROUTINE HEADER(JOB)
000002                DIMENSION IBD(3),IFD(3),ILD(3),DAT(139)
000003                DIMENSION TITLE(14)
000004                INTEGER D1,DL
000005                DATA IBD/1,1,1975/
000006                DATA TITLE/34H056 NOAA 1  NIMBUS 6     DRIFT BUOY D.V.HANSEN
000007               X          OCSLAP   10PLACE         /
000008                REWIND 33
000009                N=NUM-1
000010                READ (33) DAT
000011                D1=DAT(13)
000012                DO 10 I=1,N
000013                READ(33) DAT
000014             10 DL=DAT(13)
000015                REWIND 33
000016                IBD(1)=1
000017                IBD(2)=1
000018                IBD(3)=1975
000019                CALL UNF232(IBD(1),IBD(2),IBD(3),IFD(1),IFD(2),IFD(3),D1)
000020                IBD(1)=1
000021                IBD(2)=1
000022                IBD(3)=1975
000023                CALL UNF232(IBD(1),IBD(2),IBD(3),ILD(1),ILD(2),ILD(3),DL)
000024                IFD(3)=IFD(3)-1900
000025                ILD(3)=ILD(3)-1900
000026                CALL UNF218(IFD(3),TITLE,48,2)
000027                CALL UNF218(IFD(1),TITLE,50,2)
000028                CALL UNF218(IFD(2),TITLE,52,2)
000029                CALL UNF218(ILD(3),TITLE,54,2)
000030                CALL UNF218(ILD(1),TITLE,56,2)
000031                CALL UNF218(ILD(2),TITLE,58,2)
000032                CALL NTRAN(7,1,14,TITLE,LAP)
000033             888 IF(LAP.EQ.-1) GO TO 888
000034                PRINT 8,TITLE
000035              8 FORMAT(1X,14A6)
000036                RETURN
000037                END
```

```
@ ELT INPUT,I,7611...,54075

000001                  SUBROUTINE INPUT(A,EOF)
000002                  DIMENSION A(13900)
000003                  LOGICAL EOF
000004                  EOF=.FALSE.
000005                  CALL NTRAN(8,22)
000006                  CALL NTRAN(8,2,13900,A,L)
000007                1 IF(L.EQ.(-1)) GO TO 1
000008                  IF(L.LE.(-1)) EOF=.TRUE.
000009                  IF(EOF) CALL NTRAN(8,22)
000010                  IF(EOF) CALL NTRAN(8,10)
000011                  IF(EOF) CALL NTRAN(8,22)
000012                  IF(EOF) REWIND 33
000013                  RETURN
000014                  END
```

```
* ELT INPT2,1,77307, 66199

000001                SUBROUTINE INPT2(A,EOF)
000002                DIMENSION A(13900)
000003                LOGICAL EOF
000004                LOGICAL EOFF
000005                DATA EOFF/0/
000006                EOF=.FALSE.
000007                CALL NTRAN(8,22)
000008                IF(EOFF) GO TO 10
000009                CALL NTRAN(8,2,13900,A,L)
000010              1 IF(L.EQ.(-1)) GO TO 1
000011                IF(L.LE.(-1)) EOFF=.TRUE.
000012                IF(EOFF) GO TO 10
000013                RETURN
000014             10 CALL NTRAN(9,2,13900,A,L)
000015              2 IF(L.EQ.(-1)) GO TO 2
000016                IF(L.LE.(-1)) EOF=.TRUE.
000017                IF(EOF) CALL NTRAN(8,22)
000018                IF(EOF) CALL NTRAN(8,10)
000019                IF(EOF) CALL NTRAN(8,22)
000020                IF(EOF) CALL NTRAN(9,22)
000021                IF(EOF) CALL NTRAN(9,10)
000022                IF(EOF) CALL NTRAN(9,22)
000023                IF(EOF) EOFF=.FALSE.
000024                IF(EOF) REWIND 33
000025                RETURN
000026                END
```

```
» ELT INV,1,760412, 48045

0001                SUBROUTINE INV(RLAT1,RLON1,RLAT2,RLON2,DIST,IZ)
0002                EQRAD=6378163.
0003                PORAD=6356177.
0004                IF(CFLG)501,501,502
0005              501 FLAT=1.-PORAD/EQRAD
0006                FLAT2=FLAT*FLAT
0007                FLAT3=FLAT*FLAT2
0008                F1=FLAT+FLAT2+FLAT3
0009                F2=FLAT2*.5+FLAT3
0010                F4=FLAT2+4.*FLAT3
0011                F5=1.5*FLAT3
0012                F6=1.25*FLAT2+3.*FLAT3
0013                F7=.25*FLAT2+.5*FLAT3
0014                F8=FLAT2+4.*FLAT3
0015                F9=1.9375*FLAT3
0016                F10=.5625*FLAT3
0017                F11=4.5*FLAT3
0018                F12=.125*FLAT3
0019                F13=3.5*FLAT3
0020                F14=.5*FLAT2
0021                F15=.5*FLAT3
0022                E12=(EQRAD**2-PORAD**2)/(PORAD**2)
0023                E14=E12*E12
0024                E16=E12*E14
0025                PI=3.1415926
0026                TWOPI=6.2831853
0027                CFLG=1.
0028              502 BETA1=ATAN((1.-FLAT)*SIN(RLAT1)/COS (RLAT1))
0029                SBETA1=SIN(BETA1)
0030                CBETA1=COS(BETA1)
0031                BETA2=ATAN((1.-FLAT)*TAN(RLAT2))
0032                SBETA2=SIN(BETA2)
0033                CBETA2=COS(BETA2)
0034                DELL=RLON1-RLON2
0035                ADELL=ABS(DELL)
0036                IF(ADELL-PI)506,505,505
0037              505 ADELL=TWOPI-ADELL
0038              506 SIDEL=SIN(ADELL)
0039                CODEL=COS(ADELL)
0040                A=SBETA1*SBETA2
0041                ASQ=A*A
0042                B=CBETA1*CBETA2
0043                COPHI=A+B*CODEL
0044                SIPHI=SQRT((SIDEL*CBETA2)**2+(SBETA2*CBETA1-SBETA1*CBETA2*CODEL)*
0045               1*2)
0046                C=B*SIDEL/SIPHI
0047                EM=1.-C*C
0048                EMS=EM*EM
0049                PHI= ASIN(SIPHI)
0050                IF(COPHI)507,508,508
0051              507 PHI=PI-PHI
0052              508 PHISQ=PHI*PHI
0053                PHIC=PHISQ*PHI
0054                CSPHI=1./SIPHI
```

```
0055                CSPSQ=COSPHI*COSPHI
0056                CTPHI=COSPHI/SINPHI
0057                CTPSQ=CTPHI*CTPHI
0058                PSTCO=SINPHI*COSPHI
0059                T1=(FLAT+FLAT2+FLAT3)*PHI
0060                T2=A*(-F2*SINPHI-F4*PHISQ*CSPHI+F5*PHIC*CSPHI*CTPHI)
0061                T3=EMS*(-F6*PHI+F7*SINPHI*COSPHI+F8*PHISQ*CTPHI-F15*PHIC*CSPSQ-FLAT3*
0062               1PHIC*CTPSQ)
0063                T4=ASQ*(FLAT3*PHI+F15*SINPHI*COSPHI+FLAT3*PHIC*CSPSQ)
0064                T5=EMS*(F9*PHI-F10*SINPHI*COSPHI+F15*PHI*COPSQ-F11*PHISQ*CTPHI+
0065               1F12*SINPHI*COSPHI+F15*PHIC*CSPSQ+2.*FLAT3*PHIC*CTPSQ)
0066                COPSQ=COSPHI*COSPHI
0067                COPC=COPSQ*COSPHI
0068                T6=A*EMS*(FLAT3*SINPHI-F5*PHI*COSPHI+F11*PHISQ*CSPHI-F15*SINPHI*COPSQ-
0069               1F11*PHIC*CSPHI*CTPHI)
0070                ZLAM=C*(T1+T2+T3+T4+T5+T6)+ADELL
0071                COPHI=A+C*COS(ZLAM)
0072                SIPHI=SQRT((SIN(ZLAM)*CBETA2)**2+(SBETA2*CBETA1-SBETA1*CBETA2*
0073               1COS(ZLAM))**2)
0074                PHI= ASIN(SIPHI)
0075                PHI2=2.*PHI
0076                COSBO=(3*SIN(ZLAM))/SIPHI
0077                SINBO=SQRT(1.-COSBO*COSBO)
0078                SISQ=SINBO*SINBO
0079                SI4=SISQ*SISQ
0080                SI6=SI4*SISQ
0081                PHI3=3.*PHI
0082                COSG=(2.*A/SISQ)-COPHI
0083                IF((COSG*COSG ).GE.1. ) SISG=0.
0084                IF((COSG*COSG ).GE.1. ) GO TO 7655
0085                SISG=SQRT(1.-COSG*COSG)
0086           7655 SG=ASIN(SISG)
0087                SG4=2.*SG
0088                SG6=3.*SG
0089                A0=1.+.25*E12*SINBO*SINBO-(3.*E14/64.)*SINBO**4+(5.*E16/256.)*
0090               2SINBO**6
0091                B0=.25*E12*SINBO**2-(E14/16.)*SINBO**4+(15.*E16/512.)*SINBO**6
0092                C0=(E14/128.)*SINBO**4-(3.*E16/512.)*SINBO**6
0093                D0=(E16/1536.)*SINBO**6
0094                DIST=PORAD*(A0*PHI+B0*SIPHI*COS(SG)-C0*SIN(PHI2)*COS(SG4)+
0095               1D0*SIN(PHI3)*COS(SG6))
0096                CTAZ=0.
0097                IF(SIN(ZLAM).EQ.0.0.OR.CBETA2.EQ.0.0) GO TO 509
0098                CTAZ=(SBETA2*CBETA1-COS(ZLAM)*SBETA1*CBETA2)/(SIN(ZLAM)*CBETA2)
0099                IF(CTAZ)510,509,510
0100            509 CTAZ=.00000005
0101            510 AZ=ATAN(1./CTAZ)
0102                IF(DELL)515,514,514
0103            514 IF(DELL-PI)511,512,512
0104            511 IF(CTAZ)520,521,521
0105            520 AZ=AZ+PI
0106                GO TO 521
0107            512 IF(CTAZ)517,516,516
0108            515 IF(DELL+PI)511,511,516
0109            516 IF(CTAZ)517,518,518
0110            517 AZ=PI-AZ
0111                GO TO 521
0112            518 AZ=TWOPI-AZ
```

```
000113          521 AZ=AZ+PI
000114              AZ=AZ-TWOPI
000115              IF(AZ)513,519,519
000116          513 AZ=AZ+TWOPI
000117          519 RETURN
000118              END
```

```
@ LLT MAP,1,7664.6, 59512

000001                SUBROUTINE MAP(NUM)
000002                DIMENSION DAT(139),X(1002),Y(1002)
000003                PRINT 75,NUM
000004             75 FORMAT('  NUMBER OF POSITIONS',I5)
000005                IF(NUM.GT.1000) PRINT 1
000006                IF(NUM.GT.1000) STOP 5
000007                REWIND 33
000008                CALL SETOVR
000009                CALL PLOTS(10.,10.)
000010                YMIN=999999.
000011                XMIN=999999.
000012                XMAX=-999999.
000013                YMAX=-999999.
000014                DO 10 I=1,NUM
000015                READ(33) DAT
000016                IF(DAT(4).LT.180.) DAT(4)=DAT(4)*(-1.)
000017                IF(DAT(4).GE.180.) DAT(4)=360.0-DAT(4)
000018                CALL REC(1,DAT(3),DAT(4),D,ID,ID,ID,ID,X(I),Y(I),DAT(13))
000019                IF(X(I).LT.XMIN) XLONMN=DAT(4)
000020                IF(X(I).LT.XMIN)  XMIN=X(I)
000021                IF(X(I).GT.XMAX) XLONMX=DAT(4)
000022                IF(X(I).GT.XMAX) XMAX=X(I)
000023                IF(Y(I).LT.YMIN) XLATMN=DAT(3)
000024                IF(Y(I).LT.YMIN)   YMIN=Y(I)
000025                IF(Y(I).GT.YMAX) XLATMX=DAT(3)
000026                IF(Y(I).GT.YMAX)  YMAX=Y(I)
000027             10 CONTINUE
000028              1 FORMAT('  MORE THAN 1000 POINTS TO PLOT IS A NONO')
000029                DX=XMAX-XMIN
000030                DY=YMAX-YMIN
000031            201 XL=DX
000032                YL=DY
000033                IF(DX.LE.8.0.AND.DY.LE.8.0) GO TO 200
000034                DX=DX/2.
000035                DY=DY/2.
000036                GO TO 201
000037            200 CONTINUE
000038                DO 11 I=1,NUM
000039                X(I)=X(I)-XMIN
000040             11 Y(I)=Y(I)-YMIN
000041                CALL PLOT(1.,1.,-3)
000042                CALL SCALE(X,XL,NUM,1)
000043                CALL SCALE(Y,YL,NUM,1)
000044                 CALL LINE(X,Y,NUM,1,1,2)
000045                X1=0.
000046                X2=(XMAX-XMIN)/X(NUM+2)
000047                 Y1=0.
000048                Y2=(YMAX-YMIN)/Y(NUM+2)
000049                CALL SYMBOL(X1,Y1,0.2,3,0.,-1)
000050                CALL SYMBOL(X2,Y2,0.2,3,0.,-1)
000051                YY1=Y1-0.5
000052                YY2=Y2-0.5
000053                XX1=X1+0.5
000054                XX2=X2+0.5
```

```
000055                    CALL NUMBER(X1,Y1,0.1,PLATMN,0.,3)
000056                  CALL NUMBER(X1,YY1,0.1,XLONMN,0.,3)
000057                   CALL NUMBER(XX2,Y2,0.1,XLATMX,0.,3)
000058                  CALL NUMBER(X2,YY2,0.1,XLONMX,0.,3)
000059                  CALL PLOT(0.,0.,999)
000060                  REWIND 53
000061                  CALL BITSET
000062                  RETURN
000063                  END
```

```
      ,I ELT  MAP1,1,770/07, 005:0
000001                SUBROUTINE MAP1(NUM)
000002                DIMENSION X(1000),Y(1000)
000003                COMMON /COMX/XLAT(1000),XLON(1000),VE(1000),VN(1000),
000004               *AE(1000),AN(1000),T(1000),T1(1000),TIME(1000),BU(4761)
000005                EQUIVALENCE (X,BU(2761)),(Y,BU(3761))
000006                REWIND 33
000007                READ 500,CM,BLAT
000008            500 FORMAT(2F10.3)
000009                DO 10 I=1,NUM
000010                READ (33) DAT
000011                IF(DAT(4).LT.180.) DAT(4)=DAT(4)*(-1.)
000012                IF(DAT(4).GE.180.) DAT(4)=360.0-DAT(4)
000013                XLAT(I)=DAT(3)
000014                XLON(I)=DAT(4)
000015                CALL PCONIC(CM,DAT(3),DAT(4),BLAT,X(I),Y(I))
000016                PRINT 200,I,DAT(3),DAT(4),X(I),Y(I)
000017            200 FORMAT(1X,I5,4F15.3)
000018                X(I)=X(I)*3.937E-05
000019             10 Y(I)=Y(I)*3.937E-05
000020                XM=INT(AMIN(XLON,NUM))
000021                YM=INT(AMIN(XLAT,NUM))
000022                XMX=INT(AMAX(XLON,NUM))+1.
000023                YMX=INT(AMAX(XLAT,NUM))+1.
000024                CALL PCONIC(CM,YM,XMX,BLAT,X1,Y1)
000025                PRINT 201,YM,XMX,X1,Y1
000026                CALL PCONIC(CM,YMX,XM,BLAT,X2,Y2)
000027                PRINT 201,YMX,XM,X2,Y2
000028            201 FORMAT(1X,4F15.3)
000029                CALL SETOVR
000030                X1=X1*3.937E-05
000031                X2=X2*3.937E-05
000032                Y1=Y1*3.937E-05
000033                Y2=Y2*3.937E-05
000034                CALL PLOTS(-30.,-11.)
000035                XLEN=ABS(X2-X1)
000036                YLEN=ABS(Y1-Y2)
000037                CALL PLOT(1.,1.,-3)
000038                X(NUM+1)=X1
000039                X(NUM+2)=1.
000040                Y(NUM+1)=Y1
000041                Y(NUM+2)=1.
000042                CALL LINE(X,Y,NUM,1,1,2)
000043                X(1)=X1
000044                X(2)=X2
000045                Y(1)=Y1
000046                Y(2)=Y2
000047                Y(3)=Y1
000048                Y(4)=1.
000049                X(3)=X1
000050                X(4)=1.
000051                 CALL LINE(X,Y,2,1,-1,3)
000052                CALL PLOT(0.,0.,999)
000053                CALL BITSET
000054                REWIND 33
```

```
000055                  RETURN
000056                  END
```

```
» ELT NASA6,1,76,12,, 5156

001                 DIMENSION C(14),DAT(139,100)
002                 DIMENSION RAT(13900)
003                 EQUIVALENCE(RAT,DAT)
004                 ICT=0
005                 JCT=0
006                1 READ(5,20,ERR=100,END=100)C
007                20 FORMAT(13A6,A2)
008                 CALL UMF217(C,1,1,L)
009           C     3 IF(JCT.EQ.100) PRINT200,((DAT(I,J),I=1,139),J=1,100)
010                 3 IF(JCT.EQ.100) PRINT200,((DAT(I,J),I=1,  8),J=1,100)
011                 IF(JCT.EQ.100) CALL OUT(RAT)
012               200 FORMAT(1X,8F12.4,/(1X,10F11.4))
013                 IF(JCT.EQ.100) JCT=0
014                 IF(JCT.EQ.0) CALL CLEAR(DAT)
015                 IF(L.NE.4) GO TO 1
016                 CALL UMF217(C,53,2,I1)
017                 CALL UMF217(C,56,2,I2)
018                 IF(I1.EQ.0.AND.I2.EQ.0) GO TO 1
019                 ICT=ICT+1
020                 JCT=JCT+1
021                 DAT(2,JCT)=ICT
022                 IF(I1.GE.I2) GO TO 5
023                 DAT(5,JCT)=FLOAT(I2)
024                 XLAT=UMF230(C,24,6,2,J)
025                 XLON=UMF230(C,31,7,2,J)
026                 YLAT=UMF230(C,9,6,2,J)
027                 YLON=UMF230(C,16,7,2,J)
028                 GO TO 6
029                5 DAT(5,JCT)=FLOAT(I1)
030                 XLAT=UMF230(C,9,6,2,J)
031                 XLON=UMF230(C,16,7,2,J)
032                 YLAT=UMF230(C,24,6,2,J)
033                 YLON=UMF230(C,31,7,2,J)
034                6 DAT(3,JCT)=XLAT
035                 DAT(4,JCT)=XLON
036                 CALL UMF217(C,2,4,ID)
037                 DAT(1,JCT)=FLOAT(ID)
038                 VN=UMF230(C,39,6,2,J)
039                 VE=UMF230(C,45,7,2,J)
040                 DAT(6,JCT)=YLAT
041                 DAT(7,JCT)=YLON
042                 CALL UMF217(C,65,3,NUM)
043                 DAT(8,JCT)=FLOAT(NUM)
044                 IF(NUM.LT.1.AND.JCT.EQ.100) PRINT 200,((DAT(I,J),I=1,8),J=1,100)
045           C     IF(NUM.LT.1.AND.JCT.EQ.0) PRINT 200,((DAT(I,J),I=1,139),J=1,100)
046                 IF(NUM.LT.1.AND.JCT.EQ.100) CALL OUT (RAT)
047                 IF(NUM.LT.1.AND.JCT.EQ.100) JCT=0
048                 IF(JCT.EQ.0) CALL CLEAR(DAT)
049                 IF(NUM.LT.1) GO TO 1
050                2 LCT=0
051               22 READ(5,20,ERR=100,END=100) C
052                 CALL UMF217(C,1,1,L)
053                 IF(L.NE.5.OR.LCT.EQ.13) GO TO 3
054                 LLCT=LCT*10+9
```

```
» CLI NASATP,1,7/0351, 43665

000001                  DIMENSION YES(139,100)
000002                  DIMENSION JUNK(6)
000003                  DIMENSION A(345), K(224)
000004                  COMMON/WORK/SER(13900),DAT(139)
000005                  COMMON IF
000006                  EQUIVALENCE(YES,SER)
000007                  LOGICAL NOGOOD
000008                  DATA JUNK/61,95,75/
000009                  DATA NF/0/
000010                  DATA IFILE/-1/
000011                  LOGICAL EOI
000012                  PRINT 727
000013              727 FORMAT(' START NOW')
000014                  READ 20,NTAPES
000015               20 FORMAT(I10)
000016                  EOI= .FALSE.
000017                  ITOT=0
000018                1 CALL ACALIO('B',A,345,L,K)
000019                2 IF(L.EQ.(-1)) GO TO 2
000020                  IF(L.EQ.(-2)) GO TO 300
000021                  EOI=.FALSE.
000022                  IF(L.LE.0) CALL GTSIZ(K,L)
000023                  IF(L.LT.90) IFILE=-1
000024                  IF(L.LT.90) GO TO 100
000025                  IF(L.GT.90) GO TO 200
000026                  IF(L.LE.(-2)) GO TO 300
000027                  GO TO 1
000028              200 K=0
000029                  DO 10 I=1,892,4
000030                  K=K+1
000031                  CALL UNF201(4,A,I,ND(K),3)
000032               10 CONTINUE
000033                  CALL PROCES(ND,NOGOOD)
000034                  IF(NOGOOD) GO TO 1000
000035                  IF(NF.LT.1) GO TO 1000
000036                  DO 50 KP=1,139
000037               50 YES(KP,NF)=DAT(KP)
000038                  IF(NF.GE.100) CALL OUT(SER)
000039                  IF(NF.GE.100) CALL ZERO(SER)
000040                  IF(NF.GE.100) NF=0
000041             1000 CONTINUE
000042                  K=0
000043                  DO 101 I=1025,1916,4
000044                  K=K+1
000045                  CALL UNF201(4,A,I,ND(K),3)
000046              101 CONTINUE
000047                  IF(ND(1).GT.1008)  GO TO 1
000048                  CALL PROCES(ND,NOGOOD)
000049                  IF(NOGOOD) GO TO 1
000050                  IF(NF.LT.1) GO TO 1
000051                      DO 501 KP=1,139
000052              501 YES(KP,NF)=DAT(KP)
000053                  IF(NF.GE.100) CALL OUT(SER)
000054                  IF(NF.GE.100) CALL ZERO(SER)
```

```
000055                IF(NF.GE.100) NF=0
000056                GO TO 1
000057                GO TO 1
000058              100 CALL UNF201(4,A,4S,NFILES,S)
000059                IF(ITCT.EQ.14) NFILES=96
000060                PRINT 800,ITCT,NFILES
000061              800 FORMAT(1X,'TAPE',I5,' NUM FILES =',I10)
000062                GO TO 1
000063            C 300 IF(EOI) CALL TPOUT
000064              300 CONTINUE
000065            C     IF(EOI) NF=0
000066            C     IF(EOI) STOP
000067                EOI=.TRUE.
000068                IFILE=IFILE+1
000069                IF(IFILE.LT.NFILES) GO TO 1
000070                ITCT=ITCT+1
000071                IF(ITCT.LT.NTAPES) PAUSE
000072                IF(ITCT.LT.NTAPES)  IFILE=-1
000073                IF(ITCT.LT.NTAPES)  GO TO 1
000074                CALL NTRAN(7,22)
000075                CALL OUT(SER)
000076                CALL NTRAN(7,22)
000077                CALL NTRAN(7,9)
000078                STOP
000079                END
```

```
% ELT NASTAT,1,7.0513, 51019

0001                  SUBROUTINE NASTAT(NUM)
0002            C
0003            C     GIVES STATISTICS ON COMPONENT VELOCITIES AND ACCELERATIONS
0004            C      IN KNOTS AND USES THE FFSTSA PACKAGE
0005            C
0006                  COMMON/WORK/DAT(13),XLAT(1000),XLON(1000),VE(1000),VN(1000),
0007                 *AE(1000),AN(1000),T(1000),TT(1000),TIME(1000),PU(4761)
0008                  SF=0.03.3974
0009                  IF(NUM.GT.998) STOP 2
0010                  REWIND 33
0011                  DO 10 I=1,NUM
0012                  READ (33) DAT
0013                  IF(DAT(4).LT.180.) DAT(4)=DAT(4)*(-1.)
0014                  IF(DAT(4).GE.180.) DAT(4)=360.0-DAT(4)
0015                  XLAT(I)=DAT(3)*0.01745329
0016                  XLON(I)=DAT(4)*0.01745329
0017                10 TIME(I)=DAT(13)*1440.
0018                  N=NUM-1
0019                  DO 11 I=1,N
0020                  T(I)=(TIME(I+1)+TIME(I))/2.
0021                  CALL SPEED(XLAT(I),XLON(I),XLAT(I+1),XLON(I+1),TIME(I),TIME(I+1),
0022                 *D4,D5,D6,VE(I),VN(I),D3)
0023                  VE(I)=VE(I)*SF
0024                  VN(I)=VN(I)*SF
0025                  T(I)=T(I)/60.
0026                11 CONTINUE
0027                30 FORMAT(1X,12F10.3)
0028                  TD=T(1)
0029                  DO 25 J=1,N
0030                25 T(J)=T(J)-TD
0031                  PRINT 30,(T(K),VE(K),VN(K),K=1,N)
0032                  NN=N-1
0033                  DO 20 I=1,NN
0034                  TT(I)=((T(I+1)+T(I))/2.)-(T(2)/2.)
0035                  AE(I)=(VE(I+1)-VE(I))/(T(I+1)-T(I))
0036                20 AN(I)=(VN(I+1)-VN(I))/(T(I+1)-T(I))
0037                  PRINT 30,(TT(K),AE(K),AN(K),K=1,NN )
0038                  CALL NISHUL
0039                  CALL STRSR1(1,1,2140,N,0.,1.)
0040                  CALL STRSR1(2,1,3140,N,0.,1.)
0041                  CALL STRSR1(3,1,4140,NN,0.,1.)
0042                  CALL STRSR1(4,1,5140,NN,0.,1.)
0043                  DO 40 I=1,4
0044                  CALL STATS(I,1,50,-1,XMN,XMX,XM,SD)
0045                  PRINT 41,XMN,XMX,XM,SD
0046                41 FORMAT(' MIN=',F12.3,' MAX=',F12.3,' MEAN=',F12.3,' STANDARD DEV='
0047                 *,F12.3)
0048                40 CONTINUE
0049                  RETURN
0050                  END
```

```
. LET NOOC,1,770331, 43605

000001                SUBROUTINE NOOC(DAT,TMP,SPD,PSI)
000002                DIMENSION DAT(154)
000003                DIMENSION REC(15),IBD(3),IDT(3)
000004                DATA HEM/8HNSEW  /,IBD/1,1,1975/
000005                DATA ISW/0/
000006                DATA REC/90H05  ADAL 3
000007               X
000008                ID=DAT(1)
000009                CALL UMF216(ID,REC,14,4)
000010                ISW=ISW+1
000011                CALL UMF218(ISW,REC,18,4)
000012                IDEG=DAT(3)
000013                IF(IDEG.LT.0)CALL UMF201(1,HEM,2,REC,25)
000014                IF(IDEG.GE.0)CALL UMF201(1,HEM,1,REC,25)
000015                IDEG=IABS(IDEG)
000016                DAT(3)=ABS(DAT(3))
000017                MIN=((DAT(3)-IDEG)*60.)
000018                ISEC=((DAT(3)-IDEG)-((FLOAT(MIN))/60.))*3600.
000019                CALL UMF216(IDEG,REC,20,2)
000020                CALL UMF216(MIN,REC,22,2)
000021                CALL UMF218(ISEC,REC,24,2)
000022                IF(DAT(4).LT.180.) DAT(4)=DAT(4)*(-1.)
000023                IF(DAT(4).GE.180.) DAT(4)=360.0-DAT(4)
000024                CALL UMF201(1,HEM,4,REC,33)
000025                IF(DAT(4).LT.0.0)CALL UMF201(1,HEM,3,REC,33)
000026                DAT(4)=ABS(DAT(4))
000027                IDEG=DAT(4)
000028                MIN=((DAT(4)-IDEG)*60.)
000029                ISEC=((DAT(4)-IDEG)-((FLOAT(MIN))/60.))*3600.
000030                CALL UMF218(IDEG,REC,26,3)
000031                CALL UMF216( MIN,REC,30,2)
000032                CALL UMF216(ISEC,REC,32,2)
000033                ND=DAT(13)
000034                IBD(1)=1
000035                IBD(2)=1
000036                IBD(3)=1975
000037                CALL UMF232(IBD(1),IBD(2),IBD(3),IDT(1),IDT(2),IDT(3),ND)
000038                IHR=(DAT(13)-ND)*24.
000039                MIN=((DAT(13)-ND)-(FLOAT(IHR)/24.))*1440.
000040                IYR=IDT(3)-1900
000041                CALL UMF216(IYR,REC,35,2)
000042                CALL UMF216(IDT(1),REC,37,2)
000043                CALL UMF218(IDT(2),REC,39,2)
000044                CALL UMF218(IHR,REC,41,2)
000045                CALL UMF218(MIN,REC,43,2)
000046                ITMP=TMP*10.
000047                ISPED=SPD*10.
000048                IPSI=PSI*10.
000049                CALL UMF216(IPSI,REC,49,5)
000050                CALL UMF218(ITMP,REC,54,5   )
000051                CALL UMF216(ISPED,REC,59,5)
000052                CALL NTRAN(7,1,15,REC,LAP)
000053             888 IF(LAP.EQ.-1) GO TO 888
000054                PRINT 8765,REC
```

```
000055          8765 FORMAT(1X,15A6)
000056               RETURN
000057               END
```

```
» LET OCW,1,7611,3, 5407;

000001                  FUNCTION OCW(OC,WD)
000002                  I=OC-MOD/100.
000003                  B=OC-I*100
000004                  J=B/10.
000005                  C=B-J*10
000006                  K=C
000007                  IWORD=I*64+J*8++
000008                  OCW=IWORD
000009                  RETURN
000010                  END
```

```
$ ELT OUT,1,751923, 00277

000001                  SUBROUTINE OUT(RAT)
000002                  DIMENSION RAT(13900)
000003                  CALL INTRAN(7,22)
000004                  CALL RTRAN(7,1,13900,RAT,L)
000005                1 IF(L.EQ.(-1)) GO TO 1
000006                  RETURN
000007                  END
```

```
» ELT PCONIC,1,760813, 51023

0001                  SUBROUTINE PCONIC(CM,XLAT,XLON,BLAT,X,Y)
0002            C
0003            C     ALL COMPUTATIONS ARE BASED ON CLARK 1866 SPHEROID
0004            C     CM=CENTRAL MERIDIAN IN DEGREES
0005            C     XLAT=GIVEN LATITUDE IN DEGREES
0006            C     XLON=GIVEN LONGITUDE IN DEGREES
0007            C     BLAT=LATITUDE WHOSE INTERSECTION WITH CM IS TO BE USED FOR ORIGIN
0008            C       OF CARTESIAN COORDINATES
0009            C     X=NUMBER OF METERS TO POINT IN X DIRECTION
0010            C     Y=NUMBER OF METERS TO POINT IN Y DIRECTION
0011            C
0012                  RAD=57.2957795
0013                  IF(BLAT.GE.52.) GO TO  2
0014                  PRINT 1
0015                1 FORMAT('YOUR BASE LAT IS TOO FAR SOUTH-ERROR****')
0016                2 Y=YBASE(XLAT)-YBASE(BLAT)
0017                  SP=(SIN(XLAT/RAD))**2
0018                  DX=(CM-XLON)/RAD
0019                  P=6378206.4/SQRT(1.-(0.00 76866*SP))
0020                  X=P*DX*COS(XLAT/RAD)
0021                  Y=Y+(0.25*P*DX*DX*SP)
0022                  RETURN
0023                  END
```

```
      W ELT POLLY,1,7611 3, 54 77

000001            C                                                    ),27,17,M(YLLOP
000002                  SUBROUTINE POLLY(N,Y,X,W, )
000003            C                                                   )YU,N,P,2Z,1Z,M(YLLOP
000004            C LST SUBS CURVE FITTING VIA ORTHOGONAL POLYNOMIALS.
000005                  DIMENSION P(15,14),A(15),X(150),Y(150),W(150)
000006                  NX=2
000007                  N=4
000008                  KKK=1
000009                  K=1
000010                  IF(M-4)40,40,50
000011             40   N=N-1
000012             50   NX=NX+1
000013                  IF(KKK)110,70,110
000014             70   CONTINUE
000015                  GO TO 150
000016            110   CONTINUE
000017            150   DO 180 I=1,15
000018                  DO 180 J=1,14
000019                  P(I,J)=0.
000020            180   CONTINUE
000021                  P(1,1)=1.
000022                  XSUM=0.
000023                  YSUM=0.
000024                  DO 250 J=1,M
000025                  XSUM=XSUM+X(J)*W(J)
000026                  YSUM=YSUM+W(J)
000027            250   CONTINUE
000028                  P(2,2)=1.
000029                  P(2,1)=-XSUM/YSUM
000030                  NN=N+1
000031                  DO 540 I=3,NN
000032                  II=I-1
000033                  IX=I-2
000034                  XSUM=0.
000035                  YSUM=0.
000036                  USUM=0.
000037                  ZSUM=0.
000038                  DO 470 K=1,M
000039                  SUMY=0.
000040                  SUMX=0.
000041                  DO 420 L=1,I
000042                  IF(L.GT.1) GO TO 11
000043                  SUMY=SUMY+P(II,L)
000044                       GO TO 12
000045             11   SUMY=SUMY+P(II,L)*X(K)**(L-1)
000046             12   IF(L.GT.1) GO TO 13
000047                  SUMX=SUMX+P(IX,L)
000048                   GO TO 420
000049             13   SUMX=SUMX+P(IX,L)*X(K)**(L-1)
000050            420   CONTINUE
000051                  XSUM=XSUM+X(K)*SUMY**2*W(K)
000052                  YSUM=YSUM+SUMY**2*W(K)
000053                  USUM=USUM+X(K)*SUMY*SUMX*  (K)
000054            470   ZSUM=ZSUM+SUMX**2*W(K)
```

```
0055                B=XSUM/YSUM
0056                G=-ZSUM/ZSUM
0057                P(I,1)=-B*P(II,1)+G*P(IX,1)
0058                DO 540 J=2,I
0059                JJ=J-1
0060           540  P(I,J)=P(II,JJ)-B*P(II,J)+G*P(IX,J)
0061           550  DO 670 I=1,NN
0062                XSUM=0.
0063                YSUM=0.
0064                DO 650 K=1,M
0065                SUMZ=0.
0066                DO 620 L=1,I
0067                IF(L.GT.1) GO TO 14
0068                IF(L.EQ.1) SUMZ=SUMZ+P(I,L)
0069                GO TO 620
0070            14  SUMZ=SUMZ+P(I,L)*X(K)**(L-1)
0071           620  CONTINUE
0072                XSUM=XSUM+Y(K)*SUMZ*W(K)
0073           650  YSUM=YSUM+SUMZ**2*W(K)
0074           670  A(I)=XSUM/YSUM
0075                DO 790 I=1,NN
0076                DO 710 J=1,I
0077           710  P(15,J)=P(15,J)+P(I,J)*A(I)
0078                IF(I-NX)790,730,730
0079           730  L=I-1
0080                DO 780 K=1,I
0081                KK=K-1
0082           780  CONTINUE
0083           790  CONTINUE
0084          1000  FORMAT(1X,5I5)
0085          1001  FORMAT(3F10.2)
0086          1003  FORMAT(///12X24HTHE POLYNOMIAL OF ORDER I4,28H THAT BEST FITS THE
0087              1CURVE IS //26X10HPOWER OF X,12X11HCOEFFICIENT)
0088          1004  FORMAT(29XI4,10XE16.6)
0089          1005  CONTINUE
0090          1221  CONTINUE
0091                RETURN
0092                END
```

```
      , CALL PROCES,1,7,0,81, ,,,
```

```
000055            20 DAT(5)=AC2
000056               IF(ND(53).LT.CB.OR.ND(53).GT.CT) NOGOOD=.TRUE.                *NEW
000057               IF(ND(53).LT.  CB.OR.ND(53).GT.  CT  ) RETURN                 **-1
000058               IF(ND(51).LT.XL.OR.ND(51).GT.XT) NOGOOD=.TRUE.                *NEW
000059               IF(ND(51).LT.XL.OR.ND(51).GT.XT) RETURN                       **-1
000060               DAT(3)=CDC(ND(53),ND(54))
000061               DAT(4)=CDC(ND(51),ND(52))

                  30 DAT(3)=TAN(DAT(3))/.993305
                     DAT(3)=(ATAN(DAT(3)))*RAD
000063               DAT(4)=DAT(4)*RAD
000064               IF(IBEST.EQ.4.OR.IBEST.EQ.6) GO TO 60
000065               GO TO 61
000066            60 DAT(6)=CDC(ND(51),ND(52))
000067               DAT(7)=CDC(ND(53),ND(54))
000068            61 IF(ND(7).GT.15) ND(7)=15
000069               IF(ND(7).LT.1) ND(7)=0
000070               DAT(8)=ND(7)
000071               KYR=ND(5)/1000
000072               JYR=KYR
000073               KDAY=ND(5)-(KYR*1000)
000074               DAT(13)=KDAY+(FLOAT(ND(6))/864000.)
000075               TIME(1)=DAT(13)
000076               IND=ND(7)
000077               J=72
000078               IF(ND(7).GT.0) GO TO 888
000079               DO 889 IFX=9,139
000080            889 DAT(IFX)=0.
000081               RETURN
000082            888 CONTINUE
000083               DO 40 I=1,IND,1
000084               L=J-2
000085               MODE=0
000086               IT(I)=0
000087               IP(I)=0
000088               IWSP(I)=0
000089               KTIM=0
000090               FLD(34,2,MODE)=FLD(32,2,ND(J))
000091               FLD(28,2,IP(I))=FLD(34,2,ND(JT))
000092               FLD(30,6,IP(I))=FLD(12,6,ND(J+1))
000093               FLD(28,3,IT(I))=FLD(18,8,ND(J+1))
000094               FLD(26,2,IWSP(I))=FLD(34,2,ND(J+1))
000095               FLD(30,6,IWSP(I))=FLD(12,6,ND(J+2))
000096         C     FLD(28,3,KTIM)=FLD(18,8,ND(J+2))
000097               IF(MODE.EQ.0) GO TO 41
000098               IT(I)=IT(I)*-1
000099               IP(I)=IP(I)*-1
000100               IWSP(I)=IWSP(I)*-1
000101            41 KYR=ND(L)/1000
000102               KDAY=ND(L)-(KYR*1000)
000103               IF(KYR.EQ.76) KDAY=KDAY+365
000104               IF(KYR.EQ.77) KDAY=KDAY+731
000105               TIME(I)=KDAY+(FLOAT(ND(L+1))/864000.)
000106            40 J=J+11
000107               NSETS=ND(7)*5
000108               LAST=8+NSETS
000109               K=0
000110               DO 50 I=9,LAST,5
000111               K=K+1
000112               DAT(I)=IP(K)
```

```
000113                  DAT(I+1)=TI(K)
000114                  DAT(I+3)=INSO(K)
000115                  DAT(I+4)=TIME(K)
000116               50 CONTINUE
000117                  DAT(139)=JYR+1900
000118            C
000119                  PRINT 722,DAT(1),DAT(3),DAT(4),DAT(5),DAT(13)
000120                  NF=NF+1
000121              722 FORMAT(1X,5F15.4)
000122               70 FORMAT(1X,6F12.2,/10(1X,F10.2))
000123                  RETURN
000124                  END
```

```
$ ELT PVU,1,7701,3, 323
0001                  SUBROUTINE PVU(I,J)
0002                  COMMON/ DPK/DAT(150),X(2000),Y(2000),DX(2000),DY(2000),XPCT(320),
0003                 X YPCT(320),DST(320)
0004                  DATA X/57.2957795/,Y/63.662 3.8/,RAD/0.0174533/
0005                  DO 55 I=1,320
0006                  XPCT(I)=0.
0007               55 YPCT(I)=0.
0008                  READ(3) NUM
0009                  DO 10 I=1,NUM
0010                  READ(35) DAT
0011                  IZ=DAT(4)/6.+30
0012                  IF(DAT(4).GE.180.) IZ=(DAT(4)-180.)/6.+1
0013                  IF(DAT(4).LT.180.) DAT(4)=DAT(4)*(-1.)
0014                  IF(DAT(4).GE.180.) DAT(4)=360.-DAT(4)
0015                  XLAT=DAT(3)*RAD
0016                  XLON=DAT(4)*RAD
0017                  Z=IZ
0018                  CALL UTM(A,B,XLAT,XLON,Z,Y(I),X(I))
0019               10 CONTINUE
0020                  YMIN=XMIN(Y,NUM)
0021                  DO 11 I=1,NUM
0022               11 Y(I)=Y(I)-YMIN
0023                  XMEAN=0.
0024                  YMEAN=0.
0025                  DO 12 I=1,NUM
0026                  XMEAN=XMEAN+X(I)
0027               12 YMEAN=YMEAN+Y(I)
0028                  XMEAN=XMEAN/NUM
0029                  YMEAN=YMEAN/NUM
0030                  DO 13 I=1,NUM
0031                  DX(I)=ABS(X(I)-XMEAN)
0032                  DY(I)=ABS(Y(I)-YMEAN)
0033               13 CONTINUE
0034                  K=0
0035                   DO 14 I=1,30000,100
0036                  K=K+1
0037                  D=I
0038                  DO 17 J=1,NUM
0039                  IF(DX(J).LE.D) XPCT(K)=XPCT(K)+1.
0040                  IF(DY(J).LE.D) YPCT(K)=YPCT(K)+1.
0041               17 CONTINUE
0042                  XPCT(K)=(XPCT(K)/NUM)*100.
0043                  YPCT(K)=(YPCT(K)/NUM)*100.
0044                  DST(K)=D
0045               14 CONTINUE
0046                  XPCT(K+1)=0.
0047                  XPCT(K+2)=20.
0048                  YPCT(K+1)=0.
0049                  YPCT(K+2)=20.
0050                  DST(K+1)=0.
0051                  DST(K+2)=4000.
0052                  CALL SETOVR
0053                  CALL PLOTS(-30.,-10.,1)
0054                  CALL PLOT(0.5,9.5,-3 )
```

```
000055                CALL AXIS(0.,0.,7HY-METERS,-7,8.,0.,DST(K+1),DST(K+2))
000056                CALL AXIS(0.,0.,7HPERCENT,7,5.,90.,XPCT(K+1),XPCT(K+2))
000057                CALL LINE(DST,XPCT,K,1,-1,3)
000058                CALL PLOT(11.5,0.,-3)
000059                CALL AXIS(0.,0.,7HX-METERS,-7,8.,0.,DST(K+1),DST(K+2))
000060                CALL AXIS(0.,0.,7HPERCENT,7,5.,90.,XPCT(K+1),XPCT(K+2))
000061                CALL LINE(DST,XPCT,K,1,-1,3)
000062                CALL PLOT(0.,0.,999)
000063                CALL BITSET
000064                REWIND 33
000065                RETURN
000066                END
```

```
» ELT RA*,1,7o12o9, 4239*

000001                  DIMENSION X(2000),Y(2000),DAT(139),XX(2000),YY(2000)
000002                  COMMON/WORK/ S(13900)
000003                  RR=0.01745329
000004                  R=6378206.4
000005                  A=6378206.4
000006                  B=6356583.8
000007                  SC=0.9996
000008                  ZONE=7.
000009                  NUM=0
000010                  DO 100 I=1,1
000011                  CALL TRETOD(NUM)
000012                  CALL VCHECK(NUM)
000013                  CALL SMOOTH(NUM)
000014                  CALL DTOTPE(NUM)
000015                  REWIND 33
000016                  DO 1 I=1,NUM
000017                  READ(33) DAT
000018                  Y(I)=DAT(3)*RR
000019                  X(I)=(360.-DAT(4)) *RR
000020                  CALL UTM(A,B,Y(I),X(I),ZONE,YY(I),XX(I))
000021                  PRINT 35,DAT(15),DAT(3),DAT(4),YY(I),XX(I)
000022               35 FORMAT(1X,  5F15.2)
000023                1 CONTINUE
000024                  YS=XMIN(YY,NUM)
000025                  XS=XMIN(XX,NUM)
000026                  IYS=YS/1000
000027                  IXS=XS/1000
000028                  XS=IXS*1000
000029                  YS=IYS*1000
000030                  CALL SETOVR
000031                  CALL PLOTS(-50.,-20.5)
000032                  CALL PLOT(1.,1.,-3)
000033                  CALL AXIS(0.,0.,10HUTM ZONE 7,-10,44.,0.,XS,SC)
000034                  CALL AXIS(0.,0.,8HNORTHING,8,18.,90.,YS,SC)
000035                  XX(NUM+1)=XS
000036                  XX(NUM+2)=SC
000037                  YY(NUM+1)=YS
000038                  YY(NUM+2)=SC
000039                  PRINT 725,XS,YS,SC
000040             725  FORMAT(1X,3F16.2)
000041                  CALL LINE(XX,YY,NUM,1,1,3)
000042                  CALL PLOT(0.,0.,999)
000043                  CALL BITSET
000044                   REWIND 33
000045             100  CONTINUE
000046                  STOP
000047                  END
```

```
LET,REPORT,1,7,70,31, 4599

0001                SUBROUTINE REPORT(ID ,TAP IO)
0002                DIMENSION DAT(26),BP(26),AAS(26),BBT(26), P(26),BBS(26)
0003                DIMENSION DAT (1500),T(2200),TT(2200),S(2200),
0004               XST(2200),P(2200),PT(2200), AT(26),AP(26),
0005               XAS(26), BT(26), BP(26),BS(26),X(2000),
0006               XY(2000)
0007                COMMON/WORK/SER(13960)
0008                EQUIVALENCE(SER(1),DAT),(SER(140),T),(SER(2540),TT),(SER(4540),S),
0009               X(SER(6740),ST),(SER(9940),P),(SER(11140),PT)
0010          C     IT,IP,IS ARE THE NUMBERS OF TEMPS, ETC IN AN ORBIT
0011          C  THIS ROUTINE PRODUCES A 7 TRACK BCD TAPE OF BUOY DATA IN NODC FORMAT
0012          C     JP,JJ,JS  # OF ENGINEERING UNITS AFTER AVERAGING
0013                REWIND 33
0014                TEMP=(TEMP*9./23077+220.
0015                TST=0.
0016                JP=0
0017                JT=0
0018                JS=0
0019                DO 100 IA= 1,NJJ
0020                IT=0
0021                IP=0
0022                IS=0
0023                III=0
0024                IIP=0
0025                IIS=0
0026                DT=TST
0027                READ (33) DAT
0028                TST=DAT(13)
0029                IF((TST-DT).LT.0.058) GO TO 100
0030                N=DAT(8)
0031                IF(N.LT.2) GO TO 100
0032                IF(N.GT.26) N=26
0033          C     N= # OF SETS OF DATA IN ONE ORBIT
0034                DO 20 II=1,N
0035                ITT = 9 + (II-1)*5
0036                PRESS=OCW(DAT(ITT))
0037                TEMP=OCW(DAT(ITT+1))
0038                WSP=OCW(DAT(ITT+3))
0039                IF(DAT(13).GT.672.)     PRESS=DAT(ITT)
0040                IF(DAT(13).GT.672.)     TEMP=DAT(ITT+1)
0041                IF(DAT(13).GT.672.)     WSP=DAT(ITT+3)
0042                IF(PRESS.LT.0.0.OR.PRESS.GT.255.) GO TO 30
0043                IP=IP+1
0044                AP(IP)= PRESS
0045                BP(IP)= DAT(ITT+4)
0046                TD=BP(IP)-DAT(13)
0047                IF(TD.LT.0.) BP(IP)=INT(DAT(13))+(BP(IP)-INT(BP(IP)) )
0048                IF(TD.GT.1.) BP(IP)=INT(DAT(13))+(BP(IP)-INT(BP(IP)))
0049           30   IF(TEMP .LT.0.0.OR. TEMP.GT.255.) GO TO31
0050                IT=IT+1
0051                AT (IT)=TEMP
0052                BT (IT)=DAT(ITT+4)
0053                TD=BT(IT)-DAT(13)
0054                IF(TD.GT.1.) BT(IT)=INT(DAT(13))+(BT(IT)-INT(BT(IT)) )
```

```
000055              IF(TD.LT.0.) BT(IT)=INT(DAT(13))+(DT(IT)-INT(DT(IT)) )
000056           31 IF(ASP.LT.0.0.OR.SP.GT.2.5.) GO TO 20
000057              IS=IS+1
000058              AS (IS)=  ASP
000059              BS (IS)=  DAT(ITT+4)
000060              TD=DS(IS)-DAT(13)
000061              IF(TD.LT.0.) BS(IS)=INT(DAT(13))+(DS(IS)-INT(BS(IS)) )
000062              IF(TD.GT.1.) BS(IS)=INT(DAT(13))+(DS(IS)-INT(BS(IS)) )
000063           20 CONTINUE
000064              IF(IT.LT.2) GO TO 85
000065              DO 80 KI=2,IT
000066              IF(AT(KI).GT.AT(KI-1).AND.BT(KI).GT.BT(KI-1))  GO TO 81
000067              GO TO 82
000068           81 IIT=IIT+1
000069              AAT(IIT)=AT(KI)
000070              BBT(IIT)=BT(KI)
000071           80 CONTINUE
000072              DO 82 KI=1,IIT
000073              AT(KI)=AAT(KI)
000074              BT(KI)=BBT(KI)
000075           82 CONTINUE
000076              IT=IIT
000077           85 IF(IP.LT.2) GO TO 86
000078              DO 90 KI=2,IP
000079              IF(AP(KI).GT.AP(KI-1)) GO TO 91
000080              GO TO 90
000081           91 IIP=IIP+1
000082              AAP(IIP)=AP(KI)
000083              BBP(IIP)=BP(KI)
000084           90 CONTINUE
000085              DO 92 KI=1,IIP
000086              AP(KI)=AAP(KI)
000087              BP(KI)=BBP(KI)
000088           92 CONTINUE
000089              IP=IIP
000090           86 IF(IS.LT.2) GO TO 87
000091              DO140 KI=2,IS
000092              IF(AS(KI).GT.AS(KI-1)) GO TO141
000093              GO TO140
000094          141 IIS=IIS+1
000095              AAS(IIS)=AS(KI)
000096              BBS(IIS)=BS(KI)
000097          140 CONTINUE
000098              DO142 KI=1,IIS
000099              AS(KI)=AAS(KI)
000100              BS(KI)=BBS(KI)
000101          142 CONTINUE
000102              IS=IIS
000103           87 CONTINUE
000104          190 FORMAT(1X/)
000105              IF(IP.LT.2) GO TO 50
000106              JP= JP+1
000107              DO 40 I= 1,IP
000108              IF (AP(I).LT.AP(1)) AP(I)=AP(I)+256.
000109           40 CONTINUE
000110           50 IF(IT.LT.2) GO TO 51
000111              JT=JT+1
000112              DO 41 I=1,IT
```

```
000113              IF (AT (I).LT.AT(I)) AT(I)= T(I)+2*6.
000114           41 CONTINUE
000115           51 IF(IS.LT.2) GO TO 52
000116              JS=JS+1
000117              DO 42 I=1,IS
000118              IF (AS(I).LT. AS(I)) AS(I)=AS(I)+256.
000119           42 CONTINUE
000120           52 IF(IP.GT.1)CALL BEST(AP,PP,P(JP),PT(JP),IP)
000121              IF(IT.GT.1)CALL BEST(AT,PT,T(JT),TT(JT),IT)
000122              IF(IS.GT.1)CALL BEST(AS,PS,S(JS),ST(JS),IS)
000123          100 CONTINUE
000124        C     COMPUTE ENGINEERING UNITS 1 AT A TIME
000125        C     TOGETHER WITH MIN TIMES BETWEEN ORBITS
000126        C     TO ASSIGN VALUES TO  X=TIME AND
000127        C     Y=ENGINEERING UNIT - PLOT RESULTS
000128        C     * * * *  TEMP  * * * *
000129        C                                                  MUN,SI,PI,TI,SJ,TJ,PJ,
000130           1111 FORMAT( 1X,7I10)
000131        C                                                                  RES,.
000132           2222 FORMAT(1X,10F10.2)
000133              IF (JT.LT.2)  GO TO 70
000134              DO 60 I=2,JT
000135              X(I-1)= (TT(I)+TT(I-1))/2.
000136              Y(I-1)= T(I)-T(I-1)
000137              IF((TT(I)-TT(I-1)).LE.0.0) GO TO 177
000138          175 TRATE=Y(I-1)/(TT(I)-TT(I-1))
000139              IF(TRATE.LT.TMPMIN )   Y(I-1)=Y(I-1)+256.
000140              IF(TRATE.LT.TMPMIN )  GO TO 175
000141          177 CONTINUE
000142              Y(I-1)=Y(I-1)/(TT(I)-TT(I-1))
000143              Y(I-1)=0.1083*Y(I-1)-25.833
000144           60 CONTINUE
000145              JT=JT-1
000146              IR=0
000147              DO 10 I=1,JT
000148              IF(Y(I).GE.0.0.AND.Y(I).LT.33.) IR=IR+1
000149              IF(Y(I).GE.0.0.AND.Y(I).LT.33.)  X(IR)=X(I)
000150              IF(Y(I).GE.0.0.AND.Y(I).LT.33.)  Y(IR)=Y(I)
000151           10 CONTINUE
000152              JT=IR
000153              DO 200 I=1,JT
000154              TT(I)=X(I)
000155          200 T(I)=Y(I)
000156              DO 2001 I=2,JT
000157              IF((ABS(T(I)-T(I-1))).GT.1.1) T(I)=T(I-1)
000158         2001  CONTINUE
000159              X(JT+1)= REAL (INT(X (1)))
000160              X(JT+2)=5.
000161              Y(JT+1)=0.
000162              Y(JT+2)=4.
000163              PRINT 2222,(X(MU),Y(MU),MU=1,JT)
000164           70 IF(JP.LT.2) GO TO 71
000165              DO 61 I= 2,JP
000166              X(I-1)= (PT (I) +PT (I-1))/2.
000167              Y(I-1)= P(I)-P(I-1)
000168              IF((PT(I)-PT(I-1)).LE.0.0) GO TO 178
000169          176 PRATE=Y(I-1)/(PT(I)-PT(I-1))
000170              IF(PRATE.LT.420.) Y(I-1)=Y(I-1)+256.
```

```
      IF(PRAT..LT.620.)  GO TO 176
  178 CONTINUE
      Y(I-1)=Y(I-1)/(PT(I)-PT(I-1))
      Y(I-1)=1.3333*Y(I-1)-504.6666
   61 CONTINUE
      JP=JP-1
      IP=0
      DO 11 I=1,JP
      IF(Y(I).GT.0.0.AND.Y(I).LT.500.) IR=IR+1
      IF(Y(I).GT.0.0.AND.Y(I).LT.500.) X(IR)=X(I)
      IF(Y(I).GT.0.0.AND.Y(I).LT.500.) Y(IR)=Y(I)
   11 CONTINUE
      JP=IP
      DO 201 I=1,JP
      PT(I)=X(I)
  201 P(I)=Y(I)
      IF(JP.LT.10) GO TO 71
      X(JP+1)= REAL (INT(X(1)))
      X(JP+2)=5.
      Y(JP+1)=0.
      Y(JP)=5).
      PRINT 2222,(X(MU),Y(MU),MU=1,JP)
   71 IF (JS.LT.2) GO TO 72
      DO  62  I= 2,JS
      X(I-1)= (ST(I) + ST(I-1))/2
      Y(I-1)= S(I)-S(I-1)
      IF(Y(I-1).LT.0.)Y(I-1)=Y(I-1)+256.
      Y(I-1)=Y(I-1)/(ST(I)-ST(I-1))
      Y(I-1)=0.37931 * Y(I-1)
   62 CONTINUE
      JS=JS-1
      IR=0
      DO 12 I=1,JS
      IF(Y(I).GT.0.0.AND.Y(I).LE.50.0) IR=IR+1
      IF(Y(I).GT.0.0.AND.Y(I).LE.50.0)  Y(IR)=Y(I)
      IF(Y(I).GT.0.0.AND.Y(I).LE.50.0) X(IR)=X(I)
   12 CONTINUE
      JS=IR
      DO 202 I=1,JS
      ST(I)=X(I)
  202 S(I)=Y(I)
      X(JS+1)=REAL (INT(X (1)))
      X(JS+2)=5.
      Y(JS+2)=10.
      Y(JS+1)=0.
      PRINT 2222,(X(MU),Y(MU),MU=1,JS)
   72 CONTINUE
      REWIND 33
      IT=1
      IP=1
      IS=1
      REWIND 33
      CALL READER (NUM)
      REWIND 33
      DO 400 KXP=1,NUM
      READ(33) DAT
      TMP=-99.
      SPD=-99.
```

```
000229                PSI=-99.
000230                TIME=DAT(1)
000231                IF(JT.LT.10) GO TO 210
000232            211 IF(TIME.GT.TI(IT+1).AND.IT.LT.JT) IT=IT+1
000233                IF(IT.EQ.JT) GO TO 300
000234                IF(TIME.GT.TI(IT)) GO TO 211
000235            300 TMP=T(IT)
000236            210 IF(JP.LT.10) GO TO 220
000237            212 IF(TIME.GT.PT(IP).AND.IP.LT.JP) IP=IP+1
000238                IF(IP.EQ.JP) P(IP)=-99.
000239                IF(IP.EQ.JP) GO TO 301
000240                IF(TIME.GT.PT(IP)) GO TO 212
000241            301 PSI=P(IP)
000242            220 IF(JS.LT.10) GO TO 320
000243            213 IF(TIME.GT.ST(IS).AND.IS.LT.JS) IS=IS+1
000244                IF(IS.LT.JS) S(IS)=-99.
000245                IF(IS.EQ.JS) GO TO 302
000246                IF(TIME.GT.ST(IS)) GO TO 213
000247            302 SPD=S(IS)
000248            320 CALL NOAC(DAT,TMP,SPD,PSI)
000249            450 FORMAT(1X,8F12.2)
000250            400 CONTINUE
000251                RETURN
000252                END
                  $R
```

```
* ELI SMOOTH,1,770.07, .502

000001                SUBROUTINE SMOOTH (NUM,DAT1,DAT2)
000002          C     SMOOTHING FOR  SHIP DATA AFTER VCHECH HAS BEEN RUN
000003                COMMON/ ORK/XLAT(1000),XLON(1000),TIME(1000),TT(700),XX(700),
000004               *YY(700),DAT(13),.(700),P(15,14),PP(15,14),XP(700),YP(700),
000005               *XX1(700),XD1(700),YY1(700),YD1(700)
000006                DIMENSION WE(700),W(700),T2(2000),X2(2000),Y2(2000)
000007                REWIND 33
000008                JECT=0
000009                DO 1 I=1,NUM
000010                READ (33) DAT
000011                DID=DAT(1)
000012                XLAT(I)=DAT(3)
000013                XLON(I)=DAT(4)
000014              1 TIME(I)=DAT(13)
000015                XUU=TIME(1)
000016                DO 2 I=1,NUM
000017              2 TIME(I)=TIME(I)-XUU
000018                ITOT=0
000019                IT=TIME(NUM)-2
000020                IT=IT*4
000021                TB=2
000022                ICT=0
000023                DO 4 I=2,IT
000024                BK=-DAT1
000025                TK=DAT1
000026                ILL=10
000027          C
000028          C
000029            133 DO 3 J=1,NUM
000030                DT=TIME(J)-TB
000031                IF(DT.LT.BK.OR.DT.GT.TK) GO TO 3
000032                ICT=ICT+1
000033                TT(ICT)=TIME(J)
000034                XX(ICT)=XLON(J)
000035                YY(ICT)=XLAT(J)
000036              3 CONTINUE
000037                IF(ICT.GE.ILL) GO TO 13
000038                ICT=0
000039                TK=TK+1.
000040                BK=BK-1.
000041                GO TO 133
000042             13 BK=-DAT1
000043                TK=DAT1
000044                DO 5 K=1,ICT
000045              5 W(K)=1.
000046                CALL POLLY(ICT,XX,TT,P,W)
000047                CALL POLLY(ICT,YY,TT,PP,W)
000048                DO 6 K=1,ICT
000049                XD(K)=P(15,1)+(TT(K)*P(15,2))+(TT(K)**2.0*P(15,3))
000050                YD(K)=PP(15,1)+(TT(K)*PP(15,2))+(PP(15,3)*TT(K)**2.)
000051              6 CONTINUE
000052                DO 31 K=1,ICT
000053                IF(XX(K).LT.180.) XX1(K)=XX(K)*(-0.0174539)
000054                IF(XX(K).GE.180.) XX1(K)=(360.0-XX(K))*(0.0174539)
```

```
000055                IF(XD(K).LT.180.) XD1(K)=XD(K)*(-0.0174539)
000056                IF(XD(K).GE.180.) XD1(K)=(360.0-XD(K))*(0.0174539)
000057                YY1(K)=YY(K)*0.0174539
000058                YD1(K)=YD(K)*0.0174539
000059                CALL INV(YY1(K),XX1(K),YD1(K),XD1(K),DD,AZ)
000060                DE=SIN(AZ)*DD
000061                DN=COS(AZ)*DD
000062                WE(K)=RATE(DE)
000063             31 WN(K)=RATE(DD)
000064                CALL POLLY(ICT,XX,TT,P,WE)
000065                CALL POLLY(ICT,YY,TT,PP,WN)
000066                STT=TB
000067                ITOT=ITOT+1
000068                T2(ITOT)=TB
000069                X2(ITOT)=P(15,1)+(STT*P(15,2))+(STT*STT*P(15,3))
000070                Y2(ITOT)=PP(15,1)+(STT*PP(15,2))+(PP(15,3)*(STT**2.))
000071                IF(ITOT.LT.2) GO TO 76
000072                XPPP=0.0174539
000073                 ZX=X2(ITOT)*XPPP
000074                ZY=Y2(ITOT)*XPPP
000075                ZX1=X2(ITOT-1)*XPPP
000076                ZY1=Y2(ITOT-1)*XPPP
000077                CALL SPEED(ZY,ZX,ZY1,ZX1,1.,12.,D1,D2,D3,D4,D5,DD)
000078                IF(DD.LT.26000.) GO TO 76
000079                ITOT=ITOT-1
000080                BK=-DAT2
000081          C     ILL=ILL+1
000082                ILL=ILL+4
000083                ICT=0
000084                TK=DAT2
000085                JECT=JECT+1
000086                PRINT 999,JECT,ITOT,,DD,I
000087           999  FORMAT(1X,2I10,F12.0,I10)
000088                IF(JECT.GT.10) GO TO 77
000089                GO TO 133
000090             76 CONTINUE
000091                PRINT 75,T2(ITOT),X2(ITOT),Y2(ITOT)
000092             75 FORMAT(1X,3F15.3)
000093                ICT=0
000094                TB=TB+0.25
000095              4 CONTINUE
000096                REWIND 33
000097             77 CONTINUE
000098                REWIND 33
000099                DO 15 I=1,139
000100             15 DAT(I)=0.
000101                DO 20 I=1,ITOT
000102                DAT(1)=DID
000103                DAT(3)=Y2(I)
000104                DAT(4)=X2(I)
000105                DAT(13)=T2(I)
000106                WRITE (33) DAT
000107             20 CONTINUE
000108                REWIND 33
000109                NUM=ITOT
000110                RETURN
000111                END
```

```
ELT SORT,1,761122, 43114

      SUBROUTINE SORT(ICT)
      COMMON /WORK/ A (13900)
      COMMON/JHY/ID
      DIMENSION B(139,100)
      EQUIVALENCE(A,B)
      LOGICAL EOF
      EOF=.FALSE.
      ICT=0
      ISS=0
      REWIND 33
    1 FORMAT(I10,6F10.3)
      READ 1,ID,XLTMN,XLTMX,XLNMN,XLNMX,DAYMN,DAYMX
      PRINT1,ID,XLTMN,XLTMX,XLNMN,XLNMX,DAYMN,DAYMX
    5 CALL INPUT(A,EOF)
      IF(EOF) REWIND 33
      IF(EOF)ISS=100
      IF(EOF) PRINT 1172,ICT
 1172 FORMAT(' ICT=',I10)
      IF(ISS.GT.0.AND.ICT.LT.10)  STOP
      IF(ICT.GT.998) ICT=998
      IF(EOF) CALL CRONO(ICT)
      IF(EOF) RETURN
      IF(ID.NE.0.AND.INT(DAYMN).NE.0. AND.INT(XLTMX).EQ.0) GO TO 30
      IF(ID.NE.0.AND.INT(DAYMN).NE.0.AND.INT(XLTMX).NE.0) GO TO 10
      IF(ID.EQ.0.AND.INT(DAYMN).NE.0.AND.INT(XLTMX).NE.0)  GO TO 40
      IF(ID.NE.0.AND.INT(DAYMN).EQ.0.AND.INT(XLTMN).NE.0) GO TO 20
      PRINT 2
      STOP 2
    2 FORMAT('    *****SORT DATA ERROR U ARE BEING ZAPPED CHECK INPUT***')
   10 DO 50 I=1,100
      IF(INT(B(1,I)).EQ.ID.AND.B(3,I).GE.XLTMN.AND.B(3,I).LE.XLTMX.AND.
     . B(13,I).GE.DAYMN.AND. B(13,I).LE.DAYMX.AND.B(4,I).GE.XLNMN.AND.
     .  B(4,I).LE.XLNMX)
     X WRITE(33) (B(J,I),J=1,139)
      IF(INT(B(1,I)).EQ.ID.AND.B(3,I).GE.XLTMN.AND.B(3,I).LE.XLTMX.AND.
     . B(13,I).GE.DAYMN.AND. B(13,I).LE.DAYMX.AND.B(4,I).GE.XLNMN.AND.
     .  B(4,I).LE.XLNMX)
     X ICT=ICT+1
   50 CONTINUE
      GO TO 5
   20 DO 51 I=1,100
      IF(INT(B(1,I)).EQ.ID.AND.B(3,I).GE.XLTMN.AND.B(3,I).LE.XLTMX.AND.
     .B(4,I).GE.XLNMN.AND.B(4,I).LE.XLNMX)
     X  WRITE(33)(B(J,I),J=1,139)
      IF(INT(B(1,I)).EQ.ID.AND.B(3,I).GE.XLTMN.AND.B(3,I).LE.XLTMX.AND.
     .B(4,I).GE.XLNMN.AND.B(4,I).LE.XLNMX)
     X  ICT=ICT+1
   51 CONTINUE
      GO TO 5
   30 DO 52 I=1,100
      IF(INT(B(1,I)).EQ.ID.AND.B(13,I).GE.DAYMN.AND.B(13,I).LE.DAYMX)
     X  WRITE(33)(B(J,I),J=1,139)
      IF(INT(B(1,I)).EQ.ID.AND.B(13,I).GE.DAYMN.AND.B(13,I).LE.DAYMX)
     X ICT=ICT+1
```

```
000055              52 CONTINUE
000056                 GO TO 5
000057              40 DO 53 I=1,100
000058                 IF(B(3,I).GE.XLTMN.AND.B(3,I).LE.XLTMX.AND.B(4,I).GE.XLNMN.AND.
000059                . B(4,I).LE.XLNMX.AND.B(13,I).GE.DAYMN.AND.B(13,I).LE.DAYMX)
000060                X  WRITE(33)(B(J,I),J=1,13)
000061                 IF(B(3,I).GE.XLTMN.AND.B(3,I).LE.XLTMX.AND.B(4,I).GE.XLNMN.AND.
000062                . B(4,I).LE.XLNMX.AND.B(13,I).GE.DAYMN.AND.B(13,I).LE.DAYMX)
000063                X  ICT=ICT+1
000064              53 CONTINUE
000065                 GO TO 5
000066                 END
```

```
% ELT SORT2,I,771026, 37.+1

001                SUBROUTINE SORT2(ICT)
002                COMMON /WORK/ A (13900)
003                COMMON/JAY/ID
004                DIMENSION B(13,100)
005                EQUIVALENCE(A,B)
006                LOGICAL EOF
007                EOF=.FALSE.
008                ICT=0
009                ISS=0
010                REWIND 33
011              1 FORMAT(I10,6F10.3)
012                READ 1,ID,XLTMN,XLTMX,XLNMN,XLNMX,DAYMN,DAYMX
013                PRINT1,ID,XLTMN,XLTMX,XLNMN,XLNMX,DAYMN,DAYMX
014              5 CALL INPT2(A,EOF)
015                IF(EOF) REWIND 33
016                IF(EOF)ISS=100
017                IF(EOF) PRINT 1172,ICT
018           1172 FORMAT(' ICT=',I10)
019                IF(ISS.GT.0.AND.ICT.LT.10)  STOP
020                IF(ICT.GT.998) ICT=998
021                IF(EOF) CALL CHRONO(ICT)
022                IF(EOF) RETURN
023                IF(ID.NE.0.AND.INT(DAYMN).NE.0. AND.INT(XLTMX).EQ.0) GO TO 30
024                IF(ID.NE.0.AND.INT(DAYMN).NE.0.AND.INT(XLTMX).NE.0) GO TO 10
025                IF(ID.EQ.0.AND.INT(DAYMN).NE.0.AND.INT(XLTMX).NE.0)  GO TO 40
026                IF(ID.NE.0.AND.INT(DAYMN).EQ.0.AND.INT(XLTMN).NE.0) GO TO 20
027                PRINT 2
028                STOP 2
029              2 FORMAT('   *****SORT DATA ERROR U ARE BEING ZAPPED CHECK INPUT***')
030             10 DO 50 I=1,100
031                IF(INT(B(1,I)).EQ.ID.AND.B(3,I).GE.XLTMN.AND.B(3,I).LE.XLTMX.AND.
032               . B(13,I).GE.DAYMN.AND. B(13,I).LE.DAYMX.AND.B(4,I).GE.XLNMN.AND.
033               .  B(4,I).LE.XLNMX)
034               X WRITE(33) (B(J,I),J=1,13)
035                IF(INT(B(1,I)).EQ.ID.AND.B(3,I).GE.XLTMN.AND.B(3,I).LE.XLTMX.AND.
036               . B(13,I).GE.DAYMN.AND. B(13,I).LE.DAYMX.AND.B(4,I).GE.XLNMN.AND.
037               .  B(4,I).LE.XLNMX)
038               X ICT=ICT+1
039              50 CONTINUE
040                GO TO 5
041             20 DO 51 I=1,100
042                IF(INT(B(1,I)).EQ.ID.AND.B(3,I).GE.XLTMN.AND.B(3,I).LE.XLTMX.AND.
043               .B(4,I).GE.XLNMN.AND.B(4,I).LE.XLNMX)
044               X  WRITE(33)(B(J,I),J=1,13)
045                IF(INT(B(1,I)).EQ.ID.AND.B(3,I).GE.XLTMN.AND.B(3,I).LE.XLTMX.AND.
046               .B(4,I).GE.XLNMN.AND.B(4,I).LE.XLNMX)
047               X  ICT=ICT+1
048              51 CONTINUE
049                GO TO 5
050             30 DO 52 I=1,100
051                IF(INT(B(1,I)).EQ.ID.AND.B(13,I).GE.DAYMN.AND.B(13,I).LE.DAYMX)
052               X  WRITE(33)(B(J,I),J=1,13)
053                IF(INT(B(1,I)).EQ.ID.AND.B(13,I).GE.DAYMN.AND.B(13,I).LE.DAYMX)
054               X ICT=ICT+1
```

```
00055              52 CONTINUE
00056                 GO TO 5
00057              40 DO 53 I=1,100
00058                 IF(B(3,I).GE.XLTMN.AND.B(3,I).LE.XLTMX.AND.B(4,I).GE.XLNMN.AND.
00059                . B(4,I).LE.XLNMN.AND.B(13,I).GE.DAYMN.AND.B(13,I).LE.DAYMX)
00060                X  WRITE(33)(B(J,I),J=1,13)
00061                 IF(B(3,I).GE.XLTMN.AND.B(3,I).LE.XLTMX.AND.B(4,I).GE.XLNMN.AND.
00062                . B(4,I).LE.XLNMN.AND.B(13,I).GE.DAYMN.AND.B(13,I).LE.DAYMX)
00063                X  ICT=ICT+1
00064              53 CONTINUE
00065                 GO TO 5
00066                 END
```

```
. ELT SPOACC,1,770667, 6650

1                SUBROUTINE SPOACC(JOB)
2          C
3          C       GIVES PLOTS OF TOTAL VELOCITY AND ACCELERATION IN UNITS OF
4          C         CM/SEC AND CM/SEC/SEC VS TIME IN DAYS
5          C
6                COMMON/WORK/SER(6701),DAT(13),TIME(1000),XLAT(1000),XLON(1000),
7               *A(1000),TT(1000),T(1000),V(1000)
8                IF(JOB.GT.998) STOP 7
9                REWIND 33
0                DO 10 I=1,1000
1                READ (33) DAT
2                IF(DAT(4).LT.180.) DAT(4)=DAT(4)*(-1.)
3                IF(DAT(4).GE.180.) DAT(4)=360.0-DAT(4)
4                XLAT(I)=DAT(3)*0.01745329
5                XLON(I)=DAT(4)*0.01745329
6             10 TIME(I)=DAT(13)*1440.
7                N=NUM-1
8                DO 11 I=1,N
9                T(I)=(TIME(I+1)+TIME(I))/2.
0                CALL SPEED(XLAT(I),XLON(I),XLAT(I+1),XLON(I+1),TIME(I),TIME(I+1),
1               * D6,D5,V(I),D1,D2,D3)
2                V(I)=V(I)*1.666667
3                T(I)=T(I)/1440.
4             11 CONTINUE
5             30 FORMAT(1X,10F10.3)
6                CALL SETOVR
7                CALL PLOTS(-40.,-10.,1)
8                CALL PLOT(1.,1.,-3)
9                TD=T(1)
0                DO 25 J=1,N
1             25 T(J)=T(J)-TD
2                PRINT 30,(T(K),V(K),K=1,N)
3                V(N+1)=0.
4                V(N+2)=50.
5                T(N+1)=0.
6                T(N+2)=10.
7                CALL AXIS(0.,0.,12HTIME IN DAYS,-12,15.,0.,T(N+1),T(N+2))
8                CALL AXIS(0.,0.,13HVEL IN CM/SEC,13,8.,90.,V(N+1),V(N+2))
9                CALL LINE(T,V,N,1,1,3)
0                CALL PLOT(0.,0.,999)
1                CALL BITSET
2                REWIND 33
3                N=N-1
4                DO 20 I=1,N
5                TT(I)=((T(I+1)+T(I))/2.)-(T(2)/2.)
6             20 A(I)=(V(I+1)-V(I))/(T(I+1)-T(I))
7                PRINT 30,(TT(K),A(K),K=1,N)
8                CALL PLOT (1.,1.,-3)
9                TT(N+1)=0.
0                TT(N+2)=10.
1                A(N+1)=-4.
2                A(N+2)=1.
3                CALL AXIS(0.,0.,  'TIME IN DAYS'  ,-12,8.,0.,TT(N+1),TT(N+2))
4                CALL AXIS(0.,0.,26HACCELERATION IN CM/SEC/SEC,26,8.,90.,A(N+1),
```

```
000055                  +A(I+2))
000056                   CALL LINE(IT,A(1,1),1,1,3)
000057                   CALL PLOT(0.,0.,999)
000058                   CALL OFFSET
000059                   RETURN
000060                   END
```

```
      SUBROUTINE SPEED (LAT,LON,LAT1,LON1,T1,T2,LATM,LONM,V,VE,VN,D)
C
C     LAT AND LON ARE WGS OF FIRST POINT, LAT1 AND LON1 ARE GPS OF SECOND POIN
C     LATM AND LONM ARE MIDWAY PROG ON GT CIRCLE, T1 AND T2 ARE TIMES, V, VE,
C     AND VN ARE THE RESULTS.
C
      REAL LAT,LON, LAT1, LON1,LATM,LONM
C
C     ALL ANGLES ARE RADIANS, DISTANCES METERS, TIME SECONDS, VEL ARC IN M/SEC
C
      CALL INV(LAT,LON,LAT1,LON1,D,AZ)
      DD=D/2.
      CALL FWDGP(LAT,LON,AZ,DD,LATM,LONM,AZM)
      T=T2-T1
      V=D/T
      VE=SIN(AZM)*V
      VN=COS(AZM)*V
      RETURN
      END
```

```
% ELT TMPLT,1,760,13, 51.2

00001                 SUBROUTINE TMPLT(JOB)
00002           C
00003           C     GIVES A PLOT OF HOURS VS DAYS USING SATTELITE ACCURACY ESTIMATES
00004           C
00005                 COMMON/JOBK/SER(11500),TIME(1000),ACC(1000),HOUR(1000)
00006                 DIMENSION DAT(139)
00007                 EQUIVALENCE (DAT,SER(11360))
00008                 DO 1 I=1,NUM
00009                 READ (33) DAT
00010                 TIME(I)=DAT(13)
00011                 ACC(I)=DAT(5)
00012                 HOUR(I)=TIME(I)*1440.
00013                    HOUR(I)=AMOD(HOUR(I),24.)
00014               1 CONTINUE
00015                 ST=TIME(1)
00016                 DO 2 I=1,NUM
00017               2 TIME(I)=TIME(I)-ST
00018                 CALL SETOVR
00019                 CALL PLOTS(-91.,-10.,1)
00020                 CALL PLOT(1.,1.,-3)
00021                 CALL AXIS(0.,0.,4HDAYS,-4,TIME(NUM),0.,0.,1.)
00022                 CALL AXIS(0.,0.,4HHOUR,4,24.,90.,0.,4.)
00023                 DO 3 I=1,NUM
00024                 CALL NUMBER(TIME(I),HOUR(I),0.1,ACC(I),90.,0.)
00025               3 CONTINUE
00026                 CALL PLOT(0.,0.,999)
00027                 CALL BITSET
00028                 RETURN
00029                 END
```

```
@ ELT TOTP,1,771,20, 376,4

000001                SUBROUTINE TOTP(NUM,I1,I2)
000002          C     THIS ROUTINE READS 2 DTOTPE TAPES AND COMBINES NUM SO THAT THE
000003          C      TOTAL NUM AND ALL THE DATA MAY BE WRITTEN BACK WITH A DTOTPE
000004          C     I1 AND I2 ARE THE TAPE UNITS  THE INPUT TAPES ARE ASSIGNED TO
000005                COMMON/WORK/DAT(139)
000006                REWIND 33
000007                READ (I1) N1
000008                DO 2 I=1,N1
000009                READ (I1) DAT
000010                WRITE (33) DAT
000011              2 CONTINUE
000012                READ (I2) N2
000013                DO 3 I=1,N2
000014                READ (I2) DAT
000015                WRITE (33) DAT
000016              3 CONTINUE
000017                NUM=N1+N2
000018                REWIND 33
000019                RETURN
000020                END
```

```
      ELT TAPTO,1,7,1,97,,,
```

```
@ ELT TPOUT,1,76,209, 42593

000001                SUBROUTINE TPOUT
000002                DIMENSION DTAP(13900)
000003                REWIND 33
000004                DO 10 I=1,13900,139
000005                II=I+138
000006                READ (33) (DTAP(J),J=I,II)
000007             10 CONTINUE
000008                CALL OUT(DTAP)
000009                REWIND 33
000010                RETURN
000011                END
```

```
» ELT TPS,1,77066,0651 /

C      THIS PROGRAMS USES DROP FILE 33 DATA TO PRODUCE
C      PLOTS OF TEMPERATURE, LOAD CELL PRESSURE AND WIND SPEED VS
C      TIME IN DAYS.
       SUBROUTINE TPS(DAT,TSPAN)
       DIMENSION AAT(26),AAP(26),AAS(26),BBT(26),BBP(26),BBS(26)
       DIMENSION DAT (139),T(2200),TT(2200),S(2200),
      XST(2200),P(2200),PT(2200), AT(26),AP(26),
      XAS(26),ST(26), BT(26),BP(26),BS(26),X(2000),
      XY(2000)
       COMMON/WORK/SER(13900)
       EQUIVALENCE(SER(1),DAT),(SER(140),T),(SER(2340),TT),(SER(4540),S),
      X(SER(6740),ST),(SER(9040),P),(SER(11140),PT)
C      IT,IP,IS ARE THE NUM OF TEMPS, ETC IN AN ORBIT
C      JP,JJ,JS  # OF ENGINEERING UNITS AFTER AVERAGING
       REWIND 33
       TSPMIN=TSPAN*9.23077+220.
       TST=0.
       JP=0
       JT=0
       JS=0
       DO 100 IA= 1,NOR
       IT=0
       IP=0
       IS=0
       IIT=0
       IIP=0
       IIS=0
       DT=TST
       READ (33) DAT
       TST=DAT(13)
       IF((TST-DT).LT.0.058) GO TO 100
       N=DAT(8)
       IF(N.LT.2) GO TO 100
       IF(N.GT.26) N=26
C      N= # OF SETS OF DATA IN ONE ORBIT
       DO 20 II=1,N
       ITT = 9 + (II-1)*5
       PRESS=OCW(DAT(ITT))
       TEMP=OC (DAT(ITT+1))
       WSP=OCW(DAT(ITT+3))
       IF(DAT(13).GT.672.)     PRESS=DAT(ITT)
       IF(DAT(13).GT.672.)     TEMP=DAT(ITT+1)
       IF(DAT(13).GT.672.)     WSP=DAT(ITT+3)
       IF(PRESS.LT.0.0.OR.PRESS.GT.255.) GO TO 30
       IP=IP+1
       AP(IP)= PRESS
       BP(IP)= DAT(ITT+4)
       TD=BP(IP)-DAT(13)
       IF(TD.LT.0.) BP(IP)=INT(DAT(13))+(BP(IP)-INT(BP(IP)) )
       IF(TD.GT.1.) BP(IP)=INT(DAT(13))+(BP(IP)-INT(BP(IP)))
    30 IF(TEMP .LT.0.0.OR. TEMP.GT.255.) GO TO31
       IT=IT+1
       AT (IT)=TEMP
       BT (IT)=DAT(ITT+4)
```

```
      TD=BT(IT)-BAT(1)
      IF(TD.GT.1.) AT(IT)=INT(DAT(13))+(AT(IT)-INT(AT(IT)))
      IF(TD.LT.0.) BT(IT)=INT(DAT(13))+(BT(IT)-INT(BT(IT)))
   31 IF(ASP.LT.0.0.OR.ASP.GT.25.) GO TO 20
      IS=IS+1
      AS(IS)=ASP
      BS(IS)=BAT(IIT+4)
      TD=BS(IS)-BAT(13)
      IF(TD.LT.0.) BS(IS)=INT(DAT(13))+(BS(IS)-INT(BS(IS)))
      IF(TD.GT.1.) BS(IS)=INT(DAT(13))+(BS(IS)-INT(BS(IS)))
   20 CONTINUE
      IF(IT.LT.2) GO TO 85
      DO 80 KI=2,IT
      IF(AT(KI).GT.AT(KI-1).AND.BT(KI).GT.BT(KI-1))  GO TO 81
      GO TO 80
   81 IIT=IIT+1
      AAT(IIT)=AT(KI)
      BBT(IIT)=BT(KI)
   80 CONTINUE
      DO 82 KI=1,IIT
      AT(KI)=AAT(KI)
      BT(KI)=BBT(KI)
   82 CONTINUE
      IT=IIT
   85 IF(IP.LT.2) GO TO 86
      DO 90 KI=2,IP
      IF(AP(KI).GT.AP(KI-1)) GO TO 91
      GO TO 90
   91 IIP=IIP+1
      AAP(IIP)=AP(KI)
      BBP(IIP)=BP(KI)
   90 CONTINUE
      DO 92 KI=1,IIP
      AP(KI)=AAP(KI)
      BP(KI)=BBP(KI)
   92 CONTINUE
      IP=IIP
   86 IF(IS.LT.2) GO TO 87
      DO140 KI=2,IS
      IF(AS(KI).GT.AS(KI-1)) GO TO141
      GO TO140
  141 IIS=IIS+1
      AAS(IIS)=AS(KI)
      BBS(IIS)=BS(KI)
  140 CONTINUE
      DO142 KI=1,IIS
      AS(KI)=AAS(KI)
      BS(KI)=BBS(KI)
  142 CONTINUE
      IS=IIS
   87 CONTINUE
  190 FORMAT(1X/)
      IF(IP.LT.2) GO TO 50
      JP=JP+1
      DO 40 I= 1,IP
      IF (AP(I).LT.AP(1)) AP(I)=AP(I)+256.
   40 CONTINUE
   50 IF(IT.LT.2) GO TO 51
```

```
000113                JT=JT+1
000114                DO 41 I=1,IT
000115                IF (AT (I).LT.AT(1)) AT(I)=AT(I)+256.
000116             41 CONTINUE
000117             51 IF(IS.LT.2) GO TO 52
000118                JS=JS+1
000119                DO 42 I=1,IS
000120                IF (AS(I).LT. AS(1)) AS(I)=AS(I)+256.
000121             42 CONTINUE
000122             52 IF(IP.GT.1)CALL RLST(AP,PT,P(JP),PT(JP),IP)
000123                IF(IT.GT.1)CALL RLST(AT,PT,T(JT),TT(JT),IT)
000124                IF(IS.GT.1)CALL RLST(AS,PS,S(JS),ST(JS),IS)
000125            100 CONTINUE
000126           C      COMPUTE ENGINEERING UNITS 1 AT A TIME
000127           C      TOGETHER WITH MID TIMES BETWEEN ORBITS
000128           C      TO ASSIGN VALUES TO  X=TIME AND
000129           C      Y=ENGINEERING UNIT - PLOT RESULTS
000130           C      * * * *  TEMP  * * * *
000131           C                                                  MON,SI,PI,TI,SJ,TJ,PJ,
000132            1111 FORMAT( 1X,7I10)
000133           C                                                                    RES,
000134            2222 FORMAT(1X,10F10.2)
000135                CALL SLOVR
000136                CALL PLOTS (-90.,-10.)
000137                CALL PLOT(1.,1.,-3)
000138                IF (JT.LT.2)  GO TO 70
000139                DO 60 I=2,JT
000140                X(I-1)= (TT(I)+TT(I-1))/2.
000141                Y(I-1)= T(1)-T(I-1)
000142                IF((TT(I)-TT(I-1)).LE.0.0) GO TO 177
000143            175 TRATE=Y(I-1)/(TT(I)-TT(I-1))
000144                IF(TRATE.LT.TMPMIN )   Y(I-1)=Y(I-1)+256.
000145                IF(TRATE.LT.TMPMIN )  GO TO 175
000146            177 CONTINUE
000147                Y(I-1)=Y(I-1)/(TT(I)-TT(I-1))
000148                Y(I-1)=0.1083*Y(I-1)-23.833
000149             60 CONTINUE
000150                JT=JT-1
000151                IR=0
000152                DO 10 I=1,JT
000153                IF(Y(I).GE.0.0.AND.Y(I).LT.33.) IR=IR+1
000154                IF(Y(I).GE.0.0.AND.Y(I).LT.33.)  X(IR)=X(I)
000155                IF(Y(I).GE.0.0.AND.Y(I).LT.33.)  Y(IR)=Y(I)
000156             10 CONTINUE
000157                JT=IR
000158                X(JT+1)= REAL (INT(X (1)))
000159                X(JT+2)=10.
000160                Y(JT+1)=0.
000161                Y(JT+2)=4.
000162                CALL AXIS(0.,0.,12HTIME IN DAYS,-12 , 20.,0.,X(JT+1),10.)
000163                CALL AXIS (0.,0.,'TEMPERATURE',11,8.,90.,0.,4.)
000164                CALL LINE (X,Y,JT,1,1,3)
000165                CALL PLOT (0.,0.,999)
000166                CALL RITSET
000167                CALL PLOT (1.,1.,-3)
000168                PRINT 2222,(X(I),Y(I),I=1,JT)
000169             70 IF(JP.LT.2) GO TO 71
000170                DO 61 I= 2,JP
```

```
000171              X(I-1)= (PT (I) +PT (I-1))/2.
000172              Y(I-1)= P(I)-P(I-1)
000173              IF((PT(I)-PT(I-1)),LE.0.0) GO TO 178
000174           176 PRATE=Y(I-1)/(PT(I)-PT(I-1))
000175              IF(PRATE.LT.420.) Y(I-1)=Y(I-1)+256.
000176              IF(PRATE.LT.420.)  GO TO 176
000177           178 CONTINUE
000178              Y(I-1)=Y(I-1)/(PT(I)-PT(I-1))
000179              Y(I-1)=1.3333*Y(I-1)-554.666
000180            61 CONTINUE
000181              JP=JP-1
000182              IR=0
000183              DO 11 I=1,JP
000184              IF(Y(I).GT.0.0.AND.Y(I).LT.500.) IR=IR+1
000185              IF(Y(I).GT.0.0.AND.Y(I).LT.500.) X(IR)=X(I)
000186              IF(Y(I).GT.0.0.AND.Y(I).LT.500.) Y(IR)=Y(I)
000187            11 CONTINUE
000188              JP=IR
000189              IF(JP.LT.10) GO TO 71
000190              X(JP+1)= REAL (INT(X(1)))
000191              X(JP+2)=10.
000192              Y(JP+1)=0.
000193              Y(JP)=50.
000194              CALL AXIS(0.,0.,12HTIME IN DAYS,-12 , 20.,0.,X(JP+1),10.)
000195              CALL AXIS (0.,0.,'LOAD CELL IN PSI',16,8.,90.,0.,50.)
000196              CALL LINE (X,Y,JP,1,1,3)
000197              CALL PLOT (0.,3.,999)
000198              CALL BITSET
000199              CALL PLOT (1.,1.,-3)
000200              PRINT 2222,(X(NU),Y(NU),NU=1,JP)
000201            71 IF (JS.LT.2) GO TO 72
000202              DO  62  I= 2,JS
000203              X(I-1)= (ST(I) + ST(I-1))/2
000204              Y(I-1)= S(I)-S(I-1)
000205              IF(Y(I-1).LT.0.)Y(I-1)=Y(I-1)+256.
000206              Y(I-1)=Y(I-1)/(ST(I)-ST(I-1))
000207              Y(I-1)=0.37931 * Y(I-1)
000208            62 CONTINUE
000209              JS=JS-1
000210              IR=0
000211              DO 12 I=1,JS
000212              IF(Y(I).GT.0.0.AND.Y(I).LE.50.0) IR=IR+1
000213              IF(Y(I).GT.0.0.AND.Y(I).LE.50.0)  Y(IR)=Y(I)
000214              IF(Y(I).GT.0.0.AND.Y(I).LE.50.0) X(IR)=X(I)
000215            12 CONTINUE
000216              JS=IR
000217              X(JS+1)=REAL (INT(X (1)))
000218              X(JS+2)=10.
000219              Y(JS+2)=10.
000220              Y(JS+1)=0.
000221              CALL AXIS(0.,0.,12HTIME IN DAYS,-12 , 20.,0.,X(JS+1),10.)
000222              CALL AXIS (0.,0.,'WIND SPEED IN MPH',17,8.,90.,0.,10.)
000223              CALL LINE (X,Y,JS,1,1,3)
000224              CALL PLOT (0.,0.,999)
000225              CALL BITSET
000226              PRINT 2222,(X(NU),Y(NU),NU=1,JS)
000227            72 CONTINUE
000228              REWIND 33
```

```
000229                  IT=1
000230                  IP=1
000231                  IS=1
000232                  DO 400 KKK=1,NUP
000233                  READ(32) DAT
000234                  TMP=-99.
000235                  SPD=-99.
000236                  PSI=-99.
000237                  TIME=DAT(15)
000238                  IF(JT.LT.10) GO TO 210
000239              211 IF(TIME.GT.TT(IT ).AND.IT.LT.JT) IT=IT+1
000240                  IF(IT.EQ.JT) GO TO 300
000241                  IF(TIME.GT.TT(IT)) GO TO 211
000242              300 TMP=T(IT)
000243              210 IF(JP.LT.10) GO TO 220
000244              212 IF(TIME.GT.PT(IP).AND.IP.LT.JP) IP=IP+1
000245                  IF(IP.EQ.JP) GO TO 301
000246                  IF(TIME.GT.PT(IP)) GO TO 212
000247              301 PSI=P(IP)
000248              220 IF(JS.LT.10) GO TO 320
000249              213 IF(TIME.GT.ST(IS).AND.IS.LT.JS) IS=IS+1
000250                  IF(IS.EQ.JS) GO TO 302
000251                  IF(TIME.GT.ST(IS)) GO TO 213
000252              302 SPD=S(IS)
000253              320 PRINT 450,DAT (1),TIME,DAT(2),DAT(3),DAT(4),TMP,SPD,PSI
000254              450 FORMAT(1X,6F12.2)
000255              400 CONTINUE
000256                  RETURN
000257                  END
```

```
@I ASM UMF201,UMF201
ASSEMBLED BY UNIVAC 1108 EXEC II ASSEMBLER - 2400 000RA
THIS ASSEMBLY WAS DONE ON 07 JUN 77 AT 18:28:30
000001                                                          PROGRAM
000002       00    000000  10 00 05 13 1 000000   UMF201*      L          A5,*0,X11
000003             000001  74 00 05 13 0 000006                JZ         A5,6,X11
000004             000002  74 03 05 13 0 000006                JN         A5,6,X11
000005             000003  15 16 05 00 0 000001                AN,U       A5,1
000006             000004  27 00 15 13 1 000002                L          A1,*2,X11
000007             000005  25 16 15 00 0 000001                AN,U       A1,1
000008             000006  27 16 14 00 0 000000                L,U        A0,0
000009             000007  34 16 00 00 0 000006                DI,U       A0,6
000010             000010  24 00 14 13 0 000001                A          A0,1,X11
000011             000011  46 16 14 00 0 000001                LXI,U      A0,1
000012             000012  46 16 15 00 0 000001                LXI,U      A1,1
000013             000013  27 00 17 13 1 000004                L          A3,*4,X11
000014             000014  25 16 17 00 0 000001                AN,U       A3,1
000015             000015  27 16 16 00 0 000000                L,U        A2,0
000016             000016  34 16 02 00 0 000006                DI,U       A2,6
000017             000017  24 00 16 13 0 000003                A          A2,3,X11
000018             000020  46 16 16 00 0 000001                LXI,U      A2,1
000019             000021  46 16 17 00 0 000001                LXI,U      A3,1
000020             000022  72 10 00 15 2 000032   LOOP         EX         GETC,*A1
000021             000023  55 00 01 00 0 000046                TG         A1,(1,6)
000022             000024  26 16 15 00 0 000000                LXM,U      A1,0
000023             000025  72 10 00 17 2 000040                EX         PUTC,*A3
000024             000026  55 00 03 00 0 000046                TG         A3,(1,6)
000025             000027  26 16 17 00 0 000000                LXM,U      A3,0
000026             000030  70 01 01 00 0 000022                JGD        A5,LOOP
000027             000031  74 04 00 13 0 000006                J          6,X11
000028             000032  10 15 04 14 0 000000   GETC         L,S1       A4,0,A0
000029             000033  10 14 04 14 0 000000                L,S2       A4,0,A0
000030             000034  10 13 04 14 0 000000                L,S3       A4,0,A0
000031             000035  10 12 04 14 0 000000                L,S4       A4,0,A0
000032             000036  10 11 04 14 0 000000                L,S5       A4,0,A0
000033             000037  10 10 04 14 2 000000                L,S6       A4,0,*A0
000034             000040  01 15 04 16 0 000000   PUTC         S,S1       A4,0,A2
000035             000041  01 14 04 16 0 000000                S,S2       A4,0,A2
000036             000042  01 13 04 16 0 000000                S,S3       A4,0,A2
000037             000043  01 12 04 16 0 000000                S,S4       A4,0,A2
000038             000044  01 11 04 16 0 000000                S,S5       A4,0,A2
000039             000045  01 10 04 16 2 000000                S,S6       A4,0,*A2
000040                                                         END
                   000046  000001 000006
```

```
@I ASM UMF217,UMF217
ASSEMBLED BY UNIVAC 1108 EXEC II ASSEMBLER  2404 0006A
THIS ASSEMBLY WAS DONE ON 07 JUN 77 AT 14:20:31
000001                                                          REGISTERS
000002      00   000000  27 16 14 00 0 000000   UMF217*  L,U      A1,0
000003           000001  27 00 15 13 1 000002            L       A1,*2,X11
000004           000002  74 00 01 13 0 000005            JZ      A1,5,X11
000005           000003  74 03 01 13 0 000005            JN      A1,5,X11
000006           000004  25 16 15 00 0 000001            AN,U    A1,1
000007           000005  23 00 01 00 0 000015            L       R1,A1
000008           000006  27 16 15 00 0 000000            L,U     A1,0
000009           000007  27 00 16 13 1 000001            L       A2,*1,X11
000010           000010  25 16 16 00 0 000001            AN,U    A2,1
000011           000011  34 16 01 00 0 000006            DI,U    A1,6
000012           000012  24 00 15 13 0 000000            A       A1,0,X11
000013           000013  46 16 15 00 0 000001            LXI,U   A1,1
000014           000014  46 16 16 00 0 000001            LXI,U   A2,1
000015           000015  10 16 04 00 0 000000            L,U     A4,0
000016           000016  10 16 05 00 0 000000            L,U     A5,0
000017           000017  72 10 00 16 2 000060   LOOP     EX      GETC,*A2
000018           000020  55 00 02 00 0 000066            TG      A2,(1,6)
000019           000021  26 16 16 00 0 000000            LXM,U   A2,0
000020           000022  25 16 17 00 0 000060            AN,U    A3,060
000021           000023  74 03 03 00 0 000036            JN      A3,NONDIG
000022           000024  55 16 03 00 0 000012            TG,U    A3,10
000023           000025  74 04 00 00 0 000056            J       ILCHAR
000024           000026  10 16 05 00 0 000001            L,U     A5,1
000025           000027  31 16 00 00 0 000012   ADDIN    MSI,U   A0,10
000026           000030  24 00 14 00 0 000017            A       A0,A3
000027           000031  70 04 01 00 0 000017   JGD      JGD     R1,LOOP
000028           000032  74 02 04 00 0 000034   RETURN   JP      A4,$+2
000029           000033  11 00 00 00 0 000014            LN      A0,A0
000030           000034  06 00 14 13 1 000003            S       A0,*3,X11
000031           000035  74 04 00 13 0 000005            J       5,X11
000032           000036  24 16 17 00 0 000060   NONDIG   A,U     A3,060
000033           000037  52 16 03 00 0 000005            TE,U    A3,05
000034           000040  74 04 00 00 0 000044            J       TNEG
000035           000041  74 00 05 00 0 000031            JZ      A5,JGD
000036           000042  27 16 17 00 0 000000            L,U     A3,0
000037           000043  74 04 00 00 0 000027            J       ADDIN
000038           000044  74 01 05 00 0 000056   TNEG     JNZ     A5,ILCHAR
000039           000045  74 01 04 00 0 000056            JNZ     A4,ILCHAR
000040           000046  52 16 03 00 0 000041            TE,U    A3,041
000041           000047  74 04 00 00 0 000052            J       TPLUS
000042           000050  11 16 04 00 0 000001            LN,U    A4,1
000043           000051  74 04 00 00 0 000031            J       JGD
000044           000052  52 16 03 00 0 000042   TPLUS    TE,U    A3,042
000045           000053  74 04 00 00 0 000056            J       ILCHAR
000046           000054  10 16 04 00 0 000001            L,U     A4,1
000047           000055  74 04 00 00 0 000031            J       JGD
000048           000056  27 16 17 00 0 000000   ILCHAR   L,U     A3,0
000049           000057  74 04 00 00 0 000027            J       ADDIN
000050           000060  27 15 17 15 0 000000   GETC     L,S1    A3,0,A1
000051           000061  27 14 17 15 0 000000            L,S2    A3,0,A1
000052           000062  27 13 17 15 0 000000            L,S3    A3,0,A1
000053           000063  27 12 17 15 0 000000            L,S4    A3,0,A1
000054           000064  27 11 17 15 0 000000            L,S5    A3,0,A1
000055           000065  27 10 17 15 2 000000            L,S6    A3,0,*A1
```

```
000056                                                          FIN
                    000060  000001 000000
    UMF217  CODE    RELOCATABLE
```

```
@I ASM UMF218,UMF218
ASSEMBLED BY UNIVAC 1108 EXEC II ASSEMBLER  2400 000RA
THIS ASSEMBLY WAS DONE 0  07 JUN 77 AT 16:20:32
000001                                                  PROGRAM
000002       00    000000  10 00 05 13 1 000003   UMF218*  L          A5,*3,X11
000003             000001  15 16 05 00 0 000001            AH,U       A5,1
000004             000002  74 03 05 13 0 000005            JN         A5,5,X11
000005             000003  27 16 14 00 0 000000            L,U        A0,0
000006             000004  27 00 15 13 1 000002            L          A1,*2,X11
000007             000005  25 16 15 00 0 000001            AH,U       A1,1
000008             000006  34 16 00 00 0 000006            DI,U       A0,6
000009             000007  24 00 14 13 0 000001            A          A0,1,X11
000010             000010  46 00 14 00 0 000037            LXI        A0,M1
000011             000011  46 00 15 00 0 000037            LXI        A1,M1
000012             000012  10 00 04 13 1 000000            L          A4,*0,X11
000013             000013  12 00 02 00 0 000020            LM         A2,A4
000014             000014  74 00 02 00 0 000016            JZ         A2,%+2
000015             000015  74 00 02 00 0 000026   LOOPA    JZ         A2,BLANK
000016             000016  73 03 02 00 0 000044            DSL        A2,36
000017             000017  34 16 02 00 0 000012            DI,U       A2,10
000018             000020  24 16 17 00 0 000060            A,U        A3,060
000019             000021  72 10 00 15 2 000040            EX         PUTC,*A1
000020             000022  53 00 01 00 0 000037            TNE        A1,M1
000021             000023  26 16 15 00 0 000005            LXM,U      A1,5
000022             000024  70 01 01 00 0 000015            JGD        A5,LOOPA
000023             000025  74 04 00 13 0 000005            J          5,X11
000024             000026  27 16 17 00 0 000041   BLANK    L,U        A3,041
000025             000027  61 00 00 00 0 000020            TN         A4,
000026             000030  27 16 17 00 0 000005            L,U        A3,05
000027             000031  72 10 00 15 2 000040   LOOPB    EX         PUTC,*A1
000028             000032  27 16 17 00 0 000005            L,U        A3,05
000029             000033  53 00 01 00 0 000037            TNE        A1,M1
000030             000034  26 16 15 00 0 000005            LXM,U      A1,5
000031             000035  70 01 01 00 0 000031            JGD        A5,LOOPB
000032             000036  74 04 00 13 0 000005            J          5,X11
000033             000037  777776 777776          M1       -1,-1
000034             000040  06 15 17 14 2 000000   PUTC     S,S1       A3,0,*A0
000035             000041  06 14 17 14 0 000000            S,S2       A3,0,A0
000036             000042  06 13 17 14 0 000000            S,S3       A3,0,A0
000037             000043  06 12 17 14 0 000000            S,S4       A3,0,A0
000038             000044  06 11 17 14 0 000000            S,S5       A3,0,A0
000039             000045  06 10 17 14 0 000000            S,S6       A3,0,A0
000040                                                     END
```

```
@I ASM UMF230,UMF230
ASSEMBLED BY UNIVAC 1108 EXEC II ASSEMBLER  2409 000EA
THIS ASSEMBLY WAS DONE ON 07 JUN 77 AT 18:28:34
000001                                                          REGNAM
000002       00    000000  10 00 05 13 1 000002  UMF230*  L       A5,*2,X11
000003             000001  15 16 05 00 0 000001            AN,U    A5,1
000004             000002  27 16 14 00 0 000000            L,U     A0,0
000005             000003  74 03 05 13 0 000006            JN      A5,6,X11
000006             000004  23 00 01 00 0 000021            L       R1,A5
000007             000005  11 00 05 13 1 000003            LN      A5,*3,X11
000008             000006  01 00 05 00 0 000102            S       A5,R2
000009             000007  10 16 05 00 0 000000            L,U     A5,0
000010             000010  23 16 03 00 0 000000            L,U     R3,0
000011             000011  10 16 04 00 0 000000            L,U     A4,0
000012             000012  27 16 15 00 0 000000            L,U     A1,0
000013             000013  27 00 16 13 1 000001            L       A2,*1,X11
000014             000014  25 16 16 06 0 000001            AN,U    A2,1
000015             000015  34 16 01 00 0 000006            DI,U    A1,6
000016             000016  24 00 15 13 0 000000            A       A1,0,X11
000017             000017  46 16 15 00 0 000001            LXI,U   A1,1
000018             000020  46 16 16 00 0 000001            LXI,U   A2,1
000019             000021  72 10 00 16 2 000154  LOOP      EX      GETC,*A2
000020             000022  55 00 02 00 0 000210            TG      A2,(1,6)
000021             000023  26 16 16 00 0 000000            LXM,U   A2,0
000022             000024  25 16 17 00 0 000060            AN,U    A3,060
000023             000025  74 03 03 00 0 000116            JN      A3,NONDIG
000024             000026  55 16 03 00 0 000012            TG,U    A3,10
000025             000027  74 04 00 00 0 000143            J       TDEC
000026             000030  74 00 03 00 0 000114            JZ      A3,ZERO
000027             000031  14 16 04 00 0 000001  ADDIN     A,U     A4,1
000028             000032  31 16 00 00 0 000012            MSI,U   A0,10
000029             000033  24 00 14 00 0 000017            A       A0,A3
000030             000034  55 16 04 00 0 000012            TG,U    A4,10
000031             000035  74 04 00 00 0 000064            J       FINISH
000032             000036  70 04 01 00 0 000021  JGD       JGD     R1,LOOP
000033             000037  05 00 00 00 0 000207            SZ      UNCONV
000034             000040  74 00 04 00 0 000067  FLOAT     JZ      A4,NODIGS
000035             000041  60 00 00 00 0 000021            TP      A5
000036             000042  11 00 00 00 0 000014  LN        LN      A0,A0
000037             000043  27 16 15 00 0 000233            L,U     A1,0233
000038             000044  76 05 01 00 0 000014            LCF     A1,A0
000039             000045  27 00 14 00 0 000016            L       A0,A2
000040             000046  27 00 16 00 0 000207            L       A2,UNCONV
000041             000047  17 00 02 00 0 000102            ANM     A2,R2
000042             000050  24 16 16 00 0 000012            A,U     A2,10
000043             000051  74 03 02 00 0 000056  SCALE     JN      A2,MAXNEG
000044             000052  55 16 02 00 0 000025            TG,U    A2,21
000045             000053  74 04 00 00 0 000061            J       MAXPOS
000046             000054  76 02 00 16 0 000162            FM      A0,TENS,A2
000047             000055  74 04 00 13 0 000006  RETURN    J       6,X11
000048             000056  76 02 00 00 0 000162  MAXNEG    FM      A0,TENS
000049             000057  24 16 16 00 0 000012            A,U     A2,10
000050             000060  74 04 00 00 0 000051            J       SCALE
000051             000061  76 02 00 00 0 000206  MAXPOS    FM      A0,TENTEN
000052             000062  25 16 16 00 0 000012            AN,U    A2,10
000053             000063  74 04 00 00 0 000051            J       SCALE
000054             000064  04 00 01 00 0 000207  FINISH    S       R1,UNCONV
000055             000065  70 04 01 00 0 000073            JGD     R1,SCAN
```

```
000056  000066  74 04 00 00 0 000040          J       FLOAT
000057  000067  50 00 00 00 0 000103  NODIGS  TZ      R3
000058  000070  74 04 00 13 0 000006          J       6,X11
000059  000071  11 16 00 00 0 000000          LN,U    A0,0
000060  000072  74 04 00 13 0 000006          J       6,X11
000061  000073  72 10 00 16 2 000154  SCAN    EX      GETC,*A2
000062  000074  55 00 02 00 0 000210          TG      A2,(1,6)
000063  000075  26 16 16 00 0 000000          LXM,U   A2,0
000064  000076  53 16 03 00 0 000005          TNE,U   A3,05
000065  000077  74 04 00 00 0 000104          J       JGDS
000066  000100  25 16 17 00 0 000060          AN,U    A3,060
000067  000101  74 03 03 00 0 000151          JM      A3,ILCHAR
000068  000102  53 16 03 00 0 000015          TNE,U   A3,015
000069  000103  74 04 00 00 0 000106          J       DECF
000070  000104  70 04 01 00 0 000073  JGDS    JGD     R1,SCAN
000071  000105  74 04 00 00 0 000040          J       FLOAT
000072  000106  61 00 00 00 0 000102  DECF    TN      R2
000073  000107  74 04 00 00 0 000151          J       ILCHAR
000074  000110  27 00 17 00 0 000101          L       A3,R1
000075  000111  24 16 17 00 0 000001          A,U     A3,1
000076  000112  06 00 17 00 0 000102          S       A3,R2
000077  000113  74 04 00 00 0 000104          J       JGDS
000078  000114  23 16 03 00 0 000001  ZERO    L,U     R3,1
000079  000115  74 04 00 00 0 000121          J       BLANK
000080  000116  24 16 17 00 0 000060  NONDIG  A,U     A3,060
000081  000117  52 16 03 00 0 000005          TE,U    A3,05
000082  000120  74 04 00 00 0 000124          J       TNEG
000083  000121  74 00 04 00 0 000036  BLANK   JZ      A4,JGD
000084  000122  27 16 17 00 0 000000          L,U     A3,0
000085  000123  74 04 00 00 0 000031          J       ADDIN
000086  000124  74 01 04 00 0 000151  TNEG    JNZ     A4,ILCHAR
000087  000125  74 01 05 00 0 000151          JNZ     A5,ILCHAR
000088  000126  61 00 00 00 0 000102          TN      R2
000089  000127  74 04 00 00 0 000151          J       ILCHAR
000090  000130  50 00 00 00 0 000103          TZ      R3
000091  000131  74 04 00 00 0 000151          J       ILCHAR
000092  000132  52 16 03 00 0 000041          TE,U    A3,041
000093  000133  74 04 00 00 0 000136          J       TPLUS
000094  000134  11 16 05 00 0 000001          LN,U    A5,1
000095  000135  74 04 00 00 0 000036          J       JGD
000096  000136  52 16 03 00 0 000042  TPLUS   TE,U    A3,042
000097  000137  74 04 00 00 0 000151          J       ILCHAR
000098  000140  10 16 05 00 0 000001          L,U     A5,1
000099  000141  23 16 03 00 0 000001          L,U     R3,1
000100  000142  74 04 00 00 0 000036          J       JGD
000101  000143  61 00 00 00 0 000102  TDEC    TN      R2
000102  000144  74 04 00 00 0 000151          J       ILCHAR
000103  000145  52 16 03 00 0 000015          TE,U    A3,015
000104  000146  74 04 00 00 0 000151          J       ILCHAR
000105  000147  04 00 01 00 0 000102          S       R1,R2
000106  000150  74 04 00 00 0 000036          J       JGD
000107  000151  27 16 15 00 0 000001  ILCHAR  L,U     A1,1
000108  000152  06 00 15 13 1 000004          S       A1,*4,X11
000109  000153  74 04 00 00 0 000040          J       FLOAT
000110  000154  27 15 17 15 0 000000  GETC    L,S1    A3,0,A1
000111  000155  27 14 17 15 0 000000          L,S2    A3,0,A1
000112  000156  27 13 17 15 0 000000          L,S3    A3,0,A1
000113  000157  27 12 17 15 0 000000          L,S4    A3,0,A1
```

```
000114          000160  27 11 17 15 ) 000000            L,S5        A3,0,A1
000115          000161  27 10 17 15 2 000000            L,S6        A3,0,*A1
000116          000162  137667633766            TENS    +1*-10
000117          000163  143422701372                    +1*-9
000118          000164  146527461670                    +1*-8
000119          000165  151655376246                    +1*-7
000120          000166  155414336750                    +1*-6
000121          000167  160517426542                    +1*-5
000122          000170  164643334272                    +1*-4
000123          000171  167406111564                    +1*-3
000124          000172  172507534121                    +1*-2
000125          000173  175631463146                    +1*-1
000126          000174  201400000000                    +1.0
000127          000175  204500000000                    +10.0
000128          000176  207620000000                    +1**2
000129          000177  212764000000                    +1**3
000130          000200  216470400000                    +1**4
000131          000201  221606500000                    +1**5
000132          000202  224750220000                    +1**6
000133          000203  230461132000                    +1**7
000134          000204  233575360400                    +1**8
000135          000205  236734654500                    +1**9
000136          000206  242452013710            TEN:TEN +1**10
000137          000207                          UNCONV  RES         1
000138                                                  END
                000210  000001 000006
    UMF230  CODE    RELOCATABLE                                     23 OCT 75  16:44
```

```
@I FOR UMF232,UMF232
UNIVAC 1108 FORTRAN V LEVEL  [illegible]
THIS COMPILATION WAS DONE ON 07 JUN 77 AT 15:28:36


   SUBROUTINE UMF232    ENTRY POINT 000151

   STORAGE USED (BLOCK, NAME, LENGTH)

        0001   *CODE   000217
        0000   *DATA   000014
        0002   *BLANK  000000


   EXTERNAL REFERENCES (BLOCK, NAME)

        0003   NERR3$


   STORAGE ASSIGNMENT FOR VARIABLES (BLOCK, TYPE, RELATIVE LOCATION, NAME)

    0001   000014 310L        0001   000017 320L        0001   000142 410L        000
    0000 I 000002 J           0000 I 000001 YA



00101     1*          SUBROUTINE UMF232(M1,D1,Y1,M2,D2,Y2,DAYS)
00103     2*          IMPLICIT INTEGER (A-Z)
00104     3*          IF(M1.GT.2) GO TO 310
00106     4*          M1=M1+9
00107     5*          Y1=Y1-1
00110     6*          GO TO 320
00111     7*      310 M1=M1-3
00112     8*      320 C=Y1/100
00113     9*          YA=Y1-100*C
00114    10*          J=(146097*C)/4+(1461*YA)/4+(153*M1+2)/5+D1
00115    11*          J=J+DAYS
00116    12*          Y2=(4*J-1)/146097
00117    13*          J=(4*J-1)-146097*Y2
00120    14*          D2=J/4
00121    15*          J=(4*D2+3)/1461
00122    16*          D2=(4*D2+3)-1461*J
00123    17*          D2=(D2+4)/4
00124    18*          M2=(5*D2-3)/153
00125    19*          D2=(5*D2-3)-153*M2
00126    20*          D2=(D2+5)/5
00127    21*          Y2=100*Y2+J
00130    22*          IF(M2.LE.9) GO TO 420
00132    23*          M2=M2-9
00133    24*          Y2=Y2+1
00134    25*          GO TO 410
00135    26*      420 M2=M2+3
00136    27*      410 RETURN
00137    28*          END
```

```
@ ELT UTM,1,7008[3, 5102/

0001                  SUBROUTINE UTM(A,B,ALAR,ALOR,ZONE,ANOR,EAST)
0002                  RA=0.
0003                  RB=0.
0004                  IF(ZONE)7011,7011,7012
0005             7011 IZNE=(3.1939525-ALOR)/.1047197G
0006                  ZONE=IZNE
0007                  IRES=(3.1939525-ALOR)/.0535988-2.*ZONE
0008                  RES=IRES
0009                  ZONE=ZONE+RES
0010             7012 CONTINUE
0011             5004 CMR1=(183.-ZONE*6.)/57.295779513
0012                  IF(RA-A+RB-B)7004,7005,7004
0013             7004 CONTINUE
0014                  ECCS=(A*A-B*B)/(A*A)
0015                  SKALE=0.9996
0016                  ECPS=(A*A-B*B)/(B*B)
0017                  EN=(A-B)/(A+B)
0018                  ENS=EN*EN
0019                  ENC=ENS*EN
0020                  ENF=ENC*EN
0021                  ENFI=ENF*EN
0022                  CA=A*(1.-EN+5.*(ENS-ENC)/4.+81.*(ENF-ENFI)/64.)
0023                  CB=3.*A*(EN-ENS+7.*(ENC-ENF)/8.+55.*ENFI/64.)/2.
0024                  CC=15.*(ENS-ENC+3.*(ENF-ENFI)/4.)*A/16.
0025                  CD=35.*A*(ENC-ENF+11.*ENFI/65.)/48.
0026                  RA=A
0027                  RB=B
0028             7005 CONTINUE
0029             C    GO TO UTM ROUTINE (ALAR,ALOR,ANOR,EAST,CMR1,A ECCS ECPS CACBCCCD)
0030                  S=CA*ALAR-CB*SIN (2.*ALAR)+CC*SIN (4.*ALAR)-CD*SIN (6.*ALAR)
0031                  V=A/SQRT (1.-ECCS*SIN(ALAR)**2)
0032                  SI=SIN (ALAR)
0033                  CO=COS (ALAR)
0034                  X=61.-58.*(SI/CO)**2+(SI/CO)**4+270.*ECPS*CO**2-330.*ECPS*SI**2
0035                  DELL=CMR1-ALOR
0036                  X=X*CO**2*DELL**2/30.
0037                  X=X+5.-(SI/CO)**2+9.*ECPS*CO**2+4.*(ECPS*CO)**4
0038                  X=X*(CO*DELL)**2/12.+1.
0039                  X=X*0.5*V*SI*CO*DELL**2+S
0040                  ANOR=X*SKALE
0041                  X=(5.-18.*(SI/CO)**2+(SI/CO)**4+14.*ECPS*CO**2-58.*ECPS*SI**2)*
0042                 1CO**2*DELL**2/20.+1.-(SI/CO)**2+ECPS*CO**2
0043                  X=(X*CO**2*DELL**2/6.+1.)*V*CO*DELL*SKALE
0044                  EAST=500000.+X
0045             7002 CONTINUE
0046                  RETURN
0047                  END
```

```
. ELT VCHECK,1,7/08/07,  1:50:0
      SUBROUTINE VCHECK(NUM,SPD)
      COMMON/ DATA/ XLAT(3440),XLON(3440),TIME(3440),ISTORE(3440)
      DIMENSION KNT(7)
      IF(NUM.LT.3441) GO TO 1
      PRINT 2
    2 FORMAT('TOO MANY POINTS FOR VCHECK-ZAP')
      STOP
    1 REWIND 33
      SPD=SPD*51.48
      DO 10 I=1,NUM
      READ (33) DAT
      IF(DAT(4).LT.180.) DAT(4)=DAT(4)*(-1.)
      IF(DAT(4).GE.180.) DAT(4)=360.0-DAT(4)
      XLAT(I)=DAT(3)*0.01745329
      XLON(I)=DAT(4)*0.01745329
   10 TIME(I)=DAT(13)*1440.
      READ 4,T,YLAT,YLON
    4 FORMAT(3F10.6)
      YLAT=YLAT*0.01745329
      YLON=YLON*0.01745329
      J=0
      T=T*1440.
      DO 22 IT=1,4
   22 KNT(IT)=0
      DO 11 I=1,NUM
      IF(TIME(I).LE.T)  GO TO 11
      KK=-2
      KNT(3)=1
      KNT(4)=I+1
      CALL SPEED (YLAT,YLON,XLAT(I),XLON(I),T,TIME(I),D4,D5,V,VE,VN,D3)
  111 VE=ABS(VE*1.666667)
      VN=ABS(VN*1.666667)
      V =ABS(V *1.666667)
      IF(VE.GT.SPD)  GO TO 15
      IF(VN.GT.SPD)  GO TO 15
      IF(V .GT.SPD)  GO TO 15
      J=J+1
      ISTORE(J)=I
      YLAT=XLAT(I)
      YLON=XLON(I)
      T=TIME(I)
      KNT(1)=KNT(2)
      KNT(2)=KNT(3)
      GO TO 11
   15 KK=KK+3
      INC=KNT(KK)
      IF(KK.EQ.7.OR.INC.EQ.0)  GO TO 11
      IF(INC.GT.NUM)  GO TO 11
      CALL SPEED (XLAT(I),YLON(I),XLAT(INC),XLON(INC),TIME(I),TIME(INC),
     * D4,D5,V,VE,VN,D3)
      GO TO 111
   11 CONTINUE
      REWIND 33
      REWIND 34
```

```
000055                  IRC1=0
000056                  DO 12 I=1,J
000057                  N=LAST(I)-IRCT
000058                  DO 13 K=1,N
000059                  READ (33) DAT
000060               13 CONTINUE
000061                  IRCT=IRCT+N
000062                  WRITE(34) DAT
000063               12 CONTINUE
000064                  REWIND 33
000065                  REWIND 34
000066                  DO 14 I=1,J
000067                  READ (34) DAT
000068                  WRITE (33) DAT
000069               14 CONTINUE
000070                  REWIND 33
000071                  REWIND 34
000072                  NUM=J
000073                  RETURN
000074                  END
*K
```

```
. ELT VLOOK,1,77,66,7,    .509

0001                  SUBROUTINE VLOOK(NUM)
0002                  COMMON / ORIG/ AT(1   ),VE(2 00),VN(2000),XLAT(2000),XLON(2000),T(200
0003                 X0),XPCT(402),YPCT(402),VEL(402)
0004                 X,V(2000)
0005                  DATA RAD/0.01745329/,CMS/0.0011574/
0006                  DO 20 I=1,400
0007                  XPCT(I)=0.
0008                  YPCT(I)=0.
0009                20 VEL(I)=0.
0010                  REWIND 33
0011                  DO 10 I=1,NUM
0012                  READ(33) DAT
0013                  IF(DAT(4).LT.180.) DAT(4)=DAT(4)*(-1.)
0014                  IF(DAT(4).GE.180.) DAT(4)=360.-DAT(4)
0015                  XLAT(I)=DAT(3)*RAD
0016                  XLON(I)=DAT(4)*RAD
0017                10 T(I)=DAT(13)
0018                  DO 11 I=2,NUM
0019                  J=I-1
0020                  CALL SPEED(XLAT(J),XLON(J),XLAT(I),XLON(I),T(J),T(I),D,DD, V(J),VE
0021                 X(J),VN(J),DST)
0022                  V(J)=V(J)*CMS
0023                  V(J)=ABS(V(J))
0024                  VE(J)=VE(J)*CMS
0025                11 VN(J)=VN(J)*CMS
0026                  NUM=J
0027                  DO 14 I=1,400
0028                  VEL(I)=I
0029                  DO 17 J=1,NUM
0030                  IF(V (J).LE.VEL(I)) XPCT(I)=XPCT(I)+1.
0031                17 CONTINUE
0032                  XPCT(I)=(XPCT(I)/NUM)*100.
0033                14 CONTINUE
0034                  XPCT(401)=0.
0035                  XPCT(402)=20.
0036                  VEL(401)=0.
0037                  VEL(402)=50.
0038                  CALL SETOVR
0039                  CALL PLOTS(-30.,-10.,1)
0040                  CALL PLOT(0.5,0.5,-3)
0041                  CALL AXIS(0.,0.,19H SPEED IN CM/SEC       ,-19,8.,0.,0.,50.)
0042                  CALL AXIS(0.,0.,7HPERCENT,7,5.,90.,0.,20.)
0043                  CALL LINE(VEL,XPCT,400,1,-1,3)
0044                  CALL PLOT(0.,0.,999)
0045                  CALL BITSET
0046                  REWIND 33
0047                  RETURN
0048                  END
```

```
$ ELT VOLT,1,751,99, 926.9

000001                  SUBROUTINE VOLT(DUM)
000002                  COMMON/WORK/ S(R(13950)
000003                  DIMENSION V(3000),T(3000),DAT(139)
000004                  K=0
000005                  REWIND 53
000006                  DO 100 I=1,NUM
000007                  READ(53) DAT
000008                  N=DAT(6)
000009                  IF(N.LT.2) GO TO 100
000010                  IF(N.GT.26) N=26
000011                  DO 20 II=1,N
000012                  ITT=9+(II-1)*5
000013                  VV=DAT(ITT+1)
000014                  IF(VV.GT.0.0) GO TO 20
000015                  VV=ABS(OCW(VV))*0.085
000016                  IF(VV.LT.5.0.OR.VV.GT.20.) GO TO 20
000017                  K=K+1
000018                  V(K)=VV
000019                  T(K)=INT(DAT(13))+(DAT(ITT+4)-INT(DAT(ITT+4)))
000020                  GO TO 100
000021               20 CONTINUE
000022              100 CONTINUE
000023                  REWIND 53
000024                  CALL SETOVR
000025                  CALL PLOTS(-18.9,-10.5)
000026                  CALL PLOT(0.5,0.5,-3)
000027                  T(K+1)=(INT(T(1))/10)*10.
000028                  T(K+2)=5.
000029                  V(K+1)=5.
000030                  V(K+2)=2.
000031                  CALL AXIS(0.,0.,12HTIME IN DAYS,-12,16.,0.,T(K+1),5.)
000032                  CALL AXIS(0.,0.,5HVOLTS,5,8.,90.,V(K+1),2.)
000033                  CALL LINE(T,V,K,1,1,3)
000034                  CALL PLOT(0.,0.,999)
000035                  CALL BITSET
000036                  RETURN
000037                  END
```

```
» ELT XMAX,1,7,0.13, 51022

000001                  FUNCTION XMAX(X,N)
000002                  DIMENSION X(1)
000003                  Z=-79999990.
000004                  DO 10 I=1,N
000005                  IF(X(1).GT.Z) Z=X(1)
000006               10 CONTINUE
000007                  XMAX=Z
000008                  RETURN
000009                  END
```

```
* ELT XMIN,1,760,13, 5107

000001                  FUNCTION XMIN(X,N)
000002                  DIMENSION X(1)
000003                  Z=79999.9.
000004                  DO 10 I=1,N
000005                  IF(X(I).LT.Z) Z=X(I)
000006               10 CONTINUE
000007                  XMIN=Z
000008                  RETURN
000009                  END
```

```
* ELT ZERO,1,7512,09, 4,3
000001                  SUBROUTINE ZERO(X)
000002                  DIMENSION X(13900)
000003                  DO 1 I=1,13900
000004                1 X(I)=0.
000005                  RETURN
000006                  END
000007
```

Proceedings of the American Congress on Surveying and Mapping, 37th Annual Meeting. Washington, D.C., February 27-March 5, 1977, 177-185.

(77-211)

OBJECTIVE ANALYSIS OF LAGRANGIAN TRAJECTORY DATA

Alan Herman
and
Donald V. Hansen
National Oceanic and Atmospheric Administration
Atlantic Oceanographic and Meteorological Laboratories
Miami, Florida

BIOGRAPHICAL SKETCH

Alan Herman is an applied mathematician with the Atlantic Oceanographic and Meteorological Laboratories, AOML, Miami, Florida specializing in automatic data recovery and processing of oceanographic data. Prior to this he was a geodesist for the Naval Oceanographic Office. Mr. Herman has a bachelors degree in Mathematics and Geology from the University of the City of New York and graduate training in data processing, ocean acoustics and geophysics.

Donald V. Hansen is Director of the Physical Oceanography Laboratory, Atlantic Oceanographic and Meteorological Laboratories, NOAA, Miami, Florida. He holds a B.S. in Physics , M.S. and PhD degrees in Oceanography from the University of Washington, Seattle. He is a physical oceanographer, conducting and leading research projects on currents and dispersion processes in the ocean. He has published numerous results from investigations on estuaries, coastal, and deep ocean circulation.

ABSTRACT

This paper describes an automated method for deriving trajectories and velocities of free floating oceanographic buoys from geographic positions unequally spaced in time, and having large positional errors. The data are fit over intervals of one day to a week to a cubic curve fit by orthogonal polynomials. Distances to position coordinates from curves are computed and weights are assigned utilizing a function based on an error analysis of the navigation system. The function takes the distances as input and returns weights which represent position reliability. A new set of cubic curves is computed using the weighted positional data. These curves are spline fit, and using regressive analysis, new positions for the path are determined that are equally spaced in time. Examples from an actual project with computer generated plots of both raw and smoothed data on a Polyconic Projection are included together with a discussion of the error analysis.

INTRODUCTION

The Physical Oceanography Laboratory of the Atlantic Oceanographic and Meteorological Laboratories, Miami, Florida, is presently studying currents off the coast of Alaska by tracking free drifting buoys using the random access measurements system (RAMS) of the NIMBUS-F satellite. Buoy positions determined by this satellite often have large errors. Prerequisite to scientific analysis is the determination of the statistically most likely paths taken by the buoys.

An objective analysis procedure using explicity stated methods was devised to determine the trajectories.

Project requirements call for plots of trajectories to overlay the U.S. Geological Survey $1:10^6$ Polyconic Projection Alaskan Charts. This paper briefly describes the measurement system and the logic used in development of the computer programs for analysis and plotting. The programs are combined into a single package called "Simple Lagrangian Processing" (SLAP), and a users guide has been written and will be published as a NOAA Technical Memorandum. The paper is divided into five sections:

1. General Description of the System
2. System Characteristics and Noise
3. Elimination of large errors
4. Data Weighting and Smooth Plot Calculation
5. Plotting on a Polyconic Projection

GENERAL DESCRIPTION OF THE SYSTEM

The RAMS system (1) consists of three functional elements:

(1) The Random Access Measurement System (RAMS) located on the satellite

(2) The Buoy Transmit Terminal (BTT) located on the buoy

(3) Central ground processing facilities at Fairbanks, Alaska, and Rosmon, North Carolina.

The BTT transmits phase modulated pulses occupying about one second out of each minute. These transmissions can be received and stored by the RAMS when the satellite is within range of the BTT, which is within the cone of about five degrees above its horizon. Transmission links are usually completed on 4 to 6 orbits each day at 60° N. Positioning is accomplished by measuring the doppler shift from the known carrier frequency of the BTT and that received at the RAMS. The system was designed to have a root mean square positioning accuracy of five kilometers. Data and positioning information are stored in the RAMS until it comes in range of the ground stations to which they are telemetered. The data are then transmitted to Goddard Space Flight Center. Once each week NASA forwards the buoy data to PhOL by mail using magnetic tapes or punched cards.

SYSTEM CHARACTERISTICS AND NOISE

System characteristics and noise were determined by examining data records of several stationary buoys. The first step was to convert all latitudes and longitudes to Universal Transverse Mercator (UTM) coordinates on the Fischer Spheroid [2], so that computations could be done on a cartesian system. The UTM's were demeaned to avoid computer overflows, followed by new computation of standard deviations. The frequency distributions for the demeaned UTM positions were then printer plotted in 1000 meter intervals. Figure 1 is a typical frequency distribution plot. The shape of the curve in figure 1 approaches a Gaussian distribution.

ELIMINATION OF LARGE ERRORS

The errors analysis shows that about 90% of all fixes are accurate to within 15 kilometers although some are much worse. First order editing is designed to identify and delete these bad positions. Sequential positions which imply speeds greater than an assignable speed criterion are deleted from the data set. Near surface currents up to the order of one knot (50 km/day) or slightly greater are expected in the Gulf of Alaska. In addition a position error of 15 km in fixes implies an error velocity of 15 km/day for a one-day interval or 240 km/da for a 1.5 hour interval. A velocity cutoff of 2 knots (100 km/day) was found suitable for casting out large errors without excessive data loss. The required reverse computation to obtain the distance between two locations is done on the Fischer Spheroid using the equations derived by Sodano (3). Figure 2 shows a typical buoy path plotted prior to editing, and figure 3 is the same data set after being edited using 2 knots as the speed criterion. Figure 3 shows improvement, but still contains a high noise level and irregular data distribution.

DATA WEIGHTING AND SMOOTH PLOT CALCULATION

The task remains of further smoothing and interpolating the data. The contribution of noise to each data point must be estimated, and weights between zero (worst) and one (best) assigned for subsequent processing. This is accomplished by quadratic least squares fit to orthogonal polynomials (4) to position data components one day at a time. If less than five fixes occur during the one day period, data are added a day at a time until there are at least five data points. The distance between a data point and the curve is used to determine the weight to be assigned to that point. The weights are determined using the equation $\text{Weight} = \exp -\left(\frac{\varepsilon}{r}\right)^2$, where ε is the distance of a data point from the curve, and r is a shaping parameter, assigned a value of 8 km for this application. When all positions have been assigned a weight, the data are smoothed in a least squares sense using cubic splines. The method used is a modification of that described by Corbin (5), the differences being that the least squares polynomial fit uses weights (4), and the node points are not always at fixed intervals. The nodes are usually at two-day intervals except where data gaps exist, in which case intervals between nodes are extended a day at a time until there are data points on both sides of the gap. Regressive analysis is now used to compute positions along the path at equal time intervals. Figure 4 is a plot of smoothed positions with six-hourly positions indicated.

PLOTTING OF GEOGRAPHICS ON A POLYCONIC PROJECTION

Dr. Ferdinand Hassler, the first director of the USC&GS in 1820 devised the polyconic projection. The projection is generated by projecting parallels and meridians from the center of the earth onto a series of cones tangent at selected parallels having their apexes along an extension of the polar axis. All meridians except for the central meridian are curved lines as are all parallels. The polyconic is neither conformal nor equal area, but distortions are

very small in the area of the central meridian.

The first step in computation of polyconic coordinates was to describe a function which along the central meridian converts latitude to meters north of the equator. This was accomplished by fitting data from the meter table in Birdseye (6) to orthogonal polynomials. For the area of interest of this project, 52°N to 60°N, the following linear relationship was found to be adequate, Meters = 18.06(ϕ-52) +111299.11. The x and y distances to the longitude of interest at the same latitude are given on page 17 equation X and XI of Birdseye (6). Birdseye's equations can be closely approximated by

$$x = P\eta \cos \phi$$

$$y = 1/4 P\eta^2 \sin^2 \phi$$

where $$P = \frac{a}{(1-e^2 \sin^2 \phi)^{1/2}}$$

and

$$e = \text{eccentricity} = \sqrt{\frac{a^2 - b^2}{a^2}}$$

a = semi major axis of the earth in meters

b = semi major axis of the earth

ϕ = latitude in degrees

η = longitude difference in radians from central meridian.

The simplified method outlined above yielded errors less than 100 meters, when computations are limited to a single 1.10° chart.

ACKNOWLEDGMENTS

Thanks are due to Dr. A. Leetmaa, Dr. R. Molinari, and D. Pashinski with whom many beneficial discussions were held.

REFERENCES

1. Kellogg, W.W., M. Friedman, P. Julian "Guide for Users of the Random Access Measurement System on the NIMBUS-F Meteorological Satellite in Conjunction with Tropical Wind Energy Conversion and Reference Level Experiment NASA, Goddard Space Center, Greenbelt, Maryland, December, 1971

2. Department of Army Technical Manual TM5-241-8, "Universal Transverse Mercator Grid," Headquarters, Department of of the Army, July 1958.

3. Sodano, Emanuel M., "General Non-iterative Solution of the Inverse and Direct Geodetic Problems", XIII I.U.G.G. General Assembly at Berkeley, California, 1963.

4. Klerer, M. "Digital Computer Users Handbook," McGraw-Hill, 1967.

5. Corbin, F.L. "Least Squares Cubic Splines," AD-774, Air Force Cambridge Research Laboratories, Bedford, Massachusetts, October, 1973.

6. Birdseye, C.H. "Formulas and Tables for the Construction of Polyconic Projections," USGS Bulletin 809, U.S. Government Printing Office, 1929.

FIGURE ;

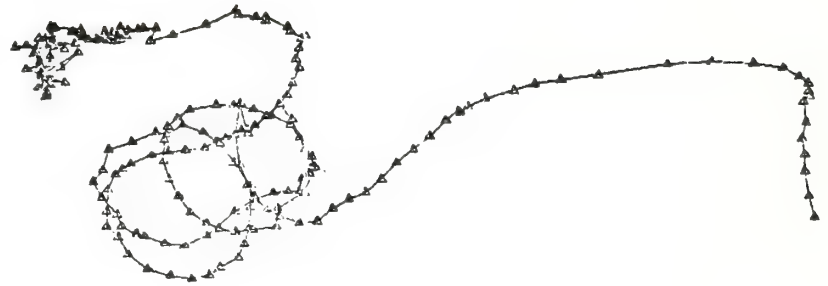
182

FIGURE 2
UNEDITED TRAJECTORY OF BUOY 1173
POLYCONIC PROJECTION

FIGURE 3
VELOCITY EDITED TRAJECTORY OF BUOY 1173
POLYCONIC PROJECTION

184

142°W
+ 61°N



59°N
147°W +

FIGURE 4
OBJECTIVELY DETERMINED TRAJECTORY OF BUOY 1173
POLYCONIC PROJECTION

Journal of Marine Research 35, No. 1, 193-220.

Low-frequency current variability and spin-off eddies along the shelf off Southeast Florida

by Thomas N. Lee[1] and Dennis A. Mayer[2]

ABSTRACT

Time series analyses of current meter records from a 6-element box array installed on the narrow shelf (<5 km) off Miami, Florida revealed two distinct current regimes. Current oscillations at the shelf break (30m isobath) appeared to be primarily produced by Florida Current spawned events, such as low frequency (periods of 2 days to 2 weeks) wave-like meanders of the Florida Current and the transient occurrence of small diameter spin-off eddies, both of which may be indirectly related to wind forcing. Velocity fluctuations along the shallow inner shelf (6m isobath) were primarily in direct response to the local wind stress. The transition between current regimes occurred within the array east-west spacing of 2 km. Current fluctuations were observed to propagate to the north at speeds ranging from 20 to 100 cm/sec and were highly coherent over the 10 km north-south array spacing for all periods greater than 2 days. Along-shelf current oscillations were mutually coherent with fluctuations in the cross-stream current measured near the Florida Current axis, and with the east-west component of the local winds, at periods of about 2 and 9 days. Cyclonic spin-off eddies appear to evolve from growing barotropic instabilities (meanders), which may initially be wind induced. They manifest themselves as warm, southward-oriented, tongue-like extrusions of Florida Current water onto the shelf. Eddy diameters range from 10 to 30 km and they extend to a depth of approximately 200m. These features occur on the average of once per week and have a life span of about 1 to 3 weeks. They contribute to shelf water mass exchange and Florida Current energy dissipation.

1. Introduction

In a recent review of continental shelf circulation, Niiler (1975) stressed the highly variable nature of horizontal currents responding energetically to atmospheric forcing, eddies and long waves from the deep sea, and tidal phenomena. He noted that the rms of these fluctuations, on time scales of a few hours to 10 days, typically exceed the seasonal means.

Lee (1970; 1975) found the high current variability on the shelf off Pompano

1. Rosenstiel School of Marine and Atmospheric Science, University of Miami, Miami, Florida, 33149, U.S.A.

2. Atlantic Oceanographic and Meteorological Laboratories, National Oceanic and Atmospheric Administration, Miami, Florida, 33149, U.S.A.

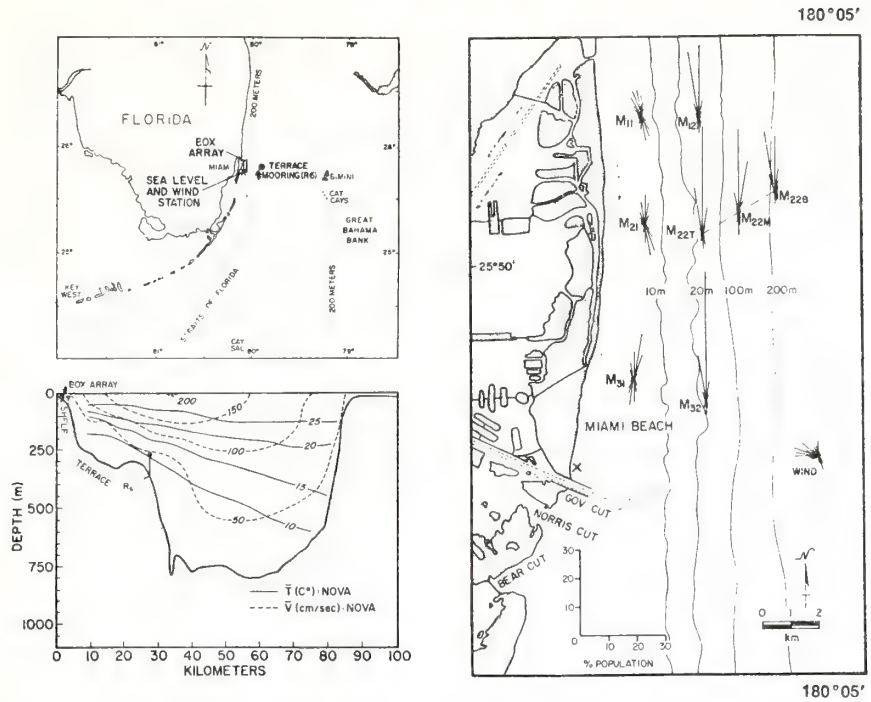


Figure 1a. Plan view of Florida Straits showing the location of the current meter box array, Terrace mooring, and the sea level and wind stations.

Figure 1b. Bottom profile of Florida Straits with current meter locations and mean temperature and current distributions based on University of Miami and Nova University observations during summer 1974.

Figure 2. Current and wind roses from 3 HrLP data for the period 9 February to 5 June, 1973 (see Table 1 for details); *x* is the location of the wind and sea level recorder.

and Boca Raton, Florida to be primarily governed by "spin-off eddies" (small diameter, cyclonic, edge-eddies) and horizontal wave-like meanders of the Florida Current front, with time scales ranging from 2 to 10 days. Mayer and Hansen (1975) observed that nearshore currents off Miami (depths <10m) were strongly correlated with the local wind stress. The shelf break (30m isobath) is approximately 3.5 km from the beach off Miami, which is about twice the shelf width off Boca Raton. This suggests that nearshore currents off Miami are somewhat isolated from events occurring along the shelf break.

2. Measurements

Eight current meters were deployed in an elongated 2 × 10 km box array on the continental shelf off Miami Beach in February, 1973 as part of a continuation of a southeast Florida coastal program begun in 1971 (Mayer and Hansen, 1975). The program was designed to provide information on circulation and exchange processes

Table 1. Mooring information and record lengths for filtered time series from current meter box array.

Station	Water Depth (m)	Instrument Depth (m)	3 HrLP* record length	40 HrLP and 40 HrHP record length	Coordinates	
M_{11}	6.1	4.9	2878	2743	25°52.9′N	80°6.4′W
M_{12}	32.0	13.7	2885	2750	25°52.9′N	80°5.2′W
M_{21}	7.3	6.1	7271	7136	25°50.8′N	80°6.3′W
M_{22T} (Top)	30.8	13.7	6774	6639	25°50.6′N	80°5.1′W
M_{22M} (Middle)	30.8	22.9	2926	2791		
M_{22B} (Bottom)	30.8	29.0	1150	1080		
M_{31}	5.8	4.6	2879	2744	25°47.8′N	80°6.6′W
M_{32}	32.0	13.7	2925	2790	25°47.4′N	80°5.1′W
Wind			3258**	3123	25°46′N	80°7.6′W

* Note: All data have time interval of 1 hour; All start times for 3 hr. low-passed (HrLP) data were 0800 GMT, 6 Feb. '73; All start times for 40 HrLP and high-passed (HP) data were 0800 GMT, 9 Feb. '73.

** Wind data have been 5 HrLP.

peculiar to this narrow, shallow shelf. The location of the current meter array relative to the Florida Straits geometry and mean temperature and current fields is shown in Figs. 1a, 1b, and 2. The local isobaths are aligned in approximately a north-south direction near the measurements. Station coordinates, depths, and record lengths are given in Table 1. The box array was maintained for approximately 4 months over the winter and early spring. Stations M_{21} and M_{22} were maintained through December, 1973 with a single current meter on each, providing about 9 months of data.

Aanderaa model RCM-4 current meters with a 10-min. sampling interval were used exclusively. The deeper stations (~ 30m) M_{12}, M_{22}, and M_{32} were of a taut wire, subsurface-float design. Station M_{22} had three meters in the vertical, the uppermost being approximately at mid-depth. The shallow stations (~ 6m) M_{11}, M_{21}, and M_{31} were all fixed tripods that mounted the meters approximately 1m above the bottom.

3. Data processing

All data were filtered to remove noise and to partition into distinct frequency bands. Three basic filters were used: 3 hr. low-pass (HrLP), 40 HrLP, and 40 hr. high-pass (HrHP). A period of 40 hrs., which falls within a spectral gap, is used to distinguish conceptually between slowly and rapidly varying processes; the latter includes tidal and inertial frequencies with periods less than 2 days but longer than 3 hrs. Table 2 summarizes the transmission characteristics of each filter. Current

Table 2. Characteristics of the digital filters used for smoothing time series data.

	3 HrLP (hr)	5 HrLP (hr)	40 HrLP (hr)	40 HrHP (hr)
6 db point 1/2 amplitude	2.5	5.0	37	37
20 db point 1/10 amplitude	2.0	4.0	30	48

meter data were first smoothed with the 3 HrLP filter then resampled hourly. The resultant time series were then filtered with the 40 HrLP and 40 HrHP to examine low and high frequency processes separately.

4. Statistics

Statistics were computed from the basic time series and are tabulated in Table 3. In addition to the means, the low and high frequency variances were calculated for the velocity component time series u(+east) and v(+north). The ratio of high passed variance (*HPV*) to total variance (*TV*), and the ratio of *TV* to the squared mean speed (μ^2) are also given. The former ratio indicates the percentage of high frequency energy in the records, and the latter ratio is of interest in analyzing the dispersion of materials.

Momentum flux calculations were computed from the velocity data and are summarized in Table 4. It is convenient to represent the velocity time series in terms of three time scales:

$$w = \langle w \rangle + \bar{w} + w' \tag{1}$$

where $w = u$ or v. The symbol $\langle\rangle$ is a time average over the record length. The overbarred term ($\bar{w}$) signifies the 40 HrLP data minus the mean, thus representing the slowly varying or low frequency processes. The primed terms (w') are 40 HrHP data and represent the rapidly varying or high frequency processes. The time averaged momentum flux, or Reynolds stress, is expressed as:

$$\langle ww \rangle = \langle w \rangle \langle w \rangle + \langle \bar{w}\,\bar{w} \rangle + \langle w'w' \rangle \tag{2}$$

Tables 3 and 4 indicate that the box array spanned two very different flow regimes. In the shallow water, mean currents were essentially zero, whereas, at the deeper stations, a net northerly flow of nearly 20 cm/sec existed. A summary of the 3 HrLP direction data is given in Fig. 2. These polar frequency distributions contain both low and high frequency processes within 10 degree class intervals. Flows at the offshore stations had a considerable bias toward the north, while those nearshore were bimodal (north and south). Approximately 70 to 75% of the total variance at the shelf break was produced by current fluctuations which had periods longer than 40 hrs. In the shallow water about 50 to 60% of the total variance was produced by low frequency currents. Also, the momentum flux ($\langle \bar{v}\,\bar{v} \rangle$ and $\langle v'\,v' \rangle$) was considerably larger at the deeper stations.

Table 3. Statistics of 3 HrLP, 40 HrLP, and 40 HrHP current meter time series.

Station	Mean Temp. $\langle T \rangle$ °C(±.05)	Mean North Component $\langle v \rangle$ cm/sec(±1.0)	Mean East Component $\langle u \rangle$ cm/sec(±1.0)	(HPV) High Passed Variance (cm/sec)²	(LPV) Low Passed Variance (cm/sec)²	Squared Mean Speed (μ^2) (cm/sec)²	HPV ÷ Total Variance (TV)	TV/μ^2
M_{11}	24.37	0.0	0.0	72.0	84.0	~1.0	.46	156
M_{12}	24.50	13.0	−1.0	145.0	308.0	170.0	.32	2.7
M_{21}	26.32	0.0	0.0	57.0	67.0	~1.0	.46	124
*M_{21}	24.27	−1.0	1.0	64.0	89.0	1.4	.42	109
M_{2eT} (Top)	26.43	18.0	0.0	206.0	654.0	324.0	.24	2.7
*M_{2eT} (Top)	24.88	15.0	0.0	140.0	370.0	225.0	.27	2.3
M_{2eM} (Middle)	24.25	10.0	1.0	97.0	190.0	101.0	.34	2.8
M_{2eB} (Bottom)	23.97	7.0	1.0	29.0	57.0	50.0	.34	1.7
M_{31}	24.45	1.0	0.0	65.0	96.0	1.0	.40	161
M_{32}	24.62	21.0	−1.0	161.0	499.0	442.0	.24	1.5
Wind		133.0±10.0	−258.0±10.0					

* These statistics are computed based on first 2750 points or approximately the first 4 months, otherwise statistics are based on the record lengths in Table 1.

The Reynolds stress estimates of Table 4 indicate a northward momentum flux toward the west of about −10 cm²/sec² for both the low and high frequency currents with little horizontal variability over the array. These estimates are believed

Table 4. Statistics of momentum flux time series (cm^2/sec^2).

	40 HrLP (± 10%)			40 HrHP (± 10%)		
	$\langle\bar{v}\,\bar{v}\rangle$	$\langle\bar{u}\,\bar{u}\rangle$	$\langle\bar{v}\,\bar{u}\rangle$	$\langle v'v'\rangle$	$\langle u'u'\rangle$	$\langle v'u'\rangle$
M_{11}	78.0	6.0	−13.0	54.0	17.0	−12.0
M_{12}	304.0	5.0	−13.0	130.0	15.0	−14.0
M_{21}	61.0	6.0	−10.0	43.0	14.0	− 9.0
*M_{21}	84.0	5.0	−10.0	50.0	15.0	− 4.0
M_{22T} (Top)	648.0	7.0	−13.0	187.0	19.0	−13.0
*M_{22T} (Top)	365.0	5.0	−13.0	128.0	12.0	−10.0
M_{22M} (Middle)	188.0	2.0	3.0	88.0	9.0	− 1.0
M_{22B} (Bottom)						
M_{31}	91.0	4.0	12.0	49.0	16.0	2.0
M_{32}	494.0	5.0	−17.0	147.0	14.0	− 8.0

* These statistics are computed based on first 2750 points or approximately the first 4 months, otherwise statistics are based on record lengths in Table 1.

to be unaffected by an artificial coordinate bias, since the mean east component (u) is essentially zero at all locations. The east-west gradient of the mean northward current, $\frac{\partial\bar{v}}{\partial x}$, was estimated from Table 3 and Fig. 1b to be about 10^{-4} sec^{-1} which results in a positive horizontal eddy viscosity, A_H, of about 1×10^5 cm^2/sec. These findings are in agreement with those of Webster (1961b) and Brooks and Niiler (this issue) for a 6 km zone on the western edge of the Florida Current, and indicate that current fluctuations in the shelf region tend to dissipate mean flow kinetic energy of the Florida Current.

5. Comparative analysis

Time series of 6-hourly current vectors, local wind, and adjusted sea level are shown in Fig. 3 for the 40 HrLP series. Coastal currents were primarily aligned with the isobaths (north-south). Currents at the shelf break (meters M_{12}, M_{22T}, M_{22M}, M_{22B}, and M_{32}) display considerable variability with fluctuation amplitudes ranging from 50 to 100 cm/sec over time scales of about 2 days to 2 weeks. These oscillations are visually coherent along the shelf break over the array spacing (10 km) and appear, for the most part, to be barotropic due to the high vertical similarity (M_{22T}, M_{22M}, and M_{22B}). Cyclonic (anticlockwise) current reversals, such as the one coded EDWARD on M_{32}, appear to be a common occurrence along the shelf break. These events were described as Florida Current spin-off eddies by Lee (1975) and will be discussed in more detail in a later section. It is difficult to detect any persistent visual correlation between shelf break currents and the local winds or sea level. A seasonal change in wind intensity occurred near the end of April with the cessation of the weekly migration of cold fronts without any apparent change in current variability.

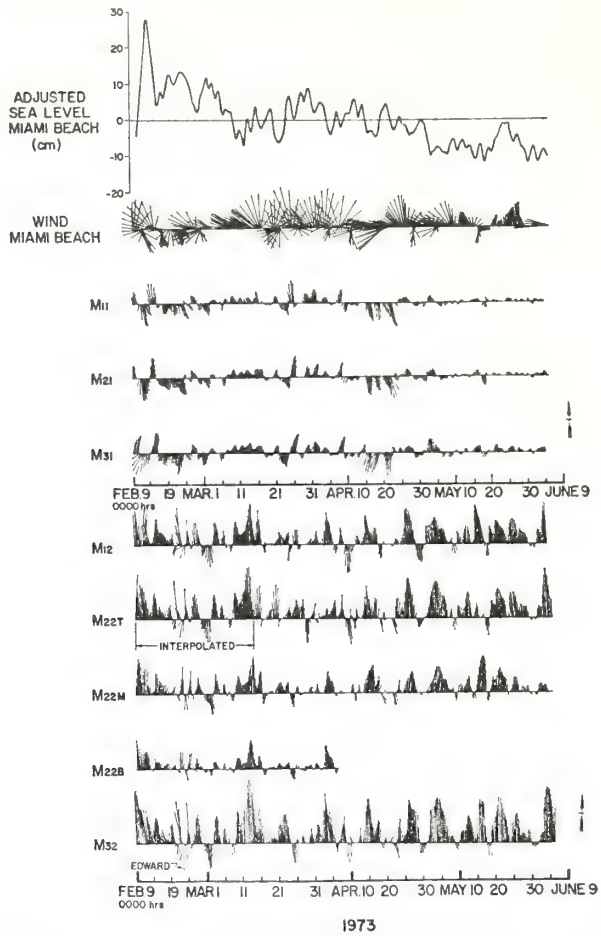


Figure 3. Time series of 6-hourly values of 40 HrLP current and wind vectors and sea level for the period 9 February to 5 June, 1973. The magnitude of the arrows corresponds to speed scales: 50 cm/sec for current and 10 m/sec for wind. Sea level has been adjusted to account for the barometric offset of atmospheric pressure.

In the shallow nearshore waters, currents had high along-shelf coherence over the array (M_{11}, M_{21}, and M_{31}) and were more clearly correlated with local winds. Visual similarity between currents at the inshore and shelf break stations is weak. The mean current along the inner shelf was approximately zero and the amplitude of the fluctuations ranged from 10 to 30 cm/sec. Current directions paralleled the coast, either to the north or south, depending on whether the wind had a component from the south or north, respectively, similar to the findings of Murray (1975). There was also a marked decrease in current speeds which occurred at the time of the summer decrease in wind speeds. Mofield and Mayer (1976) used a

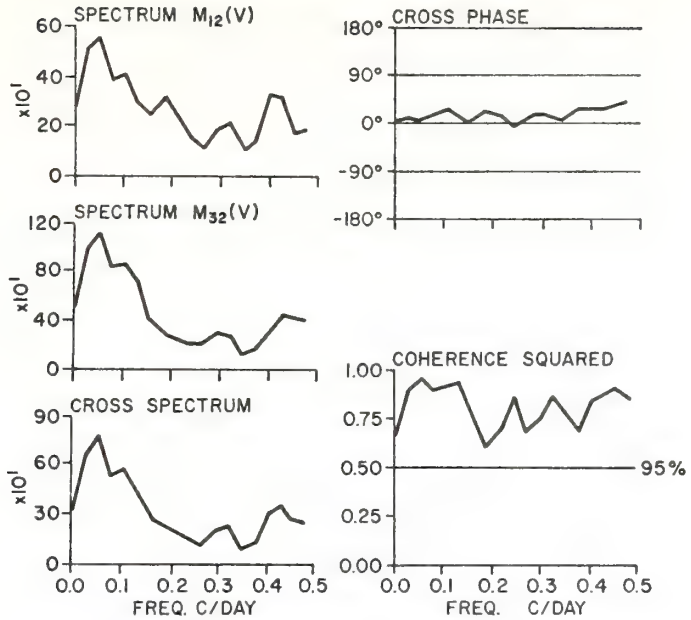


Figure 4. Spectra M_{12} vs. M_{32} ($cm^2/sec^2/CPD$) of 40 HrLP v-component series for the period 9 February to 5 June, 1973. Number of data points = 331; sample interval = 8 hrs.; lags = 56; degrees of freedom = 15.8; bandwidth = 0.035 CPD.

first-order autoregression technique to determine the longshore current response at M_{21} and M_{32} to the longshore component of the wind during the winter. He found that approximately 60% of the low frequency (periods longer than 40 hours) current variability at the inner shelf and about 12% at the shelf break were accounted for by the local wind.

Sea level set-up (set-down) at the coast appears, for the most part, to be correlated with southward (northward) winds, which is in agreement with Ekman-type downwelling (upwelling) found by Brooks and Mooers (1977). This is illustrated during February 9 to March 11, March 21 to 26, and May 1 to 16.

6. Spectrum analysis

Spectrum and cross-spectrum analyses were performed on selected time series pairs from Fig. 3 using standard Fourier transform methods (Jenkins and Watts, 1968). Only the v-component spectra are shown for they contained most of the variance, due to the north-south current alignment with the isobaths. Currents at the shelf break display four broad-band spectrum peaks centered at periods of 2.3, 3.1, 9.3, and 18.7 days (Fig. 4). At the 95% significance level, low frequency fluctuations were extremely coherent over the 10 km north-south array separation for all periods greater than two days, which account for about 75% of the total vari-

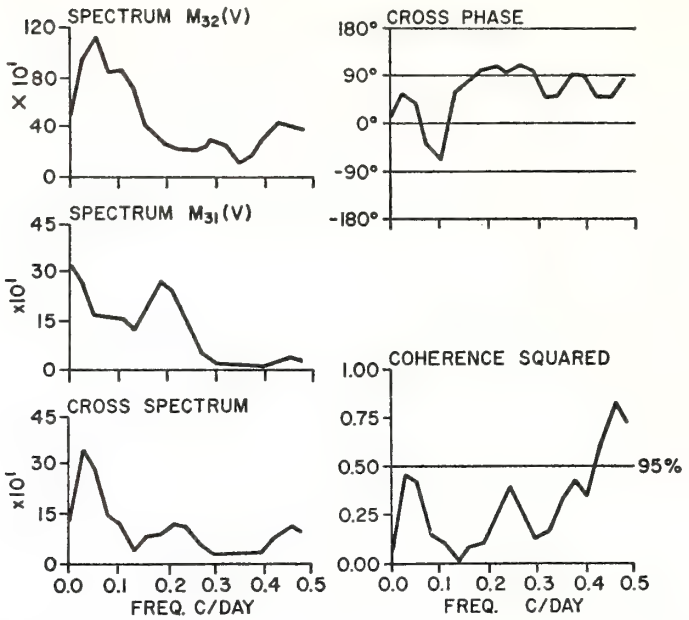


Figure 5. Spectra M_{32} vs. M_{31} ($cm^2/sec^2/CPD$) of 40 HrLP *v*-component series for the period 9 February to 5 June, 1973. Number of data points = 331; sample interval = 8 hrs.; lags = 56; degrees of freedom = 15.6; bandwidth = 0.036 CPD.

ance. Since the phase is positive for all cross-spectrum peaks, the oscillations occurred at the southern location first, which indicates a northward propagation for all low frequency motions. The periods of the coherent peaks, their coherency, phase, and 95% phase confidence limits are given in Table 5. Also shown are the corresponding wave lengths, phase speeds, and amplitudes computed over the array.

In the cross-shelf direction the only significant coherence occurred at a period of 2.2 days (Fig. 5); however, if an 80% significance level were used, then motions with periods of 2.5, 4.1, and 18-37 days would also be considered coherent. The phase is approximately +90° for all frequencies greater than 0.15 CPD, which indicates that fluctuations in the shallow water lead by about 1/4 wavelength. In the

Table 5. Linear wave properties computed from the spectra of M_{32} and M_{12}.

Period (days)	(coherence)²	Phase	95% confidence limit for Phase	Wave Length (km)	Phase Speed (cm/sec)	Amplitude (cm/sec)
18.7	.96	4.3°	±2°	905	+56	11
9.3	.92	22.7°	±3°	160	+20	14
3.1	.87	17.7°	±6°	263	+98	13
2.3	.88	27.9°	±6°	129	+65	20

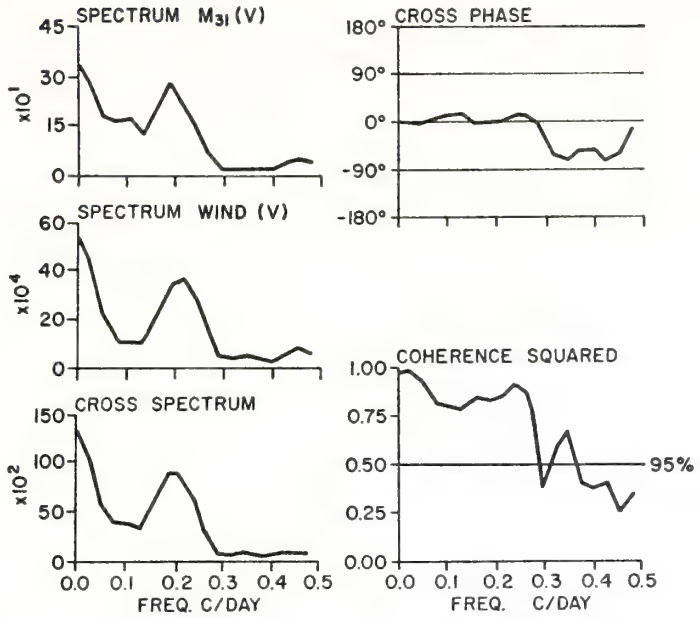


Figure 6. Spectra M_{31} vs. Miami Beach wind (cm^2/sec^2/CPD) of 40 HrLP *v*-component series for the period 9 February to 5 June, 1973. Number of data points = 328; sample interval = 8 hrs.; lags = 56; degrees of freedom = 15.6; bandwidth = 0.035 CPD.

9 to 12 day period band, oscillations at the shelf break lead by about 45°. It is again obvious that the temporal behavior of currents over the inner shelf was strikingly different from that measured at the outer shelf. The most energetic currents along the inner shelf had periodicities ranging from 4.6 to 6.2 days with a peak at 5.3 days. At the outer shelf the spectral peaks occurred at different periods with considerably higher amounts of energy.

Alongshore currents in the inner shelf waters were highly coherent with the *v*-component of the local wind for all periods longer than 3.5 days (Fig. 6). The similarity of the shape of the energy spectra and the near zero phase lags suggests that low frequency currents in these shallow waters are primarily driven by the local wind stress. In comparison, at the shelf break, the *v*-component wind was only significantly coherent (95% level) with alongshelf currents at a period of 4.1 days, with strong indication of significant coherence at 18.6 days (Fig. 7). However, the *u*-component wind was significantly correlated with current modulations at the outer shelf with periods of 37.3 and 9.3 days (Fig. 8). In addition, at periods of 4.7 and 2.2 days, the coherence is very near the 95% significance level. At the 5 day period the *u*-component wind was nearly in phase with the *v*-component current, whereas at the 9 day period the wind led by about 90° (2.2 days).

Low frequency current oscillations are not restricted to the continental shelf.

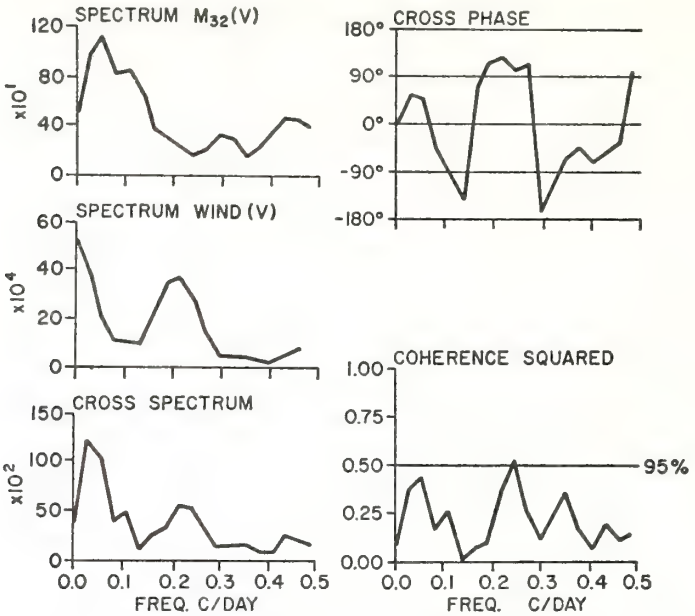


Figure 7. Spectra M_{32} vs. Miami Beach wind (cm^2/sec^2/CPD) of 40 HrLP *v*-component series for the period 9 February to 5 June, 1973. Number of data points = 328; sample interval = 8 hrs.; lags = 56; degrees of freedom = 15.6; bandwidth = 0.036 CPD.

Similar phenomena have been observed in a two-year deep current record obtained from the seaward edge of the Miami Terrace (approximately 26 km east of the box array; see Figs. 1a and 1b), located near the mean current axis of the Florida Current (Düing, Mooers, and Lee, this issue). Significant coherence occurred between the *u*-component current at this location and the *v*-component current at the shelf break for periods of 2.3 to 2.5 days and 9.3 to 12.4 days, with fluctuations at the current axis leading (Fig. 9). Comparisons with the *v*-component current from the Terrace break are not shown, but they revealed high coherence at periods of 2.3 to 2.5 days, 3.7 and 5.3 days, whereas it was low at periods of 9.3 to 12.4 days. Düing, Mooers, and Lee also observed significant coherence at periods in the 9.3 to 12.4 day range between the *v*-component current at the Terrace break and the east-west wind stress (τ_x) with the wind leading by about 90°. This is very similar to the correlation found at the shelf break with the east-west local wind.

Low frequency current fluctuations, with periods ranging from 2 days to 2 weeks, are a persistent feature of the Florida Current time domain. They were first observed by Pillsbury (1890) and later by Parr (1937). Webster (1961a) found a 7-day meander of the Florida Current front off Onslow Bay with amplitudes up to 10 km. He discovered the meander to be well correlated with onshore winds computed from north-south pressure differences that were lagged by 4.5 days, which is

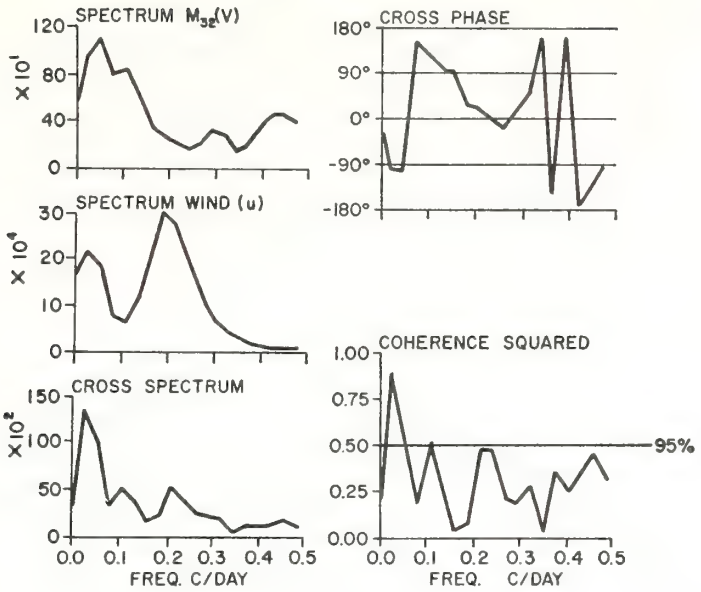


Figure 8. Spectra M_{32} (v-component) vs. Miami Beach wind (u-component) (cm²/sec²/CPD) of 40 HrLP time series for the period 9 February to 5 June, 1973. Number of data points = 328; sample interval = 8 hrs.; lags = 56; degrees of freedom = 15.6; bandwidth = 0.036 CPD.

again similar to our results and those of Düing, Mooers, and Lee. Schmitz and Richardson (1968) reported the Florida Current to be meandering on a one-week time scale with amplitudes of about 5 km in the Florida Straits. Mooers and Brooks (1977) analyzed temperature records near Miami and found several-day oscillations with amplitudes of 2 to 3°C. Düing (1975) conducted profiling from four anchored ships off Miami and noted a current modulation with 4 to 6 day time scales that was interpreted as a northward-traveling barotropic wave superimposed on the mean baroclinic current profile. The wavelength was estimated between 160 and 240 km and the phase speed was reported to be about +50 cm/sec.

It is evident that at least part of the low frequency current oscillations over the shelf are connected to similar features in the Florida Current over the Miami Terrace (Fig. 9), both of which appear to be related to wind stress. A mechanism which could account for these observations was discussed by Brooks (1975), viz., the fluctuating wind stress can produce a surface onshore-offshore Ekman transport which results in deep motions across steep bottom topography and mean current shear. As a consequence, relative vorticity is generated, which can propagate as topographically trapped waves (shelf waves). With a mean northward flow, the first two barotropic longwave modes travel to the south, with shallow water on the right. However, the shortwaves and higher modes can travel north.

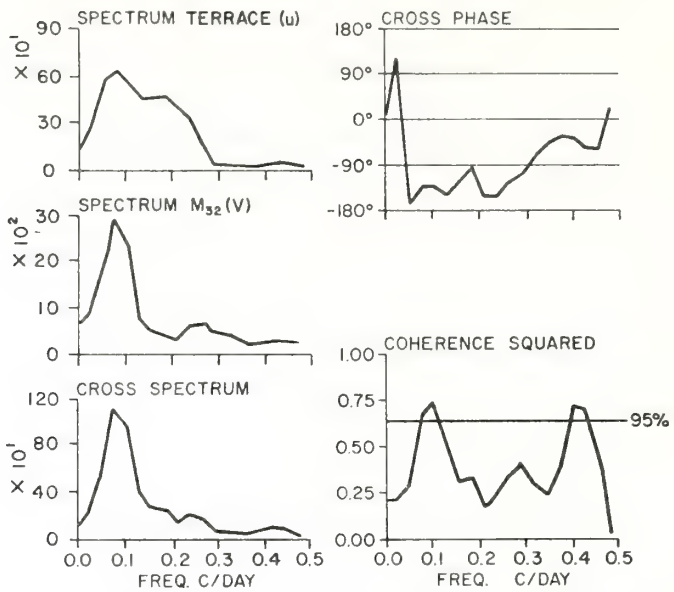


Figure 9. Spectra Terrace Break Meter (u-component) vs. M_{32} (v-component) (cm²/sec²/CPD) of 40 HrLP time series for the period 9 February to 18 April, 1973. Number of data points = 205; sample interval = 8 hrs.; lags = 56; degrees of freedom = 9.8; bandwidth = 0.036 CPD.

7. Seasonality

After removal of the box array, moorings M_{21} and M_{22} were maintained for an additional 5 months, producing record lengths of approximately 9 months. Time series of 4-hourly current vectors from these locations, along with local wind and unadjusted sea level, are shown in Fig. 10. The long current records were broken into three seasonal subsets, labeled A, B, and C, of 100 days duration and 15 days overlap. Simple statistics of these 40 HrLP series are given in Table 6.

Table 6. Basic statistics of seasonal subsets of the long 40 HrLP current series.

		u (cm/sec)				v (cm/sec)			
Mooring	Data Set	Min.	Max.	Mean	Stand. Dev.	Min.	Max.	Mean	Stand. Dev.
M_{21}	A	−5	+9	+0.9	2	−30	+28	−0.9	10
M_{22}	A	−9	+7	−0.3	2	−34	+72	+15	19
M_{21}	B	−4	+6	−0.4	2	−13	+15	+1	4
M_{22}	B	−8	+7	−0.4	3	−47	+94	+24	24
M_{21}	C	−8	+11	−0.5	3	−34	+17	−0.8	8
M_{22}	C	−10	+8	0	2	−74	+108	+18	31

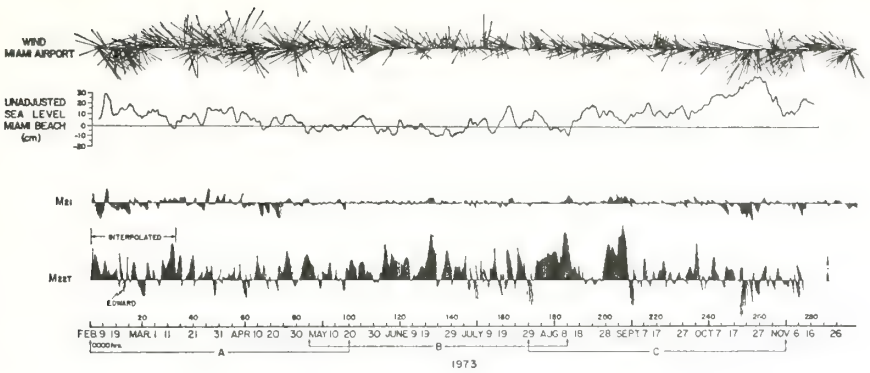


Figure 10. Time series of 4-hourly current vectors, 6-hourly wind vectors, and unadjusted sea level over the period 9 February to 3 December, 1973. The current and sea level data have been smoothed with a 40 HrLP filter. The wind record is 6-hour averages from 3-hourly Miami airport readings; speed scales are given by the magnitude of the arrows: 50 cm/sec for current and 5.4 m/sec for wind; seasonal subsets are designated by A, B, and C.

As suggested earlier (Fig. 3), the intense current variability at the shelf break is persistent throughout the year and shows little visual correlation with the local winds, which display a marked seasonal behavior. Currents at the inner shelf were

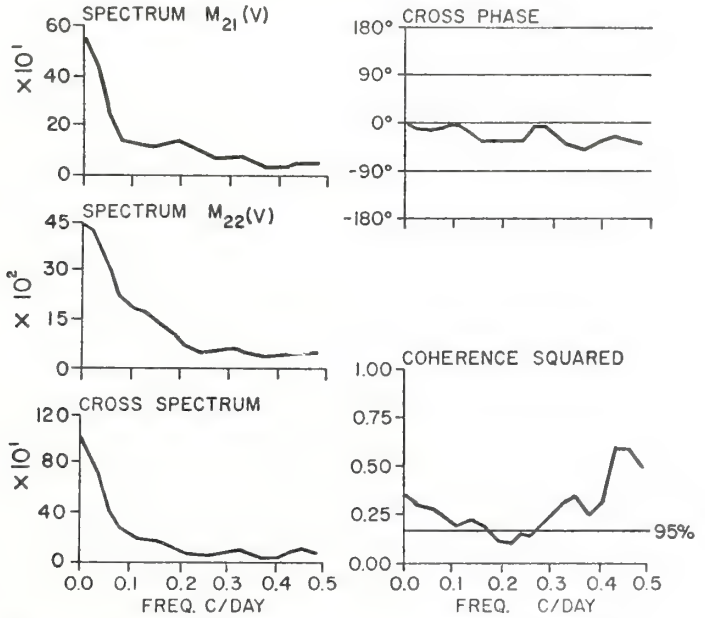


Figure 11. Spectra M_{21} vs. M_{22} (cm²/sec²/CPD) of 40 HrLP v-component series for the period 9 February to 12 November, 1973. Number of data points = 817; sample interval = 8 hrs.; lags = 56; degrees of freedom = 38.9; bandwidth = 0.036 CPD.

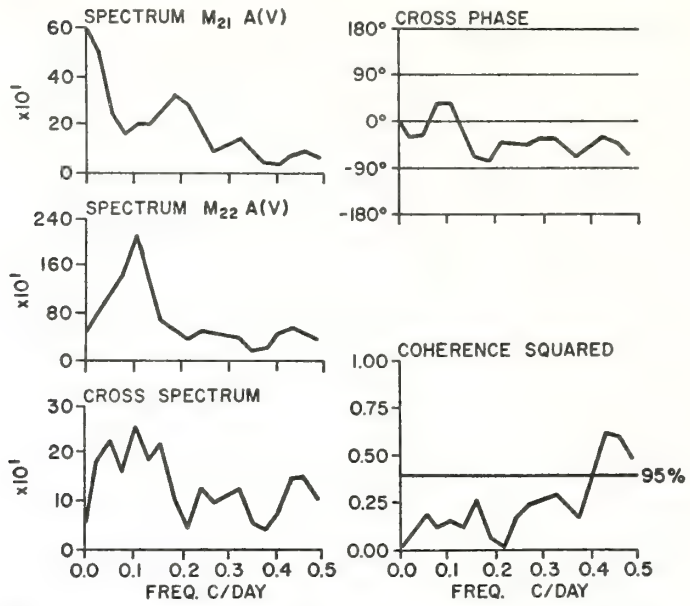


Figure 12. Spectra $M_{21}A$ vs. $M_{22}A$ ($cm^2/sec^2/CPD$) of 40 HrLP *v*-component series for the period 9 February to 20 May, 1973 (winter subset A). Number of data points = 300; sample interval = 8 hrs.; lags = 56; degrees of freedom = 14.3; bandwidth = 0.036 CPD.

highly influenced by the local wind during the two winter seasons of February through April and October through November. During the summer the smaller amplitude fluctuations appear to be related to events at the shelf break. There was a significant increase in the northerly mean current at the shelf break in the summer. A similar summer increase has been observed at the shelf break off Boca Raton, Florida by Lee (1975). These observations may reflect the summer maximum Florida Current volume transport reported by Niiler and Richardson (1973) and later confirmed by Mooers and Brooks (1977). Mean currents in the inner shelf were near zero for all seasons.

Cross-spectrum analyses were conducted with the *v*-component time series from the inner shelf and shelf break locations for the total record (Fig. 11) and seasonal subsets (Figs. 12, 13, and 14). Distinct energy peaks become lost in spectra of the total records due to the event nature of the fluctuations which occur with many different time scales and tend to produce a red spectrum when analyzed together. The cross-shelf coherence computed over the 9 months of data is above the 95% significance level for most of the low frequency spectrum except for periods of about 5 days. The negative phase indicates that fluctuations occurred first at the inner station. Spectra of the winter subset (Fig. 12) are essentially the same as that of Fig. 5, where it was shown that the 5 day peak in the inner shelf was associated

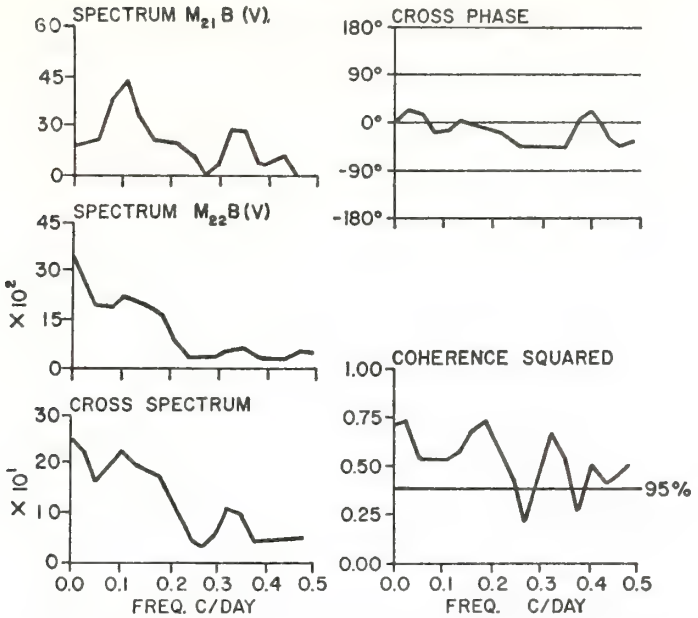


Figure 13. Spectra $M_{21}B$ vs. $M_{22}B$ ($cm^2/sec^2/CPD$) of 40 HrLP *v*-component series for the period 5 May to 13 August, 1973 (summer subset B). Number of data points = 300; sample interval = 8 hrs.; lags = 56; degrees of freedom = 14.3; bandwidth = 0.036 CPD.

with a similar period motion in the local winds. The 9 day peak at the shelf break was coherent with the *u*-component of the wind and the *u*-component of the current at the Miami Terrace break. In subset B (summer) current oscillations at the inner shelf, with periods of about 9 days, now appear as a well-defined energy peak and are coherent with similar fluctuations at the shelf break (Fig. 13). These changes are probably due to the decrease in local wind forcing which occurs with the discontinuance of winter cold fronts. The spectra of subset C (part summer and winter) do not contain any pronounced energy peaks, which reflects the mixture of time scales that are occurring during this period (Figs. 14 and 10). These numerous differences in spectra of the total data set and seasonal subsets indicate that low frequency current modulations in the shelf waters occur as transient phenomena in response to event-type forcing, such as the passage of cold fronts, which may in turn generate meanders and eddies. Thus, the shape and partition of energy in a current spectrum is to some degree dependent on the time period of the measurements. However, the statistics of the current and momentum flux time series averaged over the total record and the first 4 months showed little variation (Tables 3, 4, and 6).

8. Spin-off eddies

One of the most pronounced features of the current observations is the large

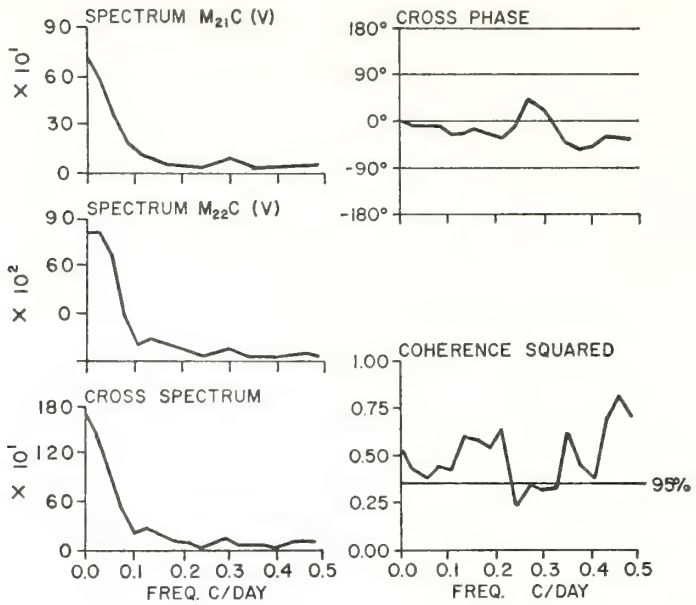


Figure 14. Spectra $M_{21}C$ vs. $M_{22}C$ ($cm^2/sec^2/CPD$) of 40 HrLP v-component series for the period 29 July to 6 November, 1973 (summer and fall subset C). Number of data points = 300; sample interval = 8 hrs.; lags = 56; degrees of freedom = 14.3; bandwidth = 0.036 CPD.

number of current reversals that do not appear to be either directly tide- or wind-induced (Figs. 3 and 10). Similar events were previously observed off Pompano and Boca Raton, Florida and were termed "spin-off eddies" (Lee, 1970; 1975). These disturbances were described as small diameter (10-30 km), cyclonic edge-eddies which form along the inshore front of the Florida Current and travel northward through the coastal waters. Vortices of this type have been frequently observed in frontal regions of strong horizontal shear (Spilhaus, 1940; Von Arx, Bumpus, and Richardson, 1955; Bang, 1971; 1973). Remote satellite thermal imagery clearly displays these features to be tongue-like, Gulf Stream extrusions coupled to a trailing band of shelf or slope waters (NOAA-NESS, 1974; DeRycke and Rao, 1973; Maul, Norris, and Johnson, 1974; Stumpf and Rao, 1975; Legeckis, 1975).

Spin-off eddies leave their signatures in a current meter record as a strong cyclonic reversal which is many times accompanied by an advection of heat and salt from the Florida Current. Fig. 10 indicates that approximately 45 reversals occurred during the total measurement period or, on the average, about one per week. However, it is difficult to determine from current meter records alone if a reversal was produced by an eddy or a propagating wave.

On February 22 and 23 the 3-dimensional thermal field of a well-developed spin-off eddy was mapped during its northward passage through the current meter array. This event is designated EDWARD in Figs. 3 and 10. Mapping was performed

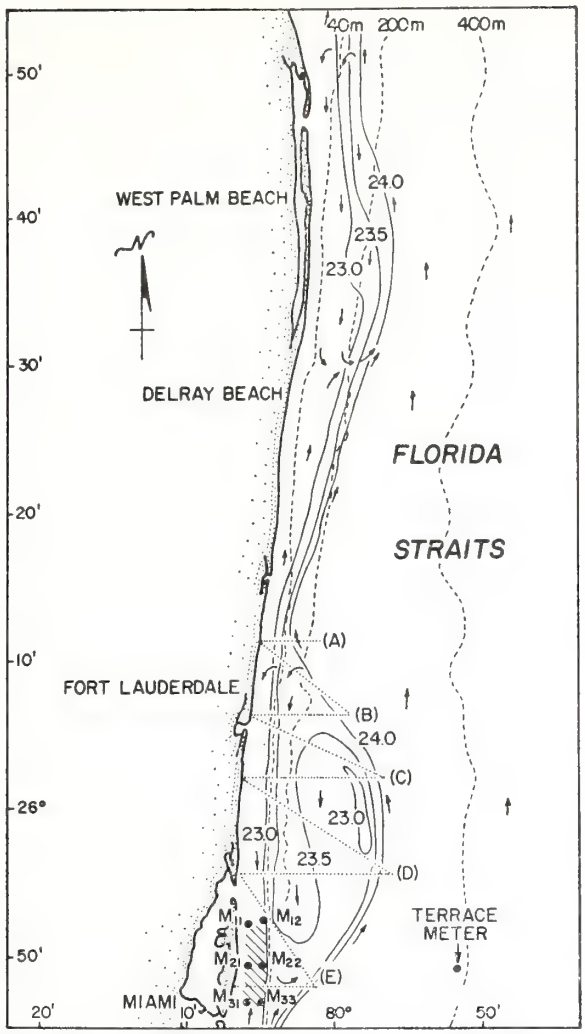


Figure 15. Composite map of surface temperature (°C) for the period 20 to 23 February, 1973. Ship tract designated by dots; temperature sections by letter (A)-(E); current meter moorings by blackened circles; arrows indicate observed current direction.

daily off Miami and Fort Lauderdale by running a saw-toothed cruise tract with a continuously recording surface thermosalinograph on a rapid vessel. A series of XBT's were released on each leg perpendicular to shore. A composite surface thermal map was constructed by translating the daily thermal maps northward at the speed of the anomaly as measured by the current meter array (Fig. 15). Mapping of the eddy event took approximately one day, from 1130 hours on the 22nd to 1200 hours on the 23rd. EDWARD appears as a warm, tongue-like southward extrusion from the Florida Current, coupled to an entrainment of cooler shelf water

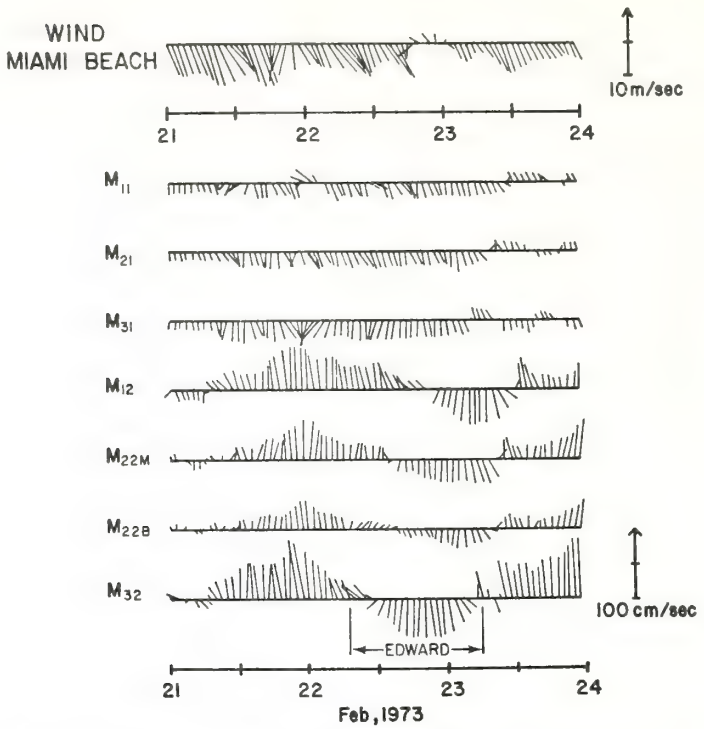


Figure 16. Time series of one-hour values of 3 HrLP current and wind vectors during the passage of a spin-off eddy (EDWARD).

along the southern boundary. This configuration is very similar to the "shingle" (Von Arx, Bumpus, and Richardson, 1955) structure observed from satellites. The oblong-shaped eddy traveled toward the north at approximately 39 cm/sec, with a length of about 34 km and width of 23 km. The northward speeds computed from the current meter array and daily displacements of the thermal maps were in good agreement. There appears to be a smaller distortion of the surface front about 80 km to the north. This feature was also observed to produce a current reversal and may be an initial growth stage of an edge-eddy. Both disturbances were associated with a larger wave-like meander of the front which had a length of 84 km and appeared to propagate to the north at the same speed as EDWARD, which indicates a period of 2.2 days.

A blow-up of the 3 HrLP current and wind data recorded during the passage of EDWARD is shown in Fig. 16. Data from current meter M_{22T} are not shown for it was not operating properly at this time. Except for a small reversal near the 23rd, the local winds were light and steady ($\sim$ 5 m/sec toward the south) over the duration of the eddy and show no direct connection. The northward movement of the event is clearly evident in the shelf break records. Currents along the inner shelf

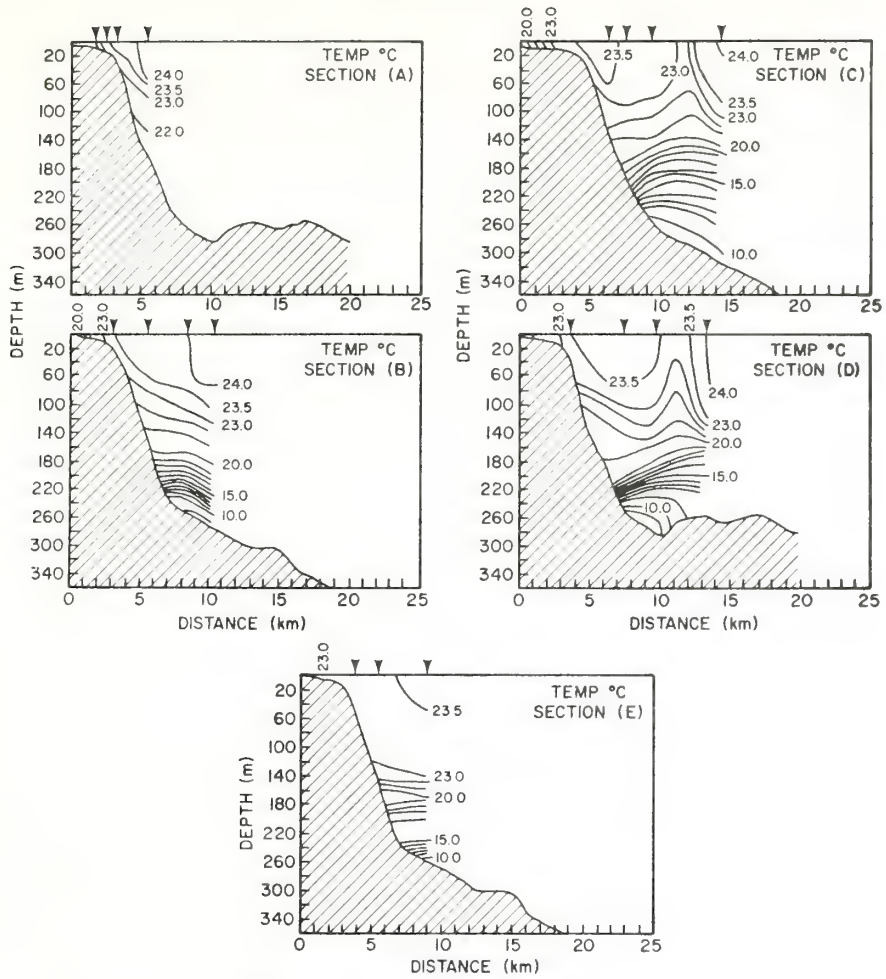


Figure 17. Temperature profiles through a spin-off eddy; section (A), 22 February, 1130-1155; section (B), 22 February, 1220-1236; section (C), 22 February, 1324-1343; section (D), 23 February, 1040-1108; section (E), 23 February, 0936-1014; arrows indicate XBT stations.

appear to be unaffected by EDWARD, indicating that it did not extend into these shallow depths (~ 6m).

The passage of a spin-off eddy also produces a strong vertical distortion of the thermal field over the slope and terrace (Figs. 17, 18a, 18b, and 18c). The up-lifted isotherms associated with the cyclonic circulation of EDWARD created a cool surface band of 23°C water near the center of the vortex. The warmer water within the southward extruding tongue is part of a homogeneous layer approximately 80m deep. The convergence of the southerly and northerly flows at the southern boundary produces an extremely turbulent surface disturbance line that is clearly visible.

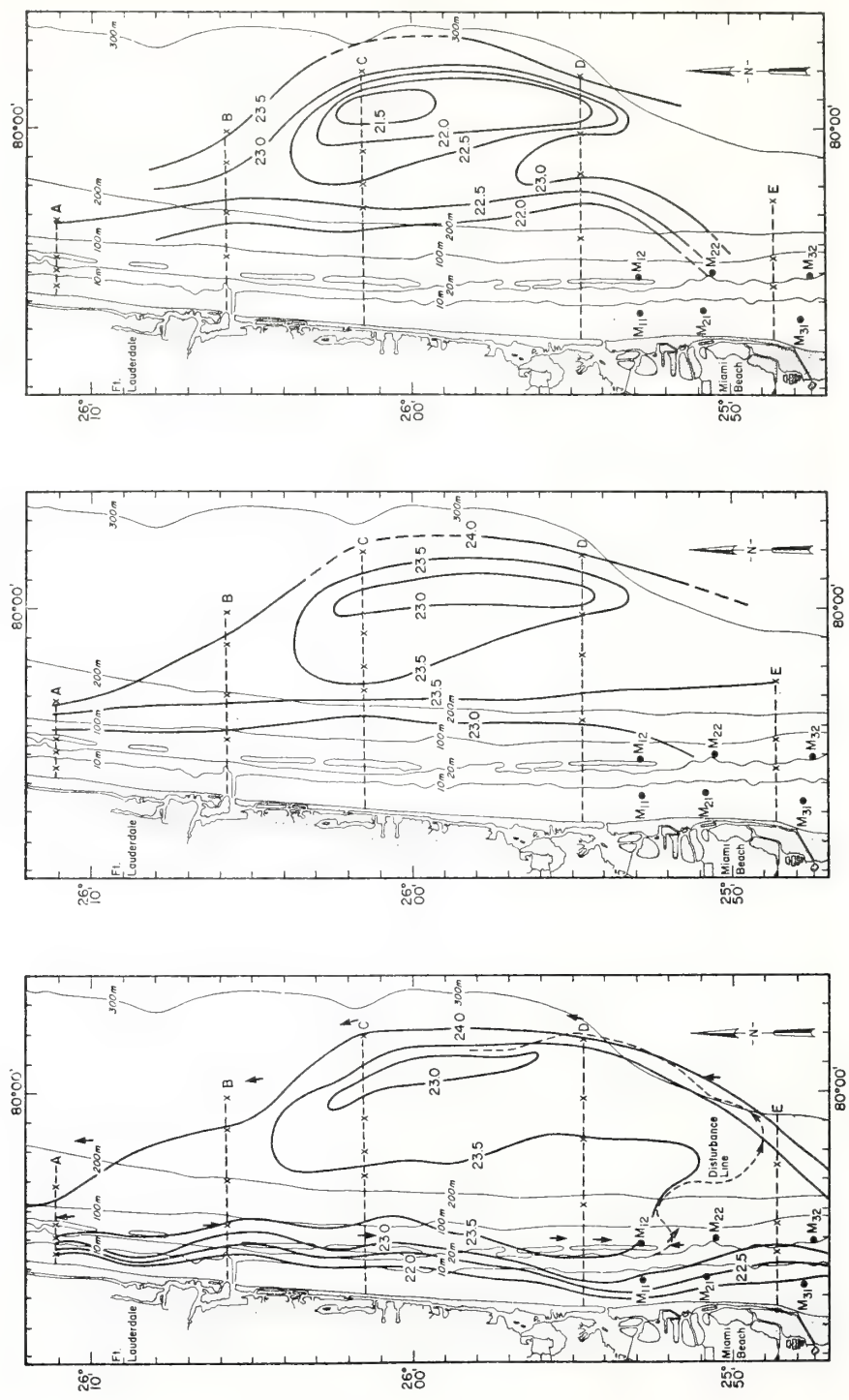


Figure 18a. Composite map of surface temperature (°C) contoured from thermosalinograph data recorded continuously along a saw-toothed cruise track on February 22 and 23. XBT stations are marked with an X.

Figure 18b. Composite map of temperature (°C) at the 50 m depth, contoured from XBT data obtained on February 22 and 23. XBT stations are marked with an X.

Figure 18c. Composite map of temperature (°C) at the 100m depth, contoured from XBT data obtained on February 22 and 23. XBT stations are marked with an X.

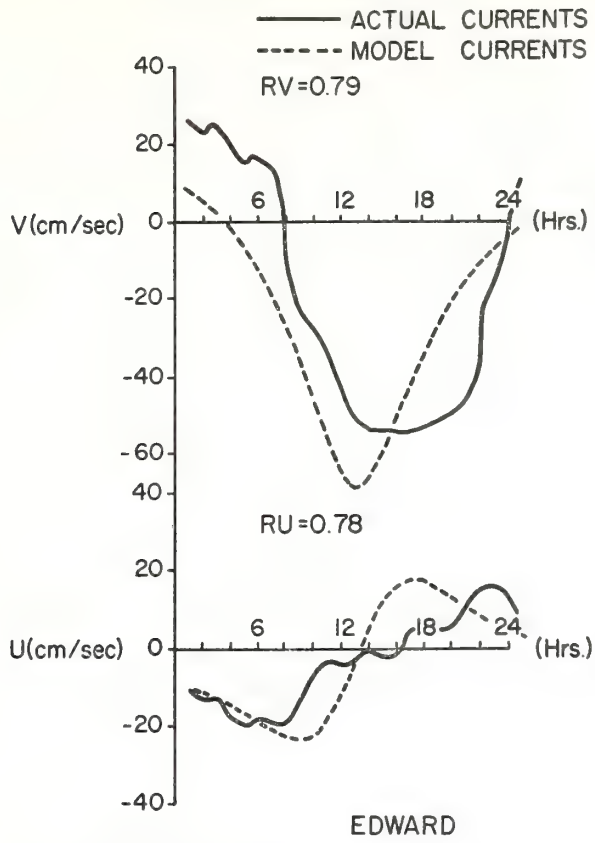


Figure 19. Actual vs. modeled currents from M_{32} 3 HrLP data. *RU* and *RV* represent the correlation coefficients for *u* and *v* components, respectively.

Effects of the eddy appear to extend to a depth of about 200-220m where the isotherms tend to become horizontal.

9. Eddy model

Since it is difficult to obtain synoptic measurements of spin-off eddies, Lee (1975) developed a kinematic model that uses current meter data to predict the horizontal dimensions, phase speed, and circulation of an eddy. This approach was used with good results on 7 vortices measured off Boca Raton; however, the only parameters available for model verifications were the observed currents and phase speeds. The event shown in Figs. 15 and 16 can be used to check the spatial predictions as well. Briefly, the model consists of a linear combination of a moving vortex pair with a uniform background current. The resulting flow is 2-dimensional in the *x*-*y* plane, with *y* positive to the north and *x* positive to the east. A vortex pair was used in order to account for the influence of the coastline (Lamb, 1945) for, when com-

bined with a uniform current, this becomes analogous to a single moving vortex in a flow near a boundary. As an eddy passes a fixed current meter, the recorded time series should resemble this combined motion.

Current meter data (M_{32}, 3 HrLP) recorded during the passage of EDWARD were tested with the above model. The actual and predicted currents as shown in Fig. 19 appear to be reasonably similar. In addition, the model predicts the eddy to have a width of 21 km, length of 36 km, phase speed of 40 cm/sec to the north, and a circulation of $4.5 \times 10^7 cm^2/sec$. These estimates are within 8% of the measured values, which is a good agreement and further substantiates the model's ability to give a reasonable representation of spin-off eddies.

10. Eddy formation

There are several candidate mechanisms that may be responsible for edge-eddy formation. Eddies are known to form in the wake of topographic anomalies, are at times generated by wind, and can form from growing instabilities. It is well documented in the literature that mesoscale eddies (rings) form east of Cape Hatteras from the growth and detachment of large-scale Gulf Stream meanders (cold core rings: Fuglister, 1971; Barrett, 1971; Parker, 1971; warm core rings: Saunders, 1971; Thompson and Gotthardt, 1971; Gotthardt, 1973). The meanders can be initiated by winds or thermohaline processes and then grow to detachment due to instabilities in the basic zonal flow (Saltzman and Tang, 1975).

Similarly, smaller diameter spin-off eddies (diameter <50 km) appear to be an evolutionary stage of a rapidly growing wave-like instability of the Florida Current front. These vortices are consistently observed in regions of large horizontal shear over a wide range of different bottom topographies and at any time of year. This suggests that their generation is not likely to be due to topographic or direct wind forcing. Also, it has been shown that a small perturbation of a region of high horizontal velocity gradients can produce a rolling up of the shear zone (Rouse, 1963) which resembles the shingle structure of the Florida Current front. In a like manner, perturbations of the front have been observed to evolve into eddies in approximately 2 days (Stumpf and Rao, 1975; Legeckis, 1975). Orlanski (1969) and Orlanski and Cox (1973) demonstrated that baroclinic instabilities can develop in the Gulf Stream and may be the source of frontal meanders in the Florida Current. However, Eady (1949) and Saunders (1973) determined that the criterion for baroclinic instability of a vortex is $\frac{R_D^2}{r^2} < 1$, where r is the eddy radius and R_D is the internal Rossby radius of deformation. For the eddy shown in Fig. 14, this ratio is approximately 3; thus, it does not appear that edge-eddies grow from amplified baroclinic waves. The criterion for barotropic instabilities to develop is satisfied if the potential vorticity distribution has one or more extrema normal to the coast (Kuo, 1949; Haurwitz and Panofsky, 1950; Lipps, 1963; Niiler and Mysak, 1971). This criterion is

met in the cyclonic shear region of the Florida Current where the instantaneous horizontal velocity profile can become strongly concave. Also, a barotropic disturbance is known to grow at the expense of kinetic energy from the mean flow (Haurwitz and Panofsky, 1950; Lipps, 1963). It was previously shown (Lee, 1975) that spin-off eddies behaved as braking mechanisms on the basic current, substantially increasing the normal energy dissipation rate of the inshore frictional region.

Due to the rapid energy dissipation, the life span of a typical spin-off eddy should be relatively short compared to the mesoscale size which can exist for years (Fuglister, 1971; Parker, 1971; Barrett, 1971). Ichiye (1966) concluded that the time (t) to reduce the vorticity in a small-scale Rankin type vortex (finite filament of constant vorticity surrounded by an irrotational field) to 1/2 its initial value is given by:

$$t = \frac{L^2}{(1.82)\, A_H} \tag{3}$$

where L is the horizontal scale of the eddy and A_H is the horizontal eddy viscosity which he computed from the semi-empirical law $A_H = 0.01\ L^{4/3}$. For the eddy displayed in Figs. 18a, b, and c, $L \cong 30$ km and $A_H \cong 4 \times 10^6 \text{cm}^2/\text{sec}$. The eddy viscosity can also be computed from the ratio of the square of the characteristic distance offshore to the center of an eddy (X) to the mean separation time of vorticities T_s, i.e., $A_H = \frac{X^2}{T_s}$, with $X = 15$ km and $T_s = 1$ week, we find that $A_H \cong 3.8 \times 10^6 \text{cm}^2/\text{sec}$. Using these values in eq. 3, the half-life of a 30 km scale edge-eddy is approximately 2 weeks. Satellite imagery indicates that this estimate is reasonable, for it is difficult to trace small-scale features on the Florida Current front in images taken more than 2 weeks apart.

11. Summary

Analysis of current meter data from the narrow continental shelf off Miami, Florida revealed that the most energetic fluctuations occurred as highly variable, low-frequency current oscillations with broad-band periods ranging from 2 days to 2 weeks. The amplitudes of these modulations were several times the means, and appear to be generated by wave-like meanders and/or eddies from the Florida Current, both of which may be causally related to wind forcing. Current fluctuations were highly coherent along the shelf break (30m isobath) over the 10 km array spacing for all periods greater than 2 days. Phase relationships indicate a northward propagation for all low frequency motions. Currents at the shelf break showed v-component spectrum peaks at periods of about 2, 3, 9, and 19 days that were mutually coherent with the u-component current near the Florida Current axis (Terrace break) and the u-component of the local wind at the common periods of

2 and 9 days. The *v*-component currents at the shelf break and at the Terrace break (Düing, Mooers, and Lee, 1977) both showed significant coherence with the east-west component of the wind around the 9 day period with the wind leading by about 90°. A similar result was found by Webster (1961a) off Onslow Bay between meanders of the Florida Current front and the east-west wind. Current oscillations along the shallow inner shelf (6m isobath) appear to be primarily driven by local winds during the winter with high coherence between the two for all periods longer than 3.5 days. The coherence between the inner shelf and shelf break locations (2 km separation) was low during this time except for periods around 2 days. During the summer, wind and inner shelf current variability decreased, whereas current variability along the shelf break remained high. In addition, current fluctuations along the inner shelf became highly coherent with those of the shelf break.

Low frequency current fluctuations are a consistent feature of the Florida Current. Oscillations over the shelf are connected to similar features over the Miami Terrace and both may be mutually related to atmospheric forcing in the form of shelf wave generation. The transient nature of the observed current modulations may, in part, be explained by the random passage of wind events, which can perturb the strongly sheared cyclonic front of the Florida Current, producing horizontal wave-like meanders (shelf-waves). Unstable barotropic modes can occur due to inflection points (potential vorticity extrema) in the horizontally sheared current, which then propagate to the north and may eventually evolve into small-scale cyclonic eddies ("spin-off eddies").

These amplified disturbances appear to dissipate kinetic energy from the mean current, behaving as braking mechanisms on the basic flow in an analogous manner as small-scale eddies in the atmosphere. Since these features occur on the average of once per week and have a life span of only about 1 to 3 weeks, their combined dissipating effect may play a significant role in the total energy balance of the Florida Current.

Edge-eddies manifest themselves as warm, southward-oriented, tongue-like extrusions of the Florida Current coupled to a trailing band of shelf or slope water. Observed eddy diameters range from 10 to 30 km and they travel to the north along the continental slope at speeds less than the mean Florida Current. They were found to extend vertically to a depth of approximately 200m. Thus, these disturbances provide a means for exchanging mass across the frontal boundary. It was estimated by Lee (1975) that the residence time of the waters on the narrow shelf off southeast Florida is largely determined by the mean separation time between spin-off eddies, or approximately one week.

Acknowledgments. The authors wish to express their appreciation to Drs. C. Rooth, C. N. K. Mooers, and D. Hansen for the time they gave in discussing many aspects of the manuscript. We are thankful for the careful preparation given the current meters by K. Majersky; the reliable attention given to current meter maintenance and deployment by R. Rutkowsky; com-

puter processing done by M. Minton; and manuscript typing by L. Neumann. Most of all, we are thankful for the personal example provided us by Bill Richardson, whose genuine interest and kind encouragement taught us a great deal more than oceanography. We are proud to be able to dedicate this paper to him. This work was partially supported by the Atlantic Oceanographic and Meteorological Laboratories of Miami, Florida under National Oceanic and Atmospheric Administration Grant No. N22-102-72(G); and the University of Miami Sea Grant Program under National Oceanic and Atmospheric Administration, Contract No. 2-35147.

REFERENCES

Bang, N. D. 1971. The southern Bengula Current region in February 1966: Part II: bathythermography and air-sea interactions. Deep-Sea Res., *18*, 209–224.

—— 1973. Characteristics of an intense ocean frontal system in the upwell regime west of Cape Town. Tellus, *25*, 256–265.

Barrett, J. R. 1971. Available potential energy of Gulf Stream rings. Deep-Sea Res., *18*, 1221–1231.

Brooks, D. A. 1975. Wind-forced continental shelf waves in the Florida Current. Ph.D. dissertation, Univ. of Miami, Miami, Florida.

Brooks, D. A. and C. N. K. Mooers. Wind-forced continental shelf waves in the Florida Current. J. Geophys. Res. (accepted)

Brooks, I. H. and P. P. Niiler. 1977. Energetics of the Florida Current. J. Mar. Res., *35*, this issue.

DeRycke, R. J. and P. K. Rao. 1973. Eddies along a Gulf Stream boundary viewed from a very high resolution radiometer. J. Phys. Oceanogr., *3*, 490–492.

Düing, W. 1975. Synoptic studies of transients in the Florida Current. J. Mar. Res., *33*, 53–73.

Düing, W., C. N. K. Mooers, and T. N. Lee. 1977. Low frequency variability in the Florida Current and relation to atmospheric forcing from 1972 to 1974. J. Mar. Res., *35*, this issue.

Eady, E. T. 1949. Long waves and cyclone waves. Tellus, *1*, 33–52.

Fuglister, F. C. 1971. Cyclonic rings formed in the Gulf Stream 1965-1966, *in* Studies in Phys. Oceanogr., A. Gordon, ed., New York, Gordon and Breach, 137–168.

Gotthardt, G. A. 1973. Observed formation of a Gulf Stream anticyclonic eddy. J. Phys. Oceanogr., *3*, 237–238.

Haurwitz, B. and H. A. Panofsky. 1950. Stability and meandering of the Gulf Stream. Trans., Amer. Geophys. Union, *31*, 723–731.

Ichiye, T. 1966. Hydrographic structure of an eddy on the edge of the Gulf Stream off Cape Hatteras. Paper presented before the 4th Amer. Geophys. Union, April, 1966. Unpublished.

Jenkins, G. M. and D. G. Watts. 1968. Spectral analysis and its applications. San Francisco, Calif., Holden-Day, Inc., 525 pp.

Kuo, H. L. 1949. Dynamic instability of two-dimensional non-divergent flow in a barotropic atmosphere. J. Meteor., *6*, 105–149.

Lamb, H. 1945. Hydrodynamics. New York, Dover Publications, 738 pp.

Lee, T. N. 1970. Demonstration of limitations and effects of waste disposal on an ocean shelf. Florida Ocean Science Institute, Environmental Protection Agency Project No. WPD 165-01(R-1)-67, Final Report, 304 pp.

—— 1975. Florida Current spin-off eddies. Deep-Sea Res., *22*, 753–765.

Legeckis, R. 1975. Applications of synchronous meteorological satellite data to the study of time dependent sea surface temperature changes along the boundary of the Gulf Stream. Geophys. Res. Letters, *2*, 435–438.

Lipps, F. B. 1963. Stability of jets in a divergent barotropic fluid. J. Atmos. Sci., *20*, 120–129.

Maul, G. A., D. R. Norris, and W. R. Johnson. 1974. Satellite photography of eddies in the Gulf Loop current. Geophys. Res. Letters, *1*, 256–258.

Mayer, D. A. and D. V. Hansen. 1975. Observations of currents and temperatures in the southeast Florida Coastal zone during 1971-1972. NOAA Tech. Rep. ERL AOML ERL 346-AOML 21, Atlantic Oceanographic and Meteorological Laboratories, Miami, Florida, 36 pp.

Mofield, H. O. and D. A. Mayer. 1976. Formulas used to analyze wind-driven currents as first-order autoregressive processes. NOAA Tech. Memo ERL PMEL-7-Pacific Marine Environmental Lab., Seattle, 21 pp.

Mooers, C. N. K. and D. A. Brooks. 1977. Fluctuations in the Florida Current, summer 1970. Deep-Sea Res. (accepted).

—— 1977. The geostrophic seasonal cycle of the Florida Current. J. Mar. Res. (in preparation).

Murray, S. P. 1975. Trajectories and speeds of wind-driven currents near the coast. J. Phys. Oceanogr., *5*, 347–360.

Niiler, P. P. 1975. A report on the continental shelf circulation and coastal upwelling. Sixteenth Gen. Assembly, Int'l. Union of Geod. and Geophys., Grenoble, France. Rev. Geophys. and Space Phys., *13*, 609–614.

Niiler, P. P. and L. A. Mysak. 1971. Barotropic waves along an eastern continental shelf. Geophys. Fluid Dyn., *2*, 273–278.

Niiler, P. P. and W. S. Richardson. 1973. Seasonal variability in the Florida Current. J. Mar. Res., *31*, 144–167.

NOAA-NESS. 1974. Experimental Gulf Stream Analysis, NOAA-2 Satellite Thermal Infrared (VHRR), U.S. Dept. Commerce, Environmental Products Group, F.O.B. #4, Room 3301, Washington, D.C. 20233.

Orlanski, I. 1969. The influence of bottom topography on the stability of jets in a baroclinic fluid. J. Atmos. Sci., *26*, 1216-1232.

Orlanski, I. and M. D. Cox. 1973. Baroclinic instability in ocean currents. Geophys. Fluid Dyn., *4*, 297–332.

Parker, C. E. 1971. Gulf Stream rings in the Sargasso Sea. Deep-Sea Res., *18*, 981–993.

Parr, A. E. 1937. Report on hydrographic observations at a series of anchor stations across the Straits of Florida. Bull. of the Binghorn Oceanogr. Coll., *6*, 1–62.

Pillsbury, J. E. 1890. The Gulf Stream—a description of methods employed in the investigation, and the results of the research. U.S. Coast and Geodetic Surv., Rep. for 1890, Appendix No. 10, 461–620.

Rouse, H. 1963. On the role of eddies in fluid motion. Amer. Scientist, 285–314.

Saltzman, B. and C. Tang. 1975. Formation of meanders, fronts, and cutoff thermal pools in a baroclinic ocean current. J. Phys. Oceanogr., *5*, 86–92.

Saunders, P. M. 1971. Anticyclonic eddies formed from shoreward meanders of the Gulf Stream, Deep-Sea Res., *18*, 1207–1219.

—— 1973. The instability of a baroclinic vortex. J. Phys. Oceanogr., *3*, 61–65.

Schmitz, W. J. and W. S. Richardson. 1968. On the transport of the Florida Current. Deep-Sea Res., *15*, 679–693.

Spilhaus, A. F. 1940. A detailed study of the surface layers of the ocean in the neighborhood of the Gulf Stream with the aid of rapid measuring hydrographic instruments. J. Mar. Res., *3*, 51–75.

Stumpf, H. G. and P. K. Rao. 1975. Evolution of Gulf Stream eddies as seen in satellite infrared imagery. J. Phys. Oceanogr., *5*, 388–393.

Thompson, B. J. and G. A. Gotthardt. 1971. Life cycle of a North Atlantic eddy. Trans., Amer. Geophys. Union, *52*, 241 (abstract only).

Von Arx, W. S., D. F. Bumpus, and W. S. Richardson. 1955. On the fine structure of the Gulf Stream front. Deep-Sea Res., *3*, 46–65.

Webster, F. 1961a. A description of Gulf Stream meanders off Onslow Bay. Deep-Sea Res., *8*, 130–143.

—— 1961b. The effects of meanders on the kinetic energy balance of the Gulf Stream. Tellus, *13*, 392–401.

Received: *February, 1976;* revised: *September, 1976.*

Printed in U.S.A. for the Sears Foundation for Marine Research,
Yale University, New Haven, Connecticut, 06520, U.S.A.
Van Dyck Printing Company, North Haven, Connecticut, 06473, U.S.A.

Limnology and Oceanography 22, No. 5, 975.

OFFICER, C. B. 1976. **Physical oceanography of estuaries** (and associated coastal waters). John Wiley and Sons, Inc., New York. xii + 465 p. $27.50.

This book presents, from the viewpoint of a geophysicist, a synthesis of the theoretical understanding of the dynamics of estuaries and a broad survey of worldwide field studies of estuaries. The scope of the material covered is impressive and comprehensive. The book starts with a fundamental discussion of the equations of motion, turbulence, boundary layers, and the hydraulics of open channel flow. Subsequent chapters deal with tidal phenomena, mixing, and pollutant dispersion.

The approach is to cement together (into a unified whole) previous investigations. Further analyses and physical insights by the author provide cohesiveness. There are problems with this ambitious effort. Notation is not uniform from beginning to end. Basic terms, symbols, and concepts when first presented are frequently undefined. Coordinate systems change. Derivations frequently refer to concepts that are introduced in subsequent chapters. Critical discussion is lacking of some of the earlier studies. Overall, the presentation is without coherence and continuity.

Notably absent is a discussion of similarity models and numerical studies of estuarine circulation. These are particularly important because they are the only ones to treat the nonlinear coupling between the salinity and velocity fields. The coupling is of crucial importance in the dynamics of estuaries. Unfortunately this omission limits the usefulness of the book.

The second half of the book is devoted to a survey of field studies of estuaries. Studies from exotic areas such as the inlets of Chile and the rivers of Japan are presented, as well as from Great Britain, Europe, and the United States. Perhaps the aim here was too ambitious. Not enough discussion is presented of any area. Some studies are only referred to in a sentence or two. My own preference would have been to use fewer examples, but to treat them more thoroughly and critically.

Despite its shortcomings, this book addresses a topic which is of special importance and provides easy access to the classical theoretical and observational studies of estuaries.

A. Leetmaa

Physical Oceanography Laboratory
AMOL
15 Rickenbacker Causeway
Miami, Florida 33149

Science 198, No. 4313, 188-189.

Effects of the Winter of 1976–1977 on the Northwestern Sargasso Sea

Abstract. *A survey was conducted in the northwestern Sargasso Sea during the spring to assess the effect and extent of the winter cooling of 1976 to 1977 on the ocean. Newly formed, well-mixed layers of 18°C water as deep as 550 meters were observed. The main thermocline south of the Gulf Stream was 100 to 150 meters deeper than it is on the average, which implies significant changes in the baroclinic transports.*

Charts of the energy exchanges between the ocean and the atmosphere show that major heat losses to the atmosphere occur in the vicinity of the Gulf Stream, east and north of Cape Hatteras (*1*). Most of the oceanic cooling occurs during the winter, and by early spring large areas south of the Gulf Stream have mixed layers as deep as 350 m with temperatures close to 18°C. During the summer a shallow, seasonal thermocline develops over this area. However, a large pool of this relatively homogeneous water continues to occupy the upper part of the water column. Because of its temperature, this water mass has become known as 18°C water (*2*). Its temperature and salinity have remained remarkably constant for decades (*3*).

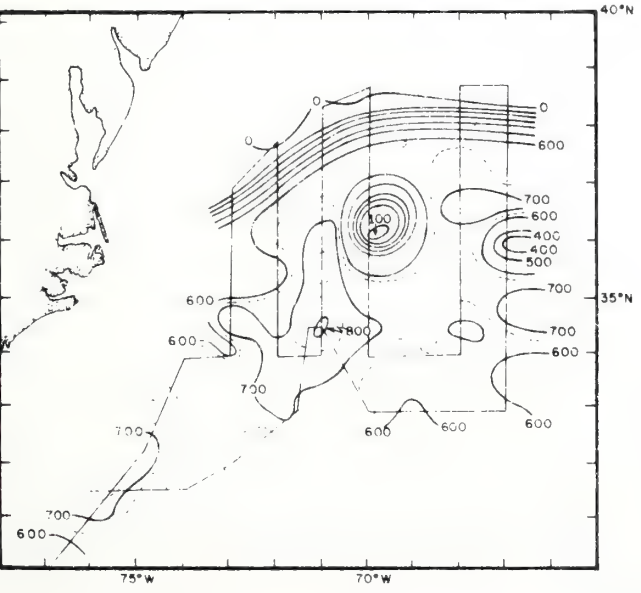
The winter of 1976 to 1977 along the eastern seaboard was notably severe. Consequently, early in 1977 a survey of the northwestern Sargasso Sea was conducted, using the R.V. *Researcher* of the National Oceanic and Atmospheric Administration, to assess the effects of this severe cooling on the ocean.

The area surveyed is shown in Fig. 1. Along the track line, expendable bathythermographs (XBT's) were dropped approximately every 24 km (13 nautical miles). Hydrographic casts, with oxygen measurements, were taken approximately 110 km (60 nautical miles) apart. These were initially taken to a depth of 1200 m, and later to 2100 m. Several were taken to the bottom. Salinity-temperature-depth casts were taken to 1200 m with almost every hydrographic cast. The depth of the 15°C isotherm from the XBT's is displayed in Fig. 1. This isotherm lies at the top of the main thermocline underlying the 18°C water, and its vertical displacement illustrates the extent to which the depth of the thermocline may have been influenced by the winter's storm activity.

The deepest regions of the thermocline lay south of the Gulf Stream, the position of which is indicated by the steep slope of the 15°C isotherm at the northern edge of the surveyed area. The deepest depression was found near 34°N, 71°W, where the 15°C isotherm reached a depth of about 800 m. The shoal areas at 36°N, 70°W and 36°N, 67°W are Gulf Stream rings. Examination of individual temperature transects taken through this region from 1969 to 1974 indicates that, on the average, the depth of the 15°C isotherm fluctuates between 600 and 700 m (*4*). Deepest values tended to occur during the spring. Occasionally these observations showed the 15°C isotherm deeper than 750 m. Thus, the thermocline this spring was as deep as or deeper than that in an average spring.

The great depth of the thermocline implies that Gulf Stream transports are higher than average. However, part of this increased transport lies to the south of the main axis of the Gulf Stream and occurs in an anticyclonic eddy surrounding the deepest depression of the thermocline. A detailed comparison between the transports this year and those previously measured is being prepared by Worthington (*5*).

The great depth of the thermocline at the end of this winter is a result of deep layers of 18°C water. Nearly homogeneous layers as deep as 550 m were observed. An example of an XBT trace that shows this is curve c in Fig. 2. Shown also for comparison are previously observed examples of deep layers of 18°C water (*2*). The mixed layer in curve c is 60 percent deeper than that in curve a. Curve c is from the region near 34°N, 71°W where the thermocline is deepest. In other areas where the 15°C isotherm was deeper than 700 m, the mixed-layer depths were comparable to that shown by curve c. In regions where the 15°C isotherm lay between 600 and 700 m, the



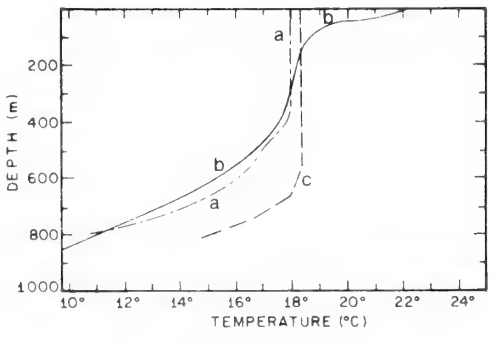


Fig. 1 (left). Depth of the 15°C isotherm in meters between 28 March and 15 April 1977. Fig. 2 (right). Temperature-depth curves: (a) R.V. *Atlantis*, hydrographic cast 1153, 28 February 1932, 34°02′N, 54°05′W; (b) R.V. *Atlantis*, hydrographic cast 5306, 11 June 1955, 34°53′N, 70°16′W; (c) R.V. *Researcher*, XBT 83, 4 April 1977, 34°39′N, 71°01′W.

traces were similar to curve a with mixed layers about 400 m deep. The temperatures of these mixed layers varied from 18.0° to 18.7°C. The coldest layers were found to the east, and the warmest layers were found near 31.5°N, 75°W. Salinities ranged from 36.47 to 36.51° per mil, and oxygen values were between 4.9 and 5.4 ml/liter. These are close to saturation values and indicate that most of these layers formed this winter.

These observations indicate that the atmosphere can, in the course of one winter, significantly change the topography of the main thermocline in the northwestern Sargasso Sea. This implies that the baroclinic volume transports in and near the Gulf Stream are also strongly affected. Worthington (6) has postulated that the Gulf Stream system, at least in part, is maintained by the thermodynamic processes that produce 18°C water. He suggested that outbreaks of polar continental air in winter cause deep vertical mixing of 18°C water south of the Gulf Stream and somehow deepen the main thermocline in this region. At present, the process that creates the deep mixed layers and deepens the main thermocline is unknown. Whether it is a convergence somehow caused by the cooling of the upper part of the water column, a convergence due to the winter wind stress distribution, or a result of some other factor needs to be clarified.

ANTS LEETMAA

Atlantic Oceanographic and Meteorological Laboratories, National Oceanic and Atmospheric Administration, 15 Rickenbacker Causeway, Miami, Florida 33149

References

1. A. F. Bunker, *Mon. Weather Rev.* **104**, 1122 (1976).
2. L. V. Worthington, *Deep-Sea Res.* **5**, 297 (1959).
3. E. Schroeder, H. Stommel, D. Menzel, W. Sutcliffe, Jr., *J. Geophys. Res.* **64**, 363 (1959).
4. U.S. Naval Oceanographic Office, *The Gulf Stream* (Washington, D.C., 1969–1974).
5. L. V. Worthington, in preparation.
6. ———, in *Studies in Physical Oceanography; A Tribute to George Wüst on His 80th Birthday*, A. L. Gordon, Ed. (Gordon & Breach, New York, 1972), pp. 169–178.

3 June 1977; revised 22 August 1977

Copyright © 1977 by the American Association for the Advancement of Science

Journal of Physical Oceanography 7, No. 5, 746-748.

Observations of Large-Scale Depth Perturbations of the Main Thermocline[1]

ANTS LEETMAA

Atlantic Oceanographic and Meteorological Laboratories, NOAA, Miami, Fla. 33149

24 August 1976 and 19 May 1977

ABSTRACT

Three trans-oceanic XBT sections (~5000 km in length) and a shorter one (~2500 km in length) were taken in the central North Atlantic in 1974 to study the distribution of the horizontal scales and amplitudes of mesoscale variability. Few features of the MODE scale (~400 km wavelength) were observed; the most dominant features had space scales of 1000–2000 km and amplitudes of 50–100 m.

1. Introduction

During 1974 the NOAA ships *Oceanographer* and *Researcher* made several traverses along the Trans-Atlantic Geotraverse (TAG) corridor (Fig. 1). This is a standard geophysical section across the central North Atlantic. In addition to geophysical measurements, hourly expendable bathythermographs (XBT's) were taken to study the oceanwide distribution of the amplitudes and scales of depth perturbations of the main thermocline. During MODE, one perturbation was observed to have an amplitude of about 100 m and a horizontal scale of 400 km. At that time, there were conjectures that such features were common and closely-packed.

The majority of the XBT's used were T-7's, which have a depth capacity of 750 m. Only when the supply of these was exhausted were T-4's (450 m probes) used. Except for the first *Oceanographer* section, during which recorder malfunctions caused several gaps in the data, few hourly observations were missed. For the three *Oceanographer* sections, the sampling interval was 28 km (16.5 n mi); for the *Researcher* section, the interval was 23 km. From Bermuda to about 25°W, three of the sections are parallel. In this region it is possible to study temporal as well as zonal variations if it is assumed that the north-south scale of any perturbations is much larger than the distance between the sections.

2. Observations

One feature of these sections is that all the isotherms below ~300 m move up and down coherently, i.e., they have the same vertical displacements. Consequently, for the purposes of this note only the depth of the 12°C isotherm is presented; it is representative of the displacements of the main thermocline. The data have been smoothed (although it was not absolutely necessary to do this) with a Hanning filter that replaces the depth of an isotherm at any spot with a depth that is one-half of the observed value at that spot plus one-fourth of the sum of the values on either side. The effect of the filter is to reduce white noise. Before filtering, missing hourly values were given depths that were linear interpolations of adjacent values.

The dominant feature of all the sections is the east-

[1] MODE Contribution No. 71.

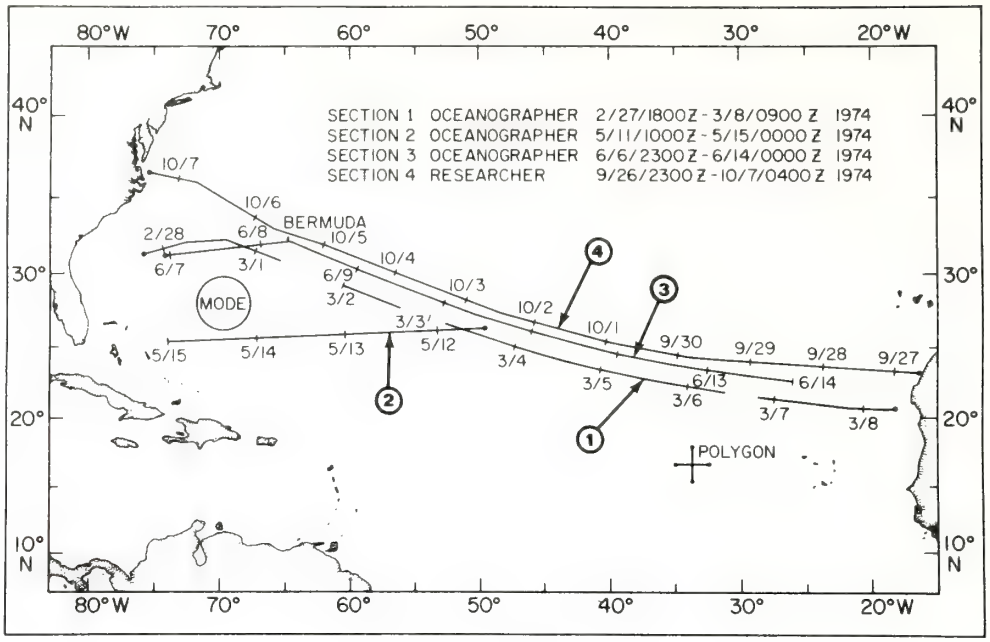


FIG. 1. Locations of XBT sections.

west slope to the thermocline (Fig. 2). Of more interest is the question as to what is the nature of the mesoscale fluctuations on these sections. Visually it can be seen that there are not many perturbations that are of the MODE scale (wavelength ~400 km). To study the perturbations more quantitatively sections 3 and 4 were selected since they are continuous across the full width of the ocean. For these sections the linear trend and mean were removed. From the remaining series the autocorrelation function and spectra were computed.

Basically the spectral computations confirmed what is apparent visually. For section 3 there is a small peak at a wavelength of ~200 km. Features of this scale can be seen to occur in figure 2 mostly at the western end of the section from 57°W to 72°W. Section 4 has a small spectral peak at ~600 km. The features that contribute to this are located between 50° and 60°W and around 25°W. Neither of these peaks is significant at the 90% confidence limit. Both sections show significantly more energy at larger wavelengths. In section 3 there is a major feature centered at 66°W. This has a wavelength of ~1000 km and an amplitude of 100 m.

Section 2 has no features at the MODE scale. A large feature is centered at 66°W with an amplitude of over 100 m. The horizontal scale of this is about 800 km. A similar feature was indicated to be present in section 3 at 66°W. This section is about ~700 km to the north of section 2 and was taken about one month later.

All of the sections are remarkably smooth between 55° and 26°W (Fig. 2). However, in this area there are large temporal variations between the sections. These appear to have horizontal scales of 1000–2000 km and amplitudes of 50–100 m. To see if these fluctuations have a clear seasonal time scale, all the hydrographic data that are on file at NODC in the 10° square centered at 25°N, 40°W were examined. These data do not

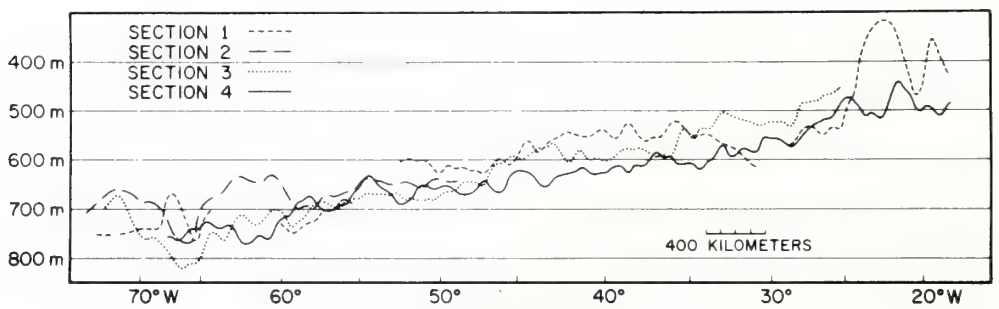


FIG. 2. Depths of 12°C isotherm.

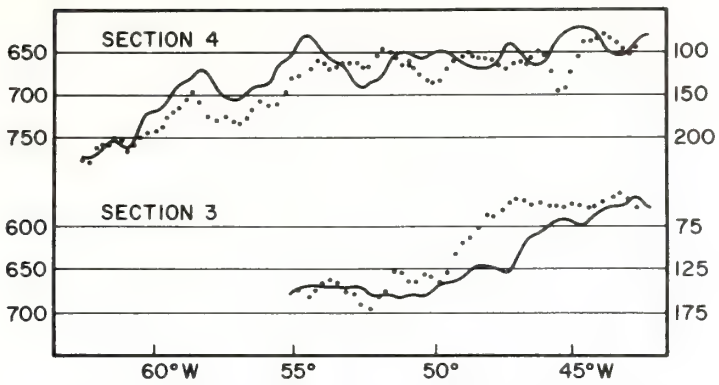


FIG. 3. Comparison between depth (m) of 12°C isotherm (solid line) and thickness change (m) of 18°C water (dotted line). Scale for thickness change is on right-hand side of figure.

show any strong seasonality; however, there was some tendency for standard deviations of the fluctuation of the depth of 12°C isotherm to be greatest during the winter. Since a total of only 117 stations was available, this result is tenuous.

In other areas, the temporal variations are much smaller. For example, between 62° and 55°W each section shows a strong east-west slope. In light of the large variations observed elsewhere, it is surprising how little this slope changes. The slope coincides with the edge of the 18°C water (Worthington, 1959). A convenient measure of the thickness of the 18°C water mass is the distance between the 18 and 20°C isotherms. The change in depth of the 12°C isotherm compensates for thickness changes in the 18°C water (Fig. 3). The thickness change is a combination of a change in depth of both the 20 and 18°C isotherms. Thus the good agreement does not result from the fact that the 12 and 18°C isotherms are almost parallel (as they are to the west of this region).

3. Summary

The purpose of these sections was to look for typical features, such as the MODE eddy, in the central Atlantic. These sections show that at these times there are few features that are characterized by both the MODE horizontal scale and amplitude. This is surprising since the sections pass through or close to the MODE, POLYGON and the proposed POLYMODE areas where such features were thought to be common. Most energetic features of this scale that are present occur on the eastern side of the ocean basin.

The most prominent features that were observed have space scales of 1000–2000 km and amplitudes of 50–100 m. The origin and time scales of these are unknown. Perhaps they are the response of the ocean to large-scale, seasonal variation of the wind field. Their large space scale makes it difficult to distinguish them from the mean circulation. Indeed some apparent variability was shown to be related to the edge of the 18°C water mass.

These results seem to indicate that the eddy field is more complex than envisioned after MODE. The MODE eddy possibly represents one realization of the eddy family. Others of different space scales have already been observed and more no doubt remain to be discovered.

Acknowledgments. The author wishes to thank M. Minton, D. V. Hansen, D. Behringer and R. Molinari, for comments that improved the manuscript. This work was partially supported by National Science Foundation-IDOE MODE A6-385.

REFERENCES

Worthington, L. V., 1959: The 18° water in the Sargasso Sea. *Deep-Sea Res.*, **5**, 297–305.

Deep-Sea Research 24, 733–742.

A study of MODE dynamics*

ANTS LEETMAA†

(*Received* 16 *June* 1976; *in revised form* 18 *November* 1976; *accepted* 30 *November* 1976)

Abstract—The feasibility of estimating horizontal divergence from variations of $(\partial\rho/\partial z)$ along density surfaces is examined. Regions of divergence are deduced from $(\partial\rho/\partial z)$ distributions and corroborated by independent evidence. One event of convergence in the near-surface layers leads to 'pooling' and also appears in the bottom pressure records. Some features in the deep water are related to regions of divergence in the main thermocline. The deep flows, in turn, are important in modifying features in the main thermocline. Vorticity changes in the near surface layers are as large as 30% of $2\Omega \sin\theta$ while those in the main thermocline and in deep water are about 10% of $2\Omega \sin\theta$.

1. INTRODUCTION

LONG PERIOD, mesoscale motions are important features in the general ocean circulation. The Mid-Ocean Dynamics Experiment (MODE) was the first major effort in the United States to study this phenomenon. Its main objectives were to obtain a descriptive and kinematic definition of the eddy field and to determine its local statistics (MODE-1 SCIENTIFIC COUNCIL, 1973). The design of MODE precluded a detailed examination of the momentum and vorticity balances. Nevertheless, a large set of measurements of many types were obtained, and estimates in order of magnitude can be made of the momentum, mass, heat, and vorticity balances.

BRYDEN (1975) has calculated each of these balances using the current meter data. In regard to the mass balance, he finds that the velocity measurements during MODE-0 are horizontally non-divergent within the estimated errors. He concludes that it is not possible to directly estimate the horizontal divergence using present moored instrumentation. In principle another technique exists for measuring this quantity. In a quasi-Lagrangian co-ordinate system in which z, the vertical co-ordinate, is replaced by ρ, the density, the rate of change of $(\partial z/\partial\rho)$ following a material element is related to the horizontal divergence (STARR, 1945). Most of the density measurements during MODE were made by conductivity–temperature–depth (CTD) or salinity–temperature–depth (STD) recorders. These sample densely in the vertical and allow good estimates to be made of $(\partial\rho/\partial z)$ or $(\partial z/\partial\rho)$.

In theory the distribution of $(\partial\rho/\partial z)$ along a density surface, used in conjunction with trajectories estimated from the dynamic height field, makes it possible to calculate the horizontal divergence. In practice, this was not possible because neither the $(\partial\rho/\partial z)$ field nor the dynamic height fields were sampled with adequate horizontal resolution. However, examination of the sign and distribution of the anomalies of $(\partial\rho/\partial z)$ is useful in identifying regions of divergence. Independent data can then be used to verify that divergence actually

* MODE-Mid-Ocean Dynamics Experiment. MODE Contribution No. 64.

† NOAA Environmental Research Laboratories, Atlantic Oceanographic and Meteorological Laboratories, 15 Rickenbacker Causeway, Virginia Key, Miami, FL 33149, U.S.A.

took place. For example, in regions of active divergence in the main thermocline, the temperatures in the deep water should be increasing or decreasing depending on the sign of the divergence. Examples presented in this paper show this to be the case. Thus there exists a relationship between features in the main thermocline and those in the deep water. Furthermore, the data suggest that the deep flows, in turn, modify the shallower features by advection. This sort of coupling has been studied extensively with two-layer models (RHINES, 1976). The 'self interaction' is an important factor in the evolution of the MODE eddy field.

II. ESTIMATING THE HORIZONTAL DIVERGENCE

An equation for absolute vorticity, $(\zeta+f)$, is

$$\frac{\mathrm{d}}{\mathrm{d}t}(\zeta+f) = -(\zeta+f)\left(\frac{\partial u}{\partial x}+\frac{\partial v}{\partial y}\right), \tag{1}$$

where $\zeta = v_x - u_y$ and f is the Coriolis parameter. Viscous terms and the terms involving horizontal derivatives of the vertical velocity are neglected. These assumptions can be shown by scale analysis to be reasonable for mesoscale motions. Under these assumptions, vorticity changes that take place are related only to the horizontal divergence. STARR (1945) showed that

$$1/(\partial z/\partial\rho)\frac{\mathrm{d}}{\mathrm{d}t}(\partial z/\partial\rho) = -\left(\frac{\partial u}{\partial x}+\frac{\partial v}{\partial y}\right)$$

or

$$1/(\partial\rho/\partial z)\frac{\mathrm{d}}{\mathrm{d}t}(\partial\rho/\partial z) = \left(\frac{\partial u}{\partial x}+\frac{\partial v}{\partial y}\right) \tag{2}$$

in a quasi-Lagrangian co-ordinate system in which z is replaced by ρ as the vertical co-ordinate. Equations (1) and (2) can be combined to obtain a relationship between the absolute vorticity and $(\partial\rho/\partial z)$. Using the MODE data set, it is possible in theory to estimate the left hand side of (2) by using dynamic height maps to determine the particle paths and speeds and the horizontal distributions of $(\partial\rho/\partial z)$ on a density surface to compute changes of $(\partial\rho/\partial z)$ along these trajectories. For several reasons it was difficult to do this.

The first problem is that the observed distributions of $(\partial\rho/\partial z)$ are very irregular. Several factors can be responsible for this. For one, the standard STD station spacing during MODE appears to have been too large to adequately map this field. This is not surprising because other MODE data sets (Katz, Sandford and Swallow, private communication) have showed that considerable variation in the temperature and velocity fields occurred on horizontal scales smaller than the standard STD grid spacing. Another possible source of difficulty is the straining of the mean density gradient by internal waves. Thus waves with high vertical wave number produce significant variations in $(\partial\rho/\partial z)$ (HAYES, JOYCE and MILLARD, 1975). Only features that persisted over days are discussed; it is unlikely that these were related to internal wave activity. A third problem is that considerable variations occurred from week to week in the dynamic height field. Even if this field was well known, the barotropic component of the current would still be undefined. Consequently, the trajectories cannot be determined.

These uncertainties, in addition to measurement errors, made it impossible to make a quantitative evaluation of (2).

Formally horizontal divergence is related to $(\mathrm{d}/\mathrm{d}t)(\partial\rho/\partial z)$. However, for the rest of this paper regions where horizontal divergence has taken place or is taking place are identified by reference to the anomalies of $(\partial\rho/\partial z)$. The rationale for doing this is as follows. Divergence, in time, leads to the formation of an anomaly in $(\partial\rho/\partial z)$. Thus anomalies do indicate regions of present or past divergences but do not indicate the magnitude of the divergence. Examination of the anomalies is also informative because they are directly related to changes in the absolute vorticity of a fluid parcel (see Section VII for a discussion).

A value of $(\partial\rho/\partial z)$ is anomalous if it lies at least one standard deviation away from the mean. Areas with anomalously high values of $(\partial\rho/\partial z)$ are regions of divergence (more precisely, regions where divergence has taken or is taking place). Conversely, areas with low values of $(\partial\rho/\partial z)$ represent regions of convergence.

It is also possible that the streamlines and anomaly fields are parallel, i.e. anomalies exist but there is no change in $(\partial\rho/\partial z)$ along a trajectory. In such a case the anomaly possibly represents a region where strong divergence took place and a 'water mass' was formed. Such an event is described in the next section.

III. THE NEAR-SURFACE LAYERS

During MODE, different parts of the water column appeared to be dominated by different dynamics. At the surface, thermal features appeared to be primarily advected by the mesoscale eddy field (Voorhis, Leetmaa and Schroeder, 1976). Beneath this, but above the main thermocline, the flow patterns are similar to those in the main thermocline, but the warm eddy appears to have a core which is identifiable by its temperature and salinity. To study this region, the average $(\partial\rho/\partial z)$ is examined between the σ_t surfaces 25.8 and 25.9. These two surfaces delimit a layer 10 to 20 m thick. The average depth of this layer is shown in Fig. 1. The areas with diagonal slashes indicate regions within this layer where $(\partial\rho/\partial z)$ is less than average, and the areas with vertical lines are regions where it is greater than average. The geostrophic flow in this layer, relative to 1500 dbar, is approximately parallel to the depth contours.

During the first week, the maximum depth of this σ_t layer, although it is not well defined by the station spacing in the vicinity of 28°N and 70°W, is between 175 and 200 m. The $(\partial\rho/\partial z)$ distribution indicates convergence possibly occurring to the south of this area near the greatest depths and divergence to the northeast. One week later, the deepest portion of this layer lies below 200 dbar. This correlates with low values of $(\partial\rho/\partial z)$ which indicate that convergence has occurred. This is supported by the fact that the average depth of the layer increased by about 25 dbar during this time. The depth of the layer does not keep increasing, but by the week of April 9, the region in which the depth is over 190 dbar has increased in size. Most of this region now has anomalously low values of $(\partial\rho/\partial z)$.

If this had been a region of convergence and an equal compensating divergence did not take place at depth, then this event should show up in the bottom pressure records at the central mooring. These records do show an increase in pressure of 6 to 7 mbar from March 25 to about April 2 (Brown, Munk, Snodgrass, Mofjeld and Zetler, 1975). Two STD stations, TRIDENT 20 and DISCOVERY 8, taken in the vicinity of the gauges also show an increase in dynamic height in the top 3000 dbar during this time of 6 to 7 cm! Most of this occurs in the top 400 dbar. A similar increase in dynamic height during this period is shown in the data from the Inverted Echo Sounders and the Temperature–Pressure recorders (Watts, 1974).

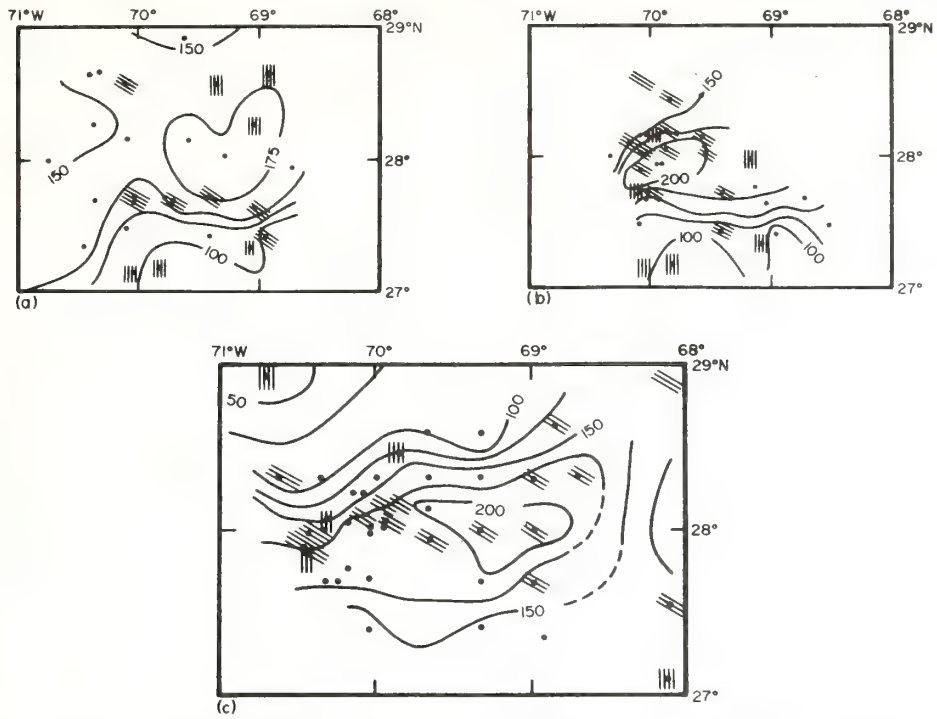


FIG. 1. Depth of the average σ_t-surface 25.8 to 25.9. The vertical lines indicate regions of anomalously high values of $(\partial\rho/\partial z)$. The diagonal slashes indicate regions with anomalously low values of $(\partial\rho/\partial z)$. (a) Week March 26 to April 1, (b) week April 2 to 8, (c) week April 9 to 15.

The interpretation of the events that appeared in the pressure gauge records was that they represented a barotropic gyre-wide response of the ocean to synoptic meteorological events (BROWN *et al.*, 1975). However, it is possible that while on long-time scales, baroclinic events are almost exactly compensated for by changes in the depth of the main thermocline, on time scales of the order of the inertial period this compensation is incomplete, and the events show up in the bottom pressure records.

From the middle of April to the end of the experiment, anomalously low values of $(\partial\rho/\partial z)$ remain associated with this depression in the σ_t surface. Thus $(\partial\rho/\partial z)$ becomes a tracer in the same sense as temperature or salinity. It appears that the MODE eddy in the near surface layers develops as a result of local convergences and advection of a warm feature from the east.

IV. FEATURES IN THE MAIN THERMOCLINE

In contrast to the near-surface layers, it does not appear possible to identify the eddy by its T–S properties on a potential density surface in the main thermocline. Similarly, the distributions of the anomalies of $(\partial\rho/\partial z)$ differ from those in the near-surface layers. In the main thermocline, anomalies occur primarily where there are indications of divergence from strong north–south velocities or where the streamlines (as indicated by the dynamic height contours) indicate that the flow might be spreading horizontally (diverging) or converging. This can be seen in Fig. 2. The vertical density gradient is examined in a layer between the potential density surfaces $\sigma_{800} = 30.6$ and 30.8. The

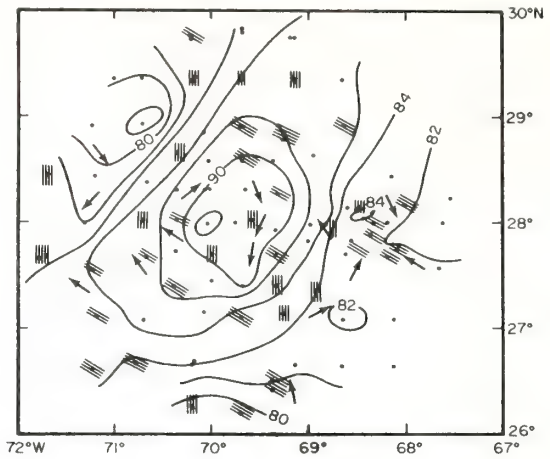


FIG. 2. Dynamic height difference between 500 and 1500 dbar in dynamic centimeters. For May 14 to 21. The arrows represent the direction of inferred flow at 3000 dbar. The shading is as in Fig. 1.

subscript 800 indicates that the potential density is referred to 800 dbar. These surfaces coincide approximately with the 12 and 10°C isotherms which lie about 90 dbar apart. In this region $(\partial\rho/\partial z)$ is approximately uniform in the vertical. About 45 values, each computed over depth intervals of 2 dbar, are in each average value.

The area of high values of $(\partial\rho/\partial z)$ around 27.5°N and 69°W occurs where there is strong southward flow. In this region, the divergence is in order of magnitude agreement with that computed from the simple vorticity balance

$$\beta v + f(u_x + v_y) = 0. \tag{3}$$

The horizontal divergence, if calculated from $\beta v/f$, is

$$\frac{2 \times 10^{-13}\,\mathrm{cm^{-1}\,s^{-1}} \times 10\,\mathrm{cm\,s^{-1}}}{7 \times 10^{-5}\,\mathrm{s^{-1}}} \sim 3 \times 10^{-8}\,\mathrm{s^{-1}}.$$

According to equation (2), the divergence is approximately

$$(\partial\rho/\partial z)^{-1} v \frac{\partial}{\partial y}(\partial\rho/\partial z) = (\partial\rho/\partial z)\frac{v}{\Delta y},$$

where Δy is the distance over which a change of $\delta(\partial\rho/\partial z)$ takes place. The observations indicate that in this region a 4% change in $(\partial\rho/\partial z)$ occurs over 100 km. For a southward velocity of $10\,\mathrm{cm\,s^{-1}}$, the divergence is $4 \times 10^{-8}\,\mathrm{s^{-1}}$. This agrees well with the previous calculation.

A similar explanation is appropriate for the region around 27.5°N and 70.5°W. In both of these regions the depth of the $\sigma_{800} = 30.6$–30.8 surface is either depressed or raised depending on whether it is a region of past convergence or divergence.

In other areas, such a simple explanation is not apparent. However, in general, low values of $(\partial\rho/\partial z)$ do occur where the streamlines (dynamic height lines) converge and high values where they diverge.

V. RELATIONSHIP OF DEEP FEATURES TO THERMOCLINE FEATURES

In the main thermocline the regions of anomalous values of $(\partial\rho/\partial z)$ are small compared to the overall size of the eddy as defined by the distance between maximum and minimum values of dynamic height (Fig. 2). If these areas represent regions of past or present divergence, and if they exist through the depth of the main thermocline, then there should be evidence for this divergence in the deep water. In areas of convergence, the temperatures at a constant depth in the deep water should be increasing, and in areas of divergence, they should be be decreasing. This is the case.

Two features of the thermal field at 3000 dbar, the development of which can be followed in time, are the maximum that is centered at about 28.3°N, 70°W and the minimum centered at 27.8°N and 69°W (see Fig. 3). Both are located where strong north–south flow extends through the main thermocline. The cold feature is associated with anomalously high values of $(\partial\rho/\partial z)$ (possible divergence) in the main thermocline and the warm features with low values of $(\partial\rho/\partial z)$. The value of the divergence was estimated in the previous section to be about $4 \times 10^{-8}\,s^{-1}$. If the scale of variation of w was the thickness of the main thermocline, i.e. 10^5 cm, then an estimate of w is $4 \times 10^{-3}\,cm\,s^{-1}$. The vertical velocity can also be estimated by assuming that the local temperature change at 3000 dbar results from vertical advection, i.e. $(\partial T/\partial t) + W(\partial T/\partial z) = 0$. The vertical gradient of potential temperature at 3000 dbar is about 0.8×10^{-3}°C dbar^{-1}. The observed temperature change was about 0.08°C in 30 days. The inferred, w is $4 \times 10^{-3}\,cm\,s^{-1}$, which agrees with the previous calculation. Thus the temperature anomalies in the deep water do appear to be linked to divergences in and above the main thermocline. It should be emphasized that these features in the deep water develop in time and that the warm feature initially is not present under the eddy in the main thermocline.

Areas of active divergence in the main thermocline do not always correlate with temperature anomalies at depth as was shown here. The comparison, as was pointed out earlier in this section, should be between the temperature change at depth and the divergence in the main thermocline. In practice such comparisons were difficult because the features in the deep water were not well resolved in time and space. However, this calculation was attempted for the temperature change at 3000 dbar between the weeks of May 14 and 21, in the region surrounding 27.5°N and 70.3°W. During this time, this area was warming at the rate of 0.03 to 0.04°C per week. The area around 27.5°N and 69°W was cooling at the rate of 0.02 to 0.03°C per week (Fig. 3). These rates are consistent with the estimates of the divergence in the main thermocline at these locations as discussed earlier in this section.

A disturbing characteristic of the thermal features in the deep water is their associated value of $(\partial\rho/\partial z)$. These were examined in the potential density layer $\sigma_{1500} = 34.74$–34.76. The mean depth of this layer is about 2100 dbar, and it is about 200 dbar thick. In this layer the cold feature appears to be associated with anomalously high values of $(\partial\rho/\partial z)$ while the warm feature appears to be associated with low values. This implies that the sign of the divergence is the same throughout most of the water column. If this is the case, then compensating convergence must occur close to the ocean bottom. There appears to be some evidence for this. The potential temperature at 5400 dbar is shown in Fig. 3b. Next to each station position is listed the difference in temperature between 5200 and 5400 dbar in mdegrees. Higher than average differences are found at the center of the warm region and lower than average differences are found to the east in the cold region. However, evidence is sparse and a definitive statement about the dynamical nature of the

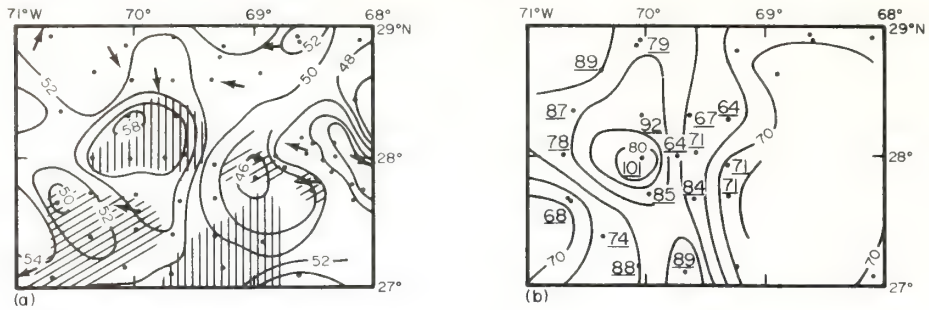


FIG. 3a. The potential temperature, $(\theta - 2.00) \times 10^2$°C, at 3000 dbar. For May 14 to 21. The arrows indicate directions of flow according to Swallow floats at 3000 dbar or SOFAR floats.

FIG. 3b. The potential temperature, $(\theta - 1.00) \times 10^2$°C at 5200 dbar. For May 14 to 21. The underlined numbers are the difference in temperature between 5400 and 5200 dbar in centidegrees.

flow close to the bottom requires a more detailed study. Thus although the temperature changes in the deep water are related to divergences in the main thermocline, little can be said about the nature of the divergences in the deep water and close to the bottom.

VI. INTERACTION IN THE WATER COLUMN

In the previous section it was shown that some thermal features in the deep water are clearly related to divergences in the main thermocline. However, it is likely that the upper parts of the water column will respond to motion in the deep water. In this section we examine this possibility. As will be shown, the deep flows are important in that they advect features in the main thermocline.

For this demonstration, something has to be said first about the deep flow field. The number of direct deep measurements is insufficient to define it well. However, a comparison of the 3000-dbar temperature maps with the deep flow measurements indicates that in a gross sense, the motion is such that looking downstream, warm water lies to the right (Figs. 3a and 4b). The intercomparison was made with both Swallow float and SOFAR float measurements. The former were at 3000 dbar, while the SOFAR floats were at about 1500 dbar. In regions of strong horizontal temperature gradient, the floats follow the temperature contours reasonably well. In weak gradient regions, this intercomparison breaks down.

The response of the upper layers to the deep flow can be seen in two ways. First, the circulation in the deep water enhances that in the main thermocline when they are in the same sense and retards it when they are opposite. This can be seen in Figs. 2, 3a, and 4. The core of the warm eddy in the main thermocline now lies over the warm feature in the deep water, whereas this was not true in April. Interestingly, over the cold cyclonic feature in the deep water the dynamic height gradients in the main thermocline vanish. This is apparently due to the upper flow and the deep flow adding destructively. Even though these features 'lock' together as postulated by RHINES (1976), there is no tendency for the flow to become barotropic in the warm eddy on this time scale (a month). It is also apparent from these figures that the eddies in the deep water and in the thermocline are of comparable scale by late May.

Another effect of the deep flow is to modify the horizontal gradients of dynamic height in the main thermocline. The arrows on the dynamic height maps in Figs. 2 and 4 show

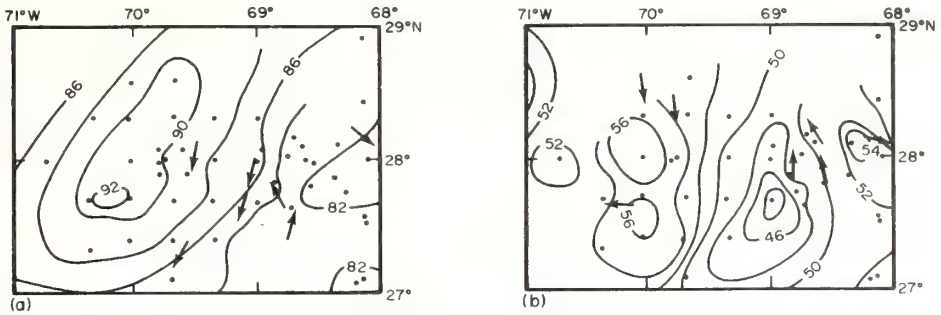


FIG. 4a. The dynamic height difference between 500 and 1400 dbar in dynamic centimeters. For May 21 to 27. The arrows represent the direction of inferred flow at 3000 dbar.

FIG. 4b. The potential temperature $(\theta - 2.00) \times 10^2$ °C, at 3000 dbar. For May 21 to 27. The arrows indicate the directions of flow according to float measurements.

the directions of flow at 3000 dbar where the horizontal temperature gradient is greater than 0.04°C (10 km)$^{-1}$. The gradients of dynamic height appear to be enhanced at 28°N, 68.8°W and 27.5°N, 69.5°W (Fig. 2). The bulge at 28°N, 71.3°W, which also is a cold tongue in the surface layers, is associated with the deep flow. Maps for other time periods show similar features.

VII. DISCUSSION

The first part of this study examined whether $(\partial\rho/\partial z)$ distributions on a density surface could be used to evaluate the horizontal divergence. For the MODE data set this could only be done qualitatively. Inadequate sampling, possible aliasing by internal waves, and inaccurate knowledge of the trajectories of water parcels prevented a quantitative evaluation. However, an analysis of the anomalies of $(\partial\rho/\partial z)$ was informative.

Strong convergence occurred in the near-surface layers in early April. This was important in the formation of the MODE eddy. Areas of major divergence or convergence that were associated with meridional flows are identified. These produced temperature changes in the deep water which in turn appear to have important feedback effects on the flow in the main thermocline.

A simple conceptual model can be applied to this interpretation of the MODE observations. In its simplest form, the model separates the ocean vertically into two layers: the thermocline and the deep water. Motions in the upper layer, particularly those in the north–south direction, produce divergences (see Section 4). These produce pressure gradients and consequently motions in the lower layer which in turn modify the gradients in the upper layer.

Although much of the physics is included in this two-layer idealization, the observations indicate that a further vertical subdivision might be appropriate. The region from beneath the surface to the top of the main thermocline differs from the main thermocline. The $(\partial\rho/\partial z)$ and salinity distributions indicate that 'pooling' can take place, i.e. the eddy in this region appears to become an identifiable water mass.

The nature of the flow at the ocean surface and close to the bottom differs from what has already been discussed. Surface features primarily are advected by the deeper flows (VOORHIS, LEETMAA and SCHROEDER, 1976). Locally this advection can result in the formation of surface fronts. Direct meteorological forcing can be of importance in this region.

It is not clear what affect this region has on the deeper flows. Still less is known about the nature of the flow close to the bottom.

An integral statement of the vorticity equation, with equation (2) substituted for the divergence, is that $(\zeta + f)\,(\partial\rho/\partial z)$ is a constant following a water parcel. Then following a water parcel it is approximately true that

$$\frac{1}{f_0 \overline{\rho_z}}\,\delta[(\zeta + f)\rho_z] \cong \delta(\partial\rho/\partial z)/\overline{(\partial\rho/\partial z)} + \delta(\zeta + f)/f_0 = 0, \tag{4}$$

where $\overline{(\partial\rho/\partial z)}$, and f_0 are mean values of the density gradient and the Coriolis parameter. The δs represent variations of these quantities. Under these approximations variations in $(\partial\rho/\partial z)$ are equivalent to variations in the absolute vorticity $(\zeta + f)$. For the three levels that were examined, the variations in $(\partial\rho/\partial z)$ were: 30% for the near-surface layers, 10% for the main thermocline, and 10% for the deep water. These percentages represent one standard deviation of the mean value. By way of comparison, f changes by only 13% over the whole MODE array. It is immediately evident that the largest $(\partial\rho/\partial z)$ or absolute vorticity changes occur in the near-surface layers. This perhaps is not too surprising since this is the most energetic region. However, it is a little surprising that the deep water and main thermocline variations are comparable. In a two-layer model changes in the thickness of one layer are compensated by thickness changes in the other layer. In such a model the deep value should be about 1/5 of the thermocline value (if the deep layer is five times as thick as the thermocline). The data indicate that a two-layer idealization is too simple.

For large-scale meridional motions, in which relative vorticity [see equation (4)] and mixing are negligible, there should be a systematic increase in $(\partial\rho/\partial z)$ from north to south. Behringer (1972) used this concept to deduce the streamlines for large scale flows in the South Atlantic and in the western Pacific off California. He found good agreement with geostrophic streamlines (dynamic height contours). As can be seen from the distribution of the anomalies in Figs. 1 and 2, the north–south distribution of $(\partial\rho/\partial z)$ is basically uniform. In fact, if averages are made of all the values in one-degree bands of latitude or longitude to get a quantitative estimate, the same result is derived. Consequently, during MODE there was no large scale meridional flow. The north–south trajectories of water parcels were probably smaller than the extent of the MODE array. As a result β-effects, relative vorticity, and $(\partial\rho/\partial z)$ changes are all comparable. There is evidence from the SOFAR float observations for limited meridional motion. However, these at times also show that the north–south trajectories can be quite long. Since the $(\partial\rho/\partial z)$ distributions are so uniform, one can speculate that the motion is dissipative in the sense that horizontal differences in $(\partial\rho/\partial z)$ are quickly eliminated.

The usefulness of this study was limited because only the anomalies of $(\partial\rho/\partial z)$ were used to deduce information about the vorticity and divergence fields. In the future, the quantity that should be examined is $(\mathrm{d}/\mathrm{d}t)(\partial\rho/\partial z)$. The formalism for doing this has been developed by McWilliams (1976). Using observations of SOFAR float trajectories and dynamic height computations from MODE he determines by objective mapping the streamfunction for the flow field. From this the relative vorticity and the stretching of vortex lines in the vertical were computed. The latter computation is equivalent to computing the horizontal divergence or

$$\left(\frac{1}{\partial\rho/\partial z}\right)\frac{\mathrm{d}}{\mathrm{d}t}(\partial\rho/\partial z).$$

A comparison of his results with these is difficult for two reasons. First, the MODE data set was not adequate to provide detailed enough maps of the streamfunction from which accurate computations of the vorticity field could be made. Secondly, there is an over-simplification in McWilliam's technique for computing the stretching term; this results in significant errors in his computation of this term. However, with more densely sampled data sets, similar techniques should allow estimation of the divergence.

REFERENCES

BEHRINGER D. W. (1972) Investigation of large scale oceanic circulation using historical hydrographic data. Ph.D. thesis, University of California, San Diego.

BROWN W. S., W. M. MUNK, F. E. SNODGRASS, H. MOFJELD and B. ZETLER (1975) MODE bottom experiment. *Journal of Physical Oceanography*, **5**, 75–85.

BRYDEN H. (1975) Momentum, mass, heat, and vorticity balances from oceanic measurements of current and temperature. Ph.D. thesis, Massachusetts Institute of Technology and Woods Hole Oceanographic Institution.

HAYES S. P., T. M. JOYCE and R. C. MILLARD, JR. (1975) Measurements of vertical fine structure in the Sargossa Sea. *Journal of Geophysical Research*, **80**, 314–319.

MCWILLIAMS J. C. (1976) Maps from the Mid-Ocean Dynamics Experiment. II. Potential vorticity and its comparison. *Journal of Physical Oceanography*, **6**, 828–846.

MODE-1 SCIENTIFIC COUNCIL (1973) MODE-1 The program and the plan. MODE Executive Office, 54-1417, Massachusetts Institute of Technology. (Unpublished manuscript.)

RHINES P. (1976) The dynamics of unsteady currents. In: *The Sea*, Vol. 6, *Marine modelling*, E. D. GOLDBERG, I. N. MCCAVE, J. J. O'BRIEN and J. H. STEELE, editors, John Wiley, in press.

STARR V. P. (1945) A quasi-Lagrangian system of hydrodynamical equations. *Journal of Meteorology*, **2**, 227–237.

VOORHIS A., A. LEETMAA and E. SCHROEDER (1976) The influence of the deep mesoscale eddies on the surface temperature in the north Atlantic subtropical convergence. *Journal of Physical Oceanography*, **6**, 953–961.

WATTS R. (1974) Inverted echo sounder. Instrument description and intercomparison report of the MODE-1 Intercomparison Group, 173 pp. MODE Executive Office, 54-1417, Massachusetts Institute of Technology. (Unpublished manuscript.)

Journal of Marine Research 35, No. 1, 1-10.

Does the Sverdrup Relation account for the Mid-Atlantic circulation?

by Ants Leetmaa,[1] Pearn Niiler,[2] and Henry Stommel[3]

ABSTRACT

A comparison is made between the geostrophic transport across selected latitudes in the North Atlantic Ocean and the theoretical transport as derived from the Sverdrup relationship. In the subtropical gyre these agree to within the error estimates. At 32°N and 24°N the interior geostrophic transports compare well with the measured values in the Florida Straits off Jacksonville.

1. Geostrophic shear on Mid-Atlantic hydrographic sections

Estimates of geostrophic shear across selected latitudes of the North Atlantic Ocean are compared to theoretical transports based on the Sverdrup relationship and the new wind-stress tabulations of Bunker (Leetmaa and Bunker, 1976). The sections chosen are shown in Fig. 1 superposed upon a chart of dynamic topography (1500 db-100 db) in dynamic millimeters (Stommel, personal communication). The sections are also listed in Table 1; both temperature and salinity profiles have been published in the atlases of Fuglister (1960) and Worthington and Wright (1970). These sections cross both the subtropical and subpolar gyres, but avoid the complex region near 40°N where the Gulf Stream System extends out into mid-ocean in a series of loops and eddies, and the existing sections seem to be dominated by what are probably transient features of large amplitude.

1. Atlantic Oceanographic and Meteorological Laboratories, NOAA, 15 Rickenbacker Causeway, Miami, Florida, 33149, U.S.A.
2. Oregon State University, School of Oceanography, Corvallis, Oregon, 97331, U.S.A.
3. Massachusetts Institute of Technology, Cambridge, Massachusetts, 02139, U.S.A.

Table 1. Sections used for geostrophic transports.

Lat	Ship	Date	Reference Stations	Longitude W	Separation (km)
59°N	*Erika*	March-	360	41°.55	1745
	Dan	April 1962	388	11°.03	
53°.5N	*Erika*	Feb.	188	15°.07	2351
	Dan	1962	221	50°.58	
32°N	*Atlantis*	Nov. 1954	5203	63°.05	4674
	Discovery II	Nov.-Dec. 1957	3646	13°.40	
24°N	*Discovery II*	Oct.	3593	20°.83	4817
		1957	3619	68°.33	
16°N	*Crawford*	Nov.	283	25°.68	3629
		1957	308	59°.70	
8°N	*Crawford*	May	—		
		1957	—		

Some degree of variability appears, of course, on all the sections as can be seen in Fig. 2 where the same relative dynamic topography shown in Fig. 1 is shown in greater detail, station by station. The observed points do not fall exactly upon a smooth line or curve, the deviations being due probably to the presence of low frequency eddies. Estimates of the total mean geostrophic shear across these sections therefore require some smoothing of the small scale features. We deem it inappropriate to sum up transports calculated between all individual stations in the manner of Wust (1957), because it puts too much weight on the stations at the extreme ends of the sections, where boundary phenomena may intervene. If the section is at a constant latitude, the total transport, of course, depends on the end stations. Instead we put more weight on mid-oceanic stations as follows.

2. The subtropical sections

Consider the data for 24°N displayed in Fig. 2. The observed points seem to lie close to a straight line, so that the slope of the dynamic topography (1500 db-100 db) is almost independent of longitude. Instead of choosing stations at the far ends of the section (which quite obviously would determine a slope unrepresentative of the mid-ocean regions), we choose two stations that define a line that visually fits the rest of the points better. These choices are shown in Fig. 2 by the larger circles: we call these "reference stations." This choice is subjective, and we will later introduce a more objective method as well. We first use these reference stations to compute the vertical distribution of geostrophic transport between the reference stations (for a discussion of geostrophic computations, see Sverdrup *et al.*, 1942). The ob-

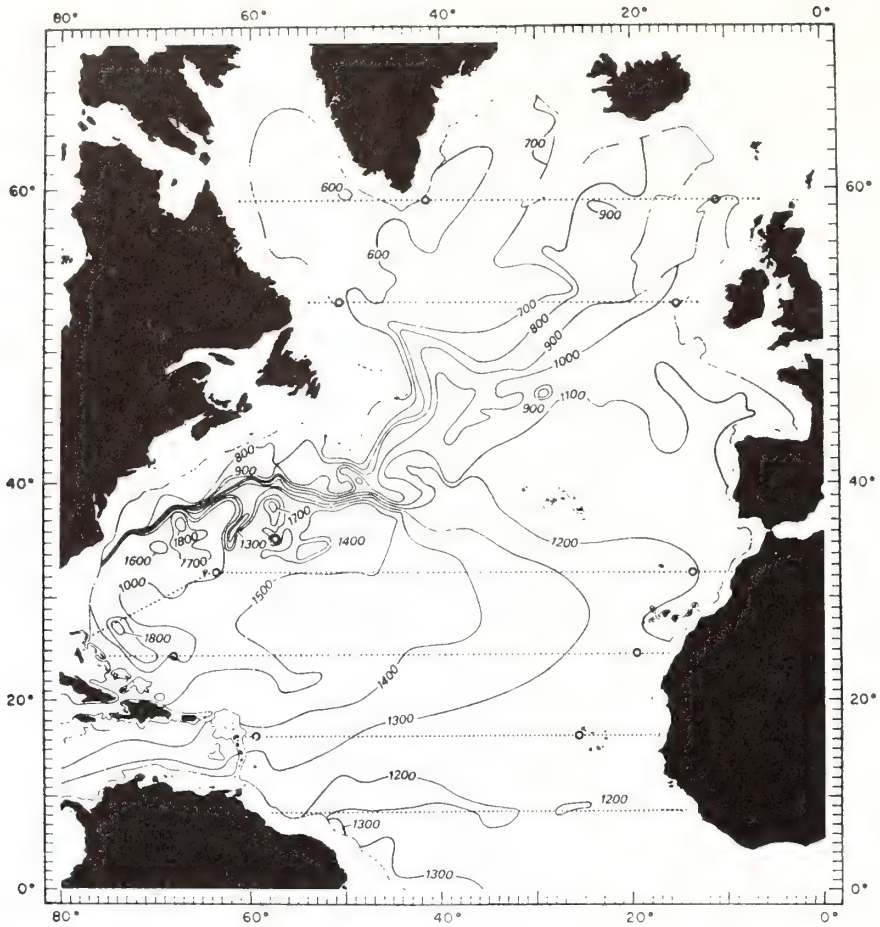


Figure 1. Chart of dynamic topography of 1500 db relative to 100 db in dynamic millimeters. Positions of the sections and reference stations used in this text are indicated.

served dynamic height differences (Fig. 2) for 32°N east of Bermuda also fit a nearly straight line. We will discuss the two sections at 24°N and 32°N first, because there is little ambiguity in finding acceptable reference stations, and uncertainties in the slope of the line thereby defined can hardly exceed 20% of what the true value is.

An example of a bad choice of reference stations is that made by Stommel (1956), before the *Discovery* stations to the east had been made. He chose in addition to *Atlantis* station 5203 (the present reference station near Bermuda), station 5210 (the low point at 50°41′W). Because this latter station now appears to be so unrepresentative of the points on the extended *Discovery* section, it is clear that Stommel over-estimated the slope by a factor of about 1.7, thus yielding an exces-

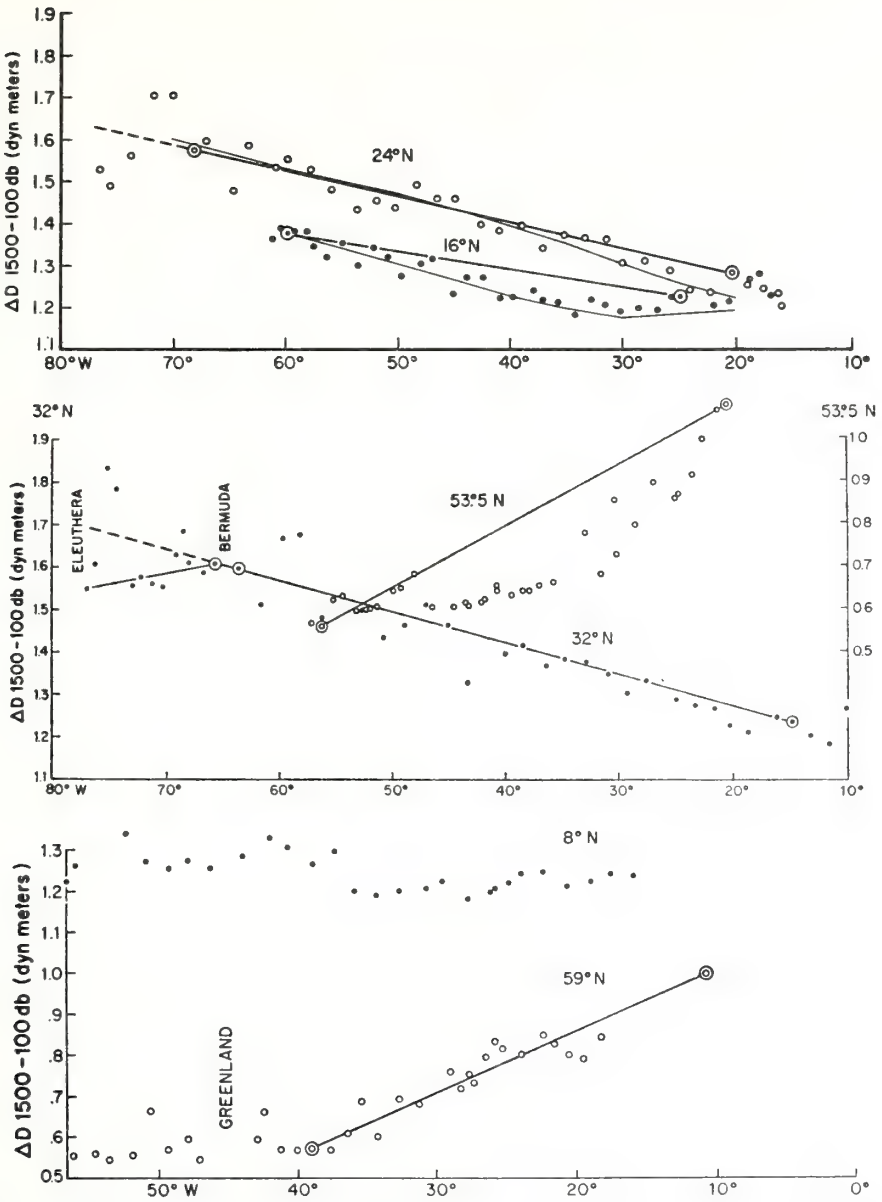


Figure 2. Dynamic height (1500 db-100 db) plotted for individual stations vs longitude on each of the east-west sections discussed. Reference stations circled. Light lines in 16°N and 24° N section display dynamic height field computed from the curl of the wind stress.

sive geostrophic shear, excessive northward abyssal flows, excessive upwelling at mid-depth, and excessive vertical eddy coefficients.

On the whole, we can expect to make reasonably good estimates of the ocean

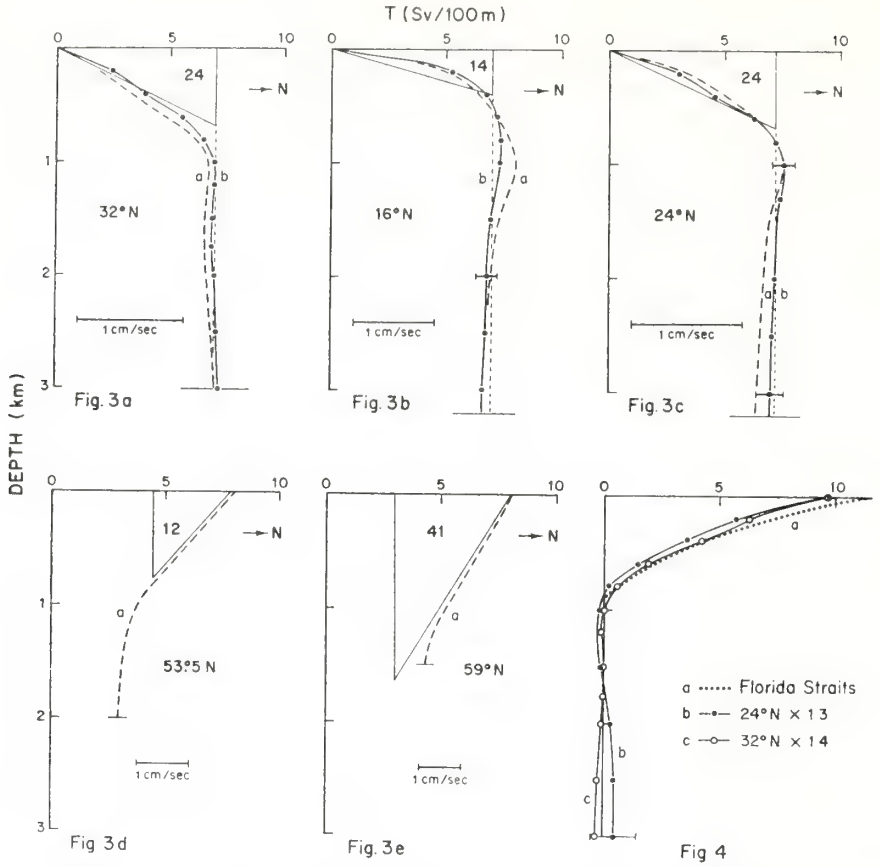


Figure 3. Vertical distribution of geostrophic transport on various sections, between reference stations in Sverdrups/100 meters depth, with zero abitrarily set at surface. (a) curves/dashed are computed from the two reference stations alone, (b) solid curves are computed from slopes determined by group means. Triangles have area corresponding to transport computed from wind-stress data, for same length of section. Error bars shown on (b) curves.

Figure 4. Vertical transport curve for Florida Straits (a) off Jacksonville—from directly measured velocity data with two other transport curves superposed: (b) extrapolated transport for 24°N (expanded transport to fill up whole ocean width), and (c) same for 32°N. The zeroes of (b) and (c) have been shifted arbitrarily to make the curves fit best by eye. Sample error bars shown at 3000 m on (b).

scale vertical distribution of geostrophic transport between reference stations on 24°N and 32°N, but only to depths above major topographic features of the Mid-Atlantic Ridge (this limits us to the upper 3200 meters).

Curves of the vertical distribution of transport (in Sverdrups/100 meters) for 24°N, 32°N, and for 16°N are given as dashed curves in Fig. 3. Note that at 16°N the dynamic topography slope depends on longitude. These were computed using

the NODC station printouts for the reference stations listed in Table 1. We do not attempt a calculation for the 8°N section, because we can see in Fig. 2 that the east-west topography is weak since this section runs along the core of the north equatorial countercurrent.

Slopes can be determined more objectively by averaging groups of station data at the western and eastern sides of the sections, and taking the differences between the mean positions of the two groups. The slope is then multiplied by the distance between the original reference stations, and the new transports displayed as solid (b) curves in Fig. 3. All transports have been drawn with reference to the surface. However, it is much more likely, as can be seen from the shapes of the curves, that the true zero of the baroclinic transport should lie somewhere in deep water as indicated by the vertical dotted lines in Fig. 3 for 32°N, 24°N, and 16°N. The curves (b) are probably better estimates than the curves (a) because the choice of reference stations made in the (a) curve calculation was based only upon representativeness in the depth interval 100 db to 1500 db and not on how the dynamic height varies with depth. Furthermore, the derivation from the group-means gives some measure of the error-bars (chosen as $\pm \sigma/\sqrt{N}$, where σ is the standard deviation of individual stations' dynamic heights from the group-means, and N =(6) is the number of stations in a group-mean). Some of these error bars are shown in Fig. 3 on the (b) curves. They increase with depth because the vertical integration from the surface accumulates noise with increasing depth and are probably too large as shown, because the residuals from the fitted sloping line are noticeably less than from the group-means.

For the 24°N section, a least squares fit was made for the dynamic height variation with depth (i.e. for each depth interval, 0-100 db, 0-200 db, etc.). Using the fit at each depth, least-squares stations were determined at 70°W and 20°W. The transport between these stations from 0 db to 800 db was 24.7 Sverdrups. For the (a) and (b) curves the same transports are 23.2 and 24.0 Sverdrups respectively. Clearly all three techniques give about the same transport in this depth range.

3. Comparison to transports from curl of wind-stress data

Estimates of the total geostrophic transport, as computed from observed wind-data, can be computed between the reference stations as differences between Sverdrup transport and Ekman transport, using the tabulations of Leetmaa and Bunker (1976). We find them to be: 12 Sverdrups (16°N), 25 Sverdrups (24°N), and 27 Sverdrups (32°N). These transports do not contain any information about the distribution of transport with depth, and they represent only an area on the diagrams in Fig. 3. We assume that the depth distribution is triangular, with fixed area, and fit suitably shaped triangles of proper area to the curves in Fig. 3. The fits shown for 16°N, 24°N and 32°N are quite good: within the likely errors and

consistent with the idea that most of the transport is indeed in the upper ocean and that the deep water has a small (within the error bars indistinguishable from zero) transport. The error bars are large enough, however, to admit uncertainty of ± 10 Sverdrups in the deep water between 1000 and 3000 decibars.

The uncertainty in the transport as computed from the curl of the stress can be as large as 30% (Leetmaa and Bunker, 1976). An error of about 5% results from underestimation of the winds by merchant vessels. Choice of a drag coefficient in the stress computation introduces an uncertainty of 10-20%. An additional error of 10% arises in the computation of the curl of the wind stress because of inadequate spatial resolution of the wind field.

Can the longitudinal structure that exists in some of the sections in Fig. 2 be explained by similar structure in the curl of the stress? The geostrophic transport, as obtained from the curl of the stress, was computed over areas 2° of latitude by 5° of longitude. If the vertical distribution of geostrophic transport is reasonably represented by a triangle (Fig. 3), the transport is related to the dynamic height change at the surface, ΔD, by the relation, $T = \frac{gH}{2f}\Delta D$ where H is the height of the triangle. Computations from the wind data give the average transport for every 5° of longitude. A ΔD can be computed for each of these and a zonal section constructed which shows the variation of ΔD with longitude. This was done for the sections at 24°N and 16°N (Fig. 2). Since only changes in the dynamic height field can be computed, the absolute value was fixed to lie close to the observed values at one end of each section. The value of H was chosen to be 500 meters for 16°N and 800 meters for 24°N. These are slightly deeper than the level to which the transport triangles are drawn but correspond more closely to our choice of the level of no motion. These choices of H make the computed and observed range of dynamic height variations agree. As can be seen, the computed shape of the dynamic height field fits the observed points remarkably well for both sections (Fig. 2). A similar computation for the 53°N section had poor agreement.

4. The subpolar sections

Turning now to the two sections that cross the subpolar grye at 53.5°N and 59°N, we see in Fig. 2 that there is a very marked dependence of slope with longitude. However, the curves are reasonably well defined, and we can choose reference stations, as shown, to embrace the major mid-ocean difference of dynamic topographic level across the sections. The transport curves (a) for these two sections are also shown in Fig. 3. No attempt to use group-means seemed worthwhile for these sections. When the wind-derived transport triangles are fitted to these curves, there is no indication of approach to zero in the deep water. Evidently there is a complicated story to tell here. The geostrophic shear extends to the bottom, and

in this respect this area is more like the western boundary regions of the subtropical gyres.

5. Comparison to measured transports in the Florida Straits

Finally we compare the interior transports to the directly observed measured values in the Florida Straits off Jacksonville at 30°N (Richardson, Schmitz, and Niiler, 1969). We suppose by continuity that the upper ocean transport southward across the full width of the subtropical ocean (excluding the Florida Straits) must correspond to a return flow at similar depths through the Florida Straits. Of course, the water does not *have* to return at the same depths, because vertical velocities and water-mass modifications must occur to some extent after water has passed southward across a section, but this may actually be minimal. Certainly deviations from liquid water conservation due to net evaporation over the Atlantic will be undetectable in our crude budgets.

We need transport estimates for the full width of the oceans, but we cannot use hydrographic data near either coast because of the higher order dynamics there, and because of the large amplitude eddies that prevail near the Gulf Stream. Evidence of enhanced eddy activity near the western ends of the 24°N and 32°N sections can be seen in Fig. 2. We therefore extrapolate the results for these sections to cover the whole width of the ocean by expanding the (a) geostrophic transport curves uniformly with depth by the factor 1.4 for 32°N and 1.3 for 24°N. These expansion factors are calculated by dividing the full ocean width by the distance between the reference stations. These two expanded curves are superposed upon the measured (Jacksonville) Florida Straits transports in Fig. 4. The comparison appears to be remarkably good. This indicates that the water does not change much in depth as it goes around the grye from the midocean into the Florida Straits. The distribution of transport with depth in the upper 1000 meters is practically the same in all three profiles; deeper transports differ indistinguishably from zero within the limits of error.

To the geostrophic transports at 32°N and 24°N should, of course, be added the Ekman transports. At 32°N this would add about two Sverdrups to the transport shown in Fig. 4. At 24°N this subtracts about three Sverdrups. Neither value changes the curves significantly. The results of the 32°N section should perhaps be compared with the Richardson, *et al.*, 1969 section at Cape Fear (33°N). The measured transport at this section was 53 Sverdrups compared to 37 Sverdrups at the Jacksonville section. However, as was noted in Richardson *et al.*, 1969, this increase was uniform with depth (barotropic). Thus the agreement for the baroclinic transport as shown in Fig. 4 still holds.

The total transports at 30°N and 33°N as estimated from the wind stress data are 35 and 34 Sverdrups respectively. At 30°N the comparison with the measured

transport is remarkably good; at 33°N the calculated and measured values are beginning to diverge.

6. Conclusion

In conclusion we believe that there is a good reason to suppose that the interior transport of the subtropical gyre of the North Atlantic is essentially consonant with the Sverdrup curl-of-the-wind-stress relationship. Our faith in a simple linear dynamic for this portion of the mean oceanic circulation is therefore strengthened.

Our conclusion, together with the results of Niiler *et al.* (1971), partly lays to rest a myth concerning discrepancies between theoretical and observed transport that began with Munk (1950) and has persisted through the years in the thinking of most of us. It has recently appeared in exaggerated form in the essay by Gill (1971). It states that observed transports exceed theoretical transports by a factor of between about 2 and 5.

This myth came about because the "observed" transports used were values obtained from measurements in the strong poleward portions of the Gulf Stream's flow while substantial return flows in a wide western boundary region near the Stream were ignored. The Stream and associated return flow are parts of a partly closed gyre of very large transport which includes substantial deep water flows (Worthington, in press). But these exotica do not extend very far into the ocean from the western coasts. Evidently the net meridional flows of the closed gyres in the western boundary regions are much less than those associated with the identifiable Gulf Stream itself, thus the discrepancies largely disappear. We believe that in the subtropics there is no demonstrable discrepancy of the kind mentioned by the above authors.

REFERENCES

Fuglister, F. C. 1960. Atlantic Ocean Atlas, Woods Hole, 209 pp.

Gill, A. E. 1971. Ocean models. Phil. Trans. Roy. Soc., London, *A 270*, 391–414.

Leetmaa, A. and Andrew Bunker. 1976. Update charts of the mean wind stress and its curl (in preparation).

Munk, W. 1950. On the wind-driven circulation. J. Met., *7*, 79–93.

Niiler, P. P., E. Simco, and R. Larue. 1971. A two-layer model of the north Atlantic thermocline. J. of Phys. Oceanogr., *1*, 257–277.

Richardson, W. S., W. J. Schmitz, and P. Niiler. 1969. The velocity structure of the Florida Current from the Florida Straits to Cape Fear. Deep-Sea Res., *16*, 225–231.

Stommel, H. 1956. On the determination of the depth of no meridional motion. Deep-Sea Res., *3*, 273–278.

Sverdrup, H. V., M. W. Johnson, and R. H. Fleming. 1942. The oceans, their physics, chemistry, and general biology. New York, Prentice-Hall, 1087 pp.

Worthington, L. V. (in press). On the North Atlantic circulation. Johns Hopkins Oceanographic Studies.

Worthington, L. V. and R. Wright. 1970. North Atlantic Atlas, Woods Hole.

Wust, G. 1957. Stromgeschwindigkeiten zur Statik und Dynamik des Atlantischen Ozeans. **Wiss. Ergebn. d. Deutschen Atlantischen expedition METEOR 1925-27. Bd VI Teil 2, Lieferung *6*, 261–420.**

Received: *November, 1976.*

Printed in U.S.A. for the Sears Foundation for Marine Research,
Yale University, New Haven, Connecticut, 06520, U.S.A.
Van Dyck Printing Company, North Haven, Connecticut, 06473, U.S.A.

Journal of Marine Research 35, No. 1, 29-47.

The annual cycle of the Gulf Loop Current Part I: Observations during a one-year time series

by George A. Maul[1]

ABSTRACT

The Gulf Loop Current is that portion of the Gulf Stream System which connects the Yucatan Current and the Florida Current in the eastern Gulf of Mexico. An experiment to test the annual cycle proposed by Leipper (1970) was conducted from August, 1972, through September, 1973. Twelve pathlines of the 22°C isotherm at 100 meters depth were made from Yucatan to the Florida Keys at 36-day intervals in conjunction with a satellite oceanography project. The sequence of pathlines shows an annual cycle of penetration into the eastern Gulf that is in phase with the historical annual cycle of current speeds and transports of the Gulf Stream, and is also reflected in tide gage sea-level records taken between Key West, Havana, and Progreso. The data suggest that an excess inflow of Yucatan Current water of $4 \times 10^6 m^3 s^{-1}$ over outflow of Florida Current water in the upper 500 meters is required to make the Loop Current grow; the outflow required to maintain static sea level conditions in the Gulf is postulated to be into the Caribbean Sea through the Yucatan Strait below this reference level. Separation of an anticyclonic eddy appears to be part of the annual cycle, which is shown to have great year-to-year variability.

1. Introduction

The portion of the Gulf Stream System in the eastern Gulf of Mexico is called the Gulf Loop Current. The flow from the Yucatan Strait penetrates northward into the Gulf to a varying degree before turning anticyclonically and exiting through the Straits of Florida. Leipper (1970) proposed an annual cycle of growth, spreading, and decay of this current system, based on data which were spaced at random intervals over two years. A sequence of current patterns designed to provide a proper time series of the Gulf Loop Current was observed in 1972-1973, and is the subject of this report.

The opportunity to observe the current at 36-day intervals for fourteen months came as part of a study in ocean color sensing from space. The Earth Resources Technology Satellite (now called LANDSAT-1) transited the study area every 18

1. National Oceanic and Atmospheric Administration, Atlantic Oceanographic and Meteorological Laboratories, Miami, Florida, 33149, U.S.A.

days. Surface observation cruises were conducted in synchronization with every second satellite overflight. Results of the investigation into the optical properties of the current and remote detection by LANDSAT were reported by Maul and Gordon (1975).

This paper is concerned with shipboard observations of the current. Later paper(s) will report the effects of observed transports through the Yucatan and Florida Straits on the heat and salt balance in the basin using concurrently observed hydrographic, sea level, meteorological, and river runoff data.

Since this paper is part of a journal dedicated to Dr. W. S. Richardson, it seems appropriate to make an acknowledgment at the outset. Bill and I had several useful conversations during the data collection stages of this work, and some of his own measurements were helpful in the analysis. It is almost impossible adequately to thank all the other persons involved, but Doctors C. Rooth, D. Hansen, D. Moore, and A. Leetmaa require a special note of gratitude.

2. Background of hydrographic observations

Early hydrographic work in the Gulf of Mexico has been summarized by Galtsoff (1954) who edited a complete overview of the biology, chemistry, geology, and physics of the area: in 1895, Lindenkohl published a map of the temperature field at 250 fm (457 m), in degrees Fahrenheit, on which the warm waters of the Caribbean could be seen flowing northward into the Gulf and penetrating deeply into the ambient thermal field; similarly the Gulf Stream, seen as a region of large horizontal temperature gradient, is shown flowing easterly and then northerly through the Straits of Florida. In an analysis of these data, Sweitzer, in 1898, reported that the circulation was a spreading of this inflow which resulted in an anticyclonic circulation around the entire Gulf basin. Parr, in 1935, reported the opposite conclusion using *Atlantis* data taken in 1933; he stated that the Gulf Stream takes the shortest path from Yucatan to the Straits of Florida. Leipper expressed this divergence of opinion as the state of knowledge in 1954 even after reviewing Dietrich's 1939 map of the salinity maximum core which, like Lindenkohl's, reflects deep penetration. Work done in the 1960's, notably by Leipper and others (Capurro and Reid, 1972), led Leipper to speculate that there was an annual cycle in the current patterns in the eastern Gulf.

Bottom topography in the eastern Gulf of Mexico is dominated by a broad shallow shelf extending north of the Yucatan Peninsula, the Campeche Bank, and another broad shallow shelf west of Florida, the west Florida Platform. The continental slopes are marked by steep escarpments along the west Florida area and northeast of Campeche. Sill depth in the Yucatan Strait is 2000 m, and in the Straits of Florida is approximately 800 m (see inset to Fig. 1). As the Yucatan Current flows along Campeche Bank, the bottom topography has been thought to control

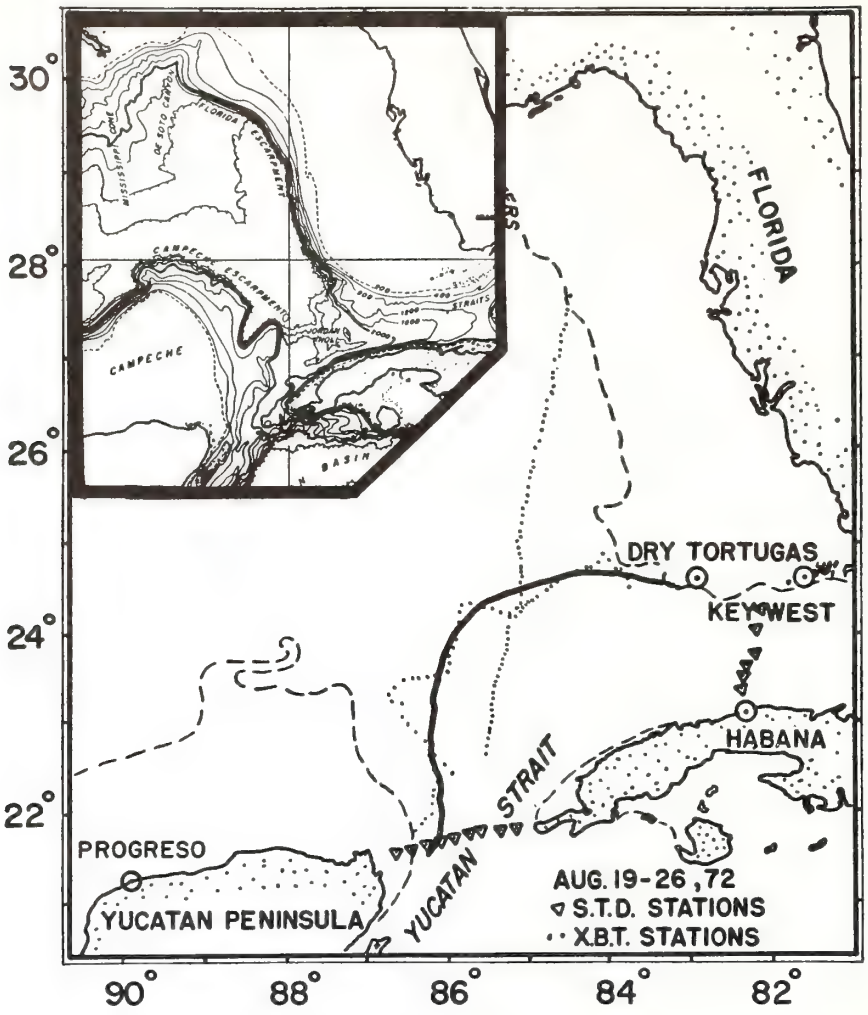


Figure 1. Example of the tracking technique is given in the main figure for August 1972. Dots are XBT drops and triangles are STD lowerings. The solid line is the pathline of the 22°C isotherm at 100 m depth. (Inset) Bottom topography in the eastern Gulf of Mexico. Contours are in meters and show the topography of the deep eastern basin surrounded by the Florida, Campeche, and Cuban Platforms.

the flow as far north as 23°30′N (Molinari and Cochrane, 1972). Above that latitude, the flow is no longer so constrained. After leaving the confines of the Campeche Bank, the Gulf Loop Current makes an anticyclonic turn in the deep water of the basin, and once again is channeled by the Florida Platform and the Cuban Platform into the Straits of Florida.

3. Observation program

Leipper showed that the 22°C isotherm at 100-m depth was a good indicator of the current in all seasons of the year. Thus the tracking strategy was to follow this isotherm with expendable bathythermographs (XBTs). The first four cruises were started in St. Petersburg. On the day of every second overpass by LANDSAT, the ship occupied the suborbital track; XBT data along the NNE-SSW tending line in Fig. 1 typify the ground track. When the ship reached the Yucatan Strait, a Salinity-Temperature-Depth (STD) profile was made at each of nine stations. After observing this hydrographic section, a zig-zag tracking pattern was initiated heading downstream, so that the average speed of the ship was boosted 1 m sec^{-1}. Typically hourly XBT's were taken. When the depth of the 22°C isotherm exceeded approximately 125 m, the ship's course was altered to the left. This course was run until the 22°C isotherm was less than 80 m, and then course was altered to the right. The pattern was continued from Yucatan around the Loop to Dry Tortugas, in all but a few cases, where weather or fuel considerations made it advisable to run for Key West. The Key West-Habana section of seven STD lowerings was occupied after a short refueling stop. From January through the end of the project (eight cruises), the cruises originated from Miami, and the Key West-Habana section was done first; this section is also a suborbital track.

After each trip, the position data were replotted and a smooth plot which is a best fit to all the navigation data was constructed. Positioning was accomplished using Loran-A, radar, visual, and celestial observations. It is difficult to estimate errors, but based on Loran-A/radar comparisons, ± 1 to ± 3 km seem reasonable. The expendable BT strip chart recorder was tested (and adjusted if necessary) before each cruise with a test canister. The average surface-bucket temperature and the average XBT-surface temperature (from the recorder) were calculated for each cruise, and the surface XBT temperature was adjusted for the difference in the average. STD stations were taken to a depth of 1000 m, or 100 m from the bottom, whichever was less. Surface calibration points were taken at each cast, and the lowering speed was about 50 m per minute. Station spacing was about 20 km, with no stations closer than 22 km (12 n mi) to foreign coasts.

4. Pathlines of the current

Conditions prior to the first cruise are summarized in Fig. 2. These data are compiled from Merrell (personal communication), Molinari and Yager (1977) and Brooks and Niiler (1975), and cover the period from 6 to 18 May, 1972. Areas where the 22°C isotherm is deeper than 125 m are stippled; the indicator isotherm is the heavy line outlining the main flow and the eddy. In this composite of their data, an anticyclonic eddy is in the process of separating as evidenced by the ridge in the topography of the 22°C isotherm extending northeast from Campeche Bank

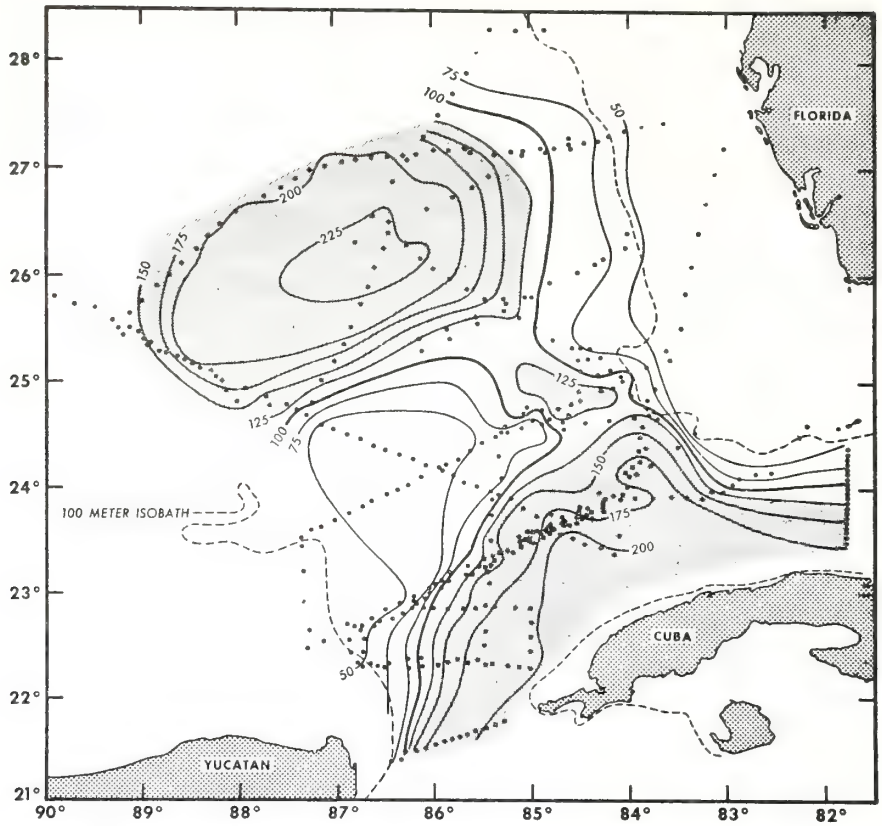


Figure 2. Depth of the 22°C isotherm in the project area, composited from data taken 6-18 May, 1972. The eddy was actively separating from the main flow, and this figure required spatial smoothing, but it does illustrate the relation of the indicator (100-m depth contour heavy) to the thermal field.

to the Florida Platform. The tracking technique would show very short radii of curvature in the zone where the separation was taking place; conversely the eddy could be missed entirely if it were not for the suborbital trackline (cf., Fig. 1). Recirculation in the eddy is already quite extensive as evidenced by the closure of the isopleths. The process of eddy separation cannot be discussed with the pathlines of the 22°C isotherm except to confirm that this did indeed occur. This eddy was observed as late as December, 1972, in the suborbital trackline near the west Florida Platform.

Pathlines of the 22°C isotherm at 100 m depth are given in Fig. 3. Dates of each survey are labeled on the appropriate pathline. The shortest tracking time was three days and the longest six days, so that near synopticity was accomplished. Hydrographic station transects of the straits added two to three days to each cruise.

In August, 1972, the 22°C isotherm extended north from Yucatan and curved in a gentle anticyclonic arc, terminating tangent to the Florida Platform near Dry Tortugas (see also Fig. 1). The August suborbital trackline data (not shown) supports the earlier discussion that the eddy observed in May had completely separated, as evidenced by the 22°C isotherm being shallower than 30 m between the eddy and the main flow.

By September, conditions had changed markedly. The initial current direction had a significant easterly component and flowed directly toward the west Florida shelf. There was evidence of Loop Current water on the shelf, and the 22°C isotherm apparently went aground well north of Dry Tortugas. By early November the current had reformed to its southernmost extent, and evidence of Florida Bay water flowing south through the Keys was noted in both the ship track and a LANDSAT image. A red tide of *Gymnodinium breve* was reported on the west Florida shelf during September. Murphy *et al.* (1975) have used these data to document partially the source of the first reported Florida east coast red tide. They hypothesized that the organisms in the west Florida shelf waters advected through the Keys where they were carried by the current through the Straits of Florida and into the coastal region north of Miami.

By December, 1972, the current had swung to the west and had penetrated into the Gulf to the same latitude as during August. At 24°N, the stream flowed in a sharp anticyclonic turn to the east. January, 1973, was the only month in which transects of the Straits were not obtained, because 25 m sec^{-1} winds and high seas forced the ship to turn back. Only four crossings were obtained, but sufficient detail permitted the observation that, for the first time in the series, the current penetrated north of Dry Tortugas (25°N).

The "spring intrusion" (Leipper, 1970) continued from February through June when the current extended to 27°N. As the current penetrated deeper into the Gulf, it also swung farther to the west. North of 24°N, the isobaths curve sharply to the west, in a region of deeper water where topographic influence becomes unlikely.

The northward penetration to almost 29°N in July, 1973, coupled with a marked cyclonic curvature off the west Florida shelf at 26°N led to the expectation of an eddy separating by the following cruise. The intrusion at 26°N from the east was not a sampling artifact; the R. V. *Bellows* obtained concurrent hydrographic station data across the shelf and out into the main current throughout this area. The furthest western extent of the current also occurred in July. A vast area of green, high chlorophyll-content water was encountered along the western boundary opposite the 26°N intrusion from the east (Ednoff, 1974).

By August, 1973, the current system extended almost to the Mississippi Delta. The eddy had not separated. Very low salinity water (24‰) was recorded by a simultaneous cruise of the R. V. *Bellows* and the R. V. *Virginia Key* all along the current edge off the Florida Shelf. Surface salinities were less than 30‰ along the

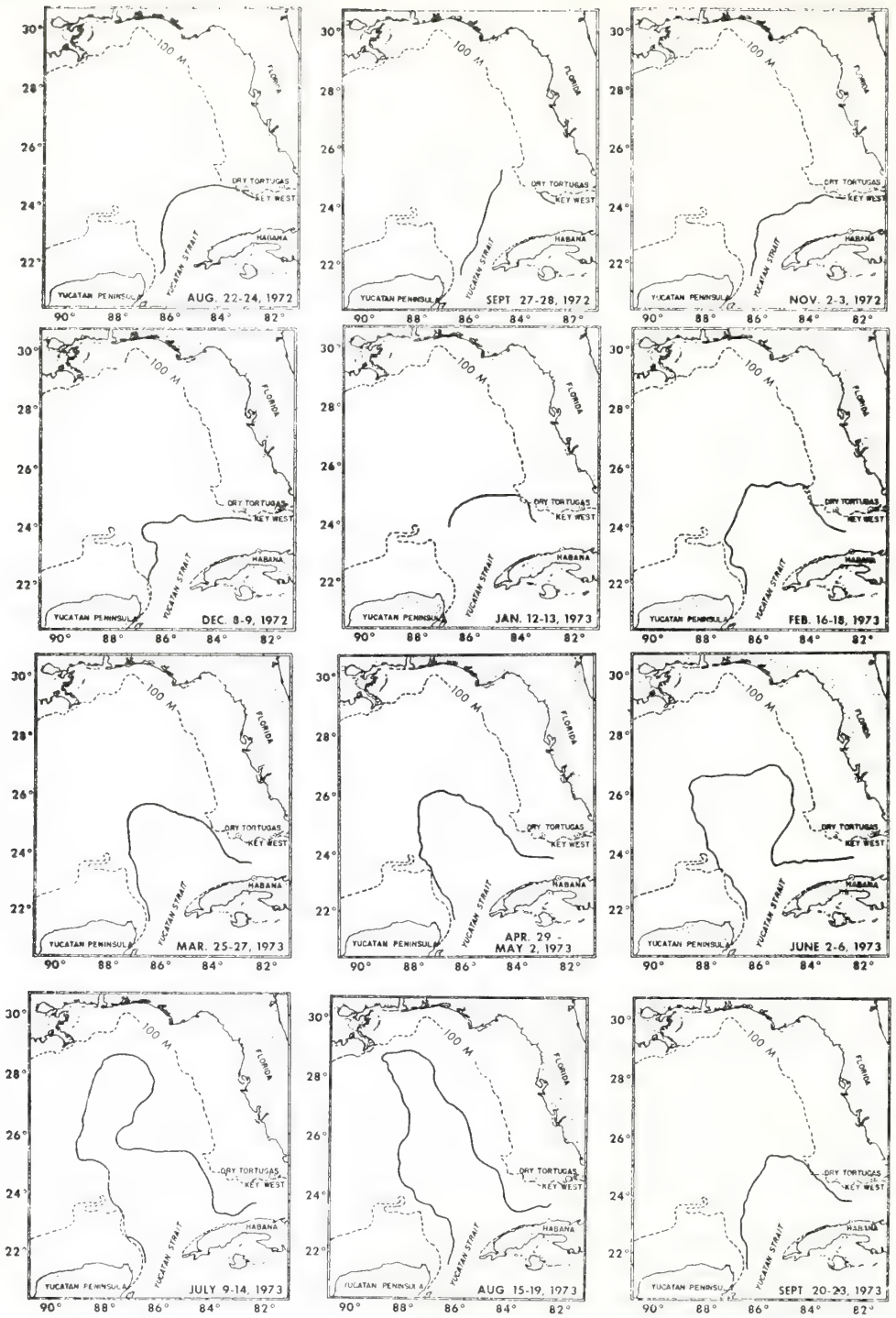


Figure 3a thru 1. Pathlines of the 22°C isotherm at 100-m depth for the period August, 1972 to September, 1973. Dashed line is the 100 m isobath. Actual dates of each survey from Yucatan to Dry Tortugas, but excluding the time required for the STD sections, are given on the lower right of each figure.

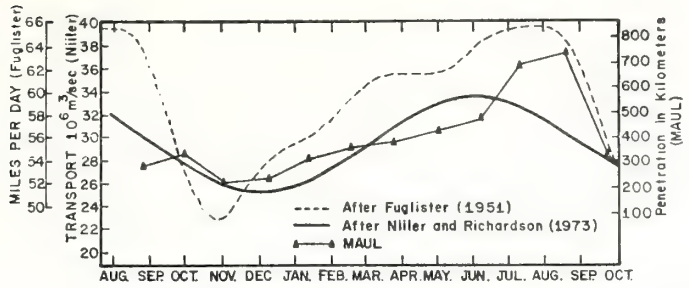


Figure 4. Annual cycle of surface drift velocity in the Straits of Florida between Cape Florida and 30°N (dashed), annual cycle in direct transport between Miami and Bimini (solid), and annual cycle of penetration of the Gulf Loop Current into the Gulf of Mexico (triangles) during 1972-73. The large decrease in penetration between August and September (right-hand side) represents the separation of an anticyclonic eddy and is a discontinuity in the penetration pattern.

cyclonic boundary in the Straits of Florida. Because the Loop Current was so close to the Mississippi Delta and there were no other large sources of fresh water, it seems probable that the source of this water was the Mississippi River. These low salinity waters were observed as far north as Georgia where salinities were still 34.5‰ (Atkinson and Wallace, 1975).

During the last cruise, September, 1973, the current was found well to the south again, at approximately the same penetration as in February. A trackline on the R. V. *Bowers*, from Ft. Myers west to 87°W and north to Pascagoula, confirmed that an anticyclonic eddy had indeed separated and that a significant change in the hydrography of the eastern Gulf had occurred in one month. There was no hint in the extensive August data that a recirculation had begun as a prelude to the eddy formation, although observations by Cochrane (Personal communication), made between the April-May and June cruises, showed substantial closure in the isotherm field in this area.

These data support the hypothesis that the eddy separation is an annual event, but by no means does it occur at the same time each year. The May, 1972 eddy and the September, 1973 event are 16 months apart, whereas spacecraft data, supported by concurrently obtained buoy tracks (W. S. Richardson, personal communication), suggest that an eddy had separated in April, 1974, a 7-month time difference. Other eddies have separated in November, 1970, and again in July or August, 1971 (J. Brucks, personal communication). Thus in each of the last 5 years, between the vernal and autumnal equinoxes, an anticyclonic eddy appears to have separated from the main current.

In Fig. 4, the northward penetration of the 22°C isotherm into the Gulf is compared with historical data. The dashed line is Fuglister's (1951) harmonic fit of

annual and semiannual terms to ship drifts in the Straits of Florida. The solid line is Niiler and Richardson's (1973) fit of a sinusoid, with an annual term only, to the direct transport measurements in the Straits of Florida. The light line with triangles is the fit of the arc distance from Cabo San Antonio (western tip of Cuba) to the pathlines of the indicator. Cochrane (1965) did an analysis similar to Fuglister's and showed that the ship drifts in the western Yucatan Strait are essentially the same as in the Straits of Florida, except that the maximum drift through Yucatan leads that through Florida by 1 month. Niiler and Richardson's curve shows the same general feature of low transports in winter and high transports in summer. They noted that the week-to-week fluctuations in the current were as much as the annual range, and further that the transports lag the annual cycle of wind stress curl over the Atlantic Ocean by 4 months. Maul (1974) reported that the slope of the 17°C isotherm in the Yucatan Strait lagged the penetration by three to four cruises. The general agreement between the three curves in Fig. 4 suggests that the variations in the Gulf Loop Current are well correlated with the annual cycle of current velocity and transport. The annual cycle of current velocity is in phase with the annual cycle of trade wind stress (Fuglister, 1951).

These data form the basis upon which Liepper's suggestion has been investigated. The pathlines indicate that: (a) there is an annual cycle of growth and decay of the Gulf Loop Current, (b) a major exchange of heat, salt, and momentum from the current into the Gulf is made through the separation of an anticyclonic eddy or current ring, and (c) the circulation in the eastern Gulf of Mexico is associated with the annual cycle of mass transport.

5. Discussion

Comparing pathlines of the 22°C isotherm with historical data averaged by months gives some indication of the variability of this current's cycle. Robinson's (1973) atlas clearly shows that the minimum penetration of the Loop occurs in March and April, whereas the maxima are in August and September. Whitaker's (1971) averages show that the minimum is in November and the maxima are in May and October. Leipper found minima in August, 1965 and November, 1965 and a maximum in August-October, 1966. From Fig. 3 it is seen that the minimum here occurred in October-November and the maximum in July-August. This summary points out the high degree of temporal variability in the Gulf Loop Current and emphasizes that the data obtained in this study are not a final description of the cycle.

Simple dynamic models of the Gulf Loop Current such as those by Ichiye (1962) and Reid (1972) suggest that the penetration of the Yucatan Current into the Gulf depends on the flow direction. Their potential vorticity-conserving model in natural

coordinates for a two-layer ocean with the lower layer at rest, is given by

$$\frac{KV - \frac{\partial V}{\partial n} + f}{D} = \text{constant} \tag{1}$$

where K is curvature, V is velocity along a streamline, $\overleftarrow{n}$ is the coordinate normal to the velocity vector, positive to the left facing downstream, f is the Coriolis parameter and D is the depth of the upper layer. In the pathlines given in an earlier section, D is a constant 100 m. If it is assumed that the velocity core is a streamline whose neighboring streamlines are nearly equidistant, $\partial V/\partial n$ is also constant. For that case, the work of Ichiye and Reid gives

$$V = \tfrac{1}{2}\, p^2 \beta \tag{2}$$

where p is the penetration of the streamline into the Gulf, and β is the meridional variation of f. Reid (1972) was careful to point out that the model only holds in deep water, that is north of Campeche Bank, and that V is an average value for the upper layer. Applying equation (2) north of Campeche during those months when bottom topography controls the flow, and at the latitude of Cabo San Antonio at other times, the velocity range is 44 to 303 cm sec^{-1} (excluding August, 1973). Forty-four cm sec^{-1} is a reasonable value for the average surface value, but 303 cm sec^{-1} is beyond the range of observations. This suggests that a geostrophic deep-water potential vorticity-conserving model is not an adequate explanation.

From Fig. 3, it can also be seen that the bottom topography of Campeche Bank did not control the current during August, September, October-November, and December, 1972, or September, 1973. During the February, March, April-May, June, and July, 1973 cruises, the 22°C pathline closely followed the 100 m isobath from the Yucatan Strait almost to 24°N. This supports Cochrane's (1965) contention that the Yucatan Current is farther to the west during periods when surface velocities are higher and these are also the months when the indicator hugs Campeche Bank. Thus, when the current is strongest in spring and summer (Molinari and Cochrane did their analysis on data observed in May 1962, 1965, and 1966), and is farther to the west, the velocity near the bottom may be sufficient for equation (1) to describe the dynamics coarsely.

Another interesting kinematic result is summarized in Fig. 5. The northern terminus of the Straits of Florida hydrographic section was near Cosgrove Lighthouse (halfway between Key West and the Dry Tortugas). The horizontal distance between Cosgrove Lighthouse and the 22°C isotherm at 100 m depth is plotted against the northward penetration of the pathline into the Gulf (measured from Cabo San Antonio). The farther north the current penetrates into the Gulf, the farther south

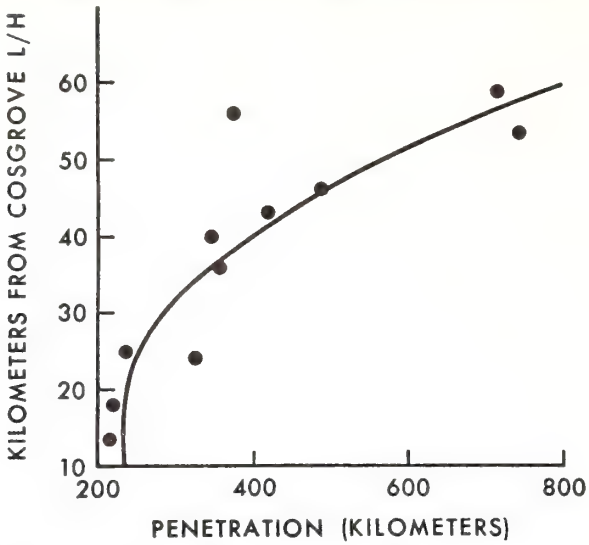


Figure 5. Distance that the 22°C isotherm at 100-m depth was found from Cosgrove Lighthouse (northern terminus of the Straits of Florida transects) versus distance from Cabo San Antonio to the northern penetration of the current into the Gulf of Mexico. The heavy line is the least-squares fit to the data. The point at 55 and 400 km represents a case where the indicator was near 100 m for three STD stations, but was chosen to be the first crossing from north to south for consistency.

it was found in the Straits of Florida. Paskausky and Reid's (1972) numerical model also shows that the current flows close to Cuba when the penetration of the Loop Current is greater, but there are no analytic models incorporating bottom topography to which these observations can be applied.

The volume of water necessary to make the Loop grow can be estimated from the length of pathlines. Assuming a mean depth (z) of 500 m for the current, pathline measurements show that 64,000 km^3 of resident Gulf water must be displaced by Yucatan water in the six months that the Loop grows. The excess transport of Yucatan water into the Gulf in this period averages 4.1×10^6 m^3 sec^{-1}. As an independent check on this value, sea-level records were studied. Cochrane (1965) showed that there is a good correlation between the monthly sea-level difference between Habana and Progreso and the average ship drift in the western Yucatan Strait; the data in Fig. 4 show a correlation between surface velocity and transport. For an upper layer flow which is in geostrophic balance in the crossstream direction, the sea-level difference across the stream is a measure of the average surface current. A transport estimate may be made by multiplying this average surface current by a mean depth for the upper layer flow, which is taken to be 500 m in this case. Marmer's (1954) mean monthly sea-level data are used. The stations are Habana (1947-1950), Key West (1930-1948), and Progreso (1947-1950). Trans-

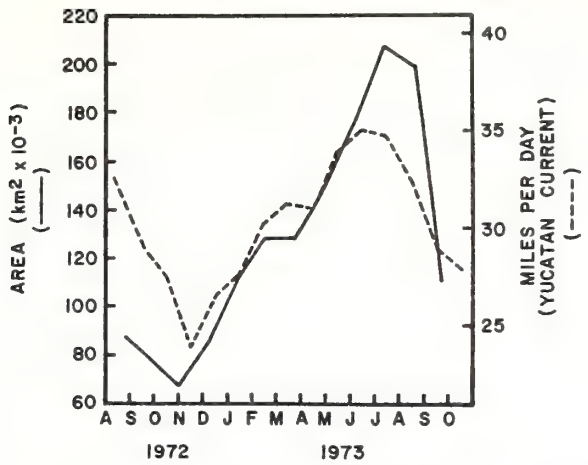


Figure 6. Annual cycle of surface area, enclosed by the 22°C isotherm in the Gulf and the Key West-Habana-Cabo San Antonio-Isla Contoy boundary, is the solid line. Dashed line is the annual cycle of surface velocities as estimated by Cochrane (1965) for the Yucatan Current from ship drift reports.

port difference between the Habana-Progreso (T_{H-P}) and the Habana-Key West (T_{H-K}) sections is then given by

$$T_{H-P} - T_{H-K} = \frac{gz}{f}(h_K - h_P) + C \tag{3}$$

where g is gravity, z is the mean depth of the current, h_K is the monthly sea level at Key West, h_P is at Progreso, and $C = (\bar{h}_K - \bar{h}_P)gz/f$, where the overbars denote mean annual sea level. Progreso and Key West are on the same side of the current, and it is assumed that the annual mean sea level along the coast is approximately the same, therefore $C = 0$. During the period that the Loop is growing, the difference $h_K - h_P = 4.88$ cm. The transport difference calculated from equation 3 is 3.8×10^6 m^3 sec^{-1} during this period.

By two independent methods, it is shown that there must be an excess inflow of Yucatan water. Jacobs (1951) estimated that evaporation exceeds precipitation in the Gulf by 35 cm per year. This would account for only $0.02 \times 10^6 \times$ m^3 sec^{-1} excess of inflow. Sea level in the Gulf does not rise 34.5 m in six months as implied by excess inflow, and the transports inferred from sea level records require that very little Gulf of Mexico water exits the Straits of Florida. This implies that Hansen and Zetler's (1972) and Schlitz's (1973) direct measurements of a net south drift at the bottom of the Yucatan Strait may have detected the major source of discharge during some phase of the growth cycle. Schlitz's estimate of the southward transport through the Yucatan Strait, based on April, 1970 data, is 4×10^6 m^3 sec^{-1} which is in excellent agreement with this discussion.

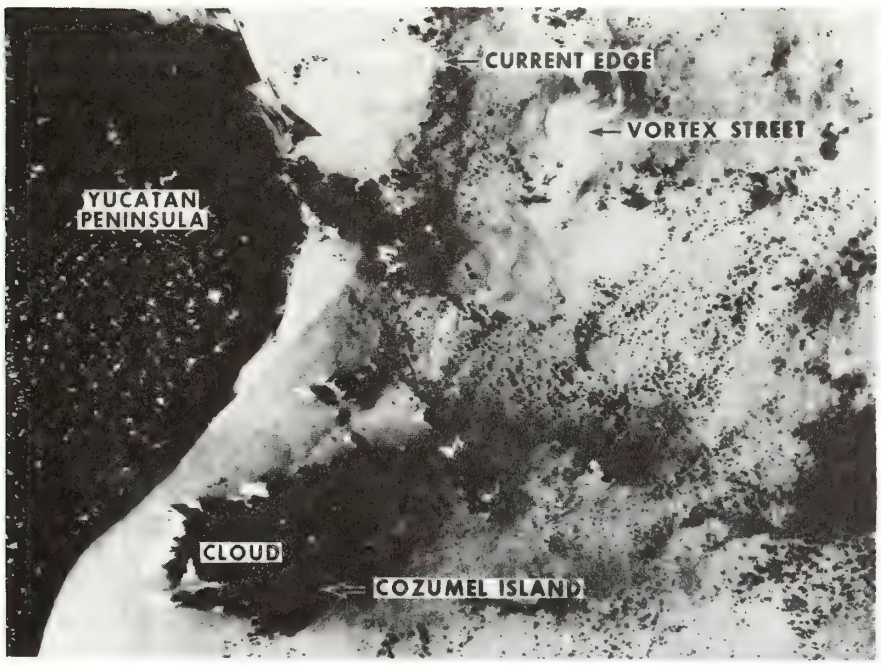
The area enclosed by the 22°C isotherm at 100-m depth along the line from Cosgrove Lighthouse to Habana, along the Cuban coast to Cabo San Antonio and across to Isla Contoy, was estimated using a polar planimeter from Fig. 3. The area enclosed by the Loop Current defines a volume of Yucatan water, and its annual cycle should be related to volume transports. As a first estimate, the transports are assumed proportional to current velocities through the Yucatan Strait, as estimated from Cochrane's ship drift studies. The comparative results are plotted in Fig. 6. The sharp decrease in area between August and September, 1973 is due to the separation of the anticyclonic eddy discussed earlier. A clear correlation exists between area and current velocities, with little phase lag between transport and the area covered by the current system. The numerical models of Wert and Reid (1972) and Paskausky and Reid (1972) attempted to relate the penetration of the Gulf Loop Current to changes in the vorticity distribution or velocity field of the Yucatan Current, but they kept the volume transport constant; Ichiye (1972) used changes in the Yucatan velocity in a rotating tank model, but did not relate the velocities to the penetration. There are no established relationships between velocity or vorticity fields in the Yucatan Current and transport, nor are there any models (except indirectly Reid (1972) or Ichiye (1962)) which use changes in transport to drive the circulation in the Gulf of Mexico.

6. Evidence of fine-scale features

The subject of oceanic eddies is increasing in importance, and is the focus of several recent multi-national studies. Besides the large eddies of May, 1972 and September, 1973 described above, a large range of smaller eddy features were observed during the year of observations. These are collectively called fine-scale features, and are discussed below.

Cochrane (1965) noted that the surface velocity field of the Yucatan Current had double maxima. It was also noted by Pillsbury in 1890 in this area and by Stommel (1966) in other portions of the Gulf Stream. It appears distinctly in Cochrane's geomagnetic-electrokinetograph profiles north of the Strait. Cochrane postulated that it occurs when the cyclonic edge of the Yucatan Current is found against the Mexican coast, and the main flow is bifurcated by Isla Cozumel; one branch passes between the island and the mainland, and the other branch passes to the east of this topographic wedge.

Fig. 7 is a computer enhanced LANDSAT image of the Yucatan Strait. This is a negative print, and thus dark tones represent areas of high radiance. The water outside the current is seen to be of lower radiance than that in the current; the radiance is dominated by a higher sea state or different glitter pattern in the current. Here the western edge of the current can be seen leaving the coast northwest of Cozumel. In the wake of the island is a spacecraft observation of an oceanic von



ıre 7. Negative print (ID 1029-15413) of computer-contrast-stretched MSS-5 (0.6-0.7 μm) ANDSAT image of Yucatan and Cozumel, Mexico, observed on 21 August, 1972. The ucatan Current's cyclonic edge can be seen emerging from between the island and the ainland. In the lee of Cozumel is a vortex pattern which causes a disturbance in the surıce velocity profile well downstream. Horizontal distance across image is 135 km.

rman vortex street; this is the oceanographic analog to similar observations in atmosphere, photographed by Gemini and Apollo astronauts in the cloud cover r the Guadeloupe Islands in the equatorial Pacific Ocean. Fig. 7 was imaged on August, 1972. The August, 1972 pathline was observed at this time, and the rent's edge and the vortex street are confirmed to be ocean features.

Surface current velocities were determined by the geostrophic method from the lrographic transect of Yucatan Strait on 21-22 August, 1972; station location is en in Fig. 1. Station spacing was very nearly 18 km, and the north component the surface speeds relative to 700 db, from Yucatan to Cuba, were: 103, 145, 119, 73, 88, 62, and 35 cm sec^{-1}. The low value of 80 cm sec^{-1}, bracketed higher values of 145 and 119 cm sec^{-1}, is in the middle of the vortex zone

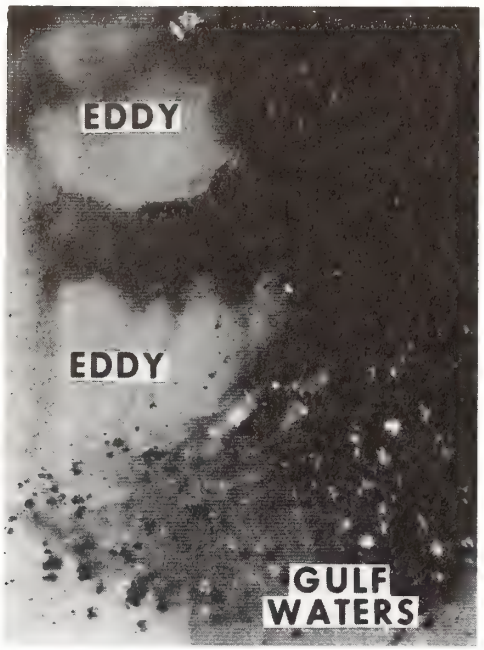


Figure 8. Negative print of computer enhanced LANDSAT MSS-4 (0.5-0.6 μm) image (ID 1153-15292) of detached eddies on the west Florida shelf observed on 22 December, 1972. Details of the boundary of these 20-km diameter Gulf Loop Current eddies show significant irregularity and nonsymmetry. Horizontal distance across the image is 45 km.

shown in Fig. 7. This cross correlation of hydrographic and satellite data is offered as evidence that the observed double maxima is caused by topographic-induced vortex generation, and explains one type of fine-scale structure as eddies imbedded in the main flow of the Yucatan Current.

Maul, Norris, and Johnson (1974) observed eddies which appeared to be embedded in the core of the current, north of Campeche Bank. These eddies were 10-30 km in diameter and were interpreted to be shear instabilities as distinguished from the von Karman vortex street observed in Fig. 7. These data cannot dismiss the possibility that the eddies in mid-Gulf are generated by Isla Cozumel. If these

eddies were shear instability features, then one could expect to find them in other areas of the stream as Stommel (1966) reported. If Cozumel was the only source of disturbance vorticity, then these eddies have been advected 600 km downstream and may be found farther. The latter seems unreasonable because of Cochrane's (1965) report that velocity profiles well upstream of Cozumel do not often exhibit these features. This may be dependent on the season of the year because the current does not always flow as close to the Mexican coast as it seems to in midsummer.

In Fig. 8, a LANDSAT image of two eddies on the west Florida Platform is shown. These appear to be spin-off eddies (Lee, 1975) which have drifted into shallow waters where the depth is less than 100 meters. Here is another example (*cf.*, Austin, 1971) of the interaction of this scale eddy with the coastal water. Austin noted that several eddies of the 20- to-50 km range were observed around the perimeter of the current in a survey in 1970. This is evidence that these features drift onto the shelf where they must exchange significant quantities of salt, heat, and momentum. Eddies such as these could interact to bring cyst stages of *G. breve* into the euphotic zone and contribute to the offshore initiation of a destructive plankton bloom.

7. Summary

This research was initially undertaken to evaluate the use of an ocean-color-sensing satellite for observing currents in the subtropics. The Gulf of Mexico was chosen as a test site because there the cyclonic boundary of the Gulf Loop Current cannot be detected by infrared techniques during the summer, and this current is the major circulation feature of the eastern Gulf. The ground-truth pathlines (Fig. 9) provided measurements of the seasonality of several optical properties across the current as well as a history of the flow itself for comparison with satellite data and for basic oceanography.

This unambiguous time series of the Gulf Loop Current based on ship observations shows that Leipper's (1970) proposition is correct in that there is an annual cycle of growth and decay, but that year-by-year variability in the patterns is significant. An anticyclonic eddy separation appears to have occurred at least once each year in the last five years.

Evidence for turbulence embedded in the core of the Gulf Loop Current is obtained from comparing velocity profiles across the Yucatan Strait with satellite imagery. Two sources of turbulence are tentatively identified: shear instability and topographic influence.

The annual cycle of growth, eddy separation, and decay of the 1972-1973 data is in phase with the annual cycle of transport of the Gulf Stream System. During the period that the Gulf Loop Current is growing, resident Gulf of Mexico waters

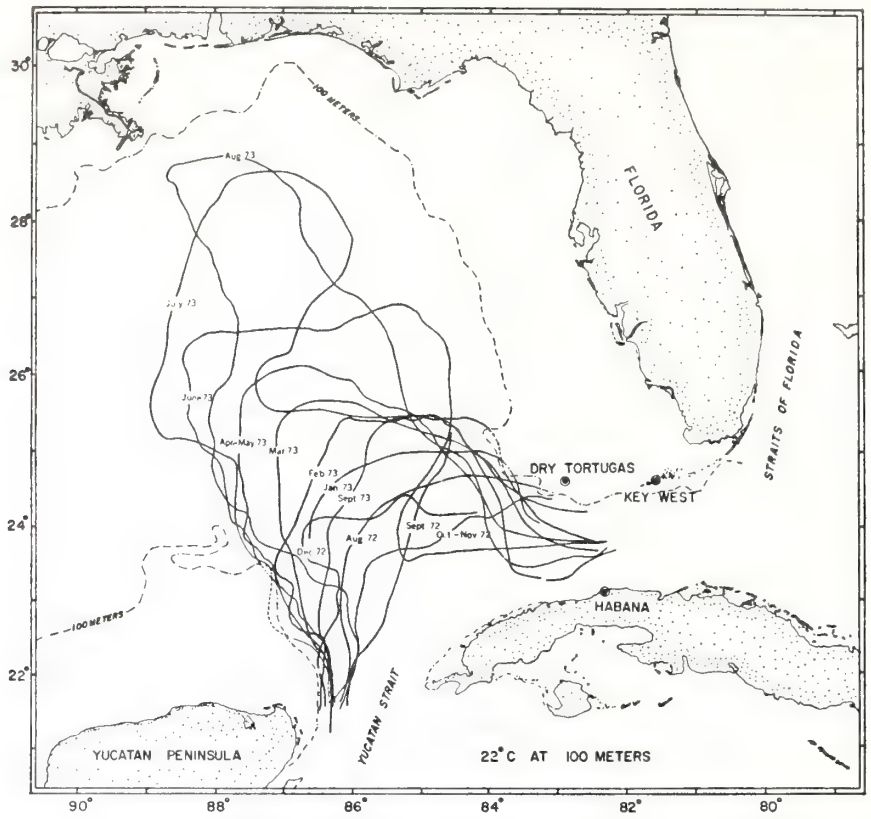


Figure 9. Compilation of pathlines of the 22°C isotherm at 100-m depth from August, 1972 through September, 1973 (see also Fig. 3). Where the indicator isotherm intersected the bottom topography, a dashed line is used to estimate its position from the other thermal data. Where the cruise started in 1 month and ended in another, both months are indicated. 100 m isobath is indicated by a dash-dot line and represents very closely the shelf break and escarpment zone.

must be displaced; this requires that 4×10^6 m^3 sec^{-1} more Yucatan water enters the basin in the upper layers through the Straits of Florida. The southward outflow appears to be near the bottom of the Yucatan Strait during part of the growth phase. Details of the balance of mass and salt were presented by the author at the second CICAR Symposium (July, 1976) and will be reported in Part II of this series of papers.

REFERENCES

Atkinson, L. P. and D. Wallace. 1975. The source of unusually low surface salinities in the Gulf Stream off Georgia. Deep-Sea Res., *23*, 913–916.

Austin, H. R. 1971. The characteristics and relationships between the calculated geostrophic current component and selected indicator organisms in the Gulf of Mexico Loop Current

system. Ph.D. Dissertation, Florida State University, Department of Oceanography, Tallahassee, 369 pp.

Brooks, I. H. and P. P. Niiler. 1975. The Florida Current at Key West: Summer 1972. J. Mar. Res., *33*, 83–92.

Capurro, L. R. A., and J. L. Reid, Eds. 1972. Contributions on the Physical Oceanography of the Gulf of Mexico. Gulf Publ., Houston, 288 pp.

Cochrane, J. E. 1965. The Yucatan Current, *in* Annual Report, Project 286, Texas A&M University, Ref. 65-17 T, College Station, 20–27.

Ednoff, M. E. 1974. Surface phytoplankton communities and their relationship to the Loop Current in the Gulf of Mexico. Master's Thesis, Florida State University, Department of Oceanography, Tallahassee, 187 pp.

Fuglister, F. C. 1951. Annual variations in current speeds in the Gulf Stream. J. Mar. Res., *10*, 119–127.

Fuglister, F. C., and A. D. Voorhis. 1965. A new method of tracking the Gulf Stream. Limnol. Oceanog., *10*, R115–R124.

Galtsoff, P. S., Ed. 1954. Gulf of Mexico—Its Origin, Waters, and Marine Life. Fishery Bulletin 89, Fish and Wildlife Service, 604 pp.

Hansen, D. V., and G. A. Maul. 1970. A note on the use of sea surface temperature for observing ocean currents. Remote Sensing of Environ., *2*, 161–164.

Hansen, D. V. 1970. Gulf Stream meanders between Cape Hatteras and the Grand Banks. Deep-Sea Res., *17*, 495–511.

Hansen, D. V. and B. D. Zetler. 1972. Deep currents in the Yucatan Strait. EOS, Transactions, A.G.U., *53*, 392.

Ichiye, T. 1962. Circulation and water mass distribution in the Gulf of Mexico. Geofis. Inter., *2*, 47–76.

—— 1972. Experimental circulation modeling within the Gulf and the Caribbean, *in* Contributions on the Physical Oceanography of the Gulf of Mexico. Gulf Publ., Houston, 213–226.

Jacobs, W. C. 1951. The energy exchange between sea and atmosphere and some of its consequences. Bull., Scripps Inst. Oceanogr., *6*, 27–122.

Lee, T. N. 1975. Florida Current spin-off eddies. Deep-Sea Res., *22*, 753–765.

Leipper, D. F. 1970. A sequence of current patterns in the Gulf of Mexico. J. Geophys. Res., *75*, 637–657.

Marmer, H. A. 1954. Tides and sea level in the Gulf of Mexico, *in* Gulf of Mexico—Its Origin, Waters, and Marine Life. Fishery Bulletin 89, Fish and Wildlife Service, 101–118.

Maul, G. A. 1974. A one year time series of the Gulf Loop Current, EOS, Transactions, A.G.U., *56*, 283.

—— 1975. An evaluation of the use of the Earth Resources Technology Satellite for observing ocean current boundaries in the Gulf Stream system. NOAA Technical Report, ERL 335-AOML 18, 125 pp.

Maul, G. A., and H. R. Gordon. 1975. On the use of the Earth Resources Technology Satellite (LANDSAT-1) in optical oceanography. Remote Sens. of Environ., *4*, 95–128.

Maul, G. A., D. R. Norris, and W. R. Johnson. 1974. Satellite photography of eddies in the Gulf Loop Current. Geophys. Res. Ltrs., *1*, 256–258.

Molinari, R. L. and J. D. Cochrane. 1972. The effect of topography on the Yucatan Current, *in* Contributions on the Physical Oceanography of the Gulf of Mexico. Gulf Publ., Houston, 149–155.

Molinari, R. L. and R. Yager. 1977. Upper layer Hydrographic conditions at the Yucatan Strait during May 1972. J. Mar. Res., *35*, this issue.

Murphy, E., K. Steidinger, B. Robert, J. Williams, and J. Jolley. 1975. An explanation of the Florida east coast *Gymnodinium breve* red tide of November 1972. Limnol. Oceanog., *20,* 481–486.

Niiler, P. P., and W. S. Richardson, Jr. 1973. Seasonal variability of the Florida Current. J. Mar. Res., *31,* 144–167.

Nowlin, W. D., Jr., and H. J. McLellan. 1967. A characterization of the Gulf of Mexico waters. J. Mar. Res., *25,* 20–59.

Paskausky, D. F., and R. O. Reid. 1972. A barotropic prognostic numerical circulation model, *in* Contributions on the Physical Oceanography of the Gulf of Mexico. Gulf Publ., Houston, 163–176.

Reid, R. O. 1972. A simple dynamical model of the Loop Current, *in* Contributions on the Physical Oceanography of the Gulf of Mexico. Gulf Publ., Houston, 157–159.

Robinson, M. K. 1973. Atlas of Monthly Mean Sea Surface and Subsurface Temperature and Depth of the Top of the Thermocline Gulf of Mexico and Caribbean Sea. Scripps Inst. Oceanogr. Reference 73-8, 105 pp.

Schlitz, R. J. 1973. Net total transport and net transport by water mass categories for Yucatan Channel based on data for April 1970. Ph.D. Dissertation, Texas A & M University, Department of Oceanography, College Station, 107 pp.

Stommel, H. 1966. The Gulf Stream. Univ. of California, Berkeley, 55–59.

Wert, R. T., and R. O. Reid. 1972. A baroclinic prognostic numerical circulation model, *in* Contributions on Physical Oceanography of the Gulf of Mexico. Gulf Publ., Houston, 177–209.

Whitaker, R. E. 1971. Seasonal variations of steric and recorded sea level of the Gulf of Mexico. Master's Thesis, Texas A & M University, Department of Oceanography, College Station, 109 pp.

Received: *November, 1976.*

Marine Technology Society Journal 11, No. 1, 5-13.

Recent Progress in the Remote Sensing of Ocean Surface Currents

George A. Maul

National Oceanic and Atmospheric Administration
Atlantic Oceanographic and Meteorological Laboratories
15 Rickenbacker Causeway, Miami, Florida 33149

Major ocean currents have surface manifestations that make them observable by spacecraft sensors. Under certain conditions, any one or a combination of the following may be used to identify the current's boundary: changes in sea surface temperature, salinity, color, sea state, sea surface topography, wave refraction patterns, and modifications to the lower atmosphere. Infrared sensors have been used most extensively to study ocean circulation; however, new instruments such as passive and active microwave sensors can sense temperature, salinity, sea state, and surface topography, and multispectral visible scanners and spectroradiometers are providing new information on ocean color and sea state. Man's role as an observer and photographer provides the highest spatial resolution to date for describing visible changes across boundaries as well as sea and swell patterns.

INTRODUCTION

Ocean currents have several sea surface manifestations that can be used singularly or in concert to locate their boundaries. Coastal currents typically have significant energy at the tidal (1-2 cycles per day; cpd) or local inertial frequencies (0.5-1.5 cpd for mid-latitudes). These frequencies are too high for the ocean's density field to adjust to the motion. Adjustment of the density field provides the conditions by which many satellite sensing techniques can be employed in studying the ocean.

The Gulf Stream off the east coast of North America is an example of a quasi-stationary current system that is well described by its density field alone. The density distribution defines that portion of the pressure field which is used to measure the geostrophic current. Frequencies associated with the boundary of this current are approximately 0.25-0.1 cpd in the Straits of Florida[1] and 0.03-0.01 cpd in the meander region off New England.[2] Geostrophic adjustment associated with low frequencies requires that the density surfaces are inclined with respect to level surfaces (surfaces of equal geopotential). The intersection of these density surfaces with the sea surface marks the so-called cyclonic boundary of the current, which is the left-hand side facing downstream in the northern hemisphere.

Figure 1 schematically represents a cross-section of a geostrophically adjusted current. The view is downstream in the northern hemisphere. Several important features should be noted: The mean density (ρ) in the current is slightly less than in the juxtaposed water to the left. Typically the surface temperature (T_s) in the current ranges from 2°C to 10°C warmer and salinity (S °/₀₀) is usually 1°/₀₀ to 2°/₀₀ higher; this is due to high insolation and evaporation in the tropical source region of the Stream. In terms of density, thermal expansion is larger than saline effects, and the average density of Gulf Stream waters is less than the slope waters along the left-hand (cyclonic) side looking north. From the hydrostatic equation,

$$H = \int_{p} \frac{dp}{\rho g} \qquad (1)$$

where g is gravity and p is pressure, it is seen that the height of the sea surface (H) is larger in the current when the integration is to some deep base pressure, say p = 2000 db. That is, there is a physical rise in the sea surface of the order of 1 m when crossing the Gulf Stream.

The last feature on this figure to be noticed is the horizontal velocity profile drawn at the top. In a geostrophically balanced system, the surface velocity (V_s) is given by

$$V_s = \frac{g}{f} \frac{\partial H}{\partial x} \qquad (2)$$

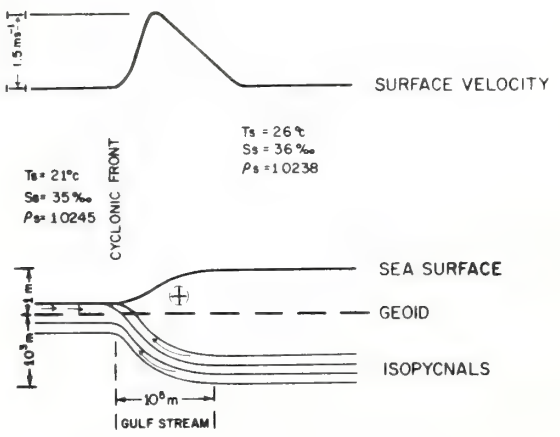
where f is the Coriolis parameter, and x is the cross-stream horizontal dimension. The horizontal velocity shear,

$\partial V_s/\partial x$, becomes a valuable feature in the study of ocean circulation from space, because it has surface manifestations. More importantly, there is some prospect of determining V_s directly from remote sensing; one example of that will be discussed later.

Associated with the horizontal motion, there appears to be a vertical circulation, which is also sketched on Figure 1.[3] Details of this motion are not fully understood, however, the effect is to have high nutrient concentrations in the euphotic zone along the cyclonic edge. These nutrients are utilized by photosynthetic organisms which are chlorophyll-bearing plants. These pigmented plant cells strongly absorb blue light, and shift the color of the sea towards the green. The phytoplankton and other associated organisms further change the optical properties of the water by increased scattering of light. Frequently, entrained sediments from the coastal regions can be detected along the current boundaries; this also modifies the optical properties of the water.[4]

When wind and waves run in opposition to the current, the local sea builds higher than when they run in the same direction. Thus the sea may be higher or lower in the current depending on the relative wind/current directions. Wave-current interaction often translates into changes in whitecap and foam distributions, changes in glitter patterns, and changes in surface wave refraction patterns.[5]

Figure 1. *Schematic cross-section sketch of a western boundary current. The flow is into the plane of the page. Note that three length scales are used: sea surface height above the geoid, depth of isopycnals below the geoid, and width of the current.*



To reiterate, when crossing into the Gulf Stream from the west, one typically encounters an increase in temperature, salinity, and perhaps sea state; the color shifts from green to deep blue, and the particulate scattering decreases; there is a rise in sea level due to steric conditions, and a sudden increase in horizontal velocity. The detection of these features of the edge of the current from spacecraft is discussed in the following sections.

INFRARED SENSING

In the 10.5 to 12.5 μm region of the electromagnetic spectrum, the ocean surface acts very nearly as a blackbody. Its radiative behavior closely follows Planck's Law with emissivities (ϵ) greater than 0.99. As a consequence of Kirchoff's Law, this requires that the source of the radiation be from the upper millimeter.[6] In the absence of whitecaps or foam, a laminar thermal boundary sublayer is postulated to exist. Heat transfer above and below this layer is dominated by turbulent processes, but molecular conduction controls the rate of heat flow through the sublayer. Infrared radiation, evaporation, and sensible heat exchange all occur within the top 0.05 mm of this sublayer, and therefore steep temperature gradients frequently exist. For this reason, "skin" temperatures of the ocean can be +0.5°C to −1.5°C different than "bulk" temperature (those measured just below the surface with a thermometer). This is of fundamental importance in determining T_s from space, but for ocean current boundary determination, the observer is looking for thermal gradients rather than for absolute temperatures.

Thermal radiation leaving the earth is modified by atmospheric absorption and emission. Clouds are opaque to the earth's radiation, which peaks at about 10μm. The radiative transfer equation for thermal radiation is

$$N_u = N_s \tau_a + \int_u^s N_a \frac{\partial \tau_a}{\partial p} dp \qquad (3)$$

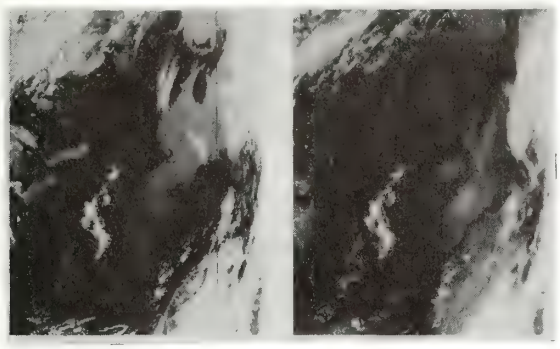
For this formulation, N is radiance, τ is transmittance, p is pressure, and the subscripts *s* and *a* are surface and atmosphere, respectively. The radiance at the top of the atmosphere (N_u) is the sum of the loss of surface radiance due to atmospheric transmittance ($N_s \tau_a$) plus the integral term which is the contribution of atmospheric radiation. Scattering is neglected in this formulation, because it is very small at these wavelengths. N and τ are tacitly assumed to be wavelength (λ) dependant.

One consequence of atmospheric transmission is that ocean surface thermal gradients are lessened at satellite altitudes. In a very moist atmosphere, an 8°C difference in T_s can be reduced to as much as 3°C in the $10.5 \leq \lambda \leq 12.5$ μm water vapor absorption window.[7] This is a fundamental restriction in infrared remote sensing of ocean current boundaries. In low latitudes where the thermal differences across oceanic fronts are small and the atmospheric moisture is high, the infrared techniques are of least value.

When radiation from the surface passes through a cloud $\tau_a \rightarrow 0$, and the spacecraft views cloud-top temperatures. Clouds are made up of liquid water, and as noted earlier, infrared photons are emitted from a very shallow depth. Low clouds often have temperatures close to the oceanic values and hence are a hindrance to proper interpretation of satellite data. Similarly, low-lying coastal lands can have near-oceanic radiances. However, in the longer visible wavelengths ($\lambda > 0.6$ μm), the reflectance of the ocean is an order of magnitude less than that of clouds and land. If both visible and infrared data are acquired si-

multaneously, then the picture elements which are cloud-free can be identified. Dual channel visible and infrared scanners aboard spacecraft are providing the data for such interpretation; an example is given in Figure 2.

Figure 2. *(A) Left hand panel is an infrared image of the east coast of North America made by the very high resolution radiometer on the NOAA-4 spacecraft.*[8] *(B) Right hand panel is the simultaneously scanned visible image of the same area. In both images, clouds appear white, the land is dark; the vertical stripe is the 33° scan angle fiducial.*



The left-hand panel of Figure 2[8] is an infrared ($10.5 \leq \lambda \leq 12.5\ \mu m$) image of the Mid-Atlantic Bight showing the coastline from Cape Hatteras to Nova Scotia. The right-hand panel is the simultaneously scanned visible ($0.6 \leq \lambda \leq 0.7\ \mu m$) image taken on 11 May 1975, at 1430 GMT. The visible image is a positive print, that is, higher radiances are lighter; the infrared is a negative print with lower radiances (i.e., cloud tops) lighter. The large feature off Nova Scotia is seen in the visible panel to be cloud, but in the infrared alone it is not clear where the cloud-sea boundary is. By comparing the images, the infrared radiance patterns are seen to be cloud-free expressions of Gulf Stream meanders, rings, eddies, and other surface thermal features. (There are some hints of these patterns in the visible image as well; this will be discussed in the section on visible imagery.) The cloud discrimination would be improved if the visible channel were in the near infrared (approximately 1 μm), where the water is more highly absorbing.

An alternate method of cloud determination involves use of the synchronous satellites that observe the earth in the same infrared band, but every 30 minutes instead of several times a day.[9,10] Using only infrared data, the 30 minute images are made into time-lapse motion pictures. Clouds have advection rates several orders of magnitude faster than ocean features, and therefore they can be readily identified against the ocean thermal background. Since the sample interval is 30 minutes, ocean features of all frequencies down to the Nyquist of 24 cpd can be studied if detectable. The spatial resolution of approximately 10 km and the mid-latitude limits of the viewing geometry are the limiting features of this sampling system.

An example of the application of the Geostationary Operational Environmental Satellite (GOES) to locating the Gulf Stream is given in Figure 3. This demonstration was made by using a 9-hour period each day on a time-available basis. Periods of cloudiness prevent all areas from being seen simultaneously, and compositing is necessary. Figure 3(A) shows the location of strong thermal fronts which are interpreted as being the cyclonic edge of the Gulf Loop Current and the Gulf Stream, the anticyclonic edge of the Stream, and the edge of rings and eddies—see also Figure 2(A). About one week is required in this demonstration and the current must be considered quasi-stationary. This is not exactly true,[10] and an improvement would be made if the data were available 24 hours a day.[11]

Figure 3. *(A) Upper panel is a composite location of strong gradients in sea surface temperature from GOES during the week 3-9 March 1976. Numbers on the figure define the date that the segment of the thermal front was observed (B) lower panel is a six-week composite showing the movement of the thermal front associated with the Gulf Stream; Figure 3(A) is one of the inputs.*[11]

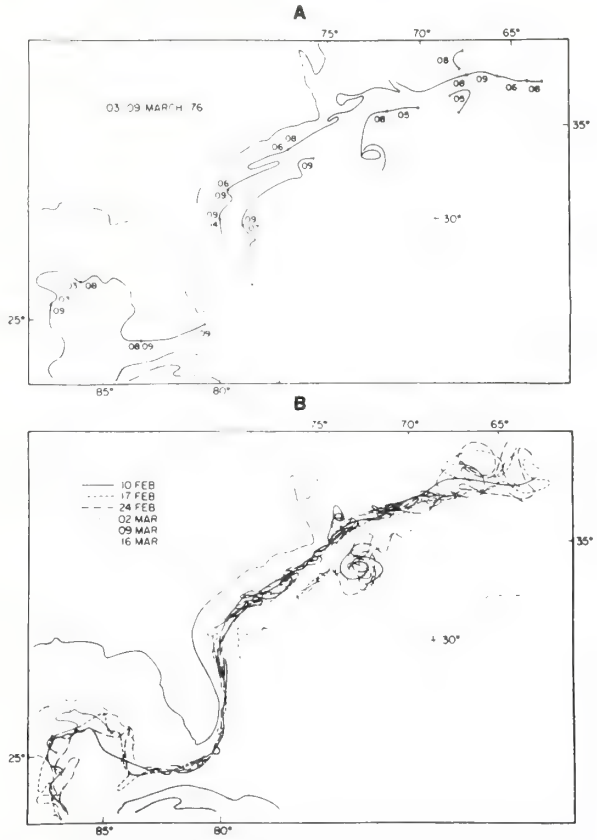


Figure 3(B) is a six-week compilation of which Figure 3(A) is one. The low-frequency growth of the Gulf Loop Current can be seen, as can meanders in the Stream, which appear to grow larger as a function of the downstream distance from the Straits of Florida. The large eddy at 33°N, 73°W appears to be drifting southwest. Long-term studies such as this (2-3 years or longer) are planned using ship data as surface truth.

Infrared satellite data are processed primarily for meteorological purposes. Many ocean features are not emphasized due to the match in the gray scale range of the film and the radiance range of the sea, land, and clouds. Improved ocean radiance resolution can be obtained by specially processing the data in such a manner that only the oceanic range is matched to the gray scale range. When this type of processing is done, most clouds saturate the film and appear white, and, as in the case of Figure 2 (A), the land and very warm water appear black. A specially designated enhancement device for the synchronous satellites to accomplish this is being considered, so film loop products for the ocean community will become available.

VISIBLE SENSING

Detection of ocean currents in the visible wavelengths ($0.4 \leq \lambda \leq 0.7\mu m$) depends on the change of ocean color and the change of sea state associated with the boundary. The spectral radiance in a finite wavelength interval ($\Delta\lambda$) at the top of the atmosphere in the visible region is given by

$$N_o(\theta, \phi) = N_a + \gamma N_s + \alpha N_d \qquad (4)$$

where N_a is the contribution of the atmosphere alone (mostly Rayleigh scattering), N_s is the contribution at the surface due to reflection from the surface, N_d is the diffuse radiance at the surface due to photons that have penetrated the ocean surface and are backscattered into the atmosphere, γ and α are atmospheric transmittance factors for N_s and N_d respectively; θ and ϕ are the nadir angle and the azimuth angle. For $\Delta\lambda$ bandwidths such as on LANDSAT or NOAA-4, $\alpha = \gamma$ in general. Changes in sea state, by which is meant changes in whitecaps, foam, glitter, etc., enter the equation only through the N_s term. Similarly, changes in the optical properties of the water itself, which provide information on the absorption and scattering of light by particles in the water are represented by N_d. The atmospheric term defines the effects of scattering, and absorption by clouds; when a cloud is in the field of view, $\delta = \gamma = 0$. For a cloud-free path, $N_a(\Delta\lambda; \theta, \phi)$ is small compared to the reflected radiance and its effect is usually neglected for ocean current boundary determination in the $0.6 \leq \Delta\lambda \leq 0.7\mu m$ interval.

Use of the second term on the right-hand side of equation 4 in locating ocean currents, is illustrated in Figure 2(B). In this VHRR visible image, $\theta = 0°$ is located near the eastern shore of Lake Ontario, and $\theta = 33°$ is along the vertical fiducial on the right-hand side. The low radiance from the Great Lakes is in contrast to the much higher values from the Gulf Stream region east of the Delmarva Peninsula. Sunglint causes the higher surface radiance from the Mid-Atlantic Bight. Comparing Figures 2(A) and (B), the edge of the Gulf Stream and the large warm core eddy are seen in both the visible and infrared images.

The explanation involves both the N_d term in equation 4 and the viewing geometry. Winds over the current were 3-7 m sec^{-1} from the northeast. As the sea generated by winds of this magnitude interact with the current, the waves steepen and form whitecaps.[12] The greatly increased wave slopes increases the diffusion of the solar beam, which reduces the observed radiance in the current as compared to that of the Slope Water [13] However, had the viewing geometry excluded specular return, the current might still have been detected by reflection of skylight from the whitecaps. In this case the current would have a higher radiance than the juxtaposed Slope Water if there were more whitecaps in the current. This latter effect has been demonstrated from LANDSAT[14] and will be an important phenomenon to exploit with the Coastal Zone Color Scanner to be flown on Nimbus G (whose observation geometry is designed to avoid sunglint).

The spectrum of diffuse radiation (N_d) is a complex function of scattering and absorption. In a simple single-scattering model, the independent variables were shown to be the total attenuation coefficient, the total scattering coefficient, and the fraction of backscattered light.[14] Each variable is also wavelength dependent, so that an infinite variety of optical conditions can combine to produce the same N_d. In the case of current boundary determinations, the highly productive water alongside the Gulf Stream cyclonic front is often higher in pigmented plant cells as well as in particulate matter. The net result is to shift the peak of the upwelling radiance spectrum toward longer wavelengths, that is towards green colors; at the same time, the radiant intensity increases due to increased scattering. When these conditions hold, the water along the cyclonic side of the stream will have a higher radiance in the absence of sea state effects. In Figure 2 (B) a boundary apparently due to differing N_d can be seen in Lake Erie. While it is unknown whether this particular boundary represents a current edge, the optical effect is similar to that used to locate the Gulf Loop Current.[4]

The interpretation is difficult here because only two channels of data are available. The $0.6 \leq \lambda \leq 0.7\ \mu m$ channel is a good choice for visible radiance and as noted earlier, was the most useful in applying LANDSAT data to the marine environment. However, since it is a valuable channel for optical oceanography, it is not the best spectral interval for cloud and sea state discrimination. Experience with LANDSAT and the experimental scanner on SKYLAB has shown that $0.9 \leq \lambda \leq 1.1\ \mu m$ is the optimum band for this purpose. Incorporation of this wavelength interval in oceanographic multispectral imagers (i.e., SEASAT) is strongly recommended in order to overcome the ambiguities of oceanic interpretation in the present system.

MICROWAVE SENSING

Microwave sensing may be considered in two ways: active systems, by which is meant radar type devices such as altimeters, scatterometers, and imaging radars, and passive or radiometer-type devices that sense the emitted microwave energy in the same sense as infrared or visible radiometers do. Many features of the edge of a current (see Figure 1) can be identified in microwave data, including sea state changes, temperature and salinity changes, the physical shape of the sea surface, and actual current speeds.[15]

Passive microwave energy is sensitive to changes in surface temperature, salinity, roughness, and foam coverage and to the presence of sea ice.[16] The transfer of radiation follows Equation 3, except that the N_λ term is a function of polarization as well as nadir angle and wavelength. Since foam transmits energy from below, transmission (τ), emissivity (ϵ), and reflectivity (ρ) all contribute to N_λ as follows:

$$N_\lambda = \tau_\lambda N_i + \epsilon_\lambda N_{BB} + \rho_\lambda N_a \qquad (5)$$

The subscripts in this expression denote the blackbody radiance (BB), the incident radiation from the atmosphere (a), and the incident radiation from the ocean (i) on the foam. The atmosphere is opaque to microwave energy at wavelengths below 1 cm due to water vapor, but between $1 \leq \lambda \leq 100$ cm (30–0.3GHz) the atmospheric transmissivity is very close to 1.0.

Measurements of thermodynamic temperature relate to N_{BB} by Planck's Law. N_{BB} can be approximated by the Rayleigh-Jeans Law at microwave wavelengths, and this is proportional to $T_\lambda \lambda^{-4}$. This simplifies the calculations in that the radiance is directly proportional to the first power of the temperature. Salinity affects ϵ, and absolute measurements by aircraft of the order of 1‰–2‰ are being reported.[17] Salinity-determining techniques measure emissivity at 21 cm and require the ancillary measurement of temperature. Salinity effects on the dielectric constant of sea water are small at $\lambda = 8$ cm. Thus a two-channel microwave sensor can provide salinity and temperature measurements in the absence of foam coverage ($\rho = 0$).

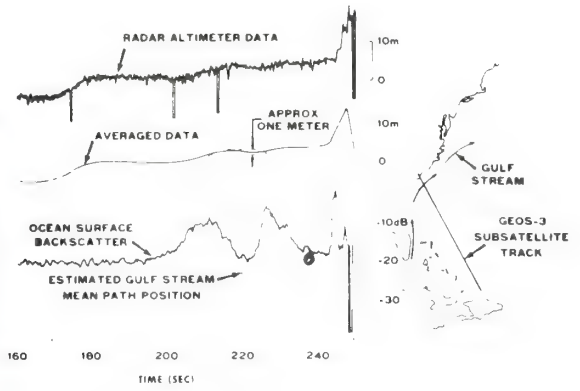
Figure 4. *Side looking airborne radar image of the ocean in the offing of Cape Hatteras.[18] Plaid pattern is an artifact of the instrument. The two diagonal streaks through the surface gravity wave patterns are associated with a strong ΔT_s. (Surface winds were 210° at 7 m. sec $^{-1}$). Horizontal distance across the image is ~20 km.*



Sea state effects on an imaging radar are shown in Figure 4. These data from a side-looking airborne radar[18] display two narrow lineations which were shown by simultaneous infrared thermometers to be associated with a large temperature gradient in the Gulf Stream front region off Cape Hatteras. These lineations are changes in the radar backscattering cross-section which suggest changes in sea state associated with (but not necessarily caused by changes in temperature). This is one application of active radar imaging in locating boundaries.

Another active radar system is the precision altimeter. It provides an all-weather suborbital measure of the topography of the sea surface. If the geoid is known in the area of interest, and tidal effects are eliminated, the surface topography can be used to estimate the absolute pressure gradients at the sea surface (see again Figure 1). Absolute pressure gradients will provide the oceanographer with a measure of surface currents (only) which can be inferred from Equation 2.

Figure 5. *GEOS-3 cross-section of the Gulf Stream off South Carolina. The estimated Gulf Stream mean path position on the satellite data (left-hand panel) corresponds to the location of the mean Gulf Stream on the inset map. Data were observed at 0955 GMT on 6 May 1975; data are received and pre-processed at the NASA Wallops Flight Center*



An example of altimetric data observed in the Gulf Stream region is given in Figure 5. The GEOS-3 sub-satellite track is from southeast to northwest. The upper profile is the radar altimeter profile (in meters), the middle profile is a smoothed plot of the altimeter, and the lower profile is the output of the automatic gain control (AGC) which is a function of the ocean surface backscatter (in dB). Time scale is arbitrarily set so that the 250 second tick mark is just inland of the Carolina coast. The estimated Gulf Stream mean path position on the data profile corresponds to the Gulf Stream position on the inset sketch. Spacecraft speed over the earth's surface is approximate'y 7 km sec^{-1}.

The large inverted "v" on the averaged altimeter data is caused by land. Two features on this profile are related to sea level: the 1 m change near 220 sec and the 3-4 m change near 175 sec. The former is near the mean position of the Gulf Stream at the continental shelf break, and the latter is near the continental rise off the Blake Plateau. Both features are observed in the gravimetric grid and are the correct sign. The one-meter rise in sea level near the mean position of the stream is of the opposite sign to what would be observed if the current alone were transited (see again Figure 1). That is, without *a priori* knowledge of the geoid, a single altimeter profile is of no value in current boundary location or surface velocity determination since

$$V_s \propto \frac{\Delta (\text{sea level - geoid})}{\Delta x} \qquad (6)$$

This requires that the accuracy to which the geoid is known must be commensurate with the requirement for ocean dynamics. Consider the ±10 cm accuracy of a radar altimeter such as planned for SEASAT. Using Equation 2 and assuming that H = ±10 cm, x = 10^7 cm (i.e., the width of the Gulf Stream), the following errors in V_s are calculated for several latitudes (ϕ):

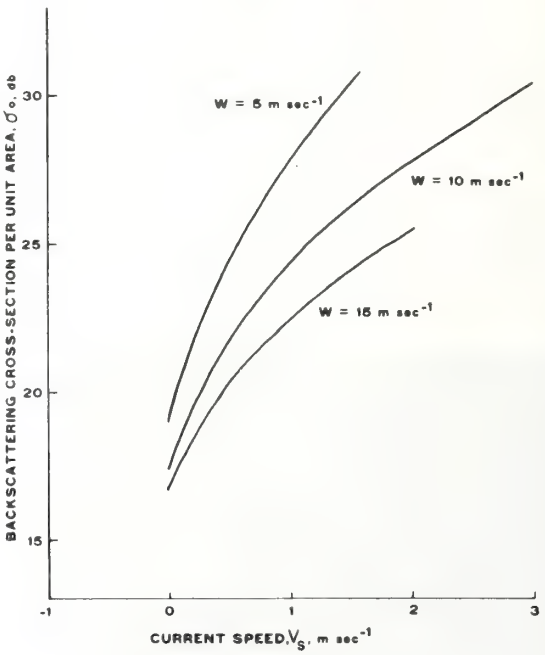
ϕ	V_s
50°	± 8.8 cm sec^{-1}
40°	± 10.5 cm sec^{-1}
30°	± 13.5 cm sec^{-1}
20°	± 19.7 cm sec^{-1}
10°	± 38.8 cm sec^{-1}

As can be seen, at the Gulf Stream latitudes (ϕ = 25° to 45°), the error is 10 per cent of the geostrophic current speed. To these errors, the inaccuracies in the geoid must be added (Equation 6). Other ocean currents have typical speeds of 15-20 cm sec^{-1}, and the ± 10 cm error can be greater than a factor of two of the current speed. One may argue that if a large number of observations were taken, ± 10 cm would lead to a good absolute determination. This is only valid for a static system unlike the ocean. In order to observe barotropic motions in the Gulf Stream at inertial and tidal frequencies,[1] many radar altimeters in orbit at the same time would be required to begin getting the coverage needed for such averaging.

Further evidence of the current can be seen in the output of the altimeter's automatic gain control (AGC) which is a function of the ocean surface backscatter (Figure 5). If there is a change in sea state associated with the Gulf Stream (as is often the case), there is an expected change in the returned signal strength. Surface winds were from the east at 2-3 m sec^{-1} when the observations were made. Mean level of the AGC output is about −20 db, with two peaks of −10 db bracketing the estimated Gulf Stream mean path position. The peaks represent areas of near specular return, perhaps zones of calm water such as those seen in Figure 2(B) south of Nova Scotia. If the Gulf Stream were flowing through such a zone, capillary waves in the current would appear because an apparent wind vector is against the flow. This is one explanation of such a change in the ocean surface backscatter signal and exemplifies the application of radar altimeter data to ocean current boundary determination.

Studies of the backscattering from radars show promise for application to many problems in radio oceanography.[19] A particularly interesting application is that of current speed determination.[15] Figure 6 is a plot of current speed (V_s) as a function of radar backscattering cross-section per unit area from a near normal incidence beam, for several wind speeds (W). If the wind velocity vector can be determined through one or several independent techniques,[9, 10] then V_s can be inferred. Alternatively, if V_s can be determined by an altimeter or a Lagrangian drifter, a refinement on W is possible. These and other microwave[20] techniques are a new and exciting horizon for remote sensing.

Figure 6. *Plot of current speed versus radar backscattering as a function of different wind speeds.*[15] *Gulf Stream current speeds are typically 1-2 m. sec* $^{-1}$ *(see also Figure 1).*



PHOTOGRAPHIC SENSING

Man's role as an observer in space was appreciated from the earlier missions, but none so fully as SKYLAB. Astronauts were for the first time given training in observing and photographing ocean features from space. This program was carried on to the recent Apollo-Soyuz Test Project and hopefully will be strengthened in the future. Many ocean circulation features such as confluences, upwelling, eddies, and other patterns that reflect currents were observed and photographed.[21] These data are providing new insight into the details of the ocean at a spatial resolution unavailable by other imaging systems.

An example of such detail is given in Figure 7 which is a hand-held photograph of turbulent mixing in the confluence region of the Falkland and Brazil currents off South America.[22] These currents are a southern hemisphere analog of the Labrador Current/Gulf Stream system in the North Atlantic. The confluence was first seen by the astronauts near the Brazil/Uruguay border and was followed for over 1000 km to sea. The color boundary showed very little mixing across the front, unlike the eddies shown in Figure 2. The eddy in Figure 7 can be seen because plankton or suspended materials cause color variations in the sea (N_d in Equation 4). The eddy appears to be anticyclonic and is possibly caused by the velocity shear along the Falkland Current.

Figure 7. *Hand-held 35 mm photograph of eddies and other turbulent expressions of the boundary of the Falkland Current taken from SKYLAB.[22] Details have been photographically enhanced by laboratory techniques. The eddy is estimated to be 60 km in diameter*



Photographic details like this are usually chance happenings. In the case of SKYLAB, however, the spacecraft transited the area several times on several consecutive days, and features such as those in Figure 7 were not only viewed several times, but they were studied with the many devices in the Earth Resources Experiment Package.

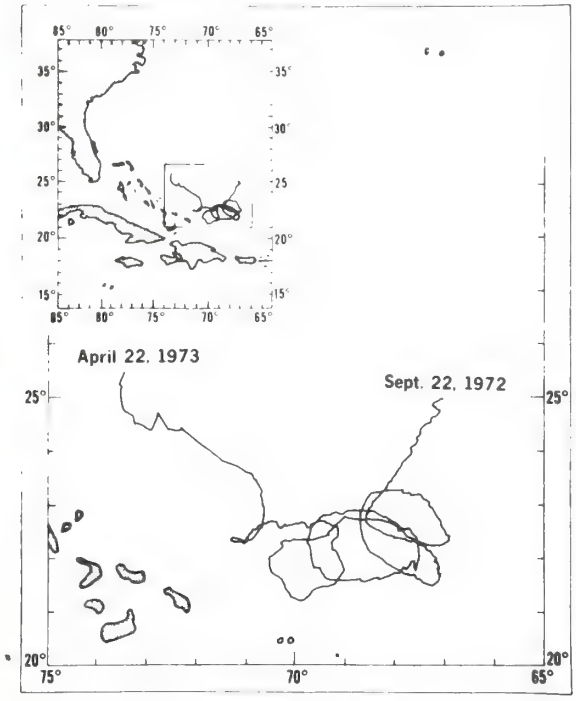
An important reason for the successful observations was the real-time communications between the crew and oceanographers at mission control. Future manned earth observing missions must exploit this communications feedback even further, so that ships and aircraft can conduct detailed studies into these interesting new-found features of the ocean's circulation.

DISCUSSION

Several techniques have been described that offer useful application to the study of ocean circulation from space. Each has advantages and disadvantages. The very high spatial resolution of visible and infrared sensors is not practical at microwave frequencies (except for synthetic apperture radars) because of limitations in antenna size. On the other hand, the microwave devices offer all-weather sensing capability but at reduced resolution.

Certain oceanic circulation features are not readily detected by their radiative properties. Under these circumstances, satellite tracking of free-drifting buoys is an important auxiliary technique. An example of interest to the problem of ocean eddies is given in Figure 8.[23] Circulation patterns in the southwestern Sargasso Sea are difficult to observe with currently available satellite data. However, with these free-drifting (quasi-Lagrangian) buoys, patterns of cyclonic and anticyclonic rotation with translation have been discovered. This very important capability must be incorporated into any ocean oriented spacecraft program.

Figure 8. *Track of free-drifting buoys in the southwestern Sargasso Sea as located by the French EOLE system.[23] Note there are two scales of motion. cyclonic motion associated with 150 km diameter eddies, and anticyclonic translation with 1000 km diameters.*



The sensing of ocean currents should be approached with multispectral techniques using visible, infrared and microwave observations supplemented by surface information from moored as well as free-drifting buoys. This will

not only provide the best opportunity to observe the feature, but will also increase the degrees-of-freedom in an automated identification scheme. One such unexplored scheme is the use of Fourier transforms in image processing for current boundary location; the higher harmonics at discontinuities being readily identified. The need in this area is not so much for new processing techniques, as it is for understanding the physical significance of various data manipulations.

Experience to date in using spacecraft measurements for studying ocean currents has identified several subjects which require special attention: Visible-Infrared multispectral scanners must have a channel near 1 μm to maximize contrast between clouds and oceanic radiances; SEASAT is an obvious choice to capitalize on this requirement. The radiance range in a particular bandwidth for ocean purposes, is quite different from meteorological or earth resources requirements; where special instruments such as to be on NIMBUS-G are not flown, ocean-tuned image display devices must be provided. Chance visual observations by SHUTTLE crews will undoubtedly lead to new discoveries about the ocean; the crews must be trained and provided with equipment that unequivocally records (in space and time) these sightings.[24] Orbit determinations on the GEOS-3 altimeter satellite will have to be improved by an order of magnitude before the data will be useful for ocean tide determinations, and two orders of magnitude for application to dynamical oceanography. Finally, there is the need to investigate the relationships between point shipboard measurements and satellite observations, particularly for the complex problems encountered in optical oceanography. Clearly, progress for satellite oceanography requires the broadest range of scientific talents if these new observation tools are to be fully exploited.

ACKNOWLEDGMENTS

The author wishes to express his appreciation to Drs. E. P. McClain and J. L. Mueller for their most helpful critical review, and to his colleagues at AOML for assistance in preparing this paper, particularly Dr. D. V. Hansen with whom there have been many fruitful discussions.

REFERENCES

[1] Duing, W. (1975). Synoptic Studies of Transients in the Florida Current, *J. Mar. Res., 33*(1), pp. 53-73.

[2] Hansen, D. V. (1970). Gulf Stream Meanders between Cape Hatteras and the Grand Banks. *Deep Sea Res., 17*, pp. 495-511.

[3] Neumann, G. and W. J. Pierson, Jr. (1966). *Principles of Physical Oceanography*, Prentice-Hall, Englewood Cliffs, N.J., pp. 224-228.

[4] Maul, G. A. and H. R. Gordon (1975). On the Use of the Earth Resources Technology Satellite (LANDSAT-1) in Optical Oceanography, *Remote Sensing of Environment, 4*, pp. 95-128.

[5] Teague, W. J. (1974). Refraction of Surface Gravity Waves in an Eddy, Scientific Report U. of Miami, Coral Gables, Fla., UM-RSMAS-No. 74034, 94 pgs.

[6] Ewing, G. and E. D. McAlister (1960). On the thermal Boundary Layer of the Ocean, *Science, 131* pp. 1374-1376.
McAlister, E. D. and W. McLeish (1969). Heat Transfer in the Top Millimeter of the Ocean. *J. Geophys. Res. 74* (13), pp. 3408-3414.

[7] Maul, G. A. and M. Sidran (1973). Atmospheric Effects on Ocean Surface and Temperature Sensing from the NOAA Satellite Scanning Radiometer, *J. Geophys. Res.*, 78(12), pp. 1909-1916.

[8] Data from the NOAA-4 meteorological satellite provided by H. M. Byrne (NOAA-AOML).

[9] Maul, G. A. and S. R. Baig (1975). A New Technique for Observing Mid-latitude Ocean Currents from Space, *Proceedings, Amer. Soc. Photogram.*, Wash. D.C., pp. 713-716.

[10] Legeckis, R. (1975). Application of Synchronous Meteorological Satellite Data to the Study of Time Dependent Sea Surface Temperature Changes Along the Boundary of the Gulf Stream, *Geophys. Res. Ltrs., 2*(10), pp. 435-438.

[11] Maul, G. A. and S. R. Baig (1976). Satellite Measurements of Gulf Stream Meanders. "Polymode News," No. 7 (unpublished manuscript).

[12] Ross, D. B. and V. Cordone (1974). Observations of Oceanic Whitecaps and their Relation to Remote Measurements of Surface Wind Speed., *J. Geophys. Res.*, 79(3), pp. 444-452.

[13] Strong, A. E. and R. J. DeRycke, (1973) Ocean Current Monitoring Employing a New Satellite Sensing Technique, *Science*, 181, pp. 482-484.

[14] Gordon, H. R. (1973). A Simple Calculation of the Diffuse Reflectance of the Ocean., *Appl. Opt., 12*, pp. 2804-2805.

[15] Parsons, C. and G. S. Brown (1976). Remote Sensing of Currents Using Backscattering Cross-Section Measurements by a Satellite Altimeter. (Submitted to *J. Geophys. Res.*)

[16] Hanson, K. J. (1972). Remote Sensing of the Ocean In: *Remote Sensing of the Troposphere*, V. E. Derr, ed., U.S. Gov't. Printing Office, Washington, D.C., pp. 22-1 to 22-56.

[17] Thomann, C. G. (1975). Remote Sensing of Salinity. *Proceedings of the NASA Earth Resources Survey Symposium*, TM X-58168, pp. 2099-2126.

[18] Data provided by D. B. Ross, NOAA-AOML.

[19] Eisenberg, R. P. (1974). Practical Considerations to the Use of Microwave Sensing from Space Platforms. In: *Remote Sensing Applied to Energy-Related Problems*. T. N. Veziroglu, ed. U. of Miami, Coral Gables, Fla., pp. S3-29 to S3-41.

[20] Molinari, R. L. (1973). Buoy Tracking of Ocean Currents. In: *Advances in the Astronautical Sciences*, F. S. Johnson, ed., Amer. Astron. Soc., Tarzana, Calif. pp. 431-444.

[21] Kaltenbach, J. L., W. B. Lenoir, M. C. McEwen, R. A. Weitenhagen, and V. R. Wilmarth, eds. (1974). SKYLAB-4 visual observations project report, NASA, JSC-09053, TM X-58142, Houston, Texas, 250 pgs.

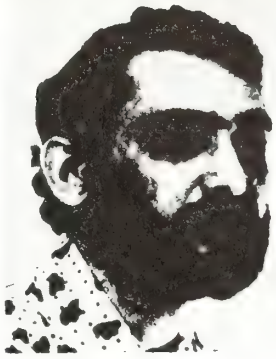
[22] Johnson, W. R. and D. R. Norris (1976). A Multispectral

Analysis of the Interface between the Brazil and Falkland Currents from SKYLAB. (Submitted to *Remote Sens. of Environ.*).

[23] Hansen, D. V. (1974). Text of presentation to AIAA Committee on Marine Systems and Technologies sponsored Symposium on Free-Drifting Buoys, NASA-LRC, Hampton, Va.

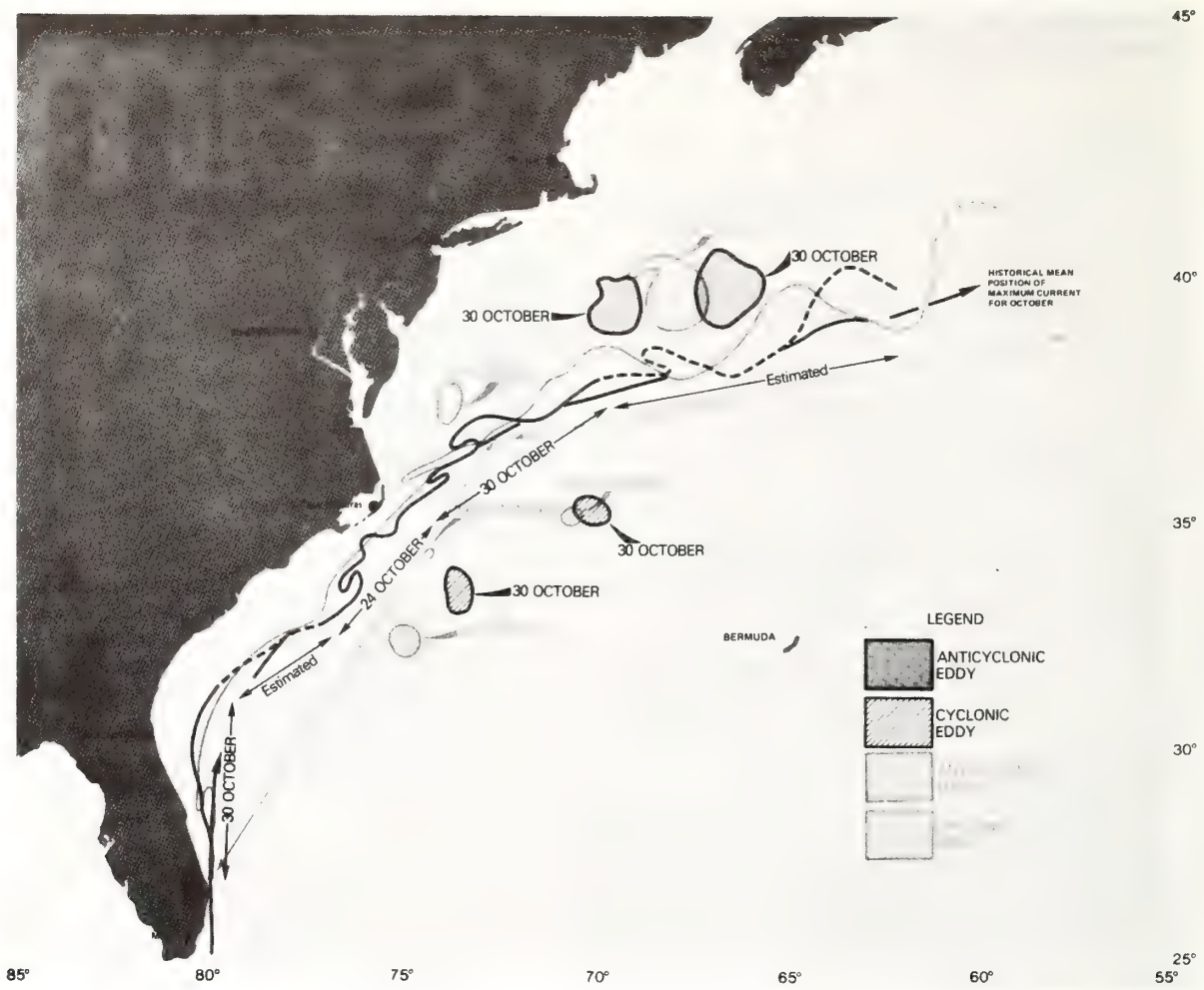
Molinari, R. L. (1973). Buoy Tracking of Ocean Currents. In: Advances in the Astronautical Series, Vol. 30, AAS, Tarzana, Ca., pp. 431-444.

[24] SKYLAB Explores the Earth (1977). NASA SP-380, in press.



George A. Maul is a physical oceanographer with NOAA's Atlantic Oceanographic and Meteorological Laboratories in Miami, Florida. He earned his B.S. degree from the State University of New York Maritime College, and his Ph.D. from the University of Miami, where he teaches a graduate course in satellite oceanography. Dr. Maul's current research interests include ocean remote sensing, radiative transfer, Gulf Stream dynamics and deep-sea tides. he has been involved in the training of the last three astronaut crews and served on the Apollo-Soyuz Test Project team. Dr. Maul is a member of the American Geophysical Union and the Optical Society of America.

Gulfstream 11, No. 10, 2-7.



Gulf Stream Position

October 1976

The northern edge is shown in blue for the beginning of the month and in orange for the end of the month. The edge was located by the strong sea surface temperature gradient north of the uniform warm core or by the 15° C isotherm at 200 meters. Solid and broken lines indicate recorded and estimated positions respectively. The position of the maximum current was calculated from H.O. Publication 571 (out of print).

Excessive cloudiness throughout the month of October made location of the Gulf Stream from satellite imagery quite difficult. Segments of the Stream's Western Wall are drawn from NOAA-5 Satellite photographs of 24 and 30 October. The positions east of 70°W, and between 77° and 80°W, are estimated largely from sea surface temperature reports from ships at sea. The area south of Cape Fear was particularly complex, with mixing of warm Gulf Stream water with Slope water behind(west of) this line.

The boundaries of the anticyclonic eddy centered near 39°45'N, 66°30'W were estimated through broken clouds; the eddy probably formed from a meander at that position earlier in the month. The anticyclonic eddy centered near 39°30'N, 69°30'W on 30 October, has moved westward from its end-of-September position at 39°40'N, 67°40'W. The cyclonic eddy at 35°15', 70°00'W is probably the same eddy seen near the end of September at 35°00'N, 70°30'W. The remaining cyclonic eddy is centered at 33°30'N, 73°30'W.

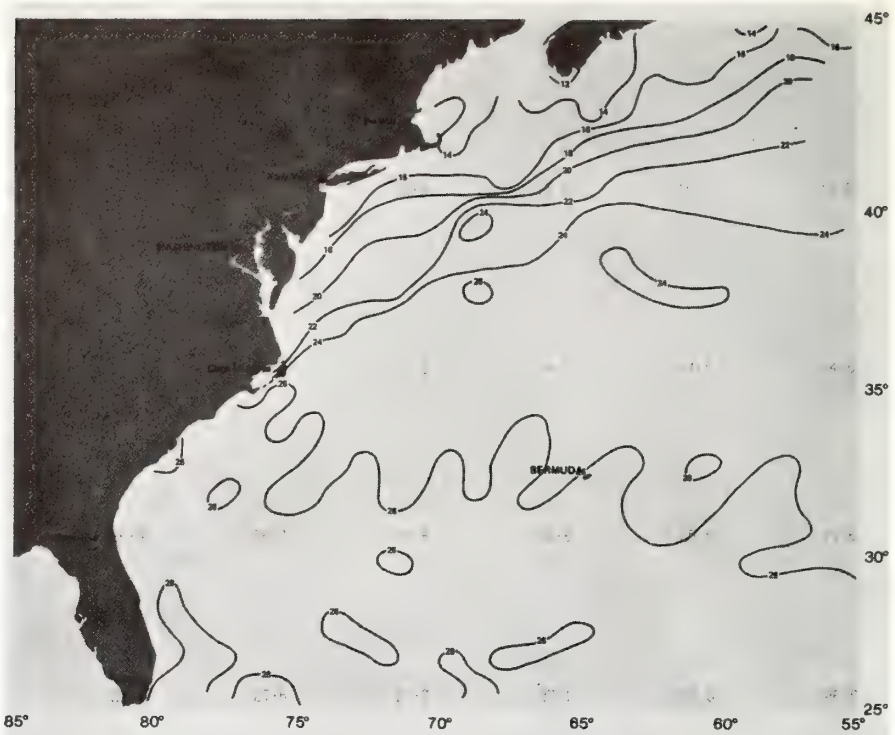

Selected Bathythermograms
October 1976
This chart shows typical near-surface thermal structure in Gulf Stream and surrounding waters. Number in lower right corner of each trace indicates date.
BERMUDA
45°
40°
35°
30°
25°
85°
80°
75°
70°
65°
60°
55°
a
b
c
d
e
f
g
h
i
j
k
l
m
n
o
p
q
r
s
t
0 m
100
200
300
400
500
0°
10°
20°
30°
4
5
5
7
9
10
10
11
11
12
12
17
19
19
19
21
22
22
23
27

3

Mean Sea Surface Temperature (° C)

October 1976

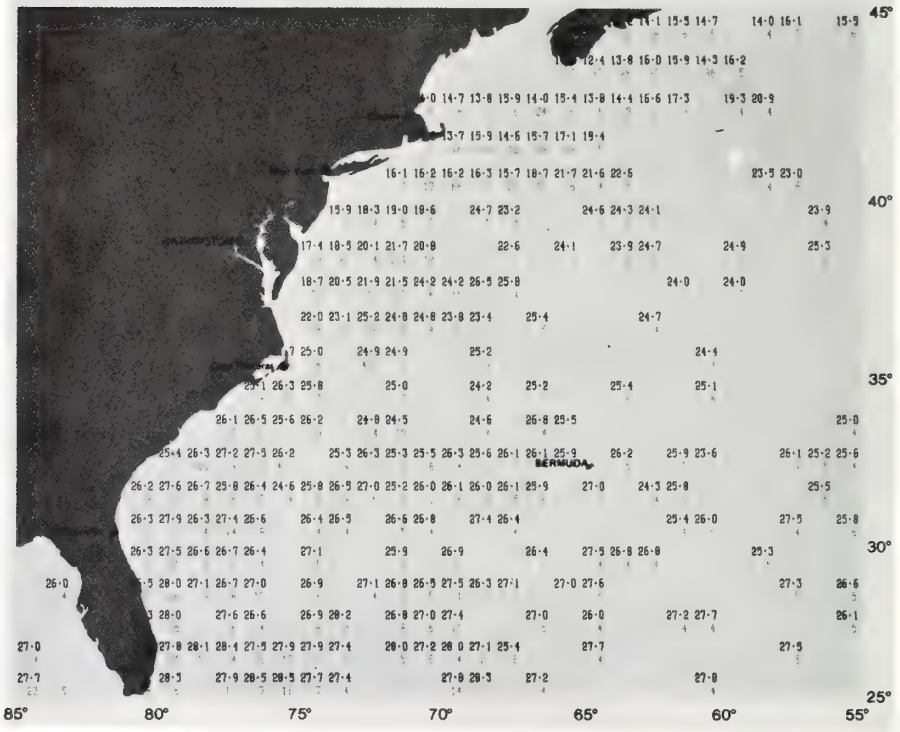
Isotherms are based on mean temperatures computed for each 1-degree quadrangle. Blue numerals indicate mean temperature by 5-degree quadrangles.



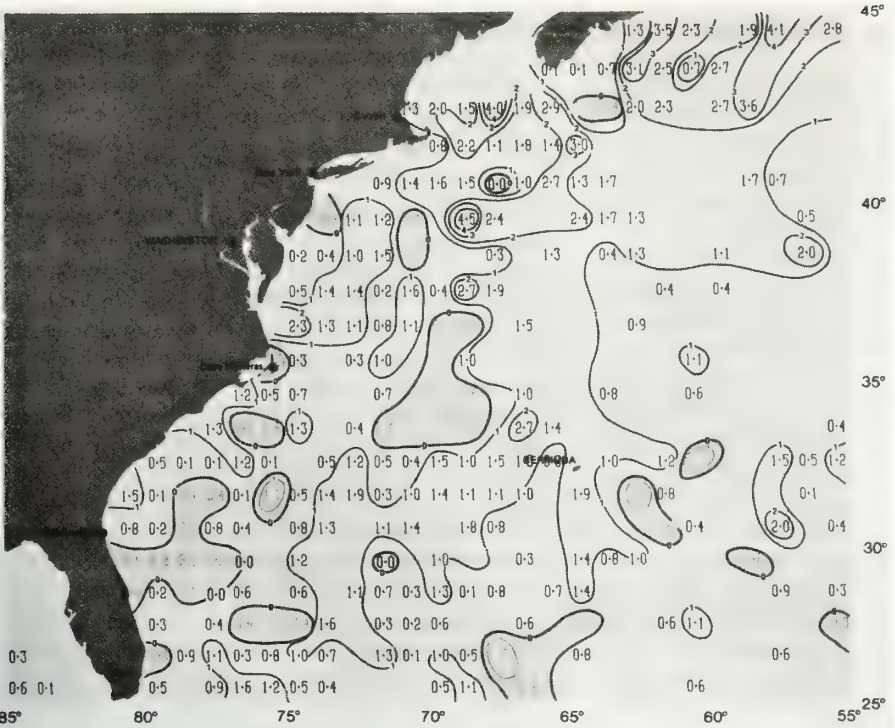
Surface Temperature Observations (° C)

October 1976

This chart is the data base for the above chart and shows mean temperature and frequency of observations for each 1-degree quadrangle. Values are shown if at least four observations were available.



4



Sea Surface Temperature Anomaly (° C)

October 1976

The anomaly is the difference between the monthly mean sea surface temperature and the historical (approximately 100 years) mean monthly value. Orange numerals indicate monthly means greater than the historical mean; blue numerals indicate monthly means smaller than the historical mean. Values were calculated if at least four observations were available.



Monthly Sea Surface Temperature Change (° C)

October 1976

Orange numerals indicate present monthly values higher than the previous month; blue numerals indicate values lower than the previous month. Values were calculated if at least four observations were available for each month.

Variability in the Gulf Stream System

In the past decade, there has been significant effort on the part of oceanographers to study time-dependent motions in the sea. Changes in the position and strength of currents within the Gulf Stream System, for example, have time scales with periods from days to years. From what is now known, parts of this system appear to have different dominate time periods as well as different scales of spatial variability. Figure 1 is a composite of information illustrating the variability in geographic position of the current from the Yucatan Strait, where the flow is first identifiable as a western boundary current , to beyond the Grand Banks, where it is known as the North Atlantic Drift.

Data for the Gulf Loop Current, Florida Current, and the Gulf Stream (Cape Hatteras to Grand Banks), are drawn from different sources, and are therefore not strictly comparable; the majority of variation for each current is, however, roughly represented by the data set for that area. The lines drawn in Figure 1 represent varying positions of an observed parameter which defines the coastward edge of the current for each area. Ship data were observed by bathythermograph or towed thermister; the satellite-observed boundary was derived from infrared sensing of the top millimeter of the water surface.

In the Gulf of Mexico, each line is an observed locus of the 22°C isotherm at 100 meters depth. This isotherm defines the coastward boundary of the main loop-current flow, which is found at an average of 14 km to the right of the satellite-sensible edge of the current facing downstream (Maul, 1975). The subsurface temperature observations were made (every 36 days, over 14 months, in 1972-73) from NOAA ships. Northward penetration of flow in the Gulf generally follows an annual cycle with maximum latitudinal extension in summer and a minimum in winter, but much year-to year variability is observed. The change from maximum to minimum northward extent occurs quite rapidly, apparently through the formation and breaking away of a large (typical diameter, 400km) anticyclonic eddy.

In the region from the Straits of Florida to Cape Hatteras, the data comprise infrared observations by the Geostationary Operational Environmental Satellite (Maul and Baig, 1976). These lines are of the extreme lefthand edge of the Stream -- defined by the strong thermal gradient at the sea surface -- and cover a 6-week period in the spring of 1976. Although the time represented by this data is short, a general study of GOES photos from the area shows that this degree of spatial variability is representative of the annual range. Minimal variability in current locations occurs in the Straits of Florida and near Cape Hatteras; maximum variability is seen off South Carolina. The GOES satellite data (photo imagery of the area every 30 minutes) often show meanders with 100-km wavelengths and periods of a week, not only in this region, but also superimposed on the main flow features in the Gulf of Mexico and off the Grand Banks.

From Cape Hatteras to the Grand Banks, each line represents a monthly locus of the 15°C isotherm at 200 meters depth (Hansen, 1970). This analysis comprises nine consecutive monthly positions drawn from data taken in 1965-66 by a Coast and Geodetic Survey ship. The statistical correlation between the 15°C isotherm at 200 meters depth, and the satellite-sensed edge of the Gulf Stream in this area, is quite similar to that of the 22°C line at 100 meters used for the Gulf of Mexico analysis; the average separation between surface and subsurface boundaries here is 15 km (Hansen and Maul, 1970). East of Cape Hatteras, the Gulf Stream seems to behave as a spatially-growing wave with periods of 1 to 2 months and wavelengths on the order of 300 km. About five to eight times a year, meanders separate from the current and form cyclonic (cold core) or anticyclonic (warm core) eddies known as Gulf Stream rings. These rings generally appear, on long-term tracking, to drift west or southwestward. Remnants of anticyclonic rings can be found throughout the New England Slope Water, and those of the cyclonic variety are found in the southwestern Sargasso Sea.

The presentation in Figure 1 is meant as a guide to the degree of spatial nonuniformity one can expect to find. New measurements by both ship and satellite reveal even more variability than outlined in the previous paragraphs: comlex patterns of mixing are being observed all along the periphery of the Stream; small eddies have been photographed that appear to be in the current itself; mesoscale eddies are evidently common throughout the Sargasso Sea. These observations suggest that the entire ocean is dominated by change with a broad spectrum of temporal and spatial scales. Indeed the mean picture of the oceans -- the atlas image -- may be largely a figment of our mathematics; one should not expect to encounter mean conditions at any given time.

George A. Maul NOAA-AOML
Miami, Florida

References

Hansen, D.V., 1970. Gulf Stream meanders between Cape Hatteras and the Grand Banks; *Deep Sea Research* 17:495-511.

Hansen, D.V., and G.A. Maul, 1970. A note on the use of sea surface temperature for observing ocean currents; *Remote Sensing of Environment* 1: 161-164.

Maul, G.A., 1975. An evaluation of the use of the Earth Resources Technology Satellite for observing ocean current boundaries in the Gulf Stream Systems; NOAA TR: ERL335-AOML 18, U.S. Gov't Printing Office, Washington, D.C., 125pp.

Maul, G.A., and S.R. Baig, 1976. Satellite measurements of Gulf Stream meanders; *Polymode News,* no. 7; unpublished manuscript.

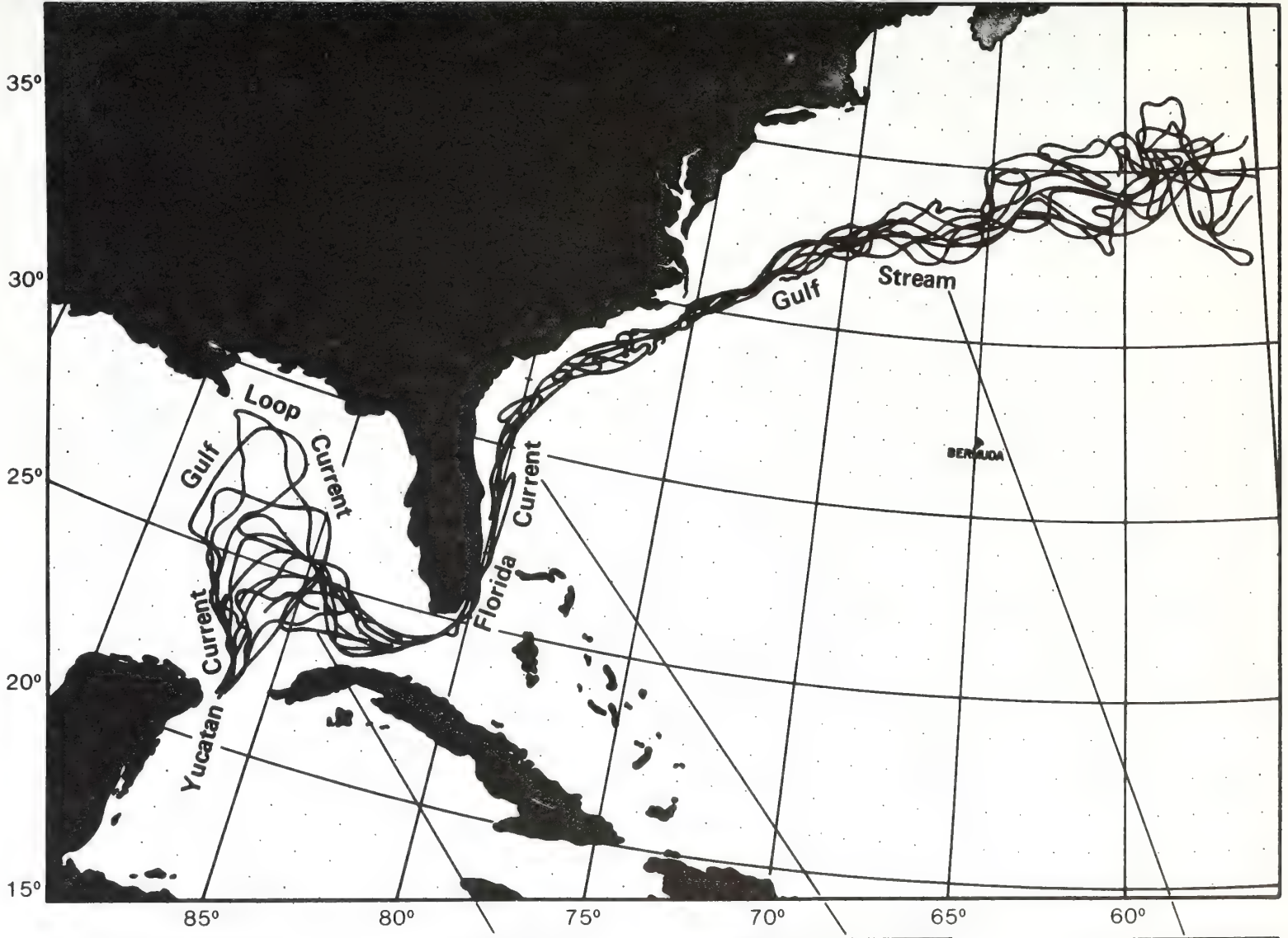


Figure 1. Variable position of currents in Gulf Stream system. Lines show coastward edge of flow, defined as follows:

Loop Current – 80-89°W
1972-73: NOAA ships
14 months/ev. 36 days
22°C isotherm @ 100m

Florida Current – 75-80°W
Spring, 76: GOES satellite
6 weeks/ev. ½ hour
temp. gradient @ sea surf.

Gulf Stream – 55-75°W
1965-66: C&GS ship
9 months/ev. month
15°C isotherm @ 200m

SKYLAB Explores the Earth, NASA SP 380, 339-352.

12

An Assessment of the Potential Contributions to Oceanography From Skylab Visual Observations and Handheld-Camera Photographs

GEORGE A. MAUL[a] *AND MICHAEL McCASLIN*[a]

FOR 84 days, the Skylab 4 crewmen had the opportunity to observe the oceans from a unique vantage point. The breadth and frequency of the survey provides a valuable and distinct view of this subject in a science long limited to a few ships for vast seas. The record of their observations gives not only improved insight into the detailed characteristics of oceanic features but also insight into the possible role space observers have in oceanographic experimentation.

This section will examine these roles by considering what has been learned in oceanography from space observations. Specifically, several interesting ocean photographs and visual observations made during the Skylab 4 mission will be discussed. Consideration of the uses and limitations of these photographs has produced a set of recommendations that the authors believe will optimize the information obtained from a space crew. The section will discuss that optimization compared to possible alternative systems for gathering the same type of data.

[a]National Oceanic and Atmospheric Administration; Atlantic Oceanographic and Meteorological Laboratories, Miami, Florida.

OBSERVATIONS

The Gulf of Nicoya on the Pacific coast of Costa Rica was photographed on January 28, 1974, at 12:25 local standard time (18:25 Greenwich mean time (GMT)) (fig. 12-1). This photograph is particularly useful because it shows detailed ocean features and includes land areas so that they can be located on a chart. The ability to determine the geographical coordinates and the time of a photograph is important in oceanography. Although a photograph demonstrates the types of features that can be seen from space, it is rarely useful for photointerpretation without such positioning information.

The striking feature of figure 12-1 is the apparent internal wave field, organized into at least three distinct packets, which can be seen on the left side of the photograph. These are interfacial waves that occur at density boundaries between layers within the water When close enough to the surface, they may appear as parallel "slicks" on the water that move with the same velocity as the waves.

Historical surveys in this region have determined the existence of a density discontinuity at a depth of approximately 30 m. Measurements from the photograph

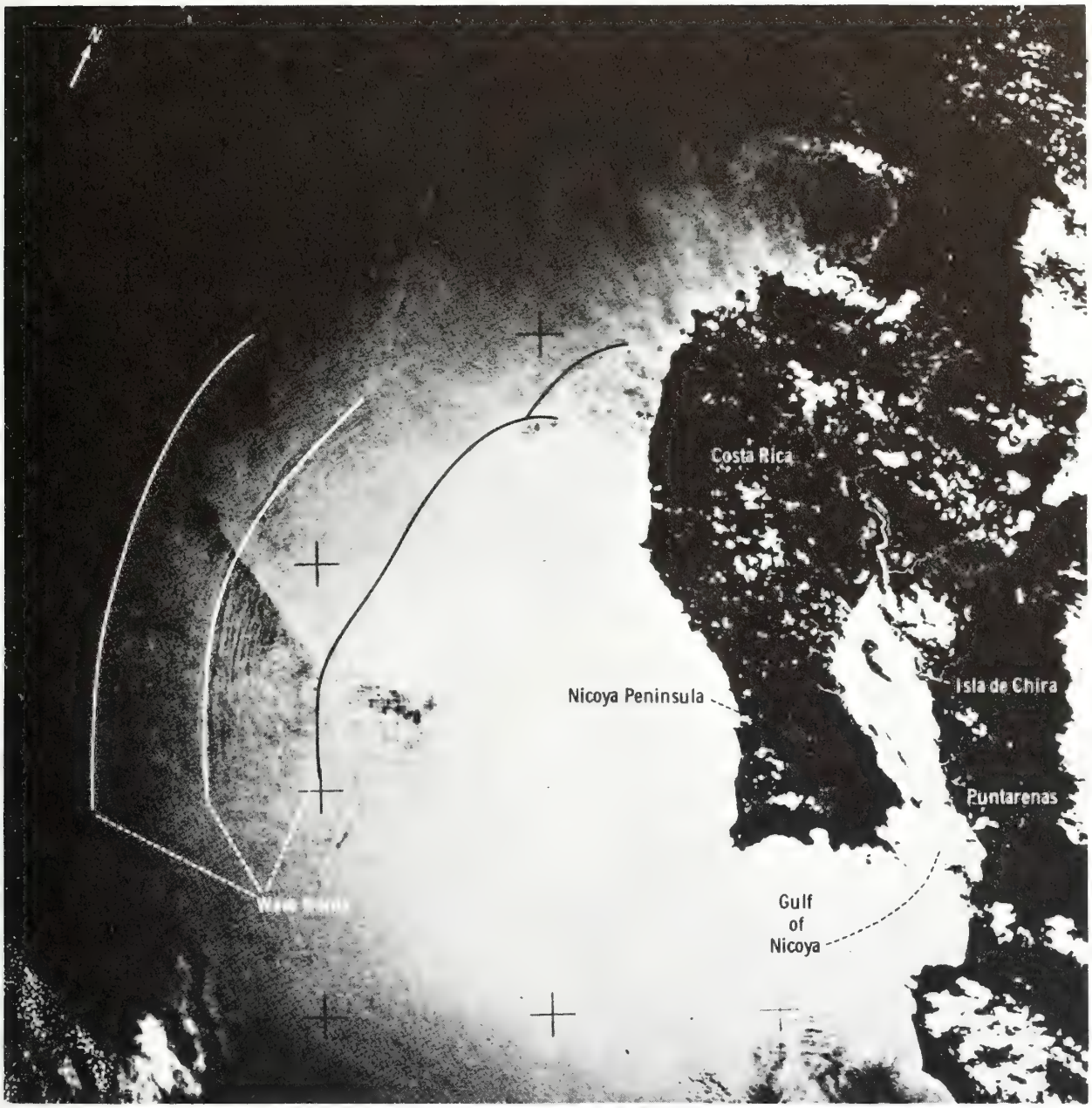


FIGURE 12-1.—Internal wave packets in the Pacific Ocean off the coast of Costa Rica. The leading edges of the three packets are identified by lines. Changes in apparent water color are due to specular return of sunglint caused by changes in capillary wave slopes. This 70-mm photograph was taken January 28, 1974, at 18:25 GMT (SL4-142-4567).

give a wavelength λ for the field of approximately 1000 m, with approximately 31 km between the fronts of the different packets. For a two-layer model:

$$C = \left[\frac{g}{k}\left(\frac{\rho - \rho'}{\rho \coth kh + \rho' \coth kh'}\right)\right]^{1/2} \qquad (12\text{-}1)$$

where C = speed of the waves, ρ = density of the lower water layer, ρ' = density of the upper water layer, g = 9.8 m sec^{-2}, h' = thickness of the upper water layer, h = thickness of the lower water layer, and $k = 2\pi/\lambda$. From equation (12-1), the wave speed is 69 cm sec^{-1}, which is within the expected range. With this speed and the distance of 31 km between packets measured on the photograph, the time between passage of the packets is 12.5 hours. This time corresponds very closely to the interval of the semidiurnal tide cycle dominant in this area, as shown by records from the tide station at Puntarenas. Such a finding supports the concept that internal or surface gravity waves are important in the dissipation of tidal energy, a parameter that affects the rotation of the Earth.

The wave fronts are curvilinear features, as revealed in the photograph. The bottom topography in this region has a U-shaped shoal that extends southwest from the Nicoya Peninsula and is a major cause of the refraction pattern seen in the photograph. Thus, the energy from the tide is transformed into internal waves that propagate into the coastal zone, where their energy is dissipated in turbulent diffusion and contributes to vertical mixing of the water.

Figure 12-1 is an example of an oceanographic feature made visible by sunglint. Ordinarily, sunglint is avoided in overwater photographs because color information is lost in the specular reflection. The Skylab 4 crewmen, however, reported that additional information could be obtained when observing and photographing the sea surface in sunglint. Sunglint covers an area of the sea surrounding the solar reflection point, which appears to be at the large island (Isla de Chira) in the Gulf of Nicoya. Within the specular region, the capillary wave facets may be tilted by the slope of the surface gravity waves such that the surface gravity wave patterns appear to be reflected.

Figures 12-2 and 12-3 are nearly consecutive photographs taken off the coast of the Republic of South Africa on December 7, at approximately 13:00 local standard time. The important features are two large-scale eddies in the left central part of figure 12-2 and an apparent water boundary visible as a color change in the center of figure 12-3. Figure 12-4 represents the best fit of these features to a Chamberlin trimetric projection. Location of the features is approximate because of the distortion in the high-oblique photograph (fig. 12-2); the small amount of land in figure 12-3 makes positioning difficult. Obliqueness in space photography involves major trade-offs between the relative ease of mapping from near-vertical images and the greater coverage and interesting angles available in oblique views. Whenever possible, land should be included in the photograph for orientation, and obliqueness may be desirable if it is necessary to include sufficient land in the picture.

An eddy with an anticyclonic rotation is shown on charts of oceanic sea-surface currents, north of the Subtropical Convergence zone between the West Wind Drift and the current systems of the central South Atlantic. (See inset to fig. 12-4.) Data taken in 1925 by the research vessel *Meteor* expedition were used to construct the charts of this region, which has few hydrographic stations. Analysis of figure 12-2 suggests that this region indeed may be one in which eddies are frequently formed; however, the sense of rotation in the Skylab data appears to be cyclonic. The color changes in the eddies indicate that the centers contain water different from the outer portion of the circulation, which is analogous to the Gulf Stream eddies observed off New England. Unfortunately, it is not possible to make quantitative measurements from the photograph to determine the water composition.

The water boundary shown in figure 12-3 exhibits the meandering sometimes characteristic of current boundaries and appears to be the Subtropical Convergence associated with the Agulhas Current. This current flows southwestward down the east coast of South Africa until it encounters the West Wind Drift zone off the Cape of Good Hope. Some idea of the flow possible in this region can be gained from the track of a free-drifting buoy that was deployed between July and October 1973 (fig. 12-4). The ability to plot the Agulhas Current and the eddies on a regular basis would be helpful to ships, particularly supertankers, that travel around the Cape of Good Hope. Westbound ships would use the current to gain extra speed, and eastbound ships would avoid the current.

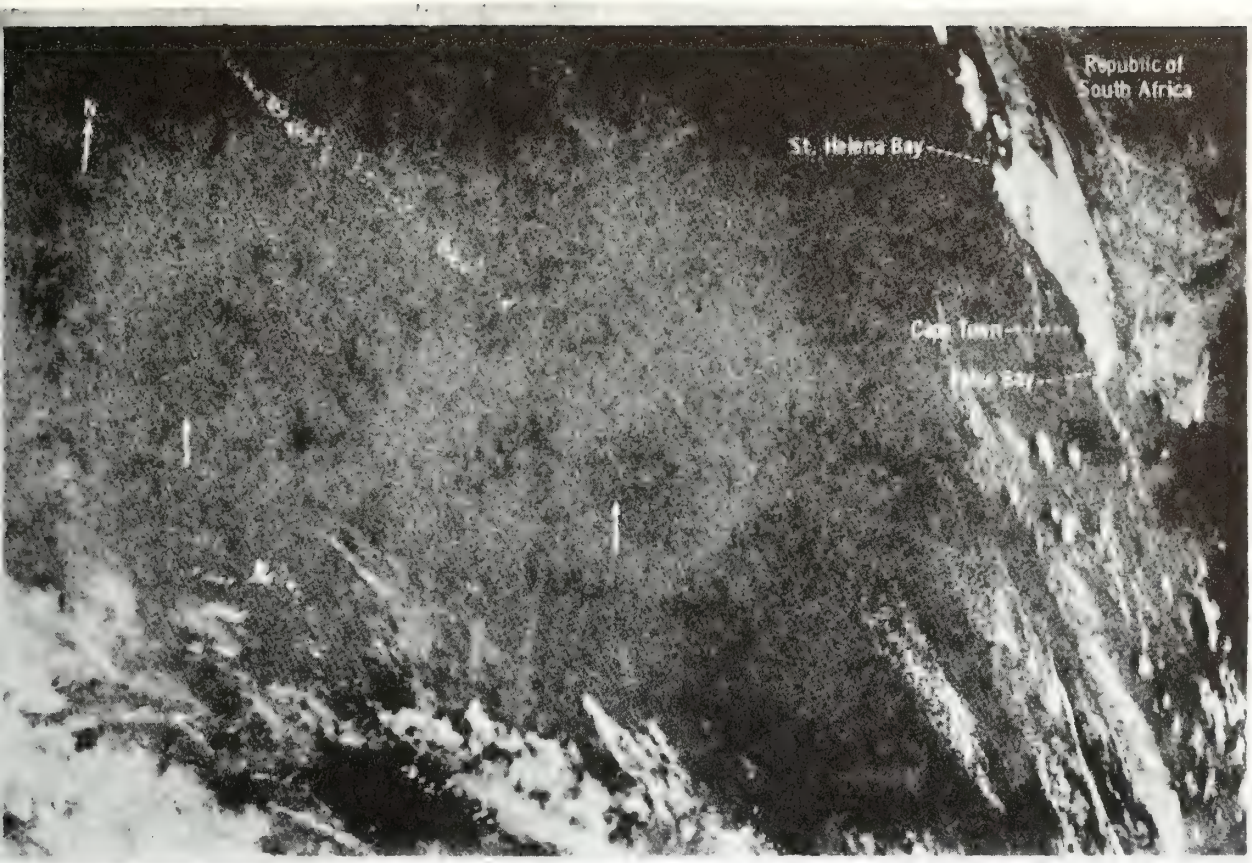


FIGURE 12-2.—Nikon 35-mm photograph showing two large eddies off the southwestern coast of South Africa (arrows pointing toward the blue water in the center). These features are 200 to 300 km in diameter and are probably cyclonic. These eddies are sketched in figure 12-4 (SL4-196-7387).

The Skylab 4 crewmen indicated that the color of the handheld-camera photographs did not reveal the detail or the vividness of their sightings. They indicated that the Skylab Earth terrain camera (S190B) photographs were more representative of what they actually saw. For example, the commander remarked that the ocean had a fine texture that resembled corduroy material. Only in examining the S190B photographs with a magnifier could he detect this common pattern, which is probably a manifestation of surface gravity waves.

The crewmen remarked that binoculars were used for at least half of their observations. This fact may explain their disappointment with the handheld-camera 70-mm photographs and the reason that the S190B products were much closer to the detail actually seen. The long focal length of the S190B camera more closely parallels their observations with binoculars. Many of the descriptions were given while using binoculars, and the relatively wide field of view of the 70-mm camera, which was used without a viewfinder, did not reproduce the observation.

Examples of colored water that may be caused by plankton, which occurs where surface water is rich in life-sustaining nutrients, are shown in figures 12-5 to 12-7. In each of these photographs, the color contrast outlines the boundary of water flow. Figure 12-5, taken on December 19 at 15:42 local standard time, shows the confluence of the Falkland Current and the Brazil Current off the east coast of Argentina. The discoloration in the Falkland Current (on December 25 at 11:03 local standard time) is shown in figure 12-6. Whether the red-

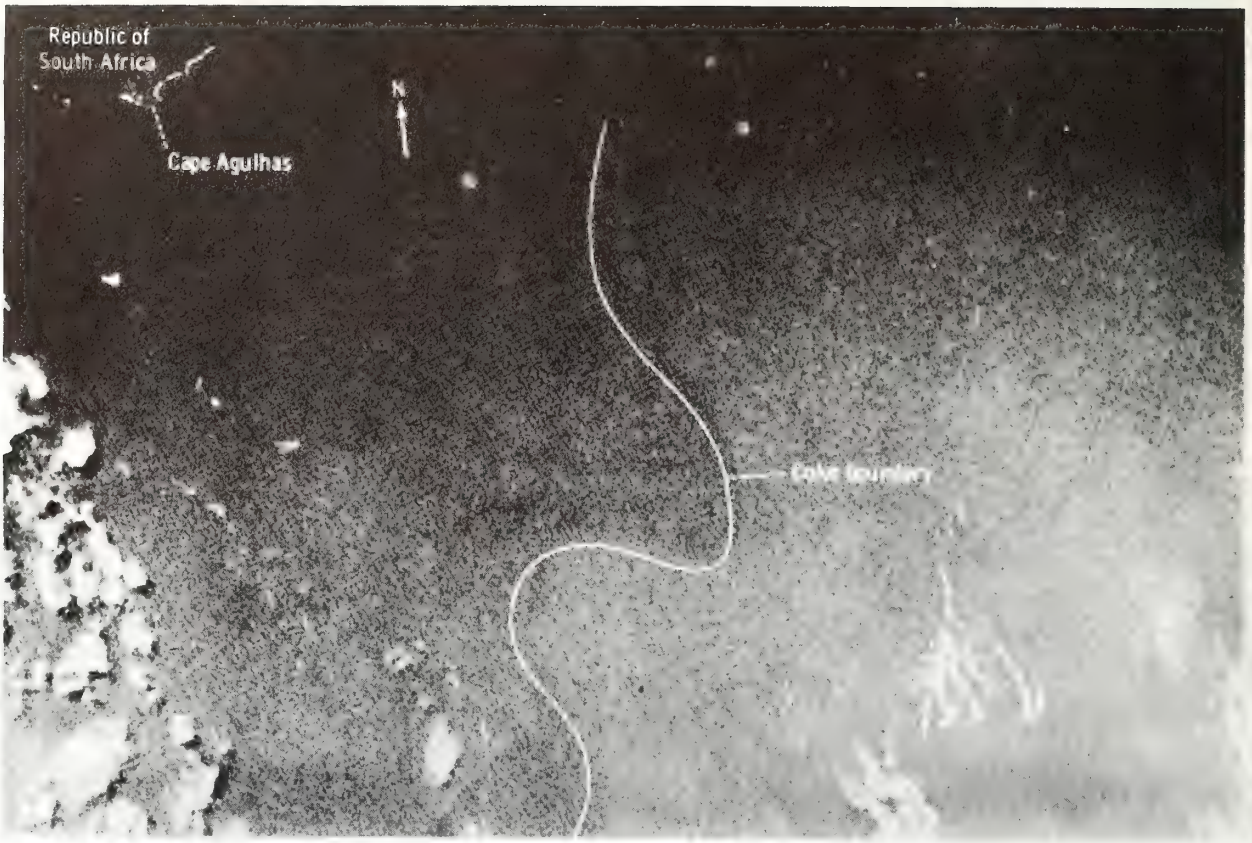


FIGURE 12-3.—Nikon 35-mm photograph showing boundary between water masses off South Africa. This color difference probably delimits the blue waters of the Agulhas Current, which has a tropical origin in the Indian Ocean, and the West Wind Drift, which has a sub-Antarctic origin. Wavelike features may grow and detach to form the eddies seen in figure 12-2, which was taken during the same overflight (SL4-196-7389).

dish color is terrigenic or biogenic is not certain, but it is known that large patches of lobster krill, common in this region at this time of year, can discolor the water. That the Falkland Current would appear bright green as it flowed northeast from Cape Horn, past the Falkland Islands, and eventually east into the South Atlantic Ocean was totally unexpected. The Skylab 4 crewmen reported that the boundary of the warm Brazil Current and the cool Falkland Current could be followed visually more than 3500 km and that the two currents formed intertwining serpentine paths, yet never showed mixing across the boundary. The growth and separation of meanders and current rings were not observed by the Skylab crew in this South Atlantic analog to the Gulf Stream-Labrador Current system. The combination of orbital groundtrack convergences at latitude 50° S permitted repeated observations of the currents during January 1974.

Unfortunately, sufficient information does not exist to orient all the photographs to a common projection and thus to construct a time series of the current. Such a time series, with the detail provided by these photographs, could be one of the most informative products of space photography. In addition, new observations by the crewmen of what appear to be plankton blooms may provide biological oceanographers with further insight into the spatial and temporal extent of these organic discolorations.

Figure 12-7 was taken at 13:23 local standard time on December 7, over the South Pacific Ocean east of New Zealand. The lower half of the picture shows a streaming event of light-colored water in the center and more

diffused patches on each side. Although there are no named currents in this region, the apparent eddying and general configuration of the central band is indicative of current activity and is probably associated with the Subtropical Convergence that passes between North Island and South Island, New Zealand.

Space photographs may prove useful in determining the occurrence and distribution of plankton blooms. Measuring the ratio of blue transmission to that of green on the color transparencies and correlating these data with surface observations may provide tools to determine plankton concentrations from space. Plankton, the base link in the oceanic food chain, is a prime indicator of areas potentially rich in sea life. Information concerning plankton distribution is important to fishermen and marine biologists.

Transmission ratios for figures 12-6 and 12-7 are given in table 12-I; each value is the mean of several individual measurements taken by a spectro-microdensitometer from different locations in the appropriate water zone. The large standard deviations are due to patchiness in the water. If other conditions (sea state, sunglint, oceanic particulates, and atmospheric scatterers) that affect the upwelling radiance from the ocean can be determined, it is possible that these ratios can be evaluated in terms of chlorophyll-a concentrations. Thus, if the photographs are calibrated in a few areas, the isopleths of the blue/green ratio may be us-

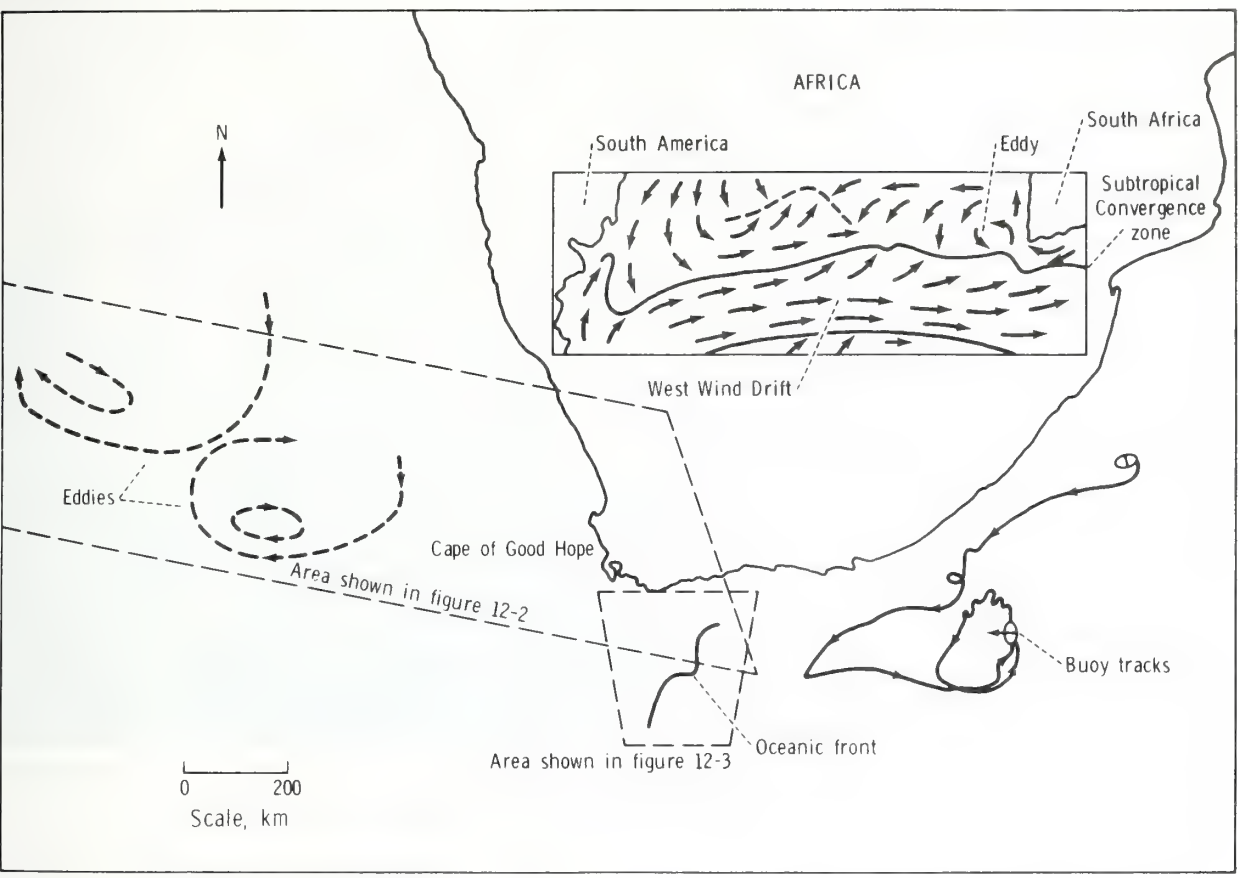


FIGURE 12-4.—Sketch of the South Atlantic Ocean off the Cape of Good Hope showing the features photographed in figures 12-2 and 12-3. The buoy track by Stavropoulos and Duncan in the Agulhas Current was made by using satellite tracking and is an indicator of representative trajectories. The boundary labeled from figure 12-3 is probably the Subtropical Convergence. Inset is a schematic map of surface currents in the South Atlantic Ocean; the solid line is the Subtropical Convergence zone.

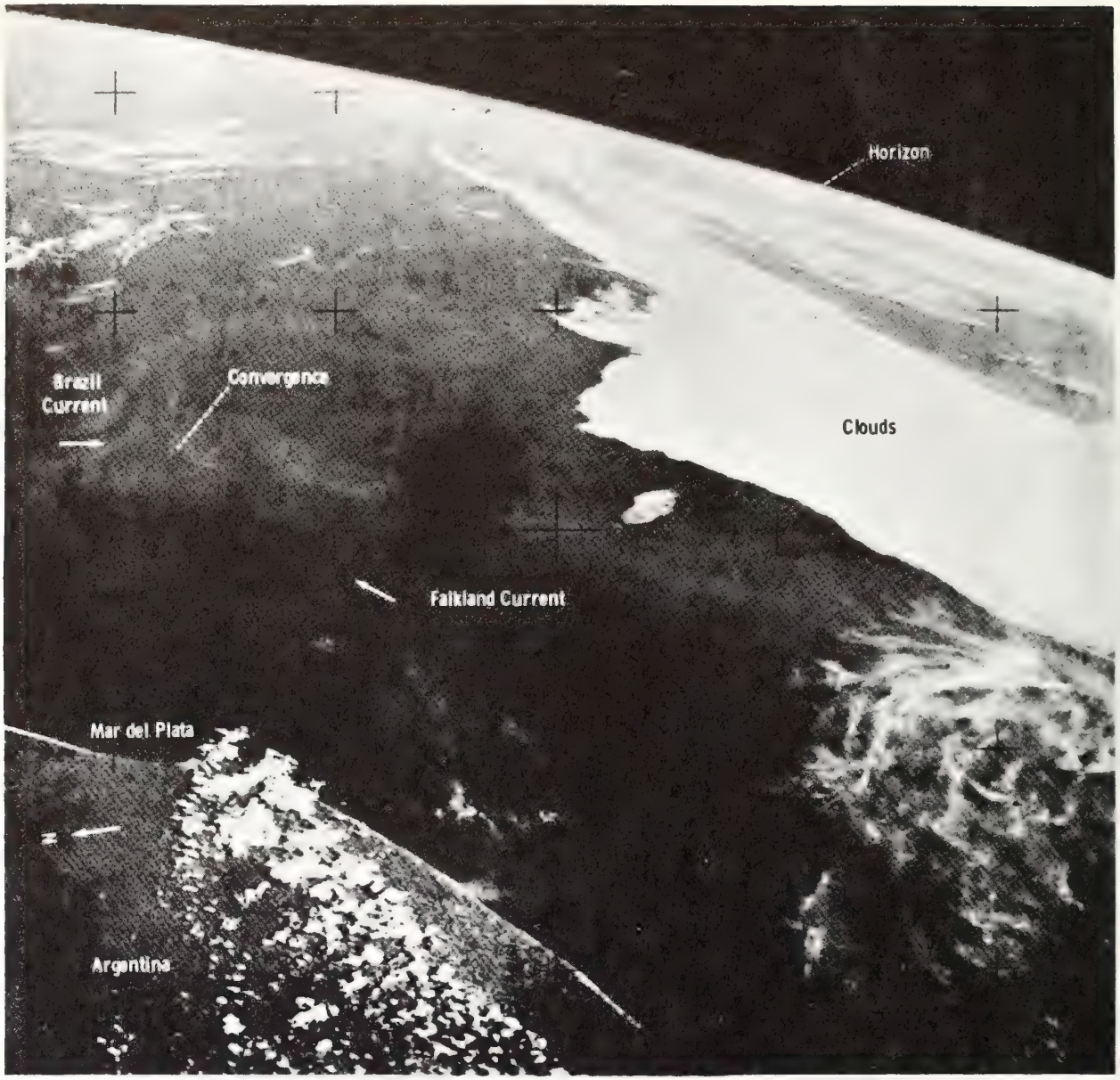


FIGURE 12-5.—East-looking view from Mar del Plata, Argentina, of the confluence of the north-flowing Falkland Current and the south-flowing Brazil Current. The light-green streaming probably marks the right-hand edge (facing downstream) of the currents and, hence, is the inshore boundary of the Brazil Current and the offshore edge of the Falkland Current (SL4-137-3690).

able as contours of pigment concentrations, which are proportional to phytoplankton populations.

Other measurements made from photographs taken by wide-angle aerial lenses have revealed a vignetting problem that seriously affects the ratios. If this problem exists, an adjustment curve must be obtained to rectify the numbers by obtaining values from a photograph of a uniform color field with the same lens. An example of such a curve is given in figure 12-8. The Skylab photographs that have been analyzed herein were taken with

TABLE 12-I.—Transmission Ratio Measured From Two Skylab Photographs[a]

Region	Transmission ratio
Figure 12-6 (SL4-137-3721)	
Front	1.57 ± 0.14
Surrounding water	2.33 ± 0.02
Plankton bloom	2.29 ± 0.06
Figure 12-7 (SL4-136-3446)	
Front	2.33 ± 0.07
Surrounding water	3.13 ± 0.51

[a]The percent transmission is measured with a spectromicrodensitometer which uses an irradiance receptor. White light is passed through the filter, then through the transparency for measurement. (Blue filter: Wratten no. 94, 455 nm; green filter: Wratten no. 93, 540 nm.)

a Hasselblad camera using various lenses, and there is no indication of any serious vignetting effect. This problem, however, should be considered in future flights, and an adjustment curve for each lens-filter combination should be prepared before the flight.

An example of mesoscale ocean eddies observed in the sunglint of a vertical photograph of the Gulf of Mexico taken on August 4 at 13:35 local standard time is shown in figure 12-9. These eddies are associated with the Loop Current in the eastern Gulf of Mexico, and their location has been correlated with the known position of this Gulf Stream-like flow. This view illustrates the important discovery that ocean features can be seen in images obtained by a seldom-used photographic technique and also provides a means of searching for other examples of eddies for a frequency-of-occurrence evaluation. In addition, air-sea interaction studies may be enhanced by studying sunglint patterns and relating them to the wind-stress vector in the atmospheric boundary layer. The photograph in figure 12-9 is one of a stereographic pair that enabled positive identification of the ocean surface features and clouds. Many potentially useful photographs have questionable value because oceanic and atmospheric features cannot be differentiated; stereophotographs or a stereographic camera would eliminate such doubts.

DISCUSSION

The usefulness of manned space vehicles to science, particularly in the area of flexibility of observation programs and routines, has been demonstrated. Communications between scientists on the ground and observers in space can significantly improve the usefulness of space observations by improving site choices and techniques. The capability to voice record the human observations gives to the scenes a perspective otherwise not available. This perspective is valuable because of the observer's visual acuity and ability to change quickly from a detailed observation to a general large-area survey. Furthermore, the relative motion of the vehicle and the Earth is a reliable aid to depth perception; for the scientists, one of the most valuable aspects of debriefing was watching the television tapes to learn how the Earth appears from orbit.

From the standpoint of oceanography, however, the space observations have not reached the full potential of their usefulness because many of the photographs cannot be geographically positioned. This limitation is critical because it prevents accumulation of time-series data, which, because most ocean features change relatively quickly, are important tools in understanding ocean dynamics. The ability to take high-oblique shots is sometimes a distinct advantage but can cause difficulty in mapping an area from the photograph. One possible approach to the problem of mapping is to try to match the photograph to weather-satellite imagery. Attempts by the authors, who used the standard archived product of the National Oceanic and Atmospheric Administration (NOAA) weather satellite NOAA-2, have not been successful because of the fairly low resolution of the satellite images (fig. 12-10) and the time difference between observations by the satellite and by the Skylab crewmen. Very-high-resolution instruments exist on the NOAA-2 satellite, however, and can be activated if sufficient warning is given. The polar-orbiting satellites are not as useful for ocean-dynamics studies as the high-resolution sensors on geosynchronous vehicles because the time difference between each observation is critical when clouds are used as common locators in manned photography and imagery.

The documentation, awkward to use and occasionally incomplete, has been one of the major problems with the Skylab photographs. The crewmen were



FIGURE 12-6.—Near-vertical photograph showing reddish discoloration embedded in the Falkland Current that is probably biogenic material. The offshore edge of the current appears as a bright green lineation, then a dark-blue zone separating the green from a lighter blue region, which is dominated by eddies approximately 15 to 20 km in diameter (SL4-137-3721).



FIGURE 12-7.—High-oblique view east of New Zealand. The light-blue meandering flow (arrow) is near the historical position of the Subtropical Convergence zone and demonstrates horizontal shear-flow instability (SL4-136-3446).

required to record their descriptions and log information such as time, camera, and lens types. This procedure hampered activities in space as well as on the ground. The technology exists to annotate each frame automatically with information such as date and time as it is taken. This automation would relieve crewmen of

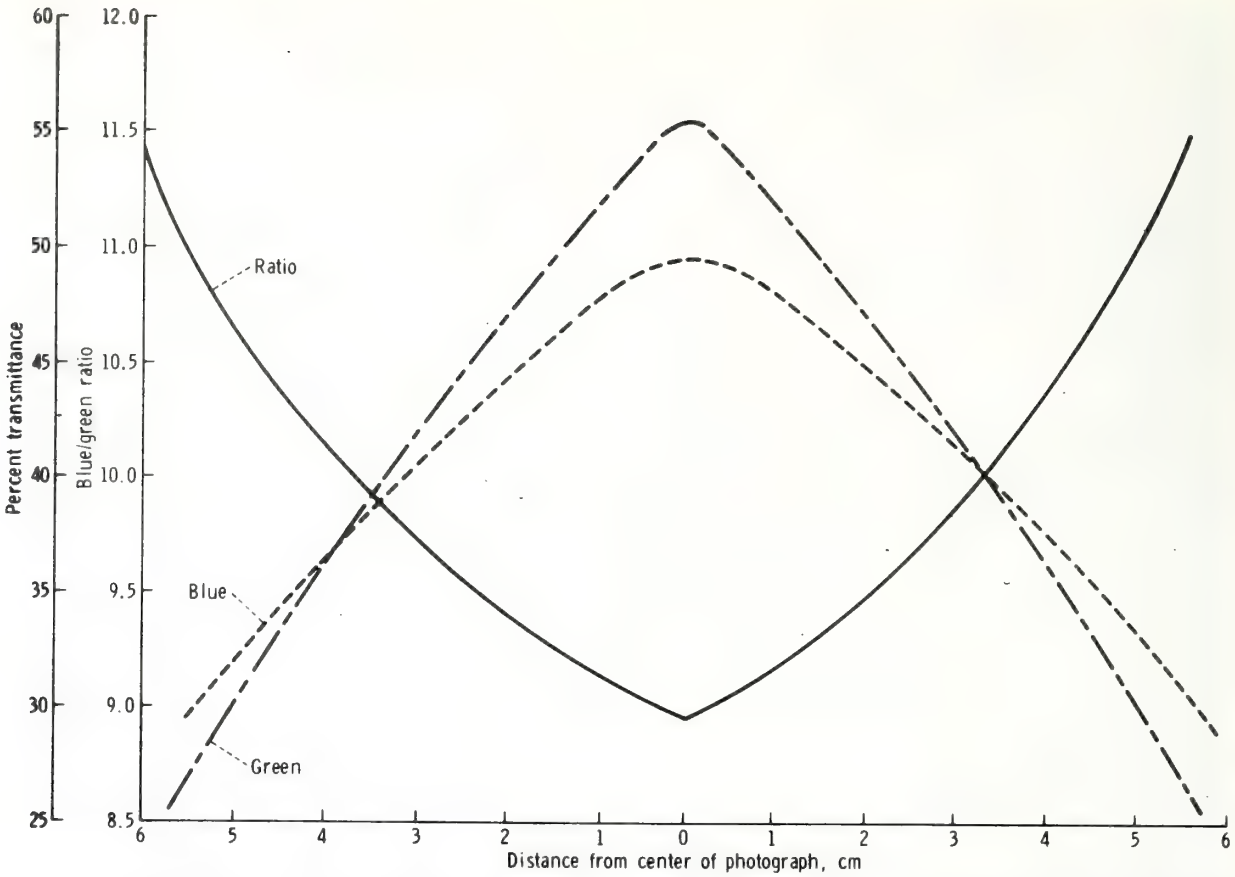


FIGURE 12-8.—Example of vignetting causing significant changes in the blue/green ratio of transmitted light measured over a uniformly blue ocean target. This result from an aircraft transparency shows that a significant correction may be necessary when using blue/green transmission ratios to assess the chlorophyll concentration in water (private communication from S. Baig).

much of their logging responsibilities and facilitate use of the photographs later. Consideration should be given also to recording other numbers such as f-stop, shutter speed, magazine and frame number, and as much other pertinent information as possible.

In addition, the camera should have a zoom lens to eliminate lens changes and should be of the single-lens reflex type. Ideally, the camera would include the functions of a pair of binoculars. Filters should be quick and easy to exchange, and the film advance should be motorized to facilitate stereophotography. Because good depth perception is important in photointerpretation, all space photographs should be taken in stereopairs. Vignetting curves should be obtained for all combinations of lenses and filters, for uniform color fields at 455, 540, and 670 nm to conform with the appropriate Wratten filters. With few exceptions, 35-mm photographs were not as interesting as 70-mm photographs, and the crew apparently found the 35-mm camera more difficult to use. Having exchangeable film packs or magazines would permit more flexible use of different film types for each photographic situation. Much research is underway in developing films for oceanographic photography; specialized alternatives to a standard color film should be investigated.

The formidable ergonomics of such a photographic system may indicate that a very-high-resolution television system would be superior. A ground-based television receiver accessible in real time could give scientists the depth perception inherent in the spacecraft motion and the sense of "being there," which cannot be obtained from a photograph. The overflights could be



FIGURE 12-9.—Vertical photograph in the eastern Gulf of Mexico showing eddies 12 to 32 km in diameter observed in the sunglint pattern. These shear-flow instabilities are not associated with any color boundary because the eddies are in the main body of the Gulf Loop Current. The serpentine feature is probably an oil slick because it is along the main shipping route to New Orleans (SL3-22-124).



FIGURE 12-10.—Oblique photograph of the Falkland Current. Computer-enhanced inset is the NOAA-2 scanning radiometer archived visible image taken the same day as the photograph. Correlation of the cloud feature in the photograph with the image is not possible for several reasons: insufficient image ground resolution, insufficient field of view in photograph, and timelag between observations. Without the ability to locate each ocean photograph, the value of the photograph is significantly diminished (SLA-143-4610).

video taped, and photographic copies of important scenes from the television image should be easy to produce.

The Skylab 4 crewmen spent several days learning to identify their location at any time over the Earth. More intensive geographical training before the mission should reduce the length of this orientation period. The experience of the Skylab 4 crewmen may be the most important link in such a training procedure and could be their most important long-term contribution to space science. Crew training for future flights should include simulated identification of ocean features at the same scale as those seen in orbit. Such simulation can be accomplished by flying aircraft missions that duplicate the resolution and color observed from space (i.e., aircraft missions can be flown without the astronauts to gather the simulated data for later instruction sessions), and by reviewing photographs and television tapes from previous space flights.

CONCLUDING REMARKS

One of the obvious characteristics of oceanographic features is that they are in constant motion. Among the dominant natural phenomena of the Earth, only meteorological events occur more rapidly than oceanographic events; Gulf Stream features, for example, may shift position significantly in 1 or 2 days. Because of these rapid, highly variable motions, an ocean observation needs to be one of a series to provide a clear idea of the dynamics involved. Identification of water types, plankton distribution and types, and other discernible parameters will become possible only if the observations are on a well-calibrated quantitative basis.

Oceanographic observations from space are useful because they provide a much-needed opportunity to survey the ocean on a scale and with a regularity that cannot be duplicated in any other manner. Handheld-camera photography has a distinct role in reconnaissance, but it cannot surpass the quantitativeness of a multispectral observation from a known attitude. Significantly, many of the most interesting ocean scenes were taken by the S190B camera, which produced very-high-resolution photographs taken from a vertical position. From the standpoint of long-term oceanographic research from space, quantitative observations are needed with accurate geographical positioning, and concurrent ocean surface observations are needed to correlate the data. The space observer can significantly augment these needs by real-time interaction with earth-bound scientists in a coordinated effort of discovery and exploration.

ACKNOWLEDGMENTS

The authors express appreciation to Dr. S. Baig, who graciously provided the spectro-microdensitometer measurements, and to Dr. S. Q. Duntley, who critically reviewed the manuscript.

Deep-Sea Research 24, 987-1004.

Bottom pressure observations in the Gulf of Mexico and Caribbean Sea

HAROLD O. MOFJELD* and MARK WIMBUSH†

(*Received* 17 *June* 1976, *in revised form* 24 *January* 1977; *accepted* 11 *March* 1977)

Abstract—During 1971 to 1974, offshore pressure gages were deployed in the Gulf of Mexico and the Caribbean Sea to measure tides and bottom pressure continuum. The observations indicate that the Gulf of Mexico has a Helmholtz resonance with a period of 1.56d. While the lack of confidence limits on theoretical cotidal charts hinders the comparison between theory and observation, the latter tend to support a model with direct astronomical forcing. The observations in the Caribbean Sea verify the general features of theoretical cotidal charts. At a six-month long station in the Eastern Caribbean, bottom pressure fluctuations with 4 to 5-d period are coherent and in phase with atmospheric waves in the Easterlies. The inverse barometer compensation appeared to be less complete in this semi-enclosed sea, spanned by weather systems, than in the open ocean. An appendix gives corrections to the response method of tidal analysis, the procedure for converting the results to harmonic constants with error estimates, and tables of analytical results.

1. BACKGROUND

To TEST theoretical models for tides and free oscillations in the Gulf of Mexico and the Caribbean Sea, offshore pressure observations were made (Fig. 1 and Table 1) during 1971 to 1973 as part of the Cooperative Investigation of the Caribbean and Adjacent Regions (CICAR). Subsequent observations in 1974 are also considered.

Gulf of Mexico

Coastal observations (ZETLER and D. HANSEN, 1970) indicate that the daily tides dominate the western and northern Gulf of Mexico, even though the semi-daily tides are favored both by co-oscillation with the Atlantic and by direct astronomical forcing. In these regions, the daily amplitudes and phases are relatively constant, and the phases are nearly opposite (180° difference in phase) to the corresponding phases in the western Atlantic and the eastern Caribbean Sea. The transition in phase occurs in the vicinity of amplitude nodes in the Straits of Florida and the Yucatan Channel.

According to MARMER (1954), a resonance of the gulf with a period near the daily tidal band causes the anomalously large daily tides. PLATZMAN (1972) developed a theoretical model of the Gulf with realistic bathymetry and using a resonance iteration technique found a Helmholtz resonance with 0.88-d period and a spatial distribution similar to the daily tides. By assumption, this model requires surface elevation nodes in

* Atlantic Oceanographic and Meteorological Laboratories Miami, FL 33149, U.S.A. Present address: Pacific Marine Environmental Laboratory, Environmental Research Laboratory, National Oceanic and Atmospheric Administration, Seattle, WA 98105, U.S.A.

† Physical Oceanography Laboratory NOVA University Dania, FL 33004, U.S.A. Present address: Graduate School of Oceanography, University of Rhode Island, Kingston, RI 02881, U.S.A.

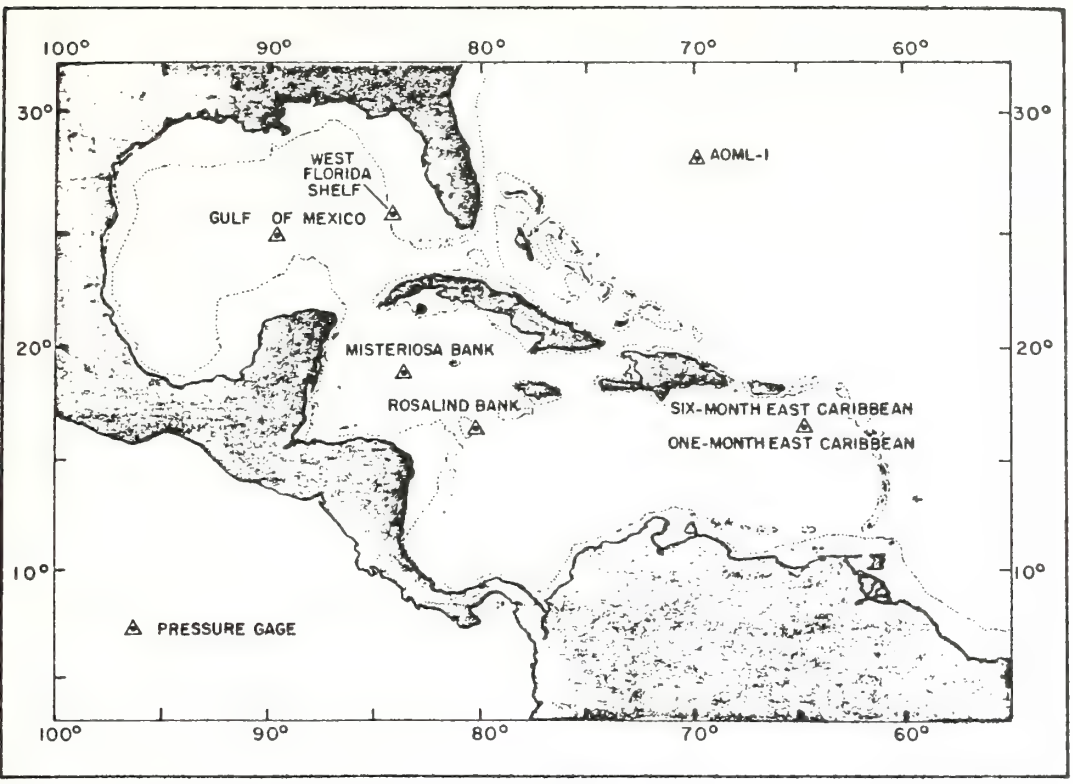


Fig. 1. Chart showing bottom pressure gage and current meter stations in the Gulf of Mexico and Caribbean Sea. Also shown is the AOML-1 station in the western Atlantic Ocean.

Table 1. Bottom pressure stations

Station	Latitude	Longitude	Depth	Starting	Ending
Misteriosa Bank	18°52.9N	83°48.3W	22 m	15July71	13Aug71
Rosalind Bank	16°36.5N	80°20.2W	31 m	15July71	14Aug71
East Caribbean					
One-Month	16°30.1N	64°54.7W	3768 m	15Sept71	19Oct71
Six-Month	16°32.5N	64°52.9W	3990 m	17May72	9Nov72
Central Gulf of Mexico	24°46.1N	89°38.9W	3461 m	11Oct72	18Jan73
West Florida Shelf	26°42.4N	84°15.0W	154 m	6Apr74	18Nov74

the Straits of Florida and in the Yucatan Channel. K. HANSEN (1974) used a Lanczos process to compute resonances (free oscillations) in the combined Gulf of Mexico–Caribbean Sea system with nodes required in the Straits of Florida and at the Antilles. The lowest gravitational resonance has a period (1.04 d) near the daily tidal band but lacks a node in the Yucatan Channel; the next higher resonance has a node in the

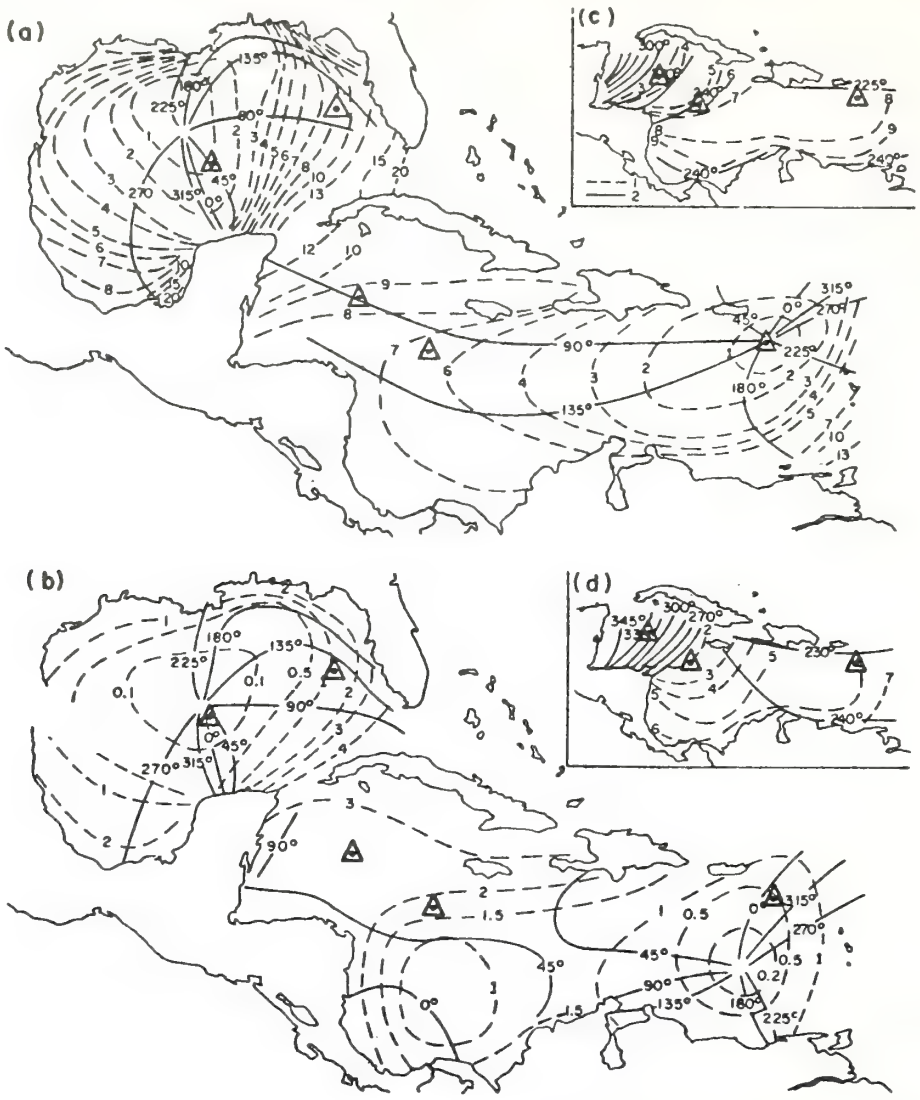


Fig. 2. Cotidal charts for the Gulf of Mexico and Caribbean Sea from the theoretical model by MICHAELOV, MELISHKO and SHCHEVELEVA (1969). Cophase lines (solid) give the Greenwich phase lag in degrees; co-amplitude lines (dashed) give amplitudes in centimetres a) semi-daily M_2 tide, b) semi-daily S_2 tide, c) daily K_1 tide, d) daily O_1 tide.

channel but has a period (0.67 d) nearer the semi-daily band. The mismatch of period and spatial distributions may be caused by the node at the Antilles not seen in the daily tides.

Theoretical work on daily tides *per se* in the Gulf of Mexico is limited to a model by GRACE (1932) of the K_1 tide. The model, which uses a small number of constant depth sections, correctly predicts a slowly varying K_1 tide is the western Gulf of Mexico but incorrectly predicts a large amplitude gradient across the Yucatan Channel.

Several models exist for the semi-daily tides in the Gulf of Mexico. Using W. HANSEN's method (1952, 1962), MICHAELOV, MELISHKO, and SHCHEVELEVA (1969) com-

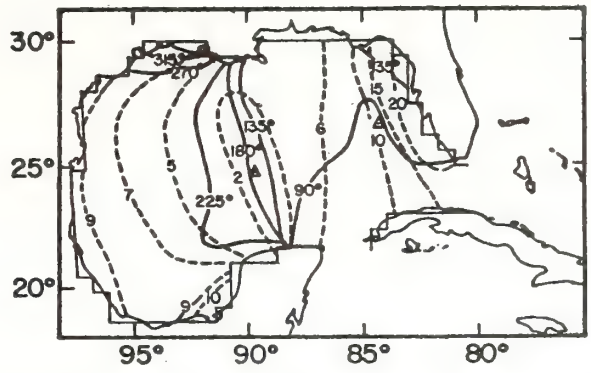


Fig. 3. Semi-daily M_2 cotidal chart for the Gulf of Mexico from the theoretical model by GRIJALVA (1971). Cophase lines (solid) give the Greenwich phase lag in degrees; co-amplitude lines (dashed) give amplitudes in cm.

puted cotidal charts (Fig. 2) for the combined Gulf of Mexico–Caribbean Sea system. Their model has a 40′ grid spacing in the gulf, uses realistic bathymetry, and neglects non-linearities, friction, and direct astronomical forcing. Observed coastal harmonic constants are used as boundary conditions. Because of an apparent singularity at the critical latitude of the daily tides, these authors did not compute the daily tides in the Gulf.

Also using W. HANSEN's (1952, 1962) method, GRIJALVA (1971) computed the M_2 tide in the gulf (Fig. 3). His model, which has a 30′ grid spacing and includes friction and direct astronomical forcing of the water (but not the sea bed), specifies the surface elevation only at the Straits of Florida and the Yucatan Channel. Grijalva attributed the lack of an amphidromic point in his model to direct astronomical forcing.

Earlier theoretical work on tides in the gulf is summarized by ZETLER and D. HANSEN (1970), while earlier work on resonances (free oscillations) is summarized by K. HANSEN (1974).

Caribbean Sea

In the eastern Caribbean Sea, coastal and island observations show that the daily tides are relatively uniform with a southward increase in phases consistent with that in the Atlantic. The amplitudes decrease slowly toward the west, decreasing more rapidly in the western Caribbean to apparent nodes in the Yucatan Channel. In the same region, there is a rapid increase in the daily phases. MICHAELOV *et al.* (1969) modelled the daily K_1 and O_1 tides in the Caribbean Sea on a 1° grid using the same assumptions they made for the gulf. Their cotidal charts (Fig. 2) reproduce the general features of the daily tides in the Caribbean Sea.

The rapid, counter-clockwise increase in semi-daily phases and the small semi-daily amplitudes indicate that each semi-daily tide forms an amphidromic system in the eastern Caribbean. The semi-daily tides increase in amplitude toward the Yucatan Channel where they dominate the tidal regime. To test the M_2 model (Fig. 2) for the Caribbean Sea by MICHAELOV *et al.* (1969), the One-Month East Caribbean station (Fig. 1 and Table 1) was occupied at the theoretical M_2 amphidromic point. The resulting pressure series was analyzed by ZETLER and CUMMINGS (1972), who found a small, but non-zero, M_2 ampli-

tude. The latter authors concluded from a study of successive 29-day series from nearby Magueyes Island that a 29-day series obtained near an amphidromic point might not yield an accurate harmonic constant for that constituent. The Six-Month East Caribbean station was therefore occupied, and results from that series are reported in this paper.

Low frequency pressure continuum

Superimposed on the tidal signal in the open ocean is a bottom pressure continuum which is not well understood. The continuum at frequencies below the daily tidal band is thought to be associated with time-dependent geostrophic currents and atmospherically induced fluctuations. For the western Atlantic Ocean, BROWN, MUNK, SNODGRASS, MOFJELD, and ZETLER (1975) found that the bottom pressure spectrum resembled the atmospheric pressure spectrum at low frequencies, but the bottom pressure and local atmospheric pressure were found to be only marginally coherent. The connection between bottom pressure and atmospheric pressure is therefore more complex than a simple deviation from the inverse barometer compensation.

If the Gulf of Mexico has a resonance near the daily tidal band as proposed by MARMER (1954), it should be apparent in the bottom pressure continuum; the pressure spectra in the gulf and the western North Atlantic should differ markedly near 1 cpd.

As discussed by RIEHL (1954), the weather in the Caribbean Sea region is dominated by waves in the Easterlies that have periods of 4 to 5 d. It is interesting to speculate about the response of the semi-enclosed Caribbean Sea to forcing by these waves.

2. INSTRUMENTATION

The pressure series from the Caribbean Sea and from the central Gulf of Mexico station were obtained using FILLOUX (1969) deep-sea tide gages. The gages have metal Bourdon tube pressure transducers exposed to the full oceanic pressure. Intercomparison studies reported by the SCOR Working Group No. 27 (1975) and by ZETLER, MUNK, MOFJELD, BROWN and DORMER (1975) show that these gages are accurate to at least 0.5 cm H^2O (relative to the mean), once a trend is removed from the data. The trend, due to creep in the Bourdon tubes, follows the logarithmic law proposed by LOMNITZ (1956, 1957) and discussed by JEFFREYS (1970). The long-term creep diverges from the Andrade's 1/3 power law proposed by FILLOUX (1969). Spurious shifts in the apparent background pressure occurred in the records from Misteriosa and Rosalind banks (Fig. 1). These shifts may be due to tilting of the gages, as observed in laboratory tests; on the bottom, the tilting could be produced by wave-induced erosion around the instrument base. The analyses were limited to sections of record for which the background pressure was stable.

The pressure record from the West Florida shelf station was obtained with a pressure-temperature gage described by WIMBUSH (1977). It used a 250-psi Vibrotron pressure sensor and a thermistor temperature sensor (to correct for a slight temperature sensitivity of the Vibrotron). Outputs of these sensors were integrated over the full sampling interval (1/8 h); the sensitivity of the system is limited by Vibrotron noise, which is very small compared with the tidal signal.

OBSERVED TIDES

Accuracy of harmonic constants

Tidal harmonic constants were obtained from the pressure series using the response method, details of which and results in standard tables are given in the Appendix.

The accuracy of the observed harmonic constants is limited by length of record and by the relative intensity of non-tidal continuum and instrument noise within the tidal bands. For the records under discussion, the non-tidal pressure continuum is the primary source of error. The spectrum of the pressure continuum typically rises appreciably around the major tidal lines, due to the phase-incoherent internal tide. Cusps around the minor lines are buried in the background.

In the deep ocean one would expect less weather-induced fluctuation of bottom pressure than at coastal sea level stations. To compare the scatter in harmonic constants from nearby deep and shallow stations, successive 29-day analyses were done on the Six-Month East Caribbean bottom pressure record and a sea-level record from Magueyes Island, 280 km away, analyzed by ZETLER and CUMMINGS (1972). Table 2 gives the means and standard deviations of the harmonic constants from these records.

Table 2. Standard deviation of harmonic constants from successive 29-day harmonic analyses at nearby shore and bottom-mounted tide stations.

	Magueyes Island* (17°58.3N, 67°02.8W)				Six-Month East Caribbean (16°32.5N, 64°52.9W)			
	Mean		Standard Dev		Mean		Standard Dev	
	H(cm)	G(deg)	H(cm)	G(deg)	H(cm)	G(deg)	H(cm)	G(deg)
N_2	0.40	52.0	0.34	66.1	0.58	128.4	0.07	5.5
M_2	0.70	52.5	0.34	38.0	0.51	155.5	0.10	13.4
S_2	0.71	348.0	0.30	30.4	1.36	45.4	0.24	10.4
K_1	7.92	233.3	0.73	5.6	8.68	232.7	0.21	1.1
O_1	5.36	227.3	0.30	3.4	6.24	227.2	0.22	1.2

* From ZETLER and CUMMINGS (1972).

Another error estimate uses the continuum spectrum, integrated over the appropriate tidal band. This estimate, which is described in the Appendix, can be obtained from series that are too short for successive analyses. The standard deviations in Tables 3 and 4 were obtained from the spectra.

Gulf of Mexico

The measured K_1 and O_1 tides (Table 3) at the central Gulf of Mexico station have at least twice the amplitudes of the corresponding tides in the western Atlantic. Although the K_1 amplitude in the western Atlantic is 1.24 times the O_1 amplitude and the astronomical K_1 forcing is 1.41 times the O_1 forcing, the O_1 amplitude exceeds the K_1 amplitude in the central gulf. Hence, the admittance (response per unit forcing) is significantly larger at lower frequencies (Fig. 4). K_1 and O_1 harmonic constants are comparable with coastal values in the western gulf, as given by ZETLER and D. HANSEN (1970). The observations support MARMER's (1954) contention that the gulf has a resonance near the daily tidal band. The increasing admittance with decreasing frequency indicates that the resonance has a frequency below (longer period than) the daily tidal band. Further evidence for the resonance is given in the section on the low frequency continuum.

Since the model by GRACE (1932) disagrees significantly with coastal values, no

Table 3. Comparison of theoretical and observed harmonic constants at the central Gulf of Mexico and West Florida Shelf stations.

	Central Gulf of Mexico Station (24°46.1N, 89°38.9W)					
	MICHAELOV, MELISHKO, and SHCHEVELEVA (1969)		GRIJALVA (1971)		Observed	
	H(cm)	G(deg)	H(cm)	G(deg)	H(cm)	G(deg)
M_2	1.0	45	~1.5	170	1.30±0.07	225.8±3.1
S_2	0.03	45	-	-	1.50±0.08	130.0±3.1
K_1	-	-	-	-	14.10±0.30	28.5±1.2
O_1	-	-	-	-	14.90±0.31	18.9±1.2

	West Florida Shelf Station (26°42.4N, 84°15.0W)					
	MICHAELOV, MELISHKO, and SHCHEVELEVA (1969)		GRIJALVA (1971)		Observed	
	H(cm)	G(deg)	H(cm)	G(deg)	H(cm)	G(deg)
M_2	8.0	110	11	88	6.74±0.07	97.1±0.6
S_2	1.3	125	-	-	3.51±0.04	102.5±0.6
K_1	-	-	-	-	12.56±0.16	12.4±0.7
O_1	-	-	-	-	11.73±0.15	5.2±0.7

comparison was made between the K_1 measured at the central Gulf of Mexico station and this theory. The measured K_1 and O_1 values are consistent with the spatial distribution of the Helmholtz resonance computed by PLATZMAN (1972), although the period is longer than the theoretical value.

The earlier K_1 and O_1 phases at the West Florida Shelf station (Fig. 4) relative to the central Gulf of Mexico station indicate that there is some progressive component to the daily tides near the Straits of Florida due to an unknown mixture of dissipation, direct forcing, and propagation to or from the Caribbean Sea. The smaller daily amplitudes (Fig. 4) are consistent with nodes in the Straits of Florida.

The observed M_2 amplitude at the central Gulf of Mexico station agrees with the model of MICHAELOV *et al.* (1969) and the model of GRIJALVA (1971). The closer agreement in M_2 phase between the latter model with observations tends to confirm Grijalva's contention that direct M_2 astronomical forcing is important in this small M_2 amplitude region of the gulf.

MICHAELOV *et al.* (1969) also computed a theoretical distribution for S_2 (Fig. 2 and Table 3) using coastal observations as boundary conditions and neglecting direct forcing. The S_2 tide is a superposition of gravitational and radiational tides. Assuming that the 0.9-cm amplitude* found by ZETLER (1971) at Key West, Florida (24°34N, 81°48W) is

* This amplitude is relatively small compared with others along the United States East Coast, as reported by ZETLER (1971).

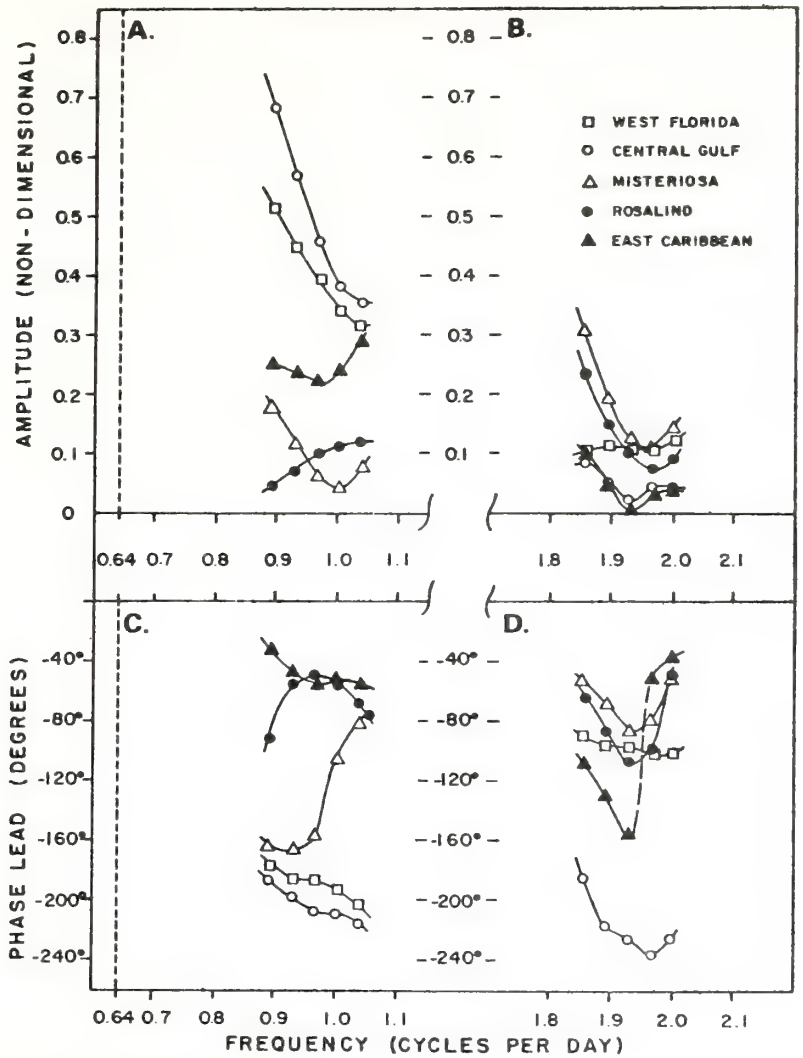


Fig. 4. Tidal admittance amplitudes computed from the bottom pressure records for the daily (A) and semi-daily (B) tidal bands and the corresponding phase leads (C) and (D). Tables of the admittances in standard form are given in the Appendix.

characteristic of the radiational S_2 tide along the Gulf Coast, the radiational S_2 dominates the boundary conditions for the S_2 model. The discrepancy between the theoretical and observed S_2 harmonic constants (Table 3) is due probably to: the neglect in the theory of nearshore wind forcing and the direct atmospheric pressure, gravitational and seabed forcing.

At the West Florida Shelf station, the theoretical M_2 tides agree reasonably well with the measured values. This result could be expected because both theories (Table 3) use nearby observed values as boundary conditions. The discrepancies may be due to tidal variations across the shelves, which are unresolved by the models.

Caribbean Sea

The observed daily tides (Table 4) verify the general features of the K_1 and O_1 cotidal charts (Fig. 2) for the Caribbean Sea presented by MICHAELOV *et al.* (1969). The theory underestimates the daily amplitudes by about 10% at the eastern stations. While the theoretical K_1 phase is 4° less than the O_1 phase at the Six-Month East Caribbean station, the observed K_1 phase is 4.7° greater than the O_1 phase. The observed K_1 tide also lags the O_1 tide at the nearby Magueyez Island station (ZETLER and CUMMINGS, 1972) and other coastal

Table 4. Comparison of theoretical harmonic constants from MICHAELOV, MELISHKO and SHCHEVELEVA (1969) and observed harmonic constants in the Caribbean Sea.

	Eastern Caribbean Sea							
	Six-Month Station (16°32.5N, 64°52.9W)				One-Month Station (16°30.1N, 64°54.7W)			
	Theoretical		Observed		Theoretical		Observed*	
	H(cm)	G(deg)	H(cm)	G(deg)	H(cm)	G(deg)	H(cm)	G(deg)
M_2	0	-	0.52±0.03	155.8±3.7	0	-	0.64	153
S_2	0.5	350	1.30±0.08	43.7±3.7	0.5	0	1.24	49
K_1	7.8	228	8.82±0.11	232.9±0.7	7.8	228	9.27	235
O_1	6.0	232	6.24±0.08	227.2±0.7	6.0	232	6.62	230

	Western Caribbean Sea							
	Misteriosa Bank Station (18°52.9N, 83°48.3W)				Rosalind Bank Station (16°36.5N, 80°20.2W)			
	Theoretical		Observed		Theoretical		Observed	
	H(cm)	G(deg)	H(cm)	G(deg)	H(cm)	G(deg)	H(cm)	G(deg)
M_2	8.7	88	7.88±0.46	84.2±3.3	6.5	105	6.63±0.35	107.0±3.0
S_2	2.6	60	3.89±0.23	55.9±3.3	1.7	50	2.51±0.13	55.6±3.0
K_1	≤ 3	280	1.58±0.19	284.3±7.0	5.0	243	4.33±0.28	235.3±3.7
O_1	≤ 1	320	3.06±0.37	347.0±7.0	2.0	250	1.89±0.12	235.5±3.7

* From ZETLER and CUMMINGS (1972), obtained from a 29-day harmonic analysis: no standard deviations given.

stations in the Caribbean Sea (U.S. Dept. of Commerce, 1942). The discrepancies are due to errors in the boundary conditions or to mislabelling of the cotidal charts because the uniformity of the tides in the eastern Caribbean precludes significant errors arising from inadequate dynamics in the model.

In the western Caribbean, the observations (Table 4) show the decrease in daily tidal amplitudes and rapid increase in daily phase lags (Fig. 2) predicted by MICHAELOV *et al.* (1969). The discrepancies between the theoretical and observed daily tides at the western Caribbean station arise from errors in the model's boundary conditions and, to a lesser extent, the influence of noise on observed harmonic constants from short records obtained at shallow stations.

The model by MICHAELOV *et al.* (1969) for the M_2 and S_2 tides in the Caribbean Sea predicts small amplitudes at the eastern Caribbean stations. Small semi-daily amplitudes are observed at these stations. As suggested for the M_2 and S_2 tides in the Gulf of Mexico, the differences between the theory and observation near a theoretical amphidrome may be due to directly forced tides and to the radiational S_2 tide. The

anomalous jump in semi-daily admittance phase (Fig. 4) at the Six-Month East Caribbean station may be due to the radiational S_2 tide near amphidromes of the gravitational, semi-daily tides.

At the western Caribbean stations, the theory (Table 4) accurately predicts the M_2 harmonic constants. While the S_2 phase is reasonably well reproduced, the theory underestimates the small S_2 amplitude.

The six-month record is sufficiently long with the low background noise to allow an analysis of the ter-daily M_3 tide arising from the C_3^3 gravitational potential. As given in Table E, the M_3 tide (0.12 cm, 48.1°G) is distinct from non-linearly generated lines in the ter-daily band.

LOW-FREQUENCY PRESSURE CONTINUUM

The records from the central Gulf of Mexico and the Six-Month East Caribbean stations are sufficiently long to permit a study of the low frequency, bottom pressure continuum. Shown in Fig. 5 are low-passed pressure series; the corresponding

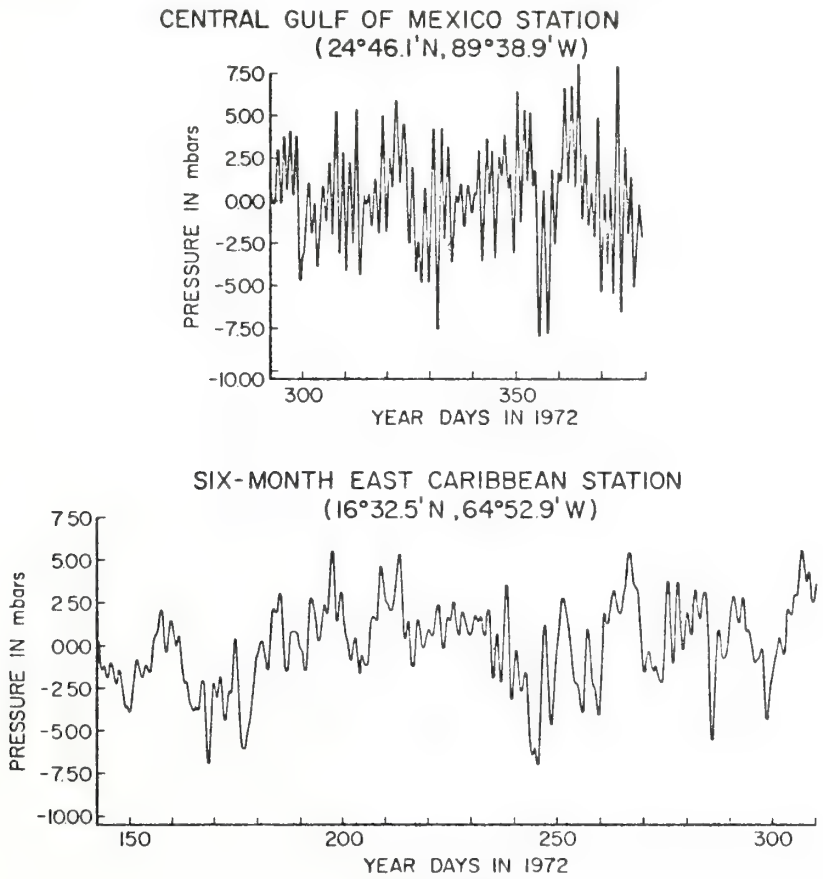


Fig. 5. Low-passed pressure records at the central Gulf of Mexico and Six-Month East Caribbean stations showing the pressure fluctuations in millibars at frequencies below the daily tidal band. The instrumental drift has been removed by subtracting a least-squares fitted logarithmic trend from each record. Note the rapid fluctuations in the central Gulf of Mexico record as contrasted with the lower frequency fluctuations at the east Caribbean station.

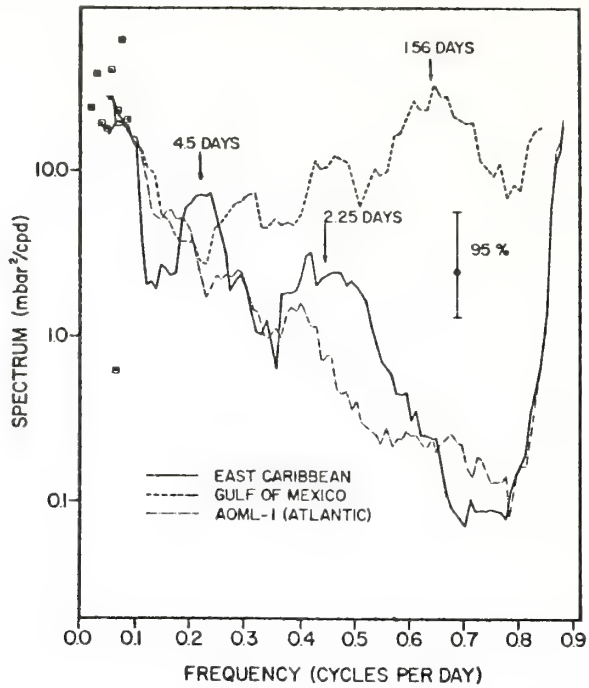


Fig. 6 Spectra of bottom pressure below the daily tidal band for the Six-Month East Caribbean, central Gulf of Mexico, and AOML-1 (Atlantic) stations. The pressure records were cosine-tapered over the first and last 10 per cent and Fourier-transformed to give primitive spectral estimates that have been smoothed with a seven point (14 degrees of freedom) box car average. The isolated points in the upper left corner are primitive spectral estimates for the east Caribbean record at and below the fortnightly frequency. Note the overall similarity between the AOML-1 and East Caribbean spectra and the peaks in the latter at 4.5 and 2.25-d periods. In contrast, the central Gulf of Mexico spectrum rises at frequencies above 0.2 cpd to a peak at 0.64 cpd (1.56 d period).

spectra are given in Fig. 6, together with the spectra at the western Atlantic AOML-1 station discussed by BROWN *et al.* (1975).

Gulf of Mexico

The Central Gulf of Mexico spectrum (Fig. 6) diverges from the AOML-1 spectrum at frequencies above 0.24 cpd, exhibiting an increase in spectral energy with higher frequency and forming a broad peak centered at about 0.64 cpd (period = 1.56 d).* After a dip centered at 0.8 cpd, this spectrum rises toward the daily tidal band. The total pressure variance between 0.049 and 0.805 cpd at the Central Gulf of Mexico Station (8.81 $mbar^2$) is three times the corresponding variance at the western Atlantic AOML-1 station (2.64 $mbar^2$). The low frequency pressure continuum observed in the gulf reinforces the contention that the gulf has a resonance with a frequency slightly below the daily tidal band.

Caribbean Sea

The pressure spectrum (Fig. 5) at the Six-Month East Caribbean station follows the general trend of the western Atlantic AOML-1 spectrum. The pressure variances between

* The spectrum from the West Florida Shelf station likewise contains a significant peak at 1.60 d.

0.046 and 0.805 cpd are 2.64 and 2.48 mbar^2, respectively. The major differences between the spectra are the pronounced peak around 0.22 cpd (4.5-d period) and its overtone seen in the Caribbean. Since the weather in this region is dominated by waves in the Easterlies with 4 to 5-d period, the bottom pressure peaks may be atmospherically forced.

A simultaneous atmospheric pressure record* from St. Croix, V. I. (17°42N, 64°44W), 130 km north and slightly east of the bottom pressure station (16°33N, 64°53W), was obtained from the National Climatic Center. The autospectra, squared coherence, and relative phase of the two records are shown in Fig. 7. Taking the 0.15-cpd spectral

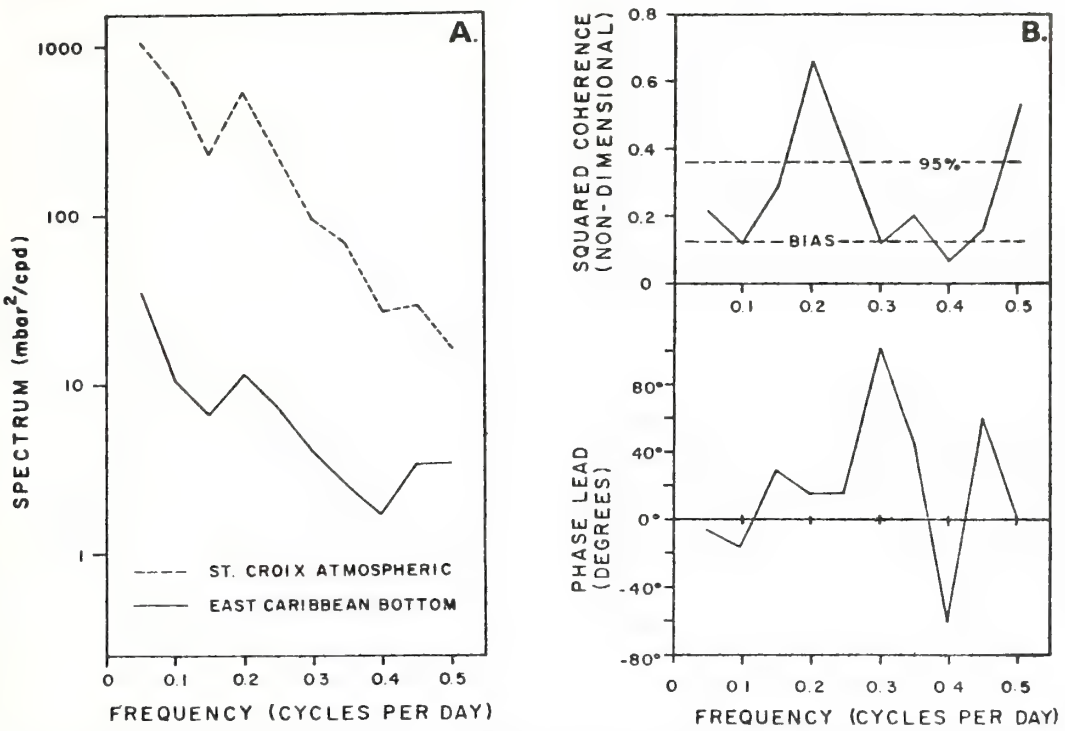


Fig. 7. Comparison of bottom pressure at the Six-Month East Caribbean station (16°33N, 64°53W) with atmospheric pressure at nearby St. Croix, V. I. (17°42N, 64°44W). The peaks in the autospectra (A) at 0.2 cpd are coherent (B) with the bottom pressure leading the atmospheric pressure by 15° at 0.2 cpd. Daily-averaged pressures were used with a 0.5-cpd Nyquist frequency.

estimates as the bases of the 0.2-cpd peaks, the corresponding amplitudes are 0.5 and 4.0 mbar for the bottom pressure and atmospheric pressure fluctuations, respectively, giving an amplitude ratio of 0.13. The fluctuations are coherent because the peak in squared coherence stands well above the 95% confidence value for rejection of the null hypothesis (i.e. that the coherence is due to random chance).

The bottom pressure fluctuations lead the atmospheric fluctuations to the north by 15°, or 4.5 h for a 0.22-cpd frequency. This is consistent with the northwestward propagation of the waves in the Easterlies as reported by RIEHL (1954). He states that the waves propagate at 12 to 15 kts (6 to 8 m s^{-1}) while the observed 4.5-h phase lead gives

* The following comparison was suggested by a reviewer.

a propagation speed of about $8\,m\,s^{-1}$, assuming that the waves propagate with a 315°T heading. The 4 to 5-d bottom pressure fluctuations observed at the Six-Month East Caribbean station are coupled strongly and in phase with atmospheric waves. This is in contrast to the low-frequency, bottom pressure fluctuations in the western Atlantic where the bottom and atmospheric fluctuations are marginally coherent. A possible explanation for the different behaviour is that the inverse barometer compensation is less complete in the semi-enclosed Caribbean Sea, where weather patterns span the basin and where water exchange is hindered by narrow, shallow passes.

DISCUSSION

The original purpose of this study was to test tidal models with offshore observations. By themselves, the few stations are not sufficient for empirical tidal charts or even to indicate whether particular features such as amphidromic points exist in a given region. When conflicting theories predict distinctly different behavior, an isolated station should discriminate between the theories. For example, the observed M_2 phase at the Central Gulf of Mexico Station favors the model by GRIJALVA (1971), which includes direct astronomical forcing, over the model by MICHAELOV *et al.* (1969), which is forced only by co-oscillation. However, it might be possible to reconcile the latter model with observations by changing boundary conditions or grid spacing. The results of tidal models are traditionally given as a single chart of amplitude and phase for a given constituent. No reliability estimates are given based on a set of numerical experiments to determine the sensitivity of the model to reasonable ranges of parameters, uncertain bathymetry, and numerical limitations. Confidence limits on the theoretical distributions are needed, just as they are for observations.

Although the daily tides dominate the Gulf of Mexico, the apparent critical-latitude singularity in the equations of motion prevented MICHAELOV *et al.* (1969) from computing daily tidal charts for the gulf. This singularity is removable, and the daily tides in the gulf can be computed by alternate numerical schemes.

ZETLER and CUMMINGS (1972) suggested that extensive observational searches for amphidromic points are unprofitable and report the recommendation by the SCOR Working Group No. 27 on Tides in the Open Ocean that emphasis should be placed on regions of maximum constituent amplitude. Such a search would also be unprofitable because the constituent amplitudes and phases vary little over large areas around these maxima. The observations should be made to discriminate between theories. The basic limitation on observational offshore tide programs is no longer the accuracy and endurance of tide gages but rather the cost of obtaining the pressure records.

Acknowledgements—Many people have contributed significantly to the research presented in this paper. The authors wish to thank the National Ocean Survey's Engineering Development Laboratory and J. J. FALKENHOFF in particular for both the design of arrays and assistance in the NOAA field program. Within AOML, F. A. NEW did much of the initial checkout and modification work on the Filloux gages. B. J. CULVERHOUSE, D. J. PASHINSKI, and R. S. JENNINGS worked with EDL and F. A. NEW on the array preparation and field work and were essential to the success of the project. R. B. STARR suggested the shallow water stations in the western Caribbean Sea. D. F. JONES designed and fabricated the arrays for those stations and supervised their installation. N. M. TARGETT was of considerable assistance in the laborious reading of pressure gage records and the subsequent data processing. Useful advice was readily given by J. H. FILLOUX, whose gages have proved to be excellent instruments for open sea bottom pressure studies.

The NOAA work was sponsored by the National Science Foundation under the agreement AG 253 for NOAA participation in the International Decade of Ocean Exploration. The Nova University work was supported by NOAA (PO 015150340) and by the National Science Foundation (Grant GA34149).

REFERENCES

BROWN W., W. MUNK, F. SNODGRASS, H. MOFJELD and B. ZETLER (1975) MODE bottom experiment. *Journal of Physical Oceanography*, **5**, 75–85.

CARTWRIGHT D. E., W. MUNK and B. ZETLER (1969) Pelagic tidal measurements—a suggested procedure for analysis. *Transactions, American Geophysical Union*, **50**, 472–477.

CARTWRIGHT D. E. and A. C. EDDEN (1973) Corrected tables of tidal harmonics. *Geophysical Journal of the Royal Astronomical Society*, **33**, 253–263.

Explanatory supplement to the astronomical emphemeris and to the American ephemeris and nautical almanac (1974) H.M.S.O., 522–564.

FILLOUX J. H. (1969) Bourdon tube deep-sea tide gauges. *Proceedings of the International Symposium on Tsunamis and Tsunamis Research*, East–West Center Press, 223–238.

GRACE S. F. (1932) The principal diurnal constituent of tidal motion in the Gulf of Mexico. *Monthly Notices of the Royal Astronomical Society, Geophysical Supplement*, **3**, 70–83.

GRIJALVA N. (1971) The M_2 tide in the Gulf of Mexico. *Geofisica Internacional*, **2**, 103–125.

GROVES G. W. (1970) Use of orthogonal functions for the analysis, prediction, and study of the tide. Hawaii Institute of Geophysics Report No. HIG-70-13, 53 pp.

HANSEN K. S. (1974) Calculations of normal modes for the American mediterranean seas. University of Chicago Technical Report No. 26. 71 pp.

HANSEN W. (1952) Gezeiten und Gezeitenstrome der halbtagigen M_2 in der Nordsee. Deutsche Hydrographischen Zeitschrift Erganzungsheft Nr. 1. 46 pp.

HANSEN W. (1962) Hydrodynamical methods applied to oceanographic problems. *Proceedings of the Symposium of Mathematical and Hydrodynamical Methods of Physical Oceanography*, **1**, 25–34

JEFFREYS H. (1970) *The earth*, 5th edition, Cambridge University Press, 525 pp.

LOMNITZ C. (1956) Creep measurements in igneous rocks. *Journal of Geology*, **64**, 473–479.

LOMNITZ C. (1957) Linear dissipation in solids. *Journal of Applied Physics*, **28**, 201–205.

MARMER H. A. (1954) Tides and sea level in the Gulf of Mexico. *Fishery Bulletin of the United States Fish and Wildlife Service*, **55**, 101–118.

MICHAELOV U. S., V. P. MELISHKO and G. I. SHCHEVELEVA (1969) Estimation of the tides and tidal currents in the Gulf of Mexico and Caribbean Sea. *Trudy, Geosudarstvennyy Okeanograficheskiy. Institute*, **96**, 146–173.

MUNK W. H. and D. E. CARTWRIGHT (1966) Tidal spectroscopy and prediction. *Philosophical Transactions of the Royal Society A*, **259**, 533–581.

PLATZMAN G. W. (1972) Two-dimensional free oscillations in natural basins. *Journal of Physical Oceanography*, **2**, 117–138.

RADOK R., W. MUNK and J. ISAACS (1967) A note on mid-ocean internal tides. *Deep-Sea Research*, **14**, 121–124.

RIEHL H. (1954) *Tropical meteorology*, McGraw-Hill, 392 pp.

SCOR Working Group No. 27 (1975) An intercomparison of open sea tidal pressure sensors. UNESCO Technical Paper in Marine Science No. 21. 67 pp.

United States Department of Commerce (1942) *Tidal harmonic constants, Atlantic Ocean including Arctic and Antarctic Regions*, TH-1. Government Printing Office, 139 pp.

WIMBUSH M. (1977) An inexpensive sea floor precision pressure recorder. *Deep-Sea Research*, 493–497.

ZETLER B. D. (1971) Radiational ocean tides along the coasts of the United States. *Journal of Physical Oceanography*, **1**, 34–38.

ZETLER B. D. and R. A. CUMMINGS (1972) Tidal observations near an amphidrome. *Geophysical Surveys*, **1**, 85–89.

ZETLER B. D. and D. V. HANSEN (1970) Tides in the Gulf of Mexico, pp. 265–275. In: *Contributions on the physical oceanography of the Gulf of Mexico*, Vol. 2, L. R. A. CAPURRO and J. L. REID, editors, Gulf Publishing Co.

ZETLER B. D., W. MUNK, H. MOFJELD, W. BROWN and F. DORMER (1975) MODE tides. *Journal of Physical Oceanography*, **5**, 430–441.

APPENDIX

Tidal analysis of the pressure records

The bottom pressure records were analyzed for tidal components by the following procedure:

Each pressure record was first divided through by $\bar{\rho}g$ to convert it to units of sea level. In practice the mean density of the water column, $\bar{\rho}$, was taken as a constant for each record. Gravity, g, was taken to be 979 cm s^{-2}, a typical value for the region.

These sea level records were then analyzed for tidal components by the response method of MUNK and CARTWRIGHT (1966).* In this method, spherical harmonic expansion of the tide-generating potential (computed from the known motions of earth, moon, and sun) are fitted to the observed data in a least squares sense. Lags and leads of the potential functions may be introduced to allow for variations with frequency of response admittances of the ocean at the observation point. These admittances are then calculated to Fourier transformation of the wrights representing the least squares fit.

For comparison with results from harmonic methods of tidal analysis, it is convenient to calculate amplitudes and phases of individual tidal lines in the spectrum. The amplitude $H(f)$ of a tidal line with frequency f is calculated by multiplying the admittance amplitude $R(f)$ by the amplitude of the tide-generating potential $H_{\mathrm{pot}}(f)$. $H_{\mathrm{pot}}(f)$ for the present historical period is given (in meters) in column 3, Table 1 of CARTWRIGHT and EDDEN (1973). The Greenwich phase $G(f)$ of the tidal line is calculated from the phase $\phi(f)$ of the admittance (defined as in MUNK and CARTWRIGHT, 1966) by the relation $G = m\pi - \phi$, where m is the species number of the tidal line.

Errors in these tidal estimates are principally due to the incoherent noise in the spectral neighbourhoods of the tidal lines. Around each tidal line a cusp-like rise in noise spectrum is observed. This is thought to be caused by baroclinic tides, which derive their energy from the barotropic tide but are rendered incoherent by the variable density structure of the ocean (RADOK, MUNK and ISAACS, 1967). With this model, the noise variance in each tide constituent is proportional to the tidal variance of the constituent, with the result that the standard error is given by

$$\sigma = \left[\frac{\mu}{2l}\right]^{1/2} \quad \sigma, \mu \ll 1$$

relative to H itself or to one radian in G, where μ is the ratio of the residual to recorded variance (i.e. the proportion of the recorded variance that is non-tidal), and l is the length of the record in months (i.e. length in days $\div 27.322$).

Tables A–E give the results of this analysis applied to the Gulf of Mexico and Caribbean bottom pressure records. The presentation follows the form recommended by CARTWRIGHT, MUNK and ZETLER (1969).

*The following corrections (many suggested by CARTWRIGHT, private communication) have been made to the formula in Appendix A of this reference. In section b. $\bar{R}_\theta/\rho_\theta$ is replaced by $(\bar{R}_\theta/\rho_\theta)^2$ as proposed by GROVES (1970). In sections d and e, $\omega_\theta = 0.4093197552 - 0.0002271109689\,2T$; T^2 is replaced by T^3 in equation A17; $-3me_{\theta 2}\sin(h_\theta p_\theta)$ is added to the r.h.s. of equation A18; $m = 0.048013285$; $-\frac{3}{2}m e_\theta \cos(h_\theta - p_\theta)$ is added within [ ] of equation A19. The International Astronomical Union 1964 astronomical constants were used throughout (see p. 492 ff of the *Explanatory supplement to the astronomical emphemeris and to the American emphemeris and nautical alamanac*, 1974).

Table A

Station: Central Gulf of Mexico — 24°46.1N 89°38.9W, depth 3461 m, 1972 October 14, 1629 - 1973 January 17, 1135 GMT

Reference: $C_2^1(0,\pm2,\pm4)$, $C_2^2(0,\pm2,\pm4)$, C_3^3

Admittances (Station/Reference)					Principal harmonic constituents			
Interval 1 cpm (0.0366011 cpd)								
Frequency (cpd)	Real	Imaginary	R	ϕ (deg)		Frequency (cpd)	H (cm)	G (deg)
0.8929346	-0.67828	0.07851	0.68281	173.40	(Q_1)	0.8932441	3.42	006.7
0.9295357	-0.53763	0.18376	0.56816	161.13	O_1	0.9295357	14.90	018.9
0.9661368	-0.40599	0.20743	0.45591	152.94				
1.0027379	-0.33624	0.18226	0.38246	151.54	(P_1)	0.9972621	4.76	028.4
1.0393390	-0.29605	0.19920	0.35683	146.06	K_1	1.0027379	14.10	028.5
Recorded variance: 304.43 cm²							±2.1%	±1.2°
Residual variance: 0.95 cm²								
1.8590714	-0.08469	0.00735	0.08501	175.04	(N_2)	1.8959820	0.63	217.3
1.8956725	-0.04168	0.03133	0.05214	143.06	M_2	1.9322736	1.30	225.8
1.9322736	-0.01438	0.01481	0.02064	134.15				
1.9688747	-0.02392	0.03446	0.04195	-124.77	(S_2)	2.0000000	1.50	130.0
					K_2	2.0054758	0.35	134.9
2.0054758	-0.03112	-0.03120	0.04407	-134.92				
							±5.4%	±3.1°
Recorded variance: 1.98 cm²								
Residual variance: 0.04 cm²								

Table B

Station: West Florida Shelf Break — 26°42.4N 84°15.0W, depth 154 m, 1974 April 6, 1407 - November 18, 2122 GMT

Reference: $C_2^1(0,\pm2,\pm4)$, $C_2^2(0,\pm2,\pm4)$, C_3^3

Admittances (Station/Reference)					Principal harmonic constituents			
Interval 1 cpm (0.0366011 cpd)								
Frequency (cpd)	Real	Imaginary	R	ϕ (deg)		Frequency (cpd)	H (cm)	G (deg)
0.8929346	-0.51272	-0.03282	0.51377	-176.34	(Q_1)	0.8932441	2.58	356.5
0.9295357	-0.44564	0.04024	0.44745	174.84	O_1	0.9295357	11.73	005.2
0.9661368	-0.39082	0.05126	0.39417	172.53				
					(P_1)	0.9972621	4.24	011.2
1.0027379	-0.33265	0.07310	0.34058	167.60	K_1	1.0027379	12.56	012.4
1.0393390	-0.29103	0.12712	0.31758	156.40				
							±1.3%	±0.7°
Recorded variance: 161.98 cm²								
Residual variance: 0.44 cm²								
1.8590714	0.00019	-0.10838	0.10838	-89.90	(N_2)	1.8959820	1.36	095.8
1.8956725	-0.01133	-0.11161	0.11218	-95.79	M_2	1.9322736	6.74	097.1
1.9322736	-0.01322	-0.10578	0.10660	-97.13				
1.9688747	-0.02223	-0.10632	0.10862	-101.81	(S_2)	2.0000000	3.51	102.5
					K_2	2.0054758	0.97	-101.7
2.0054758	-0.02463	-0.11909	0.12161	-101.68				
							±1.0%	±0.6°
Recorded variance: 30.43 cm²								
Residual variance: 0.05 cm²								

Table C

Station: Misteriosa Bank — 18°52.9N 83°48.3W, depth 22m, 1971 July 23, 0001 - August 19, 1803 GMT

Reference: $C_2^1(0,\pm2)$, $C_2^2(0,\pm2)$

Admittances (Station/Reference)					Principal harmonic constituents			
Interval 1 cpm (0.0366011 cpd)								
Frequency (cpd)	Real	Imaginary	R	¢ (deg)		Frequency (cpd)	H (cm)	G (deg)
0.8929346	-0.17160	-0.05025	0.17881	-163.68				
0.9295357	-0.11351	-0.02627	0.11651	-166.97	(Q_1)	0.8932441	0.90	343.7
0.9661368	-0.05585	-0.02316	0.06046	-157.48	O_1	0.9295357	3.06	347.0
1.0027379	-0.01062	-0.04155	0.04289	-104.34	(P_1)	0.9972621	0.50	293.3
1.0393390	0.01279	-0.07763	0.07868	-80.65	K_1	1.0027379	1.58	284.3
Recorded variance: 7.73 cm²							±12%	±7°
Residual variance: 0.24 cm²								
1.8590714	0.18556	-0.24718	0.30908	-53.10	(N_2)	1.8959820	2.30	067.8
1.8956725	0.07245	-0.17620	0.19051	-67.65	M_2	1.9322736	7.88	084.2
1.9322736	0.01251	-0.12402	0.12465	-84.24				
1.9688747	0.01819	-0.10151	0.10312	-79.84	(S_2)	2.0000000	3.89	055.9
					K_2	2.0054758	1.15	052.1
2.0054758	0.08833	-0.11333	0.14368	-52.07				
Recorded variance: 37.00 cm²							±5.8%	±3.3°
Residual variance: 0.25 cm²								

Table D

Station: Rosalind Bank — 16°36.5N 80°20.25W, depth 31 m, 1971 July 22, 0000 - August 14, 1700 GMT

Reference: $C_2^1(0,\pm2)$, $C_2^2(0,\pm2)$

Admittances (Station/Reference)					Principal harmonic constituents			
Interval 1 cpm (0.0366011 cpd)								
Frequency (cpd)	Real	Imaginary	R	¢ (deg)		Frequency (cpd)	H (cm)	G (deg)
0.8929346	-0.00116	-0.04676	0.04677	-91.42				
0.9295357	0.04080	-0.05936	0.07203	-55.49	(Q_1)	0.8932441	0.24	270.9
0.9661368	0.06519	-0.07721	0.10105	-49.82	O_1	0.9295357	1.89	235.5
1.0027379	0.06693	-0.09660	0.11752	-55.28	(P_1)	0.9972621	1.42	234.0
1.0393390	0.04566	-0.11351	0.12235	-68.09	K_1	1.0027379	4.33	235.3
Recorded variance: 13.84 cm²							±6.4%	±3.7°
Residual variance: 0.10 cm²								
1.8590714	0.10425	-0.20902	0.23357	-63.49	(N_2)	1.8959820	1.80	086.0
1.8956725	0.01110	-0.14915	0.14956	-85.74	M_2	1.9322736	6.63	107.0
1.9322736	-0.03061	-0.10035	0.10491	-106.96				
1.9688747	-0.01221	-0.07275	0.07377	-99.52	(S_2)	2.0000000	2.51	055.6
					K_2	2.0054758	0.76	049.1
2.0054758	0.06247	-0.07210	0.09540	-49.09				
Recorded variance: 22.95 cm²							±5.3%	±3.0°
Residual variance: 0.11 cm²								

Table E

Station: Six-Month East Caribbean — 16°32.5N 64°52.9W, depth 3990 m
1972 May 20, 0000 - November 9, 1309 GMT

Reference: C_2^0, $C_2^1(0,-2,\pm4)$, $C_2^2(0,\pm2,\pm4)$, C_3^3, x_1^1

Admittances* (Station/Reference) Interval 1 cpm (0.0366011 cpd)					Principal harmonic constituents			
Frequency (cpd)	Real	Imaginary	R	ϕ (deg)		Frequency (cpd)	H (cm)	G (deg)
0.8929346	0.20989	-0.13665	0.25045	-33.07	(Q_1)	0.8932441	1.26	213.2
0.9295357	0.16164	-0.17448	0.23785	-47.19	O_1	0.9295357	6.24	227.2
0.9661368	0.12927	-0.17947	0.22118	-54.24				
1.0027379	0.14436	-0.19082	0.23927	-52.89	(P_1)	0.9972621	2.85	233.2
1.0393390	0.16838	-0.23455	0.28873	-54.32	K_1	1.0027379	8.82	232.9
Recorded variance: 68.02 cm^2							±1.3%	±0.7°
Residual variance: 0.14 cm^2								
1.8590714	-0.03302	-0.09954	0.10468	-108.39	(N_2)	1.8959820	0.58	129.7
1.8956725	-0.03047	-0.03710	0.04801	-129.40	M_2	1.9322736	0.52	155.8
1.9322736	-0.00748	-0.00336	0.00820	-155.82				
1.9688747	0.02096	-0.02510	0.03270	-50.14	(S_2)	2.0000000	1.30	043.7
					K_2	2.0054758	0.32	037.5
2.0054758	0.03184	-0.02444	0.04014	-37.51				
							±6.4%	±3.7°
Recorded variance: 1.35 cm^2								
Residual variance: 0.07 cm^2								
2.8984104	-0.10248	0.11420	0.15344	131.90	M_3	2.8984104	0.12	048.1
Recorded variance: 0.035 cm^2							±**%	±**°
Residual variance: 0.027 cm^2								

* gravitational not radiational
** ν = (residual/recorded) variance = 0(1), formula inapplicable

25

NOAA Technical Memorandum ERL AOML-27, 33 pages.

SYNOPTIC AND MEAN MONTHLY 20°C TOPOGRAPHIES IN THE EASTERN GULF OF MEXICO

Robert L. Molinari

Physical Oceanography Laboratory

Atlantic Oceanographic and Meteorological Laboratories
Miami, Florida
June 1977

UNITED STATES
DEPARTMENT OF COMMERCE
Juanita M. Kreps, Secretary

NATIONAL OCEANIC AND
ATMOSPHERIC ADMINISTRATION
Robert M. White, Administrator

Environmental Research
Laboratories
Wilmot N. Hess, Director

Page

CONTENTS

Abstract..... 1

1. Introduction..... 1

2. 20°C topographies..... 1

2.1 Synoptic data..... 1

2.2 Climatological data..... 2

3. Acknowledgments..... 2

4. References..... 3

Appendix 1. 20°C topographies in the deep basin..... 4

Appendix 2. Climatological 20°C topographies..... 26

Appendix 3. Comparison of climatological and synoptic observations..... 31

SYNOPTIC AND MEAN MONTHLY 20°C TOPOGRAPHIES IN THE EASTERN GULF OF MEXICO

Robert L. Molinari
National Oceanic and Atmospheric Administration
Environmental Research Laboratories
Atlantic Oceanographic and Meteorological Laboratories
Miami, Florida

ABSTRACT. Synoptic and mean-monthly 20°C isothermal surface topographies are presented to make these data available to other investigators. Historical literature in which many of the synoptic topographies are considered are also listed. Finally, other data representations are given in which the large variability about the climatological averages is indicated.

1. INTRODUCTION

Atlantic Oceanographic and Meteorological Laboratories personnel were involved with scientists from other institutions in a "Compilation and Summation of the Historical and Existing Physical Oceanographic Data from the Eastern Gulf of Mexico" (SUSIO, 1975) for the Bureau of Land Management (BLM). One portion of this study was designed to summarize the characteristics of the deep basin circulation in the eastern Gulf of Mexico.

Temperature topographies are useful approximations to the density field and, therefore, to the geostropic circulation in the eastern Gulf of Mexico (see Leipper (1970), for instance). Thus, one of the parameters selected to describe the deep basin circulation in the BLM report was the 20°C isothermal surface topography obtained from synoptic cruise data. These topographies are presented in this report so as to provide other investigators the benefit of these data.

In addition, monthly mean 20°C topographies were computed and are presented. When available, dynamic height distributions of the sea-surface relative to 500 db were prepared and are given. Finally, some representative salinity cross-sections through the major circulation features were constructed and are included in this report.

2. 20°C TOPOGRAPHIES

2.1 Synoptic data

The National Oceanographic Data Center (NODC) of the National Oceanic and Atmospheric Administration prepared the base charts from which the contoured 20°C topographies were produced. The charts gave the station position, the data type, i.e., whether Nansen station, STD station, expendable bathy-

thermograph or mechanical bathythermograph observation, and the depth of the 20°C isotherm. If the station data did not include the depth of the 20°C surface, NODC computed the isotherm depth by linear interpolation. The charts were then subjectively contoured, and the resulting data-set is given in Appendix 1.

Appendix 1 also includes dynamic topographies of the sea-surface relative to 500 db and representative salinity cross-sections. The similarities between the dynamic and isotherm topographies, particularly in regions of strong current, demonstrate the reliability of the isotherm topography as an indicator for geostropic motions.

As discussed in the introduction, these data are presented primarily to inform other investigators of their availability. Most of the data have been discussed in other publications which considered the circulation in the eastern Gulf of Mexico, and, in particular the major flow feature in this region, the Loop Current. For instance, Nowlin and McLellan (1967) and Nowlin (1972) discussed the wintertime circulation pattern using the February to March 1962 data. Leipper (1970) based his suggestion for an annual cycle of the intrusion of the Loop Current on the 1965-1966 data-set. Nowlin and Hubertz (1972) demonstrated the summertime variability in the current regime using the June 1966 and 1967 data. Cochrane (1972) documented an eddy separation event using the 1969 observations. Finally, Maul (1975) observed a Loop intrusion cycle similar to that of Leipper in 1972-1973. Therefore, no detailed analysis of these data will be presented in this report.

2.2 Climatological data

As part of the BLM study, NODC computed average temperature values by 1° square and month from their XBT and MBT data-files. The depth of the climatological monthly 20°C surface was computed by linear interpolation from data at 5 m intervals. The mean 20°C topographies were subjectively contoured and are presented in Appendix 2.

The 150 m isopleth of the 20°C surface is located near the core of the Loop Current as indicated by the maximum gradients in the dynamic topographies. Appendix 2 also includes bi-monthly compilations of synoptic 150 m isopleths compared to climatological isopleths. These figures illustrate the large variability observed about the mean conditions.

3. ACKNOWLEDGMENTS

The compilation of these data would not have been possible without the efforts of Mr. M. Rinkel, State University System of Florida Institute of Oceanography (SUSIO); Mr. J. Cochrane, Texas A&M University; and Dr. G. Maul, NOAA, Atlantic Oceanographic and Meteorological Laboratories. This work was funded by the Bureau of Land Management, Department of Interior, through contract Number 08550-CT4-16, administered by SUSIO.

4. REFERENCES

Cochrane, J. D. (1972). Separation of an anticyclonic and subsequent developments in the Loop Current (1969). IN: Contributions on the Physical Oceanography of the Gulf of Mexico, Capurro and Reid, Editors, Gulf Publ. Co., Houston, pp. 91-106.

Leipper, D. F. (1970). A sequence of current patterns in the Gulf of Mexico. J. Geophys. Res., 75, pp. 637-657.

Maul, G. (1975). An evaluation of the use of the Earth Resources Technology Satellite for observing ocean current boundaries in the Gulf Stream system. NOAA Tech. Report ERL 355 AOML 18, 125 pp.

Nowlin, W. D. (1972). Winter circulation patterns and property distribution. IN: Contributions on the Physical Oceanography of the Gulf of Mexico, Capurro and Reid, Editors, Gulf Publ. Co., Houston, pp. 3-51.

Nowlin, W. D., and J. M. Hubertz (1972). Contrasting summer circulation patterns for the eastern Gulf: Loop Current versus anticyclonic ring. IN: Contributions on the Physical Oceanography of the Gulf of Mexico, Capurro and Reid, Editors, Gulf Publ. Co., Houston, pp. 139-148.

Nowlin, W. D., and H. J. McLellan (1967). A characterization of the Gulf of Mexico waters. J. Mar. Res., 25, pp. 29-59.

SUSIO (1975). Compilation and summation of historical and existing physical oceanographic data from the eastern Gulf of Mexico. State University System of Florida Institute of Oceanography Final Report to the Bureau of Land Management, Contract Number 08550-CT4-64.

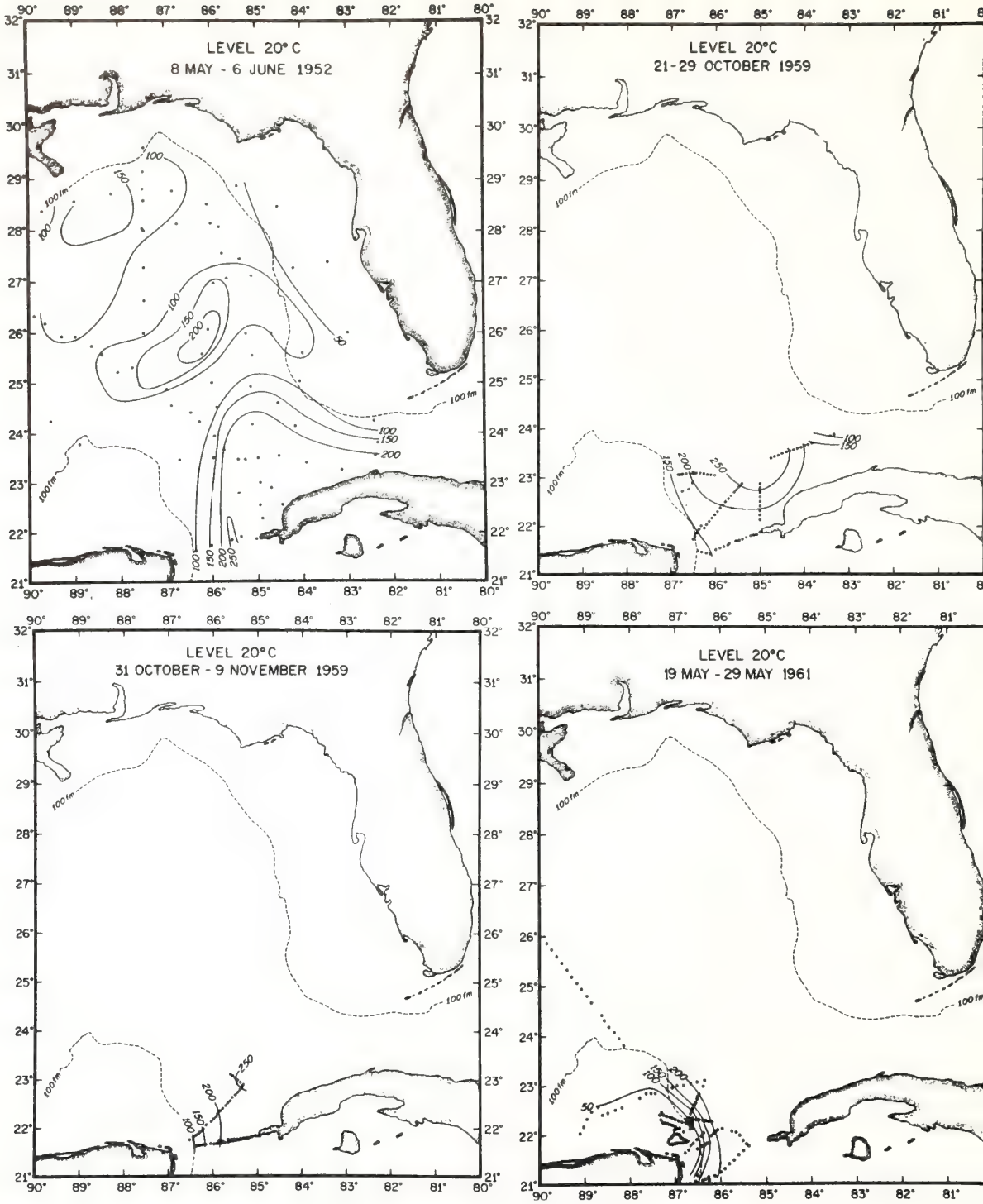
APPENDIX 1. 20°C TOPOGRAPHIES IN THE DEEP BASIN

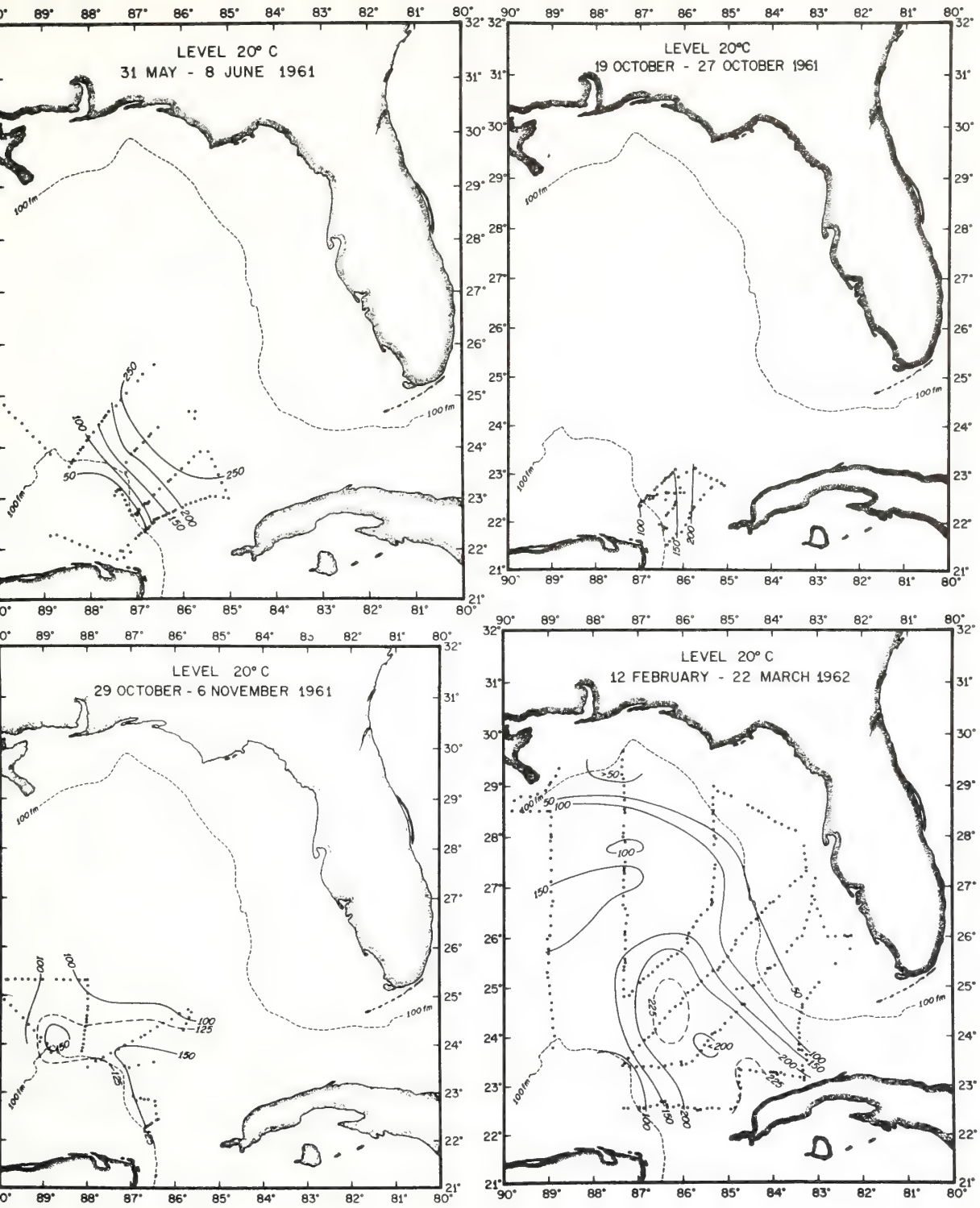
Charts indicating the depth of the 20°C isotherm surface as observed during individual and multi-ship operations have been produced by NODC. The data-sets include measurements taken by MBT, XBT, STD, and Nansen cast. In each case, a linear interpolation over the layer in which the desired isotherm occurred was performed to obtain the corresponding depth.

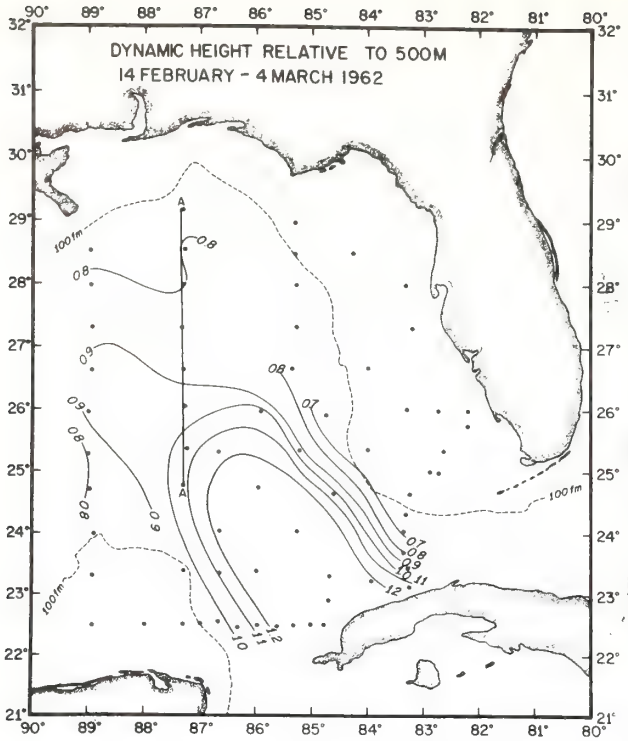
The 20°C topographies have been contoured and are presented in chronological order. Although the type of measurement, i.e., XBT, STD, etc., was indicated on the NODC chart by different symbols, only the station position, irrespective of type, is given on the following charts.

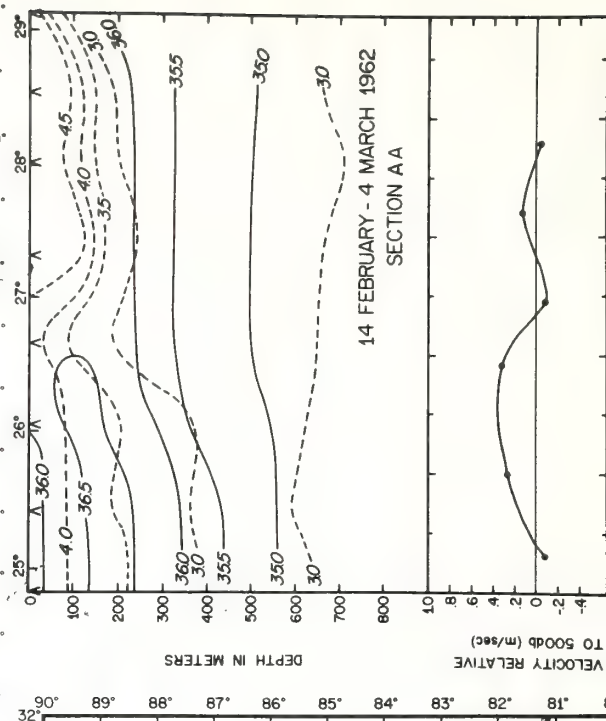
Dynamic topographies relative to 500 db are given also for those cruises in which it was felt that the spatial coverage warranted this presentation. The dynamic height values and station positions were obtained from the NODC listings provided.

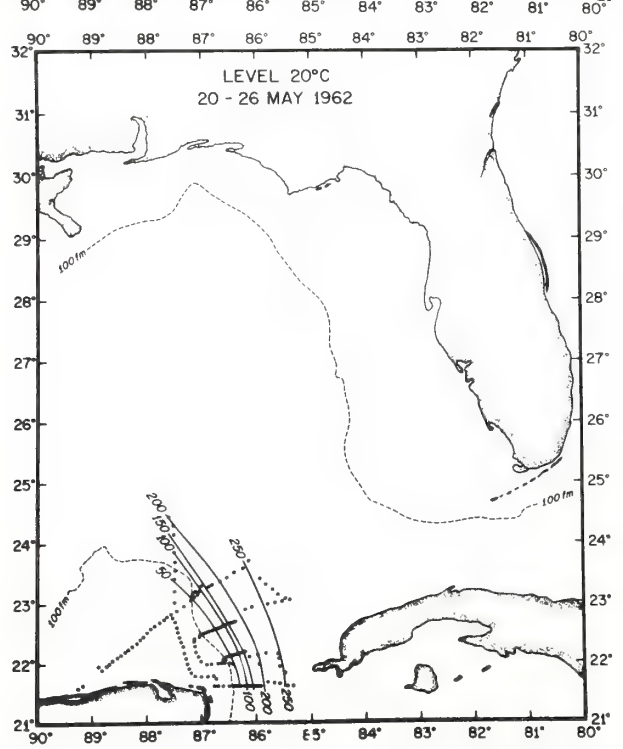
Vertical sections of salinity and oxygen, if available, are provided for those cruises in which specific features were considered. For instance, those sections through the ridge separating the main flow and a detached eddy are considered particularly informative. These sections also include geostrophic velocities relative to 500 db to define the horizontal extent of the current cores.

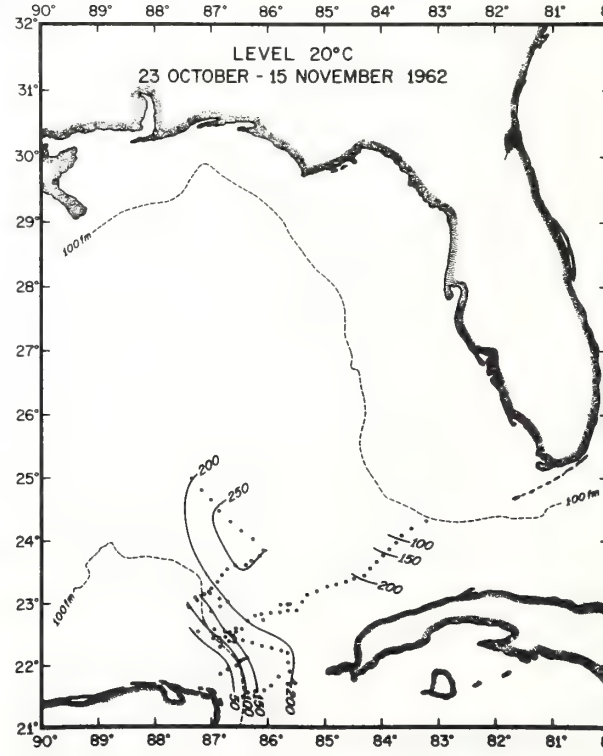

LEVEL 20° C
8 MAY - 6 JUNE 1952
LEVEL 20°C
21-29 OCTOBER 1959
LEVEL 20°C
31 OCTOBER - 9 NOVEMBER 1959
LEVEL 20°C
19 MAY - 29 MAY 1961
100 fm

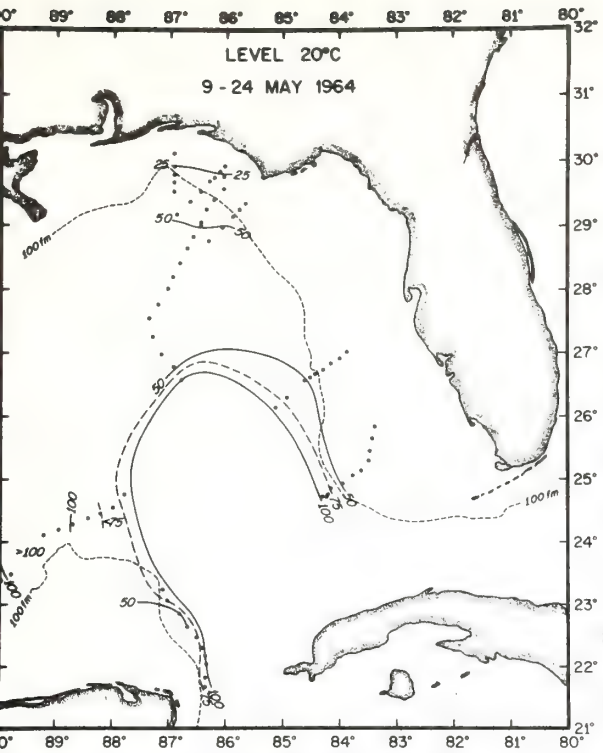

LEVEL 20° C
31 MAY - 8 JUNE 1961
LEVEL 20°C
19 OCTOBER - 27 OCTOBER 1961
LEVEL 20° C
29 OCTOBER - 6 NOVEMBER 1961
LEVEL 20° C
12 FEBRUARY - 22 MARCH 1962
100 fm

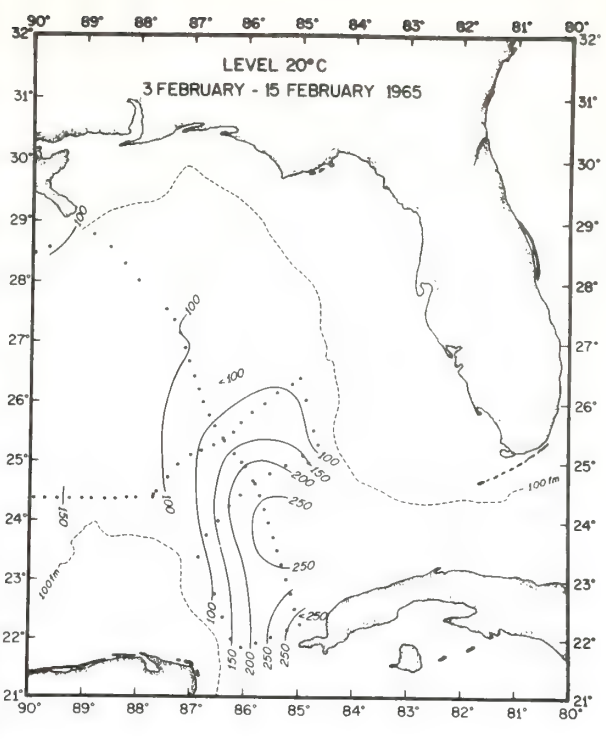

DYNAMIC HEIGHT RELATIVE TO 500M
14 FEBRUARY - 4 MARCH 1962
100fm

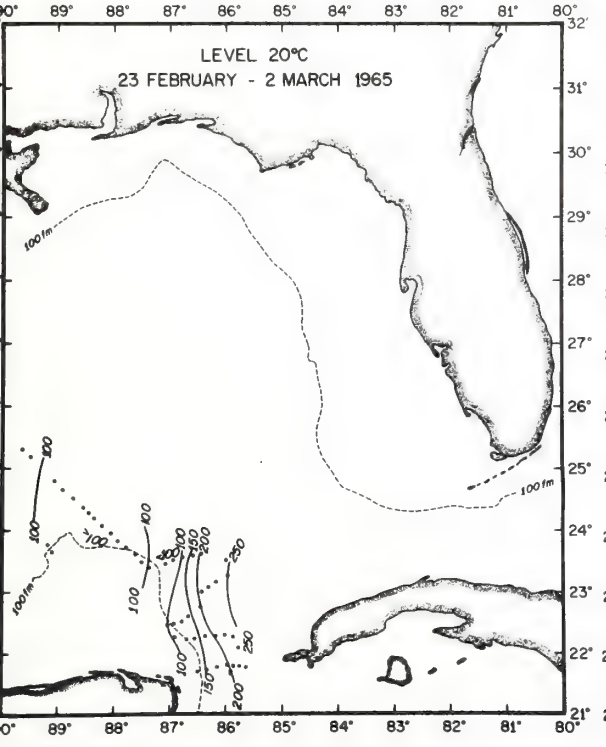

14 FEBRUARY - 4 MARCH 1962
SECTION AA
DEPTH IN METERS
VELOCITY RELATIVE TO 500db (m/sec)

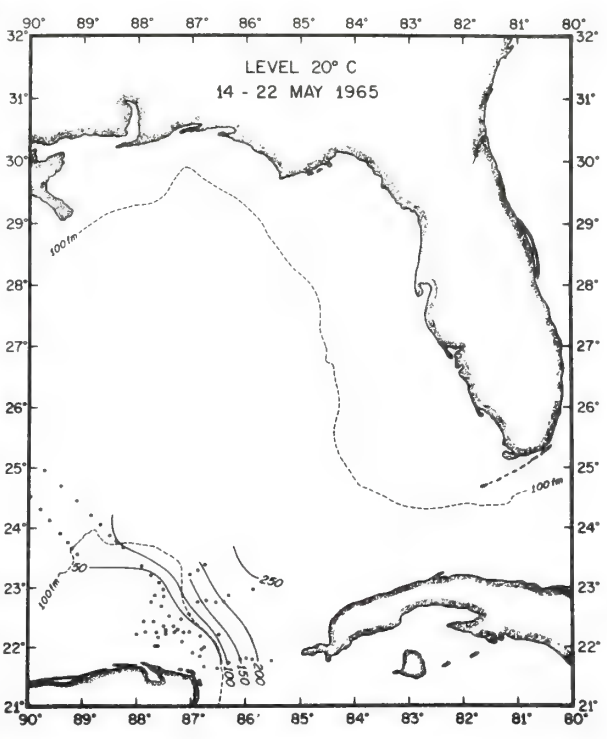

LEVEL 20°C
20 - 26 MAY 1962
100fm

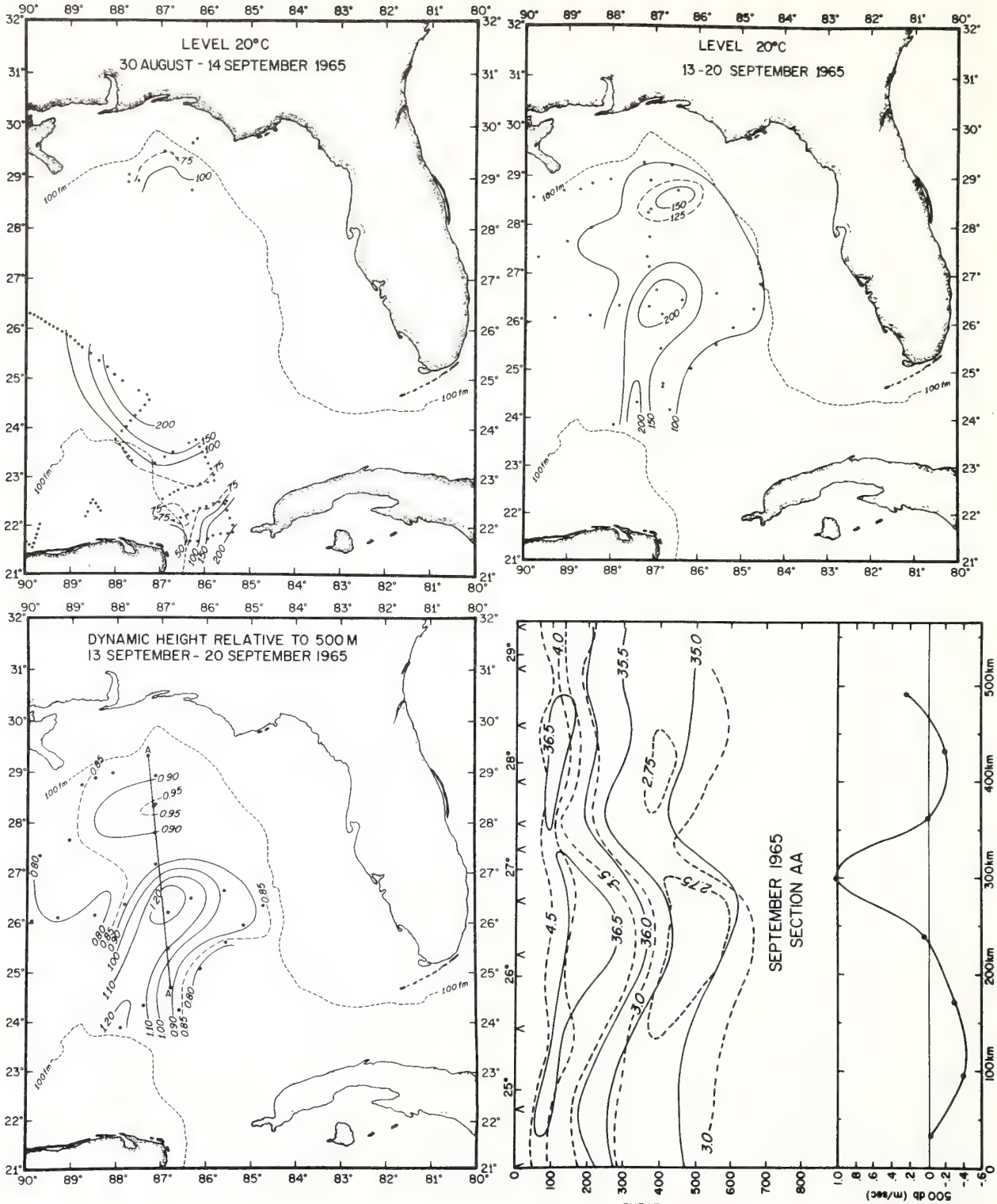

LEVEL 20°C
23 OCTOBER - 15 NOVEMBER 1962
100fm

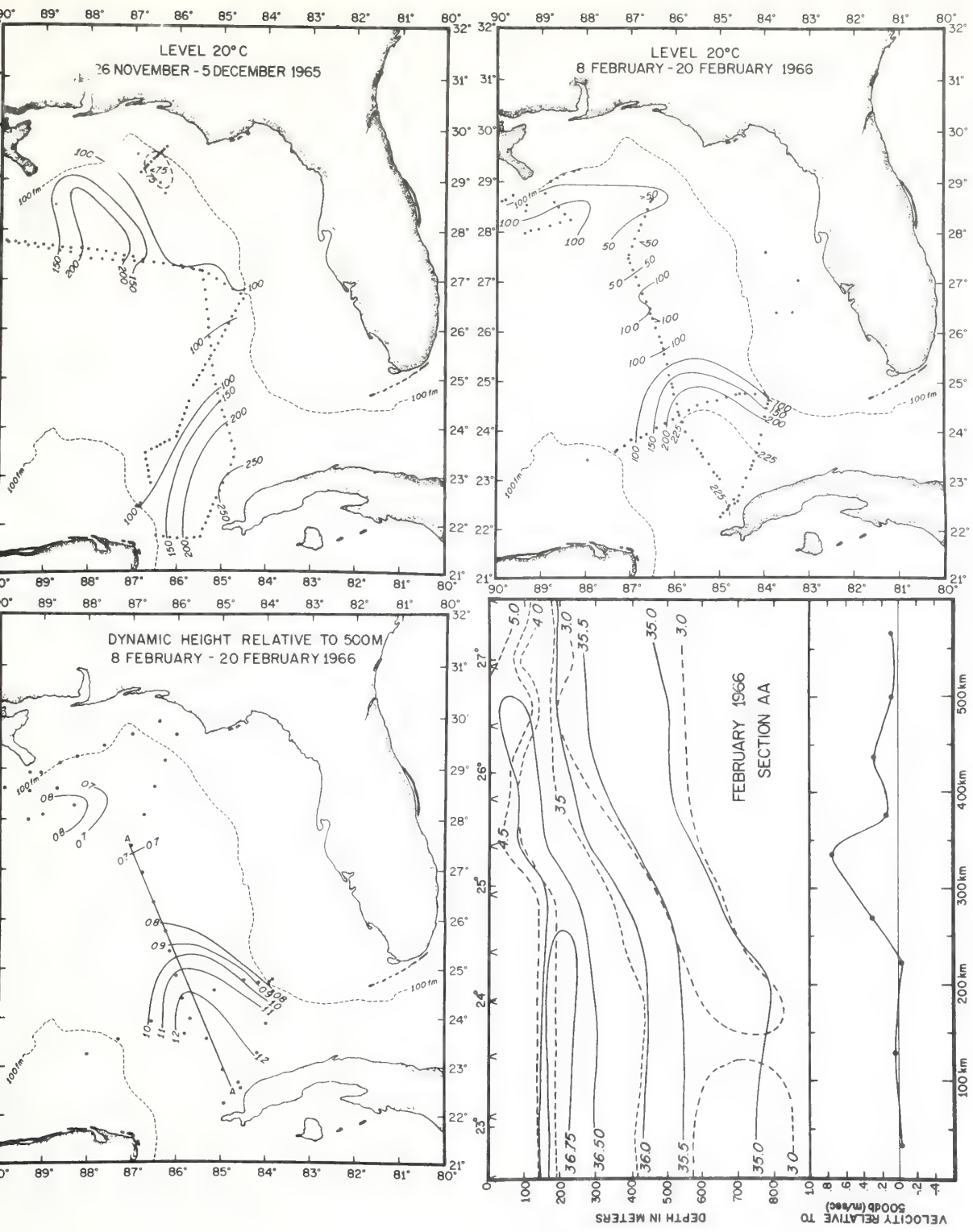

LEVEL 20°C
9 - 24 MAY 1964
100 fm

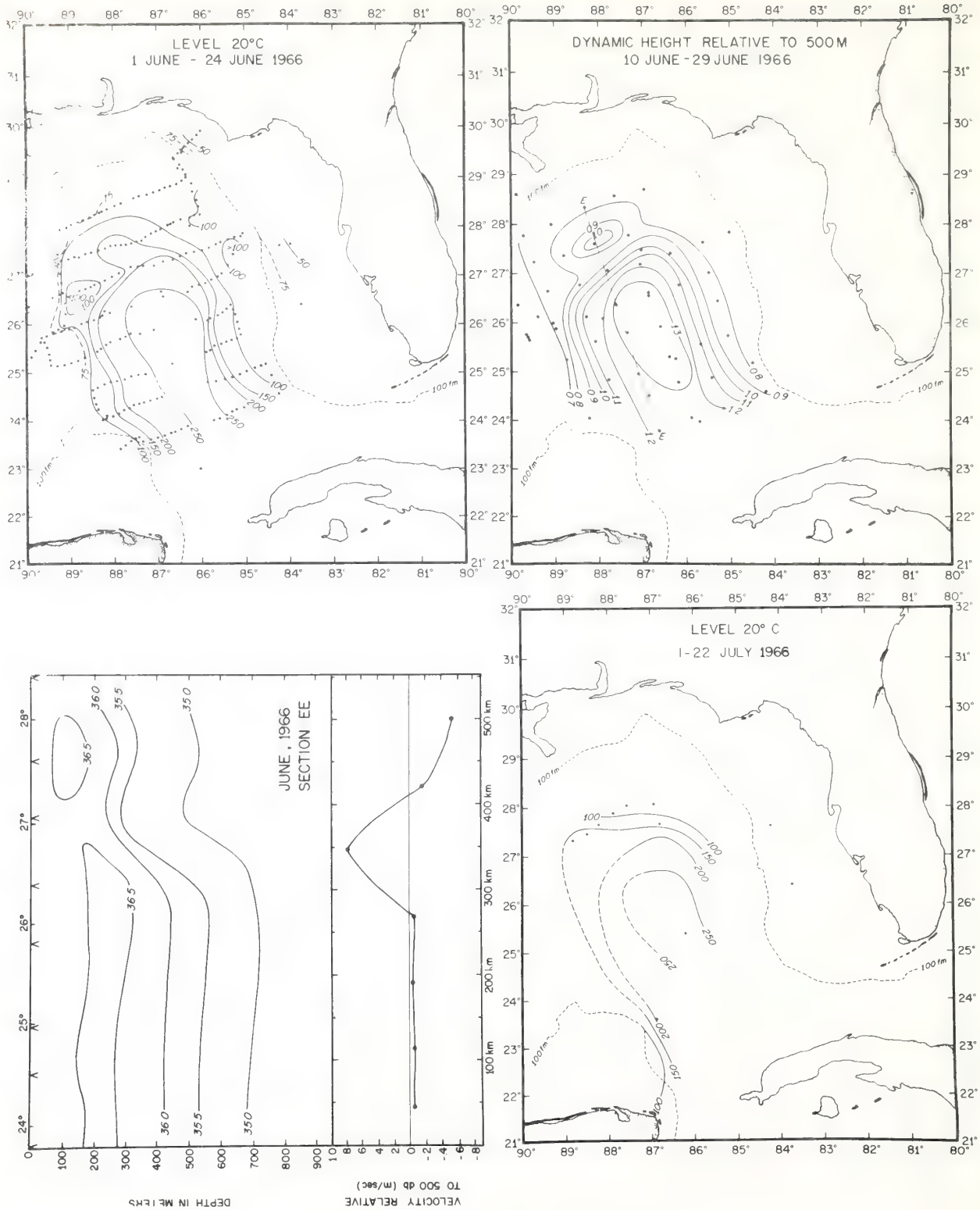

LEVEL 20°C
3 FEBRUARY - 15 FEBRUARY 1965
100 fm

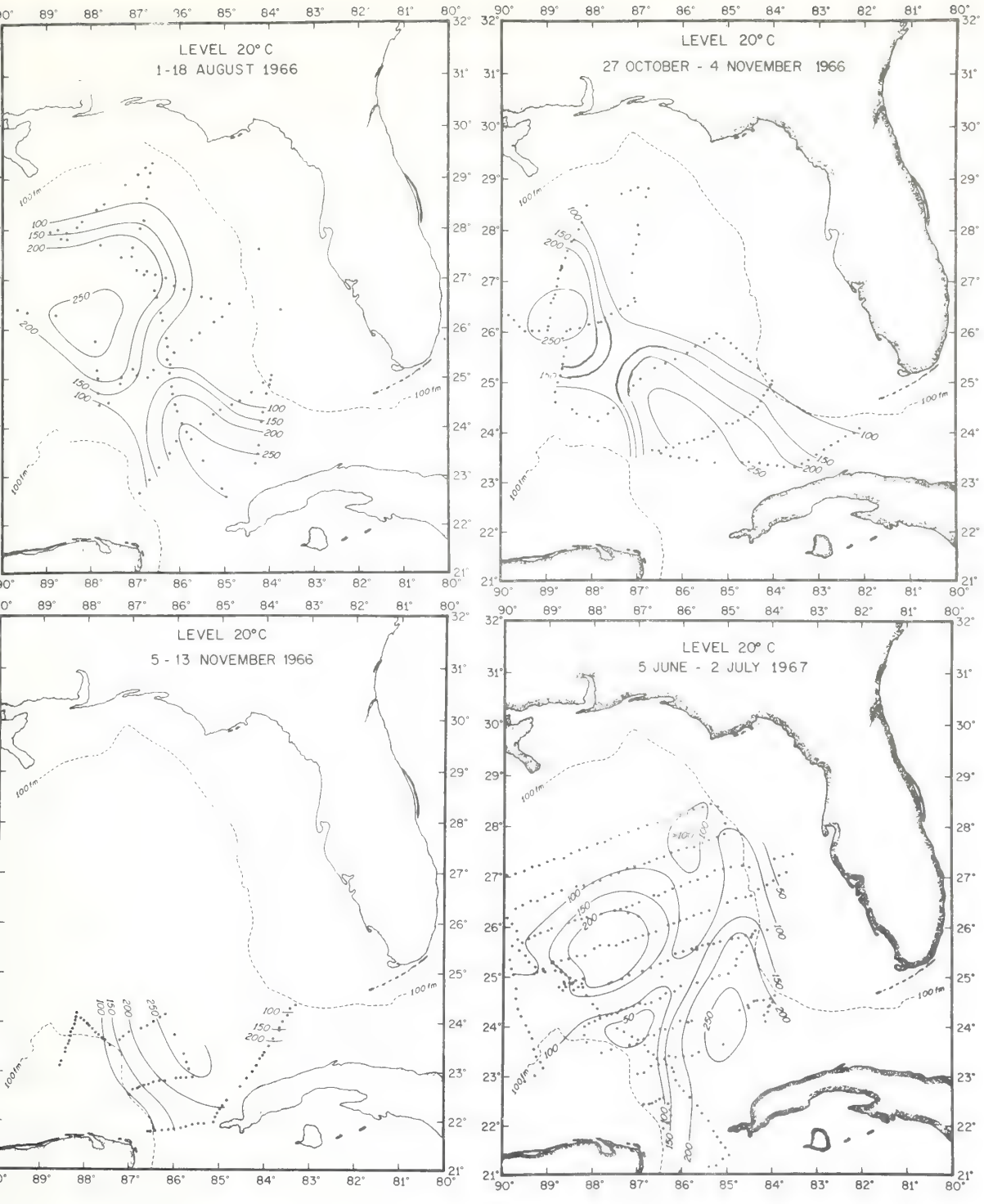

LEVEL 20°C
23 FEBRUARY - 2 MARCH 1965
100 fm

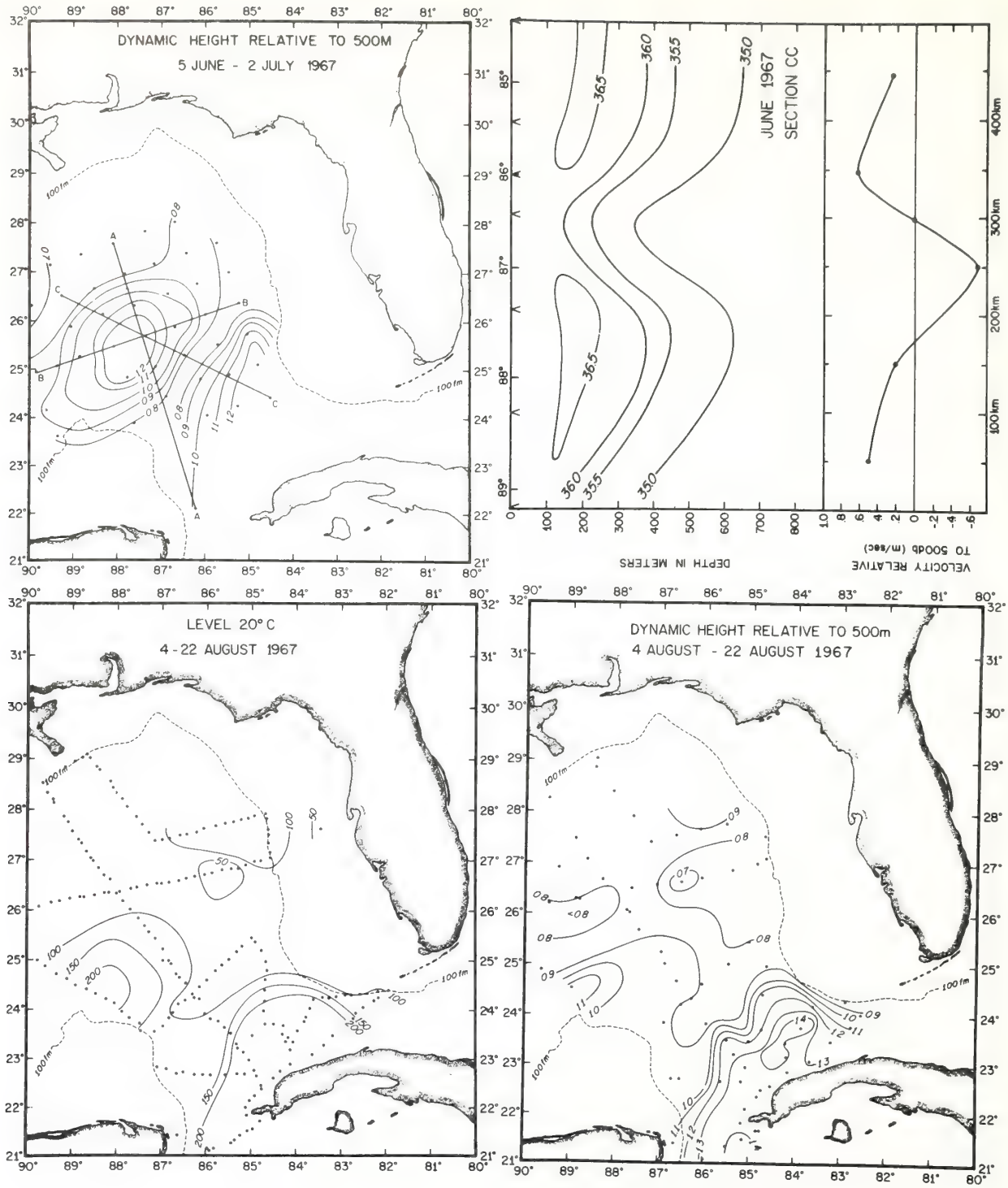

LEVEL 20° C
14 - 22 MAY 1965
100 fm

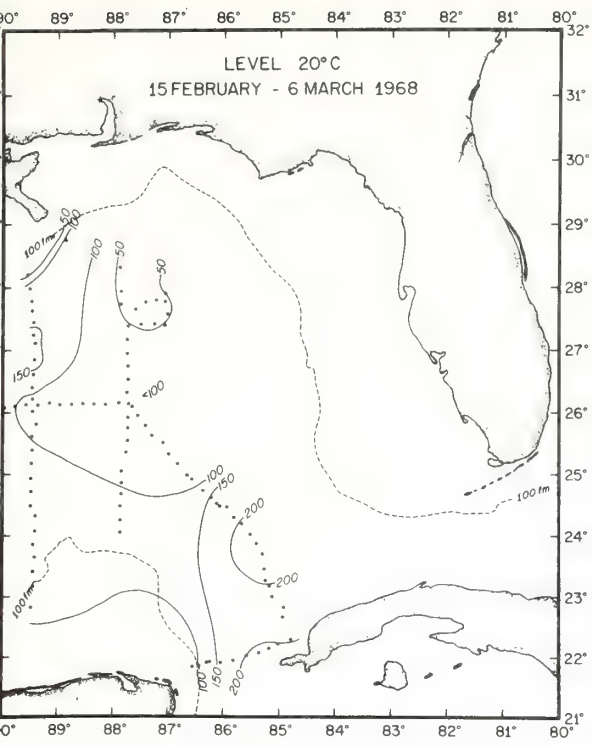

LEVEL 20°C
30 AUGUST - 14 SEPTEMBER 1965
LEVEL 20°C
13-20 SEPTEMBER 1965
DYNAMIC HEIGHT RELATIVE TO 500 M
13 SEPTEMBER - 20 SEPTEMBER 1965
SEPTEMBER 1965
SECTION AA
DEPTH IN METERS
VELOCITY RELATIVE TO 500 db (m/sec)

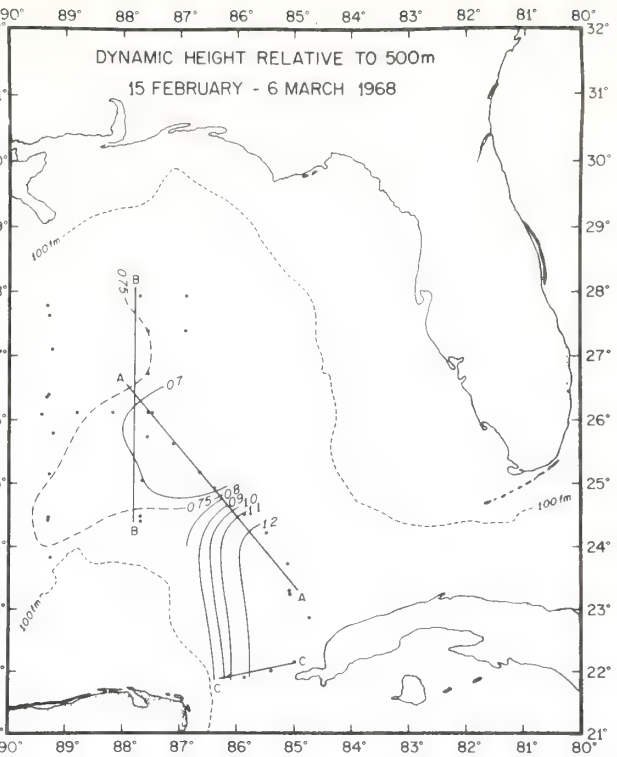

LEVEL 20°C
26 NOVEMBER - 5 DECEMBER 1965
LEVEL 20°C
8 FEBRUARY - 20 FEBRUARY 1966
DYNAMIC HEIGHT RELATIVE TO 500M
8 FEBRUARY - 20 FEBRUARY 1966
FEBRUARY 1966
SECTION AA
DEPTH IN METERS
VELOCITY RELATIVE TO 500db (m/sec)

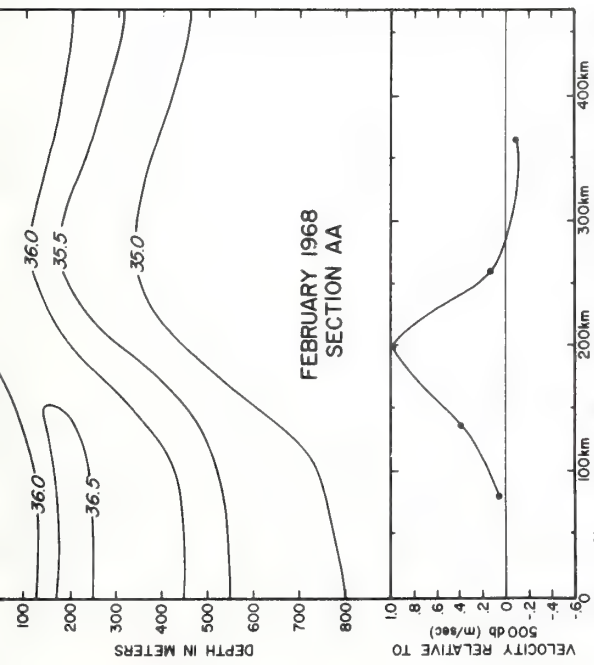

LEVEL 20°C
1 JUNE - 24 JUNE 1966
DYNAMIC HEIGHT RELATIVE TO 500M
10 JUNE - 29 JUNE 1966
LEVEL 20° C
1-22 JULY 1966
JUNE, 1966
SECTION EE
DEPTH IN METERS
VELOCITY RELATIVE
TO 500 db (m/sec)

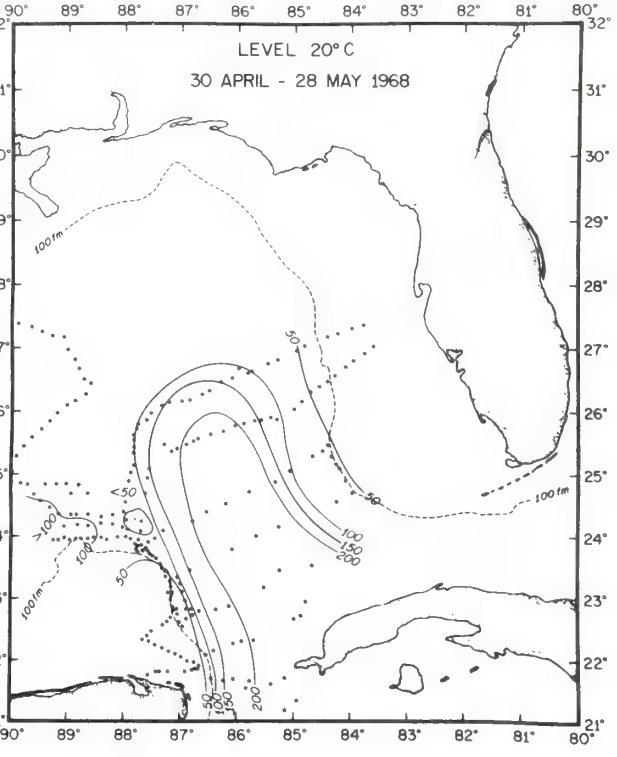

LEVEL 20° C
1-18 AUGUST 1966
LEVEL 20° C
27 OCTOBER - 4 NOVEMBER 1966
LEVEL 20°C
5 - 13 NOVEMBER 1966
LEVEL 20° C
5 JUNE - 2 JULY 1967
100 fm

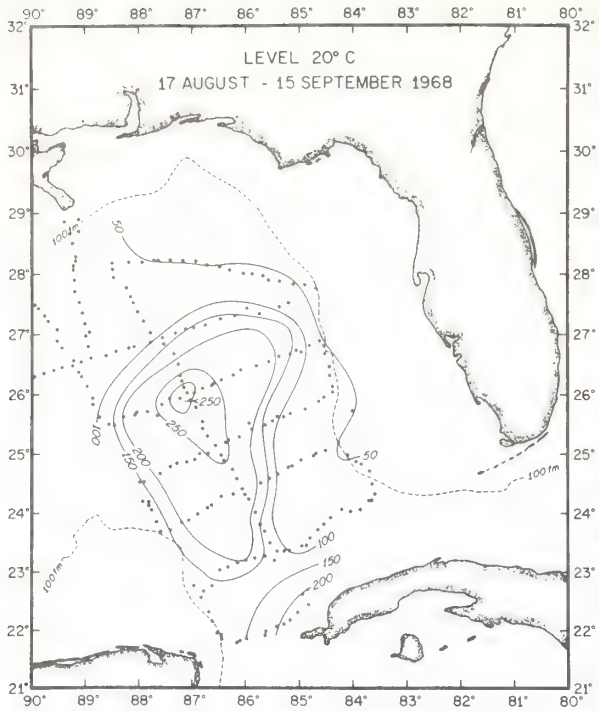

DYNAMIC HEIGHT RELATIVE TO 500M
5 JUNE - 2 JULY 1967
JUNE 1967
SECTION CC
DEPTH IN METERS
VELOCITY RELATIVE TO 500db (m/sec)
LEVEL 20° C
4 - 22 AUGUST 1967
DYNAMIC HEIGHT RELATIVE TO 500m
4 AUGUST - 22 AUGUST 1967

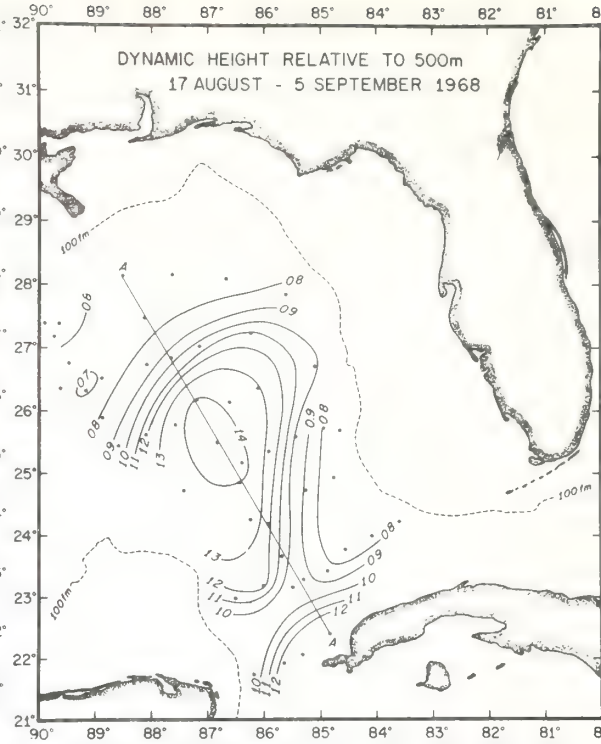

LEVEL 20°C
15 FEBRUARY - 6 MARCH 1968
100 fm

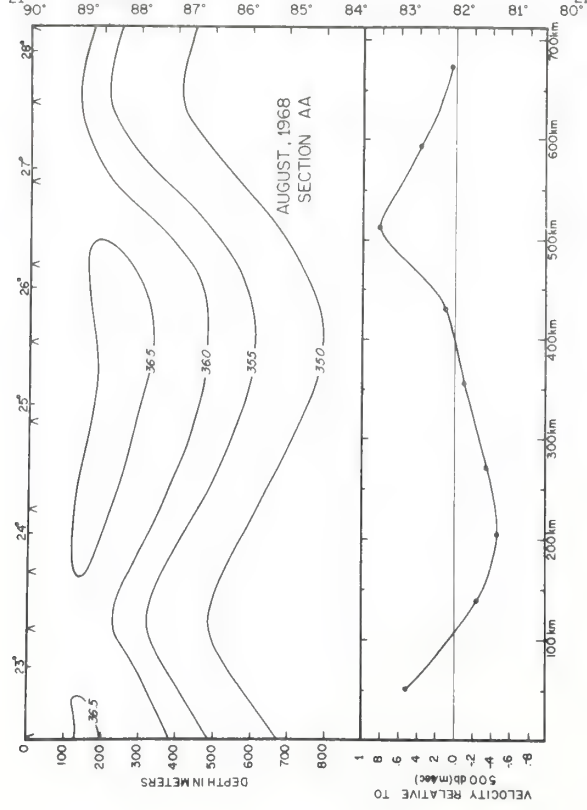

DYNAMIC HEIGHT RELATIVE TO 500m
15 FEBRUARY - 6 MARCH 1968
100 fm

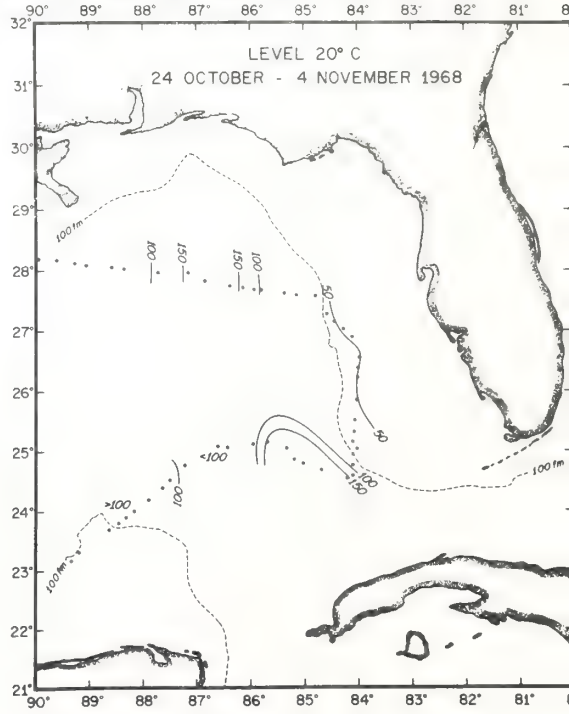

FEBRUARY 1968
SECTION AA
DEPTH IN METERS
VELOCITY RELATIVE TO 500db (m/sec)

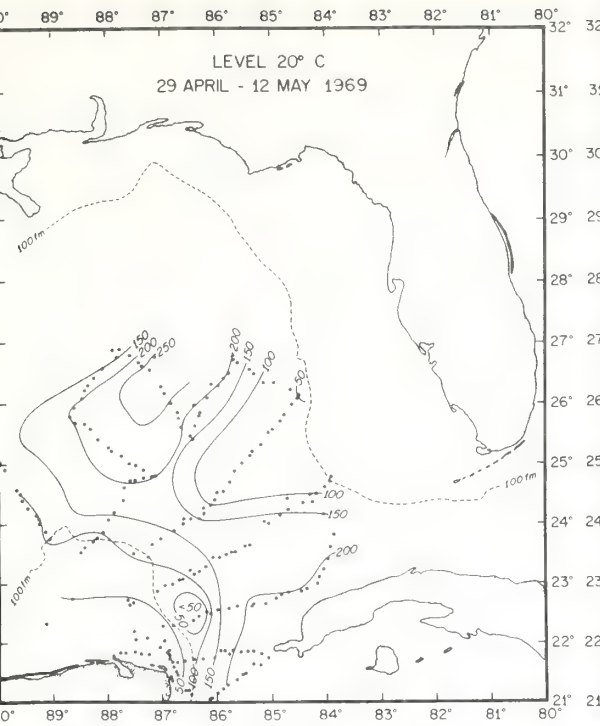

LEVEL 20°C
30 APRIL - 28 MAY 1968
100 fm

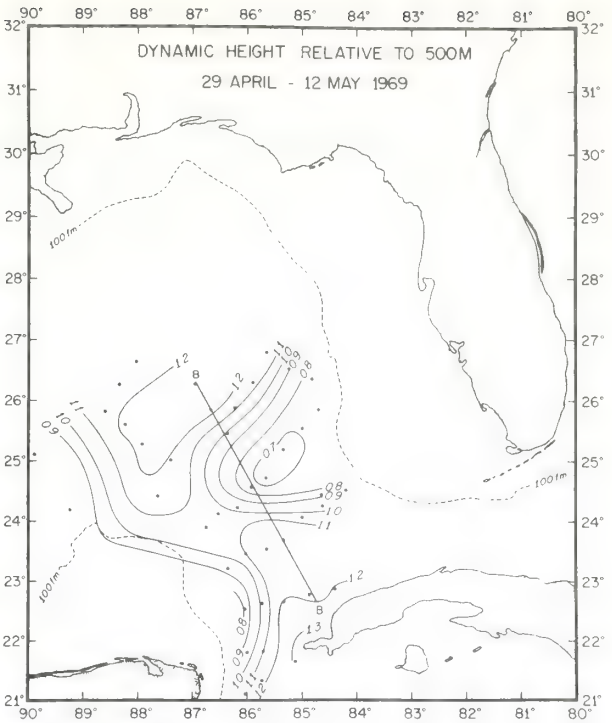

LEVEL 20° C
17 AUGUST - 15 SEPTEMBER 1968

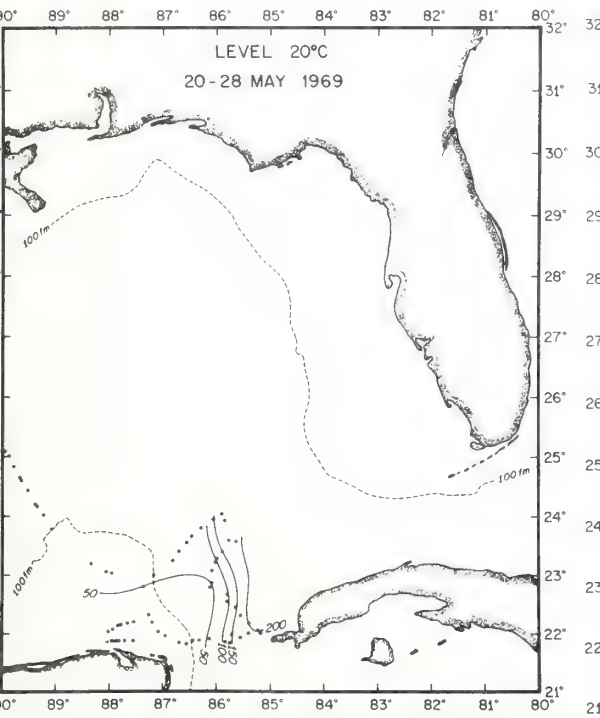

DYNAMIC HEIGHT RELATIVE TO 500m
17 AUGUST - 5 SEPTEMBER 1968

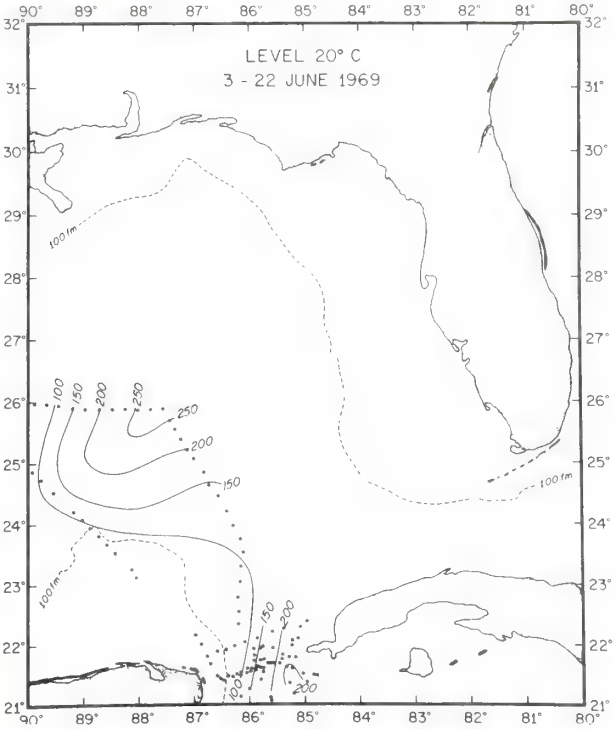

AUGUST, 1968
SECTION AA
DEPTH IN METERS
VELOCITY RELATIVE TO 500 db(m/sec)

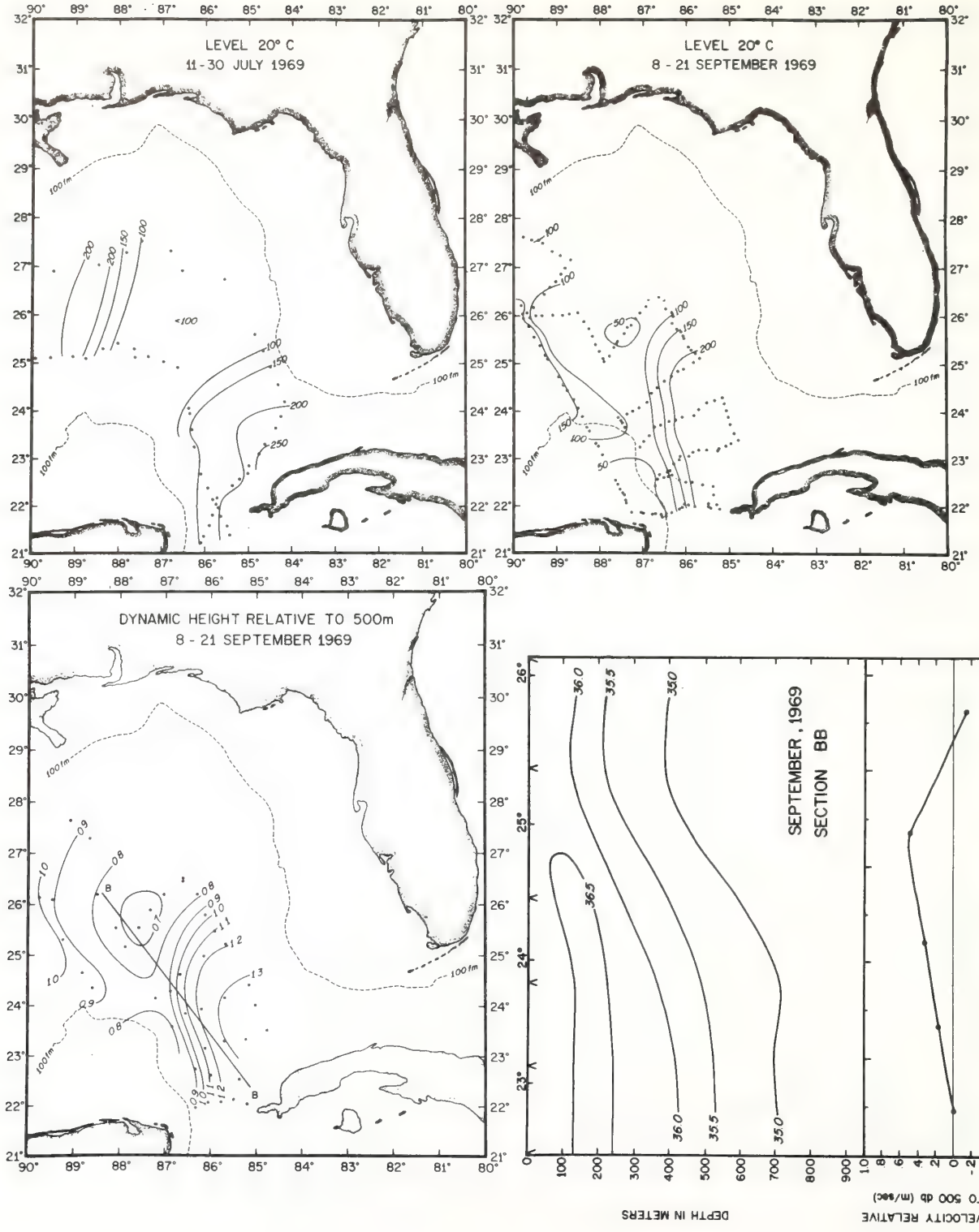

LEVEL 20° C
24 OCTOBER - 4 NOVEMBER 1968

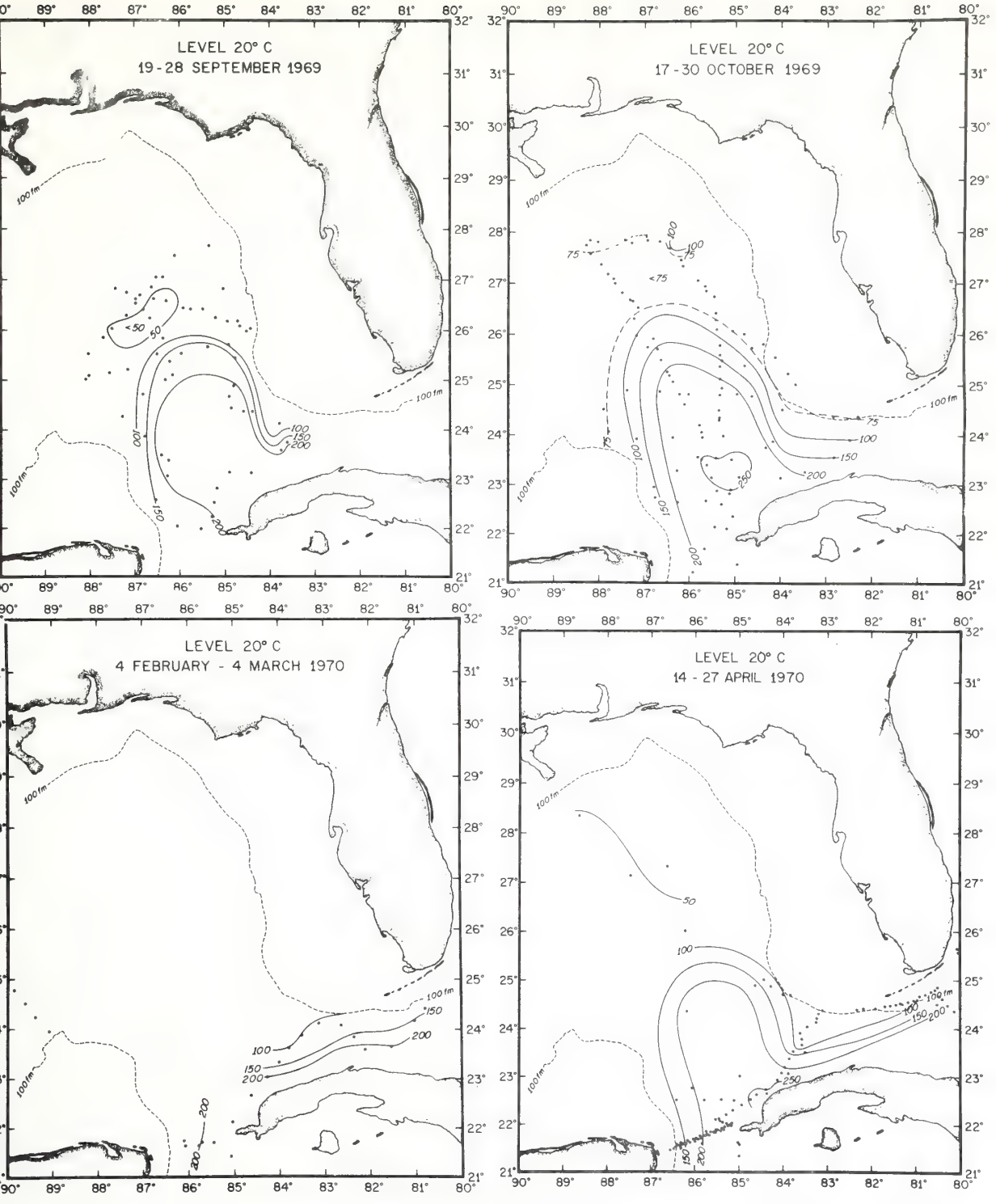

LEVEL 20° C
29 APRIL - 12 MAY 1969
100fm


DYNAMIC HEIGHT RELATIVE TO 500M
29 APRIL - 12 MAY 1969
100fm

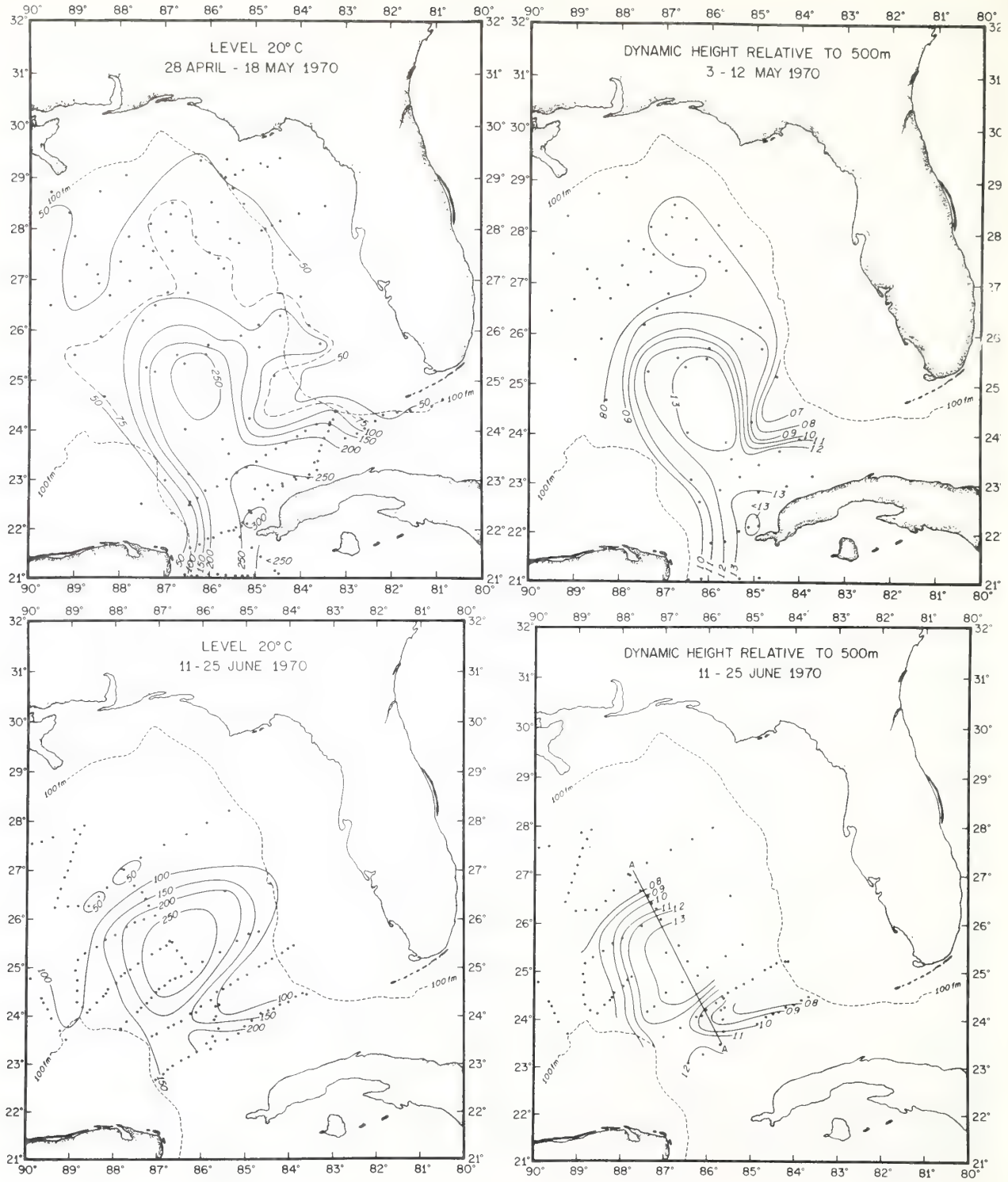

LEVEL 20°C
20-28 MAY 1969
100fm

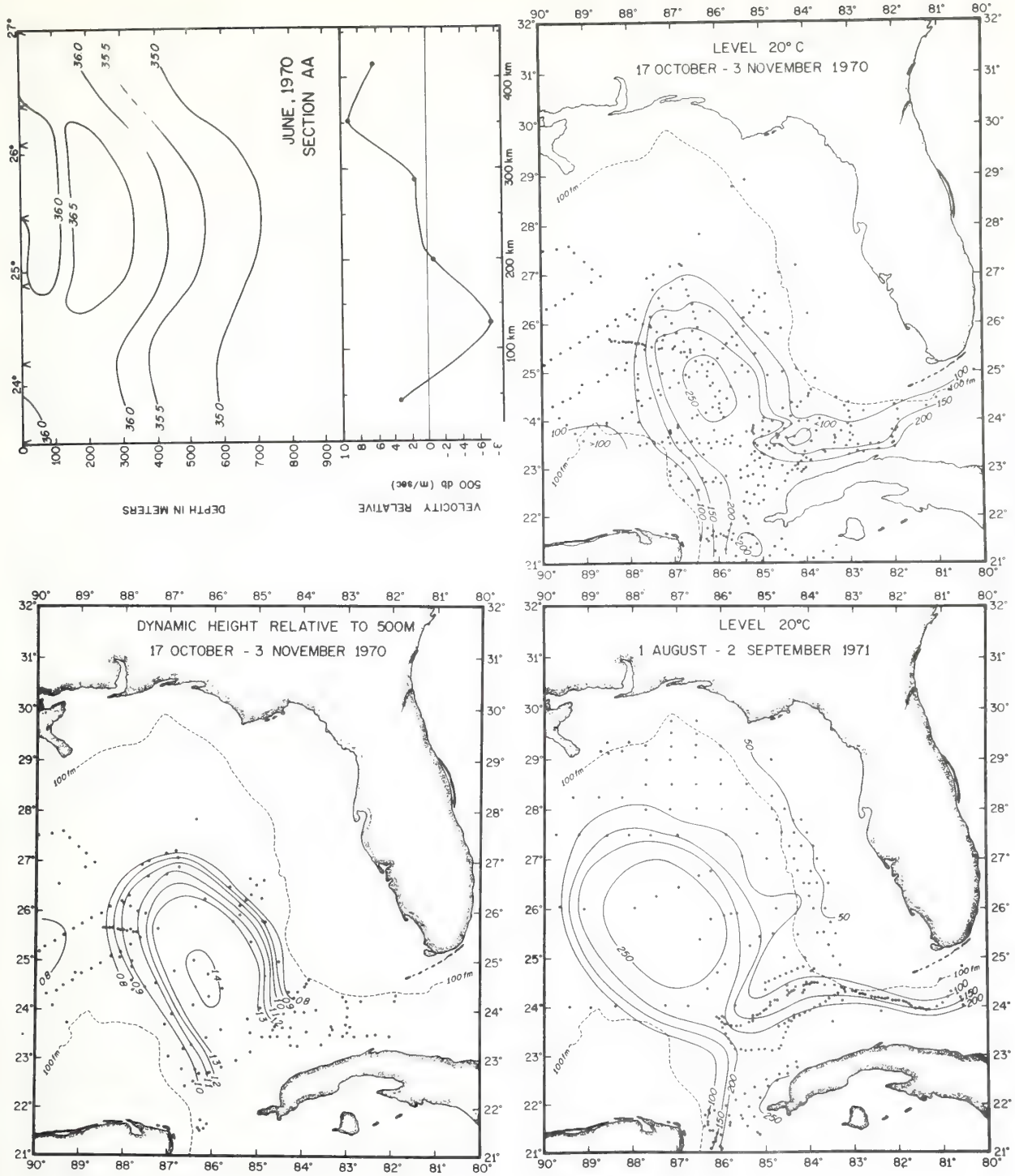

LEVEL 20° C
3 - 22 JUNE 1969
100fm

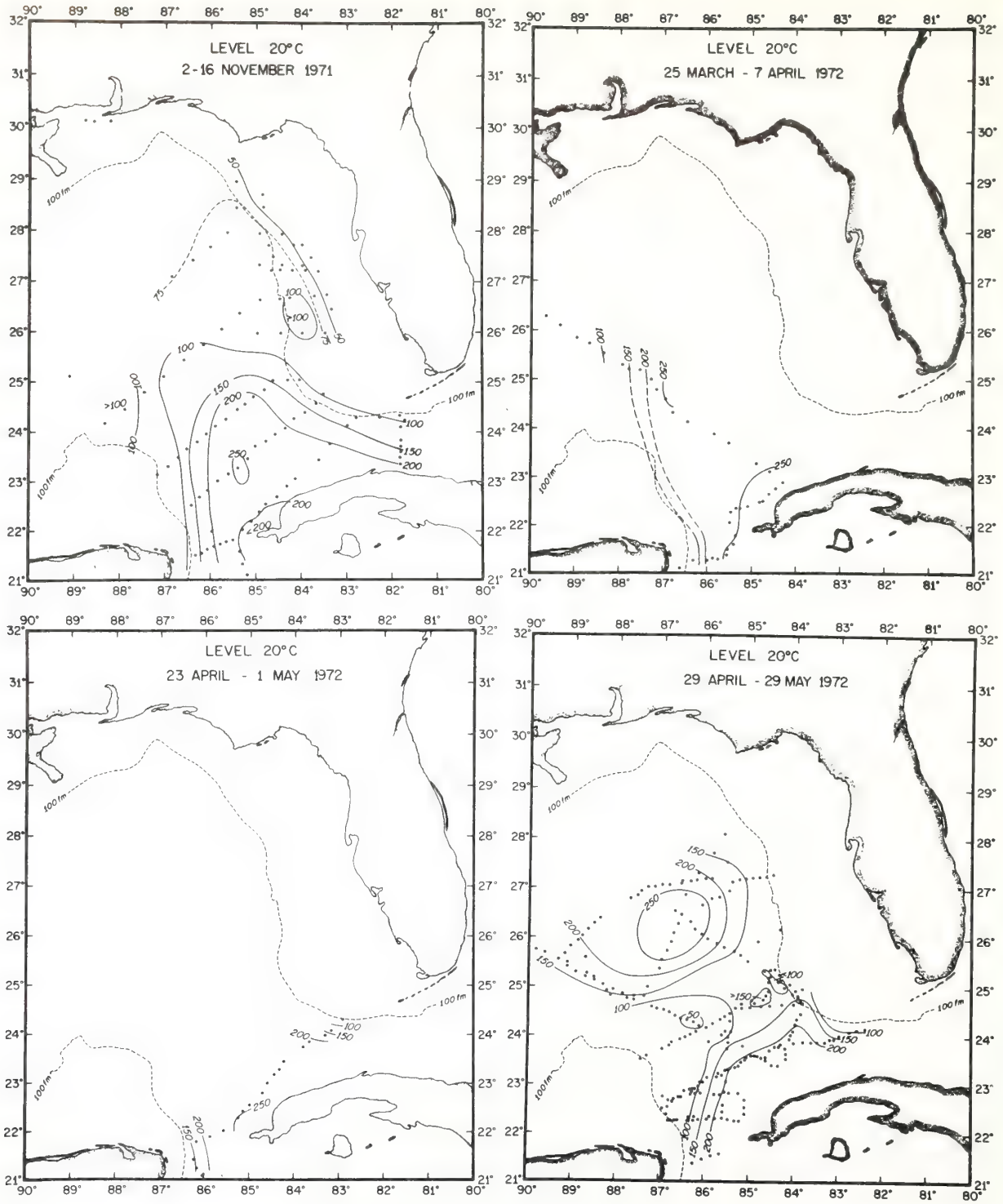

LEVEL 20° C
11 - 30 JULY 1969
LEVEL 20° C
8 - 21 SEPTEMBER 1969
DYNAMIC HEIGHT RELATIVE TO 500m
8 - 21 SEPTEMBER 1969
SEPTEMBER, 1969
SECTION BB
DEPTH IN METERS
VELOCITY RELATIVE
TO 500 db (m/sec)

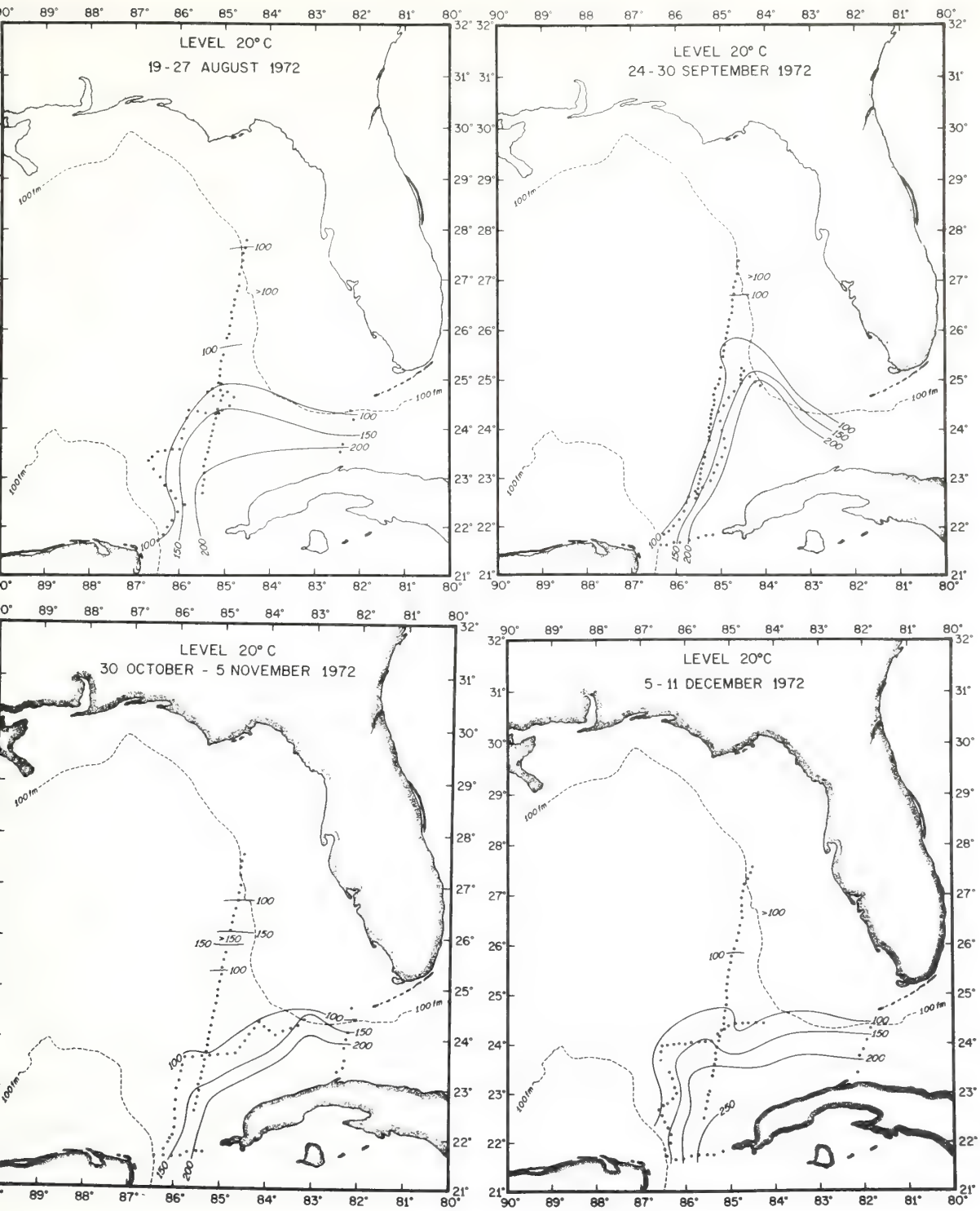

LEVEL 20° C
19-28 SEPTEMBER 1969
LEVEL 20° C
17-30 OCTOBER 1969
LEVEL 20° C
4 FEBRUARY - 4 MARCH 1970
LEVEL 20° C
14 - 27 APRIL 1970
100 fm
<50
50
100
150
200
<75
75
250

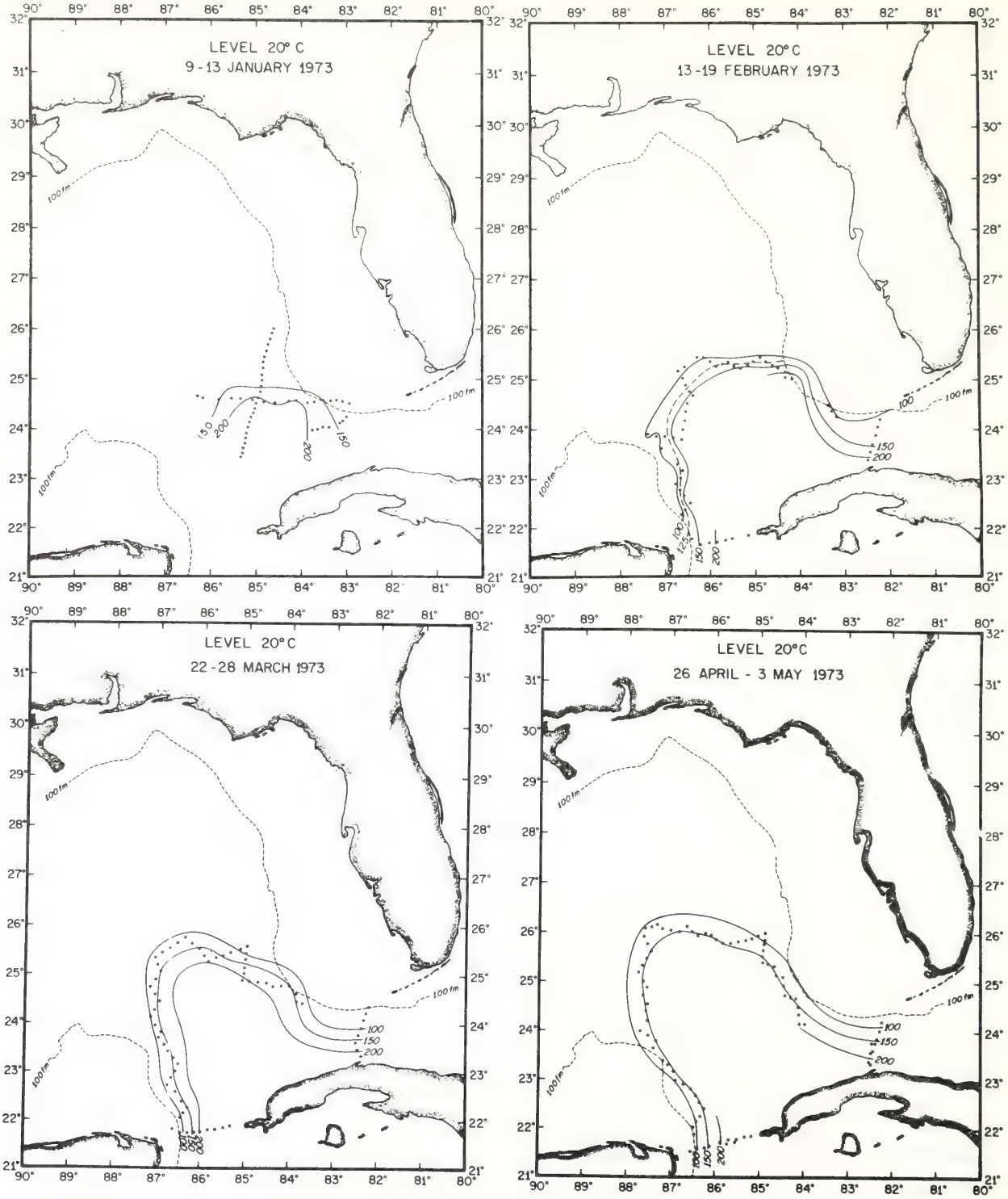
18

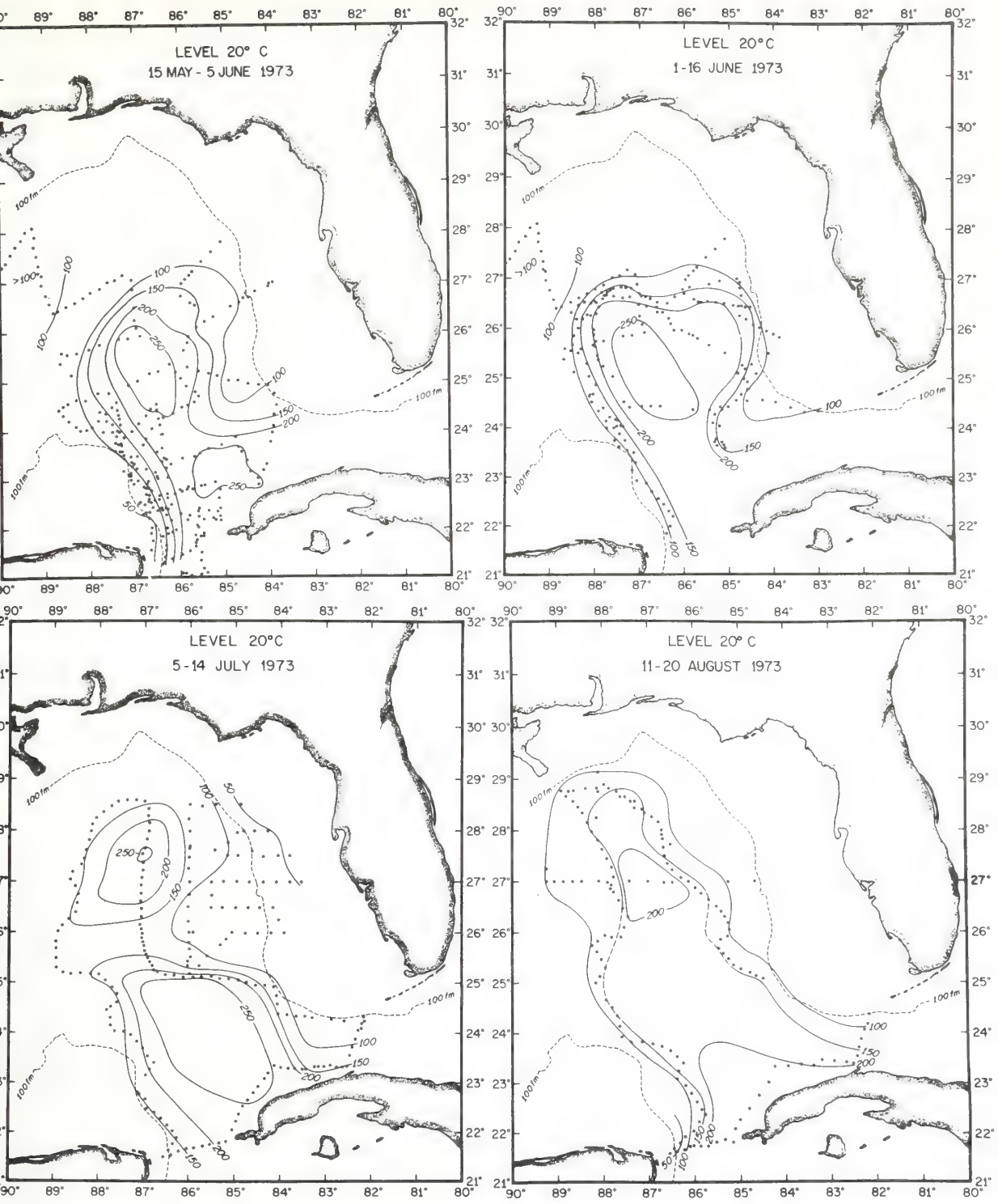

LEVEL 20° C
28 APRIL - 18 MAY 1970
DYNAMIC HEIGHT RELATIVE TO 500m
3 - 12 MAY 1970
LEVEL 20° C
11 - 25 JUNE 1970
DYNAMIC HEIGHT RELATIVE TO 500m
11 - 25 JUNE 1970

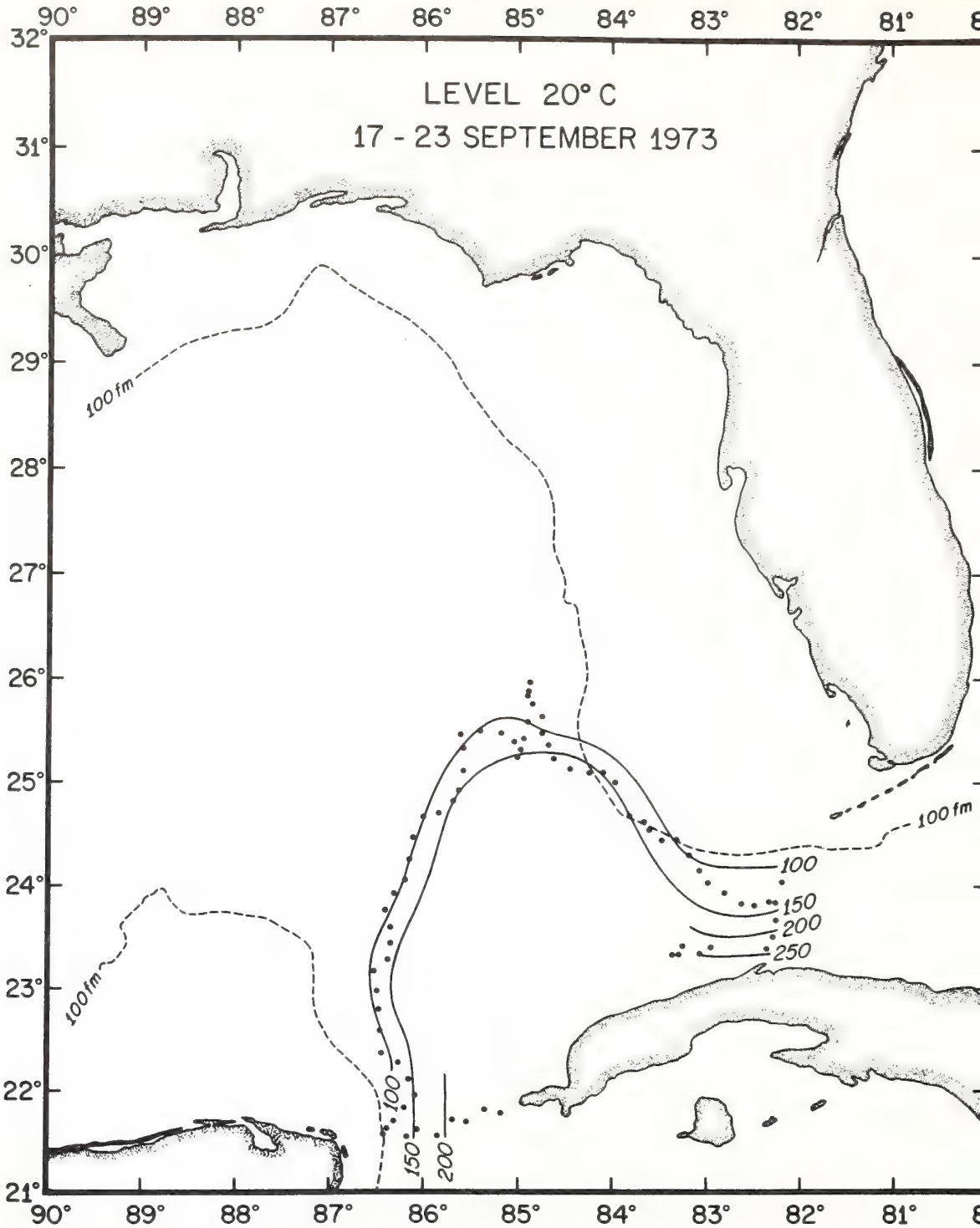

JUNE, 1970
SECTION AA
DEPTH IN METERS
VELOCITY RELATIVE
500 db (m/sec)
LEVEL 20° C
17 OCTOBER - 3 NOVEMBER 1970
DYNAMIC HEIGHT RELATIVE TO 500M
17 OCTOBER - 3 NOVEMBER 1970
LEVEL 20°C
1 AUGUST - 2 SEPTEMBER 1971


LEVEL 20°C
2-16 NOVEMBER 1971
LEVEL 20°C
25 MARCH - 7 APRIL 1972
LEVEL 20°C
23 APRIL - 1 MAY 1972
LEVEL 20°C
29 APRIL - 29 MAY 1972


LEVEL 20° C
19 - 27 AUGUST 1972
LEVEL 20° C
24 - 30 SEPTEMBER 1972
LEVEL 20° C
30 OCTOBER - 5 NOVEMBER 1972
LEVEL 20°C
5 - 11 DECEMBER 1972
100 fm
100
>100
150
200
250

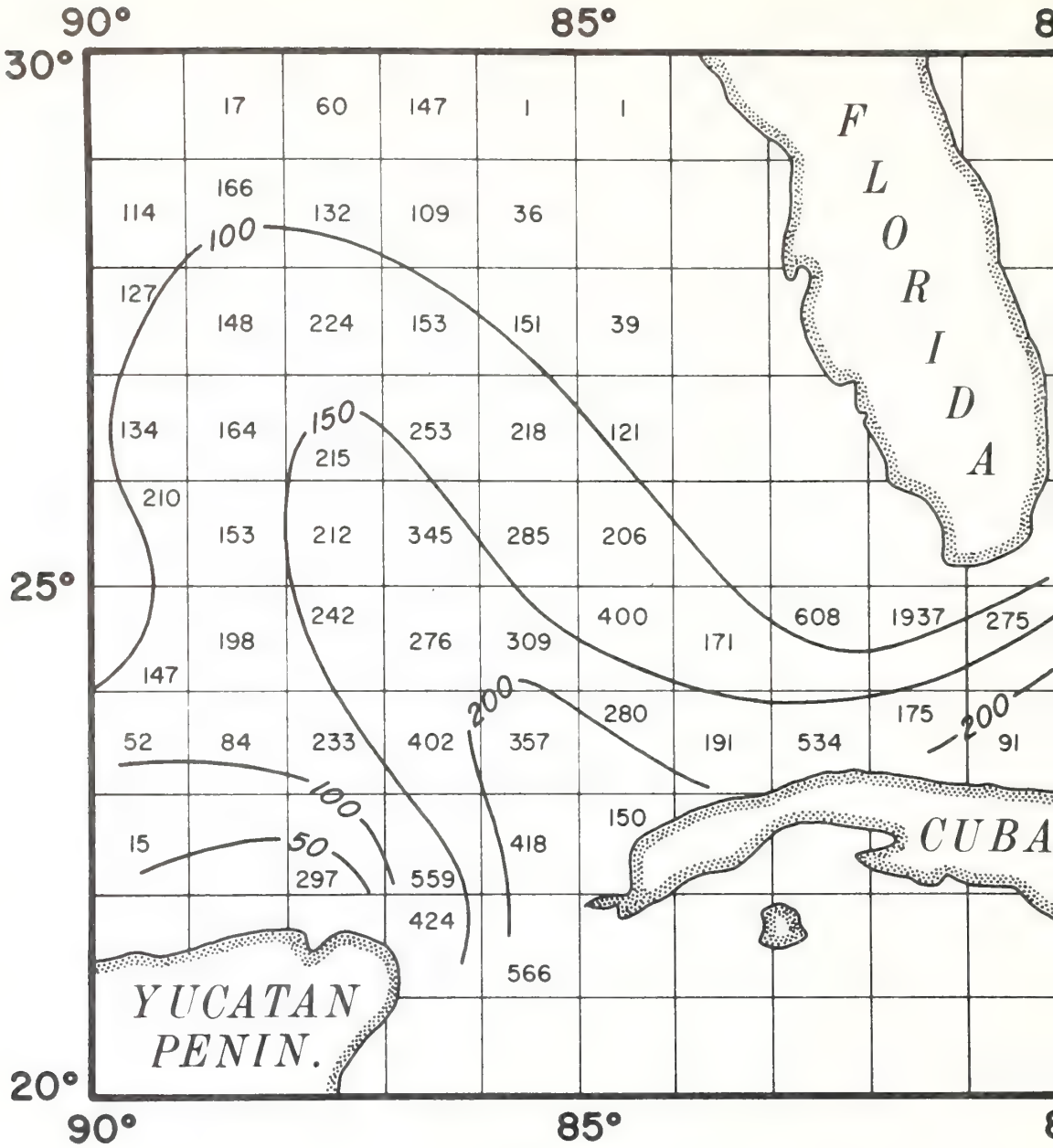

LEVEL 20° C
9-13 JANUARY 1973
LEVEL 20°C
13-19 FEBRUARY 1973
LEVEL 20°C
22-28 MARCH 1973
LEVEL 20°C
26 APRIL - 3 MAY 1973
100 fm
150
200


LEVEL 20° C
15 MAY - 5 JUNE 1973
LEVEL 20°C
1-16 JUNE 1973
LEVEL 20°C
5-14 JULY 1973
LEVEL 20° C
11-20 AUGUST 1973

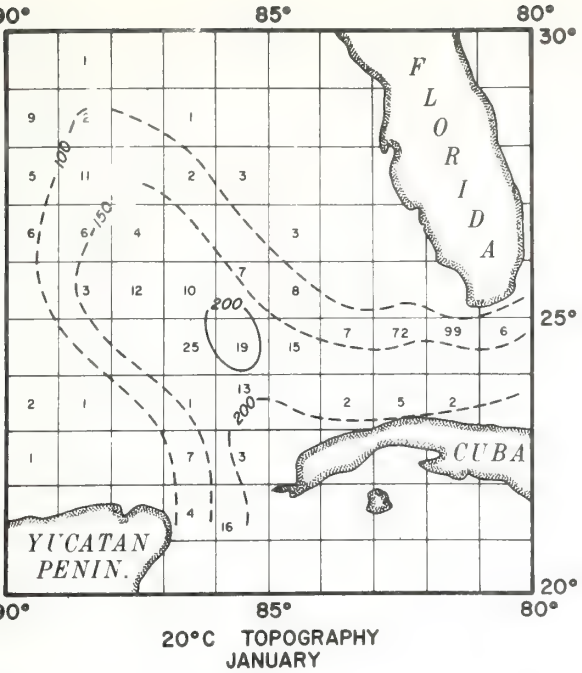

LEVEL 20° C
17 - 23 SEPTEMBER 1973
90° 89° 88° 87° 86° 85° 84° 83° 82° 81°
32° 31° 30° 29° 28° 27° 26° 25° 24° 23° 22° 21°
100 fm
100 fm
100 fm
100
150
200
250
100
150
200

APPENDIX 2. CLIMATOLOGICAL 20°C TOPOGRAPHIES

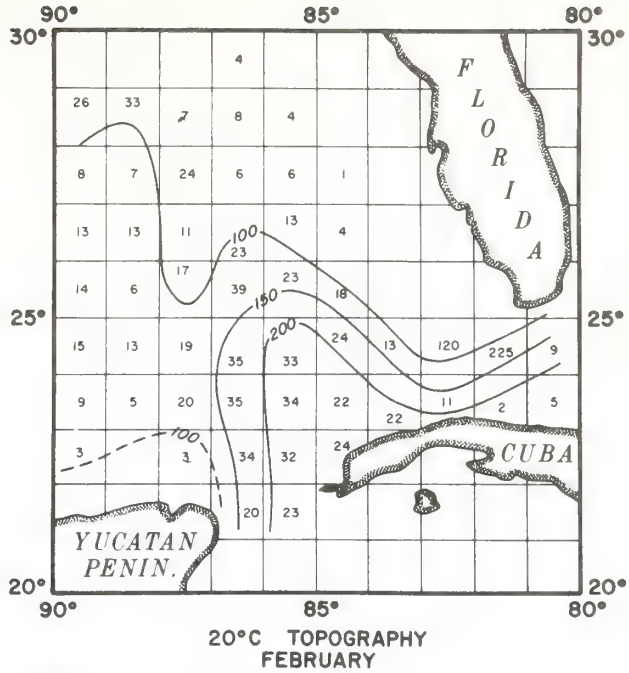
Monthly climatologies of the depth of the 20°C surface produced from NODC Listings of average temperature by 5 m depth intervals and 1° squares of latitude and longitude. The numbers within each 1° square represent the data point available. The contours are dashed in regions of few observations.



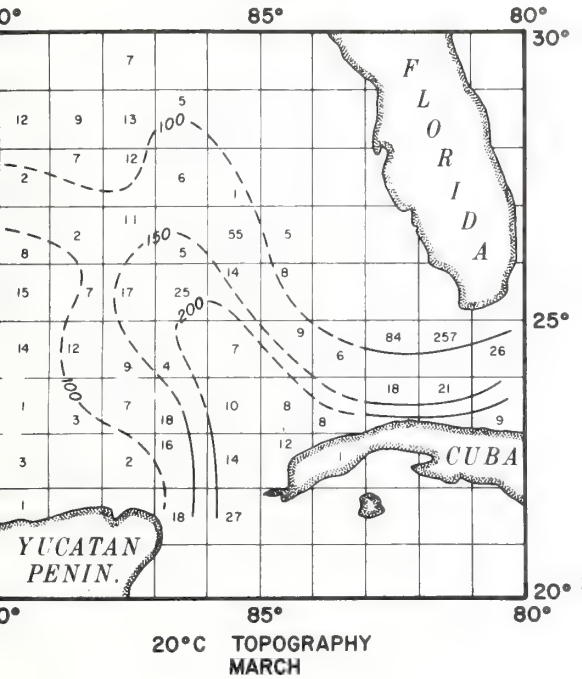
20°C TOPOGRAPHY
ANNUAL MEAN



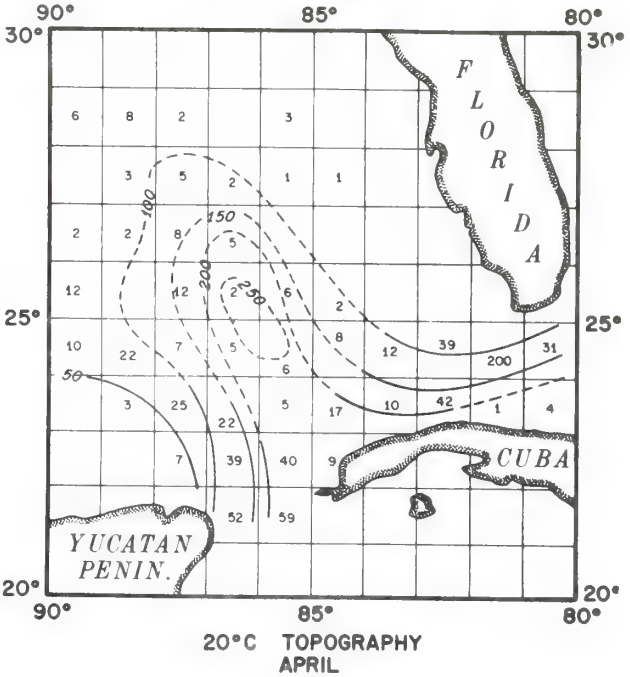
20°C TOPOGRAPHY
JANUARY



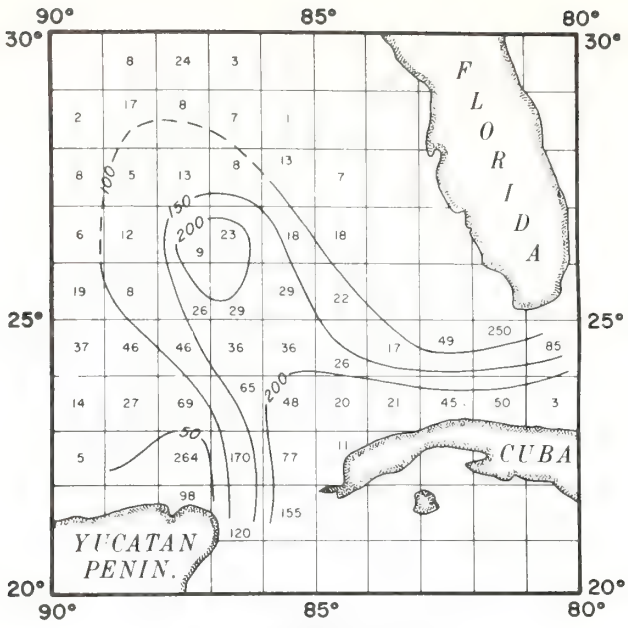
20°C TOPOGRAPHY
FEBRUARY



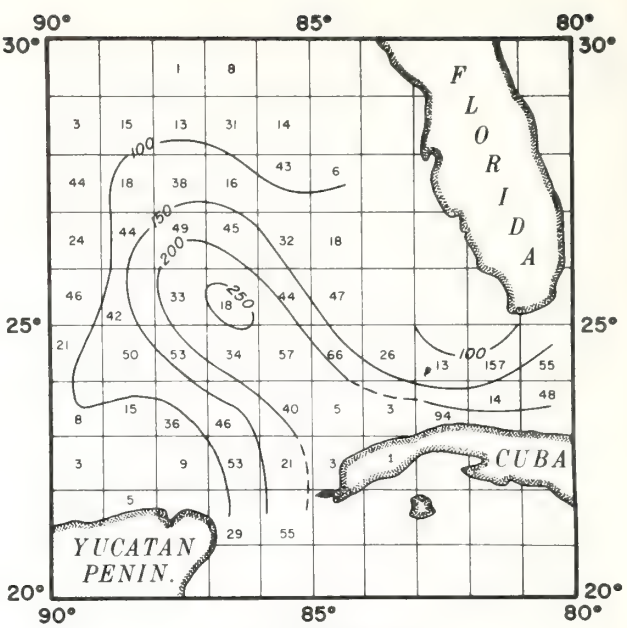
20°C TOPOGRAPHY
MARCH



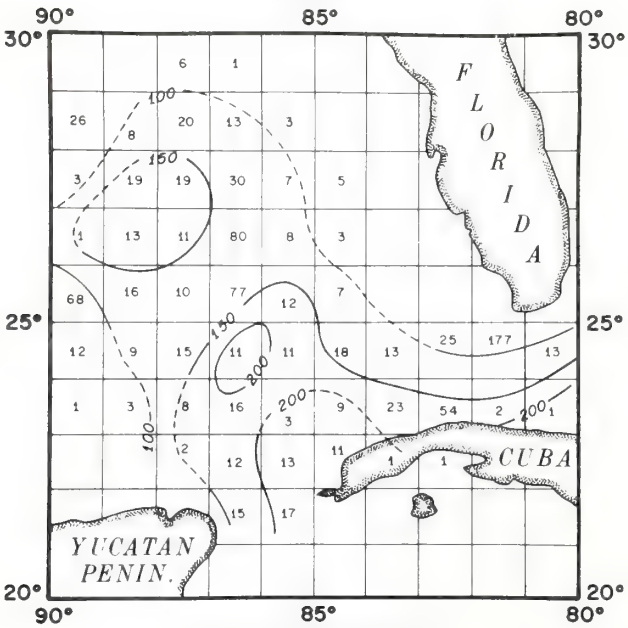
20°C TOPOGRAPHY
APRIL



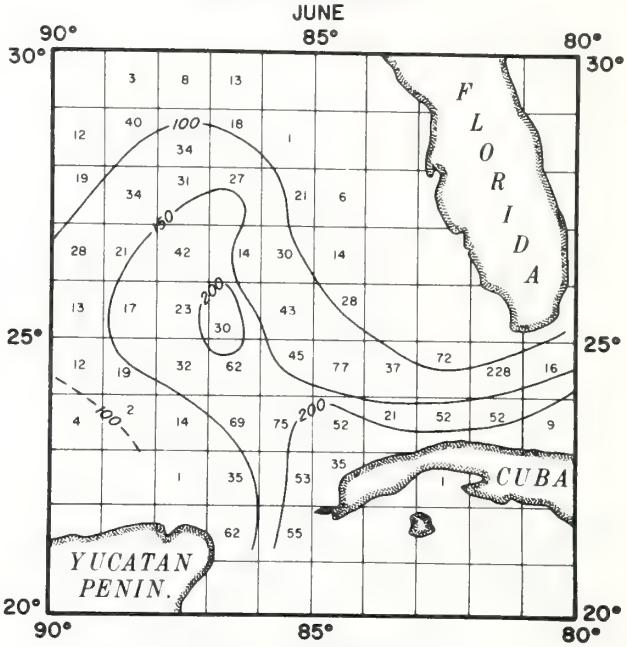
20°C TOPOGRAPHY
MAY



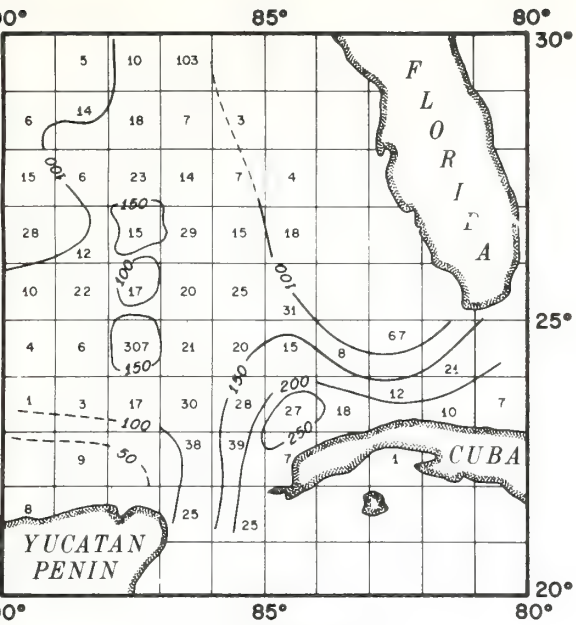
20°C TOPOGRAPHY
JUNE



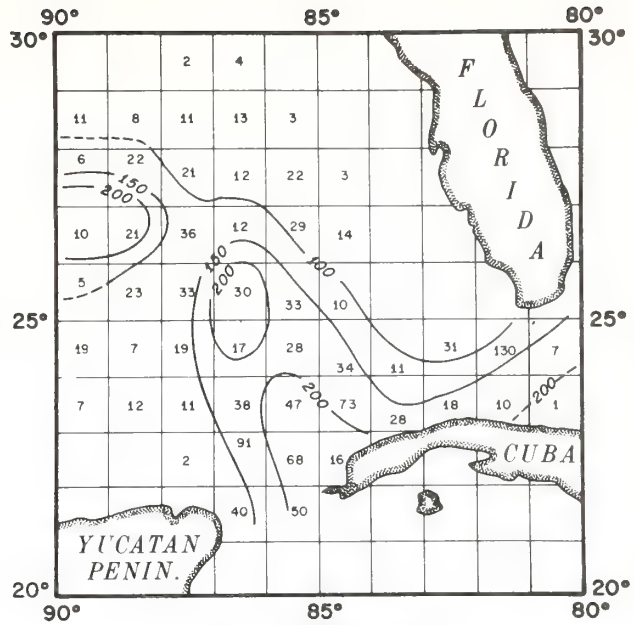
20°C TOPOGRAPHY
JULY



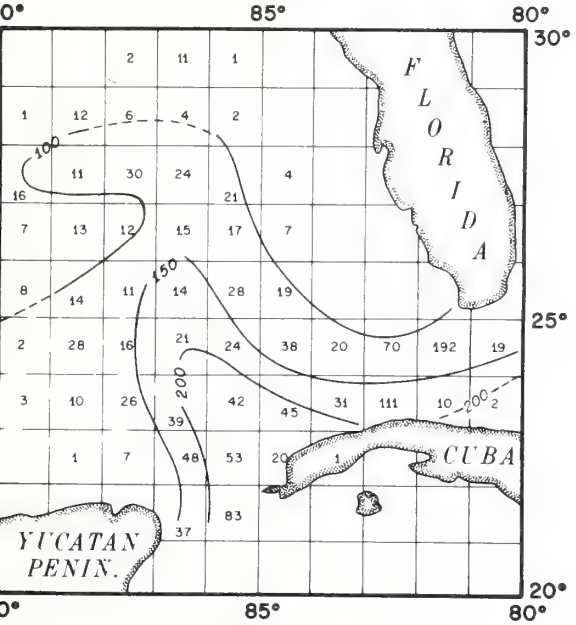
20°C TOPOGRAPHY
AUGUST



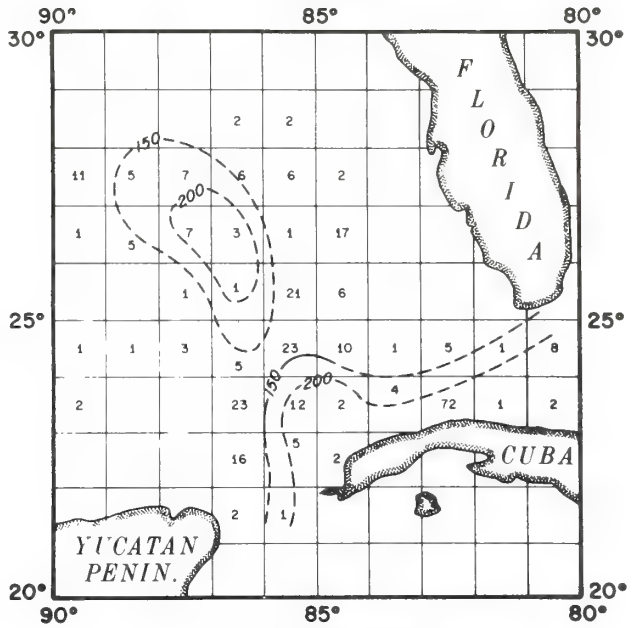
20°C TOPOGRAPHY
SEPTEMBER



20°C TOPOGRAPHY
OCTOBER



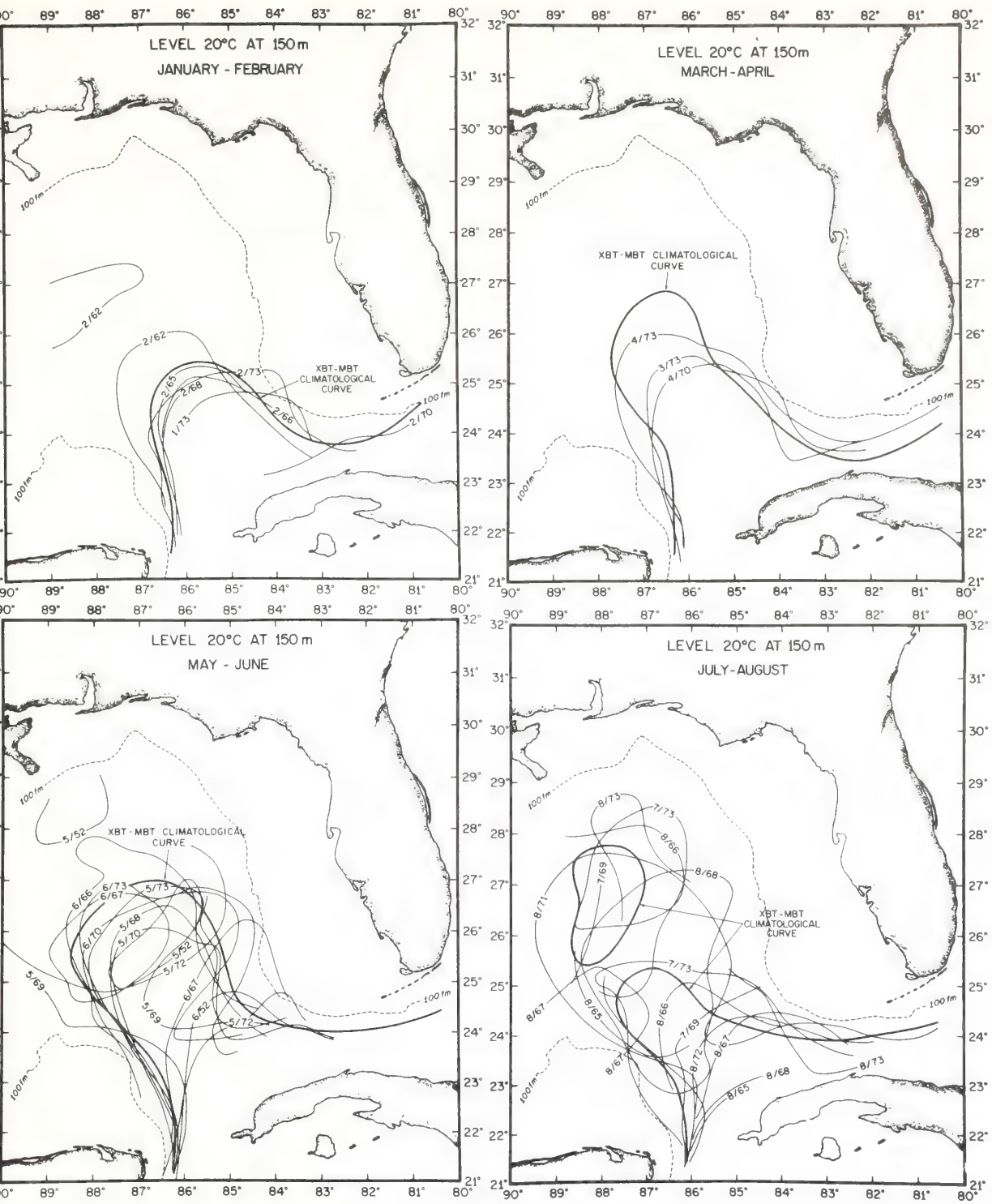
20°C TOPOGRAPHY
NOVEMBER

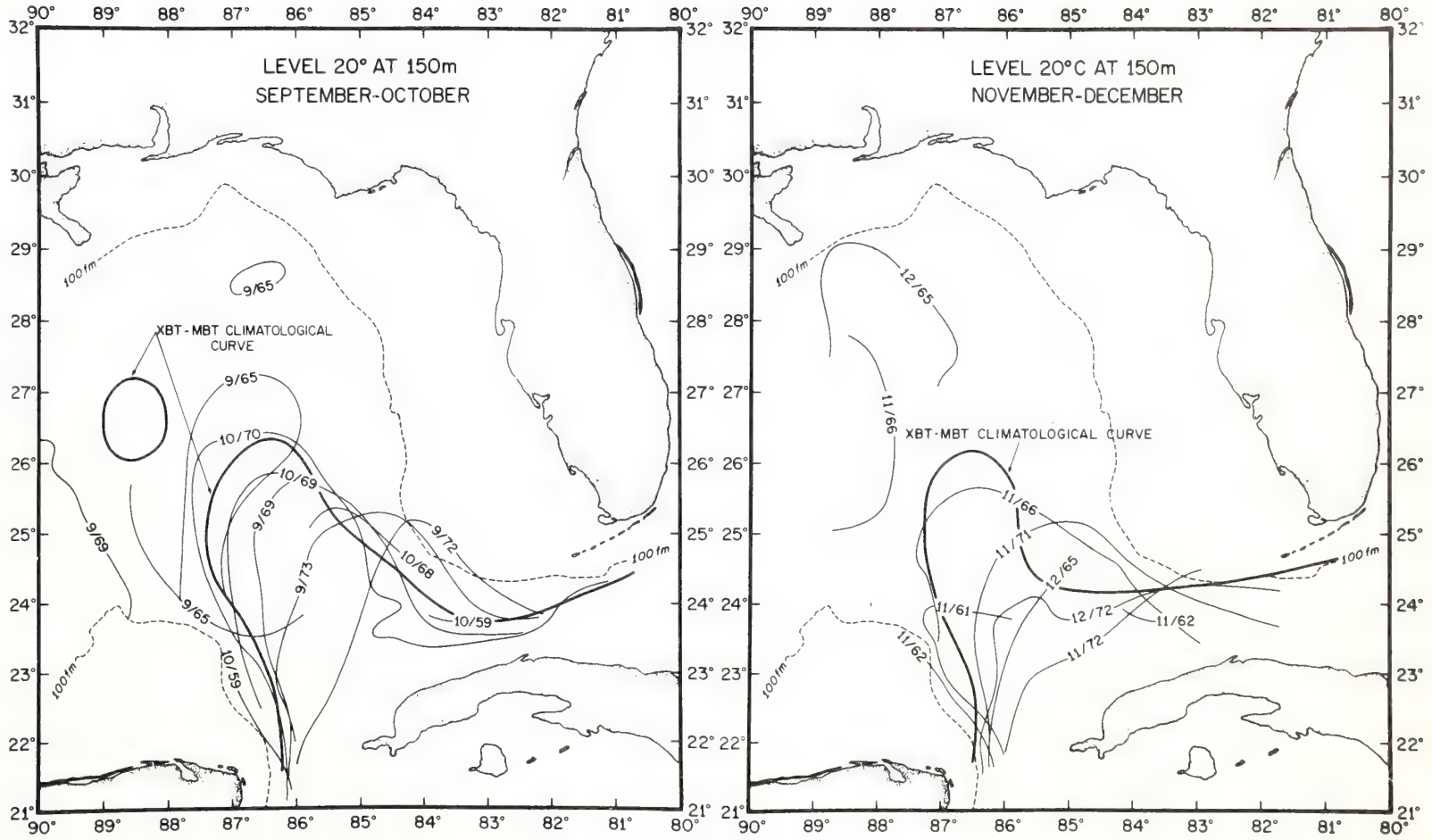


20°C TOPOGRAPHY
DECEMBER

APPENDIX 3. COMPARISON OF CLIMATOLOGICAL AND SYNOPTIC OBSERVATIONS

Bi-monthly climatological 20°C topographies were determined by averaging two months of temperature data. The 150 m contour of bi-monthly surfaces is given as the XBT-MBT climatological curve in the following figures. The 150 m contours of the 20°C for the individual cruises (denoted by month and year of the cruise) are taken from the completed 20°C topographies given in Appendix 1.


LEVEL 20°C AT 150m
JANUARY - FEBRUARY
XBT-MBT CLIMATOLOGICAL CURVE
LEVEL 20°C AT 150m
MARCH - APRIL
XBT-MBT CLIMATOLOGICAL CURVE
LEVEL 20°C AT 150 m
MAY - JUNE
XBT-MBT CLIMATOLOGICAL CURVE
LEVEL 20°C AT 150 m
JULY-AUGUST
XBT-MBT CLIMATOLOGICAL CURVE
100 fm


LEVEL 20° AT 150m
SEPTEMBER-OCTOBER
XBT-MBT CLIMATOLOGICAL CURVE
9/65
10/70
10/69
9/69
9/72
10/68
9/73
10/59
9/65
9/69
10/59
100fm
LEVEL 20°C AT 150m
NOVEMBER-DECEMBER
12/65
11/66
XBT-MBT CLIMATOLOGICAL CURVE
11/66
11/71
12/65
11/61
12/72
11/62
11/72
11/62
100fm

Drift Buoy Symposium, Hampton, Virginia, May 22-23, 1976. NASA CO-2003, 193-209.

CALCULATIONS OF DIFFERENTIAL KINEMATIC PROPERTIES FROM LAGRANGIAN OBSERVATIONS

by

Dr. R. Molinari
Atlantic Oceanographic and Meteorogical Laboratories

Dr. A. D. Kirwan, Jr.
Texas A&M University, Department of Oceanography

INTRODUCTION

In the past oceanographers have used Lagrangian data, primarily to obtain elementary fluid properties such as trajectories, velocities, and accelarations. However, meteorologists have recognized the utility of Lagrangian data in determining estimates of the differential kinematic properties, divergence, vorticity, shearing deformation, and stretching deformation. These properties are important ingredients in any description and/or explanation of fluid motions. For instance, divergence is an important factor in determining vertical motion in the ocean, vorticity can be related to the field of force that drives ocean flows, and the two deformations are important in the formation and dissipation of fronts.

The Authors: Robert Molinari received his Ph.D. in Physical Oceanography from Texas A&M University in 1970. Since 1971 he has held the position of Research Oceanographer with NOAA/AOML. His work has centered on observational and theoretical study of the Cayman Sea and the Gulf of Mexico.

Dennis Kirwan, Jr. also received his Ph.D. from Texas A&M. He has been an associate Professor at New York University and worked as a Program Director with the Office of Naval Research. More recently, he has become Research Scientist at Texas A&M and has been involved in drift buoy studies.

Two methods are presented for the calculation of these properties. One method is more readily applicable to a large number of buoys. The other approach is given to provide estimates to verify the results of the more general technique. A short description of the experiment and data analysis is given.

DATA COLLECTION AND ANALYSIS

Figure 1 is a schematic diagram of the ship-tracked buoy used in the experiment. The buoy nominally was tied to a water parcel at 40 m by a 35-ft diameter parachute.

The experiment was conducted in the western Caribbean Sea in the summer of 1971, aboard the NOAA ship RESEARCHER. The prime navigational control was supplied by a satellite positioning unit. In that region, satellite fixes can be obtained on the average every 1.5 hours. The satellite positions were supplemented by Omega fixes collected every 15 minutes. The buoys were positioned relative to the ship at each fix.

Errors are introduced into the buoy positions by the imprecision of the satellite, Omega, and radar systems. Assuming the satellite system to be the more precise of the two positioning techniques, an estimate of the Omega errors was made. An individual Omega position is accurate approximately to ±2 km. Thus, there is a very small signal-to-noise ratio when considering the 15-minute fixes.

The following smoothing procedure was applied to the Omega fixes to eliminate some of the noise in the trajectory data. Hourly fixes were obtained by taking 5-point running averages of the 15-minute component coordinates. A second degree polynomial curve was then fitted to 13 consecutive hourly fixes to arrive at the data used in the analysis.

Kirwan, in a previous talk, indicated other possible sources of error when attempting to tag a particular water parcel. Using his analysis for the drifter configuration used in this experiment, it was found that a 10 m/sec

wind could cause a 5 percent error in the estimate of the true current. This effect was not considered in reducing the data from this experiment.

A. Least Square Method

Consider a small, but finite, parcel of water, and assume that within this parcel the velocity at any point is adequately represented by the linear terms in a Taylor's expansion about the center of mass of the parcel. For a cluster of N drifters located within the parcel, the expansion yields for the velocity components of the i^{th} drifter.

$$U_i = U + g_i + \{(D + N)\, X_i\}/2 + \{(S - \zeta)Y_i\}/2$$

$$V_i = V + h_i + \{(S + \zeta)\, X_i\}/2 + \{(D - N)Y_i\}/2 \qquad i = 1,\ldots N \qquad (1)$$

The U and V are the components of the velocity of the center of mass of the parcel. The coordinates with respect to the cluster center of mass of drifter i are X_i and Y_i. The g_i and h_i represent the sum of the higher order non-linear terms in the expansion.

The differential kinematic properties are:

$$\begin{aligned} D &= \partial U/\partial X + \partial V/\partial Y \quad \text{(Divergence)} \\ \partial &= \partial V/\partial X - \partial U/\partial Y \quad \text{(Vorticity)} \\ S &= \partial V/\partial X + \partial U/\partial Y \quad \text{(Shearing deformation rate)} \\ N &= \partial U/\partial X - \partial V/\partial Y \quad \text{(Stretching deformation rate)} \end{aligned} \qquad (2)$$

The divergence, D, is a measure of the parcel volume change without change of orientation or shape. ζ, the vorticity, is a measure of the orientation change without volume or shape change of the parcel. Shape changes without change of volume or orientation are given by S and N respectively.

In equation (1), U_i, V_i, and U and V are computed from the buoy coordinates. The g and h functions, and D, N, S, and ζ can be computed by noting

that at each time the total kinetic energy density of the cluster due to small-scale turbulence is:

$$KE = \sum_{i=1}^{N} g_i^2 + h_i^2 \quad /2 \tag{3}$$

Substituting (1) into (3) shows that the kinetic energy density depends on the kinematic properties. These four parameters can be estimated by selecting values which give a minimum for the kinetic energy density. The g and h functions can then be determined from (1).

The minimum number of drifters that can be used to determine D, S, N, and ζ is three. However, this approach is readily extended to consider larger numbers of drifters. In addition, the approach generates time series of the turbulent velocities, g_i and h_i, from which direct estimates of turbulent stresses can be made.

3. Area Method

Horizontal divergence can be expressed as the fractional time rate of change of the horizontal area, A, of a parcel:

$$\frac{\partial U}{\partial X} + \frac{\partial V}{\partial Y} = \frac{1}{A}\frac{DA}{Dt} \tag{4}$$

For a triad of drifters, A is readily evaluated from the buoy positions. From the time series of A's an appropriate numerical technique is used to estimate the time rate of change.

Vorticity, shearing and stretching deformation can be evaluated by selected rotations of the velocity vectors of the three drifters. Saucier (1955) describes this technique.

RESULTS

Figure 2 is a schematic diagram of representative drogue trajectories and speeds. Four trajectories are shown. Beginning with the trajectory over the Cayman Ridge and preceeding counterclockwise around the basin, the trajectories will be numbered 1, 2, 3, and 4 for purposes of identification.

The area of figure 2 is the formation region of the Yucatan Current. The accelarations which occur during legs 2 and 3 are indicative of the formation processes occuring in the vicinity of the Yucatan Channel.

Figure 3 is a more detailed plot of the drogue trajectories of leg 1. A Universal Transverse Mercator projection is used, and the x and y coordinates are marked in kilometers. The apexes of the triangles represent drogue positions.

Also given on the figure are the velocity, accelaration, and radius of curvature of the triad center of mass. The last two curves indicate the difficulty of obtaining from these data smooth estimates for higher order derivative terms.

Figure 4 gives the divergence and vorticity as determined by the two methods. The solid lines connect the values computed by the least square approach, and the crosses represent the values computed by the area method. The triad areas (figure 4) are small and the estimates of the kinematic properties are very irregular with respect to time.

Figures 5 and 6 present the buoy trajectories and all the kinematic properties for leg 2. Again, the agreement between the two methods is good. The estimates of these parameters are smoother functions of time for this leg.

Figures 7 and 8, and 9 and 10 display the results for legs 3 and 4 respectively. The buoy speeds were lowest during leg 4, on the average 0.3 m/sec, and the triangle areas small. The kinematic property estimates given on figure 10 are very ragged, with frequent crossings of the axis. It is doubtful that these values are reliable estimates of the differential kinematic properties.

The value of the measurements is increased if the resulting data can be used to explain the dynamics of the circulation. An attempt to incorporate the data of leg 2 (figure 6) into a dynamic expression is made.

Figure 11 gives the conservation of potential vorticity relation, and the evaluation of the terms in this relation using the data of leg 2. This equation is derived by assuming no external forces (tides, winds) are acting on the flow. The terms in this expression are Z, the relative vorticity, f, the Coriolis parameter, and $\nabla\cdot\overline{V}$, the divergence. The qualitative balance of the terms for the first two days of the trajectories suggests a balance exists.

To summarize, it appears feasible to compute differential kinematic properties from drifting buoy data. In addition, if estimates are sufficiently well-behaved, some dynamical statements about the flow can be offered.

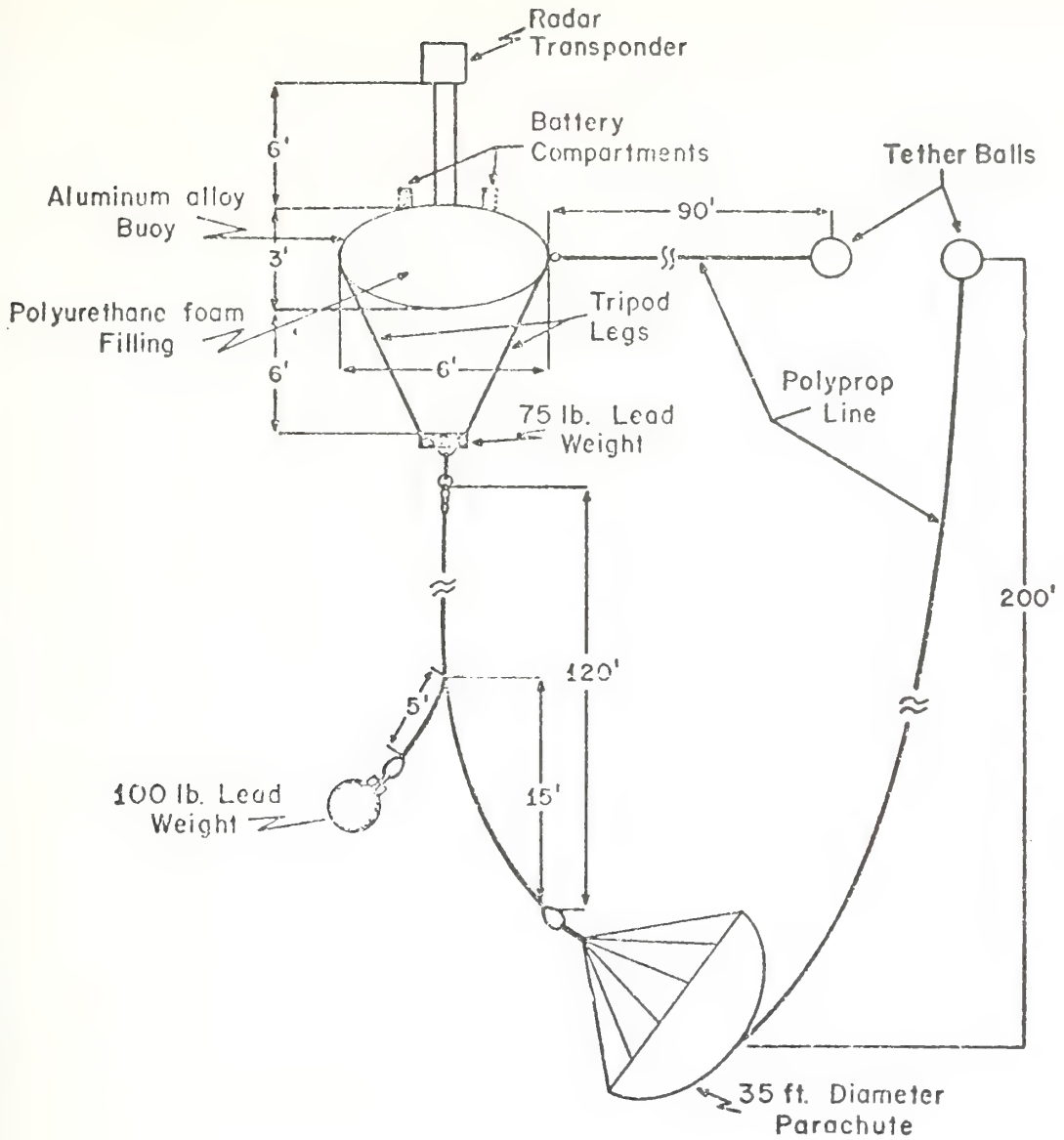

Radar
Transponder
Battery
Compartments
Tether Balls
6'
Aluminum alloy
Buoy
90'
3'
Polyurethane foam
Filling
Tripod
Legs
6'
6'
Polyprop
Line
75 lb. Lead
Weight
200'
120'
5'
100 lb. Lead
Weight
15'
35 ft. Diameter
Parachute

Figure 1.

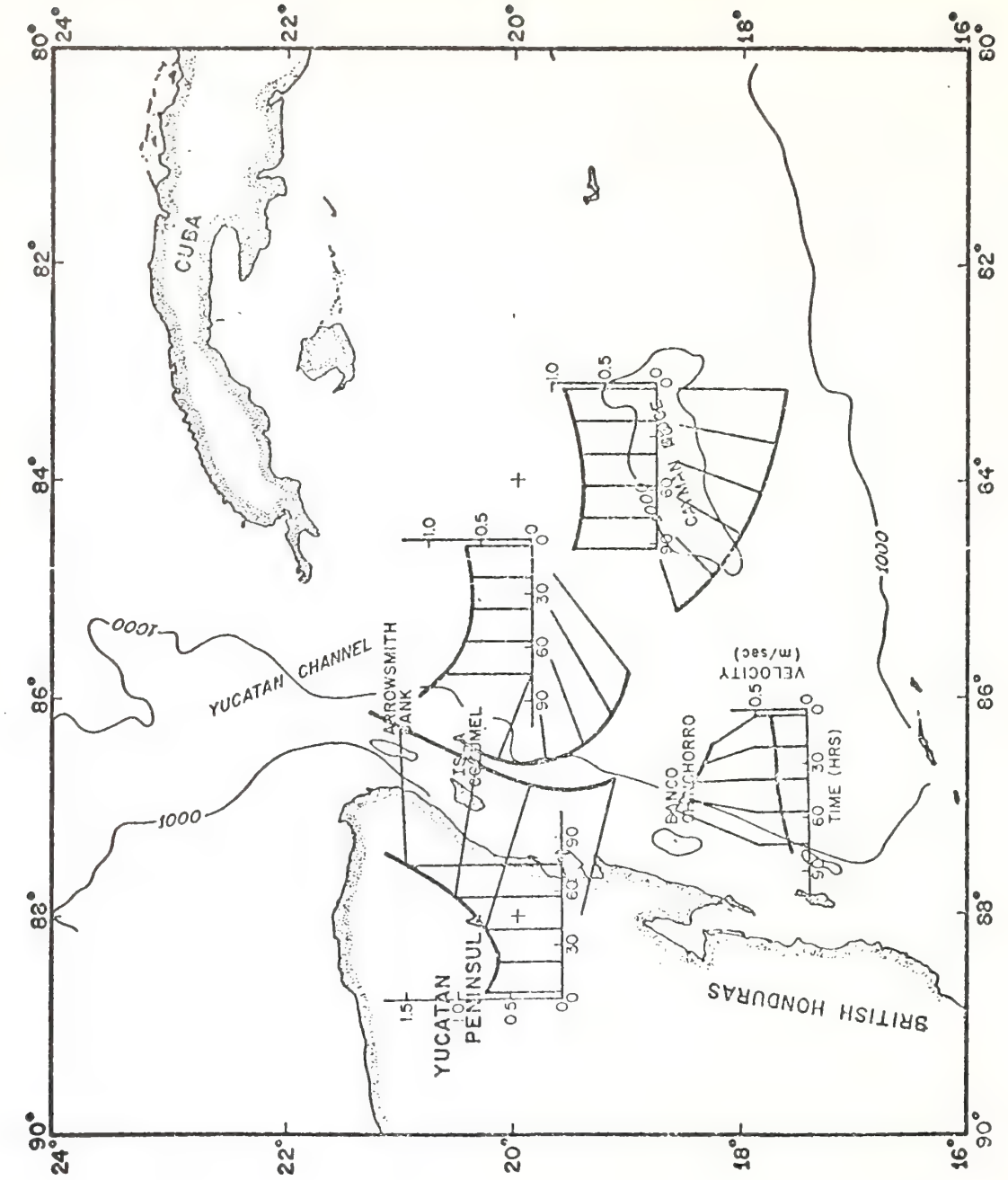

CUBA
YUCATAN CHANNEL
ARROWSMITH BANK
ISLA COZUMEL
YUCATAN PENINSULA
BANCO CHINCHORRO
CAYMAN BASIN
BRITISH HONDURAS
1000
VELOCITY (m/sec)
TIME (HRS)
80°
82°
84°
86°
88°
90°
24°
22°
20°
18°
16°

Figure 2.

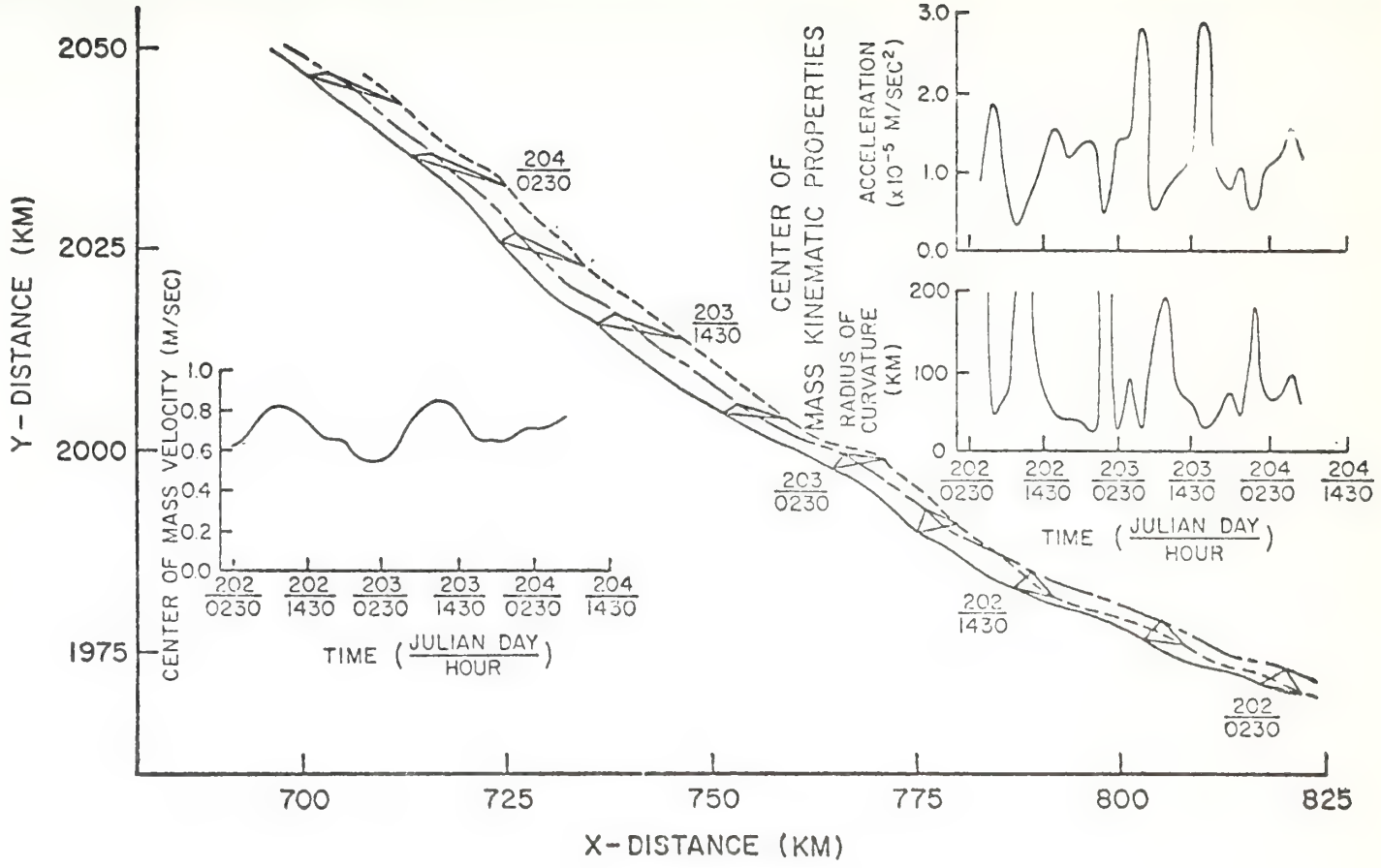

Y-DISTANCE (KM)
2050
2025
2000
1975
X-DISTANCE (KM)
700
725
750
775
800
825
CENTER OF MASS KINEMATIC PROPERTIES
204/0230
203/1430
203/0230
202/1430
202/0230
CENTER OF MASS VELOCITY (M/SEC)
1.0
0.8
0.6
0.4
0.2
0.0
202/0230
202/1430
203/0230
203/1430
204/0230
204/1430
TIME (JULIAN DAY/HOUR)
ACCELERATION (x10⁻⁵ M/SEC²)
3.0
2.0
1.0
0.0
RADIUS OF CURVATURE (KM)
200
100
0
202/0230
202/1430
203/0230
203/1430
204/0230
204/1430
TIME (JULIAN DAY/HOUR)

Figure 3.

DIVERGENCE
VORTICITY
(x 10⁻⁵/sec)
TIME
202
0530
203
0530
204
0530
4
2
0
-2
-4

Figure 4.

202

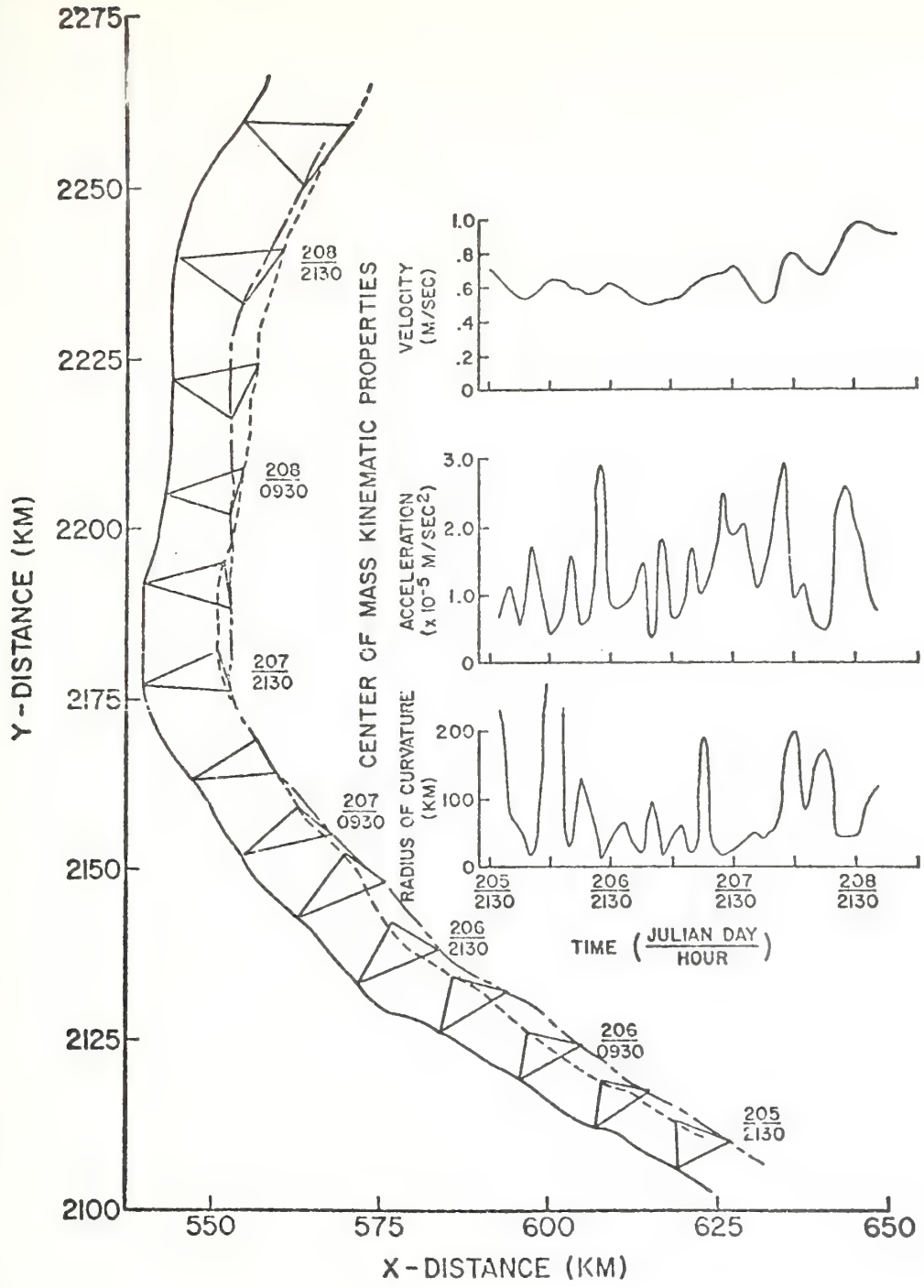

CENTER OF MASS KINEMATIC PROPERTIES
VELOCITY (M/SEC)
ACCELERATION (x 10⁻⁵ M/SEC²)
RADIUS OF CURVATURE (KM)
TIME (JULIAN DAY / HOUR)
Y-DISTANCE (KM)
X-DISTANCE (KM)
208/2130
208/0930
207/2130
207/0930
206/2130
206/0930
205/2130

Figure 5.

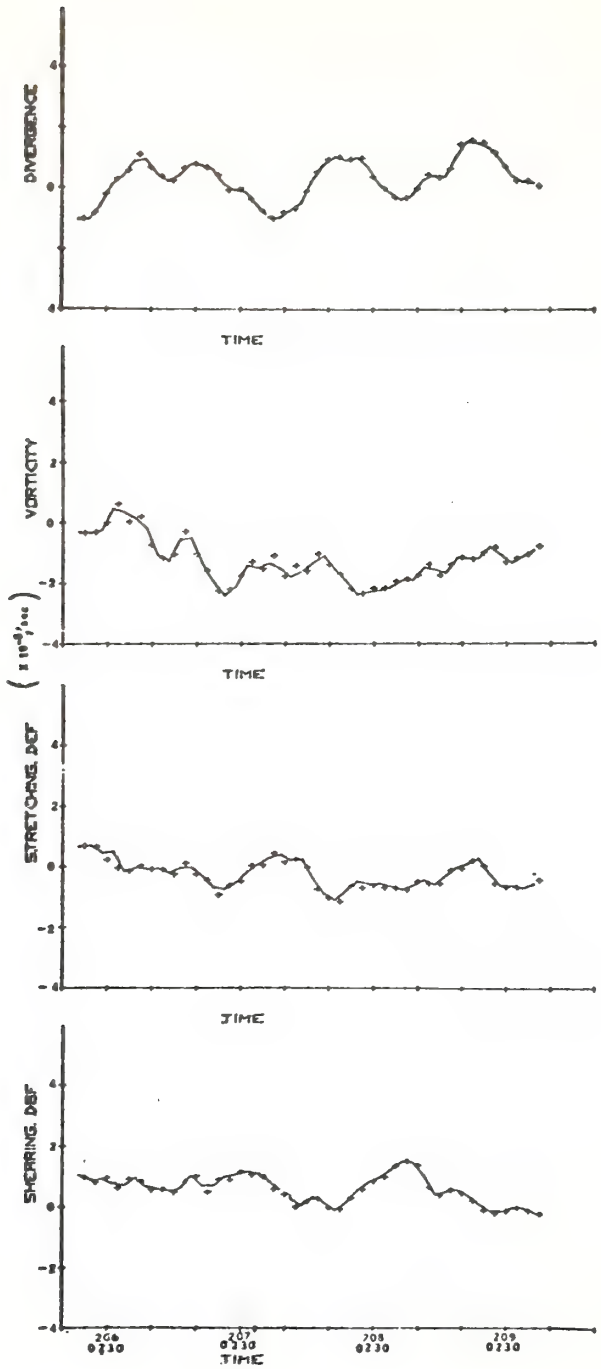

DIVERGENCE
TIME
VORTICITY
TIME
STRETCHING DEF
TIME
SHEARING DEF
206
0230
207
0230
208
0230
209
0230
TIME

Figure 6.

204

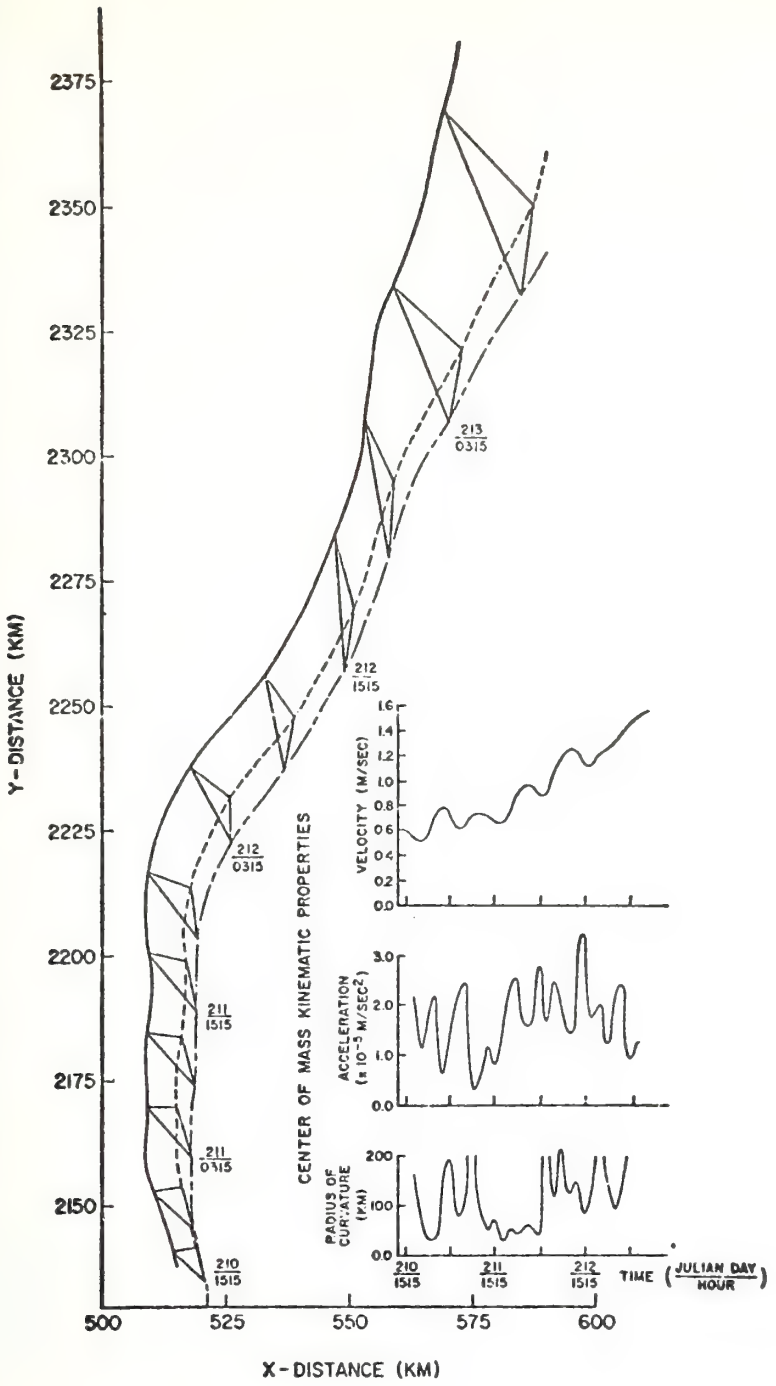

Y-DISTANCE (KM)
2375
2350
2325
2300
2275
2250
2225
2200
2175
2150
500
525
550
575
600
X-DISTANCE (KM)
213/0315
212/1515
212/0315
211/1515
211/0315
210/1515
CENTER OF MASS KINEMATIC PROPERTIES
VELOCITY (M/SEC)
ACCELERATION (x 10⁻⁵ M/SEC²)
RADIUS OF CURVATURE (KM)
210/1515
211/1515
212/1515
TIME (JULIAN DAY / HOUR)

Figure 7.

205

DIVERGENCE
VORTICITY
TIME
TIME
4
2
0
-2
-4
210
2015
211
2015
212
2015
213
2015

Figure 8.

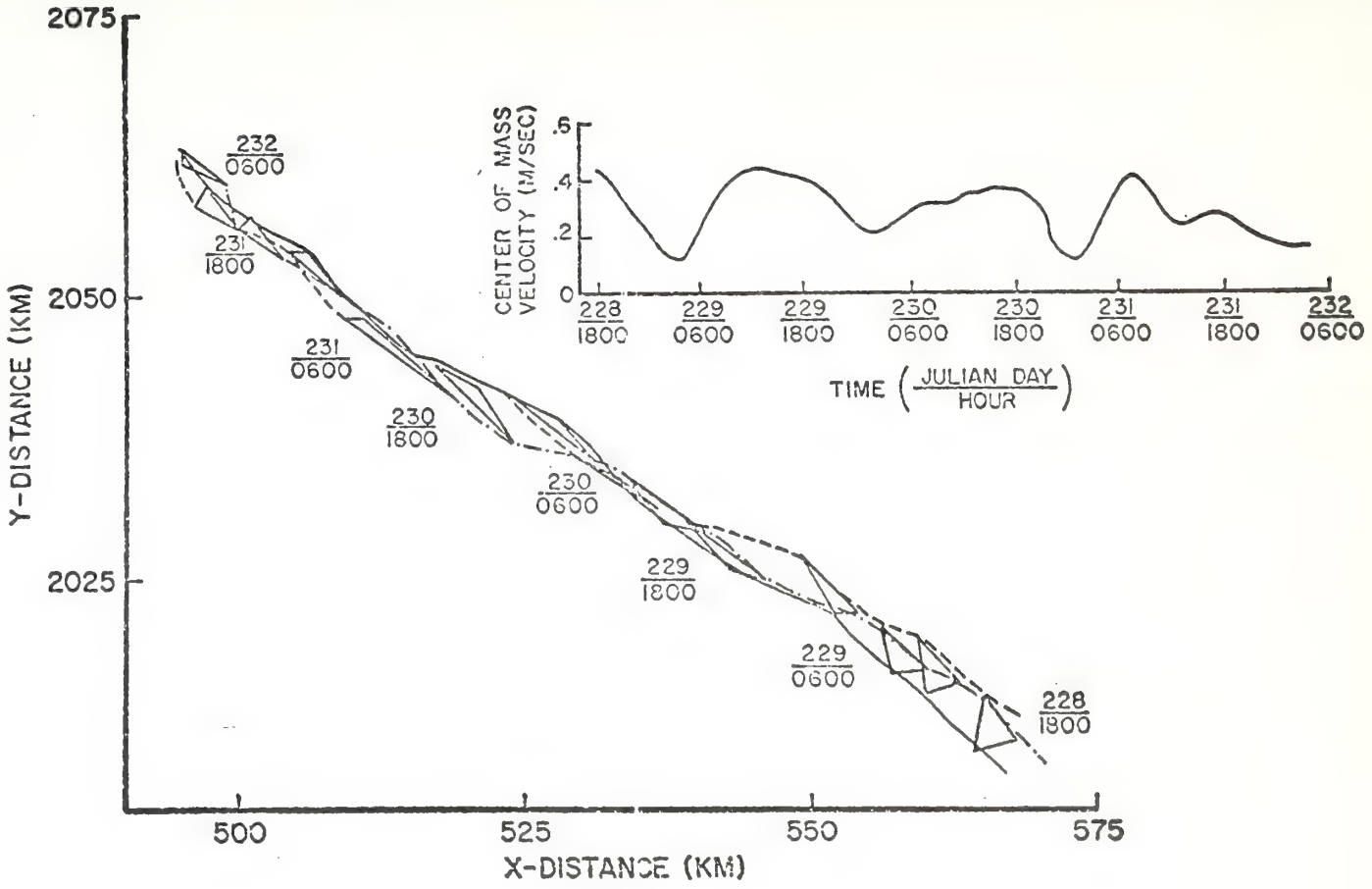

2075
2050
2025
Y-DISTANCE (KM)
500
525
550
575
X-DISTANCE (KM)
232/0600
231/1800
231/0600
230/1800
230/0600
229/1800
229/0600
228/1800
CENTER OF MASS VELOCITY (M/SEC)
.6
.4
.2
0
228/1800
229/0600
229/1800
230/0600
230/1800
231/0600
231/1800
232/0600
TIME (JULIAN DAY / HOUR)

Figure 9.

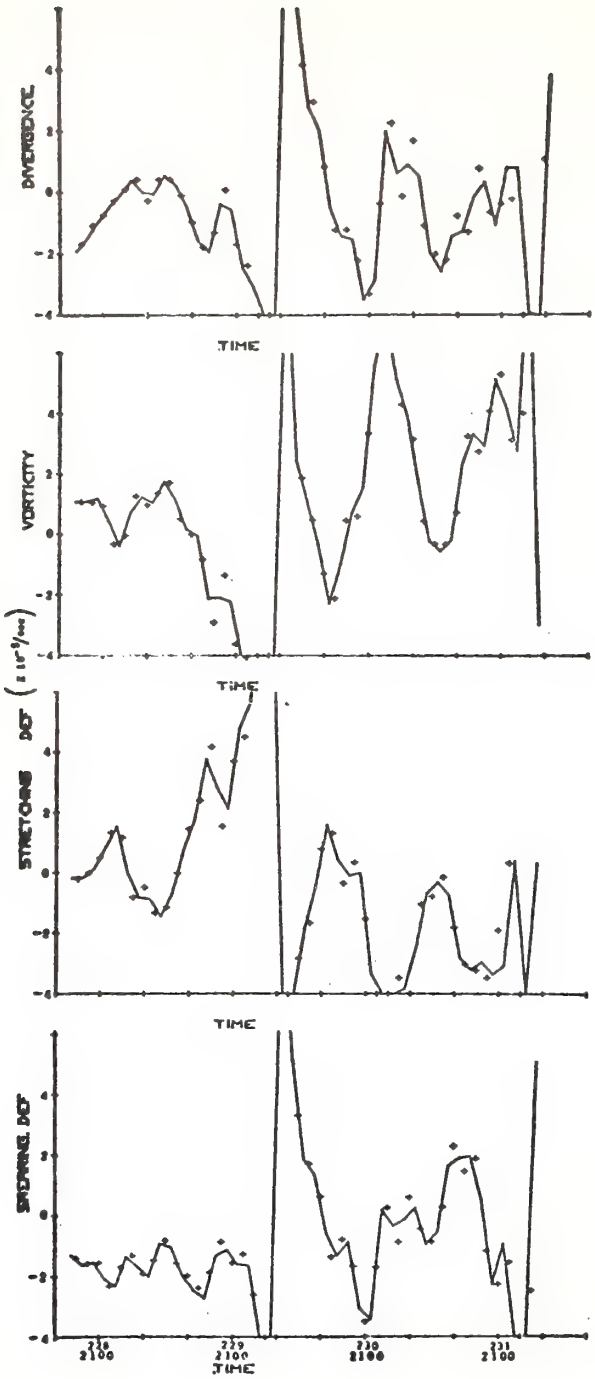


Figure 10.

208

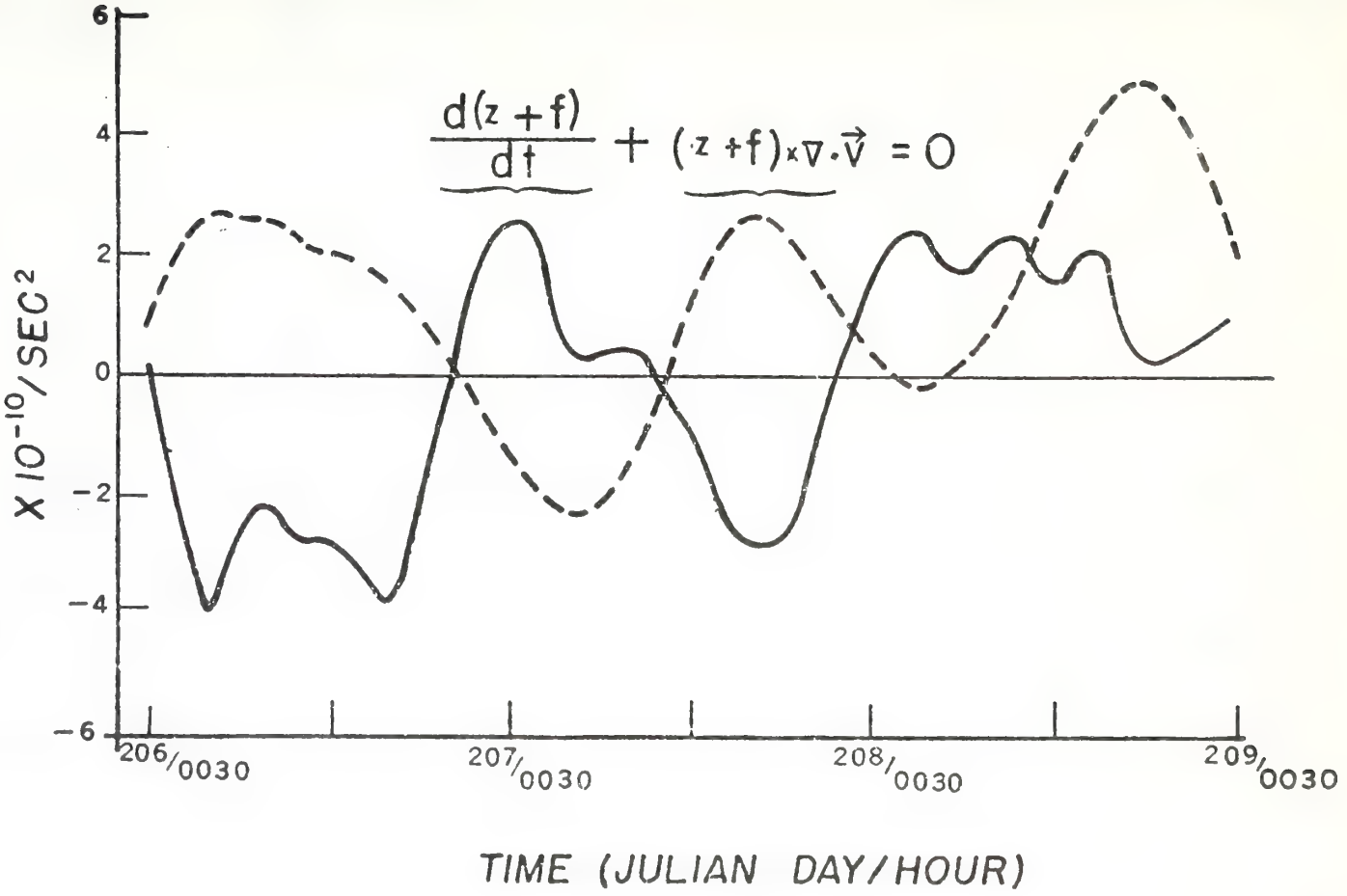

$\frac{d(z+f)}{dt} + (z+f)\times\nabla\cdot\vec{v} = 0$
6
4
2
0
−2
−4
−6
X 10⁻¹⁰/SEC²
206/0030
207/0030
208/0030
209/0030
TIME (JULIAN DAY/HOUR)

Figure 11.

Journal of Marine Research 35, No. 1, 11-20.

Upper layer hydrographic conditions at the Yucatan Strait during May, 1972

by Robert L. Molinari[1] and Robert E. Yager[2]

ABSTRACT

Average hydrographic conditions above 800m, including temperature, salinity, velocity, and volume transport, across the Yucatan Strait, during May, 1972, are presented. Direct current measurements at the surface are used as an absolute reference level for the geostrophic computations. The transport above $\sigma_t = 27.0$ is $20.8 \times 10^6 m^3/sec$ which compares favorably with measurements taken concurrently at the Straits of Florida. A subsurface countercurrent out of the Gulf of Mexico is found below 600m in the western portion of the Yucatan Strait. Relative and potential vorticity values are determined from the data; the former attaining values as high as 25% of the planetary vorticity, and the latter approximately constant across the main portion of the flow.

1. Introduction

This paper is part of a series of articles presenting the results of a summer 1972 experiment conducted in the eastern Gulf of Mexico. The primary objective of the study was to monitor the inflow and outflow conditions of the Gulf while simultaneously surveying the interior. The data were then to be used as input for numerical models planned for the area. The inflow data are listed by Molinari (1974); the outflow conditions are reported by Brooks and Niiler (1975); and the interior data are listed by Morrison *et al.* (1973), and Molinari (1974), and discussed by Morrison (1974).

In previous numerical and theoretical studies of the Gulf of Mexico, the boundary conditions at the Yucatan Strait served to force the flow in the interior of the Gulf. For instance, Paskausky and Reid (1972) and Wert and Reid (1972) in barotropic and two-layer numerical models of the Gulf respectively, varied the velocity field at the Strait while keeping the total transport constant. The results of their prognostic models indicated that this type of boundary condition could cause an interior circulation pattern similar to that observed. Reid (1972) in a simple theoretical

1. National Oceanic and Atmospheric Administration, Atlantic Oceanographic and Meteorological Laboratories, Physical Oceanography Laboratory, 15 Rickenbacker Causeway, Miami, Florida, 33149, U.S.A.
2. Nova University, 8000 North Ocean Drive, Dania, Florida, 33004, U.S.A.

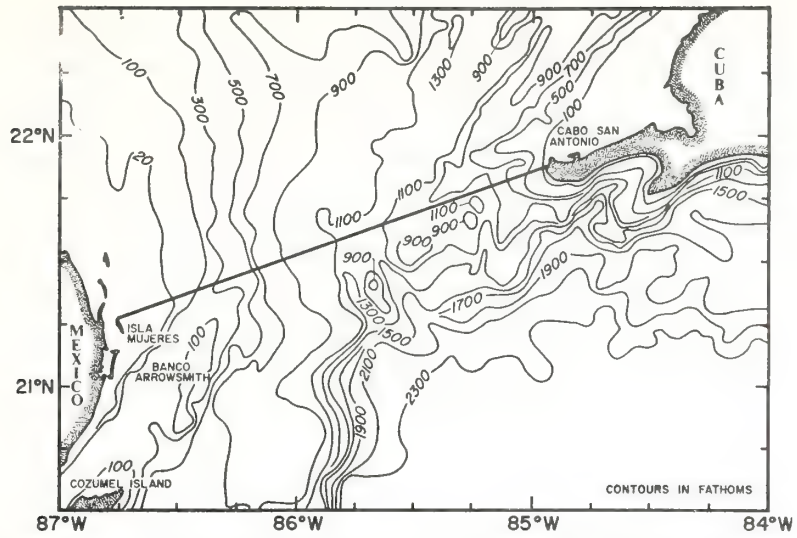


Figure 1. The bottom topography in the region of the Yucatan Strait adopted from Chart BC904N.

model was able to correlate the northernmost penetration of the current into the Gulf with relative vorticity just north of the Strait. Finally, observational studies by Cochrane (1965) and Maul (1975) suggest that the penetration of the current into the Gulf could be a function of a variable volume transport at the Strait.

This paper presents the results of an analysis of direct and indirect current measurements made from both ship and airplane in the Yucatan Strait between Isla Mujeres, Mexico, and Cabo San Antonio, Cuba (Fig. 1). In particular, average sections of those properties, velocity, transport, and vorticity, which could force the flow in the interior of the Gulf are given. When appropriate, these and other sections are compared both to the Straits of Florida sections given by Brooks and Niiler (1975) and to other sections obtained in the Yucatan Channel.

2. Experiment

A series of 15 cruises was made between Isla Mujeres, Mexico, and Cabo San Antonio, Cuba, between April 29 and May 29, 1972 (Fig. 2). STD and XBT stations were occupied along the sections. Molinari (1974) discusses the analysis techniques used to reduce the STD and XBT data. Navigation and instrument failures precluded the occupation of standard stations as originally planned.

The average T-S curve determined from the STD data is given by Molinari (1974). This curve was used to provide salinity values for both STD and XBT temperature profiles. This procedure was adopted to reduce the scatter in the deeper salinity observations due to instrumental error (Molinari, 1974), and to permit com-

Table 1. Transport to 700m or the deepest available depth.

Longitude	85°06′	85°18′	85°30′	85°42′	85°54′	86°06′	86°18′
Depth (m)	700	700	700	700	700	700	400
Transport ($\times 10^6$m^3/sec)	−0.4	2.3	4.2	3.3	3.6	2.9	4.0

putation of dynamic heights from XBT data. A two-fold increase in the amount of data available for dynamic computations was realized.

Freely falling dropsondes deployed by aircraft (see Richardson, White, and Nemeth (1972) for a description of the technique) were launched during a portion of the ship transects to measure directly the velocity and transport fields. However, because of instrument malfunctions, only the surface current speeds have been used in this analysis.

3. Average properties

Temperature, salinity, dynamic height, and surface velocity data were averaged over 12′ bands of longitude. The resulting cross-sections were assumed to represent the conditions along a line from Isla Mujeres to Cabo San Antonio (Fig. 2), a line approximately 21.5° north of due east. The mean temperature and salinity cross-sections for the one-month period are shown in Figs. 3 and 4 respectively. Mean surface velocities perpendicular to the standard section were computed from the aircraft dropsonde measurements for each band of 12′ of longitude and used as the reference speed for determination of the absolute geostrophic velocity distribution. Fig. 5 gives the geostrophic velocity section relative to these directly measured speeds. The maximum velocity of 1.04 m/sec is found at 86°18′. Speeds greater than 0.5 m/sec are found as far east as 85°48′. Countercurrents indicating flow out of the Gulf of Mexico are found from 85°42′ to 86°06′ and east of 85°18′. Similar findings of a subsurface counterflow have been reported on by Hansen (1972) and Schlitz (1973). In particular, Schlitz (1973) using the bottom as the reference level of zero velocity found outflow below the main current at 700m.

The absolute transport down to the average $27.0\sigma_t$ contour was computed for comparison with the corresponding Straits of Florida transport. This transport computed from 85°00′ to 86°36′ is 20.8 $\times$ 10^6 m^3/sec as compared to an average transport of 20.2 ($\pm$1.6) $\times$ 10^6 m^3/sec through the Straits of Florida. Since there were no surface current measurements in the segment between 86°24′ and 86°36′, the transport in this segment was computed relative to the deepest common depth between stations. The Brooks and Niiler (1975) measurements did not extend within 35 kilometers of Cuba.

Table 1 gives the transport to 700m or the deepest available depth at the center longitude of the 12′ bands, using the surface dropsonde measurements as an absolute reference level.

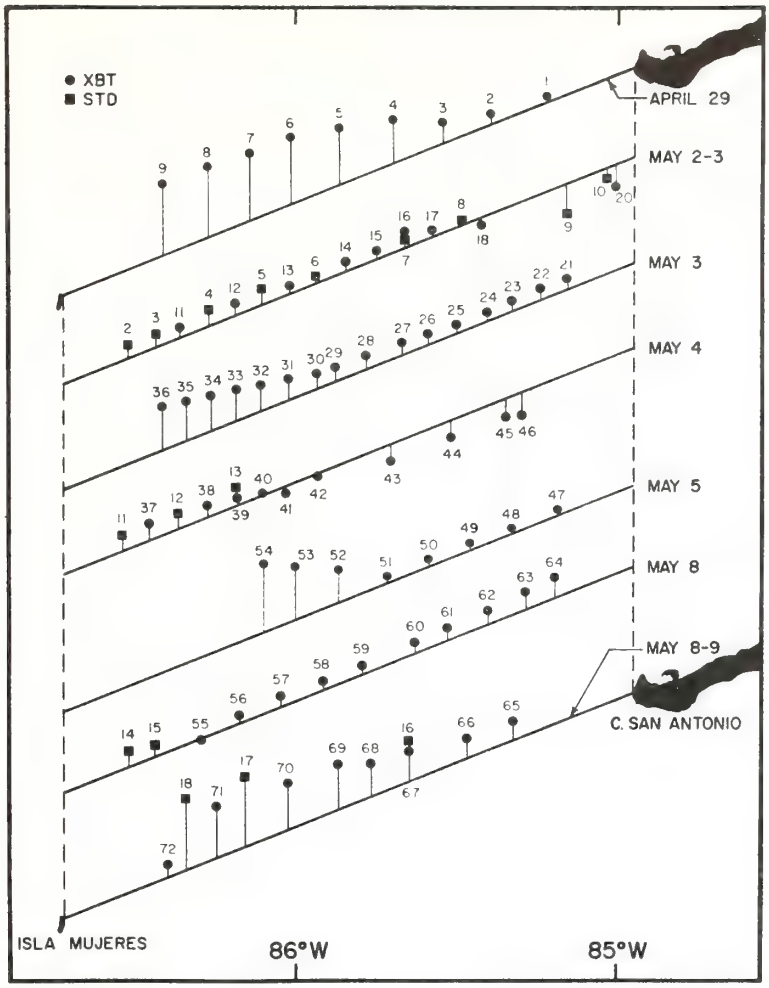
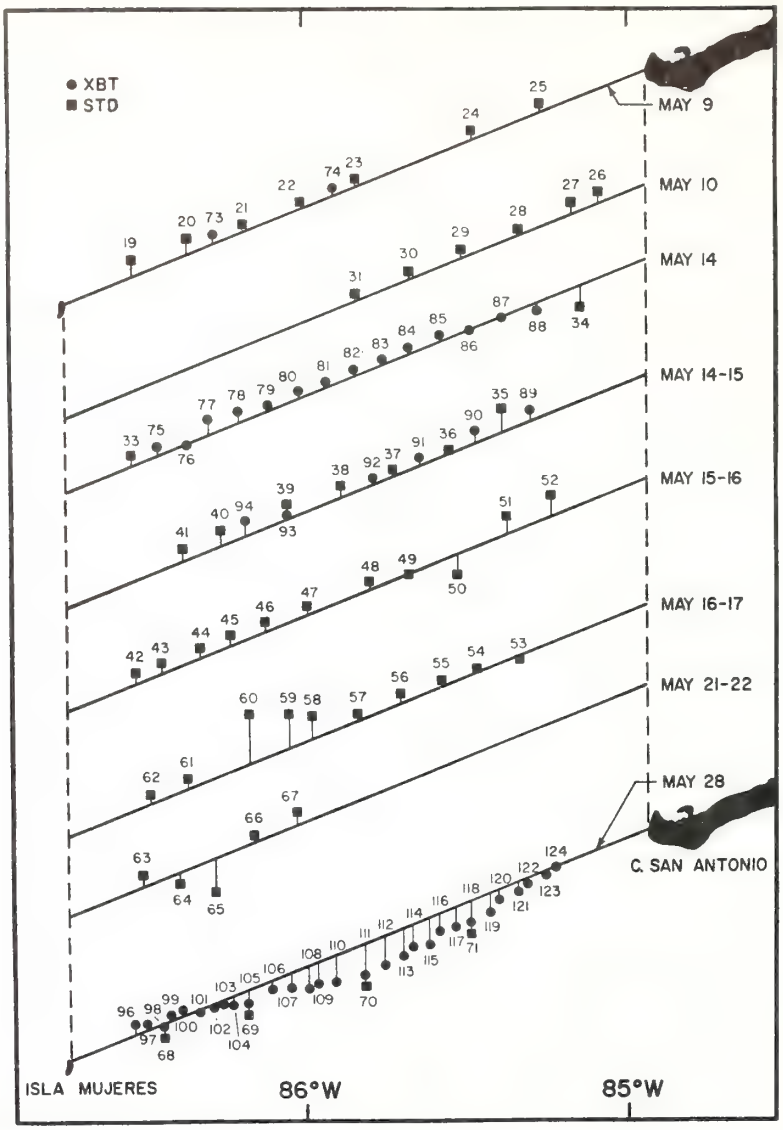


Figure 2. Station locations, and the time periods during which the sections were occupied.

Table 2. Relative and potential vorticities ($f = 5.3 \times 10^{-5}$/sec).

Longitude	85°06′	12′	18′	24′	30′	36′	42′	48′	54′	86°00′	06′	12′	18′
Velocity (m/sec)	.17		.45		.54		.60		.82		1.11		1.29
Relative Vorticity ($\times 10^5$/sec)		−1.4		−0.4		−0.3		−1.1		−1.4		−0.9	
Depth of $\sigma_t = 27.0$ contour (m)		540		510		500		450		420		390	
Potential Vorticity ($\times 10^5$/m sec)		7.2		9.6		10.0		9.3		9.2		11.2	



The average transport above 700m for this period is 19.9 $\times$ 10^6 m^3/sec. Schlitz (1973) found the average geostrophic transport above 700m during an 18 day period in April 1970 to be 22($\pm$1) $\times$ 10^6 m^3/sec.

As discussed earlier, numerical models of the Gulf of Mexico could use relative or potential vorticity or volume transport at the Yucatan Strait as a boundary condition. Table 2 lists the average relative and potential vorticities for the 12′ bands, if it is assumed that the relative vorticity, ζ, is approximated by $\partial v/\partial x$ (where v is the directly measured north component of surface speed), and the potential vorticity

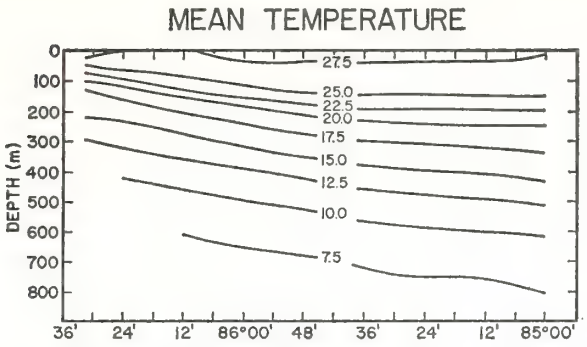


Figure 3. The mean temperature cross-section obtained by averaging all the available temperature data over 12′ bands of longitude.

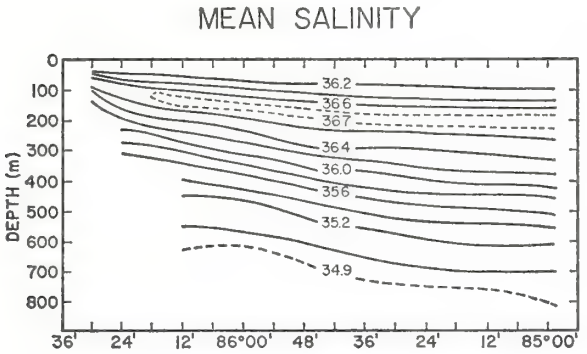


Figure 4. Same as Fig. 3, except for salinity.

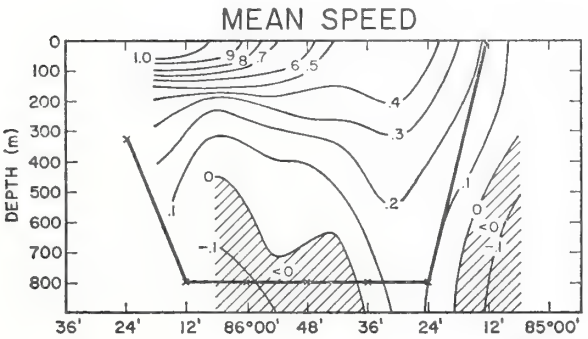


Figure 5. Geostrophic current velocities computed relative to the absolute surface speeds determined from the dropsonde measurements. Data from fifteen or more stations were available above the solid line.

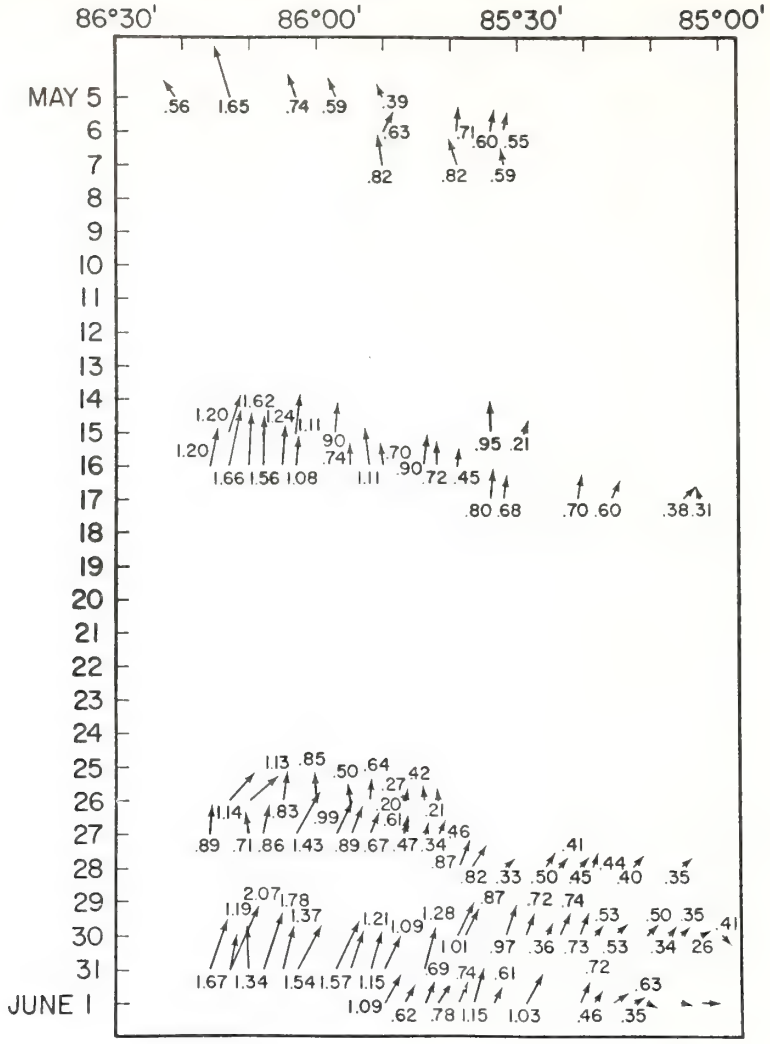


Figure 6. Surface velocity vectors determined as a function of time and position by dropsonde stations. The current speeds are given in m/sec.

by $(\zeta+f)/h$, where f is the Coriolis parameter (computed for a latitude of 21.5°N), and h is the depth of the $\sigma_t = 27.0$ contour. Table 2 shows that the relative vorticity can be as large as 25% of the planetary vorticity in the Yucatan Strait and suggests that the potential vorticity may be nearly constant in the main portion of the Yucatan Current (i.e. west of 85°24′).

4. Fluctuations

Fig. 6 is a plot of all the surface velocity vectors. There is considerable vari-

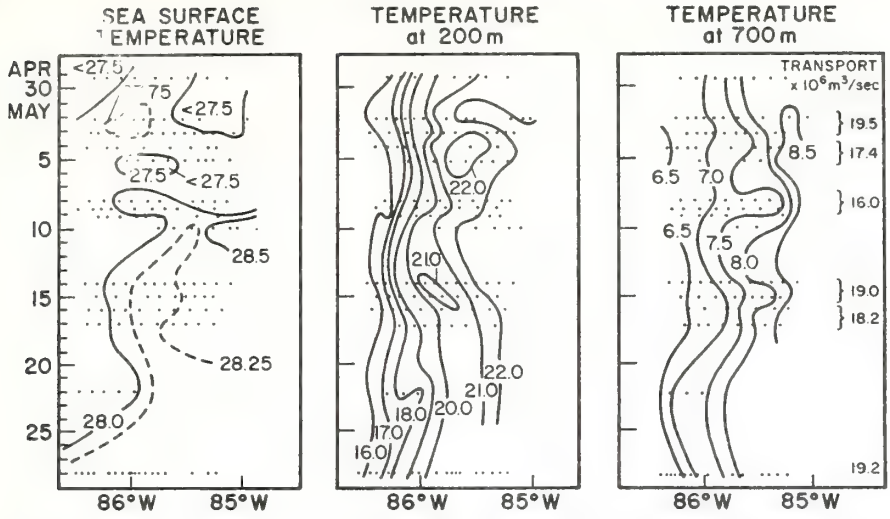


Figure 7. The change in temperature with time observed at the sea surface, 200m and 700m. Also given are geostrophic volume transports computed relative to 700m for the time periods indicated.

ability represented in these vectors; particularly in the maximum surface speeds and the width of the current with speeds greater than 1 m/sec. The amount of tidal aliasing cannot be determined from this small record, thus it is impossible to ascertain how much of this surface variability is indicative of deeper nontidal current fluctuations. It is important to note that the surface current measured by the air dropsondes is in a thin surface layer about 15 cm. thick. This layer and the floats used in the measurements may be significantly affected by local winds, and this may contribute to the variability in the surface current measurements.

A slight increase in sea surface temperature occurred during the one-month observational period (Fig. 7) but there was little cross stream sea surface temperature structure observed during the late spring survey. Satellite location of the current is precluded by this lack of horizontal temperature gradients.

The position of the maximum temperature gradients and the magnitude of these gradients at 200m and 700m varied during the experiment (Fig. 7). The variability can be indicative both of changes in the position of the Yucatan Current axis and of changes in the geostrophic speed along the axis. The axis can shift laterally by as much as 15km in a period as short as three days, May 14 to May 17, for instance. The changes in intensity appear to occur over a slightly longer interval. The period of these fluctuations can not be determined from this data set.

The geostrophic volume transport to 700 meters has been computed for each one or two day occupation of the section. This measured transport is indicated on the righthand side of Fig. 7. The average transport for the 26 day period is 18.2

($\pm$ 1.3) $\times$ 10^6 m^3/sec. The 7% variation in transport is comparable with the 9% variation measured over the same time span in the Straits of Florida at Key West (Brooks and Niiler, 1975).

5. Discussion

The results of the data analysis discussed here agree with the geostrophic velocity and transport computations done by Schlitz (1973). In particular, the existence of a deep counter current below the Yucatan Current appears in the absolute geostrophic velocity (Fig. 5). The May, 1972 transport above 700m, 19.9 $\times$ 10^6 m^3/sec, is within 10% of the value determined by Schlitz for April, 1970. However, both values are somewhat lower than the mean transport determined over many years through the Straits of Florida for April and May, reported by Niiler and Richardson (1973), 32.5 ($\pm$2.8) $\times$ 10^6 m^3/sec.

The estimates of the Straits of Florida and Yucatan Strait transports above σ_t = 27.0 are within 5% of each other. This comparison suggests that no difference in the average warm water transport between the two Straits exists during this one month period.

The transport measurements at the Yucatan Strait and Straits of Florida (Brooks and Niiler, 1975) vary 7% and 9%, respectively, over the concurrent observational period. In addition, a minimum in transport is observed at both straits during the experiment; 8 May at the Yucatan Strait (Fig. 7) and 17 May at the Straits of Florida. A similar minimum in volume transport is observed by Morrison (1974) at a repeated section in the mid-Gulf and on 9 May. Thus, the transport fluctuations observed at the Yucatan Strait could be propagating downstream to the Straits of Florida with a lag of about nine days. These fluctuations, however, appear to have only a negligible effect on the intrusion of the Loop Current as three surveys in the interior of the Gulf made between 2 and 21 May indicate little change in the configuration of the Loop Current (Morrison, 1974).

Acknowledgments. The guidance and efforts of Dr. William Richardson during the planning and execution of this experiment are remembered, and this paper is dedicated to his memory.

The long and difficult hours endured by G. Hood and T. Morrissey aboard the R. V. *Virginia Key* are gratefully acknowledged. The efforts of Jerry Ehrich during the aircraft missions were essential elements in the successful completion of the study. The data analysis efforts of M. Josselyn and D. Tidwell are also acknowledged.

REFERENCES

Brooks, I. H., and P. P. Niiler. 1975. The Florida Current at Key West: Summer 1972. J. Mar. Res., *33*, 83–92.

Cochrane, J. D. 1965. The Yucatan Current, *in* Annual Report, Project 286. Texas A&M University, Ref. 65-17 T, College Station: 20–27.

Hansen, D. V. 1972. Deep currents in the Yucatan Strait. Abstract in Trans. A. G. U., *53*, 392.

Maul, G. A. 1975. An evaluation of the use of the Earth Resources Technology Satellite for observing ocean current boundaries in the Gulf Stream System. NOAA Tech. Rept. ERL 335-AOML 18, 125 pp.

Molinari, R. L. 1974. Data from the NOAA Ship *Virginia Key* and the SUSIO Ship *Bellows*, collected during CICAR Survey Month II. NOAA Tech. Memo. ERL AOML 22, 153 pp.

Morrison, J. M. 1974. Nutrient and dissolved-oxygen distributions in the Gulf of Mexico and adjacent regions. Masters thesis, Texas A&M University, 117 pp.

Morrison, J. M., W. J. Merrell, Jr., and W. D. Nowlin, Jr. 1973. The waters of the eastern Gulf of Mexico as observed during May 1972. 1. Data collected aboard the R. V. *Alaminos*. Texas A&M Res. Found Ref. 73-10 T, 320 pp.

Niiler, P. P., and W. S. Richardson. 1973. Seasonal variability of the Florida Current. J. Mar. Res., *31*, 144–167.

Paskausky, D. F., and R. O. Reid. 1972. A barotropic prognostic numercial circulation model, *in* Contributions on the Physical Oceanography of the Gulf of Mexico, Texas A&M University Oceanographic Studies, L. R. A. Capurro and J. L. Reid, eds., Houston, Gulf Publ. Co., 163–176.

Reid, R. O. 1972. A simple dynamic model of the Loop Current, *in* Contributions on the Physical Oceanography of the Gulf of Mexico. Texas A&M University Oceanographic Studies, L. R. A. Capurro and J. L. Reid, eds., Houston, Gulf Publ. Co., 157–160.

Richardson, W. S., H. J. White, Jr., and L. Nemeth. 1972. A technique for the direct measurement of ocean currents from aircraft. J. Mar. Res., *30*, 259.

Schlitz, R. J. 1973. Net total transport and net transport by water mass categories for the Yucatan Channel based on data for April 1970. Ph.D. Dissertation Texas A&M University, College Station, Texas, 107 pp.

Wert, R. T., and R. O. Reid. 1972. A baroclinic prognostic numerical circulation model, *in* Contributions on the Physical Oceanography of the Gulf of Mexico, Texas A&M University, Oceanographic Studies, L. R. A. Capurro and J. L. Reid, eds., Houston, Gulf Publ. Co., 177–209.

Received: *1 February, 1976;* revised: *6 October, 1976.*

Printed in U.S.A. for the Sears Foundation for Marine Research,
Yale University, New Haven, Connecticut, 06520, U.S.A.
Van Dyck Printing Company, North Haven, Connecticut, 06473, U.S.A.

Science 198, 505-507.

Winter Intrusions of the Loop Current

Abstract. *Sea-surface temperature data obtained from satellite and subsurface temperature data obtained from ships are used to determine the intrusion of the The Loop Current extended considerably farther to the north during the last three winters than has been observed previously.*

The positions of intense ocean currents have traditionally been of interest to mariners, who must account for such currents in order to navigate effectively. More recently, concern about the dispersal of pollutants dumped into the oceans has created additional interest in accurately locating strong currents. There should be particular concern about this problem with regard to the Gulf of Mexico, which receives the great runoff of the Mississippi River with its load of agricultural and industrial wastes.

The circulation in the eastern Gulf of Mexico is dominated by the so-called Loop Current, which enters the Gulf through the Yucatán Straits and exits through the Straits of Florida. The path in the interior of the Gulf varies considerably with time, sometimes following a nearly direct route between the two straits, while at other times extending far to the north, forming an anticyclonic (clockwise) loop which gives the current its name.

Most of what we know about the position of the Loop is based on the assumption of geostrophic balance. Under the assumption that the vertical current shear is proportional to the horizontal gradient of mass or temperature, one can deduce that the position of strong currents coincides with the strongest depth gradients of temperature surfaces. Figure 1 shows two examples of the structure of the 20°C temperature surface in the eastern Gulf; the core of the Loop Current coincides with the positions of the large gradients observed.

Most of the temperature observations in the eastern Gulf have been made during the spring, summer, and fall. These observations have shown that the Loop Current is farthest north during the summer (*1–3*). The relatively few observations made during the winter show less developed intrusions (*2, 3*). The point of our report is that recent observations made between November 1974 and April 1977 show the northernmost intrusions of the Loop Current during the winter months.

Background. Leipper (*2*) proposed an annual cycle for the intrusion of the Loop Current, based primarily on data collected during 1965 and 1966. He found that the Loop intruded north into the Gulf during the spring. The maximum intrusion in the summer and fall occurred in one of two modes. Either the Loop Current remained continuous from the Yucatán Straits to the northeastern Gulf, or an eddy detached, leaving behind a remnant of the Loop in the southeastern Gulf. The eddy or the extended Loop drifted to the west in the fall. The minimum northward intrusion of the Loop Current was observed in the winter. Maul (*3*) found a similar cycle in 1972–73 (the data displayed in Fig. 1 were used by Maul).

Behringer, Molinari, and Festa (*4*) used the 150-m contour of the 20°C isothermal surface (which is normally found in the high-gradient region of this surface) to represent the position of the Loop Current. Figure 2 gives the maximum northern intrusion of the Loop Current from 1965 to 1977 and includes most of the data available during this time. The data obtained from 1965 through 1973 are consistent with the findings in (*2*) and (*3*).

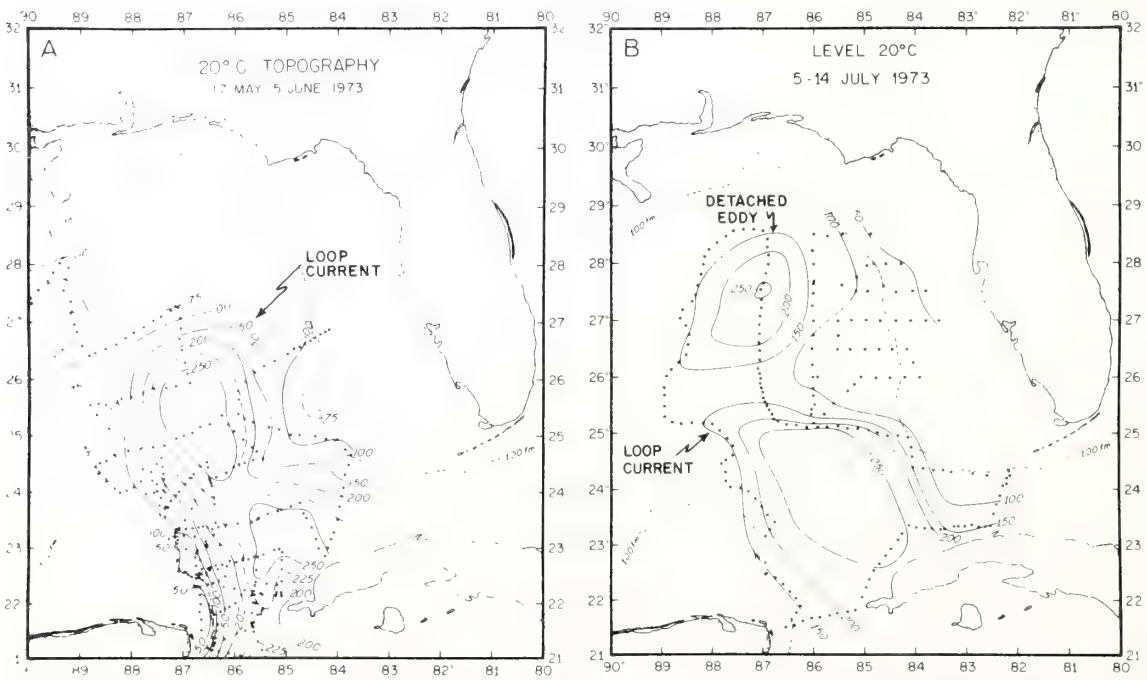


Fig. 1. Depth of the 20°C isothermal surface observed during (A) May and June and (B) July 1973. The intense currents in the eastern Gulf of Mexico are easily identified by their large horizontal temperature gradients. (A) A deep Loop Current intrusion; (B) the temperature structure after an eddy has separated from the Loop.

with the greatest northward intrusions observed from April 1972 through September 1965.

Maul (*3*) demonstrated that satellite imagery can be used to define the left side (looking downstream) of the Loop Current during the winter. The sea-surface front of the Loop Current was, on the average, 15 km to the left (looking downstream) of the subsurface core as indicated by temperature data.

Legeckis (*5*) reported on the first winter deep intrusion and eddy separation determined from direct observations during 1974 and 1975. His conclusions were drawn from maps of sea-surface temperature (SST) derived from satellite measurements.

Data sources. The Field Service Station of the National Environmental Satellite Service in Miami, Florida, produced maps of SST gradients. These were used to determine the left side of the Loop and thus define the penetration of the Loop and eddy separations during the winters of 1974–75, 1975–76, and 1976–77.

In addition, in May 1975 we began a series of cruises to study the Loop Current. The most recent survey was completed in April 1977. We have constructed topographic charts of the depth of the 20°C isothermal surface from the temperature data obtained during these cruises. We used the position of the 20°C isotherm at 150 m derived from these maps to determine the northern edge of the Loop Current, as in (*4*).

Finally, we obtained additional subsurface temperature data from the National Oceanographic Data Center. The timing of some of these observations enabled us to fill in some of the gaps in our data set. In addition, these data were used to construct 20°C isotherm topographies to compare with concurrent SST analyses of the position of the Loop Current.

Results. The few winter observations made before 1974 do not show a Loop Current intrusion north of 26°N (Fig. 2). However, from 1974 through 1977 the winter intrusions were all north of 26°N.

The subsurface temperature data we obtained from the National Oceanographic Data Center for the winter of 1974–75 show Loop Current intrusions during November 1974 and February 1975 which are consistent with the satellite observations in (*5*). Subsurface data for March 1975 confirm the winter eddy separation during early March but do not extend far enough north to verify the intrusion indicated by the SST data.

The February 1976 subsurface temperature and SST data show a similar maximum intrusion latitude. The late February and March SST data depict a northward progression of the Loop which is consistent with the May 1976 SST and subsurface position of the Loop (Fig. 2).

The SST data suggest no eddy separation before the end of May 1976. Subsurface data from May confirm the SST results in terms of the Loop's intrusion but, like the SST data, are insufficient to determine whether an eddy had detached. The eastern edge of an eddy was observed in August 1976, from which we surmise that an eddy probably separated from the Loop between May and August 1976.

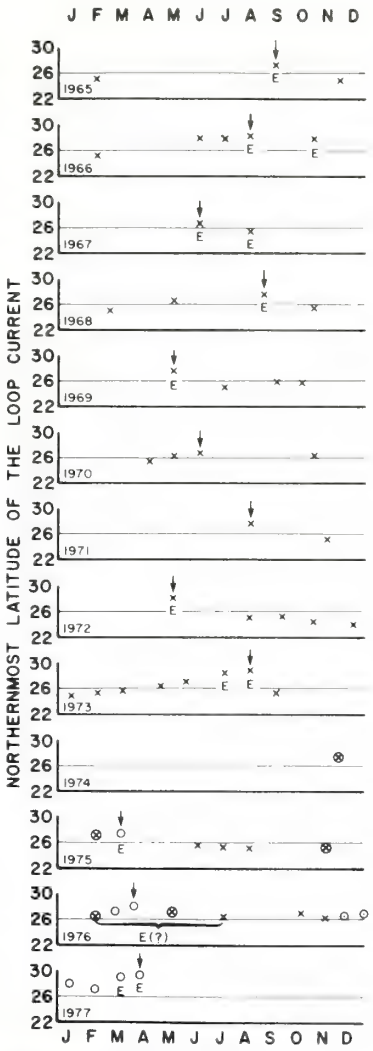


Fig. 2. Intrusion of the Loop Current as indicated by the northernmost position of the 150-m isoline of the 20°C isothermal surface (X), the edge of the current determined from satellite sea-surface temperature maps (:), or both (⊗). The arrow denotes the maximum intrusion observed during a particular year and *E* those months when the northern edge of a detached eddy was used to indicate the intrusion. The exact time of the 1976 eddy breakoff and the maximum intrusion during May 1976 could not be determined because of insufficient data.

The SST data indicate that the winter intrusions of 1976–77 were again deep and that an eddy detached in mid-March 1977. The circulation pattern derived from a limited ship survey in April 1977 is consistent with the conclusion of an earlier eddy separation event.

Discussion. Our present knowledge of the dynamics of the Loop Current is limited. The intrusion of the Loop has been related both to the relative vorticity distribution at the Yucatán Straits (*6*) and to the volume transport at this passage (*3*). However, the mechanism which establishes these conditions at the Straits are unknown. Since the Loop Current is part of the North Atlantic gyre, these conditions are probably influenced by events farther upstream in the Caribbean Sea and the Gulf of Mexico. The relation of the Gulf of Mexico to the conditions in these regions has not been established; thus we cannot say with any certainty that the recent winter intrusions are associated with anomalous winter conditions in the Caribbean Sea and the Atlantic Ocean.

In addition, the historical data set is limited, so we do not know whether winter intrusions occurred in the past and were simply not observed. Nevertheless, regardless of the reason, deep winter intrusions of the Loop Current have been heretofore unknown. The evidence presented in this report means that deepwater intrusions must now be recognized by mariners, environmentalists, and all others concerned with the position of the Loop Current.

R. L. Molinari
Atlantic Oceanographic and Meteorological Laboratories, National Oceanic and Atmospheric Administration, Miami, Florida 33149
S. Baig
National Environmental Satellite Service, National Oceanic and Atmospheric Administration, Miami, Florida 33149
D. W. Behringer, G. A. Maul
Atlantic Oceanographic and Meteorological Laboratories
R. Legeckis
National Environmental Satellite Service, National Oceanic and Atmospheric Administration, Suitland, Maryland 22023

References and Notes

1. W. D. Nowlin and J. M. Hubertz, in *Contributions On the Physical Oceanography of the Gulf of Mexico*, L. R. Capurro and J. L. Reid, Eds. (Gulf, Houston, Texas, 1972), pp. 139–142.
2. D. F. Leipper, *J. Geophys. Res.* **75**, 637 (1970).
3. G. A. Maul, *Natl. Oceanic Atmos. Adm. Tech. Rep. ERL 335-AOML 18* (1975).
4. D. W. Behringer, R. L. Molinari, J. F. Festa, *J. Geophys. Res.*, in press.
5. R. Legeckis, abstract in *Progress in Marine Research in the Caribbean and Adjacent Regions, CICAR-II Symposium, Caracas, Venezuela*, H. B. Stewart, Jr., Ed. (The editor, Miami, 1976; sponsored by Intergovernmental Oceanographic Commission with the support of the Food and Agriculture Organization, United Nations Educational, Scientific and Cultural Organization, and World Health Organization), p. 239.
6. R. T. Wert and R. O. Reid, in *Contributions On the Physical Oceanography of the Gulf of Mexico*, L. R. Capurro and J. L. Reid, Eds. (Gulf, Houston, Texas, 1972), pp. 177–209.

7. This work was partially funded by the Bureau of Land Management under BLM Interagency Agreement 085 50-1A5-26 with the NOAA Environmental Research Laboratories.

20 June 1977; revised 19 August 1977

NOAA Data Report ERL MESA-28, 93 pages. (Text only.)

NOAA Data Report ERL MESA-28

MESA NEW YORK BIGHT PROJECT
EXPANDED WATER COLUMN CHARACTERIZATION CRUISE (XWCC 10)
NOAA SHIP GEORGE B. KELEZ, 28 JUNE - 1 JULY, 1976

Robert B. Starr
John B. Hazelworth
Shailer R. Cummings
George A. Berberian

Atlantic Oceanographic and Meteorological Laboratories
Miami, Florida

Marine Ecosystems Analysis Program
Boulder, Colorado
December 1977



UNITED STATES DEPARTMENT OF COMMERCE
Juanita M. Kreps, Secretary

NATIONAL OCEANIC AND ATMOSPHERIC ADMINISTRATION
Richard A. Frank, Administrator

Environmental Research Laboratories
Milton N. Hess, Director

NOTICE

The Environmental Research Laboratories do not approve, recommend, or endorse any proprietary product or proprietary material mentioned in this publication. No reference shall be made to the Environmental Research Laboratories or to this publication furnished by the Environmental Research Laboratories in any advertising or sales promotion which would indicate or imply that the Environmental Research Laboratories approve, recommend, or endorse any proprietary product or proprietary material mentioned herein, or which has as its purpose an intent to cause directly or indirectly the advertised product to be used or purchased because of this Environmental Research Laboratories publication.

CONTENTS

	Page
Abstract	1
1. INTRODUCTION	1
2. DATA PRESENTATION	5
3. ACKNOWLEDGMENTS	6
4. REFERENCES	6
5. AREAL AND CROSS-SECTION DISTRIBUTIONS OF TEMPERATURE, SALINITY, AND SIGMA-T	8
6. STATION DATA	15

MESA NEW YORK BIGHT PROJECT
EXPANDED WATER COJUMN CHARACTERIZATION CRUISE (XWCC 10)
NOAA SHIP GEORGE B. KELEZ
28 JUNE - 1 JULY, 1976

Robert B. Starr
John B. Hazelworth
Shailer R. Cummings
George A. Berberian

During the period 28 June - 1 July 1976, an oceanographic cruise was made on the NOAA Ship George B. Kelez in the New York Bight. The objective of the cruise was to supply data to provide a base for analysis of the water characteristics and movements in the highly impacted ecosystem. This report presents the corrected physical and chemical (nutrient) data form this cruise, and describes the Neuston net towing operation and results.

Key Words: MESA, New York Bight, Physical Oceanographic Data, Nutrient Data, Neuston Net Tows.

1. INTRODUCTION

This report is a continuation in the Marine Ecosystem Analysis (MESA) Program's series of publications presenting oceanographic data from the New York Bight. In June of 1976, a cruise of 38 stations was conducted by the Atlantic Oceanographic and Meteorological Laboratories (AOML), Miami, Florida, aboard the NOAA Ship George B. Kelez. The instrumentation employed was the same as that described in previous reports (Hazelworth et al., 1974, 1975a, b, Kolitz et al, 1976) namely, an Inter Ocean Model 513-10 CSTD with associated sensors and equipment. The area of investigation was the expanded New York Bight region (Fig. 1 and Tab. 1). Cruise dates and participating AOML staff members are listed in Table 2. The physical and nutrient data obtained from the water column measurements are presented herein; the operational characteristics of the nutrient-analyses system are found in Starr et al., (1977).

This report is the eighth of a series of reports describing the physical oceanographic measurements in the expanded area. Earlier cruises were reported by Charnell et al., (1976), Starr et al., (1976, 1977), Hazelworth and Darnell (1976), Kolitz et al., (1976, 1977) and Hazelworth et al., (1977).

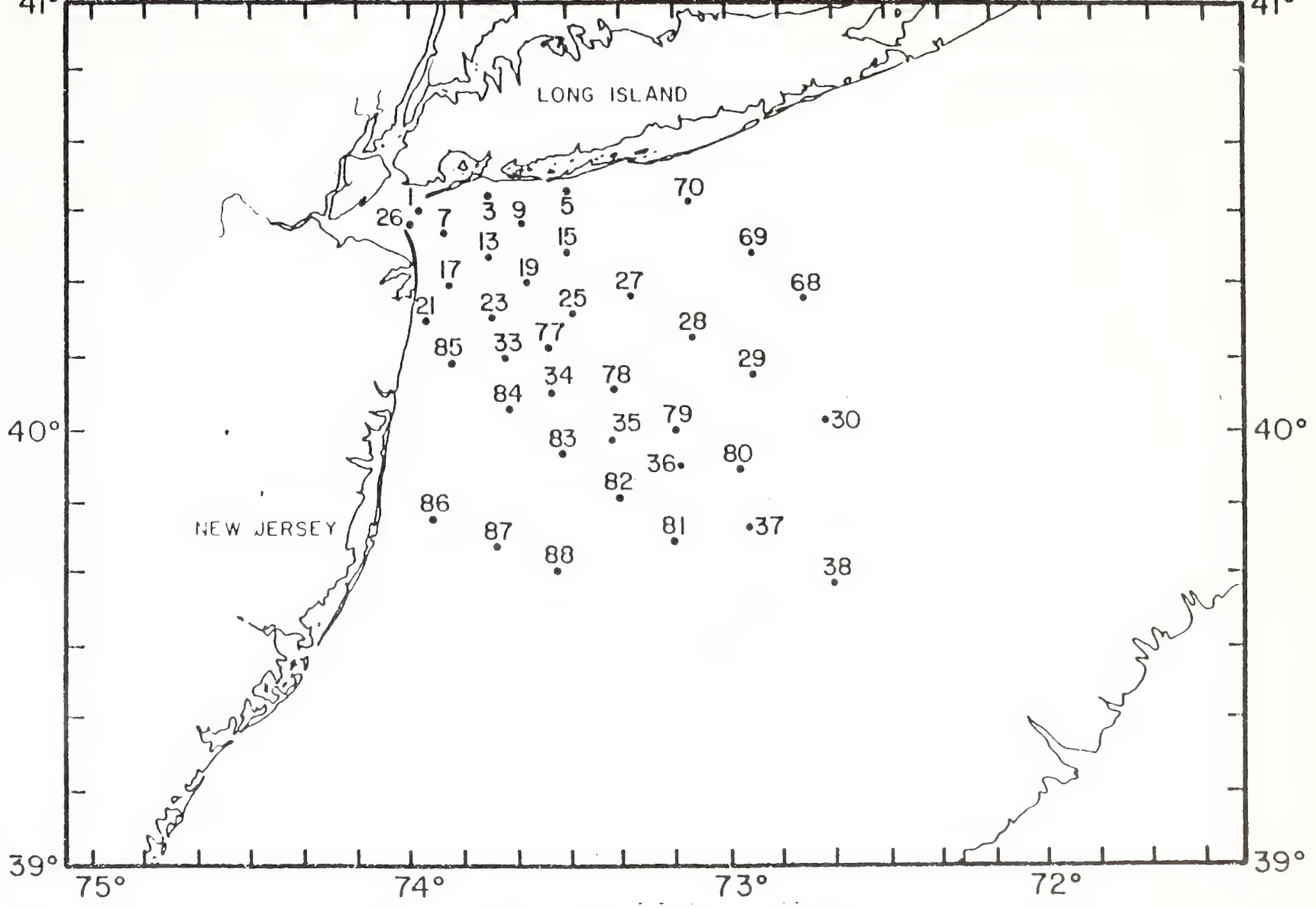


Figure 1. Stations occupied during XMC 10.

Prior reports, cited above, give detailed information on instrumentation specifications, data collection methods, and data processing techniques. The correction factors and data accuracy are given in Table 3.

Table 1. Oceanographic Station Locations

Designation	Latitude (N)	Longitude (W)	Designation	Latitude (N)	Longitude (W)
1	40°30.2'	73°57.3'	35	39°59.0'	73°21.5'
3	40°31.5'	73°48.4'	36	39°55.0'	73°06.5'
5	40°33.3'	73°32.5'	37	39°46.0'	72°57.0'
7	40°26.9'	73°53.0'	38	39°39.0'	72°39.5'
9	40°28.3'	73°39.6'	68	40°19.0'	72°46.0'
13	40°23.3'	73°47.0'	69	40°25.0'	72°55.0'
15	40°25.2'	73°30.4'	70	40°32.0'	73°07.0'
17	40°18.5'	73°51.8'	77	40°10.5'	73°34.0'
19	40°20.2'	73°37.9'	78	40°05.0'	73°21.5'
21	40°13.5'	73°56.1'	79	40°00.0'	73°09.5'
23	40°14.8'	73°45.6'	80	39°54.5'	72°57.0'
25	40°16.9'	73°28.3'	81	39°44.5'	73°10.0'
26	40°29.0'	73°59.5'	82	39°50.5'	73°20.5'
27	40°18.0'	73°17.5'	83	39°56.5'	73°30.5'
28	40°13.5'	73°07.0'	84	40°02.0'	73°41.0'
29	40°07.0'	72°54.5'	85	40°08.0'	73°51.5'
30	40°02.0'	72°41.5'	86	39°47.5'	73°57.0'
33	40°10.0'	73°41.5'	87	39°44.0'	73°45.5'
34	40°05.5'	73°31.5'	88	39°40.0'	73°30.0'

Table 2. NOAA Ship George B. Kelez
Expanded Water Column Characterization Cruise KMCC 10

Date	AOML Personnel
28 June - 1 July 1976	Robert B. Starr Chief Scientist John B. Hazelworth Shailer R. Cummings Philip G. Hanson

Table 3. Data Accuracy for Cruise XWCC 10

	Temp. °C	Salinity o/oo	Transmissivity	pH	O_2 (#1)	O_2 (#2)
Mean Data Accuracy	-0.00	+0.02	N.A.	+0.05	-0.00	Inoperative
Standard Deviation	0.03	0.05	N.A.	0.21	0.07	

The limited number of stations occupied on this cruise resulted partly from the requirement to conduct a series of Neuston net tows offshore of southern Long Island to sample the floating debris in the surface water as a result of the contamination of the Long Island beaches that had been occurring sporadically during the previous month. A total of five tows was made. The beginning and ending times and positions of these tows are listed in Table 4. The times are Eastern Daylight Saving time and the date was 1 July 1976.

Table 4. Time and Location of Neuston Net Tows

Tow No.	Times	Latitude (North)	Longitude (West)
1	1140	40°35.9'	73°17.6'
	1220	40°35.9'	73°21.4'
2	1350	40°33.5'	73°32.7'
	1450	40°33.6'	73°38.2'
3	1620	40°24.6'	73°42.8'
	1630	40°24.4'	73°42.4'
4	1740	40°33.6'	73°43.8'
	1750	40°33.8'	73°44.9'
5	1806	40°33.8'	73°45.8'
	1824	40°33.8'	73°46.4'

The first tow was made across Fire Island Inlet on ebb tide. Its contents included numerous small styrofoam fragements, a quantity of unknown fibrous material, some isopods and juvenile decapods, some wood fragments including a board about 1.5 feet long by 4 inches wide, and some sheet cork fragments. Tow number two was taken across Jones Inlet, also on ebb tide, and resulted in a much larger volume of material than the first one. It consisted of styrofoam bits, seaweed, isopods and juvenile decapods, one large and a couple of smaller charred wood fragments, and several small pieces of wood.

While proceeding westward toward East Rockaway Inlet, a message was received that the Nasau County sludge dump ship Susan Frank was leaving East Rockaway Inlet for the dump site. Consequently, since it was desired to sample one of these dumps, the Neuston net was towed in the wake of the Susan Frank during her dumping operation. The net filled and towed under in 10 minutes. The sample obtained from this sewage tow consisted of sewage sludge, styrofoam bits, a plastic bag, and what appeared to be eggs of a marine animal.

The final tows, four and five, were taken off of Atlantic Beach and East Rockaway Inlet in the late afternoon. The first one had the largest volume and consisted mostly of seaweed and styrofoam,while the second one was composed of seaweed and larval decapods. The planned transect across lower New York Bay was aborted because of approaching night and degrading visibility. The ship then returned to its berth at Floyd Bennett Field. All samples were labeled, preserved in formalin, and left at the ship base for transport to MESA Headquarters at Stony Brook, New York.

2. DATA PRESENTATION

Tables of the interpolated data and the corresponding depth profiles of temperature, salinity, sigma-t, transmissivity, pH, and dissolved oxygen are given in Section 6, Station Data. The codes used in the headings are from the National Oceanographic Data Center Manual Series (1964). The tabulated data are given at 1-m intervals from the surface to 50 m and at 10-m intervals thereafter; in addition, data are presented at the depths at which water samples were obtained and at the bottom of the cast. Profiles were produced from the corrected raw data. The symbols, explained to the left of each horizontal axis and located on the curves at 5-m intervals, identify the parameters. The listings of dissolved oxygen from the probe have had a gradient correction applied due to the very slow response characteristics of this sensor. However, because of the variable and very steep gradients,

particularly below the maximum in shallow water, this correction is only approximate in these gradients. Consequently, the statistical statement of accuracy in Table 3 for this probe only applies where there were no significant gradients. Nevertheless, the probe values do provide a good presentation of the variation of oxygen with depth in the water column that is not possible with the discreet Winkler values. On the few stations the oxygen probe malfunctioned on, the discreet Winkler values from the water samples have been substituted for the probe values. Also, when the pH probe recorded values less than 7.3 on the pH scale, these were excluded from the listings and the pH values determined on the water samples at these depths substituted in their place.

The distributions of temperature, salinity, and sigma-t are presented in Section 5: 1) horizontally at the 1-m depth (Figs. 2-4) and 2) vertically along the axis of the Hudson Shelf Valley (Figs. 5-7).

3. ACKNOWLEDGMENTS

The authors express their thanks to the officers and crew of the NOAA Ship Kelez, under the command of LCDR John Stachelhaus, for the long and diligent hours they devoted to collecting these data. The effort was sponsored by NOAA and funded in part by the NOAA Environmental Research Laboratories and the MESA Program's New York Bight Project.

4. REFERENCES

Charnell, R. L., M. E. Darnell, G. A. Berberian, B. L. Kolitz, and J. B. Hazelworth (1976): New York Bight Project, Water Column Characterization Cruises 1 and 2 of the NOAA Ship Researcher, 4-15 March and 5-14 May, 1974, NOAA Data Report MESA-18, U. S. Govt. Print., Washington, D. C., (Microfiche).

Hazelworth, J. B., B. L. Kolitz, R. B. Starr, R. L. Charnell, and G. A. Berberian (1974): MESA New York Bight Project, Water Column Sampling Cruises #1-5 of the NOAA Ship Ferrel, August-November 1973, MESA Report No. 74-2, U. S. Govt. Print. Off., Washington, D. C. 191 p.

Hazelworth, J. B., B. L. Kolitz, R. B. Starr, R. L. Charnell, G. A. Berberian, and M. A. Wiselberg (1975): MESA New York Bight Project, Water Column Sampling Cruises #6-8 of the NOAA Ship Ferrel, April-June 1974, NOAA Data Report MESA-1, U. S. Govt. Print. Off., Washington, D. C., 177 p.

Hazelworth, J. B., B. L. Kolitz, R. B. Starr, R. L. Charnell, G. A. Berberian, and M. A. Weiselberg (1975): MESA New York Bight Project, Water Column Sampling Cruises #9-12 of the NOAA Ship Ferrel, July-November 1974, NOAA Data Report MESA-3 U. S. Govt. Print. Off., Washington, D. C., 233 pp. (Microfiche).

Hazelworth, J. B. and M. E. Darnell (1977): MESA New York Bight Project, Expanded Water Column Characterization Cruises (XWCC 2 and 3) NOAA Ship Researcher, 22 February - 5 March, 9-12 April, 1975, NOAA MESA Data Report 23, U. S. Gov't Print. Off., Washington, D. C. (Microfiche). In press.

Hazelworth, J. B., S. R. Cummings, R. B. Starr, and G. A. Berberian (1977): MESA New York Bight Project Expanded Water Column Characterization Cruise (XWCC 8 NOAA Ship Kelez, April 1976, NOAA MESA Data Report, U. S. Gov't. Print. Off., Washington, D. C. In press.

Kolitz, B. L., J. B. Hazelworth, R. B. Starr, and S. R. Cummings (1977): MESA New York Bight Project. Expanded Water Column Characterization Cruises (XWCC 4-5) NOAA Ship Kelez, May-June 1975, NOAA MESA Data Report-24 U. S. Govt. Print. Off., Washington, D. C. (Microfiche). In press.

Kolitz, B. L., J. B. Hazelworth, R. B. Starr, G. A. Berberian, and S. R. Cummings (1977): MESA New York Bight Project. Expanded Water Column Characterization Cruise (XWCC 7 NOAA Ship Kelez, December 1975, NOAA MESA Data Report 26, U. S. Gov't Print. Off., Washington, D. C. (Microfiche). In press.

National Oceanographic Data Center Manual Series (1964): Processing Physical and Chemical Data from Oceanographic Stations, Part 1. Coding and Keypunching, Publication M-2, revised, U. S. Naval Oceanographic Office, Washington, D. C., 117 pp.

Starr, R. B., G. A. Berberian, and M. A. Weiselberg (1976): MESA New York Bight Project, Expanded Water Column Characterization Cruise (XWCC 1) of the R/V Advance II, January 1975, NOAA Data Report MESA-22, U. S. Gov't Print. Off., Washington, D. C., (Microfiche).

Starr, R. B., J. B. Hazelworth, and G. A. Berberian (1977): MESA New York Bight Project, Expanded Water Column Characterization Cruise (XWCC 6) NOAA Ship Kelez, September-October 1975, NOAA MESA Data Report 25, U. S. Gov't Print. Off., Washington, D. C. (Microfiche). In press.

Proceedings of IOC/FAO/UNEP International Workshop on Marine Polution in the Caribbean and Adjacent Regions, Port-of-Spain, Trinidad, 13-18 December 1976. Workshop Report No. 11, 47-79.

- 47 -

REGIONAL OCEANOGRAPHY AS IT RELATES TO PRESENT AND FUTURE POLLUTION PROBLEMS AND LIVING RESOURCES - CARIBBEAN

by D.K. Atwood

CONTENTS

		Page
1.	Introduction	49
2.	Regional Description	49
	2.1 Regional bathymetry	49
3.	Water Masses of the Caribbean Sea	49
	3.1 General features	49
	3.2 Renewal of deep water	50
	3.3 Surface water	51
4.	Circulation in the Caribbean Sea and Gulf of Mexico	52
	4.1 Ocean currents	52
	4.2 Currents in and adjacent to the Caribbean Sea and Gulf of Mexico	52
	4.3 Measurement of ocean currents	53
	4.3.1 The dynamic method of measuring ocean currents as applied to the Caribbean	53
5.	Origin of Surface Water in the Caribbean Sea and Gulf of Mexico	54
	5.1 Salinity variations	54
	5.2 Silicate-salinity relationships	55
6.	Present and Future Pollution Problems Considered in Relation to the Oceanography of the Caribbean Sea	56
	6.1 General considerations	56
	6.2 Consideration of the upper 1,500 metres of water	57
	6.3 Consideration of deep water	58
7.	Summary and Conclusions	58
	References	
	Figures and Tables	

1. Introduction

Proper planning for pollution control and abatement cannot completely be done within the framework of isolated national programmes. We must somehow develop international programmes on a regional and even global scale if we are to protect our living resources. Planning for such programmes in marine pollution requires a basic understanding of the oceanography of the region under consideration. This paper is a description of the basic physical and chemical oceanography of one such area - the Caribbean Sea.

2. Regional Description

Figure 1 shows the Caribbean-Gulf of Mexico area in relation to surrounding land and water masses. We can see that the area is relatively land-locked and that its oceanography will be affected by the adjacent North Atlantic waters. Figure 1 also shows two major rivers which empty directly into the area: the Magdalena in Colombia and the Mississippi in the United States. We shall see shortly that at least two other rivers which do not empty directly into the area, the Orinoco and Amazon, also affect it. We shall also see that pollution occurring far from the Caribbean can have definite effects on it, and that occurrences in the Caribbean will affect not only that immediate area, but areas far to the north and east (sections 4.1 and 6.2) as well.

2.1 Regional bathymetry

The land-locked nature of the Caribbean-Gulf of Mexico area is more apparent in Figure 2, where the general bathymetry is shown. We can see that the area consists of a series of deep basins varying from 4.1 to 7.1 kilometres deep and is surrounded on the north, south and west by North, South and Central America; it is partially cut off from the North Atlantic Ocean on the east and northeast by the Greater and Lesser Antilles. Water exchange with the North Atlantic Ocean occurs over the sills between these Antillean Islands. The positions of the major sills are shown in Figure 2. We can see that even the deepest of them, the Windward sill (1,600 metres) and Jungfern sill (1,815 metres) are much more shallow than even the most shallow basin. For this reason, much of the water in the Caribbean is below sill depth, causing much concern about the extent of renewal of these waters. We shall discuss some implications of this later (sections 3.2 and 6.3).

3. Water Masses of the Caribbean Sea

3.1 General features

Water masses or types are usually defined in terms of their origin. The origin of deep waters is in turn defined by the point at which the water was last at the surface of the sea where exchanges across the air-sea interface and biological activity gave it a particular salinity, temperature and oxygen concentration. After leaving the surface, the water mass can be altered only by mixing, respiratory processes, and other relatively slow chemical reactions between the water and suspended matter. Other than mixing, these processes

will have little effect on salinity and temperature; however, respiration and/or decay of detritus can alter nutrient and oxygen concentrations. During these processes, the water develops specific temperature, salinity, oxygen and nutrient characteristics, which, when considered together, can be used to identify - or "fingerprint" - the water mass. The depth at which these characteristics are most pronounced is referred to as the core depth for that water.

Figure 3 shows the approximate core depths for water types present in the Venezuela Basin of the Eastern Caribbean Sea. These same water types can be traced through the other basins and into the Gulf of Mexico. Note that above 500 metres, the core depths are noticeably more shallow in the south than in the north of the basin. This is an important fact which will have bearing on later discussions (section 4.3.1). Table 1 gives a summary of the origin and characteristics of each of these cores. Mixing occurs between water cores, and the parameters that define the adjacent cores show almost linear mixing curves. This is aptly illustrated in Figures 4 and 5, which show profiles of salinity and dissolved oxygen versus depth for the Northern Venezuela Basin. In Figure 4, we can see that the salinity curve is essentially linear between the surface mixed layer and the salinity maximum at about 175 metres (Subtropical Underwater), and again between the salinity maximum and the salinity minimum at about 800 metres (Subantarctic Intermediate Water). The oxygen profile in Figure 5 shows a slight oxygen maximum at about 300 metres for the 18°C Sargasso Sea Water (Kinard et al., 1974), a mimumum at about 700 metres for the Subantarctic Intermediate Water and another slight maximum between 1,600 and 1,800 metres. This slight maximum has been attributed by Wüst (1964) to overflow of North Atlantic Deep Water over the Jungfern sill into the deep Venezuela Basin. Again the mixing portions of the curve between cores is almost linear. The oxygen minimum at about 700 metres is due to respiration and decay of organic detritus depleting dissolved oxygen. Note that at deep depths the oxygen concentration is quite high, reflecting the cold temperature of the source of these deep waters and resulting in an enhanced oxygen solubility where the water was formed at the surface. The slight oxygen maximum at 300 metres is similarly a reflection of the enhanced oxygen solubility at that water's source in the relatively cold (18°C) Sargasso Sea during winter.

3.2 Renewal of deep water

As mentioned above (section 2.1), since much of the water in the deep basins of the Caribbean is below sill depth, there is concern over the extent to which this water is renewed. In section 3.1, we pointed out that a slight oxygen maximum in the Northern Venezuela Basin at approximately the same depth as the Jungfern sill has been interpreted by Wüst (1964) as "renewal water" flowing over that sill. We also pointed out that deep Venezuela Bottom Water is rich in oxygen and appears well ventilated in contrast to anoxic conditions which would prevail if no renewal had occurred. Therefore, either some renewal is occurring or has occurred in relatively recent time.

How much is occurring or how long ago it occurred is a question presently of concern to many researchers. Worthington (1955 a, b) has considered oxygen and temperature data taken in the Venezuela Basin from 1933

to 1954, and concluded that during that period oxygen values had dropped and the temperature increased at a rate that indicated renewal of Caribbean Bottom Water had not occurred for between 150 and 500 years. Serious doubt, however, developed as to whether oxygen data for the period were precise enough to warrant such comparison. Wüst (1964) presented potential temperature sections through the deep Caribbean passages that indicate continuity between the North Atlantic Deep Water and Caribbean Bottom Water. However, using 1963 CRAWFORD hydrographic data directly across the Jungfern and Windward sills, Worthington (1968) showed that discontinuities in the potential temperatures occurred at the sills indicating that no deep renewal was occurring at that time. More recently, work by Metcalf and Stalcup (1973), Stalcup et al. (1975), Sturges (1975), Froelich and Atwood (1974), and Atwood et al. (1976) had demonstrated that at least small amounts of cold North Atlantic Deep Water are flowing over the Jungfern sill into the deep Venezuela Basin.

Froelich and Atwood's (1974) conclusion is based on a temporal study of deep silicate data at a serial station just southwest of the Jungfern sill. Figure 6 shows profiles of dissolved silica versus depth for the North Atlantic just north of the Jungfern sill and for the Caribbean just southwest of it. The Caribbean station shows a low concentration (1-4 µm) of dissolved silica at the surface due to depletion by marine organisms, and high values (28 µm) in deep water where the silica is returned by the sinking and decay of these same organisms.

However, the curve for the North Atlantic shows a distinct difference in dissolved silica concentration at the depth of the sill (15 to 16 µm), as compared to the Caribbean water of the same depth (28 µm). Therefore, if North Atlantic Deep Water crosses over the sill, we should be able to see a dilution of dissolved silica in the Caribbean Bottom Water at least near the sill. Salinities on both sides of the sill are very close, and cannot be used to this same purpose.

Figure 7 shows the results of Froelich and Atwood's (1974) two-year temporal study of deep dissolved silicate just inside the sill. At about the sill depth and below, there is definite evidence that dilution of dissolved silica occurs, and it seems to occur sporadically. Thus, at least some renewal occurs. Worthington (personal communication) contends that the amount of renewal demonstrated is miniscule and not sufficient to have any major effect on deep Caribbean Water. However, Atwood et al. (1976) showed that this renewal can be demonstrated to have an effect on deep silicates of the northern Venezuela Basin, the mean deep silicate concentration of the northern part of the basin being some 1.5 µm less than that for the southern part. We will consider this again later (section 6.3) when we discuss possible effects of pollutants.

3.3 Surface water

We have not discussed the surface mixed layer of the Caribbean, nor does Table 1 list its origin or characteristics. This layer, and in fact the upper two hundred metres of the Caribbean, is greatly affected by circulation. We must, therefore, first consider the currents in the area before we can consider the surface water.

4. Circulation in the Caribbean Sea and Gulf of Mexico

4.1 Ocean currents

To properly understand the current structure of the Caribbean-Gulf of Mexico area, we must first consider the rest of the ocean. The basic forces exerted on the sea surface include the wind and Coriolis force. The wind exerts a frictional force on the surface of the sea which is transmitted downward because of the viscosity of the water. This tends to move the water in the direction of the wind, however, due to rotation of the earth, a second virtual force - the Coriolis - is applied at right angles to any moving body on the earth's surface. In the northern hemisphere, this deflects the body to the right. This force is zero at the equator and increases towards the poles. Usually this force is not perceptible since other forces are much larger. However, in the case of the ocean and air currents, the Coriolis force is of the same magnitude as other forces and has a definite effect on circulation.

Figure 8 presents the world's ocean current system; Table 2 gives the names of major currents, keyed to the numbers in Figure 8. Note that in each northern ocean, a clockwise gyre system exists with diffuse eastern currents and very strong currents near the western land boundaries. These latter currents are called Western Boundary Currents and include the Kuroshio and the Gulf Stream. In the southern oceans, the gyre system is counter-clockwise. The Antarctic Circumpolar Current in the extreme southern oceans is the area where the most important ocean mixing occurs, since it extends through the southern end of all three major oceans: Atlantic, Pacific and Indian.

It is clear from Figure 8 that the Caribbean-Gulf of Mexico area has inputs from the Equatorial Currents of both the North and South Atlantic and that output from the system will be soon dispersed through the entire North Atlantic gyre system.

4.2 Currents in and adjacent to the Caribbean Sea and Gulf of Mexico

Figure 9 shows the current system of the Caribbean and Gulf of Mexico as well as its inputs and outputs. Currents providing inputs are the North Equatorial Current and Guiana Current, which is an extension of the South Equatorial Current. These enter the Caribbean through the lower passages of the Lesser Antilles and become the Caribbean Current, which passes through the Caribbean, the Yucatan Straits, the southeastern Gulf of Mexico and the Straits of Florida. During this passage, various smaller currents or eddies develop which vary seasonally, such as the countercurrents in the northern Caribbean, the loop in the Gulf of Panama, and the Gulf Loop Current.

The Caribbean Current has a maximum transport of the order of 26-34 million m^3 of water per second (Gordon, 1967). Stalcup and Metcalf (1972) have shown that enough water passes through the lower passages of the Lesser Antilles to account for all of this. The same magnitude of transport occurs through the Yucatan Straits and the Straits of Florida, after which

the Caribbean Current is joined by the Antilles Current (or Canary Current) and transport reaches a value of the order of 55 million m^3 of water per second (Neumann, 1968).

4.3 Measurement of ocean currents

There are essentially three methods of measuring the magnitude and direction of ocean currents. Two are direct methods: Lagrangian measurements using drifters or drogues; and Eulerian measurements using current meters. Drifters or drogues are marked and released, and must either be tracked by ships, airplanes or satellites, or the investigator relies on recovery and return of the drifters by someone else and tries to deduce the path followed. Current meters must be moored and held relatively stationary either by securely anchored ships or by deep anchors with acoustical releases which can be triggered from a surface ship when the investigator desires. Due to the time and expense involved with drogue tracking and deep mooring of current meters, investigators often use a third indirect method of measuring ocean currents called the dynamic method.

4.3.1 The dynamic method of measuring ocean currents as applied to the Caribbean

The Caribbean Current itself can provide us with an excellent example for demonstrating the dynamic method of measuring ocean currents. At the same time, we can learn more important facts about the circulation in the Caribbean. In section 4.1, we discussed the Coriolis force which acts perpendicular to the direction of motion in such a way as to turn it to the right in the northern hemisphere. Thus, in the Caribbean, the Coriolis force is directed northward against the westward flowing Caribbean Current. This results in movement of Caribbean surface water northward until it piles up against the barrier of the Greater Antilles. This results in a slightly higher sea surface level at the north end of the Caribbean, and a "distortion" of the density field so that a pressure gradient is directed southward that just balances the Coriolis force. The result is a "distortion" in the density field that is proportional in magnitude to the current flowing west. Thus, if we can measure accurately the differences in the pressure field and relate them to a zero motion reference level, we can calculate the velocity of the current: this is basically the dynamic method. The measurement is accomplished by sampling a section of hydrographic stations along a line at right angles to the current direction, and carefully determining the salinity and temperature as a function of depth.

Figures 10 and 11 show a salinity and temperature profile across the Caribbean at 67°00'W. We note that the contours for both salinity and temperature generally slope upward towards the south just as the core depth does for the Subtropical Underwater and 18°C Sargasso Sea Water (section 3.1). The result is a greater thickness of warmer, fresher water at the north end of the section where it has been pushed by the Coriolos force creating a pressure gradient to balance it. Thus on the south end along the Venezuela coast, colder, nutrient-rich water is closer to the surface where upwelling along the coast can bring nutrients into the photic zone resulting in greater productivity. We also note that both the salinity and temperature contours turn slightly upward at the extreme north end of the section.

Figure 12 shows the current velocities calculated from the data in Figures 10 and 11. Shaded areas depict eastward flow (into the page) and unshaded, westward flow (out of the page). In Figure 12 we should note the following:

(i) The major flow of the Caribbean Current in June 1972 occurred in two branches; one between 16°00'N and 14°00'N and the other between 13°30'N and 12°00'N. Surface current velocities in these branches were very high; > 40 cm sec^{-1} and > 60 cm sec^{-1} respectively.

(ii) An extensive countercurrent covered the northern third of the section from 18°00'N to 16°00'N and had surface velocities of > 25 cm sec^{-1}. This eastward flowing current is what caused the slight upward tilt in temperature and salinity contour in the north in Figures 10 and 11.

(iii) Significant flow (> 5 cm sec^{-1}) occurs as deep as 500 metres, but not below that depth.

The seasonal nature of the eastward flowing countercurrent shown in Figure 12 is demonstrated in Figure 13, which shows velocities for the same section four months later in October, 1972. At that time, the two branches of the Caribbean Current were in approximately the same position with the same surface velocities as in June 1972, although significant velocities occurred deeper (1,000 metres). However, the counter-current consisted of only a narrow band just north of the northern branch of the Caribbean Current, and most of the northern third of the section exhibited relatively weak westward flow.

Through June 1975, data for nine such sections have been collected and reduced. Although data interpretation is not complete, it can be said that:

(i) The maximum current velocities are always in the southern half of the Caribbean.

(ii) An eastward flowing current always exists somewhere north of 14°30'N.

(iii) The net westward transport above 1,600 metres varies from about 15 to 28 million m^3 sec^{-1}.

In late 1975 and early 1976 a series of satellite-tracked Langrangian drogues were released in the eastern Caribbean and, as they were tracked, density sections such as the above were also taken. A comparison of the drogue tracks and geostrophically calculated currents indicates that the indirect measurements are essentially correct, but that the flow regime is quite variable in space and time.

5. Origin of Surface Water in the Caribbean Sea and Gulf of Mexico

5.1 Salinity variations

There is a distinct variation in surface salinity in the Caribbean with relatively high (> 35.5°/oo) salinities between January and May, with

highest salinities (> 36.5°/oo) occurring in February and March, and lower salinities between June and December, with a minimum (> 34.5°/oo) occurring in October and November. This is illustrated in Figures 14 and 15, which are adapted from Wüst (1964). The figures give a clear indication that the low salinity water that occurs in late fall enters the Caribbean from the south and east, which is the "source area" for the Caribbean Current. There has been some conjecture as to the source of this water, with some people arguing that its source is the tropical convergences close to the equator where there is extensive rainfall, and others that its source is the Amazon and Orinoco rivers which have maximum discharge between February and April (Wüst, 1964).

Tremendous amounts of water flow out from the Amazon river. Davis (1964) and Oltman (1968) report an average annual outflow equal to about 30% of all river water reaching the entire Atlantic. Wüst (1964) has summarized data through 1964 that show that the mean discharge of the Amazon is 106 to 124 m^3 sec^{-1} and a maximum discharge of 146 m^3 sec^{-1}. The Orinoco discharge is less, but still has a mean of 14 to 34 m^3 sec^{-1} and a maximum of 65 m^3 sec^{-1}. Thus, these two rivers can add between 125 and 200 m^3 sec^{-1} of fresh river water to the oceans. The surface currents depicted in Figure 9 are ideal for transporting this water into the Caribbean.

5.2 Silicate-salinity relationships

If the low-salinity surface water found in the Caribbean in October and November has its source in the Amazon and Orinoco rivers, the silicate concentration of the Caribbean surface water should show it. Due to weathering of rocks and soil, river waters carry high concentrations of dissolved silica. The Amazon and Orinoco contain 9-14 ppm dissolved silica (Livingston , 1963), whereas rain water should contain almost no dissolved silica unless it is from dust particles. Thus, if river water is the source of low-salinity Caribbean Surface Water, there should be an increase in silica as the salinity decreases. Froelich, Atwood and Polifka (1974) have reported results that show that this is exactly the case. Figure 16 shows their silicate and salinity data collected at the PESCA serial station in the Northern Venezuela Basin. It is clear that during the low-salinity periods there is a concurrent increase in dissolved silicate concentration. The same data are plotted in Figure 17 to show that there is a clear linear relationship between silicate and salinity so that there is little doubt that the low-salinity water is fluvial in origin. The authors showed a similar relationship for stations all across the Venezuela Basin, proving that the source could not be local run-off from nearby islands, and concluding that the low-salinity water originated in the Amazon and Orinoco rivers.

Since the presentation of Froelich, Atwood and Polifka's (1974) results, Carder and Schlemmer (1973) at the University of South Florida have identified nepheloid layers (layers of finely divided sediment suspended in the water column) throughout the Caribbean and Gulf of Mexico, which have sources in the Amazon and Orinoco. These layers are not restricted to the surface water, and occur at depths where particle and water densities are such that the particles remain suspended. One such layer occurs in the high salinity core of the Subtropical Underwater (Figure 3), which is at a depth where significant transport of this material can occur (Figures 12 and 13).

Another fact which should be noted in Figures 14 and 15 is the high salinities that occur along the southern portion of the Caribbean all year round as compared to salinities to the north. As discussed in section 4.3.1, this is a result of the Caribbean Current and balancing Coriolis and pressure gradient forces which have pushed the warm, lower-salinity surface water northward, exposing the upper part of the high-salinity Subtropical Underwater. As a result, cold, nutrient-rich water is closer to the surface near Venezuela and Colombia, and coastal upwelling can bring it into the photic zone, increasing productivity many times.

Another input of fresh water which has an interesting local effect is large seasonal amounts of rainfall which occur in the southwest area of the Caribbean near Panama. This rainfall produces low-salinity surface water which "floats" on the sea surface producing the anticyclonic gyre (rotation opposite to normal Coriolis-produced circulation), or loop current, near the Gulf of Panama (Figure 9).

There are various other important inputs of fresh water from rivers such as the Magdalena, Mississippi and smaller rivers draining Mexico, Central America and the United States. All of these have local importance, and the effects of the Mississippi and Magdalena on sedimentation are felt quite far from their source. However, none of these has an oceanographic impact like the Amazon and Orinoco rivers.

6. Present and Future Pollution Problems Considered in Relation to the Oceanography of the Caribbean Sea

6.1 General considerations

The foregoing sections provide an oceanographic framework in which we can consider the possible impact of present and future marine pollution. Unfortunately, we are somewhat limited in this respect, since not all of the present or potential pollution sources are known to us. Recent attempts by the Intergovernmental Oceanographic Commission to fill this gap in knowledge through the Co-operative Investigations of the Caribbean and Adjacent Regions (CICAR) have so far failed, with less than 15% of member nations responding adequately to a pollution questionnaire which was sent out to prepare for this Workshop. Nevertheless, we do know some sources and can consider what oceanographic impact any sources might have.

Based on the oceanography discussed in the foregoing sections, we can consider pollutants according to their possible effects on two categories of water:

(i) The upper 1,500 metres of the Caribbean-Gulf of Mexico area, with special emphasis on the upper 500 metres where most transport occurs, and

(ii) The deep water below the sills where renewal is a problem.

6.2 Consideration of the upper 1,500 metres of water

In sections 3, 4 and 5 we have considered the water masses present in the Caribbean and Gulf of Mexico and the currents that transport them. We have seen that these waters have origins as far away as 60°S (Subantarctic Intermediate Water) and from places as varied as the Sargasso Sea (18°C Sargasso Sea Water), the mid-latitudes of the North Atlantic (Subtropical Underwater) and the Amazon and Orinoco rivers (low-salinity surface water). Obviously, pollution of any of these sources, or of places between these sources and the Caribbean will affect the area and its living resources. For example, development in the Amazon river or Orinoco river drainage basins could increase the amount of suspended material added to the system and a portion of the pollutants deposited there, such as pesticides, herbicides, or heavy metals, will probably find its way into the Caribbean within a year.

We have also seen that water that flows through the Caribbean becomes part of the Gulf Stream and is distributed throughout the North Atlantic gyre system and eventually the entire world's oceans. Pollutants added to the water during this transit will be distributed in the same way. The time scale for such distribution is probably 1 to 5 years for the North Atlantic surface waters and over one thousand years for the entire world ocean unless the materials are removed by some process before mixing can occur.

A consideration of one type of potential pollution source in the Caribbean can serve as an example of what type of problems can occur. The Caribbean is an area of active petroleum production and refining. It is interesting to consider the current system diagrammed in Figure 9 in the light of some of the more active specific sites of petroleum and petrochemical activity such as Trinidad, St. Croix, Puerto Rico, Aruba, Curaçao, Lake Maracaibo, Jamaica and the Gulf coast of the United States where extremely large petrochemical complexes exist in the Galveston Bay and Mississippi river areas, and extensive amounts of offshore oil, gas and sulphur are produced. Added to these is the constant traffic of large and small petroleum tankers which cross the area. Even if these ships do not have accidents that result in spills of oil, they must constantly flush their tanks with ballast water, which results in significant transfer of hydrocarbons from the ship to the water (Sackett, 1974).

The reefs off the small fishing village of La Parguera, Puerto Rico, have been subjected to at least two groundings of large petroleum tankers in less than two years. One of these resulted in a major spill which extensively damaged shores and marine life. However, even more insidious than the oil spills, which can cover large areas of ocean surface and shoreline, is the organic matter that becomes dissolved in the seawater following oil spills. Brooks and Sackett (1973) surveyed the distribution of dissolved C_1- to C_4-hydrocarbons in the Gulf of Mexico, and showed important man-made sources associated with ports, offshore petroleum drilling and production operations, and open-ocean shipping activity. More recently, Sackett (1974) has presented direct evidence that large amounts of these hydrocarbons are added by underwater gas flares near oil-drilling rigs, and by ballast pumping from petroleum tankers. What the effect of these hydrocarbons on marine life can, and will, be is not completely known, but indications are that they can be deleterious.

There are no similar data on dissolved hydrocarbons in the Caribbean Sea; not even background data. However, in view of the extensive petrochemical activity bordering the Caribbean, chances are very high that hydrocarbons are being dissolved in surface sea-water throughout the area.

6.3 Consideration of the deep water

In section 3.2 we discussed the problem of renewal of deep water in the Caribbean basins, and pointed out that apparently very little renewal or flushing occurs. Thus pollutants that find their way into this water will not be flushed out. Perhaps we could adopt the perverse attitude that if we dump materals into these basins, at least we are localizing the dump; however, if pollutants are added in sufficient amounts, they could create severe problems and eventually even cause anoxic conditions.

The mechanisms by which pollutants can find their way into the deep water during a relatively short time include:

(i) As part of the suspended or nepheloid material that gradually sinks toward the bottom water. Pollutants such as pesticides or heavy metals absorb very easily on the high surface area presented by these fine particles and can be transported down as part of the absorbed phase.

(ii) As part of the sinking and decaying fragments of dead marine organisms which either ingested the material at the surface or absorbed it from the dissolved phase.

Much of this material would eventually be transported to the sediments, but, as organisms decay, a significant portion would be returned to the dissolved phase. The decay of any labile organic material will deplete the amount of dissolved oxygen, which could eventually result in anoxic conditions. Worthington (1955a) postulated that natural processes had depleted the dissolved oxygen in the deep Venezuela Basin by 0.3 ml l^{-1}, or approximately 6%, in about 20 years. Addition of large amounts of material derived from human activities could significantly increase this rate so that whatever renewal occurs could not keep up, and anoxic conditions could prevail.

We do not know just how fragile the deep-water system of the Caribbean-Gulf of Mexico is; however, until we do, great care should be exercised and we should attempt to learn more about the entire system so that we can use it to our maximum advantage while still protecting it.

7. Summary and Conclusions

In this paper we have discussed the basic oceanography of the Caribbean and Gulf of Mexico as it relates to marine pollution. We have seen that Caribbean-Gulf of Mexico pollution could have sources far from that area, and pollution in the area could affect vast areas of the world's oceans and shorelines. At the beginning of the paper, the need for international programmes in pollution monitoring, control and abatement was mentioned, and I hope that that need is more clear to us now. If anyone can have an impact on starting such programmes, it is those, such as the participants in this Workshop, who are closely involved with various governments and their pollution control agencies, which should be urged to consider such programmes for which the reading of the chapter entitled "Design of a World Monitoring System" by A.J. Lee et al. (1972) in "A Guide to Marine Pollution" is highly recommended.

Peferences

Atwood, D.K., P.N. Froelich, M.E.Q. Pilson, M.J. Barcelona and J.L. Vilen, 1976. Deep silicate content as evidence of the extent of renewal of Venezuela basin Water, submitted to Deep Sea Res.

Brooks, J.M. and W.M. Sackett, 1973. Sources, sinks, and concentration of light hydrocarbons in the Gulf of Mexico. J. Geophys. Res. 78(24): 5248-5256.

Carder, K.L., and F.C. Schlemmer II, 1973. Distribution of particles in the surface waters of the eastern Gulf of Mexico; An indicator of circulation. J. Geophys. Res. 78(27): 6286-6299.

Davis, L.C., 1964. The Amazon's rate of flow. Nat. Hist. 73(6): 15-19.

Dietrich, G., 1963. Die Meere. In: Die grosse illustrierte Landerkunde. II - Die Grosse Bertelsmann Lexikon Bibliothek, 13 : 1523-1606.

Froelich, P.N. and D.K. Atwood, 1974. New evidence for sporadic renewal of Venezuela Basin Water. Deep Sea Res. 21 : 969-975.

Froelich, P.N., D.K. Atwood and J. Polifka, 1974. Seasonal variation in the salinity-silicate structure of the upper Venezuela Basin, Caribbean Sea. Abstract 0158, EOS, Trans. of Amer. Geophys. Union 55 : 309.

Gordon, A.L., 1967. Circulation of the Caribbean Sea. J. Geophys. Res. 72 : 6207 - 6223.

Kinard, W.F., D.K. Atwood and G.S. Giese, 1974. Dissolved oxygen as evidence for the 18°C Sargasso Sea Water in the eastern Caribbean Sea. Deep Sea Res. 21 : 79-82.

Lee, A.J. et al., 1972. Design of a world monitoring system. In : A Guide to Marine Pollution. New York : Gordon and Breach. 168 pp.

Livingston, D.A., 1963. Chemical composition of rivers and lakes. In : Data of Geochemistry. U.S. Geol. Surv. Professional Paper 440-G. 64 pp.

Metcalf, W.G. and M.C. Stalcup, 1973. Caribbean inflow through the Anegada Jungfern Passage. Abstract 077, EOS, Trans. of Amer. Geophys. Union 54 : 313.

Neumann, G., 1968. Ocean Currents. New York, Elsevier Scientific Publishing Co. 352 pp.

Oltman, R.E., 1968. Reconnaissance investigations of the discharge and water quality of the Amazon River. U.S. Geol. Survey Circular 552. 16 pp.

Sackett, W.M., 1974. Paper presented as part of Chemistry of the Water Environment - Serving the Nation in the Decade Ahead. 55th Annual

Stalcup, M.C. and W.G. Metcalf, 1972. Current measurements in the passages of the Lesser Antilles. J. Geophys. Res. 77 : 1032-1049.

Stalcup, M.C., W.G. Metcalf and R.G. Johnson, 1975. Deep Caribbean inflow through the Anegada Jungfern Passage. J. Mar. Res. (Supplement) 33 : 15-35.

Sturges, W., 1975. Mixing of renewal water flowing into the Caribbean Sea. J. Mar. Res. (Supplement) 33 : 117-130.

Sverdrup, H.U., M.W. Johnson and R.H. Fleming, 1942. The Oceans : Their Physics, Chemistry and General Biology. Englewood Cliffs, N.J., Prentice-Hall, Inc. 1087 pp.

Worthington, V., 1955a. A new theory of Caribbean bottom water formation. Deep Sea Res. 3 : 82-87.

Worthington, V., 1955b. The temperature increase in the Caribbean Deep Water since 1933. Deep Sea Res. 3 : 234-235.

Worthington, V., 1968. Water circulation in the Caribbean Sea and its relationship to North Atlantic circulation. CICAR Symposium, Curaçao, Netherlands Antilles. IOC, Unesco, Paris.

Wüst, G., 1964. Stratification and Circulation in the Antillean-Caribbean Basins. New York, Columbia University Press. 201 pp.

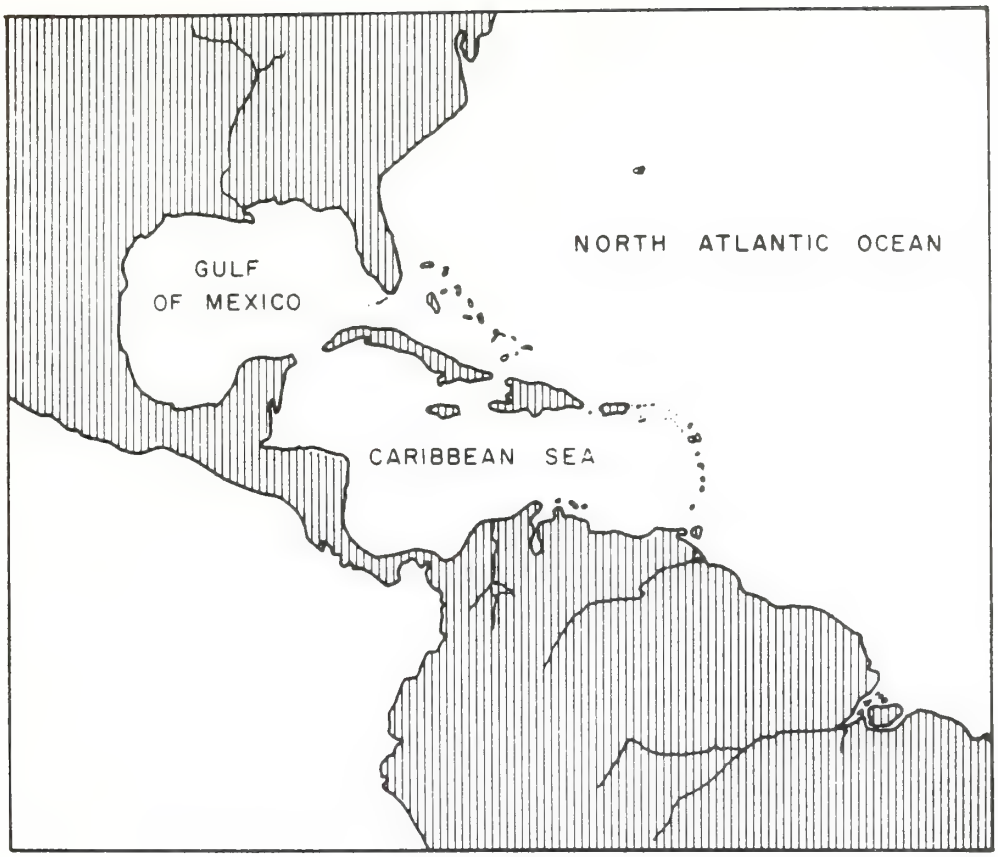
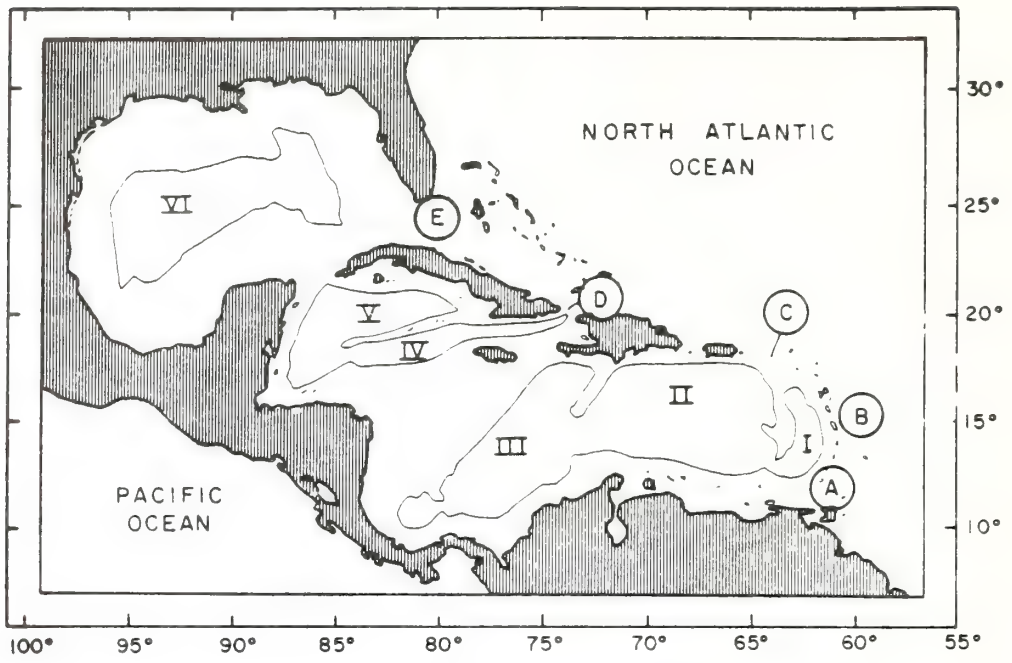


Fig. 1 The Caribbean-Gulf of Mexico region (The American Mediterranean) in relation to surrounding land and water masses and principal rivers.



I	GRENADA TROUGH	4100 m	A	GRENADA and ST. VINCENT SILLS	1000-1400 m
II	VENEZUELA BASIN	5600 m	B	ST. LUCIA SILL	800 m
III	COLOMBIA BASIN	4500 m	C	JUNGFERN SILL	1815 m
IV	CAYMAN TROUGH	7100 m	D	WINDWARD SILL	1600 m
V	YUCATAN BASIN	4600 m	E	STRAITS OF FLORIDA	800 m
VI	MEXICO BASIN	4400 m			

Fig. 2 General bathymetry of the American Mediterranean Sea showing major basins (roman numerals) and sills (letters). The names and depths of these features are given below the figure. (Adapted from Svedrup, Johnson and Fleming, 1942.)

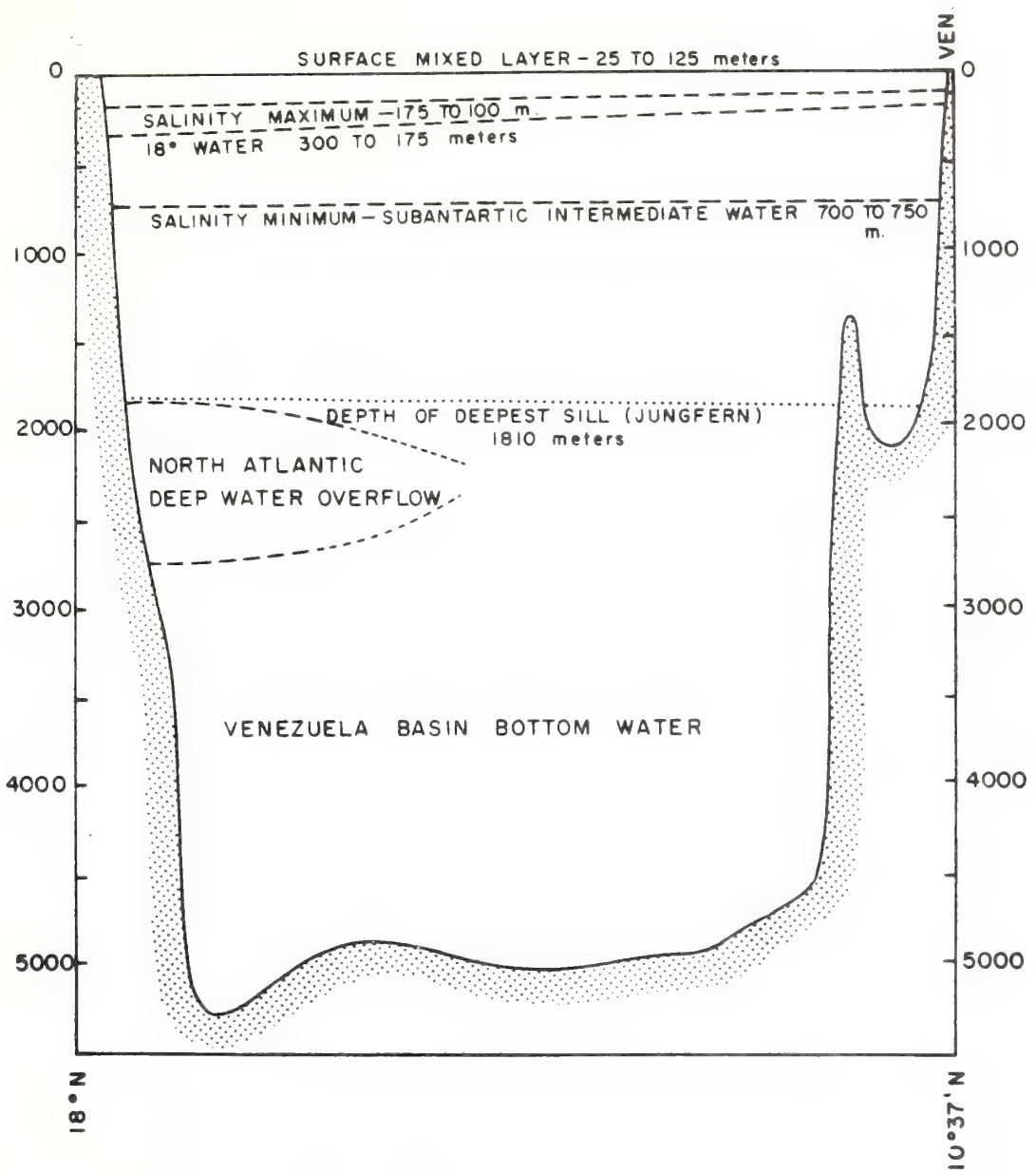


Fig. 3 Approximate core depths for water cores in the Venezuela Basin of the Caribbean Sea (adapted from data in Wüst, 1964).

Table 1

CHARACTERISTICS OF THE WATER MASSES IN THE BASINS OF THE CARIBBEAN SEA

Type of water	Origin	Temperature °C	Salinity °/oo	Oxygen ml l^{-1}	Silicate µm
Subtropical Underwater (100 to 175 m)	At the surface at 20° - 25°N & 55°W	22 to 24°	36.80 to 37.02 (maximum)	4.2 to 4.5	1.0 to 2.0
18°C Sargasso Sea Water (175 to 300 m)	At the surface of the Sargasso Sea in winter	17.9 ± 0.5°	36.50 ± 0.2	Maximum 5.0 inversion	3.0 to 5.0
Subantarctic Intermediate Water (700 to 750 m)	At the surface at 60°S	6.5 to 7.5°	34.74 (minimum)	2.86 to 3.10 (minimum)	23.0 to 27.0
North Atlantic Deep Water Overflow (1800 to 2500 m)	Flow over the Jungfern Sill into the Venezuela Basin	4.1°	34.98	4.9 to 5.1	23.0 to 25.0(1)
Bottom Water	Rate of renewal unknown	4.1°	34.98	4.9 to 5.1	27.0 to 30.0(1)

Notes : (1) In the Cayman Trough the water below 4.1°C in temperature contains as much silicate (15 µm) as is found in deep Atlantic water.

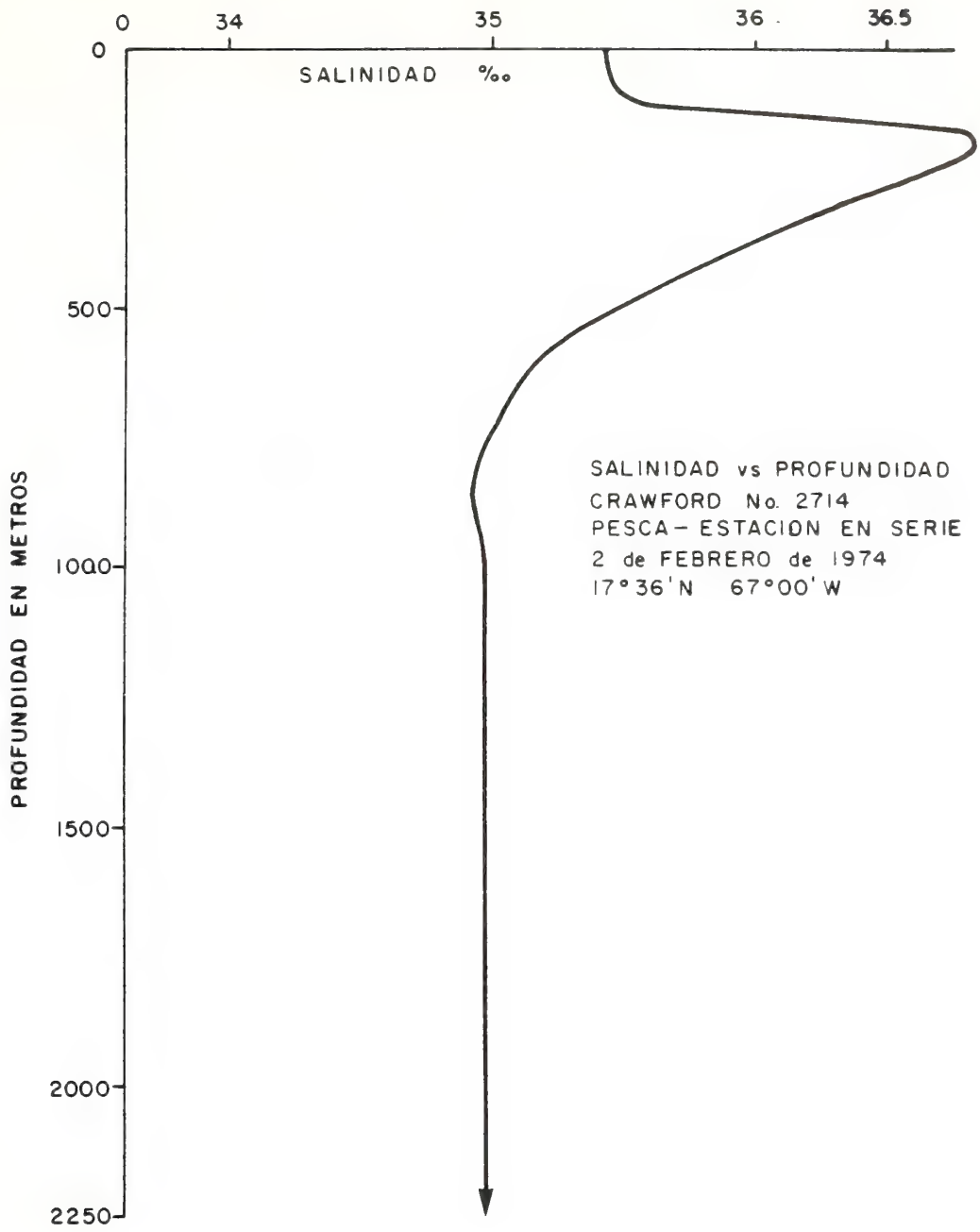


Fig. 4 Profile of salinity versus depth for R/V CRAWFORD Station Number 2714, 2 February 1974, at 17°36'N and 67°00'W (North end of Venezuela Basin). (Programa Estudios Caribe, Universidad de Puerto Rico.)

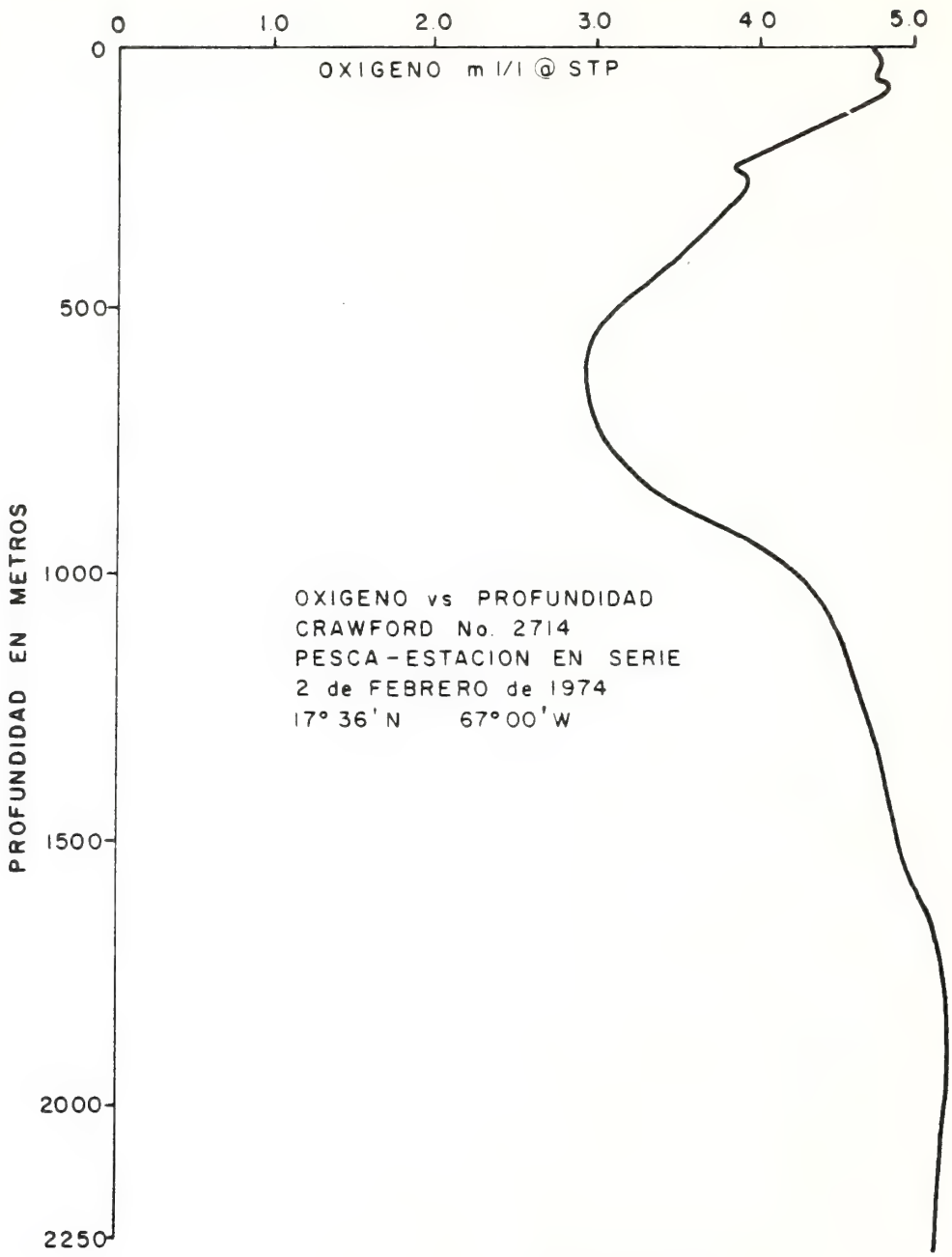


Fig. 5 Profile of dissolved oxygen versus depth for R/V CRAWFORD Station Number 2714, 2 February 1974, at 17°36'N and 67°00'W (North end of Venezuela Basin). (Programa Estudios Caribe, Universidad de Puerto Rico.)

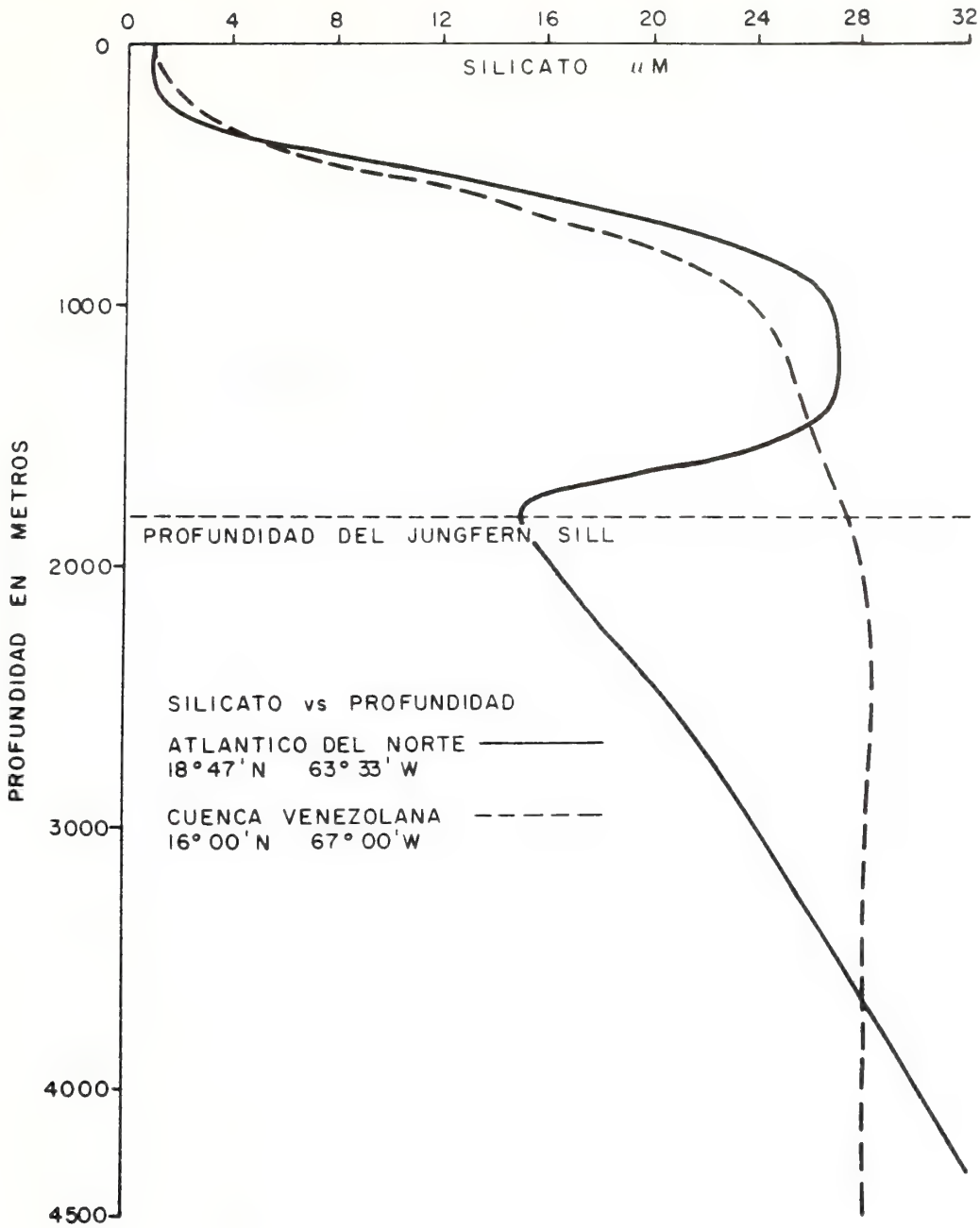


Fig. 6 Profile of dissolved silica versus depth for stations just north (18°47'N, 63°33'W, KNORR Station 198) and just southwest (17°36'N, 67°00'W, CRAWFORD Station 2714) of the Jungfern Sill. The depth of the Jungfern Sill is indicated by the horizontal dashed line.

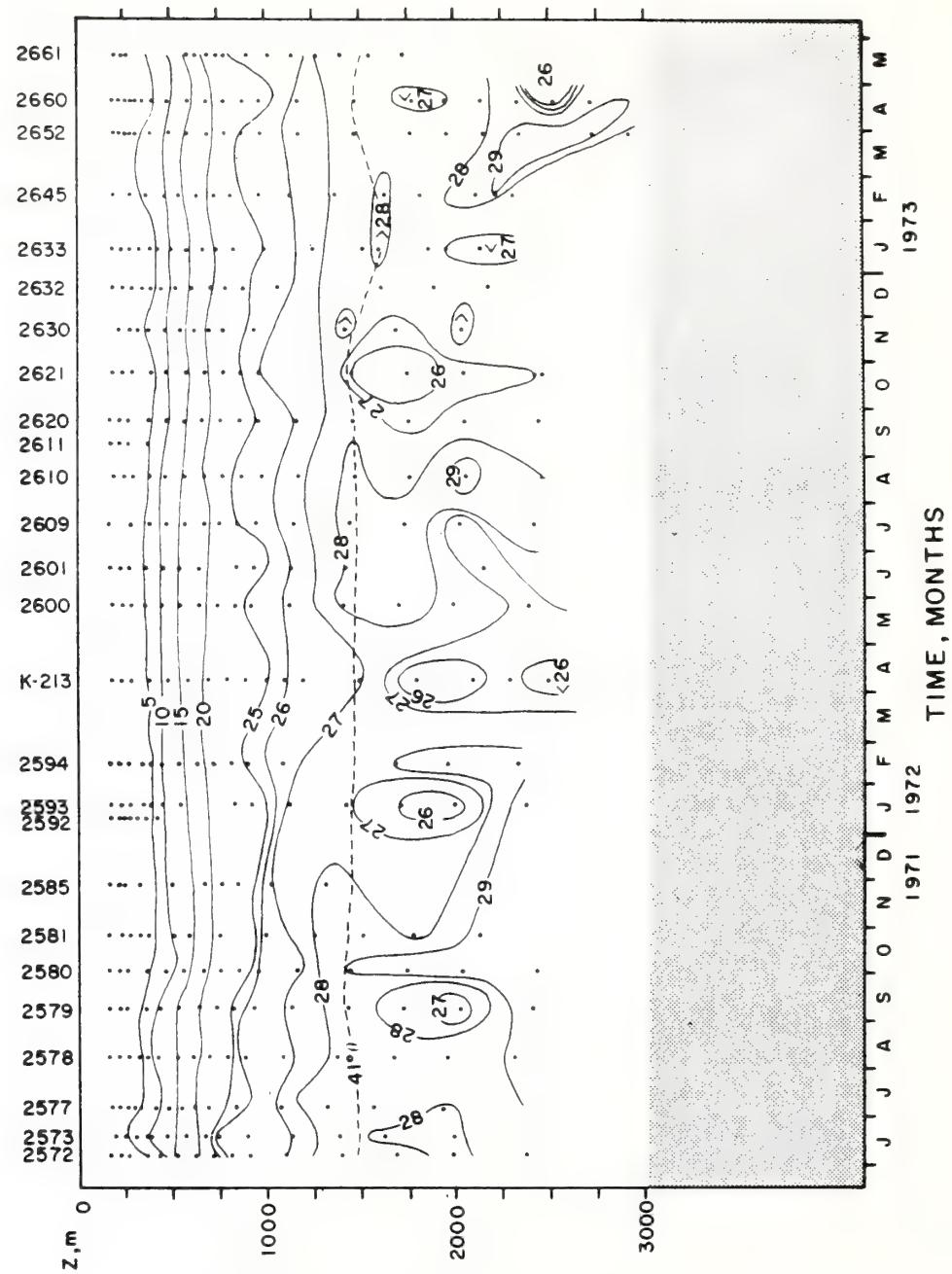


Fig. 7 Results of a two-year temporal study of dissolved silicate concentrations at the University of Puerto Rico PESCA Serial Station (17°36'N and 67°00'W).

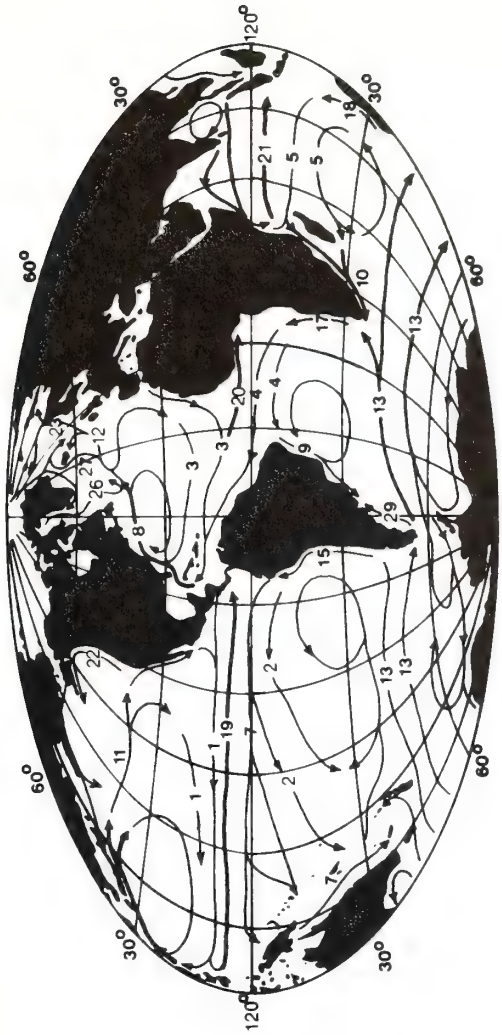


Fig. 8 Diagram of the surface circulation pattern of the oceans (after Dietrich, 1963). The names of major currents are given in the Table next to this figure according to the numbers in the figure.

Table 2

KEY TO THE CURRENTS SHOWN IN FIGURE 8

1 - 5	NORTH AND SOUTH EQUATORIAL CURRENTS	16	CANARY CURRENT
6	KUROSHIO	17	BENGUELA CURRENT
7	EAST AUSTRALIA CURRENT	18	WEST AUSTRALIA CURRENT
8	GULF STREAM	19 - 21	EQUATORIAL COUNTERCURRENTS
9	BRAZIL CURRENT	22	ALASKAN and ALEUTIAN CURRENTS
10	AGULHAS CURRENT	23	NORWEGIAN CURRENT
11	NORTH PACIFIC CURRENT	24	WEST SPITZBERGEN CURRENT
12	NORTH ATLANTIC CURRENT	25	EAST GREENLAND CURRENT
13	ANTARCTIC CIRCUMPOLAR CURRENT	26	LABRADOR CURRENT
14	CALIFORNIA CURRENT	27	IRMINGER CURRENT
15	PERU CURRENT	28	OYA CHIO
		[illegible]	FALKLAND CURRENT

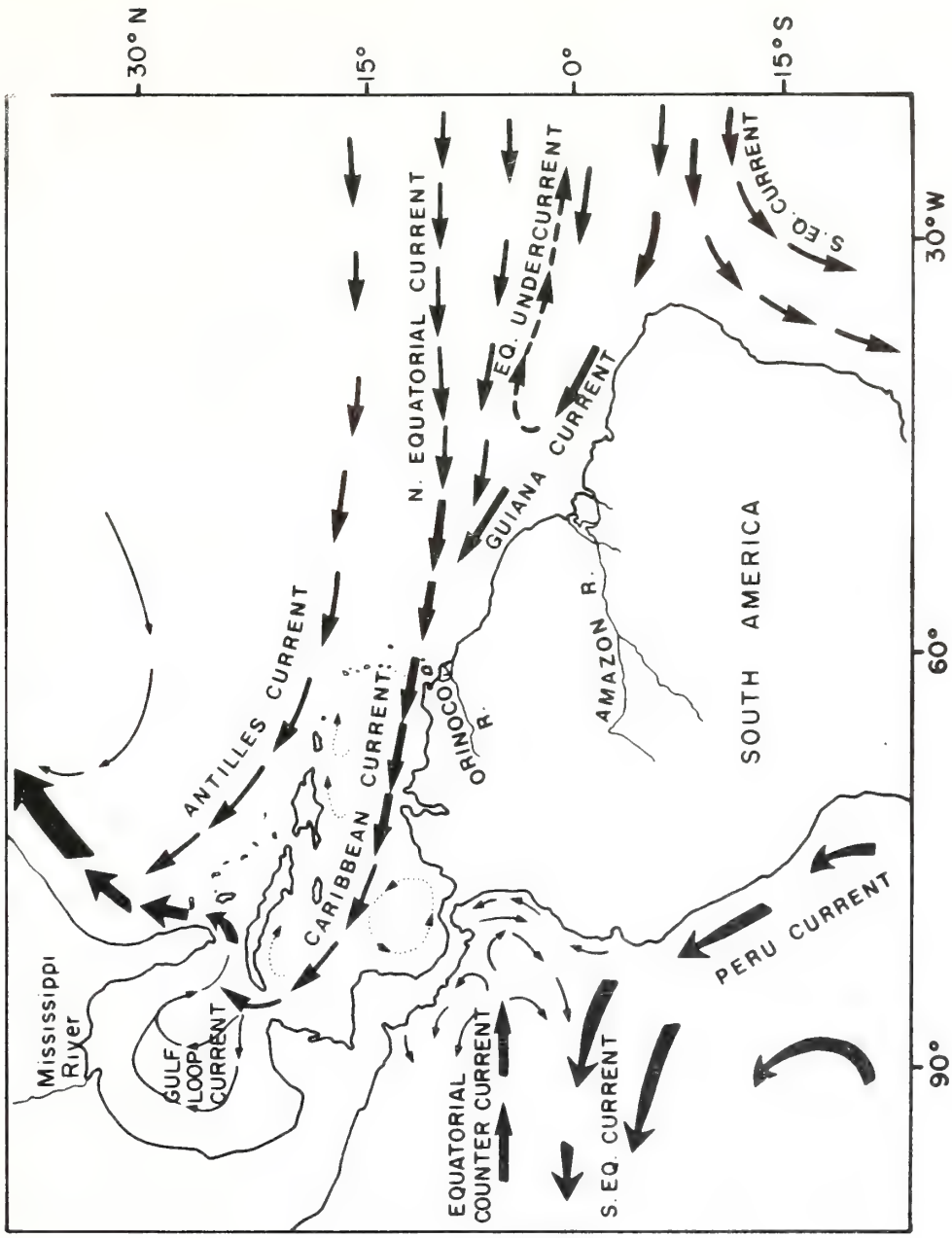


Fig. Schematic representation of surface currents in and adjacent to the Caribbean Sea and Gulf of Mexico, as well as the northwest coast of South America.

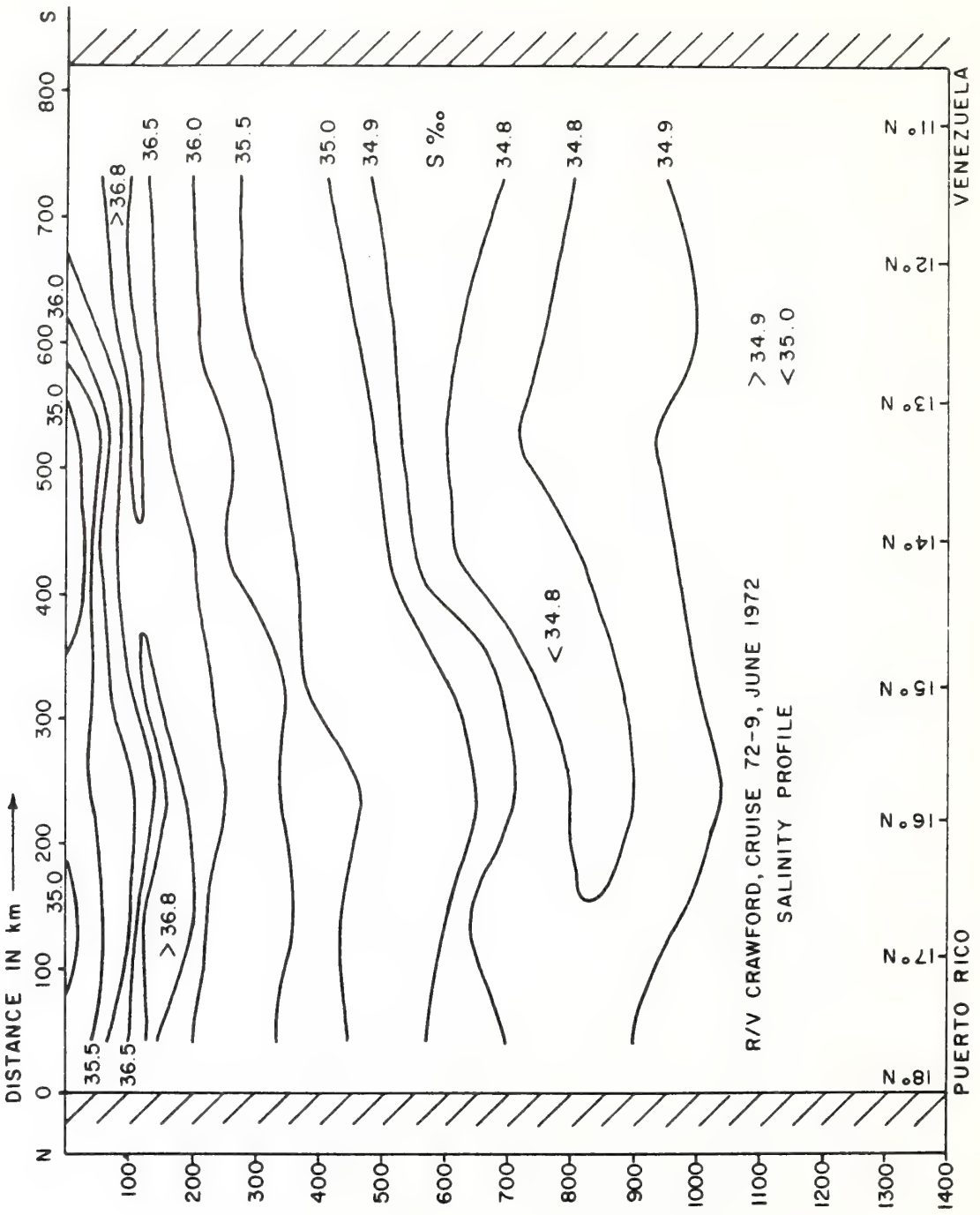


Fig. 10 Contours of salinity versus depth and latitude along 67°00'W from 18°00'N to 11°00'N. R/V CRAWFORD PESCA Cruise 72 - 9 June 1972, Stations 2601 to 2608.

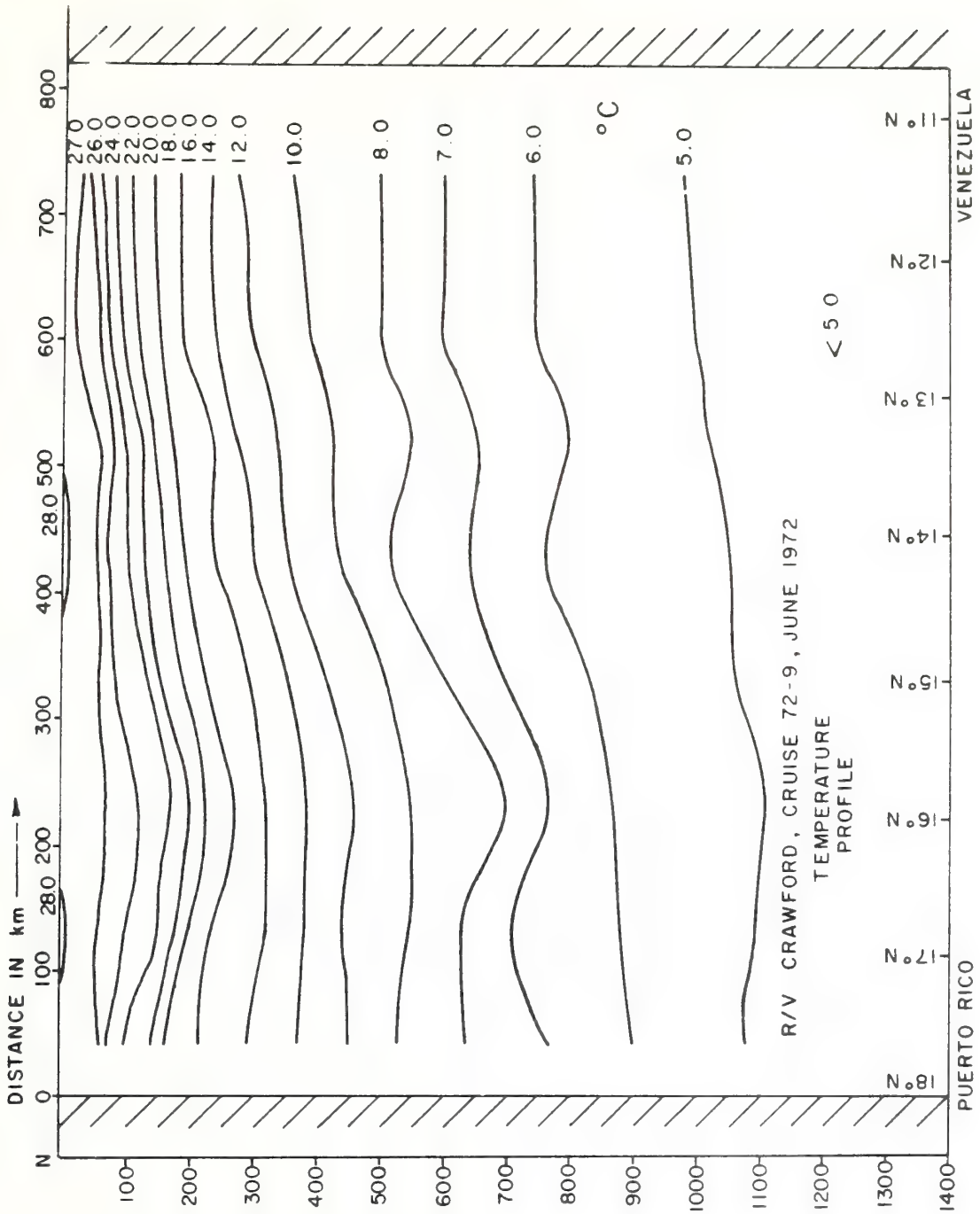


Fig. 11 Contours of temperature versus depth and latitude along 67°00'W from 18°00'N to 11°00'N. R/V CRAWFORD PESCA Cruise 72 - 9 June 1972, Stations 2601 to 2608.

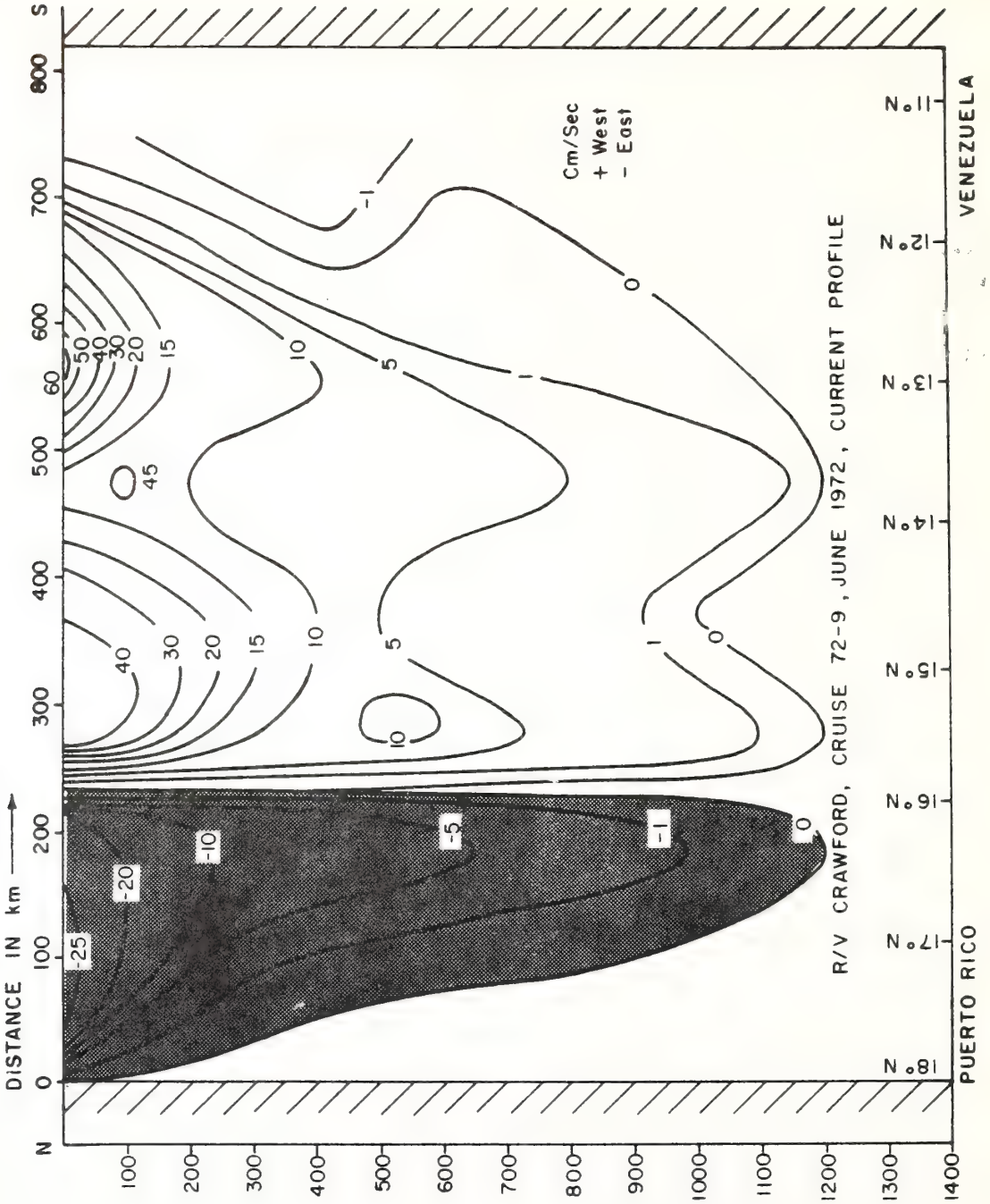


Fig. 12 Velocities along 67°00'W, determined by the dynamic method using salinity and temperature data depicted in Figs. 10 and 11. R/V CRAWFORD Cruise 72 - 9 June 1972, Stations 2601 to 2608. Velocities are in cm sec^{-1}. Positive values are westward flowing and negative ones are eastward flowing. Shaded areas are eastward flowing (into page).

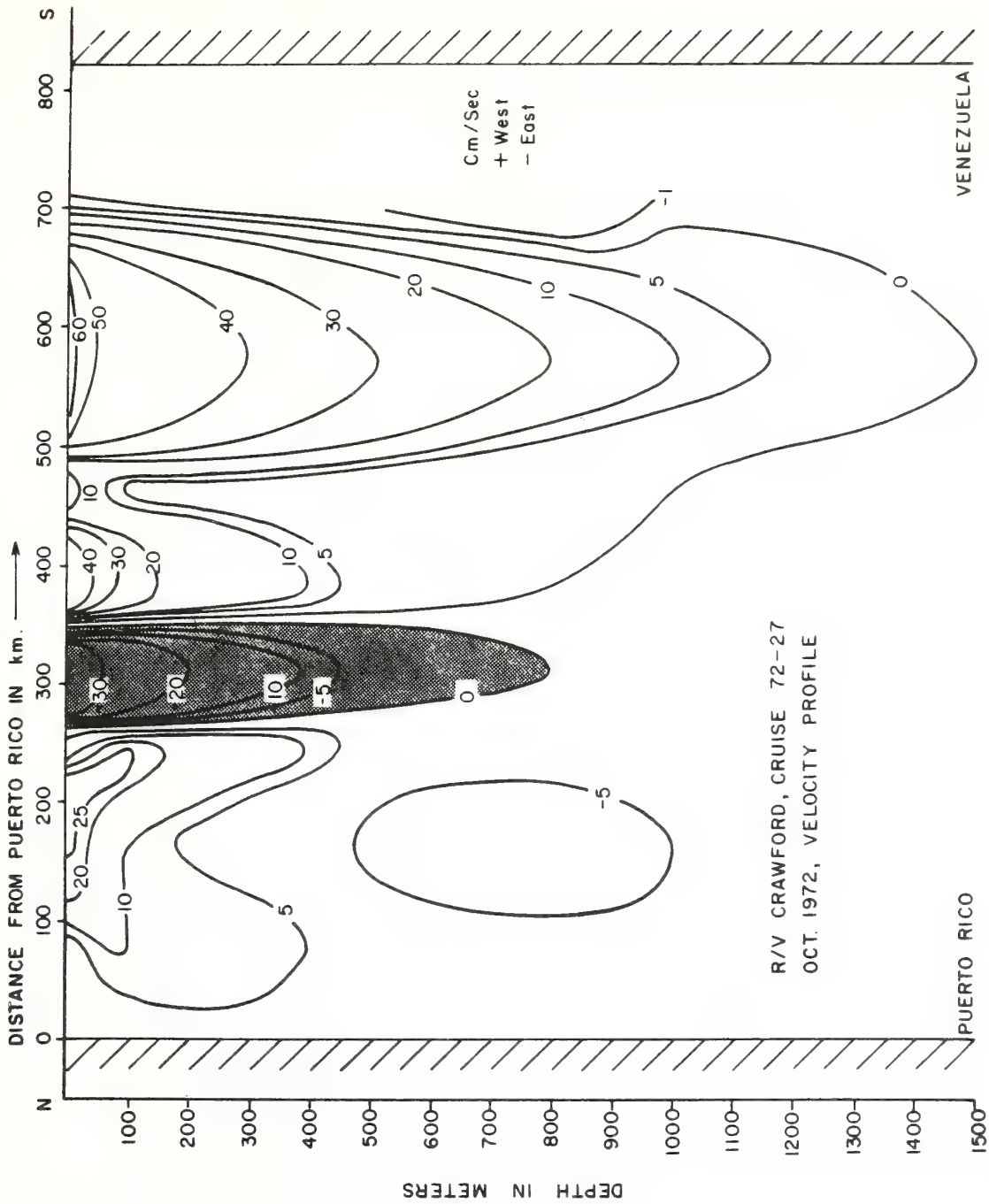


Fig. 13 Velocities along 67°00'W determined by the dynamic method in October 1972, R/V CRAWFORD Cruise 72-27, Stations 2621 to 2629. Velocities are in cm sec^{-1}. Positive values are westward flowing and negative ones are established eastward flowing. Shaded areas are eastward flowing (into page).

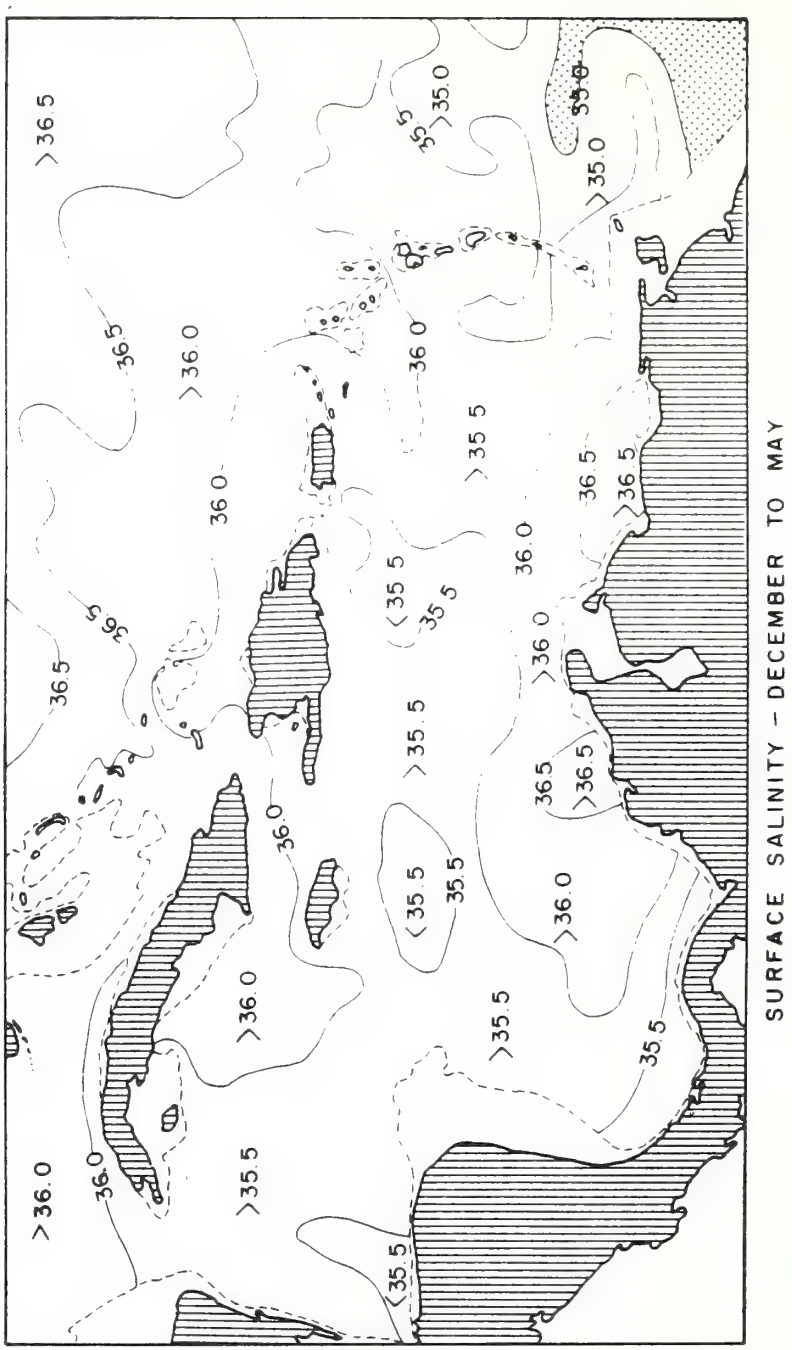


Fig. 14 Sea-surface contours of mean salinity in the Caribbean Sea between December and May (after Wüst, 1964).

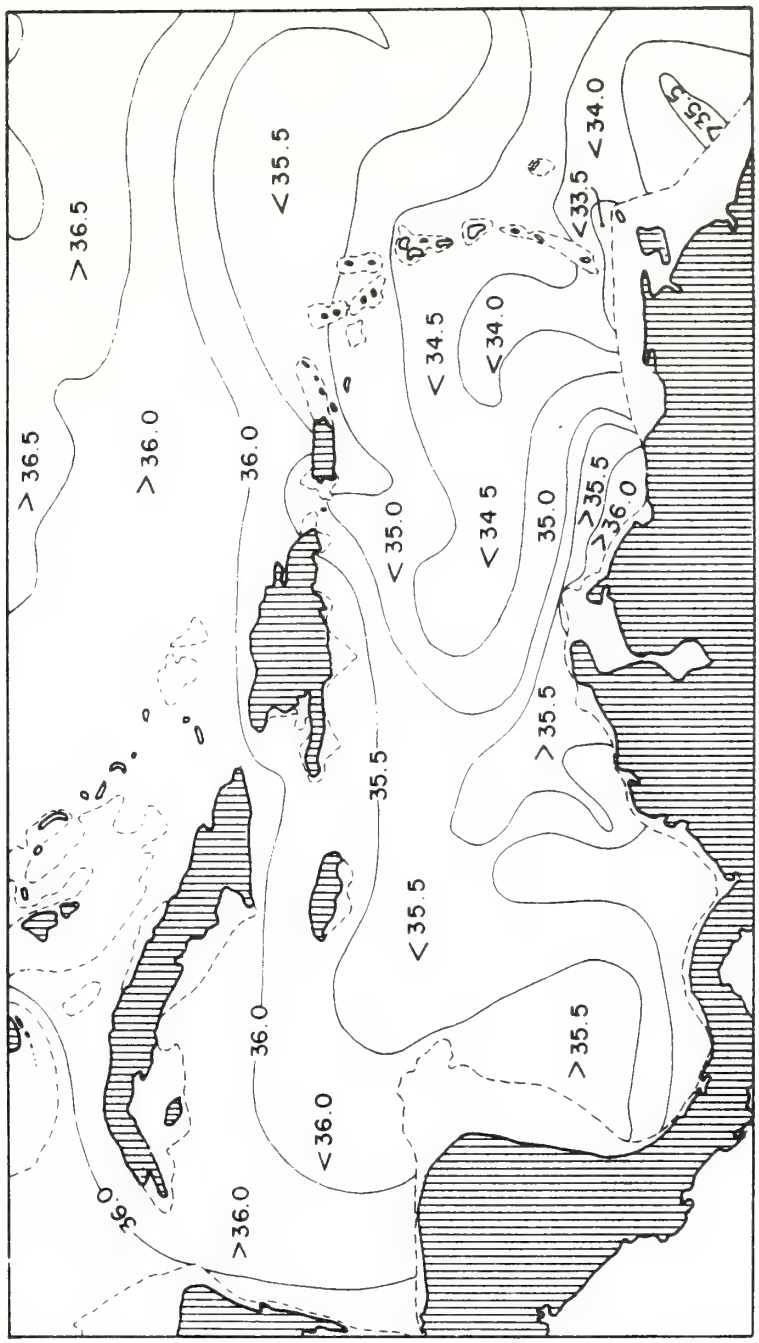


Fig. 15 Sea-surface contours of mean salinity in the Caribbean sea between June and November (after Wüst, 1964).

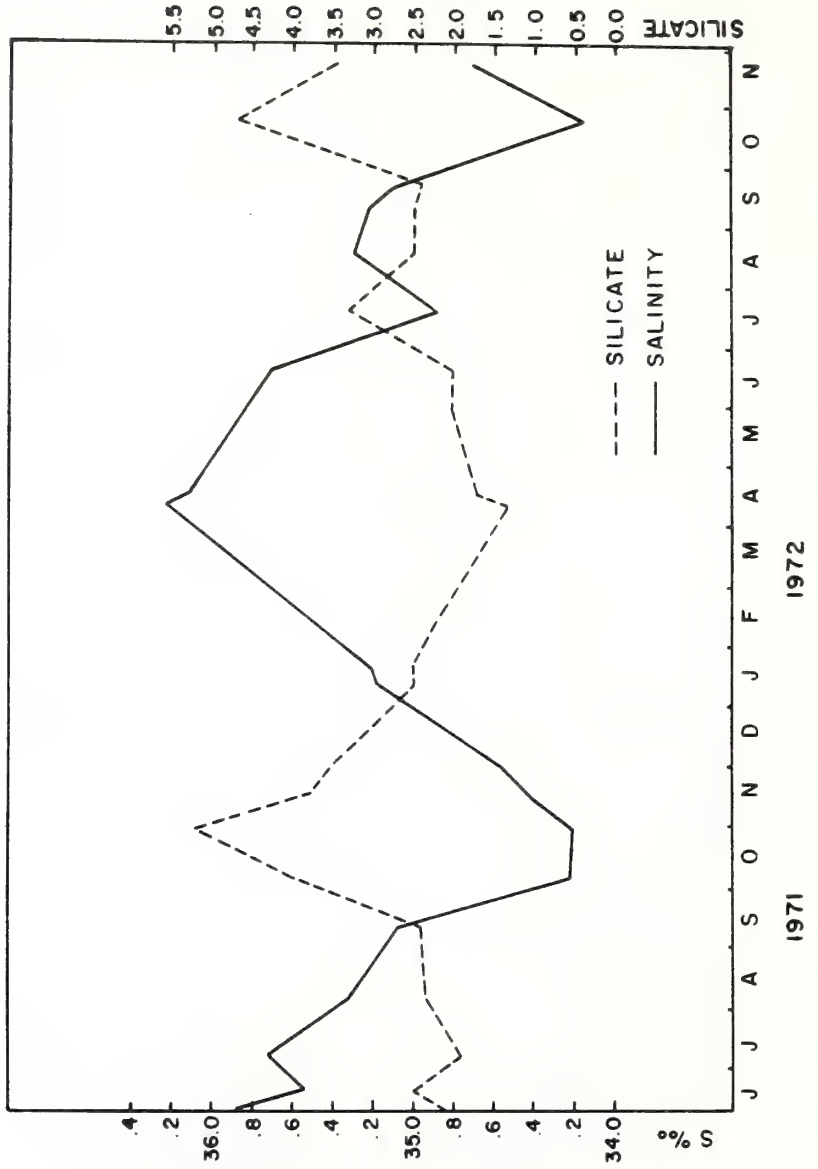


Fig. 16 Plots of dissolved silicate concentration and salinity for surface waters at the PESCA Serial Station for 1971 and 1972 at 17°36'N and 67°00'W.

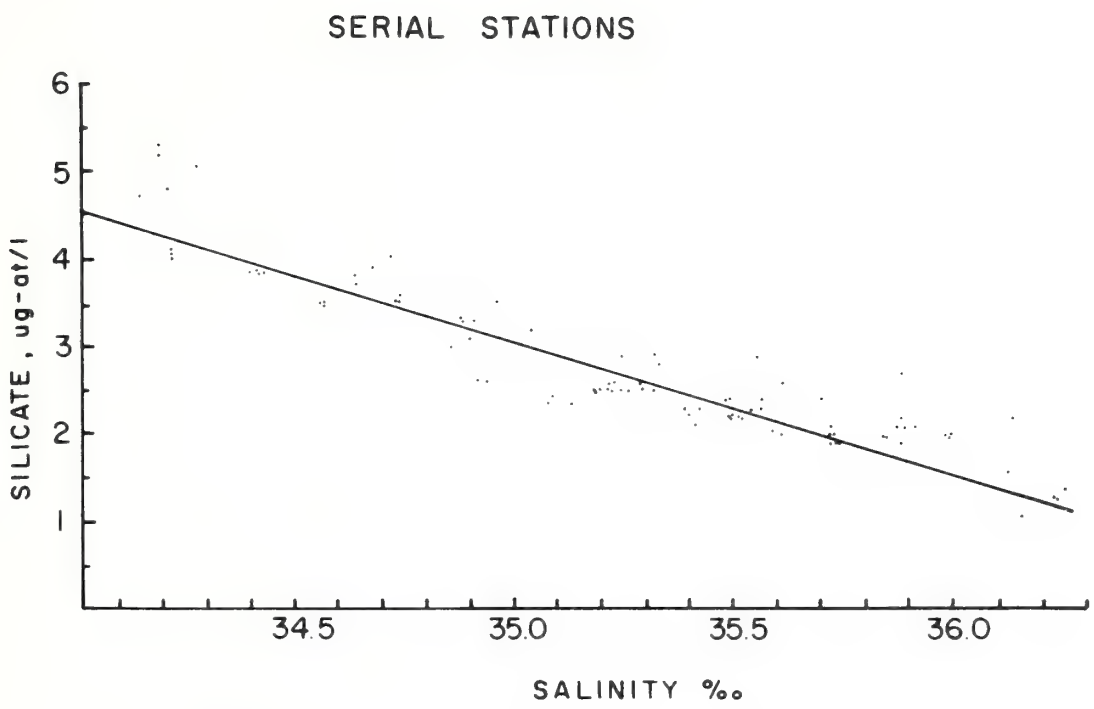


Fig. 17 Plot of dissolved silica concentration against salinity for surface waters at PESCA Serial Station (17°36'N and 67°00'W) in 1971 and 1972.

Symposium Volume of the International Conference on Heavy Metals in the Environment, Toronto, Canada, 1977, 183-204.

METAL SPECIES IDENTIFICATION IN THE ENVIRONMENT A MAJOR CHALLENGE FOR THE ANALYST

Adriana Y. Cantillo
and
Douglas A. Segar

National Oceanic and Atmospheric Administration
Atlantic Oceanographic and Meteorological Laboratories
15 Rickenbacker Causeway, Virginia Key
Miami, Florida 33149

ABSTRACT

The role of trace metals in the environment is critically dependent upon the nature of the chemical species in which they occur. Toxicity and availability to organisms, and solubility in natural waters are among the factors which may be totally different for different chemical species of the same metals. Historically, metal analysis in the environment has been primarily concerned with total metal concentrations. However, identification and determination of individual metal species is becoming increasingly necessary.

Traditional analytical techniques for metals do not distinguish among chemical species, while traditional techniques for organic compounds usually eliminate metal-organic compounds during separation prior to the determination step. These techniques are, therefore, not well suited to investigations of metal-organic species in the environment. However, a new family of analytical instruments, in which atomic spectral analysis is employed for the detection of components separated by various types of chromatography, has recently been developed. The first of these, flameless atomic absorption-gas chromatography, has already been used to dramatically improve our knowledge of the occurrence and transformation of volatile organo-metallics in the environment. This technique and, for non-volatile metal organic compounds, flameless atomic absorption-high pressure liquid chromatography will probably be the major tools used in metal species analysis in the environment in the next several years. Chromatography-mass spectrometry combinations and such techniques as electron spin resonance will also be necessary in this area of research, but are less likely to fulfil the eventual need for low cost reliable routine analysis of identified metal-organic compounds in environmental samples.

RÉSUMÉ

Le rôle des oligo-éléments métalliques dans l'environnement dépend fortement de la nature des espèces chimiques dont ils font partie. La toxicité et la disponibilité aux organismes, ainsi que la solubilité dans les eaux naturelles, sont quelques-uns des facteurs qui peuvent varier considérablement pour les différentes espèces chimiques d'un même métal. Historiquement, l'analyse des métaux dans l'environnement portait principalement sur la déterminiation des concentrations de métal total. Cependant, l'identification et la détermination des espèces métalliques particulières devient de plus en plus nécessaire.

Les techniques classiques d'analyse des métaux ne s'occupent pas de déterminer les différentes espèces chimiques, alors que les techniques classiques pour l'analyse des composés organiques prévoient habituellement l'élimination des composés organo-métalliques pendant l'isolement qui précède l'étape du dosage. Ces techniques ne sont donc pas très appropriées à l'étude des espèces de composés organo-métalliques dans l'environnement. Toutefois, on a mis au point récemment une nouvelle famille d'instruments analytiques basés sur l'utilisation de l'analyse du spectre atomique pour la détection des composés séparés par différents types de chromatographie. La première de ces techniques, l'absorption atomique sans flamme combinée à la chromatographie gazeuse, a déjà contribuer à améliorer de façon importante nos connaissances sur l'existence et les transformations des composés organo-métalliques volatils dans l'environnement. Cette technique et, pour les composés organo-métalliques non volatils, l'absorption atomique sans flamme combinée à la chromatographie liquide à haute pression, constituera probablement l'une des principales technique d'analyse des espèces métalliques dans l'environnement au cours des prochaines années à venir. Des combinaisons de la chromatographie et de la spectrométrie de masse, ainsi que de techniques comme la résonance du spin électronique, seront également nécessaires pour ce type de recherche, mais il est peu probable qu'elles pourront répondre à un besoin éventuel d'appareils d'analyse de routine fiables et peu coûteux pour le dosage de composés organométalliques identifiés dans des échantillons prélevés dans l'environnement.

INTRODUCTION

Trace metals are present in the environment in many different chemical forms. These chemical forms may be broadly classified into three groups; inorganic compounds, simple and inorganically complexed ions, and metal-organic compounds. In the environment inorganic compounds of trace metals are generally found only in solid phases, although these solid phases may exist in colloidal suspension in natural waters. Transport of metals across biological membranes requires that the metal be in solution. Therefore, elements in solid phases must normally be chemically converted to ionic or organically combined form in solution before they can enter the biosphere. Such conversion may take place either in the bulk liquid phase of aquatic systems or in the aqueous phases generated by organisms for this purpose, for example the intestinal fluids of the vertebrates. Once a metal has been taken up by an organism through its external membrane, the subsequent transport of the

metal to other parts of the organism usually also takes place in solution. Each different chemical species of an element has its own characteristic rate of diffusion and spectrum of reactions with the molecules that form living cell tissue. Therefore, the speciation of the element both in natural waters and in biological fluids, such as blood and vacuole solutions, is critically important in determining the function and effects of the metal upon the organism. For example, copper is known to be considerably more toxic to various aquatic organisms when present in ionic form than it is when chelated with organic compounds (e.g. Steeman Nielsen and Wium-Andersen 1970; Lewis *et al.* 1973; Morris and Russell 1973). Methylmercury is known to be more readily accumulated and more toxic than inorganic mercury (Wood 1974).

Little is known about the speciation of metals in environmental solutions. The two major reasons for this lack of knowledge are the great diversity of species that exist, and the analytical problems associated with identifying and determining individual species at extremely low concentrations. The environmental analyst has been primarily concerned, in the past decade or so, with the very difficult problems of analysis of the total concentration of a trace metal at parts per billion or lower concentrations in natural solutions. Most of the problems associated with the determination of total metal concentration have now been solved. Therefore, we should expect to find a stronger emphasis on the development of methodology for metal species identification and quantitation in the next few years. Biological effects of trace metals will be better understood only when a detailed knowledge of speciation is obtained.

Many investigations have been carried out in recent years on certain aspects of the speciation of metals in solution. However, primarily because of limitations in the available instrumental techniques, these have normally been concerned with inorganically complexed ions, metal complexes with simple organic compounds, and, more recently, volatile organometallics. In this paper, we intend to review briefly the various new analytical techniques that are applicable to metal species identification. In particular we will discuss the potential of two simple and inexpensive new techniques, the interface of atomic spectroscopy with gas chromatography and liquid chromatography respectively.

METAL SPECIES IN THE ENVIRONMENT

The simplest form of a metal in solution is the "free" ion. Coordination compounds of the ion will form if suitable ligands are available. Since water molecules act as ligands, ions in solution are normally hydrated (Fig. 1). In

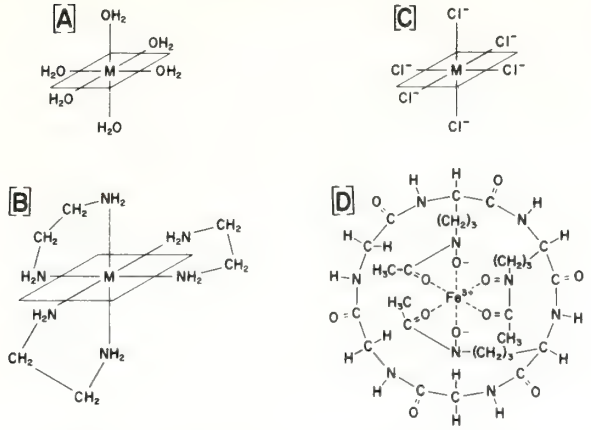


Fig. 1. Examples of coordination compounds found in environmental samples (A) Hydroxy-metal complex (B) chloro-complex (C) metal ethylene diamine tetracetic acid chelate complex (D) Ferrichrome, a Ferric ion chelate complex.

natural waters, simple inorganic ligands, such as hydroxylchloride, and sulphate ions, are present and can replace one or more of the water molecules in the hydrated ion complex. (Fig. 1). Complexes of this type are generally not strong ion complexes but ion pairs held by weak electrostatic forces. Most of these species will, therefore, be indistinguishable from one another and from the free ions, during analyses which use techniques involving acidification or the use of a strong complexing agent. The equilibria existing among these species can, however, be investigated from thermodynamic calculations (Sillen 1961; Zirino and Yamamoto 1972) and by polarographic techniques (Baric and Branica 1967; Zirino and Healy 1970, 1972).

Many organic compounds have electron donor groups and can, therefore, coordinate with metal ions. In general these complexes are weak unless the organic molecule has two or more donor groups which can coordinate with the same metal ion forming stable, closed ring, metal chelates (Fig. 1). Many naturally occurring and synthetic organic compounds have chelating ability and, therefore, the number of possible metal chelates in the environment is very large. The metal chelates have stability constants which can vary over many orders of magnitude. In many instances, because of the stereo-chemical requirements of complex formation, the stability constant of a specific organic molecule may range over many orders of magnitude among different metals. Chelates in the environment may be classified into two types, "labile" and "non-labile". Labile chelates such as EDTA-metal complexes are such that

small changes of pH may markedly affect the stability of the complex, and the complexed metal ion may readily exchange with uncomplexed ions of the same metal in solution. Non-labile chelates are those with extremely high stability constants, usually with a large organic molecule forming a cage structure around the metal ion, and whose metal ion is not readily exchangeable with other metal ions in solution.

Examples of these "non-labile" complexes are vitamin B_{12} (cobalamin) and the ferrichromes (Fig. 1). The distinction between non-labile and labile complexes is purely arbitrary. However, as the analytical approach to these two types of complexes will be somewhat different, the distinction has a functional value.

In addition to metal chelates, three other types of metal-organic compounds may be found in the environment: those with direct metal to carbon bonds (organo-metallics), salts of organic acids, and complexes with π-electron donating compounds.

Complexes with π-electron donating systems include such compounds as ferrocene, in which a ferrous ion is sandwiched between two cyclopentadiene molecules (Fig. 2) and Zeise's salt in which a platinum ion is complexed with an ethylene molecule (Fig. 2). These compounds are not generally stable and probably will have little importance in the environment, although they may be present in petroleum oils and tars.

Transition metal salts of organic acids are unlikely to be important in natural systems. However, the alkaline earth metal carbamate salts may be important in the calcium/phosphate cycles in the environment. The formation of soluble calcium carbamino-carboxylates (Fig. 3) is thought to be responsible for the dissolution of bones and teeth under suitable conditions (Neuberg *et al.* 1957).

Organometallic compounds have become the subject of intense interest in environmental chemistry within the last decade. This interest began with the identification of methylmercury as the chemical species primarily responsible for Minamata disease (Irukayama *et al.* 1961). Organometallic compounds are formed when the metal atom is bonded directly to one or more carbon atoms as in lead tetraethyl (Fig. 3). Many organometallic

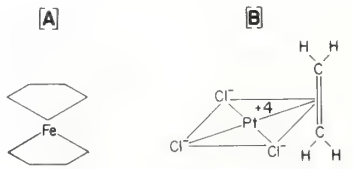


Fig. 2. Examples of π electron complexes (A) Ferrocene (B) Zeise's salt.

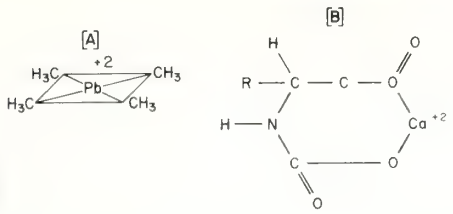


Fig. 3. Examples of (A) organo metallic compound, tetramethyl lead (B) calcium carbamino-carboxylate.

compounds have been synthesized by man. However, most of these are not stable in the environment. The environmental analyst is concerned mainly with the alkyl and aryl compounds of a few elements: Hg, Pb, Se, As, I, and possible several others.

IMPORTANCE OF METAL ORGANIC SPECIES IN NATURAL WATERS

Because the nature of metal organic compounds in natural waters is not well known, the effects of these species are not well understood. However, some effects are known, and they can be classed into two areas; the control of solubility, volatility, and oxidation state, and the control of availability or toxicity to organisms.

The complexing of metals by organic matter in natural waters will increase the solubility of the metal if the complex itself is soluble. The "solubilization" effect of chelation has been observed for a number of elements (e.g. Koshy *et al.* 1969a, 1969b; Desai *et al.* 1970; Park and Hood 1959). However, there is some doubt whether chelation with naturally occurring organics yields true soluble complexes or colloidal complexes in fresh waters (Shapiro 1964), and whether chelation can significantly affect solubility of elements in ocean waters with low dissolved organic matter concentrations (Duursma and Sevenhuysen 1966).

Some chelates are insoluble, and chelation of a metal can lead to their precipitation. In natural systems there is an abundance of particulate matter containing organic compounds which may chelate dissolved metals, and so remove them from solution (e.g. Pillai *et al.* 1971).

The control of metal solubility is often critical to the fate of elements in the environment. For example, in water and wastewater treatment processes, chelated contaminant metals may not be removed as are the simple

metal ions (USPHS 1956; Bender *et al.* 1970). In addition, the control of solubility of metals may have profound influences upon the corrosion of metals in the environment. A metal surface may be either more rapidly dissolved or stabilized by chelation effects on the surface, and the principal action of fouling organisms in mediating corrosion may be due to release of extracellular organic chelators.

Some organically combined species of metals are not ionised in solution and are volatile. Such species as tetramethyl lead and methylated selenium compounds (Wong *et al.* 1975), methyl iodide (Lovelock *et al.* 1972), elemental mercury (Wood 1974), and an unknown cadmium species (Huey *et al.* 1975) may be transported from aquatic systems into the atmosphere because of this volatility. Speciation thus plays a vital role in contaminant transport processes at the air-water interface, particularly as natural waters generally have surface slicks which tend to concentrate the un-ionized metal-organic compounds. Hydrophobic metal organic compounds may be responsible for the high concentration of toxic metals found at the air-sea interface (Duce *et al.* 1972), and neuston species may well be exposed to a different spectrum of metal species than other aquatic organisms.

In certain instances, chelation of a metal may stabilize a metal in an oxidation state which is not otherwise stable. For example, chelation by natural organic matter can stabilize ferrous iron in aerated natural waters and retard its oxidation to ferric iron (Theis and Singer 1974).

The chemical species of an element is of critical importance in controlling the toxicity and availability of the element to organisms. Many organometallics are considerably more toxic to organisms than are the inorganic metal ions themselves, for example, methyl mercury and methyl arsenic (Wood 1974). In addition, the chelation of a metal in solution can change its toxicity to organisms. Copper ions in solution are extremely toxic to a variety of organisms. However, if the copper is chelated its toxicity is considerably reduced (Steeman Nielsen and Wien Andersen 1970; Lewis *et al.* 1973; Morris and Russell 1973). More subtle effects of chelation on living organisms have been reported by many investigators concerned with understanding the factors which control the productivity of planktonic algae. The presence of a chelating agent such as EDTA (ethylene diamine tetraacetic acid) is either essential to, or accelerates, the growth of marine phytoplankton (e.g. Johnson 1964; Barber 1973; Barber and Ryther 1969). It is not clear whether the function of such chelation is to reduce the toxicity of the ionic form of some elements to the plankton, or alternatively to solubilize and make such essential elements as iron and manganese available for uptake. Probably both mechanisms are important for different elements and in different environmental situations.

ANALYTICAL TECHNIQUES FOR METAL-ORGANICS IN ENVIRONMENTAL SOLUTIONS

Reports of the analytical determination of individual metal organic species were virtually non-existent until recent years. The presence of metal-organic compounds in natural waters has been inferred from differential analysis of metal ions in oxidised and unoxidised samples (Williams 1964; Hood 1967; Slowey *et al.* 1967; Stiff 1971; Alexander and Corcoran 1967; Foster and Morris, 1971) from various toxicity and growth experiments (Steeman Nielson and Wium Andersen 1970; Lewis *et al.* 1973; Morris and Russell 1973; Johnson 1964; Barber 1973; Barber and Ryther 1969), and from solubility considerations (Shapiro 1964; Koshy *et al.* 1969a, 1969b; Desai *et al.* 1970, Park and Hood 1959; Theis and Singer 1974; etc.). At least one specific compound, cyanocobalamin (vitamin B_{12}), has been determined by biological assay and colorimetric techniques (Riley 1965). In addition, a number of volatile organometallics have recently been chemically determined in natural systems by gas chromatographic techniques which will be discussed below. The reason for the paucity of data can be better understood by considering some of the characteristics of techniques currently used for environmental chemical analysis.

Analytical techniques commonly used for trace metal analyses in environmental samples include neutron activation, atomic absorption and emission, X-ray fluorescence, isotope dilution mass spectrometry, colorimetry, and polarography. With the exception of colorimetry and polarography each of these analytical techniques will normally determine the total quantity of metal present in the determinative step regardless of chemical species. Any deviation from this principle, when a metal compound is present in the determinative step, but not included in the analysis, is considered to be a matrix interference in the analysis. Colorimetry and polarography, on the other hand, will normally determine only the concentration of the free ion of the element in one specific oxidation state. In practice any species in equilibrium with this ionic state with rapid kinetics will affect the determination, since long plating times and anodic stripping techniques are usually necessary for polarographic determination of metals at the concentrations normally encountered in natural waters.

Except for the analysis of a few elements by neutron activation, flameless atomic absorption, polarography and colorimetry, preconcentration and separation of the metal must be carried out before determination in natural waters. This step is necessary because of inadequate analytical sensitivity and matrix interferences, and it involves such procedures as ion exchange and solvent extraction. These procedures are invariably selective for

only certain chemical species. Therefore, the total metal is not determined. Often the separation procedure is preceded by an oxidation step to destroy oxidisable metal species and permits the metal in these species to be included in the analytical result.

The general principle behind most analytical procedures for metals in environmental samples is, therefore, to determine the total metal regardless of its chemical form. The problems encountered in intercalibration studies of the determination of trace elements in natural waters may be partly related to the failure of some techniques to achieve this goal. The recent success of flameless atomic absorption for direct determination of some metals in natural water samples (Segar and Cantillo 1976; Ediger 1973) should help to minimize such problems in the future.

In the study of organic compounds in natural systems, the limited value of data concerning the concentration of total carbon was recognized many years ago. Therefore, analytical techniques were sought which could determine specific organic molecules. Direct techniques, except bio-assay, cannot be used for analysis of individual compounds and almost all environmental organic analyses involve complex separation procedures to isolate individual compounds for detection and quantitation. The separation procedures are usually highly selective for a particular group of organic compounds and, therefore, normally exclude metal organic compounds from the final determination step. The final determination is usually carried out by some combination of a chromatographic final separation and detection with a non-specific detector. Gas and liquid column chromatography are the most extensively used of all final separation techniques, although thin layer chromatography, electrophoresis, field desorption mass spectrometry, and other techniques are used in certain specific analyses. The detection that follows the final separation is usually based upon some general property of the organic molecule itself (e.g. colorimetric reactions, ultraviolet absorption, combustion energy or ionization, thermal conductivity, molecular mass) and therefore, is not specific to one type of organic molecule. The specificity of the analysis for the type of organic molecule that is being determined is normally introduced in the prior separation procedures.

A number of detection systems which are selective for one type of functional group are widely used, for example, electron capture detectors selective for halogen containing compounds, colorimetric reactions such as that of ninhydrin with amino nitrogen groups, thermionic detectors selective for phosphorus containing compounds, and mass spectrometers used in the mass fragmentography mode to be selective for compounds containing a fragmenting functional group of known mass. This last system, with a mass spectrometer acting as the detector is perhaps the most versatile and powerful

analytical system currently available to environmental chemists. However, its limitations include very high cost and the difficulty of interfacing mass spectrometers with separation systems other than gas chromatographs.

The enormous success of the interfaced gas chromatograph-mass spectrometer system in isolating, identifying, and determining specific organic compounds in environmental samples, provided the background necessary for the genesis of the first of a new hierarchy of interfaced analytical systems designed for the analysis of individual metal-containing organic and inorganic species. This was the combination of a gas chromatograph with an atomic absorption spectrophotometer as the element specific detector. The first such instruments were developed for analysis of alkyl mercury compounds (Gonzalez and Ross 1972; Longbottom 1972). Elemental and alkylated mercury compounds were separated in a gas chromatograph. The effluent compounds were reduced to elemental mercury by combusting in a flame or heating in a tube furnace, and the elemental mercury was passed through an absorption cell in the atomizer compartment of the atomic absorption spectrophotometer. Prior to these applications, spectral detection for gas chromatography had been limited almost entirely to the flame photometric detector (Juvet and Durbin 1966; Zado and Juvet 1966). The flame photometric detector is not ideally suited to measure atomic emission due to the wide wavelength band pass of the monochromator used, and the difficulty in compensating for flame background and temperature variations caused by organic and other inorganic species in the column effluent. It has, therefore, been used primarily as a selective detector for phosphorus and sulfur by monitoring broad band molecular emission. Juvet and his co-workers (Juvet and Dubin 1966; Zado and Juvet 1966) did demonstrate the potential utility of the flame photometric detector for element-specific atomic emission, but little use of their techniques has subsequently been made.

The use of flameless atomic absorption analysis for detection of mercury compounds separated by a gas chromatograph was important because it represented the first use of a truly element-specific detection system for chomatography, with sufficient sensitivity to be used for environmental sample analyses, and with a remarkable degree of freedom from interferences. The advantages of the specificity of atomic absorption detection may be illustrated by the analysis of methyl mercury in fish tissue. The various steps necessary for this analysis using gas chromatography, and both electron capture and atomic absorption detection, are illustrated in Figure 4. Because the atomic absorption detector is insensitive to non-mercury containing compounds in fish tissues, which are detected by the electron capture detector, most of the tedious sample clean-up procedure is eliminated.

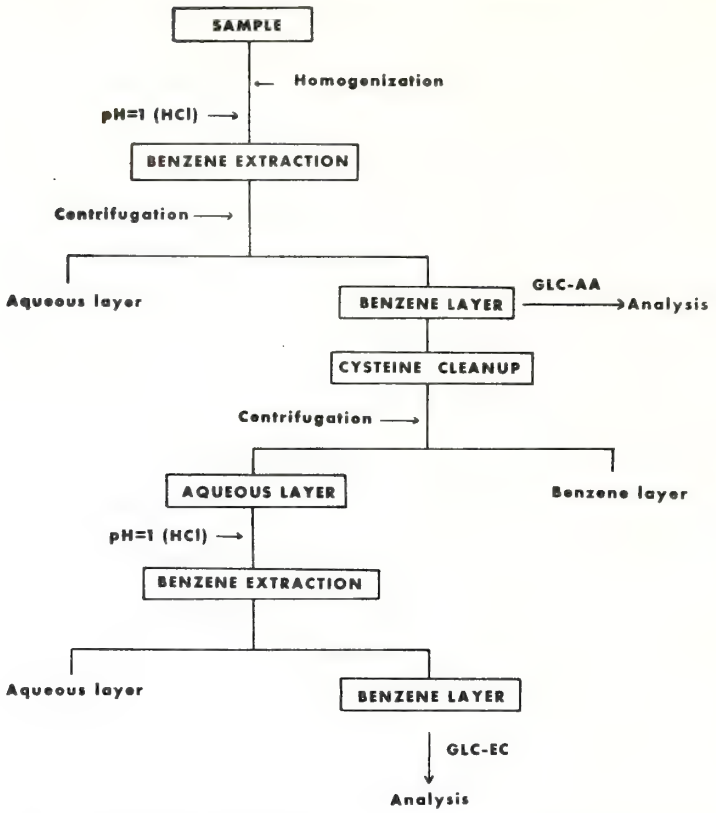


Fig. 4. Analysis scheme for alkyl mercury compounds in fish tissues by gas liquid chromatography with electron capture or atomic absorption detection.

Although the gas chromatography-atomic absorption instrumentation described by Gonzales and Ross (1972) and Longbottom (1972) is ideal for mercury compounds, it cannot be used for compounds of other elements. Mercury is the only metal which forms an unreactive monatomic gas with significant vapor pressures at low temperatures. Atoms of other metals formed by thermal or combustive decomposition of their compounds cannot be passed through a low temperature transfer line and cell for atomic absorption. Segar and Gonzalez (1973) described two gas chromatographic-atomic absorption spectrophotometer combinations which overcame this limitation by decomposing the metal compounds to atoms in the atomic absorption

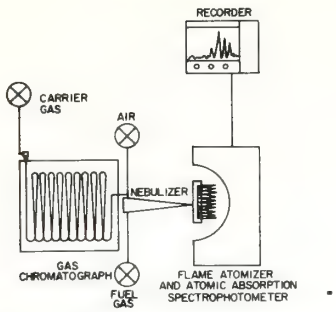


Fig. 5. Schematic of flame atomic absorption gas-liquid chromatograph (FAAGLC).

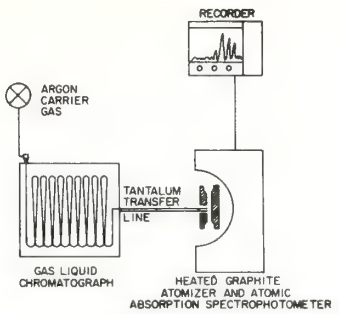


Fig. 6. Schematic of non flame atomic absorption gas-liquid chromatograph (NFAAGLC).

spectrophotometer atomizer itself. The simplest system involved the passage of the chromatograph effluent gasses through a heated transfer line into a compressed air stream, at the point of its introduction to the nebulizer chamber of a standard flame atomic absorption spectrophotometer (Fig. 5). This system, although simple, does not provide very high sensitivity for metal analysis, and a second system was developed (Segar and Gonzalez 1973; Segar 1974) in which the gas chromatograph effluent was passed directly into the center of the heated graphite tube of a flameless atomic absorption atomizer, which was maintained at a temperature sufficient to decompose the metal-organic compounds (Fig. 6). With this technique, dilution of the column effluent with air is avoided and the analytical sensitivity is considerably enhanced. The utility of this technique was demonstrated by analysis of lead alkyl compounds in gasoline samples. The gas chromatograph and interface used were crude, and no attempt to optimize all of the relevant chromatographic or atomic absorption parameters was made. Despite this, the results obtained were excellent. A typical set of chromatograms obtained with 2 μl injections of gasoline, and no instrumental scale expansion on the atomic absorption spectrophotometer readout is shown in Fig. 7, and the results of an analysis of a standard lead alkyl mixture are shown in Table 1.

The sensitivity of the gas chromatographic flameless atomic absorption spectrophotometric technique can be considerably improved by collecting individual chromatographic peaks as they exit the chromatographic column and by atomizing each peak instantaneously in the flameless atomizer. In this mode of operation, the absolute analytical sensitivity is essentially the same as that which can be obtained by the normal mode of individual injections into

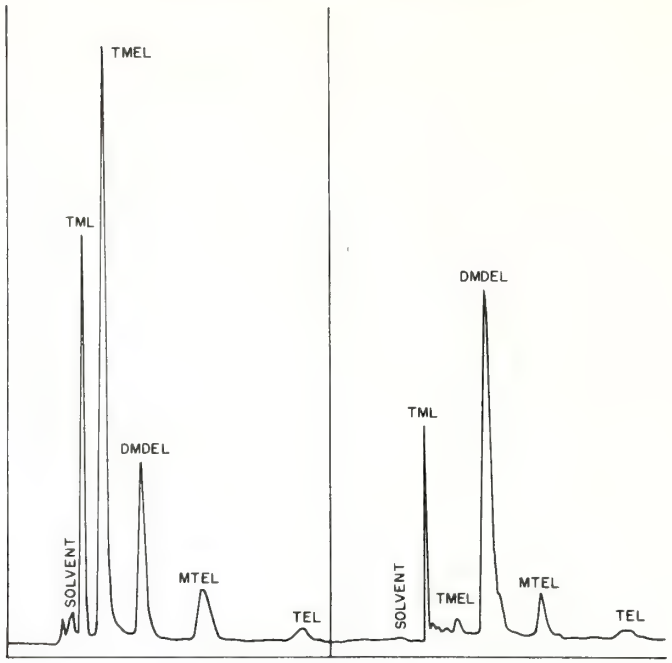


Fig. 7. Separation of lead alkyls from two commercial gasoline samples by flameless atomic absorption gas chromatograph. 2 μl gasoline injected. Continuous atomization detector mode. No scale expansion on atomic absorption spectrophotometer. TML = tetramethyl lead, TMEL = trimethyl ethyl lead. DMDEL = dimethyl diethyl lead, MTET = methyl triethyl lead, TEL = tetraethyl lead.

TABLE 1

Analysis of Dupont TMX50 by flameless atomic absorption gas chromatography.

TMX50 diluted with hexane to conc. of 57.1 ppm total Pb, injection 21, maximum absorbance reading for dimethyl diethyl lead 0.22 absorbance. Peak areas calculated from peak height times half base width.

Compound	Percent in mixture	
	Manufacturer's spec.	Analysis
Tetra methyl lead	4.6	4.5
Trimethyl ethyl lead	24.8	21.6
Dimethyl diethyl lead	41.2	45.0
Methyl triethyl lead	24.8	24.5
Tetra ethyl lead	4.6	4.4

the flameless atomizer. However, the collection of the metal organic compounds as they are eluted in separate peaks from the chromatographic column is difficulty. Two methods have been investigated: the individual chromatographic effluent compounds may be collected in separate cold traps by a valve switching arrangement, the compounds being evaporated by rapid heating, then passed directly into the flameless atomizer with a minimum gas volume. This arrangement is complex and offers only small sensitivity advantages over the continuous mode of detector operation. Alternatively, the flameless atomizer can be temerature programmed in such a manner that, during the passage of a chromatographic effluent peak through the atomizer, the temperature is sufficient to decompose the metal-organic compound but not sufficient to volatilize or atomize the metal. The metal, therefore, accumulates on the walls of the atomizer and may be atomized instantaneously by increasing the atomizer temperature for a few seconds immediately following the collection of each chromatographic effluent peak. Many difficulties are inherent in the development of optimum conditions for the use of this technique, and it can be used only for those metal organic-compounds which are decomposed at low temperatures relative to the temperature required to volatilize the metal. Nevertheless, the technique has been applied successfully to the analysis of perfluoroacetylacetonates of chromium, and careful design and optimization of the gas chromatograph-atomic absorption interface and control sequences should enable this technique to be used for many other compounds. A modification of the heated "T" tube graphite atomizer designed by Robinson and co-workers (Loftin *et al.* 1970; Robinson *et al.* 1972) would probably be considerably better suited to this technique than present commercial atomizers. The decomposition and deposition of the chromatographic effluent could be achieved on the carbon bed in the side arm of the atomizer and could be aided by adding suitable reactive gases or vapours such as oxygen to this "T" tube to achieve decomposition of the metal organic compound at low temperatures.

Since the introduction of atomic absorption detectors for gas chromatography in 1972, the method has been adopted for routine analysis of many organo-metallics in environmental samples. Alkylated mercury compounds have been routinely determined in fish tissues and other samples (Gonzalez and Ross 1972). Interest has also been revived in the use of the microwave emission detector for analysis of mercury compounds and alkyl arsenic acids after gas chromatographic separation (Talmi 1975; Talmi and Bostick 1975), and of metal β-diketone chelates separated by gas chromatography (Kawaguchi *et al.* 1973; Dagnall *et al.* 1973). The gas chromatograph-microwave emission combination has also been used to determine the total concentrations of

selenium, arsenic and antimony in environmental samples after preparation of volatile metal derivatives from metals in the sample. (Talmi and Andren 1974; Talmi and Norvell 1975). Lead alkyls in gasoline samples have been routinely determined by flame (Coker 1975) and flameless (Segar 1974) atomic absorption gas chromatography. Lead and selenium alkyls have been determined in air, and the vapor phase above sediments and cultures, by flameless atomic absorption gas chromatography with a simplified heated quartz tube atomizer (Chau *et al.* 1975a, 1975b, 1975c; Wong *et al.* 1975). Volatile mercury and cadmium species in algal cultures have also been determined by flameless atomic absorption gas chromatography (Huey *et al.* 1975). Van Loon and Radziuck (1975) and Van Loon *et al.* (1976) have described an ingenious inexpensive quartz "T" tube furnace with a simple gas chromatographic column installed in the arm of the furnace. This remarkably simple device has been used successfully for flameless atomic absorption gas chromatography of organo-selenium compounds and for the investigation of selective volatilization characteristics of metals from various matrices during thermal vaporization.

The combination of gas chromatographic separation with atomic spectral detection is now a well established analytical technique which enables environmental analysts to investigate, for the first time, many volatile metal species. However, much still remains to be done to optimize the instrumentation and develop applications. Unfortunately very few metal-organic species in the environment are sufficiently volatile that they can be separated by gas chromatography. Atomic absorption spectrophotometry can, however, be readily used as a detection technique for liquid chromatography. For flame atomic absorption or emission detection, the effluent of the chromatographic column can simply be passed directly into the nebulizer inlet of the flame atomizer (Manahan and Jones 1973; Umebayashi and Kitagishi 1975; Freed 1975). The combination of flame detectors and liquid chromatography suffers from two major drawbacks: the sensitivity is poor, and the flame uses large quantities of sample destructively, prohibiting collection of column effluent fractions for further characterization. Both of these drawbacks may be reduced by interfacing the liquid chromatograph with a flameless atomic absorption spectrophotometer. The flameless atomic absorption-high pressure liquid chromatograph was first described by Segar and Gonzalez (1973). Early experiments with this system were successful, but in order to obtain the maximum potential the instrumentation required development. Although the development is not yet complete the probable configuration of the instrumentation is shown schematically in Fig. 8. The column effluent is passed through an injection valve, which injects between 5 and 50 μl of the effluent into a heated graphite furnace atomizer through a tantalum capillary.

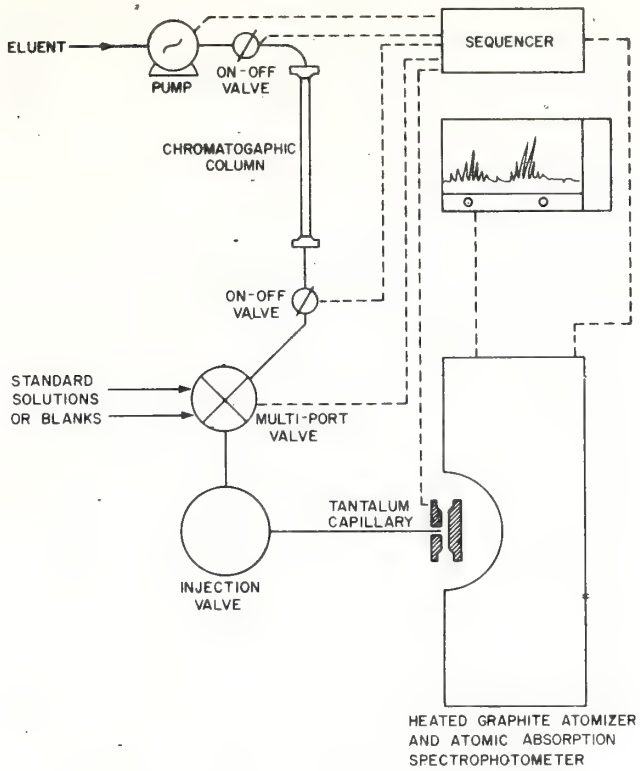


Fig. 8. Schematic of non flame atomic absorption-high pressure liquid chromatograph (NFFA HPLC).

The tantalum capillary is, at present, left permanently in place in the injection port of the atomizer. However, improved reproducibility of injection should be achieved by using a non-wettable teflon capillary, which is inserted into the atomizer injection port only during sample injection (Weltz 1975; Pickford and Rossi 1972). A sequencer controls the operations of the high pressure liquid chromatograph, atomic absorption spectrophotometer, injection valve, and a multi-port sampling valve (Fig. 8). The multi-port sampling valve permits automated injection of standard and blank solutions to calibrate the atomic absorption spectrophotometer at intervals. Two electrically operated on-off valves are provided, before and after the chromatographic column (Fig. 8). These valves may be closed during the analysis cycle of the flameless atomic absorption spectrophotometer and reopened to permit only sufficient volume

to pass the column for the subsequent injection. In this mode, almost all of the column effluent is used for injection into the atomic absorption detector, and very high sensitivity and high resolution may be achieved with small samples and small chromatographic columns. In an alternative mode, the two on-off valves may be left permanently open, and the bulk of the column effluent which passes directly through the injection valve may be collected in a fraction collector. The atomic absorption spectrophotometer analysis sequence time may be set at any value above the minimum required for drying, ashing, atomizing, and cool down cycles of the heated graphite atomizer (usually 30-180 seconds depending upon the matrix, element determined, and sample injection volume). The atomic absorption detector in the continuous flow mode still provides high sensitivity, but the major portion of any metal-containing fraction eluted from the column may be collected for further characterization. The applications of this instrumentation to the analysis of metal-organic species in environmental samples promise to be extensive particularly in view of its capability of working with small samples and very low concentrations of the metal species. The partially developed equipment has already been used for preliminary analysis of metal species in natural seawater separated on molecular exclusion gels (Sephadex). An example of the separation of metal fractions in natural sea water obtained with this instrumentation is shown in Fig. 9. The results of these separations are difficult to interpret because of the adsorptive properties of the gel used (Gjessing 1965). Further research is currently being carried out using microporous glass or silica beads in place of the Sephadex gels.

One potentially valuable application of flameless atomic absorption high pressure liquid chromatography under investigation is the estimation of stability constants of metal complexes with naturally occuring organics, by modifications of the gel filtration technique of Hummel and Dreyer (Hummel and Dreyer 1962; Mantoura and Riley 1975). Stability constants can be estimated at natural concentrations of metal using only very small quantities of the

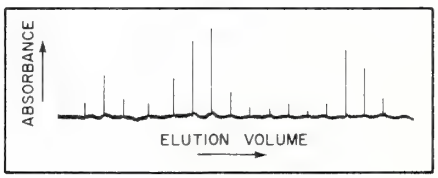


Fig. 9. Chart recording for typical separation of copper species in sea water by NFAAHPLC using gel molecular exclusion chromatography, continuous column flow and interval sampling.

organic compound. Isolates of naturally occuring trace organic compounds can, therefore, be investigated without the necessity to isolate large quantities of the compound.

The combination of chromatographic separation and atomic spectral analysis is simple and relatively inexpensive. Only minor modifications of equipment already used in most environmental analytical laboratories are required, or alternatively, very simple equipment may be constructed specifically for this purpose (e.g. Van Loon and Radziuk 1975). The flameless atomic absorption gas, and high pressure liquid chromatographs, and the modifications of them that are sure to appear, are likely to constitute the major analytical tools with which the environmental analyst meets the challenge of investigating the nature of metal-organic species in the environment, and subsequently determining them in routine manner. Other techniques such as polarography, electron spin resonance, and electrophoresis will undoubtedly be vital to some investigations but are unlikely to provide the broad range of capabilities of chromatography-atomic spectroscopy techniques. Perhaps the only techniques more versatile than the chromatography-atomic spectroscopy combinations are chromatography-mass spectrometry configurations. Gas chromatography-mass spectrometry is already used extensively, and liquid chromatography-mass spectrometry combinations have been developed recently (Jones and Yang 1975; McLafferty *et al.* 1975). Undoubtedly these techniques will be important research tools. However, the expensive equipment required and the sophisticated nature of the mass spectrometry technique do not lend themselves to its use for routine sample analysis.

The recently developed analytical techniques that we have discussed provide the environmental analyst with a new set of tools that will enable him to address the problems of metal speciation. However, the techniques are not yet fully developed and their potential is as yet, relatively unexplored.

REFERENCES

Alexander J.E., and Corcoran E.F., 1967. The distribution of copper in tropical seawater., Limnol. and Oceanogr., 12:236-42.

Bache C.A., and Lisk D.J., 1971. Gas chromatographic determination of organic mercury compounds by emission spectrometry in a helium plasma, Analyt. Chem., 43:950-2.

Barber R.T., 1973. Organic ligands and phytoplankton growth in nutrient-rich seawater., In Trace Metals and Metal-Organics Interaction in Natural Waters, Ed. P.C. Singer, Ann Arbor Science, Mich.

Barber R.T., and Ryther J.H., 1969. Organic chelators: factors affecting primary production in the Cromwell current upwelling., J. Exp. Mar. Biol., 3:191-199.

Baric A., and Branica M., 1967. Polarography of sea water I. Ionic state of cadmium and zinc in seawater., J. Polarog. Soc., 13:4-8.

Bender M.E., Matson W.R., and Jordan R.A., 1970. On the significance of metal complexing agents in secondary sewage effluents., Environ. Sci. & Technol., 4:520-1.

Chau Y.K., Wong P.T.S. and Goulden P.D., 1975a. Paper read at Fifth International Conference on Atomic Spectroscopy, 25-29 Aug., at Monash University, Melbourne, Australia.

Chau Y.K., Wong P.T.S. and Goulden P.D., 1975b. Determination of alkyl lead and selenium compounds in the atmosphere by GC-AAS system. Paper read at International Conference on Heavy Metals in the Environment. 27-31 Oct. 1975. Toronto, Canada.

Chau Y.K., Wong P.T.S. and Goulden P.D. 1975c. Gas chromatography atomic absorption method for the determination of dimethyl selenide and dimethyl diselenide. Analyt. Chem. 47:2279-81.

Coker D.T., 1975. Determination of individual and total lead alkyls in gasoline by a simple rapid gas chromatography/atomic absorption spectrometry technique., Analyt. Chem., 47:386-89.

Dagnall R.M., West T.S. and Whitehead P., 1973. The determination of volatile metal chelates by using a microwave excited emissive detector. Analyst, 98:647-54.

Desai M.V.M., Mathew E., and Ganguly A.K., 1970. Differential interaction of marine humic and fulvic acids with alkaline earth and rare earth elements. Curr. Sci., 39:429-33.

Duce R.A., Quinn J.G., Olney C.E., Piotrowicz S.R., Ray B.J., and Wade T.L., 1972. Enrichment of heavy metals and organic compounds in the surface microlayer of Narragansett Bay, Rhode Island., Science, 176:161-3.

Duursma E.K. and Sevenhuysen W., 1966. Note on chelation and solubility of certain metals in seawater at different pH values., Ned. J. Sea Res., 3:95-106.

Ediger R.D., 1973. A review of water analysis by atomic absorption., At. Abs. Newsletter., 12:151-7.

Foster P. and Morris A.W., 1971. The seasonal variation of dissolved ionic and organically associated copper in the Menai Straits, Deep Sea Res., 18:231-6.

Freed D.J., 1974. Flame photometric detector for liquid chromatography., Analyt. Chem., 47:186-7.

Gjessing E.T., 1965. Use of 'Sephadex' gel for the estimation of molecular weight of humic substances in natural water., Nature, 207:1091-2.

Gonzalez J.G., and Ross R.T., 1972. Interfacing of an atomic absorption spectrophotometer with a gas-liquid chromatograph for the determination of trace quantities of alkyl mercury compounds in fish tissue., Anal. Lett., 5:683-94.

Hood D.W., 1967. Chemistry of the oceans: some trace metal-organic associations and chemical parameter differences in the top one meter of surface., Environ. Sci. Tech., 1:303-305.

Huey C.W., Brinckman F.E., Iverson W.P. and Grim S.O., 1975. Bacterial volatalization of cadmium. Paper read at International Conference on Heavy Metals in the Environment., 27-31 Oct., Toronto, Canada.

Hummel J.T., and Dryer W.J., 1962. Measurement of protein binding phenomena by gel filtration. Biochem. Biophys. Acta., 63:530-532.

Irukayama K., Kondo T., Kai F., and Fujiki M., 1961. Studies on the origin of the causative agent of Minimata disease. I. Organic mercury compounds in fish and shellfish from Minimata Bay., Kumamoto Med., J., 14:157-69.

Johnson R., 1964. Seawater, the natural medium of phytoplankton II. Trace metals and chelation, and general discussion., J. Mar. Biol. Ass. U.K., 44:87-109.

Jones P.R. and Yang S.K., 1975. A liquid chromatograph-mass spectrometer interface., Analyt. Chem., 47:1000-2.

Juvet R.S. and Durbin R.P., 1966. Characterization of flame photometric detector for gas chromatography., Analyt. Chem., 38:565-9.

Kawaguchi K., Sakamoto T. and Mizuike A., 1973. Emission spectrometric detection of metal chelates separated by gas chromatography, Talanta, 20:321-6.

Koshy E., Desai M.V.M., and Ganguly A.K., 1969a. Studies on organo-metallic interactions in the marine environment. Part 1. Interaction of some metallic ions with dissolved organic substances in seawater., Curr. Sci., 38:555-8.

Koshy E., Desai M.V.M., and Ganguly E.K., 1969b. Studies on organo-metallic interactions in the marine environment. Part 2. Interaction of metallic ions with humic acid from a marine sediment., Curr. Sci., 38:582-6.

Lewis A.G., Whitfield P., and Ramnarine., 1973. The reduction of copper toxicity in a marine copepod by sediment extract., Limnol. and Oceanogr., 18:324-5.

Loftin H.P., Christian C.M., and Robinson J.W., 1970. The continuous determination of lead in air., Spectroscopy Lett., 3:161-74.

Longbottom J.E., 1972. Inexpensive mercury-specific gas chromatographic detector., Analyt. Chem., 44:1111-2.

Lovelock J.E., Maggs R.J., and Rasmussen R.A., 1972. Atmospheric dimethyl sulphide and the natural sulphide cycle., Nature, 273:452-3.

McLafferty F.W., Knutti R., Venkataraghaven R., Arpino P.J., and Dawkins B.G., 1975. Continuous mass spectrometric monitoring of a liquid chromatograph with subnanogram sensitivity using an on-line computer., Analyt. Chem., 47:1503-5.

Manahan S.E., and Jones D.R., 1973. Atomic absorption detector for liquid-liquid chromatography., Analyt. Lett., 6:745-53.

Mantoura R.F.C., and Riley J.P., 1975. The use of gel filtration in the study of metal binding by humic acids and related compounds., Analyt. Chem. Acta., 78:193-200.

Morris O.P., and Russell., 1973. Effect of chelation on toxicity of copper., Mar. Poll. Bull., 4:159-60.

Neuberg C., Grauer A., Kriedl M. and Lowry H., 1957. The role of the carbamate reaction in the calcium and phosphorous cycles in nature., Archiv. Biochem. Biophys., 70:70-85.

Park K., and Hood D.W., 1959. Effect of organic material on the solubility of calcium carbonate in seawater., In Preprints of the Intern. Oceanogr. Cong., New York., ed. M. Sears, pp. 873-875. Amer. Assoc. Adv. Science.

Pickford C.J., and Rossi G., 1972. Analysis of high purity water by flameless atomic absorption spectroscopy I. Use of an automated sampling system., Analyst., 97:647-52.

Pillai T.N.V., Desai M.V.M., Mathew E., Ganapathy S., and Ganguly A.K., 1971. Organic materials in the marine environment and associated metallic elements., Curr. Sci., 40:75-81.

Riley J.P., 1965. Analytical chemistry of seawater. In Chemical Oceanography Vol. 2., eds. J.P. Riley and G. Skirrow., pp. 295-424., London, Academic Press.

Robinson J.W., Slevin P.J., Hindman G.D., and Wolcott D.K., 1972. Non-flame atomic absorption in the vacuum ultraviolet region. The direct determination of mercury in air at the 184.9 nm resonance line. Analyt. Chim. Acta., 61:431-9.

Segar D.A., 1974. Flameless atomic absorption gas chromatography., Analyt. Lett., 7:89-95.

Segar D.A., and Cantillo A.Y., 1976. The direct determination of trace metals in seawater by flameless atomic absorption. p. 56-81. In Analytical Chemistry in Oceanography., ed., T.R.P. Gibb, Advances in Chemistry Series. No. 147, American Chemical Society, Washington, D.C.

Segar D.A., and Gonzalez J.G., 1973. Vapour phase sample injection for flame and flameless atom reservoir atomic absorption. Paper read at Fourth International Conference on Atomic Spectroscopy, 29 Oct. -2 Nov., Toronto, Canada.

Shapiro J., 1964. Effect of yellow organic acids on iron and other metals in water., J. Amer. Water Works Assoc., 58:1062-82.

Sillen L.G., 1961. The physical chemistry of seawater. In Oceanography, ed. M. Sears. pp. 549-81, Washington D.C., Am. Assoc. Adv. Sci.

Slowey J.F., Jeffrey L.M., and Hood D.W., 1967. Evidence for organic complexed copper in seawater. Nature., 214:377-378.

Steeman Nielsen E., and Wium-Andersen S., 1970. Copper ions as poison in sea and in fresh water., Mar. Biol., 6:93-7.

Stiff M.J., 1971. The chemical states of copper in polluted fresh water and a scheme of analysis to differentiate them., Water Res., 5:585-99.

Talmi Y., 1975. The rapid sub-picogram determination of volatile organo-mercury compounds by gas chromatography with a microwave emission spectrometric detector system., Analyt. Chim. Acta., 74:107-17.

Talmi Y., and Andren A.W., 1974. Determination of selenium in environmental samples using gas chromatography with a microwave emission spectrometric detection., Analyt. Chem., 46:2122-30.

Talmi Y., and Bosbick D.T., 1975. Determination of alkylarsenic acids in pesticide and environmental samples by gas chromatography with a microwave emission spectrometric detection system. Analyt. Chem., 47:2145-50.

Talmi Y., and Norvell V.E., 1975. Determination of arsenic and antimony in environmental samples using gas chromatography with a microwave emission spectrometric system., Analyt. Chem., 47:1510-73.

Theis T.L., and Singer P.C., 1974. Complexation of Iron (II) by organic matter and its effect on Iron (II) oxygenation, Environ. Sci. Technol., 8:569-73.

Umebayashi M., and Kitagishi K., 1975. Direct attachment of atomic absorption spectrophometer to a liquid chromatograph for the identification, estimation, and continuous monitoring of metal ions and metal chelates. Paper read at Fifth International Conference on Atomic Spectroscopy, 25-29 Aug., Monash University, Melbourne, Australia.

United States Public Health Service, 1956. Interaction of heavy metals and biological sewage treatment processes., U.S. Public Health Service Publication No. 999-WP-22., Robert A. Taft Sanitary Engineering Center.

Van Loon J.C., and Radziuk B., 1975. A quartz "T" tube furnace-atomic absorption spectroscopy system for metal speciation studies. In Press.

Van Loon J.C., Radzuick B., and Silvester M.D., 1975. A "T" tube furnace for the investigation of metal species by AAS. Paper read at Fifth International

Conference on Atomic Spectroscopy, 25-29 Aug., Monash University, Melbourne, Australia.

Welz B., 1975. Influence of sample preparation on accuracy and precision in flameless AA. Paper read at Fifth International Conference on Atomic Spectroscopy, 25-29 Aug., at Monash University, Melbourne, Australia.

Williams P.M., 1969. The association of copper with dissolved organic matter in sea water., Limnol and Oceanogr. 14:156-158.

Wong P.T.S., Chau Y.K., Luxon P.L., and Silverberg B., 1975. Methylation of lead and selenium in the environment. Paper read at International Conference on Heavy Metals in the Environment, 27-31 Oct., Toronto, Canada.

Wood J.M., 1974. Biological cycles for toxic elements in the environment., Science, 183:1049-58.

Zado F.M., and Juvet R.S., 1966. A new selective-nonselective flame photometric detector for gas chromatography., Analyt. Chem., 38:569-73.

Zirino A., and Healy M.L., 1970, Inorganic zinc complexes in seawater., Limnol and Oceanogr., 15:956-8.

Zirino A., and Healy M.L., 1972. pH-controled differential voltammetry of certain trace transition elements in natural waters., Environ. Sci. and Technol., 6:243-9.

Zirino A., and Yamamoto S., 1972. A pH dependent model for the chemical speciation of copper, zinc, cadmium, and lead in seawater., Limnol and Oceanogr., 17:661-71.

Middle Atlantic Continental Shelf and the New York Bight, Special Symposia 2, 1976, M.G. Gross, ed. (the American Society of Limnology and Oceanography, Inc.) 240-248.

Carbohydrates and organic carbon in New York Bight sediments as possible indicators of sewage contamination[1]

Patrick G. Hatcher and Larry E. Keister

Atlantic Oceanographic and Meteorological Laboratories, NOAA, 15 Rickenbacker Causeway, Miami, Florida 33149

Abstract

Sediments of the New York Bight were analyzed for total organic carbon (TOC) and total carbohydrates (TCH). The TCH:TOC ratio was significantly more elevated than comparable sediments from other areas. High TCH:TOC values ($\geq$30) may be attributed to sewage-derived materials which contribute significant quantities of refractory organic matter to the bight annually. Nonanthropogenic sources of organic matter to these sediments have little or no influence on TCH:TOC except near the shelf break. The TCH:TOC ratio may be useful as a qualitative and semiquantitative indicator of sewage-derived organic matter in sediment deposits. The observed TCH:TOC ratios suggest that organic material being deposited in the Christiaensen Basin and mud patches near Long Island is predominantly of sewage origin, and that seaward of the apex, the sedimentary organic matter becomes less influenced by sewage-derived organic matter and oceanic organic matter becomes a more significant fraction.

Increasing alarm has been expressed over the potential threat of sewage-derived chemical and biological contaminants accumulating on the beaches along coasts of the New York Bight. Consequently, a means of identifying and quantifying sewage-derived materials is of great interest.

Visual observations of sediment samples resembling "black mayonnaise" have been used in an attempt to map areas of "sludge" accumulation (Harris 1974). Sewage sludge constituents such as tomato seeds and human artifacts have been used elsewhere as sewage indicators with varying degrees of success (Shelton 1971). In the New York Bight, the distribution of organic matter in sediments was used to delineate the spatial extent of sewage contamination (Pearce 1972). More recently, in connection with the Coastal Water Research Project off southern California, various toxic heavy metals and chlorinated insecticides have been been used as qualitative indicators of sewage contamination (South. Calif. Coastal Water Res. Proj. 1974). These parameters can serve only as qualitative or semiqualitative indicators. A positive quantitative tracer for sewage is lacking.

Sewage is a complex and heterogeneous mixture of organic and inorganic materials. As it is incorporated into marine sediments, the resultant mixture becomes even more complex. Organic matter from sewage and natural sources becomes intermixed with the inorganic components of both sewage and natural materials, so we must first segregate organic from inorganic components of the sediments. The inorganic components are generally predominant in bight sediments as the organic matter content is usually <20% of dry weight (Pearce 1972). The overwhelming presence of natural silt and sand-sized particles may limit the usefulness of inorganic constituents as sewage indicators. Because the organic content of natural sediments is low and that of sewage is so high, admixture of sewage with natural sediments, even in small percentages, should substantially affect the nature of the resultant organic matter. By examining the nature of the organic matter in sediments of the bight we may be able to estimate the relative amount of the organic matter that is derived from sewage.

As part of the Marine EcoSystems Analysis Program, an organic geochemical investigation of New York Bight sediments was

[1] This study was conducted at the Atlantic Oceanographic and Meteorological Laboratories of NOAA as part of the NOAA–MESA Program, New York Bight Project.

initiated. Samples were collected from the bight apex and Hudson Shelf Valley and from other study areas being investigated as part of the MESA Program (Fig. 1). Our findings indicate that total organic carbon (TOC) and total carbohydrates (TCH), together as a ratio (TCH:TOC), may be used as qualitative and even semiquantitative indicators of sewage-derived materials in sediments.

We wish to acknowledge M. H. Hulbert, F. W. Nastav, R. Young, P. A. McGillivary, and our colleagues at the Atlantic Oceanographic and Meteorological Laboratories in Miami for their contributions. We would also like to thank the officers and crew of the NOAA ship *Ferrel* for their technical assistance and members of the NOAA/MESA program for their aid, advice, and support.

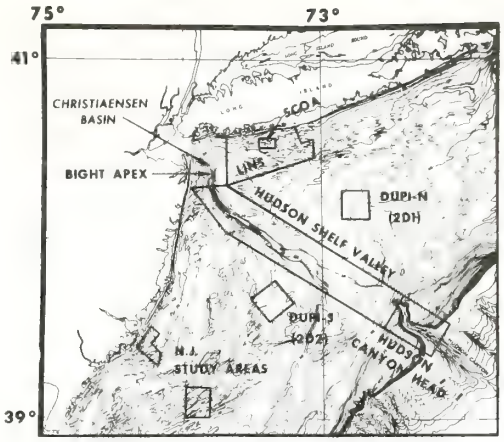


Fig. 1. Index map of the New York Bight showing the MESA geology study areas. SCOA—Suffolk County outfall area; LINS—Long Island nearshore; 2D1 and 2D2—alternate dumpsites.

Methods

Sediment samples taken with a Shipek sampler in fall 1973 were freeze-dried, and aliquots were analyzed in duplicate for total organic carbon (TOC) by a dry combustion technique (Konrad et al. 1970; Hatcher 1974). Other aliquots were analyzed in duplicate and, in some cases, triplicate for total carbohydrate (TCH) by the phenol-sulfuric acid method (Artem'yev 1970; Gerchakov and Hatcher 1972).

Results and discussion

TOC in sediments of the New York Bight—Gross (1970, 1972) analyzed various sediment samples from the New York Bight and Raritan Bay areas for TOC and noticed an enrichment of organic matter (TOC = 5%) over typical open shelf sands. Both areas are located in regions of relatively low hydraulic energy and therefore are less exposed to severe scour and erosion than open shelf sediments. These areas, therefore, act as sediment traps for muds and other fine-grained particles entrained in the water column, be they of natural or contaminant origin. Since Hunt (1961) and Froelich et al. (1971) have pointed out that TOC is inversely related to the mean size distribution of the sediment particles, we would expect the TOC to be greater in muds than in sands of the bight. It seems possible that the distribution observed by Gross (1970) may be explained, at least partially, by this phenomenon.

Pearce (1972) has determined total organic matter in various sediment samples from the bight apex and found the concentrations to be on the order of 10–20% organic matter in the mud and silt deposits of the Christiaensen Basin, which is a low topographic feature in the apex (Fig. 1). The sediments of one area in the Christiaensen Basin had an organic matter concentration >20% dry weight. This area was classified as a dead sea, devoid of the large numbers of benthic organisms typical of other similar muddy environments. The sediments were identified as black, oily muds having a consistency similar to that of mayonnaise.

In our investigation, TOC values were obtained for sediments in the bight apex and adjacent Hudson Shelf Valley (Fig. 2). Values range from less than 0.1% (dry wt) in some sands to about 5% in some silty muds found in the topographic lows. A strong correlation is observed between the bathymetry of the area shown in Fig. 1 and TOC distribution.

Although the sediments in the axis of the shelf valley and the Christiaensen Basin are all similar in grain size, some spatial dif-

ferences exist in TOC concentrations. The TOC isopleths indicate a down-valley depletion of muds high in organic carbon. It seems that these muds may be originating from the Christiaensen Basin at the head of the shelf valley. This area of the apex has silty muds relatively high in TOC (Gross 1970). However, enrichment in TOC alone cannot be taken as indicative of sewage contamination.

Carbohydrates and carbohydrate:TOC ratios—Analyses of marine sediments for carbohydrates are scarce in the literature, and no previous data are available concerning the carbohydrate content of New York Bight sediments. Our studies were initiated to measure the TCH of the sediments. The distribution as a function of dry sediment weight is shown in Fig. 3: the pattern is strikingly similar to that of TOC with the high concentrations located in the Christiaensen Basin and down the axis of the shelf valley.

To obtain a qualitative source indicator for organic matter in the bight, we report carbohydrate concentration as a percentage of TOC. In doing so, this parameter (TCH:TOC) becomes independent of sediment dry weight or of absolute concentration of organic matter and, as shown later, it more nearly defines the type of organic matter present.

The distribution of TCH:TOC in the sediments of the bight is presented in Fig. 4. Values generally range from 20 to 60 with highs located near the Long Island shore, the head of the shelf valley, and in the shelf valley itself. Since this parameter more nearly typifies the nature of the organic matter, the contours suggest that a source of organic matter exists at the head of the shelf valley and the organic material is being diluted seaward within it.

We propose that the major source of this high carbohydrate organic matter is sewage. The assumptions supporting this proposition are based on literature reports concerning the TCH:TOC ratio of various types of organic matter present in the environment. In the following discussion attention is focused on the TCH:TOC ratio of terrestrial material, phytoplankton, and sewage, since these are the major sources of organic matter in the bight. We attempt to show how the TCH:TOC ratio of each source constituent contributes to the TCH:TOC ratio in sediments of the bight.

Terrestrially derived organic matter is typically low in carbohydrates (Kononova 1966), the TCH:TOC ratio being on the

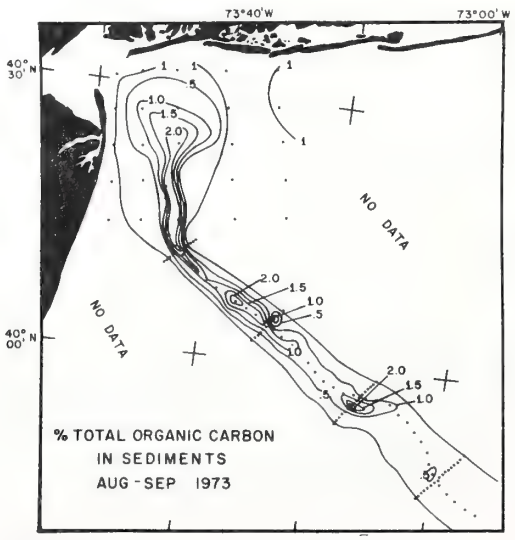


Fig. 2. Distribution of total organic carbon in sediments (dots represent sampling stations).

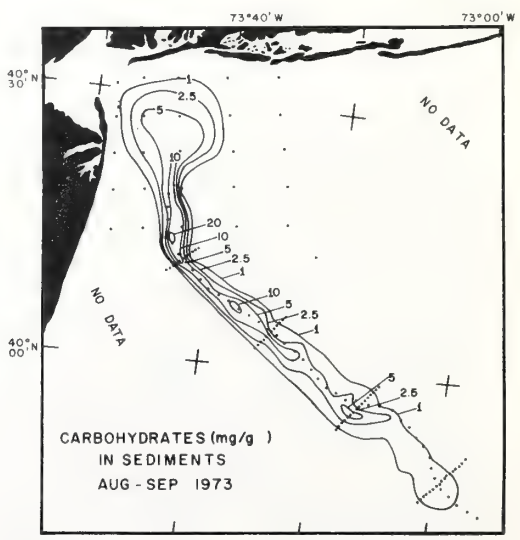


Fig. 3. Distribution of total carbohydrates in sediments.

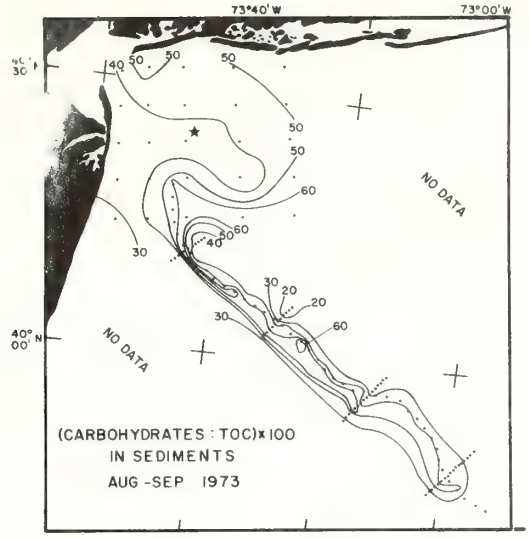


Fig. 4. TCH:TOC ratio in sediments. Star designates sewage sludge dumpsite.

order of 10–20. Waksman and Stevens (1929) showed that typical sawgrass peats had a TCH:TOC ratio of about 5—indication that a significant fraction of the carbohydrates, which are abundant in the living plants, are rapidly degraded bacterially. Waksman and Hutchings (1935) showed that a large fraction of the organic matter in various types of soils could be present as cellulose and hemicelluloses, giving a TCH:TOC ratio of up to 50; however, most of the values ranged from 10–20. Since organic matter undergoes substantial bacterial decomposition in aerobic soils, it is expected that most of the remaining carbohydrates are typically composed of resistant carbohydrates such as cellulose and hemicelluloses, and even this material undergoes bacterial decomposition with time. In fact, only small amounts of cellulose are found in materials older than the Pleistocene (Vallentyne 1963). Soils, therefore, are expected to exhibit a relatively high TCH:TOC ratio in early stages of deposition; however, this ratio decreases to essentially zero after about 10^6 years. This time frame may well apply to the terrestrial material transported to the New York Bight, because, according to Meade (1969), the net transport of fine muds in the Hudson River estuary is landward. The trapping of terrestrial material is rather efficient in this estuary and relatively little is expected to be deposited in the bight. The contribution of terrestrial material to the TCH:TOC in the bight is therefore expected to be negligible.

A major fraction of the particulate matter in the oceans, especially in nearshore areas, is composed of living planktonic plants and animals. These organisms contain substantial amounts of carbohydrates, and the TCH:TOC ratio is often around 30–80 (Strickland 1965). Easily hydrolyzable sugars such as glucose and galactose compose the major fraction of the carbohydrates with more resistant carbohydrates such as cellulose and hemicellulose composing a minute fraction (Parsons et al. 1961).

Handa (1967) observed that, with increasing depth in the oceans, the particulate carbohydrates decrease from 35 μg/liter at the surface to 10 μg/liter at 200 m and that, below this depth, the concentrations do not vary. He pointed out that, within the 200-m surface layer, a major portion of the carbohydrates is mineralized. Only the resistant polysaccharides survive this bacterial decomposition. It is expected that the TCH:TOC ratio would decrease rapidly as phytoplankton cells become part of the detritus and settle to the sediments.

As particulate detritus settles to the sediment, an increase in the decomposition rate takes place, usually within the top few centimeters. The detritus is subjected to bacterial decay, which further decreases the amounts of labile carbohydrates and even resistant carbohydrates. The net result is a decrease in TCH:TOC if the carbohydrates being decomposed are more labile than other fractions of the organic matter (TOC). So, for marine phytoplankton, whose carbohydrates are predominantly labile, a continuously decreasing TCH:TOC will occur as the organisms die and are buried in the sediments. For example, the surface sediments of the Santa Barbara Basin, where organic matter is primarily derived from phytoplankton, have a TCH:TOC ratio of 5 (Degens 1967). Sediments from an experimental Mohole (Rittenberg et al. 1963) had a TCH:TOC of 0.4 at the

surface, decreasing to less than 0.1 at a depth of 40 m. In sediments from the eastern continental shelf of the USSR, the TCH:TOC ratio was <2 (Shabarova 1955).

A large fraction of sedimentary detritus in coastal areas is derived from phytoplankton. Malone (in press) has measured the annual productivity in the New York Bight apex as 370 g/m² of carbon. This represents the most significant annual input of organic matter to the bight apex when compared to that of the Hudson River (Meade 1969) and of dumped wastes (Gross 1972). However, if phytoplankton was the major source of organic matter to sediments of the bight, the TCH:TOC ratio would be about 10 or less. Sediments of the New York Bight have a larger TCH:TOC ratio, suggesting the presence of a major organic component other than phytoplankton.

Sewage contains a substantial amount of carbohydrates, mostly in the form of cellulose and hemicellulose (Hunter and Heukelekian 1965). Its TCH:TOC ratio is about 30 (Hatcher unpublished data). After sewage is introduced into the marine environment, it undergoes microbial decomposition and a fraction of the organic matter (TOC) is lost. The cellulose and hemicelluloses may not undergo equivalent decomposition in such a relatively short period of time; TCH:TOC may therefore increase as the organic matter undergoes early stages of decomposition. With increased biodegradation, TCH:TOC for sewage-derived organic matter may increase to values ranging from 40 to 60 or greater. These values were estimated based on our observations of the TCH:TOC distribution in the bight. We do not expect a high TCH:TOC to be derived from either terrigenous material or phytoplankton. As stated earlier, the TCH:TOC of sediments derived from each of these sources is observed to decrease with depth in the sedimentary column. Decomposition thereby decreases the TCH:TOC ratio of terrigenous organic matter and phytoplankton-derived organic matter. Our inability to explain high values such as 50 or 60 as being derived from a high TCH:TOC source other than that of sewage leads us to assume that decomposition of sewage increases its TCH:TOC.

Input of sewage to the bight occurs via ocean disposal of sewage sludge, ocean outfalls, and outfalls within the Hudson River. In addition, dredge spoils from the Hudson River estuary, barge-dumped in the bight, are likely to contain large amounts of sewage-derived materials. The total amount of organic matter of sewage origin can thus be calculated, based on the values of Gross (1972), to be roughly half that supplied by primary productivity. However, we believe that, of the organic matter which eventually settles to the sediment, the portion derived from sewage should constitute a major fraction. This is due primarily to the fact that sewage materials are relatively less biodegradable than phytoplankton detritus, and a larger portion of the former is apt to be retained in the surface layers of sediment.

Since the organic matter in sediments of the bight is derived mostly from the two aforementioned sources (phytoplankton and sewage) the resultant TCH:TOC will, in general, be a weighted average of TCH:TOC from each source, the weight factor of each being based on its relative contribution to the sediment organic matter. A high TCH:TOC ratio of 40–50 should indicate that the organic matter contains relatively large amounts of sewage-derived materials. It follows that a TCH:TOC ratio of 20 or less should indicate that the sediment organic matter is composed of phytoplankton organic matter alone or in combination with a smaller amount of sewage. It is obvious, from the previous discussion, that the TCH:TOC ratio is mostly used in a qualitative manner and, at best, a semiquantitative fashion. By semiquantitative, we mean that, in measuring TCH:TOC of a sediment, it is possible to delineate only whether the individual sources contribute a large or small percentage to the organic matter. Before making any more quantitative estimates of source contribution, substantially more information must be obtained on the various sources of organic matter to the bight. First, there must be better estimates of the total inputs of terrigenous matter and phytoplankton to the bight apex. Second, in situ

measurements should be made to determine the change in TCH:TOC of various source materials with decomposition. Due to the difficulty of the aforementioned tests, it seems doubtful that all the proper experiments necessary to render the TCH:TOC ratio quantitative will ever be performed. For now, our best hopes are for semi-quantitative estimates of source inputs. In the following discussion we address several regions of the bight and attempt to estimate the relative contribution of sewage to the organic matter in sediments based on the TCH:TOC ratio.

Various sedimentary facies were sampled in the bight, and a wide range of sediment types exists. Samples collected near the Long Island shore and in the apex have a high TCH:TOC ratio (40–60) as shown in Fig. 4. The few samples collected in this area do not necessarily give a true indication of the range of values to be expected. Several additional cruises were made to collect more samples from this area. These cruises were code-named substrate monitoring program (SUMP) and substrate inventory sampling (SIS). The SUMP cruise was designed to obtain sediment samples every ¼ mi along two lines: one extending from the sewage sludge dumpsite to within ½ mi of Atlantic Beach, Long Island, and the other extending from the New Jersey coast to Cholera Bank (73°44′W) along 40°25′N lat (Fig. 5). The SIS cruise was designed to obtain sediments on a dense grid along the Long Island shoreline extending from Rockaway Point to Jones Beach (Fig. 6). The TOC and TCH:TOC data for selected samples from both cruises are presented in Table 1. In general, the sands have a TCH:TOC ranging from 50–60 and a TOC <1%. The silty or black muds have a TCH:TOC of 40–50 and a TOC >1%.

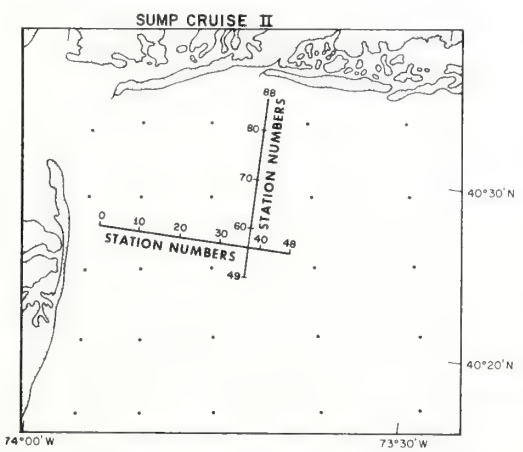


Fig. 5. Tracklines and sample locations for SUMP cruise, January 1974.

The silty muds located in the Christiaensen Basin (SUMP samples 29, 21, 33) and in various sections of the SIS area (SIS samples P-23, P-21, Q-30) were similar to those described (Harris 1974) as having a black "mayonnaisey" consistency which is most likely imparted by the amount of sewage or sewage-derived materials present. The silty muds from both areas have a similar TCH:TOC suggesting that the organic matter is of similar origin. As stated, the high TCH:TOC suggests that the source of this organic matter is predominantly sewage.

The sands located along the Long Island shore typically have a higher TCH:TOC than the silty muds of the same area. Here again, the high TCH:TOC strongly suggests that organic matter is of sewage origin. However, the organic matter (TOC) has most likely undergone more biological decomposition and the ratio has been elevated by this process.

In speculating about the distribution and fate of sewage-derived materials along the Long Island shore and in the apex, we suggest that sewage is being dispersed throughout the apex and that it accumulates mostly in topographic lows. However, some of the sewage particles settle and are trapped within the sands where they undergo more biological decomposition than if they had settled in the mud patches or topographic lows.

We must also point out that while organic matter in the muds may be primarily derived from sewage or sewage sludge, the muds themselves are far from being similar to sewage sludge. Almost an order of magnitude difference exists between the TOC of sewage sludge (≃40%) and that of the silty muds (3–5%). Obviously a substantial amount of decomposition, dissolution, or

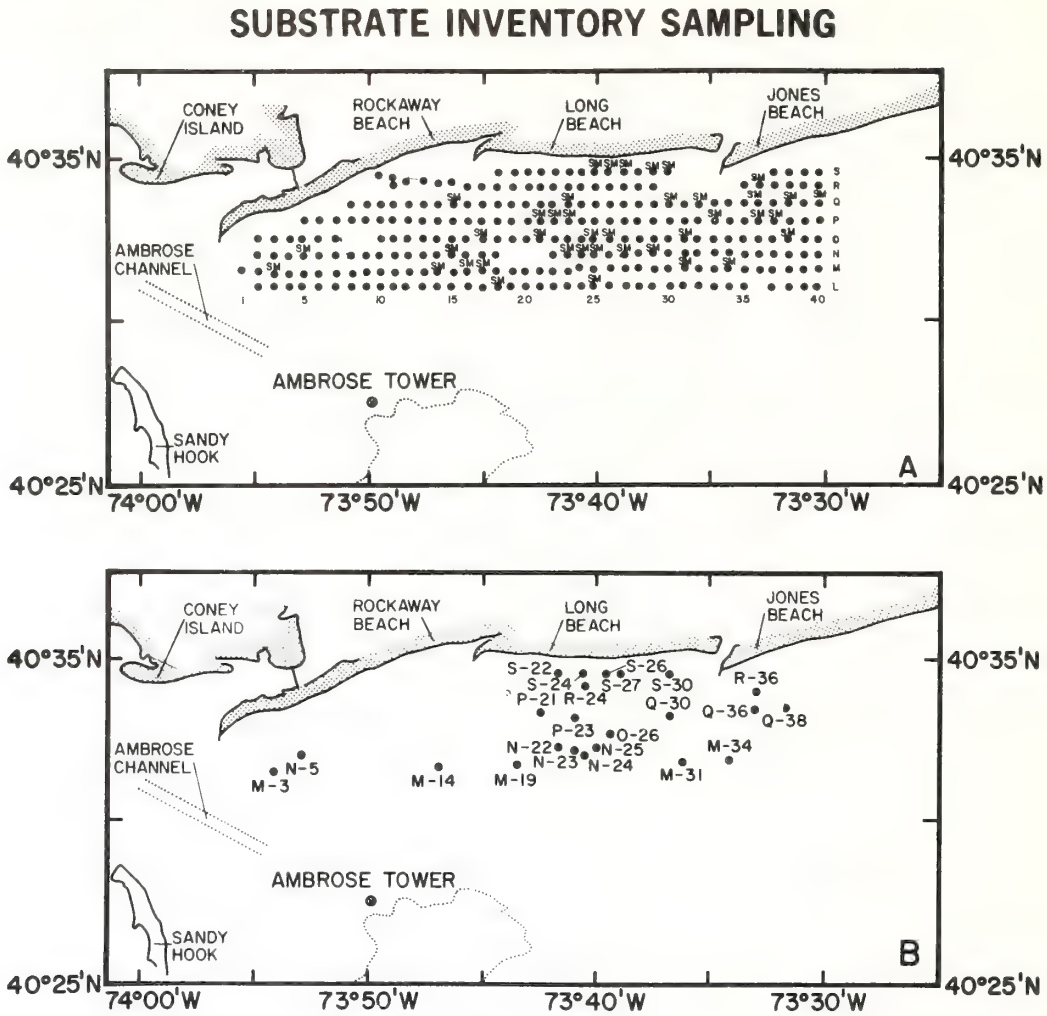


Fig. 6. Sampling locations for SIS cruise (June 1974). A—Proposed grid; B—station locations of samples taken for organic analyses.

dilution of the sewage sludge organic matter must occur before it is incorporated in the sediments. Sewage-derived materials, therefore, comprise only a minor fraction of the dry weight in silty muds. An even smaller amount of sewage-derived materials exists in the sandy sediments.

Sandy sediments near the New Jersey coastline have high TCH:TOC (30–40) values, but not nearly as high as those from the Long Island shoreline. Again, sewage must play a large role in supplying organic matter to the sediments. However, the supply of organic matter may be influenced by the Hudson River, whose plume almost always flows south along the New Jersey coastline. Although the organic matter in the Hudson plume may be primarily of sewage origin, a smaller fraction may consist of terrestrial and phytoplankton organic matter having a lower TCH:TOC ratio. The resultant mixture of sewage and terrestrial material imparts a TCH:TOC of 30–40 to the sediments in contrast to the 50–60 value expected if they were similar to the Long Island sands.

Sands located on the outer continental shelf, adjacent to the Hudson Shelf Valley, have a much lower TCH:TOC ratio, varying from 18–30. We would expect that or-

Table 1. Bulk organic properties of SUMP and SIS sediments.

SUMP			SIS		
Sta.	% TOC	TCH:TOC	Sta.	% TOC	TCH:TOC
9	0.46	35	M-3	0.09	52
11	2.99	42	M-14	0.77	53
13	1.40	30	M-19	0.15	57
15	0.64	44	M-31	0.71	57
21	2.45	39	M-34	0.23	43
23	1.96	52	N-5	0.09	53
25	1.64	61	N-22	0.08	54
28	1.26	58	N-23	0.28	52
29	2.85	52	N-24	0.08	44
31	5.08	43	N-25	0.05	50
33	3.85	49	O-26	1.20	40
35	3.04	65	P-21	2.31	47
58	0.35	41	P-23	5.21	46
62	0.41	56	Q-30	1.86	51
66	0.84	52	Q-36	0.18	42
69	0.48	62	Q-38	1.99	41
78	0.05	40			
82	0.17	47			
85	0.12	54			
88	0.10	64			

ganic materials present in the bight apex should contribute little to the organic matter of sediments in this offshore region, due simply to dilution processes as the materials are transported there. Oceanic material, therefore, becomes a more significant contributor to the sedimentary organic matter. The TCH:TOC ratio would, therefore, be expected to be more representative of phytoplankton detritus (ca. 10 or less). The fact that TCH:TOC is higher (18–30) indicates that sewage or terrestrial organic matter is still present.

Within the Hudson Shelf Valley, which extends from just south of the apex area out to the shelf break, the sediments are primarily fine-grained silty muds and TCH:TOC varies from 30–60 (Fig. 4). The TCH:TOC ratio in silty muds at the head of the shelf valley, along the axis, is about 60. As we progress seaward, the TCH:TOC ratios in muds of the axis steadily decrease to values of 30 or less. The fact that TCH:TOC decreases probably indicates that nonsewage-derived components (phytoplankton) constitute a more significant fraction of the organic matter in the muds at greater distances from shore.

The muds located just south of the Christiaensen Basin in the Hudson Shelf Valley have a relatively high TCH:TOC ratio (50–60). The sedimentary environment is similar to that found in the Christiaensen Basin, and the TCH:TOC ratio would be expected to be similar. However, the values are closer to those found in the sands near the Long Island shoreline than to those of muds of the Christiaensen Basin. It seems likely that the organic matter, if derived from the same source as Christiaensen Basin muds, has undergone more decomposition. It is possible that the muds of the Hudson Shelf Valley are derived from muds being deposited in the Christiaensen Basin and that these are being resuspended and redeposited in the shelf valley. This resuspension, transport, and redeposition effectively subject the sewage-derived organic matter to increased decomposition, thereby increasing the TCH:TOC ratio.

As we have pointed out, the TCH:TOC ratio may be used to semiquantitatively measure the relative contribution of sewage to the sediment organic matter of the bight. This measure, however, only relates to that part of the sediment which is organic. The inorganic fraction of the sediment may be derived from different sources. This is especially true for sands where the fine and coarse fractions are transported by differ-

ent mechanisms and forces. So, in order to estimate the absolute amount of sewage-derived materials in the sediments, we must take into account both the TCH:TOC ratio and the absolute amount of organic matter. We must also attempt to define the amounts of sewage-derived inorganic components, since these may contribute equally as much to the sediment weight. As little is known of inorganic constituents at this time, we must rely on TCH:TOC and TOC to measure semiquantitatively only the contribution of sewage-derived organic matter to the sediment.

References

ARTEM'YEV, V. YE. 1970. Carbohydrates in bottom sediments of the central Pacific. Oceanology **10**: 508–513.

DEGENS, E. T. 1967. Diagenesis of organic matter, p. 343–390. *In* G. Larsen and G. V. Chilingar [eds.], Diagenesis in sediments. Elsevier.

FROELICH, P., B. GOLDEN, AND O. H. PILKEY. 1971. Organic carbon in sediments of the North Carolina continental rise. Southeast. Geol. **13**: 91–97.

GERCHAKOV, S. M., AND P. G. HATCHER. 1972. Improved technique for analysis of carbohydrates in sediments. Limnol. Oceanogr. **17**: 938–943.

GROSS, M. G. 1970. Analysis of dredged wastes, fly ash and waste deposits, New York metropolitan region. Mar. Sci. Res. Center Tech. Rep. 7, SUNY, Stony Brook.

———. 1972. Geologic aspects of waste solids and marine waste deposits, New York metropolitan region. Geol. Soc. Am. Bull. **83**: 3163–3176.

HANDA, N. 1967. Identification of carbohydrates in marine particulate matters and their vertical distribution. Rec. Oceanogr. Works Jap. **9**: 65–73.

HARRIS, W. H. 1974. Sewage sludge expansion, migration, accumulation, and identification, Nassau Co., New York inner continental shelf. U.S. Congress, Senate, Committee on Public Works, Subcommittee on Environmental Pollution; sewage sludge hazard to Long Island beaches: Hearing, 93rd Cong. 93-H52, p. 297–330.

HATCHER, P. G. 1974. A study of the organic geochemistry of Mangrove Lake, Bermuda. M.S. thesis, Univ. Miami.

HUNT, J. M. 1961. Distribution of hydrocarbons in sedimentary rocks. Geochim. Cosmochim. Acta **22**: 37–49.

HUNTER, J. V., AND H. HEUKELEKIAN. 1965. The composition of domestic sewage fractions. J. Water Pollut. Control Fed. **37**: 1142–1163.

KONONOVA, M. M. 1966. Soil organic matter, 2nd ed. Pergamon.

KONRAD, J. G., G. CHESTER, AND D. R. KEENEY. 1970. Determination of organic and carbonate carbon in freshwater lake sediments by a microcombustion procedure. J. Thermal Anal. **2**: 199–208.

MALONE, T. C. In press. Phytoplankton productivity, nutrient recycling, and energy flow in the inner New York Bight. NOAA-MESA Tech. Rep.

MEADE, R. H. 1969. Landward transport of bottom sediments in estuaries of the Atlantic Coastal Plain. J. Sediment. Petrol. **39**: 222–234.

PARSONS, T. R., K. STEPHENS, AND J. D. H. STRICKLAND. 1961. On the chemical composition of eleven species of marine phytoplankters. J. Fish. Res. Bd. Can. **18**: 1011–1016.

PEARCE, J. B. 1972. The effects of solid waste disposal on benthic communities in the New York Bight, p. 404–411. *In* M. Ruivo [ed.], Marine pollution and sea life. Fish. News.

RITTENBERG, S. C., AND OTHERS. 1963. Biochemistry of sediments in experimental Mohole. J. Sediment. Petrol. **33**: 140–172.

SHABAROVA, N. T. 1955. The biochemical composition of deep-water marine mud deposits (ocean-bottoms). Biokhimiya **20**: 146–151.

SHELTON, R. G. J. 1971. Sludge dumping in the Thames estuary. Mar. Pollut. Bull. **2**: 24–27.

SOUTHERN CALIFORNIA COASTAL WATER RESEARCH PROJECT. 1974. Annual report. SCCWRP, El Segundo, Calif.

STRICKLAND, J. D. H. 1965. Production of organic matter in primary stages of the marine food chain, p. 478–610. *In* J. P. Riley and G. Skirrow [eds.], Chemical oceanography. Academic.

VALLENTYNE, J. R. 1963. Geochemistry of carbohydrates, p. 456–502. *In* I. A. Breger [ed.], Organic geochemistry. Pergamon.

WAKSMAN, S. A., and I. J. HUTCHINGS. 1935. Chemical nature of organic matter in different soil types. Soil Sci. **26**: 113–137.

———, AND K. R. STEVENS. 1929. Contribution to the chemical composition of peat. 3. Chemical studies of two Florida peat profiles. Soil Sci. **21**: 271–279.

Marine Sediment Transport and Environmental Management, D.J. Stanley and D.J.P. Swift, eds. (John Wiley & Son, Inc.). Chapter 19, 461-477.

CHAPTER 19

Chemistry and Continental Margin Sedimentation

PATRICK G. HATCHER and DOUGLAS A. SEGAR

Atlantic Oceanographic and Meteorological Laboratories, Miami, Florida

The coastal zone is an area that has been defined as the junction between two major biomes where the land meets the ocean (Ketchum, 1972). Since many processes in both environments are intensified at their boundaries, the continental shelves, although limited in size, are areas of dynamic change. Therefore, the coastal zone has been known as an area of intense hydraulic, depositional, chemical, and biological activity.

The chemical transformations occurring during sedimentation on the continental shelf are of fundamental importance in environmental processes such as the corrosion of materials, removal of contaminants from the water column, provision of food for benthic organisms, renewal of nutrient supplies in the water column, and transport of sediment.

Whenever man has used the ocean, chemical changes have been brought about in that environment. These effects are at their greatest on the continental margins where man's presence is pervasive and his impact increasingly intense. Shipping, ocean dumping, river discharge, offshore drilling, dredging, and bottom trawling all affect the chemistry of the ocean ecosystem, often in subtle ways. The change presenting probably the greatest potential for environmental degradation is the addition of toxic contaminants to the ecosystem. Solid phases are good scavengers for many contaminants so that perhaps the most important feature of continental shelf sedimentation from an environmental standpoint is the detoxification of contaminants and their removal to the sediments. Such removal may be essentially permanent or may be only temporary, with the toxic chemical species being released during diagenesis and bioturbation of the sediments.

THE SIGNIFICANCE OF THE SHELF ENVIRONMENT TO MAN'S ACTIVITIES

Aside from being the most productive areas in the world oceans, the continental shelves are the nursing grounds for a majority of the commercially important marine organisms. The nations of the world annually harvest over 10 billion pounds of commercial fish from the coastal zone (Pruter, 1972). Therefore, the natural balance of the shelf environment is important to the many fisheries that have established themselves along the coast. Although the bounty is plentiful, the natural processes that control the populations are delicately balanced. Biological systems of the shelf are subjected to extreme chemical and physical changes in their environment, and many organisms subsist at or near their tolerance limits for such changes. Any imbalance in these environmental conditions (especially chemical) may alter the biological structure.

The shelf environment provides an abundance of mineral resources. Recently, the supply of petroleum products has become critically short. The continental shelves house a tremendous supply of untapped oil. In the United States alone the amount exceeds five times the present known land reserve of oil (American Gas Association, 1971). It is expected that extensive drilling for oil will occur on our continental shelves in the near

future. The shelf environment will feel the impact, with its delicate chemical balance threatened by petroleum products, some of which are highly toxic.

The large sand and gravel deposits located near metropolitan areas such as New York and Boston are a significant resource (Schlee et al., 1971). The demand for large quantities of sand and gravel in the building industry has generated interest in these deposits as a valuable source for the expanding needs of the future. Mining of these deposits could alter the biological and chemical balance of the shelf by releasing excess nutrients, organic materials, and toxic substances which had previously been removed from the natural chemical cycle.

Various recreational activities such as boating, sport fishing, and swimming constitute important uses of the continental shelf. Loss of aesthetic quality of water and sediment would directly impact these recreational facilities. Inversely, the ever increasing use of the continental shelf for recreation has led to a steady decline in water quality over the years, again endangering the delicate chemical and biological balance.

Finally, because of its proximity to land and its accessibility, the coastal zone has been, for centuries, the area where major population centers and industries have evolved. The continental shelf has felt this effect through the centuries. Now, as populations increase, the shelf is becoming endangered by the many chemical and biological wastes associated with urban growth. In metropolitan New York alone, 4.6 million metric tons of wastes are being dumped onto the shelf annually. These wastes include dredged material, construction wastes, acid-iron wastes, and sewage sludge (Gross, 1972). Obviously, the chemical constituents present in these wastes have a significant effect on the chemical and biological balance in the New York Bight.

CHEMICAL CHARACTERISTICS OF NEARSHORE SEDIMENTS

Bottom sediments are extremely complex mixtures of many different solid phases. Deep-sea sediments are predominantly fine-grained in texture. In contrast, nearshore sediments comprise a large range of grain sizes. Because of the many physical forces tending to redistribute these sediments, the spatial heterogeneity in composition is very large.

The principal phases of marine sediments include biologically and abiologically produced carbonates, alumino-silicate minerals, quartz, iron and manganese hydroxide phases, biogenic silica, and biologically produced organic matter. The relative proportions of these components are determined by a multitude of factors. However, one factor is predominant in the coastal zone the presence of river runoff. Despite the relatively high productivity of many coastal areas, calcium carbonate contents of continental margin sediments are low particularly adjacent to the major river systems. The major components of shelf sediments are quartz, amorphous silica, various feldspars, clay minerals, and a wide variety of heavy minerals all of which are characteristic of river drainage.

Coastal sediments in most instances differ from deep ocean sediments only in the wider range of concentrations of organic matter and trace components. Coastal sediments can range from 0.2 to 10% organic carbon (Gross, 1972) or in anoxic basins up to as much as 7% organic carbon (Richards, 1965). Generally, nearshore sediments have relatively high silica contents derived from river runoff. Exceptions are found where this runoff is quantitatively small or where carbonate precipitation occurs, as in the Bahamas. The trace element concentrations of nearshore sediments generally are lower than in deep ocean sediments and tend to approximate those of igneous rocks (Table 1). This is simply a reflection of the dominance of erosional debris from the continents in most nearshore sediments.

TABLE 1. The Distribution of Trace Elements in Marine Sediments and Igneous Rocks

Trace Element	Igneous Rocks* (ppm)	Nearshore Sediments† (ppm)	Deep-Sea Clays‡ (ppm)
Cr	65	100	77
V	130	130	330
Cu	42	48	570
Pb	13	20	160
Ni	50	55	290
Co	19	13	120
Sn	2	21	20
Ba	530	750	2200
Sr	340	<250	590
Zr	150	160	150
Ga	17	19	20

* Average trace element content of basalts, granites, and granodiorites. Adapted from Turekian and Wedepohl (1961).

† Adapted from Wedepohl (1960) with the exception of Sn and Sr which are taken from El Wakeel and Riley (1961).

‡ Adapted from El Wakeel and Riley (1961), Goldberg and Arrhenius (1958), and Young (1954).

Organic matter in nearshore sediments is generally a complex mixture arising from a multiplicity of sources. Inputs derived from the leaching of terrigenous organic

matter and from phytoplankton in shelf waters all combine to form this complex mixture. Although the major portion of organic matter is uncharacterized, some of the more significant contributors are known. These include humic acids which are primarily derived from terrigenous soils (Kononova, 1966), carbohydrates, amino acids, and proteins. Carbohydrates generally constitute approximately 5% of the organic matter (Rittenberg et al., 1963; Degens, 1967). However, in some cases, up to 35% of the organic matter is composed of carbohydrates (Segar et al., 1975; Hatcher and Keister, in preparation). Amino acids generally constitute between 10 and 90% of the organic matter in Recent shelf sediments (Degens, 1967). Other components such as fatty acids, hydrocarbons, phenolic compounds, and aromatic compounds constitute less than 1% of the organic matter.

SOURCES OF CHEMICAL CONSTITUENTS

The river transport of sediment to the oceans has been estimated at approximately 3.6×10^{15} g/year (Turekian, 1971). However, only a small fraction reaches the deep sea with the major portion being deposited on the continental shelf and slope. The primary constituents of these sediments are quartz, various feldspars, clay minerals, and others which are primarily dependent on the igneous rock compositions in the watersheds. The organic matter so derived is characteristic of soil organic matter from the watershed and therefore is high in humic materials.

Hydrogenous components constitute a major fraction of continental shelf sediments. These include materials resulting from the formation of solids from dissolved components by inorganic reactions in the water column (Goldberg, 1954). Carbonates, phosphates, some silicates, sulfates, oxides, and hydroxides are the major components of this class.

Biogenous material is another significant component of sedimentary material on the continental shelf. This includes carbonate shell debris, siliceous skeletons, and indigenous organic matter.

A small but often significant fraction of marine sediments is eolian-transported material. Volcanic and windblown debris and, more recently, volatile synthetic organic materials and industrial trace metal aerosols are all introduced to marine sediments via the atmosphere.

EFFECTS OF COASTAL PROCESSES ON THE DISTRIBUTIONS OF CHEMICAL SPECIES

Importance of the Estuarine Interface

Most of the chemical species, including contaminants, reach the ocean via the rivers of the world. They enter the oceans both in solution and as suspended particles. As river water mixes with seawater, significant changes take place in the physical and chemical environment in the water column. Ionic strength is increased and the pH usually rises significantly. These changes produce dramatic shifts in the equilibria between the solid and dissolved phases. In this context, the estuarine interface should be defined as including not only the estuary itself but also the area of open ocean within which the bulk of marine sediments are initially deposited.

The changes in equilibria occurring between dissolved and particulate chemical species in passing the estuarine interface are poorly known. The general events observed for trace metals (Turekian, 1971) and many organic compounds are as follows:

1. The increased concentrations of major ions in solution compete effectively for adsorption and ion and ligand exchange sites on particle surfaces, releasing the sorbed contaminants to solution (Kharkar et al., 1968).
2. The increased ionic strength and conductivity of the solution induces a "salting out" effect that causes finely divided colloidal and particulate matter to aggregate and settle out.
3. The increased pH and ionic strength together interact to reduce the solubility of a number of elements. Iron and manganese precipitate as hydroxides, and aluminum, silicon, and several other elements may precipitate as complex hydrated oxides. Dissolved organic materials such as fulvic and humic acids may also precipitate at this interface.

The three processes known to occur in the estuarine interface take place at different rates and at different geographical locations in the mixing zone determined by a complex of environmental factors not yet understood. Turekian (1971) has described the general features of trace metal cycles in Long Island Sound (Fig. 1). The Sound is essentially the seaward end of an estuary, fresh water being added at the southern end and from numerous rivers and streams along both its shorelines. The chlorosity distribution (Fig. 2) indicates that progressive mixing with seawater takes place along the length of the Sound. At the eastern end of the Sound, seawater enters as a bottom layer and lower salinity water leaves at the surface, predominantly in the upper 20 ft of the water column. The distributions of dissolved cobalt, nickel, and silver in and just outside the Sound are all similar (Figs. 3–5). Despite the considerable river-borne input of industrial contaminants and natural metals, the dissolved trace element concentrations are relatively uniform along the length of Long Island Sound. In fact, the water leaving the Sound appears to have somewhat lower trace metal concentrations that the sea-

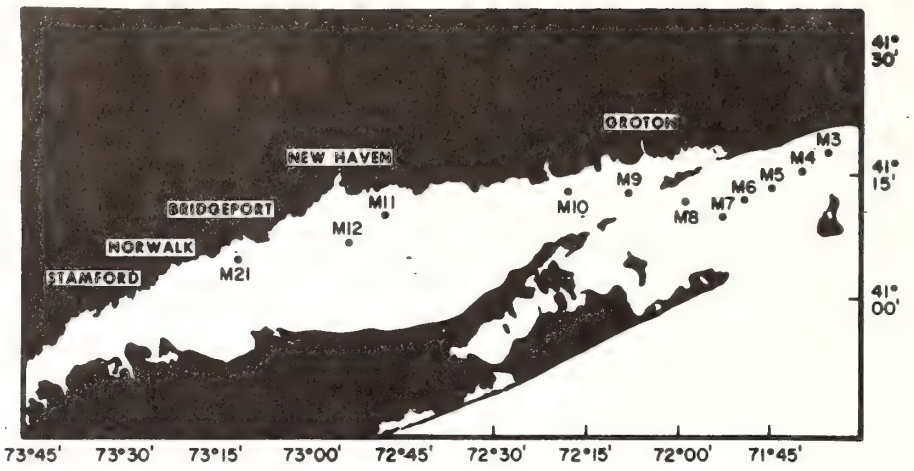


FIGURE 1. *Long Island Sound showing longitudinal transect stations. Modified from Turekian (1971).*

water entering. This illustrates the efficiency with which sedimentation processes in the estuarine interface remove contaminants from the water column.

Mechanism of Scavenging from Solution

In order to be able to predict and understand the fate of dissolved solids added to the oceans in the coastal zone, we must establish the mechanisms by which these elements or compounds are removed from seawater and added to the sediments. The scavenging mechanisms of elements, particularly trace metals, have been the subject of extensive study during the history of oceanography. Despite this effort, we still have only a very incomplete knowledge of the factors that control the concentrations of most elements in solution.

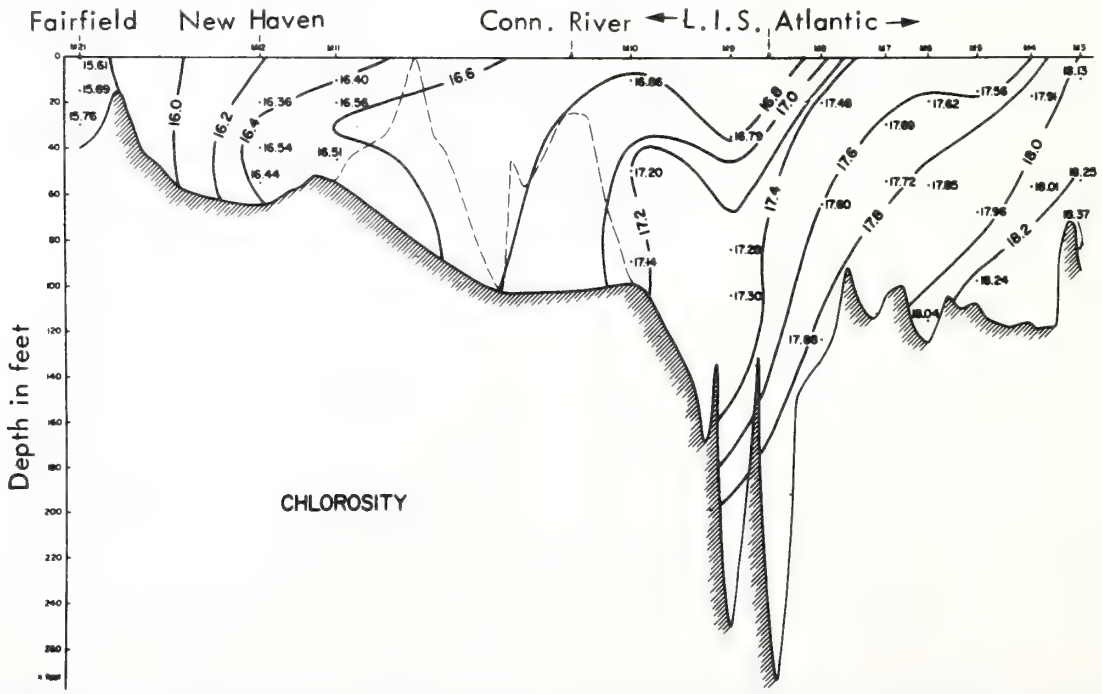
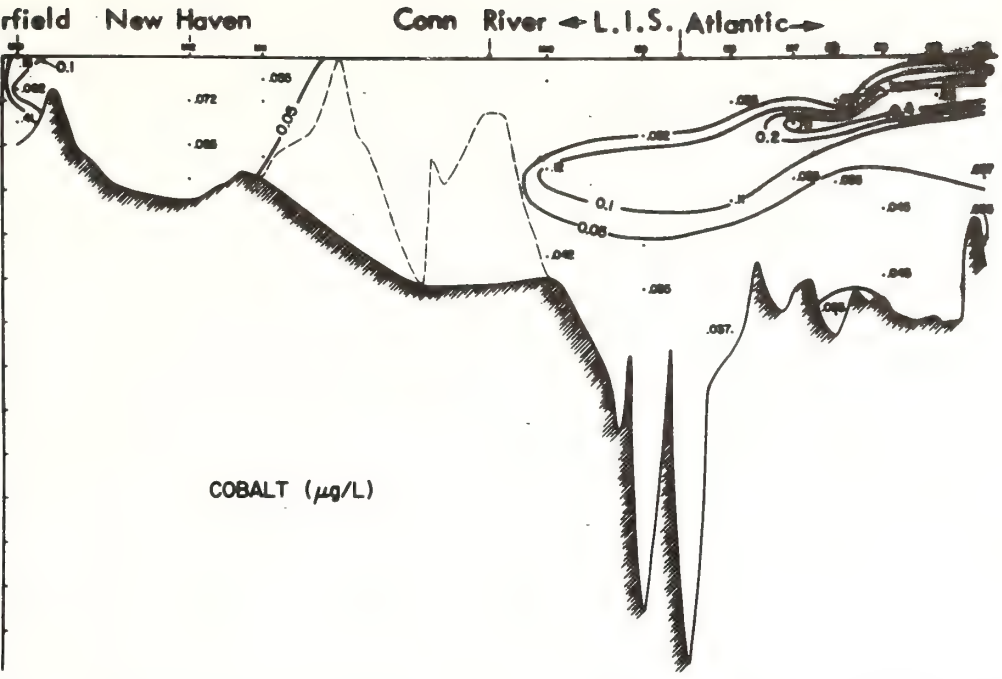
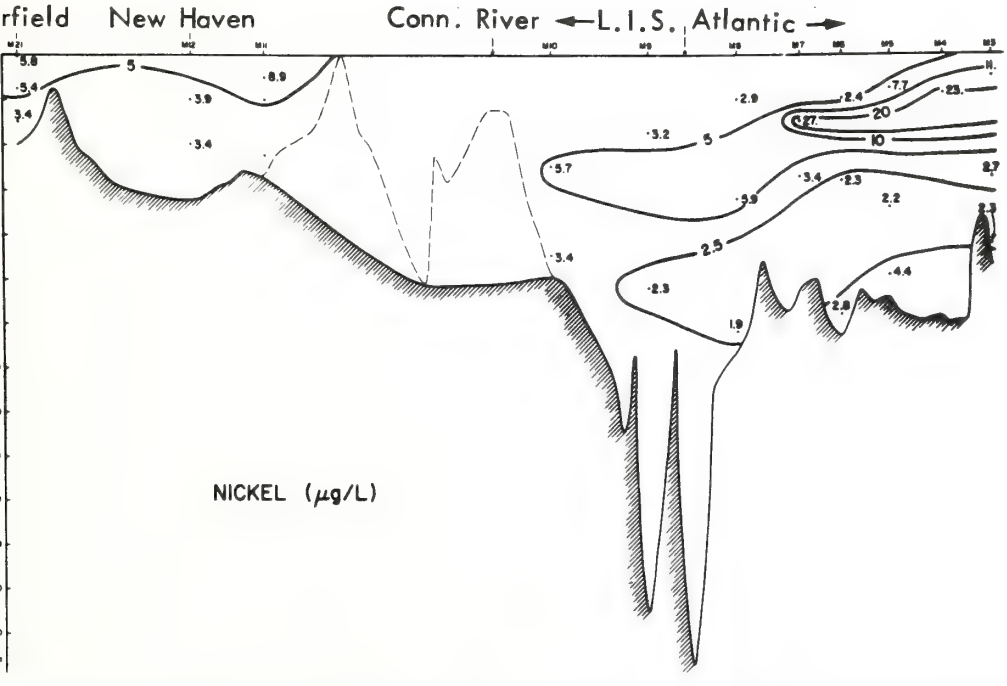


FIGURE 2. *Chlorosity distribution on longitudinal section of Long Island Sound, summer 1964. Modified from Turekian (1971).*



RE 3. *Cobalt distribution on a longitudinal section of Long Island Sound, summer 1964. Modified from ian (1971).*



RE 4. *Nickel distribution on a longitudinal section of Long Island Sound, summer 1964. Modified from ian (1971).*

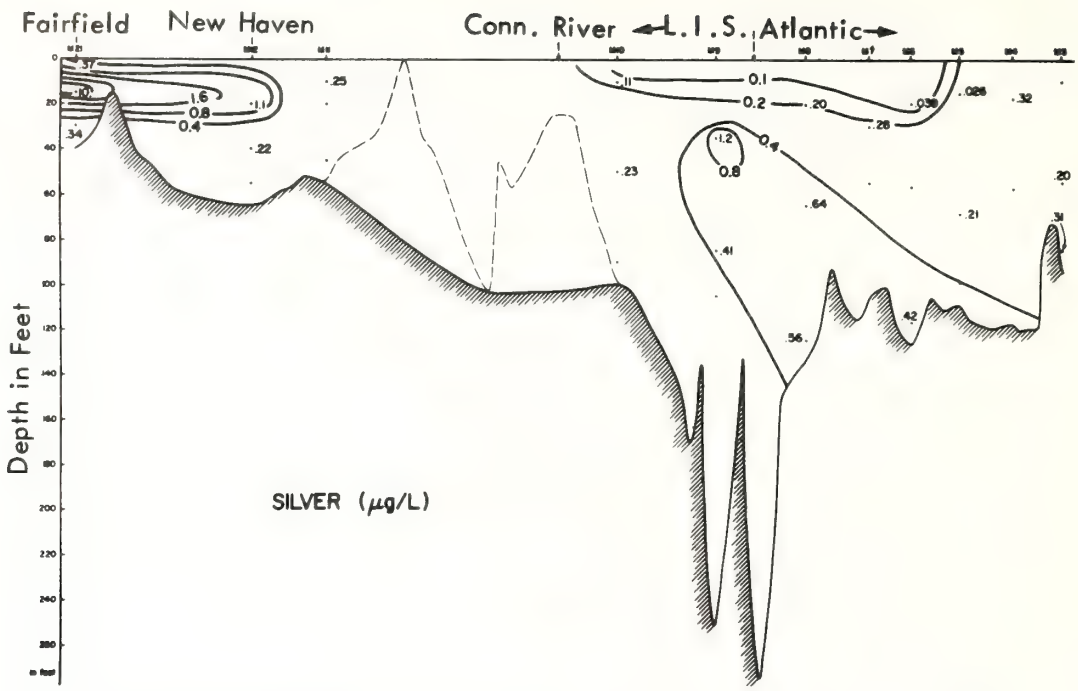


FIGURE 5. *Silver distribution on a longitudinal section of Long Island Sound, summer 1964. Modified from Turekian (1971).*

Krauskopf (1956) conducted a theoretical and experimental evaluation of direct precipitation, adsorption, and biological scavenging processes in controlling the concentration of various elements in seawater. His conclusions have remained little changed despite the considerable amount of subsequent research. The concentrations of all but a very few elements (Ca, Sr, Ba) in open ocean water are many times below their solubilities. Therefore, direct precipitation of their insoluble salts cannot occur. An exception to this rule occurs in anoxic waters (e.g., Norwegian fjords, Black Sea, etc.) where precipitation of many elements with extremely insoluble sulfides may occur. Another exception occurs at the estuarine interface. River waters, having a lower ionic strength and lower pH than ocean water, contain high concentrations of elements such as silicon, aluminum, iron, and manganese. These elements all have very insoluble hydrated oxides which precipitate at the interface.

The chemical interactions between solid surfaces and solutes are extremely complex. Mechanisms such as adsorption, ion exchange, ligand exchange, coprecipitation, and mixed crystal formation can all lead to the scavenging of elements or organic compounds from solution. Krauskopf (1956) showed that hydrous manganese and ferric oxides, organic detritus from different sources, and certain clay minerals are all effective in removing metals from seawater, whereas quartz and calcium carbonate are not. Lowman et al. (1966) have observed the precipitation or scavenging of several elements in experiments where filtered river and seawater were mixed.

The ocean waters of the continental margins generally contain much larger quantities of suspended particles than are found in the deeper oceans (Manheim et al., 1970; Buss and Rodolfo, 1972). In addition, a large fraction of the particles suspended in the coastal zone have been recently introduced to the marine environment and are out of equilibrium with the dissolved phase. The surface activity of such particles is therefore great, and they are potentially efficient scavengers of dissolved trace components. Hence, the coastal zone is an area where efficient scavenging of allochthonous constituents occurs.

Composition of Seawater and the Concept of Residence Time

Knowledge of sediment chemistry is important for its application to studies of the transport of elements and organic compounds among the solid, dissolved, and biological phases. Over 75 elements have been detected or determined in solution in seawater as well as many organic compounds (Riley and Chester, 1971). These dis-

solved components are not in equilibrium with solid phases in the oceans. Therefore, transfers take place between the dissolved phase and both nonliving and living solid particles in the ocean. As there is a constant supply of dissolved components to the oceans from the land, the net effect of these transports for most elements or compounds is a loss from the water to the sediments. Marine sediments act as a sink for material added to the ocean, although the removal and deposition may be either temporary or permanent.

The upper few centimeters of sediments generally contain trace elements in excess of those found in all of the overlying water column including suspended particulates and biota. This is illustrated by the distributions of Co, Fe, Mn, and Zn in a Texas Bay ecosystem (Parker et al., 1963); see Table 2. Similar distributions have been observed in coastal ecosystems in many parts of the world. As the upper layer of sediments in the continental shelf undergoes extensive bioturbation and reworking by wave, tide, and current energy, transport of chemical compounds between the overlying water column and the sediments down to depths of 10 cm or more will take place readily and will be more rapid than similar processes in the deep ocean where diffusion is the dominant transport mechanism.

TABLE 2. Distribution of Total Mass of Cobalt, Iron, Manganese, and Zinc in Water, Sediments, and Biota of a Texas Salt Marsh

	Mass (mg/m^2)			
Element	Bay Water (1 m depth)	Sediments (upper 3 cm)	Plants	Animals
Co	0.5	12.0	3.8	0.0012
Fe	30	30,000	1,496	0.414
Mn	5	2,740	700	0.075
Zn	8	900	350	0.173

Source Adapted from Parker et al. (1963).

The composition of river water is very different from that of the ocean. Some elements, notably sodium, potassium, chlorine, calcium, magnesium, and strontium, are found in very much lower concentrations in river water than in seawater. Others (trace transition elements, aluminum, and silicon) are found in higher concentrations in river discharge than in the ocean. As the composition of river water has not changed drastically over geological time, the composition of the oceans does not necessarily reflect the accumulation of river water in the ocean basins. Water itself is removed from the oceans by evaporation and recycled by rainfall. About 0.002% of the water in the oceans is recycled by this mechanism each year. Although some dissolved salts are entrained in aerosols and recycled by rivers, another mechanism (removal to the sediments) must be operative in order for the present concentrations of elements in the ocean to have been achieved. The concentrations of elements in seawater therefore represent a balance between their input from rivers and atmospheric aerosols and their removal to the sediments.

From a knowledge of the total quantity of an element dissolved in the ocean and either the rate of input from land or the sedimentation rate, the mean residence time of an element in seawater can be calculated (Goldberg, 1965). The mean residence time is simply the time it would take new inputs to double the existing concentration in the absence of removal mechanisms. The residence time is also the length of time required for sedimentation to remove all of an element from the oceans if no new inputs were made and if the sedimentation rate for the element did not depend on its concentration. The observed residence times for various elements range from as little as 100 up to hundreds of millions of years (Riley and Chester, 1971). The alkali and alkaline earth elements have residence times in excess of 10^6 years, as the processes of sedimentation do not efficiently scavenge them from solution. In contrast, elements such as aluminum, iron, chromium, titanium, beryllium, and thorium have residence times of less than 1000 years. No calculated residence times are available for organic compounds because of the limited knowledge of their concentration, distribution, and degradation rates in rivers, the ocean, and marine sediments.

Mean residence time defines the average length of time that any atom will spend in the ocean before being removed to the sediments. However, the residence time of some compounds may be much shorter in the coastal zone where sedimentation is more intense. In addition, the sedimentation of elements may occur much more rapidly than calculated from sediment accumulation rates, as much of the biologically sedimented matter will be readily decomposed and elements returned to the water column. Such internal cycling of elements will not affect the ocean mean residence time but may be critically important in determining the short-term fate of contaminants introduced to the ocean.

Influence of Seasonal Changes

Although different for the various geographical areas, the seasonal variations in water column physics and chemistry greatly influence the distribution of chemical species in shelf sediments.

In the spring, the water column is relatively uniform in chemical composition except at the mouth of major rivers. There, a halocline often exists because of the increased river flow which also supplies dissolved and particulate chemical species to the water column. Increased sunlight causes an increase of photosynthetic activity with its associated production of large quantities of organic matter and other biogenous materials.

Organisms extract many chemical species (both natural and contaminant) from the dissolved state during growth. These species are either returned to the water column or retained in the sediments when the organisms die. Bordovskiiy (1965) points out that biological production is concentrated just shoreward of the continental slope and just seaward of the shore zone, and that biogenic organic matter in association with fine suspended sediments settles in depressions on the shelf. The Hudson Shelf Valley is one such depression where deposition of fine sediments has increased the total organic carbon concentrations compared to the sandy shelf sediments (Fig. 6).

In the summer months, solar heating of the water column creates a thermal stratification in most temperate regions. During this time, photosynthetic activity is reduced because of depletion of nutrients in the surface layers. The sedimentation of biogenic material therefore decreases.

Reduced wind and wave activity are characteristic of the summer months. The various sedimented materials accumulate and postdepositional changes begin to occur in sediments little disturbed except by burrowing and filter-feeding organisms.

In the fall and winter months, wind and wave activity increase, thereby breaking up the thermocline. The water column becomes mixed, replenishing nutrients to the surface layer, and photosynthetic activity may increase if light is available. Because of the increased hydraulic energy which ultimately affects most areas of the shelf, sediments now are resuspended and transported away from the original deposition site. This affects the distribution of chemical constituents in the sediments as precipitation and dissolution processes occur. Chemical species formed in the sediments by postdepositional processes may be dissolved and reprecipitated elsewhere.

Influence of Sediment Transport Processes

Erosion of nearshore or shoreface sediments can supply tremendous amounts of sedimentary materials to the shelf (see Chapter 14). These and other shelf sediments

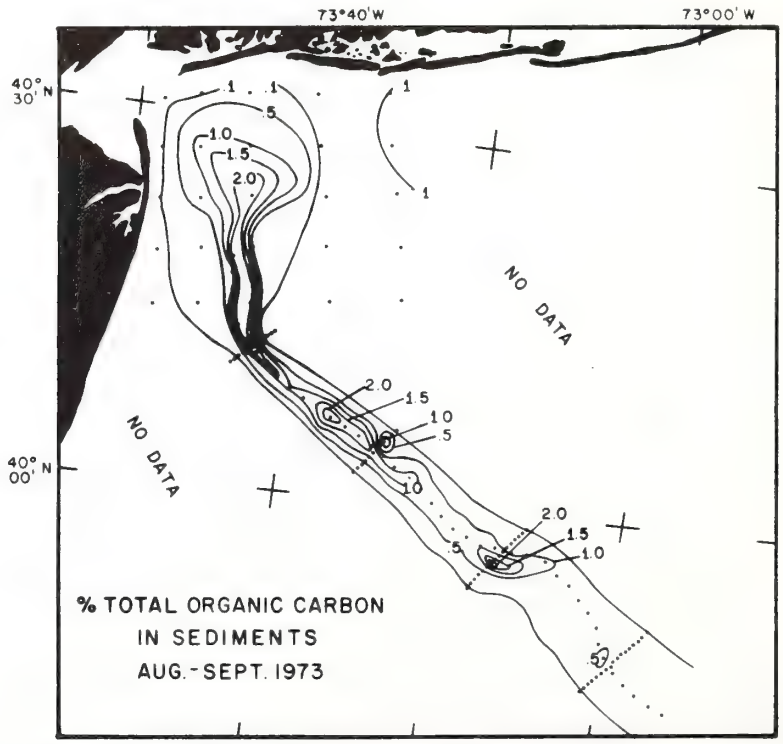


FIGURE 6. *The total organic carbon (percent dry weight) in sediments of the New York Bight (the dots represent the sampling stations).*

are distributed by various transport processes. The chemical compositions of shelf sediments at different locations are determined by both physical sorting and chemical changes occurring during transport. Dissolution and precipitation of various chemical phases occur. Deposited organic materials, for example, are subjected to microbial decomposition processes leading to dissolution of more labile materials and retention of the refractory material. For this reason, organic matter associated with highly mobile sediments takes on a more refractory character than organic matter associated with sediments accumulating in low-energy environments. As organic matter is usually associated with fines (Hunt, 1961; Bordovskiiy, 1965; Froelich et al., 1971) the high organic carbon concentration in mud bottoms on the shelf is not unexpected. Studies in the New York Bight (Fig. 6) and the Hudson Canyon (Fig. 7; Keller, 1973) indicate that organic carbon contents are highest in the depressions. Similar considerations may also be important in controlling the trace element distributions (Fig. 8).

Effects of Tidal Excursions

In the open ocean, tidal variations are small. However, as sea meets land, tidally induced fluctuations in the water level have a profound effect on erosional processes, and thereby on the distributions of chemical compounds.

Along the eastern coast of the United States, the tidally drained coastal wetlands are primarily characterized by grassy marshes and mangrove swamps. These wetlands are highly productive areas (Teal and Teal, 1969) with the detritus feeders forming the base of the food chain. They are also notable as sinks for sediments and as nutrient traps (Grant and Patrick, 1969). Although they are important scavengers of certain chemical species, the coastal wetlands release other compounds such as organic matter in the form of humic materials. With each ebb and flood tide, chemical exchange takes place between the tidal flats and the shelf waters. Many of the outgoing chemical constituents eventually precipitate on the shelf.

Influences of the Benthic Communities

As light penetrates to the bottom in many parts of the shelf and as production of detritus in the overlying water column is high, the shelf sediments support diverse and often abundant benthic biota. Attached macroalgae, various filter-feeding organisms, numerous classes of worms, and an abundance of microbial species are constantly altering the chemical balance at or below the sediment-water interface. These organisms utilize the various sedimented components as food sources, with their biomass and excreta becoming important components of shelf sediments. It is estimated that 75% of the benthic fauna on the shelf depends on detritus and associated organisms for a food source (Riley and Chester, 1971). A large proportion of organic matter produced by photosynthetic organisms is hydrolyzed by bacteria before reaching the sediments (Menzel and Goering, 1966). However, in shelf sediments, as much as 30 to 60% of

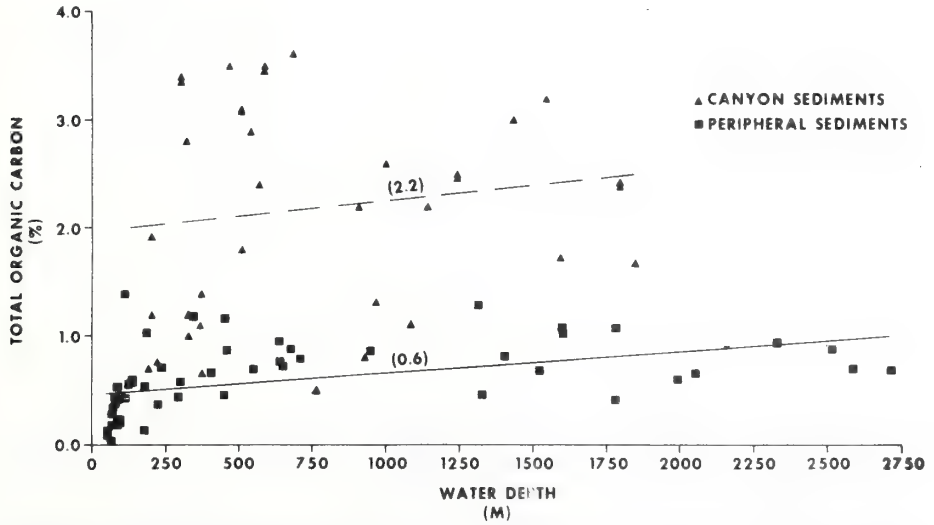


FIGURE 7. *The total organic carbon (percent dry weight) in sediments of the Hudson Canyon and adjacent shelf. From Keller (1973).*

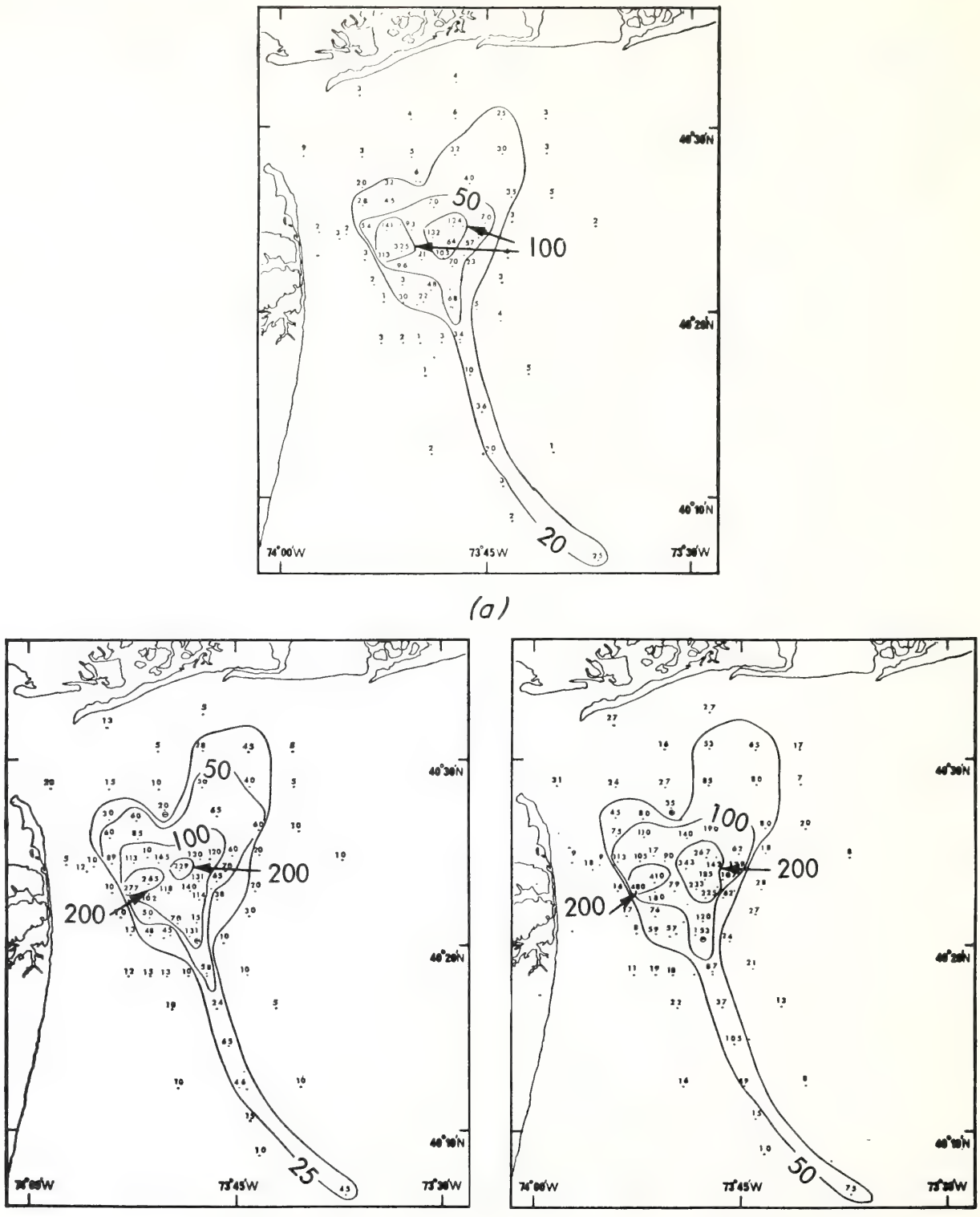


FIGURE 8. *Distribution of copper* (a), *lead* (b), *and zinc* (c) *in surface sediments from the New York Bight* (μg/g). *From Carmody et al.* (1973).

the organic matter is hydrolyzable and readily available to benthic organisms as a food source (Bordovskiiy 1965); see Table 3. A large portion of this readily hydrolyzable organic matter forms the cellular substance of bacterial biomass. As the organic matter is hydrolyzed or decomposed, a large fraction is returned to the water column as inorganic nutrients and other organic compounds (Riley and Chester, 1971).

TABLE 3. Distribution of Readily Hydrolyzable Organic Matter in Recent Bering Sea Sediments (Mean Data)

Type of Sediment	Total Organic Carbon (TOC) (% of dry sediment)	Content of Readily Hydrolyzable Carbon	
		% of Sediment	% of TOC
Medium-grained sands	0.32	0.19	59.4
Coarse silts	0.76	0.21	27.6
Fine silt muds	0.97	0.26	26.7
Silt-clay muds	1.38	0.30	21.8
Clay muds	0.54	0.14	25.7

Source. After Bordovskiiy (1965).

Chemical Changes in Sediments After Deposition

After deposition, sediments undergo diagenetic chemical changes that tend to bring them more nearly into equilibrium with their aqueous environment. This environment itself changes significantly. Oxygen in the sedimentary pore waters is consumed as organic matter introduced to the sediments is bacterially degraded. Unless the oxygen is renewed, sulfide formation takes place as bacteria utilize sulfate for oxidation of the organic matter. Within undisturbed sediments, diffusion is the only mechanism leading to renewal of oxygen in the pore waters (Fig. 9). Diffusion also permits solutes released during bacterial decomposition and chemical equilibrium to be released from the sediments. This is an extremely slow process. Transport of significant quantities of solutes through even 1 cm of sediment depth requires many years or even hundreds of years. Nevertheless, the distribution of elements in the sediments can be affected by postdepositional diffusion as illustrated by the distribution of manganese in certain deep-sea sediments and their pore waters (Fig. 2). Manganese is released to solution as its relatively soluble sulfide and diffuses upward, precipitating again in the oxidizing zone at the sediment surface. In this instance, manganese is not released into the water column, but elements or compounds released by sediments and not resorbed or precipitated may well diffuse out into the water column.

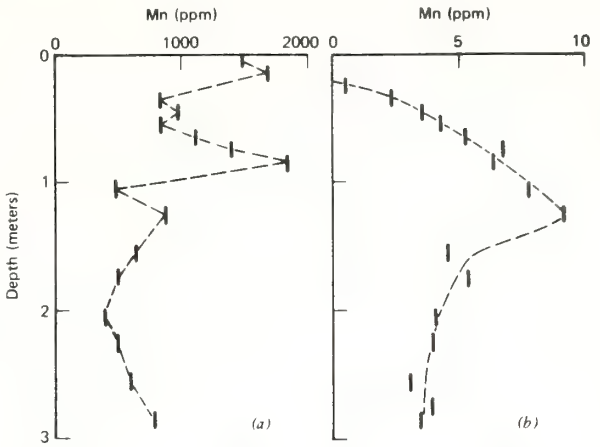


FIGURE 9. *The distribution of manganese in the sediment and interstitial water of an Arctic deep-sea core.* (a) *Distribution of manganese in the sediment.* (b) *Distribution of manganese in the interstitial water. From Riley and Chester (1971).*

In the coastal zone, sediments are continually resuspended and reworked both by biological action and by wave, tide, and current energy. Unless the sedimentation rate of organic matter is very rapid, the sedimentary pore waters do not maintain permanent concentrations of sulfide but are intermittently flushed with oxygenated seawater. Two important conditions must be fulfilled for metals and other constituents to be released to solution during diagenesis and transported back into the overlying water column. First, the decomposition of most of the detrital organic matter reaching the sediments and the equilibration of inorganic phases with seawater must take place before permanent burial is achieved. Migration of solutes into the overlying water column may thus take place by advective processes which are considerably faster than diffusion. Second, the periodic renewal of oxygen in the pore waters is necessary to either prevent metal sulfide precipitation or permit reoxidation and dissolution of such sulfides if they are formed. It is probable that significant release of metals and organic compounds occurs from coastal sediments particularly from organic matter and solid material dumped into the ocean directly. Unfortunately very little is known about these processes, although increased concentrations of dissolved trace metals have been observed in the water column close to the sediments in estuaries (J. H. Carpenter, personal communication), in the coastal zone, and even in the deep oceans (Segar, unpublished data). More information is required before it can be established with any degree of confidence whether or not the rapid removal of contaminants to the sediments at the estuarine interface and at outfalls and dumpsites is permanent or only temporary. Clearly this

is important, as contaminants permanently held in the sediments can have little interaction with the biosphere.

Organic components undergo extensive diagenesis in the top layers of sediment. Proteins are immediately hydrolyzed by bacteria to free amino acids (Lindblom and Lupton, 1961; Hare, 1969) which dissolve in the pore waters and, later, may diffuse out. In fact, it has been suggested that extensive migration of amino acids occurs in certain coastal sediments (Rittenberg et al., 1963). Carbohydrates also undergo extensive hydrolysis to free sugars with increasing burial time (Degens et al., 1964; Hatcher, 1974). Since free sugars represent an important nutritional substance for many organisms, this process may be important in determining the ability of a particular sediment to support various benthic biota. In addition to carbohydrates and proteins, other relatively labile organic constituents undergo early diagenetic changes. These result in a predominance of resistant humiclike materials below the first few meters of shelf sediments.

Over geological time, organic constituents of coastal sediments undergo more extensive alteration and some may eventually be transformed to petroleum. Fatty acids may be converted to petroleum alkanes (Cooper and Bray, 1963; Eisma and Jurg, 1969). Chlorophyll derivatives may be converted to aromatic compounds and to the branched-chain components of crude oil (Orr et al., 1958). Various other changes in organic matter composition of sediments with time have also been delineated (Eglinton, 1969).

CHEMICAL FACTORS AFFECTING PHYSICAL PROPERTIES AND ERODIBILITY OF SEDIMENTS ON THE SHELF

Physical processes affect the distribution of chemical components in shelf sediments. Conversely, the chemical properties also exert a significant influence on the physical properties of sediments. No studies appear to have been reported concerning the influence of chemical properties on the susceptibility of sediment on the seafloor to erosion and resuspension. Variations in sediment physical properties due to chemical factors may be expected to affect sediment stability and ultimately sediment transport. A few studies have reported the relationships among chemical species and the mass physical properties of sediments. Chemical cementation and cohesion appear to be two properties largely controlled by sediment chemistry.

The effects of silica, carbonate minerals, and amorphous oxides on sediment cementation have been reported by Nacci et al. (1974). Organic compounds such as barnacle cements are also important cementing agents. Cementation of mineral grains affects the transport of materials on the shelf by controlling both erodibility and effective particle size of the eroded material.

The cohesive property of a sediment is strongly affected by its organic components (Soderblom, 1966). Studies on various terrestrial soils have indicated that polysaccharides exert tremendous binding forces between mineral grains (Martin, 1971). Hulbert and Given (1975) suggest that organic matter may be important in determining the cohesive property (shear strength) of marine sediments. Bacterial mucus is composed mostly of mucopolysaccharide secretions and may also have an effect on the cohesion of finer particles on the shelf (see Chapter 18).

The ionic strength of pore waters has been shown to affect the cohesion of sediments (Lambe, 1958). The ionic chemical species control the electrostatic attractions of the clays within the bulk sediments.

Cementation and cohesion of a sediment occur because of chemical interactions between sediment grains. The amount of hydraulic activity needed to resuspend or transport the sediment increases with increased cohesion and cementation. For example, muds in the axis of the Hudson Shelf Valley are not swept away by currents which are known to be sufficient for transport of fine sands (Lavelle et al., 1975). Cohesion obviously plays a major role in maintaining the integrity of the substrate.

IMPACT OF HUMAN ACTIVITIES ON SEDIMENT CHEMISTRY

The oceans and their underlying sediments contain quantities of trace metals and natural organic materials that are vast when compared to the quantities that man releases. However, contaminant release by man takes place primarily at point sources in the coastal zone such as rivers, outfalls, and ocean dumpsites. Contaminant materials are mixed only slowly into the ocean, while they are often rapidly scavenged by the coastal sedimentation process. Therefore, anomalies have been observed in the chemistry of sediments close to shore which may be ascribed with reasonable certainty to human activities (Gross, 1972; NOAA, 1975; Segar and Pellenbarg, 1973).

Introduction of Contaminants

Anomalous sediment chemistry may be observed in areas of the shelf zone where man's activity is intense, although historical data are often missing and it is difficult to establish that these anomalies are not natural.

The sediment close to a power plant cooling water outfall at Turkey Point in Florida has anomalously high concentrations of a number of trace elements including V, Cu, and Ni (Segar and Pellenbarg, 1973); see Fig. 10. These anomalously high concentrations could be caused by emission of particulate metals from the power plant, emission of dissolved metals that are subsequently scavenged by entrained particles, or by concentration of naturally occurring metals due to geochemical or ecological changes other than direct metal release by the power plant.

In the New York Bight, dumpsites for sewage sludge, cellar dirt, dredge spoil, and acid waste have been used for many years (Gross, 1972). Anomalously high sedimentary concentrations of metals (Fig. 4) are found in the New York Bight but only in the topographic depressions (Carmody et al., 1973). Anomalous concentrations are not found immediately at the dumpsites themselves. It is probable that the dumped material, which is predominantly fine-grained, is simply redistributed by the active sediment transport processes of the continental shelf. Clearly in the absence of historical sediment chemistry data, the sediment transport processes must be understood before it can be concluded with certainty that the anomalous concentrations in the topographic lows are caused by contaminant material.

In addition to the metal contaminants, many synthetic organic compounds not found naturally are added to the oceans. Many of these compounds are not easily biodegraded (e.g., polychlorobiphenyls) and are concentrated in the sediments. Detectable concentrations of these types of compound have been found in many marine sediments, particularly those from the continental shelf (e.g., Murray and Riley, 1973). Recent studies of DDT and PCB compounds in sediments off the coast of California (McDermott and Heesen, 1974; Young, 1974) have indicated that increased levels of these contaminants are directly traceable to municipal waste effluents.

In the past decade, increasing concern has arisen over pollution of the shelf environment by petroleum products. More than 1 billion tons of crude oil and oil products is transported across the continental shelf each year. Oil spillage by accidental disasters such as the Torrey Canyon, by bilge pumping, and by tanker deballasting, contribute possibly between 5 and 10 million tons of petroleum per year to the marine environment (Ehrhardt and Blumer, 1972). Crude oil entering the marine environment is first subjected to extensive evaporation and dissolution, with the remaining fractions coagulating into floating tar lumps that may eventually settle to the sediments (Morris and Butler, 1973). Petroleum products also sorb to particulate matter and eventually become incorporated into sediments. In the process, they become available to the marine food chain and pose a long-term toxicity problem (Tissier and Oudin, 1973). Aromatic hydrocarbons are naturally present in very low concentrations in unpolluted sediments (Brown et al., 1972). However, their rate of incorporation into the sediments of heavily polluted areas is significant enough to achieve toxic levels (Tissier and Oudin, 1973).

Introduction of Radioactive Wastes

Recently the ocean dumping of radioactive wastes has aroused some concern for the shelf sediment environment. Peaceful uses of nuclear reactors, fuel fabrication plants, and reprocessing plants contribute on the order of 10^5 Ci/year (National Academy of Sciences, 1971). Iodine-151, strontium-90, cesium-137, tritium, argon-39, and krypton-88 are radionuclides that present major problems in the environment. Nuclear testing is also a potential hazard as atmospheric fallout is expected to affect shelf sediments.

Dredging and Mining Operations

Dredging and mining operations have increased recently as a result of accelerating urbanization and land development. Any sediment disturbance imposes an effect on the shelf environment as the sediment/water equilibrium is destroyed. Release of contaminants that have previously been removed from the system poses a significant stress on areas affected by mining operations. Additionally, entrainment of fine, silty material into the water column causes oversiltation which destroys the delicate food-gathering mechanisms of many filter-feeding organisms. The release of large quantities of sulfides and organic matter causes the water column to be stripped of essential oxygen for respiration. The decrease in water clarity affects light penetration, thereby decreasing photosynthetic activity.

Ocean Dumping

Large quantities of waste material including dredge spoil, solid wastes, incinerator residue, garbage, sewage sludge, chemical wastes, discarded military equipment and munitions, and construction debris are disposed of annually by dumping in the coastal zone (NOAA, 1974). For example, in the New York metropolitan area alone, 10^7 tons of sewage sludge, 2×10^7 tons of dredge spoil, and 6×10^6 tons of chemical wastes are annually released to the New York shelf environment (Environmental Protection Agency, 1975). This amount of contamination is bound to have an effect on the chemistry of the

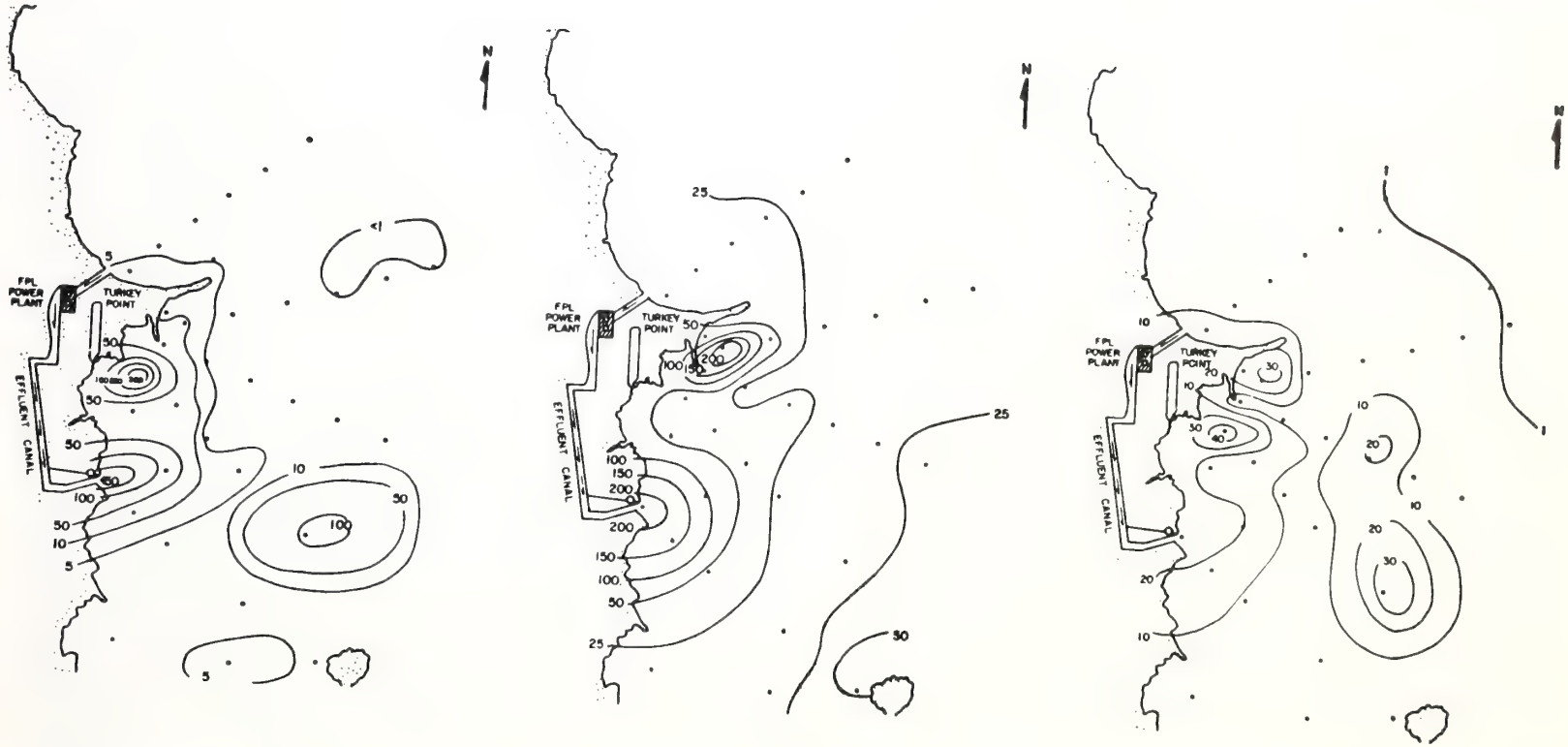


FIGURE 10. *Concentrations (μg/g) of nickel (left), vanadium (center), and copper (right) in surface sediments of the area of Biscayne Bay, Florida, adjacent to the Turkey Point power plant cooling water discharge. Modified from Segar and Pellenbarg (1973).*

sediments. The most notable changes that can be attributed to the sewage are the increase in organic carbon concentration in the sediments near the dumpsites, the increase in levels of trace metals (Carmody et al., 1973), and the reduction of the dissolved oxygen concentrations through BOD (Sandy Hook Laboratory, 1972). In fact, sediments in the dumpsite area have been labeled the "dead sea" because of the general absence of benthic organisms (Pearce, 1972).

SUMMARY

Chemical interactions involving sediments of the continental margins are extremely complex. River drainage with its associated chemical constituents, biological intensification, wind and wave activity, depositional and erosional processes, and last but not least the presence of man with his waste products interact to produce an extremely dynamic chemical ecosystem on the continental shelf. This complexity and the resulting heterogeneity have made it extremely difficult to describe the chemical characteristics of the coastal zone and the chemical interactions therein.

Nearshore sediments are complex mixtures of allochthonous and autochthonous constituents whose grain size range varies considerably between samples collected within several meters of each other. The relative proportions of allochthonous and autochthonous constituents varies as a function of distance from shore and proximity to major rivers. Aside from certain subtropical areas, the major components of shelf sediments are silica, various feldspars, clay minerals, a variety of heavy minerals, and a complex mixture of organic materials. The sources of the various constituents have been only partially and poorly identified. River transport supplies not only the shelf but also the deep oceans with considerable quantities of many of the various chemical compounds encountered in sediments and the water column. Both hydrogenous and biogenous components also comprise a significant fraction of shelf sediments. Eolian-transported constituents are thought to be only minor fractions in all marine sediments.

As chemical constituents are supplied to the shelf environment, various processes tend to redistribute these components among solid and dissolved phases. The most important of these processes occur when river water encounters ocean water at the estuarine interface. The increase in ionic strength causes various soluble and colloidal particles to precipitate. These precipitates scavenge other chemical constituents from solution. This process is an important regulating factor in the geochemical balance of many trace components in the world's oceans.

Several variations are extremely important in shelf waters. Seasonal changes in biological activity and river flow coupled to changes in the hydraulic regime constantly modify the nature and amounts of chemical compounds reaching shelf sediments. In addition, the redistribution of materials by sediment transport processes is seasonally dependent, and the sediments of the shelf have a continuously altering seafloor distribution. Different chemical constituents are associated with different particle sizes of material. Therefore physical sorting of shelf sediments affects the distribution of these constituents on the shelf.

Tidal fluctuations aid in movement of sediments and cause a corresponding effect on the distribution of chemical species. Although bioturbation is not considered to be a sediment transport process by some, it substantially affects the distribution of chemical constituents on the seafloor.

Once deposited, organic and inorganic chemical compounds undergo diagenesis whereby they are solubilized or precipitated. Diffusion, advection, and bioturbation all serve to transport the products of diagenesis within the sedimentary column and into the water column.

Just as physical and biological processes alter the distribution of chemical constituents on the shelf, variations of chemical constituents influence the physical processes of sedimentation. Cohesion and cementation of mineral grains may be controlled by organic and inorganic chemical agents, and these parameters affect the sediment transport processes.

The most important influence on the distribution of chemical constituents on the shelf in many areas is the presence of man and his many waste disposal and industrial practices. Adjacent to large urban centers, the shelf is constantly being supplied contaminants resulting from man's inability to recycle waste materials effectively. The shelf is used as a convenient repository for such materials as dredge spoils, cellar dirt, sewage and sewage sludge, chemical wastes, radioactive wastes, petroleum products, discarded military equipment, and various other chemical contaminants. Although the oceans are thought to be capable of assimilating vast quantities of our waste products, it is becoming clear that disposal of even limited quantities of contaminants in the shelf zone may cause critical problems. The chemistry of the shelf ecosystem is in a state of dynamic equilibrium, which may be destroyed if present practices are continued. Recent studies have indicated that the present contaminant loadings have caused significant changes in the chemistry of coastal sediments.

ACKNOWLEDGMENTS

We thank the NOAA Marine Ecosystem Analysis (MESA) program for their support of the New York Bight investigation.

REFERENCES

American Gas Association (1971). Reserves of crude oil, natural gas liquids, and natural gas in the United States and Canada and the U.S. productive capacity as of December 31, 1970. *Am. Gas Assoc., Am. Pet. Inst., Can. Petrol. Assoc.*, **25**: 1–256.

Bordovskiiy, O. K. (1965). Accumulation of organic matter in bottom sediments. *Mar. Geol.*, **3**: 33–82.

Broecker, W. S. (1974). *Chemical Oceanography*. New York: Harcourt Brace & Jovanovich, 214 pp.

Brown, F. S., H. J. Baedecker, A. Nissenbaum, and I. R. Kaplan (1972). Early diagenesis in a reducing fjord, Saanlich Inlet, British Columbia—III. Changes in organic constituents of sediment. *Geochim. Cosmochim. Acta*, **36**: 1185–1203.

Buss, B. A. and T. S. Rodolfo (1972). Suspended sediments in continental shelf waters off Cape Hatteras, North Carolina. In D. J. P. Swift, D. B. Duane, and O. H. Pilkey, eds., *Shelf Sediment Transport: Process and Pattern*. Stroudsburg, Pa.: Dowden, Hutchinson & Ross, pp. 263–279.

Carmody, D. J., J. B. Pearce, and W. E. Yasso (1973). Trace metals in sediments of New York Bight. *Mar. Pollut. Bull.*, **4**: 132–135.

Cooper, J. E. and E. E. Bray (1963). A postulated role of fatty acids in petroleum formation. *Geochim. Cosmochim. Acta*, **27**: 1113–1127.

Degens, E. T. (1967). Diagenesis of organic matter. In G. Larsen and G. V. Chilingar, eds., *Diagenesis in Sediments*. Amsterdam: Elsevier, pp. 343–390.

Degens, E. T., J. H. Reuter, and K. N. F. Shaw (1964). Biochemical compounds in offshore California sediments and sea waters. *Geochim. Cosmochim. Acta*, **28**: 45–63.

Eglinton, G. (1969). Organic geochemistry. The organic chemist's approach. In G. Eglinton and M. T. J. Murphy, eds., *Organic Geochemistry*. Berlin and New York: Springer-Verlag, pp. 20–73.

Eglinton, G. and M. T. J. Murphy, eds. (1969). *Organic Geochemistry*. Berlin and New York: Springer-Verlag, 828 pp.

Eisma, E. and J. W. Jurg (1969). Fundamental aspects of the generation of petroleum. In G. Eglinton and M. T. J. Murphy, eds., *Organic Geochemistry*. Berlin and New York: Springer-Verlag, pp. 676–698.

El Wakeel, S. K. and J. P. Riley (1961). Chemical and mineralogical studies of deep-sea sediments. *Geochim. Cosmochim. Acta*, **25**: 110–146.

Environmental Protection Agency (1975). *Ocean Disposal in the New York Bight*. Technical Briefing Report #2, USEPA, Region II, 86 pp.

Ehrhardt, M. and M. Blumer (1972). The source indentification of marine hydrocarbons by gas chromatography. *Environ. Pollut.*, **3**: 179–194.

Froelich, P., B. Golden, and O. H. Pilkey (1971). Organic carbon in sediments of the North Carolina continental rise. *Southeast. Geol.*, **13**: 91–97.

Goldberg, E. D. (1954). Marine geochemistry. *J. Geol.*, **62**: 249–265.

Goldberg, E. D. (1965). Minor elements in sea water. In J. P. Riley and G. Skirrow, eds., *Chemical Oceanography*, Vol. 1. New York: Academic Press, pp. 163–196.

Goldberg, E. D. and G. O. S. Arrhenius (1958). Chemistry of the Pacific pelagic sediments. *Geochim. Cosmochim. Acta*, **13**: 153–212.

Grant, R. R., Jr. and R. Patrick (1969). Tinnisum Marsh as a water purifier. In *Two Studies of Tinnisum Marsh, Delaware and Philadelphia Counties*. Washington, D.C.: Pa. Conserv. Found., pp. 80–118.

Gross, M. G. (1972). Geologic aspects of waste solids and marine waste deposits, New York metropolitan region. *Geol. Soc. Am. Bull.*, **83**: 3163–3176.

Hare, P. E. (1969). Geochemistry of proteins, peptides, and amino acids. In G. Eglinton and M. T. J. Murphy, eds., *Organic Geochemistry*. Berlin and New York: Springer-Verlag, pp. 438–463.

Hatcher, P. G. (1974). A study of the organic geochemistry of Mangrove Lake, Bermuda. M.S. Thesis, University of Miami, Florida. 231 pp.

Hood, D. W., ed. (1971). *Impingement of Man on the Oceans*. New York: Wiley-Interscience, 738 pp.

Hulbert, M. H. and D. N. Given (1975). Geotechnical and chemical property relationships for Wilkinson Basin, Gulf of Maine, sediments. *J. Sediment. Petrol.* (in press).

Hunt, J. M. (1961). Distribution of hydrocarbons in sedimentary rocks. *Geochim. Cosmochim. Acta*, **22**: 37–49.

Keller, G. K. (1973). Sedimentary dynamics within the Hudson submarine canyon. *Proc. of Symposium Relations sédimentaires entre estuaires et plateaux continentaux, Bordeaux, France, July 1973*, p. 49.

Ketchum, B. H. (1972). *The Water's Edge: Critical Problems of the Coastal Zone*. Cambridge, Mass.: MIT Press, 393 pp.

Kharkar, D. P., K. K. Turekian, and K. K. Bertine (1968). Stream supply of dissolved silver, molybdenum, antimony, selenium, chromium, cobalt, rubidium, and cesium to the oceans. *Geochim. Cosmochim. Acta*, **32**: 283–298.

Kononova, M. M. (1966). *Soil Organic Matter*, 2nd ed. New York: Pergamon, 544 pp.

Krauskopf, K. B. (1956). Factors controlling the concentrations of 13 rare metals in sea water. *Geochim. Cosmochim. Acta*, **9**: 1–32B.

Lambe, W. T. (1958). The structure of compacted clay. *J. Soil Mech., Found. Div.*, Pap. **1654**: 1–34.

Lavelle, J. W., G. H. Keller, and T. L. Clarke (1975). Possible bottom current response to surface winds in the Hudson shelf channel. *J. Geophys. Res.*, **80**: 1953–1956.

Lindblom, G. and M. D. Lupton (1961). Microbial aspects of organic geochemistry. *Dev. Ind. Microbiol.*, **2**: 9–22.

Lowman, F. G., K. K. Phelps, R. McClin, V. Roman De Vega, I. Oliver de Padovani, and R. J. Garcia (1966). Interactions of the environmental and biological factors on the distribution of trace elements in the marine environment. In *Disposal of Radioactive Wastes into Seas, Oceans and Surface Waters*. Vienna: IAEA, pp. 249–266.

McDermott, D. J. and T. C. Heesen (1974). Inventory of DDT in sediments. In *Coastal Water Research Project, Annual Report, 1974*, pp. 123–129.

Manheim, F. T., R. H. Meade, and G. C. Bond (1970). Suspended matter in surface waters of the Atlantic Continental margin from Cape Cod to the Florida Keys. *Science*, **167**: 371–376.

Martin, J. P. (1971). Decomposition and binding action of polysaccharides in soil. *Soil Biol. Biochem.*, **3**: 33–41.

Menzel, D. W. and J. J. Goering (1966). The distribution of organic detritus in the ocean. *Limnol. Oceanogr.*, **11**: 333–337.

Morris, B. F. and J. N. Butler (1973). Petroleum residues in the

Sargasso Sea and on Bermuda beaches. *Proc. Conf. Prevention and Control Oil Spills, 1973*, pp. 521–529.

Murray, A. J. and J. P. Riley (1973). The determination of chlorinated aliphatic hydrocarbons in air, natural waters, marine organisms and sediments. *Anal. Chim. Acta*, **65**: 261–270.

Nacci, V. A., W. E. Kelly, H. C. Wang, and K. R. Demars (1974). Strength and strain characteristics of cemented deep-sea sediments. In A. L. Inderbitzen, ed., *Deep-Sea Sediments, Physical and Mechanical Properties*. New York: Plenum Press, pp. 129–150.

National Academy of Sciences (1971). *Radioactivity in the Marine Environment*. Washington, D.C.: Natl. Acad. Sci., 272 pp.

NOAA (1974). *Report to the Congress on Ocean Dumping and Other Man-Induced Changes to Ocean Ecosystems, October 1972 through December 1973*, 84 pp.

NOAA (1975). *Technical Background Relating to Offshore Dumping Assessment—An Interim Report*. In R. L. Charnell, ed., NOAA Tech. Memo., ERL, MESA-1, 83 pp.

Orr, W. L., K. O. Emery, and J. R. Grady (1958). Preservation of chlorophyll derivatives in sediments off Southern California. *Bull. Am. Assoc. Pet. Geol.*, **42**: 925–962.

Parker, P. L., A. Gibbs, and R. Lawler (1963). Cobalt, iron and manganese in a Texas bay. *Publ. Inst. Mar. Sci., Univ. Texas*, **9**: 28–32.

Pearce, J. B. (1972). The effects of solid waste disposal on benthic communities in the New York Bight. In M. Ruivo, ed., *Marine Pollution and Sea Life*. London: FAO Publ., pp. 404–411.

Pruter, A. T. (1972). Foreign and domestic fisheries for groundfish, herring, and shellfish in continental shelf waters off Oregon, Washington, and Alaska. Woods Hole, Mass. Workshop on Critical Problems of the Coastal Zone, unpublished paper, 16 pp.

Richards, F. A. (1965). Anoxic basins and fjords. In J. P. Riley and G. Skirrow, eds., *Chemical Oceanography*, Vol. I. New York: Academic Press, pp. 611–646.

Riley, J. P. and R. Chester (1971). *Introduction to Marine Chemistry*. New York: Academic Press, 465 pp.

Riley, J. P. and G. Skirrow (1965). *Chemical Oceanography*. New York: Academic Press, Vol. 1, 712 pp.; Vol. 2, 508 pp.

Rittenberg, S. C., K. O. Emery, J. Hulsemann, E. T. Degens, R. C. Fay, J. H. Reuter, J. R. Grady, S. H. Richardson, and E. E. Bray (1963). Biogeochemistry of sediments in experimental Mohole. *J. Sediment. Petrol.*, **33**: 140–172.

Sandy Hook Laboratory (1972). *The Effects of Waste Disposal in New York Bight*. Final report submitted to U.S. Army Corps of Engineers, Coastal Eng. Res. Cent, 762 pp.

Schlee, J., D. Folger, and C. O'Mara (1971). *Bottom Sediments of the N.E. U.S.: Cape Cod to Cape Ann, Mass.* USGC Open File Report and Misc. Geol. Invest. Rep. No. 1-746.

Segar, D. A., P. G. Hatcher, G. A. Berberian, L. E. Keister, and M. A. Weiselberg (1975). The chemical and geochemical oceanography of the New York Bight apex region as it pertains to the problem of sewage sludge disposal. Part III. In R. L. Charnell, ed., *Technical Background Relating to Offshore Dumping Assessment—An Interim Report*. NOAA Tech. Memo., ERL, MESA-1, pp. 62–83.

Segar, D. A. and R. E. Pellenbarg (1973). Trace metals in carbonate and organic rich sediments. *Mar. Pollut. Bull.*, **4**: 138–142.

Soderblom, R. (1966). Chemical aspects of quick clay formation. *Eng. Geol.*, **1**: 415–431.

Stumm, W. and J. J. Morgan (1970). *Aquatic Chemistry, An Introduction Emphasizing Chemical Equilibria in Natural Waters*. New York: Wiley-Interscience, 583 pp.

Teal, J. M. and M. Teal (1969). *Life and Death of the Salt Marsh*. New York: Audubon Ballantine.

Tissier, M. and J. L. Oudin (1973). Characteristics of naturally occurring and pollutant hydrocarbons in marine sediments. *Proc. Conf. Prevention and Control Oil Spills, 1973*, pp. 205–214.

Turekian, K. K. (1971). Rivers, tributaries and estuaries. In D. W. Hood, ed., *Impingement of Man on the Oceans*. New York: Wiley-Interscience, pp. 9–74.

Turekian, K. K. and K. H. Wedepohl (1961). Distribution of the elements in some major units of the earth's crust. *Geol. Soc. Am. Bull.*, **72**: 175–191.

Wedepohl, K. H. (1960). Suprenanalytische Untersuchungen an Tiefseetonen aus dem Atlantik, Ein Beitrag zue Deutung der Geochemischen Sonderstellung von pelagischen tonen. *Geochim. Cosmochim. Acta*, **18**: 200–231.

Young, D. R. (1974). DDT and PCB in dated sediments. In *Coastal Water Research Project, Annual Report, 1974*, pp. 135–137.

Young, E. J. (1954). Trace elements in recent marine sediments. *Geol. Soc. Am. Bull.*, **65**: 13–29.

Bulletin of Environmental Contamination and Toxicology 17, No. 4, 491-498.

Steroids as Sewage Specific Indicators in New York Bight Sediments

Patrick G. Hatcher, Larry E. Keister, and Philip A. McGillivary
NOAA, Atlantic Oceanographic and Meteorological Laboratories
15 Rickenbacker Causeway, Miami, Fla. 33149

ABSTRACT

Sediments of the New York Bight were examined for steroidal compounds and found to contain relatively large amounts of coprostanol and 24 β-ethyl coprostanol. These steroids were found to be derived from sewage, and it is suggested that they be used as sewage tracers in marine sediments.

INTRODUCTION

The New York Bight has recently received much attention in the field of environmental pollution. The National Oceanic and Atmospheric Administration (NOAA) has been conducting a multidisciplinary study (Marine EcoSystems Analysis Program, MESA) to assess the impact of waste disposal in the Bight. Currently, the municipalities of New York City are dumping 3.7×10^6 metric tons/year of sewage sludge, 9.7×10^6 metric tons/year of dredge spoil, 2.0×10^6 metric tons/year of contruction rubble, and 2.2×10^6 metric tons/year of acid-iron wastes in the New York Bight (EPA, 1975). Additionally, undetermined amounts of sewage, sewage effluents, and chemical wastes are being released directly into the Bight or enter via the Hudson-Raritan river system (MUELLER and JERIS, 1975). Much of this waste material eventually settles to become part of the sediment in the Bight. GROSS (1972) stated that the major supply of sedimentary materials to the Bight was from anthropogenic sources. HATCHER and KEISTER (1975) suggest that most of the organic sedimentary matter in the Apex area is of sewage origin.

Recently some alarm has been expressed over the probable encroachment of black silty muds onto the beaches of Long Island (HARRIS, 1974). Pockets of black mud having a "mayonnaise" consistency similar to that of sewage sludge have been detected near the beaches (CHARNELL, 1974; HARRIS, 1975). HATCHER and KEISTER (1975) suggested that the ratio of total carbohydrates to total organic carbon serves as a

semi-qualitative measure of sewage contamination. However, controversy subsequently arose due to the inability to positively determine specific identifiers which would classify the source of these black muds as sewage. By examining and comparing New York Bight sediments and sewage sludge, we now present steroids as suitable sewage tracers.

Steroids are minor constituents of both plants and animals (IKAN et al., 1975). Plants and more primitive species of the animal kingdom contain such a wide variety of steroids that taxonomic identifications are often made based on their steroid contents. In a comprehensive review on the occurrence of steroids in higher plants and animals, AUSTIN (1970) found cholesterol to predominate over other steroids.

Although steroids are minor components of plants and animals, they resist microbial degradation for much longer periods of time than other biolipids (RHEAD et al., 1971). ATTAWAY and PARKER (1970) found steroids present in a 2000-year-old sediment. Sediments as old as 130,000 years have been found to contain steroids (HENDERSON et al., 1971). This degree of preservation makes steroids useful biological markers for long periods of time.

Due to their taxonomic specificity, steroids may also provide distinctions between marine or terrestrial sources and anthropogenic sources such as sewage (ATTAWAY and PARKER, 1970; TABAK et al., 1972; KIRCHMER, 1971). This capability is quite useful, especially in the coastal zone where organic matter in sediments may be derived from a multitude of sources including sewage. In addition to being a mixture of plant and animal remains, sewage contains unique steroids derived from mammalian fecal matter (ENEROTH et al., 1964). These compounds are thought to arise from the reduction of sterols to stanols by mammalian intestinal microflora (ROSENFELD et al., 1954; MATTHEWS and SMITH, 1968).

The steroids found in human excreta are predominantly cholesterol, coprostanol, coprostanone, β-sitosterol, methyl cholesterol, and ethyl coprostanol (ENEROTH et al., 1964). Cholesterol, β-sitosterol, and methyl cholesterol have been identified in the marine environment (MATTHEWS and SMITH, 1968; ATTAWAY and PARKER, 1970; GAGOSIAN, 1975). However, coprostanol and ethyl coprostanol have not been detected in unpolluted marine sediments (ATTAWAY and PARKER, 1970; IKAN et al., 1975). Due to the miniscule contribution of marine mammals to oceanic biomass (RILEY and CHESTER, 1971), such mammalian fecal steroids would be present in the natural marine environment only in extremely

insignificant amounts. While several microorganisms have been found to reduce cholesterol to coprostanol (EYSSEN et al., 1973; PARMENTIER and EYSSEN, 1974), their presence is unreported in the marine environment. However, if these organisms were active in marine sediments, we would expect to find detectable amounts of coprostanol due to the ubiquitous presence of cholesterol. Coprostanol has not been detected in uncontaminated marine sediments, and it is unlikely that its bacterial production is occurring. Discounting the natural production of coprostanol and 24 β-ethyl coprostanol, we believe their presence in the marine environment to be of contaminant origin. MATTHEWS and SMITH (1968) as well as EGLINTON et al. (1975) also suggest that these steroids are possible identifiers of sewage when detected in the environment. Coprostanol in the dissolved state has previously been used as a sewage tracer in fresh water systems contaminated by sewage effluents (TABAK et al., 1972; KIRCHMER, 1971; DOUGAN and TAN, 1973). We therefore examined the steroids of a suspected sewage-contaminated sediment of the New York Bight and a sample of sewage sludge. We were specifically interested in steroids of fecal origin.

METHODS

Freeze-dried sediments and sewage sludge were Soxhlet extracted with a benzene:methanol (1:1 v/v) solution. Each extract was saponified in 0.5N KOH in methanol. The saponified solutions were then acidified with HCl, mixed with water, and extracted with CCl_4. The CCl_4 extracts were evaporated to dryness and the residues esterified with BF_3/methanol for preparation of the fatty acid esters which will be discussed elsewhere. Water was then added to each of the solutions which were subsequently extracted with hexane. The hexane extracts were placed on 30 x 1 cm silica gel columns and eluted with 0.5, 2.5, and 2.0 column volumes of hexane, benzene, and methanol, respectively. The methanol fractions were evaporated to dryness and treated with BSA (N, O, bis-trimethylsilylacetamide) to form the trimethyl silyl ethers of alcoholic compounds. The resulting solutions were chromatographed on a Tracor 550 using glass columns packed with 3% OV-1 on Chromosorb W (HP), and the temperature was programmed from 100° to 270°C at 4°/min. The peak areas were calculated with a Hewlett-Packard 3380A electronic integrator. Concentrations were estimated by injecting known amounts of solution and relating the areas of each component to the flame detector molar response for a cholesterol standard. The steroids were identified

by retention data given by ENEROTH et al. (1964) and confirmed by combined gas chromatography-mass spectrometry (DuPont 490-B). The gas chromatographic peaks were checked for purity by scanning the mass spectrometer repeatedly as the peaks eluted. Although the chromatograms may be congested, the steroid peaks are sufficiently separated to allow quantitative analysis.

RESULTS AND DISCUSSION

One sediment sample was taken during a NOAA/MESA cruise in September 1973 from the topographic depression (Christiaensen Basin) in the Apex of the New York Bight, near the sewage sludge dumpsite. This sediment was observed to have a black "mayonnaise" appearance. The other sample (P-21) was taken in June 1974 aboard the R/V VENTURE, from within one mile of Atlantic Beach, Long Island. This sample had a similar consistency to that of the Christiaensen Basin sample, as it came from a localized accumulation of mud near the beach. The gas chromatograms for the BSA-treated methanol eluates of both sediments are presented in Fig. 1 (1 and 2). A large variety of compounds such as fatty alcohols and hydroxy fatty acids are present in addition to the steroid derivatives which are designated by letters. The major steroids found in both sediments are coprostanol (peak A), cholesterol (B), β-sitosterol (D), and 24 β-ethyl coprostanol (C). The sample mass spectra of these four compounds are presented in Fig. 2. The cholesterol and β-sitosterol are present in significant amounts and are generally dominant in marine sediments (IKAN et al., 1975). The presence of coprostanol and of 24 β-ethyl coprostanol immediately drew our attention. These steroids offer ideal sewage tracers, since they are found as major steroids in human excrement (ENEROTH et al., 1964; TABAK et al., 1972). Their natural contribution is unreported and is generally considered non-detectable in open ocean sediments. Their presence in New York Bight sediment samples links the source of the major organic component in these muds to sewage. The measured concentrations of coprostanol in the Christiaensen Basin and P-21 sediments are 4.8 and 5.2 ppm, respectively, indicating a similar level of sewage contamination. It is especially interesting that the near-shore mud (P-21) is as contaminated as that of the Christiaensen Basin, an area known to be heavily impacted by sewage (GROSS, 1972).

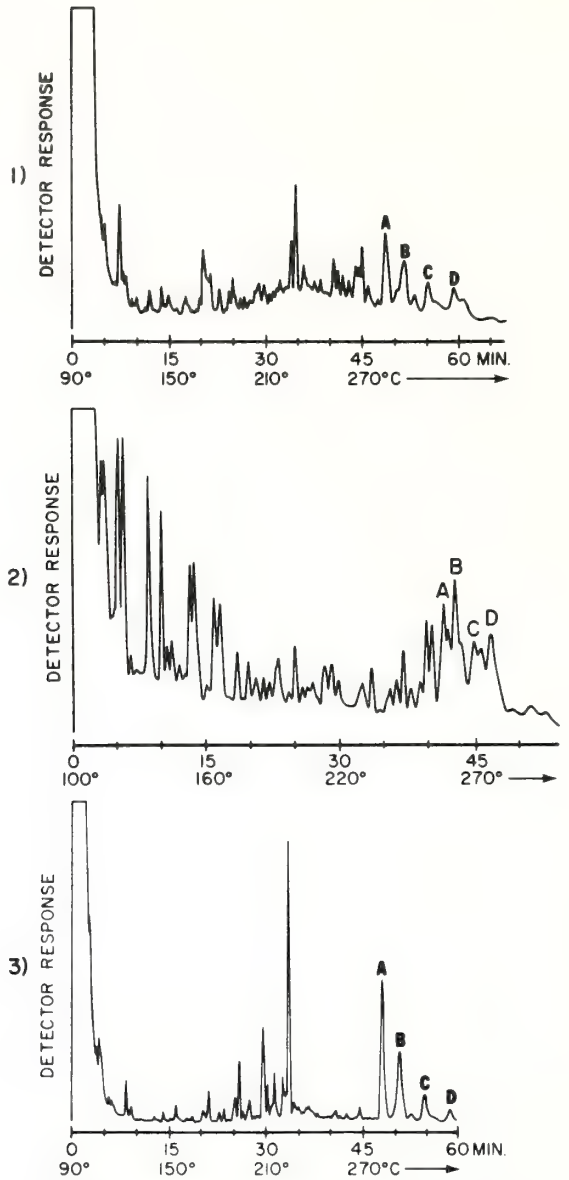


Figure 1. The gas chromatograms of the BSA-treated methanol eluate of the Christiaensen Basin mud (1), the P-21 sample (2), and the Ward's Island sewage sludge (3). A 6'x1/8" o.d. glass column packed with 3% OV-1 on chromosorb W(HP) was used in (1) and (3). A 6'x1/4" o.d. glass column packed with the same material was used in (2).

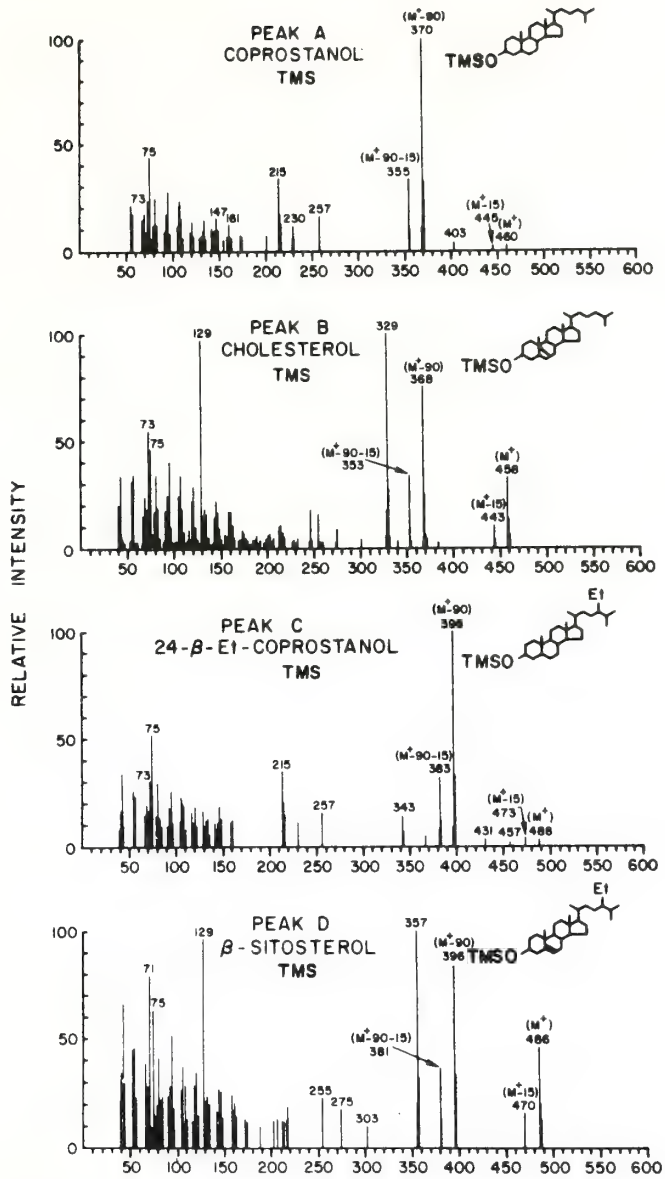


Figure 2. The mass spectra of the TMS derivatives of coprostanol, cholesterol, 24β-ethyl coprostanol, and β-sitosterol in the Christiaensen Basin mud sample.

To confirm our observations that sewage was the source of coprostanol, we analyzed a sample of sewage sludge from Ward's Island sewage treatment facility in New York City. The chromatogram of the BSA-treated methanol eluate is shown in Fig.1(3). In this fraction cholesterol and β-sitosterol are noticeably present, but the great quantity of coprostanol and 24 β-ethyl coprostanol confirmed our beliefs that sewage is the source of these steroids in the Christiaensen Basin and in the sample near the Long Island shoreline.

The coprostanol concentration of Ward's Island sewage sludge is 5800 ppm. Realizing that roughly 0.3×10^6 tons of sewage sludge sludge solids are added to the Bight annually (EPA, 1975), it is not too surprising to find relatively high levels of coprostanol in New York Bight sediments.

In conclusion, we point out that New York Bight sediments are contaminated with sewage resulting from either ocean dumping of sludge or from outfalls. Coprostanol or 24 β-ethyl coprostanol can be used to identify sewage contamination in sediments on both a horizontal and vertical sedimentary profile.

ACKNOWLEDGEMENTS

We would like to thank the MESA, New York Bight Project for their financial assistance and Mr. George A. Berberian for his comments on the manuscript.

REFERENCES

ATTAWAY, D. and P.L. PARKER: Science 169, 674(1970).
AUSTIN, J.: Advances in Steroid Biochemistry and Pharmacology, ed. by Briggs, New York, NY, Academic Press, 1970.
CHARNELL, R.: Assessment of Offshore Dumping; Technical Background. NOAA Tech. Memo ERL, MESA-1, 1975.
DOUGAN, J., and L. TAN: J. Chromatogr. 86, 107(1973).
EGLINTON, G., B.R.T. SIMONEIT, and J.A. ZORO: Pro. R. Soc. Land. 189, 415(1975).
ENEROTH, P., K. HELLSTROM, and R. RYHAGE: J. Lipid Res. 5, 245(1964).
EYSSEN, H.J., G.G. PARMENTIER, F.C. COMPERNOLLE, G. DE PAUW, and M. PIESSEN-DENEF: Eur. J. Biochem. 36, 411(1973).
GAGOSIAN, R.B.: Geochim. Cosmochim. Acta 39, 1443 (1975).
GROSS, M.G.: Geol. Soc. Am. Bull. 83, 3163(1972).
HARRIS, N.H.: Symposium on the Middle Atlantic Continental Shelf and New York Bight, Nov. 1975.
HATCHER, P.G., and L.E. KEISTER: Symposium on the Middle Atlantic Continental Shelf and New York

Bight, Nov. 1975.
HENDERSON, W., W.E. REED, and G. STEEL: Advances in Organic Geochemistry, ed. by Gaertner and Wehner, Oxford, Pergamon Press, 1971.
IKAN, R., M.J. BAEDECKER, and I.R. KAPLAN: Geochim. Cosmochim. Acta 39, 195(1975).
KIRCHMER, C.J.: 5 Beta-cholestan-3 Beta-ol: An indicator of fecal pollution. PhD thesis, Univ. of Fla., Gainesville FL, 1971.
MATTHEWS, W.P., and L.L. SMITH: Lipids 3, 239(1968).
MUELLER, J.A., and J.S. JERIS: Symposium on the Middle Atlantic Continental Shelf and New York Bight, Nov. 1975.
PARMENTIER, G.G., and H.J. EYSSEN: Biochim. Biophys. Acta 348, 279(1974).
RHEAD, M.M., G. EGLINTON, and G.H. DRAFFAN: Chem. Geol. 8, 277(1971).
RILEY, J.P., and R. CHESTER: Introduction to Marine Chemistry, New York, Academic Press, p. 219.
ROSENFELD, R.S., D.K. FUKUSHIMA, L. HELLMAN, and T.F. GALLAGHER: J. Biol. Chem. 211, 301(1954).
TABAK, H.H., R.N. BLOONHUFF, and R.L. BUNCH: Developments in Industrial Microbiology, Vol. 13, Washington DC, Am. Inst. Biol. Sci., 1972.
U. S. EPA: Ocean disposal in the New York Bight; Tech. Briefing Report #2, 1975.

Middle Atlantic Continental Shelf and the New York Bight, Special Symposia 2, 1976, M.G. Gross, ed. (the American Society of Limnology and Oceanography, Inc.) 220-239.

Oxygen depletion in the New York Bight apex: Causes and consequences

Douglas A. Segar[1] *and George A. Berberian*

Atlantic Oceanographic and Meteorological Laboratories, NOAA, 15 Rickenbacker Causeway, Miami, Florida 33149

Abstract

Dissolved oxygen concentrations in waters of the New York Bight apex are near saturation except in summer when a stable thermocline exists and concentrations in the lower layer can drop to 10% of saturation.

Mass balances of oxygen and carbon cycles in the apex were examined. Photosynthetically produced carbon accounts for most of the oxygen demand, particularly in summer. Oxygen demand due to sewage sludge and dredge spoils is small compared to that from organic carbon produced in situ. Oxygen demand of particulate and dissolved organics in the estuarine discharge may be as great as the sewage sludge and dredge spoils together.

Midsummer primary productivity in the apex is high due to nutrient inputs, particularly nitrogen. Most nitrogen, supplied to the apex in forms suitable to support photosynthetic production, comes from the discharge of the Hudson-Raritan-Passaic systems. Most of this nitrogen comes from liquid effluents of sewage treatment plants discharged to the rivers.

Ocean dumping in the bight apex does not cause the low oxygen concentrations found in summer. These are caused primarily by nitrogen supply from rivers. Improvement in dissolved oxygen concentrations could be achieved by removing nitrogen from sewage treatment plant effluents.

The impact of man's activities on the New York Bight, particularly the inner bight, has been appreciable (NMFS 1972). One probable cause of the reported degradation of benthic communities in the bight apex is the low oxygen concentration in bottom waters during summer (NMFS 1972). Low oxygen values have been observed in the region of the sewage sludge and dredge spoil dumpsites (Corwin 1970; NMFS 1972; Horne et al. 1971; Ketchum et al. 1951). It has been assumed generally that the oxygen demand of dumped material is responsible for removing the oxygen from the water. Studies of man's impact on the New York Bight supported by NOAA's Marine EcoSystems Analysis (MESA) Program included the question of low oxygen concentrations in the apex of the bight.

Distribution and seasonal variation of dissolved oxygen in the New York Bight

In 1948–1949 the first observations of low oxygen concentrations, about 50% saturation, in the bottom waters of this area were made (Ketchum et al. 1951). In September 1969 Corwin (1970) found oxygen at 26% of saturation while Horne et al. (1971) reported saturation values as low as 10% at the center of the dumping area. In 1969–1970 investigators from the Sandy Hook Laboratory found the lowest oxygen concentrations during summer when a strong thermocline was present. During winter the well mixed water column was essentially saturated with oxygen (NMFS 1972).

Distributions and seasonal cycles of certain dissolved and suspended particulate chemical species in the apex were studied on cruises made between April 1974 and March 1975. On each cruise continuous vertical profiles of salinity, temperature, and depth were obtained at a series of stations with an InterOcean model 513-10 CSTD. A General Oceanics model 1015 rosette multibottle array, equipped with General Oceanics 10-liter model 1070 top-drop Niskin bottles, was interfaced with the CSTD system. Water samples were obtained at the surface (1 m) and at intervals of 10 m to the bottom with a bottom sample about 2 m above the sediment–water interface. Each water sample was analyzed for salinity, dissolved oxygen, pH, nitrate, nitrite, phosphate, silicate, total suspended particulate

[1] Present address: NOAA, Code C61, Rockville, Maryland 20852.

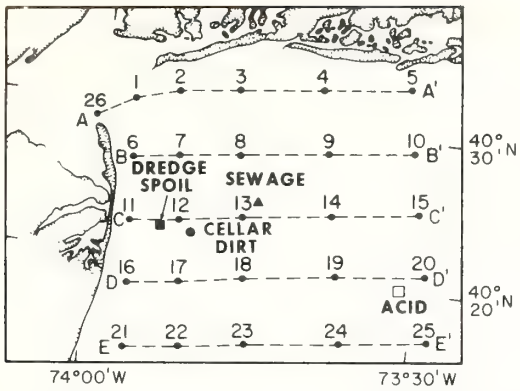


Fig. 1. Station locations, designated dumpsites, and transects (A'–A', B'–B', etc.) for which vertical sections are plotted in Figs. 3–7, 11–15, and 17–18.

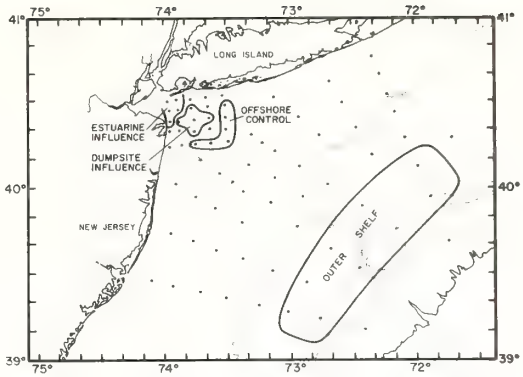


Fig. 2. Extended sampling grid, showing designated regimes for which average values are calculated (*see text*). Station grid sampled 26 February–3 March 1975.

load, particle size distribution, suspended total organic carbon and nitrogen, suspended total carbohydrates and total proteins, and dissolved metals including Fe, Mn, Cd, Cu, and Zn (Cantillo et al. 1976).

Seven cruises were carried out between April and November 1974 at 36-day intervals to coincide with ERTS (Earth Resour. Technol. Satellite) overpasses. Cruise dates were 16–20 April, 6–9 May, 10–13 June, 16–19 July, 21–24 August, 29 September–2 October, and 4–7 November. A grid of 25 stations (26 in September and November) was occupied (Fig. 1). An additional cruise was carried out in the period 26 February–3 March 1975; this cruise occupied a series of 64 stations over a larger area (Fig. 2).

Oxygen analyses were performed by the Winkler titration (Strickland and Parsons 1968). Percentage saturations of oxygen were calculated from these values and the salinity and temperature with the equations of Weiss (1970).

Vertical sections of percentage saturations of oxygen in the apex regions are shown in Figs. 3–7 for cruises in April, June, August, September, and November. In April the water column was almost isothermal but was weakly stratified with lower salinity water at the surface (Hazelworth et al. 1975*a*). The water column was almost saturated or slightly supersaturated with oxygen, although lower saturations occurred consistently in the lower layer (Fig. 3). By June the waters were stratified. Although near-surface waters were saturated or supersaturated with oxygen, the oxygen saturations in subthermocline waters had dropped, falling below 80% near the bottom in extensive areas of the apex (Fig. 4). In August (Fig. 5) with a well stratified water column, the area and depth of low oxygen waters were considerably extended, and saturation values as low as 28% were observed. By late September (Fig. 6) surface water temperatures had fallen, and the stratification was less well defined. The oxygen saturation values, although still lower near the bottom than at the surface, were not as low as they had been during midsummer. During the November cruise and for a number of days immediately before it, the weather was mild, and it was unusually calm and sunny in the New York area. The water column had cooled, and the thermocline had been partly destroyed by mixing. In this unusual situation, oxygen saturation values were variable and generally low (Fig. 7). Low oxygen waters extended to the surface. Rates of re-aeration would have been slow due to the surface film integrity that resulted from the extremely calm seas.

Lowest oxygen concentrations observed in summer were about 2 mg/liter. Investigators from the Sandy Hook Laboratory observed oxygen concentrations as low as 1 mg/liter in waters within 1 m above the sediment–water interface during 26 August–6 September, immediately after our August cruise (Thomas et al. 1976). They also con-

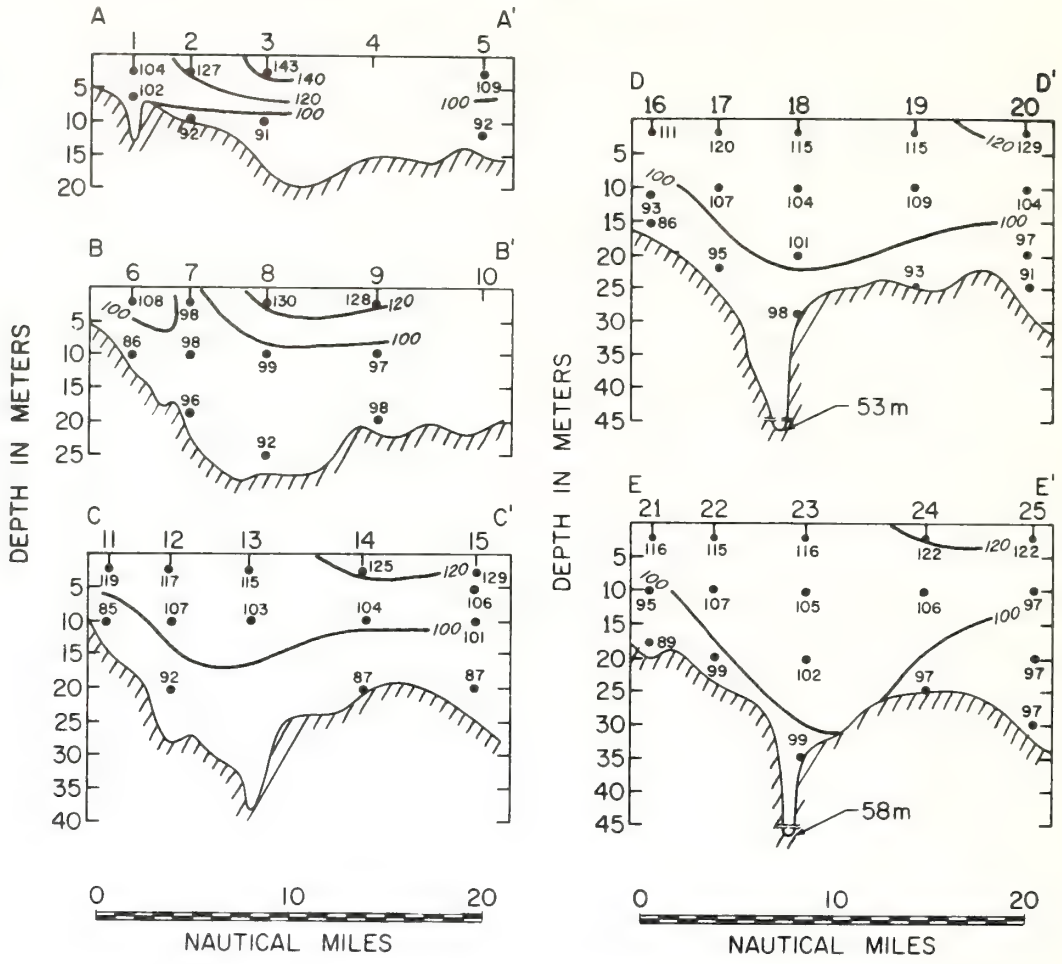


Fig. 3. Percent of saturation of dissolved oxygen in the apex, 16–20 April 1974.

firmed that large areas of the bight apex had bottom water with low oxygen concentrations.

There is considerable evidence that oxygen concentrations below about 4 mg/liter are responsible for changes in species composition and the abundance of marine organisms (Rheinheimer 1972; Vidaver 1972). The effects of low oxygen concentrations in the apex may therefore be responsible, at least in part, for some of the reported degradations in marine biological communities (NMFS 1972; Pararas-Carayannis 1973).

Processes affecting oxygen concentrations

The low oxygen concentrations could be due either to oxygen demand within the apex or to inflows of low oxygen water. Several considerations suggest that although low oxygen waters may enter from outside, this source is quantitatively less important in maintenance of low oxygen concentrations than oxygen demand within the apex itself.

Water entering the apex must come as a low salinity discharge from Lower New York Bay or from the open shelf. Low salinity water from Lower New York Bay was thought to be responsible for some of the low saturation water found in the open waters of the apex (Horne et al. 1971). However, measurements of oxygen concentrations and percent saturation in the discharge area itself do not support this view

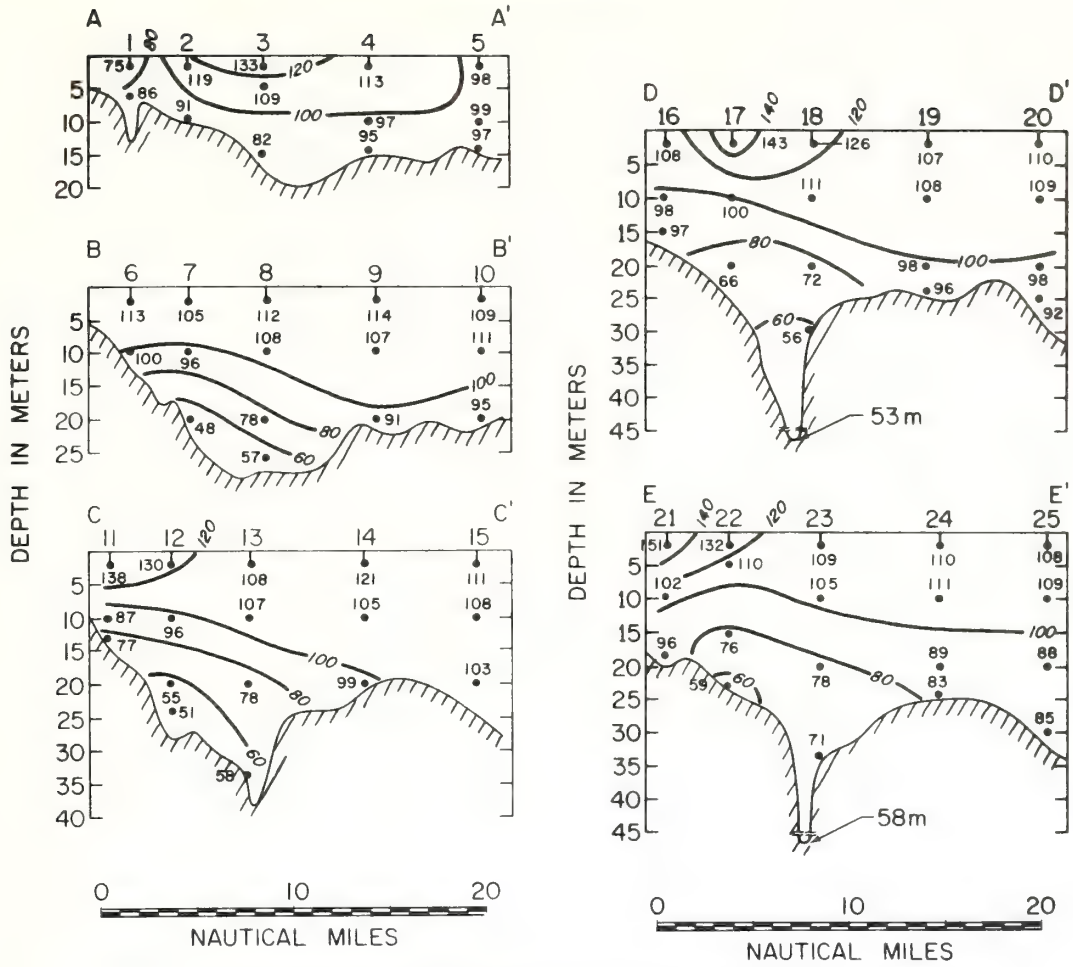


Fig. 4. Percent of saturation of dissolved oxygen in the apex, 10–13 June 1974.

(J. E. Alexander and I. Duedall personal communications; Figs. 3–7: stations 1, 2, 6, and 26). Oxidizable material in the estuarine discharge exerts an oxygen demand and influences dissolved oxygen concentrations. Such oxygen demand takes place within the apex itself and is discussed below.

Water entering the apex from the open shelf does not have anomalously low oxygen concentrations. Water below the thermocline on the Atlantic shelf was essentially saturated or slightly undersaturated with oxygen in September 1969 (Corwin 1970). Also, our data indicate that a substantial fraction of the oxygen must be removed from the water column within the bight apex. The average oxygen concentration and percent saturation for samples below the thermocline can be calculated by averaging all values for samples below 10 m. The thermocline is generally between 10 and 20 m (Hazelworth et al. 1975*a*,*b*). Averages have been calculated for groups of stations representing the dumpsite region (stations 8, 12, 13, 14, and 18—Fig. 8) and the outer edge of the apex through which exchange of water with the open shelf must take place (stations 10, 15, 20, 23, 24, and 25—Fig. 8—referred to as offshore control). Consistently throughout the year oxygen saturations and concentrations within the apex (dumpsite influenced region) are lower than at the ocean boundary (Figs. 9 and 10). Dissolved oxygen in wa-

ters at the ocean boundary of the apex is near saturation throughout the year. Therefore, the bulk of the oxygen depletion must take place through oxygen-demanding processes in the apex itself.

Waters with low percent saturation of oxygen are consistently found in the deeper portion of the Hudson Shelf Valley (station 23, Figs. 3–7). If all bottom water in the apex were derived from northward flow in the axis of the shelf valley, then the low oxygen concentrations in the apex might be due to influx of low oxygen water through this section. However, the data from waters outside the apex during June and September 1975 (unpublished data) suggest that this is not the case. Low oxygen waters at station 23 are not found at stations farther south in the shelf valley, except within several meters of the bottom. Current meter data from the Hudson Shelf Valley axis indicate that, during summer, mean flow near the seabed is slow and reversible, although net movement is normally southward (Lavelle et al. 1975). The quantity of oxygen-poor water that could be introduced to the apex by the slow mean flow in the shelf valley axis is insufficient to account for much of the oxygen depletion in the apex, even if this flow were permanently northward.

There are several sources of oxygen demand in the apex: oxidation of sewage sludge, organic material and sulfides in

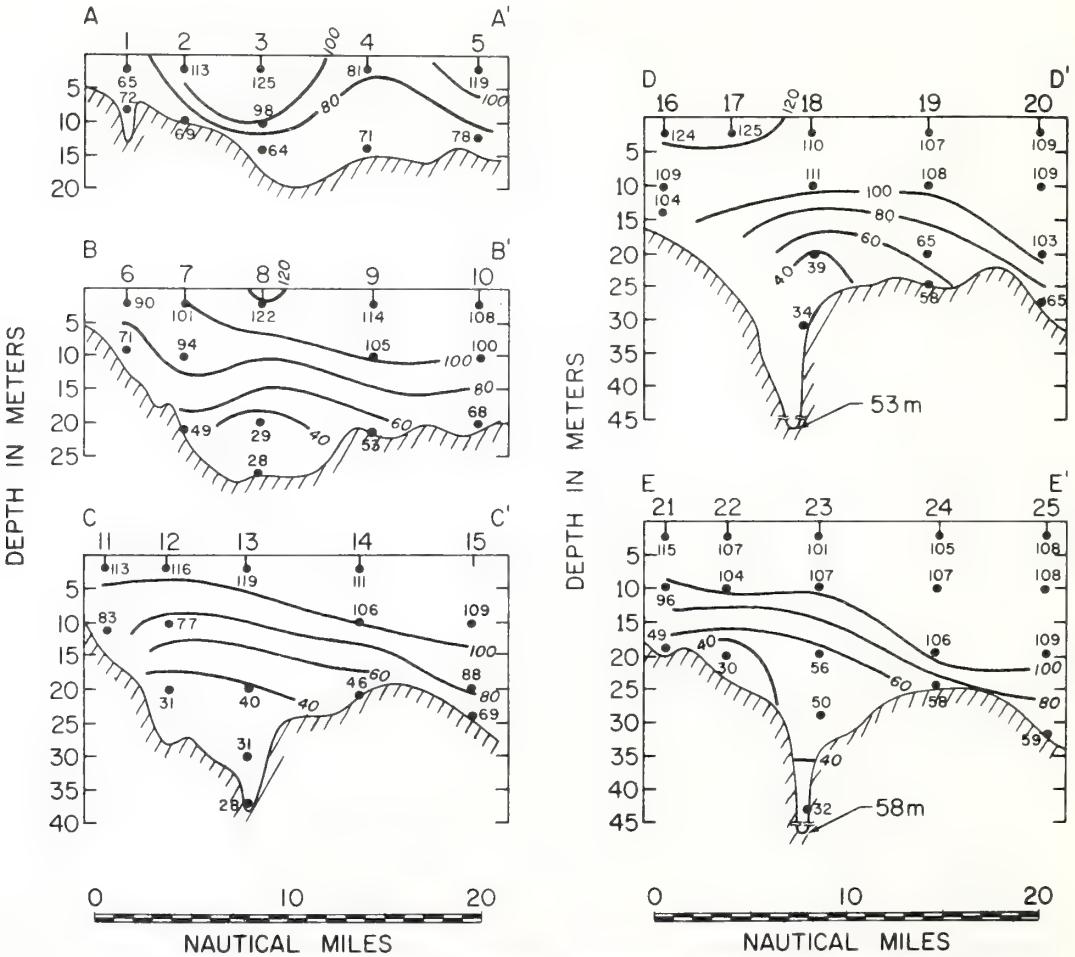


Fig. 5. Percent of saturation of dissolved oxygen in the apex, 21–24 August 1974.

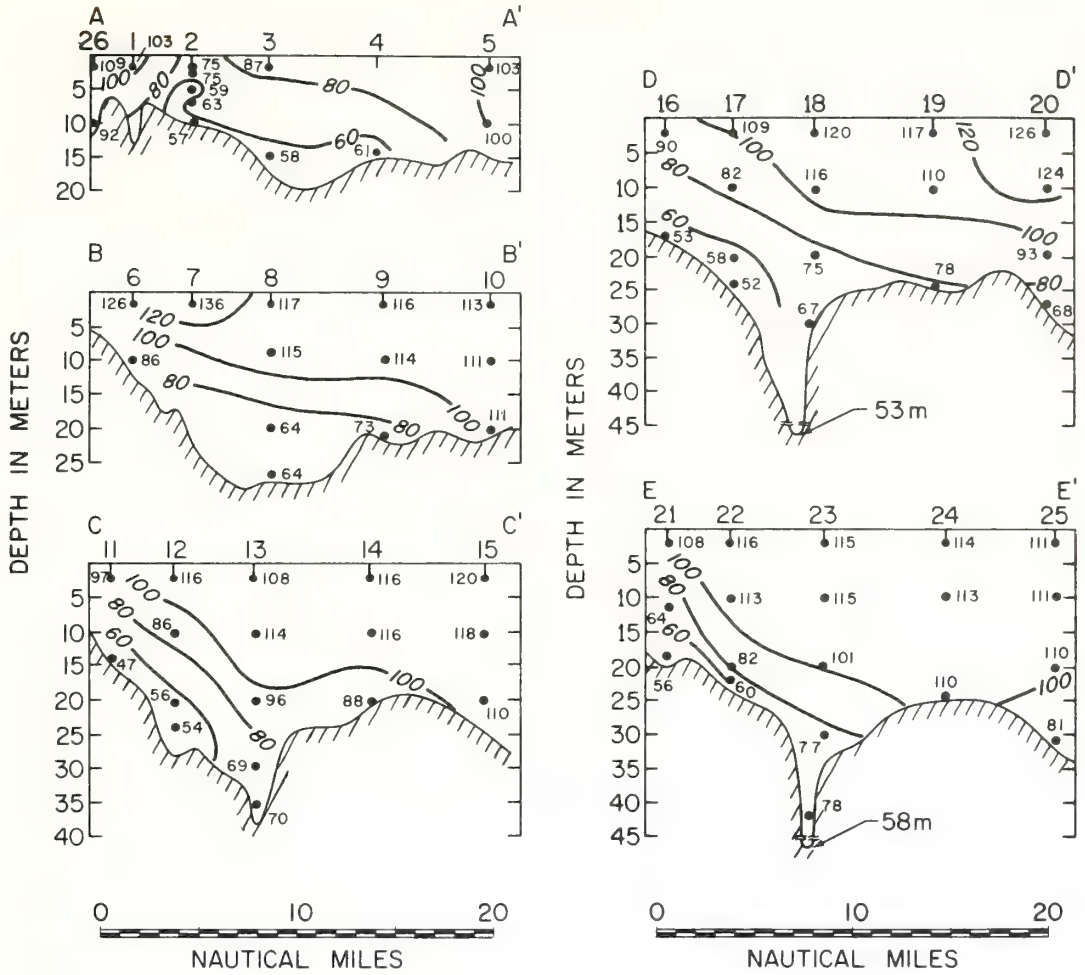


Fig. 6. Percent of saturation of dissolved oxygen in the apex, 29 September–2 October 1974.

dredge spoils, organic matter introduced in the estuarine discharge, acid wastes, and organic matter produced by photosynthesis. The chemical oxygen demand of acid wastes is small (Mueller et al. 1975). Potential oxygen demands of the four significant sources can be estimated. For this purpose, the apex is assumed to be 2,400 km² in area, or the region covered by our apex sampling grid (Fig. 1). This area represents quite well the area of the ocean where exchange with the southwest flow of the open shelf is somewhat restricted (Charnell and Hansen 1974). Amounts of total organic carbon input per day from the four sources are estimated in Table 1 and oxygen demands in

Table 1. Approximate total organic carbon inputs to the apex (kg oxidizable C per day).

Sewage sludge dumping*	1.1×10^5
Dredge spoil dumping*	5.4×10^5
Primary production†	
Average	2.2×10^6
Summer	6.5×10^6
Estuarine input	
Particulate‡	7.3×10^4
Dissolved§	$\simeq1\times10^6$

* From Mueller et al. (1975).

† Calculated from Malone (1976). Productivity interpolated between stations and integrated over 2,400 km² apex.

‡ Average mean flow rate of estuarine discharge of Raritan Bay 850 m³/s (Mueller et al. 1975). Total particulate organic carbon 0.6 mg/liter (Hatcher unpublished data).

§ Assumes mean discharge of Raritan Bay 850 m³/s (Mueller et al. 1975) and about 10 mg/liter of dissolved organic carbon (Alexander et al. 1974). Considerable uncertainty exists as to the dissolved organic carbon estimate.

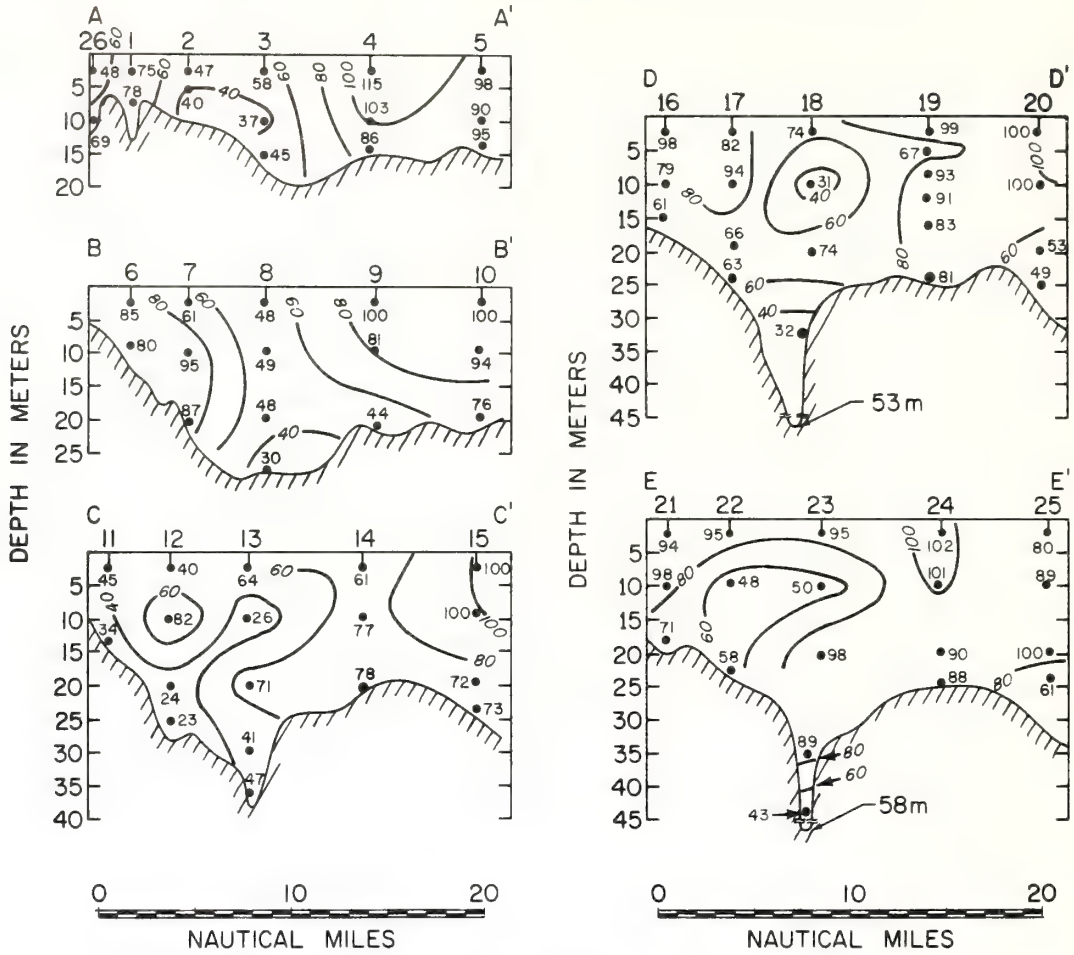


Fig. 7. Percent of saturation of dissolved oxygen in the apex, 4–7 November 1974.

Table 2. The major oxygen demand is from decomposition of photosynthetically produced organic matter, especially in summer. Ocean dumping is quantitatively less important. The river input may be quantitatively important. Analytical uncertainties of dissolved organic carbon concentrations in the river are such that the river input (Tables 1 and 2) is probably overestimated.

Four types of particulate organic matter having similar densities and size ranges are introduced to the apex through surface waters. Therefore, similar fractions of each type of organic matter will be transported vertically downward through the thermocline in summer, except that some dredge spoil and sewage sludge organics may be entrained with the rapidly settling mineral material.

Organic matter from sewage sludge, dredge spoils, and the estuarine outflows is

Table 2. Total potential oxygen demand from major sources in the apex (kg O_2 per day).

Sewage sludge dumping*	1.1×10^6
Dredge spoil dumping*	2.1×10^6
Primary production†	
Average	5.7×10^6
Summer	1.7×10^7
River input†‡	$\simeq5\times10^6$

* From COD data (Mueller et al. 1975).
† From organic carbon (Table 1) and Redfield ratio of carbon to oxygen (Redfield et al. 1963). Assumes complete oxidation.
‡ Considerable uncertainty exists.

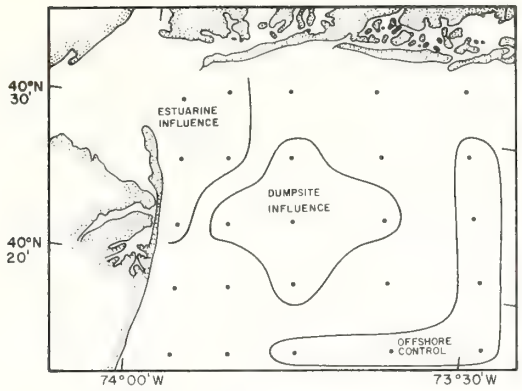


Fig. 8. Stations designated estuarine influenced, dumpsite influenced, and offshore control, for which average concentrations are calculated (*see text*).

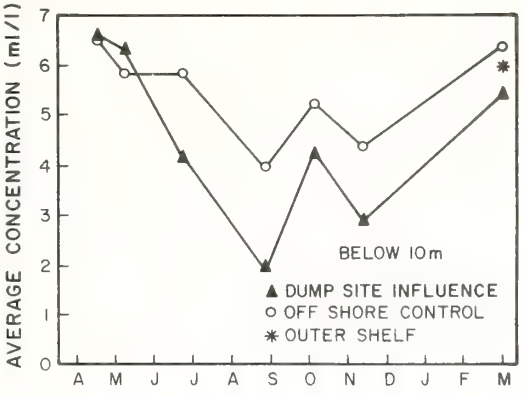


Fig. 10. Seasonal variation of average dissolved oxygen concentration in the water column below 10-m depth in the apex. (*See Figs. 2 and 8.* N.B. 1 ml/liter = 1.43 mg/liter. The latter units are used in the text.)

already partially oxidized. It will, therefore, be more refractory and oxidize slower than the organic matter produced by phytoplankton in the apex.

Mean residence times of low density particles in the apex are estimated to be not more than several weeks (Segar and Cantillo 1976). The proportion of organic matter introduced in dredge spoils or sewage sludge which is oxidized during residence in the apex will be lower than the proportion of photosynthetically produced material oxidized, assuming they have similar mean residence times in the apex. The dominance of the photosynthetic material over other sources in oxygen uptake in the lower layer of the apex is, therefore, probably underestimated in Tables 1 and 2.

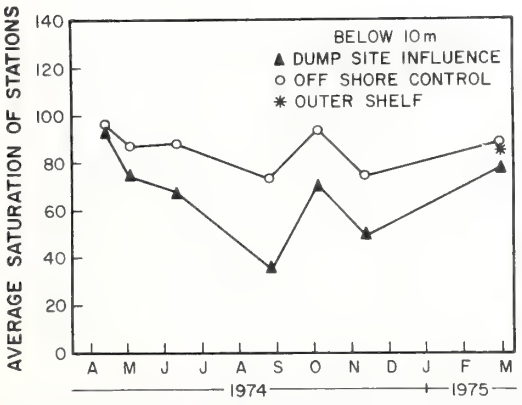


Fig. 9. Seasonal variation of average percent of saturation of dissolved oxygen in the water column below 10-m depth in the apex. (*See Figs. 2 and 8.*)

If the water were saturated, the total quantity of dissolved oxygen below 10 m in the apex in summer would be about 2×10^8 kg ($\simeq$8 mg O_2/liter in 2.6×10^{13} liters of water). Total oxygen demand of sewage sludge, dredge spoils, and summer primary production ($\simeq2\times10^7$ kg O_2/d: Table 2) is sufficient to deplete the dissolved oxygen in this water layer in about 10 days. Some oxygen demanding material will be transported out of the apex before being oxidized, and, in the surface layer, some oxygen will be replaced from the atmosphere by photosynthesis. Additionally, much organic matter will be oxidized before being transported below the thermocline. Observed oxygen depletion (average of about 50% saturation) could be achieved if half of the total oxygen demand ($\simeq1\times10^7$ kg O_2/d) occurs below the thermocline and if the residence time of water in the apex is about 1 week (Ketchum et al. 1951). As the mean residence time calculated by Ketchum et al. (1951) probably underestimates the residence time of water below the thermocline in summer, the total oxygen demand in the lower layer required to produce the observed depletion is probably $<1\times10^7$ kg O_2/d.

Decomposition of organic matter and utilization of oxygen may take place either

in the sediments or in the water column. Seabed oxygen consumption in the apex has been determined, and both geographical and temporal variations have been examined (Thomas et al. 1976). Total seabed oxygen demand in the 2,400-km^2 area considered, during summer, estimated from these data is about 1.1×10^6 kg/d. This is small compared to the oxygen demand inputs listed in Table 2. Therefore, most oxygen utilization must occur in the water column, perhaps concentrated in the euphotic zone and near the seabed where suspended sediment concentrations are highest (Drake 1974). Rates of oxidation will be high in the euphotic zone, as much of the easily oxidized organic matter will be oxidized before organic detritus is transported below the thermocline. Rates of oxidation will also be high near the bottom due to the presence of resuspended sediments. Sediments utilize oxygen considerably faster when resuspended (Berg 1970).

Oxygen uptake rates of the waters in the bight apex are not well defined. The only available data appear to be those of Thomas et al. (1976) who measured the oxygen consumption of water samples taken in summer, close to the sediment–water interface at a number of stations, coincident with seabed oxygen consumption measurements. The total oxygen demand of the water column below a depth of 10 m during summer in the apex calculated from these data is

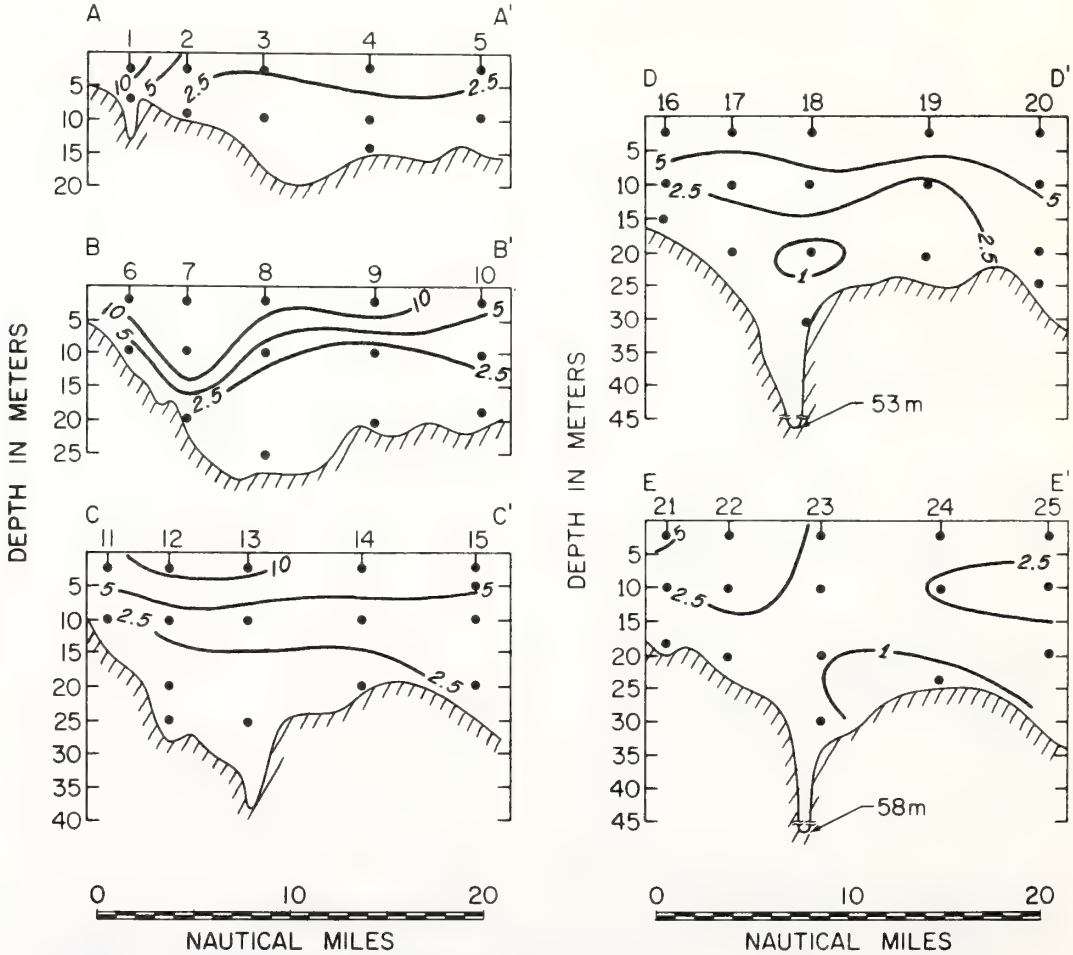


Fig. 11. Dissolved nitrate and nitrite (μg atoms N/liter) in the apex, 16–20 April 1974.

about 10^7 kg O_2/d—about ten times the seabed oxygen consumption—but the estimate is not good because the data are sparse.

Total oxygen consumption in the apex below a depth of 10 m, including seabed and water column consumption, is estimated to be about 10^7 kg O_2/d. This is comparable to the total oxygen demand inputs to the apex listed in Table 2.

Primary production and nutrients

Malone (1976) showed that mean primary production in the apex is 370 g C m^{-2} yr^{-1}; Mandelli et al. (1970) found a mean annual production of 420 g C m^{-2} yr^{-1} within the region extending to 5 mi south of Long Island. Primary productivity in waters outside the apex has been estimated by Ryther and Yentsch (1958) to decrease from 160 to 100 g C m^{-2} yr^{-1} going from 50 to 1,000 m deep. Therefore, the apex productivity is high compared to offshore values. Much of the excess production takes place in midsummer when productivity farther offshore is reduced because of nutrient depletion.

Several factors influence the productivity of oceanic phytoplankton. The availability of light and of the micronutrients nitrogen and phosphorus normally controls the productivity in coastal waters (Harvey 1963). In the New York Bight little is known about the relative importance of these two factors.

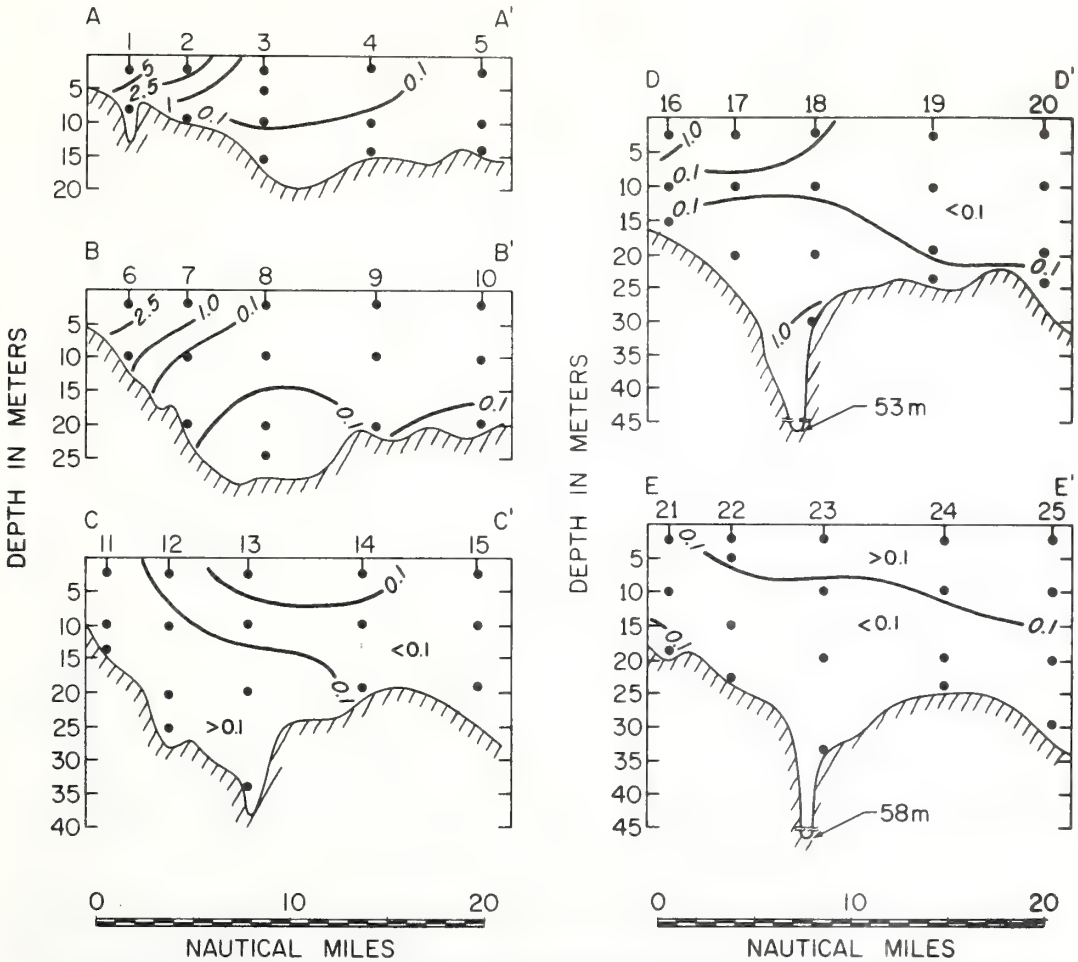


Fig. 12. Dissolved nitrate and nitrite (μg atoms N/liter) in the apex, 10–13 June 1974.

Ryther and Dunstan (1971) concluded that phytoplankton growth in the bight is nitrogen limited. They based this on the distribution of dissolved inorganic nitrogen and phosphorous in September 1969 and on bioassay experiments with *Skeletonema costatum*. From a study of productivity, light intensity, and chlorophyll *a*, Malone (1976) concluded that phytoplankton growth in the apex is light limited. However, he qualified this statement by noting that the low dissolved inorganic nitrogen to phosphorus ratios found in the bight could indicate that nitrogen is a growth limiting factor in summer in the outer portion of the apex.

Dissolved inorganic nitrogen (nitrate and nitrite) distributions in the apex between April and November 1974 are shown in Figs. 11–15. Highest concentrations are always associated with the plume of waters from Lower New York Bay. The plume normally lies along the New Jersey coast. The dissolved inorganic nitrogen concentrations in the surface layer of the center and outer part of the apex drop almost to zero and remain low during summer (Fig. 16). However, the dissolved inorganic nitrogen in the estuarine discharge area (stations 26, 1, 2, 6, 7, and 11: Fig. 1) remains higher throughout the year, as it does in the water below 10-m depth (Fig. 16).

Our dissolved inorganic nitrogen values do not include ammonia which may constitute the major fraction of inorganic nitrogen

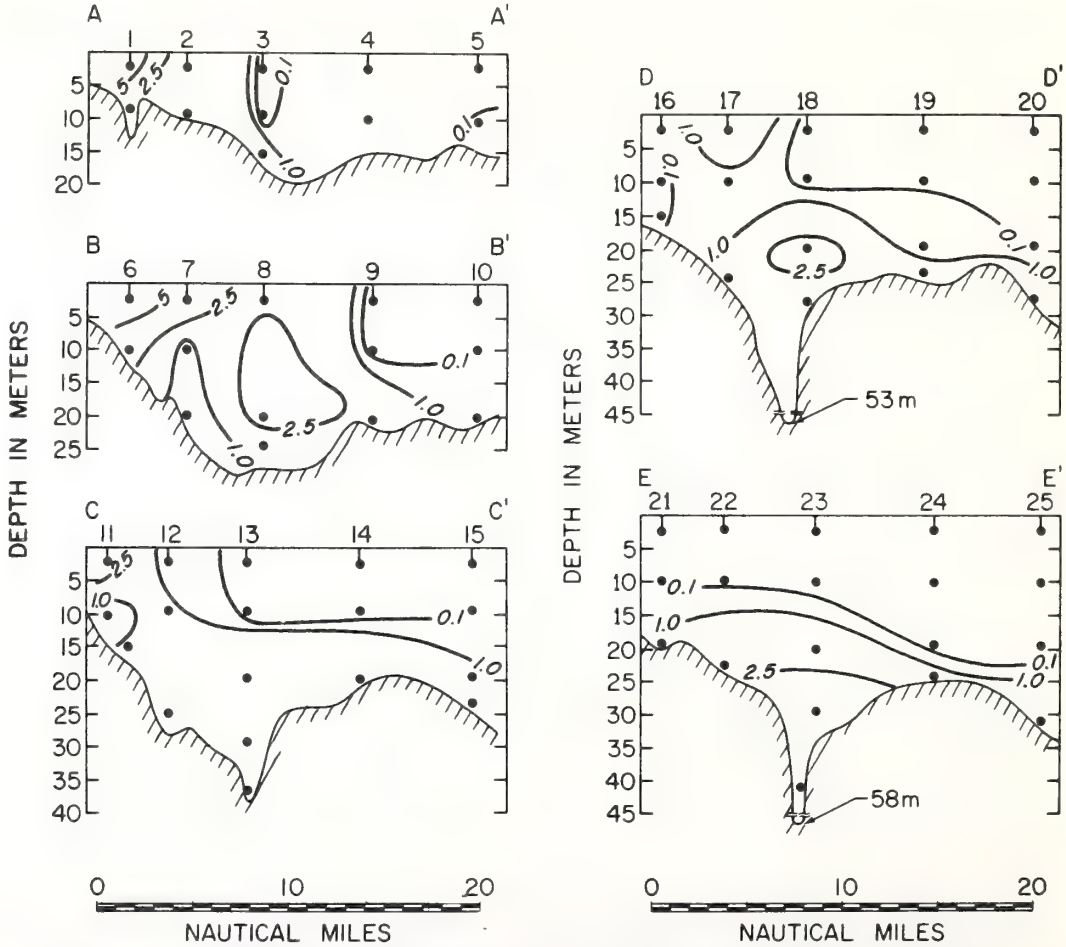


Fig. 13. Dissolved nitrate and nitrite (μg atoms N/liter) in the apex, 21–24 August 1974.

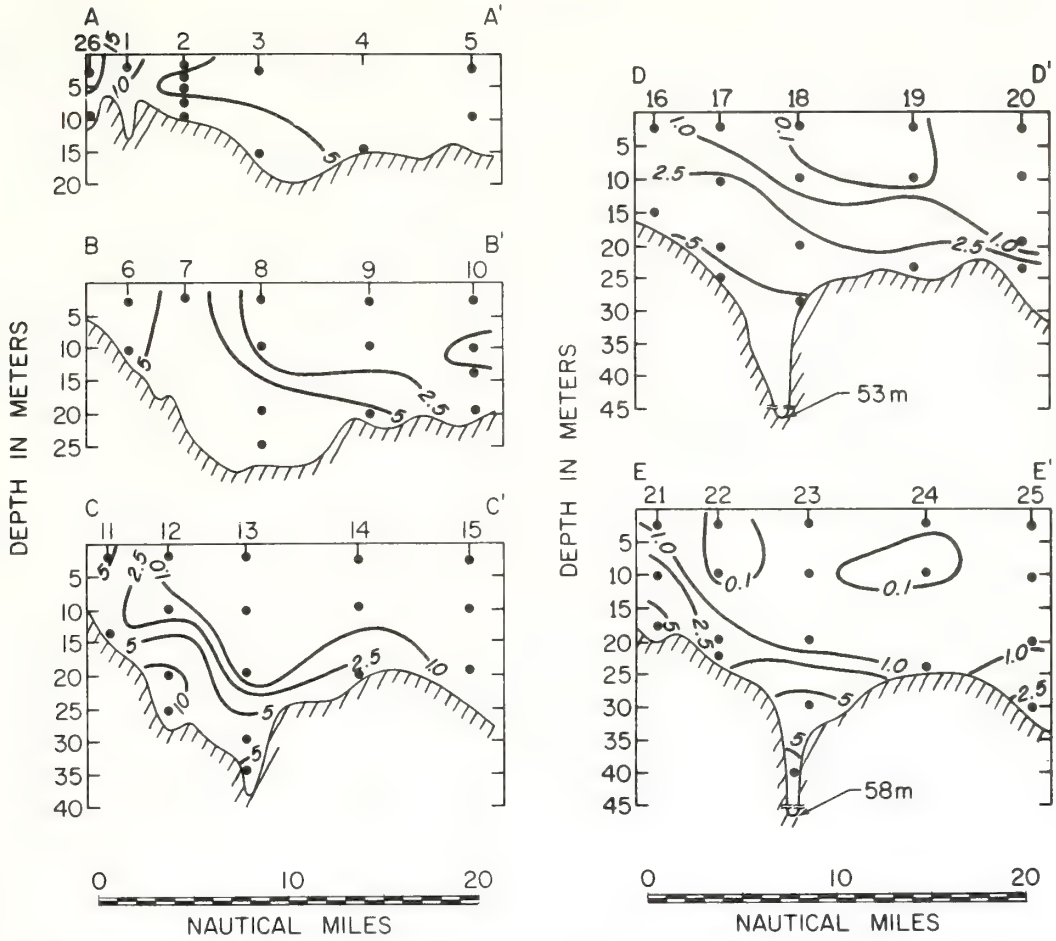


Fig. 14. Dissolved nitrate and nitrite (μg atoms N/liter) in the apex, 29 September–2 October 1974.

in the surface waters in summer when nitrate and nitrite are depleted (Cooper 1933). Ammonia originates primarily from decomposition of organic matter in the surface water, either by bacteria or zooplankton feeding and excretion and is rapidly reassimilated by phytoplankton. Ammonia is added to the apex both from the estuarine discharges and dumping of sewage sludge and dredge spoils (Duedall et al. 1975). However, phytoplankton generally exhibits a marked preference for ammonia-nitrogen over nitrate and nitrite (Harvey 1963; Dugdale and Goering 1967). If the quantity of ammonia supplied to the apex were sufficient to support all of the primary production in the apex, then the nitrate and nitrite would not be depleted.

Malone (1976) reported ammonia concentrations in the bight apex from April to August 1974. His data suggest that ammonia may be the most significant fraction of dissolved inorganic nitrogen in the water column below the thermocline, particularly where low oxygen concentrations occur during midsummer. Ammonia is regenerated from organic matter by bacterial decomposition—the process which is also primarily responsible for the reduction in oxygen concentrations.

Ammonia concentrations observed by Malone (1976) in surface waters of the

bight apex during summer were generally high only near the estuarine discharge. In the rest of the apex, concentrations were close to the analytical detection limit.

Dissolved inorganic phosphate distributions in June and August 1974 are shown in Figs. 17 and 18 and the seasonal variation in Fig. 19. Although low phosphate concentrations are observed in summer, they remain above those normally associated with growth limitation (Fuhs et al. 1972). Like dissolved inorganic nitrogen, the highest phosphorus concentrations are found in the discharge from Lower New York Bay, while higher values are almost always found in water below 10 m than are found in the upper 10 m (Fig. 19).

The atom ratio of dissolved inorganic nitrogen to dissolved inorganic phosphorus in open oceans is about 15:1, the same ratio that is generally found in phytoplankton cells (Redfield 1958). However, in areas of restricted circulation and high biological activity, this ratio can change. Usually it becomes lower because nitrogen is removed from the surface layers more rapidly than phosphorus due to its slower regeneration from decomposing organic matter (Ryther and Dunstan 1971). Very low values of this ratio where phosphorus is more abundant than nitrogen are found only in areas where nitrogen is limiting for phytoplankton growth. The variation in the ratio of dissolved inorganic nitrogen to dissolved inor-

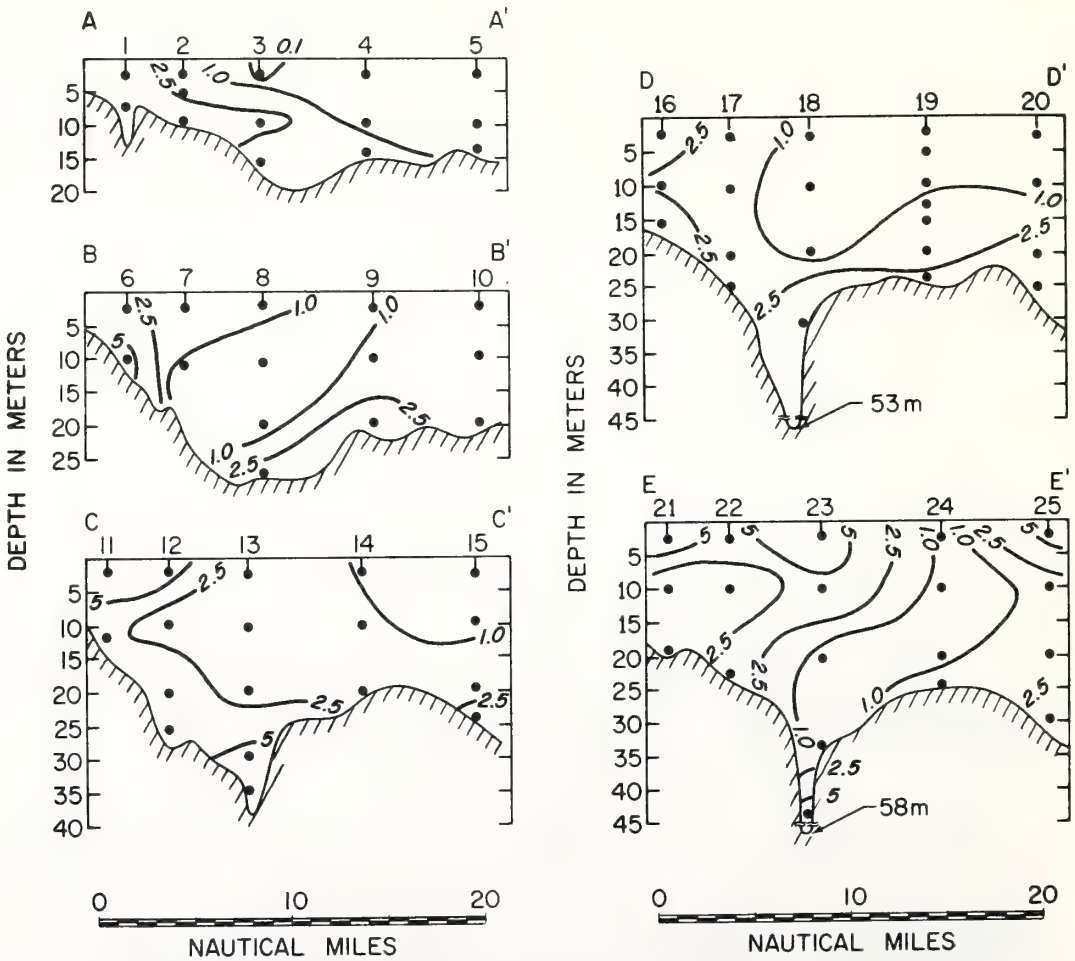


Fig. 15. Dissolved nitrate and nitrite (μg atoms N/liter) in the apex, 4–7 November 1974.

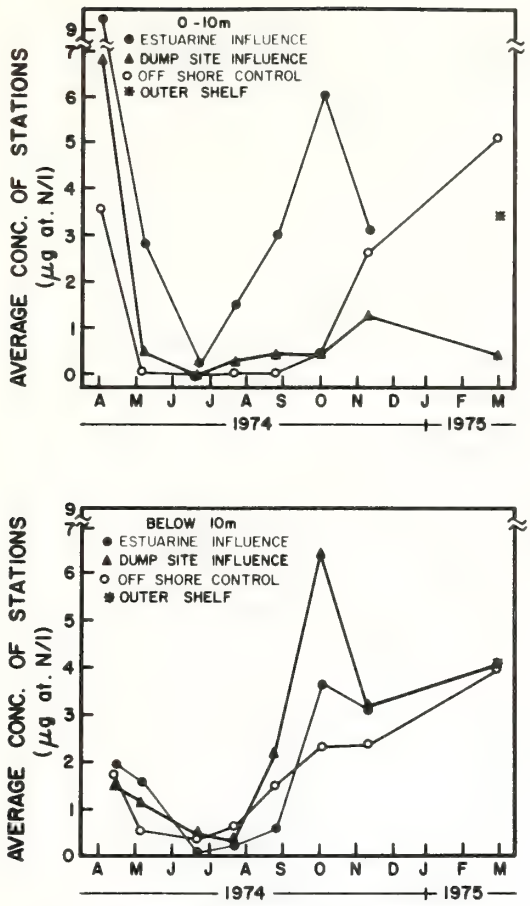


Fig. 16. Seasonal variation of average dissolved nitrate and nitrite, 10 m and above, and below 10-m depth in the apex for estuarine and dumpsite influenced regions, offshore control, and winter average for outer shelf region. (*See Figs. 2 and 8.*)

ganic phosphorus for surface waters in the bight is shown in Fig. 20. The ratio does not include ammonia-nitrogen and would be higher with this included, particularly in summer. However, Malone's (1976) data indicate that the ratio with ammonia included would be no more than two or three times the summer values in Fig. 20. The ratio, even corrected for ammonia, is extremely low throughout summer. Note that the estuarine water consistently has higher N:P ratios than the central apex (dumpsite influenced), and the stations farthest offshore consistently have the lowest N:P ratio.

We interpret the data as follows. During winter, productivity in the apex is light limited. In spring, as light intensity increases, productivity in and near the turbid estuarine plume is light limited, while areas outside sustain phytoplankton blooms, stripping surface waters of nitrogen. When nitrogen becomes limiting in the outer area of the apex, the total production of the apex region is also limited by nitrogen, even though the growth rate in the more turbid inner apex remains light limited. All of the nitrogen supplied to the surface layer of the apex is consumed by phytoplankton growth within the apex during this summer period. Organic matter produced is partially reoxidized in the surface waters, releasing some nitrogen for recycling. The remaining organic matter is transported below the thermocline and oxidized, becoming the primary cause of the low oxygen values observed in this water mass.

It is possible that some intense localized phytoplankton blooms in the New York Bight apex in spring and summer are caused by mixing high-nutrient low-transparency estuarine water with nutrient-depleted clear ocean water. If the edge of the turbid estuarine plume is sharp, as it often appears to be from satellite images, then phytoplankton in a very restricted area at the interface will have an adequate nutrient supply and will not be light limited, due to settling out of some estuarine-derived suspended particles.

The sources of nitrogen input to surface waters of the apex during the summer stratified period include dumped waste materials, estuarine discharge, atmospheric fallout and washout, and mixing across the thermocline. The last of these is likely to be small. Water entering the apex from the outer shelf during midsummer is depleted of dissolved inorganic nitrogen (Figs. 12, 13, and 16) except for near-bottom waters. It is difficult to estimate the amount of nitrogen transported into the apex from the outer shelf because the dynamical information available is limited. However, if the differential between water entering the apex and that leaving were 1 μg atom N/liter, the flushing time were 7 days, and all of the nitrogen thus supplied were brought into

the surface layer and made available for photosynthesis, then the rate of input would be about 1×10^5 kg N/d. This estimate is probably too high, as the concentration differential is less than 1 μg atom N/liter in surface waters moving in and out of the apex in midsummer, and inhibition of vertical mixing by the thermocline will prevent much of the nitrogen introduced in the deeper water from being made available for photosynthesis. Therefore, the supply of nitrogen to the apex for photosynthesis from the outer shelf is probably small compared to the other sources whose inputs are estimated in Table 3. In any event, nitrogen from outside the apex would be supplied irrespective of man's presence and, therefore, cannot account for the high productivity of the apex in comparison to other continental shelf regions.

Table 3. Total nitrogen supplied to the apex (kg N per day).

Sewage sludge dumping*	1.7×10^4
Dredge spoil dumping*	6.3×10^4
River input†	1.2×10^5
Atmospheric input*	6.4×10^4‡

* From Mueller et al. (1975); total Kjeldahl nitrogen.
† From Garside et al. (1976); summer value, winter is 1.6×10^5.
‡ Considerable uncertainty.

Table 3 gives estimates of nitrogen inputs to the apex from dumping sewage sludge and dredge spoils, from the atmosphere, and from estuarine input. The river input is the major contributor as suggested by the

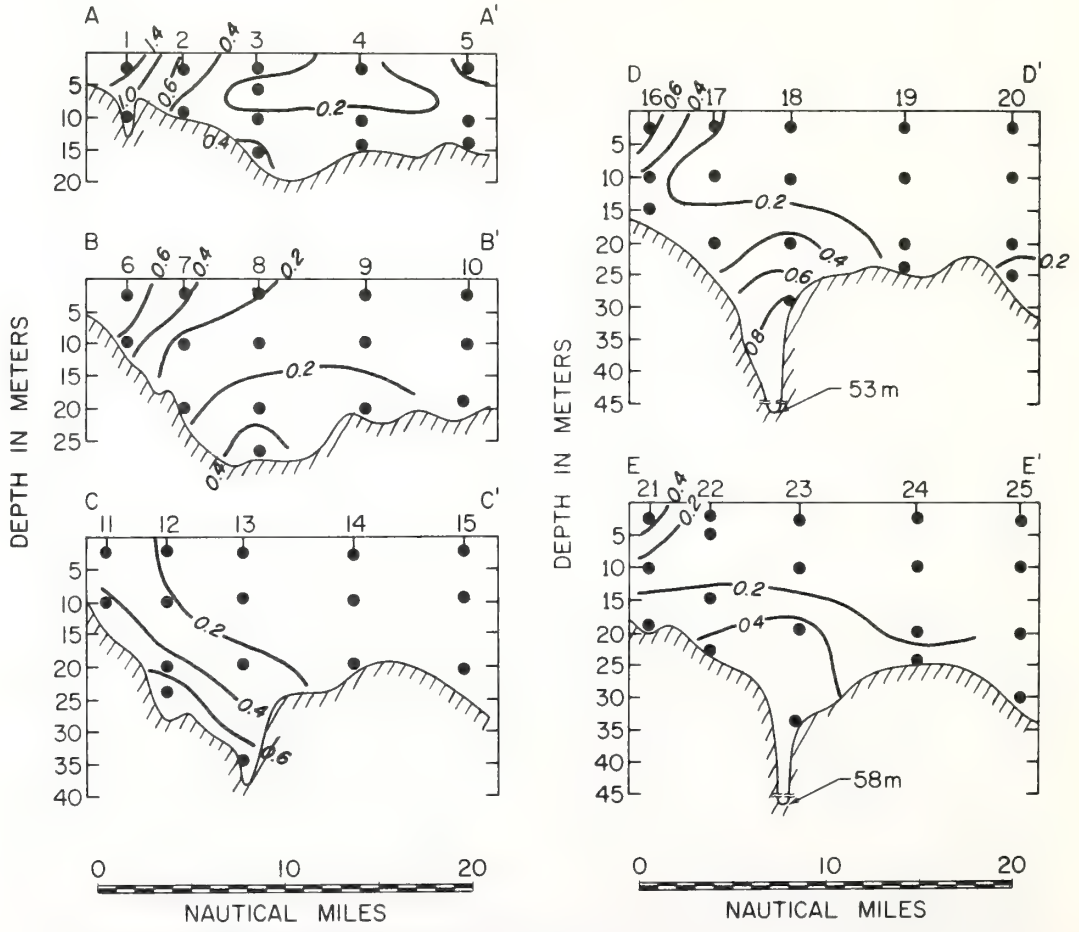


Fig. 17. Dissolved reactive phosphorus (μg atoms P/liter) in the apex, 10–13 June 1974.

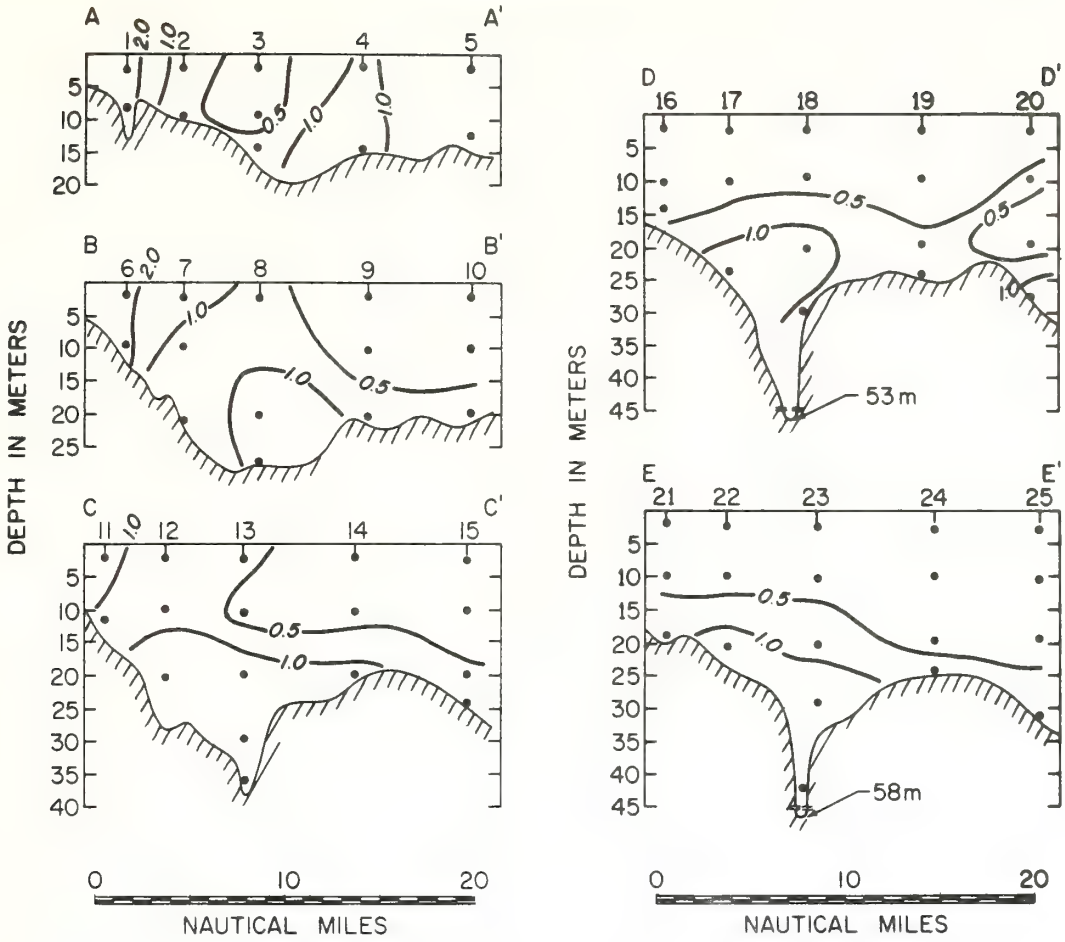


Fig. 18. Dissolved reactive phosphorus (μg atoms P/liter) in the apex, 21–24 August 1974.

nitrogen distributions (Figs. 11–16). In fact, the importance of the river input is probably underestimated in Table 3. The quantities of nitrogen calculated for the dredge spoils and sewage sludge are total Kjeldahl nitrogen values. Much of the nitrogen is organically bound (Mueller et al. 1975) and will not be available for phytoplankton growth before being transported either out of the apex or below the thermocline. Garside et al. (1976) included most but perhaps not all of the inorganic nitrogen which is introduced to the river with sewage or sewage treatment plant effluents in their estimate of estuarine input. Other sources of nitrogen to the rivers, although comparatively small, are not negligible. Mueller et al. (1975) estimated estuarine input of total Kjeldahl nitrogen plus nitrate and nitrite to the apex to be 3.4×10^5 kg N/d.

It is noteworthy that the atmospheric dust and rain input of nitrogen to the bight apex may be significant compared even to the river input and that it consists almost entirely of inorganic nitrogen which is readily available to organisms. However, there is considerable uncertainty about the accuracy of the atmospheric input estimate.

If the only nitrogen supplied to the apex euphotic zone were from the estuarine outflow (1.2×10^5 kg N/d), and no recycling of the nitrogen in the surface waters took place, the C:N ratio of the phytoplankton produced in summer would be 63. Values of

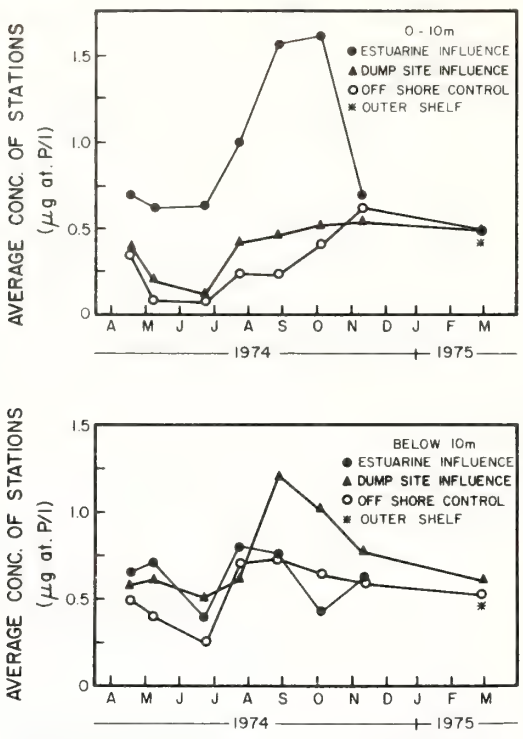


Fig. 19. Same as Fig. 16 for average dissolved reactive phosphorus.

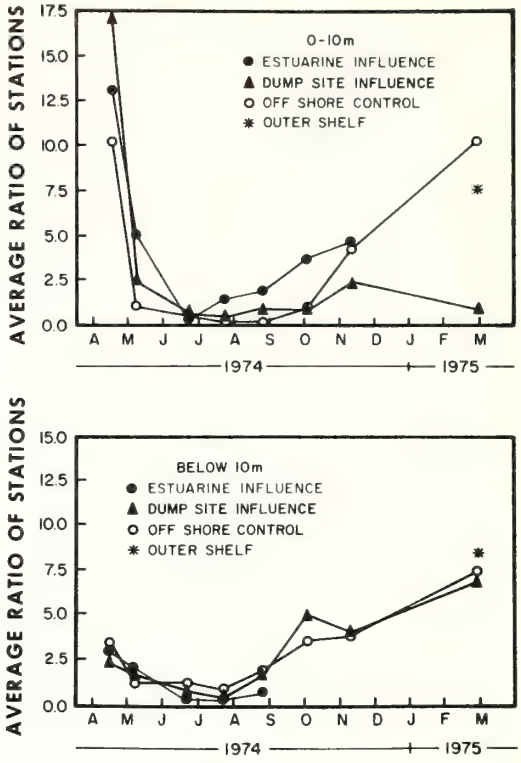


Fig. 20. Same as Fig. 16 for atom ratio of dissolved nitrate and nitrite nitrogen to dissolved reactive phosphorus.

the C:N ratio this high are unknown, but values as high as 20 have been observed in nitrogen limited phytoplankton (Caperon and Meyer 1972), while a ratio of 7 is considered normal (Redfield et al. 1963). The estimate of Garside et al. (1976) for nitrogen input by the estuary is certainly too small, and a substantial proportion of the phytoplankton nitrogen will be regenerated and reutilized within the surface layer before being transported below the thermocline. Therefore, nitrogen from the estuary is enough to sustain much of the phytoplankton production in the apex.

Consequences

The above conclusions have considerable importance for decisions concerning the necessary steps to reduce the deleterious effects of man's activities on the New York Bight ecosystem. The NOAA-MESA Project was designed specifically to aid the transfer of scientific knowledge to the environmental manager's decision-making process. Therefore, it is relevant to review briefly the content of this paper in terms of impending decisions concerning the disposal of sewage sludge generated in the New York–New Jersey metropolitan area.

The Environmental Protection Agency has declared its intent to consider halting all dumping at the present sewage sludge dumpsite in 1976 (EPA 1974). The dumpsite would be moved to a position about 65 nmi from the entrance to Lower New York Bay. The extra distance that the sludge would have to be transported translates into a considerable additional expenditure by local authorities.

Conclusions reached in this paper indicate that the removal of the sewage sludge and/or dredge spoil input to the water column in the New York Bight apex would probably have little effect on the low oxygen concentrations observed in the lower water layer in summer. In fact, the decrease in suspended solids and, therefore, turbidity

might increase the productivity of the apex during times when light limitation exists. Thus, removing sewage sludge and/or dredge spoil inputs could conceivably extend the period when very low oxygen concentrations occur, even though the directly added oxygen demand would be reduced.

Low oxygen concentrations in the bight apex are, however, not the only cause for concern about ocean dumping in the New York Bight apex. Toxic metals, organic compounds, and pathogenic microorganisms are introduced with the dumped material. Segar and Cantillo (1976) demonstrated that stopping sewage sludge dumping in the apex would have little effect on trace metal concentrations within it, but that stopping dredge spoil dumping might significantly reduce these concentrations. Similarly, less extensive studies by MESA personnel suggest that sewage sludge dumping is probably not the major source of organic contaminants such as pesticides and hydrocarbons in the apex. In addition, no evidence exists that pathogenic microorganisms have been transferred from dumped materials to man by way of the oceans.

We conclude that the removal of the sewage sludge dumpsite alone will have little beneficial effect on the New York Bight apex. Removal of both sewage sludge and dredge spoil dumpsites would have only marginal benefits. However, dumping these materials at offshore alternate sites would have potentially harmful effects on the biota living in a region of ocean not presently as heavily impacted by man as is the apex. In fact, the recommendation of the NOAA-MESA Project is that, unless some as yet unidentified critical impact of sewage sludge in the New York Bight becomes known, sewage sludge should continue to be dumped at the present location until EPA phases out ocean dumping entirely in 1981 (Wallace 1976). At the same time, every effort should be made to expedite a solution to the entire sewage treatment problem.

Low oxygen concentrations are perhaps the most critical environmental problem so far identified in the bight apex. Any significant increase in the nitrogen input to the apex would further reduce the oxygen concentrations. The apex is eutrophic. If nitrogen input, particularly from the rivers, were to increase significantly, then it is likely that anoxia would occur. Anoxia is well known in fjords and lakes where the oxygen demand input to bottom water layers is smaller than in the New York Bight but where the flushing time is longer. If anoxic conditions develop in the bight, they would occur episodically. The balance of oxygen demanding processes against flushing of the apex with more oxygen-rich waters and oxygen resupply from the atmosphere is controlled by weather conditions. Fish kills, sulfide release to the atmosphere, and beach contamination associated with anoxia in fjords might well be in the future for New York unless steps are taken to limit nitrogen loading of the rivers. The principal source of nitrogen to the rivers emptying to the New York Bight is wastewater discharge. Therefore, this problem is intimately linked with the sewage sludge disposal problem.

We believe that the possibility that anoxic conditions in New York Bight waters may be caused by nutrient loading, is of sufficient concern that the problem of nutrient removal from wastewater discharges, i.e. better treatment of sewage rather than deeper ocean disposal of sewage sludge, should be examined closely by the New York and New Jersey municipalities and the appropriate agencies.

ADDENDUM (4 October 1976): During May and June 1976 unusual weather conditions obtained in the New York Bight with winds from the south and southwest during a 5-week period. During this time upwelling of cold nutrient-rich water probably occurred, which added to the existing high productivity of *Ceratium tripos*. *Ceratium* had been observed in unusually large numbers along the mid-Atlantic coast during February and succeeding months. At the end of the onwelling period conditions were anoxic and near anoxic in extensive areas of the bight near the New Jersey shore, large quantities of decomposing *C. tripos* were observed in a mat close to the sediments,

and fish and shellfish mortalities were recorded. The anoxic conditions have persisted at least through September 1976. An interim report ("Mortalities of fish and shellfish associated with anoxic bottom water in the Middle Atlantic Bight" NOAA, Middle Atlantic Coastal Fisheries Center, Sandy Hook, N.J., September 1976) stated

> A major environmental event that has affected the sport and commercial fisheries along the New Jersey shore occurred in New York Bight this summer [1976]. The immediate impact includes fish and shellfish mortalities and unusual fish distribution patterns and/or concentrations. Long-term effects, including interruption of spawning, mortalities of eggs and larvae, and disruption of food chains may be as significant to the resource as the actual numbers of organisms killed.

This anoxic episode likely would have been geographically smaller and less persistent, and may in fact not have occurred, had the problem of river nitrogen contamination from sewage treatment plant effluents discussed here not existed to aggravate natural conditions.

References

ALEXANDER, J. E., R. HOLLMAN, AND T. WHITE. 1974. Heavy metal concentrations in the New York Bight. Final Rep. NOAA-MESA, New York Bight Project Contract 4-35262. New York Ocean Sci. Lab. Montauk.

BERG, R. H. 1970. The oxygen demand of resuspended bottom sediments. Tech. Rep. Seattle Univ. NTIS PB 228-263.

CANTILLO, A. Y., G. A. BERBERIAN, P. G. HATCHER, L. E. KEISTER, AND D. A. SEGAR. 1976. Chemistry data of water column sampling cruises No. 6–12 of the NOAA ship *Ferrel*, April–November 1974. NOAA Data Rep. MESA New York Bight Project. In press.

CAPERON, J., AND J. MEYER. 1972. Nitrogen limited growth of marine phytoplankton. 2. Uptake kinetics and their role in nutrient limited growth of phytoplankton. Deep-Sea Res. **19**: 619–632.

CHARNELL, R. L., AND D. V. HANSEN. 1974. Summary and analysis of physical oceanography data collected in the New York Bight apex during 1969–70. MESA Rep. 74–3. NOAA-ERL. 44 p.

COOPER, L. H. N. 1933. Chemical constituents of biological importance in the English Channel. Pt. 1. Phosphate, silicate, nitrate, nitrite, ammonia. J. Mar. Biol. Assoc. U.K. **18**: 677–728.

CORWIN, N. 1970. Reduced data reports for *Atlantis II* 52, and *Goswald* 140, Appendix 1. Tech. Rep. Ref. 70-15, Woods Hole Oceanogr. Inst.

DRAKE, D. E. 1974. Suspended particulate matter in the New York Bight apex, Sept.–Nov. 1973. NOAA Tech. Rept. ERL 318-MESA 1.

DUEDALL, I. W., M. J. BOWMAN, AND H. B. O'CONNORS, JR. 1975. Sewage sludge and ammonium concentrations in New York Bight apex. Estuarine Coastal Mar. Sci. **3**: 457–463.

DUGDALE, R. C., AND J. J. GOERING. 1967. Uptake of new and regenerated forms of nitrogen in primary productivity. Limnol. Oceanogr. **12**: 196–206.

EPA. 1974. Ocean dumping in the New York Bight since 1973. Tech. Briefing Rep., Region 2, Surveillance and Analysis Div.

FUHS, G. W., S. D. DEMMERLE, E. CANELLI, AND M. CHEN. 1972. Characterization of phosphorus-limited plankton algae. Am. Soc. Limnol. Oceanogr. Spec. Symp. **1**: 113–133.

GARSIDE, C., T. C. MALONE, O. A. ROELS, AND B. C. SHARFSTEIN. 1976. An evaluation of sewage derived nutrients and their influence on the Hudson estuary and New York Bight. Estuarine Coastal Mar. Sci. **4**: In press.

HARVEY, H. W. 1963. The chemistry and fertility of sea water. Cambridge Univ.

HAZELWORTH, J. B., B. L. KOLITZ, R. B. STARR, R. L. CHARNELL, G. A. BERBERIAN, AND M. A. WEISELBERG. 1975*a*. Water sampling cruises No. 6–8 of NOAA ship *Ferrel*, April–June 1974. NOAA Data Rep. MESA-1. New York Bight Project.

———, ———, ———, ———, AND ———. 1975*b*. Water sampling cruises No. 9–12 of NOAA ship *Ferrel*, July–Nov. 1974. NOAA Data Rep. ERL MESA-3. New York Bight Project.

HORNE, R. A., A. J. MAHLER, AND R. C. ROSSELLO. 1971. The marine disposal of sewage sludge and dredge spoil in the waters of New York Bight. Rep. U.S. Army, Corps of Engineers, Coastal Eng. Res. Center, contract DACW72-70-C-0030.

KETCHUM, B. H., A. C. REDFIELD, AND J. C. AYERS. 1951. The oceanography of the New York Bight. Pap. Phys. Oceanogr. Meteorol. **12**(1): 46 p.

LAVELLE, J. W., G. H. KELLER, AND T. L. CLARKE. 1975. Possible bottom response to surface winds in the Hudson shelf channel. J. Geophys. Res. **80**: 1953–1956.

MALONE, T. C. 1976. Phytoplankton productiy ity in the apex of the New York Bight: Environmental regulation of productivity/chlorophyll *a*. Am. Soc. Limnol. Oceanogr. Spec. Symp. **2**: 260–272.

MANDELLI, E. P., P. R. BURKHOLDER, T. E. DOHENY, AND R. BRADY. 1970. Studies of primary productivity in coastal waters of southern Long Island, New York. Mar. Biol. **7**: 156–160.

MUELLER, J. A., J. S. JERIS, A. R. ANDERSON, AND C. HUGHES. 1975. Contaminant inputs to the

New York Bight. Rep. MESA Program. *Also* 1976. NOAA Tech. Memo. ERL MESA-6.

National Marine Fisheries Service. 1972. The effects of waste disposal in the New York Bight. Nine sections (NTIS acquisition AD-739531 through AD739539). Summary Final Rep. (AD743936). NOAA-NMFS.

Pararas-Carayannis, G. 1973. Ocean dumping in the New York Bight: An assessment of environmental studies. Tech. Memo. 39. U.S. Army, Corps of Engineers Coastal Eng. Res. Center. 159 p.

Redfield, A. C. 1958. The biological control of chemical factors in the environment. Am. Sci. **46**: 205–222.

———, B. H. Ketchum, and F. A. Richards. 1963. The influence of organisms on the composition of seawater, p. 26–77. *In* M. N. Hill [ed.], The sea, v. 2. Interscience.

Rheinheimer, G. 1972. Dissolved gases, bacteria, fungi, and blue-green algae, p. 1456–1469. *In* O. Kinne [ed.], Marine ecology, v. 1, part 3. Wiley-Interscience.

Ryther, J. H., and W. M. Dunstan. 1971. Nitrogen, phosphorus and eutrophication in the coastal marine environment. Science **171**: 1008–1013.

———, and C. S. Yentsch. 1958. Primary production of continental shelf waters off New York. Limnol. Oceanogr. **3**: 327–335.

Segar, D. A., and A. Y. Cantillo. 1976. Trace metals in the New York Bight. Am. Soc. Limnol. Oceanogr. Spec. Symp. **2**: 171–198.

Strickland, J. D. H., and T. R. Parsons. 1968. A practical handbook of seawater analysis. Bull. Fish. Res. Bd. Can. 167.

Thomas, J. P., W. C. Phoel, F. W. Steimle, J. E. O'Reilly, and C. A. Evans. 1976. Seabed oxygen consumption—New York Bight Apex. Am. Soc. Limnol. Oceanogr. Spec. Symp. **2**: 354–369.

Vidaver, W. 1972. Dissolved gases, plants, p. 1471–1489. *In* O. Kinne [ed.] Marine ecology, v. 1, part 3. Wiley-Interscience.

Wallace, D. H. 1976. Letter to G. M. Hansler, Regional Administrator, Region 2, EPA, p. 199–202. *In* Evaluation of proposed sewage sludge dumpsite areas in the New York Bight. NOAA Tech. Memo. ERL MESA-11.

Weiss, R. F. 1970. The solubility of nitrogen, oxygen, and argon in water and seawater. Deep-Sea Res. **17**: 721–736.

Middle Atlantic Continental Shelf and the New York Bight, Special Symposia 2, 197
M.G. Gross, ed. (the American Society of Limnology and Oceanography, Inc.) 171-19

Trace metals in the New York Bight

Douglas A. Segar[1] *and Adriana Y. Cantillo*

Atlantic Oceanographic and Meteorological Laboratories, NOAA, 15 Rickenbacker Causeway, Miami, Florida 33149

Abstract

Large quantities of trace metals are introduced to the New York Bight apex from many sources. Distributions of dissolved Mn, Fe, Cd, Cu, and Zn are extremely nonuniform in the waters of the apex due to the many sources and complex reactions taking place. Estuarine discharge and dredge spoil dumping are major sources, while sewage sludge and acid waste dumping are minor sources for most elements studied. Much of the dissolved Cu and Fe occurs in a chemical form that is not extractable by chelation/solvent extraction, even after acidification. The quantity of this metal fraction increases with distance from the Hudson-Raritan estuary. Loss from solution of some elements, notably Mn, occurs when estuarine water mixes with oceanic water. Metals, particularly Zn, are released to solution during ocean dumping of sewage sludge and other materials. Concentrations of dissolved metals in the apex are higher than on the open shelf and higher in summer than in spring and fall. This suggests that the apex flushes slower in summer, as inputs do not vary significantly with season.

Budget calculations show that contaminant metals, exemplified by Cu and Zn, do not accumulate in the apex but are rapidly removed either to the estuaries or the surrounding shelf waters. Mean residence times of contaminant metals in the apex waters are less than 6 months, perhaps considerably less

Many activities in the New York metropolitan region produce significant quantities of waste products containing trace metals at concentrations above those normally found in materials introduced to the environment naturally. Atmospheric dust and rainfall, freshwater runoff from land, urban and industrial liquid effluents, and solid wastes dumped into the ocean all provide unnaturally high levels of trace metals to the ocean in the New York Bight. These inputs are concentrated in the apex region of the bight (Fig. 1) where most of the river input takes place, where almost all of the solid waste dumping is concentrated (Mueller et al. 1975), and where atmospheric dust loads apparently are highest (Duce et al. 1976).

Perhaps the first realization of the magnitude of problems associated with metal discharges to the ocean came with the diagnosis of organic mercury as the cause of Minimata disease (Irukayama et al. 1961). The first studies of trace metal contamination of the New York Bight were reported in 1970 (Gross 1970*a*,*b*). Much remains to be learned about the transport, reactions, and ultimate fate of metals in the bight. Here we describe the results of some of the early stages of an investigation of trace metal cycles in the apex.

Methods

The availability of data concerning the concentrations of trace metals in New York Bight sediments and some organisms (Gross et al. 1971; NMFS 1972; Carmody et al. 1973) caused us to direct our initial sampling and analysis toward trace metals in dissolved and suspended particulate states.

Distributions of trace metals and the variability of these distributions with season were investigated between April 1974 and March 1975. On each cruise, continuous vertical profiles of salinity, temperature, and depth were obtained with an Inter Ocean model 513-10 CSTD. The CSTD was interfaced with a General Oceanics model 1015 rosette multibottle array equipped with

[1] Present address: NOAA, Code C61, Rockville, Maryland 20852.

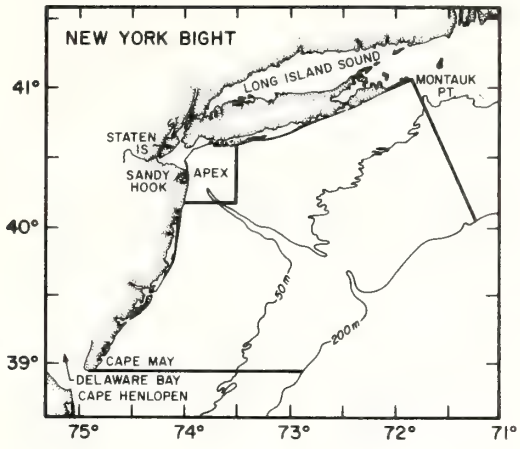


Fig. 1. New York Bight, showing apex area.

General Oceanics model 1070 10-liter top-drop Niskin bottles. Water samples were collected at the surface (1 m), at 10-m intervals, and at about 2 m above the sediment–water interface. Each water sample has been analyzed for salinity, dissolved oxygen, pH, nitrate, nitrite, phosphate, silicate, total suspended load, particle size distribution, suspended total organic carbon, suspended total carbohydrates and total proteins, and the dissolved trace metals Fe, Mn, Cd, Cu, and Zn (Cantillo et al. 1976). Some suspended sediment samples are currently being analyzed for mineralogy and inorganic composition (Betzer personal communication).

Seven cruises were conducted at 36-day intervals between April and November 1974 and occupied 25 or 26 stations in the bight apex (Fig. 2). A single additional cruise in February–March 1975 occupied a series of 64 stations (Fig. 3).

Samples for trace metal analyses were drawn from the Niskin sampler and filtered through a 0.4-μ Nuclepore membrane filter, with great care being taken to minimize atmospheric contamination. Filtered samples were collected in precleaned 1-liter linear polyethylene bottles and acidified immediately with 1 ml/liter of silica redistilled concentrated nitric acid. Samples from the first cruise (16–20 April 1974) were not filtered.

Analyses for total Fe, Mn, Cu, Cd, and Zn were performed with a Perkin Elmer 503 atomic absorption spectrophotometer by direct injection of the sample into a Perkin Elmer HGA 2100 heated graphite atomizer (Segar and Cantillo 1976). Zn was determined only on cruises after July 1974. The

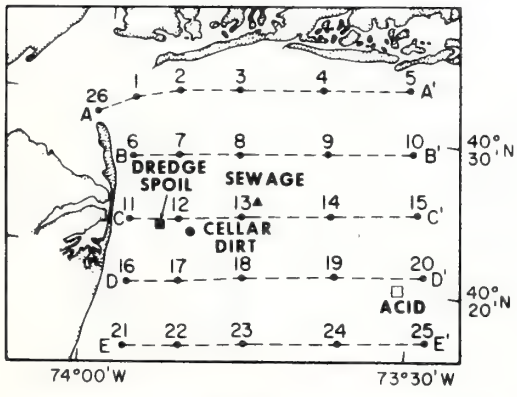


Fig. 2. Station locations in the apex. Designated dumpsite locations and transect designation (A'–A', B'–B', etc.) for which vertical sections are plotted in Figs. 4–7 and 12–28.

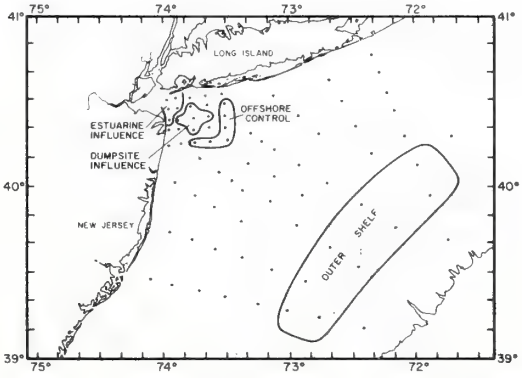


Fig. 3. Extended sampling area occupied 26 February–3 March 1975, showing station locations and regimes: estuarine and dumpsite influenced, offshore control, and outer shelf for which average concentrations are calculated and shown in Figs. 30–34.

analytical precision determined from multiple aliquots from the same sample storage bottle was better than ±10% for concentrations of metals in excess of 10 times the instrumental detection limit (ca. 0.3 ppb for Fe, Mn, and Cu, and 0.01 ppb for Cd and Zn). Generally only single samples were taken from each Niskin sampler. Random duplicates were obtained on several cruises and analyzed. Overall precision of the sampling and analysis was better than ±15% for concentrations in excess of ten times the instrumental detection limit (Segar and Cantillo 1975).

Results and discussion

April 1974 data (unfiltered samples)—Analyses of samples from the first cruise (16–20 April 1974) were performed without filtering. Samples were acidified and allowed to stand for several weeks and the subsample for analysis was taken carefully from the bottle without shaking. Our analytical technique does not discriminate between chemical or physical forms of the element (Segar and Cantillo 1975), so these analyses include all of the metal whether dissolved or remaining in suspension. The

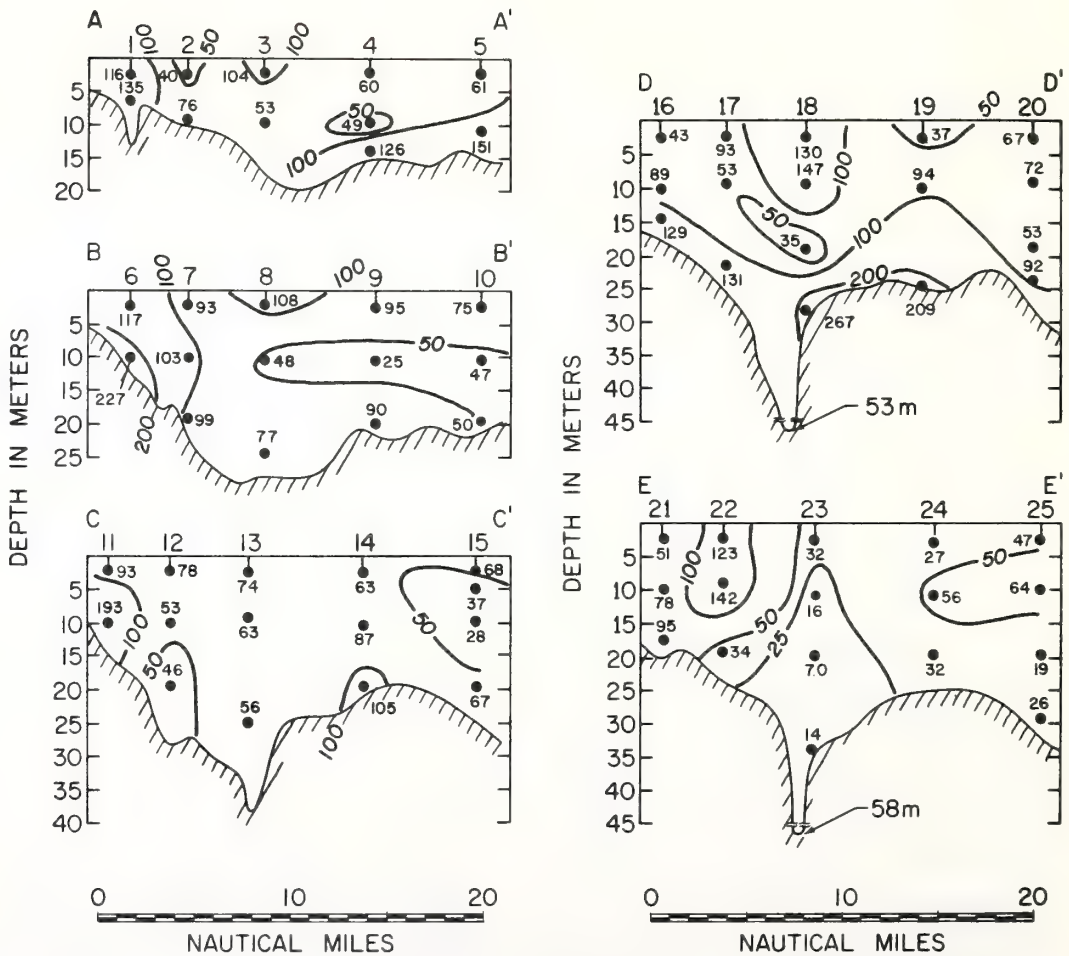


Fig. 4. Total dissolved and particulate iron (μg/liter) in the apex, 16–20 April 1974.

analysis includes the dissolved and weak acid-soluble metal, but excludes metal associated with coarse mineral fractions. The distributions of total particulate plus dissolved Fe, Mn, Cu, and Cd for the April 1974 cruise are shown in Figs. 4–7. There is considerable variation in metal concentration between stations and with depth. Although our sampling density is inadequate to describe this variability, certain features are clear. The lower salinity surface water discharging from Lower New York Bay (Fig. 8) contains high concentrations of both Mn and Fe, but Cd and Cu concentrations do not seem to be strongly influenced by the estuarine discharge. Fe, but not Mn, is also found in high concentrations in water near the sediment–water interface over much of the apex. The absence of this layer in the rest of the apex may be a sampling artifact since samples often could not be taken near the sediment–water interface,

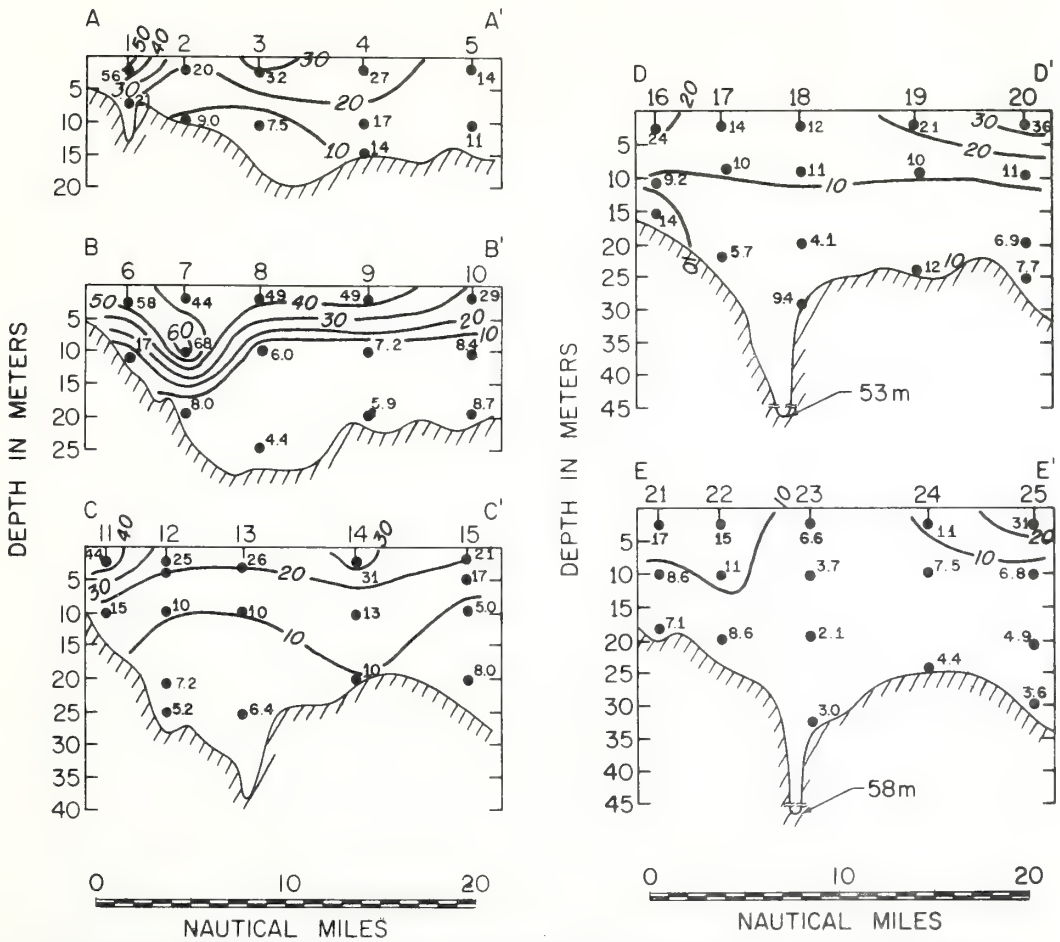


Fig. 5. Total dissolved and particulate manganese (μg/liter) in the apex, 16–20 April 1974.

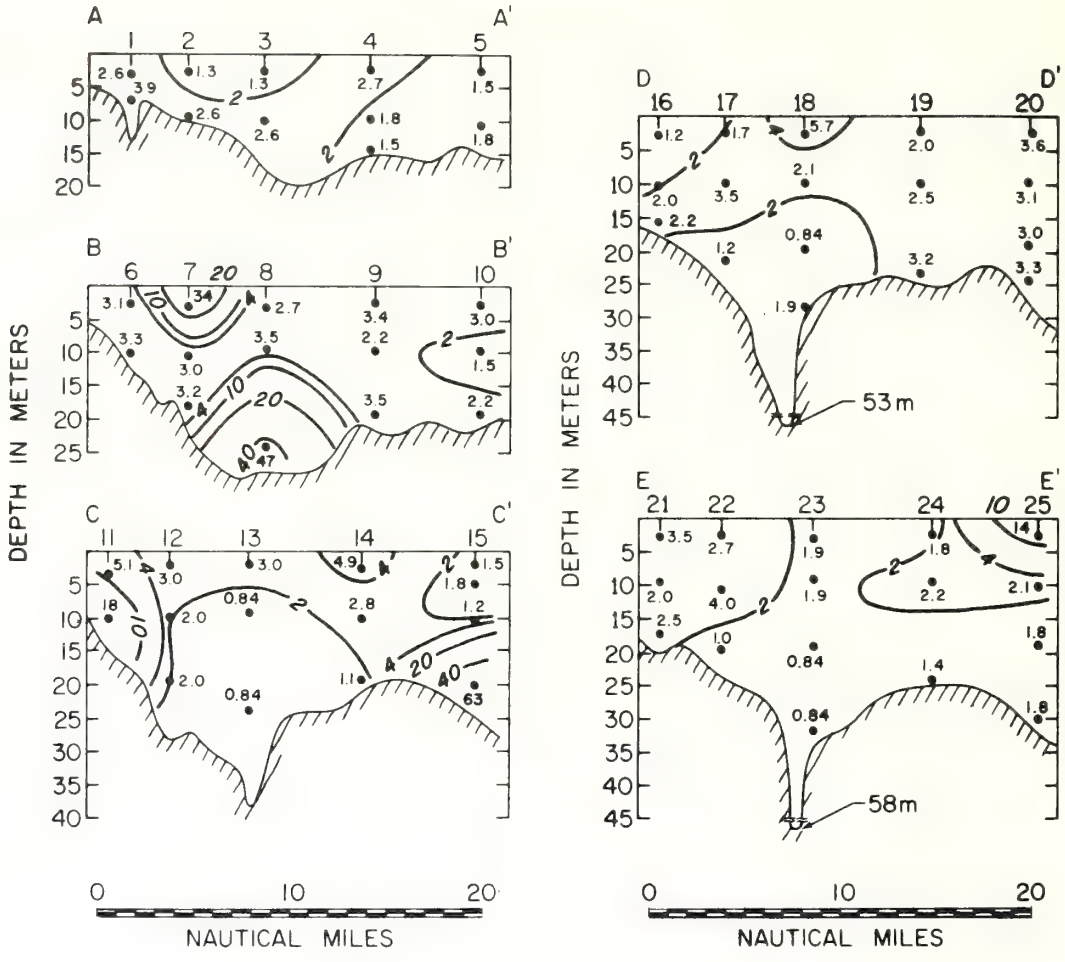


Fig. 6. Total dissolved and particulate copper (μg/liter) in the apex, 16–20 April 1974.

particularly during rough weather. This layer of water with high Fe concentrations may be the nepheloid layer containing high concentrations of fine particles. Such particles, if representative of resuspended bottom sediments, would contain considerably higher concentrations of Fe than of Mn, Cd, and Cu, and most of this Fe should be soluble in weak acid (Gross et al. 1971).

Concentrations of Mn and Fe plotted against salinity (Figs. 9 and 10) suggest that total Fe concentrations are useful in tracing water mass mixing. Iron added to the New York Bight in low salinity river discharge is mixed conservatively with the high salinity-low Fe concentration water of the open ocean. However, at high salinities iron is also introduced to the water column from the sediments. Hence, the complex distribution of points in Fig. 9.

The plot of Mn against salinity does not show any Mn input at high salinities and, because of the curvature, suggests that Mn injected by the low salinity discharge is not conservative but is lost from the water column during mixing with the high salinity-

low Mn water. In Fig. 11, Fe concentrations are plotted against those of Mn. The distribution suggests a three end-member mixing diagram with almost all of the points falling on two straight lines representing two distinct Mn:Fe ratios. Two water masses, low Mn-high Fe and high Mn-high Fe, are mixing simultaneously with low Mn-low Fe water. Points falling on the high Mn-Fe ratio line are almost all surface or near-surface samples, while those falling on the low Mn-Fe ratio line are deeper samples. The implication is that little mixing takes place between the lower and upper layers when the water column is stratified. In addition, the limited data available here suggest that total Fe:Mn ratios or Fe:Mn ratios in suspended particulates may serve as a tracer for suspended sediment mixing.

Cu and Cd concentrations in the apex during April (Figs. 6 and 7) seem to be almost uniform except in a few isolated areas. These high values could either represent poor data or reflect the inadequacy of the sampling density in describing the small-scale variations in concentration. The latter seems more probable (*see below*).

May–November 1974 data (filtered samples)—Six apex cruises followed the April cruise (6–9 May, 10–13 June, 16–19 July, 21–24 August, 29 September–2 October, 4–7 November). The quantity of low salinity

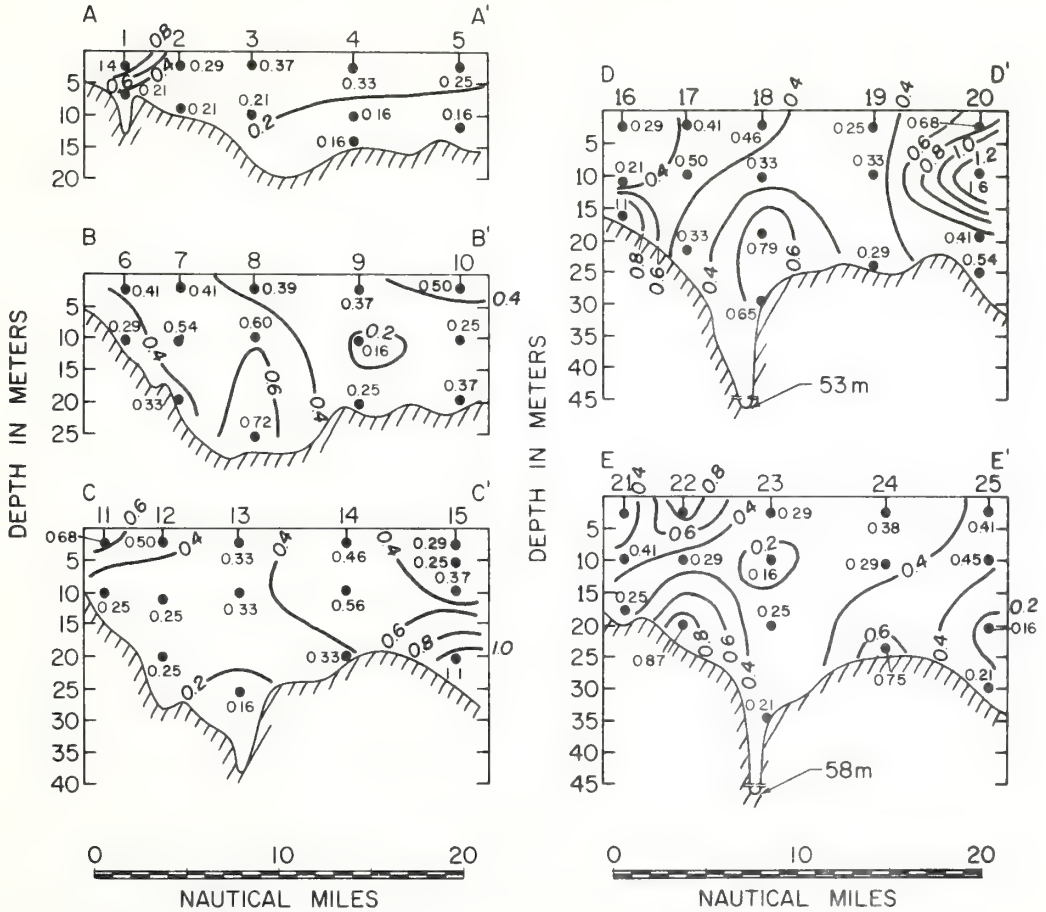


Fig. 7. Total dissolved and particulate cadmium (μg/liter) in the apex, 16–20 April 1974.

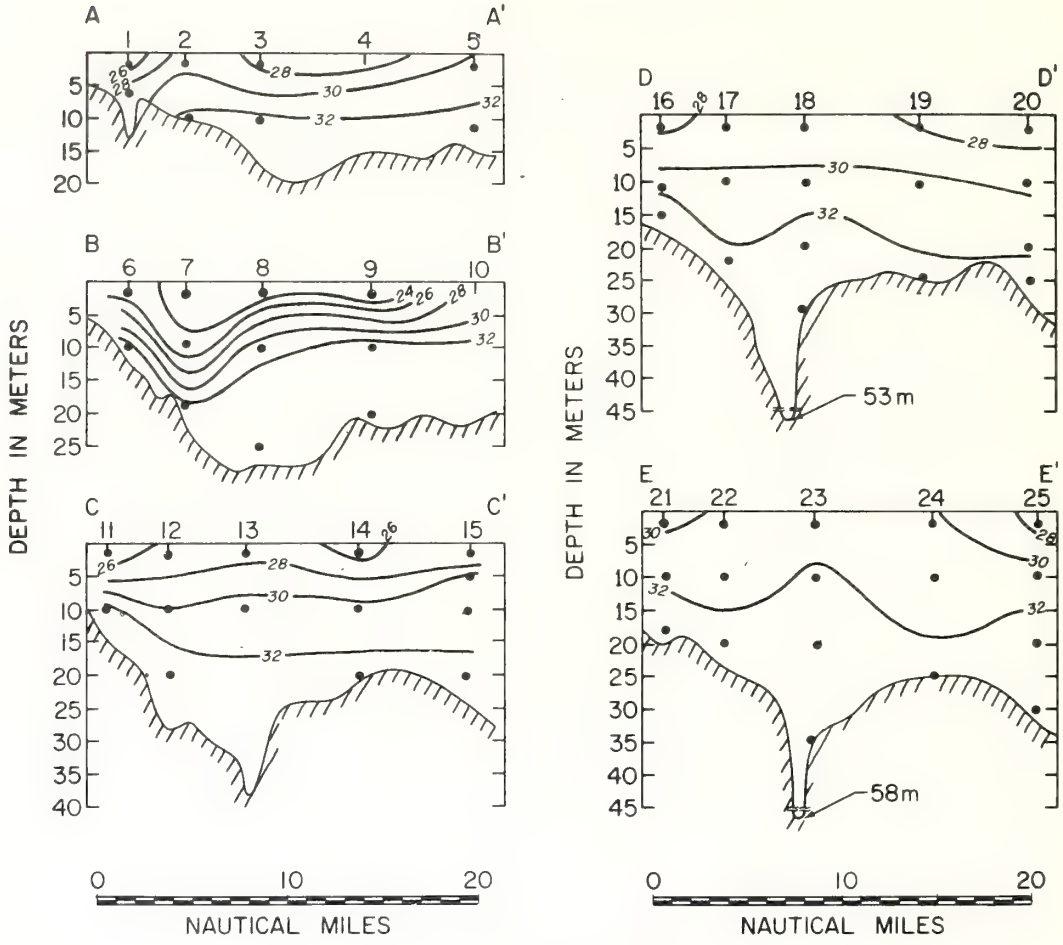


Fig. 8. Salinity (‰) in the apex, 16–20 April 1974.

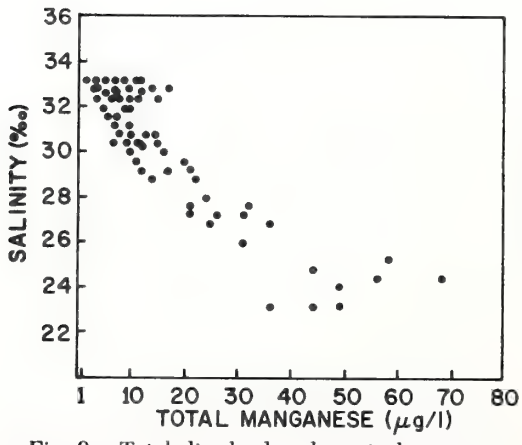


Fig. 9. Total dissolved and particulate manganese in the apex as a function of salinity, 16–20 April 1974.

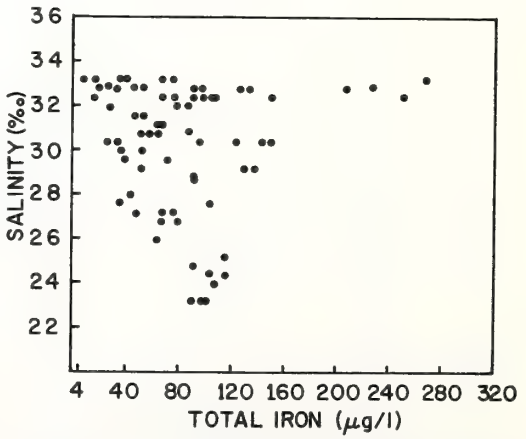


Fig. 10. Total dissolved and particulate iron in the apex as a function of salinity, 16–20 April 1974.

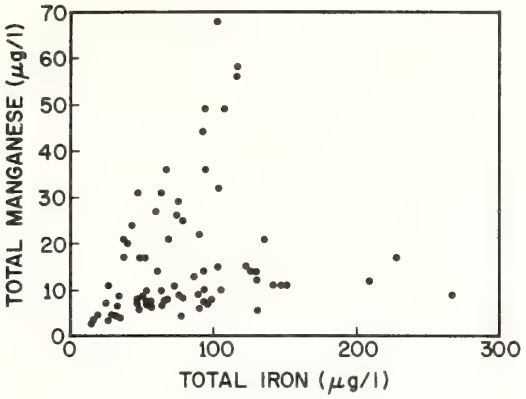


Fig. 11. Total dissolved and particulate iron in the apex as a function of total dissolved and particulate manganese, 16–20 April 1974.

water discharging from Lower New York Bay was less and average salinities throughout the apex were always several parts per thousand higher during this period than during April (Hazelworth et al. 1975*a*,*b*). All samples collected on these later cruises were filtered through 0.4-μ Nuclepore membrane filters and acidified immediately after they were brought aboard ship. Analyses thus determine the total elemental concentration in solution. Station 26 was occupied only on the cruises in September and November, and Zn was determined only on samples from these and the August cruise.

Distributions of total dissolved iron in June, July, August, and September are

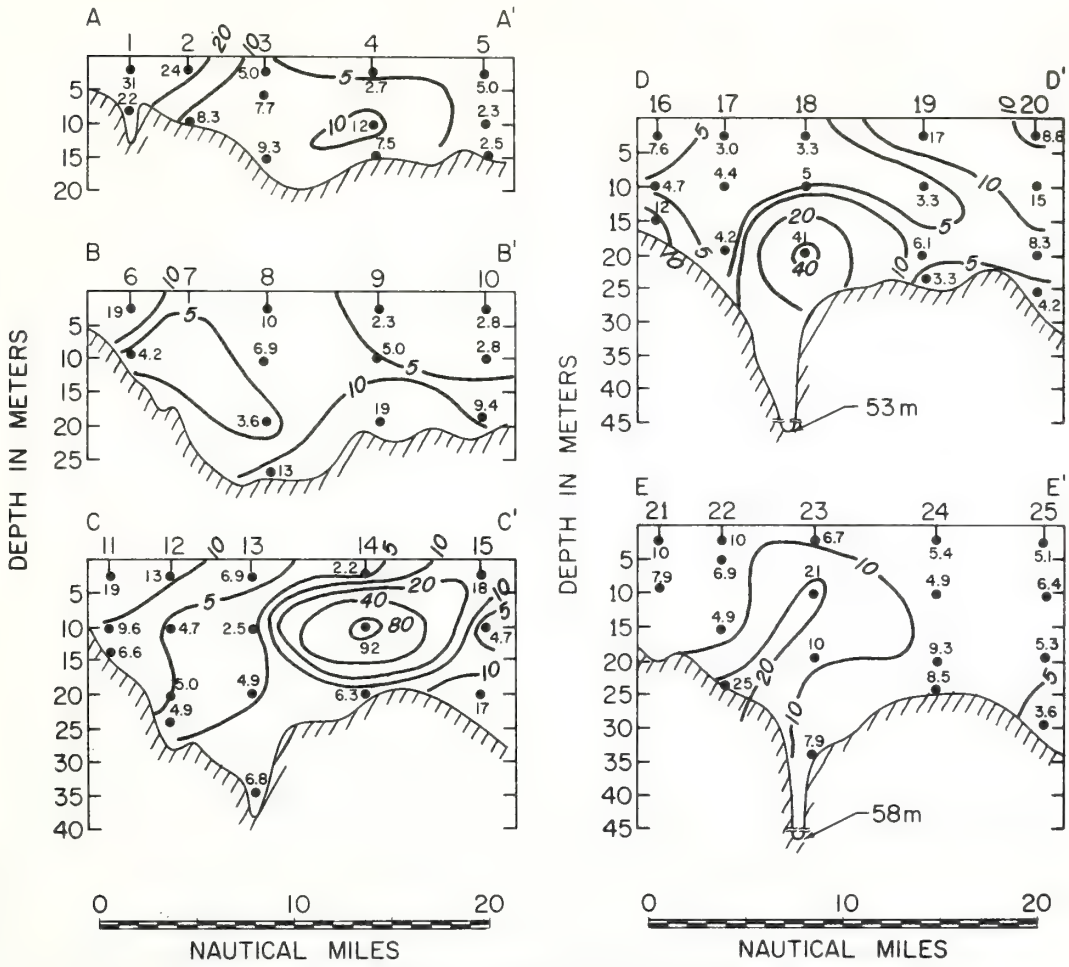


Fig. 12. Total dissolved iron (μg/liter) in the apex, 10–13 June 1974.

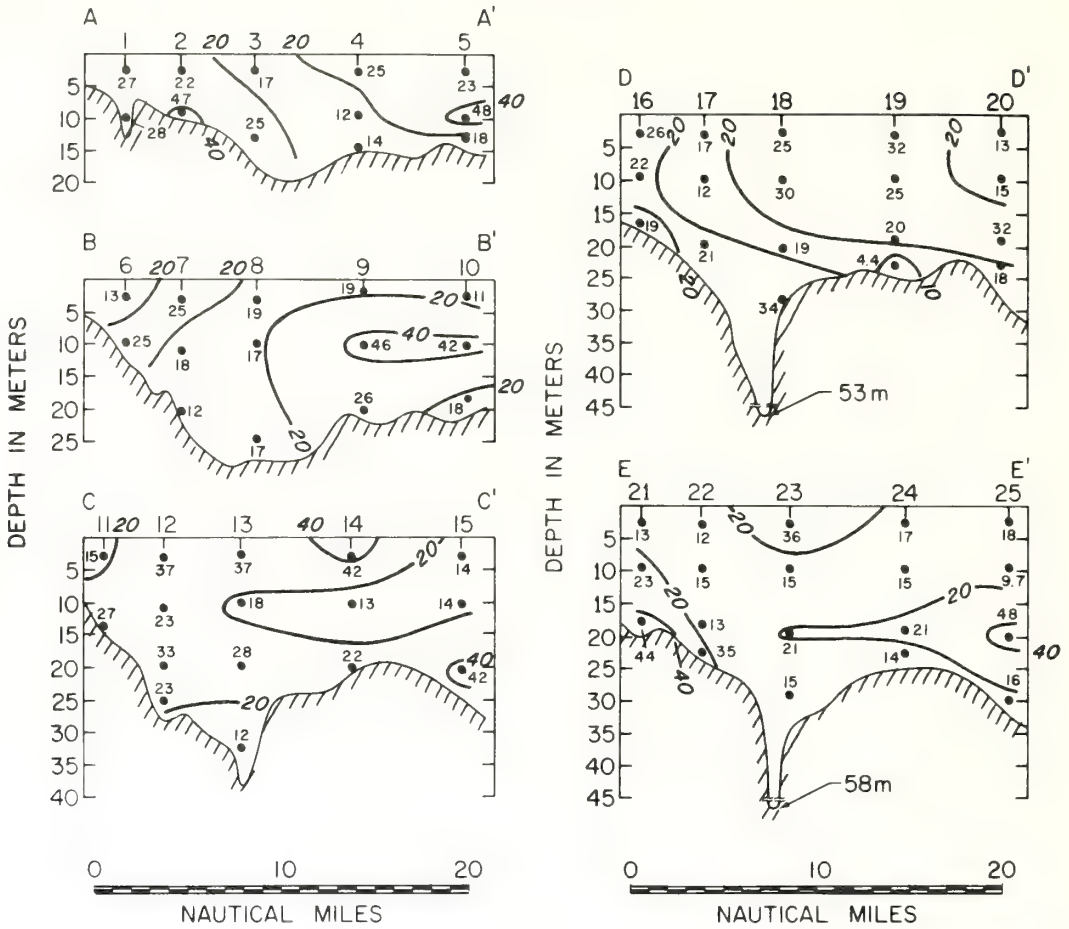


Fig. 13. Total dissolved iron (μg/liter) in the apex, 16–19 July 1974.

shown in Figs. 12–15. The June distribution suggests significant Fe inputs from the estuary; during other months no such input is apparent. Distributions are generally nonuniform with higher concentration regions of water often occurring either to the north or south of the acid waste dumpsites (*see Fig. 2*). Uniform concentrations tend to occur at a particular sampling depth over large distances, despite relatively large changes in concentration with depth. This is particularly apparent in July (Fig. 13) and suggests that little vertical mixing of dissolved species takes place, at least across the thermocline. High dissolved Fe concentrations were not generally found close to the sediment–water interface. This contrasts with the April observations of total acid-soluble iron discussed above and supports our hypothesis that the excess iron near the bottom is particulate and occurs in a nepheloid layer.

Total dissolved Mn distributions for the June, July, August, and September cruises are shown in Figs. 16–19. The Mn distributions are more consistent than those of Fe. High Mn concentrations are always found near the sediment–water interface. Some-

what higher concentrations are also generally observed in the surface water east of the sewage sludge dumpsite and north of the acid waste dumpsite. The excess Mn in these surface waters may come from the acid waste, which contains appreciable quantities of Mn (Gross 1970*b*) and probably disperses northward with the surface drift (Charnell et al. 1975).

High dissolved Mn concentrations in the bottom waters of the bight are probably caused by loss of reduced Mn from anoxic sediments. The Mn will be oxidized and reprecipitated, but the oxidation process is slow (Morgan 1971), particularly when dissolved oxygen concentrations are low (Segar and Berberian 1976).

The Cu concentrations in June, July, and September (Figs. 20–22) are rather uniform, ranging between about 2 and 4 ppb over most of the apex. However, concentrations in the estuarine outflow and apparently in cells of surface water north of the acid waste dumpsite are usually somewhat higher than concentrations elsewhere in the apex. The region north of the acid waste dumpsite is where high Mn concentrations are also found. Cells of high Cu

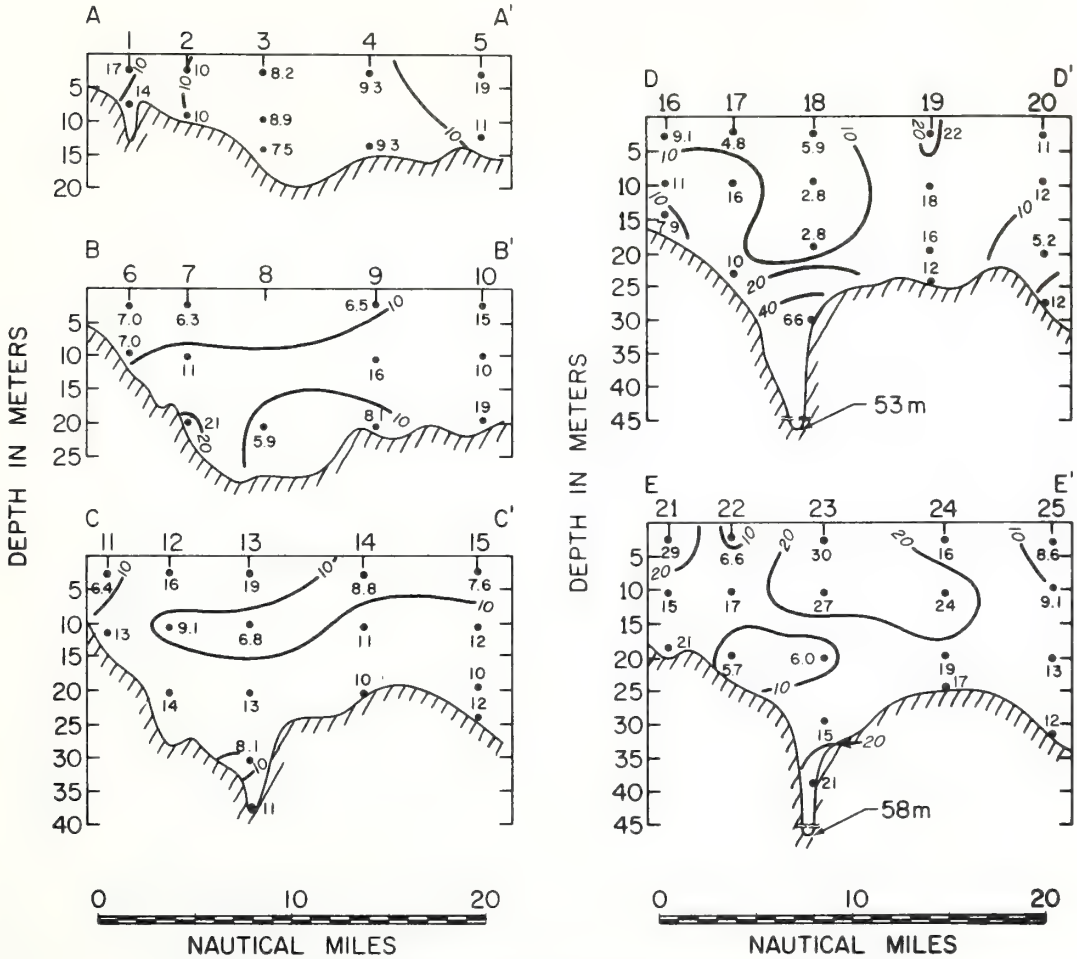


Fig. 14. Total dissolved iron (μg/liter) in the apex, 21–24 August 1974.

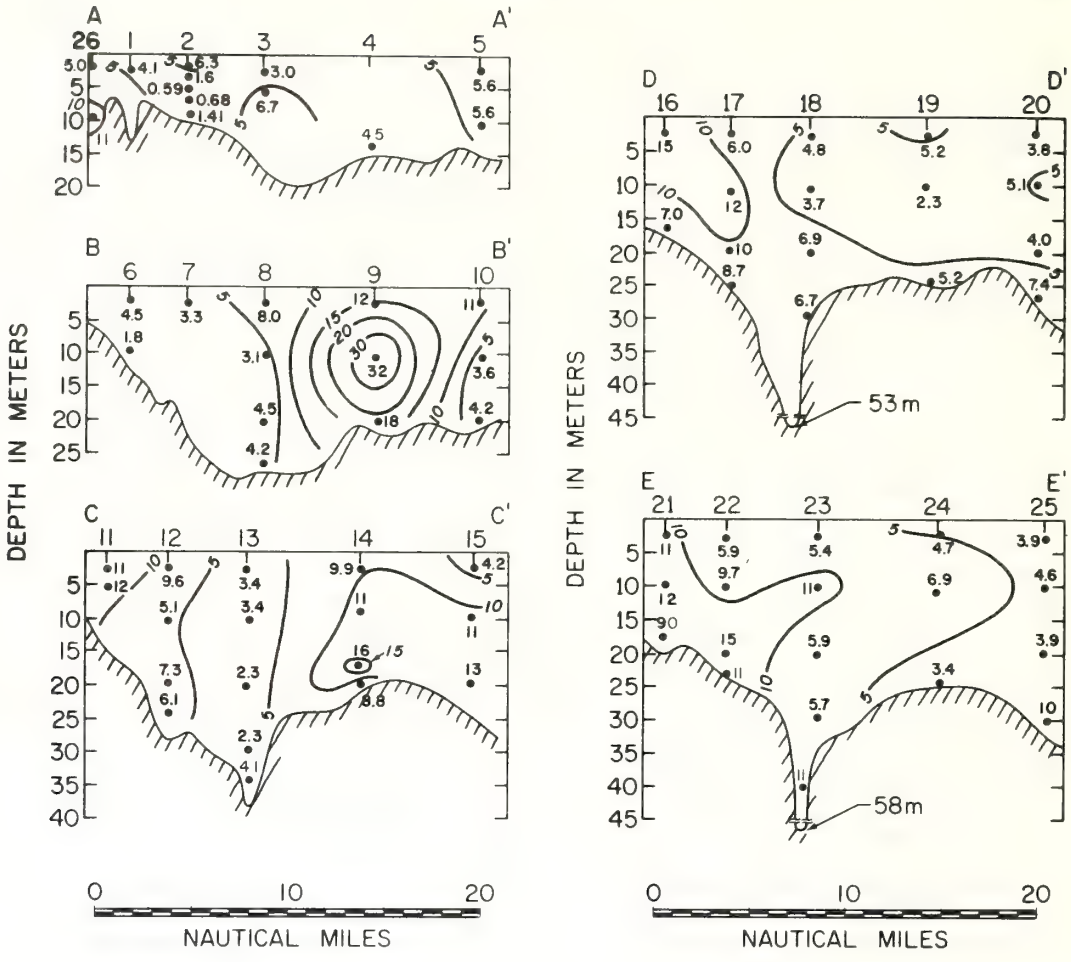


Fig. 15. Total dissolved iron (μg/liter) in the apex, 29 September–2 October 1974.

concentration are found in deeper waters but generally not extending to the deepest sample. They appear to be associated with the regions where high Mn and low oxygen concentrations are observed. Perhaps, they are generated by biological decomposition and associated Cu release or by oxidation of sulfides in resuspended bottom sediments. If the latter were the case, then the deepest samples would show lower concentrations, due either to scavenging by nepheloid layer particles or to sulfide reprecipitation.

Cd concentrations in June, July, and September (Figs. 23–25) do not vary greatly throughout the apex, although the estuarine outflow and near-bottom samples tend to have higher concentrations than waters elsewhere in the apex. Areas of high Cd concentration water were observed, but no obvious pattern can be delineated.

Zn concentrations in August, September, and November (Figs. 26–28) are high compared to reported values for other coastal areas (Morris 1971; Windom et al. 1971; Windom and Smith 1972; Butterworth et al. 1972; Abdullah et al. 1972; Steele et al. 1973; Preston 1973). However, the lowest values found in the outer stations in September

(Fig. 27) are within the range reported for other regions.

Estuarine waters entering the apex have Zn concentrations above background there. Concentrations near the sediment–water interface are often high, and discrete cells of Zn-rich water are observed.

The most striking features of the Zn distributions are the high surface concentrations at stations 23 and 24 in August (Fig. 26) and the high concentrations at stations 12 and 13 in August (Fig. 26) and station 13 in September (Fig. 27). Station 13 is located almost at the sewage sludge dumpsite, and high Zn concentrations there are probably caused by release of Zn to solution during sewage sludge disposal. The high concentrations at stations 23 and 24 in August are possibly due to releases of Zn from acid wastes.

The highest zinc concentrations observed were below levels known to be acutely toxic to marine organisms. But the concentrations are high enough and may be persistent enough to cause concern about potential chronic toxic effects (Connor 1972; Brown and Ahsanullah 1971).

It is relevant at this point to consider the validity of trace metal data showing cells of water with anomalous concentration.

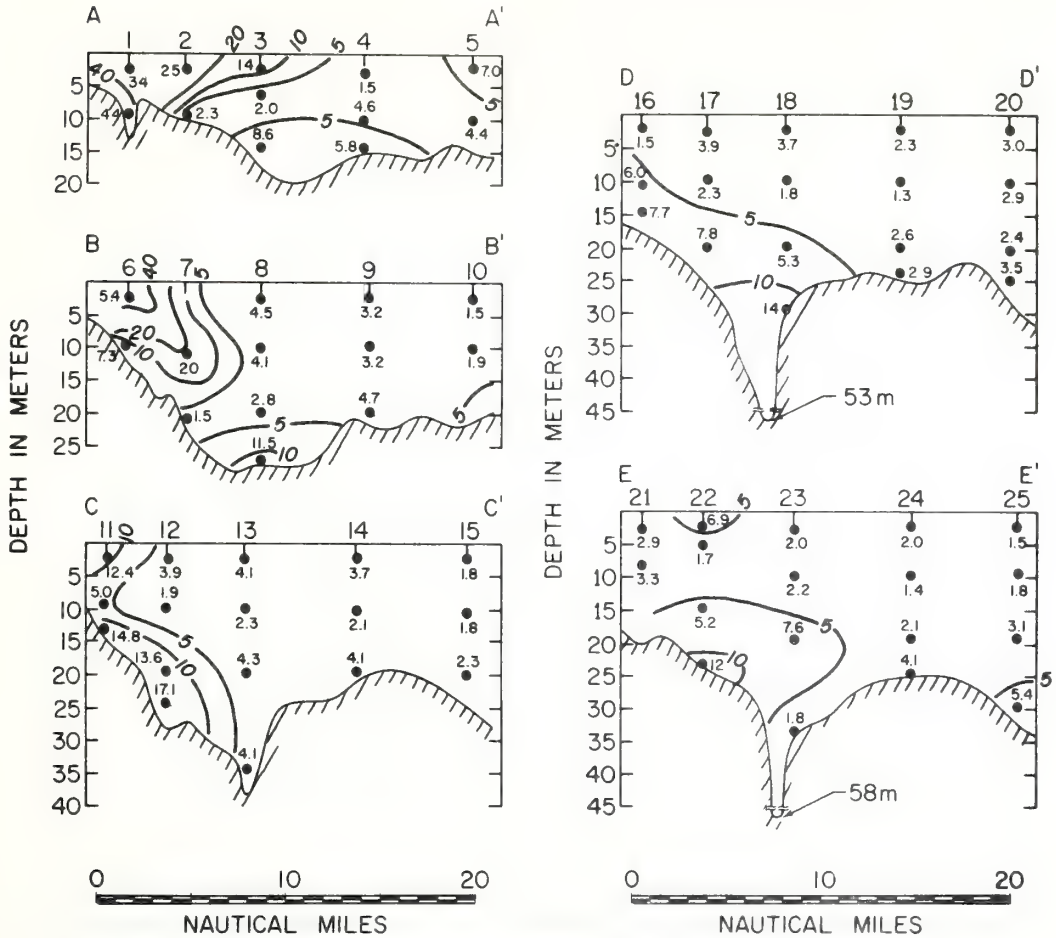


Fig. 16. Total dissolved manganese (μg/liter) in the apex, 10–13 June 1974.

Often the anomalous water is characterized by only a single data point. In such instances it is possible that analytical error is responsible for the anomaly. However, we believe that our anomalous values are genuine, with perhaps one or two exceptions. We have sampled the same stations twice, several days apart, usually obtaining good agreement between successive samplings, even when observed concentrations were anomalous compared to other areas. In addition, the vertical and horizontal integrity and the repetition of the high Zn concentration at station 13, a phenomenon clearly explicable by known chemical processes, convince us that such features elsewhere are significant although less easily explained.

Samples from the August cruise were analyzed for V and Ni after extraction with ammonium pyrollidine dithiocarbamate into methyl isobutyl ketone. Vanadium concentrations were generally below the detection limit (ca. 0.2 μg/liter), while Ni concentrations ranged from about 0.5 to 7 μg/liter. Both metals occurred in higher concentrations in the estuarine influenced region (V ca. 3 μg/liter) and were uniformly low

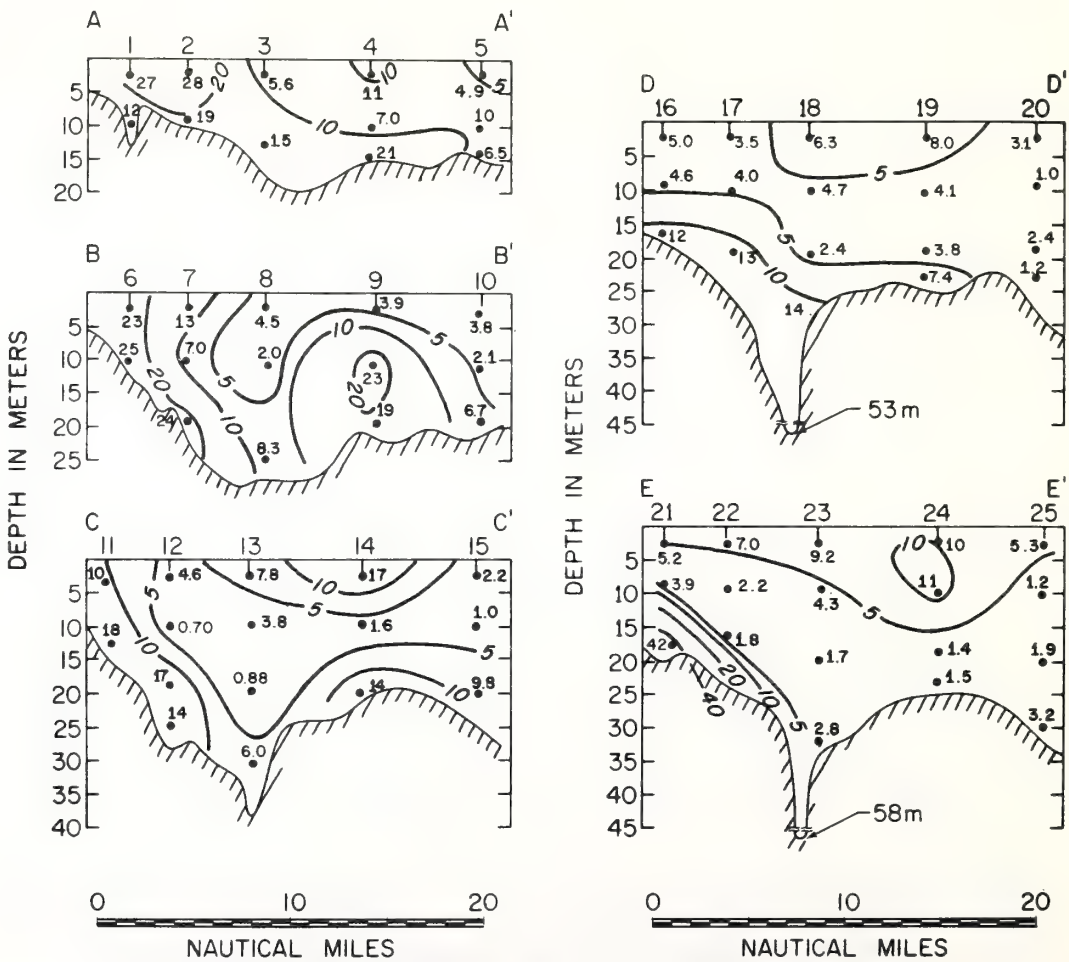


Fig. 17. Total dissolved manganese (μg/liter) in the apex, 16–19 July 1974.

throughout the rest of the apex. In the outer areas of the apex, concentrations of Ni in surface waters (1–2 μg/liter) were generally somewhat higher than in deeper water (0.5–1 μg/liter).

Seasonal variations—To simplify the data so that seasonal trends and geographical variations might be more easily understood, average metal concentrations for several regimes were calculated. The average concentration, including all depths sampled, was calculated for each cruise for four areas (Fig. 29): estuarine influenced (stations 1, 2, 6, 7, and 11), dumpsite influenced (stations 8, 12, 13, 14, and 18), offshore control (stations 10, 15, 20, 23, 24, and 25), and, for our single expanded grid cruise (26 February–3 March 1975), outer shelf (Fig. 3). These averaged data are plotted for Fe, Mn, Cu, Cd, and Zn in Figs. 30–34. Several observations can be made.

1. Outer shelf stations had lower average concentrations of each metal except Cd than the apex in winter. In winter the outer shelf stations had lower average Mn concentrations than the average concentrations in the apex at any time of year.

2. Average surface layer Mn concentrations in the estuarine influenced regions

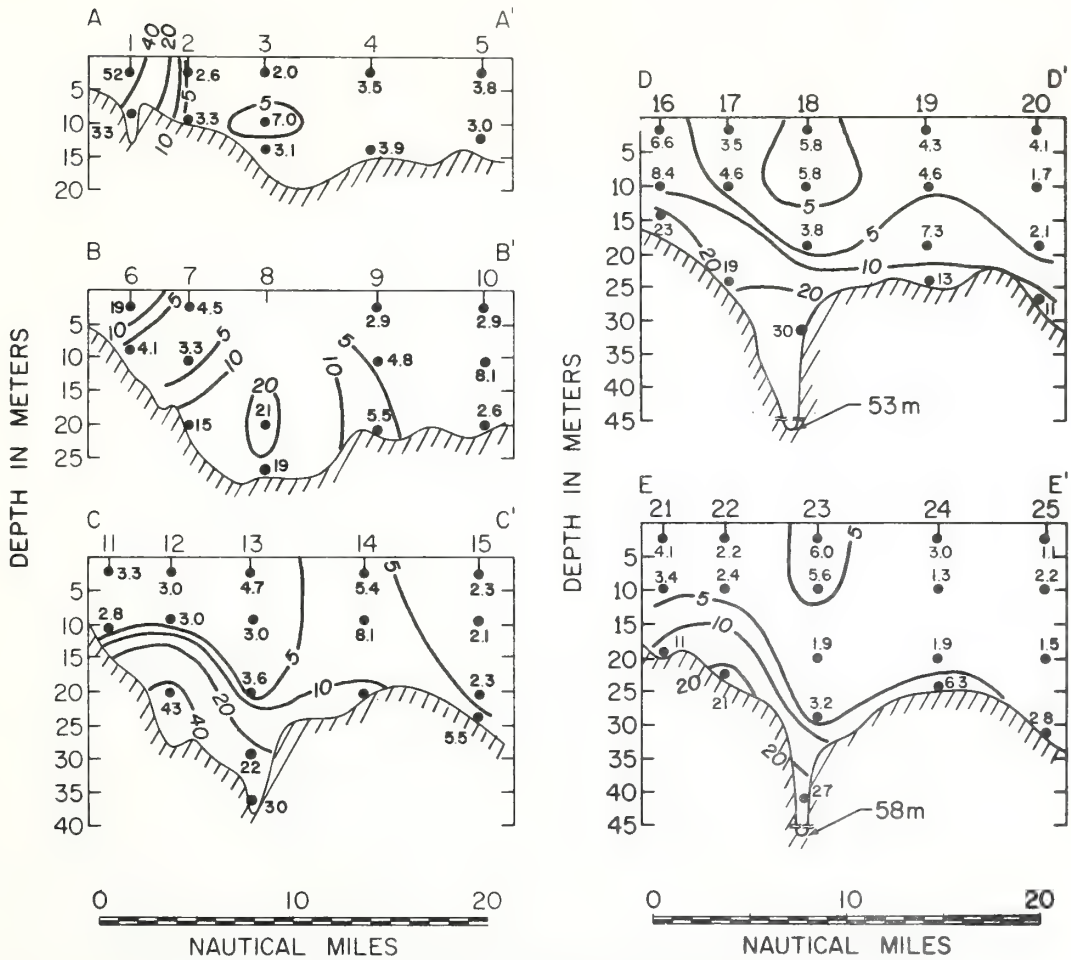


Fig. 18. Total dissolved manganese (μg/liter) in the apex, 21–24 August 1974.

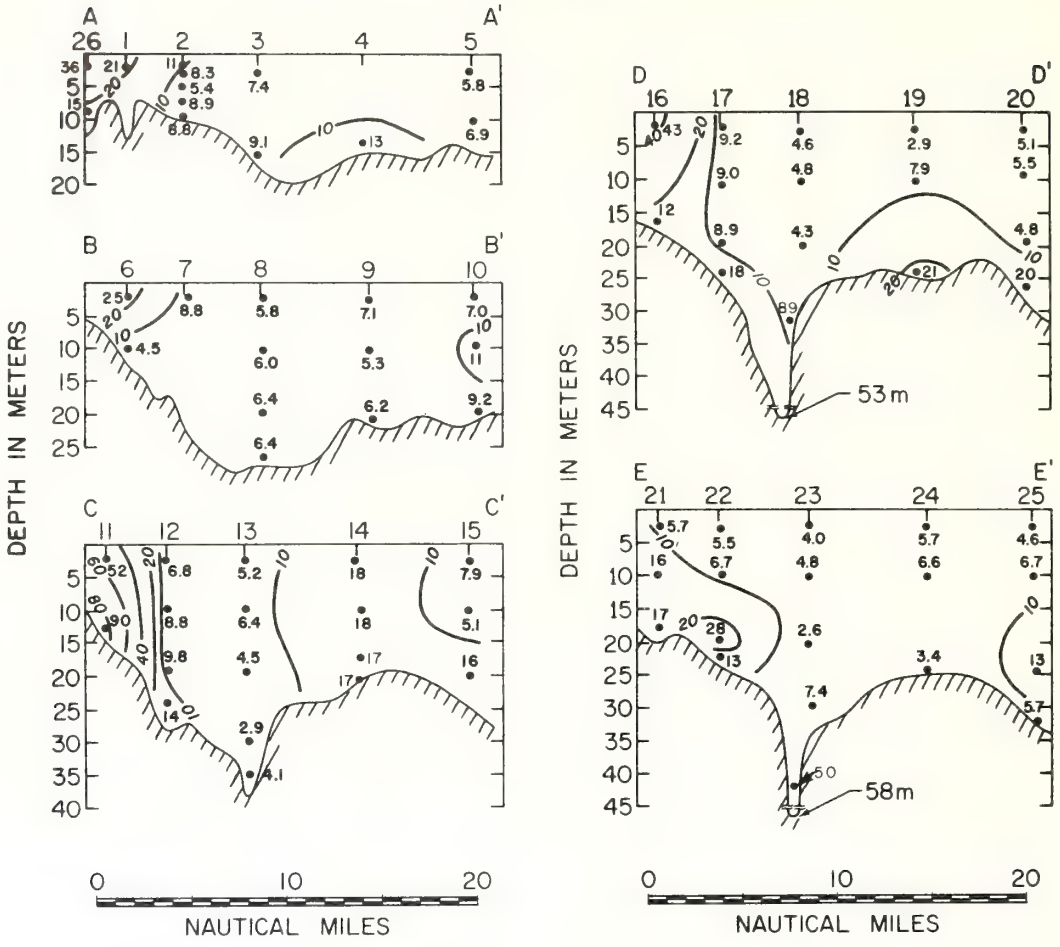


Fig. 19. Total dissolved manganese (μg/liter) in the apex 29 September–2 October 1974.

were always higher than the average concentrations offshore where Mn was rather uniform. This suggests that the estuary is a major source of dissolved manganese. Mn added from dumping must be precipitated or remain in the suspended phase.

3. The estuary seems to be a significant source of high Cd and Zn concentrations only at certain times.

4. In no instance is the average concentration of a metal in the dumpsite region significantly higher than in the rest of the apex, although the concentration of Zn in the immediate vicinity of the sewage sludge dumpsite is often anomalously high (Figs. 26–28).

5. Surface and lower layer (below 10-m depth) average metal concentrations are not significantly different except for Mn. Average lower layer Mn concentrations in the dumpsite region are significantly higher than surface concentrations. The differential is caused by high near-bottom Mn concentrations in this region where oxygen

concentrations are low and reduced Mn is probably diffusing from the sediments.

6. Concentrations of each metal in the apex were lower during spring and fall than during summer or midwinter. High summer concentrations are probably caused by restricted circulation and the consequent longer residence time and higher equilibrium concentration of contaminants during this season. High concentrations in winter, particularly in the deeper water, are probably caused by release of dissolved trace metals from resuspended sediments, as the winter cruise took place in the days immediately following a storm.

7. Average Zn and Cd concentrations in the bight are higher than reported in other coastal waters. Cu, Fe, and Mn concentrations are high but within the range reported for contaminated coastal waters (Morris 1971; Windom et al. 1971; Slowey and Hood 1971; Butterworth et al. 1972; Abdullah et al. 1972; Sundaraj and Krishnamurthy 1972; Steele et al. 1973; Preston 1973; Sankaranarayanan and Reddy 1973). High concentrations of the various metals observed in the bight may be due either to analytical methodology differences (our method determines essentially total dis-

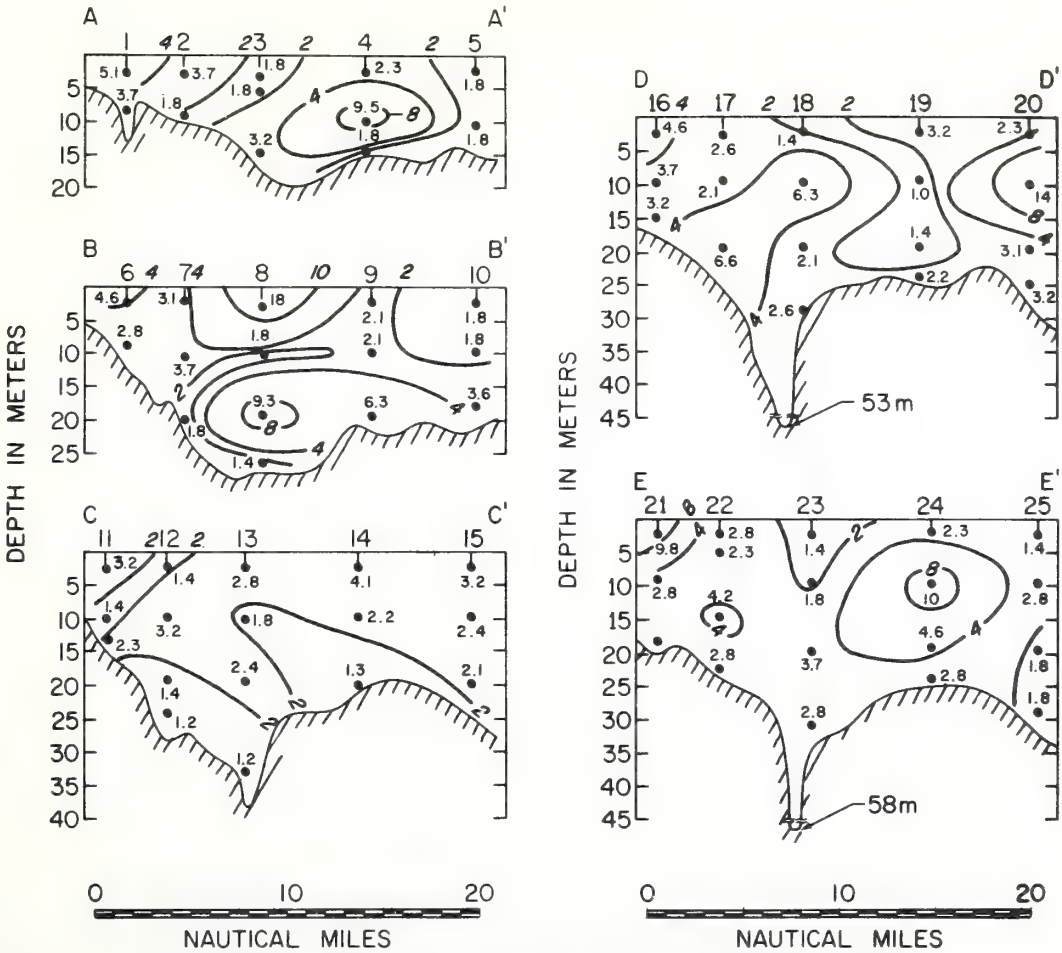


Fig. 20. Total dissolved copper (μg/liter) in the apex, 10–13 June 1974.

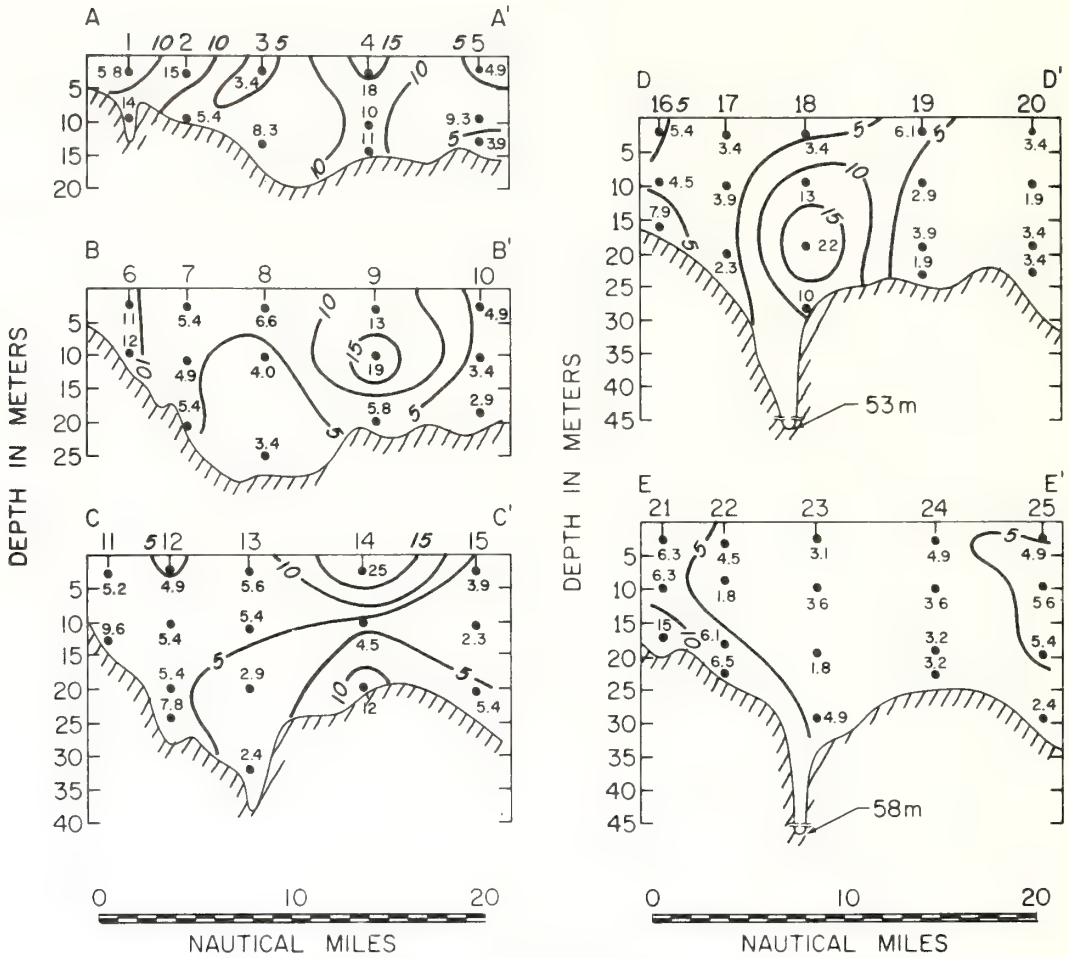


Fig. 21. Total dissolved copper (μg/liter) in the apex, 16–19 July 1974.

solved metal) or to the impact of man's contamination or to both.

Some considerations on metal speciation—A new analytical technique was used which determines the total metal concentration in the sample without regard to chemical form (Segar and Cantillo 1975). The results obtained were compared with analyses performed by separating metals from the salt matrix by chelation with ammonium pyrollidine dithiocarbamate (APDC) and extraction with methyl isobutyl ketone (MIBK). The extractive analyses were carried out by standard additions using a modification of the method of Kremling and Petersen (1974). Excellent agreement was found between methods for each metal examined if analysis was carried out on water samples from the estuarine discharge region. However for Fe and Cu and possibly Cd, Zn, and Mn in samples from outside the estuarine influence, concentrations found by the total analysis method were much higher than those obtained by the extraction method. The extraction of standard additions was quantitative from all samples regardless of origin.

Total Cu and extractable Cu are plotted against one another for samples from the August apex cruise in Fig. 35. Points lying

between the two straight lines represent agreement between the two values and therefore 100% extractability within the estimated errors of the two analyses. Samples with quantitatively extractable Cu were predominantly taken at the surface in the area of estuarine influence, whereas points lying progressively to the right of this line (i.e. <100% extractability) derive from deeper samples or samples from progressively farther offshore. Salinity variations were relatively small in the apex during this cruise, the lowest salinity sample being about 28‰. No obvious relationship existed between salinity and either total copper or extractable copper concentrations.

Apparently in the open shelf waters of the bight apex metals occur in a form that is not present in the estuarine discharge and is not extracted by APDC/MIBK even when the sample has been acidified to pH 1 and stored for several weeks before analysis. The inextractable metal may be the fraction released by oxidation of seawater samples (Corcoran and Alexander 1964; Hood 1967; Williams 1969; Slowey and Hood 1971), and it may be organically associated. However, if it is organically associated metal, it is surprising that it does not seem to be present in the estuarine water which has a high dissolved organic carbon concentration (Alexander and Alexander in press).

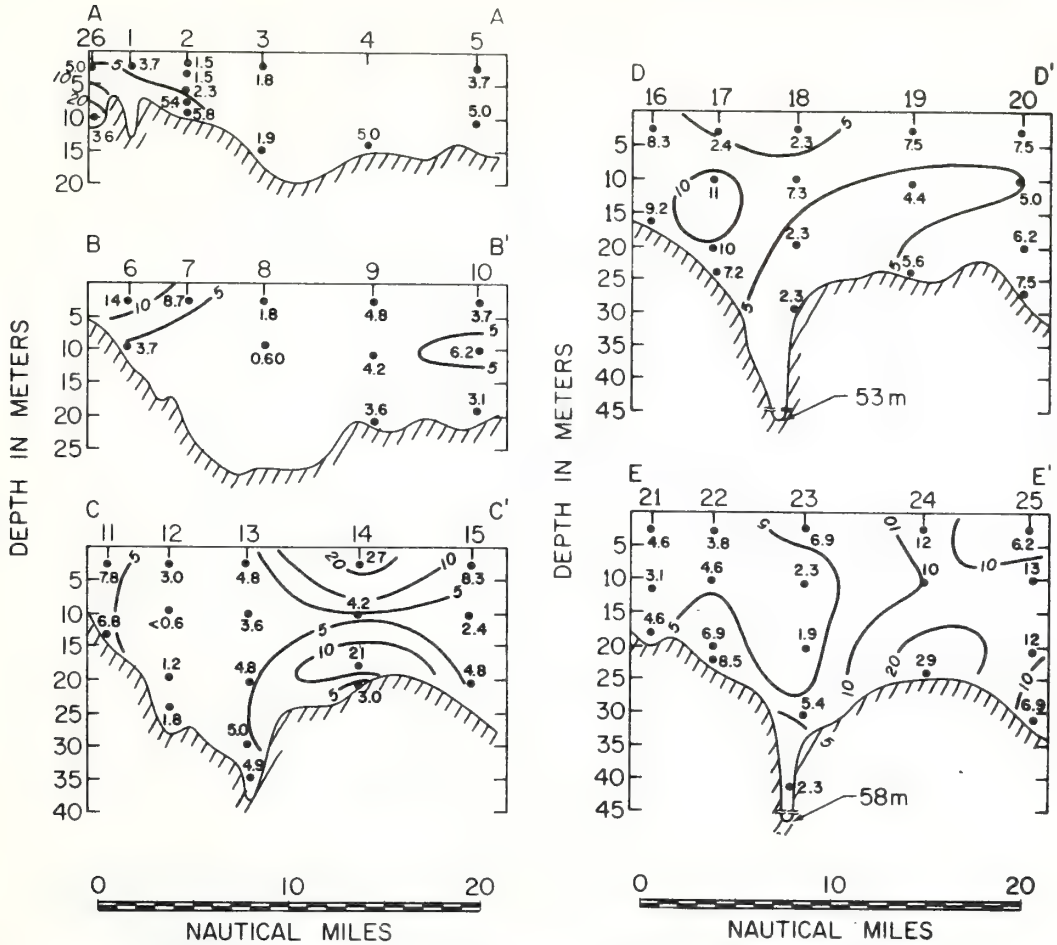


Fig. 22. Total dissolved copper (μg/liter) in the apex, 29 September–2 October 1974.

Metal budgets—Budgets for trace metals in the bight can be made only imprecisely because existing data are inadequate. We lack adequate estimates for most metal inputs and for the distribution of most trace metals in the New York Bight ecosystem. At this time, reasonable budget calculations can be made for Cu and Zn.

The total quantity of Cu and Zn in the apex, a region defined by our 26 station grid (Fig. 2), with an area of 2,400 km^2 has been estimated from data discussed above. The quantity of these metals in the upper 1 cm of the sediments of the apex has been calculated from the data of Carmody et al. (1973) (Table 1). The amount of each metal in the water column is comparable to the amount in the upper 1 cm of sediment. Only the upper few centimeters of sediment are able to exchange elements with the water column and the biota (Duursma and Gross 1971). As the deposition rates in the bight are generally low (G. Freeland per-

Table 1. Total metal in the apex (tonnes).

	Cu	Zn
Average water column*	212	1,500
Sediments (upper 1 cm)	410	855

* Dissolved metal only.

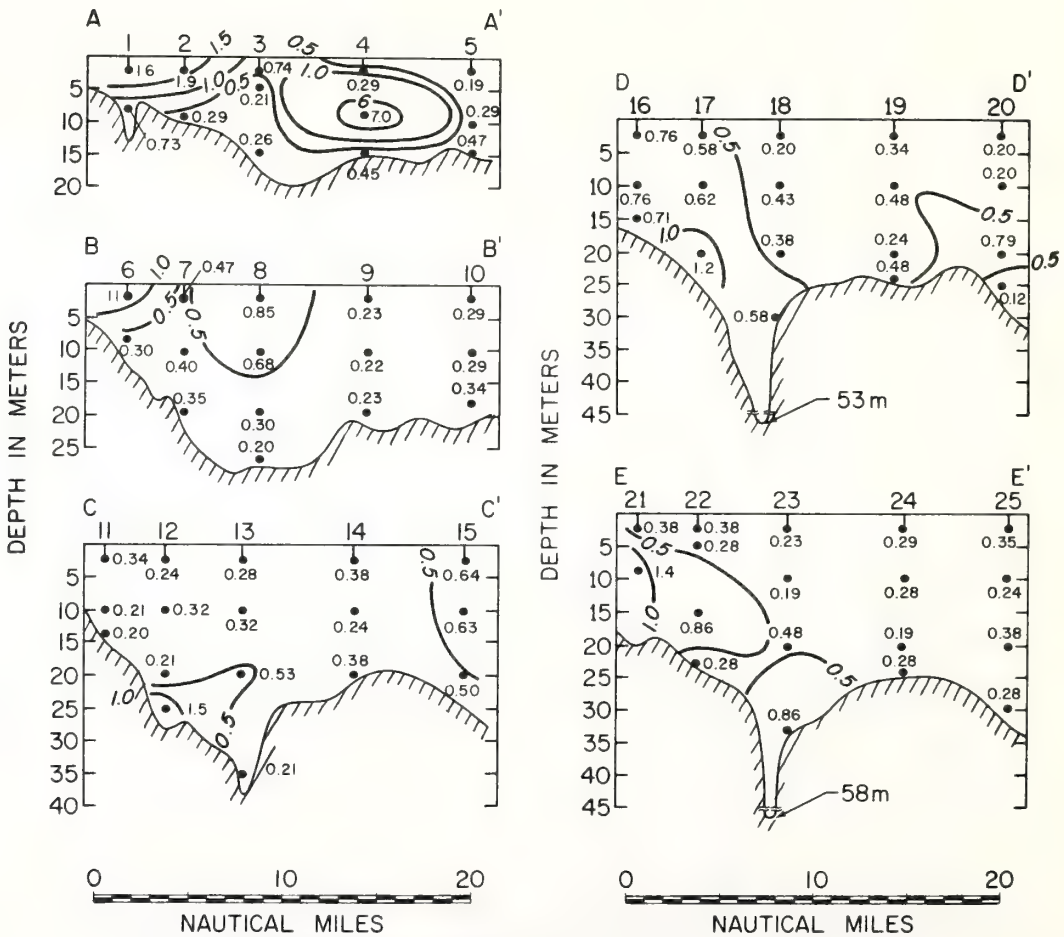


Fig. 23. Total dissolved cadmium (μg/liter) in the apex, 10–13 June 1974.

sonal communication), and as some equilibrium exists between sediments and water, this implies that an appreciable fraction of Cu or Zn (and probably other elements) added as dissolved contaminants to the bight apex must stay in solution until either taken up by organisms or physically transported out of the apex.

The total quantity of metal in the water column, as calculated in Table 1, does not include metal incorporated in suspended particles. Some idea of the relative magnitudes of suspended and dissolved metals can be obtained by comparing the concentrations in samples collected in the apex in April, which were not filtered, and those collected later in the year, which were. This comparison is made by averaging all trace metal analyses for the April cruise and averaging all trace metal analyses for the six subsequent apex cruises (Table 2). However, an accurate estimate of the total particulate metal cannot be made from Table 2 because the April hydrographic conditions and, presumably, metal distributions were different from those in the other sampling periods. Also, the April analyses do not include any metal that might be present in the acid-insoluble settleable fraction of the suspended particulates. Nevertheless, from

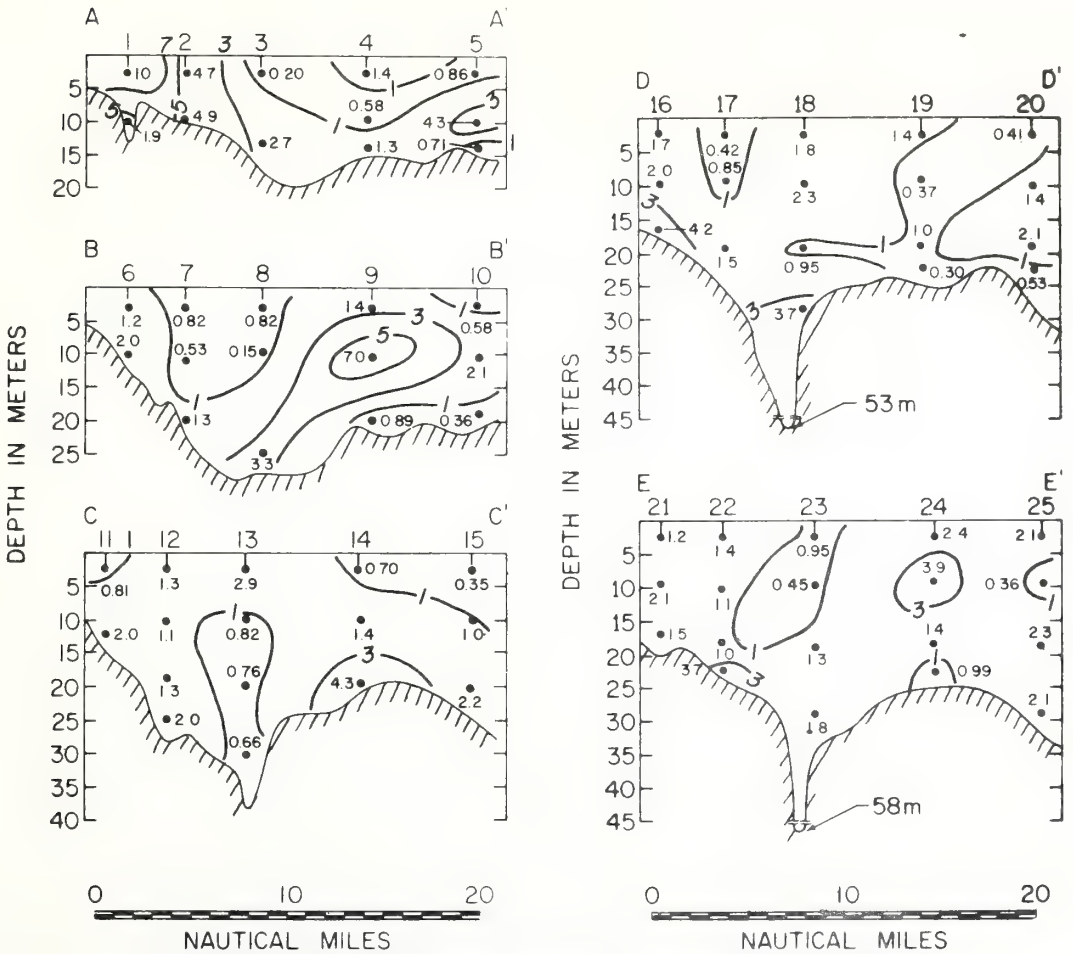


Fig. 24. Total dissolved cadmium (μg/liter) in the apex, 16–19 July 1974.

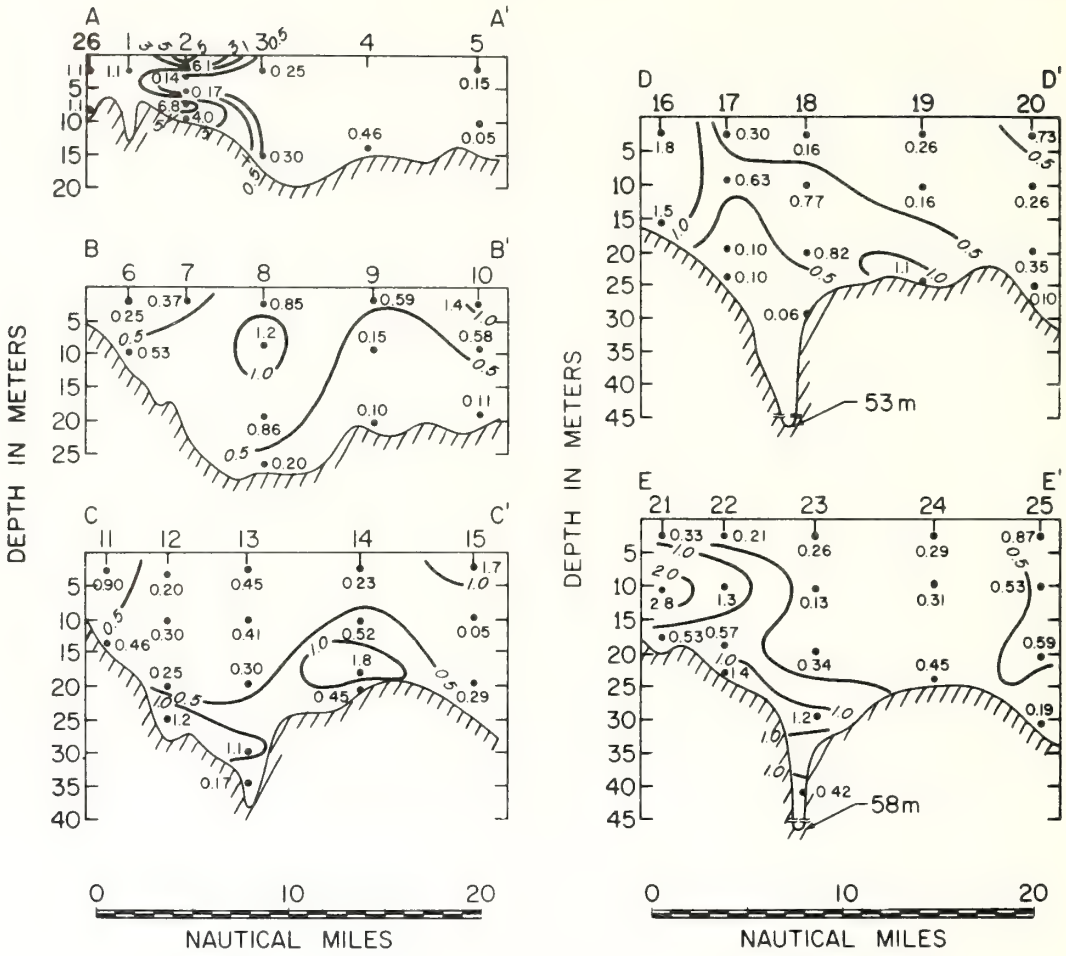


Fig. 25. Total dissolved cadmium (μg/liter) in the apex, 29 September–2 October 1974.

Table 2, and from total suspended load data and preliminary analyses of concentrations in suspended matter (Betzer personal communication), it seems that while Fe and Mn may be present in significant quantities in the suspended phase, Cu, Cd, and Zn will be found predominantly in the dissolved phase. Therefore, suspended Cu, Cd, and Zn are present in only small quantities in the bight apex, and the values in Table 1 underestimate the total metal contents of the water column by at most a few percent.

Table 2. Average metal concentration for all stations (ppb).

	Apr*	May–Nov†
Fe	82	12
Mn	17	8.0
Cu	4.2	4.5
Cd	0.42	0.82
Zn	—	32

* Includes dissolved, plus acid-soluble particulate metal.
† Dissolved metal only.

Cu and Zn inputs to the apex from various sources are estimated in Table 3. It is apparent from these estimates that both acid waste dumping and atmospheric input of Cu are negligible, and of Zn are small,

Table 3. Inputs of metals to the apex (tonnes per day).

	Cu	Zn
Sewage sludge*	0.7	1.8
Dredge spoils*	6.3	7.3
Acid wastes*	0.05	0.2
Atmospheric input†	0.02	0.4
River runoff		
Mueller et al. (1975)	6.2	17
River flow rate × concn	0.48	3

* From Mueller et al. (1975).
† From Mueller et al. (1975), scaled to 2,400 km², assuming uniform fallout.

compared to other sources. Dredge spoils appear to be the dominant source for each metal, although river inputs may be large—perhaps comparable to dredge spoil dumping. Even if the low estimates are correct, input of metals from sewage sludge is no greater than that from the estuarine discharge. Evidently caution must be exercised in using concentrations or ratios of trace metal concentrations to identify sewage sludge in apex sediments (Harris 1974).

Differences between the two estimated values of input from the rivers (Table 3) are large. The estimates of Mueller et al. (1975) are almost certainly too high. Their estimates are made by summing the discharges of wastewater and industrial effluents to the lower parts of the Hudson-Raritan-Passaic estuary and New York Bay,

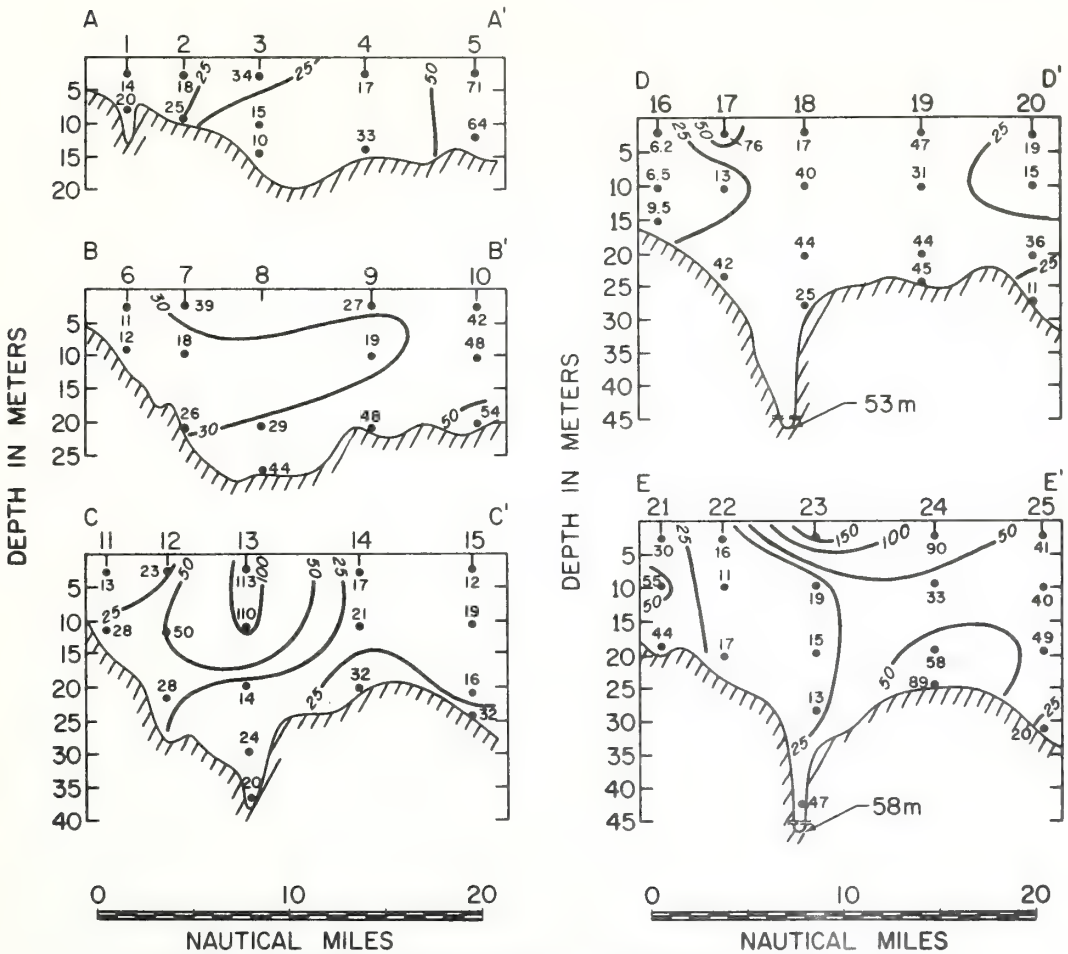


Fig. 26. Total dissolved zinc (μg/liter) in the apex, 21–24 August 1974.

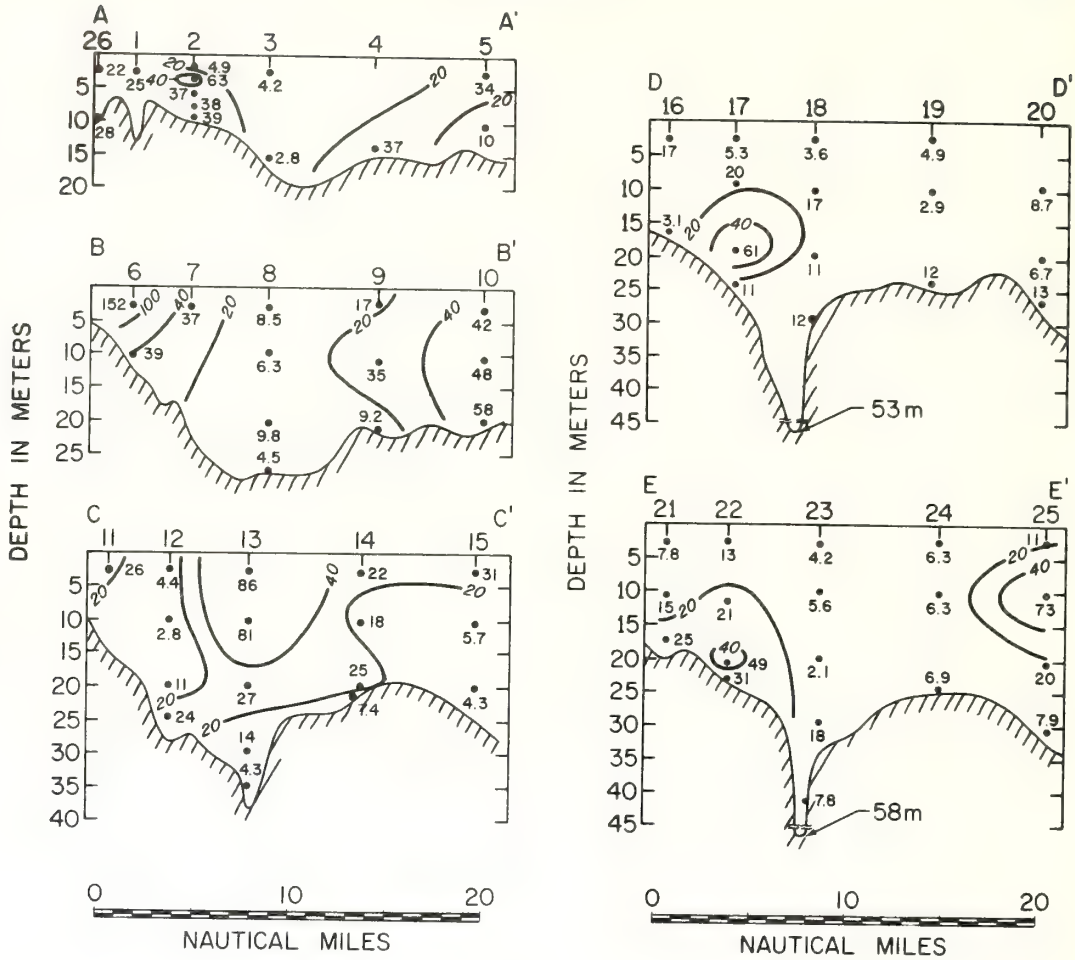


Fig. 27. Total dissolved zinc (μg/liter) in the apex, 29 September–2 October 1974.

together with loads carried by these rivers from their upper reaches. However, a large fraction of the metal contaminants added to the estuary will not be transported to the bight but are probably deposited in the estuary. The deposited material is transported to the bight as dredge spoils. If the estuary has no net accumulation or depletion of contaminants, then the input calculated by Mueller et al. (1975) should be equal to the sum of the actual estuarine transport and the dredge spoil removal. If the estuarine discharge calculated from the mean river flow rates and metal concentrations are added to the dredge spoil input, the sum does approximate the Mueller et al. (1975) estimate of input to the rivers.

The river input of metals, which is calculated from the mean flow rate multiplied by the average metal concentration in water at the mouth of Lower New York Bay (Table 3), is only a crude approximation. Tidal exchange, neglected here, may create a significant net transport of metals either into or out of Lower New York Bay. Better estimates cannot be made from existing data. As long as metal concentrations in low salinity discharges are consistently equal to

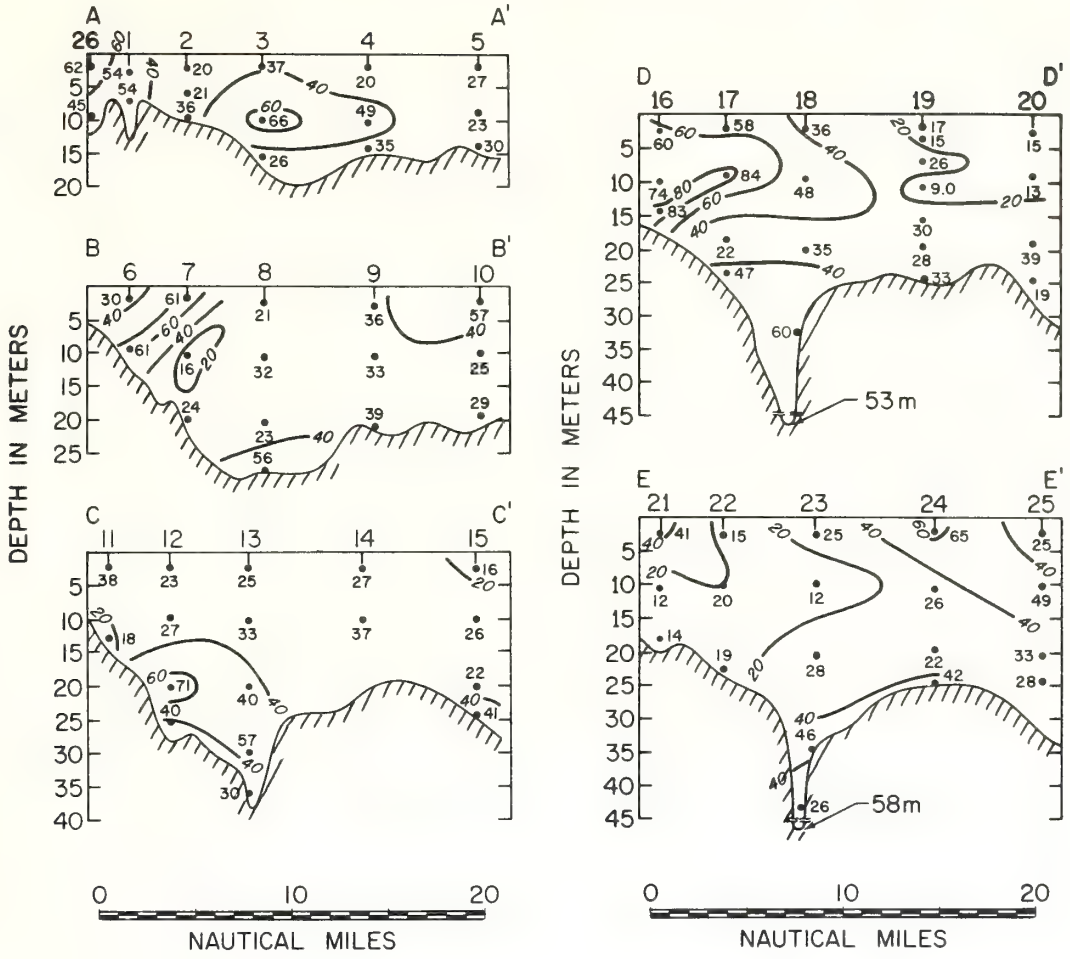


Fig. 28. Total dissolved zinc (μg/liter) in the apex, 4–7 November 1974.

or higher than that in the high salinity return flow to the estuary, input estimates calculated from mean river flow will be minimum values. Limited data for Cu and Zn concentrations in the estuarine discharge (Alexander and Alexander in press) suggest that this condition is fulfilled.

Input rates from the combined dredge spoil and sewage sludge dumping (Table 3) are sufficient to provide the metals contained in the upper 1 cm of sediments in the apex (Table 1) in as little as 94 days for Zn and 59 days for Cu. Net sediment accumulation rates in the New York Bight apex are considerably smaller than this. In fact most of the apex has been eroded slightly between 1936 and 1973 (G. Freeland personal communication). Net accumulation occurred only at the dredge spoil site, $\simeq 1\times 10^8$ m^3 in 37 years (G. Freeland personal communication), and is sufficient to account for only about half of the volume of dredge spoils dumped during this period ($\simeq 2\times 10^8$ m^3). These data indicate that much of the solid material dumped into the apex is rapidly dispersed and transported

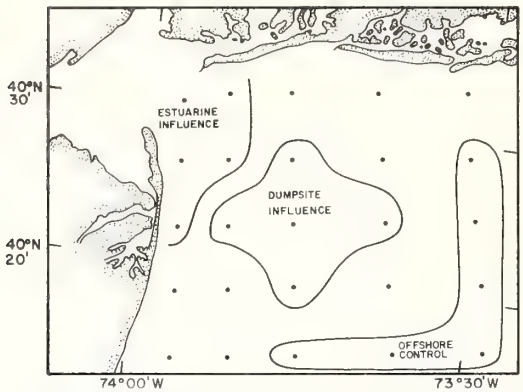


Fig. 29. Stations designated estuarine influenced, dumpsite influenced, and offshore control.

from it, presumably seaward and possibly back to the estuaries.

Some idea of the rate of removal of contaminant metals from the apex can be obtained by calculating maximum mean residence times for Cu and Zn in the apex from the input data in Table 3 and the total metal content of the apex from Table 1. Estimates of maximum residence times (Table 4) have been calculated by assuming that there is no input of metals from the seawater entering the apex and that, first, there is no net sedimentation in the apex and, second, half of the dredge spoils accumulate in the sediments (G. Freeland

Table 4. Calculated mean residence time (days) of Cu and Zn in the apex.

	No net sediment accumulation		Accumulation of 50% of dredge spoils in sediments	
	Max*	Min†	Max*	Min†
Cu	28	16	48	21
Zn	118	56	165	65

* River input calculated from average concentration × average flow rate.
† River input from Mueller et al. (1975).

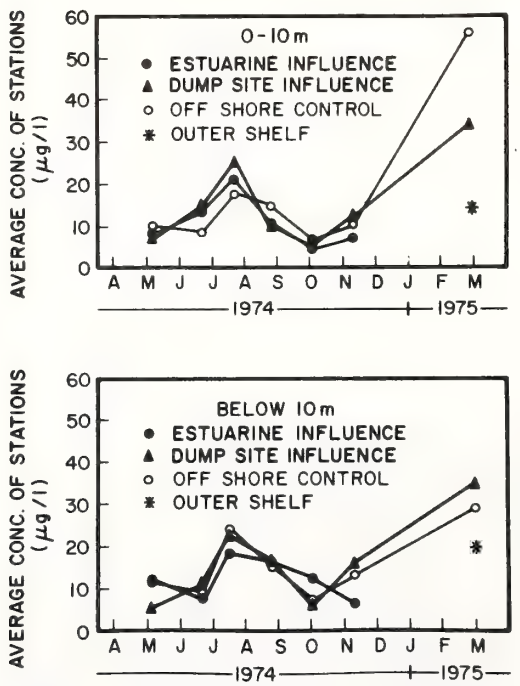


Fig. 30. Seasonal variation of average total dissolved iron in the apex, above and below 10-m depth for estuarine and dumpsite influenced, and offshore control regions, and winter average for outer shelf regime. (*See Figs. 3 and 29.*)

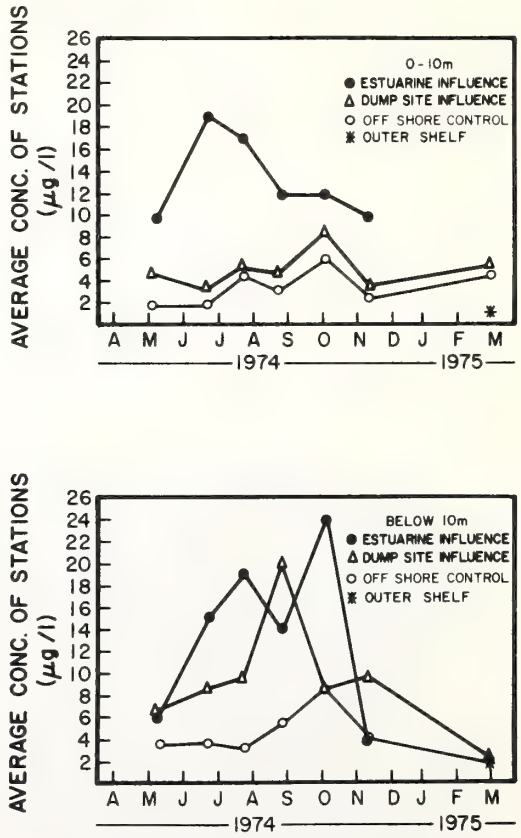
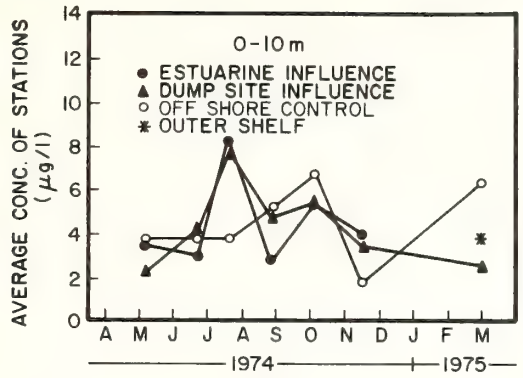


Fig. 31. Same as Fig. 30 for manganese.



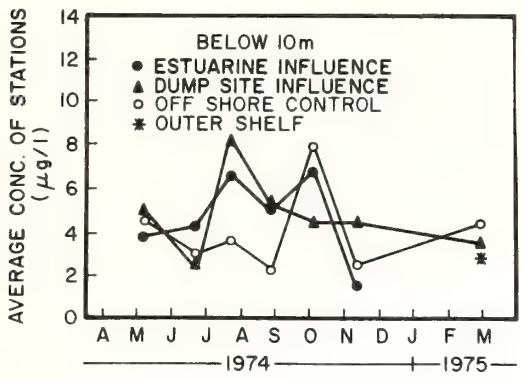
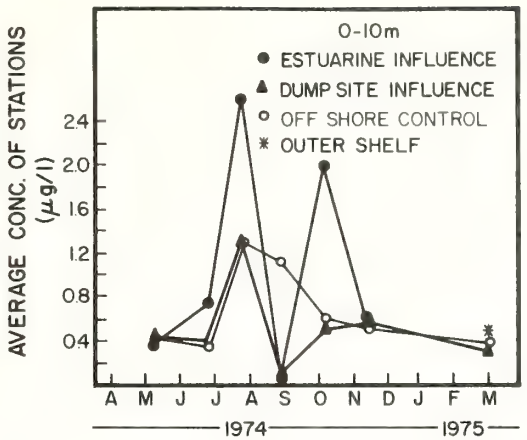


Fig. 32. Same as Fig. 30 for copper.



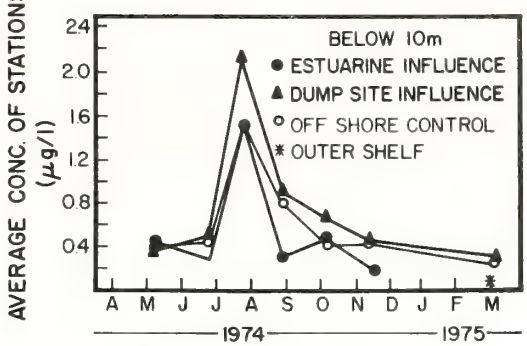
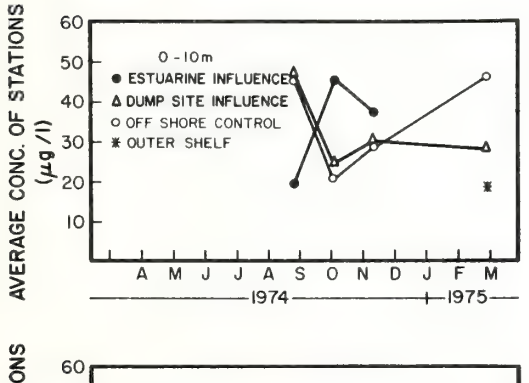


Fig. 33. Same as Fig. 30 for cadmium.



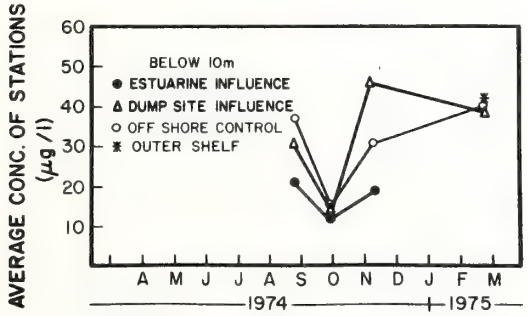


Fig. 34. Same as Fig. 30 for zinc.

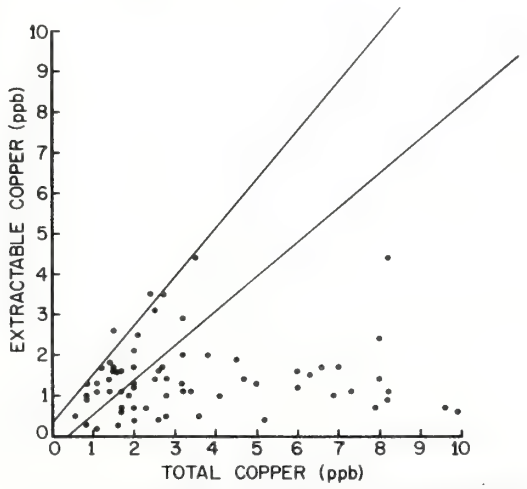


Fig. 35. Dissolved extractable (APDC/MIBK) copper and total dissolved copper in the apex, 21–24 August 1974. Solid lines represent approximate error limits. Samples with values lying between solid lines have ≃100% extractable copper. Samples to right of lines have <100% extractable copper.

personal communication) and there is no net sedimentation otherwise. In each case the extreme values of the estuarine input rate from Table 3 have been used to establish separate estimates. The residence times estimated by assuming zero inputs of metals from seawater entering the apex are maximum values as seawater flushing the apex does contain metals. Input rate estimates of metals from the ocean are very imprecise due to poor data concerning the flushing rate of the apex and the concentrations of metals in seawater outside it. Inputs from the ocean probably exceed those from other sources by as much as a factor of three and the true mean residence times of Cu and Zn in the apex, will, therefore, be as much as a factor of four smaller than estimated in Table 4. In any event the true mean residence times of Cu and Zn cannot exceed 6 months and are probably 10–50 days.

Flushing time of apex waters has been estimated from salt balance studies to be about 1 week (Ketchum et al. 1951). Therefore, it appears that contaminants as represented by Cu and Zn are removed from the apex only a little slower than the water column is flushed, and resuspension of sedimentary contaminants and transport of particulate material out of the apex must constitute a very efficient process.

ADDENDUM (4 October 1976): Since the preparation of this paper there have been three reports (Contract Rep. D-75-4, D-76-1, and D-76-7 of the Dredged Material Res. Program, U.S. Army Waterways Exp. Sta., Vicksburg, Miss.) that in laboratory experiments Mn and Cd but not Fe, Cu, and Zn are released to solution during dredged material dispersal and sedimentation in seawater. Re-examination of our data shows that high concentrations of Mn (Figs. 16–19) and Cd (Figs. 23–25), but not Fe, Cu, or Zn, were generally observed in near-bottom water at the station (No. 12) nearest to the designated dredge spoil dumpsite. It is likely that the high concentrations of Mn and Cd at this and adjacent stations are caused by the dumping of dredged material.

References

ALEXANDER, J. E., AND E. C. ALEXANDER. In press. The chemical oceanography of New York Bight. MESA New York Bight Atlas Monogr. Ser. 2.

ABDULLAH, M. I., L. E. ROYLE, AND A. W. MORRIS. 1972. Heavy metal concentrations in coastal waters. Nature **235**: 158–160.

BROWN, B., AND M. AHSANULLAH. 1971. Effect of heavy metals on mortality and growth. Mar. Pollut. Bull. **2**: 182–187.

BUTTERWORTH, J., P. LESTER, AND A. NICKLESS. 1972. Distribution of heavy metals in the Severn estuary. Mar. Pollut. Bull. **3**: 72–74.

CANTILLO, A. Y., G. A. BERBERIAN, P. G. HATCHER, L. E. KEISTER, AND D. A. SEGAR. 1976. Chemistry data of water column sampling cruises No. 6–12 of the NOAA Ship *Ferrel*, April–November 1974. NOAA Data Rep. MESA New York Bight Project. In press.

CARMODY, D. J., J. B. PEARCE, AND W. E. YASSO. 1973. Trace metals in sediments of New York Bight. Mar. Pollut. Bull. **4**: 132–135.

CHARNELL, R. L., D. A. MAYER, AND D. V. HANSEN. 1975. Physical oceanography, p. 1–15. *In* R. L. Charnell [ed.], Assessment of offshore dumping; technical background. NOAA Tech. Rep. TM ERL MESA-1.

CONNOR, P. M. 1972. Acute toxicity of heavy metals to some marine larvae. Mar. Pollut. Bull. **13**: 190–192.

CORCORAN, E. F., AND J. E. ALEXANDER. 1964. The distribution of certain trace elements in tropical sea water and their biological significance. Bull. Mar. Sci. **14**: 594–602.

DUCE, R. A., G. T. WALLACE, JR., AND B. J. RAY. 1976. Atmospheric trace metals over the New York Bight. NOAA Tech. Rep. MESA. In press.

DUURSMA, E. K., AND M. G. GROSS. 1971. Marine sediments and radioactivity, p. 147–160. *In* Radioactivity in the marine environment. Natl. Acad. Sci.

GROSS, M. G. 1970*a*. Preliminary analyses of urban wastes, New York metropolitan region. Mar. Sci. Res. Center Tech. Rep. 5, SUNY, Stony Brook.

———. 1970*b*. Analysis of dredged wastes, fly ash, and waste chemicals, New York metropolitan region. Mar. Sci. Res. Center Tech. Rep. 7, SUNY, Stony Brook.

———, J. A. BLACK, R. J. KALIN, J. R. SCHRAMEL, AND R. N. SMITH. 1971. Survey of marine waste deposits, New York metropolitan region. Mar. Sci. Res. Center Tech. Rep. 8, SUNY, Stony Brook.

HARRIS, W. H. 1974. Sewage sludge expansion, migration, accumulation and identification, Nassau County, New York inner continental shelf. U.S. Congress, Senate, Committee on

Public Works, Subcommittee on Environmental Pollution; sewage sludge hazard to Long Island beaches. Hearing, 93rd Cong. 93-H52, p. 297–330.

HAZELWORTH, J. B., B. L. KOLITZ, R. B. STARR, R. L. CHARNELL, G. A. BERBERIAN, AND M. A. WEISELBERG. 1975*a*. Water sampling cruises No. 6–8 of NOAA ship *Ferrel*, April–June 1974. NOAA Data Rep. MESA-1. New York Bight Project.

———, ———, ———, ———, ———, AND ———. 1975*b*. Water sampling cruises No. 9–12 of NOAA ship *Ferrel*, July–Nov. 1974. NOAA Data Rep. ERL MESA-3. New York Bight Project.

HOOD, D. W. 1967. Chemistry of the oceans: Some trace metal-organic association and chemical parameter differences in top one meter of surface. Environ. Sci. Technol. **1**: 303–305.

IRUKAYAMA, K., T. KONDO, F. KAI, AND M. FUJIKI. 1961. Studies on the origin of the causative agent of Minimata disease 1. Organic mercury compound in the fish and shellfish from Minimata Bay. Kumamoto Med. J. **14**: 157–169.

KETCHUM, B. H., A. C. REDFIELD, AND J. C. AYERS. 1951. The oceanography of the New York Bight. Pap. Phys. Oceanogr. Meteorol. **12**(1): 46 p.

KREMLING, K., AND H. PETERSEN. 1974. Ammonium pyrollidine dithiocarbamate-methyl isobutyl ketone extraction system for the determination of copper and iron in 1 cm^3 of sea water by flameless atomic absorption spectrometry. Anal. Chim. Acta **70**: 35–39.

MORGAN, J. J. 1971. Principles and applications of water chemistry, p. 561–624. *In* S. D. Faust and J. V. Hunter [eds.], Organic compounds in aquatic environments. Dekker.

MORRIS, A. W. 1971. Trace metal variations in sea water of the Menai Straits caused by a bloom of *Phaeocystis*. Nature **233**: 427–428.

MUELLER, J. A., J. S. JERIS, A. R. ANDERSON, AND C. HUGHES. 1975. Contaminant inputs to the New York Bight. Rep. MESA Program. *Also* 1976. NOAA Tech. Memo. ERL MESA-6.

NATIONAL MARINE FISHERIES SERVICE. 1972. The effects of waste disposal in the New York Bight. Nine sections (NTIS acquisition AD-739531 through AD739539); Summary Final Rep. (AD743936). NOAA-NMFS.

PRESTON, A. 1973. Heavy metals in British water. Nature **242**: 95–97.

SANKARANARAYANAN, V. N., AND C. V. E. REDDY. 1973. Copper content in the inshore and estuarine waters along the central west coast of India. Current Sci. **42**: 223–224.

SEGAR, D. A., AND G. A. BERBERIAN. 1976. Oxygen depletion in the New York Bight apex: Causes and consequences. Am. Soc. Limnol. Oceanogr. Spec. Symp. **2**: 220–239.

———, AND A. Y. CANTILLO. 1975. Direct determination of trace metals in sea water by flameless atomic absorption, p. 56–81. *In* T. R. P. Gibb [ed.], Analytical chemistry in oceanography. Adv. Chem. Ser. 147.

SLOWEY, J. F., AND D. W. HOOD. 1971. Copper, manganese and zinc concentrations in Gulf of Mexico waters. Geochim. Cosmochim. Acta **35**: 121–138.

STEELE, J. H., A. D. MCINTYRE, R. JOHNSON, I. G. BAXTER, G. TOPPING, AND H. D. DOOLEY. 1973. Pollution studies in the Clyde Sea area. Mar. Pollut. Bull. **4**: 153–157.

SUNDARAJ, V., AND K. KRISHNAMURTHY. 1972. The distribution of copper in Porto Novo waters. Current Sci. **41**: 315–317.

WILLIAMS, P. M. 1969. The association of copper with dissolved organic matter in seawater. Limnol. Oceanogr. **14**: 156–158.

WINDOM, H. L., K. C. BECK, AND R. SMITH. 1971. Transport of trace metals to the Atlantic Ocean by three southeastern rivers. Southeast. Geol. **12**: 169–181.

———, AND R. E. SMITH. 1972. Distribution of cadmium, cobalt, nickel, and zinc in southeastern United States continental shelf waters. Deep-Sea Res. **19**: 727–730.

PENN STATE UNIVERSITY LIBRARIES
A0000728327 45